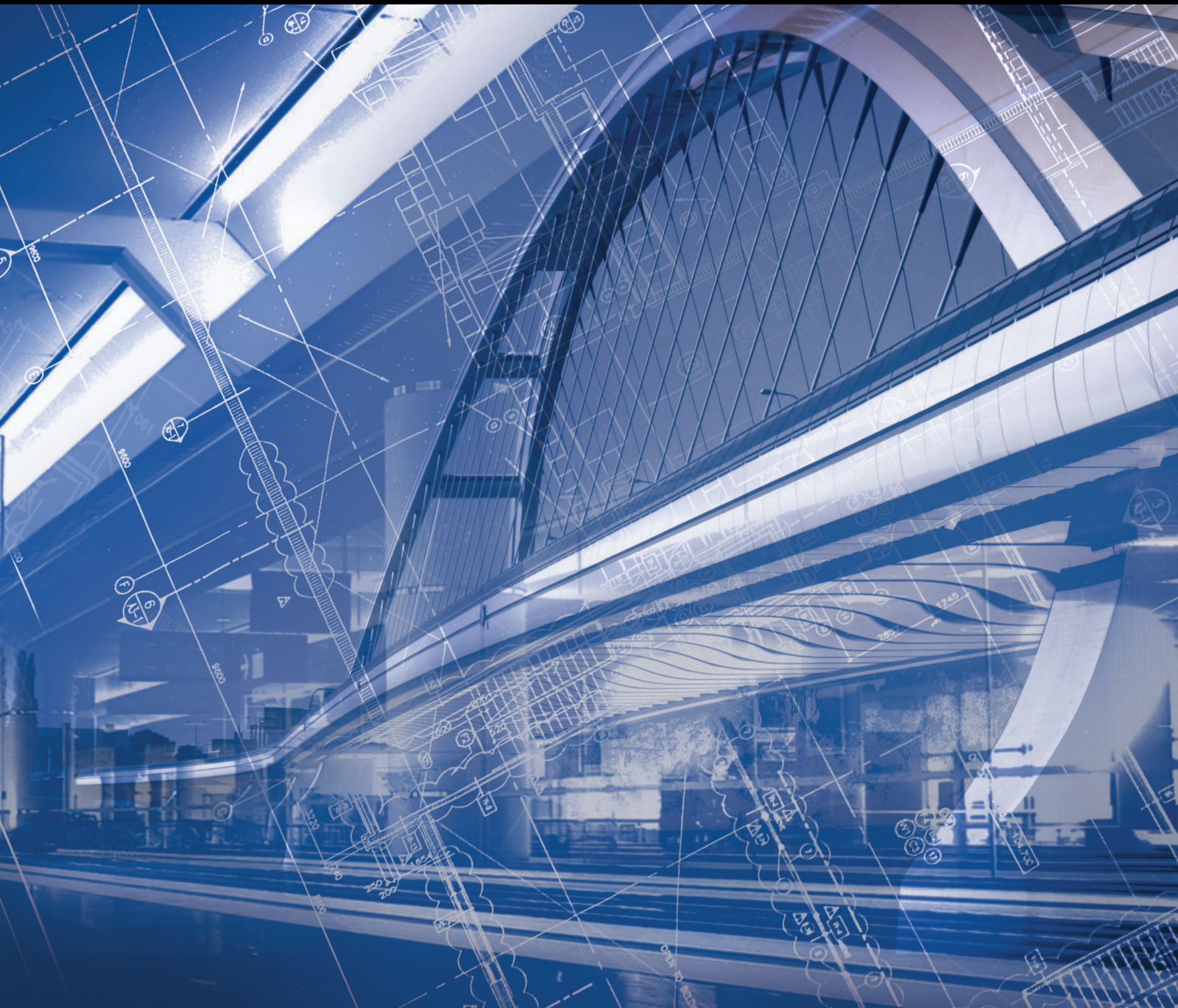# Heat, Flow and Deformation in Rock Masses in Extreme Conditions

Lead Guest Editor: Hailing Kong
Guest Editors: Chen Cao, Zhiqiang Yin, and Bisheng Wu

Heat, Flow and Deformation in Rock Masses in Extreme Conditions

Heat, Flow and Deformation in Rock Masses in Extreme Conditions

Lead Guest Editor: Hailing Kong
Guest Editors: Chen Cao, Zhiqiang Yin, and Bisheng Wu

Chayut Ngamkhanong, Thailand
Trung Ngo, Australia
Tengfei Nian, China
Mehdi Nikoo, Canada
Youjun Ning, China
Olugbenga Timo Oladinrin, United Kingdom
Oladimeji Benedict Olalusi, South Africa
Timothy O. Olawumi, Hong Kong
Alejandro Orfila, Spain
Maurizio Orlando, Italy
Siti Aminah Osman, Malaysia
Walid Oueslati, Tunisia
SUVASH PAUL, Bangladesh
John-Paris Pantouvakis, Greece
Fabrizio Paolacci, Italy
Giuseppina Pappalardo, Italy
Fulvio Parisi, Italy
Dimitrios G. Pavlou, Norway
Daniele Pellegrini, Italy
Gatheeshgar Perampalam, United Kingdom
Daniele Perrone, Italy
Giuseppe Piccardo, Italy
Vagelis Plevris, Qatar
Andrea Pranno, Italy
Adolfo Preciado, Mexico
Chongchong Qi, China
Yu Qian, USA
Ying Qin, China
Giuseppe Quaranta, Italy
Krishanu ROY, New Zealand
Vlastimir Radonjanin, Serbia
Carlo Rainieri, Italy
Rahul V. Ralegaonkar, India
Raizal Saifulnaz Muhammad Rashid, Malaysia
Alessandro Rasulo, Italy
Chonghong Ren, China
Qing-Xin Ren, China
Dimitris Rizos, USA
Geoffrey W. Rodgers, New Zealand
Pier Paolo Rossi, Italy
Nicola Ruggieri, Italy
JUNLONG SHANG, Singapore

Nikhil Saboo, India
Anna Saetta, Italy
Juan Sagaseta, United Kingdom
Timo Saksala, Finland
Mostafa Salari, Canada
Ginevra Salerno, Italy
Evangelos J. Sapountzakis, Greece
Vassilis Sarhosis, United Kingdom
Navaratnarajah Sathiparan, Sri Lanka
Fabrizio Scozzese, Italy
Halil Sezen, USA
Payam Shafigh, Malaysia
M. Shahria Alam, Canada
Yi Shan, China
Hussein Sharaf, Iraq
Mostafa Sharifzadeh, Australia
Sanjay Kumar Shukla, Australia
Amir Si Larbi, France
Okan Sirin, Qatar
Piotr Smarzewski, Poland
Francesca Sollecito, Italy
Rui Song, China
Tian-Yi Song, Australia
Flavio Stochino, Italy
Mayank Sukhija, USA
Piti Sukontasukkul, Thailand
Jianping Sun, Singapore
Xiao Sun, China
T. Tafsirojjaman, Australia
Fujiao Tang, China
Patrick W.C. Tang, Australia
Zhi Cheng Tang, China
Weerachart Tangchirapat, Thailand
Xiaxin Tao, China
Piergiorgio Tataranni, Italy
Elisabete Teixeira, Portugal
Jorge Iván Tobón, Colombia
Jing-Zhong Tong, China
Francesco Trentadue, Italy
Antonello Troncone, Italy
Majbah Uddin, USA
Tariq Umar, United Kingdom
Muahmmad Usman, United Kingdom
Muhammad Usman, Pakistan
Mucteba Uysal, Turkey

Ilaria Venanzi, Italy
Castorina S. Vieira, Portugal
Valeria Vignali, Italy
Claudia Vitone, Italy
Liwei WEN, China
Chunfeng Wan, China
Hua-Ping Wan, China
Roman Wan-Wendner, Austria
Chaohui Wang, China
Hao Wang, USA
Shiming Wang, China
Wayne Yu Wang, United Kingdom
Wen-Da Wang, China
Xing Wang, China
Xiuling Wang, China
Zhenjun Wang, China
Xin-Jiang Wei, China
Tao Wen, China
Weiping Wen, China
Lei Weng, China
Chao Wu, United Kingdom
Jiangyu Wu, China
Wangjie Wu, China
Wenbing Wu, China
Zhixing Xiao, China
Gang Xu, China
Jian Xu, China
Panpan, China
Rongchao Xu, China
HE YONGLIANG, China
Michael Yam, Hong Kong
Hailu Yang, China
Xu-Xu Yang, China
Hui Yao, China
Xinyu Ye, China
Zhoujing Ye, China
Gürol Yildirim, Turkey
Dawei Yin, China
Doo-Yeol Yoo, Republic of Korea
Zhanping You, USA
Afshar A. Yousefi, Iran
Xinbao Yu, USA
Dongdong Yuan, China
Geun Y. Yun, Republic of Korea

Hyun-Do Yun, Republic of Korea
Cemal YİĞİT, Turkey
Paolo Zampieri, Italy
Giulio Zani, Italy
Mariano Angelo Zanini, Italy
Zhixiong Zeng, Hong Kong
Mustafa Zeybek, Turkey
Henglong Zhang, China
Jiupeng Zhang, China
Tingting Zhang, China
Zengping Zhang, China
Zetian Zhang, China
Zhigang Zhang, China
Zhipeng Zhao, Japan
Jun Zhao, China
Annan Zhou, Australia
Jia-wen Zhou, China
Hai-Tao Zhu, China
Peng Zhu, China
QuanJie Zhu, China
Wenjun Zhu, China
Marco Zucca, Italy
Haoran Zuo, Australia
Junqing Zuo, China
Robert Černý, Czech Republic
Süleyman İpek, Turkey

Contents

Contents

Research Article

Analysis on Loose Circle of Surrounding Rock of Large Deformation Soft-Rock Tunnel

Rui Wang,[1] **Yiyuan Liu,**[1] **Xianghui Deng** (iD),[1] **Yu Zhang,**[1] **Xiaodong Huang,**[2] **and Xiao Ding**[1]

[1]*School of Civil and Architecture Engineering, Xi'an Technological University, Xi'an 710021, China*
[2]*Xi'an Shaanxi Road and Bridge Group Co. Ltd, Xi'an 710000, China*

Correspondence should be addressed to Xianghui Deng; xianghuideng@xatu.edu.cn

Received 5 June 2020; Revised 4 October 2020; Accepted 22 October 2020; Published 17 November 2020

Academic Editor: Hailing Kong

With the rapid development of tunnel construction in China, deep buried and long tunnel projects are emerging in areas with complex engineering geological conditions and harsh environment, and thus large deformation of tunnels under conditions of high in situ stress and soft rock becomes increasingly prominent and endangers engineering safety. Therefore, it is of great significance to control the deformation and improve the stability of surrounding rock by analyzing the thickness and distribution law of loose circle according to the unique mechanical properties and failure mechanism of surrounding rock of large deformation soft-rock tunnel. Based on unified strength theory, this paper deduces the radius calculation formula of the loose circle by considering the influence of intermediate principal stress. Furthermore, the theoretical calculations and field tests of the loose circle in the typical sections of grade II and III deformation of Yuntunbao tunnel are carried out, and the thickness and distribution law of loose circle of surrounding rock of large deformation soft-rock tunnel is revealed. The results show that the formula based on the unified strength criterion is applicable for a large deformation tunnel in soft rock.

1. Introduction

With the development of transportation facilities in western mountainous areas of China, more and more tunnels are built in soft rock areas with high in situ stress. Soft rock is featured by low strength and strong expansibility [1–3], so it is easy to produce large deformation due to high in situ stress extrusion or improper technical measures, which will affect the stability of surrounding rock [4–8]. The deformation is usually characterized by large deformation, fast deformation rate, long duration, various failure forms, and large damage scope, bringing about considerable losses to the project [9–11]. When the tunnel is built in this kind of environment, problems such as large rheology and large displacement are constantly emerging, which will lead to serious underground excavation accidents under complex geological conditions [12–14]. Because the stress redistribution after tunnel excavation will form a ring-shaped fracture zone within a certain range in its section space, that is, the loose circle of surrounding rock [15], of which the distribution range and

law have a great influence on the stability of surrounding rock [16–19]. The larger the loose circle is, the worse the stability of surrounding rock is, and the more difficult the tunnel support is. So it is of great significance to study systematically the thickness and distribution law of loose circle of surrounding rock of large deformation soft-rock tunnel for controlling the deformation and improving the stability of surrounding rock.

So far, theoretical analysis and field measurement are mainly adopted in the study of a loose circle of surrounding rock both at home and abroad. Currently, the theoretical research of the radius of the loose circle is mainly in the theory of elastoplastic mechanics and numerical simulation. Dube et al. [20] determined the radius of the "broken zone" by using the graphic method based on the elastic-plastic analysis. Later on, Whitaker determined the size of the loose circle and the amount of convergence generated by the method of mathematical simulation through the data of the laboratory. Based on the "Convergence-Confinement" method, Serrano et al. [21] obtained the mathematical

expression to determine the radius of the loose circle. Li et al. [22] used the theory of elastic-plastic mechanics to deduce the analytical solutions of stress, displacement, and range of plastic zone in different stages and explained the stress and displacement of surrounding rock in practical engineering. Xia et al. [23] used the finite element method to regress the peak value of the effective stress of the element and revealed the range of the surrounding rock loose circle through numerical simulation. By using the acoustic detector, the changing law of the loose circle under the blasting dynamic load of the tunnel in front of the coal mine driving was obtained. Yu et al. [24] used the maximum axial force of bolt to determine the scope of surrounding rock loose area and plastic area theoretically and put forward the calculation formula of the radius of the plastic area and loose area after the surrounding rock deformation stopped.

For the field test of the radius of the loose circle, many experts and scholars have studied a lot. Toshio Maejima et al. [25] described an evaluation of the loose circle based on monitored stress of rock. At the same time, in observational design and construction procedures, by monitoring the loosening behavior and correctly predicting and analyzing the subsequent behavior of the cavern, the cavern supporting system was optimized. Golebiowski [26] presented using the GPR method for the location of the loose circle in the river embankments. The changeable-offset profiling he proposed in the paper gave wider possibilities in GPR detection of the loose circle distribution in levees than standard, zero-offset, reflection profiling. Czaja [27] determined the methodology of GPR measurements in flood embankments investigation by investigating the nonuniformity of the loose and saturated zones in the flood dike. Hong Dinhpuc [28] studied the excavation damaged zone of the hydropower station EDZ by using the geophysical testing method (acoustic wave and digital borehole camera technology). The results show that the damage of caverns surrounding rock masses is usually induced by the redistribution of stress undisturbed rock mass in the caverns excavation process. Huotari-Halkosaari [29] integrated geophysical and geological research methods to provide information for possible faults and weak zones near the new metro line. For detection of loose zones located in the flood levee, Golebiowski Tomislaw and Malysa Tomasz [30] carried out with the use of short-offset reflection profiling technique, and radargrams were subjected to standard signal processing.

In summary, the thickness of the loose circle of surrounding rock is greatly affected by the buried depth of surrounding rock, initial in situ stress, and support parameters; especially in the large deformation tunnel of soft rock, the thickness of the loose circle is also greatly different. Therefore, it is essential to determine the radius of the loose circle by combining theory with the field test. However, the researches on the radius of the loose circle of large deformation soft rock are still in a relatively scarce stage at present. Based on the systematic classification of large deformations, the thickness formula of the loose circle in surrounding rock of large deformation soft-rock tunnel is

derived based on unified strength criterion, and then the thickness and distribution law of loose circle of Yuntunbao tunnel is analyzed with field acoustic wave test.

2. Concept and Classification of Large Deformation of Soft Rock

Large deformation of soft rock is caused by the fact that the displacement of surrounding rock cannot be effectively restrained by conventional supporting structure and construction method after the deep buried or expansible surrounding rock meets water, which leads to the deformation far exceeding the allowable range in the code or the reserved range in design (some scholars defined it as the deformation exceeding 3% of tunnel diameter), and it does not converge for a long time, and even causes large-scale plastic failure.

The large deformation of surrounding rock has obvious characteristics of fluid-plastic deformation and shows progressive expansion characteristic and obvious time effect. It often leads to the destruction of the tunnel support structure, such as cracking and falling of primary support concrete, distortion, and even breaking of the steel frame, causing great difficulties in construction.

Surrounding rocks of large deformation in the soft rock are V-grade. However, there are still significant differences in crown settlement and surrounding convergence values between different tunnels or different sections of the same tunnel. Therefore, it is necessary to systematically classify large deformation of soft rock for the accurate design of tunnel construction method, supporting type, lining type, and thickness and effectively guaranteeing the construction safety and reducing project cost.

Experts and scholars at home and abroad generally divided the classification standard of large deformation of soft rock into two stages: design and construction. In the design stage, one or more factors, such as deformation amount (U_a), relative deformation amount (U_a/a), strength-stress ratio (R_b/σ_v), and initial in situ stress (σ_v), are taken as the index to initially determine the classification standard. Moreover, corresponding design measures for prevention and control are put forward. In the construction stage, the classification standard is further refined and the deformation management standard is put forward according to site geological conditions and construction deformation. At present, the most representative classification standard in China is shown in Table 1.

The internal cause of large deformation of soft-rock tunnel is that the initial stress field has higher tectonic stress and lower rock mass strength. That is, the Strength-Stress ratio (R_b/σ_v) is relatively small, showing the most intuitive appearance of large deformation. Therefore, the Strength-Stress ratio (R_b/σ_v) and deformation amount of surrounding rock (U_a) are used as indexes to classify large deformation in this paper. Referring to the existing quantitative standards at home and abroad, the classification standard of large deformation of soft rock is shown in Table 2.

Table 1: Representative classification standards for large deformation of soft rocks in China.

Experts and scholars	Grade	Classification index			
		σ_v (MPa)	R_b/σ_v	U_a (cm)	U_a/a (%)
China railway erju construction [31]	I	5~10	0.33~0.2	—	4~7
	II	10~15	0.2~0.125	—	7~10
	III	>15	<0.125	—	>10
Xu Linsheng et al. [31]	I	—	—	15~30	1.5~3
	II	—	—	30~50	3~5
	III	—	—	>50	>5
Zhang Zhidao [31]	I	—	—	—	3~6
	II	—	—	—	6~10
	III	—	—	—	>10
Liu Zhichun et al. [31]	I	5~10	0.5~0.25	—	3~5
	II	10~15	0.25~0.15	—	5~8
	III	>15	<0.15	—	>8
Li Guoliang et al. [31]	I	—	0.25~0.15	—	1.5~3
	II	—	0.15~0.1	—	3~5
	III	—	<0.1	—	>5

Table 2: Classification standard for large deformation of soft rock.

Surrounding rock classification	I	II	III
Strength-stress ratio ($R_b/\sigma_{\max}$)	0.5~0.25	0.15~0.25	<0.15
Deformation amount (cm)	20~40	40~60	>60
Large deformation degree	Slightly large deformation	Medium-large deformation	Severe large deformation

3. Theoretical Calculation of Loose Circle of Surrounding Rock of Large Deformation Soft-Rock Tunnel

Most large deformation soft-rock tunnels have higher tectonic stress, sometimes even greater than gravity stress. Therefore, the influence of intermediate principal stress on rock mass strength and stress state should be considered in the elastic-plastic analysis. Although the traditional Mohr-Coulomb strength criterion and Hoek–Brown strength criterion have been matured in the elastic-plastic calculation of loose circle of the surrounding rock, it failed to consider the influence of intermediate principal stress, leading to inaccurate analysis results. The unified strength criterion not only takes the influence of intermediate principal stress into account but could also degenerate into Mohr-Coulomb strength criterion and Hoek–Brown strength criterion, and thus it is widely used in the engineering field. Therefore, the unified strength criterion is adopted for the theoretical calculation of the thickness of the loose circle of large deformation soft-rock tunnel.

3.1. Calculation Model.
In the elastic-plastic stress analysis of circular tunnels, solving the plane strain problems, the basic assumptions of the mechanical model are as follows: (1) the tunnel section is equivalent to a circular one with infinite length; (2) the initial in situ stress P is hydrostatic pressure; that is, the lateral pressure coefficient is 1; (3) the surrounding rock is homogeneous, isotropic, and incompressible, and the body force effect is not taken into account. The stress state of the surrounding rock is shown in Figure 1.

3.2. Elastoplastic Analysis of Thickness of Surrounding Rock Loose Circle.
The unified strength criterion is expressed as follows:

$$F = \sigma_\theta \frac{1 - \sin\varphi}{1 + \sin\varphi} - \frac{1}{1 + b}\left(b\sigma_2 + \sigma_r\right)$$
$$= \frac{2c\cos\varphi}{1 + \sin\varphi}, \sigma_2 \leq \frac{1}{2}\left(\sigma_\theta + \sigma_r\right) + \frac{\sin\varphi}{2}\left(\sigma_\theta - \sigma_r\right), \quad (1)$$

$$F' = \frac{\left(\sigma_\theta + b\sigma_2\right)}{1 + b}\frac{1 - \sin\varphi}{1 + \sin\varphi} - \sigma_r$$
$$= \frac{2c\cos\varphi}{1 + \sin\varphi}, \sigma_2 \geq \frac{1}{2}\left(\sigma_\theta + \sigma_r\right) + \frac{\sin\varphi}{2}\left(\sigma_\theta - \sigma_r\right). \quad (2)$$

where c is the cohesive force of surrounding rock; φ the internal friction angle of surrounding rock; σ_2 the intermediate principal stress; σ_r the radial stress; σ_θ the tangential stress; b the influence coefficient of intermediate principal stress, which represents the coefficient of principal shear stress and normal stress of relevant surface on the degree of influence on material destroy, and the value range is $0 \leq b \leq 1$. The formula [29] for calculation of b is shown as follows:

$$\begin{cases} b = \dfrac{1 + \alpha - B}{B - 1}, \\[2mm] B = \dfrac{\sigma_t}{\tau_s}, \\[2mm] \alpha = \dfrac{\sigma_t}{\sigma_c}, \end{cases} \quad (3)$$
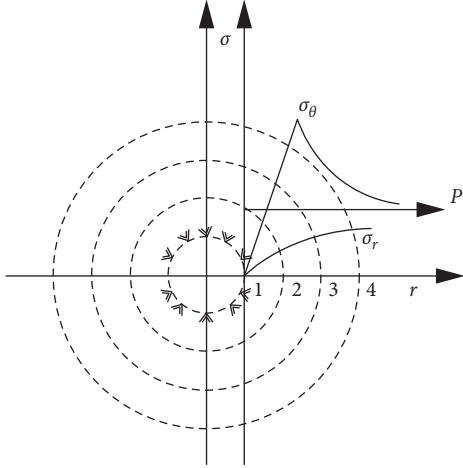
FIGURE 1: Stress diagram of elastic-plastic surrounding rock state.

where σ_c is the compressive strength of geotechnical materials; σ_t the tensile strength; τ_s the shear strength.

For plane strain problems, when the material enters the plastic state, the longitudinal axial stress is the intermediate principal stress σ_2, which approximately takes the average value of radial stress σ_r and tangential stress σ_θ. Therefore, the intermediate principal stress in equation (1) can be expressed as follows:

$$\sigma_2 = \frac{m}{2}(\sigma_r + \sigma_\theta), \tag{4}$$

where m is the intermediate principal stress coefficient, and the value range is $0 < m \leq 1$. According to the Levy–Miss hypothesis, for incompressible plastic materials, m = 1.

Substituting equation (4) into equation (1), we have the following:

$$\frac{\sigma_\theta - \sigma_r}{2} - \frac{\sigma_\theta + \sigma_r}{2}\frac{2(1+b)\sin\varphi}{2+b(1+\sin\varphi)} = \frac{2(1+b)c\cos\varphi}{2+b(1+\sin\varphi)}, \tag{5}$$

in that way, $\sin\varphi_t = 2(1+b)\sin\varphi/2 + b(1+\sin\varphi)$, $c_t = 2(1+b)c\cos\varphi/2 + b(1+\sin\varphi)\cdot 1/\cos\varphi_t$, so equation (5) can be simplified as follows:

$$F = \frac{\sigma_\theta - \sigma_r}{2} - \frac{\sigma_\theta + \sigma_r}{2}\sin\varphi_t = c_t\cos\varphi_t, \tag{6}$$

3.2.1. Basic Equation. The equilibrium equation under axisymmetric condition can be expressed as follows:

$$\frac{d\sigma_r}{dr} + \frac{\sigma_r - \sigma_\theta}{r} = 0, \tag{7}$$

The geometric equation is shown as follows:

$$\varepsilon_r = \frac{du}{dr}, \varepsilon_\theta = \frac{u}{r}, \tag{8}$$

where r is the distance from any point of the surrounding rock to the center of the circle; u the radial displacement.

3.2.2. Elastic Region Analysis. Under the axisymmetric stress condition, the stress in the elastic region can be obtained by stress boundary condition and single-valued condition of displacement:

$$\begin{cases} \sigma_{re} = P_0\left(1 - \frac{r_0^2}{r^2}\right) + \sigma_R\frac{r_0^2}{r^2}, \\[2mm] \sigma_{\theta e} = P_0\left(1 + \frac{r_0^2}{r^2}\right) - \sigma_R\frac{r_0^2}{r^2}, \end{cases} \tag{9}$$

In addition,

$$\sigma_{\theta e} + \sigma_{re} = 2P_0, \tag{10}$$

where r_0 is the excavating radius of the tunnel; σ_R the radial stress at the elastoplastic interface.

3.2.3. Plastic Region Analysis. Equation (5) can be reorganized as follows:

$$\sigma_{\theta p} = \frac{1 + \sin\varphi_t}{1 - \sin\varphi_t}\sigma_{rp} + \frac{2c_t\cos\varphi_t}{1 - \sin\varphi_t}. \tag{11}$$

By substituting equation (11) into equation (7), it can be arranged as follows:

$$\frac{1 - \sin\varphi_t}{2\sin\varphi_t}\ln\left(\frac{2\sin\varphi_t}{1 - \sin\varphi_t}\sigma_{rp} + \frac{2c_t\cos\varphi_t}{1 - \sin\varphi_t}\right) = \ln r + C_0, \tag{12}$$

where C_0 is integral constant.

Based on the boundary conditions, as $r = r_0$, then $\sigma_{rp} = P_i$. And, therefore,

$$C_0 = \frac{1 - \sin\varphi_t}{2\sin\varphi_t}\ln\left(\frac{2\sin\varphi_t}{1 - \sin\varphi_t}\sigma_{rp} + \frac{2c_t\cos\varphi_t}{1 - \sin\varphi_t}\right) - \ln r_0. \tag{13}$$

By substituting equation (13) into equation (12), the equation can be expressed as follows:

$$\sigma_{rp} = (P_i + c_t\cot\varphi_t)\left(\frac{r}{r_0}\right)^{2\sin\varphi_t/1-\sin\varphi_t} - c_t\cot\varphi_t. \tag{14}$$

By substituting equation (14) into equation (11), thus the expression for $\sigma_{\theta p}$ can be obtained as follows:

$$\sigma_{\theta p} = \frac{1 + \sin\varphi_t}{1 - \sin\varphi_t}(P_i + c_t\cot\varphi_t)\left(\frac{r}{r_0}\right)^{2\sin\varphi_t/1-\sin\varphi_t} - c_t\cot\varphi_t. \tag{15}$$

Equations (14) and (15) are the expressions of stress in the plastic region of the surrounding rock of the tunnel.

3.2.4. Solution of Radius of Plastic Region and Loose Circle. At the elastic-plastic interface, that is, $r = R_p$, both σ_r and σ_θ satisfy the equation of state for both elastic and plastic regions, then $\sigma_{\theta e} = \sigma_{\theta p}$, $\sigma_{re} = \sigma_{rp}$. Based on equation (10),

there is $\sigma_{\theta p} + \sigma_{rp} = 2P_0$. And combining equation (14) with equation (15), the following equation can be obtained:

$$\left(\sigma_{\theta p} + \sigma_{rp}\right)|_{r=R_p} = \frac{2}{1 - \sin \varphi_t} \left(P_i + c_t \cot \varphi_t\right) \left(\frac{r}{r_0}\right)^{2 \sin \varphi_t / 1 - \sin \varphi_t} \\ - 2c_t \cot \varphi_t = 2P_0. \tag{16}$$

The radius R_p of the plastic region and the radial stress σ_R at the elastic-plastic interface can be obtained with equation (16), as follows:

$$R_p = r_0 \left[\frac{\left(1 - \sin \varphi_t\right)\left(P_0 + c_t \cot \varphi_t\right)}{P_i + c_t \cot \varphi_t}\right]^{1 - \sin \varphi_t / 2 \sin \varphi_t}, \\ \sigma_R = P_0 \left(1 - \sin \varphi_t\right) - c_t \cos \varphi_t. \tag{17}$$

According to the definition of the loose circle, the tangential stress of surrounding rock is equal to initial in situ stress on the boundary of the loose circle, that is, $\sigma_\theta = P_0$. Thus, equation (15) can be simplified as follows:

$$\sigma_{\theta p} = \frac{1 + \sin \varphi_t}{1 - \sin \varphi_t} \left(P_i + c_t \cot \varphi_t\right) \left(\frac{r}{r_0}\right)^{2 \sin \varphi_t / 1 - \sin \varphi_t} \\ - c_t \cot \varphi_t = P_0. \tag{18}$$

The radius R_0 of the loose circle is solved through the above formulas, and it can be expressed in the following form:

$$R_0 = r_0 \left[\frac{\left(P_0 + c_t \cot \varphi_t\right)\left(1 - \sin \varphi_t\right)}{\left(P_i + c_t \cot \varphi_t\right)\left(1 + \sin \varphi_t\right)}\right]^{1 - \sin \varphi_t / 2 \sin \varphi_t}. \tag{19}$$

Formula (19) shows that the radius R_0 of the loose circle is related to the tunnel excavating radius r_0, rock mass strength c and φ, intermediate principal stress b, initial in situ stress field P_0, and support reaction P_i.

4. Engineering Application

4.1. Engineering Situation.
The newly built Yuntunbao Tunnel is the dominant engineering of the Chengdu–Lanzhou Railway Dedicated Passenger Line located near Anguan Village, Anhong Township, Songpan County, Aba Prefecture, Sichuan Province. The tunnel with a length of 22,923.419 m starts at the mileage DK213 + 350 at the entrance and ends at the mileage DK236 + 390 at the exit. It is a superlong single-tunnel double-track tunnel. The excavation span is 15.3 m and height 13.99 m, and the inner contour arch wall is a single-center circle with a radius of 8.5 m. The clearance section is shown in Figure 2. The tunnel is divided into seven transverse tunnels and one outlet work area for construction. No. 7 transverse tunnel passes through the Shidaguan arc structure belt, and it is located in the front arc area of the Jiaochang mountain-shape structural belt. The

tunnel runs roughly in parallel with the Minjiang fault zone, and it is seriously affected by regional faults, with the development of small and medium-sized folds, rock fragmentation, and joint development. After geological surveying and mapping and drilling, some unfavorable geological effects such as landslides and debris flows exist in the tunnel site, and high stress with maximum principal stress of 10 MPa exists in the deep burying section. The bulk of surrounding rock is carbonaceous phyllite, mainly composed of sericite, chlorite, and quartz. The fine-grained scales have crystalline texture, low strength, thin-layer, poor integrity, and powder after excavation. Large deformation of soft rock occurs during construction, even serious invasion of initial support and distortion, and fracture of structural steel frames, among which the section DK234 + 190~DK234 + 350 is the most serious, as shown in Figure 3.

4.2. Theoretical Calculation.
The conclusion that the tunnel section with large deformation is V-grade surrounding rock can be obtained based on-site geological survey and laboratory test. According to the *Code for Design of Railway Tunnel* (TB 10003-2016) and geological conditions, the initial support design parameters of the Yuntunbao Tunnel are shown in Table 3.

The large deformation of Yuntunbao Tunnel is classified according to Table 2, and theoretical calculation of surrounding rock loose circle is carried out on large deformation grade II DK234 + 205 section and large deformation grade III DK234 + 318 section of soft rock in No. 7 transverse tunnel, in order to make a profound study about the influence of large deformation of soft rock on the loose circle of Yuntunbao Tunnel. The relevant mechanical parameters of surrounding rock based on field tests are shown in Table 4. Gravity stress is taken as initial in situ stress. According to the *Code for Design of Railway Tunnel* (TB 10003-2016), the vertical surrounding rock pressure at the arch of the deep-buried tunnel is calculated by formula $q = \gamma \times 0.45 \times 2^{s-1} \times [1 + i(B - 5)]$, and the horizontal pressure is calculated by the uniform load formula $e = \lambda q$. From the measured results, it is known that there is high in situ stress in this section, so $\lambda = 1.2$. Meanwhile, the relative mechanical parameters of surrounding rock in Table 4, such as compressive strength σ_c, compressive strength σ_t, and shear strength τ_s, are introduced into formula (3), and the influence coefficient of intermediate principal stress b is obtained. The related calculation results are shown in Table 5.

Formula (19) shows that the radius of loose circle R_0 is related to the excavation radius of tunnel r_0, rock mass strength c and φ, intermediate principal stress b, and initial in situ stress field P_0 are related to support reaction P_i. In practical engineering, the excavation radius, lithology, and initial stress state of the tunnel have been determined, and the thickness of the loose circle can only be affected by
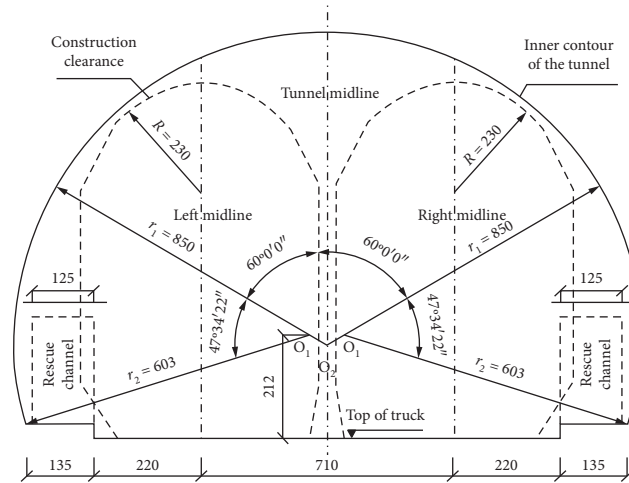
Figure 2: Tunnel clearance section.

| (a) | (b) |

Figure 3: Failure form of initial support. (a) Severe beyond-limit deformation of initial support. (b) Distortion of structural steel frames.

Table 3: Initial support parameters table.

Surrounding rock grade	C30 shotcrete (cm)	Mesh reinforcement (cm)	Anchor (cm)	Steel frames (cm)
V	25	$\phi 8@20 \times 20$	$L = 400, \phi 22@120 \times 100$	I20b@80

Table 4: Relevant mechanical parameters of surrounding rock.

Cross section mileage	Cohesion c (kPa)	Internal friction angle φ (°)	Bulk density γ (kN/m³)	Compressive strength σ_c (MPa)	Compressive strength σ_t (MPa)	Shear strength τ_s (MPa)
DK234 + 205	31	32	22	4.98	0.77	0.68
DK234 + 318	30	33	22	4.83	0.76	0.67

changing the support reaction P_i. Therefore, the thickness of the loose circle caused by different bearing capacity ratios of the initial support structure in surrounding rock pressure is calculated separately. The calculation results of the thickness of the loose circle of the typical section are shown in Table 6, and the curve is drawn, as shown in Figure 4.

TABLE 5: Calculation table of surrounding rock pressure.

Cross section mileage	Large deformation grade	Area	Buried depth h (m)	Excavation height H_t (m)	Lateral pressure coefficient λ	Influence coefficient of intermediate principal stress b	Initial in situ stress P(kPa)	Surrounding rock pressure P(kPa)
DK234 + 205	II-grade	Vault	200	13.99	1.2	0.168	4400	321.552
		Side wall					5280	385.682
DK234 + 318	III-grade	Vault	250	13.99	1.2	0.171	5500	321.552
		Side wall					6600	385.682

TABLE 6: The calculation values of loose circles of grade II and III large deformation section (m).

Cross section mileage	Area	Thickness of loose circle at different bearing capacity ratios of the support structure R_0										
		0	10%	20%	30%	40%	50%	60%	70%	80%	90%	100%
DK234 + 205	Vault	24.08	18.02	14.64	12.39	10.75	9.47	8.45	7.61	6.89	6.27	5.73
	Side wall	26.59	19.19	15.35	12.88	11.11	9.76	8.68	7.80	7.05	6.41	5.85
DK234 + 318	Vault	24.66	18.52	15.15	12.92	11.30	10.04	9.03	8.20	7.49	6.88	6.34
	Side wall	27.06	20.00	15.81	13.37	11.63	10.31	9.25	8.38	7.64	7.01	6.45

(a)

(b)
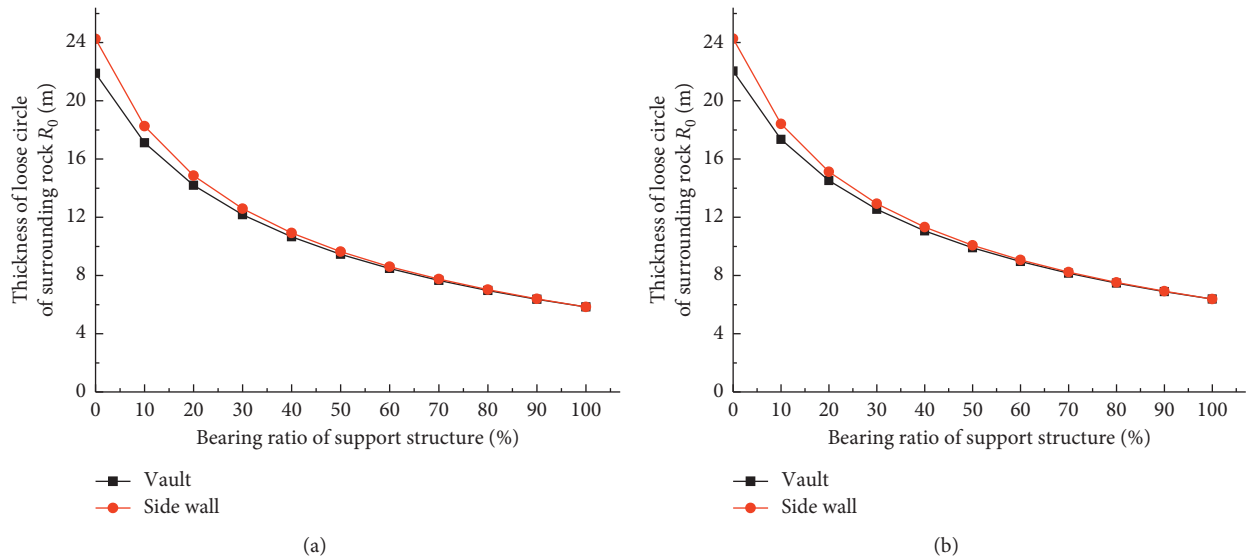
FIGURE 4: The curve of theoretical calculation of loose circle. (a) DK234+205 section. (b) DK234+318 section.

From Table 6 and Figure 4, it can be concluded that

(1) The higher the large deformation grade of soft rock, the worse the quality of surrounding rock and the thicker the loose circle.

(2) As a whole, there is little difference in the distribution of the loose circles of surrounding rock of tunnel on cross sections. Still, due to the influence of high in situ stress on the initial in situ stress field, the phenomenon that loose circle of the side wall is slightly larger than that of the vault.

(3) With the increase of support resistance P_i(i.e., the ratio of support structure bearing capacity increases), the theoretical calculation radius of loose circle decreases gradually.

4.3. Field Test

4.3.1. Test Scheme. RSM-SY5 (T) nonmetallic acoustic wave test detector produced by Zhongyan in Wuhan was used to test the loose circle of surrounding rock. DK234 + 205 section of grade II soft rock with large deformation and DK234 + 318 section of grade III soft rock with large deformation were selected for testing. Both sections were selected from the No.7 cross tunnel of the Yuntunbao tunnel. Considering the surrounding rock condition, cross section area, reliability of data, operability, and cost of test, four test holes are laid on each test section, located on the left and right sides of the sidewall 2 m and 5 m away from the track surface of the tunnel. The diameter and depth of the test holes are 40 mm and 10 m, respectively, which are
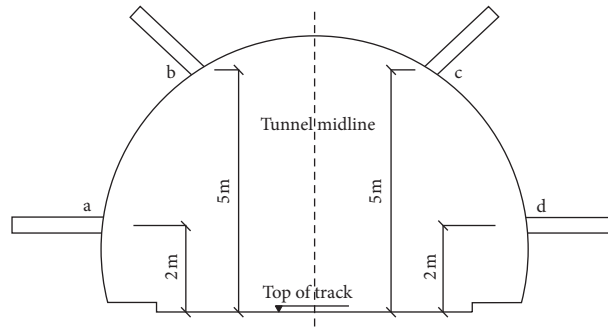
FIGURE 5: Hole layout.
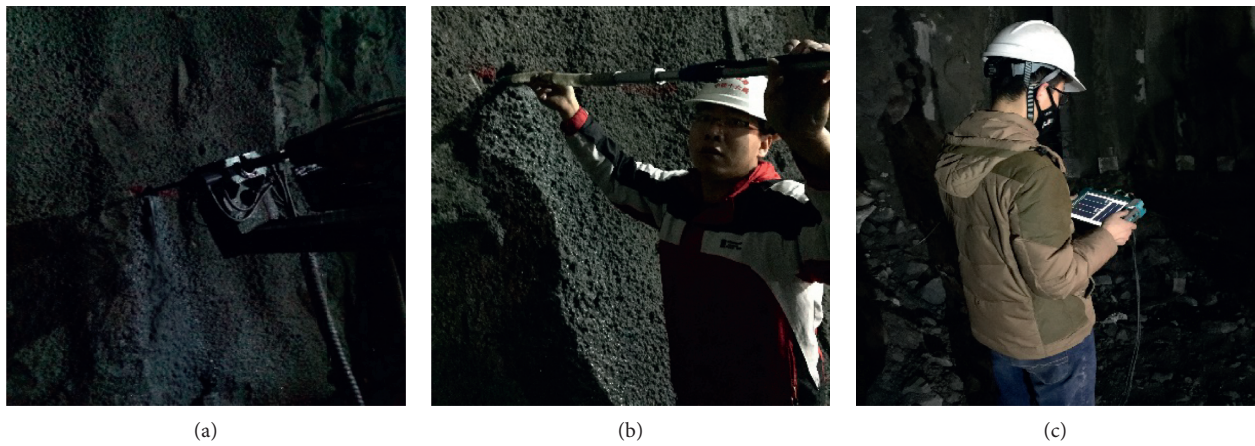
FIGURE 6: Field test of the loose circle. (a) Drilling holes, (b) installing probes, (c) collecting data.
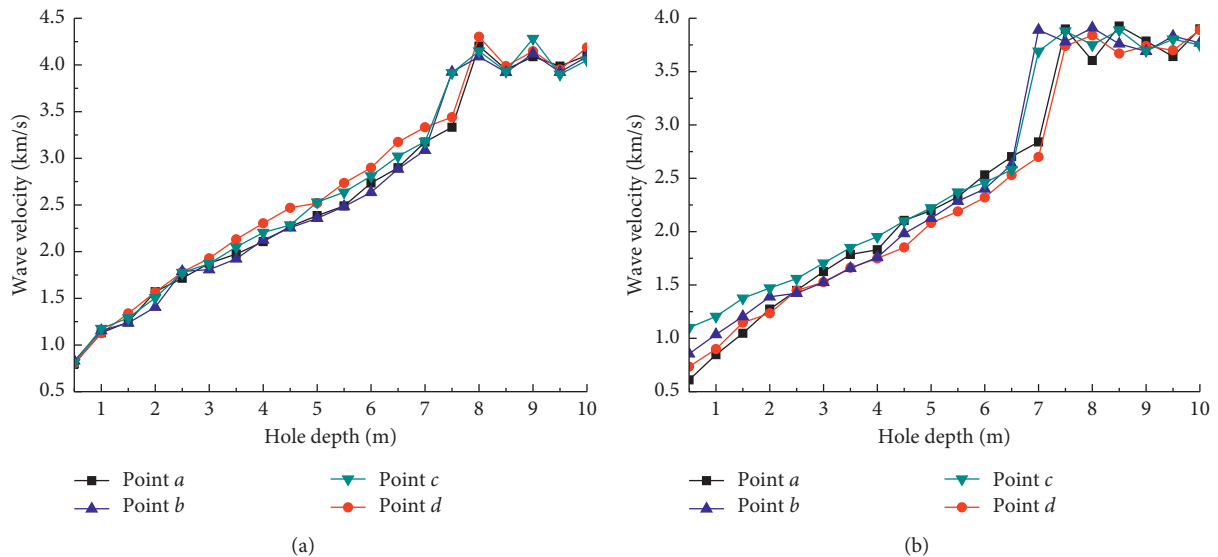
FIGURE 7: Hole depth-wave velocity curve of sections. (a) DK234 + 205 section. (b) DK234 + 318 section.

perpendicular to the excavation face. The locations of test holes are shown in Figure 5.

The field test is divided into five steps [32]: ① drilling; ② cleaning; ③ putting a probe into the testing hole; ④ injection; ⑤ moving measuring rod and starting the test, pulling out the rod by 0.5 m at a time until the whole rod is consumed to complete the test. Part of the operation process of the engineering site is shown in Figure 6.

TABLE 7: Measured values of loose circles and surrounding rock pressures of typical section (m).

Cross section mileage	Test items	Hole location			
		1	2	3	4
DK234 + 205	Loose circle (m)	7~7.5	6.5~7	6.5~7	7~7.5
	Surrounding rock pressure (kPa)	304.7	259.3	241.2	288.4
DK234 + 318	Loose circle (m)	7.5~8	7~7.5	7~7.5	7.5~8
	Surrounding rock pressure (kPa)	322.6	279.1	251.3	307.7

4.3.2. Analysis of Test Results. The longitudinal wave velocity of surrounding rock at different depths is measured in typical sections. The hole depth-wave velocity curves of each measuring point are plotted, as shown in Figure 7.

In Figure 7, the position where longitudinal wave velocity of rock has catastrophe occurrences is taken as the boundary of the loose circle, so the loose circle of the sidewall (points a and d) of DK234 + 205 section of grade II soft rock with large deformation ranging from 7 m to 7.5 m, the loose circle of the vault (points *b* and *c*) ranging from 6.5 m to 7 m, the loose circle of the sidewall (points a and d) of grade III soft rock with large deformation ranging from 7.5 m to 8 m, and the loose circle of the vault (points *b* and *c*) is 7.7 m to 7.5 m, as shown in Table 7.

From Table 7, the pressure of surrounding rock measured at each measuring point is about 80% of the theoretical value of surrounding rock pressure, and the values of thickness of loose circle measured at section DK234 + 205 of grade II and section DK234 + 318 of grade III soft rock with large deformation are basically consistent with the theoretical calculation values when supporting structure bears 80% of surrounding rock pressure. It shows that the theoretical calculation results are reliable, and according to the existing construction scheme, the surrounding rock stress has been released by 20% when the initial support construction is completed. At the same time, by monitoring and measuring, the peripheral convergence of section DK234 + 205 of grade II and section DK234 + 318 of grade III soft rock with large deformation is 475 mm and 662 mm, respectively, which are far beyond the standard and should be classified as large deformation. The main cause of large deformation is due to the supporting structure, which is not constructed in time and the insufficient length of the bolt which cannot provide enough support reaction.

5. Conclusions

Based on unified strength criterion, in this paper, there is the deduction of the formula for calculating the radius of the loose circle of surrounding rock in the tunnel, theoretical calculation, and field test of surrounding rock loose circle for typical sections of grade II and III soft rock with large deformation which is carried out in Yuntunbao Tunnel and analyzes the distribution range and law of loose circle of surrounding rock in large deformation tunnel of soft rock. The main conclusions are as follows:

(1) Based on the objective fact that high in situ stress exists in large deformation tunnel in soft rock, a formula for calculating the radius of the loose circle is derived with unified strength criterion and considering the influence of intermediate principal stress on the stress state of surrounding rock.

(2) In a large deformation tunnel of soft rock, with the upgrade of large deformation, the quality of surrounding rock becomes worse. Supporting resistance decreases and the thickness of the loose circle increases continuously. Moreover, due to the influence caused by high in situ stress, the distribution of the loose circle on the cross section is larger than that on side wall of the arch.

(3) The field measurement results of the loose circle of surrounding rock in the Yuntunbao tunnel are close to the theoretical calculation values when the supporting structure bears 80% of surrounding rock pressure. The thickness of the loose circle of the vault and the sidewall of grade II large deformation section is from 6.5 m to 7.0 m and 7.0 m to 7.5 m, respectively, and that of grade III large deformation section is from 7.0 m to 7.5 m and 7.5 m to 8.0 m, respectively. It shows that the formula for calculating the radius of the loose circle based on the unified strength criterion is applicable for a large deformation tunnel in soft rock.

(4) The peripheral convergences of grade II large deformation section and grade III large deformation section of Yuntunbao Tunnel reach 475 mm and 662 mm, respectively, which are far above the limit and should be classified as large deformation. The length of the bolt can be optimized according to the thickness of the loose circle, so as to provide sufficient support reaction, which controls the displacement of surrounding rock and ensures the safety of the structure.

Data Availability

The raw/processed data required to reproduce these findings cannot be shared at this time as the data also form part of an ongoing study.

Conflicts of Interest

The authors declare that they have no conflicts of interest.

Acknowledgments

References

[1] O. Kenzo, T. Tatsuya, and T. Fumio, "Deformation characteristics of sedimentary soft rock evaluated by field and laboratory tests and full-scale behaviour," *Journal of the Society of Materials Science Japan*, vol. 44, pp. 856–861, 1995.

[2] C. Yit-Jin and C. Sheng, *Evaluation of Influence Parameters for Soft Rock Tunnel*, Geotechnical Special Publication, Denver, CO, USA, 2007.

[3] M. Iwata, A. Yashima, and K. Sawada, "Local behavior of pore water pressure during plane-strain compression of soft rock," *Springer Series in Geomechanics and Geoengineering*, vol. 5, pp. 211–227, 2011.

[4] O. Kenzo, T. Tatsuya, and T. Fumio, "Deformation characteristics of sedimentary soft rock evaluated by full-scale excavation, field and laboratory investigation and liner back-analysis," *Proceedings of the Japan Society of Civil Engineers*, vol. 487, pp. 177–186, 1994.

[5] T. Fumio and L. Wang, "Brief review of the strength and deformation characteristics of sedimentary soft rock," *Chinese Journal of Rock Mechanics and Engineering*, vol. 22, pp. 872–893, 2003.

[6] D. C. Peckley and T. Uchimura, "Strength and deformation of soft rocks under cyclic loading considering loading period effects," *Soils and Foundations*, vol. 49, no. 1, pp. 51–62, 2009.

[7] D. Sterpi and G. Gioda, "Visco-Plastic behaviour around advancing tunnels in squeezing rock," *Rock Mechanics and Rock Engineering*, vol. 42, no. 2, pp. 319–339, 2009.

[8] S. Archer and V. Rasouli, "A log based analysis to estimate mechanical properties and in-situ stresses in a shale gas well in North Perth Basin,"vol. 81, pp. 163–174, in *Proceedings of the 1st International Conference on Petroleum and Mineral Resources*, vol. 81, pp. 163–174, WIT Press, Kurdistan, Iraq, 2013.

[9] M. S. A. Siddiquee and A. Hamdi, "A time-dependent double hardening model for soft rock," *Advances in Civil Engineering*, vol. 2019, no. 2, pp. 1–18, 2019.

[10] L. R. Sousa, *Learning With Accidents And Damage Associated To Underground Works*, pp. 7–39, Taylor and Francis – Balkema, Oxfordshire, UK, 2006.

[11] R. L. Sousa and H. H. Einstein, "Risk analysis during tunnel construction using Bayesian networks: porto Metro case study," *Tunnelling and Underground Space Technology*, vol. 27, no. 1, pp. 86–100, 2012.

[12] M. C. Acar and B. Kaya, "Models to estimate the elastic modulus of weak rocks based on least square support vector machine," *Arabian Journal of Geoences*, vol. 13, no. 14, 2020.

[13] Y. Xue, T. Teng, F. Dang, Z. Ma, S. Wang, and H. Xue, "Productivity analysis of fractured wells in reservoir of hydrogen and carbon based on dual-porosity medium model," *International Journal of Hydrogen Energy*, vol. 45, no. 39, pp. 20240–20249, 2020.

[14] Y. Xue, P. G. Ranjith, F. Dang et al., "Analysis of deformation, permeability and energy evolution characteristics of coal mass around borehole after excavation," *Natural Resources Research*, vol. 29, pp. 1–19, 2020.

[15] Q. Zeng, E. Wang, and S. Wang, "Comparison between plastic radius around a circular opening derived from Hoek-Brown failure criterion and calculated through modified Fenner formula," *Journal of Shenyang Jianzhu University (Natural Science)*, vol. 24, pp. 933–938, 2008.

[16] L. L. Ngueyep Mambou, J. Ndop, and J.-M. B. Ndjaka, "Numerical investigations of stresses and strains redistribution around the tunnel: influence of transverse isotropic behavior of granitic rock, in situ stress and shape of tunnel," *Journal of Mining Science*, vol. 51, no. 3, pp. 497–505, 2015.

[17] X. Zhang, F. M. He, and S. G. XuLi, "Study on the large deformation characteristics and disaster mechanism of a thin-layer soft-rock tunnel," *Advances in Civil Engineering*, vol. 2020, no. 6, 15 pages, Article ID 8826337, 2020.

[18] I. Tao, N. Vlachopoulos, and M. S. Diederichs, "Assessing fracturing mechanisms and evolution of excavation damaged zone of tunnels in interlocked rock masses at high stresses using a finite-discrete element approach," *Journal of Rock Mechanics and Geotechnical Engineering*, vol. 11, no. 4, pp. 701–722, 2019.

[19] I. Vazaios, N. Vlachopoulos, and M. S. Diederichs, "Mechanical analysis and interpretation of excavation damage zone formation around deep tunnels within massive rock masses using hybrid finite-discrete element approach: case of Atomic Energy of Canada Limited (AECL) Underground Research Laboratory (URL) test tunnel," *Canadian Geotechnical Journal*, vol. 56, no. 1, pp. 35–59, 2019.

[20] X. Zhou and G. Song, "Theory research situation of foreign surrounding rock loose circle support theory," *Mine Construction Technology*, vol. 6771 pages, 1994.

[21] A. Serrano, C. Olalla, and I. Reig, "Convergence of circular tunnels in elastoplastic rock masses with non-linear failure criteria and non-associated flow laws," *International Journal of Rock Mechanics and Mining Sciences*, vol. 48, no. 6, pp. 878–887, 2011.

[22] L. Ming, X. Mao, Y. Yu et al., "Stress and deformation analysis on deep surrounding rock at different time stages and its application," *International Journal of Mining Science and Technology*, vol. 22, pp. 301–306, 2012.

[23] H. B. Xia, Y. Xu, and Y. Zhang, "Numerical simulation and experimental analysis of roadway surrounding rock loose circle under blasting vibration," in *Proceedings of the 2013 4th International Conference on Digital Manufacturing and Automation*, pp. 850–854, IEEE Computer Society, Shangdong, China, 2013.

[24] Y. X. Yu, B. P. Chen, T. Zhang et al., "Back analysis on deformation and failure zone distribution laws of surrounding rock in deep-buried soft rock tunnel," *Journal of Railway Engineering Society*, vol. 34, pp. 46–52, 2017.

[25] T. Maejima, H. Morioka, T. Mori, and K. Aoki, "Evaluation of loosened zones on excavation of a large underground rock cavern and application of observational construction techniques," *Tunnelling and Underground Space Technology*, vol. 18, no. 2-3, pp. 223–232, 2003.

[26] T. Golebiowski, "Changeable-offset GPR profiling for loose zones detection in levees," in *Proceedings of the 14th European Meeting of Environmental and Engineering Geophysics of the Near Surface Geoscience Division of EAGE*, European Association of Geoscientists and Engineers, Porto, Portugal, 2008.

[27] K. Czaja, "Application of GPR and computer modelling in flood embankment investigation," in *Proceedings of the 75th European Association of Geoscientists and Engineers Conference and Exhibition, European Association*, pp. 6246–6248, London, UK, 2013.

[28] D. P. Hoang, G. L. Xu, Z. P. Li et al., "Investigation of failure mechanism and process on excavation damaged zone/Disturbed zone (EDZ) of underground engineering in rock," in *Proceedings of the ISRM VietRock 2015 International Workshop*, pp. 1–9, International Society for Rock Mechanics, Hanoi, Vietnam, 2015.

[29] T. K. T. Huotari-Halkosaari, M. H. Wennerstöm, and I. A. S. Suppala, "Study of integrated geophysical and geological research methods on mapping weakness structures in bedrock at urban areas," in *Proceedings of the Near Surface Geoscience 2016-22nd European Meeting of Environmental and Engineering Geophysics*, European Association of Geoscientists and Engineers, 2016.

[30] G. Tomislaw and M. Tomasz, "Application of GPR method for detection of loose zones in flood levee. 1st conference of the international water association IWA," *EDP Sciences*, vol. 30, pp. 1–11, 2018.

[31] G. Li, Z. Liu, and Y. Zhu, "On the large squeezing deformation law and classification criteria for the Lanzhou-Chongqing Railway Tunnels in soft and high geostress rocks," *Modern Tunnelling Technology*, vol. 52, pp. 62–68, 2015.

[32] Ministry of Housing and Urban-Rural Development of the People's Republic of China and General Administration of Quality Supervision, Inspection and Quarantine of the People's Republic of China, *Standard for Test Methods of Engineering Rock Mass (GB/T 50266-2013)*, China Planning Press, Beijing, China, 2013.

Research Article

Instability Model of a Coal Wall with Large Mining Height under Excavation Unloading Conditions

Lei Li [1,2] **and Feng zhang** [3,4]

[1]*Business Division of Mining Design of Tiandi Technology Co., Ltd., Beijing 100013, China*
[2]*Mining Research Division of China Coal Research Institute, Beijing 100013, China*
[3]*State Key Laboratory of Mining Response and Disaster Prevention and Control in Deep Coal Mines,*
Anhui University of Science and Technology, Huainan, Anhui Province 232001, China
[4]*State Key Laboratory of Water Resource Protection and Utilization in Coal Mining, Beijing 100120, China*

Correspondence should be addressed to Lei Li; lilei@tdkcsj.com

On the basis of the stress field characteristics of surrounding rocks at a coal wall on a working face with a large mining height, the theories of unloading rock mass mechanics and fracture mechanics were used to establish a model of the excavation unloading field effect of the coal wall, and its instability mechanism under the action of unloading stress field was analyzed. Results show that the coal mining process is the unloading process of coal and rock masses, and the stress field of surrounding rocks at the coal wall turns into an unloading stress field that consists of original and unloading stresses. Under the action of unloading stress field, cracks in the coal wall will undergo instability, propagation, and combination in the form of composite-type cracks and will gradually evolve into a wedge structure. The wedge stability is inversely related to roof pressure P_0, unloading force T, and intersection angle φ of structural planes. Elevating the wall-supporting force P_h, the initial supporting force of supports on the working face and the cohesion C of coal body can effectively control the occurrence of coal wall caving accidents and contribute to the safe mining of working faces with a large mining height.

1. Introduction

Fully mechanized underground coal mining with a large mining height is the development direction of thick coal mining in China. However, enlarging the mining height aggravates the probability of coal wall caving on the working face [1–3] and restricts the application of fully mechanized coal mining technology in thick coal seam. Current methods of theoretically analyzing coal wall caving causes and mechanism, such as crack-layer plate structural model [4–6], compressive bar structural model [7, 8], wedge stability model [9], mechanical model of coal wall sliding surface [10], or coal wall shear failure model [11], neglect the influence of the coal mining-induced unloading effect. The theory of unloading rock mass mechanics states that the excavation process of rock and earth masses is actually a

mechanical unloading process of rock masses [12]. Jointed rock masses in the loading process generally have good mechanical properties, but rock masses are turned from compressive state into tensile state under excavation unloading, and their mechanical properties will be rapidly degraded; as a result, the mechanical characteristics of rock masses under unloading condition are inconsistent with those under loading condition [13–15]. Therefore, the coal rock mass near the coal wall formed by coal seam excavation is analyzed as an unloading rock mass, which conforms to the characteristics of the engineering rock mass, and it has practical engineering significance. On the basis of the theories of unloading rock mass and fracture mechanics, the fracture instability mechanism of a coal wall under the action of unloading stress field was investigated, the fracture instability criterion for the coal wall and the influencing factors

of its instability were acquired, and a new framework of using the theory of unloading rock mass mechanics to analyze coal wall fracture instability was opened.

2. Characteristics of Coal Excavation-Induced Unloading Field Effect

2.1. Principle of Unloading Analysis. The theory of unloading rock mass mechanics posits that excavation unloading effect is equivalent to applying a reverse tensile stress in the rock mass under initial stress. Thus, unloading stress can be equivalent to a tensile stress that acts upon the initial rock mass, and its maximum value is $\sigma_0 + R_t$ (σ_0 is the initial stress, R_t is the tensile strength of rock mass, and $\sigma_0 + R_t$ is the equivalent tensile strength of rock mass). The unloading problem of rock mass during mining can be decomposed into the joint action model of initial and mining unloading stresses, as shown in Figure 1, where $\triangle\sigma$ is the unloading stress.

2.2. Stress Field of the Coal Body nearby the Coal Wall and Its Failure. In coal excavation process, the coal body nearby the coal wall will also bear the action of the excavation-induced unloading stress in addition to the stress of the primary rock. The stress condition is shown in Figure 2.

Given that original cracks or defects exist in the coal body, the quality of the coal nearby the coal wall will be gradually degraded under the unloading stress field that consists of primary rock stress (compressive stress) and unloading stress (tensile stress). After the excavation of the roadway, the original rock stress is redistributed, and the stress concentration appears in the surrounding rock of the roadway, which generally does not exceed 5 times the radius of the roadway. For the coal body nearby the coal wall of the working face with a large mining height, the coal wall will easily experience tensile or shear failure under the joint action of compressive and tensile stresses. When lateral confining pressure is moderate and lower than brittle-plastic transition value, the coal wall can easily undergo dislocation or shear failure [5, 16]. The occurrence of the above-mentioned failure mode is closely related to crack propagation and coalescence.

2.3. Mechanical Analysis of Crack Propagation. For the convenience of analysis, this study assumes that an oblique crack exists in the coal body, where its length is $2a$ and its dip angle is β. The crack propagation model, as shown in Figure 3, is established under the action of unloading stress field. Given the existence of unloading stress, crack propagation is controlled by types I and II stress intensity factors K_I and K_{II}, and its propagation characteristics can be described by a composite-type crack model. In accordance with the superposition principle, the stress intensity factor at the crack end, as shown in Figure 3, can be expressed as the superposition of stress intensity factor caused by simple loading [17] (Figure 4). Therefore, the stress intensity factor of the composite-type crack is expressed as below.
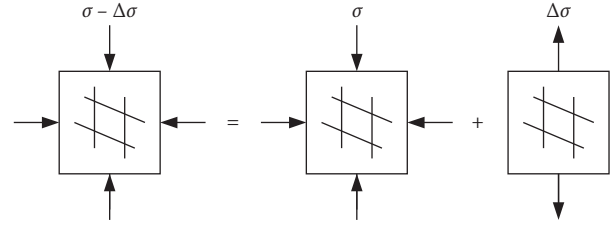
FIGURE 1: Graph of unloading field effect.

$$\left.\begin{array}{l} K_I = \left(\triangle\sigma \sin^2\beta - \sigma\right)\sqrt{\pi a}, \\ K_{II} = \triangle\sigma\sqrt{\pi a}\sin\beta\cos\beta. \end{array}\right\} \tag{1}$$

According to the theory of the maximum circumferential stress in fracture mechanics [18–20], the breaking angle θ_0 of the composite-type crack satisfies the following condition:

$$k_I \sin\theta_0 + k_{II}(3\cos\theta_0 - 1) = 0. \tag{2}$$

Its fracture criterion is

$$\left[K_I\cos^2\frac{\theta_0}{2} - \frac{3}{2}K_{II}\sin\theta_0\right]\cos\frac{\theta_0}{2} = K_{IC}. \tag{3}$$

We set $\alpha = K_I/K_{II}$. Then, we have

$$\alpha = \frac{\triangle\sigma \sin^2\beta - \sigma}{\triangle\sigma\sin\beta\cos\beta}. \tag{4}$$

From equation (2), we can obtain the following:

$$\cos\theta_0 = \frac{3 \pm \sqrt{\alpha^4 + 8\alpha^2}}{\alpha^2 + 9}, \tag{5}$$

$$\cos\frac{\theta_0}{2} = \pm\sqrt{\frac{1 + \cos\theta_0}{2}},$$

$$= \pm\sqrt{\frac{\alpha^2 + 12 \pm \sqrt{\alpha^4 + 8\alpha^2}}{2(\alpha^2 + 9)}}. \tag{6}$$

From comprehensive formulas (3), (4), and (5), we can get

$$\begin{aligned} &\left[\frac{\alpha^3 + 12\alpha \pm \alpha\sqrt{\alpha^4 + 8\alpha^2}}{2(\alpha^2 + 9)}\right. \\ &\left. -\frac{3}{2\alpha}\left(1 - \frac{9 \pm 3\sqrt{\alpha^4 + 8\alpha^2}}{\alpha^2 + 9}\right)\right] \\ &* \left(\pm\sqrt{\frac{\alpha^2 + 12 \pm \sqrt{\alpha^4 + 8\alpha^2}}{2(\alpha^2 + 9)}}\right), \\ &= \frac{K_{IC}}{\triangle\sigma\sqrt{\pi a}\sin\beta\cos\beta}. \end{aligned} \tag{7}$$

(a)

(b)
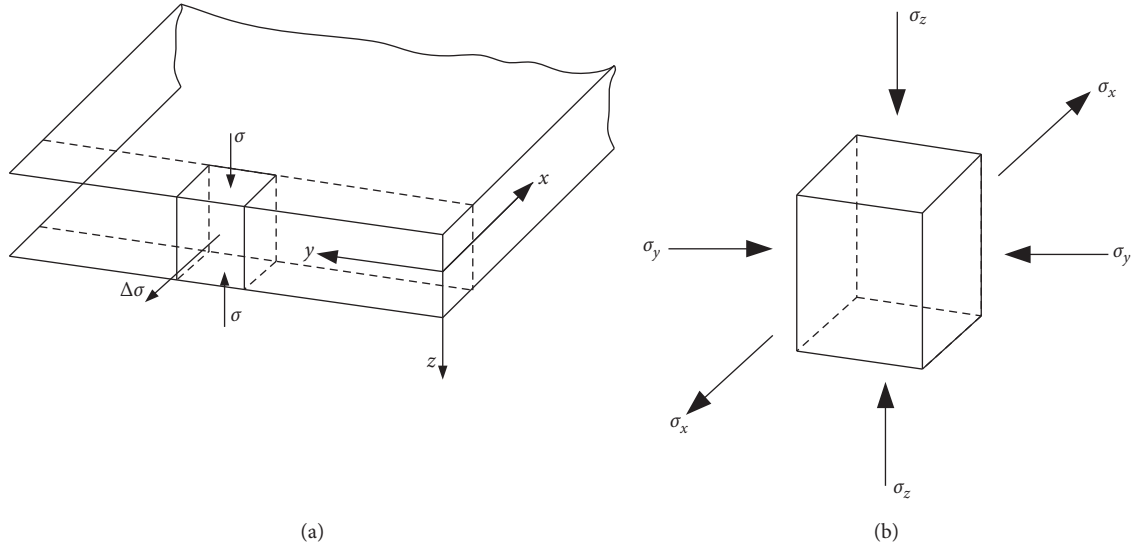
FIGURE 2: Unloading stress field in the coal body at the coal wall. Force diagram of the (a) coal body and (b) coal units at the coal wall on the working face.

We set $m = K_{IC}/\triangle\sigma\sqrt{\pi a}\sin\beta\cos\beta$ and $0 < \theta_0 < \pi/2$. Then, equation (8) of α about m can be solved, and equation (4) can be combined to determine the relationships among ultimate compressive stress σ, unloading stress $\triangle\sigma$ (tensile stress), crack angle β, fracture toughness K_{IC}, and initial crack length a, as shown in equation (9).

$$\alpha = \frac{m}{3} - \frac{2^{1/3}\left(30m^2 - m^4\right)}{3m\left(-216m^2 + 153m^4 + 2m^6 + 3\sqrt{3}\sqrt{1728m^4 + 1552m^6 + 435m^8 + 36m^{10}}\right)^{1/3}},$$
$$+ \frac{\left(-216m^2 + 153m^4 + 2m^6 + 3\sqrt{3}\sqrt{1728m^4 + 1552m^6 + 435m^8 + 36m^{10}}\right)^{1/3}}{32^{1/3}m}, \tag{8}$$

$$\sigma = \triangle\sigma\left(\begin{array}{l}\sin\beta - \dfrac{m}{3} - \dfrac{2^{1/3}\left(30m^2 - m^4\right)}{3m\left(\begin{array}{c}-216m^2 + 153m^4 + 2m^6 \\ +3\sqrt{3}\sqrt{1728m^4 + 1552m^6 + 435m^8 + 36m^{10}}\end{array}\right)^{1/3}} \\ + \dfrac{\left(\begin{array}{c}-216m^2 + 153m^4 + 2m^6 \\ +3\sqrt{3}\sqrt{1728m^4 + 1552m^6 + 435m^8 + 36m^{10}}\end{array}\right)^{1/3}}{32^{1/3}m}\cos\beta\end{array}\right)\sin\beta. \tag{9}$$

When the crack angle β and the material fracture toughness K_{IC} are determined, the ultimate compressive stress σ declines with the increase in the unloading stress $\triangle\sigma$. With the continuous advancement of the working face during the coal mining process, the stress in the coal body in front of the working face is gradually concentrated. The unloading stress is also gradually enlarged. When the compressive and unloading stresses satisfy equation (9), the crack in the jointed coal body will undergo instability, propagation, and combination. This condition will lead to a coal wall caving event during operation under a large mining height. When the composite-type crack in the coal body is propagated, its propagation direction will not be along the direction of the dip angle of original crack any longer, but it will present propagation at the angle of θ_0. Therefore, the instability form of the coal body at the coal wall with a large quantity of cracks is not a simple layer-crack plate structure but an irregular polyhedron of a certain dip angle. This deduction can be verified through the characteristic analysis and statistics of many field caving accidents.
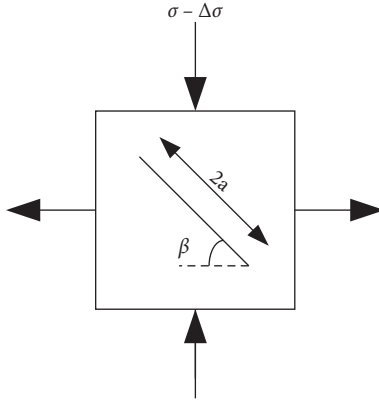
FIGURE 3: Composite crack propagation model.

3. Instability Criterion for Wedge Structure at the Coal Wall

The characteristic statistics of a large number of field coal wall caving accidents indicates that the geometric characteristics of the irregular polyhedron formed by instability, propagation, and combination of composite-type cracks can be simplified into a wedge structural model [9, 21]. The stability of the coal wall can be analyzed through the stability of the wedge structure. The analytical model of wedge stability is constructed, as shown in Figure 5, to obtain the instability criterion for the coal wall wedge. In the figure, planes I and II are the structural planes that form after crack propagation and combination in the coal body. The line of intersection between these planes is BD, and a wedge with quadrangular points ABCD is formed.

The dead weight of the wedge is set as G, the roof pressure as P_0, the unloading force as T, the horizontal wall-supporting force provided by wall-supporting plates as P_h, and the structural plane intersection angle as φ. The line of intersection BD is taken as x-axis, and the vertical line of the

outward intersection is taken as y-axis to establish the coordinate system shown in Figure 5(b).

The force N perpendicular to the line of intersection BD between structural planes is

$$N = (P_0 + G)\cos\varphi + (P_h - T)\sin\varphi. \tag{10}$$

The force τ parallel to the line of intersection BD between structural planes is

$$\tau = (P_0 + G)\sin\varphi - (P_h - T)\cos\varphi. \tag{11}$$

N is decomposed into N_I perpendicular to structural plane I, and N_{II} is perpendicular to structural plane II. We assume that the included angles between vertical plane of line of intersection BD, which passes through structural planes I and II, and two structural planes are θ_1 and θ_2. The sliding direction of wedge is also assumed parallel to the line of intersection of the two structural planes, as shown in Figures 5(c) and 5(d). Then, it has

$$\begin{aligned} N_I &= N\sin\theta_1, \\ N_{II} &= N\sin\theta_2. \end{aligned} \tag{12}$$

The wedge stability coefficient K can be expressed as

$$K = \frac{f_I N_I + f_{II} N_{II} + C_I S_I + C_{II} S_{II}}{(P_0 + G)\sin\varphi - (P_h - T)\cos\varphi}, \tag{13}$$

where f_I and f_{II} are the sliding coefficients of structural planes I and II, respectively; C_I and C_{II} are their cohesion coefficients; and S_I and S_{II} are the areas of their sliding surfaces.

By combining equations (10), (12), and (13), the expression of stability coefficient K is determined as in equation (14). When $K < 1$, the wedge at the coal wall will undergo instability failure to cause coal wall caving. When $K \geq 1$, the wedge will not experience any instability failure or the caving phenomenon.

$$K = \frac{f_I[(P_0 + G)\cos\varphi + (P_h - T)\sin\varphi]\sin\theta_1 + f_{II}[(P_0 + G)\cos\varphi + (P_h - T)\sin\varphi]\sin\theta_2 + C_I S_I + C_{II} S_{II}}{(P_0 + G)\sin\varphi - (P_h - T)\cos\varphi}. \tag{14}$$

In investigating the change relations of wedge stability with roof pressure, unloading force, and intersection angle between structural planes, we assume $\theta_1 = \theta_2$, $f_I = f_{II}$, $C_I = C_{II}$, and $S_I = S_{II}$. Then, equation (14) can be simplified into the following form:

$$K = \frac{2f_I\left[\begin{array}{c}(P_0 + G)\cos\varphi \\ +(P_h - T)\sin\varphi\end{array}\right]\sin\theta_1 + 2C_I S_I}{(P_0 + G)\sin\varphi - (P_h - T)\cos\varphi}. \tag{15}$$

A single-factor analysis by assigning values to the influencing parameters of wedge stability shows that, as roof pressure P_0, unloading force T, and intersection angle φ between structural planes increase, the wedge stability is

degraded. Moreover, the influence degrees of unloading force T and intersection angle φ are high, as shown in Figure 6.

As the wall-supporting force P_h and cohesion C of structural planes increase, wedge stability is also enhanced [9]. However, as the coal seam is continuously mined forward, the coal quality at the coal wall will be continuously degraded due to the existence of the excavation unloading effect, and its cohesion and internal frictional angle are continuously decreased, which further aggravates the wedge instability. Thus, on a working face with a large mining height, elevating wall-supporting force P_h, cohesion C of coal body, and initial supporting force of supports on the working face can improve the wedge stability.
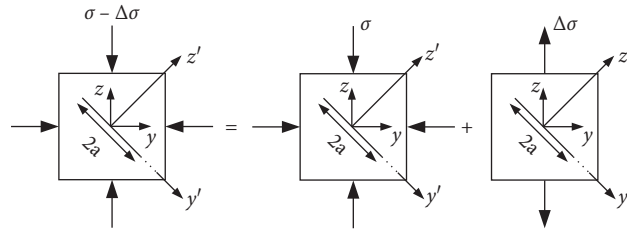
FIGURE 4: Superposition of stress intensity factor.
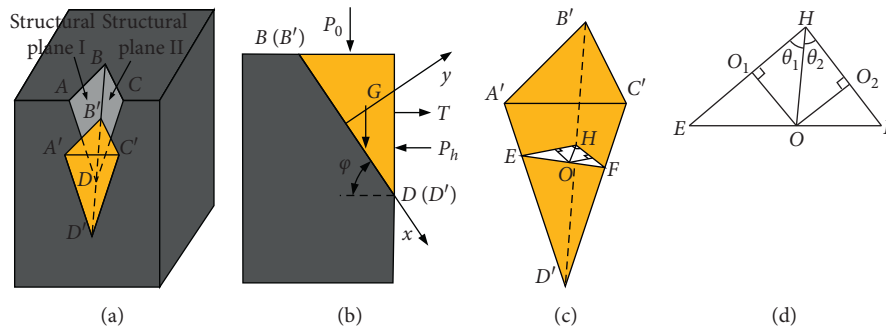
FIGURE 5: Analytical model of wedge stability at the coal wall.
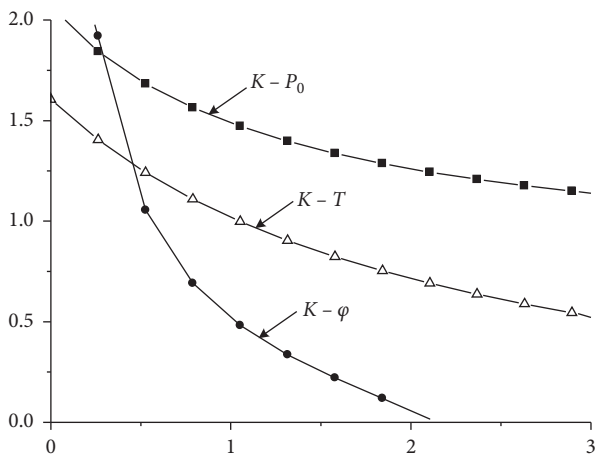
FIGURE 6: Diagram of unloading field effect.

4. Stability Control Technology of the Coal Wall with a Large Mining Height

The wedge instability mechanism at the coal wall indicates that improving the wedge stability helps enhance the stability of the coal wall and control coal wall caving. Therefore, the following measures can be taken to control coal wall caving in engineering practice

Wall-supporting force P_h should be elevated. The stability of the coal wall on the working face with a large mining height, especially for "three-soft" coal seam, is poor due to the unloading effect. However, enlarging the wall-supporting force can generate a certain compensating and weakening effect on the unloading force. Thus, after the coal is cut through a coal machine, the wall-supporting plate should be timely opened to guarantee wedge stability.

Cohesion C of the coal body at the coal wall should be elevated. Coal seam grouting or water injection can improve coal properties, increase coal wall cohesion, enlarge internal frictional angle, and enhance antishear ability and overall stability.

Initial supporting force of supports should be elevated. Initial supporting force is the force used by supports to proactively support the roof. The supports should be timely lifted after coal cutting and support advancing, and roof-contacted filling should be carried out to ensure sufficient initial supporting force, effectively mitigate rotation and subsidence of roof strata, keep peak supporting pressure away from the coal wall, and relieve coal wall pressure P_0. Accordingly, the wedge stability of coal wall can be controlled.

The advancement of the working face should be properly accelerated. The accelerated advancement of the working face shortens the exposure time of the coal wall and relieves the influence degree of the coal excavation unloading effect. Meanwhile, it also reduces the action time of the supporting pressure on the coal wall and the degree of coal damage and degradation. Accordingly, the coal wall caving degree can be decreased.

5. Conclusions

The coal mining process is the unloading process of coal and rock masses. The characteristics of coal excavation-induced unloading stress field were analyzed using the theory of unloading rock mass mechanics. The results showed that the stress field of surrounding rocks at the coal wall would be turned into an unloading stress field that consisted of original and unloading stresses.

Under the action of unloading stress field, the cracks in the coal wall would undergo instability, propagation, and combination in the form of composite-type cracks and be gradually evolved into a wedge structure. Meanwhile, the propagation criterion for composite-type cracks under the existence of unloading stress was given in accordance with the theory of fracture mechanics.

The wedge instability criterion of the coal wall was obtained by establishing a mechanical model of the wedge stability of the coal wall. Specifically, when $K < 1$, the coal wall wedge would experience instability failure to cause coal wall caving. In addition, the wedge stability would be degraded, and the coal wall could easily undergo caving with the increase in roof pressure P_0, unloading force T, and intersection angle φ between structural planes.

The stability of the coal wall could be improved by elevating the wall-supporting force P_h, the coal cohesion C, and the initial supporting force and by properly accelerating the advancement of the working face to provide a guarantee for safe mining of working faces with a large mining height.

Data Availability

The data underlying the findings of this paper are publicly available.

Conflicts of Interest

The authors declare no conflicts of interest.

Acknowledgments

References

[1] S.-H. Tu, Y. Yong, Y. Zhen et al., "Research situation and prospect of fully mechanized mining technology in thick coal seams in China," *Procedia Earth and Planetary Science*, vol. 1, no. 1, pp. 35–40, 2009.

[2] X. Z. Ma and G. X Xie, "Coal wall spalling mechanism and control technology of fully mechanized high cutting longwall coal mining face," *Chinese Journal of Coal Science Technology*, vol. 36, pp. 1–4, 2008, in Chinese.

[3] X. J. Wang, X. S. Qian, L. Q. Ma et al., "Research on large mining height technique for thick coal seams," *Chinese Journal of Coal Science Technology*, vol. 26, pp. 212–216, 2009, in Chinese.

[4] X. X. Miao, L. Q. An, and M. H. Zhai, "Model of rock barest for extension of slip fracture in palisades," *Journal of China University of Mining and Technology*, vol. 8, pp. 15–19, 1999, in Chinese.

[5] X. C. Zhang, X. X. Miao, and T. Q. Yang, "The layer-crack-plate model and testing study of the rock burst in mines," *Chinese Journal of Rock Mechanics and Engineering*, vol. 18, pp. 507–511, 1999, in Chinese.

[6] H. L. Zhang, L. G. Wang, and H. Qin, "Study of spalling mechanism and control techniques of mining roadway," *Chinese Journal of Rock Mechanics and Engineering*, vol. 31, pp. 1462–1466, 2012, in Chinese.

[7] X. W. Yin, S. H. Yan, and Y. An, "Characters of the rib spalling in fully mechanized caving face with great mining height," *Chinese Journal Mine Safety Science and Engineering*.vol. 25, pp. 222–225, 2008, in Chinese.

[8] Y. Ning, "Mechanism and control technique of the rib spalling in fully mechanized mining face with great mining height," *Journal of China Coal Society*, vol. 34, pp. 50–52, 2009, in Chinese.

[9] Y. Yuan, S. H. Tu, X. T. Ma et al., "Coal wall stability of fully mechanized working face with great mining height in "three soft" coal seam and its control technology," *Chinese Journal Mine Safety Science and Engineering*.vol. 29, pp. 21–25, 2012, in Chinese.

[10] H. J. Hao and Y. Zhang, "Stability analysis of coal wall in full-seam cutting workface with fully-mechanized in thick seam," *Chinese Journal of Liaoning Technical University*, vol. 24, pp. 489–491, 2005, in Chinese.

[11] J. C. Wang, "Mechanism of the rib spalling and the controlling in the very soft coal seam," *Journal of China Coal Society*, vol. 32, pp. 785–788, 2007, in Chinese.

[12] J. L. Li, *Unloading Rock Mass Mechanics*, China Water Power Press, Beijing, China, 2003, in Chinese.

[13] X. P. Zhou, Q. L. Ha, Y. X. Zhang et al., "Analysis of localization of deformation and complete stress strain relation for mesoscopic heterogenous brittle rock materials when axial stress isohel constant while lateral confinement is reduced," *Chinese Journal of Rock Mechanics and Engineering*, vol. 24, pp. 3236–3245, 2005, in Chinese.

[14] H. L. Hu, *Study on Sensitivity of Stable Parameters for Rock Slope and Mechanical Parameters of Excavation Unloading Rock Mass*, Three Gorges University. College of Civil and Hydropower Engineering, Yichang: China, 2008, in Chinese.

[15] J. L. Pei, J. F. Liu, and J. Xu, "Experimental study of mechanical properties of layered marble under unloading condition," *Chinese Journal of Rock Mechanics and Engineering*, vol. 28, pp. 2496–2502, 2009, in Chinese.

[16] L. N. D. Germanovich, A. V. Yskin, N. M. Syrul Nikov et al., "A model of the deformation and fracture of brittle materials with cracks under uniaxial compression," *Mechanics of Solids*, vol. 28, pp. 116–1288, 1993.

[17] B. K. Atkinson, *Fracture Mechanics of Rock*, Seismological Press, Beijing, China, 1992.

[18] Y. D. Li, *Theory and Application of Fracture Mechanics*, Weapon Industry Press, Beijing, China, 2005, in Chinese.

[19] Q. Gao, *Engineering Fracture Mechanics*, Chongqing University press, Chongqing, China, 1996, in Chinese.

[20] L. S. Tang, P. C. Zhang, and Y. Wang, "Propagation of the complex cracks in rocks without water pressure," *China Journal of Acta Scientiarum Naturalium Universitatis Sunyatseni*, vol. 41, pp. 83–90, 2002, in Chinese.

[21] Q. Gao, X. J. Yi, and X. Y. Zhao, "Discussion and analysis of wedge sliding and its stability," *China Journal of Subgrade Engineering*, vol. 12, pp. 115-116, 2008, in Chinese.

Research Article

Experimental Study on Lateral Permeability Evolution of Sandstone under Seepage-Damage Coupling

Dongdong Pang,[1,2,3] **Feisheng Feng** [ID],[1,3] **Guanghui Jiang** [ID],[4] **Dongjing Xu** [ID],[5] **and Xiaohan Wang** [ID][2]

[1]*State Key Laboratory of Mining Response and Disaster Prevention and Control in Deep Coal Mine, Anhui University of Science and Technology, Huainan 232001, China*
[2]*School of Mining and Safety Engineering, Anhui University of Science and Technology, Huainan 232001, China*
[3]*Key Laboratory of Coal Mine Safety and Efficiently Caving of Ministry of Education, Anhui University of Science and Technology, Huainan, Anhui 232001, China*
[4]*School of Civil Engineering, Ludong University, Yantai 264025, China*
[5]*Shandong Prov Key Lab Deposit Mineralizat & Sedim, Shandong University of Science and Technology, Qingdao 266590, Shandong, China*

Correspondence should be addressed to Feisheng Feng; fsfeng21@qq.com

To analyze the internal pore evolution law of aquifer rock in a coal mining front under the coupling effect of stress and seepage and the influence on the water inrush performance of the working face, research on the working face was conducted to improve the RTR-1000 high-temperature and high-pressure rock triaxial mechanical testing system, using hollow cylindrical and complete sandstone samples and by considering the stress change law in the actual mining process as the reference loading path. At the initial stage of loading, the permeability of sandstone demonstrates a rapid downward trend within a small range of stress change, with a decline rate of 50%. At lower permeabilities, the fluctuation is small; the plastic and failure stages are transient, and the relationship curve between the horizontal permeability and the axial confining pressure of sandstone is divided into compaction, multiple fluctuations, surrender, and failure. In several stages, the sandstone lateral permeability experiment under the coupling effect of stress and seepage demonstrates that the permeability of the aquifer in the coal mining front is significantly reduced after the original rock stress is disturbed by mining, suggesting that the water inrush calculation of the traditional water-flowing fractured zone and caving zone aquifer rock permeability experiment is inaccurate. Further research can deepen the stress and seepage coupling evolution process under the action of working face water inrush.

1. Introduction

Underwater coal mining inevitably involves problems such as water gushing on the working face, water inrush into the tunnel, and groundwater seepage. The interaction between the coal strata and groundwater influences the coal seam and groundwater, and there exists a coupling problem between seepage and stress. The coupling of seepage and stress is manifested mainly when seepage occurs; the water pressure caused by seepage acts on the rock and changes its condition.

Changes in the external influences of rock stress change the internal crack seepage features, seepage, and stress coupling mainly through the seepage characteristics of the fracture [1–6]. Snow determined the stress under the action of the permeability coefficient expression through a set of parallel fracture experiments [7]. Oda used statistical methods to express the tensor of the crack and obtain the relationship between stress and seepage [8–10]. Barton et al. proposed a relationship between the permeability coefficient and the effective stress by studying the mechanical properties of

fractures [11]. Reichenberger et al. proposed a finite volume method for vertex centers that can be used for the complete coupling of two-phase flow in porous media fractures [12]. Hoteit and Firoozabadi proposed an effective numerical model of incompressible two-phase flow in cracked media [13]. Helmig et al. studied the model coupling of multiphase flow in porous media [14]. Peratta and Popov developed a new numerical method for three-dimensional (3D) modeling of flows and transient solute transport in cracked porous media, thereby providing accurate and effective treatment of 3D complex geometric shapes and inhomogeneity [15]. Zhao et al. proposed a stress and seepage coupling research method based on digital image technology under the same conditions [16]. The digital image was obtained by segmentation, and the spatial distribution information was extracted. Linear interpolation is a 3D digital analysis model that was established to determine the stress of the spatial structure and seepage spatial division of the cataclastic rock mass characteristics. Wang and Zhang proposed a numerical simulation method for fracture propagation and closure under seepage stress coupling that was modeled using the extended finite element method based on the research background of fractures and voids [17]. Gui et al. reported that the primary cause of karst water inrush was the coupling effect of mining stress and bottom seepage [18]. Yi, Xiao, Tan, Ferfera, Chen, and Sheng-Qi Yang et al. conducted rock damage experiments on rocks of different lithologies and concluded that the permeability of rocks changes significantly after damage [19–24]. Shan and Lai, Sheikh and Pak, Guo et al., and Zhang et al. conducted related research on stressing osmotic coupling using numerical simulation, establishing numerical models of rock stress-strain-permeability coupling, and preliminary studies on the mechanism of stress-seepage coupling [25–28]. Ding and Xu, Shi and Durucan, Weeks, and Wang and Yakushev. conducted permeability studies in different directions under the condition of convective solid coupling [29–32]. The results indicated that permeability in different directions varies significantly under the same experimental conditions. The aforementioned research has laid the theoretical foundation for investigation in this study of the coupling of underground stress and permeability under the condition of damage caused by coal mining. However, there has been little experimental research on the change rule of horizontal permeability under mining pressure, particularly for the pseudotriaxial rock mechanics test system. The stress application can be conducted in two ways. In the first method, vertical in situ stress under confining pressure and horizontal in situ stress under axial pressure and confining pressure are applied to test the change law of axial permeability of rock with increasing confining pressure. The horizontal in situ stress in two directions is significantly different from the actual horizontal in situ stress, and the applied magnitude of the vertical in situ stress can only be smaller than that of the horizontal in situ stress, which is significantly different from the actual conditions. In the second method, the vertical in situ stress is applied under axial pressure, and the horizontal in situ stress is applied under confining pressure, which better simulates the actual

stress. The conventional permeability measurement can only measure the axial permeability; thus, the permeability measurement method must be improved to obtain the lateral permeability measurement of the conventional pseudo-triaxial apparatus.

2. Materials and Methodology

2.1. Experimental Design. The China University of Mining and Technology (Beijing) RTR-1000 high-temperature and high-pressure rock triaxial mechanical testing system can implement program design through rock experiments under different stress conditions of stress path loading, which creates conditions for simulating the stress change environment of in situ experiments. The permeability test does not include a test of transverse permeability; thus, the permeability test of the test system was modified to enable the measurement of the lateral permeability of the rock specimen. The rock specimen was sandstone; its buried depth was $270\,m$, bulk density was $20.5\,kN/m^3$, tensile strength was $0.62\,MPa$, and elastic modulus was $0.62 \times 104\,MPa$. The modifications are illustrated in Figure 1.

In comparison with the original permeameter, the improved permeameter changes the internal conductivity and rock sample specifications. The penetration path adds a guide gasket to one side of the test piece. The test piece is a cylindrical specimen with length L and radius r_e. A hole with radius r_w is drilled along the axial direction, as depicted in Figure 1.

2.2. Calculation Method for Permeability after Device Improvement. In comparison with gases, liquids have lower compressibility, higher density, and viscosity and rarely deviate from Darcy's law during permeability measurement. Under the same pressure gradient, the viscosity of the liquid volume flow is considerably higher than the gas viscosity, and a higher liquid density compensates to some extent for the influence of viscosity related to inertia resistance [33]. Thus, the vertical flow due to gravity cannot be ignored during permeability measurement. The Darcy expression of permeability measured by laminar fluid considering the effect of gravity is [34]

$$v_s = \frac{q}{A} = \frac{-C_1 k}{C_2 \mu}\left(\frac{dp}{ds} - \frac{\rho g}{C_4}\frac{dz}{ds}\right), \tag{1}$$

where S is the distance along the flow direction; υ_s is the volumetric flow rate of the fluid flowing through the unit void medium per unit time; Z is the ordinate, increasing downward; ρ is the fluid density; (dp/ds) is the pressure gradient along the flow direction of s; μ is the fluid viscosity; k is the permeability of the medium; q is the volume velocity; A is the cross-sectional area perpendicular to the streamline; and C_1, C_2, and C_4 are constants to ensure uniformity of units.

For the transverse seepage test, there is no vertical component in the flow direction; therefore, it is considered as $(dz/ds) = 0$. The permeability calculation formula for the fluid can be obtained by integration of Formula (1).

(a)

(b)
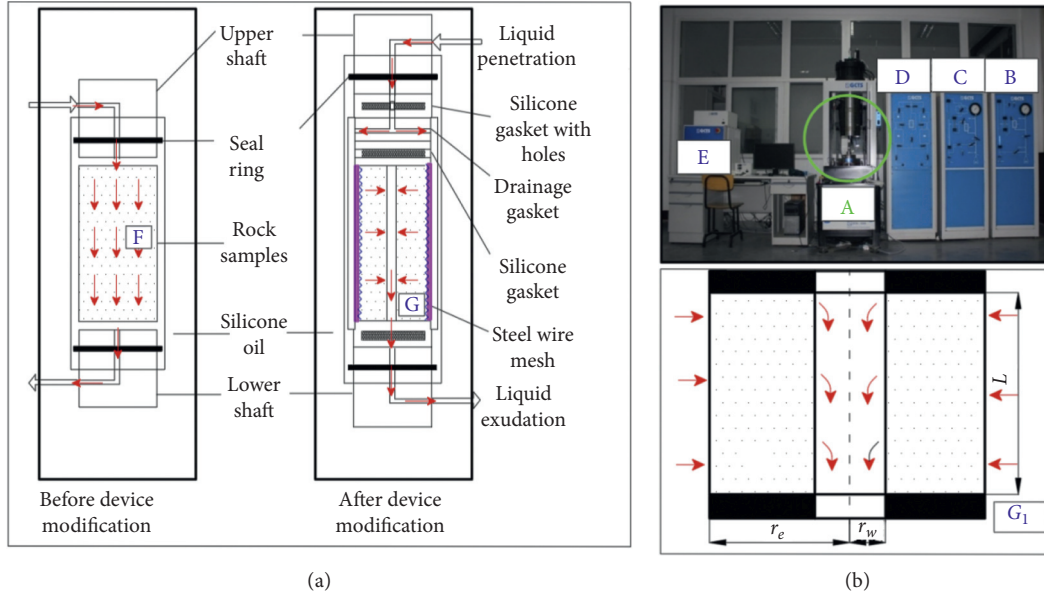
FIGURE 1: Comparison of flow paths before and after improvement of the RTR-1000 seepage test system. A: penetration test system; B: hole pressure supercharger; C: confining pressure supercharger; D: permeameter; E: console; F: traditional rock specimen; G: hollow cylinder rock specimen; G_1: profile of hollow cylinder rock specimen with seal rings.

$$k = \frac{C_2 \mu q}{C_1 G_f (p_1 - p_2)}, \tag{2}$$

where G_f is the geometric factor for the length, calculated by Formula (3) for radial flow.

$$G_f = \frac{2\pi L}{\ln[(r_e/r_w)]}, \tag{3}$$

where L is the sample length; r_e is the sample radius; and r_w is the internal diameter.

2.3. Experimental Process.

During the test, different sensors must be installed, including the confining pressure sensor, pore pressure sensor, axial pressure sensor, and axial displacement sensor. Because the surface of the test piece has a wire mesh, no strain gauge is directly added to the surface of the test piece; the displacement sensor on the indenter is used for calculating the strain. Using water as the permeable medium would pose a risk to the safety of the equipment owing to leakage. Thus, kerosene was used as the osmotic medium in the experiment. Before the experiment, the test piece was saturated with aviation kerosene and wrapped with a layer of steel wire mesh. The main function of the steel wire mesh is to provide a flow channel for the fluid to diffuse to the outer surface of the test piece. The hardness of the steel wire mesh should not be too high, for ease of wrapping the test piece and to avoid the risk of puncturing the heat-shrinkable tube. If the diameter of the steel wire mesh hole is too large, then heat-shrinkable tube deformation may hinder the surface uniformity of the penetration medium on the surface. If the diameter of the wire mesh is too small, then the wire hole ratio may be too large, which may reduce the oil inlet cross-sectional area of the outer surface, thereby affecting the experimental results. The size of the filter mesh was between 20 and 30, the material used was 304 stainless steel, the recommended wire diameter was 0.21 mm, and the side length of the hole was 1.10 mm. The length of the wire mesh was slightly larger than that of the test piece; the test piece was placed between the upper head and the lower head of the pressure chamber. The expanded width of the steel wire mesh was slightly larger than the circumference of the cylindrical sample. After wrapping the steel wire mesh, a heat-shrinkable tube was placed on the periphery to seal the test piece and the upper and lower heads. In the experiment, after a specific axial confining pressure was applied, a pore pressure supercharger was used to apply the osmotic pressure P_1 using aviation kerosene, which converged horizontally from the outer surface of the sample to the center hole and flowed out of the instrument through the hole in the lower head. The experimental samples before and after the experiment are illustrated in Figure 2.

The experimental rock samples were taken from the medium coarse sandstone in the roof of the 16-3 coal seam in the Mindong mining area. The sample dimensions were as follows: height $L = 100$ mm, section radius $r_e = 25$ mm, and inner drill hole radius $r_w = 4$ mm. The initial test confining pressure p_c was 10 MPa, and the initial axial pressure p_A was 10 MPa. The permeation medium was kerosene, with a dynamic viscosity $\mu = 2.5 \times 10^{-3}$ Pa.s and a radial flow $G_f = 342.86$ mm. According to the relationship between the kerosene flow rate and the time series, the flow velocity was calculated at a stable time.

3. Results

There are two main purposes of the experiment: to study the change rule of transverse permeability under the action of
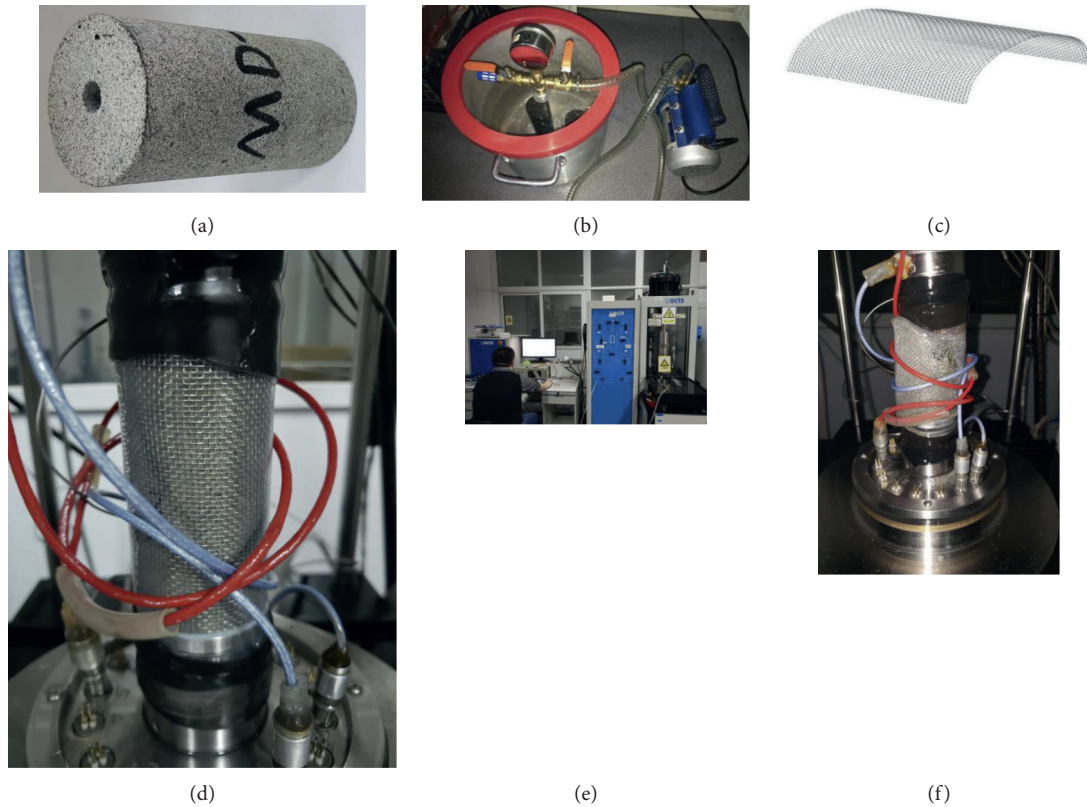
FIGURE 2: Diagram before and after the horizontal penetration test sample. (a) Pre-experiment (rock samples). (b) Pre-experiment (saturation device). (c) Pre-experiment (steel wire mesh). (d) Pre-experiment. (e) During experiment. (f) After completion of experiment.

mining abutment pressure in the standard environment and to provide a constitutive relation equation for the subsequent numerical construction of stress-seepage coupling and disaster prediction. According to the in situ experiments, the vertical stress and horizontal stress values of the distant rocks in the process of advancing on the working face were calculated according to the literature and the formula, and a lateral permeability test of the aquifer rocks under mining-induced stress was conducted. The test process considers the basic needs of the experiment. Each group of samples was tested three times.

To conveniently study the law of transverse permeability change and ensure the experimental effect, the unit of axial pressure increase was changed to 0.5 MPa and 0.25 MPa, and the unit of confining pressure decrease was changed to 1 MPa. The original rock stress was 10 MPa according to the axial pressure and the confining pressure, and the experimental process was programmed according to the loading path given in Table 1. When the flow rate was stable, the stress was changed to the next stress state in the loading path; this process continued until the rock was broken. The permeability of Darcy flow was calculated by substituting the final seepage flow results into Formula (2). The permeability

coefficient and measured strain data of MD-1 sandstone are presented in Table 1.

4. Discussion

In contrast to the variation rule of permeability in traditional total stress-strain, this study focuses on the variation rule of horizontal permeability of an aquifer under the influence of mining stress. The data in Table 1 consider the axial pressure as the abscissa and the permeability, confining pressure, and axial strain as the ordinate. A plot of the relationships is depicted in Figure 3.

As depicted in Figure 3, according to the stress change path of the aquifer in the process of coal seam advancement, MD-1 sandstone exhibits the correlation curve of horizontal permeability, axial pressure, and confining pressure, which are divided into compaction, multiple fluctuations, yield, and failure stages. To better explain the results, the key points in the figure are marked. Point A represents the original rock stress state; point B is the end point of the compaction stage; point C is the highest point in the middle stage; point D is the elastic-plastic boundary point; point E is the collapse failure point.

TABLE 1: MD-1 sandstone loading path and permeability statistics.

Axial compression/MPa	10.0	10.5	11	11.5	12.0	12.5	13.0	13.5	14
Confining pressure, MPa	9	9	9	9	9	9	9	9	9
Permeability, $\times 10^{-9}$ mm^2	1.54	0.672	0.879	0.825	0.915	0.641	0.795	0.882	0.672
Axial compression, MPa	14.5	15.0	15.5	16.0	16.5	17	17.5	18.0	18.5
Confining pressure, MPa	8	7	6	5	5	5	5	5	5
Permeability, $\times 10^{-9}$ mm^2	0.76	0.889	0.969	0.107	0.106	0.128	0.893	0.811	0.923
Axial compression, MPa	19.0	19.5	20	20.5	21.0	21.5	22.0		
Confining pressure, MPa	5	4	4	4	4	4	4		
Permeability, $\times 10^{-9}$ mm^2	0.084	1.12	0.977	0.943	1.12	1	200		
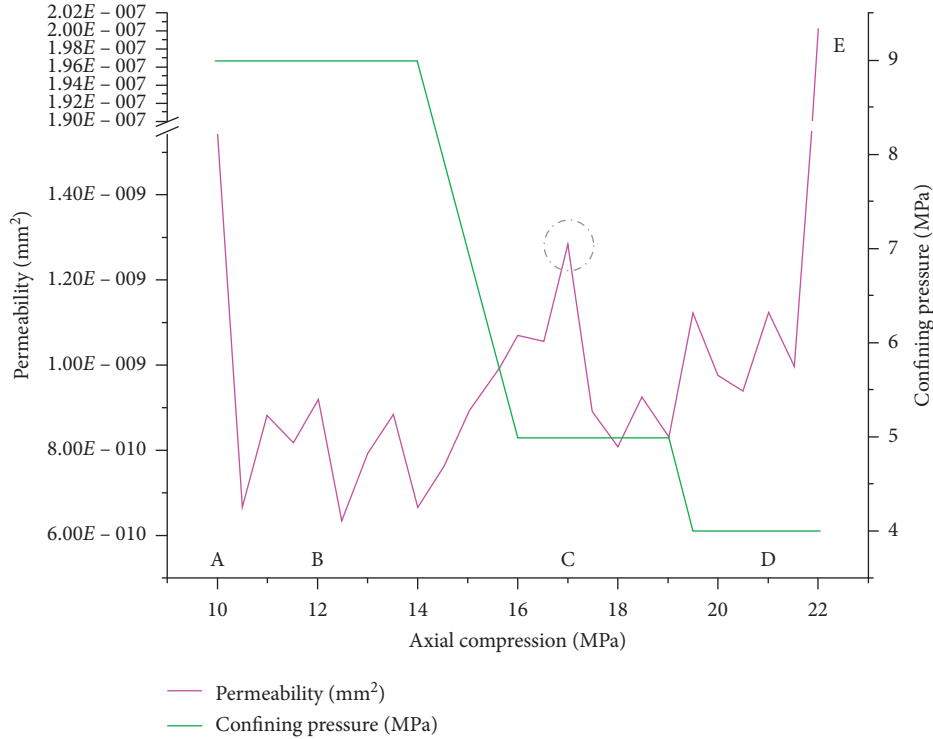
FIGURE 3: Relationship between permeability and stress state of MD-1 sandstone.

4.1. Separate Analysis of Different Sections.

In AB section, when the stress increased from the original rock stress by 0.5 MPa axial pressure, the permeability decreased sharply from 1.54×10^{-9} mm^2 to 6.72×10 mm^2, a decrease of 56%, mainly due to the high porosity of the rock specimen, a water-rich aquifer rock. Although the original rock stress has been loaded, the greater porosity is compacted under the additional pressure, producing a rapid nonlinear decline trend. This stage is the first compaction period of fracture [35].

In BC section, in the early stage, the confining pressure remains constant at 10 MPa. As the axial pressure continues to increase by 0.5 MPa each time, the permeability presents a small amplitude of vibration and does not show a significant increase or decrease trend. When some large fractures are compacted, the permeability of the rock decreases sharply; however, there exist a large number of parallel and vertical fractures on the cross-section of the rock in the axial direction. As the axial pressure increases, the fractures perpendicular to the axial direction are compressed, and the fractures parallel to the axial direction are opened, producing a random vibration. The later stage of the BC section represents the confining pressure unloading period, wherein the axial pressure is unchanged and the confining pressure is reduced. The permeability changes immediately and demonstrates an obvious increase, which is consistent with the reduction law of confining pressure [36]. Thus, the confining pressure plays a decisive role in the permeability change during this period, which includes the first shock period and the first growth period of permeability.

In the CD section, when the confining pressure remains at 5 MPa and the axial pressure continues to increase at a rate of 0.5 MPa each time, the permeability coefficient exhibits a small decrease and then increases sharply, reaching 1.28E-9 mm^2 at the highest point in the medium term, before rapidly decreasing and fluctuating, as shown in the AC and CD sections. Both these sections are stress change environments in which the confining pressure first remains
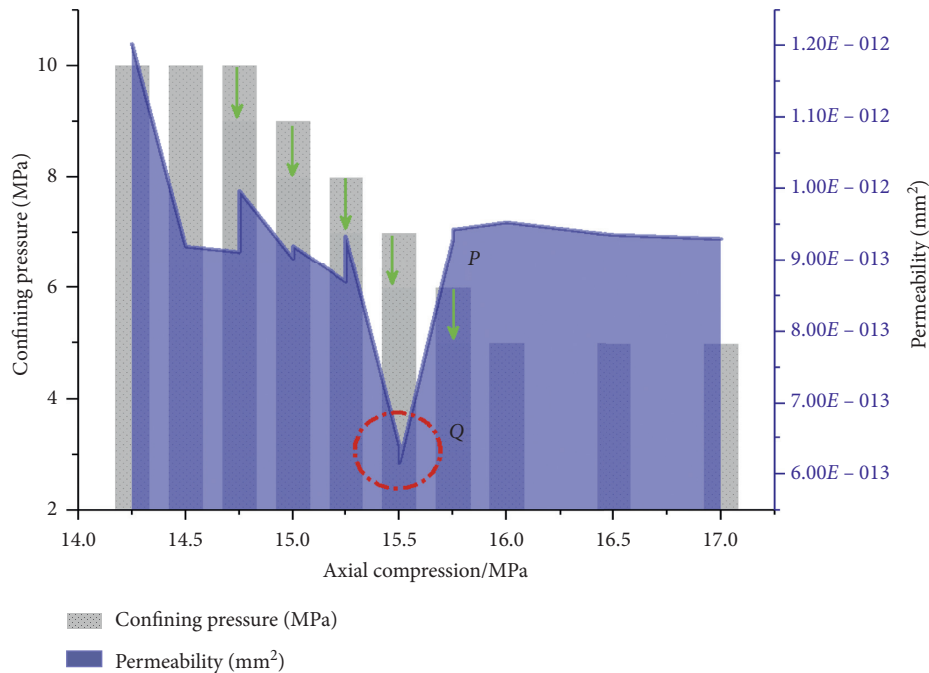
FIGURE 4: Relationship between permeability and stress state in section of nonactual changing load area in MD-2 sandstone.

unchanged and then decreases as the axial pressure gradually increases. The curve shows a high degree of similarity. The permeability first decreases rapidly and then fluctuates within a range. When the confining pressure decreases, the permeability increases immediately. After the confining pressure decreases significantly, the permeability undergoes a new equilibrium process [37]. Once the confining pressure is relieved, the compaction-fluctuation-axial pressure failure of the rock sample under axial pressure is observed. This stage includes the second compaction period, second shock period, and second growth period of permeability.

In the DE section, when the confining pressure remains at 4 MPa and the axial pressure continues to increase at a rate of 0.5 MPa each time, the permeability decreases twice in succession and then increases sharply to 2E-7 mm². The final permeability is 218 times the permeability in the original rock stress state; thus, the permeability change of the aquifer rock under the mining stress loading path is completed [38].

To better understand the influence of the confining pressure and axial pressure on the permeability of the rock stratum, MD-2 is added to a section of nonactual changing load area; that is, there is no such change trend in the actual process, but it only prolongs the unloading span and has no influence on the experimental results. In the loading process, axial pressure =14.75 MPa, confining pressure =10 MPa, confining pressure unloads at 1 MPa, and axial pressure increases at 0.25 MPa, both of which occur separately and alternately. This stress loading path does not exist in the actual stress state of the sample. The relationship between the final permeability and the stress state is depicted in Figure 4.

The green arrows in the figure indicate that an experiment of unloading 1 MPa under the same axial and confining pressures was conducted. The results indicate that the permeability increases four times during the five unloadings

of confining pressure and the permeability decreases once. As shown by the blue line in the figure, the horizontal permeability decreases slightly in the Q area. After five times of increasing 0.25 MPa under the same axial and confining pressures, the permeability decreases four times, as shown by the magenta line in the figure. A significant increase in lateral permeability occurs in the QP section, demonstrating that the increase in axial pressure tends to reduce the lateral permeability, mainly due to the effect of axial compression and compaction. The decrease in confining pressure tends to increase the lateral permeability, mainly due to the effect of confining pressure unloading and expansion. However, when the two factors act together, the differences in the action weight result in a wave of permeability. The influence weight of the confining pressure and axial pressure on the transverse permeability is related to the stress environment and the damage state of the rock sample. The crack direction and propagation scale of the internal fracture of the rock affect the transverse permeability within a small range.

The two sets of data reflect consistency at the macro level. The permeability coefficient exhibits a sharp decline and then stabilizes and fluctuates slightly, surging with the change in stress state. This process differs from the rule shown in the traditional sandstone total stress-strain relationship curve. First, the sandstone permeability exhibits a rapid downward trend in the small range of stress change at the initial stage of loading. Subsequently, the permeability is low with small fluctuations. Second, it exhibits a small wave peak value in the middle-later period of loading; however, the wave peak value is lower than the permeability under the original rock stress. Third, the rock undergoes a short plastic stage and a failure stage. The main reason why these three points differ from the traditional sandstone total stress-strain curve is that the coal seam roof strata simulated in this

experiment are under the influence of mining stress. The relationship between stress and permeability, different loading paths, and the experimental research subject is based on the lateral permeability of the rock and the different seepage directions. For the law of the experimental results, the pressure loading path was drawn according to the change trend of the confining pressure of No. III. In numerical simulation research, only the vertical pressure and permeability must be combined. The relationship between the horizontal permeability and the axial pressure of sandstone obtained from the experiment is divided into two sections; each section is fitted with a quadratic curve equation, which is used as the constitutive relation equation for later numerical simulation of the correlation between stress and permeability. This formula is not a theoretical derivation but has significance in practical engineering, particularly for mining areas under complex hydrogeological conditions. A more accurate constitutive equation has a better effect on the prediction of water inflow and the migration law of the groundwater flow field.

5. Conclusion

(1) Through the design of a hollow cylinder specimen, the original permeability testing experiment was changed from a vertical seepage mode of the permeability medium to a seepage mode from the outside to the inside. Furthermore, through the derivation transformation of the Darcy expression of the permeability measurement of the laminar fluid considering the influence of gravity, an accurate improved permeability calculation formula that is suitable for similar experimental conditions can be deduced. The measurement of horizontal permeability is a scientific reference.

(2) Through the improved test method, it was found that the sandstone specimen increased the axial pressure and decreased the confining pressure on the basis of the original rock stress. With the change in stress, the permeability first decreased sharply, then stabilized, fluctuated slightly, and increased sharply.

Data Availability

The datasets generated for this study are available from the corresponding author upon request.

Conflicts of Interest

The authors declare that they have no conflicts of interest.

Acknowledgments

References

[1] X. Qian, C. Xia, Y. Gui, X. Zhuang, and Q. Yu, "Study on flow regimes and seepage models through open rough-walled rock joints under high hydraulic gradient," *Hydrogeology Journal*, vol. 27, no. 4, pp. 1329–1343, 2019.

[2] Z.-Q. Yin, Z. X. Hu, Z. D. Wei et al., "Assessment of blasting-induced ground vibration in an open-pit mine under different rock properties," *Advances in Civil Engineering*, vol. 2018, Article ID 4603687, 10 pages, 2018.

[3] Z. Yin, W. Chen, H. Hao et al., "Dynamic compressive test of gas-containing coal using a modified split Hopkinson pressure bar system," *Rock Mechanics and Rock Engineering*, vol. 53, no. 2, pp. 815–829, 2020.

[4] Z. Wen, S. Jing, Y. Jiang et al., "of the fracture law of overlying strata under water based on the flow-stress-damage model," *Geofluids*, vol. 201912 pages, 2019.

[5] F. Tian, J. Yan, X. Li, and S. Luo, "A peak-strength strain energy storage index for rock burst proneness of rock materials," *International Journal of Rock Mechanics and Mining Sciences*, vol. 117, pp. 76–89, 2019.

[6] H. Zhang, M. Tu, H. Cheng, and Y. Tang, "Breaking mechanism and control technology of sandstone straight roof in thin bedrock stope," *International Journal of Mining Science and Technology*, vol. 30, no. 2, pp. 259–263, 2020.

[7] D. T. Snow, "Rock fracture spacings, openings and porosities," *Journal of the Soil Mechanics & Foundations Division*, vol. 94, no. 1, pp. 73–91, 1968.

[8] M. Oda, "An equivalent continuum model for coupled stress and fluid flow analysis in jointed rock masses," *Water Resources Research*, vol. 22, no. 13, pp. 1845–1856, 1986.

[9] M. Oda, "A method for evaluating the effect of crack geometry on the mechanical behavior of cracked rock masses," *Mechanics of Materials*, vol. 2, no. 2, pp. 163–171, 1983.

[10] M. Oda, Y. Hatsuyama, and Y. Ohnishi, "Numerical experiments on permeability tensor and its application to jointed granite at Stripa Mine, Sweden," *Journal of Geophysical Research Solid Earth*, vol. 92, no. 8, 1987.

[11] N. Barton, K. S. Bandis, and K. Bakhtar, "Strength, deformation and conductivity coupling of rock joints," *International Journal of Rock Mechanics and Mining Sciences & Geomechanics Abstracts*, vol. 22, no. 3, pp. 121–140, 1985.

[12] V. Reichenberger, H. Jakobs, P. Bastian, and R. Helmig, "A mixed-dimensional finite volume method for two-phase flow in fractured porous media," *Advances in Water Resources*, vol. 29, no. 7, pp. 1020–1036, 2006.

[13] H. Hoteit and A. Firoozabadi, "An efficient numerical model for incompressible two-phase flow in fractured media," *Advances in Water Resources*, vol. 31, no. 6, pp. 891–905, 2008.

[14] R. Helmig, B. Flemisch, M. Wolff, A. Ebigbo, and H. Class, "Model coupling for multiphase flow in porous media," *Advances in Water Resources*, vol. 51, pp. 52–66, 2013.

[15] A. Peratta and V. Popov, "A new scheme for numerical modelling of flow and transport processes in 3D fractured porous media," *Advances in Water Resources*, vol. 29, no. 1, pp. 42–61, 2006.

[16] J. Zhao, L. Yin, and W. Guo, "Stress-seepage coupling of cataclastic rock masses based on digital image technologies," *Rock Mechanics and Rock Engineering*, vol. 51, no. 8, pp. 2355–2372, 2018.

[17] C. Wang and Q.-Y. Zhang, "Study of the crack propagation model under seepage-stress coupling based on XFEM,"

Geotechnical and Geological Engineering, vol. 35, no. 5, pp. 2433–2444, 2017.

[18] H. Gui, H. Qiu, W. Qiu, S. Tong, and H. Zhang, "Overview of goaf water hazards control in China coalmines," *Arabian Journal of Geosciences*, vol. 11, no. 3, p. 49, 2018.

[19] J. Yi, H. L. Xing, J. J. Wang, and Z. H. Xia, Y. Jing, "Pore-scale study of the effects of surface roughness on relative permeability of rock fractures using lattice Boltzmann method," *Chemical Engineering Science*, p. 209, Article ID 115178, 2019.

[20] W. J. Xiao, D. M. . Zhang, and X. J. Wang, "Experimental study on progressive failure process and permeability characteristis of red sandstone under seepage pressure," *Engineering Geology*, vol. 265, Article ID 105406, 2020.

[21] Q. G. Tan, J. Y. Li, Y. L. . Kang, X. Zhang et al., "Changes in pore structures and porosity-permeability evolution of saline-lacustrine carbonate reservoir triggered by fresh water-rock reaction," *Journal of Hydrology*, vol. 580, Article ID 124375, 2019.

[22] F. M. R. Ferfera, J. P. Sarda, M. Boutéca, and O. Vincké, "Experimental study of monophasic permeability changes under various stress paths," *International Journal of Rock Mechanics and Mining Sciences*, vol. 34, no. 3-4, 370 pages, Article ID 2147483647, 1997.

[23] X. Chen, J. Yu, C. a. Tang, H. Li, and S. Wang, "Experimental and numerical investigation of permeability evolution with damage of sandstone under triaxial compression," *Rock Mechanics and Rock Engineering*, vol. 50, no. 6, pp. 1529–1549, 2017.

[24] S.-Q. Yang, P. Xu, and Y.-H. Huang, "Experimental investigation on triaxial mechanical and permeability behavior of sandstone after exposure to different high temperature treatments," *Geothermics*, vol. 69, pp. 93–109, 2017.

[25] P. F. Shan and X. P. Lai, "Numerical simulation of the fluid-solid coupling process during the failure of a fractured coal-rock mass based on the regional geostress," *Transport in Porous Media*, vol. 124, no. 3, pp. 1061–1079, 2018.

[26] B. Sheikh and A. Pak, "Numerical investigation of the effects of porosity and tortuosity on soil permeability using coupled three-dimensional discrete-element method and lattice Boltzmann method," *Physical Review E*, vol. 91, no. 5, Article ID 053301, 2015.

[27] W. Guo, J. Zhao, and L. Yin, "Simulating research on pressure distribution of floor pore water based on fluid-solid coupling," *Arabian Journal of Geosciences*, vol. 10, p. 5, 2017.

[28] J. Zhang, F. J. Biao, S. C. Zhang, and X. X. Wang, "A numerical study on interference between different layers for a layer-by-layer hydraulic fracture procedure," *Petroleum Science and Technology*, vol. 32, no. 12, pp. 1512–1519, 2014.

[29] W. T. Ding and W. J. Xu, "Study on the multiphase fluid-solid interaction in granular materials based on an LBM-DEM coupled method," *Powder Technology*, vol. 335, pp. 301–314, Article ID S0032591018303590, 2018.

[30] J. Q. Shi and S. Durucan, "Modelling laboratory horizontal stress and coal permeability data using S&D permeability model," *International Journal of Coal Geology*, vol. 131, pp. 172–176, 2014.

[31] E. P. Weeks, "Determining the ratio of horizontal to vertical permeability by aquifer-test analysis," *Water Resources Research*, vol. 5, no. 1, pp. 196–214, 1969.

[32] A. Wang and V. S. Yakushev, "Analytical model of the linear inflow to a horizontal well with hydraulic fractures in low-permeability reservoirs," *Fluid Dynamics*, vol. 52, no. 3, pp. 351–362, 2017.

[33] D. L. Brown, *Multiscale methods for fluid-structure interaction with applications to deformable porous media*, Ph.D. thesis, Dissertations & Theses-Gradworks, Cincinnati, USA, 2013.

[34] S. A. Mathias, S. Nielsen, and R. L. Ward, "Storage coefficients and permeability functions for coal-bed methane production under uniaxial strain conditions," *Transport in Porous Media*, vol. 130, no. 2, pp. 627–636, 2019.

[35] A. A. DiGiovanni, D. J. Fredrich, W. A. Holcomb, and W. Olsson, "Microscale damage evolution in compacting sandstone," *Geological Society, London, Special Publications*, vol. 289, no. 1, pp. 89–103, 2007.

[36] Y. L. Zhao, J. Z. Tang, Y. Chen et al., "Hydromechanical coupling tests for mechanical and permeability characteristics of fractured limestone in complete stress-strain process," *Environmental Earth Sciences*, vol. 76, no. 1, pp. 1–18, 2017.

[37] Y. Zhao, L. Zhang, W. Wang, C. Pu, W. Wan, and J. Tang, "Cracking and stress-strain behavior of rock-like material containing two flaws under uniaxial compression," *Rock Mechanics and Rock Engineering*, vol. 49, no. 7, pp. 2665–2687, 2016.

[38] L. Wang, J. F. Liu, J. L. Pei, H. N. Xu, and Y. Bian, "Mechanical and permeability characteristics of rock under hydro-mechanical coupling conditions," *Environmental Earth Sciences*, vol. 73, no. 10, pp. 5987–5996, 2015.

Research Article

A Discussion of Stability and Engineering Verification of Thin Immediate Roof under Uniform Load of the Rectangular Coal Roadway

Linsheng Gao,[1,2] **Yueping Wang** [2] **Er-hui Zhang,**[2] **Liang Cheng,**[3] **and Rui Peng** [2]

[1]*School of Mineral Engineering, Xi'an University of Science and Technology, Xi'an, Shanxi 710054, China*
[2]*School of Safety Engineering, North China Institute of Science and Technology, Beijing 101601, China*
[3]*Zhongshan Haofa Real Estate Development Co., Ltd., Zhongshan, Guangzhou 528400, China*

Correspondence should be addressed to Yueping Wang; ypwang@ncist.edu.cn

Roadway roof is a key factor in roadway stability. At present, the analysis of roof stability is mainly based on numerical calculations and field measurements with a relatively weak theoretical basis and inadequate research studies on the loading mechanism of the roof. In this paper, a mechanical calculation model of immediate direct roof under uniform load of rectangular coal roadway is established. The stress distribution and roof subsidence in the roof are calculated theoretically and verified by the numerical calculation, physical tests, and engineering applications. Based on the classical beam solution theory, the stress distribution and sinking of the thin immediate roof under uniform load are obtained and verified by numerical calculations. The results are highly consistent. Two types of thin direct roof failure under uniform load are analyzed: the failure of the normal cross section caused by the bottom tensile stress and the failure of the inclined section caused by the combined effect of the tensile stress in the abdominal area and compressive stress. The stability of thin immediate roof under uniform load of the rectangular coal roadway was tested in 1905s mining roadway of Great Wall Number #3 coal excavation field. This research can further fill in blanks of the loading mechanism of the roadway roof and provide theoretical and pragmatic values to control the roadway pressure and rock stratum as well as the scientific references to the design of the anchor bolt supporting system.

1. Introduction

In coal mining, the stability of the roadway roof is one of the keys to ensure the safe and efficient production of the mine. However, the existing researches fail to provide a clear stability mechanism and sufficient theories about the supporting system for the roadway roof [1–5]. In the initial study of the roadway surrounding rock stability, the self-supporting capacity of the surrounding rock was often neglected. The bolt support plays a role of suspension or provides support resistance to the surface of the roadway [1, 6, 7]. With the development of anchor bolt technology, people gradually recognize that the pressure of the roadway surrounding rock has been mainly born by the surrounding rock itself with the surrounding rock as the primary load carrier and the supporting system as the secondary load carrier [8, 9]. The

bearing capacity of the surrounding rock of the roadway was firstly proposed in the Terzaghi theory [10]. The Protodyakonov theory [11] suggests that the pressure imposed on the supporting system originated from the weight of loose rocks in the collapse arch of the surrounding rock. The Austrian method [12] theory indicates that the self-bearing capacity of the surrounding rock plays a dominating role in achieving the stability of the surrounding rock. The core idea of the Austrian method lies in making use of the self-bearing capacity of the surrounding rock to support the roadway surrounding rock, forming a combined support system along with the external supporting structure through focusing on the self-bearing capacity of the surrounding rock [13].

As the researches regarding the stability of the roadway surrounding rock develop further, people are aware of

certain load bearing structure included in the roadway surrounding rock, which benefits the optimization of the roadway surrounding rock [14]. Salamon et al. proposed the energy supporting theory, suggesting that supporting structure and surrounding rock of a roadway interact with each other and deformed together. Man-chu [15] conducted the discontinuous deformation analysis (DDA) and found out that the alternate layout of the high preloaded long and short anchor bolts was critical to achieve the supporting structure with high stability. In addition, the anchor bolts in radial pattern can achieve a better control of the roadway roof than those in vertical pattern. Chen et al. [16] believe that the surrounding rock has substantial self-bearing capacity, indicating the limited supporting role of the external supporting structure. Many factors can contribute to the pressure of the surrounding rock including the embedded depth of the tunnel, the tunnel sizes and shapes, the physicomechanical properties, and the flexibilities of the supporting system. Zhao et al. [17] analyze the constraint of the anchor bolts to the expandability of the tunnel rocks through analyzing the interaction between the rock mass dilatancy and bolt support in underground engineering and suggest that the anchor bolt supporting system can effectively improve the pressure environment adjacent to the tunnel and inhibit the expansion of highly pressurized rocks in the area with low pressure.

Improvements are needed in the present researches. All research results fail to include the strength parameters of the coal body, which tends to impact the load bearing capacity of the surrounding rock. Some parameters cannot be obtained, resulting in the gap between the theories and the field

applications. Without the quantitate versification, the accuracy is questionable. In this paper, a mechanical calculation model of thin direct roof under uniform load of rectangular coal roadway is established to analyze the mechanism behind the roof collapse. In addition, the results were applied to the field for verification.

2. Stress Theoretical Calculation of the Thin Immediate Roof under Uniform Load of Rectangular Coal Roadway

2.1. Theoretical Calculation Model. The thin immediate roof of the roadway, as the study object, bears the evenly distributed load from the top, which often originates from the weight of the top rock layer, with the lateral horizontal stresses at both sides. The roof also bears the vertical stress and shear stress imposed by the coal body. The stress distribution firstly increased and decreased subsequently from the roadway center to the sides, which is equivalent to the bearing loads and stresses mentioned in Section 3, with different orientations [18]. The thin immediate roof under uniform load is considered as a beam structure under the plane stresses, as demonstrated in Figure 1.

The load imposed on the thin immediate roof by the coal body can be calculated based on equation (1). However, compared with the coordinates in Figure 1, the coordinates in Figure 2 moved by $b/2$ in length to the left, which results in a new equation to calculate the load imposed on the thin immediate roof by the coal body, provided as follows [19]:

$$\sigma_y = \left[\frac{C_0}{\tan \varphi_0} + \left(\frac{1 + \sin \varphi}{1 - \sin \varphi} \right) P_x + \frac{2C \cos \varphi}{1 - \sin \varphi} \right] \exp \left[\frac{2 \tan \varphi_0 (1 + \sin \varphi)}{m(1 - \sin \varphi)} x \right] - \frac{C_0}{\tan \varphi_0},$$

$$\tau_{xy} = \left[C_0 + \left(\frac{1 + \sin \varphi}{1 - \sin \varphi} \right) P_x \tan \varphi_0 + \frac{2C \cos \varphi \tan \varphi_0}{1 - \sin \varphi} \right] \exp \left[\frac{2 \tan \varphi_0 (1 + \sin \varphi)}{m(1 - \sin \varphi)} x \right],$$

$$(1)$$

$$\sigma_y = \begin{cases} 0, & \left(0 \leq x < \frac{b}{2} \right), \\ K_1 \exp \left[K_2 \left(x - \frac{b}{2} \right) \right] - \frac{C_0}{\tan \varphi_0}, & \left(\frac{b}{2} \leq x \leq x_0 \right), \end{cases}$$

$$\sigma_{ye} = (k_0 - 1) \gamma H \exp \left[-\alpha (x - x_0) \right] + \gamma H; \quad (x > x_0),$$

$$(2)$$

where $x_0 = x_s + b/2$; $K_1 = C_0/\tan \varphi_0 + (1 + \sin \varphi/1 - \sin \varphi) P_x + 2C \cos \varphi/1 - \sin \varphi$; and $K_2 = 2 \tan \varphi_0 (1 + \sin \varphi)/ m(1 - \sin \varphi)$.

2.2. Calculation

2.2.1. Load Intensity, Shear Force, and Moment of the Thin Immediate Roof under Uniform Load of Rectangular Coal Roadway. In contrast with the classic beam theory, the thin immediate roof under uniform load bears not only the

vertical load but also the shear stress load at the bottom due to the lateral coal body [20]. Figure 2 demonstrates a magnified section at x point from the original point, which was selected from the beam shown in Figure 1. F_q and M_q refer to shear force of the left cross section and the moment, respectively. When x was increased by dx, F_q and M_q were increased by dF_q and dM_q accordingly.

All internal forces included in the selected section are taken to be positive. Following $\sum F_q = 0$ and $\sum M_q = 0$, the following equation is obtained:
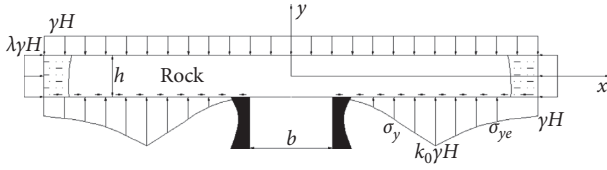
FIGURE 1: Mechanical model of thin immediate roof.

$$F - (F + dF) + (\sigma_y - \gamma H)dx = 0,$$

$$-M + (M + dM) - Fdx - (\sigma_y - \gamma H)dx\frac{dx}{2} + \tau_{xy}\frac{h}{2}dx = 0,$$

(3)

where M is the center moment of the thin immediate roof, N·m and h is the thickness of the thin immediate roof m.

After skipping the high-order trace $(\sigma_y - \gamma H)dx\,(dx/2)$, the internal forces can be expressed as follows:

$$\frac{dF}{dx} = \sigma_y - \gamma H,$$

(4)

$$\frac{dM}{dx} = F - \tau_{xy}\frac{h}{2}.$$
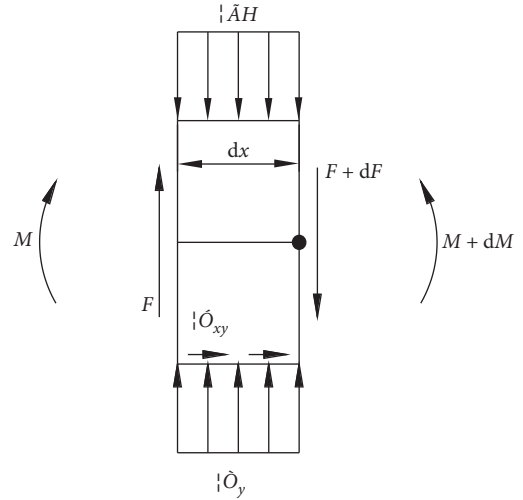
FIGURE 2: The model of the relationship of internal forces of thin immediate roof.

2.2.2. *Horizontal Stress of the Thin Immediate Roof under Uniform Load of Rectangular Coal Roadway.* According to equation (4), the internal shear force of the thin immediate roof under uniform load can be expressed as follows:

$$F = \begin{cases} -\gamma H x, & \left(0 \leq x < \dfrac{b}{2}\right), \\[2em] \dfrac{K_1}{K_2}\left\{\exp\left[K_2\left(x - \dfrac{b}{2}\right)\right] - \exp\left[K_2\left(x_0 - \dfrac{b}{2}\right)\right]\right\} \\[1em] \quad -\left(\dfrac{C_0}{\tan\varphi_0} + \gamma H\right)(x - x_0) - \dfrac{(k_0 - 1)\gamma H}{\alpha}, & \left(\dfrac{b}{2} \leq x \leq x_0\right), \\[2em] -\dfrac{(k_0 - 1)\gamma H}{\alpha}\exp[-\alpha(x - x_0)], & (x > x_0), \end{cases}$$

(5)

where K_1 and K_2 are parameters to be determined.

$$
M = \begin{cases}
-\gamma H \dfrac{x^2}{2} + K_3, & \left(0 \le x < \dfrac{b}{2}\right), \\[2ex]
\left(\dfrac{K_1}{K_2^2} + \dfrac{K_1 h \tan \varphi_0}{2K_2}\right) \exp\left[K_2\left(x - \dfrac{b}{2}\right)\right] - \dfrac{K_1}{K_2}\exp\left[K_2\left(x_0 - \dfrac{b}{2}\right)\right]x \\[2ex]
\quad - \left(\dfrac{C_0}{\tan \varphi_0} + \gamma H\right)\left(\dfrac{x^2}{2} - xx_0\right) - \dfrac{(k_0 - 1)\gamma H}{\alpha}x + K_4, & \left(\dfrac{b}{2} \le x \le x_0\right), \\[2ex]
\dfrac{(k_0 - 1)\gamma H}{\alpha^2}\exp\left[-\alpha(x - x_0)\right] - \dfrac{K_1 h \tan \varphi_0}{2K_2}\exp\left[K_2\left(-x - \dfrac{b}{2} + 2x_0\right)\right], & (x > x_0),
\end{cases}
\tag{6}
$$

where K_3 and K_4 are parameters to be determined.

$$
K_3 = K_4 + \frac{K_1}{K_2^2} + \frac{K_1 h \tan \varphi_0}{2K_2} - \frac{bK_1}{2K_2}\exp\left[K_2\left(x_0 - \frac{b}{2}\right)\right] - \frac{C_0 b^2}{8\tan\varphi_0} + \frac{bx_0}{2}\left(\frac{C_0}{\tan\varphi_0} + \gamma H\right) - \frac{b(k_0 - 1)\gamma H}{2\alpha},
$$

$$
K_4 = \frac{(k_0 - 1)\gamma H}{\alpha}\left(\frac{1}{\alpha} + x_0\right) - \left(\frac{K_1}{K_2^2} + \frac{K_1 h \tan \varphi_0}{K_2}\right)\exp\left[K_2\left(x_0 - \frac{b}{2}\right)\right] + \frac{K_1}{K_2}\exp\left[K_2\left(x_0 - \frac{b}{2}\right)\right]x_0 - \frac{x_0^2}{2}\left(\frac{C_0}{\tan\varphi_0} + \gamma H\right).
\tag{7}
$$

The horizontal stress of the thin immediate roof at the roadway width is obtained as follows:

$$
\sigma_{qt} = \frac{K_3 - \gamma H(x^2/2)}{W} - \frac{2K_1}{hK_2}\tan\varphi_0\exp\left[K_2\left(x_0 - \frac{b}{2}\right)\right] + \frac{K_1}{hK_2}\tan\varphi_0.
\tag{8}
$$

Considering the impact of the lateral loads on the thin immediate roof, the horizontal stress is calculated as follows:

$$
\sigma_{qt} = \frac{K_3 - \gamma H(x^2/2)}{W} - \frac{2K_1}{hK_2}\tan\varphi_0\exp\left[K_2\left(x_0 - \frac{b}{2}\right)\right]
$$
$$
+ \frac{K_1}{hK_2}\tan\varphi_0 + \lambda\gamma H.
\tag{9}
$$

2.2.3. Deposition of the Thin Immediate Roof under Uniform Load of Rectangular Coal Roadway.

The deposition of the thin immediate roof at the roadway width satisfies the following equation:

$$
EIw'' = Mdx,
\tag{10}
$$

where w is the deflection of the thin immediate roof (the deposition), m; E is the elastic modulus of the thin immediate roof, GPa; and I is the moment of inertia, m_4.

Integrating equation (5), the bending moment of the thin immediate roof under uniform load is obtained as follows:

The moments of the thin immediate roof continue when $x = b/2$ and $x = x_0$. Following equation (6), K_3 and K_4 are calculated as follows:

The thin immediate roof adopts a symmetric structure with a zero-center tangle. The deposition of the roof is calculated based on equation (10) as follows:

$$
EIw = \iint Mdx + K_5,
\tag{11}
$$

where K_5 is a parameter to be determined.

This problem is an infinite statically indeterminate problem, requiring the determination of the vertical displacement of the coal bodies on both sides before the solution. To simplify the calculation, assuming that the deformation somewhere in the coal body is zero as the deformation coordination condition, the following equation is obtained:

$$
K_5 = -\frac{x_q^2}{2}K_3 + \gamma H \frac{x_q^4}{24},
\tag{12}
$$

where x_q is the point where the deformation is assumed at zero in the plastic zone.

x_q depends on the width of the plastic zone within the coal seam. When the hardness of the coal is high, a relatively smaller value of x_q is selected, which is equivalent to the half of the roadway width. In case of low hardness, the point with zero deformation migrates to the deep area of the coal seam, resulting in the following equation:

$$x_q = \frac{2}{b} + \frac{m}{2\tan\varphi_0}\left(\frac{1-\sin\varphi}{1+\sin\varphi}\right)\ln\left[\frac{\eta\gamma H + (C_0/\tan\varphi_0)}{C_0/\tan\varphi_0 + (1+\sin\varphi/1-\sin\varphi)P_x + 2C\cos\varphi/1-\sin\varphi}\right], \quad (13)$$

where η is a parameter to be determined.

The deposition of the roof is calculated as follows:

$$w = \frac{x^2 - x_q^2}{2EI}K_3 + \gamma H\frac{x_q^4 - x^4}{24EI}. \quad (14)$$

Under the panel strain, the deposition of the roof is calculated as follows:

$$w = \frac{1-\mu^2}{2EI}K_3\left(x^2 - x_q^2\right) + \frac{1-\mu^2}{24EI}\gamma H\left(x_q^4 - x^4\right). \quad (15)$$

3. Numerical Calculations and Verification of the Stress of the Thin Immediate Roof under Uniform Load of Rectangular Coal Roadway

A model was established based on FLAC3D, whose dimension is $100 \times 30 \times 1$ m. The dimension of the road is 4.8×4 m with a 3 m roof and 23 m bottom, constituting a total of 36,000 units, as shown in Figure 3. The top, bottom, left, and right sides of the model are fixed with an evenly distributed load of 2.5 MPa at the top, excluding the weight of the coal seam.

The vertical stress and horizontal stress of the thin immediate roof under the evenly distributed load are demonstrated in Figure 4.

As shown in Figure 4, the peak coefficient of lateral support stress was 1.75 with a plastic zone width at 3.72 m through the theoretical calculation. In the case of 5.8 m thickness of the think immediate roof, the numerical calculation suggested that the vertical stress peak coefficient of the thin immediate roof was 1.64, while the theoretical calculation indicated a plastic zone width at 3.46 m. The theoretical and numerical calculations were compared and are illustrated in Figure 5.

As demonstrated in Figure 4, the horizontal stress of the thin immediate roof is consistent, including the theoretically calculated result and the numerically calculated result at 5.8 m thickness of the thin immediate roof. The maximum difference was limited to 0.67 MPa. However, in the case of 3 m thickness of the thin immediate roof, the maximum difference was as high as 5.2 MPa.

The relatively large difference at 3 m thickness of thin immediate roof is caused by the selected value of α. In the theoretical calculation, α was obtained based on the counterbalance of the lateral vertical stress of the contact surface, whose curve was divided into two sections: positive exponential function on the left and negative exponential function on the right. However, the numerical calculation suggests that the aforementioned curve was followed at 5.8 m thickness of the thin immediate roof. When the thickness of the thin immediate roof was 3 m, fluctuation was observed around the stress peak. The positive lateral vertical stress was selected. Figure 6 provides the detailed distribution of the lateral vertical stress.

According to Figure 6, when the thickness of the thin immediate roof was 3 m, fluctuation was observed around the stress peak. The stress fluctuation resulted in the tolerances of the calculation of parameter α, leading to the tolerance of the lateral vertical stress distribution. To resolve this issue, a correction factor was introduced. The comparison of the corrected result and the numerical calculation was conducted and is illustrated in Figure 7.

According to Figure 7, at the correction factor of 1.5, two calculations yielded the closest results. Therefore, for the thin immediate roof, the tolerance caused by the fluctuation of the vertical stress needs to be corrected for obtaining an accurate result.

4. Analysis of the Collapse Mechanism of the Thin Immediate Roof under Uniform Load of Rectangular Coal Roadway

A thinner immediate roof under uniform load leads to a higher possibility of normal section failure. On the other hand, a thicker immediate roof under uniform load leads to a higher possibility of an oblique section failure. The following analysis is conducted from two perspectives including the normal section and the oblique section.

4.1. Analysis of the Normal Section Collapse Mechanism of the Thin Immediate Roof under Uniform Load of Rectangular Coal Roadway

4.1.1. Forces on the Normal Section of the Thin Immediate Roof under Uniform Load. When the load imposed on the thin immediate roof under uniform load is relatively small, the internal moment is relatively small in the thin immediate roof, whose forces are similar to the homogeneous elastomer beams. The stress distribution of the pressurized zone and tensile zone forms a triangle shape, as demonstrated in Figure 8(a).

When the load imposed on the thin immediate roof under uniform load increases, the stress distribution of the tensile zone tends to bend instead of staying as a straight line, which is due to a higher compression capacity of the rock than the tensile capacity. The curve of the tensile zone stress distribution develops toward the neutral axis. When the moment reaches the strain limit of the tensile zone boundary, the normal section will break, as demonstrated in Figure 8(b). At this moment, the stress distribution of the pressurized zone is still close to a triangle shape, while the stress distribution of the tensile zone has developed into a curve.

The key to preventing the failure of the normal section of the thin immediate roof lies in controlling the stratum strain at the bottom. The truss structure or anchor bolts (cables) along with the steel belts can be used. The ideal situation is to ensure that the thin immediate roof experiences failures
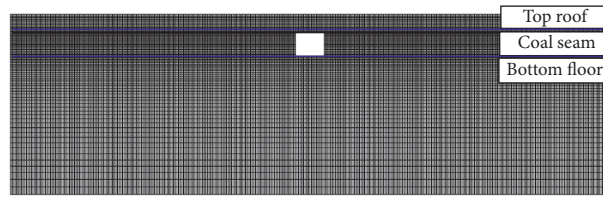
FIGURE 3: Numerical model of stress of thin immediate roof under uniform load.

(a)

(b)
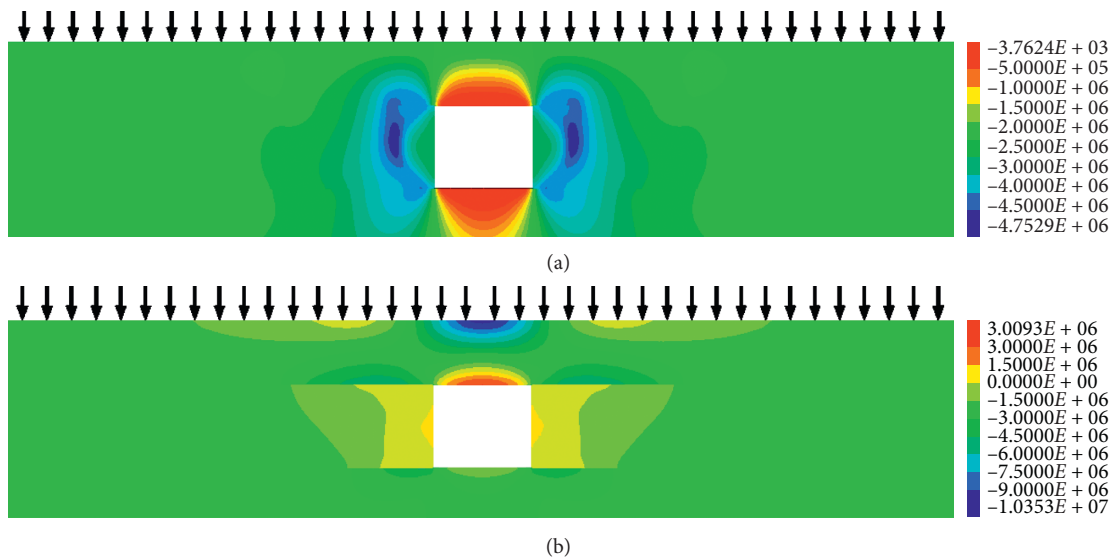
FIGURE 4: The stress of thin immediate roof under uniform load. (a) The cloud diagram of the vertical stress. (b) The cloud diagram of the horizontal stress.
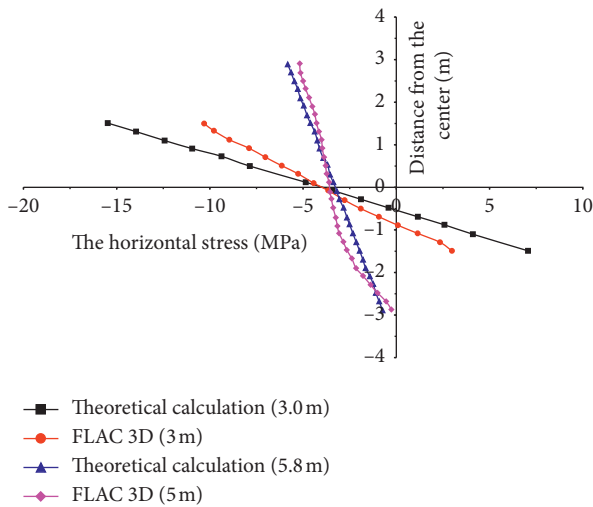
FIGURE 5: The horizontal stress at the center of thin immediate roof under uniform load.
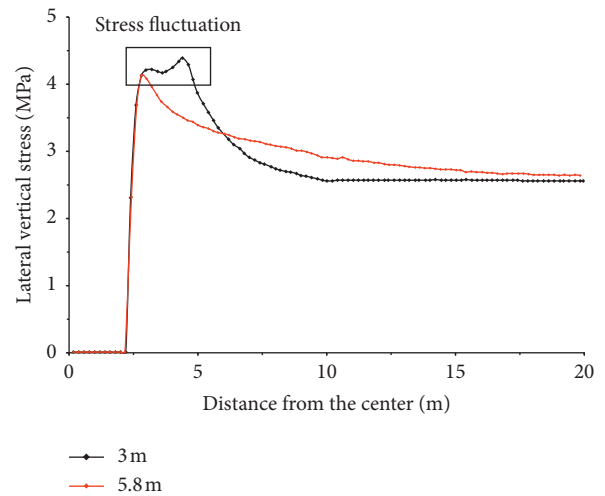
FIGURE 6: The lateral vertical stress.

simultaneously in the pressurized zone and tensile zone, making full use of the self-bearing capacity of the rock stratum. When cracks develop at the lower section of the thin immediate roof, the load born by the tensile zone is transferred to the tie rods or steel belts (reference to the steel bar mechanism in the steer bar and concrete beam construction; and the tie rods in the truss structure or the steel belts and ladder beams in the standard anchor bolts are equivalent to the tensile reinforcement steel bars in the steel bar and concrete structure). The tie rods or steel belts tend to bear higher forces. Meanwhile, the neutral axis moves upward, transferring the tensile force to the tie rods and steel
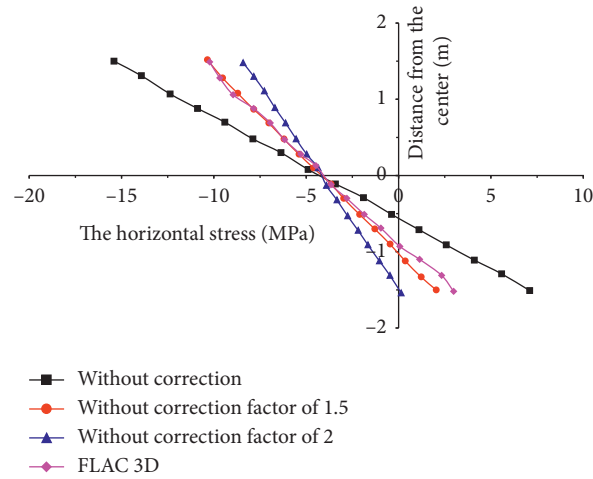
Figure 7: The corrected horizontal stress distribution at the center of thin immediate roof under uniform load.

(a)

(b)

(c)

(d)
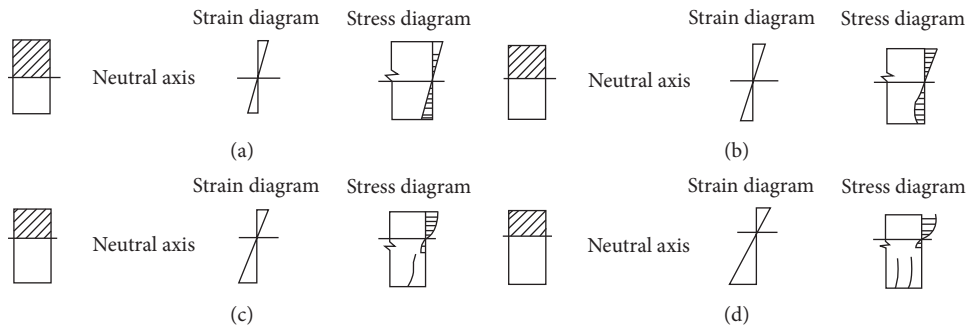
Figure 8: The mechanical characteristic of normal section of thin immediate roof under uniform load.

(a)

(b)

(c)
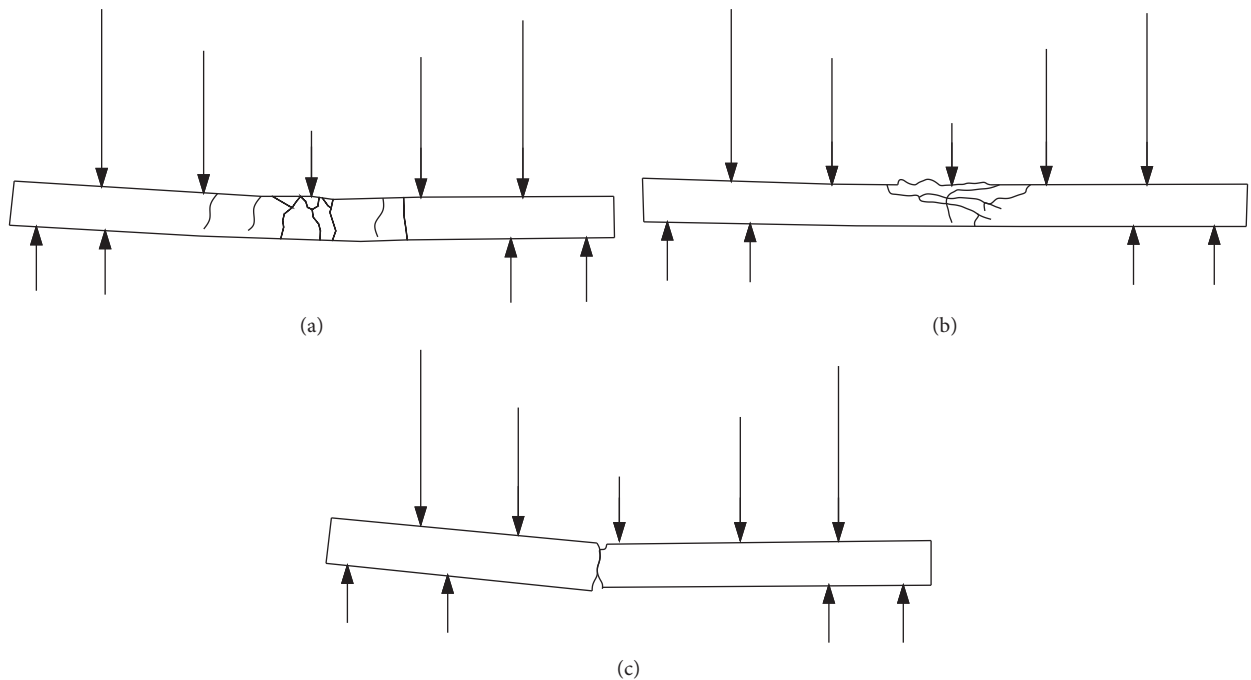
Figure 9: The failure form of normal section of thin immediate roof under uniform load. (a) The under-reinforced beam failure. (b) The over-reinforced beam failure. (c) The low-reinforced beam failure.
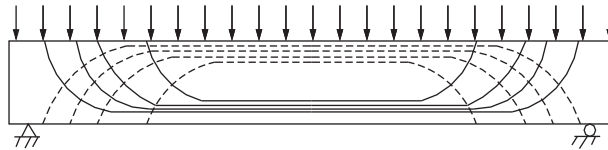
FIGURE 10: The principal stress trajectory of thin immediate roof under uniform load.
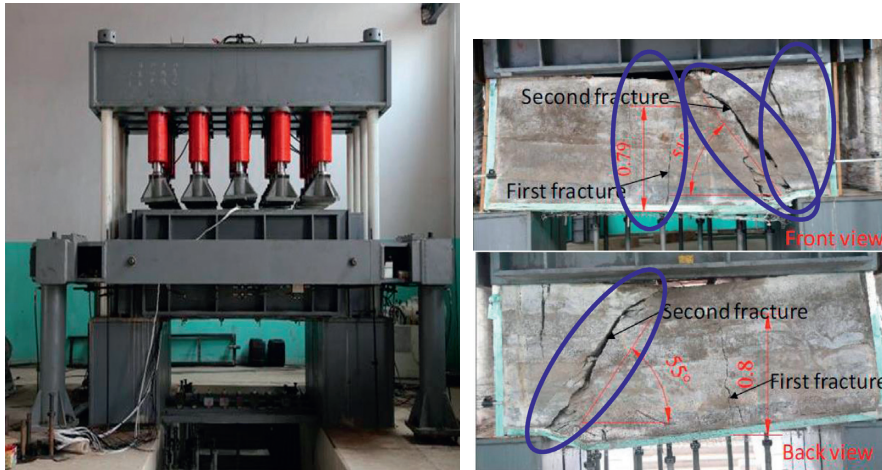
(a)
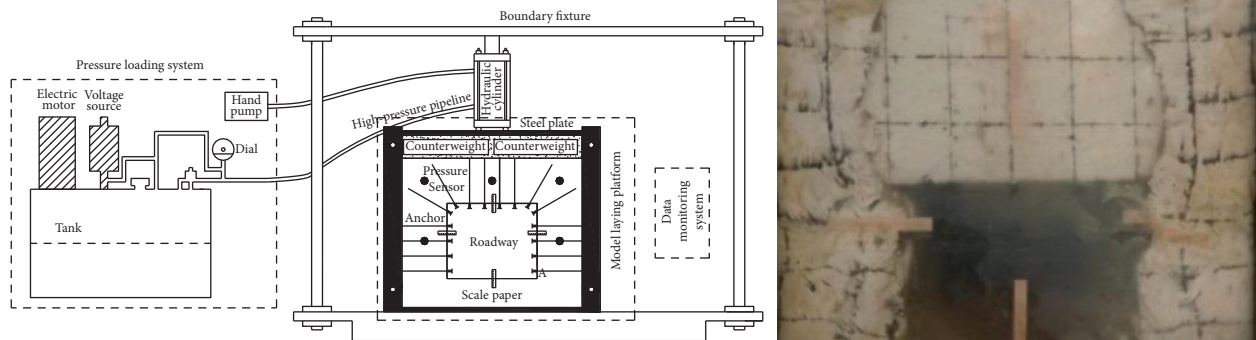
(b)

Research on key technology of
surrounding rock control of 1905S
backstoping face in Changcheng
No.3 Mine
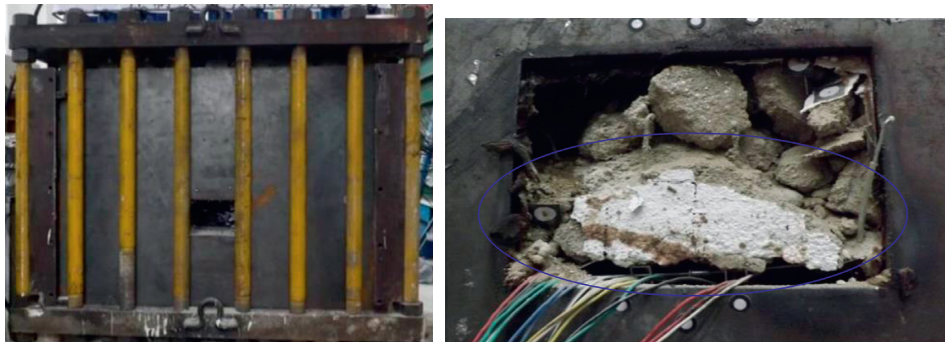
(c)

FIGURE 11: The experiment validation of oblique section failure of thin immediate roof under uniform load. (a) The test device and the failure of the thin immediate roof in the literature [20]. (b) The test device and the failure of the thin immediate roof in the literature [1]. (c) The roof collapse of the Great Wall Number #3 coal mining field.

belts. The loaded stratum demonstrates more plastic features, resulting in a curved stress distribution, as demonstrated in Figure 8(c).

When the load imposed on the thin immediate roof under uniform load reaches extreme, the tie rods or steel belts tend to yield, leading to the drastic deposition of the thin immediate roof and section failure, as demonstrated in Figure 8(d).

4.1.2. Collapse Mechanism of the Thin Immediate Roof under Uniform Load.
Referencing the failures of the concrete beams, the collapses of the thin immediate roof can be divided into three categories: the under-reinforced beam failure, the over-reinforced beam failure, and the low-reinforced beam failure, as shown in Figure 9.

The under-reinforced beam failure is featured with the early yield of the tie rods or the steel belts. The section does not break until the stratum edge of the load zone is crushed, which is categorized as the ductile failure. The tie rods and steel belts demonstrated drastic plastic deformation during the process, leading to the deposition of the thin immediate roof, as demonstrated in Figure 9(a). This type of failure is often accompanied with early warnings. The over-reinforced beam failure is featured with the early crushing of the stratum in the load zone without the yield of the tie rods or steel belts. The failure occurs suddenly due to the crushing of the stratum without any clear warning, which is categorized as the brittle failure, as demonstrated in Figure 9(b). For the low-reinforced beam failure, the failure occurs once the tensile rock stratum develops cracks, which is categorized as the brittle failure, as demonstrated in Figure 9(c).

4.2. Collapse Mechanism Analysis of the Thin Immediate Roof under Uniform Load of Rectangular Coal Roadway.
The principal tensile stress and load stress on the thin immediate roof under uniform load can be expressed, respectively, as follows:

$$\sigma_{tp} = \frac{\sigma_{qt}}{2} + \sqrt{\frac{\sigma_{qt}^2}{4} + \tau_{qt}^2},$$

$$\sigma_{cp} = \frac{\sigma_{qt}}{2} - \sqrt{\frac{\sigma_{qt}^2}{4} + \tau_{qt}^2}, \tag{16}$$

where σ_{tp} is the principal tensile stress, MPa, and σ_{cp} is the principal load stress, MPa.

When overlooking the impact of the bottom lateral shear stress load on the internal shear stress, the shear stress at the center of the thin immediate roof can be expressed as follows:

$$\tau_{qt} = \frac{F}{8I}h^2 = \frac{3F}{2h}, \tag{17}$$

where τ_{qt} is the shear stress of the thin immediate roof, MPa.

The angle between the principal tensile stress and the beam axis can be expressed as follows:

$$\tan(2\alpha_{qt}) = -\frac{\tau_{qt}}{2\sigma_{qt}} = -\frac{3F}{\sigma_{qt}h}, \tag{18}$$

where α_{qt} is the angle between the principal tensile stress and the axis.

The principal stress trajectory of thin immediate roof under uniform load can be described in Figure 10.

The low positive stress and high shear stress were observed at the neutral axis with a 45° principle tensile stress direction. When the load increased at the thin immediate roof to reach the tensile limit of the stratum, cracks developed. Oblique cracks were developed along the principle vertical tensile stress in the abdominal area, which was named as abdominal shear oblique cracks. From the principal stress trajectory, the principle tensile stress closer to the roadway was dominated by the horizontal direction. Without any additional support, short and vertical cracks tend to develop, slowly expanding to the load zone, which are called bending shear diagonal cracks.

The shear-span ratio reflects the relative ratio of normal stress and shear stress on the oblique section, indicating the relative ratio of the bending moment of the section to the shear force to some extent, which holds a deciding meaning to the failure of the oblique section and can be expressed as follows:

$$\vartheta = \frac{M}{Fh}, \tag{19}$$

where ϑ is the shear-span ratio.

Introducing equations (5) and (6) into equation (19), the following equation is obtained:

$$\vartheta = \frac{x}{2h} - \frac{K_3}{\gamma Hxh}. \tag{20}$$

Around the center of the thin immediate roof, the moment plays a vital role in the roof failure, leading to high possibilities of normal section failure. Due to the lower shear-span ratio at both roof sides, the principal stress trajectory follows a pattern of short cylinders, leading to high possibilities of oblique section failure. In other words, the stratum in the oblique section tends to be sliced into small oblique cylinder units by the abdominal shear oblique cracks, ending with the ultimate failure. The load bearing capability is relatively high for this type of failure, which depends on the load strength of the stratum and is categorized as the brittle failure.

Some previously conducted experiments have also verified the oblique failures of the thin immediate roof under uniform load, as demonstrated in Figure 11. In spite of some deviations from the test conditions and the theoretical calculation, the general pattern and rule demonstrated are consistent.

In the simulation demonstrated in Figure 11(a), small cracks developed in the thin immediate roadway roof, suggesting the normal section failure of the thin immediate roof. However, due to the constraint generated from the steel belts, the crack development was limited to a relatively small width. The principle tensile stress led to the failure of the
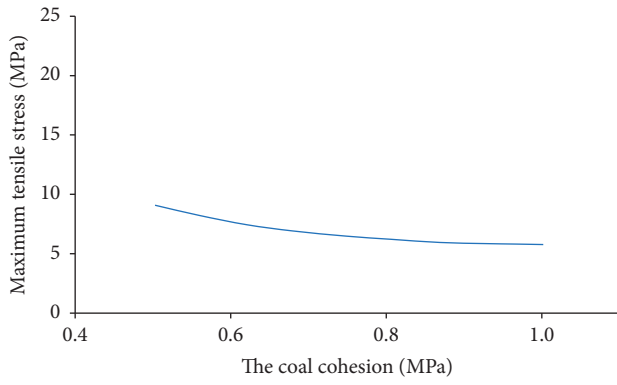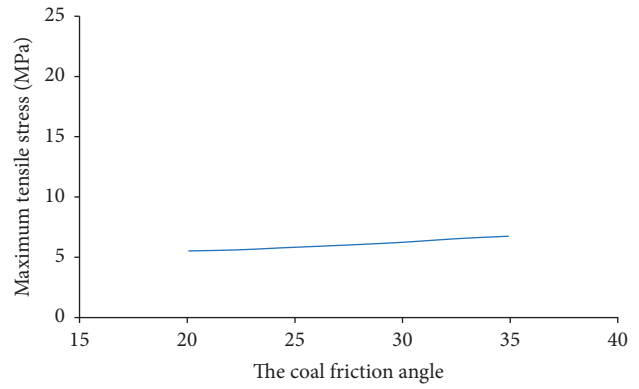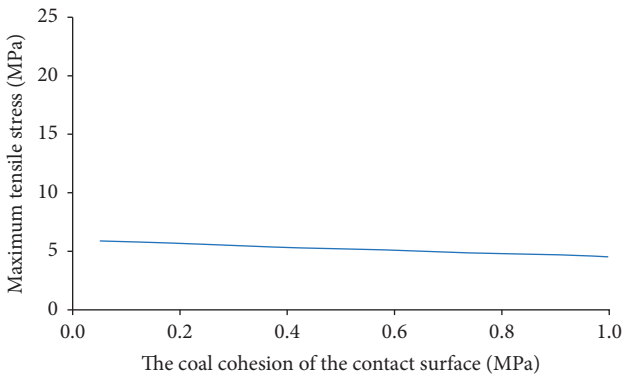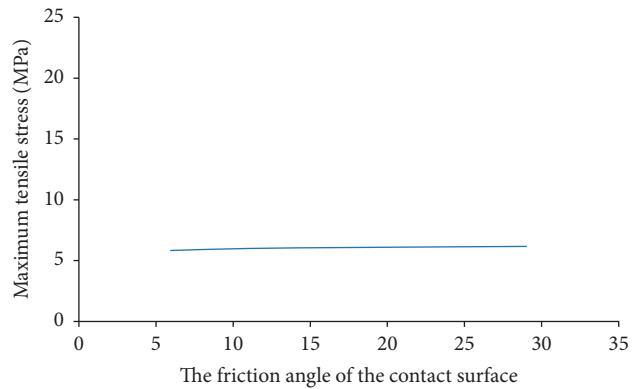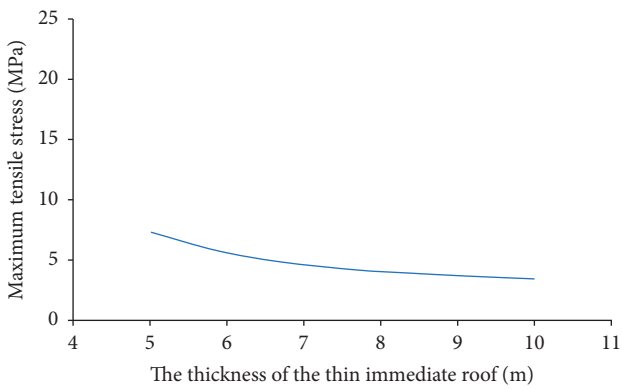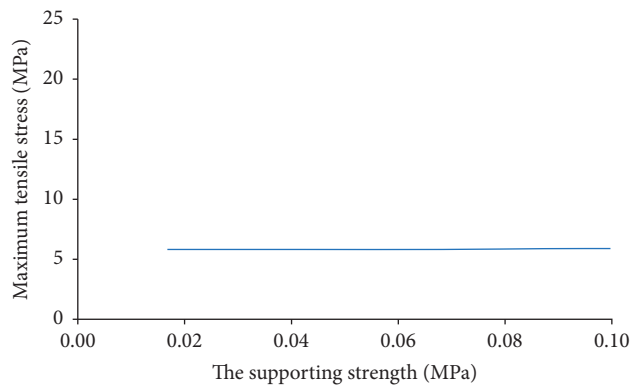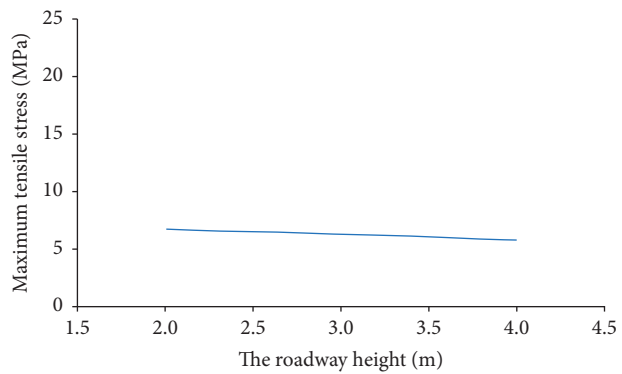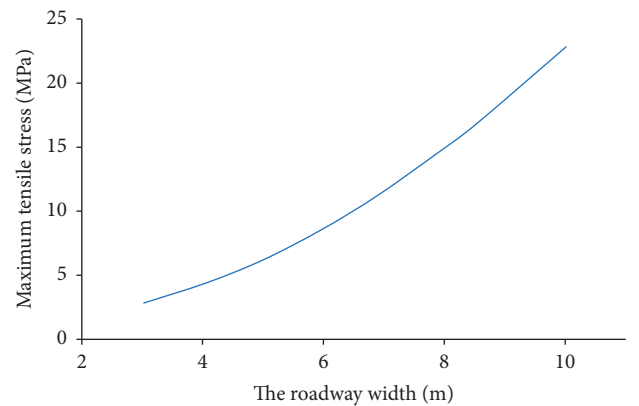
Figure 12: Parameter analysis of maximum tensile stress of thin immediate roof under uniform load. (a) The coal cohesion. (b) The coal friction angle. (c) The coal cohesion of the contact surface. (d) The friction angle of the contact surface. (e) The thickness of the thin immediate roof. (f) The supporting strength. (g) The roadway height. (h) The roadway width.
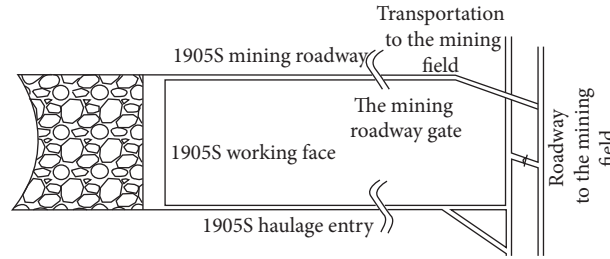
FIGURE 13: Layout of 1905S working face.

TABLE 1: Properties of coal and immediate roof of 1905S entry.

Stratum	Thickness (m)	Tensile strength (MPa)	Compressive strength (MPa)	Elastic modulus (GPa)	Poisson's ratio	Cohesion (MPa)	Internal friction angle (°)
Immediate roof	1.8	5.09	98.75	46.3	0.22	8.47	33.9
Coal seam	4.0	—	4.39	7.86	0.31	1.51	25.3
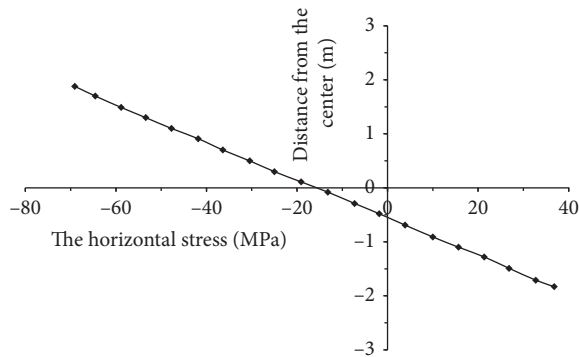
FIGURE 14: Horizontal stress in the middle of 1905S air-return entry.

oblique section, which is similar to the failure of the oblique load. Clear damaged stratum can be observed in the front view in the right bottom corner of the roof. After the failure, the cracks continued to grow driven by the principle tensile stress. Due to the inclined anchor bolts, no collapse occurred; only cracks occurred. The experiment demonstrated in Figure 11(b) simulated the roadway sides and the roof. Compared with Figure 11(a), the following differences were observed. ① No crack was observed in the roof center due to unevenly distributed load caused by different loading methods, resulting in a low load in the center and high loads at sides. ② The oblique cracks at the roof bottom moved toward the center. The roadway movement can be evaluated based on the black lines marked in Figure 11(b), suggesting that the roadway movements had some impact on the crack development of the thin immediate roof and further influenced the stability of the thin immediate roof, which failed to be included in the theoretical calculation mentioned above. Figure 11(c) demonstrates the physical simulation tests to the hard and thin roof. Five times of the original

vertical stress (the original vertical stress was about 17.5 MPa) was imposed on the roof, resulting in the development of the through oblique cracks. Despite the anchor bolts, collapse still occurred in arch shapes. Three experiments illustrate the failures of the oblique section of the thin immediate roof. The development of the through oblique cracks without sufficient supports can lead to roof collapse.

5. Parameter Analysis of the Maximum Tensile Stress of the Thin Immediate Roof under Uniform Load of Rectangular Coal Roadway

The maximum tensile stress for the thin immediate roof locates at the center of the thin immediate roof. When the tensile stress exceeds the tensile strength of the stratum, the normal section failure can occur easily. Therefore, the maximum tensile stress at the roof center was selected for parameter analysis with the roof thickness of 5.8 m to avoid the lateral vertical stress fluctuation, as demonstrated in Figure 12. The basic parameters are the same as those included in the numerical calculation model.

According to Figure 12, when other parameters stay unchanged, (1) the coal internal friction angle and the cohesion, the friction angle and the cohesion of the contact surface, the support strength (0~0.1 MPa), and the roadway height have limited impact on the maximum tensile stress; (2) the thickness of the thin immediate roof has a relatively high impact on the maximum tensile stress; and as the roof thickness increases, the maximum tensile stress decreases accordingly; the classic beam theory is no longer applicable for the roof with extreme thicknesses due to the increased tolerances; (3) the roadway width has a significant impact on the maximum tensile stress of the thin immediate roof; as the roadway width increases, the maximum tensile stress increases approximately linearly.

TABLE 2: Rock bolt support parameters of 1905S roadway.

	Anchor bolt					Anchor cable				
Parameter	Length (mm)	Distance (mm)	Row distance (mm)	Diameter (mm)	Preload (kN)	Length (mm)	Number/row	Row distance (mm)	Diameter (mm)	Preload (N·m)
Roof	2400	1200	1200	22	200	6500	2	2400	17.8	200
Two sides	2400	1200	1200	22	200	—	—	—	—	—
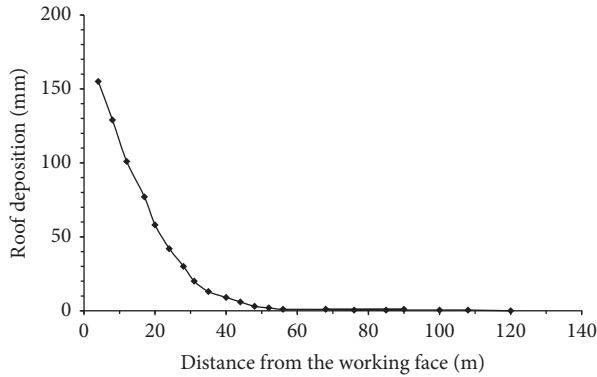
FIGURE 15: Roof deposition of 1905S haulage entry.
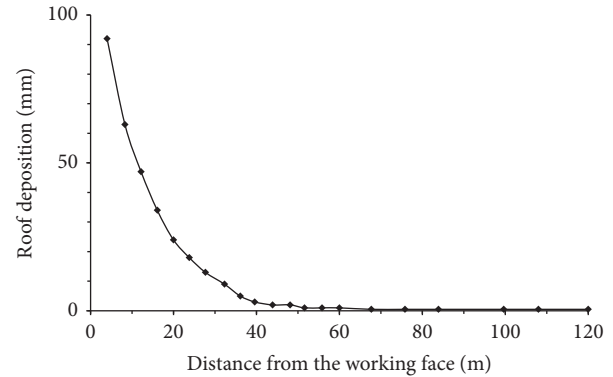
FIGURE 16: Roof deposition of 1905S air-return entry.

6. Engineering Verification of the Stability of the Thin Immediate Roof under Uniform Load of Rectangular Coal Roadway

The thin immediate roof under uniform load is mainly suitable for the roadway under the thin bedrock and the roadway with the hard-immediate roof. The engineering verification was conducted in 1905S mining roadway of Great Wall Number #3 coal excavation field.

1905S mining roadway of Great Wall Number #3 coal field locates at number #9 coal seam, with a total roadway length of 2665 m, whose inclined angle is 12~24°, with average at 17°. The embedded depth of the 1905S haulage entry is about 700 m with a 600 m embedded depth of the mining roadway. Solid coal is surrounding the work face. The detailed work surface is demonstrated in Figure 13.

The immediate roof of 1905S mining roadway is made out of limestone, whose mechanical properties are listed in Table 1.

According to Table 1, the 1905S roadway roof has high hardness, meeting the conditions of the thin immediate roof. However, more parameters are needed to calculate the forces born by the roof. The horizontal stress was taken by equating to the vertical stress. The coal cohesion was taken as 1/2 of the coal rock block. The cohesion of the coal contact surface was taken as 1/10 of the rock block. The friction angle of the coal rock body was taken equating to the coal rock block. The friction angle in the rock contact surface is 10° with the peak stress coefficient at 2. The theoretical calculation of the horizontal stress at the center of the thin immediate roof is shown in Figure 14.

According to Figure 14, the area 1.2 meters away from the roof center is the tensile stress zone when no mining is conducted. Under mining, the roadway bore a higher load.

The tensile stress at the lower section of the roof exceeded the tensile strength, transforming the linear distribution into a curved distribution toward the neutral axis. When the tensile stress at the tensile zone boundary reached the limit, the section tended to crack. To prevent the development of cracks, anchor bolts were installed on the site to enhance the roof stability.

The section of 1905S air-returning roadway takes the shape of an oblique rectangle with a cross section width of 5400 mm, a low top of 3910 mm, and a high top of 4680 mm. The roadway is supported by anchor cable and net, anchor rod is $\Phi 22 \, \text{mm} \times 2400 \, \text{mm}$ high strength bolt, steel pallet is $150 \times 150 \times 10 \, \text{mm}$, each anchor has two MSK2835 resin cartridges, row spacing between bolts is $1200 \times 1200 \, \text{mm}$, roof W steel belt is $5200 \times 280 \times 3 \, \text{mm}$, high (low) steel belt is $2600 \, (1400) \times 280 \times 3 \, \text{mm}$, top steel strand anchor cable is $\Phi 17.8 \times 6500 \, \text{mm}$, each with four MSK2835 resin cartridges, steel plate is $300 \times 300 \times 12 \, \text{mm}$, and row spacing is 2400 mm, two per row. The main parameters of bolt support are presented in Table 2.

The actual roof depositions of the 1905S roadway surrounding rock were measured and presented in Figures 15 and 16.

The forces on the roof anchor bolts of the 1905S haulage entry were measured through the dynamometer on site and are presented in Figure 17.

According to Figures 15 to 17, the following results are obtained: (1) With a relatively weak anchor supporting system, the deformations of two roadways were limited under one-time excavation effect. The roof deposition of 1905S haulage entry was about 180 mm, while the 1905S air-returning roadway experienced a total of 120 mm in deposition, which is consistent with the theoretical calculations. (2) The forces on the anchor bolts experienced limited variances

(a)

(b)
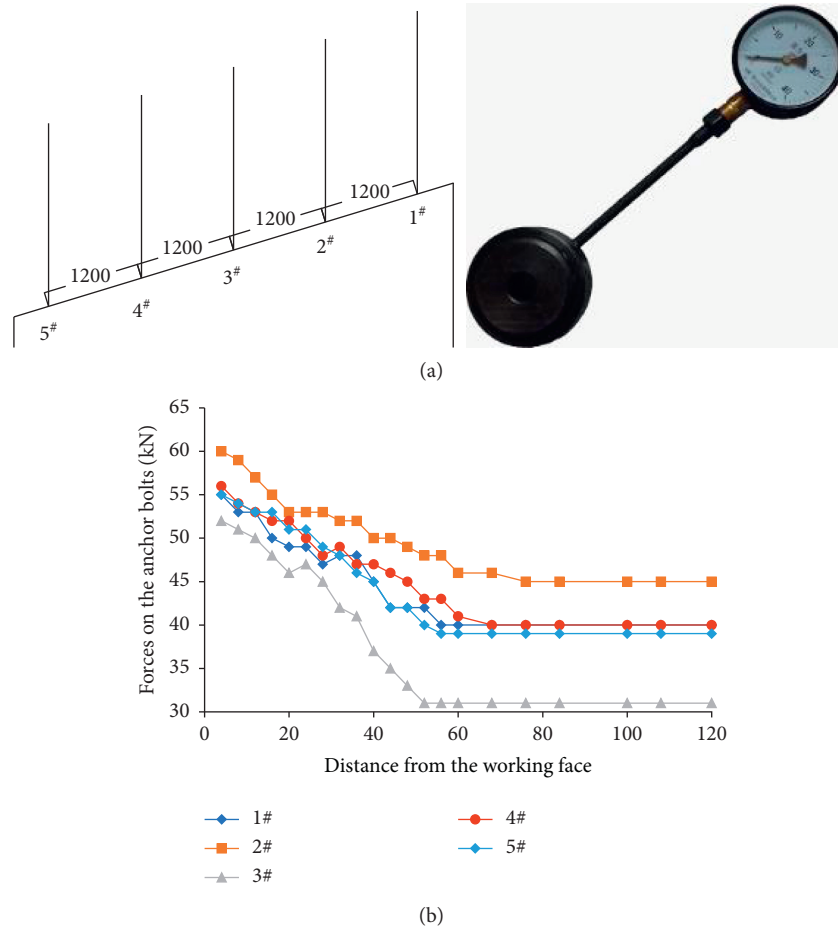
FIGURE 17: Rock bolt force of 1905S haulage entry. (a) Bolt dynamometer and number. (b) Bolt force.

50 meters beyond the working face. The forces on the anchor bolts experienced some increases within 50 meters from the working face, as high as 30 kN. The increase was relatively small, suggesting that the vertical deformation of the surrounding rock within the supporting range of the anchor bolts was limited, validating the selection of the classical beam theory for the study of the roof stability in this study.

7. Conclusions

(1) The stress distribution and deposition of the thin immediate roof under uniform load of rectangular coal roadway were obtained through the theoretical calculations.

(2) The stress theoretical calculations and the numerical calculations of the thin immediate roof under uniform load were compared and a consistent trend was obtained, especially at 5.8 m thickness of the thin immediate roof. However, the differences between the theoretical calculations and the numerical calculations were relatively large at 3 m thickness of the thin immediate roof, which was caused by the fluctuations observed around the lateral supporting stress peak, resulting in tolerances among

parameters. After the introduction of the correction factors, the differences were significantly reduced, rendering the consistency between the theoretical calculations and the numerical calculations.

(3) Two failures of the thin immediate roof under uniform load were identified: the normal cross section failure caused by the bottom tensile stress and the failure of the oblique section caused by the combined effect of the tensile stress in the abdominal area and compressive stress.

(4) The parameter analysis of the maximum tensile stress based on the theoretical equation reveals that the coal internal friction angle and cohesion, the friction angle and the cohesion of the contact surface, the support strength, and the roadway height have limited impact on the maximum tensile stress. The thickness of the thin immediate roof has a relatively high impact on the maximum tensile stress. As the roof thickness increases, the maximum tensile stress decreases accordingly. The classic beam theory is no longer applicable for the roof with extreme thicknesses due to the increased tolerances. The roadway width has a significant impact on the maximum tensile stress of the thin

immediate roof. As the roadway width increases, the maximum tensile stress increases approximately linearly.

(5) The stability of the thin immediate roof under uniform load was tested and verified on the 1905S mining roadway of Great Wall Number #3 mine. Under most of circumstances, the thin immediate roof with high hardness is stable consistently.

Data Availability

The data used to support the findings of this study are available from the corresponding author upon request.

Conflicts of Interest

The authors declare that they have no conflicts of interest regarding the publication of this paper.

Acknowledgments

References

[1] W. Shen, J. Bai, W. Li, and X.-Y. Wang, "Prediction of relative displacement for entry roof with weak plane under the effect of mining abutment stress," *Tunnelling and Underground Space Technology*, vol. 71, pp. 309–317, 2018.

[2] Y. Yu, H. Xing, and F. Cheng, "Study on load transmission mechanism and limit equilibrium zone of coal-wall in extraction opening," *Journal of China Coal Society*, vol. 37, no. 10, pp. 1630–1636, 2012.

[3] Y. Zhang, L. Cheng, J. Yang, and J. Ming, "Bearing characteristic of composite rock-bolt bearing structure under different bolt support density," *Journal of Mining and Safety Engineering*, vol. 32, no. 2, pp. 305–309, 2015.

[4] Y. Pan, S. Gu, and Y. Qi, "Analytic solution of tight roof's bending moment, deflection and shear force under advanced supercharger load and supporting resistance before first weighting," *Chinese Journal of Rock Mechanics and Engineering*, vol. 32, no. 8, pp. 1544–1553, 2013.

[5] H. Kang, J. Li, J. Yang, and F. Gao, "Investigation on the influence of abutment pressure on the stability of rock bolt reinforced roof strata through physical and numerical modeling," *Rock Mechanics & Rock Engineering*, vol. 50, no. 2, pp. 1–15, 2016.

[6] Z. Zhao, W. Wang, L. Wang et al., "Compression-shear strength criterion of coal-rock combination model considering interface effect," *Tunnelling and Underground Space Technology*, vol. 47, pp. 193–199, 2015.

[7] W. Shen, J. Bai, X. Wang, and Y. Yu, "Response and control technology for entry loaded by mining abutment stress of a thick hard roof," *International Journal of Rock Mechanics and Mining Sciences*, vol. 90, pp. 26–34, 2016.

[8] S. Sinha and Y. P. Chugh, "An evaluation of roof support plans at two coal mines in Illinois using numerical models," *International Journal of Rock Mechanics & Mining Sciences*, vol. 82, pp. 821–829, 2016.

[9] S. Bastola and Y. P. Chugh, "Shear strength and stiffness properties of bedding planes and discontinuities in the immediate roof rocks overlying the no. 6 coal seam in Illinois," in *Proceedings of the ISRM 2015*, Montreal, Canada, March 2015.

[10] Y. P. Chugh and S. Sinha, "Numerical modeling of roof support plans at 4-way coal mine intersections," in *Proceedings of the 49th US Rock Mechanics/Geomechanics Symposium*, San Francisco, CA, USA, June 2015.

[11] B. Wang, W.-J. Wang, F.-J. Zhao et al., "Study of bolt anchoring effect based on self-bearing characteristics of roadway surrounding rock," *Rock and Soil Mechanics*, vol. 35, no. 7, pp. 1965–1972, 2014.

[12] N. Ma, X. Zhao, Z. Zhao et al., "Stability analysis and control technology of mine roadway roof in deep mining," *Journal of China Coal Society*, vol. 40, no. 10, pp. 2287–2295, 2015.

[13] L. I. Ji, N. Ma, and Z. Ding, "Heterogeneous large deformation mechanism based on change of principal stress direction in deep gob side entry and control," *Journal of Mining & Safety Engineering*, vol. 35, no. 4, pp. 670–676, 2018.

[14] C. Carranza-Torres, "Analytical and numerical study of the mechanics of rockbolt reinforcement around tunnels in rock masses," *Rock Mechanics and Rock Engineering*, vol. 42, no. 2, pp. 175–228, 2009.

[15] R. Y. Man-chu, *Application of Shi's Discontinuous Deformation Analysis to the Study of Rock behavior*, Department of Civil Engineering College of Engineering University of California Berkeley, Berkeley, CA, USA, 1991.

[16] S. Chen, Q. Qian, and M. Wang, "Problems of deformation and bearing capacity of rock mass around deep buried tunnels," *Chinese Journal of Rock Mechanics and Engineering*, vol. 24, no. 13, pp. 2203–2210, 2005.

[17] X. Zhao, M. Cai, and M. Cai, "Mutual influence between shear dilatation ofrock mass and rebar support around underground excavation," *Chinese Journal of Rock Mechanics and Engineering*, vol. 29, no. 10, pp. 2056–2062, 2010.

[18] W. Wang, C. Yuan, W. Yu et al., "Stability control method of surrounding rock in deep roadway with large deformation," *Journal of China Coal Society*, vol. 41, no. 12, pp. 2921–2931, 2016.

[19] China University of Mining and Technology, *CHENG Liang Structure Characteristic and Stability Analysis Method of Rectangle Coal Roadway Roof and Engineering Validation*, China University of Mining and Technology, Xuzhou, China, 2018.

[20] X. Yang, C. Hu, M. He et al., "Study on presplitting blasting the roof strata of adjacent roadway to control roadway deformation," *Shock and Vibration*, vol. 2019, Article ID 3174898, 16 pages, 2019.

Research Article

Study on Stress Relief of Hard Roof Based on Presplitting and Deep Hole Blasting

Peng Gong [iD],[1,2] **Yongheng Chen** [iD],[2] **Zhanguo Ma,**[1,2] **and Shixing Cheng** [iD][1]

[1]*State Key Laboratory for Geomechanics and Deep Underground Engineering, China University of Mining and Technology, Xuzhou 221116, Jiangsu, China*
[2]*School of Mechanics and Civil Engineering, China University of Mining and Technology, Xuzhou 221116, Jiangsu, China*

Correspondence should be addressed to Peng Gong; gongpeng1220@126.com

For the problem that the hard roof causes wider end-mining coal pillar, and the roadway is greatly affected by mining, this paper took Shanxi Luning Coal Mine as the engineering background; based on the stress distribution characteristics of the coal pillar, the calculation method of the limit end-mining coal pillar size was given; considering the formation conditions and transmission forms of the advanced abutment stress, a method combining presplitting and deep hole blasting was proposed to weaken the advanced abutment stress. The numerical simulation was used to analyze the stress distribution of coal pillars, which was verified by on-site industrial tests. The results showed that the presplitting can achieve the blocking of stress. The closer it is to the peak of the abutment stress, the better the blocking effect. Deep hole blasting can weaken the source of the advanced abutment stress and reduce the peak of abutment stress. With the combination of the two blasting methods, the end-mining coal pillar size of Luning Coal Mine can be reduced to 60 m. The method combining presplitting and deep hole blasting can effectively reduce the end-mining coal pillar size and reduce the impact of mining on the deformation of the dip roadway.

1. Introduction

The hard roof suspension structure is not easy to collapse, which will lead to an increase in the peak value of the advanced abutment stress and the effect range [1, 2]. When the mining panel is close to the dip roadway, if the size of the reserved coal pillar is insufficient, the energy released by the roof fracture and the mining stress will have a serious impact on the remote roadway [3–5]. Therefore, the roads are often protected by increasing the size of the coal pillars, resulting in waste of coal resources.

The pressure relief methods for hard roofs are mainly divided into three types: hydraulic fracturing, water injection weakening, and physical blasting. The principle is to reduce the integrity of the rock mass by weakening the load-carrying capacity or blocking the transmission of the internal force of the rock layer; from the perspective of reducing the integrity of the rock mass, people initially used water injection to change the rock properties to weaken it, but this method is not suitable for hard roofs with dense structures; the current more mature method is physical blasting; artificial cracks are formed by blasting and interpenetrate with the original cracks under the pressure of the mine so that the roof is easy to collapse and the stress concentration in front of the coal wall is reduced. Blasting pressure relief has a lot of research in theory and practical application; Xia et al. [6] used shallow hole blasting to reduce the roof pressure in front of the mining panel and then combine grouting reinforcement technology to improve the stability of roadway surrounding rock; Zuo et al. [7] used theory, and the method of numerical simulation was used to study the evolution behavior of the stress field induced by deep hole blasting. Zhou et al. [8] analyzed the internal dynamic response of coal pillars during the mining process using PFC software. In recent years, there have also been studies using hydraulic fracturing techniques to increase the degree of rock fragmentation.

The main way to block the transmission of stress in the rock layer is to create a fracture surface inside the rock layer, weaken the bearing stress generated by the suspended ceiling structure, and change the distribution of the bearing stress field from the source. At present, the technology is widely used in the gob-side entry retaining. For example, Liu et al. [9] and Chen et al. [10] have studied the roof structure and pressure relief effect in the roadway along the gob. Hu [11] established a mechanical model of gob-side entry retaining related to the strength of the support and calculated a reasonable presplitting height; Huang et al. [12] used directional hydraulic fracturing to cut the outer roof of the coal pillar to achieve the purpose of protecting the roadway. In recent years, some people have used directional presplitting technology to control the advanced abutment stress and cyclic pressure. Yang et al. [13, 14] respectively adopted directional hydraulic fracturing technology and directional energy gathering blasting technology to presplit the front roof of the mining panel, thereby shortening the cyclic pressure step to reduce the energy accumulated in front of the coal wall.

It can be seen from previous studies that although hydraulic pressure has been applied in the field as an emerging technology to control the advanced abutment stress, the fracturing process is not easy to control and is seriously affected by the original cracks in the rock mass. The development of physical blasting technology has been very mature, but it mostly stays in the application research of a single method and fails to combine the advantages of multiple blasting methods to achieve efficient control of the pressure field. In this paper, based on the actual background of the project, considering the stress distribution inside the coal pillar and the advantages of various blasting methods, this paper proposes a pressure relief method combining presplitting blasting and deep hole blasting to control the advanced abutment stress through numerical simulation and industrial experiments to study the effect of pressure relief.

2. Research on Coal Pillar Stress Distribution and Roadway Stability

2.1. Coal Pillar Stress Distribution and Size Calculation. Reasonable width of the end-mining coal pillar should ensure the stability of the roadway surrounding rock while reducing the size as much as possible to improve resource utilization. The redistribution of initial rock stress field was caused by roadway excavation. As shown in Figure 1, the broken area I, plastic area II, and elastic area III are formed in turn along the roadway. The broken area and plastic area can be collectively called the limit equilibrium area. In the initial mining period, the mining panel is far away from the roadway, and the advanced abutment stress of the mining panel is also distributed in 3 areas, and the original rock stress zone IV still exists between the mining panel and roadway. With the advancement of the mining panel, the influence range of the advanced abutment stress continues to move forward, and the original rock stress zone gradually decreases. According to rock mechanics, 5% of the original

rock stress is selected as the boundary between the elastic zone and the original rock stress field. When the elastic area of the abutment stress field overlaps with the surrounding rock stress area of the roadway, the roadway will gradually become unstable and be destroyed. Therefore, the width of the limit end-mining coal pillar is the sum of the range I and II of the surrounding rock stress area of the roadway and the area I, II, and III of the advanced abutment stress zone.

The range of the advanced abutment stress zone is the sum of the width of the limit equilibrium zone x_1 and the width of the elastic zone x_2. x_1, and x_2 can be calculated by the following [15] equations:

$$x_1 = \frac{M(1 - \sin\varphi)}{2f(1 + \sin\varphi)} \ln\left\{\frac{K\gamma H(1 - \sin\varphi)}{\tau_0 \cot\varphi(1 + \sin\varphi)}\right\}, \qquad (1)$$

$$x_2 = \frac{M\beta}{2f} \ln\frac{K}{1.05}, \qquad (2)$$

where x_1 is the width of the plastic zone; x_2 is the width of the elastic zone; M is the thickness of the coal seam, 4.0 m; f is the friction angle, 31°; f is the friction factor between the coal seam and the roof and floor, 0.16; τ_0 is the cohesion, 0.6 MPa; H is the coal seam depth, 500 m; γ is the average bulk density of the overburden rock, 25 kN/m³; K is the maximum stress concentration factor, 3.0; β is the lateral pressure coefficient, 2.0.

For the surrounding rock stress field of rectangular roadway, in the absence of structural stress, as shown in Figure 2, it should be equivalent to a circular roadway with the circumscribed circle of the roadway as the cross-section. Then, use the method of elastic-plastic limit equilibrium theory and assign a certain correction coefficient to calculate. The radius Rb of the limit equilibrium zone of the surrounding rock of the roadway can be obtained by the following equation:

$$R_b = \eta R_0 \left\{ \left[\frac{(p + c \cdot ctg\varphi)(1 - \sin\varphi)}{c \cdot ctg\varphi}\right]^{((1 - \sin\varphi)/2\sin\varphi)} - 1 \right\}, \qquad (3)$$

where p is the original rock pressure; R_0 is the circumscribed circle radius of the roadway; c is the cohesive force; f is the friction angle in the coal body; η is the correction coefficient, 0.8.

Taking the above parameters into equations (1)–(3), $x_1 = 18.6$ m, $x_2 = 65.3$ m, and Rb = 2.6 m, so the theoretical minimum width of the end-mining coal pillar is $L = x_1 + x_2 + $ Rb $= 86.5$ m.

2.2. Effect of Advanced Abutment Stress on Roadway. The main roof has the characteristic of transmitting horizontal force in the direction of propulsion, which has a significant impact on the pressure of the stope. The harder the main roof, the more the weight of the overlying strata will be transferred to the surrounding rock mass, resulting in an increase in the range of the advanced abutment stress field. Therefore, the hard main roof is not only the source of the advanced abutment stress but also the main transmission

Figure 1: Stress distribution of the end-mining coal pillar.

Figure 2: Equivalent roadway profile.

holes on both sides of the PVC pipe. The shaped jet penetrates and tears in a predetermined direction around the explosion hole to form an initial guide crack, which provides accurate orientation for the further effect of blasting stress wave and detonation gas, as well as the directional expansion of cracks, thereby forming a fracture surface and destroying the integrity of the roof. At present, this method is mostly used to presplit the roof above the roadway, the side roof of the gob collapses under the pressure of overburden to protect the roadway. Based on this idea of cutting off the stress transmission path, it is possible to achieve the blocking of the advanced abutment stress transmission in the roof.

During the coal seam mining, the roadway is mainly affected by two kinds of stress, namely, the redistribution of static stress after mining and the dynamic load caused by other factors such as rock fracture. The advanced presplitting will form a fault-like loosening and weakening zone around the blast hole, which will block the transmission of stress in the rock layer. (1) Blocking the transmission of static load: the macro performance of presplitting is the formation of crack surface; the contact area of the rock mass on both sides of the crack is greatly reduced, and the joint force is lost at the crack so that the ability of the roof to transmit force is weakened, and there is no ability to resist bending, shearing, and tensile. At the same time, the degree of loosening and weakening under the action of abutment pressure is increased, and the strength is further reduced. (2) Weakening the propagation of stress waves: dynamic loads such as rock fracture, collapse, and blasting propagate in the rock body in the form of stress waves. When stress waves encounter weak interfaces such as fissures caused by blasting on the transmission path, wave projection and reflection will occur, which will weaken the transmission of dynamic loads in the rock layer. Therefore, the advanced presplit blasting will block the advanced stress of the stope from the two aspects of dynamic and static loading.

path of the abutment stress. As shown in Figure 3, based on the above two characteristics of the main roof, a stress blocking blasting pressure relief technology is proposed. First, the main roof is presplitted to block the propagation of stress. Then, reduce the roof integrity through advanced deep hole blasting. On the one hand, the internal stress will be transferred to the deep part due to the increased rock fracture. On the other hand, after the mining panel has been mined, the broken roof will collapse directly under the pressure of the overlying rock layer and will not produce a suspended roof structure, weakening the advanced abutment stress from the source. Through this combination of "prevention and treatment," the size of coal pillars and the effect of the advanced abutment stress on the stability of the surrounding rock are reduced.

3. Mechanism of Stress Blocking and Relief

3.1. Stress Blocking with Presplitting. The presplitting is based on the directional energy gathering blasting technology [16–18] so that the detonation product forms a super-high pressure and density shaped jet along the dire. As shown in Figure 4, the energy gathering hole is formed by drilling

3.2. Attenuation of Stress in Blasting Crack Zone. In order to study the blocking effect of the blasting fracture zone on the stress wave, the stress wave generated in the stope can be simplified as a plane wave, because the longitudinal wave velocity is much greater than the shear wave velocity, and the blasting fracture zone is perpendicularly incident. Therefore, the blocking of the dynamic load is regarded as the attenuation of the vertical stress wave incident on the
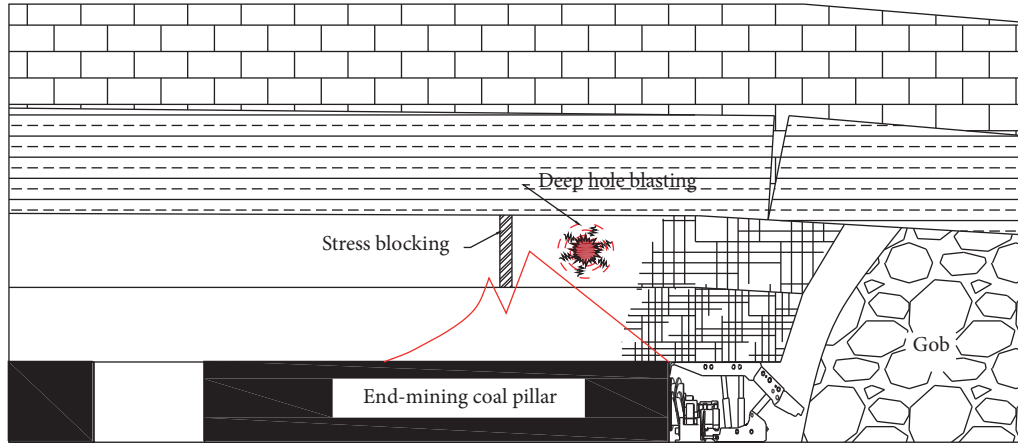
FIGURE 3: Schematic diagram of stress blocking and blasting relief.
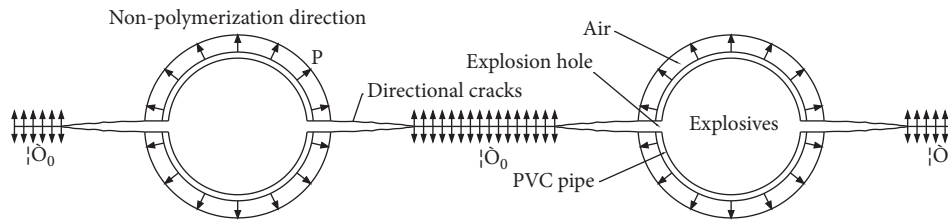
FIGURE 4: Directional energy gathering blasting.

multilayer medium. As shown in Figure 5, σ_0 is the initial peak stress value of the incident layer of the stress wave, and σ_{max} is the peak stress value after passing through the n-layer medium. The peak stress σ_{max} after n-layer medium can be obtained from [19] the following equation:

$$\sigma_{max} = 2^n \prod_{k=0}^{n-1} \frac{\rho_{n+1} v_{n+1} \left(\sum_{k=1}^{n} d_k\right)^{\alpha_{n+1}}}{\left(\rho_n v_n + \rho_{n+1} v_{n+1}\right)\left(\sum_{k=1}^{n+1} d_k\right)^{\alpha_{n+1}}} \sigma_0, \qquad (4)$$

where ρ is the density of the medium; v is the wave velocity of the wave propagating in the medium; d is the thickness of the medium; α is the attenuation coefficient.

It can be known from the wave theory that when a wave is transmitted from a medium with a small wave impedance into a medium with a high wave impedance, the peak value of the wave is enhanced, and vice versa. A large number of cracks around the blast hole will cause multiple reflections of the stress wave to increase the propagation distance, and the attenuation of the stress wave will increase with the increase of the propagation distance. In addition, the redistribution of the medium state due to the work of the stress wave on the broken rock mass around the blast hole will also consume wave energy. When the stress wave propagation distance is the same, the more media layers passing through, the richer the media properties, and the faster the stress wave decay, so the blast fracture zone can effectively attenuate the stress wave generated in the rock layer.

4. Establishment of Numerical Simulation Model

4.1. Model Parameters and Boundary Condition. Using the numerical simulation software Fast Lagrangian Analysis of Continua in 3 Dimensions (FLAC3D) to build a numerical calculation model with the 22115 mining panel of Luning Coal Mine as the research object. As shown in Figure 6, the dimensions of the model were $392 \text{ m} \times 373 \times \text{m} \times 93 \text{ m}$, including one mining panel and three dip roadways. Boundary conditions limit the horizontal displacement of the four sides, fixed constraints are applied at the bottom, and the top is set as a free surface. The vertical rock stress is applied at the top of the model to simulate the weight of the overburden, and based on field tests, lateral pressure is applied to the four sides of the model with a coefficient of 1.5. The calculation uses the Mohr–Coulomb model, and the physical and mechanical parameters of each rock layer are measured by on-site sampling and laboratory tests, as shown in Table 1.

The simulation involves deep hole blasting and stress wave transfer research. It is necessary to set up matching dynamic calculation conditions. For FLAC3D dynamic calculation, three aspects must be considered: dynamic load and boundary conditions, mechanical damping, and wave propagation in the model. When an explosion occurs in the rock and soil body, a blasting compression wave will first produce a compaction effect on the inner wall of the blast hole. The compression wave attenuates sharply after reaching the peak and rebounds after the load disappears.
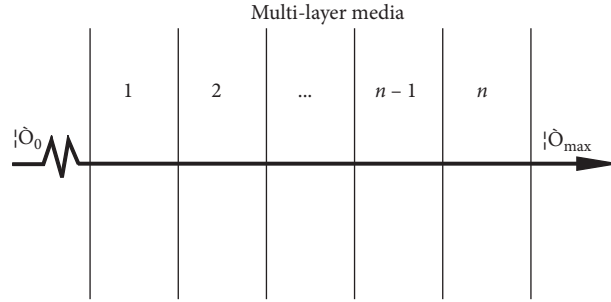
FIGURE 5: Normal transmission model of the stress wave in multilayer medium.
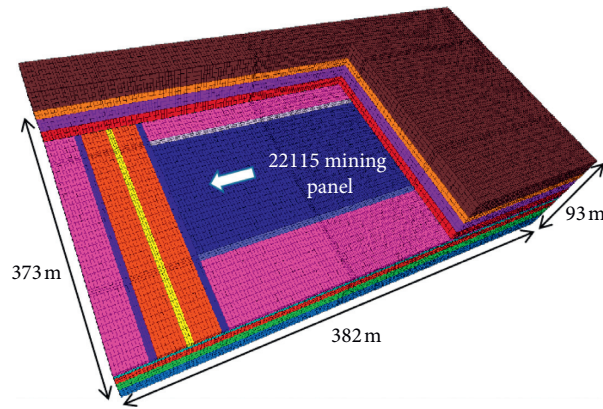
FIGURE 6: Overall view of the numerical simulation model.

TABLE 1: Main rock model parameters.

Group name	Lithology	Bulk (GPa)	Shear (GPa)	Cohension (MPa)	Friction (°)	Tension (MPa)	Density (kg/m^3)
Main roof	Sandstone	6.11	3.15	3.6	32	2.95	2600
Immediate roof	Sandy mudstone	5.61	3.97	3	31	3.33	2577
False roof	Carbon mudstone	3.03	1.32	1	23	1.3	1368
Coal seam	2# coal	3.03	1.32	1	23	1.68	1368
Immediate floor	Mudstone	9.53	5.17	2.8	32	3.5	2624
Main immediate	Siltstone	1.01	6.05	3	38	6.06	2625

Therefore, the triangle wave with loading and unloading process can be used as the power source in the calculation [20]; the dynamic loading equation is shown in equation (5), where the total time course is 0.06 s, and the loading section lasts 0.01 s, unloading the segment lasts 0.05 s, the peak load is 20 MPa, and the dynamic load and curve are shown in Figure 7.

$$
\begin{cases}
A(\tau) = \dfrac{A}{t_0} \cdot \tau, & 0 \leq \tau < t_0, \\[2ex]
A(\tau) = A - \dfrac{A}{t_1 - t_0} \cdot (\tau - t_0), & t_0 \leq \tau < t_1, \\[2ex]
A(\tau) = 0, & t \geq t_1,
\end{cases}
\tag{5}
$$

where t_0 is the loading time; t_1 is the unloading time; τ is the time variable; A is the peak load.

The damping of rock and soil mainly comes from internal friction and a large number of joint surfaces. The damping mode determines the form of dynamic load attenuation. The FLAC3D dynamic calculation module provides three damping modes, of which Rayleigh damping itself is frequency-dependent, but the frequency-independent characteristics of the rock and soil body can be obtained within a certain range by adjusting appropriate parameters. The parameters of Rayleigh damping include the minimum critical damping ratio ε_{min} and the minimum center frequency ω_{min}. For geotechnical materials, the critical damping ratio generally ranges from 2% to 5%. In this paper, $\varepsilon_{min} = 0.05$ is directly adopted; the center frequency of the damping can be simplified to the natural frequency f of the model instead. The natural frequency can set the model to elastic constitutive and apply gravity without solving damping to solve a certain number of steps to make the model oscillate. The response of key nodes in the model determines the size of the natural frequency. As shown in
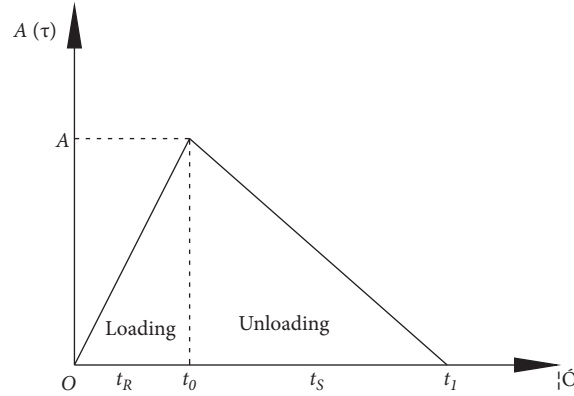
FIGURE 7: Dynamic load curve.
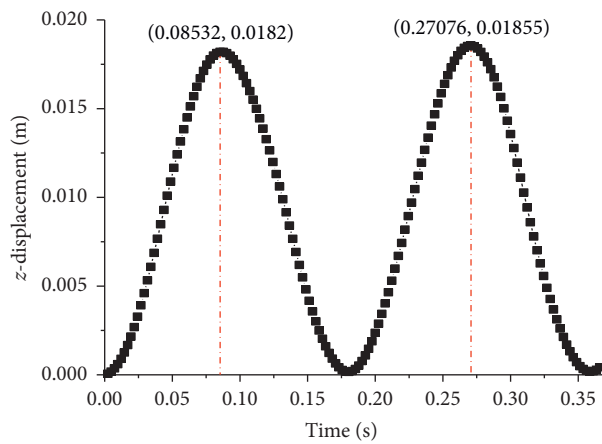
FIGURE 8: Overall view of the numerical simulation model.

TABLE 2: Dynamic parameters.

Peak load (MPa)	Loading time t_R (s)	Unloading time t_S (s)	Minimum critical damping ratio	Minimum center frequency (Hz)
20	0.01	0.05	0.05	5.12

Figure 8, the two adjacent peaks of the displacement time-history curve taken from vibration are a vibration period T, and the minimum center frequency can be obtained from equation (6) as $\omega_{\min} = 5.12$ Hz. The dynamic load parameters required for the simulation are shown in Table 2.

$$\omega_{\min} \approx f = \frac{1}{T}, \tag{6}$$

where $\omega_{\min}$ is the minimum center frequency; f is the natural frequency; T is the vibration period.

In the calculation, the dynamic load is applied to the internal nodes of the model, and only the application of the viscous boundary can effectively reduce the reflection effect generated by the boundary. In addition, the size of the grid in dynamic calculation is closely related to the dynamic load frequency, and the frequency of the input wave and the wave velocity characteristics of the system both affect the numerical accuracy of the wave transmission. Therefore, the grid space element size ΔL must be less than about one-tenth

to one-eighth of the wavelength associated with the highest frequency f component of the input wave, as in equation (7). The application of the dynamic load and the determination of the grid size in the entire process are completed by the software built-in programming language fish, and in order to increase the calculation speed, a dynamic multistep calculation mode is adopted.

$$\Delta L \leq \lambda (0.1 \sim 0.125), \tag{7}$$

where ΔL is the grid space element size; λ is the wavelength.

4.2. Simulation Scheme. The focus of this study is the blocking of stress transmission by directional presplit blasting and the effect of deep hole blasting on weakening the advanced abutment stress. With the combination of the two methods, the purpose of shortening the range of the advanced abutment stress field is achieved. The simulation is performed by the following steps: (1) firstly, coal mining is

carried out in the conventional way, and the limit coal pillar size is determined based on the advanced abutment stress range, based on the coal pillar size determination principle given above. (2) Presplitting at different horizontal distances of the advancing mining panel, according to different stress blocking effects give the best presplitting position. (3) After determining the presplitting position, deep hole blasting dynamic load is applied to study the pressure relief effect under the combination of the two methods.

4.3. Effect of Blasting on Coal Pillar Stress Field Distribution

4.3.1. Determination of Coal Pillar Size. It can be seen from Figure 9 that when the mining panel is far away from the roadway, the roadway is not disturbed, and the original rock stress area exists in the coal pillar stress field. The range of the advanced abutment stress field is about 80 m, and the peak stress is about 22 MPa. The stress field of the roadway surrounding rock is about 30 m, and the peak stress is about 16 MPa. The advanced abutment stress field advances with the mining of the mining panel. When the coal pillar width is reduced to 115 m, the original rock stress area gradually disappears, and the two stress fields elastic areas begin to superimpose each other, and the stress value is the result of linear superposition. When the size of the coal pillar is reduced to 85 m, the advanced abutment stress field reaches the disturbance boundary of the surrounding rock stress field of the roadway. As the size of the coal pillar continues to decrease, the degree of disturbance in the roadway intensifies, causing the peak value of the surrounding rock stress field to increase rapidly, and the roadway gradually becomes unstable. It can be seen that without taking any measures, the end-mining coal pillar size is about 80–85 m.

4.3.2. Stress Blocking Effect Analysis. In order to study the influence of the presplitting blasting position on the stress blocking effect, presplitting was carried out at the horizontal distances of 20 m, 35 m, 50 m, and 65 m from the mining panel, respectively, to simulate the redistribution state of the advanced abutment stress field after directional presplitting. Assuming that blasting generates a blasting cavity with a width of 0.2 m and a blasting weakened area with a radius of 2 m, a horizontal stress monitoring line is arranged along the midpoint of the coal seam height to record the change trend of the stress in the coal pillar, as shown in Figure 10.

As can be seen from Figure 10, the presplit blasting destroyed the rock mass around the blast hole, resulting in the formation of a plastic failure zone around the blast hole. The rock mass inside the area was loosely broken, the bearing capacity was weakened, and a local stress drop was observed. By comparing the stress curves at different presplitting locations, we can see that, when presplitting at 20 m ahead of the mining panel, the presplitting position is close to the stress peak area and the stress gradient is large, so the presplitting location is severely damaged under the action of dynamic load, and the stress drops by 3 MPa compared to the case without presplitting at the same location. The range of the stress rise zone is reduced, and the entire advanced
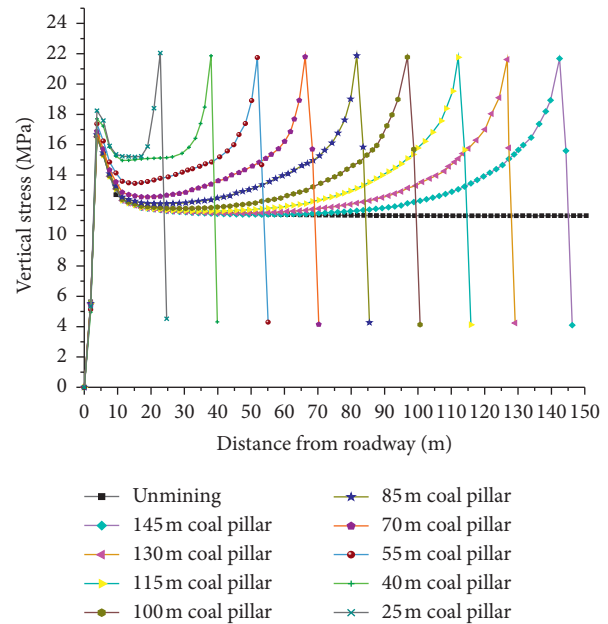
FIGURE 9: Stress curve with different widths of the coal pillar.

bearing stress range is reduced from 85 m to 55 m. The presplitting of the mining panel at 35 m showed the same characteristics, but the degree of stress reduction was only 1.7 MPa, and the range of the advanced abutment stress was shortened to 70 m. When the presplitted mining panel is 50 m and 65 m, due to the balanced stress distribution on both sides of the presplitted position, only the stress reduction phenomenon is shown at the presplitted position, but the range of the advanced abutment stress is not reduced.

4.3.3. The Effect of Deep Hole Blasting on the Advanced Abutment Stress Field. The artificial cracks produced by the advanced deep hole blasting intersect with the original cracks, which makes the roof collapse with mining, weakening the source of the advanced abutment stress. Under the influence of mining stress, the roof in front of the coal wall is broken more and the bearing capacity is reduced. As shown in Figure 11, the peak stress is reduced from 22 MPa to 18 MPa, and the area of increased stress shifts deeper. After the deep hole blasting, the stress concentration is reduced overall, and the stress change gradient is reduced. The presplitting position shows that the degree of stress blocking is weaker than that before. The field range was further reduced to 55 m.

By arranging measuring points at 10 m on both sides of the presplitting zone and recording the speed-time curve of the measuring points, the propagation of stress waves in the roof and the blocking effect of cracks on dynamic loads were studied. Figure 12 shows the vibration time-history curves of the nodes in the horizontal and vertical directions of the top plate, respectively. As can be seen from Figure 12(a), the entire vibration time-history at the location of measuring point 1 lasts about 0.06 s. The curve is triangular and consistent with the dynamic load of the analog input. The peak value is $53 \times 10{-2}$ cm/s. With the increase of the propagation distance of the stress wave and

(a)

(b)

(c)

(d)
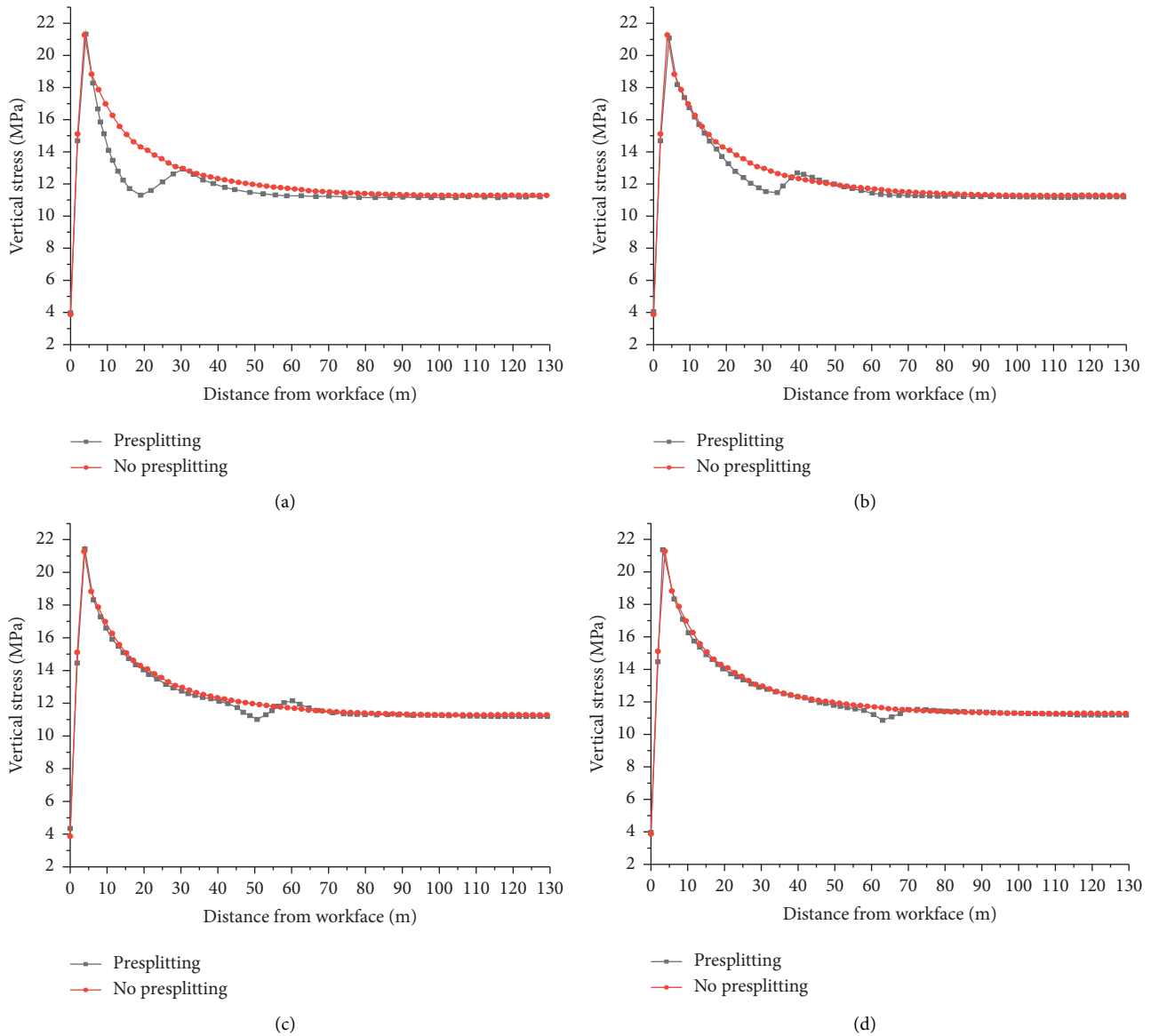
FIGURE 10: Vertical stress curves at different presplitting positions. (a) 20 m ahead mining panel. (b) 35 m ahead mining panel. (c) 50 m ahead mining panel. (d) 65 m ahead mining panel.

the existence of damping, the amplitude decreases to 38×10^{-2} cm/s at the presplitting zone, and transmission and reflection phenomena occur at the presplitted surface, because the distances between the measuring points 1 and 3 to the crack are the same. At about 0.2 s, the vibration waveform was simultaneously monitored at measuring point 3 and measuring point 1, and the amplitudes were attenuated to 17×10^{-2} cm/s and 14×10^{-2} cm/s, respectively. The transmitted wave is attenuated by 68% compared to the incident wave. Although no dynamic load is applied in the direction perpendicular to the rock layer, due to the overall vibration of the rock layer and the reflection of the wave in the fissure, the vibration waveforms are monitored at measurement points 1 and 3, and the amplitude of the waveform in the y direction is much smaller than that in the x direction. The crack surface cannot transmit the vibration in the y direction, so the vibration waveform is not recorded at the

monitoring point 2. It can be seen that the crack has a significant blocking effect on the dynamic load.

5. Field Application

5.1. Project Overview. The 22115 mining panel of Shanxi Luning Coal Mine is close to the track dip, belt dip, and return dip. The depth is about 500 m, the mining panel width is 207 m, and the thickness of the coal seam in the minable section is 4.0 m, and the inclination angle is 4°. The immediate roof is mudstone and siltstone with a thickness of 12 m, and the main roof is fine-grained sandstone with a thickness of 8 m. The hard roof is not easy to collapse, which leads to a large range of advanced abutment stress. It is easy to affect the stability of the surrounding rock when it is close to the roadway. As shown in Figure 13, in the past, when the 80 m
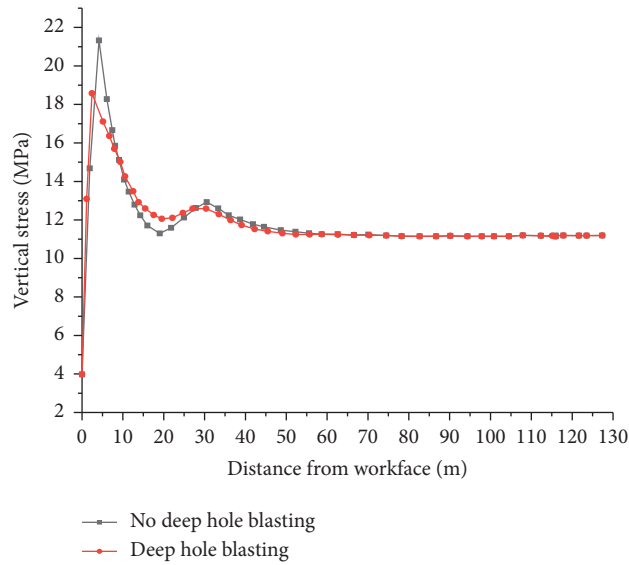
Figure 11: Vertical stress curves under deep hole blasting.

(a)

(b)
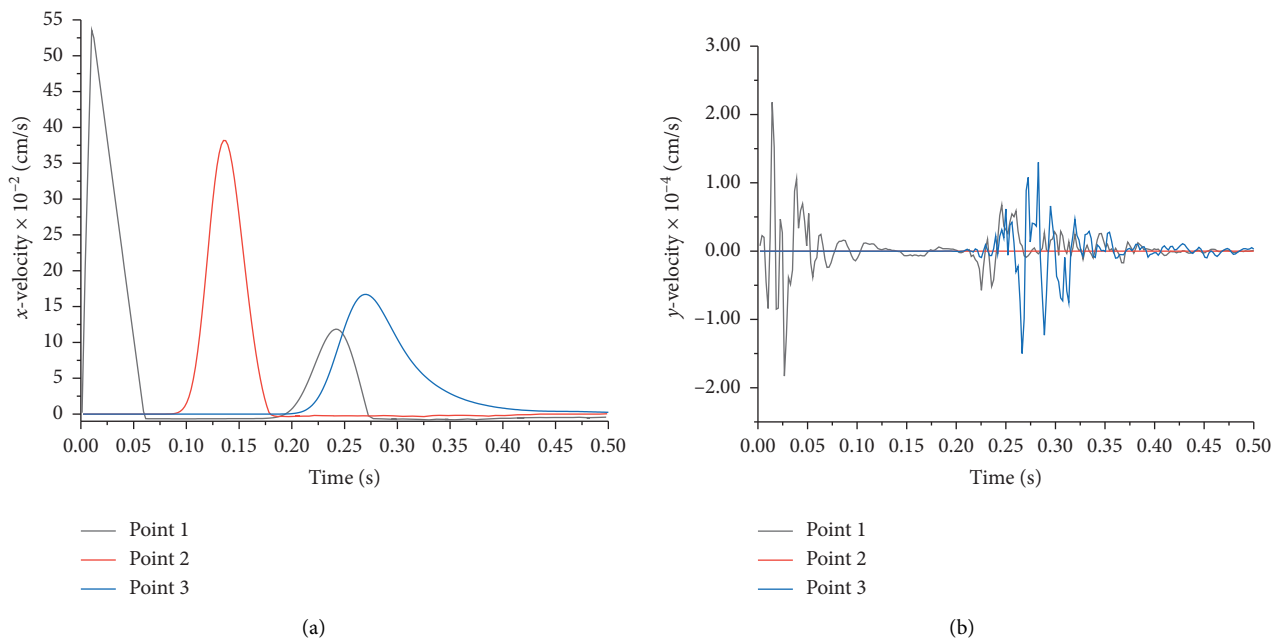
Figure 12: Speed-time curve of measuring point. (a) x-velocity. (b) y-velocity.

coal pillars were left, the surrounding rock of the roadway often had problems such as roofing and spalling rib. The roadway can only be protected by increasing the size of the coal pillar, resulting in a serious waste of coal resources.

5.2. Blasting Plan and Effect Monitoring. Through the combination of directional energy gathering blasting and advanced periodic deep hole blasting, the range of advanced abutment stress and the peak value of stress are reduced. The roof collapse is promoted to protect the safety of roadway and mining panel production. As shown in Figure 14, combined with the previous analysis, the end-mining coal pillar size is

designed to be 60 m, and firstly the directional presplit blasting is carried out 15 m in front of the end-mining line. Drilling obliquely upwards from the two roadways, the blast holes are distributed in a fan shape. Advanced periodic deep hole blasting is carried out during the normal mining of the mining panel, and every three blast holes are arranged in a group of fan-shaped ones. The blast hole parameters [21, 22] are designed according to the geological conditions of the working area and blasting requirements.

The monitoring mainly measures the advanced abutment stress. As shown in Figure 14, the measuring stations are respectively arranged on the both side of presplitting line, and each station is arranged with three measuring points. It

(a)

(b)

(c)
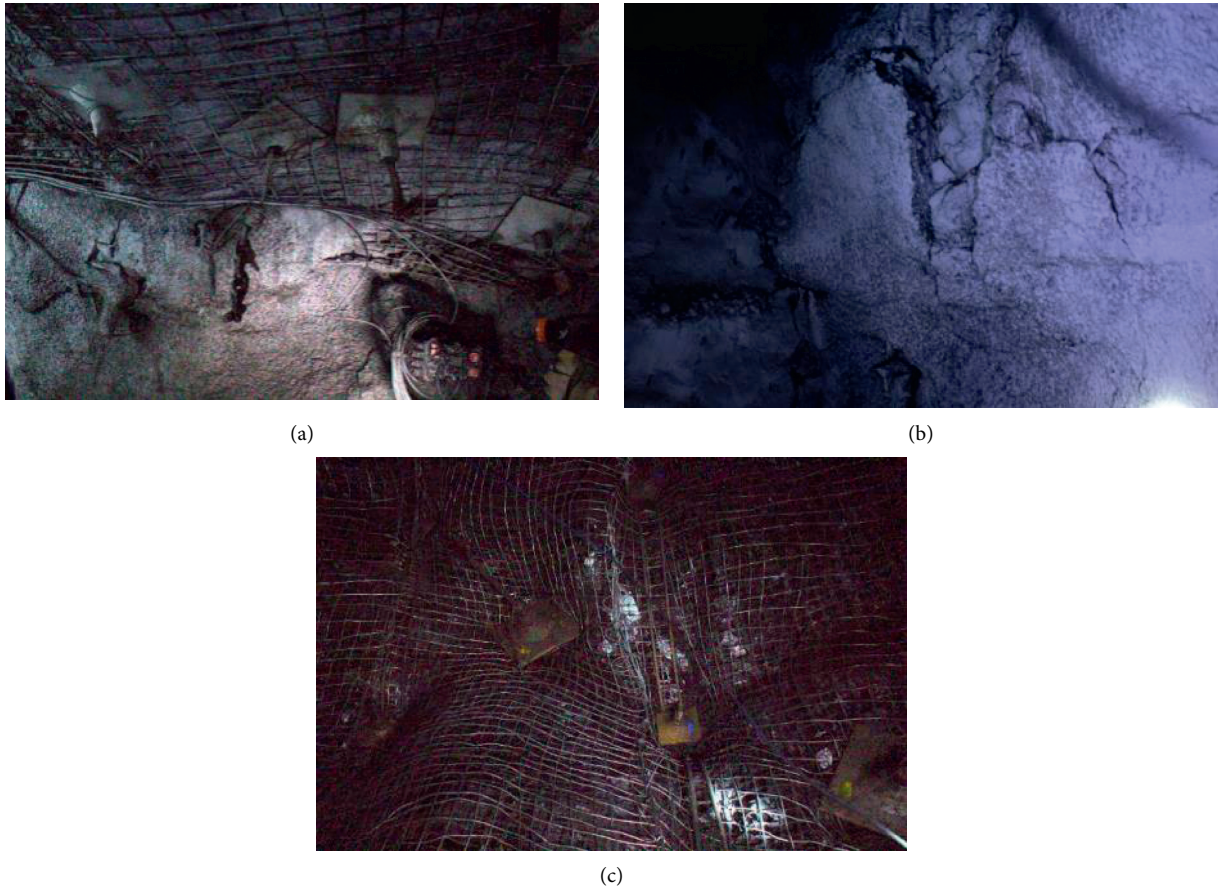
Figure 13: Roadway damage forms. (a) Roof collapse. (b) Spalling rib. (c) Anchor failure.
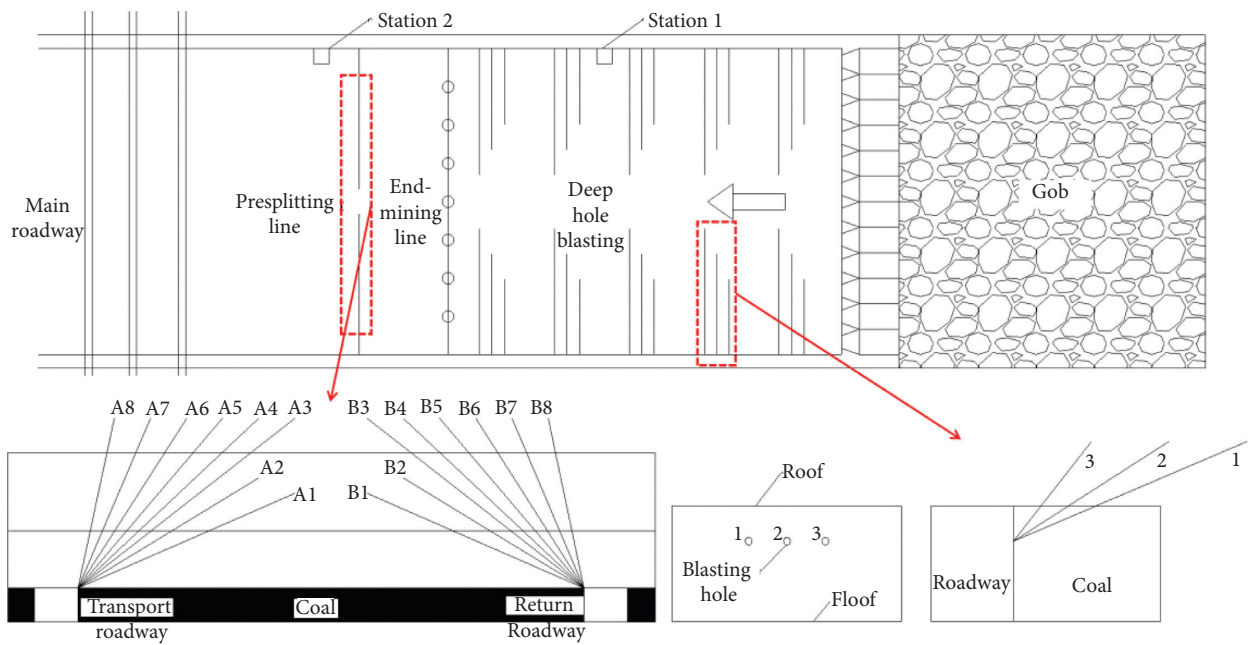
Figure 14: Blasting plan and blast hole layout.
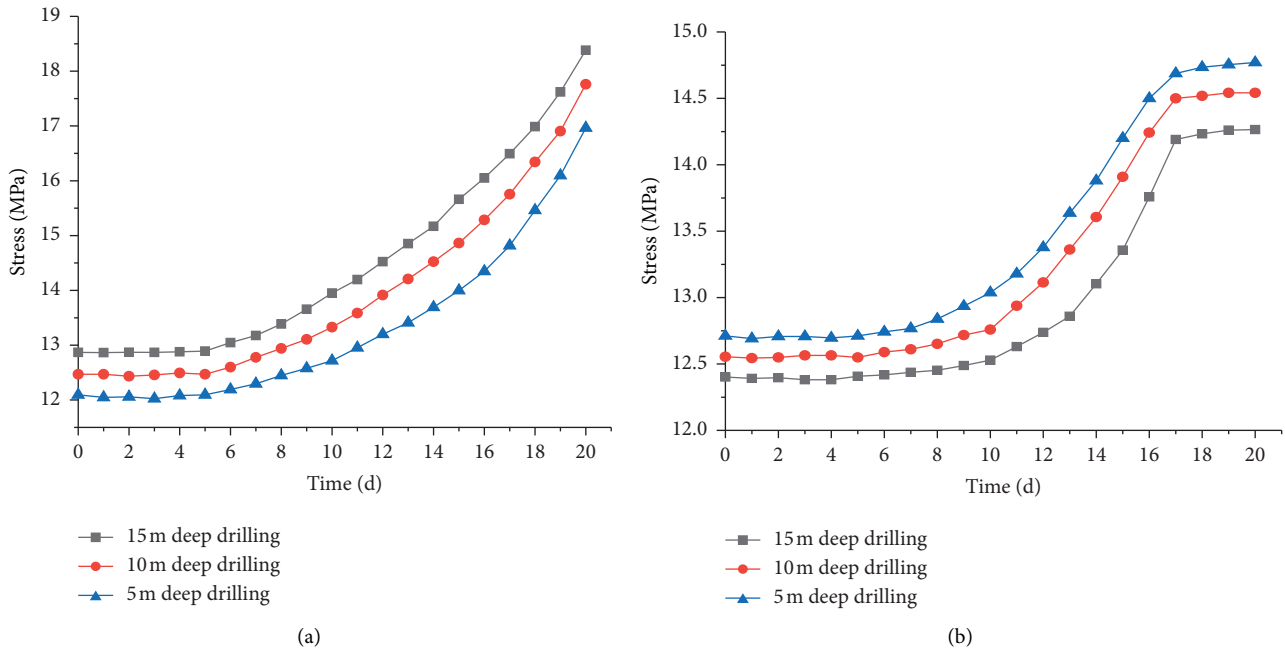
FIGURE 15: Abutment pressure monitoring curve. (a) Station 1. (b) Station 2.

can be seen from the monitoring result curve in Figure 15 that the number of days of stress increase of station 1 is about 16 days, and the value of station 2 remains unchanged after 9 days of pressure increase due to the stop of mining. Starting from the time point when the pressure count value began to increase, the stress value of station 1 increased by an average of 5 MPa, and the stress value of station 2 increased by an average of 2 MPa within 9 days; the value of the advanced abutment stress decreased significantly. Calculated by considering the daily advance of mining 4 m and the layout of the station, after the blasting pressure relief technology was proposed in use, the advanced abutment stress range was reduced from 80 m to 55 m.

6. Conclusion

This paper considers the problem that the width of the end-mining coal pillar is large under hard roof conditions and the roadway is strongly affected by mining. Through the analysis of the distribution characteristics of the stress field inside the coal pillar, the calculation principle of the coal pillar size was obtained. Based on the formation conditions and transfer forms of the advanced abutment stress, a pressure relief technique using a combination of directional presplitting and deep hole blasting was proposed, and the pressure relief effect was studied through numerical simulation and field tests. The main conclusions are as follows:

(1) The size of the limit end-mining coal pillar is the sum of the range of the advanced abutment stress field and the stress field range of the roadway limit equilibrium area. When the stress disturbance boundary of the advanced abutment stress field overlaps with the boundary of the roadway stress

field limit equilibrium zone, the surrounding rock gradually becomes unstable;

(2) The fracture surface formed by presplitting blasting leads to a decrease in the degree of rock layer connection, which can not only block the transmission of the static stress field in the stope but also cause attenuation of the dynamic load. Advanced deep hole blasting reduces the source of the advanced abutment stress by reducing the integrity of the roof and shortening the distance between one ceiling and the other ceiling;

(3) Numerical simulation analysis shows that the effect of presplitting blasting on stress is related to the gradient of the stress field. The closer the presplitting surface is to the peak of the advanced abutment stress, the more obvious the effect of stress blocking;

(4) The combination of presplitting blasting and deep hole blasting effectively controls the advanced abutment stress. The industrial test of 22115 mining panel shows that the surrounding rock of the downhill roadway remains stable even when the size of the end-mining coal pillar is shortened to 60 m.

Data Availability

The data used to support the findings of this study are included within the article.

Conflicts of Interest

The authors declare that there are no conflicts of interest regarding the publication of this paper.

References

 [1] N. Li, B. Huang, X. Zhang, T. Yuyang, and B. Li, "Characteristics of microseismic waveforms induced by hydraulic fracturing in coal seam for coal rock dynamic disasters prevention," *Safety Science*, vol. 115, pp. 188–198, 2019.

 [2] D. Ma, H. Duan, W. Liu, X. Ma, and M. Tao, "Water-sediment two-phase flow inrush hazard in rock fractures of overburden strata during coal mining," *Mine Water and the Environment*, vol. 39, no. 2, pp. 308–319, 2020.

 [3] A.-Y. Cao, L.-M. Dou, X. Luo, Y.-D. Zheng, J.-L. Huang, and K. Andrew, "Seismic effort of blasting wave transmitted in coal-rock mass associated with mining operation," *Journal of Central South University*, vol. 19, no. 9, pp. 2604–2610, 2012.

 [4] Q. Zhang, E. Wang, X. Feng et al., "Rockburst risk analysis during high-hard roof breaking in deep mines," *Natural Resources Research*, vol. 29, no. 6, pp. 4085–4101, 2020.

 [5] G. Wang, S. Gong, L. Dou, W. Cai, X. Yuan, and C. Fan, "Rockburst mechanism and control in coal seam with both syncline and hard strata," *Safety Science*, vol. 115, pp. 320–328, 2019.

 [6] J. Xia, Y. Cheng, M. Zhao, C. Liu, and Y. Wen, "Study on mining technology of shallow hole + deep hole shrinkage method with ductule grouting in advance for roof reinforcement," *IOP Conference Series: Earth and Environmental Science*, vol. 295, Article ID 042123, 2019.

 [7] J. Zuo, Z. Li, S. Zhao, Y. Jiang, H. Liu, and M. Yao, "A study of fractal deep-hole blasting and its induced stress behavior of hard roof strata in bayangaole coal mine, China," *Advances in Civil Engineering*, vol. 2019, Article ID 9504101, 14 pages, 2019.

 [8] Z. Zhou, Y. Zhao, W. Cao, L. Chen, and J. Zhou, "Dynamic response of pillar workings induced by sudden pillar recovery," *Rock Mechanics and Rock Engineering*, vol. 51, no. 10, pp. 3075–3090, 2018.

 [9] H. Liu, J. Dai, J. Jiang, P. Wang, and J. Yang, "Analysis of overburden structure and pressure-relief effect of hard roof blasting and cutting," *Advances in Civil Engineering*, vol. 2019, Article ID 1354652, 14 pages, 2019.

[10] Y. Chen, S. Ma, Y. Yang, N. Meng, and J. Bai, "Application of shallow-hole blasting in improving the stability of gob-side retaining entry in deep mines: a case study," *Energies*, vol. 12, no. 19, p. 3623, 2019.

[11] T. Hu, "Study on the parameters of roadside support after the cantilever beam of the basic roof with height of fracture zone cut by deep-hole blasting," *IOP Conference Series: Earth and Environmental Science*, vol. 283, Article ID 012038, 2019.

[12] B. Huang, J. Liu, and Q. Zhang, "The reasonable breaking location of overhanging hard roof for directional hydraulic fracturing to control strong strata behaviors of gob-side entry," *International Journal of Rock Mechanics and Mining Sciences*, vol. 103, pp. 1–11, 2018.

[13] J. Yang, C. Liu, and B. Yu, "Application of confined blasting in water-filled deep holes to control strong rock pressure in hard rock mines," *Energies*, vol. 10, no. 11, p. 1874, 2017.

[14] B. Chen, C. Liu, and J. Yang, "Design and application of blasting parameters for presplitting hard roof with the aid of empty-hole effect," *Shock and Vibration*, vol. 2018, Article ID 8749415, 16 pages, 2018.

[15] G. R. Feng, "Study on rational width of the end-mining coal pillar of extra-thick mining panel in permo-carboniferous igneous rock intrusion area," *Journal of Mining & Safety Engineering*, vol. 36, no. 1, pp. 87–94, 2019, in Chinese.

[16] L. X. Xie, Q. B. Zhang, J. C. Gu et al., "Damage evolution mechanism in production blasting excavation under different stress fields," *Simulation Modelling Practice and Theory*, vol. 97, Article ID 101969, 2019.

[17] W. Yuan, S. Liu, W. Wang et al., "Numerical study on the fracturing mechanism of shock wave interactions between two adjacent blast holes in deep rock blasting," *Earthquake Engineering and Engineering Vibration*, vol. 18, no. 4, pp. 735–746, 2019.

[18] Z. Liu, A. Cao, G. Liu, and J. Li, "Experimental research on stress relief of high-stress coal based on noncoupling blasting," *Arabian Journal for Science and Engineering*, vol. 43, no. 7, pp. 3717–3724, 2018.

[19] X. Xu, M. He, C. Zhu, Y. Lin, and C. Cao, "A new calculation model of blasting damage degree-Based on fractal and tie rod damage theory," *Engineering Fracture Mechanics*, vol. 220, p. 106619, 2019.

[20] J. Hu, X. Zhang, Y. Gao, Z. Ma, X. Xu, and X. Zhang, "Directional presplit blasting in an innovative no-pillar mining approach," *Journal of Geophysics and Engineering*, vol. 16, no. 5, pp. 875–893, 2019.

[21] G. Yue et al., "Optimal layout of blasting holes in structural anisotropic coal seam," *PLoS One*, vol. 14, no. 6, Article ID e0218105, 2019.

[22] P. Bańka, H. Badura, and M. Wesołowski, "The possibility of increasing the efficiency of accessible coal deposits by optimizing dimensions of protective pillars or the scope of exploitation," *IOP Conference Series: Materials Science and Engineering*, vol. 268, Article ID 12005, 2017.

Research Article

Study on the Mechanical Relationship among the Backfilling Mining Support, Roof Rock Beam, and Gangue Filling Body in Comprehensive Mechanized Filling Mining Process

Zhimin Huang [1], **Lei Zhang** [1], **and Zhanguo Ma**[2]

[1]*School of Materials Science and Physics, China University of Mining & Technology, Xuzhou, Jiangsu 221116, China*
[2]*State Key Laboratory for Geomechanics and Deep Underground Engineering, School of Mechanics and Civil Engineering, China University of Mining & Technology, Xuzhou, Jiangsu 221116, China*

Correspondence should be addressed to Lei Zhang; cumtzl@126.com

Based on the theory of elastic foundation beam, the mechanical model of the backfilling mining support-roof rock beam-gangue filling body under the condition of comprehensive mechanized filling mining is established. The foundation coefficient of each part is determined, and the subsidence of each part of roof rock beam is calculated. It is found that the initial filling height is the decisive factor to control the subsidence and migration stability of each part of the roof rock beam. Properly increasing the pushing force of backfilling-coal mining hydraulic support on the filling body can also effectively control the roof subsidence. The comprehensive mechanized filling mining process was studied by similar simulation experiments, it is found that the influence law of initial filling height on roof rock beam subsidence is the same as that of theoretical analysis, and the experimental measurement values and fitting function relationships are consistent with the theoretical calculation results.

1. Introduction

In recent years, under the guidance of the concepts of "green mining" and "scientific mining" [1, 2], the scientific mining of coal has made rapid development [3–8]. The comprehensive mechanized solid filling mining technology solves the organic combination problem of "three down" mining technology and comprehensive mining technology and realizes the production mode of high mining rate, high yield, high efficiency, and low cost under buildings [9, 10]. A large number of engineering practices put forward higher and higher requirements for basic research on strata control theory and mechanical properties of filling body under the condition of filling mining. Many scholars have carried out a lot of theoretical and experimental studies in this regard [11–22]. In the process of filling coal mining, after the filling body is tamped by the hydraulic support of filling coal mining, it will replace the raw coal to support the overlying strata, so that the movement and fracture of the overlying strata are significantly reduced. Therefore, on one hand, no

caving zone will be formed, and on the other hand, the height of the fracture zone will be greatly decreased, and there may even be no fracture zone. The goaf is filled with gangue. The filling body is in the form of scattered fragments and granular structure, and its movement process is in the form of consolidation and compaction. Most of the strata above are curved subsidence zones, the rock mass structure is relatively complete, and the strata are cut regularly by the layers, so that the structure body presents a layered structure of normal heterogeneity and tangential homogeneity. The deformation form of rock mass structure is the bending deformation of beam or slab [23]. Under the condition of filling mining, the filling body has a strong control effect on the overlying strata, and the roof subsidence and internal force are greatly reduced; therefore, in theory, the basic roof or key layer is generally regarded as the beam or plate on the elastic foundation to consider the interaction between the roof, support, and filling body. The foundation coefficient of the filling body reflects the supporting role of the filling body, and its value is directly related to the compaction

mechanical characteristics of the gangue filling body. Therefore, on the basis of fully understanding the mechanical properties of the gangue filling body, a more accurate mechanical model of "backfilling mining support-roof rock beam-filling body" need to be established, which has important theoretical value and practical significance for improving the theoretical system of the relationship between strata movement and support surrounding rock in solid filling coal mining.

Based on the elastic foundation beam theory, this paper establishes the mechanical model of the backfilling mining support-roof rock beam-gangue filling body. The influence of initial filling height and compaction force of filling support on the subsidence of roof rock beam is studied by solving the differential equation of the subsidence of roof rock beam under the condition of comprehensive mechanized filling mining, and the results are verified by similar simulation experiments.

2. Mechanical Model of "Backfilling Mining Support-Roof Rock Beam-Filling Body" and the Analysis

2.1. Mechanical Model. Under the condition of comprehensive mechanized mining and dense filling, rock beam, coal body and filling body can be regarded as elastic foundation, and the mechanical model of elastic foundation beam of roof rock beam is established. The relationship among backfilling mining support, roof rock beam, and filling body is shown in Figure 1(a), and the mechanical model is shown in Figure 1(b).

In Figure 1, the roof can be regarded as an infinitely long elastic foundation beam of unit width, with thickness of h. The weight of the overlying strata produces a distributed load of concentration q on the beam. The leading force of the front coal seam on the roof is $p_1(x)$, and the thickness of the coal seam is H_0. The overlying strata is supported by the backfilling mining support within the top control area, with force $p_2(x)$ and length of l, and the mined area outside the top control area of the mining face is supported by the gangue filling body, with force $p_3(x)$.

The coordinate origin O is selected at the coal wall. The positive direction of the x-axis is to the right, and the positive direction of the y-axis is downward. This paper discusses the near horizontal coal seam, and horizontal left is the advancing direction of mining face. The horizontal position x is taken as the independent variable and the displacement function $y(x)$ is taken as the basic unknown quantity. Under the action of load q, the subsidence of roof rockbeam at the coal wall is h_0. On the side of goaf, the subsidence of roof rock beam at the position of maximum roof distance control is $h_0 + h_1$, and h_1 is the subsidence before the roof rock beam touches the gangue filling body.

Based on the Winkler foundation assumption, the subsidence equation of roof rock beam under the condition of comprehensive mechanized filling mining can be listed as

$$EI \frac{0^4 y}{0 x^4} = q + \gamma h - p_1, \quad x < 0, \tag{1}$$

$$EI \frac{0^4 y}{0 x^4} = q + \gamma h - p_2, \quad 0 \le x \le l, \tag{2}$$

$$EI \frac{0^4 y}{0 x^4} = q + \gamma h - p_3, \quad x > l. \tag{3}$$

Among them, the coal body and filling body are simplified as the elastic foundation, meeting Winkler foundation assumption:

$$\begin{aligned} p_1 &= k_1 y \quad (x < 0), \\ p_3 &= k_3 (y - h_0 - h_1) \quad (x > l). \end{aligned} \tag{4}$$

For the support force p_2, according to the working conditions of the comprehensive mechanized filling mining, considering that the active support function of the filling hydraulic support is mainly to make the rear roof beam of the support resist the bending and sinking of the roof, the active load of the support is assumed to be:

$$p_2 = p_a + \frac{p_b - p_a}{l} x, \quad 0 \le x \le l. \tag{5}$$

In equations (1)–(3), E and I are the elastic modulus and section inertia moment of the roof rock beam respectively, and γ is the bulk density of the rock beam, k_1 is the foundation coefficient of the coal seam and k_3 is the foundation coefficient of filling gangue. p_a and p_b are the support loads at the front and back of the support, respectively.

Equation (1) is solved firstly. For the form of the homogeneous equation corresponding to equation (1), let

$$\alpha_1 = \frac{\sqrt{2}}{2} \sqrt[4]{\frac{k_1}{EI}}. \tag{6}$$

The general solution is

$$\begin{aligned} y_0 &= e^{\alpha_1 x} (A_1 \sin \alpha_1 x + A_2 \cos \alpha_1 x) \\ &\quad + e^{-\alpha_1 x} (A_3 \sin \alpha_1 x + A_4 \cos \alpha_1 x). \end{aligned} \tag{7}$$

The special solution is $y^* = (q + \gamma h)/k_1$; therefore, the solution of equation (1) can be expressed as: $y = y_0 + y^*$.

Because the rock beam is not affected by mining at the far end of both sides, there are $y = (q + \gamma h)/k_1$ when $x = -\infty$.

By substituting the general solution, we can get $A_3 = A_4 = 0$.

Therefore, the solution of equation (1) is

$$y_1 = e^{\alpha_1 x} (A_1 \sin \alpha_1 x + A_2 \cos \alpha_1 x) + \frac{q + \gamma h}{k_1}, \quad x < 0. \tag{8}$$

Using the same method, let $\alpha_2 = (\sqrt{2}/2)\sqrt[4]{k_3/EI}$, the solution of equation (3) can be obtained as follows:

$$y_3 = e^{-\alpha_2 x} (C_3 \sin \alpha_2 x + C_4 \cos \alpha_2 x) + \frac{q + \gamma h}{k_3} + h_0 + h_1, \quad x > l. \tag{9}$$

(a)

(b)
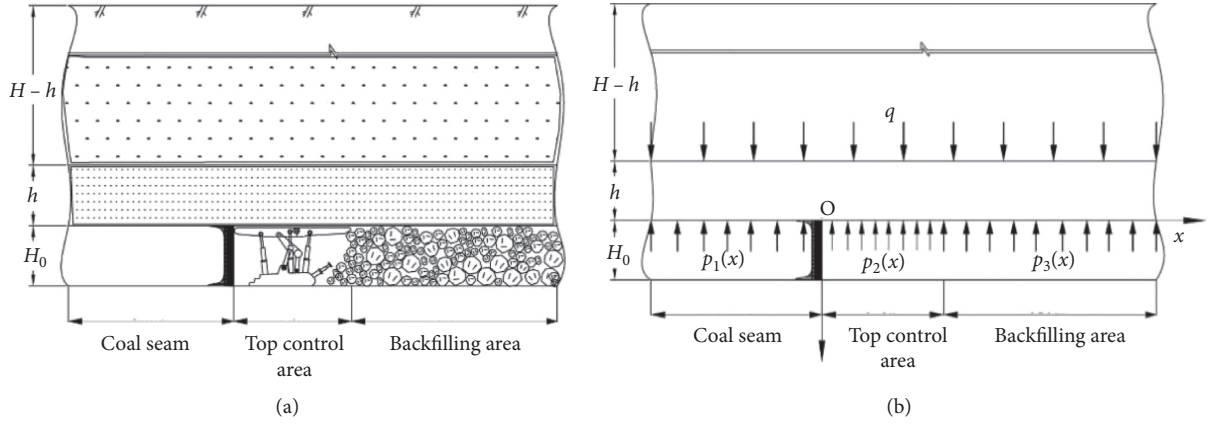
FIGURE 1: Mechanical model of backfilling mining support-roof rock beam-filling body.

Finally, equation (2) is solved through integration directly, the solution is

$$y_2 = \frac{p_a - p_b}{120EIl}x^5 + \frac{q + \gamma h - p_a}{24EI}x^4 + B_1 x^3 + B_2 x^2$$
$$+ B_3 x + B_4, \quad 0 \le x \le l. \tag{10}$$

The coefficients A_1, A_2, B_1, B_2, B_3, B_4, C_3, and C_4 in equations (8)–(10) can be obtained by using the boundary continuity conditions of the boundary between the support and the coal wall ($x = 0$) and the boundary between the support and the filling body ($x = l$):

$$x = 0: \begin{cases} y_1 = y_2, \\ y_1' = y_2', \\ y_1'' = y_2'', \\ y_1''' = y_2''', \end{cases}$$

$$x = l: \begin{cases} y_2 = y_3, \\ y_2' = y_3', \\ y_2'' = y_3'', \\ y_2''' = y_3'''. \end{cases} \tag{11}$$

As the foundation coefficient k in Winkler foundation model is related to the deformation modulus E_s and the thickness H of the foundation, when both sides of the compression layer are free of deformation,

$$k = \frac{E_s}{H}. \tag{12}$$

In the questions studied above, for k_1, H is the mining height H_0, while for k_3, H is the height of the filling body foundation H_3, which is affected by the allowable pressure height of the support during the filling mining process and the initial filling rate. H_3 can be expressed as

$$H_3 = H_0 - h_0 - h_1. \tag{13}$$

Similarly, for k_1, E_s is the deformation modulus of the solid coal foundation E_{s0}; while for k_3, E_s corresponds to the deformation modulus of the filling body foundation E_{s3}. E_{s3}

is mainly affected by the compaction force of the support on the filling body during the filling mining process. According to the compaction mechanical property test of the slag mixture filling body [24], it can be seen that there is a linear relationship between E_{s3} and the compaction stress σ, and can be expressed as

$$E_{s3} = a_4 + b_4 \sigma. \tag{14}$$

Therefore, k_1 and k_3 can be expressed as

$$k_1 = \frac{E_{s0}}{H_0},$$
$$k_3 = \frac{E_{s3}}{H_3} = \frac{a_4 + b_4 \sigma}{H_0 - h_0 - h_1}, \tag{15}$$

where H_3 is the thickness of the foundation, which is equal to the initial filling height h_g of the filling area, so k_3 can also be expressed as

$$k_3 = \frac{E_{s3}}{h_g} = \frac{a_4 + b_4 \sigma}{h_g}. \tag{16}$$

It can be seen that for a given gangue filling material, the value of k_3 is affected by two factors, the initial filling height h_g and the compaction stress σ that the filling body bears. Substituting equation (16) into (8)–(10) can get the relationship among the amount of roof rock beam subsidence and h_g, σ, H_0, E, I, k_1, etc.

Taking a coal mine in Shanxi Province, China, as an example for analysis, take $h = 4$ m, $H_0 = 3$ m, $E = 10$ GN/m^2, $I = 5.33$, $q = 3.11$ MPa, $\gamma = 25$ kN/m^3, $p_a = 0.73$ MPa, $p_b = 0.80$ MPa, $l = 7.5$ m, and $k_1 = 0.6$ GN/m^2. According to equation (14), the fitting coefficient of primary slag mixture ($a_4 = -433702$, $b_4 = 15.987$) is selected, then equation (17) can be obtained:

$$E_s = -433702 + 15.987\sigma. \tag{17}$$

The relationship among y_1, y_2, y_3, and h_g and σ will be discussed below. Substituting the above parameters into equations (8) to (10), the expressions for y_1, y_2, and y_3 can be obtained as follows:

$$y_1 = 0.00535 + e^{0.23x}\left[A_2 \cos(0.23x) + A_1 \sin(0.23x)\right], \tag{18}$$

$$y_2 = B_4 + B_3 x + B_2 x^2 + B_1 x^3 + 1.939 \times 10^{-6} x^4 - 1.459 \times 10^{-9} x^5, \tag{19}$$

$$y_3 = 3 - h_g + \frac{3.21 \times 10^6 h_g}{-433702 + 15.987\sigma} + e^{-2.081\times10^{-3}x\left((-433702+15.987\sigma)/h_g\right)^{1/4}}$$
$$\left\{C_4 \cos\left[2.081 \times 10^{-3} x \left(\frac{-433702 + 15.987\sigma}{h_g}\right)^{1/4}\right] + C_3 \sin\left[2.081 \times 10^{-3} x \left(\frac{-433702 + 15.987\sigma}{h_g}\right)^{1/4}\right]\right\}. \tag{20}$$

In the equation, the coefficients A_1, A_2, B_1, B_2, B_3, B_4, C_3, and C_4 are all related to σ and h_g. For each set of σ and h_g values, the specific expressions of y_1, y_2, and y_3 can be obtained. The effects of σ and h_g on y_1, y_2, and y_3 will be discussed below, respectively.

2.2. Effect of Initial Filling Height on Roof Rock Beam Subsidence.

The roof's subsidence amount $y_1|_{x=0}$ at the coal wall $x = 0$, the roof's subsidence amount y_2 above the support and the roof's subsidence amount y_3 above the gangue filling body are calculated in the condition of the compaction stress $\sigma = 2\,\text{MPa}$ and $h_g = 1.8\,\text{m}$, 2.1 m, 2.4 m, 2.7 m and 2.85 m respectively, which are substituted into equations (18)–(20). The results are shown in Figure 2.

It can be seen from the figure that when the filling body is subjected to the pushing and pressing stress of 2 MPa of the support tamping mechanism, different positions of the roof rock beams sink in different degrees after filling. For dense filling mining, under the pushing and pressing action of tamping mechanism, the filling body can be connected to the top basically. However, due to mining, a certain subsidence occurs before the roof hits the gangue, so the initial filling height h_g is also different. The magnitude of h_g has a significant effect on the subsidence of the roof rock beam.

First of all, the larger h_g is, the smaller the final stable subsidence of the roof rock beam above the filling area is. When $h_g = 1.8\,\text{m}$, the filling height is 60% of the mining height, and the final stable subsidence of the roof above the filling area is 1.38 m; when $h_g = 2.4\,\text{m}$, the filling height is 80% of the mining height, and the final stable subsidence of the roof above the filling area is 0.85 m; when $h_g = 2.85\,\text{m}$, the filling height is 95% of the mining height, and the final stable subsidence of the roof above the filling area is only 0.44 m.

Secondly, subsidence y_3 of the rock beam above the filling body increases with the increase of the distance x from the coal wall. After a certain distance is filled, the subsidence of the rock beam above the filling body can reach stability, so h_g has a great influence on the distance of the final stable subsidence of the roof rock beam. When $h_g = 2.85\,\text{m}$, $x = 25\,\text{m}$ (filling distance behind the support is about 17 m), y_3 tends to be stable; when $h_g = 2.4\,\text{m}$, $x = 30\,\text{m}$ (filling distance behind the support is about 22 m), y_3 tends to be stable; when $h_g = 1.8\,\text{m}$, $x = 40\,\text{m}$ (filling behind the support is about 32 m), y_3 tends to be stable.

Thirdly, no matter what the height of h_g is equal to, the subsidence y_2 of the rock beam above the support increases with the increase of x, and basically satisfies the linear relationship. The subsidence at the front end of the support is small, and the subsidence at the back end of the support is large. At the same time, the subsidence of the roof above the support decreases with the increase of h_g.

Finally, the subsidence $y_1|_{x=0}$ of coal wall decreases with the increase of h_g, and basically satisfies the linear relationship. The filling height increases from 60% to 95% of the mining height, which can reduce the subsidence of the coal wall from 0.199 m to 0.067 m, a decrease of nearly 2/3. It can be seen that increasing the initial filling height can effectively control the subsidence and migration stability of each part of roof rock beam.

2.3. The Influence of Compaction Force of Self-Ramming Backfill Mining Hydraulic Support on the Subsidence of Roof Rock Beam.

When $h = 4\,\text{m}$, $H_0 = 3\,\text{m}$, $E = 10\,\text{GN/m}^2$, $I = 5.33$, $q = 3.11\,\text{MPa}$, $\gamma = 25\,\text{kN/m}^3$, $p_a = 0.73\,\text{MPa}$, $p_b = 0.80\,\text{MPa}$, $l = 7.5\,\text{m}$, $k_1 = 0.6\,\text{GN/m}^2$, $a_4 = -433702$, $b_4 = 15.987$, $h_g = 2.4\,\text{m}$, and σ is taken as 1.0 MPa, 1.5 MPa, 2.0 MPa, 2.5 MPa, 3.0 MPa respectively, $y_1|_{x=0}$, y_2, y_3 are calculated during equations (17)~(20). The influence of filling push pressure stress on the subsidence of roof rock beam is discussed, as shown in Figure 3.

It can be seen from the figure that when the self-ramming backfill mining hydraulic support exerts different amounts of compaction force on the filling body, the amount of subsidence of the roof rock beam will also change in different sizes.

First of all, σ has a great influence on the final stable subsidence of the roof rock beam in the filling area. The larger σ is, the smaller the final subsidence is. It can also be seen that when σ increases from 1.0 MPa to 2.0 MPa, the final subsidence of y_3 decreases by 0.25 m; when σ increases to 3.0 MPa, the final subsidence of y_3 only decreases by 0.09 m. Therefore, when the compaction stress is about 2.0 MPa, the subsidence of the roof rock beam can be effectively controlled. If the compaction stress is increased more on this basis, this control effect will not increase significantly.

Secondly, σ also has a certain influence on the distance of the final stable subsidence of the roof beam above the filling area. When $\sigma = 3.0\,\text{MPa}$, $x = 25\,\text{m}$ (filling distance behind the support is about 17 m), y_3 tends to be stable; when $\sigma = 1.0\,\text{MPa}$, $x = 45\,\text{m}$ (filling distance behind the support is about 37 m). y_3 tends to be stable. It can be observed that the smaller the compaction stress is, the longer the unstable area of roof subsidence movement is.

(a)

(b)

(c)
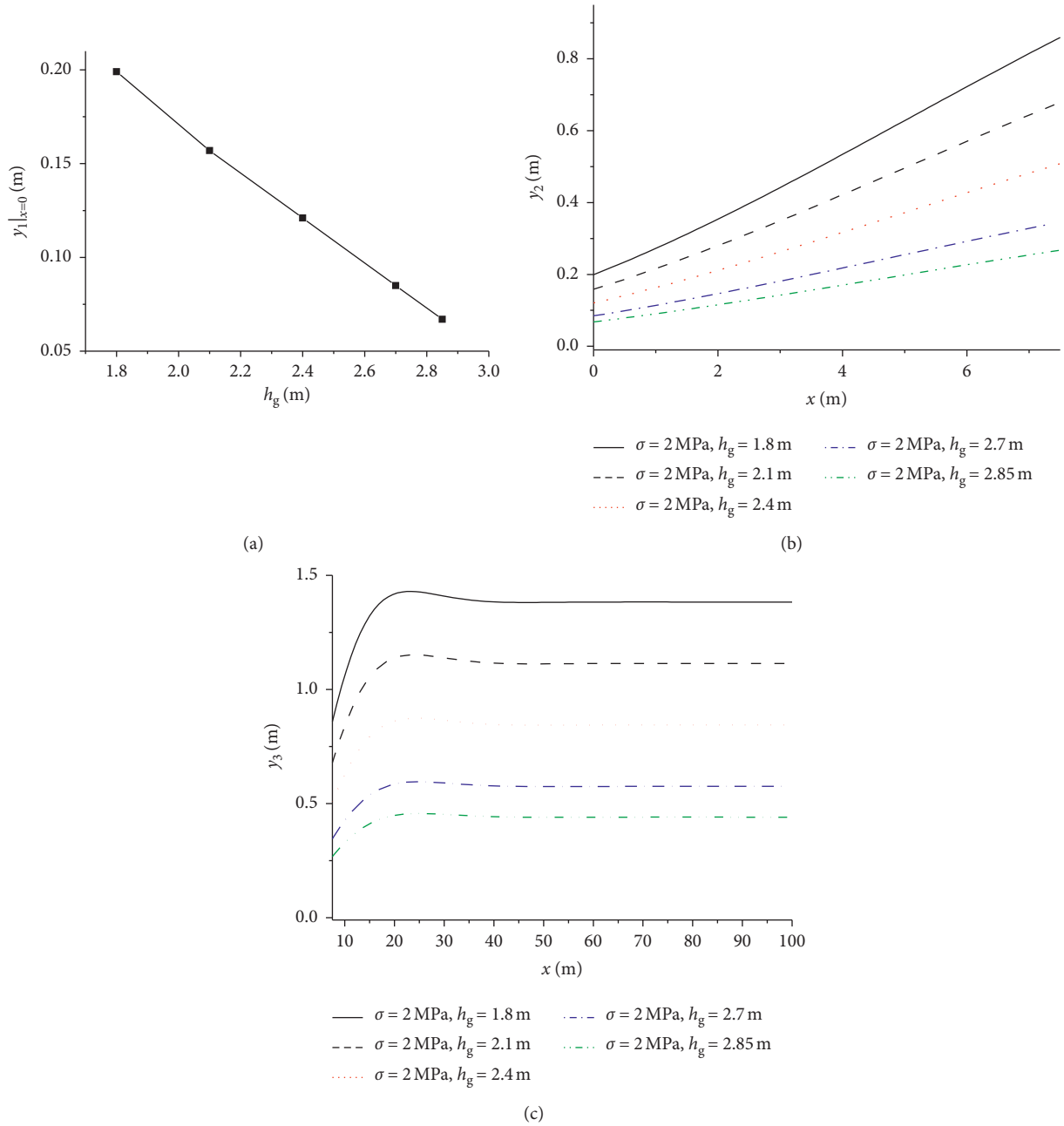
FIGURE 2: Roof's subsidence amount with different h_g. (a) Roof's subsidence amount of coal wall. (b) Roof's subsidence amount above the support. (c) Roof's subsidence amount above the gangue filling body.

Thirdly, when the compaction stress σ changes, the subsidence y_2 of the rock beam above the support still increases with the increase of x, and basically satisfies the linear relationship. The subsidence at the front end of the bracket is small, and the subsidence at the back end of the bracket is large. At the same time, the subsidence of the roof decreases with the increase of σ.

Finally, the subsidence $y_1|_{x=0}$ of coal wall decreases with the increase of σ, but it is nonlinear. In general, σ has little effect on the subsidence of coal wall. It can be seen that increasing the compaction stress σ of the support can effectively compact the back part of the backfilling body and

increase its deformation modulus, thus controlling the subsidence and instability range of the roof rock beam.

3. Physical Simulation of Comprehensive Mechanized Filling Mining

Similar material simulation experiment is not only intuitive and repeatable, but also an experimental method with good condition control flexibility and high efficiency. Therefore, it has become an important means to study the characteristics of strata movement and the law of mine pressure change in mining engineering. In this paper, on the basis of the

(a)

(b)

(c)
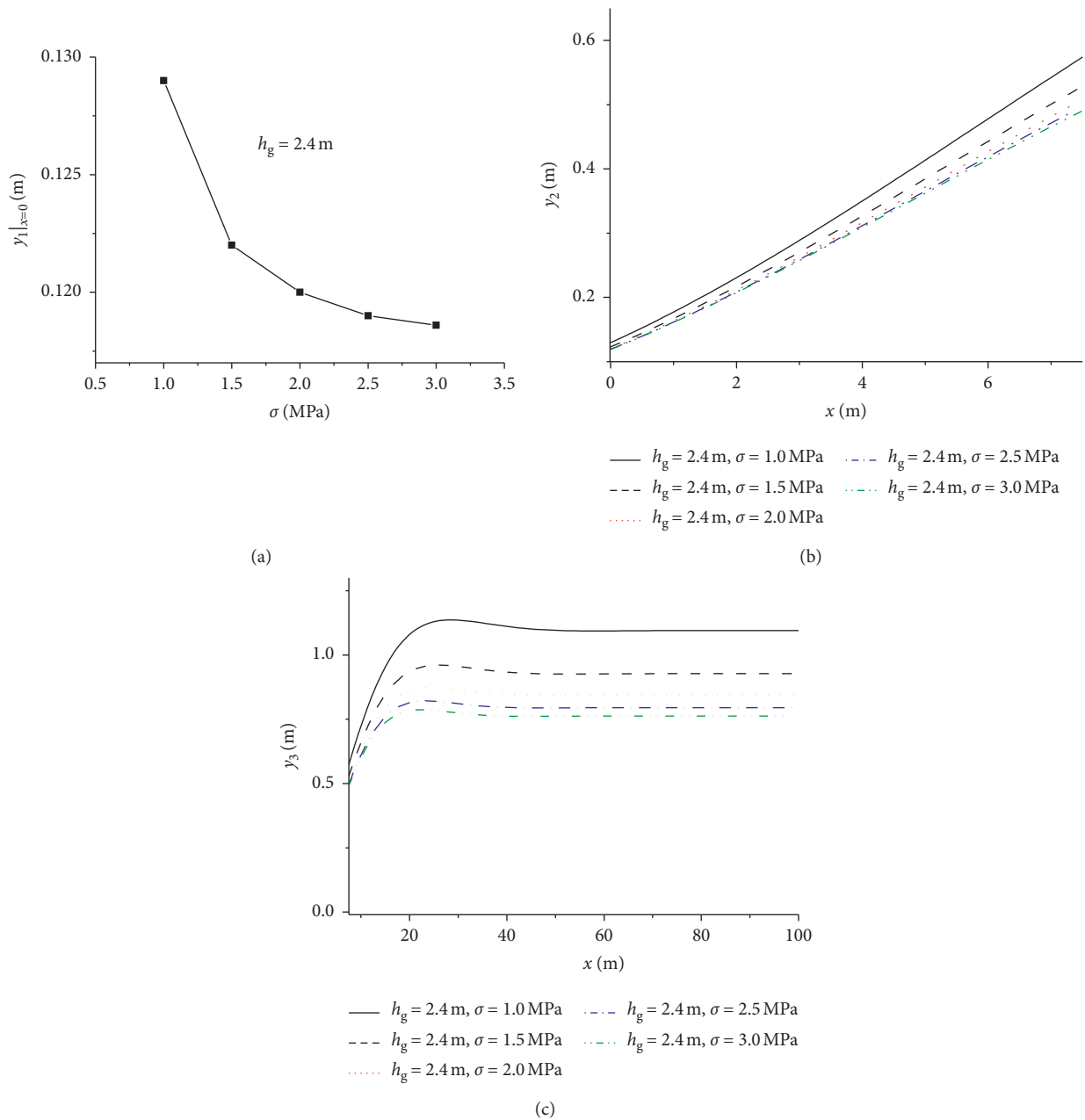
FIGURE 3: Roof's subsidence with different σ. (a) Roof's subsidence of coal wall. (b) Roof's subsidence above the support. (c) Roof's subsidence above the gangue filling body.

theoretical study of the mechanical model of filling mining, with the help of similarity theory, the simulation experiment of similar materials is carried out to observe the movement, failure, and stress change of rock strata in the process of filling mining and verify the theoretical calculation results.

3.1. Equipments and Materials of Similar Material Model Experiment.
In a similar material model experiment, the plane model test bench with the length × height × width = 2.50 m × 1.50 m × 0.20 m of the State Key Laboratory of Coal Resources and Safe Mining of China University of Mining and Technology is used. The upper part of the test bench is

equipped with cylinder loading system, and the model can be loaded by air pump. The image acquisition uses the digital photogrammetry system [24] independently developed by China University of Mining and Technology to track and shoot the whole process with fixed camera position and accurately calculate the movement of each point of the rock stratum through the image processing software in the later stage. During the model laying process, the Earth pressure cells are embedded, and the digital high-speed strain gauge is connected to monitor the rock stress of each layer during the experiment. The support model is pressurized by a manual hydraulic oil pump to adjust the height and support force of the support.

In the similar model, the following similar materials of rock stratum were selected: aggregate: ordinary fine-grained river sand after screening (particle size is less than 3 mm); cementitious material: gypsum, cement, calcium carbonate; layered material: mica powder. Before making the model, the aggregate and cement were weighed according to different proportions, mixed and stirred evenly with water, and the similar material experiment pieces were made, and their mechanical properties were measured after drying. After repeated tests, the final proportion of model materials was determined to meet the requirements of mechanical similarity.

High-density foam, low-density foam, and sponge material were selected for different height combinations to form 6 kinds of similar materials of filling body, as shown in Table 1. These six materials were tested for the characteristics of compaction strength. At the same time, according to the compaction test curve of the original slag mixture filling body [25], the theoretical value of stress and strain of the model material of the filling body used in the similar model was calculated according to the mechanical similarity ratio. The theoretical values were compared with the compaction curves of six model materials of the filling body, as shown in Figure 4. Among them, the stress-strain curve of No. 6 material was the closest to the theoretical curve, so this paper finally determined that No. 6 model material was selected as the model material of the filling body.

3.2. Experiment Scheme and Process of Similar Material Models.

The aforementioned coal mine is in Shanxi Province, China. The coal seams mined in the working face are located in the strata of the Shanxi formation of the Permian system, which are continental lacustrine deposits. The structure of the coal seams is simple, the thickness of the coal seams is stable and minable, the average thickness of the coal seams is 3 m, and the average dip angle of the coal seams is 7°. It can be approximately considered as a horizontal coal seam. The direct roof of 2# coal seam is composed of sandy mudstone and fine sandstone, and the direct floor of 2# coal seam is composed of mudstone. The coal seam is 125 m deep, with roads and buildings on the ground. The lithological characteristics of the strata above and below the coal seam are shown in Table 2.

In order to study the interaction relationship among support, roof rock, and filling body under the condition of filling and fully mechanized mining, two parallel similar models were laid. Under the condition that the mining height is fixed and the initial filling height is different, the movement law of the strata is simulated. When the model was mined, both sides of the seam were cut, and no boundary was left, which is used to simulate the deformation law from the comprehensive mechanized solid filling mining face to the direction of the middle part of the stope.

The geometric similarity ratio of both models was $\alpha_l = (y_m/y_p) = (z_m/z_p) = (1/27)$. The mounting height was 1.015 m, and the total thickness of the simulated rock stratum was 27.41 m, of which the thickness of the coal seam was 3 m. The bulk density similarity coefficient of the model

was $\alpha_{\gamma 0} = (\gamma_{mi}/\gamma_{pi}) = 0.60$. According to the similarity simulation theory, the elastic modulus similarity coefficient is the product of the geometric similarity ratio and the bulk density similarity ratio. After calculation, its value was $\alpha_E = (1/44)$, the upper loading was 0.06 MPa to simulate the gravity of the 105 m overburden. The mixture ratios of similar materials of rock stratum are shown in Table 3.

In the actual filling and mining process, the filling body is pushed after being filled into the mined-out area to make it connect to the top. Therefore, in the experiment, the combined height of foam and sponge was made to reach the mining height first, and the process of compressing the sponge was used to simulate the initial pushing process. Since the initial filling heights of the two models were different, when the combined height of the foam and sponge reached the initial filling height under the action of the compressive force of 10 kPa, the height of each material was finally determined according to the principle of the height ratio of the No.6 model material. Similar model experiment scheme and the combination design of foam and sponge of backfilling materials are shown in Table 4.

After the model was laid, the corresponding displacement measuring points were arranged, and three rows of displacement measuring lines were arranged from bottom to top, with the vertical heights of 0.27 m, 0.36 m, and 0.80 m, respectively. Each row of displacement measuring lines was arranged with 19 measuring points from right to left, with a spacing of 12.5 cm. Each row of displacement measuring lines was arranged with 19 measuring points, measuring point ① was located at a position 12.5 cm from the right edge, and then measuring point ②~measuring point ⑲ were arranged in sequence from right to left, with the distance 12.5 cm between each other. After conversion according to the similarity ratio, in the actual rock stratum, the corresponding position of measuring point ① was the position where the mining length was 3.375 m from the right boundary, and the corresponding position of measuring point 2 was the position where the mining length was 6.75 m. By analogy, the actual distance between each two measuring points was 3.375 m.

During the experiment, all kinds of materials and equipment required were prepared first, the river sand, gypsum, calcium carbonate and cement, and other materials were screened and fully air-dried, then laid the model. After air-drying, corresponding displacement measuring points were arranged, the digital high-speed strain gauge was connected, and the cylinder was then loaded from the top of the model until the model was fully stable. The boundary effect was considered in the similar material model experiment. In order to reduce the influence of the boundary effect, both sides of the model were cut. The specific experiment steps were as follows: (1) Excavated from right to left without leaving a boundary on the right. Excavated 25 cm for the first time, put in the support model, and set the initial support force and height of the support according to each scheme. After the model was fully stabilized, data were recorded, photos were taken, and the photo number was recorded. (2) Excavated 5 cm, data were recorded, photos were taken, and the photo number was recorded. (3) Moved

TABLE 1: Combination design of wood and sponge for different filling ratios.

No.	Height of high-density foam (cm)	Height of low-density foam (cm)	Height of sponge (cm)	Height ratio (high-density foam:low-density foam:sponge)
1	7.5	0	3	5 : -- : 2
2	10	0	1	10 : -- : 1
3	6.6	2.4	2	33 : 12 : 10
4	8	0	2	8 : -- : 2
5	4.25	5	2	17 : 20 : 8
6	9	0	2	9 : -- : 2

(a)
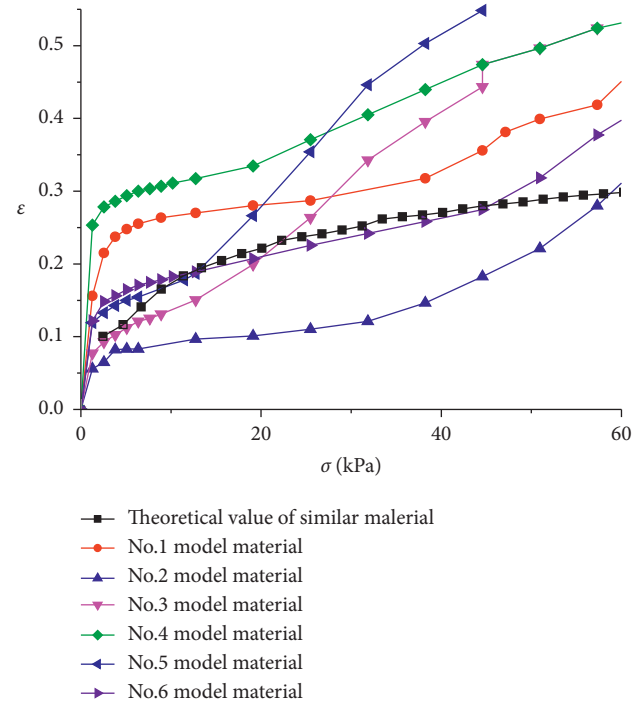
(b)

FIGURE 4: Compaction test photos and curves of similar materials of filling body. (a) Compaction test photos. (b) Compaction test curves.

the support 5 cm forward and fill it at the rear. After the model was fully stabilized, data were recorded, photos were taken, and the photo number was recorded. (4) Repeated steps (2) to (3) until the model was fully mined and filled.

3.3. Influence of Initial Filling Height on Deformation of Roof Rock and Backfilling Body.
The initial filling heights of Model I and Model II were 6.67 cm and 10.56 cm, respectively, which were 60% and 95% of the mining height. The deformation law of surrounding rock and filling body and the change law of pressure cell data during the filling mining process were recorded. The actual photos of the mining length of 20 m, 32 m, and 49 m are shown in Figure 5. The displacement of roof strata was tracked and analyzed by using image processing software Photoinfor. The displacement was calculated according to the pixel coordinates of the

image, and the displacement nephogram and vector diagram were obtained, as shown in Figures 6 and 7. The displacement of every measuring point of line 1 above the coal seam in the process of filling mining was extracted, and the result is shown in Figure 8.

It can be seen from Figures 5–8 that when the initial filling height is 60% of the mining height (model I), the movement of rock strata is very obvious. When the mining length is 8 m (Figure 6(a)), the roof above the goaf begins to sink, and the maximum subsidence of the rock strata above the broken direct roof is 0.01 m. When the mining length was 20 m, the roof above the goaf began to sink more obviously, the maximum subsidence was 0.30 m, and discontinuous cracks began to appear in the roof strata (as shown by the red dotted line in Figure 5(a)), and the first relatively complete rotary area appeared (as shown in the red quadrilateral in Figure 6(b)); the displacement of measuring

TABLE 2: The lithological characteristics of the strata.

Stratum position	Rock name	Lithology description	Depth (m)	Thickness (m)
	Siltstone	Dark grey; broken locally; uneven cross section and inclined fracture.	105.30	1.17
	Sandy mudstone	Dark grey; flat section, small wavy bedding, and inclined fracture.	110.95	5.65
	Siltstone	Dark grey; highly-weathered and broken locally; flat section.	114.90	3.95
	Sandy mudstone	Dark grey; wavy bedding; vertical fracture.	117.10	2.20
Overlying strata	Fine-grained sandstone	Light grey; broken locally; sub angular in shape and medium in sorting.	119.05	1.95
	Mudstone	Dark grey; highly-weathered; flat section and inclined fracture.	120.30	1.25
	Fine-grained sandstone	Light grey; not weathered; medium sorted; cross bedded, subangular, vertical fracture, and occasionally inclined fracture.	122.65	2.35
	Sandy mudstone	Dark grey; flat section; strongly weathered.	123.15	0.50
	Coal	Black, massive and fragmentary; glass luster.	124.80	1.65
Coal seam	Mudstone	Dark grey; highly-weathered; flat section; wavy bedding; inclined fracture.	125.05	0.25
	Coal	Black, massive and fragmentary; glass luster.	125.66	0.61
Floor stratum	Mudstone	Grey; highly-weathered; wavy bedding; flat section and inclined fracture.	131.05	5.39

TABLE 3: Layer programs and mixture ratios of similar model.

Rock layer name	Model thickness (m)	Layer number	Mass per layer (kg)	Sand (kg)	Cement (kg)	Calcium carbonate (kg)	Gypsum (kg)	Water (kg)
Siltstone	0.043	2	17.333	13.000	0.000	2.167	2.167	1.733
Sandy mudstone	0.209	6	27.901	20.926	0.000	3.488	3.488	2.790
Siltstone	0.146	4	29.259	23.407	0.000	1.756	4.096	2.926
Sandy mudstone	0.081	2	32.593	24.444	0.000	4.074	4.074	3.259
Fine-grained sandstone	0.072	2	28.889	26.000	2.022	0.000	0.867	2.889
Mudstone	0.046	2	18.519	15.873	0.000	0.794	2.646	1.852
Fine-grained sandstone	0.087	3	23.210	17.407	0.000	1.741	4.062	2.321
Sandy mudstone	0.019	1	14.815	11.111	0.000	1.852	1.852	1.481
Coal	0.111	3	29.630	25.926	0.000	2.593	1.111	2.963
Mudstone	0.120	5	31.941	23.956	0.000	2.396	5.590	3.194

TABLE 4: Similar model experiment scheme and combination design of foam and sponge for two models.

	Actual mining height (m)	Actual initial filling height (m)	Height of high density foam (cm)	Height of sponge (cm)	Combined height after initial compression (cm)
ModelI	3.0	1.8	5.45	5.65	6.67
ModelII	3.0	2.85	8.64	2.46	10.56

points ① and ② of line 1 above the coal seam also began to increase significantly (Figure 8(a)). When the mining length was 32 m, the first rotary area continued to sink and gradually turned to the horizontal direction (Figure 6(c)), small cracks began to appear in front of it (as shown by the red dotted line in Figure 5(b)), and a second rotary area appeared (as shown in the red quadrilateral in Figure 6(c)); the displacement of measuring points ①, ②, and ③ of measuring line 1 above the coal seam increased stepwise (Figure 8(a)), and the maximum subsidence was 0.87 m.

When the mining length was 40 m, the second rotary area basically formed and turned (Figure 6(d)), and there were

many cracks on the roof. The speed of displacement increase of measuring points ①, ②, and ③ of line 1 above the coal seam slowed down. The displacement of measuring points ④ and ⑤ increased at a larger speed (Figure 8(a)), and the maximum subsidence was 1.14 m. When the mining length was 49 m, the cracks on the roof above the first rotary area gradually closed, the roof above the working face started to produce small cracks (as shown by the red dotted line in Figure 5(c)), and the third rotary area appeared (as shown in the red quadrilateral in Figure 6(e)). The displacement of measuring points ①, ②, and ③ tended to be stable, and the increase speed of displacement of measuring point ④ slowed

(a)

(b)

(c)

(d)

(e)

(f)
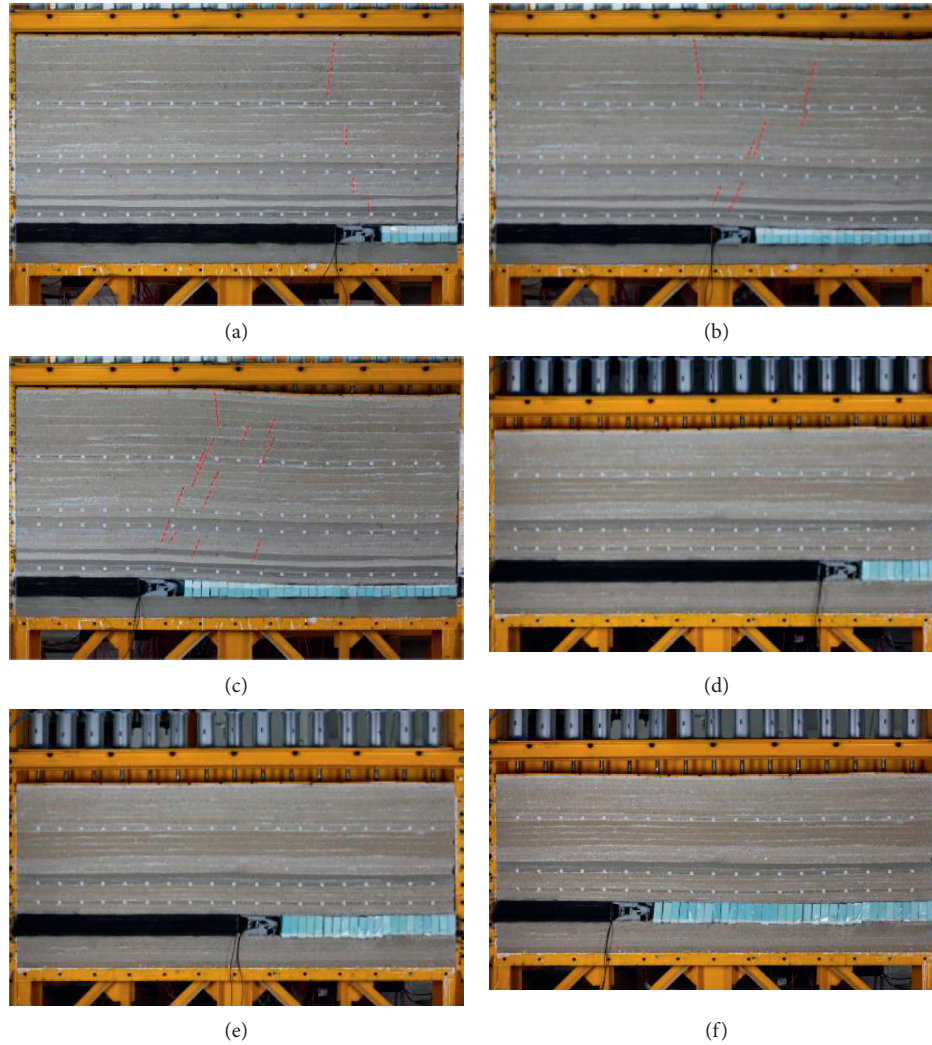
FIGURE 5: The process of mining and filling and the change of rock strata displacement. (a) Model I, mining length 20 m. (b) Model I, mining length 32 m. (c) Model I, mining length 49 m. (d) Model II, mining length 20 m. (e) Model II, mining length 32 m. (f) Model II, mining length 49 m.

down, with the maximum subsidence of 1.21 m. When the mining length was 57 m (Figure 6(f)), the third rotary area was basically formed, and there were more cracks in the roof. At the same time, the first two areas continued to sink, and the second area turned to the horizontal direction gradually; the displacement of measuring point ④ tended to be stable, and the increase speed of displacement of measuring point ⑤ slowed down, the maximum subsidence was 1.27 m. When the mining length was 65 m (Figure 6(g)), the third area rotated, the cracks in the first two areas were basically closed, the displacement of measuring points ⑥ to ⑧ continued to increased rapidly, and the maximum subsidence was 1.36 m.

On the whole, when the initial filling height is 60% of the mining height, the roof sinks obviously. During the mining process, the movement of the roof is similar to the traditional caving method, the periodic fracture occurs, and the masonry beam structure is formed. However, the comprehensive mechanized filling and mining method of mining and filling at the same time well limits the scope and speed of

roof collapse, so that the roof can basically maintain integrity. The filling body is gradually compacted during the advancing period of the mining face, and each rotary area of the roof gradually contacts the filling body in the process of rotation, and the filling body is initially compacted. After the completion of rotation, in the stage of horizontal subsidence, the filling body is fully compacted; only at this time, the filling body can play the role of supporting the roof and controlling the roof subsidence. It can also be seen from the change of the measuring point displacement that after the mining face pushes over the measuring point, the roof strata sink rapidly at first, after 20∼30 m of filling, then gradually sink slowly until they are stable. The final stable subsidence of the roof is 1.36 m in the experiment, which is in good agreement with the theoretical calculation value of 1.38 m when $h_g = 1.8$ m (60% of the mining height) in Section 2.2.

It can be seen from Figures 5–8 that when the initial filling height is 95% of the mining height (model II), the overall subsidence of the rock stratum is relatively small.

(a)

(b)

(c)

(d)

(e)
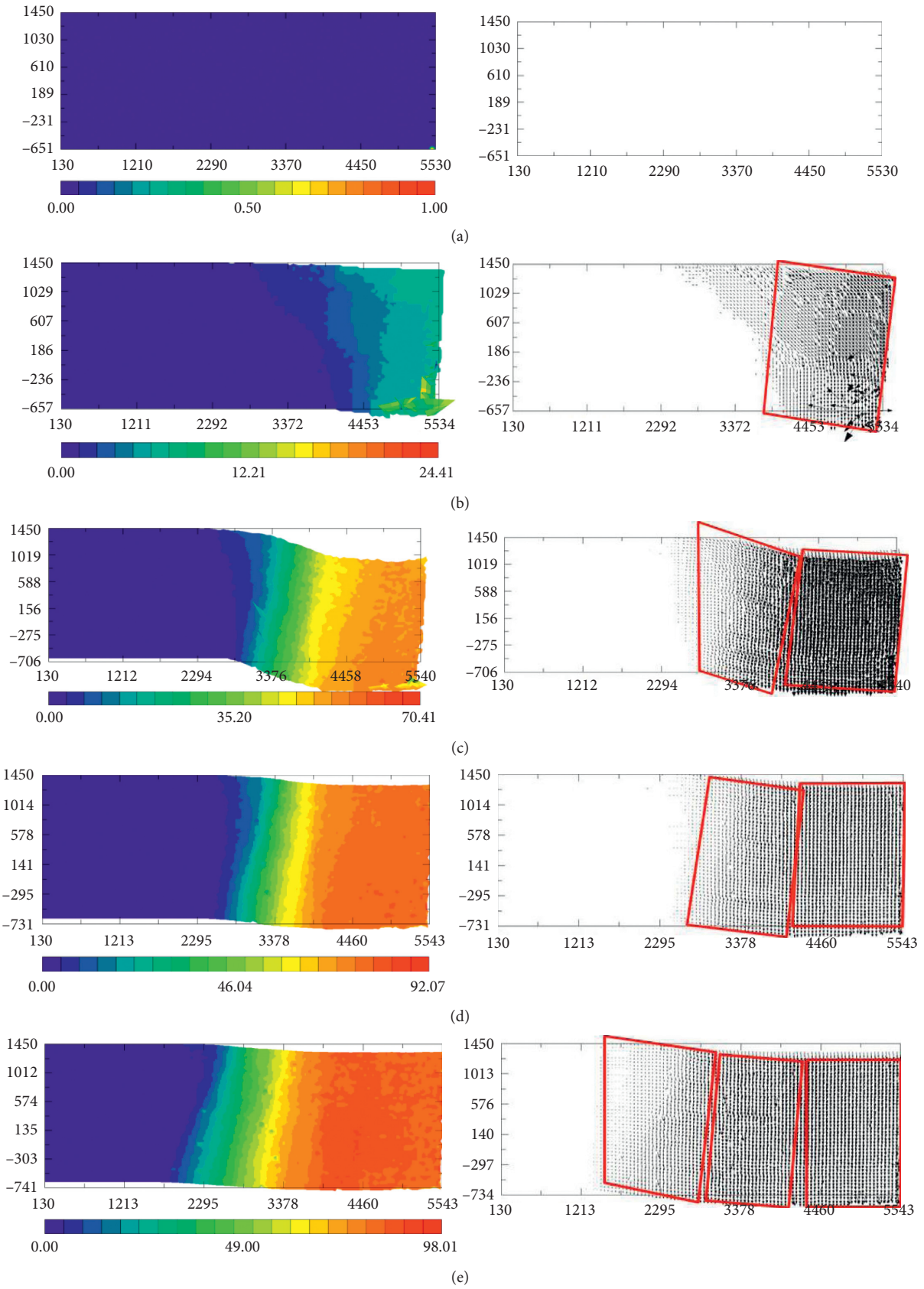
Figure 6: Continued.
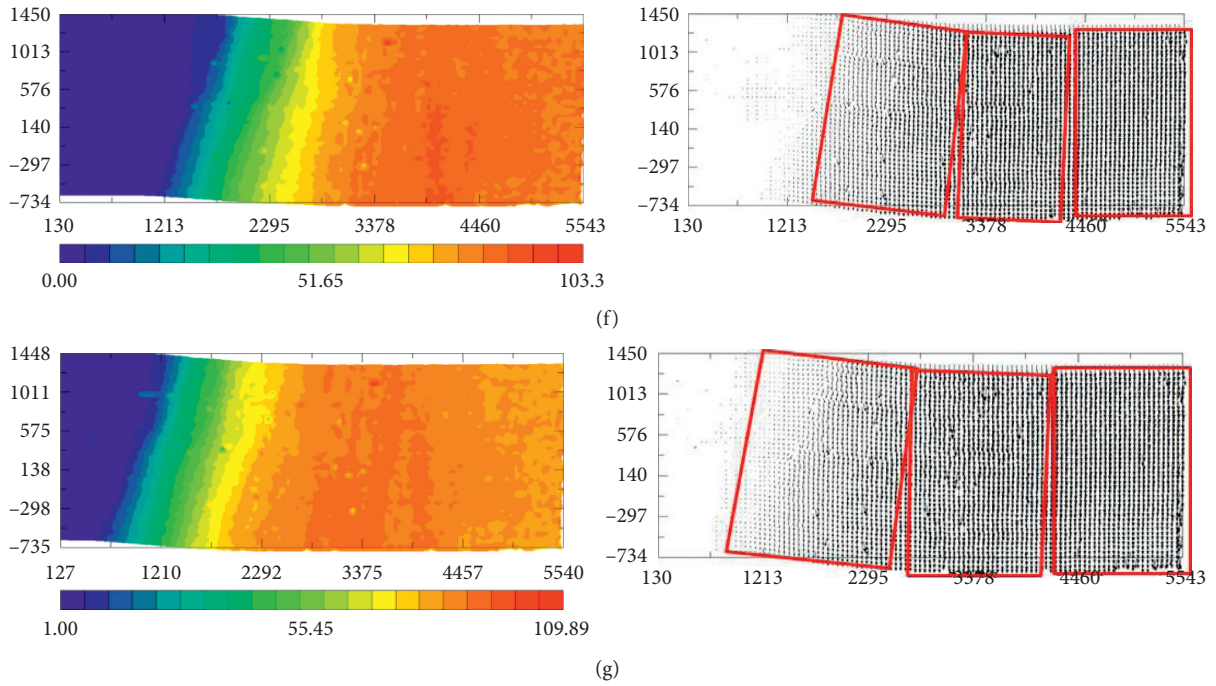
Figure 6: Displacement nephograms and vector diagrams of rock strata in the process of mining and filling of model I: (a) mining length 8 m, (b) mining length 20 m, (c) mining length 32 m, (d) mining length 40 m, (e) mining length 49 m, (f) mining length 57 m, and (g) mining length 65 m.

Figure 7: Continued.

(g)
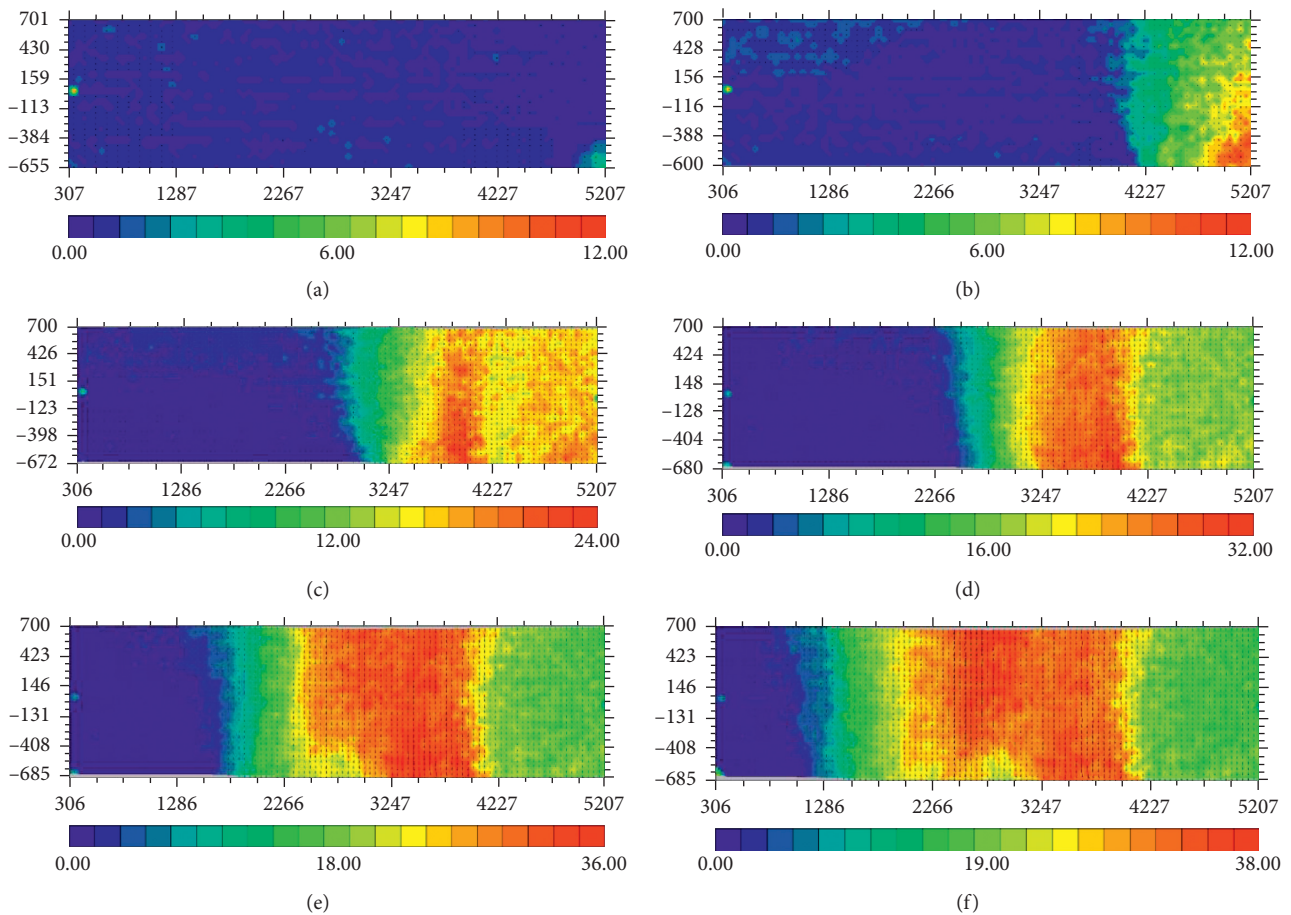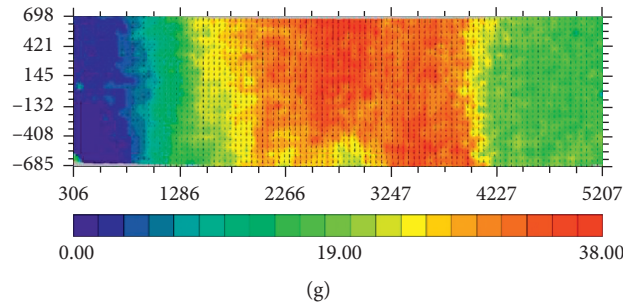
FIGURE 7: The process of mining and filling and the change of rock strata displacement in model II: (a) mining length 8 m, (b) mining length 20 m, (c) mining length 32 m, (d) mining length 40 m, (e) mining length 49 m, (f) mining length 57 m, and (g) mining length 65 m.

(a)

(b)
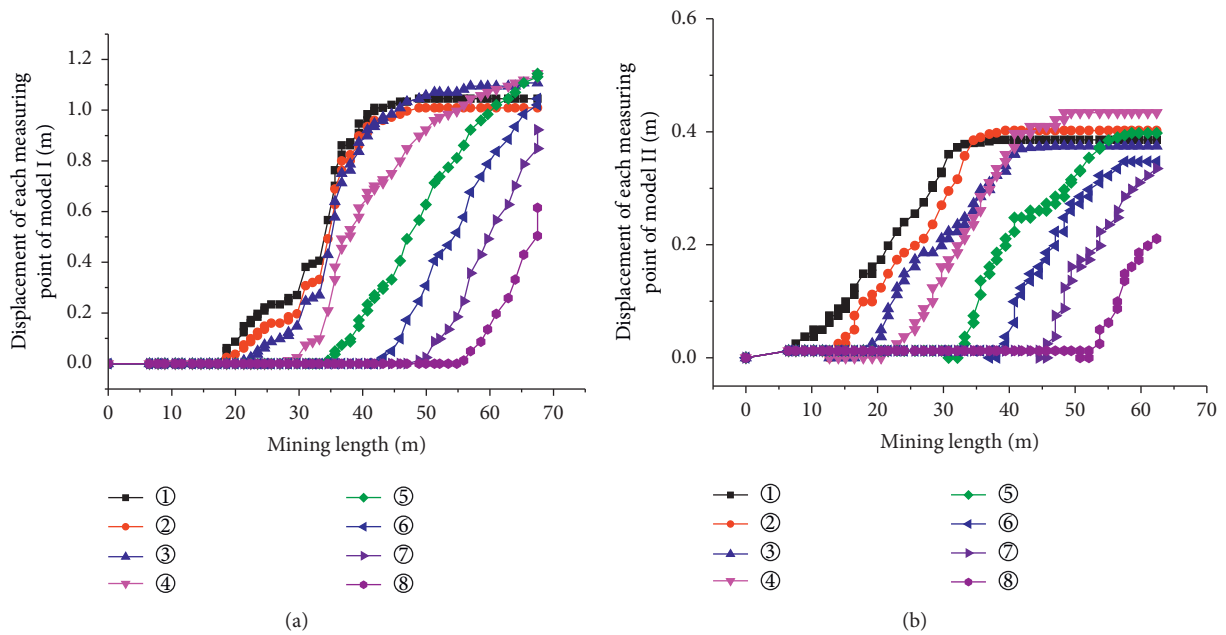
FIGURE 8: The displacements of the measuring points in the line 1 in the process of mining and filling: (a) model I and (b) model II.

During the entire mining and filling process, no obvious bending of the roof strata was observed, only small subsidence occurred (Figures 5(d)–5(f)). When the mining length is 20 m (Figure 7(b)), the maximum subsidence is only 0.14 m; when the mining length is 40 m (Figure 7(d)), the maximum subsidence is only 0.39 m; when the mining length is 65 m (Figure 7(g)), the maximum subsidence is only 0.47 m, which is in good agreement with the theoretical calculation value of 0.44 m when $h_g = 2.85$ m (95% of the mining height) in Section 2.2. The displacement of each measuring point of measuring line 1 above the coal seam does not show an episodic increase, but it continues to increase steadily after the mining face pushes over the measuring point and reaches a stable value after filling about 22 m. This distance is also very close to the theoretical calculation value of filling distance $x = 25$ m corresponding to the stable subsidence of the roof in the filling area in Section 2.2. This shows that when the initial filling height is 95% of the mining height, the filling body can replace the coal seam to support the roof timely and play an important
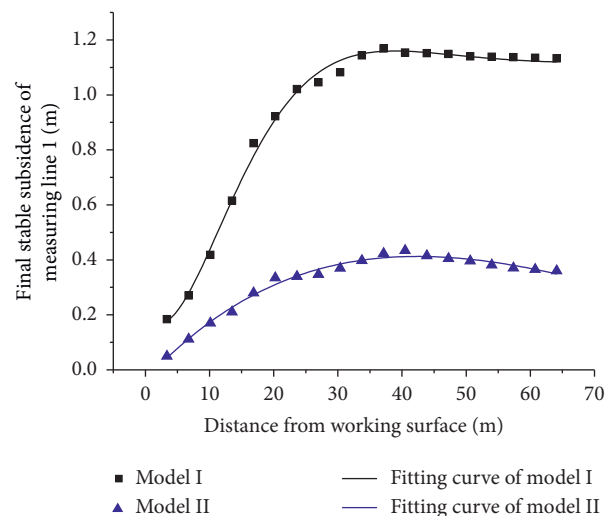
FIGURE 9: Experiment value and fitting curve of the final stable subsidence of measuring line 1 in two models.

role in controlling the subsidence and migration of roof rock beams.

In conclusion, the initial filling height has a significant effect on the movement and subsidence of the overlying strata in the process of mining and filling. After the completion of the process of mining and filling, the final subsidence displacement of each measuring point on measuring line 1 of the two models is recorded and compared, as shown in Figure 9. It can be seen that with the increase of the distance away from the mining face, that is, the increase of the filling length, the final subsidence of each model roof presents the trend of rapid increase at first and then gradually stabilizes. The final stable subsidence of model I is about 1.1 m, which is only about 0.4 m in model II. The filling distance corresponding to the stable subsidence of the roof also decreases with the increase of the initial filling height. In model I, after 35 m of filling, the roof subsidence gradually stabilized; in model II, after 22 m of filling, the roof subsidence becomes stable.

The final subsidence curves of roof measuring line 1 of model I and model II are function-fitted, as shown in Figure 9. The fitting function is

$$\begin{aligned}
\text{model I}: \quad & y = e^{-0.086x}\left[-1.340\sin(0.086x) - 0.912\cos(0.086x)\right] + 1.119, \\
\text{model II}: \quad & y = e^{-0.015x}\left[2.021\sin(0.015x) + 0.326\cos(0.015x)\right] - 0.362.
\end{aligned} \tag{21}$$

The form of fitting function is the same as that of theoretical formula (9). The correlation coefficients of fitting are 0.996 and 0.985, respectively, which has a good fitting result. This shows that the similar simulation experiment results are consistent with the theoretical calculation values of roof subsidence law.

4. Conclusion

Based on the theory of elastic foundation beam, the mechanical model of the backfilling mining support-roof rock beam-gangue filling body is established. Under the condition of comprehensive mechanized filling mining, the subsidence differential equation of roof rock beam is solved, and the foundation coefficient in the model is discussed in combination with the compaction mechanical property of gangue filling body. The subsidence displacements of roof at the coal wall, above the support and above the filling body are obtained. On the basis of similarity theory and mechanical test of similar materials of gangue filling body, simulation experiments of filling mining were carried out. From the theoretical analysis and experimental observation, the influence of initial filling height and compaction force of filling support on the subsidence of roof rock beam is discussed respectively. Some conclusions can be drawn as follows:

(1) The initial filling height is the decisive factor to control the subsidence and migration stability of each part of the roof rock beam. The larger the initial filling height is, the smaller the final subsidence of each part of the roof rock beam is, and the shorter the corresponding filling length is when the roof rock beam above the filling area reaches the final stable subsidence.

(2) The compaction force of the backfilling mining support on the gangue filling body has a certain influence on the subsidence of roof rock beam, which is mainly reflected in the filling area. Appropriately increasing the compaction force of the support can compact the backfilling body effectively and increase its deformation modulus, thus controlling the subsidence and unstable range of the roof rock beam. When the compaction stress is about 2.0 MPa, the subsidence of roof rock beam can be effectively controlled. If the compaction stress is increased, this control effect will not increase significantly.

(3) In view of the two cases where the initial filling height is 60% and 95% of the mining height, respectively, two similar simulation experiment models are set up to carry out the simulation experiment research on the filling mining process. The experiment results show that the maximum subsidence of the roof rock beam and the corresponding filling length when the roof rock beam reaches the final stable subsidence are consistent with the theoretical calculation value. The experiment curve fitting function of the final subsidence is consistent with the expression form of the theoretical calculation result. In addition, similar simulation experiment can better reflect the movement characteristics of roof strata during the entire filling mining process.

The mechanical model and research results presented in this paper shed light on better understanding of the interaction among support, roof rock beam, and backfilling body in the process of comprehensive mechanized backfilling mining.

Data Availability

The data used to support the findings of this study are available from the corresponding author upon request.

Conflicts of Interest

The authors declare no conflicts of interest.

Acknowledgments

References

[1] M.-G. Qian, J.-l. Xu, and X.-X. Miao, "Green technique in coal mining," *Journal of China University of Mining &. Technology*, vol. 32, no. 4, pp. 343–348, 2003.

[2] M.-G. Qian, X.-X. Miao, J.-l. Xu et al., "On scientized mining," *Journal of Mining & Safety Engineering*, vol. 25, no. 1, pp. 1–10, 2008.

[3] M.-G. Qian, X.-X. Miao, and J.-l. Xu, "Resources and environment harmonics (green) mining and its technological system," *Journal of Mining & Safety Engineering*, vol. 23, no. 1, pp. 1–5, 2006.

[4] M.-G. Qian and J.-l. Xu, "Concept and technical framework of sustainable mining," *Journal of China University of Mining &. Technology (Social Sciences)*, vol. 13, no. 3, pp. 1–7, 2011.

[5] J.-X. Zhang, Q. Zhang, A. J. S. Spearing, M. Xiexing, G. Shuai, and S. Qianga, "Green coal mining technique integrating mining-dressing-gas draining-backfilling-mining," *International Journal of Mining Science and Technology*, vol. 27, no. 1, pp. 17–27, 2017.

[6] X.-X. Miao and J.-X. Zhang, "Key technologies of integration of coal mining gangue washing-backfilling and coal mining," *Journal of China Coal Society*, vol. 39, no. 8, pp. 1424–1433, 2014.

[7] F. Ju, J.-X. Zhang, Y.-L. Huang et al., "Waste filling technology under condition of complicated geological condition working face," *Procedia Earth & Planetary Science*, vol. 1, no. 1, pp. 1220–1227, 2009.

[8] X.-x. Miao, J.-X. Zhang, and M.-M. Feng, "Waste-filling in fully-mechanized coal mining and its application," *Journal of China University of Mining and Technology*, vol. 18, no. 4, pp. 479–482, 2008.

[9] Y.-J. Zhou, "Study on suitability evaluation of full-mechanized solid back-filling mining technology for difficult-to-mine resource," Doctoral dissertation, China University of Mining & Technology, Xuzhou, China, 2012.

[10] L. Wang, "Study and application on coordination degree of scientific coal mining system," Doctoral dissertation, China University of Mining & Technology (Beijing), Beijing, China, 2015.

[11] Y.-L. Huang, J.-X. Zhang, B.-F. An, and Q. Zhang, "Overlying strata movement law in fully mechanized coal mining and backfilling longwall face by similar physical simulation," *Journal of Mining Science*, vol. 47, no. 5, pp. 618–627, 2011.

[12] J.-C. Wang and S.-L. Yang, "Research on support-rock system in solid backfill mining methods," *Journal of China Coal Society*, vol. 35, no. 11, pp. 1821–1826, 2010.

[13] Z.-G. Ma, J.-Q. Fan, K. Sun, G.-Z. Zhao, and Y.-G. Pan, "Study on stope stability during repeated mining with fully- mechanized solid filling technology in residual coal pillar area,"

[14] J. Zhang, Q. Zhang, Y. Huang, J. Liu, N. Zhou, and D. Zan, "Strata movement controlling effect of waste and fly ash backfillings in fully mechanized coal mining with backfilling face," *Mining Science and Technology (China)*, vol. 21, no. 5, pp. 721–726, 2011.

[15] Z.-G. Ma, T. Lan, Y.-G. Pan, J.-G. Ma, and F.-H. Zhu, "Experimental study of variation law of saturated broken mudstone porosity during creep process," *Chinese Journal of Rock Mechanics and Engineering*, vol. 28, no. 7, pp. 1447–1454, 2009.

[16] Z. Ma, R. Gu, Z. Huang, G. Peng, L. Zhang, and D. Ma, "Experimental study on creep behavior of saturated disaggregated sandstone," *International Journal of Rock Mechanics and Mining Sciences*, vol. 66, no. 1, pp. 76–83, 2014.

[17] Z. Huang, Z. Ma, L. Zhang, P. Gong, Y. Zhang, and F. Liu, "A numerical study of macro-mesoscopic mechanical properties of gangue backfill under biaxial compression," *International Journal of Mining Science and Technology*, vol. 26, no. 2, pp. 309–317, 2016.

[18] Z.-M. Huang, Z.-G. Ma, L. Zhang, D.-W. Yang, S.-H. Guo, and D.-P. Liu, "Numerical simulation of the particle flow during the vibration, pushing, and pressing procedure of the backrilling body," *Journal of Mining & Safety Engineering*, vol. 34, no. 4, pp. 789–794, 2017.

[19] F. Ju, P. Huang, S. Guo, M. Xiao, and L. Lan, "A roof model and its application in solid backfilling mining," *International Journal of Mining Science and Technology*, vol. 27, no. 1, pp. 139–143, 2017.

[20] X. Du, G. Feng, T. Qi, Y. Guo, Y. Zhang, and Z. Wang, "Failure characteristics of large unconfined cemented gangue backfill structure in partial backfill mining," *Construction and Building Materials*, vol. 194, pp. 257–265, 2019.

[21] F. Wang, B. Jiang, S. Chen, and M. Ren, "Surface collapse control under thick unconsolidated layers by backfilling strip mining in coal mines," *International Journal of Rock Mechanics and Mining Sciences*, vol. 113, pp. 268–277, 2019.

[22] Y. Zhang, S. Cao, N. Zhang, and C. Zhao, "The application of short-wall block backfill mining to preserve surface water resources in northwest China," *Journal of Cleaner Production*, vol. 261, Article ID 121232, 2020.

[23] Z. Liu, "Compaction properties of gangue and it's application in backfilling coal mining," Doctoral dissertation, China University of Mining & Technology, Xuzhou, China, 2014.

[24] Y.-H. Li and H.-W. Jing, "Software development of a digital speckle correlation method and its application," *Journal of China University of Mining & Technology*, vol. 37, no. 5, pp. 635–640, 2008.

[25] Z.-G. Ma, Z.-M. Huang, J.-Q. Fan, G.-Z. Zhao, K. Sun, and F. Liu, "Experimental research on compacting characteristics of open-air slag mixture," *China Coal*, vol. 38, no. 7, pp. 36–38, 2012.

Research Article

Study on the Porosity of Saturated Fragmentized Coals during Creep Process and Constitutive Relation

Peng Gong [1,2] **Zhanguo Ma** [1,2] **Yongheng Chen** [2] **Shixing Cheng** [1] **and Kelong Li** [2]

[1] *State Key Laboratory for Geomechanics and Deep Underground Engineering, China University of Mining and Technology, Xuzhou, Jiangsu 221116, China*
[2] *School of Mechanics and Civil Engineering, China University of Mining and Technology, Xuzhou, Jiangsu 221116, China*

Correspondence should be addressed to Zhanguo Ma; 1044@cumt.edu.cn

Pore abundance and deformation characteristics of saturated fragmentized coals during creep process are of significant meaning to the study on ground sediment in the mined-out area. The law of porosity variation of saturated fragmentized coals during creep process and its creep constitutive model were studied by using the self-developed multiphase coupling creep test device. And, results have indicated that the porosity logarithm of fragmentized coal during creep process shows a linear negative correlation with the time $\ln(n-a) = -ct + \ln b$, and the porosity decrease is evidently divided into three phases. In addition, when the stress level is relatively low, the porosity decreases slowly; when the stress level rises up, the porosity decreases quickly; when the stress level remains stable finally, the porosity is smaller. Under the equal stress, as the grain size of fragmentized coals decreases, the porosity tends to decrease, and as the grain size of fragmentized coal tends to be stable, the porosity tends to increase; the creep constitutive equation of fragmentized coals with different grain sizes was established by using the Kelvin–Voigt model, and the correlation analysis shows that the Kelvin–Voigt creep model of fragmentized coals is reasonable.

1. Introduction

Coal is an inhomogeneous and porous media [1], and thus compaction and bearing problems of fragmentized coals are quite common during coal mining. With the impact of external forces, coals are constantly crushed, densified, and compacted; meanwhile, some relevant physical and mechanical properties of fragmentized coals are changed, which can cause some engineering problems such as overburden movement, ground sediment [2–5], and side slope instability in the mined-out area. The study on the law of porosity variation of fragmentized coals during creep process [6–11] and its creep constitutive equation lays a theoretical foundation for resolving engineering problems such as the evaluation of deformation of ground sediment in the mined-out area. But, among current analyses of fragmentized rocks [12–14], few can systematically analyze the porosity variation law of fragmentized rocks during creep in terms of different stress and different grain sizes; in the description of creep deformation law, regression analysis means, such as

logarithm fitting and fit exponential decay, are usually adopted, but its constitutive relation is not analyzed, and its creep deformation mechanism is explained from the perspective of the material prosperity of fragmentized rocks.

2. Test Equipment and Test Methods

2.1. Coal Sample. In order to study the law of porosity variation of fragmentized coals with different grain sizes under different loads during compaction and creep process, fragmentized coals with five grain sizes are selected, whose uniaxial compressive strength is 15 MPa. Their grades and sizes are shown in Table 1, and fragmentized coals and preparation instruments are shown in Figure 1(a).

2.2. Test Equipment. It is easy for loose and fragmentized coals without confining pressure to flow transversely under axial load; thus, they cannot bear heavy loads, but fragmentized coals in special sites such as the roadway of the coal

Table 1: Grades and sizes of fragmentized coals.

Grades	Grade symbol	Size (mm)
1	m1	20.0~25.0
2	m2	15.0~20.0
3	m3	10.0~15.0
4	m4	5.0~10.0
5	m5	2.5~5.0

Figure 1: Classification of particle size: (a) 20.0~25.0 mm. (b) 15.0~20.0 mm. (c) 10.0~15.0 mm. (d) 5.0~10.0 mm. (e) 2.5~5.0 mm.

mining face have strong confining pressure. In consideration of this, the self-developed multiphase coupling creep test device of fragmentized coals is designed which applies the leadscrew system to provide loads, as shown in Figure 1(b). When it reaches certain pressure, the power supply can be cut off, and it relies on leadscrew self-locking to provide pressure to avoid too much energy consumption during the long-time test. The deformation test adopts an FT81 displacement sensor and an LVDV-3 digital indicator. In addition, one spherical hinge needs to be added above the pressure-bearing deformation instrument to avoid unbalance loading due to pedestal or spring imbalance.

The assembly height of the compaction apparatus of fragmentized coals is 300 mm (140 mm high piston and 170 mm long cylinder barrel). The inner diameter of the cylinder barrel is 100 mm, and the wall thickness is 15 mm; during processing, ordinary No. 45 steel is fully quenched to enhance hardness and prevent fragmentized coal edges from scratching the inner wall and increasing the resistance; cylinder barrel bottom and pedestal are linked by bolts. The maximum axial loading pressure designed for the deformation instrument is 180 MPa.

2.3. Test Methods. Firstly, the deformation instrument is assembled and filled with the sample of statured fragmentized coals to be tested. In consideration of the displacement instrument stroke and the estimated maximum deformation, those uncompressed fragmentized rocks are controlled to be 128 mm high and are slightly shaken to be dense for each time; finally, they are divided into two groups for test under the load of 8 and 12 Mpa, respectively.

Test procedures are as follows: the sample of saturated fragmentized coals is loaded to the working load, and the loading process is recorded; the saturated drip is opened, and water is fed to the compaction apparatus at the appropriate time under the symphonic effect to maintain the coal sample always under the saturation state; each group of deformation instruments provides two sets of displacement testing systems, and the displacement reading is the average value; the load is observed daily in a fixed time interval, the load is compensated when necessary, and the displacement data and time are recorded. Each type of test is divided into 3~5 groups, and the average value of test data is the final result. For test schemes with results of significant dispersion, test groups are added until three groups draw the similar conclusion.

3. The Law of Porosity Variation with Time

Porosity refers to the ratio of pore volume between particles to total volume of fragmentized media, namely,

$$n = \frac{V_s - V_z}{V_{sz}}, \tag{1}$$

where n denotes the porosity of fragmentized coals, V_{sz} denotes the total volume of fragmentized coals before test, V_s denotes the total volume of fragmentized coals during test, and V_z denotes the volume of solid particles in fragmentized coals.

3.1. Influence of Stress Level on the Porosity of Fragmentized Coals. Stress level produces a significant impact on the porosity of fragmentized coals, and the relation curve between the porosity of fragmentized coals and the time under different stress levels is obtained from two groups of tests under different loads, as shown in Figures 2∼3.

It can be seen from Figure 2 that under the stress of 8 Mpa, the porosity variation of coal samples with different grain sizes is periodic. When Grain Size 1 plummets at 69.12×10^4 (s), the porosity decreases to 0.154 66; when Grain Size 2 plummets at 60.48×10^4 (s), the porosity decreases to 0.185 85, and when it plummets at 86.4×10^4 (s) for the second time, the porosity decreases to 0.185 62; when Grain Size 3 plummets at 51.84×10^4 (s), the porosity decreases to 0.162 38, and when it plummets at 69.12×10^4 (s) for the second time, the porosity decreases to 0.162 27; when Grain Size 4 plummets at 51.84×10^4 (s), the porosity decreases to 0.170 80; when Grain Size 5 plummets at 51.84×10^4 (s), the porosity decreases to 0.212 09. The above phenomena are difficult to observe in the short-time creep test.

It can be seen from Figure 3 that under the stress of 12 Mpa, the porosity variation of coal samples with different grain sizes is periodic. When Grain Size 1 plummets at 34.56×10^4 (s), the porosity decreases to 0.112 20, when it plummets at 51.84×10^4 (s) for the second time, the porosity decreases to 0.112 06, and when it plummets at 103.68×10^4 (s) for the third time, the porosity decreases to 0.111 77; when Grain Size 2 plummets at 34.56×10^4 (s), the porosity decreases to 0.174 02, and when it plummets at 51.84×10^4 (s) for the second time, the porosity decreases to 0.173 68; when Grain Size 3 plummets at 17.28×10^4 (s), the porosity decreases to 0.122 84, and when it plummets at 69.12×10^4 (s) for the second time, the porosity decreases to 0.122 25; when Grain Size 4 plummets at 34.56×10^4 (s), the porosity decreases to 0.140 31; when Grain Size 5 plummets at 43.2×10^4 (s), the porosity decreases to 0.172 52, and when it plummets at 60.48×10^4 (s) for the second time, the porosity decreases to 0.172 25.

During the creep of fragmentized coals, the decrease in the porosity of fragmentized coals with five grain sizes is basically divided into three phases. Phase I: the porosity varies quickly and tends to decrease; in this phase, slippage, malposition, and deformation occur between particles of fragmentized coals. Due to the large void between coal particles, the apparent volume decreases quickly, and then the porosity reduces quickly.

Phase II: the porosity changes very quickly and tends to slow down; in this phase, slippage and malposition seldom happen to fragmentized coal particles, and the fragmentized coal particles form a self-supporting structure; as the stress continues to be loaded, under the squeezing impact, (1) particle surface edges are fragmentized, and internal gap diffuses and forms fractures which expand and cause deformation. (2) Some particles slide slightly and cause plastic flow.

Phase III: the porosity changes more slowly than the first two phases, and gradually tends to be stable; due to the attrition crushing in Phase II, a larger gap exists between coal particles and is filled with fine coal particles after fragmentized. As the stress continues to be loaded, the gap between particles becomes smaller and is difficult to be filled; thus, the entire state of coal particles tends to be a critical stable skeleton structure, and deformation tends to be stable.

As shown by the curve, the porosity of fragmentized coals varies with time under two different stresses; when the stress is 8 MPa, the porosity decrease corresponding to Grain Sizes 1–5 in the entire creep process is 5.44%, 10.19%, 6.45%, 6.64%, and 2.34%, respectively; when the stress is 12 MPa, the porosity decrease corresponding to Grain Sizes 1–5 in the entire creep process is 4.41%, 7.89%, 8.11%, 1.94%, and 4.00%, respectively. When the stress increases from 8 MPa to 12 MPa, the porosity decrease corresponding to Grain Sizes 1∼5 is 27.73%, 6.43%, 24.71%, 17.85%, and 18.78%, respectively. In case of lower load level, slippage and malposition seldom happen to fragmentized coal particles, and fragmentized coal particles can form a self-supporting structure earlier because there are few particle surface edges fracture, internal fracture expansion, and particles plastic flow, and slower porosity decreases due to weak squeezing effect between fragmentized coal particles; as the stress level rises up, more slippage and malposition happen to fragmentized coal particles, and fragmentized coal particles form a self-supporting structure late because there are more particle surface edges fracture, internal fracture expansion, and particles plastic flow due to strong squeezing effect between fragmentized coal particles, so that the porosity decreases quickly, and finally stabilized porosity is smaller.

3.2. Influence of Grain Size on Porosity of Fragmentized Coals. Grain size produces a significant impact on the porosity of fragmentized coals, and the relation curve between the porosity of fragmentized coals with different grain sizes and time under different stress levels is obtained from tests, as shown in Figure 4.

Figure 5(a) shows that under the stress of 8 MPa, the porosity decreases quickly at early creep, and at 8.64×10^4 (s), the porosity of samples corresponding to Grain Sizes 1∼5 is 0.163 562, 0.206 678, 0.173 566, 0.182 943, and 0.217 181, respectively. Afterwards, it goes through three stages of obvious decay. In Phase I until 34.56×10^4 (s), the porosity of samples corresponding to Grain Sizes 1∼5 decreases to 0.155 049, 0.188 101, 0.163 554, 0.172 351, and 0.212 414,

(a)

(b)

(c)

(d)

(e)
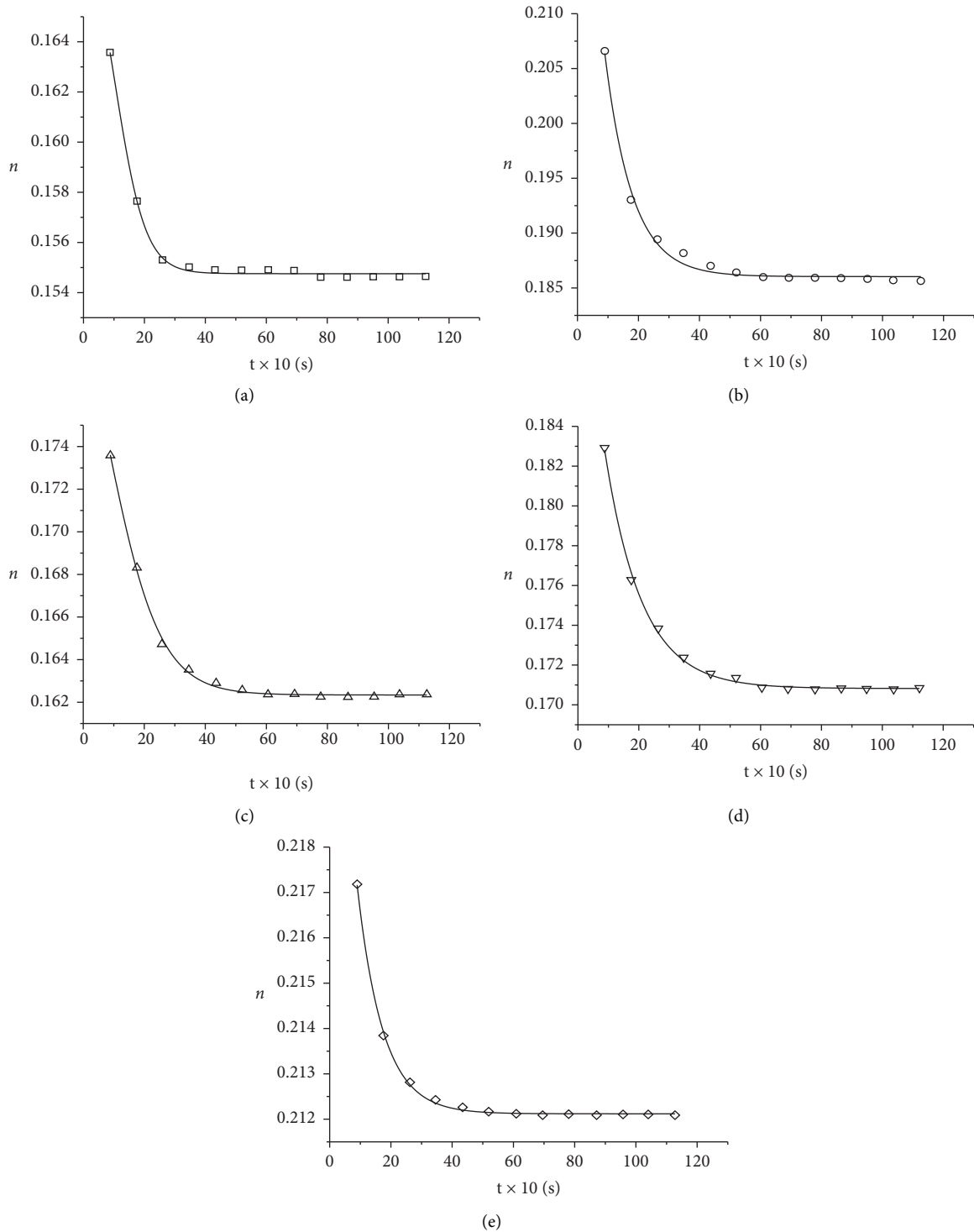
FIGURE 2: Relation curves between porosity of fragmentized coals and time under the stress of 8 MPa. (a) m1. (b) m2. (c) m3. (d) m4. (e) m5.

respectively; in Phase II until 51.84×10^4 (s), the porosity of samples corresponding to Grain Sizes 1~5 decreases to 0.154 919, 0.186 297, 0.162 593, 0.171 318, and 0.212 174, respectively; in Phase III until 112.32×10^4 (s), the porosity of samples corresponding to Grain Sizes 1~5 decreases to 0.154 658, 0.185 619, 0.162 379, 0.170 800, and 0.212 094. Targeted

at the porosity of the first catastrophe point, the porosity of samples corresponding to Grain Sizes 2~5 increases by 21.32%, 5.49%, 11.16%, and 37.00%, respectively.

Figure 5(b) shows that under the stress of 12 MPa, the porosity decreases quickly at early creep, and at 8.64×10^4 (s), the porosity of samples corresponding to Grain Sizes 1~5
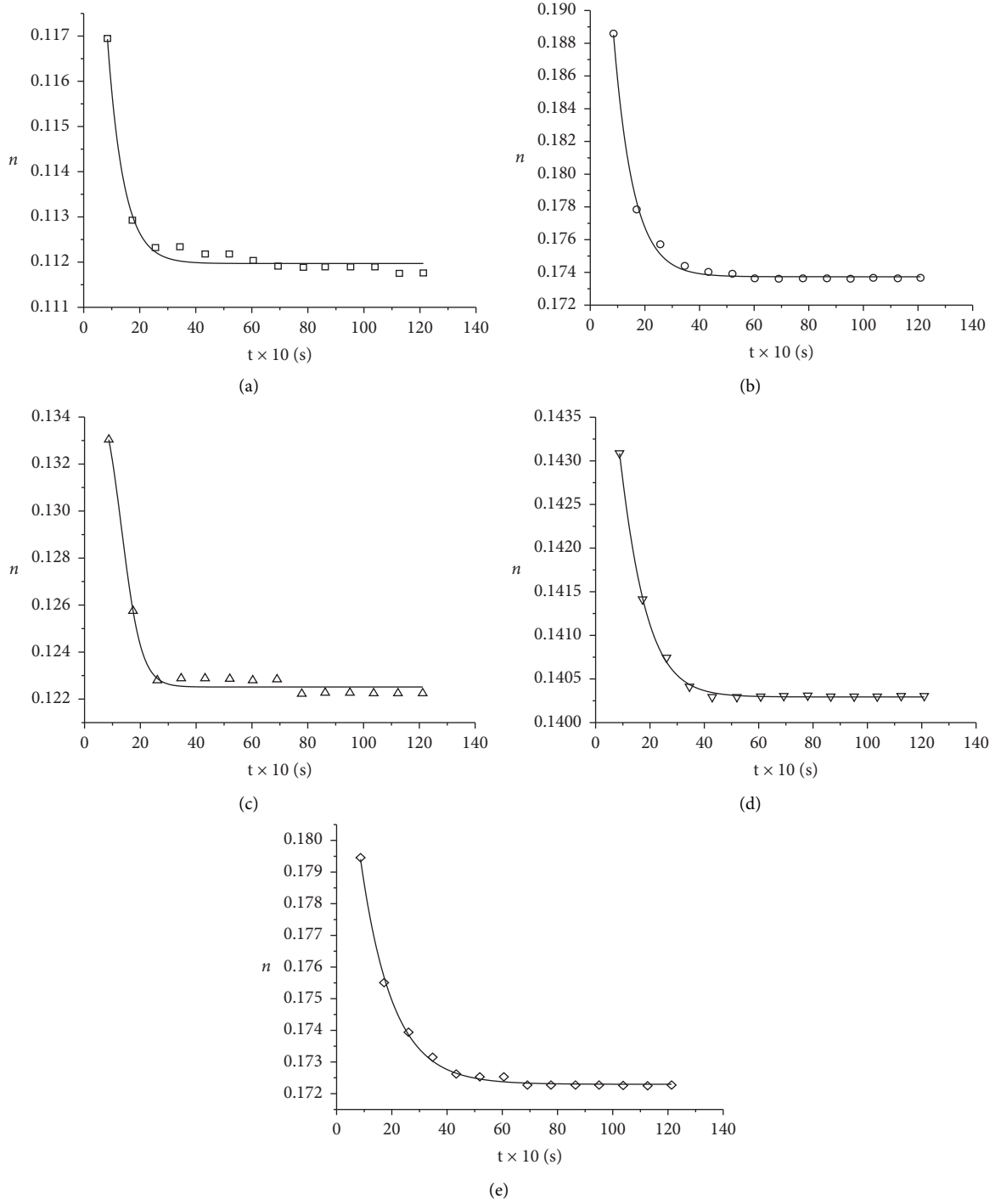
Figure 3: Relation curves between the porosity of fragmentized coals and time under the stress of 12 MPa. (a) m1. (b) m2. (c) m3. (d) m4. (e) m5.
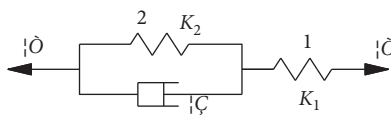
Figure 4: Kelvin–Voigt model. 1, Hook model; 2, Kelvin Model.
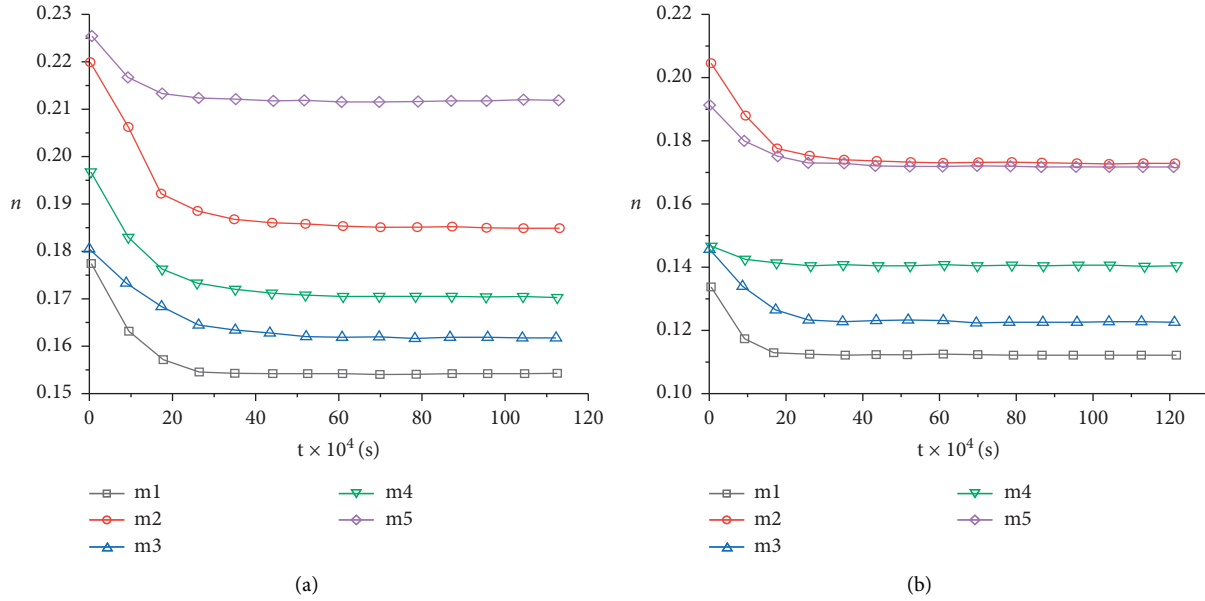
FIGURE 5: Influence of grain size on the porosity of fragmentized coals. (a) 8 MPa. (b) 12 MPa.

is 0.116 921, 0.188 551, 0.133 041, 0.143 082, and 0.179 431, respectively. Afterwards, it goes through three stages of obvious decay. In Phase I until 34.56×10^4 (s), the porosity of samples corresponding to Grain Sizes 1~5 decreases to 0.112 343, 0.174 373, 0.122 839, 0.140 419, and 0.173 135, respectively; in Phase II until 51.84×10^4 (s), the porosity of samples corresponding to Grain Sizes 1~5 decreases to 0.112 199, 0.173 908, 0.122 614, 0.140 308, and 0.172 518, respectively; in Phase III until 120.91×10^4 (s), the porosity of samples corresponding to Grain Sizes 1~5 decreases to 0.111 767, 0.173 675, 0.122 252, 0.140 308, and 0.172 253. Targeted at the porosity of the first catastrophe point, the porosity of samples corresponding to Grain Sizes 2~5 increases by 55.22%, 9.34%, 24.99%, and 54.11%, respectively.

Under the equal stress, as the grain size of fragmentized coal particles decreases, the porosity tends to decrease; as the grain size of fragmentized coal particles tends to be stable, the porosity tends to increase.

3.3. Regression Analysis of the Porosity Variation with Time. According to the regression analysis of the porosity variation of fragmentized coals with five grain sizes and under two stresses with time, the regression equation and relation coefficient are obtained and shown in Table 2.

Under two stresses, the porosity logarithm of fragmentized coals during creep process shows a linear negative correlation with the time, namely,

$$\ln (n - a) = -ct + \ln b, \tag{2}$$

where n denotes the porosity of fragmentized coals; t denotes the time; a, b, and c are the regression coefficients. As the creep time increases, the a value infinitely nears the final porosity after creep. Under the stress of 8 MPa, the a value of Grain Sizes 1~5 corresponding to samples is 0.1548, 0.1860, 0.1623, 0.1708, and 0.2121, respectively, which tends to

increase with the decrease in grain size; under the stress of 12 MPa, the a value of Grain Sizes 1~5 corresponding to samples is 0.1120, 0.1738, 0.1225, 0.1403, and 0.1723, respectively, which tends to increase with the decrease in grain size. The a value tends to increase with the decrease in grain size and tends to decrease with the increase in load.

4. Creep Constitutive Model of Saturated Fragmentized Coals

The creeping property of fragmentized coals refers to the long-term mechanical effect suffered by fragmentized coals. The creeping property and law of fragmentized coals can be explained by establishing the creep constitutive equation. It can be found from the analysis of test results that early instantaneous strain and deformation limit of long-term creep exist during the entire creep test process of fragmentized coals. Therefore, Kelvin–Voigt is selected to describe the creep law of fragmentized coals and disclose its constitutive relation. A correlation analysis is conducted on the Kelvin–Voigt model, and a comparison is conducted with the previously common fitting curve of the first index decay to verify the reasonability of creep constitutive relation of fragmentized coals described by the Kelvin–Voigt model.

4.1. Model Building of Creep Constitutive Model of Fragmentized Coals. In broad sense, the Kelvin–Voigt model of the creep constitutive model is shown in Figure 4.

Under the condition of applying the constant load $\sigma_0 = \sigma_1 = \sigma_2$,

$$\varepsilon_1 = \varepsilon_2 = \varepsilon_3 = \frac{\sigma_0}{K_1} + \frac{\sigma_0}{K_2} \left[1 - \exp\left(-\frac{K_2}{\eta} t \right) \right]. \tag{3}$$

When $t = 0$, $\varepsilon_0 = \sigma_0/K_1$, where ε_0 is the instantaneous deformation, which is independent from time and is realized by the H element (element 1).

TABLE 2: Fitted equation coefficients of fragmentized coals under different axial stresses.

Grain size (in mm)	Regression coefficient	Axial stress: 8 MPa	Axial stress: 12 MPa
m1 (20–25)	A	0.1548	0.1120
	B	0.2839	0.0233
	C	0.0676	0.1800
m2 (15–20)	A	0.1860	0.1738
	B	0.0538	0.0483
	C	0.1118	0.1375
m3 (10–15)	A	0.1623	0.1225
	B	0.0231	0.0365
	C	0.0815	0.1430
m4 (5–10)	A	0.1708	0.1403
	B	0.0250	0.0071
	C	0.0845	0.1075
m5 (2.5–5)	A	0.2121	0.1723
	B	0.0141	0.0150
	C	0.1187	0.0865
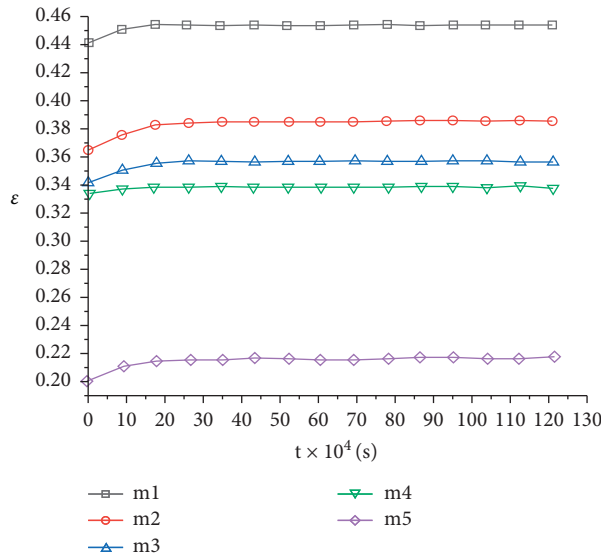
FIGURE 6: The ε-t relation of fragmentized coals with different grain sizes under the stress of 12 MPa.

TABLE 3: Kelvin–Voigt model parameter table of fragmentized coals with different grain sizes under the stress of 12 MPa.

Parameter	Grain size				
	m1	m2	m3	m4	m5
K_1 (MPa)	27.1675	32.84006	35.049762	35.8090186	59.8890943
K_2 (MPa)	964.286	586.9565	790.2439	3056.60377	733.031674
η (MPa·s)	$5.4\,E + 07$	67363268	86390175	351439009	63883287.3

When $t \longrightarrow \infty$, $\varepsilon_{\infty} = \sigma_0/K_1 + \sigma_0/K_2$, ε_0 is obtained, where ε_{∞} denotes that finally the creep tends to be stable and is the sum of instantaneous deformation of two Hooke bodies.

During the creep test, the ε-t relation of fragmentized coals with different grain sizes is shown in Figure 6.

The analysis of the ε-t relation during the creep test of fragmentized coals and the creep model parameters of

fragmentized coals with different grain sizes are shown in Table 3.

4.2. Reasonability Analysis of the Creep Constitutive Model of Fragmentized Coals. The constitutive equation of fragmentized coals with different grain sizes can be obtained by the Kelvin–Voigt model and based on the material creeping

TABLE 4: Fitting parameter table of the first index decay of fragmentized coals with different grain sizes under the stress of 12 MPa.

Parameter grain size	m1	m2	m3	m4	m5
A	−0.0123	−0.02073	−0.01528	−0.0397	−0.01618
B	5.48016	10.01032	9.60959	10.76907	9.20648
C	0.45403	0.38592	0.35751	0.33906	0.21664

□ Real measuring points of creep test
--- Fitting curve of first index decay
— Creep curve of Kelvin–Voigt model

(a)

□ Real measuring points of creep test
--- Fitting curve of first index decay
— Creep curve of Kelvin–Voigt model

(b)

□ Real measuring points of creep test
--- Fitting curve of first index decay
— Creep curve of Kelvin–Voigt model

(c)

□ Real measuring points of creep test
--- Fitting curve of first index decay
— Creep curve of Kelvin–Voigt model

(d)

FIGURE 7: Continued.

(e)

FIGURE 7: Kelvin–Voigt model and the fitting curve of first index decay of fragmentized coals with different grain sizes. (a) m1. (b) m2. (c) m3. (d) m4. (e) m5.

TABLE 5: Comparison of correlation coefficients of the Kelvin–Voigt model and the fitting curve of first index decay of fragmentized coals with different grain sizes.

Grain size correlation coefficient	m1	m2	m3	m4	m5
Exponential decay curve fitting	0.99937	0.99549	0.99439	0.99866	0.99835
Kelvin–Voigt creep model	0.99965	0.995799	0.9954751	0.9988852	0.9989241

property of fragmentized coals. Hereby, the reasonability and precision of the Kelvin–Voigt model need to be further analyzed.

In the past research studies on the creeping property of fragmentized rocks, the exponential decay fitted equation is mostly adopted to describe the creep process of fragmentized rocks. According to the analysis of the ε-t relation of fragmentized coals with different grain sizes as shown in Figure 6, the fitted equation of the first index decay ε-t can be obtained:

$$\varepsilon = A \cdot \exp\left(-\frac{t}{B}\right) + C. \tag{4}$$

Parameters of the fitted equation of the first index decay ε-t are shown in Table 4.

Kelvin–Voigt model and the fitting curve of first index decay of fragmentized coals with different grain sizes are shown in Figure 7.

On the basis of creep test data of the saturated fragmentized coals and through the statistical correlation analysis and calculation according to the Kelvin–Voigt model and the fitting curve of the first index decay of fragmentized coals with different grain sizes, their correlation coefficients are shown in Table 5.

As shown in Table 5, according to the creep constitutive relation of fragmentized coals described by the creep model, the curve correlation coefficient at all grain sizes reaches above 0.995; at all grain sizes, the correlation coefficient between the Kelvin–Voigt creep model of fragmentized coals and test data is larger than the past fitting curve of the first index decay, indicating that compared with the fitting curve of the first index decay, the creep constitutive equation of fragmentized coals established by the Kelvin–Voigt model is more precise, and the latter is reasonable; in addition, the creep constitutive equation of fragmentized coals established by the Kelvin–Voigt model can explain the creep test process of saturated fragmentized coals from the perspective of the material property of fragmentized coals.

5. Conclusions

According to the analysis of the porosity variation laws of fragmentized coals with five grain sizes during creep process under two stresses and its creep constitutive relation, the following conclusions are drawn:

(1) Under two stresses, the porosity logarithm of fragmentized coals during creep shows a linear

negative correlation with the time: ln(n–a) = –ct + lnb.

(2) The porosity decrease is evidently divided into three phases. Phase I: slippage, malposition, and deformation occur between particles of fragmentized coals, and porosity decreases quickly. Phase II: slippage and malposition seldom happen to be fragmentized coal particles, and the fragmentized coal particles form a self-supporting structure; as the stress continues to be loaded, under the squeezing impact, the porosity changes relatively quickly and tends to decrease. Phase III: due to the attrition crushing in Phase II, a larger gap exists between coal particles and is filled with fine coal particles after fragmentized. As the stress continues to be loaded, the gap between particles becomes smaller and is difficult to be filled; thus, the entire state of coal particles tends to be a critical stable skeleton structure, and deformation tends to be stable.

(3) When the stress level is lower, the porosity decreases slowly; when the stress level rises up, the porosity decreases quickly; finally when the stress level remains stable, the porosity is smaller.

(4) Under the equal stress, as the grain size of fragmentized coal decreases, the porosity tends to decrease, and as the grain size of fragmentized coal tends to stabilize, the porosity tends to increase.

(5) The creep constitutive equation of fragmentized rocks with different grain sizes was established by using the Kelvin–Voigt model; the correlation analysis shows that the curve correlation coefficient reaches above 0.995, and at various grain sizes, the Kelvin–Voigt creep model and test data correlation coefficient are larger than the past fitting curve of the first index decay, indicating the Kelvin–Voigt creep model of fragmentized coals is reasonable.

Data Availability

The data used to support the findings of this study are included within the article.

Conflicts of Interest

The authors declare that there are no conflicts of interest regarding the publication of this paper.

Acknowledgments

References

[1] Xu Jiang, LuQi, X. Wu, and D. Liu, "The fractal characteristics of the pore and development of briquettes with different coal particle sizes," *Journal of Chongqing*, vol. 34, pp. 81–89, 2011, in Chinese.

[2] J. E. Turney, *Subsidence above Inactive Coal Mines: Information for the Homeowner*, Colorado Geological Survey, Colorado Mined Land Reclamation, Division Inactive Mine Reclamation Program, and Department of Natural Resources, Golden, CO, USA, 1985.

[3] C. Zhang, J. Liu, Y. Zhao, P. Han, and L. Zhang, "Numerical simulation of broken coal strength influence on compaction characteristics in goaf," *Natural Resources Research*, vol. 29, no. 4, pp. 2495–2511, 2020.

[4] S. Li, "Stability study of fluid-solid coupled dynamic system of seepage in accumulative broken rock," *Arabian Journal of Geosciences*, vol. 13, no. 14, 2020.

[5] C. Zhang and L. Zhang, "Permeability characteristics of broken coal and rock under cyclic loading and unloading," *Natural Resources Research*, vol. 28, no. 3, pp. 1055–1069, 2019.

[6] M. Zhan-guo, G.-L. Guo, R.-H. Chen, and M. Xian-biao, "An experimental study on the compaction of water-saturated over-broken rock," *Chinese Journal of Rock Mechanics and Engineering*, vol. 24, no. 7, pp. 1139–1144, 2005, in Chinese.

[7] C. H. Scholz, "Mechanism of creep in brittle rock," *Journal of Geophysical Research*, vol. 73, no. 10, pp. 3295–3302, 1968.

[8] H. W. Zhou, L. Zhang, X. Y. Wang, T. L. Rong, and L. J. Wang, "Effects of matrix-fracture interaction and creep deformation on permeability evolution of deep coal," *International Journal of Rock Mechanics and Mining Sciences*, vol. 127, p. 104236, 2020.

[9] M. Li, J. Zhang, G. Meng, Y. Gao, and A. Li, "Testing and modelling creep compression of waste rocks for backfill with different lithologies," *International Journal of Rock Mechanics and Mining Sciences*, vol. 125, p. 104170, 2020.

[10] P. N. Hagin and M. D. Zoback, "Viscous deformation of unconsolidated sands–part 1: time-dependent, frequency dispersion, and attenuation," *Geophysics*, vol. 69, no. 3, pp. 653–861, 2004.

[11] W. He, A. Hajash, and D. Sparks, "Creep compaction of quartz aggregates: effects of pore-fluid flow--A combined experimental and theoretical study," *American Journal of Science*, vol. 303, no. 2, pp. 73–93, 2003.

[12] F. M. Chester, J. S. Chester, A. K. Kronenberg, and A. Hajash, "Subcritical creep compaction of quartz sand at diagenetic conditions: effects of water and grain size," *Journal of Geophysical Research*, vol. 112, no. B6, p. B06203, 2007.

[13] A. K. Parkin, "Creep of rockfill," in *Advances in Rockfill Structure*, pp. 221–239, Kluwer Academic Publishers, London, UK, 1992.

[14] Z. Ma, P. Wang, Z. Guo-zhen, and K. Sun, "Test study on the changing of the porosity for water-saturated granular shale during its creep," in *Proceedings of the 44th US Rock Mechanics Symposium and the 5th US/Canada Rock Mechanics Symposium*, Salt Lake City, UT, USA, June 2010.

Research Article

A New Unified Solution for Circular Opening considering Different Strength Criteria and the Postpeak Elastic Strain Form

Xuyang Shi ,[1] **Wei Zhou** ,[1] **Liang Chen** ,[2] **Qingxiang Cai,**[1] **Ming Li,**[2] **Zhaolin Li,**[1] **and Boyu Luan**[1]

[1]*School of Mines, China University of Mining & Technology, Xuzhou, Jiangsu 221116, China*
[2]*State Key Laboratory for Geomechanics and Deep Underground Engineering, China University of Mining & Technology, Xuzhou, Jiangsu 221116, China*

Correspondence should be addressed to Wei Zhou; loutian1982@126.com and Liang Chen; chenliang_cumt@126.com

The strength criterion is an extremely important basis for evaluating the stability of surrounding rock and optimizing the support pressure design. In this paper, nine different strength criteria are summarized and simplified based on the reasonable assumption. Then, a new unified criterion equation is established, which includes all strength theories proposed by this paper. Meanwhile, a new unified closed-form solution for circular opening based on the newly proposed unified criterion equation is deduced with the infinite and finite external boundary combining with the nonassociative flow rule under plane strain conditions. In the plastic zone, four different elastic strain assumptions are applied to solving the plastic zone deformation considering the effect of rock mass damage. The solution's validity is also verified by comparison with the traditional solution. Finally, the influences of strength criteria, dilation coefficient, elastic strain form of plastic zone, and rock mass damage on the mechanical response of surrounding rock are discussed in detail. The research result shows that TR and VM criteria give the largest plastic zone radius, followed by IDP, MC, and MDP criteria, and seem to underestimate the self-strength of rock mass; The CDP criterion gives the smallest plastic zone radius and may overestimate the self-strength of rock mass; UST0.5, GSMP, GMC, and GLD criteria that reasonably consider the effect of internal principal stresses give an intermediate range and can be strongly recommended for evaluating the mechanics and deformation behavior of surrounding rock; as the dilation coefficient gradually increases, the dimensionless surface displacement presents the nonlinear increase characteristics; the deformation of plastic zone and the ground response curve, which are closely related to the strength criteria, are also greatly influenced by the elastic strain assumption in the plastic zone and rock mass damage degree. The assumption that the elastic strain satisfies Hook's law (Case 3) may be more reasonable compared with the continuous elastic strain (Case 1) and thick-walled cylinders (Case 2) assumptions; in addition, the Young's modulus power function damage model seems to give more reasonable solution for the deformation of plastic zone and is suggested to be a preferred method for solving plastic displacement. The research results can provide very important theoretical bases for evaluating the tunnel stability and support design reliability of different lithology rock masses in underground engineering.

1. Introduction

Accurate prediction for the stress and displacement distribution of circular opening plays a crucial role in evaluating the mechanics and deformation behavior of rock mass in civil, mine, and oil engineering and natural gas development engineering. The circular opening may include tunnel, vertical shaft, boreholes, and pile foundation holes. In the

early stage, many closed-form solutions of circular opening are obtained by regarding the outer boundary as the infinite boundary with association or nonassociative flow rules [1–9]. However, the semianalytical solutions considering the finite boundary are rarely deduced because of the complexity of the calculation process [6, 10–13]. In practice, it is possible to calculate the outer boundary as an infinite boundary only if it is much larger than the diameter of circular opening.

Therefore, this simplified calculation method has certain limitations in many geological engineering, such as shallow-buried tunnel.

As for most of the analyses reported in the past, the solutions were given considering different yield criteria, such as linear Mohr–Coulomb (MC), Tresca (TR), and nonlinear Hoek–Brown (HB) criteria [2, 4–9, 14–17]. Nevertheless, the above studies did not consider the effect of intermediate principal stress on the mechanical response of surrounding rock. Many research results have shown that the intermediate principal stress exerts significant influence on the failure behavior of rock mass [6]. In addition, for rock mass as a natural geological material, the yield failure criterion is more complicated under the influence of internal crack and joint. Therefore, it is extremely difficult to reconcile the calculation results with the field measured results if only one or two yield criteria are used to predict the stresses and displacement behavior of surrounding rock. In this paper, as shown in Table 1, different yield criteria, such as Mogi–Coulomb (GMC) [9, 10], Drucker–Prager (CDP, MDP, and IDP) [3, 4, 14, 28–30], Generalized Lade–Duncan (GLD) [31, 35], Generalized SMP (GSMP) [18, 27, 31], and von Mises (VM) criteria [15, 26], will be summarized and simplified and then used to study the mechanical response of rock mass.

For an elastic-brittle plastic rock mass, the postpeak deformation is closely related to the assumed form of elastic strain in the plastic zone. Brown et al. researched the ground response curve for the rock tunnel by assuming that the elastic strain in the plastic region was equal to that on the elastic-plastic interface [36]. Sharan presented a series of new closed-form solutions for the prediction of displacements around circular openings in a brittle rock mass with nonlinear Hoek–Brown criterion by regarding the elastic strain of plastic zone as the thick-walled cylinder [16, 37]. Yu and Zhang and Reed et al. held that the elastic strain in the plastic zone satisfied the generalized Hooke's theorem and then derived the deformation of plastic zone with non-associative flow laws [9, 38–40]. In addition, Park summarized the above three different definitions for elastic strains in the plastic zone and analyzed the deformation law of plastic zone with Mohr–Coulomb and Hoek–Brown criteria under three different case conditions [9]. However, the postpeak Young's modulus attenuation along the radii direction is ignored in this study.

In this paper, different yield criteria of rock mass are firstly summarized and then a unified yield criterion form is derived by simplifying the above criteria. Next, a new closed-form solution for stresses and deformation distribution around a circular opening subjected to the hydrostatic pressure at the finite or infinite outer boundary is also obtained with the new proposed unified yield criterion. In the plastic zone, five different definitions for elastic strains in the plastic zone and nonassociated flow rule are adopted to establish the radii displacement solution. The correctness of the solution is also verified by comparison with a series of traditional solution and numerical simulation results. Finally, the influences of strength theory and elastic strain definitions of plastic zone on the mechanical response of surrounding rock are discussed in detail.

2. Brief Description of Yield Criterion

2.1. Mohr–Coulomb Criterion.
The linear Mohr–Coulomb criterion is widely used in geotechnical engineering because of its simple expression form. However, the influence of intermediate principal stress on rock mass failure is ignored. In addition, the triaxial strength of rock mass obtained by MC criterion deviates greatly from the measured data under the high confining pressure conditions. The following is the governing equation for MC criterion based on the cohesion c and internal friction angle φ [1, 14, 39]:

$$\sigma_1 = N\sigma_3 + \sigma_c, \tag{1}$$

where N is a constant which is a function of the internal friction angle and σ_c is the uniaxial compressive strength (UCS). They can be expressed as follows:

$$N = \frac{(1 + \sin\varphi)}{(1 - \sin\varphi)},$$
$$\sigma_c = \frac{(2c\cos\varphi)}{(1 - \sin\varphi)}. \tag{2}$$

2.2. Tresca Criterion.
The Tresca (TR) criterion is a simplified form of MC criterion and assumes that the failure will occur if the maximum shear stress $\tau_{\max}$ inside any plane of rock mass reaches a critical value [1, 15]. As shown in Figure 1, the yield curve of TR criterion is a regular hexagon, which is inscribed in the circular yield curve of the von Mises (VM) criterion in π-plane. The expression form is

$$\left(\frac{\sigma_1 - \sigma_3}{2}\right) = \tau_{\max} = c. \tag{3}$$

The TR criterion can be considered as a special case where the internal friction angle equals zero in the MC criterion. Equation (2) can be rewritten as

$$f(\sigma_1, \sigma_3) = \sigma_1 - \sigma_3 - 2c = 0. \tag{4}$$

2.3. Generalized Lade–Duncan Criterion.
In early 1973, the Lade–Duncan criterion has been firstly proposed by considering the intermediate principal stresses based on the triaxial compression test for noncohesive soil. The initial expression form can be written as follows:

$$\frac{(I_1)^3}{I_3} = K_{\text{Lade}}, \tag{5}$$

where I_1 and I_3 are, respectively, the first and third principal stress invariants of friction material. K_{Lade} is the material constant which is closely related to internal friction angle:

$$K_{\text{Lade}} = \frac{(3 - \sin\varphi)^3}{(1 + \sin\varphi)(1 - \sin\varphi)^2}, \tag{6}$$

$$I_1 = \sigma_1 + \sigma_2 + \sigma_3, \tag{7}$$

TABLE 1: A summary on the yield criterion under plane strain conditions.

Failure criterion	Initial yield criterion	Simplified yield criterion ($\sigma_1 = \xi_j\sigma_3 + Y_j$)	Linearity	Intermediate principal stress
Mohr–Coulomb (MC) [1, 14]	$\sigma_1 = (1 + \sin\varphi/1 - \sin\varphi)\sigma_3 + (2c\cos\varphi/1 - \sin\varphi)$	$\xi_{MC} = (1 + \sin\varphi/1 - \sin\varphi); Y_{MC} = (2c\cos\varphi/1 - \sin\varphi)$	Linear	No
Tresca (TR) [15]	$(\sigma_1 - \sigma_3/2) = \tau_{\max} = c$	$\xi_{TR} = 1$ $Y_{TR} = 2c$	Linear	No
Generalized Lade–Duncan (GLD) [18–23]	$((I_1')^3/I_3') = K_{Lade}$, $K_{Lade} = ((3 - \sin\varphi)^3/(1 + \sin\varphi)(1 - \sin\varphi)^2)$;	$\xi_{GLD} = \eta_{GLD}$ $Y_{GLD} = (\eta_{GLD} - 1)\sigma_i$	Nonlinear	Yes
Mogi–Coulomb (GMC) [2, 24, 25]	$\frac{1}{3}\sqrt{(\sigma_1 - \sigma_2)^2 + (\sigma_2 - \sigma_3)^2 + (\sigma_1 - \sigma_3)^2} = q_1((\sigma_1 + \sigma_2 + \sigma_3)/3) + q_2$ $q_1 = (2\sqrt{2}/3)\sin\varphi$ $q_2 = (2\sqrt{2}/3)c\cos\varphi$	$\xi_{MGC} = (\sqrt{6} + 3q_1/\sqrt{6} - 3q_1)$ $Y_{MGC} = (6q_2/\sqrt{6} - 3q_1)$	Linear	Yes
von Mises (VM) [15, 26]	$\sqrt{((\sigma_1 - \sigma_2)^2 + (\sigma_2 - \sigma_3)^2 + (\sigma_1 - \sigma_3)^2/6)} = \sqrt{J_2} = (2c/3)$	$\xi_{VM} = 1$ $Y_{VM} = (4c/\sqrt{3})$	Nonlinear	Yes
Generalized SMP criterion (GSMP) [18, 27]	$(I_1^1 I_2^1/I_3^1) = K_{GSMP}$ $K_{GSMP} = 8\tan^2\varphi + 9$	$\xi_{GSMP} = \eta_{GSMP}$ $Y_{GSMP} = (\eta_{GSMP} - 1)\sigma_i$	Nonlinear	Yes
Circumscribe Drucker–Prager (CDP) [1, 3, 4, 28–30]	$\sqrt{J_2} = k - \alpha I_1$ $k = (6c\cos\varphi/\sqrt{3}\,(3 - \sin\varphi))$ $\alpha = (2\sin\varphi/\sqrt{3}\,(3 - \sin\varphi))$ The expression form is the same as CDP.	$\xi_{CDP} = (1 + 3\alpha/1 - 3\alpha)$ $Y_{CDP} = (2k/1 - 3\alpha)$	Nonlinear	Yes
Middle Circumscribe Drucker–Prager (MDP) [28]	$k = (6c\cos\varphi/\sqrt{3}\,(3 + \sin\varphi))$ $\alpha = (2\sin\varphi/\sqrt{3}\,(3 + \sin\varphi))$			Yes
Inscribe Drucker–Prager (IDP) [31]	The expression form is the same as CDP. $k = (\sqrt{3}\,c\cos\varphi/\sqrt{(3 + \sin^2\varphi)})$ $\alpha = (\sin\varphi/\sqrt{(9 + 3\sin^2\varphi)})$ If $\sigma_2 \leq (\sigma_1 + \sigma_3)/2 - ((\sigma_1 - \sigma_3)\sin\varphi)/2$			Yes
Unified strength theory (UST) [5, 6, 32–34]	$F = ((1 - \sin\varphi/1 + \sin\varphi))\sigma_1 - ((b\sigma_2 + \sigma_3/1 + b)) = ((2c\cos\varphi/1 + \sin\varphi));$ If $\sigma_2 \geq (\sigma_1 + \sigma_3)/2 - (\sigma_1 - \sigma_3)\sin\varphi/2$ $F' = (1 - \sin\varphi/(1 + b)(1 + \sin\varphi))(\sigma_1 + b\sigma_2) - \sigma_3 = (2c\cos\varphi/1 + \sin\varphi)$	$\xi_{UST} = (2 + b + (2 + 3b)\sin\varphi/(2 + b)(1 - \sin\varphi))$ $Y_{UST} = (4(1 + b)c\cos\varphi/(2 + b)(1 - \sin\varphi))$	Linear	Yes
Generalized twin shear stress criterion (GTSS) [5, 6]	When $b = 1$, UST is equal to GTSS.	$\xi_{GTSS} = (3 + 5\sin\varphi/3(1 - \sin\varphi))$ $Y_{GTSS} = (8c\cos\varphi/3(1 - \sin\varphi))$	Linear	Yes

The compressive stress is positive and the tensile stress is negative $(\sigma_1 \geq \sigma_2 \geq \sigma_3)$; b is the intermediate principal stress coefficient; $\eta_{LD} = (1/4)[\sqrt[3]{K_{Lade}} - 1 + \sqrt{(\sqrt[3]{K_{Lade}} - 1)^2 - 4}]^2$; $\eta_{SMP} = (1/4)[\sqrt{K_{SMP}} - 1 + \sqrt{K_{SMP} - 3 - 2\sqrt{K_{SMP}}}]^2$; $\sigma_i = c\cot\varphi$.
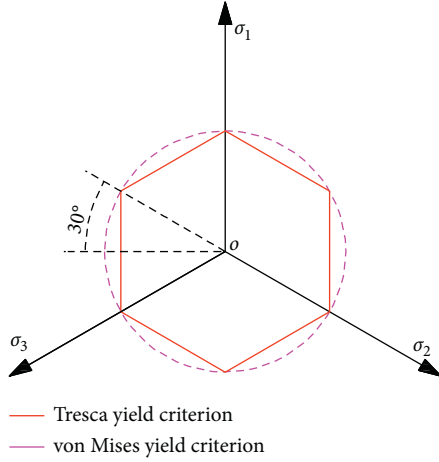
FIGURE 1: Tresca and von Mises criterion in the π-plane.

$$I_3 = \sigma_1 \sigma_2 \sigma_3. \tag{8}$$

In 1999, the Lade–Duncan criterion was modified by Ewy so that it could reasonably describe the strength characteristics of cohesive soil by introducing bound stress (σ_0) [35]. Its generalized expression is also given as

$$\frac{(I_1')^3}{I_3'} = K_{\text{Lade}}, \tag{9}$$

where I_1' and I_3' are, respectively, the first and third principal stress invariants of cohesive-friction material:

$$
\begin{aligned}
I_1' &= (\sigma_1 + \sigma_0) + (\sigma_2 + \sigma_0) + (\sigma_3 + +\sigma_0), \\
I_3' &= (\sigma_1 + \sigma_0)(\sigma_2 + \sigma_0)(\sigma_3 + +\sigma_0),
\end{aligned} \tag{10}
$$

where σ_0 is the bound stress: $\sigma_0 = c \cot \varphi$. For the non-cohesive soils, under plane strain conditions, the internal principal stress can be expressed as

$$\sigma_2 = \sqrt{\sigma_1 \sigma_3}. \tag{11}$$

By substituting equations (7), (8), and (11) into equation (6), the Lade–Duncan criterion can be rewritten as

$$\sigma_1 = \left(\frac{1}{4}\right)\left[\sqrt[3]{K_{\text{Lade}}} - 1 + \sqrt{\left(\sqrt[3]{K_{\text{Lade}}} - 1\right)^2 - 4} \right]^2 \sigma_3 = \eta_{\text{Lade}} \sigma_3. \tag{12}$$

For the cohesive-friction material, according to the coordinate translation method [18, 19], the generalized Lade–Duncan (GLD) criterion will be obtained by integrating equation (12).

$$\sigma_1 + \sigma_0 = \left(\frac{1}{4}\right)\left[\sqrt[3]{K_{\text{Lade}}} - 1 + \sqrt{\left(\sqrt[3]{K_{\text{Lade}}} - 1\right)^2 - 4} \right]^2$$

$$\cdot (\sigma_3 + \sigma_0) = \eta_{\text{Lade}}(\sigma_3 + \sigma_0).$$

$$f(\sigma_1, \sigma_3) = \sigma_1 - \eta_{\text{Lade}}\sigma_3 - (\eta_{\text{Lade}} - 1)\sigma_0 = 0. \tag{13}$$

2.4. Generalized SMP Criterion.
Considering the effect of internal principal stress, H. Matsuoka and T. Nakai proposed the SMP criterion, which could be expressed by three principal stress invariants [31]:

$$\left(\frac{I_1 I_2}{I_3}\right) = K_{\text{SMP}}, \tag{14}$$

where I_2 is the second principal stress invariant and K_{SMP} is the material constant in the SMP criterion:

$$K_{\text{SMP}} = 8 \tan^2 \varphi + 9, \tag{15}$$

$$I_2 = \sigma_1 \sigma_3 + \sigma_1 \sigma_2 + \sigma_2 \sigma_3. \tag{16}$$

For the frictional material, by introducing equations (7), (8), (11), and (16) into equation (14), another form of SMP criterion will be deduced.

$$\sigma_1 = \left(\frac{1}{4}\right)\left[\sqrt{K_{\text{SMP}}} - 1 + \sqrt{K_{\text{SMP}} - 3 - 2\sqrt{K_{\text{SMP}}}} \right]^2$$

$$\cdot \sigma_3 = \eta_{\text{GSMP}} \sigma_3. \tag{17}$$

As the GLD criterion, according to the coordinate translation method, the generalized SMP criterion will be given as [18]

$$\sigma_1 + \sigma_0 = \left(\frac{1}{4}\right)\left[\sqrt{K_{\text{SMP}}} - 1 + \sqrt{K_{\text{SMP}} - 3 - 2\sqrt{K_{\text{SMP}}}} \right]^2$$

$$\cdot (\sigma_3 + \sigma_0) = \eta_{\text{GSMP}}(\sigma_3 + \sigma_0).$$

$$f(\sigma_1, \sigma_3) = \sigma_1 - \eta_{\text{GSMP}}\sigma_3 - (\eta_{\text{GSMP}} - 1)\sigma_0 = 0. \tag{18}$$

As shown in Figure 2, compared with the yield curve of MC criterion in the π-plane, the GLD and GSMP criteria are nonlinear and the cross-sectional area of GLD criterion is the largest, followed by the GSMP criterion.

2.5. Mogi–Coulomb Criterion.
Based on Mog's theory [24], Al-Ajmi and Zimmerman found that the polyaxial test data could be fitted by linear relationships in $\tau_{\text{oct}} - \sigma_{m,2}$ space.

$$\tau_{\text{oct}} = a\sigma_{m,2} + b, \tag{19}$$

$$\tau_{\text{oct}} = \left(\frac{1}{3}\right)\sqrt{(\sigma_1 - \sigma_2)^2 + (\sigma_1 - \sigma_3)^2 + (\sigma_2 - \sigma_3)^2}, \tag{20}$$

$$\sigma_{m,2} = \left(\frac{\sigma_1 + \sigma_2 + \sigma_3}{3}\right), \tag{21}$$

where $\sigma_{m,2}$ is the mean normal stress and τ_{oct} is octahedral shear stress. The parameters a and b can be related exactly to the Coulomb strength parameter:
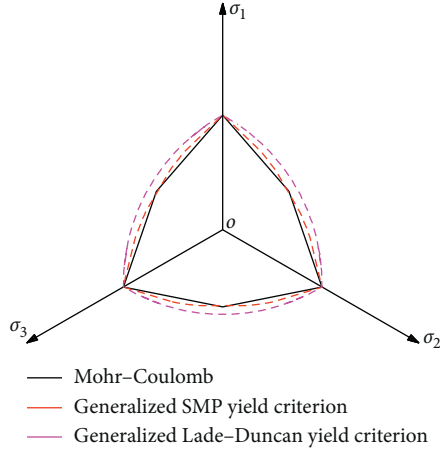
Figure 2: Comparison of MC, GLD, and GSMP criteria in the π-plane under plane strain condition.

$$a = \left(\frac{2\sqrt{2}}{3}\right)\sin\varphi,$$

$$b = \left(\frac{2\sqrt{2}}{3}\right)c\cos\varphi. \tag{22}$$

As the von Mises criterion, we take $\sigma_2 = ((\sigma_1 + \sigma_3)/2)$. Then, the Mogi–Coulomb (GMC) criterion can be obtained by integrating equations (19), (20), and (21).

$$f(\sigma_1, \sigma_3) = \sigma_1 - \left(\frac{\sqrt{6} + 3a}{\sqrt{6} - 3a}\right)\sigma_3 - \left(\frac{6b}{\sqrt{6} - 3a}\right) = 0. \tag{23}$$

2.6. Unified Strength Theory.

Based on the twin shear yield criterion, the unified strength theory (UST) is established by considering the influence of all the stress components on the material yield failure [32–34]. In geotechnical engineering, the cohesion and internal friction angle are usually used to represent this yield theory. The yield function can be expressed as follows [5, 6]:

If $\sigma_2 \le ((\sigma_1 + \sigma_3)/2) - ((\sigma_1 - \sigma_3)/2)\sin\varphi$,

$$f(\sigma_1, \sigma_3) = \left(\frac{1 - \sin\varphi}{1 + \sin\varphi}\right)\sigma_1 - \left(\frac{b\sigma_2 + \sigma_3}{1 + b}\right) = \left(\frac{2c\cos\varphi}{1 + \sin\varphi}\right). \tag{24a}$$

If $\sigma_2 \le ((\sigma_1 + \sigma_3)/2) - ((\sigma_1 - \sigma_3)/2)\sin\varphi$,

$$f(\sigma_1, \sigma_3) = \frac{1 - \sin\varphi}{(1 + b)(1 + \sin\varphi)}(\sigma_1 + b\sigma_2) - \sigma_3 = \left(\frac{2c\cos\varphi}{1 + \sin\varphi}\right). \tag{24b}$$

where b represents the yield parameter related to the intermediate principal stress, which can reflect the effect of the intermediate principal shear stress and the positive stress on the yield failure of the rock material, and $0 \le b \le 1$. As shown in Figure 3, if $b = 0$, UST will translate into the MC criterion; if $b = 1$, UST is converted into general twin shear strength
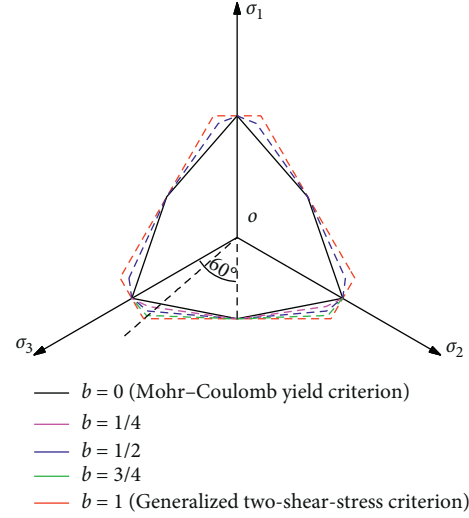
Figure 3: Unified strength theory yield curve in the π-plane [16].

(GTSS) criterion; if $0 < b < 1$, UST is a series of other ordered new strength criteria.

Just like Sections 2.3 and 2.6, if $\sigma_2 = ((\sigma_1 + \sigma_3)/2)$, $\sigma_2 \ge ((\sigma_1 + \sigma_3)/2) - ((\sigma_1 - \sigma_3)/2)\sin\varphi$ can be judged by substituting $\sigma_2 = ((\sigma_1 + \sigma_3)/2)$ into equation (24a) or equation (24b). Therefore, UST can be rewritten as

$$f(\sigma_1, \sigma_3) = \sigma_1 - \frac{2 + b + (2 + 3b)\sin\varphi}{(2 + b)(1 - \sin\varphi)}\sigma_3$$

$$- \frac{4(1 + b)c\cos\varphi}{(2 + b)(1 - \sin\varphi)} = 0. \tag{25}$$

2.7. Drucker–Prager Criterion.

The Drucker–Prager (DP) criterion is an extension of the von Mises criterion, which takes into account the effect of intermediate principal stress and hydrostatic pressure on yield failure of the materials. It can be expressed as

$$f(I_1, J_2) = \sqrt{J_2 + \alpha I_1 - k} = 0, \tag{26}$$

where the parameters α and k are the material constants, which can be determined from the slope and the intercept of the failure envelope. The parameter k is related to the cohesion and internal friction angle of rock mass. The parameter α is only related to the friction angle. Therefore, the Mohr–Coulomb parameter can be used to depict the DP criterion. By comparison with the yield curve of MC criterion in the π-plane (see Figure 4), the DP criteria can be divided into Circumscribe Drucker–Prager (CDP) criterion, Middle Circumscribe Drucker–Prager (MDP) criterion, and Inscribe Drucker–Prager (IDP) criterion.

(i) When the yield curve of DP criterion is the circumcircle of MC criterion, the material parameters α and k for the CDP criterion can be obtained by [4, 28]
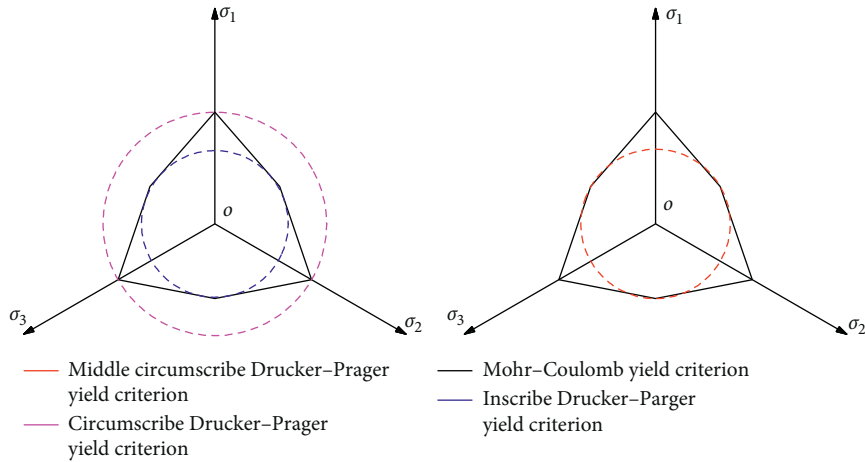
FIGURE 4: Drucker–Prager yield criterion curve in the π-plane.

$$\alpha = \frac{2\sin\varphi}{\sqrt{3}\,(3-\sin\varphi)},$$

$$k = \frac{6c\cos\varphi}{\sqrt{3}\,(3-\sin\varphi)}. \tag{27a}$$

(ii) When the yield curve of DP criterion is the inscribed circle of MC criterion, the solution of parameters α and k for the IDP criterion presented by Vekeens et al. [31] is

$$\alpha = \frac{\sin\varphi}{\sqrt{\left(9+3\sin^2\varphi\right)}},$$

$$k = \frac{\sqrt{3}c\cos\varphi}{\sqrt{\left(3+\sin^2\varphi\right)}}. \tag{27b}$$

(iii) When the yield curve of DP criterion is between CDP and IDP, the material parameters α and k for the MDP criterion are expressed as follows:

$$\alpha = \frac{2\sin\varphi}{\sqrt{3}\,(3+\sin\varphi)},$$

$$k = \frac{6c\cos\varphi}{\sqrt{3}\,(3+\sin\varphi)}. \tag{27c}$$

As shown in Sections 2.6 and 2.7, we take $\sigma_2 = ((\sigma_1 + \sigma_3)/2)$. Then, the Drucker–Prager criterion can be deduced by solving equation (26).

$$f(\sigma_1, \sigma_3) = \sigma_1 - \left(\frac{1+3\alpha}{1-3\alpha}\right)\sigma_3 - \left(\frac{2k}{1-3\alpha}\right) = 0. \tag{28}$$

2.8. Establishment of Unified Criterion Equation. As shown in Table 1, the unified equation of different yield criterion can be summarized based on the above analysis under plane strain conditions.

$$f(\sigma_1, \sigma_3) = (\sigma_1 - \xi_j)(\sigma_3 - Y_j) = 0, \tag{29}$$

where the subscript "j" represents different yield criteria and ξ_j and Y_j are the material constants of different criteria, which can be divided into two different cases. When $\xi_j = 1$, equation (29) corresponds to the TR and VM criteria; when $\xi_j \neq 1$, equation (29) represents other criteria. Therefore, it can be regarded as a unified criterion equation to research the mechanical response of rock mass.

3. Problem Description

3.1. Establishment of Calculating Model. Figure 5 shows that a circular opening is excavated in a finite, isotropic, homogeneous elastic-brittle plastic rock mass subjected to an inner pressure σ_0 at the inner radii R_0 and a hydrostatic pressure p_0 at the external radius R_2. As σ_0 gradually decreases, the displacement will occur and the plastic zone with the radii R_1 will firstly develop around the circular opening when the maximum principal stress and minimum principal stress satisfy the initial yield condition. The influence of the rock mass weight in the plastic zone on the radial displacement and inner pressure is ignored. In this paper, the brittle plastic rock mass is introduced to research the postpeak mechanical behavior of rock material. As shown in Figure 6, the strength of the rock mass suddenly drops after peak load and then the postpeak softening behavior of strength parameters will occur. In other words, the postpeak cohesion c_{res}, internal friction angle φ_{res}, Young's modulus E_{res}, and Poisson's ratio ν_{res} are used to solve the stress and displacement distributions in the plastic zone.

Under the axisymmetric plane strain conditions, when $p_0 > \sigma_0$, the hoop stress σ_θ and radial stress σ_r are, respectively, maximum principal stress and minimum principal stress; the tangential strain ε_θ and radial strain ε_r are, respectively, maximum principal strain and minimum principal strain. Accordingly, the unified criterion equation can be rewritten as follows:
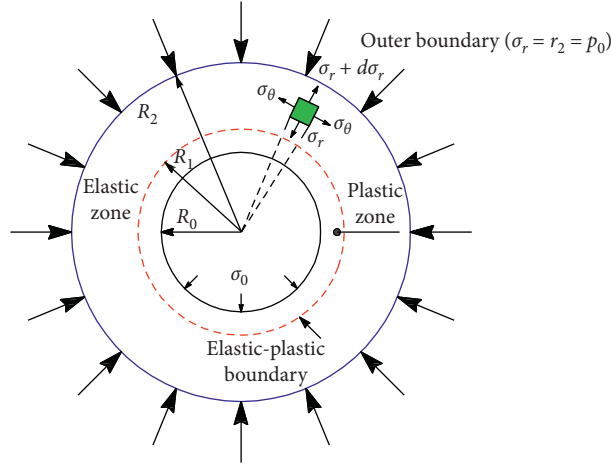
FIGURE 5: Calculation model of the circular opening with finite or infinite boundary.

(a)

(b)
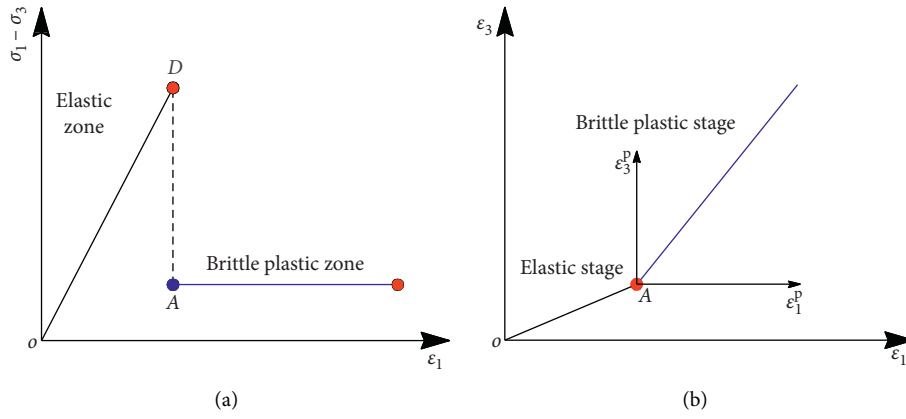
FIGURE 6: Postpeak failure behavior of brittle plastic rock mass.

$$\sigma_{\theta(i)} = \xi_j^{\text{ini}} \sigma_{r(i)} + Y_j^{\text{ini}} \text{ for peak stage,} \tag{30a}$$

$$\sigma_{\theta(i)} = \xi_j^{\text{res}} \sigma_{r(i)} + Y_j^{\text{res}} \text{ for postpeak stage,} \tag{30b}$$

where the subscript "i" represents different zones ($i = 1, 2$), ξ_j^{ini} and Y_j^{ini} are the initial strength parameters, respectively, and ξ_j^{res} and Y_j^{res} are the residual strength parameters, respectively.

3.2. Based Equation. For the axisymmetric plane strain problem, the equilibrium differential equation can be expressed as (ignoring the body force of rock masses) [29, 30, 39]

$$\left(\frac{d\sigma_{r(i)}}{dr} \right) + \left(\frac{\sigma_{r(i)} - \sigma_{\theta(i)}}{r} \right) = 0. \tag{31}$$

The geometric equation, based on the small deformation assumption, can be denoted as

$$\varepsilon_{r(i)} = \left(\frac{\partial u_{r(i)}}{\partial r} \right),$$

$$\varepsilon_{\theta(i)} = \left(\frac{u_{r(i)}}{r} \right), \tag{32}$$

where $u_{r(i)}$ is the radial displacement. Both the radial displacement u_{R_1} and radial contact stress σ_{R_1} should be continuous at the elastic-plastic interface, respectively. Therefore, the boundary conditions around the circular opening can be summarized as

$$\begin{cases} r = R_0, \sigma_{r(1)} = \sigma_0, \\ r = R_1, \sigma_{r(1)} = \sigma_{R_1}, u_{r(1)} = u_{R_1}, \\ r = R_2, \sigma_{r(2)} = p_0. \end{cases} \tag{33}$$

4. The New Unified Solution of Circular Opening

4.1. A Semianalytical Solution with the Finite External Boundary. According to the elastic mechanics theory, the stresses and displacement in the elastic zone can be deduced by regarding it as a hollow thick-wall cylinder subjected to an inner pressure σ_{R_1} at the internal boundary $r = R_1$ and a hydrostatic pressure p_0 at the external boundary $r = R_2$ as follows:

$$\sigma_{r(2)} = \frac{(R_2 R_1)^2 (\sigma_{R_1} - p_0)}{R_2^2 - R_1^2} \left(\frac{1}{r^2}\right) + \left(\frac{R_2^2 p_0 - R_1^2 \sigma_{R_1}}{R_2^2 - R_1^2}\right), \tag{34a}$$

$$\sigma_{\theta(2)} = -\frac{(R_2 R_1)^2 (\sigma_{R_1} - p_0)}{R_2^2 - R_1^2} \left(\frac{1}{r^2}\right) + \left(\frac{R_2^2 p_0 - R_1^2 \sigma_{R_1}}{R_2^2 - R_1^2}\right), \tag{34b}$$

$$u_{r(2)} = \left(\frac{1 - \nu - 2\nu^2}{E}\right)\left(\frac{R_2^2 p_0 - R_1^2 \sigma_{R_1}}{R_2^2 - R_1^2}\right) r$$
$$+ \left(\frac{1 + \nu}{E}\right)\frac{(R_2 R_1)^2 (p_0 - \sigma_{R_1})}{R_2^2 - R_1^2}\left(\frac{1}{r}\right), \tag{34c}$$

where E and ν are the initial Young's modulus and initial Poisson's ratio, respectively. The initial yield failure condition should be satisfied at the elastic-plastic interface. Therefore, the radial contact stress σ_{R_1} can be derived by substituting equations (34a) and (34b) into equation (30a) under different yield criteria:

$$\sigma_{R_1} = \frac{(2p_0 - Y_j^{\mathrm{ini}})R_2^2 + R_1^2 Y_j^{\mathrm{ini}}}{(1 + \xi_j^{\mathrm{ini}})R_2^2 + (1 - \xi_j^{\mathrm{ini}})R_1^2}. \tag{35}$$

Obviously, the stresses in the plastic zone should satisfy the equilibrium differential equation and are easily deduced by submitting equation (30b) into equation (31) as well as combining with the boundary condition $\sigma_{r(1)} = \sigma_0$ at $r = R_0$. However, for $\xi_j^{\mathrm{res}} = 1$ and $\xi_j^{\mathrm{res}} \neq 1$, the stress solutions in the plastic zone are inconsistent.

(i) f $\xi_j^{\mathrm{res}} \neq 1$, the unified stresses solution in the plastic zone will be obtained as

$$\sigma_{r(1)} = \left(\sigma_0 + \frac{Y_j^{\mathrm{res}}}{\xi_j^{\mathrm{res}} - 1}\right)\left(\frac{r}{R_0}\right)^{\xi_j^{\mathrm{res}} - 1} - \left(\frac{Y_j^{\mathrm{res}}}{\xi_j^{\mathrm{res}} - 1}\right), \tag{36a}$$

$$\sigma_{\theta(1)} = \xi_j^{\mathrm{res}}\left(\sigma_0 + \frac{Y_j^{\mathrm{res}}}{\xi_j^{\mathrm{res}} - 1}\right)\left(\frac{r}{R_0}\right)^{\xi_j^{\mathrm{res}} - 1} - \left(\frac{Y_j^{\mathrm{res}}}{\xi_j^{\mathrm{res}} - 1}\right). \tag{36b}$$

Here, the subscript "j" represents MC, GMC, GLD, GSMP, CDP, MDP, IDP, UST, and GTSS criteria.

Then, the radii of plastic zone can be determined by considering the boundary condition $\sigma_{r(1)} = \sigma_{R_1}$ at the elastic-plastic interface. By integrating equation (35) and equation (36a), the nonlinear function between R_1 and R_2 can be established as follows:

$$\left[(1 + \xi_j^{\mathrm{ini}})R_2^2 + (1 - \xi_j^{\mathrm{ini}})R_1^2\right]\left[\left(\sigma_0 + \frac{Y_j^{\mathrm{res}}}{\xi_j^{\mathrm{res}} - 1}\right)\right.$$
$$\left.\cdot \left(\frac{R_1}{R_0}\right)^{\xi_j^{\mathrm{res}} - 1} - \frac{Y_j^{\mathrm{res}}}{\xi_j^{\mathrm{res}} - 1}\right] = (2p_0 - Y_j^{\mathrm{ini}})R_2^2 + R_1^2 Y_j^{\mathrm{ini}}. \tag{37}$$

(ii) If $\xi_j^{\mathrm{res}} = 1$, the unified stress solutions of plastic zone based on the TR and VM criteria are

$$\sigma_{r(1)} = \sigma_0 + Y_j^{\mathrm{res}} \ln\left(\frac{r}{R_0}\right), \tag{38a}$$

$$\sigma_{\theta(1)} = \sigma_0 + Y_j^{\mathrm{res}}\left[1 + \ln\left(\frac{r}{R_0}\right)\right]. \tag{38b}$$

As the solution for equation (41), the nonlinear function between R_1 and R_2 based on the VM and TR criterion can be also deduced as follows:

$$\left[(1 + \xi_j^{\mathrm{ini}})R_2^2 + (1 - \xi_j^{\mathrm{ini}})R_1^2\right]\left[\sigma_0 + Y_j^{\mathrm{res}} \ln\left(\frac{R_1}{R_0}\right)\right]$$
$$= (2p_0 - Y_j^{\mathrm{ini}})R_2^2 + R_1^2 Y_j^{\mathrm{ini}}. \tag{39}$$

In practice, the external radius R_2 is a constant. The approximate solution for R_1 in equations (37) and (39) can be obtained by using the numerical calculation methods such as the least square method and Newton iteration method. Then, the stresses and displacement in elastic zone can be determined by equations (34a), (34b), and (34c).

In the plastic zone, the total hoop strain $\varepsilon_{\theta(1)}$ and radial strain $\varepsilon_{r(1)}$ are, respectively, composed of elastic strain and plastic strain. Therefore, the total strain can be expressed as

$$\begin{cases} \varepsilon_{\theta(1)} = \varepsilon_{\theta(1)}^e + \varepsilon_{\theta(1)}^p, \\ \varepsilon_{r(1)} = \varepsilon_{r(1)}^e + \varepsilon_{r(1)}^p, \end{cases} \tag{40}$$

where $\varepsilon_{\theta(1)}^e$ and $\varepsilon_{r(1)}^e$ are, respectively, the hoop elastic strain and radial elastic strain in the plastic zone; $\varepsilon_{\theta(1)}^p$ and $\varepsilon_{r(1)}^p$ are the hoop plastic strain and radial plastic strain of plastic zone, respectively.

For axisymmetric plane strain problems, the plastic strain relationships can be established by considering the small strain theory and nonassociated flow rule [5, 9].

$$\varepsilon_{r(1)}^p + \beta \varepsilon_{\theta(1)}^p = 0, \tag{41}$$

where β is the dilation coefficient: $\beta = (1 + \sin\psi)/(1 - \sin\psi)$. ψ is the dilation angle.

By substituting equations (32) and (41) into equation (44), the following differential equation for the radial displacement in the plastic zone can be derived as

$$\left(\frac{\partial u_{r(1)}}{\partial r}\right) + \beta\left(\frac{u_{r(1)}}{r}\right) = \varepsilon^e_{r(1)} + \beta\varepsilon^e_{\theta(1)} = f(r). \tag{42}$$

From equation (42), it can be seen that the radial displacement is closely related to the elastic strain form in the plastic zone.

Then, the following function can be obtained by solving equation (42) as follows:

$$u_{r(1)} = \frac{1}{r^\beta}\int_{R_1}^r f(r)r^\beta dr + u_{R_1}\left(\frac{R_1}{r}\right)^\beta, \tag{43}$$

where u_{R_1} is the radial displacement at the elastic-plastic interface. It can be easily determined by taking $r = R_1$ in equation (34c) as follows:

$$u_{R_1} = \left(\frac{1 - \nu - 2\nu^2}{E}\right)\left(\frac{R_2^2 p_0 - R_1^2 \sigma_{R_1}}{R_2^2 - R_1^2}\right)R_1$$

$$+ \left(\frac{1+\nu}{E}\right)\left(\frac{R_2^2 R_1\left(p_0 - \sigma_{R_1}\right)}{R_2^2 - R_1^2}\right). \tag{44}$$

In order to obtain the radial displacement of plastic zone, the expression for elastic strain should be firstly determined. Generally, four different definitions for elastic strain can be used to research the deformation behavior of rock mass in the plastic zone.

(1) Case 1: it is assumed that the elastic strain in the plastic region is equal to that on the elastic-plastic interface. Then, the elastic strains can be expressed as [36]

$$\begin{cases} \varepsilon^e_{\theta(1)} = \left(\frac{u_{r(2)}}{r}\right)_{r=R_1} = \left(\frac{1 - \nu - 2\nu^2}{E}\right)\left(\frac{R_2^2 p_0 - R_1^2 \sigma_{R_1}}{R_2^2 - R_1^2}\right) + \left(\frac{1+\nu}{E}\right)\left(\frac{R_2^2\left(p_0 - \sigma_{R_1}\right)}{R_2^2 - R_1^2}\right). \\ \\ \varepsilon^e_{r(1)} = \left(\frac{\partial u_{r(2)}}{\partial r}\right)_{r=R_1} = \left(\frac{1 - \nu - 2\nu^2}{E}\right)\left(\frac{R_2^2 p_0 - R_1^2 \sigma_{R_1}}{R_2^2 - R_1^2}\right) - \left(\frac{1+\nu}{E}\right)\left(\frac{R_2^2\left(p_0 - \sigma_{R_1}\right)}{R_2^2 - R_1^2}\right). \end{cases} \tag{45}$$

Then, the function $f(r)$ is

$$f(r) = \left(\frac{\left(1 - \nu - 2\nu^2\right)(1+\beta)}{E}\right)\left(\frac{R_2^2 p_0 - R_1^2 \sigma_{R_1}}{R_2^2 - R_1^2}\right)$$

$$- \left(\frac{(1+\nu)(1-\beta)}{E}\right)\left(\frac{R_2^2\left(p_0 - \sigma_{R_1}\right)}{R_2^2 - R_1^2}\right) = \delta_{\text{case1}}. \tag{46}$$

By substituting equation (46) into equation (43), the radial displacement in the plastic zone can be derived as follows:

$$u^{\text{case1}}_{r(1)} = \left(\frac{\delta_{\text{case1}}}{(1+\beta)}\right)\left(\frac{r^{\beta+1} - R_1^{\beta+1}}{r^\beta}\right) + u_{R_1}\left(\frac{R_1}{r}\right)^\beta. \tag{47}$$

(2) Case 2: by regarding the plastic zone as the thick-wall cylinder subjected to the inner pressure σ_0 at $r = R_0$ and radial contact stress σ_{R_1} at $r = R_0$, the elastic strain in the plastic zone can be written as [19, 39]

$$\begin{cases} \varepsilon^e_{\theta(1)} = \frac{1 + \nu_{\text{res}}}{E_{\text{res}}}\left[(1 - 2\nu_{\text{res}})C_1 - \left(\frac{C_2}{r^2}\right)\right], \\ \\ \varepsilon^e_{r(1)} = \left(\frac{1 + \nu_{\text{res}}}{E_{\text{res}}}\right)\left[(1 - 2\nu_{\text{res}})C_1 + \frac{C_2}{r^2}\right], \end{cases} \tag{48}$$

where $C_1 = ((\sigma_{R_1} - p_0)R_1^2 - (\sigma_0 - p_0)R_0^2/R_1^2 - R_0^2)$ and $C_2 = (R_1^2 R_0^2(\sigma_0 - \sigma_{R_1})/R_1^2 - R_0^2)$. Therefore, the function $f(r)$ is

$$f(r) = \left(\frac{1 + \nu_{\text{res}}}{E_{\text{res}}}\right)\left[(1+\beta)(1 - 2\nu_{\text{res}})C_1 + (1-\beta)\frac{C_2}{r^2}\right],$$

$$= \delta_1^{\text{Case2}}(1+\beta) + \delta_2^{\text{Case2}}(1-\beta)r^{-2}, \tag{49}$$

where $\delta_1^{\text{Case2}} = (1 + \nu_{\text{res}}/E_{\text{res}})(1 - 2\nu_{\text{res}})C_1$ and $\delta_2^{\text{Case2}} = (1 + \nu_{\text{res}}/E_{\text{res}})C_2$.

By submitting equation (49) into equation (43), we can obtain the radial displacement of plastic zone as follows:

$$u_{r(1)}^{\text{case2}} = \left(\frac{1}{r^\beta}\right)\left[\delta_1^{\text{Case2}}\left(r^{\beta+1} - R_1^{\beta+1}\right) - \delta_2^{\text{Case2}}\left(r^{\beta-1} - R_1^{\beta-1}\right)\right]$$
$$+ u_{R_1}\left(\frac{R_1}{r}\right)^\beta. \tag{50}$$

(3) Case 3: adopting Hooke's law, the elastic strains in the plastic zone can be written as follows [27]:

$$\begin{cases} \varepsilon_{\theta(1)}^e = \dfrac{(1 + \nu_{\text{res}})}{E_{\text{res}}}\left[(1 - \nu_{res})\sigma_{\theta(1)} - \nu_{\text{res}}\sigma_{r(1)}\right]. \\[2mm] \varepsilon_{r(1)}^e = \dfrac{(1 + \nu_{\text{res}})}{E_{\text{res}}}\left[(1 - \nu_{res})\sigma_{r(1)} - \nu_{\text{res}}\sigma_{\theta(1)}\right]. \end{cases} \tag{51}$$

Then, the function $f(r)$ can be expressed as follows:

$$f(r) = \frac{1 + \nu_{\text{res}}}{E_{\text{res}}}\left[(1 - \nu_{\text{res}} - \beta\nu_{\text{res}})\sigma_{r(1)} \right.$$
$$\left. + (\beta - \nu_{\text{res}} - \beta\nu_{\text{res}})\sigma_{\theta(1)}\right]. \tag{52}$$

(i) If $\xi_j^{\text{res}} \neq 1$, the function $f(r)$ will be rewritten by substituting equations (36a) and (36b) into equation (52) as follows:

$$f(r) = \left(\frac{1 + \nu_{\text{res}}}{E_{\text{res}}}\right)\left[\delta_1^{\text{case3}}\left(\frac{r}{R_0}\right)^{\xi_j^{\text{res}}-1} - \delta_2^{\text{case3}}\right], \tag{53}$$

where $\delta_1^{\text{case3}} = (\sigma_0 + (Y_j^{\text{res}}/\xi_j^{\text{res}} - 1))[1 + \beta\xi_j^{\text{res}} - (1 + \xi_j^{\text{res}})(\nu_{\text{res}} + \beta\nu_{\text{res}})]$ and $\delta_2^{\text{case3}} = (1 - 2\nu_{\text{res}})(1 + \beta)(Y_j^{\text{res}}/\xi_j^{\text{res}} - 1)$.

By substituting equation (53) into equation (43), the radial displacement in the plastic zone can be derived as follows:

$$u_{r(1)}^{\text{case3}} = \left(\frac{1 + \nu_{\text{res}}}{E_{\text{res}}}\right)\left(\frac{1}{r^\beta}\right)\left[\frac{\delta_1^{\text{case3}}}{\left(\xi_j^{\text{res}} + \beta\right)R_0^{\xi_j^{\text{res}}-1}}\left(r^{\xi_j^{\text{res}}+\beta} - R_1^{\xi_j^{\text{res}}+\beta}\right)\right.$$
$$\left. - \frac{\delta_2^{\text{case3}}}{(1 + \beta)}\left(r^{1+\beta} - R_1^{1+\beta}\right)\right] + u_{R_1}\left(\frac{R_1}{r}\right)^\beta. \tag{54}$$

(ii) If $\xi_j^{\text{res}} = 1$, the function $f(r)$ can be obtained by substituting equations (38a) and (38b) into equation (52) as follows:

$$f(r) = \left(\frac{1 + \nu_{\text{res}}}{E_{\text{res}}}\right)\left[\delta_3^{\text{case3}}\ln\left(\frac{r}{R_0}\right) + \delta_4^{\text{case3}}\right], \tag{55}$$

where $\delta_3^{\text{case3}} = (1 - 2\nu_{\text{res}})(1 + \beta)Y_j^{\text{res}}$ and $\delta_4^{\text{case3}} = (1 - \nu_{\text{res}} - \beta\nu_{\text{res}})\sigma_0 + (\beta - \nu_{\text{res}} - \beta\nu_{\text{res}})(\sigma_0 + Y_j^{\text{res}})$.

By submitting equation (55) to equation (43), the radial displacements for TR and VM criterion in the plastic zone are

$$u_{r(1)}^{\text{case3}} = \left(\frac{1 + \nu_{\text{res}}}{E_{\text{res}}}\right)\left(\frac{1}{r^\beta}\right)\left\{\frac{\delta_3^{\text{case3}}}{1 + \beta}\left[r^{1+\beta}\ln\left(\frac{r}{R_0}\right) - R_1^{1+\beta}\ln\left(\frac{R_1}{R_0}\right)\right]\right.$$
$$\left. + \left[\frac{\delta_4^{\text{case3}}}{1 + \beta} - \frac{\delta_3^{\text{case3}}}{(1 + \beta)^2}\right]\left(r^{1+\beta} - R_1^{1+\beta}\right)\right\} + u_{R_1}\left(\frac{R_1}{r}\right)^\beta. \tag{56}$$

(4) Case 4: the mechanical behavior of rock mass is closely related to its damage degree in the plastic zone. The higher damage usually leads to larger deformation behavior. Then, the attenuation of Young's modulus should be considered in the plastic zone. In this case, the power function attenuation model of Young's modulus along the radius direction is introduced to research the deformation behavior in the plastic zone [6]:

$$E(r) = E_{\text{res}}\left(\frac{r}{R_0}\right)^m.$$
$$m = \frac{\log(E/E_{\text{res}})}{\log(R_1/R_0)}. \tag{57}$$

(i) If $\xi_j^{\text{res}} \neq 1$, the function $f(r)$ will be rewritten by substituting equation (57) into equation (53) as follows:

$$f(r) = \left(\frac{1 + \nu_{\text{res}}}{E_{\text{res}}}\right)\left(\frac{R_0}{r}\right)^m\left[\delta_1^{\text{case3}}\left(\frac{r}{R_0}\right)^{\xi_j^{\text{res}}-1} - \delta_2^{\text{case3}}\right]. \tag{58}$$

By substituting equation (58) into equation (43), the radial displacement in the plastic zone can be derived. In fact, the expression form is the same as that in equation (54):

$$u_{r(1)}^{\text{case3}} = \left(\frac{1 + \nu_{\text{res}}}{E_{\text{res}}}\right)\frac{1}{r^\beta}\left[\left(\frac{\delta_1^{\text{case3}}}{\left(\xi_j^{\text{res}} + \beta - m\right)R_0^{\xi_j^{\text{res}}-m-1}}\right)\right.$$
$$\cdot\left(r^{\xi_j^{\text{res}}+\beta-m} - R_1^{\xi_j^{\text{res}}+\beta-m}\right) - \left(\frac{\delta_2^{\text{case3}}}{(1 + \beta - m)R_0^{-m}}\right)$$
$$\left.\cdot\left(r^{1+\beta-m} - R_1^{1+\beta-m}\right)\right] + u_{R_1}\left(\frac{R_1}{r}\right)^\beta. \tag{59}$$

(ii) If $\xi_j^{\text{res}} = 1$, the function $f(r)$ can be obtained by substituting equation (57) into equation (55) as follows:

$$f(r) = \left(\frac{1 + \nu_{\text{res}}}{E_{\text{res}}}\right)\left(\frac{R_0}{r}\right)^m\left[\delta_3^{\text{case3}}\ln\left(\frac{r}{R_0}\right) + \delta_4^{\text{case3}}\right]. \tag{60}$$

By introducing equation (60) to equation (43), the expression form for radial displacement is similar to equation (56):

$$
\begin{aligned}
u_{r(1)}^{\text{case3}} =& \left(\frac{1+\nu_{\text{res}}}{E_{\text{res}}}\right)\frac{1}{r^\beta}\left\{\frac{\delta_3^{\text{case3}}R_0^m}{1+\beta-m}\left[r^{1+\beta-m}\ln\left(\frac{r}{R_0}\right)\right.\right. \\
&\left.- R_1^{1+\beta-m}\ln\left(\frac{R_1}{R_0}\right)\right] + \left[\frac{\delta_4^{\text{case3}}}{1+\beta-m} - \frac{\delta_3^{\text{case3}}}{(1+\beta-m)^2}\right] \\
&\left.\cdot R_0^m\left(r^{1+\beta-m}-R_1^{1+\beta-m}\right)\right\} + u_{R_1}\left(\frac{R_1}{r}\right)^\beta.
\end{aligned}
$$
(61)

4.2. The Closed-Form Solution with the Infinite External Boundary.

For the deep underground engineering, a circular opening subjected to an inner support pressure σ_0 at $r = R_0$ and hydrostatic pressure p_0 at infinite external boundary is a special case of the axisymmetric thick-wall cylinder. The stress and displacement solutions can be obtained through the same solving process as that in Section 4.1. When $R_2 \longrightarrow \infty$, the stresses in the elastic zone can be easily deduced by equations (34a) and (34b) as follows:

$$
\sigma_{r(2)} = p_0 - \left(p_0 - \sigma_{R_1}\right)\left(\frac{R_1}{r}\right)^2,
$$
(62a)

$$
\sigma_{\theta(2)} = p_0 + \left(p_0 - \sigma_{R_1}\right)\left(\frac{R_1}{r}\right)^2.
$$
(62b)

Accordingly, the stress distribution for deep circular opening in the plastic zone can be also calculated by equations (36a) and (36b) for $\xi_j^{\text{res}} \neq 1$ or equations (38a) and (38b) for $\xi_j^{\text{res}} = 1$. In addition, the unified radial contact stress σ_{R_1} for different criteria can be rewritten by taking $R_2 \longrightarrow \infty$ in equation (35) as follows:

$$
\sigma_{R_1} = \frac{\left(2p_0 - Y_j^{\text{ini}}\right)}{\left(1 + \xi_j^{\text{ini}}\right)}.
$$
(63)

As shown in equation (37), if $\xi_j^{\text{res}} \neq 1$, the radius of plastic zone for deep circular opening can be easily deduced as follows:

$$
R_1 = R_0 \sqrt[\xi_j^{\text{res}}]{\frac{\left(\left(2p_0 - Y_j^{\text{ini}}\right)/\left(1+\xi_j^{\text{ini}}\right)\right) + \left(Y_j^{\text{res}}/\left(\xi_j^{\text{res}}-1\right)\right)}{\left(\sigma_0 + Y_j^{\text{res}}/\left(\xi_j^{\text{res}}-1\right)\right)}}.
$$
(64a)

As shown in equation (39), if $\xi_j^{\text{res}} = 1$, the unified radius solution of plastic zone based on TR and VM criteria is

$$
R_1 = R_0 e^{\frac{\left(2p_0 - Y_j^{\text{ini}}\right)/\left(1+\xi_j^{\text{ini}}\right)-\sigma_0}{Y_j^{\text{res}}}}.
$$
(64b)

For the deep underground engineering, the real displacement far away from the tunnel surface is almost zero after the tunnel excavation. Hence, the initial displacement

values, that is, $\left((1 - \nu - 2\nu^2)p_0 r/E\right)$, caused by the hydrostatic pressure should be ignored at the infinite boundary $(R_2 \longrightarrow \infty)$. Therefore, the radial displacement caused by tunnel excavation in the elastic zone should be rewritten as follows:

$$
u_{r(2)} = \frac{(1+\nu)\left(p_0 - \sigma_{R_1}\right)}{E}\left(\frac{R_1^2}{r}\right).
$$
(65)

The radial displacement at the elastic-plastic interface can be determined by equations (64a) and (64b) as follows:

$$
u_{R_1} = \frac{(1+\nu)\left(p_0 - \sigma_{R_1}\right)}{E}R_1.
$$
(66)

Just as the calculation method of radial displacement in Section 4.2, four different assumptions about the elastic strain forms are also used to research the deformation behavior of rock mass in the plastic zone.

(1) Case 1: with the assumption of the constant elastic strain at the elastic-plastic interface, as the calculation methods in equations (45) and (46), the function $f(r)$ can be easily deduced by integrating equations (65) and (32) as follows:

$$
f(r) = -\frac{(1+\nu)(1-\beta)}{E}\left(p_0 - \sigma_{R_1}\right) = \delta_{\text{case1}}.
$$
(67)

Then, the radial displacement of plastic zone for deep circular opening will be obtained by introducing equations (67) and (66) into equation (43). The expression form is consistent with equation (47) except for the parameters δ_{case1} (taking equation (67)) and u_{R_1}(taking equation (66)).

(2) Case 2: as shown in equations (49) and (50), the radial displacement for deep circular opening can be also obtained by regarding the plastic zone as the thick-wall cylinder. The expression is the same as that in equation (50) except for u_{R_1} (equation (66)) and σ_{R_1} (equation (63)).

(3) Case 3: by adopting generalized Hooke's law for removing the effect of initial hydrostatic pressure p_0, the elastic strain in the plastic zone can be expressed as follows:

$$
\begin{cases}
\varepsilon_{\theta(1)}^e = \frac{(1+\nu_{\text{res}})}{E_{\text{res}}}\left[(1-\nu_{\text{res}})\left(\sigma_{\theta(1)} - p_0\right) - \nu_{\text{res}}\left(\sigma_{r(1)} - p_0\right)\right]. \\
\varepsilon_{r(1)}^e = \frac{(1+\nu_{\text{res}})}{E_{\text{res}}}\left[(1-\nu_{\text{res}})\left(\sigma_{r(1)} - p_0\right) - \nu_{\text{res}}\left(\sigma_{\theta(1)} - p_0\right)\right].
\end{cases}
$$
(68)

Then, the function $f(r)$ can be expressed as follows:

$$
\begin{aligned}
f(r) =& \left(\frac{1+\nu_{\text{res}}}{E_{\text{res}}}\right)\left[(1-\nu_{\text{res}} - \beta\nu_{\text{res}})\sigma_{r(1)}\right. \\
&\left.+ (\beta - \nu_{\text{res}} - \beta\nu_{\text{res}})\sigma_{\theta(1)} + (2\nu_{\text{res}} - 1)(1+\beta)p_0\right].
\end{aligned}
$$
(69)

(i) If $\xi_j^{\text{res}} \neq 1$, the radial displacement for deep circular opening can be deduced by calculation methods similar to those discussed in Section 4.1. Its expression is the same as that in equation (54), but the constant δ_2^{case3} in equation (54) needs to be replaced by

$$\delta_{22}^{\text{case3}} = (1 - 2\nu_{\text{res}})(1 + \beta)\left[\frac{p_0 - Y_j^{\text{res}}}{\left(\xi_j^{\text{res}} - 1\right)}\right]. \quad (70)$$

(ii) If $\xi_j^{\text{res}} = 1$, the radial displacement for TR and VM criteria can be also obtained by substituting equations (38a), (38b), and (69) into equation (43). The expression is in accordance with equation (56); after that the constant δ_4^{case3} in equation (56) is replaced by

$$\delta_{44}^{\text{case3}} = (1 - \nu_{\text{res}} - \beta\nu_{\text{res}})\sigma_0 + (\beta - \nu_{\text{res}} - \beta\nu_{\text{res}})\left(\sigma_0 + Y_j^{\text{res}}\right) \\ + (2\nu_{\text{res}} - 1)(1 + \beta)p_0. \quad (71)$$

(4) Case 4: in this case, the influence of rock mass damage degree on the mechanical and deformation behavior of surrounding rock is taken into account by assuming Young's modulus attenuation along the radius direction. As discussed in Section 4.1, for $\xi_j^{\text{res}} \neq 1$, the radial displacement for deep circular opening in the plastic zone can be determined through the constant δ_2^{case3} in equation (59) replaced by the value $\delta_{22}^{\text{case3}}$ in equation (70). In addition, for $\xi_j^{\text{res}} = 1$, the radial displacement based on TR and VM criteria will be calculated by the constant δ_4^{case3} in equation (61) replaced by the value $\delta_{44}^{\text{case3}}$ in equation (71).

5. The Theoretical and Practical Value

The new unified closed-form solution obtained in Section 4.1 with a finite boundary can be regarded as a semianalytical solution due to solving equations (37) and (39) by a numerical calculation. In addition, the new closed-form solution for a deep circular opening in Section 4.2 with an infinite boundary is a true analytical solution. The new closed-form solution with the infinite and finite external boundary can be used to predict the stress and displacement of circular opening excavated in an elastic-brittle plastic rock mass under different yield criteria. Actually, the circular opening maybe includes a borehole, vertical shaft, and deep- or shallow-buried tunnel. In addition, the new unified solution proposed in this paper is a series of traditional solutions rather than one specific solution. The solution based on the MC, GMC, TR, VM, GLD, GSMP, DP (CDP, MDP, and IDP), UST, and GTSS yield criteria can be obtained from the new unified solution by making ξ_j and Y_j take different parameters (as shown in Table 1). Therefore, the new unified solution has a broader engineering application scope and can be more appropriate for different lithology rock masses.

Zhang et al. [6], Park and Kim [9], and Chen et al. [17] carried out relevant theoretical research on the new closed-form solution of circular opening as discussed in Sections 4.1 and 4.2. However, the solution by Zhang et al. was based on the unified strength theory and ignored the influence of the other criteria on the mechanical response of rock mass. Hence, the application of this solution has some limitations for different lithology rock masses. Chen's solution, based on the elastic, perfectly plastic model and Mohr-Coulomb criterion, did not reflect the effect of internal principal stress and strength parameter attenuation. In addition, Park and Kim [9] analyzed the deformation law of plastic zone by using three different definitions for elastic strains in the plastic zone with Mohr-Coulomb (MC) and Hoke-Brown (HB) criteria. However, the solution based on the finite external boundary was not given. For the shallow-buried tunnel, it may not be reasonable to regard the outer boundary of circular tunnel as the infinite boundary. Moreover, the internal principal stress and Young's modulus attenuation are also ignored in this paper. When j = UST, the new unified solution proposed by this paper will be converted to the results by Zhang et al. [6] except for Case 1 and Case 2. When j = MC $\nu_{\text{res}} = \nu$, $c_{\text{res}} = c$, $\varphi_{\text{res}} = \varphi$, and $E_{\text{res}} = E$, the solution based on this paper will be transformed into the solution by Chen et al. [17]. Meanwhile, Park and Kim's solution based on MC criterion is a special case in Section 4.2 of this paper except for Case 4. Therefore, the new unified closed-form solution obtained in this paper is a series of results, and it is suitable for a wide range of rock masses and engineering backgrounds. Meanwhile, it can provide a broader yield criterion for the engineering application as well.

6. Correctness Verification and Parameter Analysis

6.1. A Comparison with the Traditional Solution. Park et al. summarized three different definitions for elastic strains in the plastic zone (see Cases 1~3 in Section 4.2) and analyzed the deformation law of plastic zone with Mohr-Coulomb criterion [9]. However, the Young's modulus and Poisson's ratio attenuation were ignored. In fact, it can be obtained by taking $E_{\text{res}} = E$, $\nu_{\text{res}} = \nu$, $\xi_j = \xi_{\text{MC}}$, and $Y_j = Y_{\text{MC}}$ in this paper. To further verify the correctness of the calculation results for deep circular opening in Section 4.2, the solution by Park et al. will be presented as a comparison with the solution proposed by this paper. The geometrical and physical parameters for circular opening are shown in Table 2.

The radial displacements obtained by Park are shown in Figure 7 in this paper. It can be seen that the calculation results in this paper are in accordance with Park's closed-form solution. Therefore, the closed-form solution proposed by this paper is correct and can be regarded as an extension of Park's solution. In other words, this paper's solution has a more wide application in practice engineering.

TABLE 2: Geometrical and physical parameters of circular opening.

Parameters	Rock type by Park and Kim (2006) [10]	
	Hard rock	Soft rock
Radius of opening, R_0 (m)	1	1
Initial stress, σ_0 (MPa)	1	1
Internal pressure, p_{in} (MPa)	0	0
Young's modulus, E (MPa)	50,000	5000
Poisson's ratio, ν	0.2	0.2
Shear modulus, G (MPa)	20833	2083
c (MPa)	0.173	0.276
φ (deg)	55	35
c_{res} (MPa)	0.061	0.055
φ_{res} (deg)	52	30

(a)

(b)

(c)

(d)
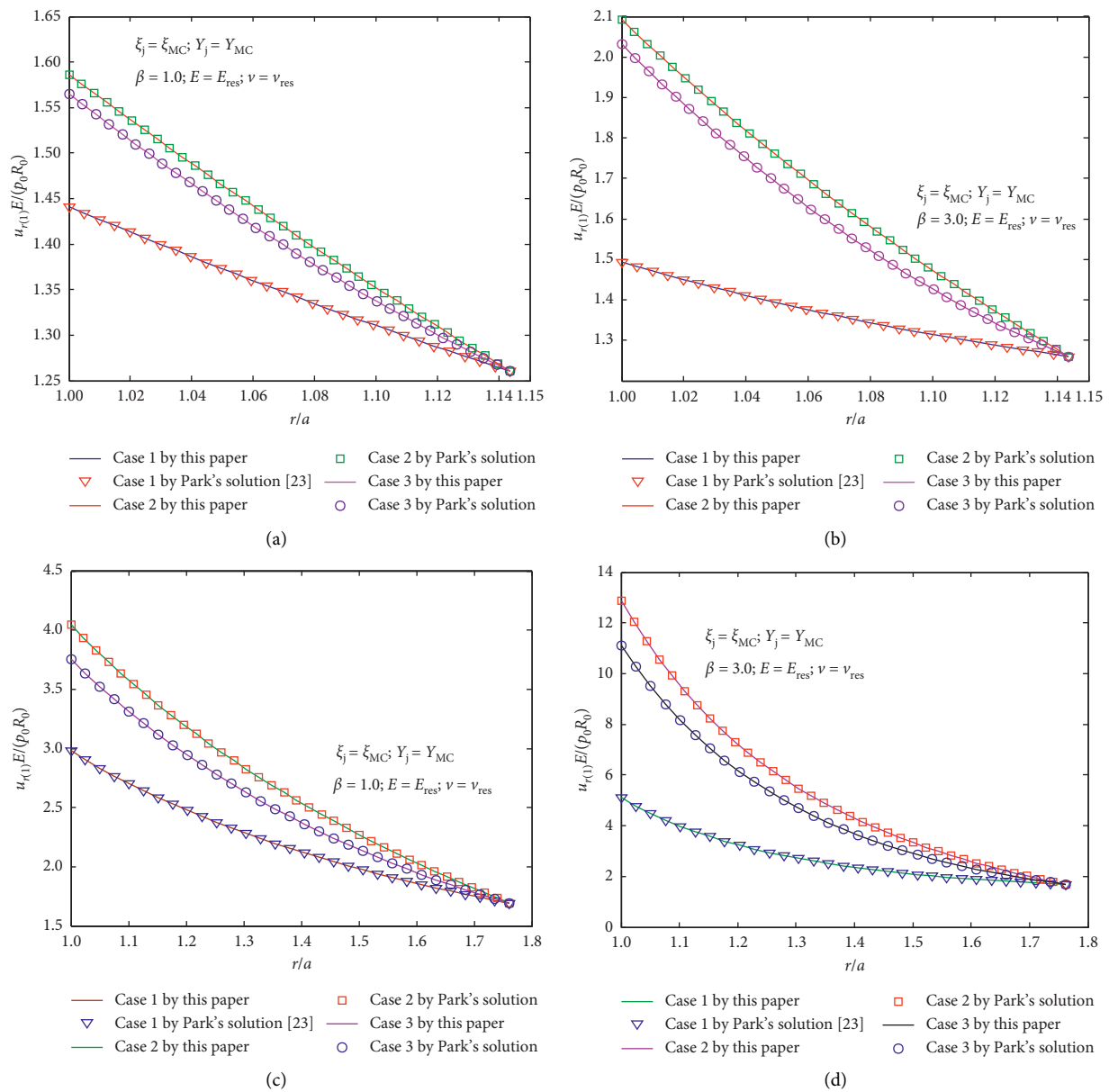
FIGURE 7: Comparison with the traditional solution. (a) Radial displacement (data: hard rock, $\beta = 1.0$). (b) Radial displacement (data: hard rock, $\beta = 3.0$). (c) Radial displacement (data: soft rock, $\beta = 1.0$). (d) Radial displacement (data: soft rock, $\beta = 3.0$).

6.2. Parameters Analysis

6.2.1. The Effect of the Strength Yield Criteria.
As previously mentioned, the strength criteria exert an extremely important effect for evaluating the mechanical response and deformation behavior of surrounding rock. For studying the influence of strength theories on the stresses and displacement of surrounding rock, the mechanical and geometrical parameters of circular tunnel are shown in Table 3.

The stresses distribution laws under different strength criteria are shown in Figure 8. Meanwhile, the dimensionless radius of plastic zone and critical inner pressure at the elastic-plastic interface are presented in Table 4. It can be seen that the dimensionless values ((R_1/R_0) and (σ_{R_1}/p_0)) show the characteristics of $TR > VM > IDP > MC > MDP > UST0.5 > GSMP > GMC > GLD > GTSS > CDP$. Compared with the traditional solution obtained by MC criterion, the dimensionless value ((R_1/R_0)) calculated by TR and VM criteria obviously increases by 125.26% and 78.53%, respectively. This is mainly because the TR and VM criteria only regard the rock mass as friction-less bonding material and ignore the impact of friction effect on the mechanical properties of the rock mass so that the bearing capacity of rock mass is underestimated. Therefore, the calculation result is obviously larger than the solution obtained by other criteria. The MC criterion does not take the effect of the intermediate principal stress into account and it is easy to underestimate the bearing capacity of rock mass. Therefore, the deformation of surrounding rock calculated by MC criterion may be slightly larger. The IDP and MDP criteria underestimate the influence of internal principal stresses, so the calculation results may also be larger than the solution obtained by UST0.5, GSMP, GMC, GLD, CDP, and GTSS criteria. Meanwhile, the result obtained by CDP criterion is minimal compared with other criteria's solutions. In fact, the criterion overestimates the effect of intermediate principal stresses on rock mass strength and may not be reasonable in practical engineering. In addition, the calculation results ((R_1/R_0)) obtained by UST0.5, GSMP, GMC, and GLD criteria are close to each other within the range of 1.294–1.347. The above four criteria seem to be more reasonable considering the effect of intermediate principal stress on yield strength of rock masses.

From the above analysis, it can be seen that the UST0.5, GSMP, GMC, and GLD criteria can be strongly recommended for evaluating the mechanics and deformation behavior of surrounding rock, followed by IDP, MDP, GTSS, and MC criteria. The TR, VM, and CDP criteria are not recommended to be used for underground engineering.

6.2.2. The Effect of Dilation Coefficient.
As shown in Figure 9, the dilation coefficient has an extremely important influence on the surface displacement of surrounding rock. As the parameter β gradually increases, the dimensionless surface displacement ($u_0E/(p_0R_0)$) presents the nonlinear increase characteristics. However, the increasing rate of surface displacement under different yield criteria is significantly different. For instance, as shown in Table 5, β increases from 1.0 to 3.0, and the dimensionless value

($u_0E/(p_0R_0)$), respectively, increases by 38.12% for MC criterion, 16.94% for GSMP criterion, 18.30% for UST0.5 criterion, and 29.58% for MDP criterion under Case 1 condition. Therefore, the effect of dilation coefficient should be considered in the design of tunnel support parameters and strength.

6.2.3. The Effect of Elastic Strain Form and Rock Mass Damage.
In this study, the geometrical and mechanical parameters of circular tunnel are shown in Table 3 (soft rock). Figure 10 presents the influence of elastic strain form in the plastic zone on the surface displacement of surrounding rock. From the above analysis, the relevant conclusions can be summarized as follows:

(i) The radial displacement of plastic zone is closely related to the selection of the elastic strain form. Case 2 has the greatest effect on the radial displacement of plastic zone, followed by Case 3. Then, the results obtained by Case 2 are minimal. For example, when $r = R_0$ (tunnel surface), compared with Case 1, the dimensionless surface displacement ($u_0E/(p_0R_0)$), respectively, increases by 0.272 for Case 2 and 0.206 for Case 3 with an increasing rate of 16.47% for Case 2 and 12.46% for Case 3 under GLD criterion.

(ii) Meanwhile, the influence of elastic strain form on the radial displacement of plastic zone is also closely related to the strength criterion. For example, the dimensionless surface displacements $u_0E/(p_0R_0)$ are, respectively, 1.926 for Case 2 and 1.860 for Case 3 under GLD criterion. However, the value significantly increases by 18.32% for Case 2 and 31.71% for Case 3 under GTSS criterion.

When the rock mass enters the plastic zone, its mechanical and deformation behavior are closely related to the rock damage degree. Generally, Young's modulus attenuation could be used to indicate the damage degree of rock mass. The influence of rock mass damage degree on the surface displacement of surrounding rock is shown in Figure 11.

(iii) It can be seen that the radial displacement of plastic zone is closely related to the selection of Young's modulus attenuation model. Compared with Case 3 ($E_{res} = E$), Case 4 has the greatest effect on the radial displacement of plastic zone. Case 3 ($E_{res} = 0.65E$) is the second. For example, as shown in Table 6, compared with Case 3 ($E_{res} = E$), the dimensionless surface displacements ($u_0E/(p_0R_0)$) of Case 3 ($E_{res} = 0.65E$) and Case 4 increase by 0.163 and 0.074 with an increasing rate of 7.49% and 3.40%, respectively, under the GTSS criterion.

(iv) In addition, the influence of Young's modulus attenuation on the radial displacement of plastic zone is closely related to the strength criterion. For Case 3 ($E_{res} = 0.65E$) and Case 4, the dimensionless surface displacements ($u_0E/(p_0R_0)$) of surrounding rock are 1.971 and 1.911, respectively, under the

TABLE 3: The mechanical and geometrical parameters of circular opening.

p_0 (MPa)	σ_0 (MPa)	R_0 (m)	$E_{res} = E$ (GPa)	$\nu_{res} = \nu$	$c_{res} = c$ (MPa)	$\varphi_{res} = \varphi$ (°)	β
25	0	3	3	0.25	7.2	18.3	1.0

(a)

(b)

(c)

(d)
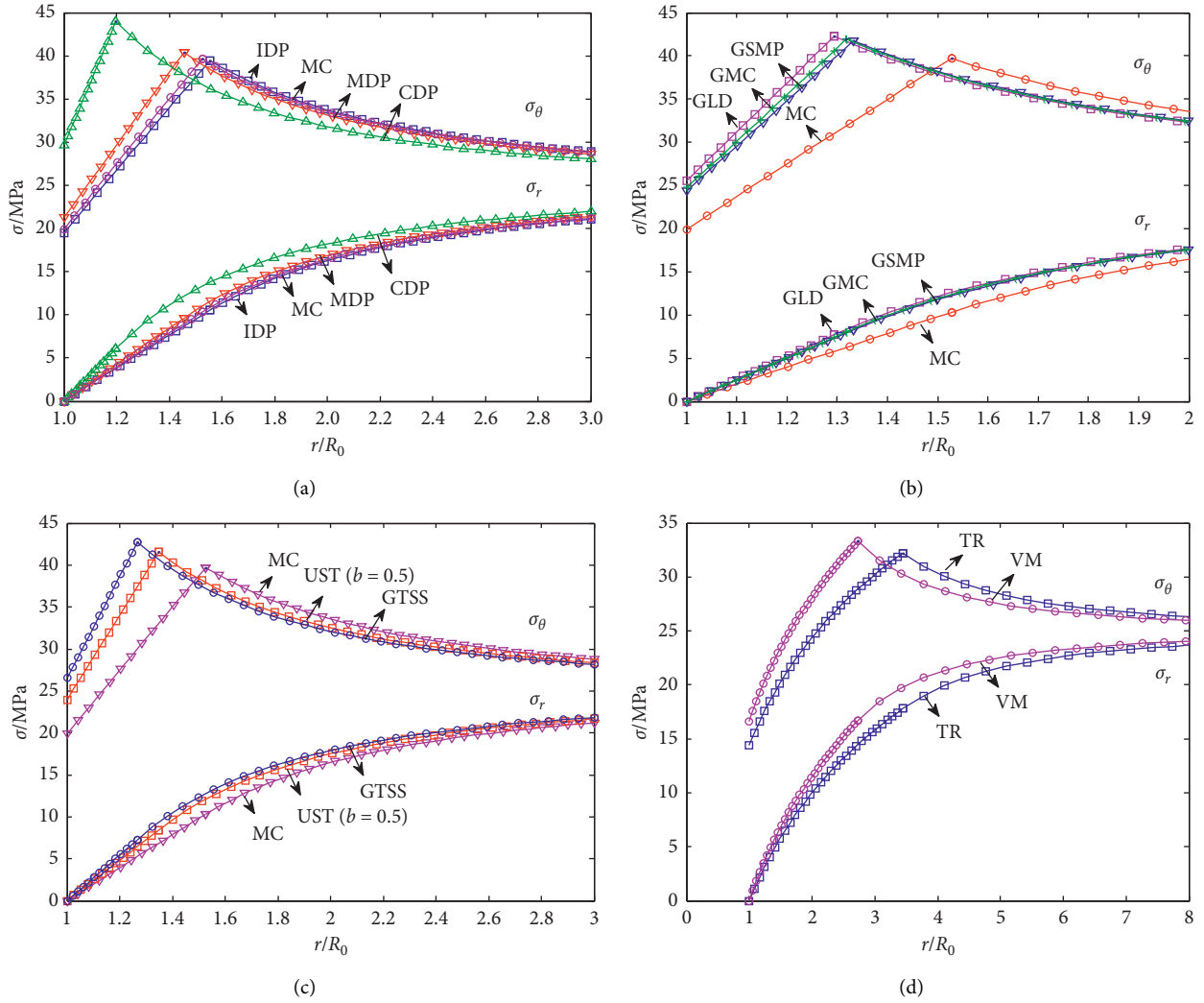
FIGURE 8: The stresses distributions law under different criteria.

TABLE 4: The radius of plastic zone and critical inner pressures under different criteria.

Strength criterion	(R_1/R_0) (σ_{R_1}/p_0)	Strength criterion	(R_1/R_0) (σ_{R_1}/p_0)
MC	1.528 (0.413)	VM	2.728 (0.667)
GMC	1.318 (0.322)	IDP	1.556 (0.422)
GLD	1.294 (0.308)	MDP	1.456 (0.386)
GSMP	1.332 (0.329)	CDP	1.198 (0.242)
TR	3.442 (0.712)	UST$_{0.5}$	1.347 (0.337)
GTSS	1.266 (0.291)	—	—

GLD criterion. However, when taking the GSMP criterion, the value significantly increases by 25.82% and 24.54% compared with the GLD criterion, respectively.

Figure 12 illustrates the effect of elastic strain form on the ground response curve. From Figure 12, it can be seen that the surface displacement of surrounding rock presents the change characteristic of Case 2 solution > Case 3

(a)

(b)
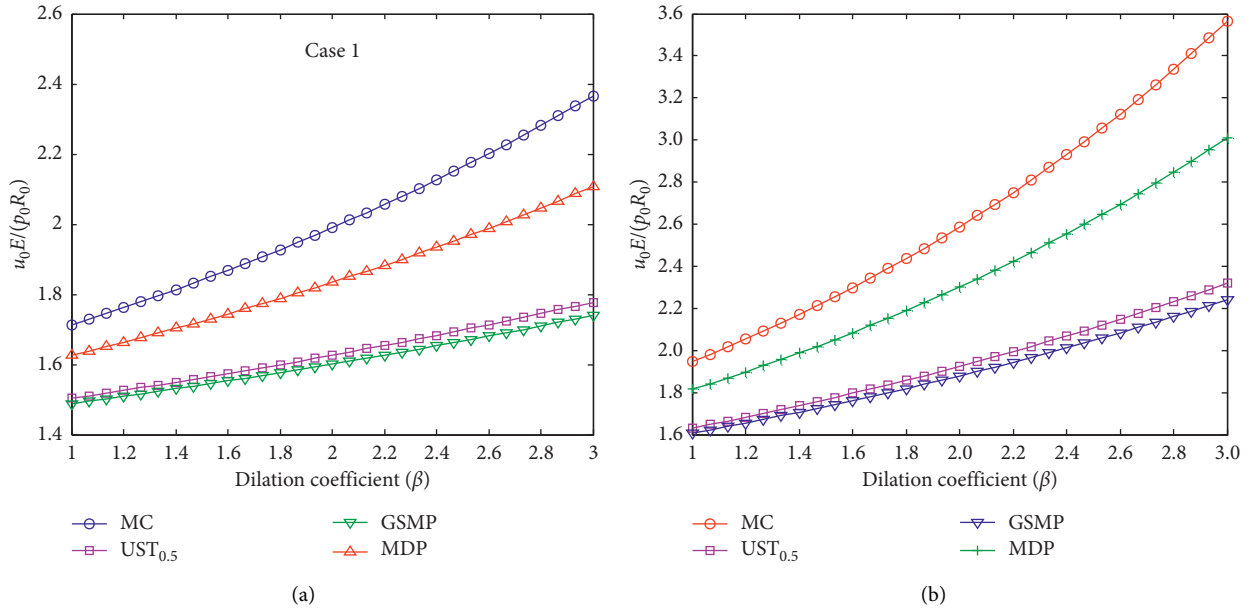
FIGURE 9: The effect of dilation coefficient on the surface displacement.

TABLE 5: The surface displacement value $(u_0 E/(p_0 R_0))$ of the circular tunnel.

	Parameter (β)	MC	GSMP	$UST_{0.5}$	MDP
	1.0	1.713	1.488	1.503	1.626
Case 1	2.0	1.990	1.601	1.626	1.834
	3.0	2.366	1.740	1.778	2.107
	1.0	1.945	1.607	1.630	1.815
Case 2	2.0	2.5867	1.879	1.924	2.302
	3.0	3.567	2.241	2.320	3.011

(a)

(b)
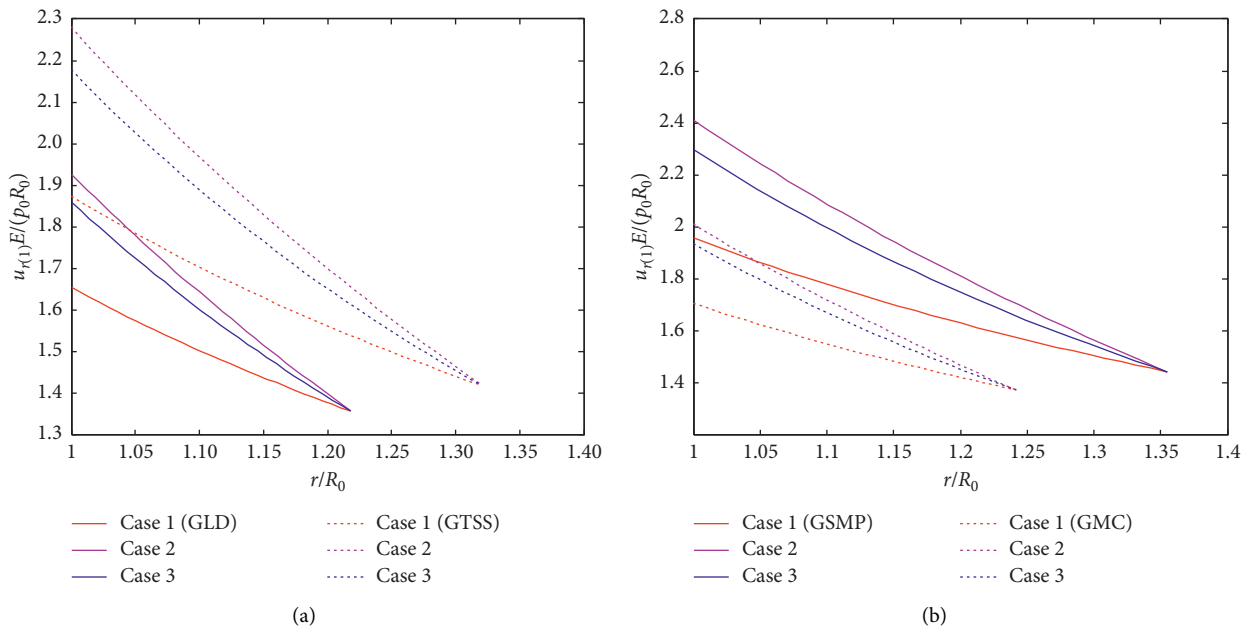
FIGURE 10: The effect of elastic strain form on the radial displacement.

(a)

(b)
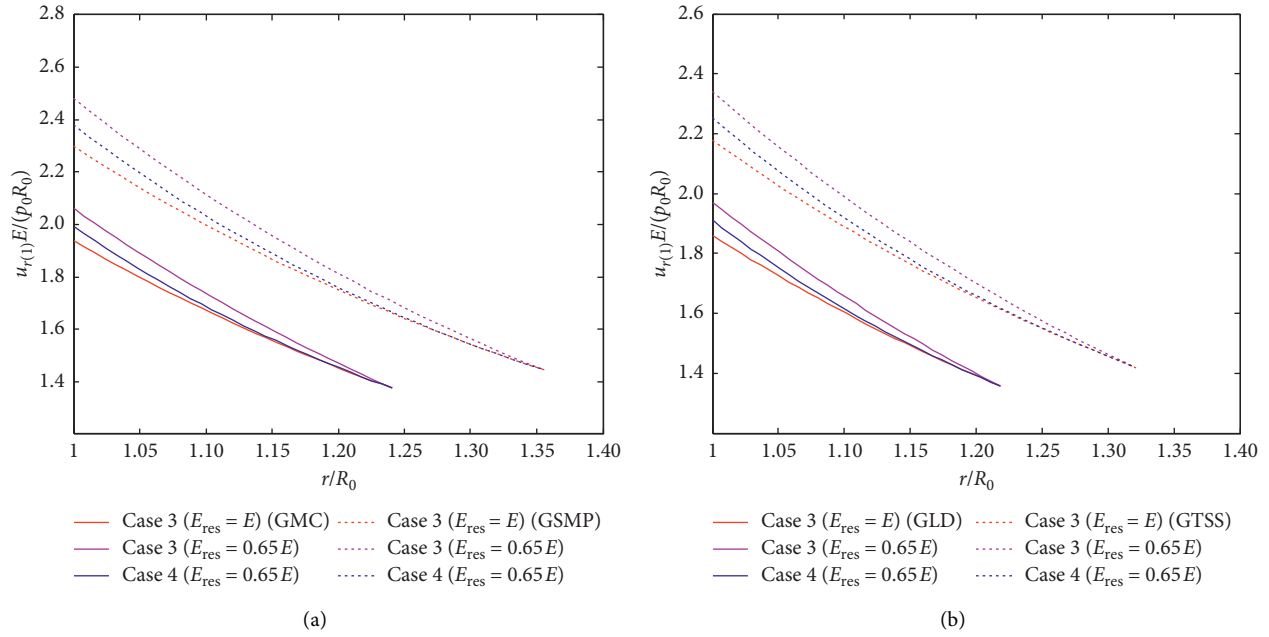
FIGURE 11: The effect of rock mass damage on the radial displacement.

TABLE 6: The dimensionless surface displacement $(u_0 E/(p_0 R_0))$ of the circular tunnel.

		GLD	GTSS	GMC	GSMP
Case 3	$m = 0, E_{res} = E$	1.860	2.177	1.937	2.297
	$m \neq 0, E_{res} = 0.65E$	1.971	2.340	2.061	2.480
Case 4	$m \neq 0, E_{res} = 0.65E$	1.911	2.251	1.993	2.380

(a)

(b)

FIGURE 12: Continued.

(c)
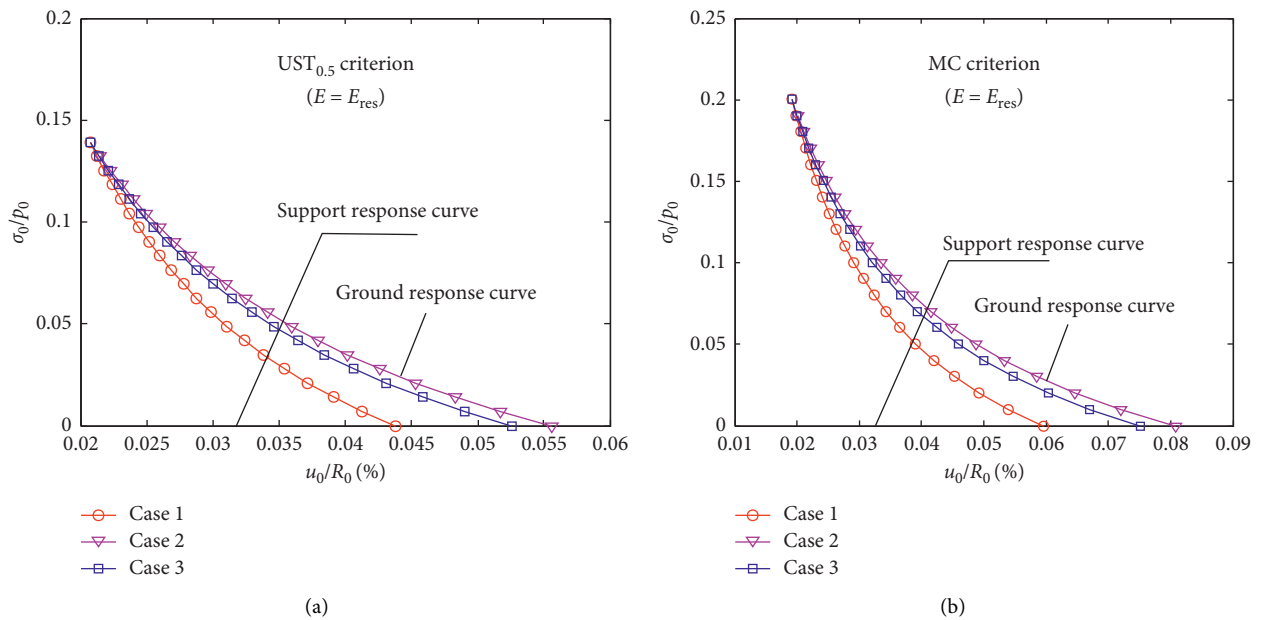
(d)
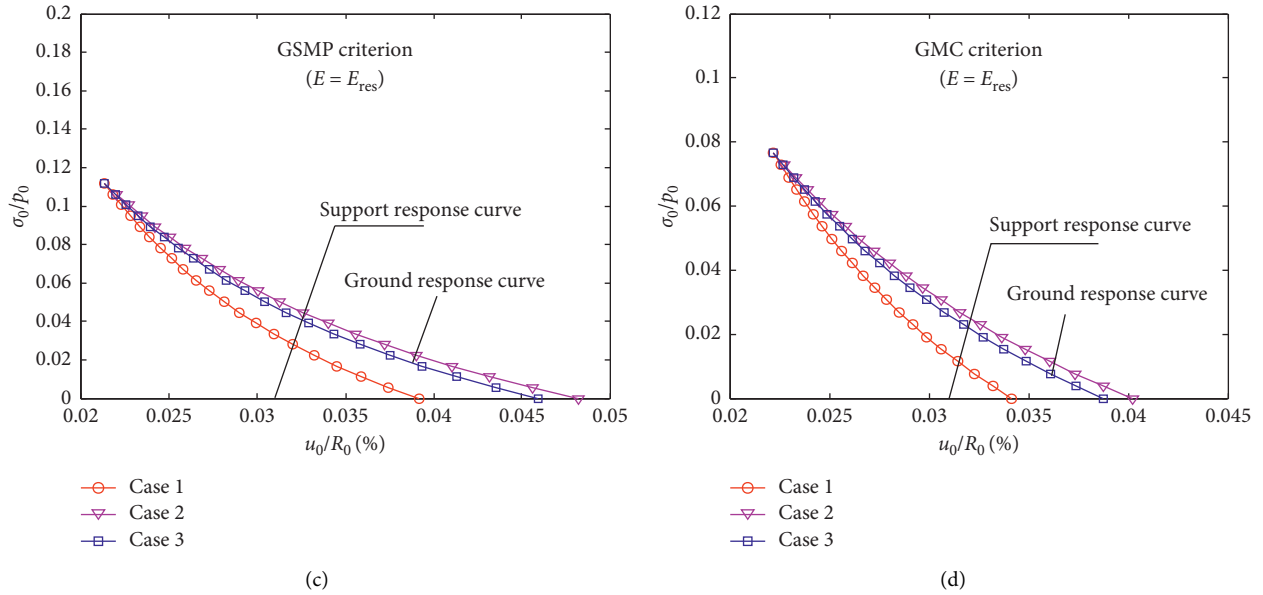
FIGURE 12: The effect of elastic strain form on the ground response curve (note: Young's modulus attenuation is ignored in Case 3).

(a)

(b)
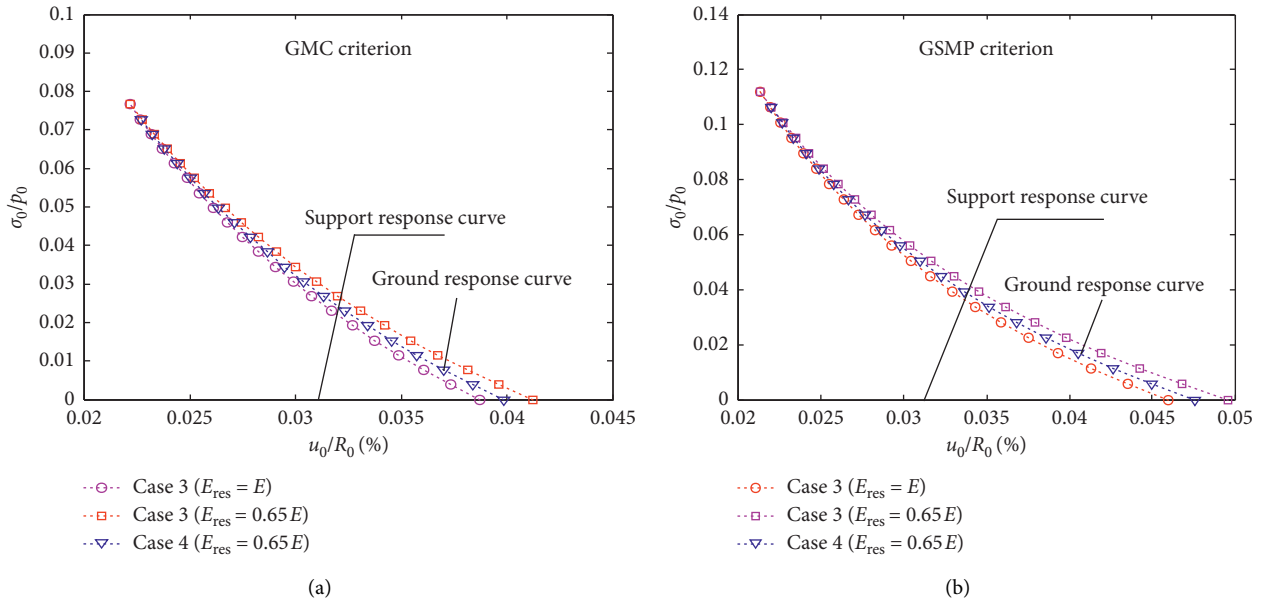
FIGURE 13: The effect of rock mass damage on the ground response curve.

solution > Case 1 solution when the support pressures are equal under the same strength criterion. For example, when $(\sigma_0/p_0) = 0$, compared with Case 2, the surface displacements of surrounding rock decrease, respectively, by 26.37% for Case 1 and 7.13% for Case 3 under the MC strength criterion or by 18.84% for Case 1 and 4.76% for Case 3 under the GSMP strength criterion. From the above analysis, we can see that the support strength design should satisfy the relationship of Case 2 > Case 3 > Case 1 under the same deformation conditions. In fact, the support strength predicted by using Case 2 is relatively large, while that predicted by using Case 1 is relatively small.

In addition, the change characteristic of the ground response curve is closely related to the section of strength criterion. For instance, when $(\sigma_0/p_0) = 0$, the surface displacement $((u_0/R_0))$ increases, respectively, by 74.46% for the MC criterion, 14.68% for GSMP criterion, and 28.17% for UST0.5 criterion by comparison with the GMC criterion under Case 1 condition. The main reason for the above results is that the different strength criteria are different in evaluating the bearing capacity of rock mass. For example, the MC criterion does not consider the effect of intermediate principal stress and then it is easy to underestimate the bearing capacity of rock mass. Therefore, the surface

displacement obtained by MC criterion is larger than that obtained by other criteria under the same support pressure.

The ground and support response curves under GMC and GSMP criteria are shown in Figure 13 considering different Young's modulus attenuation models. It is shown that the damage degree of rock mass has an extremely important influence on the ground response curve. For instance, when $\sigma_0/p_0 = 0$, compared with Case 3 ($E_{res} = E$), the surface displacements of surrounding rock increase, respectively, by 7.96% for Case 3 ($E_{res} = 0.65E$) and 3.59% for Case 4 under GSMP criterion. In other words, when the Young's modulus attenuation is ignored (Case 3 ($E_{res} = E$)), the deformation of the surrounding rock and support force will be underestimated; however, when a residual value of Young's modulus is assumed in the plastic zone (Case 3 ($E_{res} = 0.65E$)), the deformation of the surrounding rock and support force will be overestimated. So, the Young's modulus power function attenuation model (Case 4) seems to present more reasonable results and is recommended for optimizing support parameters design and evaluating stability of surrounding rock in deep underground engineering.

7. Conclusions

By summarizing and simplifying different strength theories, a new unified criterion equation is firstly proposed based on the certain assumption. Then, a new unified closed-form solution for circular opening based on the newly proposed unified criterion equation is deduced with the infinite and finite boundary combining with the nonassociative flow rule. In the plastic zone, four different elastic strain assumptions are applied to solving the plastic zone deformation considering the effect of rock mass damage. Then, the validity of the solution is also verified by comparison with the traditional solution. Finally, the influences of strength criterion effect, dilation coefficient, elastic strain form, and rock mass damage on the mechanical response of surrounding rock are discussed in detail. The primary conclusions can be summarized as follows:

(1) The selection of strength criterion has an extremely important effect on the stresses, plastic zone radius, and critical inner pressure distributions of surrounding rock. For the radius of plastic zone, the calculation results obtained by TR and VM criteria which ignore the impact of friction effect are obviously the largest, followed by IDP, MC, and MDP criteria. The result obtained by CDP criterion which overestimates the effect of intermediate principal stresses on rock mass strength is minimal compared with other criteria's solutions. In addition, the calculation results obtained by UST$_{0.5}$, GSMP, GMC, and GLD criteria which reasonably consider the effect of internal principal stresses give an intermediate range. Therefore, UST$_{0.5}$, GSMP, GMC, and GLD criteria can be strongly recommended for evaluating the mechanics and deformation behavior of surrounding rock, followed by IDP, MDP, GTSS, and MC criteria. TR, VM, and CDP criteria are not recommended to be used.

(2) The influence of dilation coefficient on the surface displacement of surrounding rock is closely related not only to the assumption form of elastic strain in the plastic zone but also to the strength criteria. As the dilation coefficient gradually increases, the dimensionless surface displacement presents the nonlinear increase characteristics. Therefore, the support parameters design should take the influence of the dilation coefficient into account.

(3) The elastic strain assumption forms in the plastic zone have a significant important effect on the deformation of plastic zone and ground response curve by ignoring the effect of rock mass damage. Case 1 gives a smallest deformation and seems to overestimate the plastic bearing capacity of rock mass; however, Case 2 gives a largest deformation and maybe underestimates the plastic bearing capacity of rock mass. Therefore, Case 3 may be more reasonable for evaluating stability of surrounding rock and optimizing support strength design.

(4) The effects of Young's modulus attenuation on the deformation of the plastic zone and ground response curve are related to the selection of the Young's modulus attenuation model and also closely related to the strength criterion. When ignoring the continuity of Young's modulus attenuation, the deformation of surrounding rock is easy to be overestimated or underestimated. So, the Young's modulus power function attenuation seems to give more reasonable results.

Data Availability

Data supporting the results of this study are included in the article.

Conflicts of Interest

The authors declare that there are no conflicts of interest regarding the publication of this paper.

Acknowledgments

References

[1] T. Ogawa and K. Y. Lo, "Effects of dilation and yield criterion on displacement around tunnels," *Canadian Geotechnical Journal*, vol. 24, no. 1, pp. 100–113, 1987.

[2] A. M. Al-Ajmi and R. W. Zimmerman, "Stability analysis of vertical boreholes using the Mogi–Coulomb failure criterion," *International Journal of Rock Mechanics & Mining Sciences*, vol. 43, no. 8, pp. 1200–1211, 2006.

[3] X. J. Wang, M. X. Chen, X Chang et al., "Studies of application of Drucker-Prager yield criterion to stability analysis," *Rock and Soil Mechanics*, vol. 30, no. 12, pp. 3733–3738, 2009.

[4] C. G. Zhang, C. L. Zhang, F. Zhou et al., "The strength theory effect in elastic-plastic analysis of a circular tunnel," *Chinese Journal of Geotechnical Engineering*, vol. 20, no. 10, pp. 1–8, 2017.

[5] L. Chen, X. B. Mao, Y. L. Chen et al., "A new unified solution for circular tunnel based on a four-stage constitutive model considering the intermediate principal stress," *Advances in Civil Engineering*, vol. 2018, p. 14, 2018.

[6] C. Zhang, J. Zhao, Q. Zhang et al., "A new closed-form solution for circular openings modeled by the unified strength theory and radius-dependent young's modulus," *Computers & Geotechnics*, vol. 42, no. 42, pp. 118–128, 2012.

[7] C. Carranza-Torres, "Elasto-plastic solution of tunnel problem using the generalized form of the Hoek-Brown failure criterion," *International Journal of Rock Mechanics and Mining Sciences*, vol. 41, no. 3, pp. 480–1, 2004.

[8] D. Ma, M. Rezania, H. S. Yu, and H. B. Bai, "Variations of hydraulic properties of granular sandstones during water inrush: effect of small particle migration," *Engineering Geology*, vol. 217, pp. 61–70, 2017.

[9] S. K. Sharan, "Exact and approximate solutions for displacements around circular openings in elastic-brittle-plastic Hoek-Brown rock," *International Journal of Rock Mechanics and Mining Sciences*, vol. 42, no. 4, pp. 542–549, 2005.

[10] K. H. Park and Y. J. Kim, "Analytical solution for a circular opening in an elastic-brittle-plastic rock," *International Journal of Rock Mechanics and Mining Sciences*, vol. 43, no. 4, pp. 616–622, 2006.

[11] Y. Wang, "Ground response of circular tunnel in poorly consolidated rock," *Journal of Geotechnical Engineering*, vol. 122, no. 9, pp. 703–708, 1996.

[12] S. Q. Xu and M. H. Yu, "The effect of the intermediate principal stress on the ground response of circular openings in rock mass," *Rock Mechanics & Rock Engineering*, vol. 39, no. 2, pp. 169–181, 2006.

[13] X. Chen, C. P. Tan, and C. M. Haberfield, "Numerical evaluation of the deformation behaviour of thick-walled hollow cylinders of shale," *International Journal of Rock Mechanics & Mining Sciences*, vol. 37, no. 6, pp. 947–961, 2000.

[14] R. Rahimi and R. Nygaard, "Comparison of rock failure criterion in predicting borehole shear failure," *International Journal of Rock Mechanics & Mining Sciences*, vol. 79, Article ID IJRMMSD1500037, 2015.

[15] W. M. Huang and X. Y. Gao, "Tresca and von mises yield criterion: a view from strain space," *Philosophical Magazine Letters*, vol. 84, no. 10, pp. 625–629, 2004.

[16] S. K. Sharan, "Analytical solutions for stresses and displacements around a circular opening in a generalized Hoek-Brown rock," *International Journal of Rock Mechanics and Mining Sciences*, vol. 45, no. 1, pp. 78–85, 2008.

[17] X. Chen, C. P. Tan, and C. M. Haberfield, "Solutions for the deformations and stability of elastoplastic hollow cylinders subjected to boundary pressures," *International Journal for Numerical & Analytical Methods in Geomechanics*, vol. 23, no. 8, pp. 779–800, 2015.

[18] J. M. Zhu, Z. X. Wu, H. T. Zhang et al., "Study of residual stress of rock based on Lade-Duncan and SMP strength criterion," *Chinese Journal of Rock Mechanics and Engineering*, vol. 31, no. 8, pp. 1715–1720, 2012.

[19] X. Q. Yang, Z. Z. Zhu, H. E. Shi-Xiu et al., "Researches on failure criterion of lade-Duncan, Matsuoka-nakai and ottosen," *Chinese Journal of Geotechnical Engineering*, vol. 28, no. 3, pp. 337–342, 2006.

[20] P. V. Lade and M. K. Kim, "Single hardening constitutive model for frictional materials III. Comparisons with experimental data," *Computers & Geotechnics*, vol. 6, no. 1, pp. 31–47, 1988.

[21] D. Ma, H. Y. Duan, X. B. Li, Z. H. Li, Z. L. Zhou, and T. B. Li, "Effects of seepage-induced erosion on nonlinear hydraulic properties of broken red sandstones," *Tunnelling and Underground Space Technology*, vol. 91, Article ID 102993, 2019.

[22] X. Ma, J. W. Rudnicki, and B. C. Haimson, "The application of a Matsuoka-Nakai-Lade-Duncan, failure criterion to two porous sandstones," *International Journal of Rock Mechanics & Mining Sciences*, vol. 92, pp. 9–18, 2017.

[23] P. V. Lade, "Cubical triaxial tests on cohesionless soils," *Soil Mechanics and Foundation Engineering*, vol. 99, no. 10, pp. 793–812, 1973.

[24] A. M. Al-Ajmi and R. W. Zimmerman, "Relationship between the parameters of the Mogi and Coulomb failure criterion," *International Journal of Rock Mechanics and Mining Sciences*, vol. 42, no. 3, pp. 431–439, 2005.

[25] D. Ma, H. Y. Duan, Q. Zhang, J. X. Zhang, W. X. Li, Z. L. Zhou et al., "A numerical gas fracturing model of coupled thermal, flowing and mechanical effects," *Computers, Materials & Continua*, vol. 65, no. 3, pp. 2123–2141, 2020.

[26] T. R. Rogge and C. F. Sieck, "He use of NONSAP to compare the Von Mises and a modified Von Mises yield criterion," *Computers & Structures*, vol. 17, no. 5, pp. 705–710, 1983.

[27] H. Matsuoka and D. Sun, "Extension of spatially mobilized plane (SMP) to frictional and cohesive materials and its application to cemented sands," *Soils & Foundations*, vol. 35, no. 4, pp. 63–72, 1995.

[28] D. Ma, J. J. Wang, X. Cai et al., "Effects of height/diameter ratio on failure and damage properties of granite under coupled bending and splitting deformation," *Engineering Fracture Mechanics*, vol. 220, Article ID 106640, 2019.

[29] D. Ma, H. Y. Duan, W. T. Liu, X. T. Ma, and M. Tao, "Water-sediment two-phase flow inrush hazard in rock fractures of overburden strata during coal mining," *Mine Water and the Environment*, vol. 39, no. 2, pp. 308–319, 2020.

[30] C. J. Deng, G. J. He, and Y. R. Zheng, "Studies on Drucker-Prager yield criterions based on M-C yield criterion and application in geotechnical engineering," *Chinese Journal of Geotechnical Engineering*, vol. 28, no. 6, pp. 735–739, 2006.

[31] C. A. M. Veeken, J. V. Walters, C. J. Kenter et al., "Use of plasticity models for predicting borehole stability," *International Journal of Rock Mechanics and Mining Sciences & Geomechanics Abstracts*, vol. 27, no. 6, p. 379, 1989.

[32] M. H. Yu, S. Y. Yang, S. C. Fan et al., "Unified elasto-plastic associated and non-associated constitutive model and its engineering applications," *Computers & Structures*, vol. 71, no. 6, pp. 627–636, 1999.

[33] M. H. Yu, "Advances in strength theories for materials under complex stress state in the 20th century," *Advances in Mechanics*, vol. 34, no. 4, pp. 529–560, 2004.

[34] M. H. Yu, *Unified Strength Theory and its Applications*, Springer-Verlag, Berlin, Germany, 2004.

[35] R. T. Ewy, "Wellbore-stability predictions by use of a modified lade criterion," *Spe Drilling & Completion*, vol. 14, no. 2, pp. 85–91, 1999.

[36] E. T. Brown, J. W. Bray, B. Ladanyi et al., "Ground response curves for rock tunnels," *Journal of Geotechnical Engineering*, vol. 109, no. 1, pp. 15–39, 1983.

[37] S. K. Sharan, "Elastic–brittle–plastic analysis of circular openings in Hoek–Brown media," *International Journal of Rock Mechanics & Mining Sciences*, vol. 40, no. 6, pp. 817–824, 2003.

[38] H. S. Yu, *Cavity Expansion Methods in Geomechanics*, Kluwer Academic Publishers, New York, NY, USA, 2000.

[39] Q. Zhang, B. S. Jiang, X. S. Wu, H. Q. Zhang, and L. J. Han, "Elasto-plastic coupling analysis of circular openings in elasto-brittle-plastic rock mass," *Theoretical and Applied Fracture Mechanics*, vol. 60, pp. 60–67, 2012.

[40] M. B. Reed, "Stresses and displacements around a cylindrical cavity in soft rock," *Ima Journal of Applied Mathematics*, vol. 36, no. 3, pp. 223–245, 1986.

Research Article

Solid-Gas Flow Characteristics of Drilling Bit-Rod Integral Structure

Hongtu Zhang,[1,2,3] Ouya Zhang,[1] Le Wei,[4] and Banghua Yao [2,3]

[1]*School of Safety Science and Engineering, Henan Polytechnic University, Jiaozuo, Henan 454003, China*
[2]*State Key Laboratory Cultivation Base for Gas Geology and Gas Control, Henan Polytechnic University, Jiaozuo, Henan 454003, China*
[3]*State Collaborative Innovation Center of Coal Work Safety and Clean-Efficiency Utilization, Jiaozuo 454003, China*
[4]*China Coal Technology and Engineering Group Chongqing Research Institute, Chongqing 400037, China*

Correspondence should be addressed to Banghua Yao; yaobanghua@126.com

Sampling based on negative pressure pneumatic conveying method is an important theory in determining coal bed methane (CBM) content. The coal-gas two-phase flow path is an integrated structure composed of polycrystalline diamond compact (PDC) bit and drilling rod. In this work, CFD-DEM coupling numerical simulation was adopted to study the solid-gas flow characteristics of an integrated structure having PDC bit and gas velocity pipe under different gas velocity and solid mass flow rates. The results showed that the gas phase had a reverse velocity zone at the PDC bit. The reverse velocity zone gradually decreased with increase of gas velocity. In addition, a high-velocity band in drill pipe became apparent for the particle phase; there was an obvious bottom flow characteristic at the PDC bit and an area of the highest layer thickness in the drill pipe. Under the same gas velocity, the location of the area of the highest layer thickness shifted from the drill bit with the increase of solid mass flow rate. Increase in the gas velocity resulted in a rapid increase of the velocity of coal particles, while the bottom flow characteristics of coal particles weakened and the suspension flow gradually appeared. The results of this study are of great significance for optimizing the gas velocity based on negative pressure pneumatic conveying technique.

1. Introduction

Pneumatic conveying is a common method for transportation of bulk material over long distance in industries such as petrol, agriculture, mining, and chemical due to its efficiency, adaptability, and operability. A typical pneumatic conveying consists of feeder equipment, pipelines, and power device. Gas velocity, solid-gas ratio, pressure drop, and flow pattern are the main factors for evaluating the pneumatic conveying system. The solid-gas flow characteristics of pneumatic conveying under different operating parameters are key factor for optimizing the system.

Although experiments can effectively investigate the flow pattern, pressure drop, and particle concentration of pneumatic conveying under different operating parameters, it is difficult to determine the optimal parameters for complex and uneconomical solid-gas flow.

The development of CFD (computational fluid dynamics) has proved to be a useful alternative method for investigating pneumatic conveying. Many works on pneumatic conveying have been carried out using CFD-DPM. Huber et al. [1] calculated the dispersed gas-solid flows in pipe systems using CFD-DPM which included all important effects, such as turbulence, two-way coupling, particle transverse lift forces, and particle-wall collisions including wall roughness and interparticle collisions. Lain et al. [2] investigated the different flow characteristics of channel and pipe flow under different effects, such as wall roughness and the degree of coupling (i.e., two- or four-way) via Euler–Lagrange. Sommerfeld et al. [3] studied the parameters influencing dilute phase pneumatic conveying through pipe systems.

The DPM neglects the particle-particle interaction [4], because it more suited for the study of dilute phase flow [5].

When researchers need more information about the particle behavior, for example, the particle degradation during pneumatic conveying, particle-particle interaction should not be neglected. To obtain more particle information, Tsuji et al. [6] proposed a new CFD-DEM method (computational fluid dynamics-discrete element method), which has been widely used in petrol, agriculture, mining, and chemical industries. Akhshik et al. [7, 8] investigated the drilling cuttings flow characteristics in petrol industry under different pipeline rotations by the CFD-DEM coupling method. In agriculture industry, Li et al. [9] studied the grain motion in the air-and-screen cleaning device of combining harvester by the CFD-DEM method. Dai et al. [10] investigated the motion simulation and tested threshed grains in tapered threshing and transmission device for plot wheat breeding based on CFD-DEM. In chemical industry, Kruggel-Emden et al. [11] studied the rope formation and dispersion of nonspherical particles during pneumatic conveying in a pipe bend by the CFD-DEM. Kumar [12] studied the pressure drop in the bend. Korevaar et al. [13] revealed the particle charging mechanism during the pneumatic conveying. The CFD-DEM method was also used to study the physical mechanisms involved in slug transport and pipe blockage during horizontal pneumatic conveying [14].

In the mining industry, Shao et al. [15] studied the flow characteristics of drilling cuttings during coal bed methane extraction drilling while Zhou et al. [16] revealed the distribution law of fine sealing material particles in the narrow channels of coal seam during the secondary sealing process of gas drainage drilling.

However, it is noteworthy that previous works on the flow characteristics of pneumatic conveying paid more attention to the characteristics of the solid-gas flow into the rod, while there is insufficient study about the physical structure effect of the solid-gas flow into the rod.

The prerequisite for efficient CBM extraction is determination of its precise gas content. A typical application of pneumatic conveying is the sampling method based on negative pressure pneumatic conveying for determining the content of coal bed methane in underground coal mines. Before the coal sample is collected, the gas-coal flowed into the bit-drilling rod structure by the bit firstly and then to the drilling rod during the sampling process. And the gas-coal flow in the bit-drilling rod structure affected the sampling process. Therefore, studying the gas-coal flow characteristics inside the structure composed of bit-drill rod had an important guiding for optimizing the design of sampling drilling bit-drill rod structure.

In this work, the integrated structure of the coal-gas flow path during the drilling bit-rod was constructed. The CFD-DEM numerical simulation method was then applied to study the coal-gas flow characteristics under different operating parameters.

2. Geometry and Mesh

The bit is based on a common PDC three-wing bit and there are three fluid holes, which are evenly distributed on the circumference. Simplifying the PDC bit structure with fluid holes, the inclination angle is 30° and the center diameter is 0.02 m. The total effective fluid holes cross-sectional area formed is equal to the cross-sectional area of the circular surface of rod with diameter of 0.04 m. In this study, the total geometric structure length was 5 m with an improved PDC drill bit and a section of drill rod with inner diameter of 0.04 m. And the improved PDC bit had three fluid holes with inclination angle of 30 degrees each and a total effective cross section area equaled that of the drill rod, the actual diagram of the bit, and the drill rod as shown in Figure 1. The drilling rod has a diameter of 40 mm, leading to an integrated structure which constitutes the bit-drilling rod (0–5 m) model. Gambit 2.4.6 preprocessing software was used to model and mesh the grid into blocks: the grid part of the drill bit adopts Trid type, Tet/hybrid unit, interval size = 0.005; the connecting part of the drill pipe is of Copper type, Hex/Wedge unit, interval size = 0.02, as shown in Figure 1 (the part of the drill pipe is a partial schematic diagram). For verification, the mesh independent of the calculation was 16384, 34610, and 66542, respectively. The pressure drop and the difference between the calculated results at the same gas velocity are shown in Table 1.

3. CFD-DEM Coupling Simulation

3.1. CFD-DEM Coupling Simulation Process. In this work, two commonly used numerical software applications FLUENT and EDEM were selected as the CFD and DEM operation platforms, respectively. The CFD-DEM simulation procedure is as follows: the particle phase is added after the gas phase flow field reaches a steady state. The gas phase calculates convergence within a single time step; the particles then update the motion state according to the gas phase data in the grid unit. In the new time step, the gas phase flow information is updated according to the state of particle motion in the grid cell and reaches the convergence state. Back and forth cycling continues until a steady state is reached; the calculation procedure is as shown in Figure 2.

FLUENT-EDEM coupling algorithm has two coupling methods, namely, Lagrange and Euler. Compared with the Euler–Lagrangian method, the Euler-Euler coupling method fully considers the force between the particle-fluid phase, particle-particle, and particle-wall surface. Besides, Euler-Euler coupling can be used in both dilute phase and dense phases. Therefore, the Euler-Euler coupling method was used in the current study.

3.2. Solid Phase Governing Equation. Newton's second kinetic equation was adopted to describe the particle motion, and the coal particle i motion equation is as follows:

Particle i motion can be described by the following equation:

$$F_I = m_i \ddot{v}_i, \tag{1}$$

$$M_i = I_i \ddot{\theta}_i, \tag{2}$$

(a)

(b)

(c)
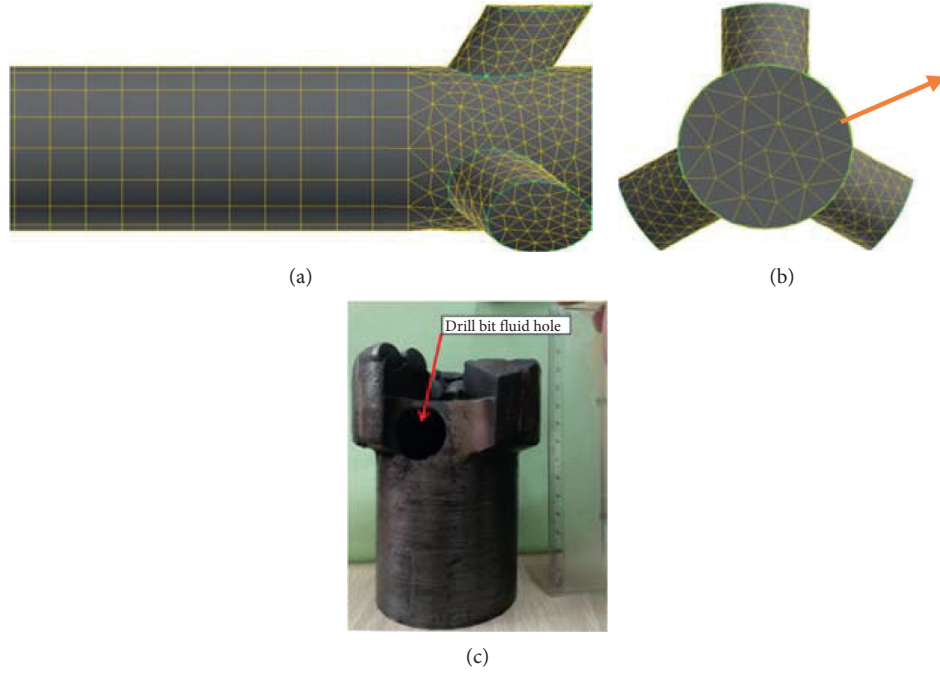
Figure 1: The meshing of drilling bit meshing.

Table 1: The details for the grid independence study.

Mesh number	Pressure (Pa)	Error (%)
16384	1976	
34610	2062	4.35
66542	1985	
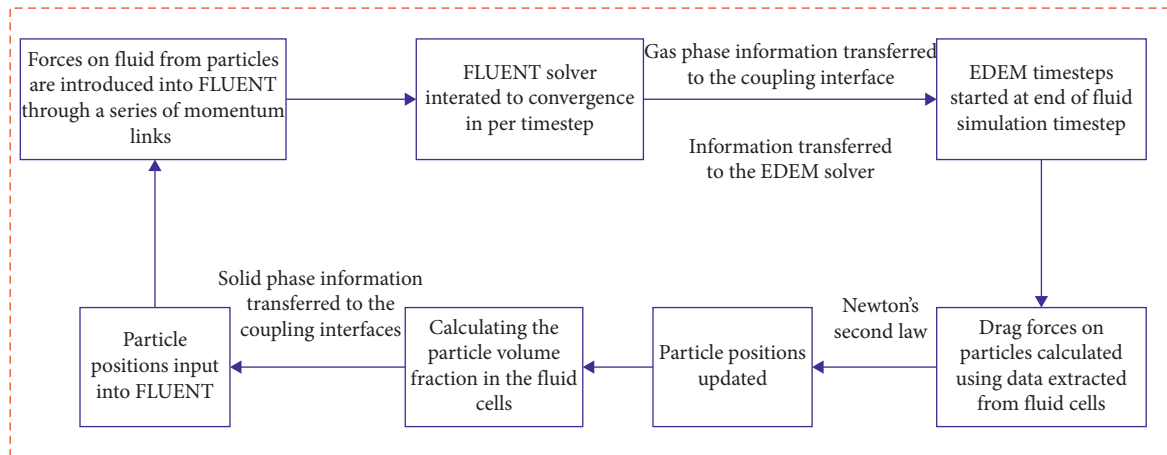
Figure 2: The process of FLUENT-EDEM coupling method.

where $\ddot{v}_i$ and $\ddot{\theta}_i$ are particle i acceleration and angle velocity. m_i and I_i are particle i mass and inertia moment. F_i and M_i are accumulated force and accumulated moment.

In this work, the Hertz–Mindlin nonsliding contact model was adopted [17].

The coal particle is subjected to drag force, gravity, particle-particle interaction force, buoyancy, pressure gradient force, lift force, virtual mass force, and other forces. Pressure gradient force, lift force, and virtual mass force are negligible compared with drag force, gravity, and coal particle-coal particle force. Therefore, the force Fi of coal particle can be expressed as previously reported [18]:

$$F_i = m_i g + f_{p-g,i} + \sum_{j=1}^{k_i} \left(f_{c,ij} + f_{d,ij} \right). \tag{3}$$

The Grun, Wen, and Yu drag force model was used to describe the drag force $f_{p-g,i}$ [19]:

$$f_{c,ij} = f^c_{n,ij} + f^c_{t,ij},\quad(4)$$

$$f^c_{n,ij} = \frac{4}{3}E^*\sqrt{R^*}\sigma_n^{1.5},\quad(5)$$

$$f^c_{t,ij} = -2\sqrt{\frac{5}{6}}\beta\sqrt{S_n m^*}v_n^{rel},\quad(6)$$

$$\beta = \frac{\ln e}{\sqrt{\ln^2 e + \pi^2}},\quad(7)$$

$$S_n = 2Y^*\sqrt{R^*\delta_n},\quad(8)$$

where $f^c_{n,ij}$ is normal contact force, $f^c_{t,ij}$ is tangential contact force, E^* is equivalent Young's modulus, R^* is coal particle equivalent radius, δ_n is normal overlap, m^* is equivalent mass, v_n^{rel} is normal component of relative velocity, e is restitution coefficient, S_n is normal stiffness, and β is damping coefficient:

$$f_{d,ij} = f^d_{n,ij} + f^d_{t,ij},\quad(9)$$

$$f^d_{n,ij} = -S_t\delta_t,\quad(10)$$

$$S_t = 8G^*\sqrt{R^*\delta_n},\quad(11)$$

$$f^d_{t,ij} = -2\sqrt{\frac{5}{6}}\beta\sqrt{S_t m^*}v_t^{rel},\quad(12)$$

where $f^d_{t,ij}$ is tangential damping force, $f^d_{n,ij}$ is normal damping force, δ_t is tangential overlap, m^* is equivalent mass, v_t^{rel} is relative velocity tangential component, S_t is tangential stiffness, and G^* is equivalent shear modulus.

Rolling friction torque T_i is

$$T_i = -\mu_t F_t R_i \omega_i,\quad(13)$$

where μ_t is rolling friction coefficient, F_n is coal particle-surface normal contact force, R_i is distance from coal particle sphere center to contact point, and ω_i is particle angular velocity.

3.3. Gas Phase Governing Equation.
The RNG k-ε turbulence model was used to solve the gas phase governing equations. Both the turbulent kinetic energy and the discrete rate adopted the second-order upwind scheme; the pressure term dispersion scheme was PRESTO, the momentum term discrete scheme was QUICK, and the pressure-velocity coupling applied the SIMPLE algorithm.

3.4. Time Step Setting.
The time step was determined by Rayleigh time step T_R:

$$T_R = (0.1631\sigma + 0.8766)^{-1}\pi d_p\sqrt{\frac{\rho_p}{G}},\quad(14)$$

where σ is Poisson's ratio and G is coal particle shear modulus.

3.5. Simulation Conditions Setting.
Setting of gas phase conditions: according to the empirical formula, when the coal particle size is 1 mm, its suspension velocity is 5.97 m/s. For the pneumatic conveying empirical process of the coal particle in a suspended transport state, the air velocity needs to be 2 to 2.5 times the coal particle suspension velocity. Therefore, the gas velocity is selected as 15 m/s, 20 m/s, and 25 m/s. The velocity is evenly distributed perpendicular to the entrance and the exit condition is the pressure boundary. The wall has no slip boundary conditions and the time step is $3e-05$ s.

Setting of coal particle phase conditions: the method of dynamically generating coal particle was adopted, assuming that coal particle flows into the three fluid holes uniformly into the bit-drilling rod (0 m ∼ 5 m). Taking ∅ 94 mm PDC bit as an example, the density of coal particle is 1450 kg/m³, and the mass of coal particle produced when drilling 1 m is about 10 kg. The mass flow rate of coal shavings in a single fluid hole is then taken as 0.02 kg/s, 0.03 kg/s, 0.04 kg/s, and 0.05 kg/s (expressed in terms of single hole coal shavings mass flow rate), corresponding to the total coal mass flow rate of 3.6 kg/min, 5.4 kg/min, 7.2 kg/min, and 9 kg/min, respectively. The time step of coal particle phase is $6e-07$ s. The specific simulation conditions are shown in Table 2. The physical property parameters such as coal particle and wall surface are shown in Table 3.

4. Results and Discussion

4.1. Model Validation.
In order to verify the accuracy of the CFD-DEM calculation method and turbulence model selected in this work, refer to the relevant experimental data of the horizontal dilute phase pneumatic conveying of Naveh [20] for verification. Pressure drop is main parameters for pneumatic conveying and is used for validation in this study. Figure 3 shows the pressure drop of simulated results under different gas velocities, which were compared with experimental pressure drop data by Naveh.

4.2. Coal-Gas Flow in the Drilling Bit-Rod Integral Structure of 0 m∼5 m.
In this work, 12 cases were carried out at 3 s for each case. The flow pattern of coal particle in the bit-drilling rod (0–5 m) depicts the acceleration and deposition characteristics of coal particle at the initial stage of entering the bit, which intuitively reflects the coal particle in the drilling and the propensity to block the pipeline inside the rod. The pattern of coal particle flowing out of the drilling rod area showed the acceleration characteristics of coal particle under different conditions and ability of transporting the coal particles. The distribution of the number of coal particles along their flow direction at the same gas velocity particle flow rate and different gas velocities further reflects the gas velocity's ability of transporting coal particles and their flow patterns. The velocity of coal particle is obtained and the proportion of different velocities indicates the influence of

TABLE 2: Simulation cases setting.

Case	Coal mass flow rate (kg·s⁻¹)	Gas velocity (m·s⁻¹)
1	0.02×3	15
2	0.02×3	20
3	0.02×3	25
4	0.03×3	15
5	0.03×3	20
6	0.03×3	25
7	0.04×3	15
8	0.04×3	20
9	0.04×3	25
10	0.05×3	15
11	0.05×3	20
12	0.05×3	25

TABLE 3: Physical parameters of coal and wall.

Parameter	Unit	Value
Coal density	km·m⁻³	1450
Coal Poisson's ratio	—	0.201
Coal shear modulus	Pa	$1.4e9$
Coal particle radius	mm	1
Steel density	km·m⁻³	7400
Steel Poisson's ratio	—	0.25
Steel shear modulus	Pa	$8.24e10$
Coal restitution coefficient	—	0.5
Coal static friction coefficient	—	0.6
Coal rolling friction coefficient	—	0.05
Coal steel restitution coefficient	—	0.5
Coal steel static friction coefficient	—	0.4
Coal steel rolling friction coefficient	—	0.05
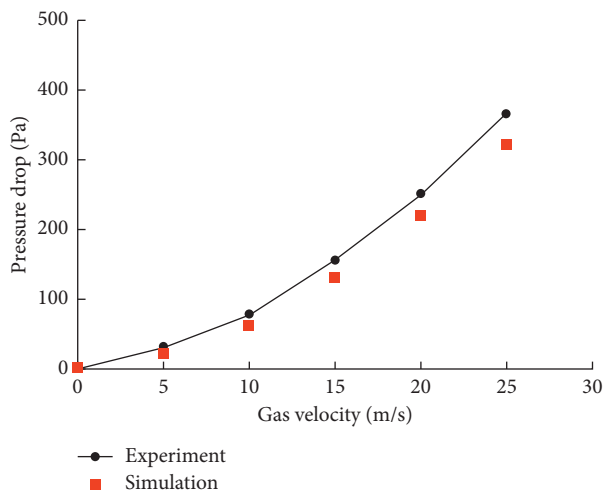
FIGURE 3: Comparison of pressure drop at different gas velocities ($d = 1.44$ mm and $D = 52.5$ mm).

gas velocity on the acceleration process of coal particle and depicts the flow pattern of coal particle at different positions. Therefore, at the same gas velocity, the output coal cuttings have different flow rate bit-drilling rod 0–0.5 m of coal particle flow pattern (Z direction 0 m~0.5 m in this model), flowing out of the drilling rod area (at this time in the model, the direction of coal particle in Z direction is 4.5 m~5 m); the

same coal particle flow rate has different gas velocity, number of coal particles at different positions, velocity of coal particle obtained, and proportion of different velocities.

After the gas flows into the bit-drilling rod (0–5 m), the coal particle influences the gas flow. Gas velocity is an important parameter to characterize the airflow. The change of gas velocity reflects the influence of coal particle on airflow. The influence of coal particle on the airflow is most obvious in the bit-gas velocity rod (0–0.5 m) section. Therefore, the gas velocity contour in the bit-gas velocity rod (0–0.5 m) segment (0–0.5 m in Z direction in this model) at different coal particle flow rates in the gas phase is revealed.

4.3. Coal-Gas Flow in the Drilling Bit-Rod Integral Structure of 0–0.5 m

(1) The coal-gas flow characteristic in the bit-drilling rod (0 m~0.5 m) section under different mass flow rates of coal particles at gas velocity of 15 m/s is as shown in Figure 4.

When the coal particle entered into the bit-rod through fluid holes under mass flow rate of 0.02 kg/s, an obvious bottom flow characteristic along the flow direction appeared, and a small amount of coal particle accumulated at the end. When the coal particle mass flow rate was 0.03 kg/s, the amount of coal particle increased at the bottom of the drill pipe, the highest layer thickness point appeared at about 0.33 m, the accumulation of coal particle at the end of the drill bit increased, the flow of coal particle was the highest after the layer thickness point, and part of the coal particle started to accelerate and formed a suspension. When the coal particle mass flow rate of reached 0.04 kg/s, the highest layer thickness point moved in the direction of flow. The thickness of the coal particle layer was thicker than that of 0.03 kg/s, and a small amount of coal particle in the upper part of the drilling rod was suspended. When the coal particle mass flow rate reached 0.05 kg/s, the accumulation of coal particles at the end of the drilling rod and the thickness of the coal particles further increased, and the thickest layer of coal particle advanced again along the direction of flow.

When the gas flowed into the bit, a high-velocity strip formed at the axial center of the bit with the coal particle mass flow rate of 0.02 kg/s. Along the flow direction, the strip in the high-velocity zone was distributed on the upper part of the drilling rod and its width gradually decreased to 0.30 m. There was a reverse velocity zone within a certain range near the end of the bit. The strip range of the high-velocity zone was extended along the flow direction, and a thin strip-shaped high-velocity zone was formed on the upper part of the drilling rod, and the range of the velocity zone in the opposite direction of the end of the bit was reduced when the coal particle mass flow rate was 0.03 kg/s. When the coal mass flow rate increased to 0.04 kg/s and 0.05 kg/s, the band range

(a)

(b)
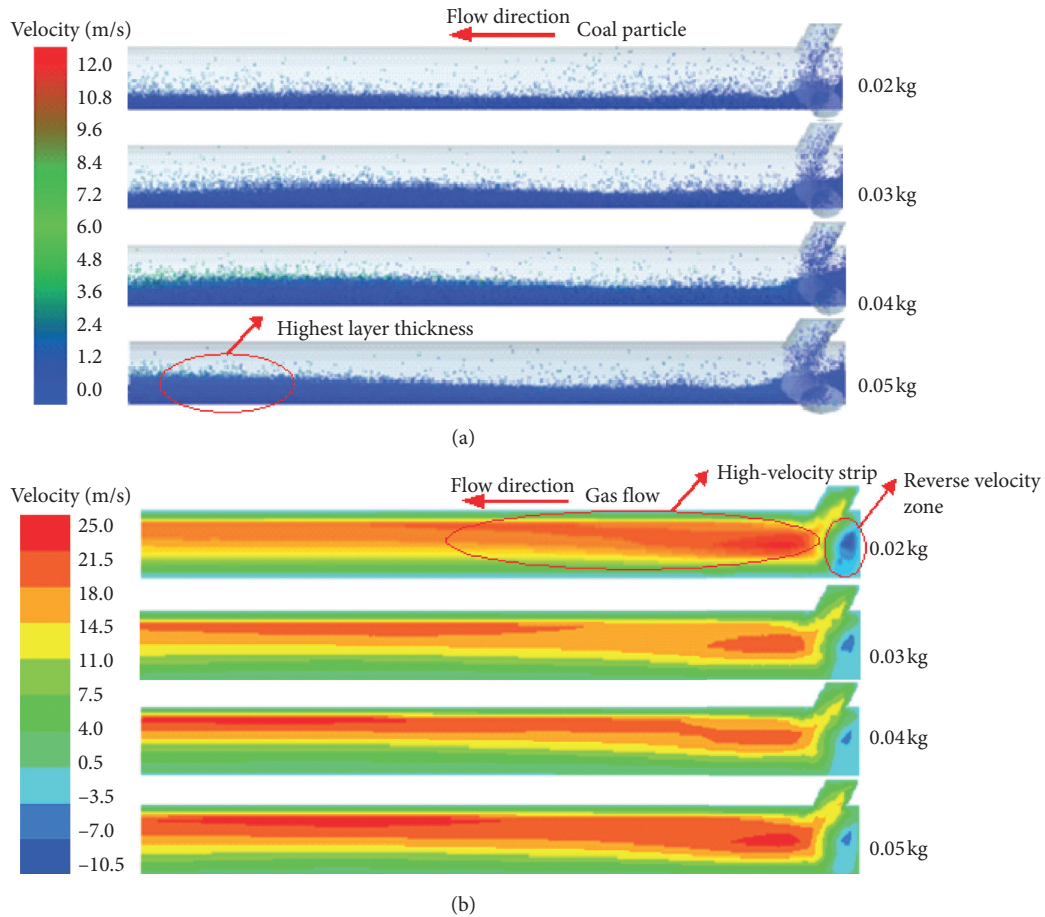
FIGURE 4: The coal-gas flow characteristic in drilling bit-rod integral structure 0~0.5 m under gas velocity of 15 m/s ($t = 3$ s).

of the gas high-velocity area increased, and the reverse direction velocity area slightly changed.

(2) The coal-gas flow states at drilling bit-rod integral structure 0 m~0.5 m section are shown in Figure 5, when the gas velocity was 20 m/s at different coal particle mass flow rates.

When the coal particle flow rate was 0.02 kg/s, there was a higher particle concentration at the 0 m to 0.25 m section. The coal particle concentration decreased along the flow direction; the movement and suspension motion of coal particle became more dispersed and pronounced, respectively. There was a small amount of coal particle suspension movement at the end of the drilling bit. When the coal particle mass flow rate was 0.03 kg/s, the coal particle of the highest thickness point in the drilling rod was at 0.1 m~0.15 m and pipe bottom flow occurred. The accumulation of coal particle at the end of the drilling bit increased along the flow direction. After the coal particles flowed past the highest layer thickness point, the amount of suspended coal particles increased and their concentration in the upper part of the drilling rod became low, and the concentration of coal particles in the lower part became high. The thickness of coal particles at the

bottom of the pipe changed slightly along the flow direction. At a coal particle mass flow rate of 0.04 kg/s, the highest layer thickness point appeared at 0.1 m~0.15 m, the amount of suspended coal particles decreased, the thickness of the coal particle layer increased, and the accumulation of coal particle at the end of the drilling bit increased.

Compared to coal particle mass flow rate of 0.04 kg/s, the coal particle accumulation at the end of the drilling bit and the thickness of the coal particle layer increased under coal particle mass flow rate of 0.05 kg/s.

When the gas flowed into the drilling bit, a high-velocity strip formed at its axial center and a reverse velocity range appeared near its end when the coal particle mass flow rate was 0.02 kg/s. When the coal particle mass flow rate was 0.03 kg/s, the length of the strip in the high-velocity zone extended to 0.4 m and the zone became larger, while the range of the velocity zone decreased in the opposite direction. When the coal particle mass flow rate increased to 0.04 kg/s and 0.05 kg/s, respectively, the high-velocity zones extended to 0.5 m, and the strip widths were wider than those in the opposite direction, while the velocity zone slightly changed in the reverse direction.

(a)

(b)
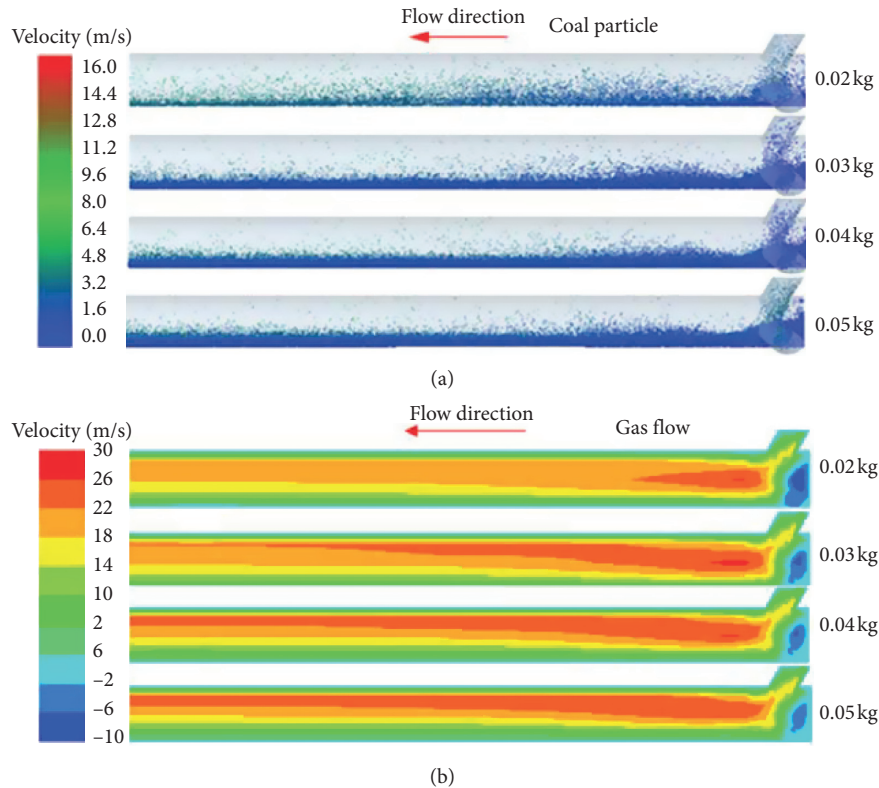
FIGURE 5: The coal-gas flow characteristic in drilling bit-rod integral structure 0~0.5 m under gas velocity of 20 m/s ($t = 3$ s).

(3) The coal-gas flow states at drilling bit-rod integral structure 0 m~0.5 m section are shown in Figure 6, when the gas velocity was 25 m/s at different coal particle mass flow rates.

When the coal particle mass flow rate was 0.02 kg/s, the movement of the coal particle in the drilling rod became more dispersed, and there was a small accumulation of coal particles at its end. At a coal particle mass flow rate of 0.03 kg/s, a typical pipe bottom flow appeared, and the accumulation of coal particles at the end of the drilling bit increased. The thickness of coal particles at the bottom of the pipe gradually decreased along the flow direction. When the coal particle mass flow rate was 0.04 kg/s, the bottom flow characteristics of the pipe strengthened. When the coal particle mass flow rate reached 0.05 kg/s, the accumulation of coal particle at the end of the drilling rod further increased.

A high-velocity strip formed at the axial center of the drilling bit when the gas flowed into it under coal particle mass flow rate of 0.02 kg/s. The high-velocity zone strip was distributed along the flow direction on the upper part of the drilling rod, and its width decreased gradually. There was a range of reverse velocity within a certain range near the end of the drilling bit. When the coal particle mass flow rate was 0.03 kg/s, the width of the strip in the high-velocity zone became wider than that under 0.02 kg/s, while the change in velocity zone in the opposite direction was not apparent. When the airflow flowed to 0.5 m in the flow direction, the coal particle mass flow rate increased to 0.04 kg/s and

0.05 kg/s, respectively, and the strip width of the high-velocity zone became wider than that of the former, while the reverse direction velocity zone was slightly decreased.

4.4. Coal Particle Flow in Drilling Rod at 4.5 m~5.0 m

(1) The states of coal-air flow at 4.5 m~5 m section of the drilling rod under different coal particle mass flow rates are as shown in Figure 7 at gas velocity of 15 m/s.

When the coal particle mass flow rate was 0.02 kg/s, a small amount of coal particles flew through this section, and some of them were suspended in motion. When the coal particle mass flow rate reached 0.03 kg/s, the number of coal particles increased. A small amount of coal particles was distributed on the upper part of the drilling rod. When the coal particles mass flow rate reached 0.04 kg/s, both the number of coal particles that flowed through this section and those suspended in the upper part of the drilling rod increased, and the bottom flow characteristics were obvious. When the coal particles mass flow rate reached 0.05 kg/s, the characteristics of the bottom flow of the pipe were more obvious, and the number of coal particles suspended in the upper part of the drilling rod slightly increased.

(2) The coal-air flow states of the 4.5 m~5 m section of the drilling rod under different coal particle mass flow rates are as shown in Figure 8 when the gas velocity was 20 m/s.

(a)

(b)
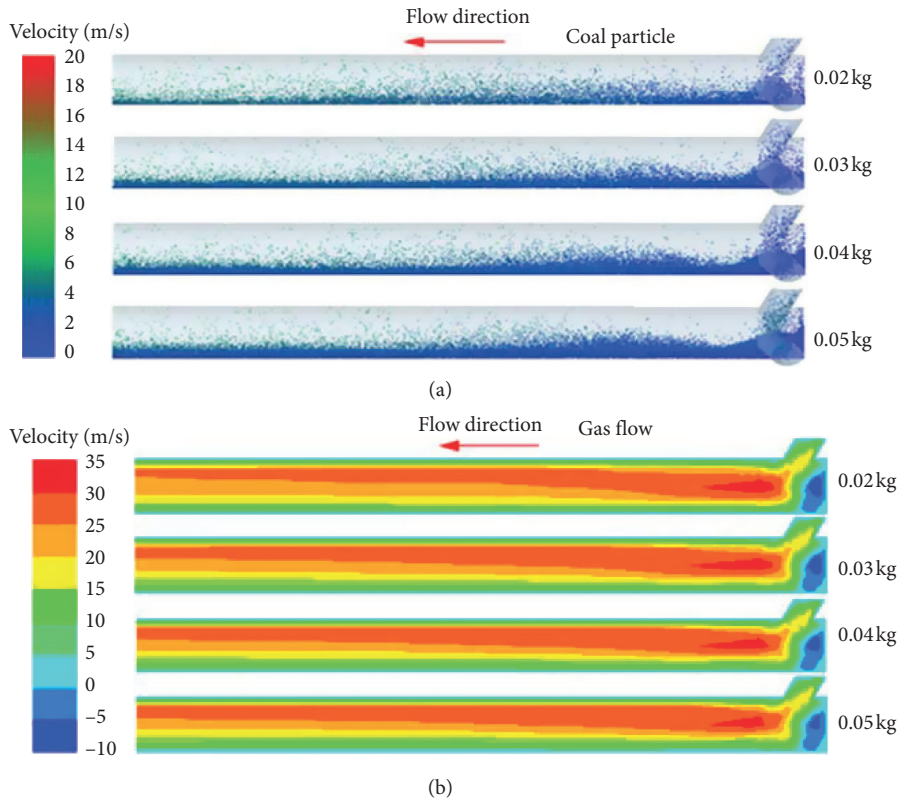
FIGURE 6: The coal-gas flow characteristic in drilling bit-rod integral structure 0~0.5 m under gas velocity 25 m/s ($t = 3$ s).
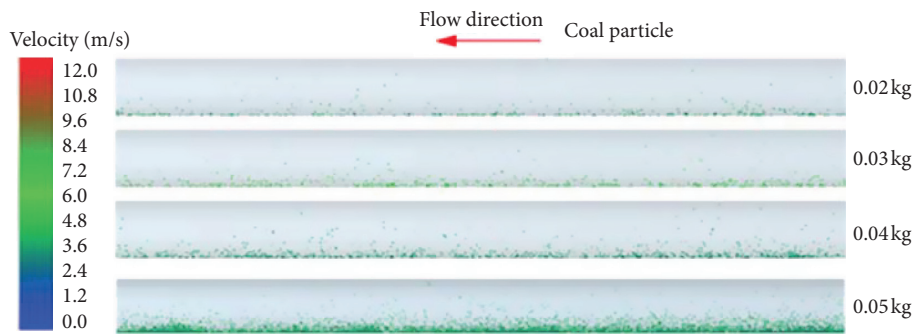
FIGURE 7: The coal-gas flow characteristic in drilling rod at 4.5~5.0 m under gas velocity 15 m/s ($t = 3$ s).
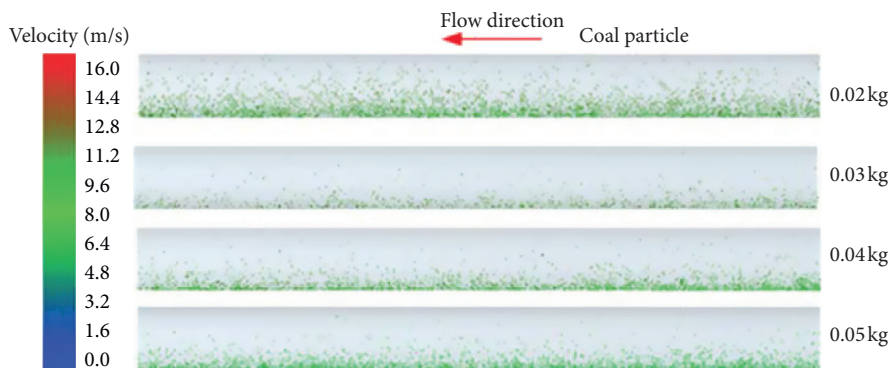
FIGURE 8: The coal-gas flow characteristic in drilling rod at 4.5~5.0 m under gas velocity of 20 m/s ($t = 3$ s).

When the coal particle mass flow rate was 0.02 kg/s, all the coal particles were approximately in suspension flow state and the coal particle velocity was around 10 m/s. When the coal particle mass flow rate reached 0.03 kg/s, the amount and velocity of coal particles flowing through this part decreased compared with those at 0.02 kg/s and the motion of coal particles was distributed in the middle and lower part of the drilling rod. When the coal particle mass flow rates were 0.04 kg/s and 0.05 kg/s, the amount of coal particles flowing through this part changed slightly, while the particle velocity increased.

(3) The coal-air flow states of the 4.5–5 m section of the drilling rod under different coal particle mass flow rates are as shown in Figure 9 when the gas velocity was 25 m/s.

When the coal particle mass flow rates were 0.02 kg/s and 0.03 kg/s, the coal particles in the drilling rod were in a suspended flow motion, and the high-velocity coal particle suspension motion was at the upper part of the drilling rod. When the coal particle mass flow rate reached 0.04 kg/s and 0.05 kg/s, the coal particles in the drill pipe were mostly in a suspended state, while a small quantity of low-velocity coal particles moved along the direction of the bottom of the rod, indicating a slight bottom flow. Figures 8–10 showed the flow patterns of coal particles in the 4.5 m–5 m section along the flow direction under different conditions. This section reflects the flow pattern after the coal particle flowed into the drilling rod after an acceleration distance of 4 m.

When the gas velocity was 15 m/s, the amount of coal particle at 0–0.5 m gradually increased with the coal particle mass flow rate that increased from 0.02 kg/s to 0.05 kg/s, while the energy obtained by a single coal particle decreased under the same gas velocity. When the coal particles reached the 4.5–5.0 m section, the coal particle velocity was higher and more evenly distributed on the drilling rod cross section when the coal particle mass flow rate was 0.02 kg/s. As the coal particle mass flow rate increased, the bottom flow characteristics became obvious and the coal particle velocity was lower. As the coal particle mass flow rate increases, the coal particle flow state characteristics at the tube bottom gradually strengthen. Only a part of high-velocity coal particle was distributed in the upper part of the drilling rod. When the gas velocity increased to 20 m/s and 25 m/s, respectively, the kinetic energy of a single coal particle increased and more coal particles accelerated to the suspension velocity. Therefore, the suspension characteristics of the coal particles increased with the increasing gas velocity in the range of 4.5–5 m for the drilling rod.

4.5. Gas Flow in the Drilling Bit-Rod Integral Structure of 0 m~0.5 m.
There were high-velocity area and reverse velocity area in the opposite direction of the 0–0.5 m section of the drilling rod, as shown in Figure 10. The three fluid holes of the drilling bit were evenly distributed along the circumference, and the coal-gas flowed into the drilling bit and converged at the axis of the drill rod, forming a high-velocity

area. The cross-sectional area of the drilling bit fluid hole was smaller than that of the drilling rod. When the gas flowed into the drilling bit, a secondary flow was generated in the drilling bit by part of the gas flow. Therefore, a reverse velocity area formed at the center of the end. The range of high-velocity area expanded with increase in coal particle mass flow rate, while the range of the reverse velocity area decreased.

Along the flow direction, the high-velocity strip was in the upper region of the drilling rod. This was because the coal particles flowed into the drilling bit at lower velocity and accelerated due to the drag and gravitational forces. In the zone of 0 m to 0.5 m, there was a bottom flow for the self-gravity. The flow channel of the gas moved upward while the high-velocity area moved forward along the flow direction with increasing coal particles as shown in Figures 6–8. At the same gas velocity, with continuous acceleration of coal particles, the flow pattern transitioned from bottom flow to uniform suspended flow. Consequently, the impact of the bottom coal on the air flow gradually reduced, and the high-velocity band of gas flow gradually disappeared while the distribution of the air flow field changed to the distribution characteristics of "high center, low wall." As the coal particle mass flow rate increased, its influence on the air flow gradually increased within 0 m~0.5 m, leading to extension and expansion of the range of high-velocity zone along the direction of flow. The range of the reverse velocity area gradually reduced for the coal particle mass flow rate of the same gas velocity and thus increased the influence of coal particle on the gas flow field and weakened the secondary flow intensity of the gas flow at the end of the drilling bit. Therefore, the influence of coal particle on the gas phase flow field cannot be neglected.

4.6. Coal Flow in Drilling Bit-Rod Integral Structure of 0 m~5 m.
To further analyze the particle flow characteristics of the drilling bit-rod integral structure of 0~5 m, four aspects including the proportion, velocity, length of the bottom flow characteristic, and the acceleration distance of the suspension of coal particles at different locations were studied.

4.6.1. Proportion of Coal Particle at Different Locations.
The coal particle number distribution along the flow direction could reflect the acceleration and movement characteristics of coal particles under this condition, as well as the ability of transporting coal particles under different gas velocities, and could also provide the basis for determining the flow pattern of coal particle. The ratio of the number of coal particles at different positions is defined as the ratio of the number of coal particles at a certain position to the total number of coal particles near the drilling bit under steady flow. The statistical results are as shown in Figure 11.

Figure 11 shows that when the coal particle mass flow rate was 0.02 kg/s, the proportion of coal particle in the 0–0.5 m section to the total coal particle was 44.67% under gas velocity of 15 m/s. When the gas velocity increased to 20 m/s, the proportion of coal particle decreased to 32.48%,

Flow direction

Velocity (m/s)   Coal particle

0.02 kg

0.03 kg

0.04 kg

0.05 kg
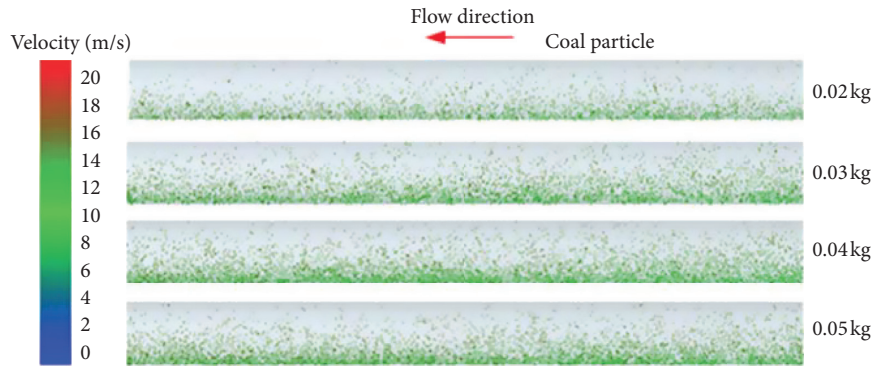
FIGURE 9: The coal-gas flow characteristic in drilling rod 4.5~5.0 m under gas velocity 25 m/s ($t = 3$ s).

High velocity area

Second flow area
(reverse velocity area)

Flow direction
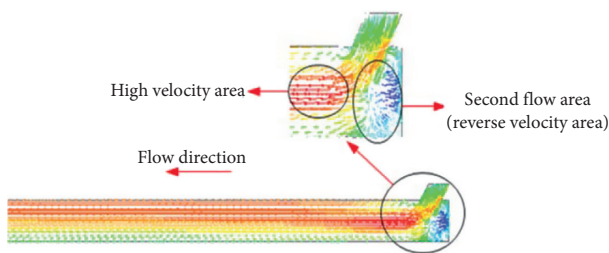
FIGURE 10: The gas phase flow vector of drilling bit-rod integral structure of 0~0.5 m.

which was 27.27% lower than that at 15 m/s. At a gas velocity increase of 25 m/s, the proportion of coal particles in the 0 m~0.5 m section was 20.92% in comparison to the total coal particles. This was also a reduction of 53.17% and 35.60% compared with 15 m/s and 20 m/s, respectively.

Figure 11 shows that when the coal particle mass flow rate was 0.03 kg/s, the proportion of coal particle in the 0 m~0.5 m section to the total coal particle was 57.98% under a gas velocity of 15 m/s. On the one hand, when the gas velocity increased to 20 m/s, the proportion of coal particle decreased to 40.72%, which was 29.27% lower than that at 15 m/s. On the other hand, when the gas velocity increased to 25 m/s, the proportion of coal particle in the 0 m~0.5 m section was 28.55% of the total coal particle. Thus, the proportion of coal particles reduced by 50.7% and 29.89% compared with those under 15 m/s and 20 m/s, respectively.

When the coal particle mass flow rate was 0.04 kg/s, the proportion of coal particle in the 0 m~0.5 m section to the total coal particle was 76.49% under a gas velocity of 15 m/s. When the gas velocity increased to 20 m/s, the proportion of coal particle decreased to 41.34%, which was 45.96% lower than that at 15 m/s; when the gas velocity increased to 25 m/s, the proportion of coal particles in the 0 m~0.5 m section to the total coal particles was only 31.83%. Thus, the proportion of coal particles reduced by 58.38% and 22.98% compared with those under 15 m/s and 20 m/s, respectively.

When the coal particle mass flow rate was 0.05 kg/s, the proportion of coal particles in the 0 m~0.5 m section to the total coal particle was 80.30% under gas velocity of 15 m/s. When the gas velocity increased to 20 m/s, the proportion of coal particles decreased to 46.0%, which was 42.71% lower

than that at 15 m/s; when the gas velocity increased to 25 m/s, the proportion of coal particles in the 0 m~0.5 m section to the total coal particle was only 34.50%. Therefore, the proportion of coal particles reduced by 57.04% and 25.01% compared with those at 15 m/s and 20 m/s, respectively.

Coal particle distribution of drilling bit-rod integral structure in the 0 m~0.5 m section of exhibited the following characteristics: the lower the gas velocity, the greater the amount of coal particles distributed in the drilling bit in 0 m~0.5 m section under the same coal particle mass flow rate, and the distribution of coal particles gradually decreased along the flow direction. The coal particle in the 0 m~0.5 m section was significantly reduced, and the distribution of coal particle along the flow direction tended to be balanced with the increase of gas velocity. The higher the gas velocity, the higher the the kinetic energy per unit mass of coal particles; thus, the coal particle moved fast inside the drilling rod.

4.6.2. Velocity of Coal Particles at Different Locations. The velocity distribution of coal particles at the same gas velocity and different coal particle mass flow rates is as shown in Figures 12–15.

Figure 12 shows that part of the coal particle velocity was in the range of 3 m/s and only a small number of coal particles had a velocity of 3 m/s to 4.5 m/s in the 0 m to 0.5 m section having a gas velocity of 15 m/s. In the 1 m~3 m section, the velocity of most coal particle was about 6 m/s, and the velocity of a few coal particles reached 7.5 m/s. Within the 3 m~5 m section, the velocity of coal particles was mostly above 6 m/s, and the highest velocity realized was about 9 m/s.

When the gas velocity increased to 20 m/s, a small quantity of coal particles had a velocity of less than 3 m/s in the 0–0.5 m section. The velocity of coal particles was mainly above 6 m/s at 2 m, and it increased to 12 m/s at 5 m.

When the gas velocity increased to 25 m/s, the number of coal particles having a velocity of less than 3 m/s was further reduced in the 0 m to 0.5 m section. The velocity of coal particle was more than 6 m/s at 2 m, and it increased to more than 12 m/s at 5 m.

Figure 13 shows that when the gas velocity was 15 m/s, the coal particle velocity was less than 2.25 m/s in the
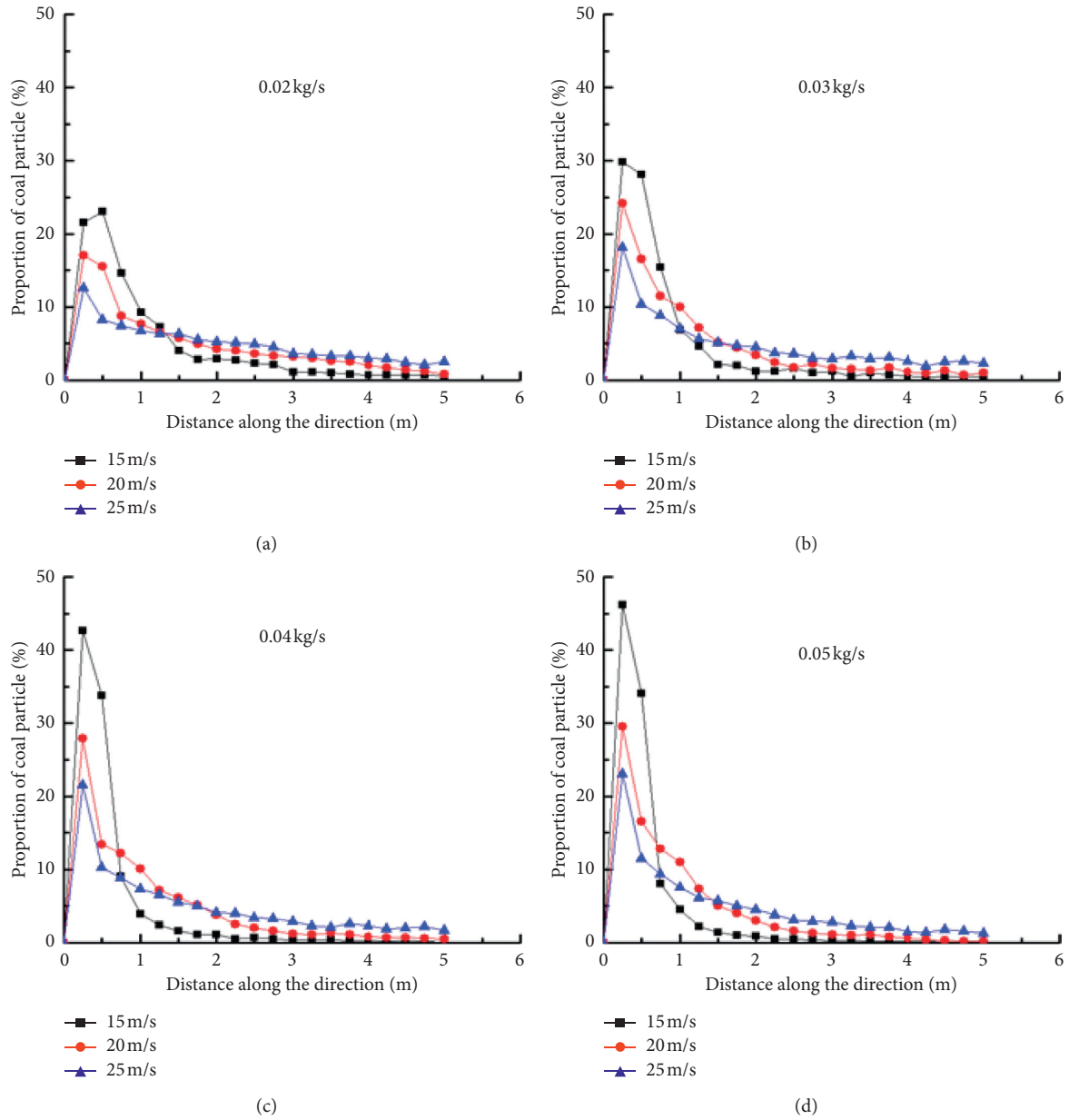
FIGURE 11: Particle number distribution along the flow direction.

0 m~0.5 m section; in the 1–3 m section, the velocity of most of the coal particles was about 6 m/s, and a small quantity of the coal particle had a velocity of 7.5 m/s. In the 3~5 m section, the velocity of coal particle was mostly above 6 m/s, and the highest velocity realized was about 9 m/s.

When the gas velocity increased to 20 m/s, only a small quantity of coal particle velocity was within the range of 3 m/s in the 0 m~0.5 m section. At the position of 3 m, the coal particles velocity was mostly above 6 m/s, while at 5 m the velocity of coal particle increased to 9 m/s.

When the gas velocity increased to 25 m/s, the number of coal particles having a velocity of 3 m/s reduced further in the 0–0.5 m section, while in the 0–2 m section the coal particle accelerated to above 6 m/s at about 2.25 m. All the coal particle velocities increased to above 12 m/s at 5 m.

Figure 14 shows that when the gas velocity was 15 m/s, the coal particles velocity was less than 1.6 m/s in the 0 m~0.5 m section, while a few particles velocities increased to 6 m/s; in the 1 m~2.75 m section, most of the coal particles velocity was approximately 3 m/s, and the velocity of most of the coal particle s was below 6 m/s at 5 m.

When the gas velocity increased to 20 m/s, the coal particle velocity was within the range of 6 m/s in the 0 m~0.5 m section. At 2.75 m, the velocity of the coal particles was mostly above 6 m/s and their velocity increased to 9 m/s at 5 m.

When the gas velocity increased to 25 m/s, most of the coal particles velocity was within 9 m/s in the 0 m–0.5 m section, and their velocity was above 6 m/s at about 2.5 m. However, all the coal particle velocities had increased to more than 11 m/s at 5 m.
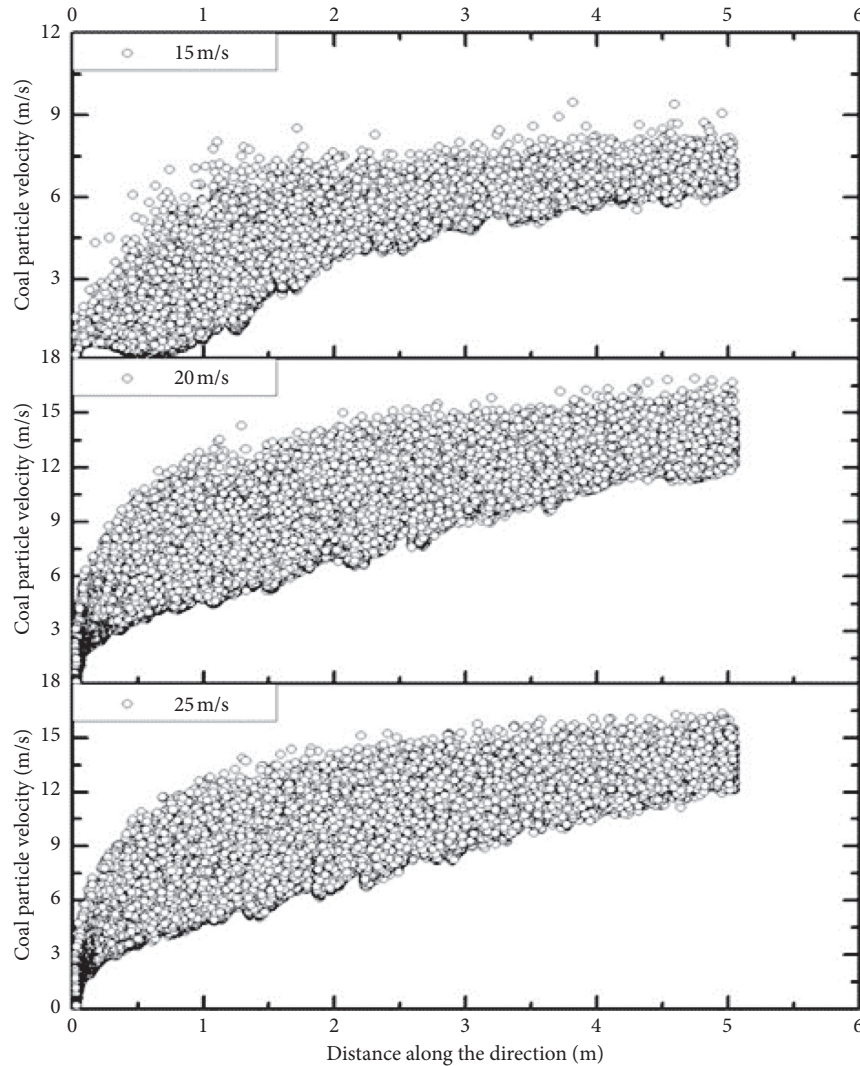
FIGURE 12: Coal particle velocity distribution along the flow direction with particle generation rate of 0.02 kg/s ($t = 3.0$ s).

According to Figure 15, when the gas velocity was 15 m/s, the coal particle velocity was less than 1.6 m/s in the 0 m~0.5 m section, while the velocity of a few particles increased to 6 m/s; in the 1 m~2.75 m section, most of the coal particles had a velocity of 3 m/s, and their velocity in this section was mostly below 6 m/s at 5 m.

At a gas velocity of 20 m/s, the coal particle velocity was within the range of 6 m/s in the 0 m~0.5 m section. At 2.75 m, the velocity of coal particles was mostly above 6 m/s and at 5 m their velocity increased to 9 m/s.

When the gas velocity increased to 25 m/s, most of the coal particle velocity was within 9 m/s in the 0 m–0.5 m zone, and t velocity was above 6 m/s at 2.5 m. All the coal particle velocities increased to more than 11 m/s at 5 m.

4.6.3. Proportion of Coal Particles at Different Locations. Quantitative characterization of the number of coal particles having the same velocity in the 0 m~5 m section of bit-drill rod can quantify the acceleration characteristics of coal particle under different conditions. The ratio of coal particle

velocity at different positions was defined as the ratio of coal particle number at a certain velocity at a position to the total number of coal particles in the 0 m–5 m section, as shown in Figure 16.

Figure 16 depicts the fact that when the coal particle mass flow rate was 0.02 kg/s, the quantity of coal particles with a velocity of 0 m/s to 6 m/s had about 2.58% of the total coal particle with a gas velocity of 15 m/s. When the gas velocity increased to 20 m/s, the proportion of coal particle with velocity of 0 m/s to 6 m/s increased to 30.24%, which was equivalent to an increment of 1071.46%. When the gas velocity reached 25 m/s, the proportion of coal particles with a velocity of 0 m/s~6 m/s increased to 58.35%, which was an increment of 92.90% compared to the gas velocity of 20 m/s.

When the coal particle mass flow rate was 0.03 kg/s, 2.16% of the amount of coal particle with velocity 0 m/s to 6 m/s had a gas velocity of 15 m/s. When the gas velocity reached 20 m/s, the proportion of particle with velocity with 0–6 m/s increased to 18.74%, which was an increment of 765.58%. When the gas velocity increased to 25 m/s, the proportion of coal particle with a velocity of 0 m/s~6 m/s
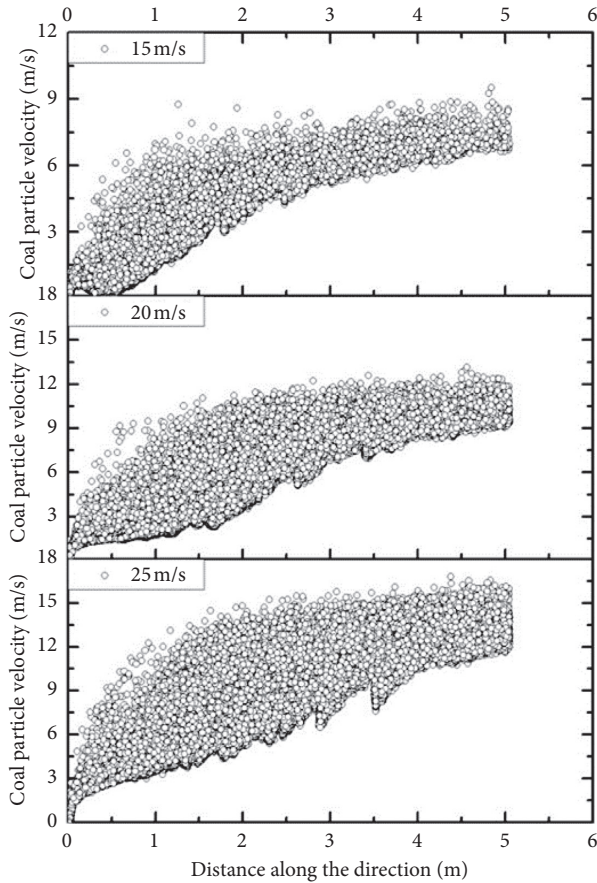
FIGURE 13: Coal particle velocity distribution along the flow direction with particle generation rate of 0.03 kg/s ($t = 3.0$ s).

FIGURE 14: Particle velocity distribution along the flow direction with particle generation rate of 0.04 kg/s ($t = 3.0$ s).

increased to 43.02%, which was equivalent to an increment of 129.56% compared to that of gas velocity of 20 m/s.

When the coal particle mass flow rate was 0.04 kg/s, of total amount of coal particle with velocity of 0 m/s to 6 m/s, about 1.70% had a gas velocity of 15 m/s. When the gas velocity increased to 20 m/s, the proportion of particle with velocity of 0 m/s to 6 m/s increased to 15.56%, representing an increment of 813.59%. When the gas velocity reached 25 m/s, the proportion of coal particle with velocity of 0 m/s~6 m/s increased to 36.48%, which was an increment of 134.56% compared to the gas velocity of 20 m/s.

When the coal particle mass flow rate was 0.05 kg/s, the amount of coal particle with a velocity 0 m/s to 6 m/s had 0.88% of the total coal particle gas velocity of 15 m/s. When the gas velocity reached 20 m/s, the proportion of particle with velocity of 0 m/s to 6 m/s had the total coal particle that increased to 10.85%, which was an increase of 1132.96%. When the gas velocity reached 25 m/s, the proportion of coal particle with 0 m/s~6 m/s in the total coal particle increased to 31.89%, which was an increment of 193.88% compared to the gas velocity of 20 m/s.

4.6.4. Bottom Flow Length and Acceleration Suspension Distance. The acceleration of coal particle to the suspension velocity under the action of gas was the prerequisite for suspension flow. Correspondingly, the coal particle underwent an accelerated motion at the bottom of the drill rod. As the coal particle velocity increased, the bottom flow characteristics disappeared and gradually changed to suspension flow. Bottom flow length, which is the distance from the end of the drill bit when the significant bottom flow characteristic appears as it disappears along the flow direction (0 m~5 m), was defined. Suspension acceleration distance was defined as the coal particle flow distance from where it enters the drill rod to where the particle velocity reaches the suspension velocity under different working conditions. The bottom flow length and suspension acceleration distance under different conditions are as shown in Figures 17(a) and 17(b), respectively.

Figure 17 depicts the fact that the bottom flow length was about 2.25 m and 4.81 m when the coal particle mass flow rate was 0.02 kg/s and 0.03 kg/s with gas velocity 15 m/s, respectively. When the coal particle mass flow rate increased to 0.04 kg/s and 0.05 kg/s, there was still a significant bottom flow at 5 m. When the gas velocity increased to 20 m/s, the characteristic of bottom flow reduced significantly, and the bottom flow length was about 1.7 m, 2.37 m, 3.27 m, and 3.68 m when the coal particle mass flow rate was 0.02 kg/s, 0.03 kg/s, 0.04 kg/s, and 0.05 kg/s, respectively. When the gas velocity was 25 m/s, the effect of bottom flow length was little under coal particle flow rate of 0.02 kg/s and 0.03 kg/s and
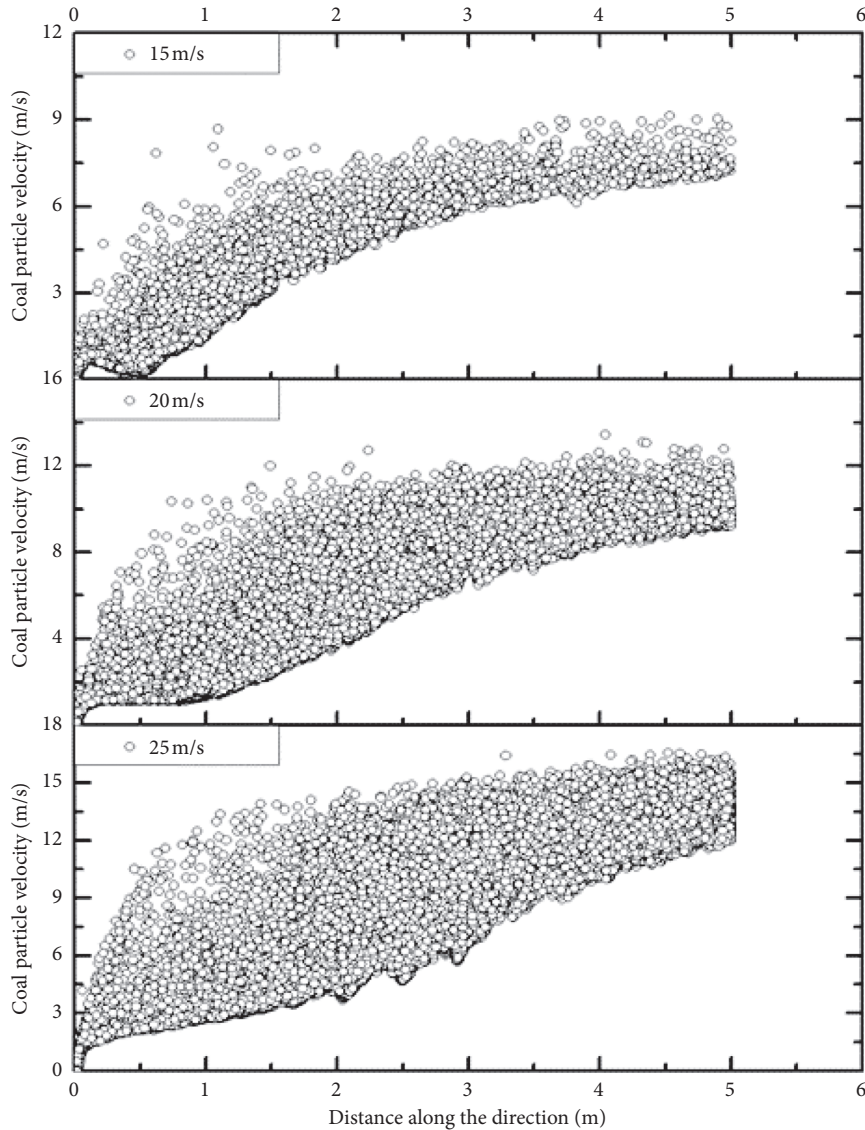
Figure 15: Particle velocity distribution along the flow direction with particle generation rate of 0.05 kg/s ($t = 3.0$ s).

reduced to 1.58 m and 2.11 m, respectively. Conversely, the bottom flow length under coal particle flow rate 0.04 kg/s and 0.05 kg/s had greater influence, with reduction to 2.74 m and 2.85 m, respectively.

The coal particle flowed into the drilling bit and moved along the drill rod bottom because the gas velocity was too low to timely accelerate the coal particles under the gas velocity of 15 m/s. The coal particle velocity distribution in the 0 m–0.5 m part was within 3 m/s, 2.25 m/s, 1.6 m/s, and 0.93 m/s, respectively, which were far less than the suspension velocity of coal particle (6 m/s) when the coal particle mass flow rates were 0.02 kg/s, 0.03 kg/s, 0.04 kg/s, and 0.05 kg/s, as shown in Figures 5 to 7, and the proportions of coal particle in this section were 44.67%, 57.98%, 76.49%, and 80.30%, respectively. The more the quantity of particles,

the more the particle-particle interaction, leading to a remarkable agglomeration effect of coal particle [20], thus increasing the particle suspension velocity, particle gravity, and the bottom flow characteristics. Therefore, the bottom flow characteristics of coal particle became more and more pronounced with the coal particle mass flow rate increasing at gas velocity of 15 m/s.

When the gas velocity reached 25 m/s, the initial drag force provided by the gas flow to the coal particle increased by 55% compared with that of gas velocity of 20 m/s, and the acceleration energy of the coal particle increased. Therefore, the coal particle accelerated faster under lower coal particle mass flow rate, and the proportion of higher coal particle velocity increased, especially the proportion of coal particle velocity higher than the suspension velocity that increased to
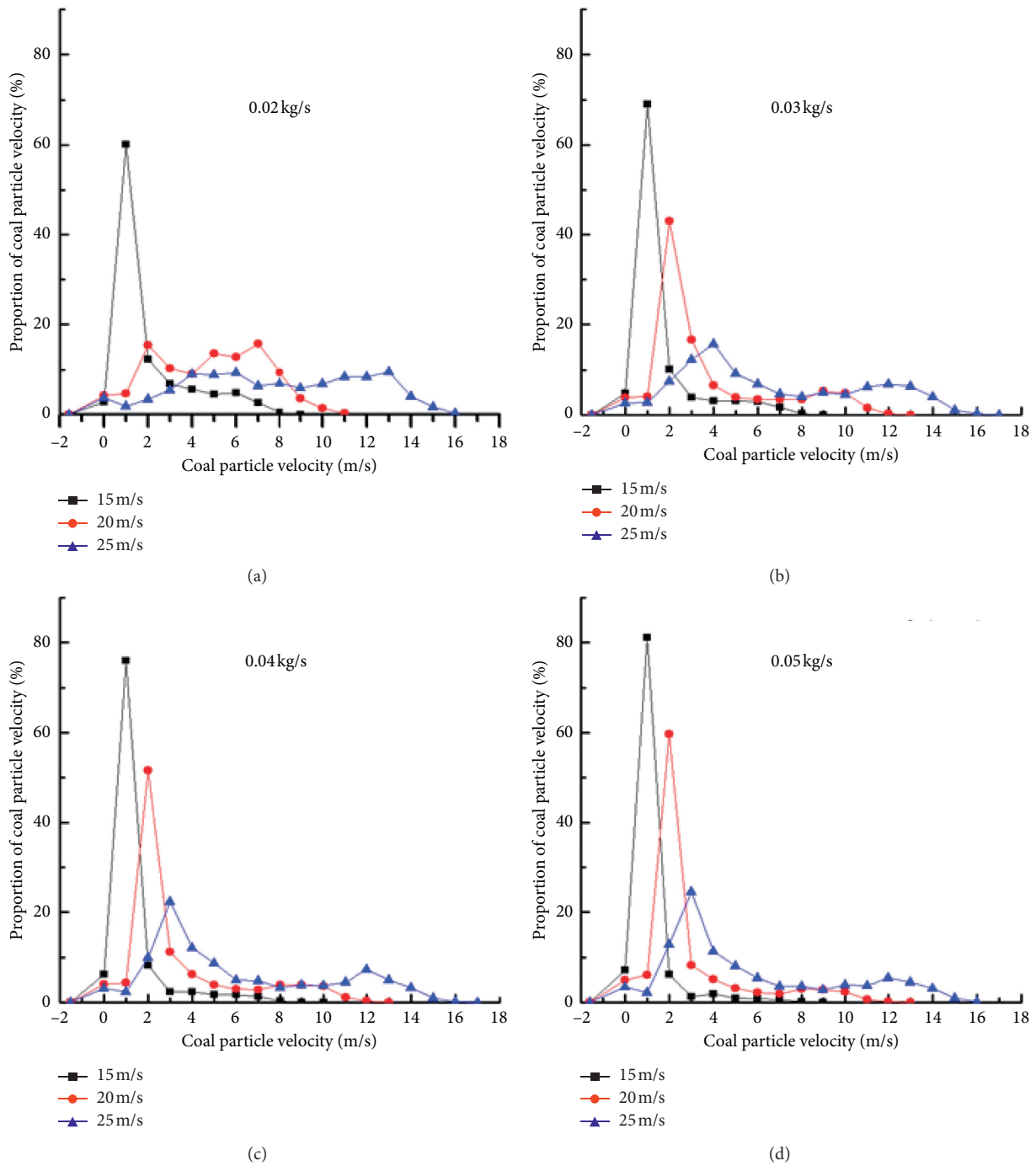
FIGURE 16: Percentage of different particle velocities.

58.35%, 43.01%, 36.49%, and 31.89%, while the proportion of coal particle fell to 20.92%, 28.55%, 31.83%, and 24.50% correspondingly. Therefore, the bottom flow characteristics of coal particle were further weakened compared with 20 m/s.

It is noteworthy that there was an area of high coal particle thickness in the 0–0.5 m section of bit-drill rod with obvious bottom flow characteristics. After passing through this area, some of the coal particles quickly changed into a suspension state because an increased coal particle layer thickness was equivalent to a reduction in the

flow area of the gas flow, leading to an increase of the gas velocity. At the same time, the drag between the coal particle and gas increased, and the rate of acceleration increased. Secondly, the increase in the airflow velocity, according to Bernoulli equation, increased the static pressure of the lower part of the drill pipe b than that in the upper part. The pressure gradient force promoted the upward movement of coal particles. Suspended coal particle also flowed in the upper part of the drill rod. Therefore, the bottom flow characteristics of coal particle in the drill
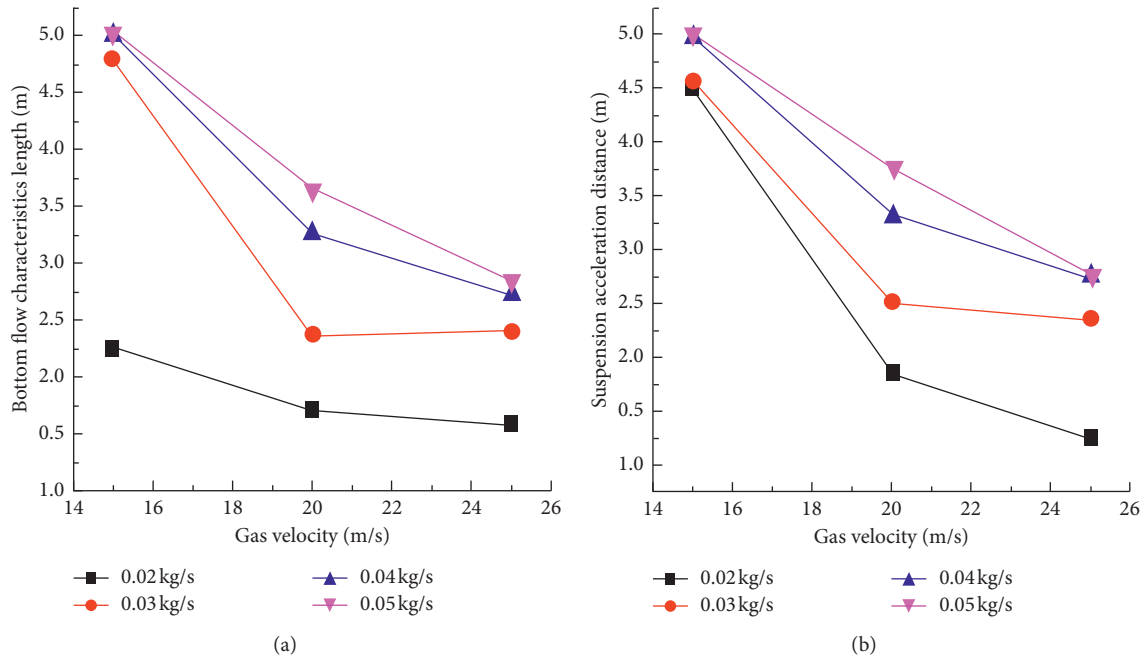
FIGURE 17: The characteristic length of bottom flow and the suspension acceleration distance.

rod decreased in the 0–0.5 m section with increasing gas velocity.

5. Conclusions

In this work, the CFD-DEM coupled numerical simulation method is applied to the special PDC drill-drill pipe flow structure. The following conclusions are drawn from the results:

(1) For the gas phase, there was a reverse velocity zone at the PDC bit. With increasing gas velocity, the reverse velocity zone gradually shrinked; and there was a high-velocity band in the drill rod. As the gas velocity increased, the high-velocity strip gradually became apparent.

(2) For the particle phase, at the PDC bit, there was an obvious bottom flow characteristic, and there was an area of the highest layer thickness in the drill rod part. At the same gas velocity, the area of the highest thickness layer advanced with the increasing of coal particle mass flow rate.

(3) The velocity of coal particle increased rapidly with the gas velocity, the bottom flow characteristics of coal particle weakened, and the suspension flow gradually appeared.

(4) For the application of sampling method based on negative pressure pneumatic conveying, the values of gas velocity and coal particle mass flow rate should be determined according to the actual engineering conditions for successful sampling.

It is noteworthy that the particle size of coal or rock drilling particle was distributed in 0.25~3 mm according to the hardness of the coal or rock formation in engineering practices. However, because the particles number is an important factor affecting the calculation efficiency of the CFD-DEM coupled simulation method and the particle size distribution of coal particles obtained in the field, a fixed particle size of 2 mm was selected in this study. The gas-solid flow characteristics under different particle size distributions will be paid more attention subsequently.

Data Availability

The raw/processed data required to reproduce these findings cannot be shared at this time as the data also form part of an ongoing study.

Conflicts of Interest

The authors declare that they have no conflicts of interest regarding this work.

Acknowledgments

References

[1] N. Huber and M. Sommerfeld, "Modelling and numerical calculation of dilute-phase pneumatic conveying in pipe systems," *Powder Technology*, vol. 99, no. 1, pp. 90–101, 1998.

[2] S. Laín and M. Sommerfeld, "Numerical calculation of pneumatic conveying in horizontal channels 645 and pipes: detailed analysis of conveying behaviour," *International Journal of Multiphase Flow*, vol. 39, no. 646, pp. 105–120, 2012.

[3] M. Sommerfeld and S. Lain, "Parameters influencing dilute-phase pneumatic conveying through pipe systems: a computational study by the Euler/Lagrange approach," *The Canadian Journal of Chemical Engineering*, vol. 93, no. 1, pp. 1–17, 2015.

[4] N. A. Patankar and D. D. Joseph, "Modeling and numerical simulation of particulate flows by the Eulerian-Lagrangian approach," *International Journal of Multiphase Flow*, vol. 27, no. 10, pp. 1659–1684, 2001.

[5] M. Mezhericher, T. Brosh, and A. Levy, "Modeling of particle pneumatic conveying using DEM and DPM methods," *Particulate Science and Technology*, vol. 29, no. 2, pp. 197–208, 2011.

[6] Y. Tsuji, T. Kawaguchi, and T. Tanaka, "Discrete particle simulation of two-dimensional fluidized bed," *Powder Technology*, vol. 77, no. 1, pp. 79–87, 1993.

[7] S. Akhshik, M. Behzad, and M. Rajabi, "CFD-DEM simulation of the hole cleaning process in a deviated well drilling: the effects of particle shape," *Particuology*, vol. 25, pp. 72–82, 2016.

[8] S. Akhshik, M. Behzad, and M. Rajabi, "CFD-DEM approach to investigate the effect of drill pipe rotation on cuttings transport behavior," *Journal of Petroleum Science and Engineering*, vol. 127, pp. 229–244, 2015.

[9] H. Li, Y. Li, F. Gao, Z. Zhao, and L. Xu, "CFD-DEM simulation of material motion in air-and-screen cleaning device," *Computers and Electronics in Agriculture*, vol. 88, pp. 111–119, 2012.

[10] F. Dai, X. Song, W. Zhao et al., "Motion simulation and test on threshed grains in tapered threshing and transmission device for plot wheat breeding based on CFD-DEM," *International Journal of Agricultural and Biological Engineering*, vol. 12, no. 1, pp. 66–73, 2019.

[11] H. Kruggel-Emden and T. Oschmann, "Numerical study of rope formation and dispersion of non-spherical particles during pneumatic conveying in a pipe bend," *Powder Technology*, vol. 268, pp. 219–236, 2014.

[12] A. Kumar, S. Gupta, K. Pal, and D. R. Kaushal, "CFD modeling for pressure drop in pneumatic conveying through pipe bend," *International Journal of Advances in Engineering Sciences*, vol. 4, no. 3, pp. 16–19, 2014.

[13] M. W. Korevaar, J. T. Padding, M. A. Van Der Hoef, and J. A. M. Kuipers, "Integrated DEM-CFD modeling of the contact charging of pneumatically conveyed powders," *Powder Technology*, vol. 258, pp. 144–156, 2014.

[14] I. Lecreps, O. Orozovic, T. Erden, M. G. Jones, and K. Sommer, "Physical mechanisms involved in slug transport and pipe blockage during horizontal pneumatic conveying," *Powder Technology*, vol. 262, pp. 82–95, 2014.

[15] B. Shao, Y. Yan, X. Yan, and Z. Xu, "A study on non-spherical cuttings transport in CBM well drilling by coupled CFD-DEM," *Engineering Applications of Computational Fluid Mechanics*, vol. 13, no. 1, pp. 579–590, 2019.

[16] F. Zhou, S. Hu, Y. Liu, C. Liu, and T. Xia, "CFD-DEM simulation of the pneumatic conveying of fine particles through a horizontal slit," *Particuology*, vol. 16, pp. 196–205, 2014.

[17] J. Wei, H. Zhang, Y. Wang, Z. Wen, B. Yao, and J. Dong, "The gas-solid flow characteristics of cyclones," *Powder Technology*, vol. 308, pp. 178–192, 2017.

[18] A. Di Renzo and F. P. Di Maio, "Comparison of contact-force models for the simulation of collisions in DEM-based granular flow codes," *Chemical Engineering Science*, vol. 59, no. 3, pp. 525–541, 2004.

[19] G. A. Bokkers, M. Van Sint Annaland, and J. A. M. Kuipers, "Mixing and segregation in a bidisperse gas-solid fluidised bed: a numerical and experimental study," *Powder Technology*, vol. 140, no. 3, pp. 176–186, 2004.

[20] R. Naveh, N. M. Tripathi, and H. Kalman, "Experimental pressure drop analysis for horizontal dilute phase particle-fluid flows," *Powder Technology*, vol. 321, pp. 355–368, 2017.

Research Article

Type I Fracture Toughness Test of Rock-like Materials Based on the Particle Flow Method

Ling Yue,[1] Bangyong Yu [ID],[1] Chengxi Zhao,[1] Fei Guo,[2,3] and Fei Huang[4]

[1]*Institute of Construction Engineering, Changzhou Vocational Institute of Engineering, Changzhou 213164, Jiangsu, China*
[2]*Ministry of Education Key Laboratory of Geological Disaster of Three Gorges Reservoir Area, China Three Gorges University, Yichang 443002, Hubei, China*
[3]*National Field Observation and Research Station of Landslides, Three Gorges Reservoir Area of Yangtze River, China Three Gorges University, Yichang 443002, China*
[4]*China Design Group Co., Ltd., Nanjing 210014, Jiangsu, China*

Correspondence should be addressed to Bangyong Yu; yby_cumt@126.com

In order to investigate the feasibility and reliability of the three-dimensional particle flow method in simulating the type I fracture toughness test, four types of numerical samples were established by particle flow code PFC^{3D}: straight crack three-point bending (SC3PB), edge cracked flattened semicircular disc (ECFSD), cracked chevron notched Brazilian disc (CCNBD), and edge cracked flattened ring (ECFR). Three models with different strength parameters (group A, group B, and group C) were established for each type, in which group A parameters are obtained from the concrete model, group B parameters are applied for simulating marble, and group C parameters are for granite. The type I fracture toughness and the failure form of each model are obtained by conducting the numerical test, and the curves of load versus displacement of loading point are recorded. The numerical test results show that, with the same strength parameter, the maximum difference in test results of each specimen type is 0.39 MPa·m$^{1/2}$. The K_{IC} of ECFR specimen is 0.13–0.28 MPa·m$^{1/2}$ smaller than that of CCNBD specimen, and the K_{IC} of ECFSD specimen is slightly higher than that of CCNBD sample. The K_{IC} of SC3PB specimen is 0.06–0.21 MPa·m$^{1/2}$ smaller than that of the CCNBD sample. When the loading rate is less than 0.01 m/s, the effect of loading rate on fracture toughness can be reduced to less than 0.1 MPa·m$^{1/2}$.

1. Introduction

The research of theoretical and laboratory test for type I fracture toughness K_{IC} of rock materials is relatively mature [1]. Typical test methods include three-point bending test, compact tensile test, and Brazilian splitting test, and the specimen types of SC3PB, CCNBD, and SR are commonly used.

Zhang et al. [2] found that the fracture toughness of the sample without notch is higher, and the discreteness in results is obtained. Cui et al. [3] reviewed the testing methods of type I fracture toughness of rocks, compared the results by different methods, and explained the causes of these differences. Wei et al. [4] think that the results of three-point bending test are more stable and reliable, and it

is recommended to use the formula proposed by ASTM. Ayatollahi et al. [5] found that the larger the diameter specimen, the higher the type I fracture toughness. The research results of Meng et al. [6] and Yang et al. [7] show that as the center angle of the platform Brazil sample increases, the failure mode becomes complex. The most appropriate platform angle is 20°. Huang et al. [8, 9] study the influence of different particle sizes on load-displacement curves and failure modes by PFC^{2D}. The results show that the generation of secondary cracks is mainly affected by particle sizes. The size effect in particle flow software simulation has been studied by Wong et al. [10]. It was found that the increase of particle size would cause the increment in fracture toughness and crack initiation stress. The deformation characteristics of sandstone and granite are

researched under different stress path by Peng et al. [11–14], Wang et al. [15], and Shang et al. [16], and the energy characteristics during crack propagation are studied. It is found that the most sensitive parameter for stage identification is the volumetric strain. With the increment of confining pressure, the development and connection direction of cracks are inhibited, and the length of the final fracture surface decreases. The test process and results of SR and CCNBD specimens are studied by Cui et al. [17, 18]. The results suggest significant size effects of CCNBD specimens. As the specimen diameters increase, the variance in fracture toughness K_{IC} of SR and CCNBD specimen becomes smaller. The facture surface of SR specimen is rougher than that of CCNBD. It is also found that fracture toughness test results can be more consistent by the specimen with larger diameter than the ISRM suggested "minimum effective diameter 75 mm." Based on the boundary effect theory, the fracture toughness of rock is studied by Guan et al. [19]. The real material parameters without size effect of different rock types are constructed, and the results are used to predict the fracture trend.

Experimental study on the fracture toughness of CCNBD specimen and the size effect was conducted by Wu et al. It is proposed that the results can be modified by geometric shape function, and then the real fracture toughness of rock can be obtained. In semicircular bending (SCB) test, the support type influence on rock fracture toughness is researched by Bahrami et al. [20]. The results of finite element method and laboratory tests show that different support types and the friction between the specimen and the bottom supports have great influence on results. The fracture toughness K_{IC} of lapilli-ash tuff is researched by Wong et al. [21] with two typical semicircular bending specimens. The fracture toughness K_{IC} measured by semicircular bending (SCB) method is found to be lower than that using cracked chevron notched semicircular bending (CCNSCB) method. The CCNBD method produces more scattered results.

In laboratory tests of rock fracture toughness K_{IC}, the sample processing is relatively difficult, and the test results are scattered. Therefore, numerical simulation method is widely used to test rock fracture toughness. Most of the numerical tests are simulated by two-dimensional software, and three-dimensional numerical calculation method has not been widely discussed. In this study, four types of sample are selected, and three-dimensional particle flow numerical simulation is used to test the type I fracture toughness of the samples. The results are compared and analyzed, which provides a reference for numerical test of fracture toughness.

2. Establishing a Numerical Model

2.1. Microparameters of the Model. Particle flow software PFC is widely used to simulate the deformation and failure process of elastic-plastic materials, such as rock, soil, and concrete, which can show the mechanical properties and failure mechanism from a micro perspective. By adjusting the parameters of particle and bond model, the mechanical characteristics of numerical model can be similar to actual

materials. Failure process can be obtained by monitoring the number and location of microcracks and the stress in model. In order to study the applicability of numerical simulation in rock materials with different strength, three groups of micro parameters (group A, B, and C) are selected for calculation and analysis (see Tables 1–3), among which the strength parameters are lowest in group A and highest in group C.

The parameters in group A are calibrated according to the results of direct shear test in the laboratory. The parameters in group B are the micro parameters for marble taken by Huang et al. [22]. The parameters of group C are modified based on the Brazil split test curve for granite. The uniaxial compressive strength of numerical models can be used to calibrate parameters, and the test results show that the strength is 78.4 MPa with group A parameters, 106.8 MPa with group B parameters, and 142.1 MPa with group C parameters.

As PFC^{2D} is used in reference [17], the rationality of micro parameters in three-dimensional particle flow simulation needs to be further tested and modified. The details of parameter calibration in group A are as follows:

(1) Mix cement, sand, and water evenly by the mass ratio of $1:1:0.4$, put them into a cubic mold sized $15 \, cm \times 15 \, cm \times 15 \, cm$ (as shown in Figure 1), and vibrate them tightly. After placing for 1 day, demold them and cure them at room temperature for 28 days; then, a similar model sample can be obtained [23], whose physical and mechanical properties are close to actual rock.

(2) Carry out uniaxial compress test and direct shear test on samples under different normal stress (as shown in Figure 2); then, normal stress and shear stress during the test are recorded and plotted in Figure 3. The test results show that the cohesion *c* of the sample is 5.09 MPa, and the internal friction angle φ is 44.8° (as shown in Figure 3). The uniaxial compressive strength of samples is 82.3 MPa.

(3) Establish PFC^{3D} numerical models of the same size, and carry out numerical test with the micro parameters of Huang et al. [13]. Modify these parameters until the test results are closer to those of the laboratory test; then, plot the results in Figure 3. The test results show that the cohesion *c* of the sample is 4.93 MPa and the internal friction angle φ is 46.7° (as shown in Figure 3); take the micro parameters as group A.

The calibration and modification of parameters in group C are as follows:

(1) Cylindrical specimens sized $\phi 50 \, mm \times 25 \, mm$ are made with intact granite; then, a series of Brazil disk split tests and uniaxial compress tests are conducted with these specimens (as shown in Figure 4). The load-displacement curves of the test are recorded in Figure 5. According to the procedures, during the Brazil tests, the loading rate is controlled as 0.1 MPa/s. The uniaxial compress strength of granite samples is 142.3 MPa.

TABLE 1: Particles microscopic parameters of group A.

Particle parameters					Parallel bond parameters				
Density $(kg \times m^{-3})$	Ratio of particle size	Contact modulus (GPa)	Contact stiffness $(k_n \times k_s^{-1})$	Friction coefficient	Bond modulus (GPa)	Ratio of bond stiffness $(pb\_k_n \times pb\_k_s^{-1})$	Normal bond strength (GPa)	Shear bond strength (MPa)	Multiplier of radius
1850	1.6	2.3	2.0	0.45	2.3	2.0	11	15	1.0

TABLE 2: Particles microscopic parameters of group B.

Particle parameters					Parallel bond parameters				
Density $(kg \times m^{-3})$	Ratio of particle size	Contact modulus (GPa)	Contact stiffness $(k_n \times k_s^{-1})$	Friction coefficient	Bond modulus (GPa)	Ratio of bond stiffness $(pb\_k_n \times pb\_k_s^{-1})$	Normal bond strength (MPa)	Shear bond strength (MPa)	Multiplier of radius
2700	1.66	55	2.2	0.5	55	2.2	80	80	1.0

TABLE 3: Particles microscopic parameters of group C.

Particle parameters					Parallel bond parameters				
Density $(kg \times m^{-3})$	Ratio of particle size	Contact modulus (GPa)	Contact stiffness $(k_n \times k_s^{-1})$	Friction coefficient	Bond modulus (GPa)	Ratio of bond stiffness $(pb\_k_n \times pb\_k_s^{-1})$	Normal bond strength (MPa)	Shear bond strength (MPa)	Multiplier of radius
2800	1.66	5.0	3.0	0.8	35	3.0	70	140	1.0

FIGURE 1: Similar model sample mold.
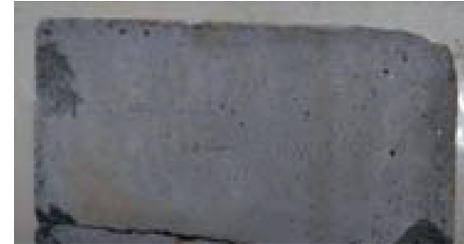
FIGURE 2: Direct shear test of similar model sample.

(2) Establish the numerical model of particle flow and carry out the numerical test according to step (1), and then adjust the micro parameters of the model repeatedly, until the load-displacement curves of numerical test agree well with those of laboratory tests (as shown in Figure 5). The parameters are taken as group C.

Based on the above micro parameters, 12 numerical models of SC3PB, ECFSD, CCNBD, and ECFR were established, respectively, among which SC3PB and CCNBD models have been widely used, and ECFSD and ECFR are new type models studied by Zhang [24]. The size and loading form of models are shown in Figures 6–9. According to Potyondy et al. [25], the particle size can be selected as 3–4% of the model size, and numerical tests are carried out for each model.

2.2. Controlling the Loading Rate. Displacement loading is used in the test. In order to select an optimal loading rate, the SC3PB and CCNBD sample models are established with parameters in group A, and the test is executed under three loading rates of 0.05 m/s [9], 0.01 m/s, and 0.002 m/s [26]. The strength curves of the two samples under different loading rates are obtained, respectively (as shown in Figures 10 and 11).

Elastic stages of the curves, under different loading rates, are almost the same. The slower the loading rate, the lower the peak strength of the curve. For SC3PB sample, K_{IC} is
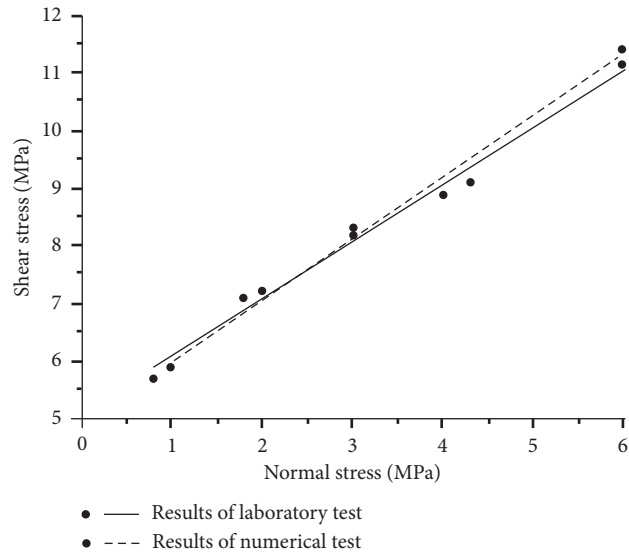
FIGURE 3: Shear stress-normal stress curve of sample.

FIGURE 4: Brazil disk split test with granite specimens.
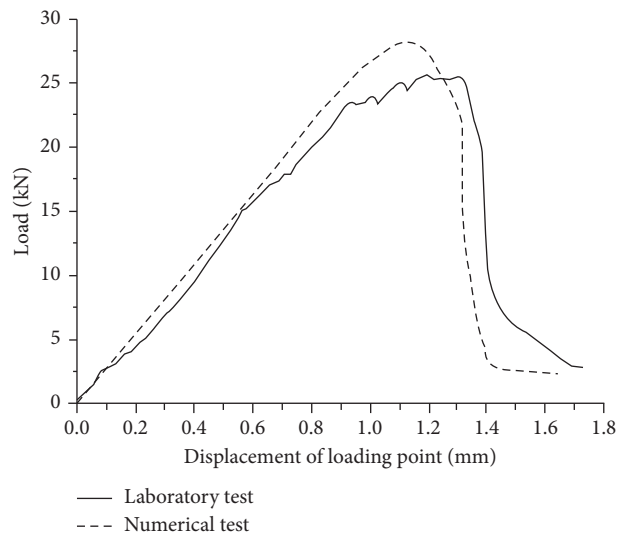
FIGURE 5: Load-displacement curve of Brazil test (parameter of group C).

$S = 100\,\text{mm}; a = 20\,\text{mm}; B = 40\,\text{mm}; H = 20\,\text{mm}$

(a) (b)
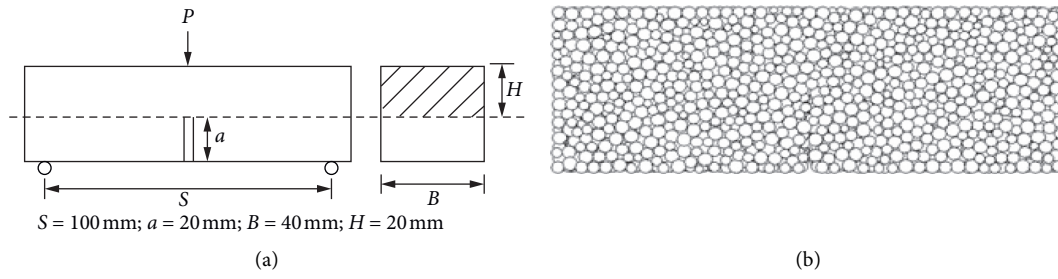
FIGURE 6: Three-point bending beam model. (a) Model size. (b) PFC^{3D} model.

$R = 40\,\text{mm}; a = 20\,\text{mm}; a = 10^{\circ}; B = 30\,\text{mm}$

(a) (b)
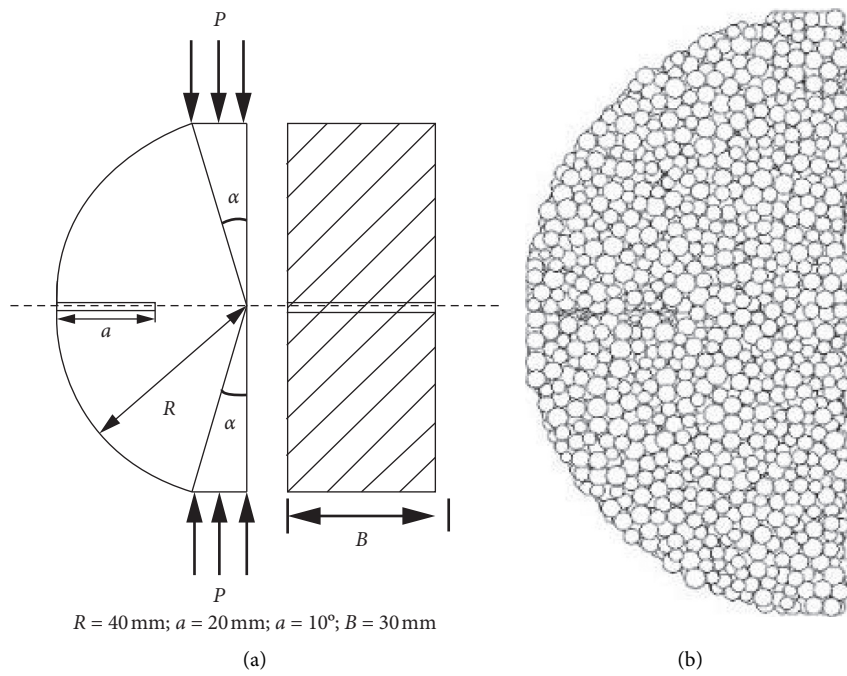
FIGURE 7: Edge cracked flattened semicircular disc model. (a) Model size. (b) PFC^{3D} model.

$R = 40\,\text{mm}; a_0 = 7.4\,\text{mm}; a_1 = 20\,\text{mm}; B = 30\,\text{mm}$

(a) (b)
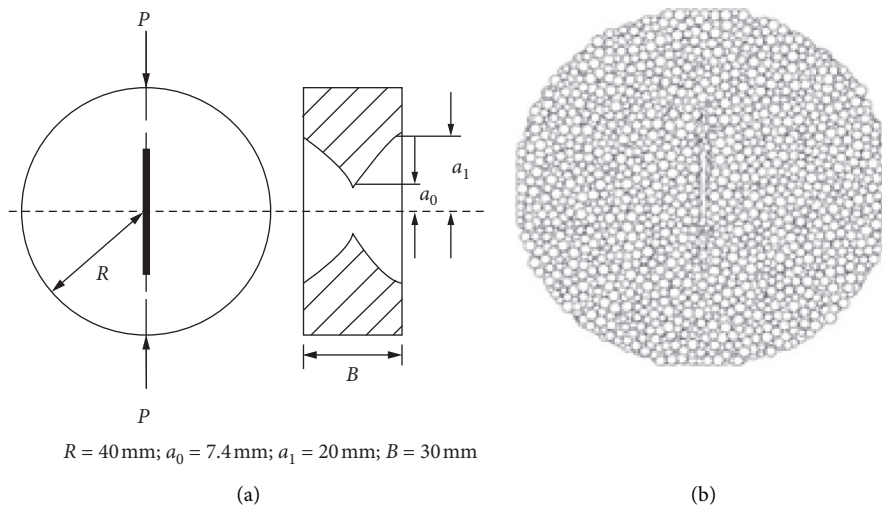
FIGURE 8: Cracked chevron notched Brazilian disc model. (a) Model size. (b) PFC^{3D} model.

$R = 40\,\text{mm}$; $r = 200000\,\text{mm}$; $a = 7\,\text{mm}$; $a = 10°$; $B = 30\,\text{mm}$

(a)   (b)
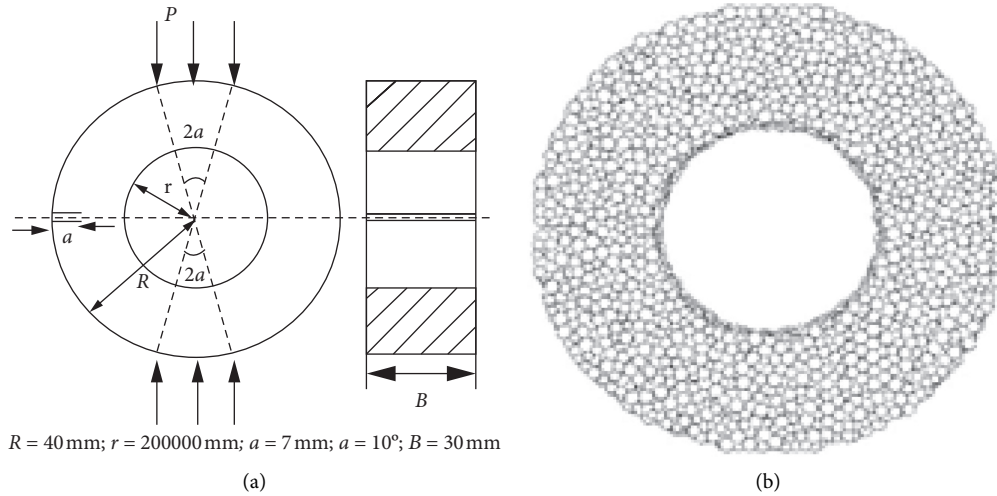
FIGURE 9: Edge cracked flattened ring model. (a) Model size. (b) PFC^{3D} model.
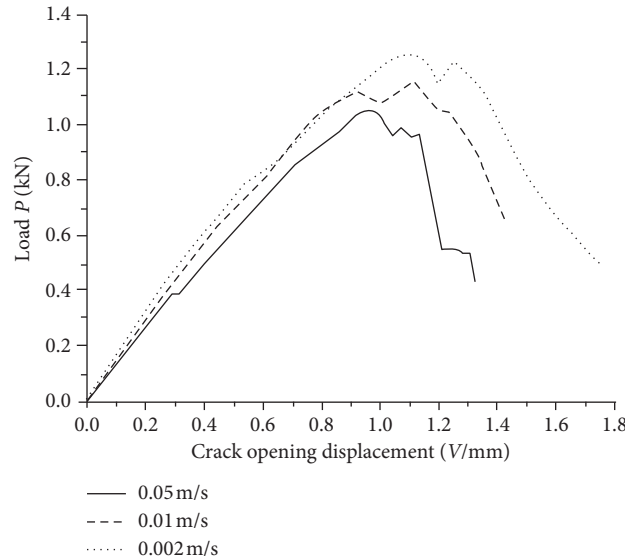
FIGURE 10: P-V curve of the three-point bending test under different loading rates.

calculated by substituting the first load platform in the curve into formulas (1) and (2) [27]:

$$K_{IC} = \frac{PS}{BW^{3/2}} f\left(\frac{a}{W}\right), \tag{1}$$

$$f\left(\frac{a}{W}\right) = \frac{3(a/W)^{1/2}}{2(1 + 2a/W)(1 - a/W)^{3/2}} [1.99 - (a/W) \cdot (1 - a/W)(2.15 - 3.93a/W + 2.7a^2/W^2)], \tag{2}$$

where P is the load value, kN; s is the nominal span, mm; W is the specimen height, mm; B is the specimen thickness, mm; and a is the prefabricated crack length, mm.

For CCNBD samples, K_{IC} is calculated by substituting the maximum load [5] in test by formulas (3)–(6) [28]:

$$K_{IC} = Y^*_{\min} \frac{P_{\max}}{\sqrt{2RB}}, \tag{3}$$

$$Y^*_{\min} = ue^{v\alpha_1}, \tag{4}$$

$$u(\alpha_0, \alpha_B) = 0.2553 + 0.0925\alpha_B + 0.0327\alpha_0 + 0.1929\alpha_0^2 + 0.3473\alpha_0^3 - 0.9695\alpha_0^4, \tag{5}$$

$$v(\alpha_0, \alpha_B) = 2.4404 - 0.8582\alpha_0 - 1.2698\alpha_B + 0.469\alpha_0\alpha_B + 0.7345\alpha_0^2 + 0.4819\alpha_B^2, \tag{6}$$

where $Y^*_{\min}$ is critical strength factor; $\alpha_0 = a_0/R$, the dimensionless initial crack length; $\alpha_1 = a_1/R$, the dimensionless maximum crack length; $\alpha_B = a_B/R$, the dimensionless specimen thickness; and $P_{\max}$, the local maximum load, kN.
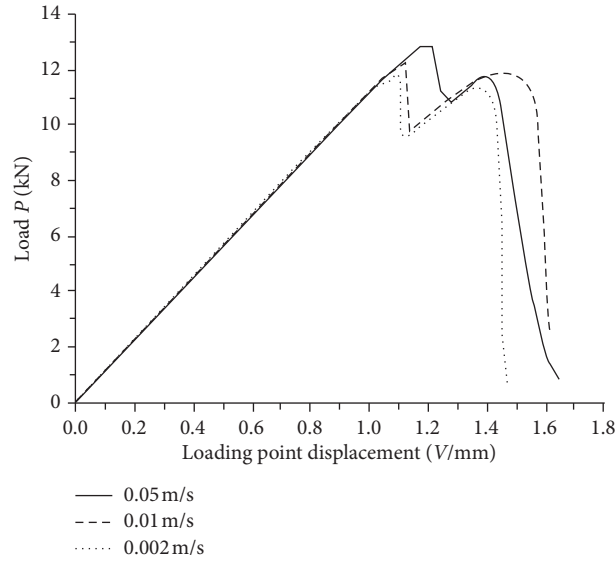
FIGURE 11: *P-v* curve of the CCNBD test under different loading rates.

The fracture toughness of the samples under various loading rates is listed in Table 4. The results of SC3PB samples, with the error of 0.16 MPa·m$^{1/2}$, are greatly affected by loading rate. The results of CCNBD samples are almost close to the error of 0.08 MPa·m$^{1/2}$. With the decrease of loading rate, the influence of loading rate becomes smaller. The slower the loading rate is, the closer the test is to the quasi-static loading. With the same displacement, there is less damage in the sample, and the results are more accurate. Therefore, theoretically, the loading rate should be controlled relatively low, but considering the calculation efficiency of numerical simulation, the loading rate should be increased properly under the condition that the results are accurate enough. According to the above test, the loading rate of this test is controlled as 0.01 m/s.

3. Results of the Numerical Test

3.1. Three-Point Bending Test Results. For numerical test, first of all, the rationality and validity of the test results should be preliminarily judged. Through monitoring the generation and distribution of microcracks in the model, the failure form of the sample can be observed (as shown in Figures 12–14). The black part in the figure represents the microcracks produced by the bond failure between particles. Among them, Figures 12(a), 13(a), and 14(a) show the crack initiation, Figures 12(b), 13(b), and 14(b) show the crack propagation, and Figures 12(c), 13(c), and 14(c) show that the specimen is damaged when the crack propagates to a certain stage. It is found that, in the samples with different strength, the microcracks are first generated from the tip of the preformed groove and gradually expand, indicating that the failure of the model is caused by the growth of the groove, so the numerical test is reasonable and effective.

Then, record the curve of load *P*-crack opening displacement *V* in the test (as shown in Figure 15). According

to the test results, $P_A = 1.11$ kN, $P_B = 2.99$ kN, $P_C = 3.27$ kN; substituting these values into formula (1), the K_{IC} of model A1 is calculated as 0.92 MPa·m$^{1/2}$, K_{IC} of model B1 is 2.49 MPa·m$^{1/2}$, and K_{IC} of model C1 is 2.72 MPa·m$^{1/2}$.

3.2. ECFSD Test Results. During the test, the distribution of microcracks in the model is shown in Figures 16–18. It is found that a small number of microcracks, at the crack initiation stage, appear at the loading point and the prefabricated crack end. Then, the prefabricated crack propagation stops after about 5 mm, and a large number of microcracks appear at the two loading points. Crushing along the loading direction is the main failure mode of the sample.

In B2 model, the crack occurs at the loading points firstly and then occurs at the end of precrack (as shown in Figure 17). The fracture in the direction of diameter caused by stress concentration at both ends of the specimen is the main cause of specimen failure.

Record the curve of load *P*-displacement *V* in the test (as shown in Figure 19), and substitute the local minimum value on the curve into the following formula [19]:

$$K_{IC} = Y_{max} \frac{P_{min}}{\sqrt{RB}}, \qquad (7)$$

where Y_{max} is the dimensionless stress intensity factor [17], $Y_{max} = 1.0756$; *R* is the radius of sample, mm; P_{min} is the local minimum load, kN; and the other symbols are the same as before.

According to the test results, $P_{Amin} = 6.22$ kN, $P_{Bmin} = 14.9$ kN, $P_{Cmin} = 16.3$ kN; then, K_{IC} of models can be calculated. The results show that $K_{IC} = 1.11$ MPa·m$^{1/2}$ for A2 model, $K_{IC} = 2.66$ MPa·m$^{1/2}$ for B2 model, and $K_{IC} = 2.91$ MPa·m$^{1/2}$ for C2 model. The observation of the loading process shows that the local minimum value P_{min} of the load curve corresponds to the crack initiation and

TABLE 4: Test results of fracture toughness under different loading rates.

Loading rate	0.05 m/s	0.01 m/s	0.002 m/s
SC3PB	1.04	0.92	0.88
CCNBD	1.19	1.13	1.11

(a)   (b)   (c)
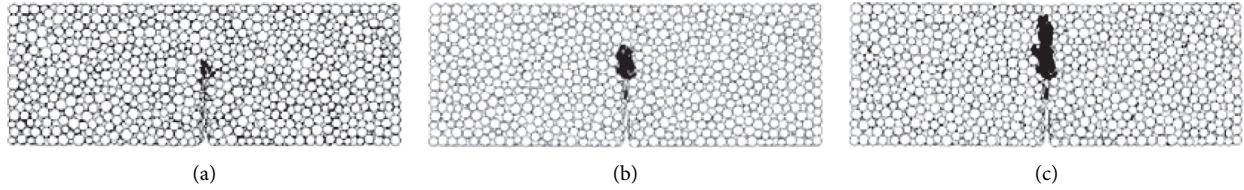
FIGURE 12: Microcracks distribution in SC3PB specimen (A1). (a) Crack initiation. (b) Crack growth. (c) Specimen failure.

(a)   (b)   (c)
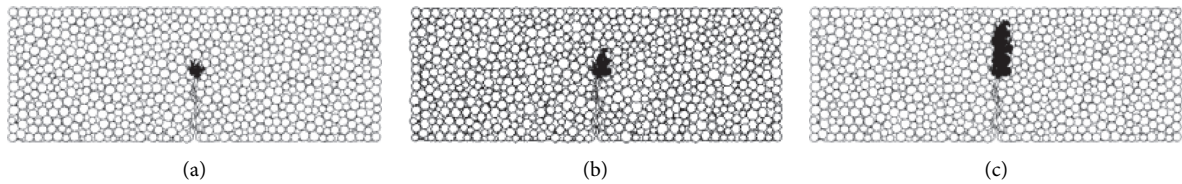
FIGURE 13: Microcracks distribution in SC3PB specimen (B1). (a) Crack initiation. (b) Crack growth. (c) Specimen failure.

(a)   (b)   (c)
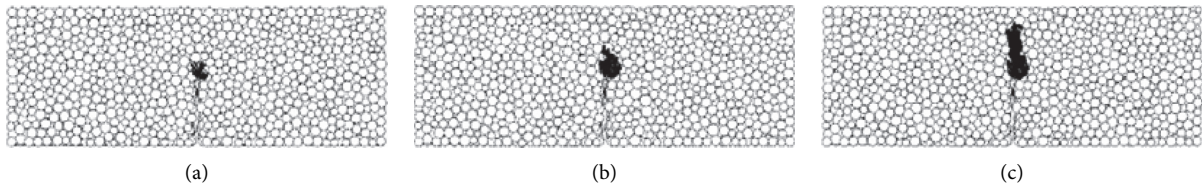
FIGURE 14: Microcracks distribution in SC3PB specimen (C1). (a) Crack initiation. (b) Crack growth. (c) Sample failure.
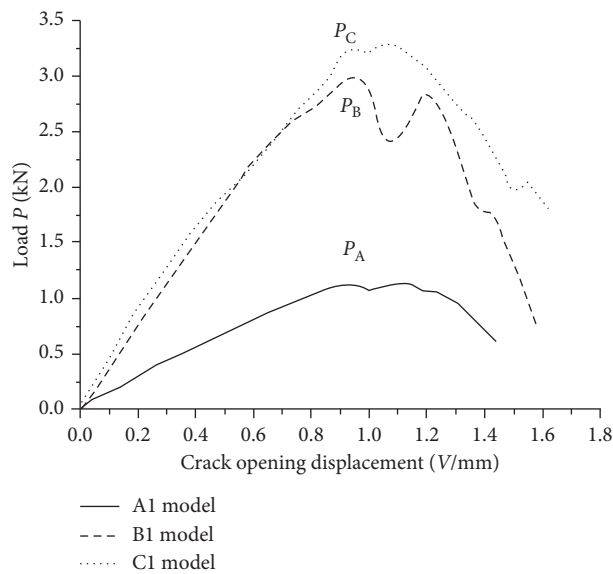
FIGURE 15: P-V curve of the three-point bending test.
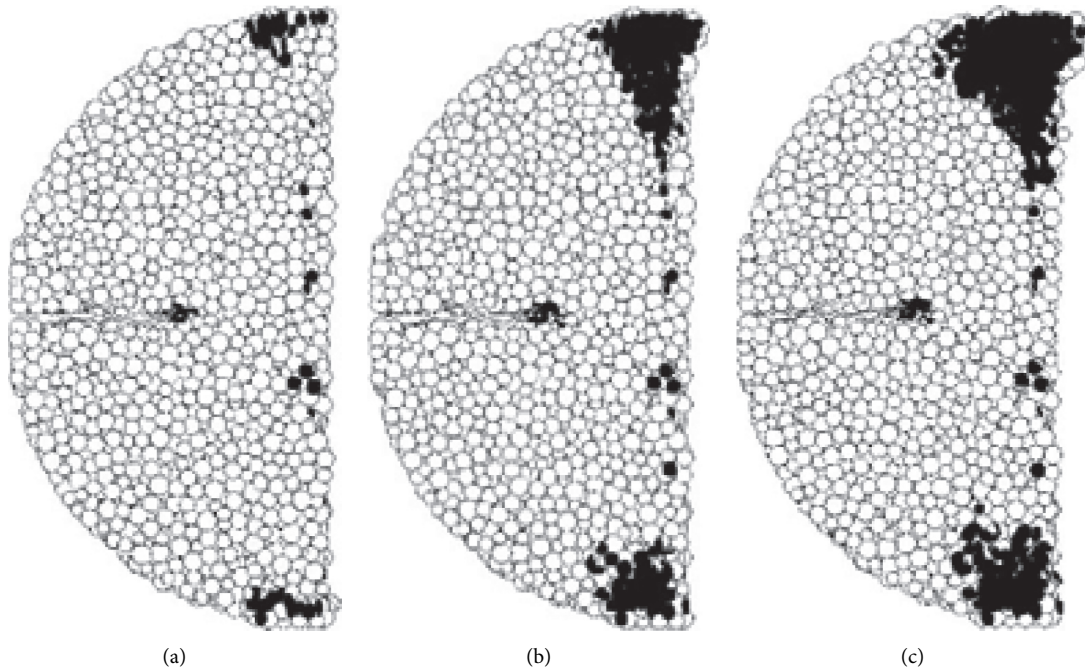
FIGURE 16: Microcracks distribution in ECFSD specimen (A2). (a) Crack initiation. (b) Crack growth. (c) Sample failure.
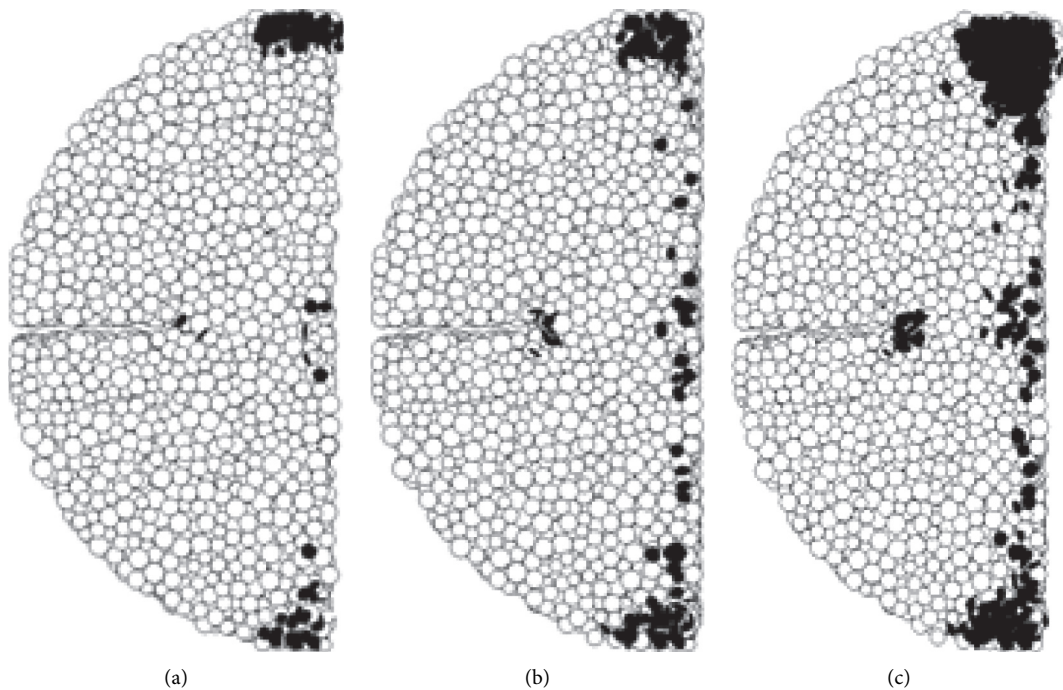
FIGURE 17: Microcracks distribution in ECFSD specimen (B2). (a) Crack initiation. (b) Crack growth. (c) Sample failure.

propagation stage of the prefabricated crack. At this time, the specimen is not completely damaged. As the loading continues, the load curve increases, and the second peak value may exceed the first.

3.3. CCNBD Test Results. The distribution of microcracks in the models is shown in Figures 20–22. It is found that microcracks occur at the loading points of the sample and the end of precut groove firstly, then the precut groove begins to propagate, and the microcracks run through the sample along the diameter direction finally. A number of

(a)   (b)   (c)
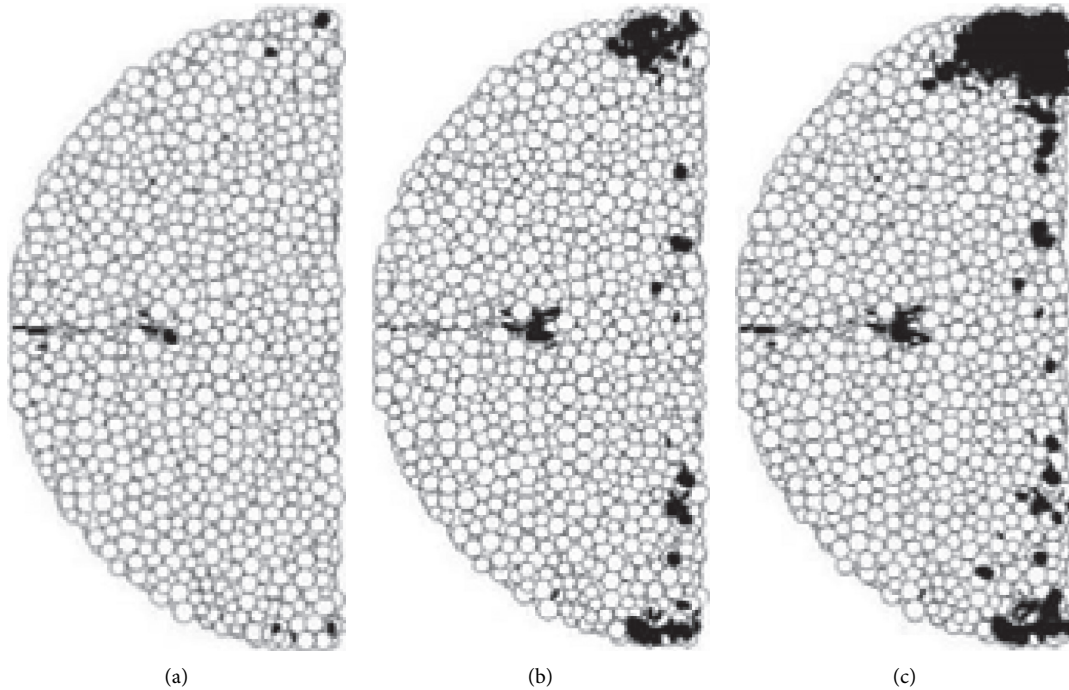
FIGURE 18: Microcracks distribution in ECFSD specimen (C2). (a) Crack initiation. (b) Crack growth. (c) Sample failure.
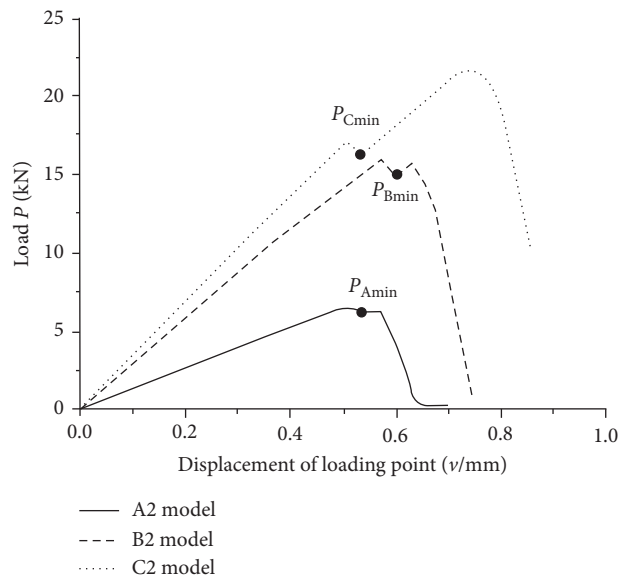
FIGURE 19: P-v curve of the ECFSD test.

microcracks near the loading platform occur because of the local fracture caused by the stress concentration.

The curve of load P-displacement v is recorded in the test (as shown in Figure 23), and the maximum load in the test is substituted into formulas (3)–(6), for calculation.

According to the test results, $P_{Amax} = 12.2$ kN, $P_{Bmax} = 18.4$ kN, $P_{Cmax} = 20.4$ kN; then, K_{IC} of models are calculated. The results show that $K_{IC} = 1.13$ MPa·m$^{1/2}$ for A3

model, $K_{IC} = 2.55$ MPa·m$^{1/2}$ for B3 model, and $K_{IC} = 2.83$ MPa·m$^{1/2}$ for C3 model.

3.4. ECFR Test Results. The distribution of microcracks in the model is shown in Figures 24–26. In the process of loading, the vertical microcracks are produced on the inner wall of the samples firstly; then, the cracks propagate
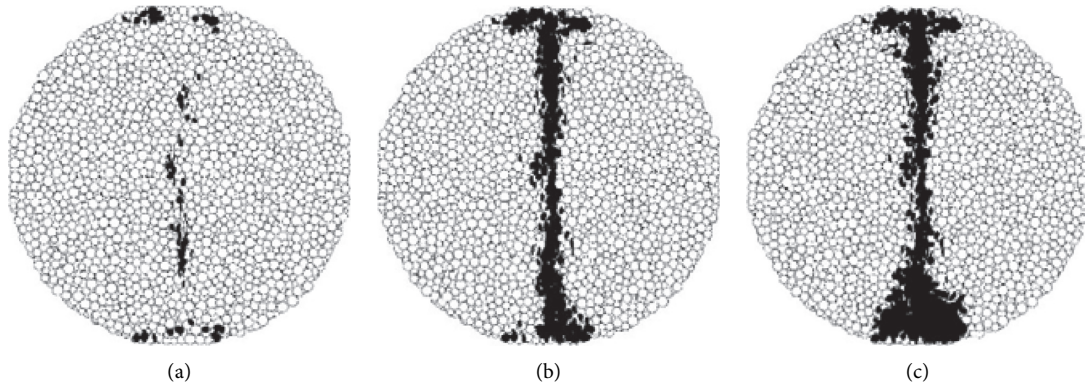
FIGURE 20: Microcracks distribution in CCNBD specimen (A3). (a) Crack initiation. (b) Crack growth. (c) Sample failure.
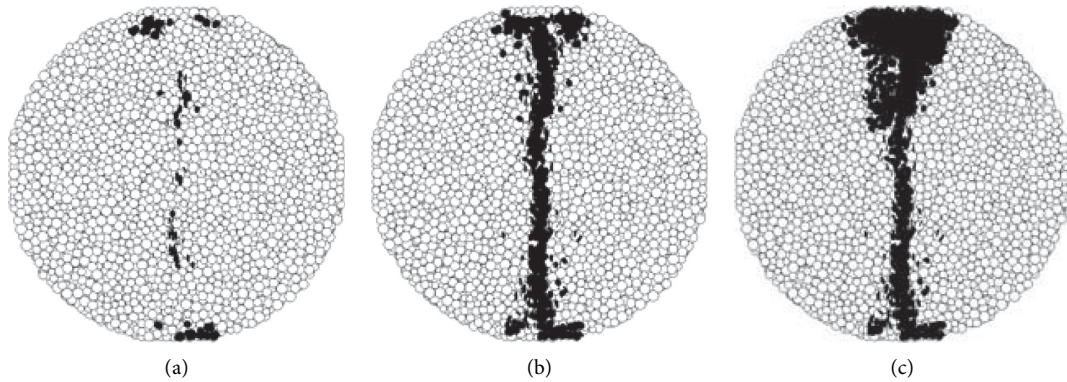
FIGURE 21: Microcracks distribution in CCNBD specimen (B3). (a) Crack initiation. (b) Crack growth. (c) Sample failure.
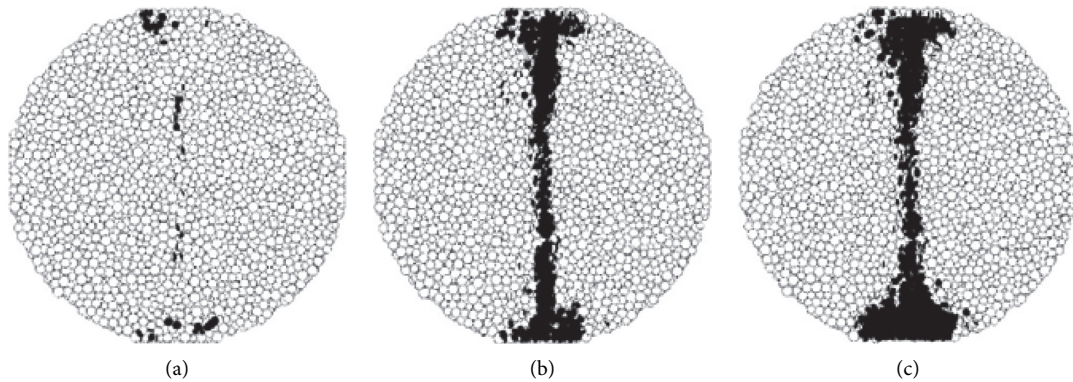
FIGURE 22: Microcracks distribution in CCNBD specimen (C3). (a) Crack initiation. (b) Crack growth. (c) Sample failure.

gradually from the inside to the outside along the loading direction and run through the samples. At the same time, the precut cracks also propagate to the inside of the samples. Tensile failure also occurs in the right half of the ring.

The curve of load P-displacement v is shown in Figure 27. According to reference [17], the local minimum load P_{min} is substituted into formula (7), where $Y_{max} = 1.0468$, $P_{Amin} = 5.71$ kN, $P_{Bmin} = 13.0$ kN, $P_{Cmin} = 15.2$ kN, and the results are as follows: $K_{IC} = 1.00$ MPa·m$^{1/2}$ for A4 model, $K_{IC} = 2.27$ MPa·m$^{1/2}$ for B4 model, and $K_{IC} = 2.65$ MPa·m$^{1/2}$ for C4 model.

4. Analysis of Test Results

In each group of samples, SC3PB and CCNBD samples are damaged by the propagation of precut cracks, while ECFSD
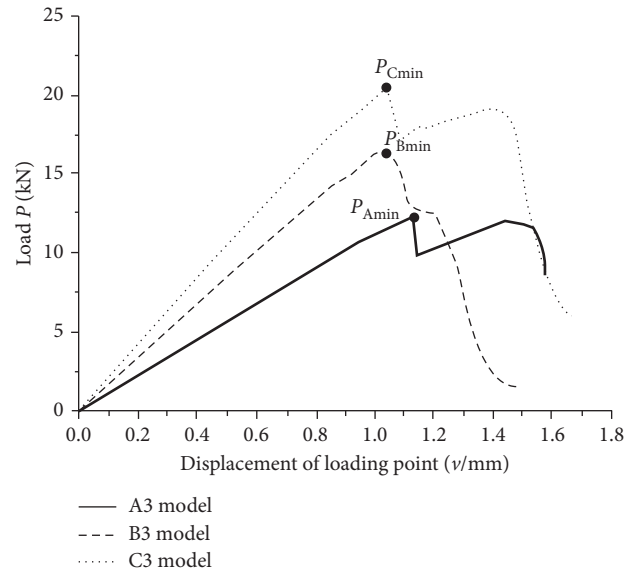
FIGURE 23: P-v curve of the CCNBD test.
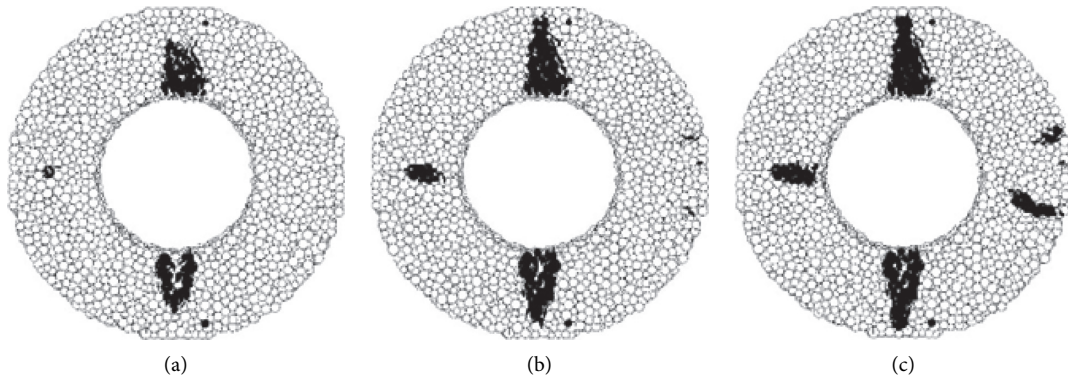
FIGURE 24: Microcracks distribution in ECFR specimen (A4). (a) Crack initiation. (b) Crack growth. (c) Sample failure.
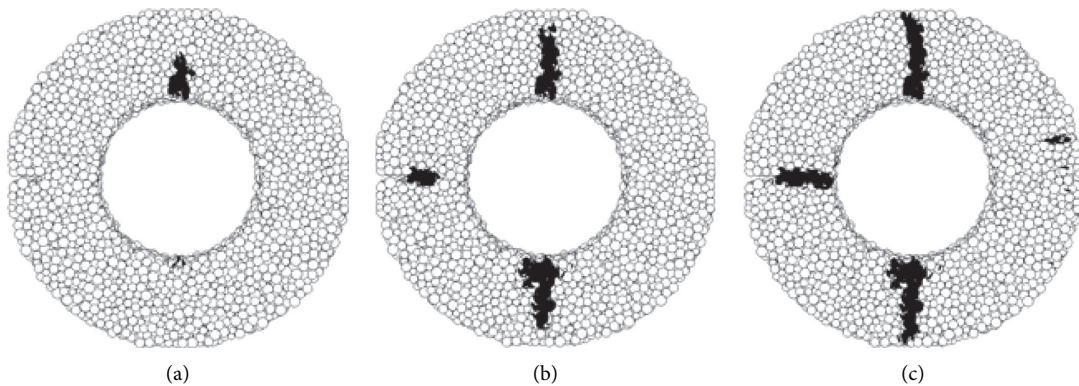
FIGURE 25: Microcracks distribution in ECFR specimen (B4). (a) Crack initiation. (b) Crack growth. (c) Sample failure.

and ECFR samples are damaged by not only the propagation of precut cracks, but also the coalescence of vertical cracks. The load-displacement curve of each specimen will decrease slightly and then increase again, which is caused by stress release after crack initiation. By comparing the fracture toughness of each model (see Table 5), it can be found that,

(a)   (b)   (c)
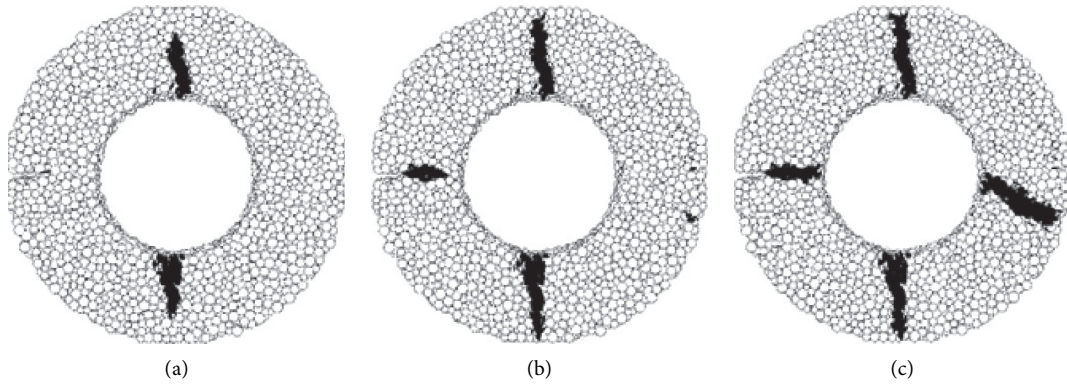
FIGURE 26: Microcracks distribution in ECFR specimen (C4). (a) Crack initiation. (b) Crack growth. (c) Sample failure.
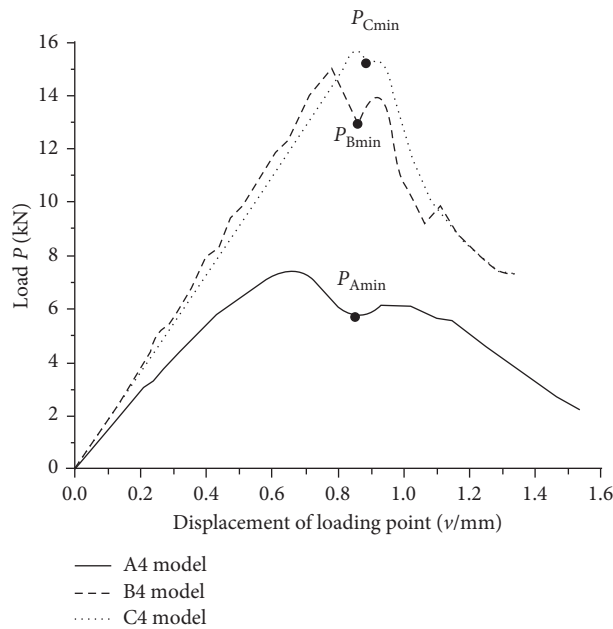
FIGURE 27: P-v curve of the ECFR test.

in group A, the difference between the four sample types is 0.21 MPa·m$^{1/2}$. In group B, the difference between the four sample types is 0.39 MPa·m$^{1/2}$. In group C, the difference between the four sample types is 0.26 MPa·m$^{1/2}$. On the whole, the fracture toughness of the ECFR samples is smaller than that of the ECFSD and CCNBD samples (Tables 4 and 5).

By comparing the distribution of microcracks in each model, it can be found that, in ECFSD and CCNBD samples, both the crack growth and the fracture of the loading point can be obtained. The short crack propagation distance in the ECFSD specimen is not the main reason for specimen failure. It is because the crack tip is within the width covered by specimen loading platform as precut crack propagating. In the contact diagram (as shown in Figure 28), the black line represents the pressure between particles, and the thickness of the line represents the

magnitude of force. It is explicit that the specimen is compressed along the vertical direction, and the precut crack tip will not undergo tensile failure anymore, so the crack will not further expand. Under a lower loading rate, there are fewer microcracks outside the propagation path in the CCNBD specimen, which makes the results relatively accurate.

The ECFR specimen can be regarded as a platform Brazilian disk specimen with edge crack and central circular hole. Compared with the disk or half-disk specimen, the ring-like specimen is more prone to compression deformation.

The calculated results are closely related to the ratio of internal and external radius r/R, the ratio of crack length to external diameter a/R, and other geometric parameters. There are many microcracks outside the crack propagation path, which has a certain influence on the test results.

TABLE 5: Test results of fracture toughness (MPa·m$^{1/2}$).

	SC3PB sample	ECFSD sample	CCNBD sample	ECFR sample
A model	0.92	1.11	1.13	1.00
B model	2.49	2.66	2.55	2.27
C model	2.72	2.91	2.83	2.65
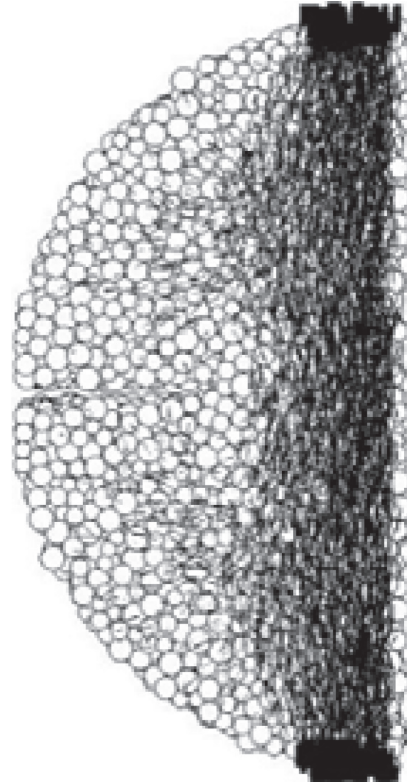
FIGURE 28: Contact force between particles in the ECFSD model.

5. Conclusions

The fracture toughness test of rock with 4 types of specimens is researched by the numerical simulation method of particle flow. The failure forms and load-displacement curves are analyzed and compared. The conclusions in this research are listed as follows:

(1) The results of the numerical test are reasonable and effective. The maximum difference between the test results of different samples with the same strength parameter is 0.39 MPa·m$^{1/2}$.

(2) When the loading rate is reduced to 0.01 m/s, the effect of loading rate on fracture toughness can be reduced to less than 0.1 MPa·m$^{1/2}$. So, the loading rate of 0.01 m/s is reasonable.

(3) During the loading process, the microcracks occur in multiple areas in ECFR specimens. The test results of ECFR specimens are 6%–11% smaller than those of CCNBD specimens. For ECFSD specimens, there are many microcracks generated along the loading direction as the propagation of prefabricated crack. The test load is larger than the other specimens, so

the fracture toughness of ECFSD specimens is 0.08–0.11 MPa·m$^{1/2}$ larger than that of CCNBD specimens.

(4) The SC3PB and CCNBD specimens are spilt along the loading direction because of the propagation of prefabricated crack, and the test results of SC3PB are 0.06–0.21 MPa·m$^{1/2}$ less than those of CCNBD specimens.

Data Availability

The article data used to support the findings of this study are included within the article.

Conflicts of Interest

The authors declare that there are no conflicts of interest regarding the publication of this paper.

Acknowledgments

References

[1] J. A. Franklin, Z. Sun, and B. K. Atkinson, "Suggested methods for determining the fracture toughness of rock," *International Journal of Rock Mechanics and Mining Science & Geomechanics Abstract*, vol. 25, no. 2, pp. 71–96, 1988.

[2] S. Zhang and Q. Z. Wang, "Determination of rock fracture toughness by split test using five types of disc specimens," *Rock and Soil Mechanics*, vol. 30, no. 1, pp. 12–18, 2009.

[3] Z. D. Cui, D. A. Liu, G. M. An, and M. Zhou, "Research progress in model I fracture toughness testing methods for rocks," *Journal of Test and Measurement Technology*, vol. 23, no. 3, pp. 189–196, 2009.

[4] J. Wei, W. C. Zhu, R. F. Li, L. L. Niu, and Q. Y. Wang, "Experiment of the tensile strength and fracture toughness of rock using notched three point bending test," *Journal of Water Resources and Architectural Engineering*, vol. 14, no. 3, pp. 128–132, 2016.

[5] M. R. Ayatollahi and J. Akbardoost, "Size and geometry effects on rock fracture toughness: mode I fracture," *Rock Mechanics and Rock Engineering*, vol. 47, no. 2, pp. 677–687, 2014.

[6] J. J. Meng, P. Cao, K. Zhang, and P. Tan, "Brazil split test of flattened disk and rock tensile strength using particle flow code," *Journal of Central South University(Science and Technology)*, vol. 44, no. 6, pp. 2449–2454, 2013.

[7] S. Q. Yang, Y. H. Huang, and X. R. Liu, "Particle flow analysis on tensile strength and crack coalescence behavior of brittle rock containing two pre-existing fissures," *Journal of China University of Mining and Technology*, vol. 43, no. 2, pp. 220–226, 2014.

[8] Y. H. Huang and S. Q. Yang, "Particle flow simulation on marco- and meso-mechanical behavior of red sandstone containing two pre-existing non-coplanar fissures," *Chinese Journal of Rock Mechanics and Engineering*, vol. 33, no. 8, pp. 1644–1653, 2014.

[9] Y. H. Huang and S. Q. Yang, "Particle flow simulation on fracture characteristics and crack propagation mechanism of holed-cracked Brazilian disc specimen," *Rock and Soil Mechanics*, vol. 35, no. 8, pp. 2269–2277, 2014.

[10] L. N. Y. Wong and X.-P. Zhang, "Size effects on cracking behavior of flaw-containing specimens under compressive loading," *Rock Mechanics and Rock Engineering*, vol. 47, no. 5, pp. 1921–1930, 2014.

[11] K. Peng, J. Zhou, Q. Zou, and F. Yan, "Deformation characteristics of sandstones during cyclic loading and unloading with varying lower limits of stress under different confining pressures," *International Journal of Fatigue*, vol. 127, no. 10, pp. 82–100, 2019.

[12] K. Peng, Z. Liu, Q. Zou, Q. Wu, and J. Zhou, "Mechanical property of granite from different buried depths under uniaxial compression and dynamic impact: an energy-based investigation," *Powder Technology*, vol. 362, pp. 729–744, 2020.

[13] K. Peng, H. Lv, F. Z. Yan, Q. L. Zou, X. Song, and Z. P. Liu, "Effects of temperature on mechanical properties of granite under different fracture modes," *Engineering Fracture Mechanics*, vol. 226, p. 106, 2019.

[14] K. Peng, Y. Wang, Q. Zou, Z. Liu, and J. Mou, "Effect of crack angles on energy characteristics of sandstones under a complex stress path," *Engineering Fracture Mechanics*, vol. 218, p. 106, 2019.

[15] Y. Wang, X. Shang, and K. Peng, "Relocating mining microseismic earthquakes in a 3-D velocity model using a windowed cross-correlation technique," *IEEE Access*, vol. 8, pp. 37866–37878, 2020.

[16] X. Y. Shang and H. Tkalčić, "Point-Source inversion of small and moderate earthquakes from P-wave polarities and P/S amplitude ratios within a hierarchical bayesian framework: implications for the geysers earthquakes," *Journal of Geophysical Research: Solid Earth*, vol. 125, no. 2, 2020.

[17] Z.-D. Cui, D.-A. Liu, G.-M. An, B. Sun, M. Zhou, and F. Q. Cao, "A comparison of two ISRM suggested chevron notched specimens for testing mode-I rock fracture toughness," *International Journal of Rock Mechanics and Mining Sciences*, vol. 47, no. 5, pp. 871–876, 2010.

[18] Z. D. Cui, D. A. Liu, G. M. An, M. Zhou, and Z. Q. Li, "Research for determining mode I rock fracture toughness K_{IC} using cracked chevron notched Brazilian disc specimen," *Rock and Soil Mechanics*, vol. 31, no. 9, pp. 2743–2748, 2010.

[19] J. F. Guan, G. S. Qian, W. F. Bai, X. H. Yao, and J. W. Fu, "Method for predicting fracture and determining true material parameters of rock," *Chinese Journal of Rock Mechanics and Engineering*, vol. 37, no. 5, pp. 1146–1160, 2018.

[20] B. Bahrami, M. R. Ayatollahi, A. M. Mirzaei, and M. Y. Yahya, "Support type influence on rock fracture toughness measurement using semi-circular bending specimen," *Rock Mechanics and Rock Engineering*, vol. 53, no. 5, 2019.

[21] N. Wong, T. Guo, and W. Lam, *Experimental Study on Two Semi-circular Bending Methods for Mode I Fracture Toughness Determination in Tuff*, pp. 17–20, Seattle, Washington, DC, USA, 2018.

[22] D. Huang and X. Q. Li, "Numerical simulation research on characteristic strength of marble based on development of microcrack," *Rock and Soil Mechanics*, vol. 38, no. 1, pp. 253–262, 2017.

[23] Y. L. Zhao, W. Wan, W. J. Wang, and P. C. Zhao, "Compressive-shear rheological fracture of rock-like cracks and subcritical crack propagation test and fracture mechanism," *Chinese Journal of Geotechnical Engineering*, vol. 34, no. 6, pp. 1050–1059, 2012.

[24] C. G. Zhang, Y. Zhou, J. R. Yang, and Q. Z. Wang, "A serious of edge cracked flattened ring (disc) specimens for determining fracture toughness: numerical analysis and calibration results," *Chinese Journal of Rock Mechanics and Engineering*, vol. 33, no. 8, pp. 1546–1555, 2014.

[25] D. O. Potyondy and P. A. Cundall, "A bonded-particle model for rock," *International Journal of Rock Mechanics and Mining Sciences*, vol. 41, no. 8, pp. 1329–1364, 2004.

[26] M. J. Jiang, H. Chen, and F. Liu, "A microscopic bond model for rock and preliminary study of numerical simulation method by distinct element method," *Chinese Journal of Rock Mechanics and Engineering*, vol. 32, no. 1, pp. 15–23, 2013.

[27] Q. Z. He and Z. N. Li, *Engineering Fracture Mechanics*, Beijing University of Aeronautics and Astronautics Press, Beijing, China, 1993.

[28] L. Z. Wu, X. M. Jia, and Q. Z. Wang, "A new stress intensity factor formula of cracked chevron notched Brazilian disc (CCNBD) and its application to analyzing size effect," *Rock and Soil Mechanics*, vol. 25, no. 2, pp. 233–237, 2004.

Research Article

Research on the Deformation and Control Technology of Surrounding Rock in Entry Retaining along the Gob Side

Meng Zhang,[1] Hui He,[1] Yu Zhang,[1,2] Xin Jin,[1] Xinyu Liang,[1] Yidong Zhang ![ORCID],[3] and Hongjun Guo[4]

[1]*School of Civil & Architecture Engineering, Xi'an Technological University, Xi'an 710021, China*
[2]*Shaanxi Key Laboratory of Loess Mechanics and Engineering, Xi'an University of Technology, Xi'an 710048, China*
[3]*State Key Laboratory of Coal Resources and Mine Safety, China University of Mining & Technology, Xuzhou 221116, China*
[4]*Jiangsu Vocational Institute of Architectural Technology, Xuzhou 221116, China*

Correspondence should be addressed to Yidong Zhang; ydzhang@cumt.edu.cn

This paper studies and introduces the successful case of gob-side entry retaining technology and the typical mining pressure law in Luan mining area, which is the main mining coal seam in Qinshui coalfield. Qinshui coalfield has an estimated coal reserve of 300 billion tons, accounting for 9.58% of the total national coal reserve in China, especially anthracite, chemical coal, and coking coal. The methods of field investigation, theoretical analysis, physical experiment, and industrial test are adopted. Through the field investigation, theoretical analysis, physical experiments, and industrial test, the following conclusions have been drawn in this study: (1) A thorough engineering geological investigation was conducted on the entry retaining along the gob side on noncoal pillar mining working face, which covers multiple periods of mining process including the roadway excavation period, primary mining period, primary mining stability period, and secondary mining influence period. A series of analysis and tests were conducted such as core sampling, rock mechanics property testing, borehole detection, and flexible formwork support evaluation, which laid a foundation for identifying the mining pressure law of gob-side entry retaining by using noncoal pillar mining. (2) The mining pressure law was studied through the collection of the field measurements taken from the entry retaining along the gob side on noncoal pillar mining working face. The keys to achieve the roadway surrounding rock stability through noncoal pillar mining are obtained. According to the study, the stability control of retained roadway surrounding rock mainly depends on the stability of top coal, coal side, and shoulder angle coal. (3) In this study, a roadway reinforcement scheme is proposed to improve the surrounding rock control technology for gob-side entry retaining by noncoal pillar mining, whose effectiveness has been verified by a series of industrial test. Therefore, the wide adoption of the noncoal pillar mining method in Number #3 coal mine can significantly relieve the predicament of coal pressing under a large number of buildings in Luan mining area, which provides insightful guidance to the coal-free pillar mining in the whole Luan mining area.

1. Introduction

Entry retaining along the gob side refers to that in order to recover the protective coal pillars reserved in the traditional mining method, the roadway in the upper section is resupported by certain technical means and left to the next section for use. This is of practical significance to the technical transformation of production mine, relaxation of mining relationship, and extension of mine life. Luan mining area contains a total of 10 planned mines and 8

production mines, namely, Shigejie mine, Wuyang mine, Zhangcun mine, Changcun mine, Wangzhuang mine, Tunliu mine, Sima mine, and Gaohe mine. No 3# coal seam is the main mining area. Locating in the eastern part of Qinshui coalfield, the mining area is about 44–77 km long from north to south and 63.1 km wide from east to west. The total area of the mining area is about 2052.8 km². Ordovician limestone is the basement of the coal measures in the mining area, and the coal-bearing strata are mainly Carboniferous and Permian strata, with Shanxi Formation of the Lower

Permian and Taiyuan Formation of the Upper Carboniferous as the main bodies. No 3# coal seam locates in the middle and lower parts of Shanxi Formation as the main mineable coal seam in this area. In addition, Nos. 6, 9, 14, and 15-2# coal seams are only partially minable. Under the event that no pillar is utilized in the mining process of No.3 coal, a higher coal recovery rate can be achieved by eliminating the pillar and additional constructions [1–3]. Therefore, the study of the mining pressure law of 3# coal seam mining can provide insightful guidance to the coal-free pillar mining in the whole Luan mining area. During the study, a typical mine called Gaohe was selected as the main study subject [4–6].

2. Engineering Overview

2.1. Engineering Geological Overview of E1316 Intake Entry. The current production capacity of Gaohe mine is 8.0 mt/a, which belongs to high-yield and high-efficiency mine. E1316 intake entry is surrounded by the E1316 working face at the south side, the goaf of E1315 working face on the north side, and five main roadways on the west side, which serve as the auxiliary transportation roadway of the south wing at +450 m level. The E1316 intake entry is located in the 3# coal seam with a total length of 1087 m and drivage along the roadway floor. The specific roadway location is shown in Figure 1. Gaohe mine is a typical high-gas mine. The absolute gas emission volume of the mine is as high as $253.92\,m^3/min$. Considering that it has the high gas content and emission, the ventilation mode of E1316 working face was changed from the "Y-type + High pumping roadway" ventilation mode to the "W-type + High pumping roadway" ventilation mode to optimize the ventilation system and recover coal resources as much as possible. In addition, the noncoal pillar mining was implemented.

No. $3^{#}$ coal seam in the E1316 working face is deposited in the Shanxi Formation of the Permian as lagoon facies. The working face locates in a syncline structural area with a stable coal seam thickness ranging from 6.2 m to 7.1 m and an average coal thickness of 6.5 m. The whole coal is sandwiched with a layer of carbonaceous mudstone, whose thickness ranges from 0.10 m to 0.35 m with an average thickness of 0.20 m. The coal seam has a dip angle of 1° to 7° and an average inclination of 5°. The depth of coal seam is 430.123 m–446.942 m, and the average distance from 9# coal seam is about 64.7 m. The test results of rock (coal) mechanical properties are summarized in Table 1.

2.2. Introduction of E1316 Intake Entry Support

2.2.1. Roadway Support Form. The details of the roadway support section are shown in Figure 2(a) with roadway support parameters shown in Table 2. Due to the production needs, E1316 intake entry was reinforced by the adoption of a shelf structure as shown in Figure 2(a).

2.2.2. Details of the Flexible Formwork Support. The strength of the flexible formwork support in E1316 intake entry was achieved through the application of the C30 concrete to the E1316 intake entry flexible formwork wall. The concrete parameters are provided in Table 3.

3. Law of Mine Pressure of the Gob-Side Entry Retaining during the First Mining Period

3.1. Deformation Law of Surrounding Rock of Gob-Side Entry Retaining

3.1.1. Pressure Observation Station. The surface displacement of entry is monitored by the cross point method. Before the mining of E1315 working face, the mine pressure observation stations are arranged in the ventilation roadway of E1315 working face with No. 1# station set at 270 meters away from the cut hole and No. 2# stationset at 330 meters away from the cut hole. The location of the station and the observation objects are shown in Figure 1 and Table 4, respectively.

3.1.2. Law of Mine Pressure Appearance along the Gob-Side Entry Retaining in Front of E1315 Working Face

(1) Surface Deformation Law of Entry. After processing the deformation observation data obtained from No. 1# measuring point, an entry deformation curve was developed and is presented in Figure 3.

As demonstrated in Figure 3, the surface deformation of the gob-side entry retaining in front of E1315 working face can be divided into three stages:

(1) No mining influence stage: beyond 72 meters in front of the working face, the entry in this section is basically not affected by the mining. The cumulative deformation of entry roof and floor is limited with the entry maintenance in good condition.

(2) Low mining influence stage: with the advancing of the working face, in the range of 32–72 m ahead of the working face, the advance abutment pressure of the working face causes the increases of the subsidence rate of the roof, floor, and two sides of the entry gradually. The collected field data suggest that the average moving rate of the two sides is 8.63 mm/d with a maximum moving rate of 23 mm/d. Meanwhile, the average moving rate of the roof and floor is 5.6 mm/d with a maximum moving rate of 12 mm/d. In this stage, the cumulative deformation of the two sides is 138 mm with a total of 90 mm cumulative deformation in the roof and floor.

(3) High mining influence stage: as the working face advances, in the range of 0–32 m, the deformation rate of the entry increases dramatically. The average moving rate of the two sides is 18 mm/d, with a maximum moving rate of 27 mm/d. Meanwhile, the average moving rate of the roof and floor is 20.7 mm/d, with a maximum moving rate of 54 mm/d.

Therefore, advanced supporting systems should be installed within 72 m of the influence range of entry.
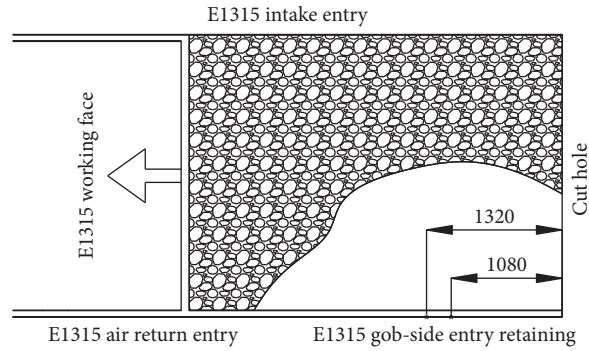
FIGURE 1: The layout of E1316 working face and entry.

TABLE 1: Mechanical parameters of coal.

Name	Type	Compressive strength (MPa)	Tensile strength (MPa)	Cohesion (MPa)	Internal friction angle (MPa)	Modulus of elasticity (GPa)	Poisson's ratio
Main roof	Packsand	46.63	4.96	7.76	36	28.85	0.20
Direct roof	Sandy mudstone	23.44	3.85	4.68	33	3.69	0.27
3# coal	3# coal	9.49	1.12	2.12	30	1.53	0.27
Direct floor	Siltstone	28.51	3.71	5.98	35	24.49	0.17

3.1.3. Law of Mine Pressure Appearance along the Gob-Side Entry Retaining at the Rear of the E1315 Working Face. Figure 4 shows the deformation and deformation rate curve of the 2# measuring point. The surface deformation of the gob-side entry retaining at the rear of the E1315 working face can be divided into two stages.

No. 2# measuring station is 330 m away from the cut hole, locating at 201 meters behind the current working face. The cumulative displacement of the roof and floor reached 1121 mm with a total of 1070 mm cumulative displacement at sides. The roof subsidence is the most severe one, followed by the floor subsidence and lateral substance. The deformation of the coal pillar side in advance entry was not as severe as the solid coal side. At the beginning of the mining of the working face, the deformation was observed at the measuring station, which locates at about 10 meters ahead of the working face. Gradually, the roadway deformation speed increased. The roof and floor moved at the maximum rate of 72 mm/d, with the maximum rate of two sides at 28.5 mm/d. A "step sinking" on the roof in front of the working face was identified, which led to the rapid increase of deformation rate.

After retaining the entry, the deformation speed of the entry firstly increased significantly and then decreased gradually. When the distance between the measuring station and the back of the working face reached 32 m, the roof and floor moved at a rate of 14 mm/d with intensified deformation speed. The roof and floor moved at the maximum rate of 45 mm/d, with a maximum rate of the two sides at 28.5 mm/d. When the distance reached 40–60 m behind the working face, the deformation of the entry became severe and continued for a whole week. It was presumed that the main roof of the working face collapses for the first time.

Meanwhile, the advancing distance of the working face was 80–100 m. The deformation of the retaining entry near the No. 2 measuring station grew stable.

(1) The increasing stage of deformation speed of the working face after mining: within a certain range after the working face was pushed, the immediate roof above the goaf failed and collapsed, accompanied by the main roof failure and rotation sinking. The entry deformation speed reached the maximum [7–10]. Simultaneously the maximum deformation rate of the two sides reached 27.5 mm/d and the maximum moving rate of the roof and floor was as high as 42.5 mm/d in the radius of 80 m behind the working face. In this whole stage, the cumulative deformation at both sides of the entry reached 655 mm with 752 mm cumulative deformation in the roof and floor.

(2) The decreasing stage of deformation speed of the working face after mining: as the bearing capacity of the filling wall increased, the key blocks at the end of the working face gradually stabilized under the support of the lower falling rock and filling body, resulting in the decreasing deformation speed of the surrounding rock of the entry. Within the range of 80–192 m behind the working face, the deformation speed of the entry gradually decreased, resulting in a maximum moving rate of 11.7 mm/d at two sides and a maximum moving rate of 12 mm/d in the roof and floor [11, 12]. The cumulative deformation at both sides of the entry reached 302 mm, and the cumulative deformation of the roof and floor was as high as 270 mm.
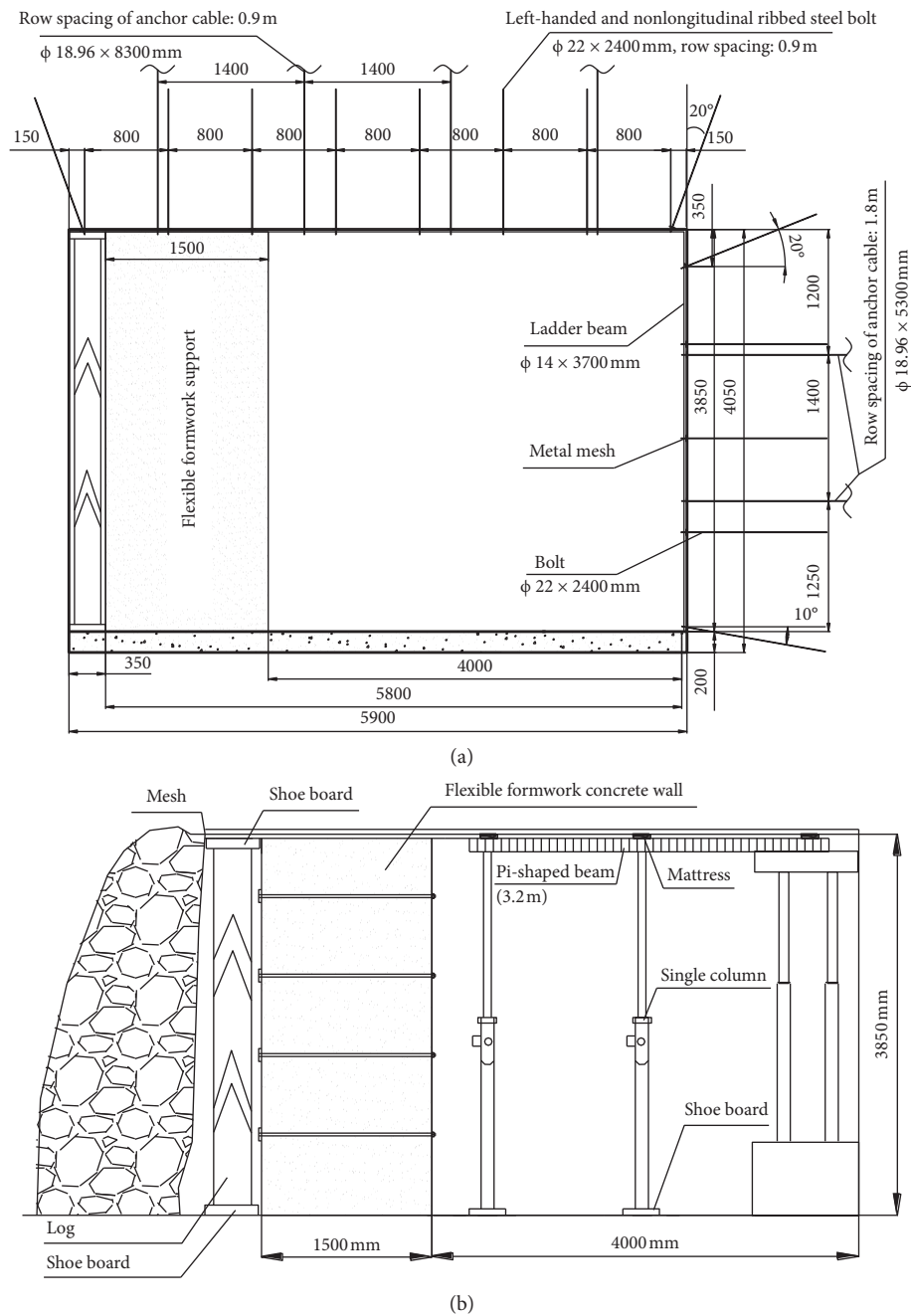
FIGURE 2: Roadway support form. (a) The supporting profile of the intake entry. (b) The shelf supporting profile of E1316 intake entry.

(3) The stable stage of deformation speed of the working face after mining: the rotary subsidence of overburden strata on the roof grew stable gradually 190 m behind the working face. The deformation speed of the surrounding rock followed a similar trend. No visible crack and failure were observed in the filling wall. Despite that, the entry wall was rated as the low stress area, and the plastic zone of the entry surrounding rock had penetrated the coal body. Both sides moved at the maximum rate of 3.5 mm/d with the maximum rate of 3 mm/d in the roof and floor.

3.2. Supporting Stress in Coal Pillar along the Gob-Side Entry Retaining, the Load Distribution, and the Variation Law of Flexible Formwork Support Body

3.2.1. Pressure Variation of Single Prop. As shown in Figure 5, the pressure of single hydraulic prop in advance support of roadway was monitored. The curves were developed with the collected data and corresponding analysis.

The analysis of the working resistance of single hydraulic prop before mining suggested that the working resistance of the prop continued to increase in the range of 0–35 m before

Table 2: Roadway support parameters.

The name of roadway		E1316 intake entry
The gross section	Digging width (mm)	5900
	Digging height (mm)	4050
	Excavating area (m^2)	23.90
The net section	Net width (mm)	4000
	Net height (mm)	3850
	Net area (m^2)	15.40
The row and line space between roof bolts (mm)		800 × 900
The row and line space between floor bolts (mm)		900 × 900
Layout of roof anchor cable		Four or four layouts
The row and line space between anchor cables (mm)		1400 × 900
Layout of floor anchor cable		Two or two layout
The row and line space between anchor cables (mm)		1400 × 1800
Layout of ladder beam	Side (single reinforcement)	Φ14 × 3700
	Roof (double reinforcement)	Φ14 × 5000
Layout of mesh (mm)	Side	4200 × 950
	Roof	5300 × 950

Table 3: The parameters of pump injected concrete.

Concrete components	Cementitious material	Water	Aggregate		Admixture
			Stone	Sand	
Name of concrete base material	Cement	Water	Stone	Sand	Admixture
1 m^3 concrete base material quality	550 kg	220 kg	800 kg	765 kg	1 kg

Table 4: Observations of mine pressure.

NO	Observation contents	Observation instrument
1[#]	Surface deformation	Self-made wedge
2[#]	Surface deformation	Self-made wedge

(a)

(b)
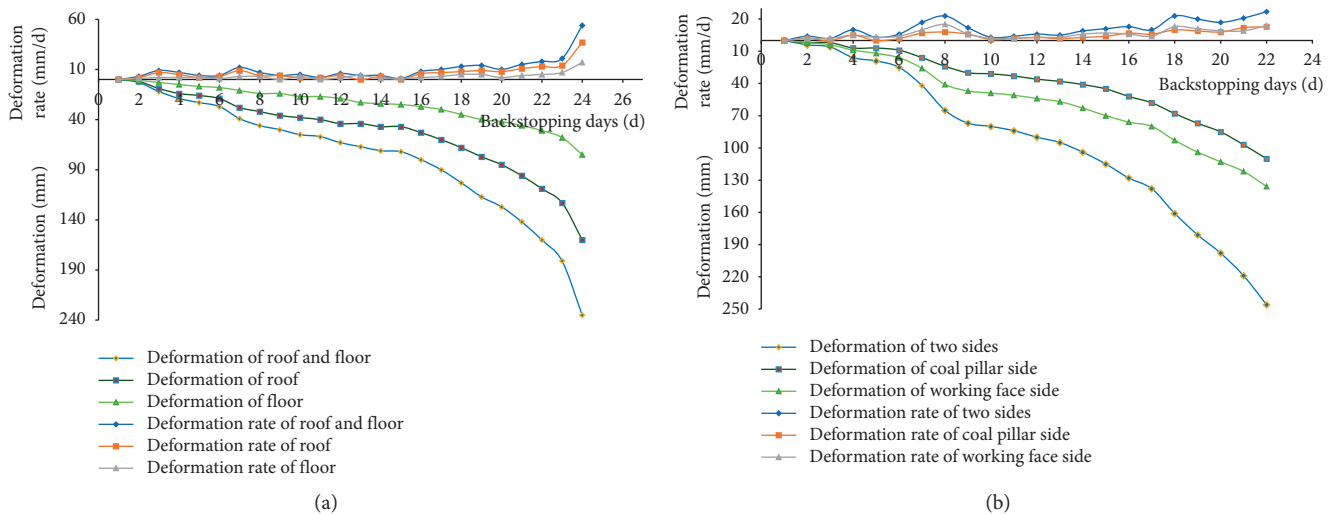
Figure 3: The entry deformation curve. (a) The deformation rate of roof and floor. (b) The deformation rate of two sides.

the working face. The pressure of the prop at the coal pillar side was the highest, followed by the working face. Due to the advance abutment pressure, the prop pressure continued to rise. After mining, due to the increased distance between the single prop and the working face, the pressure of the single prop experienced increments firstly and decrement at

(a)

(b)
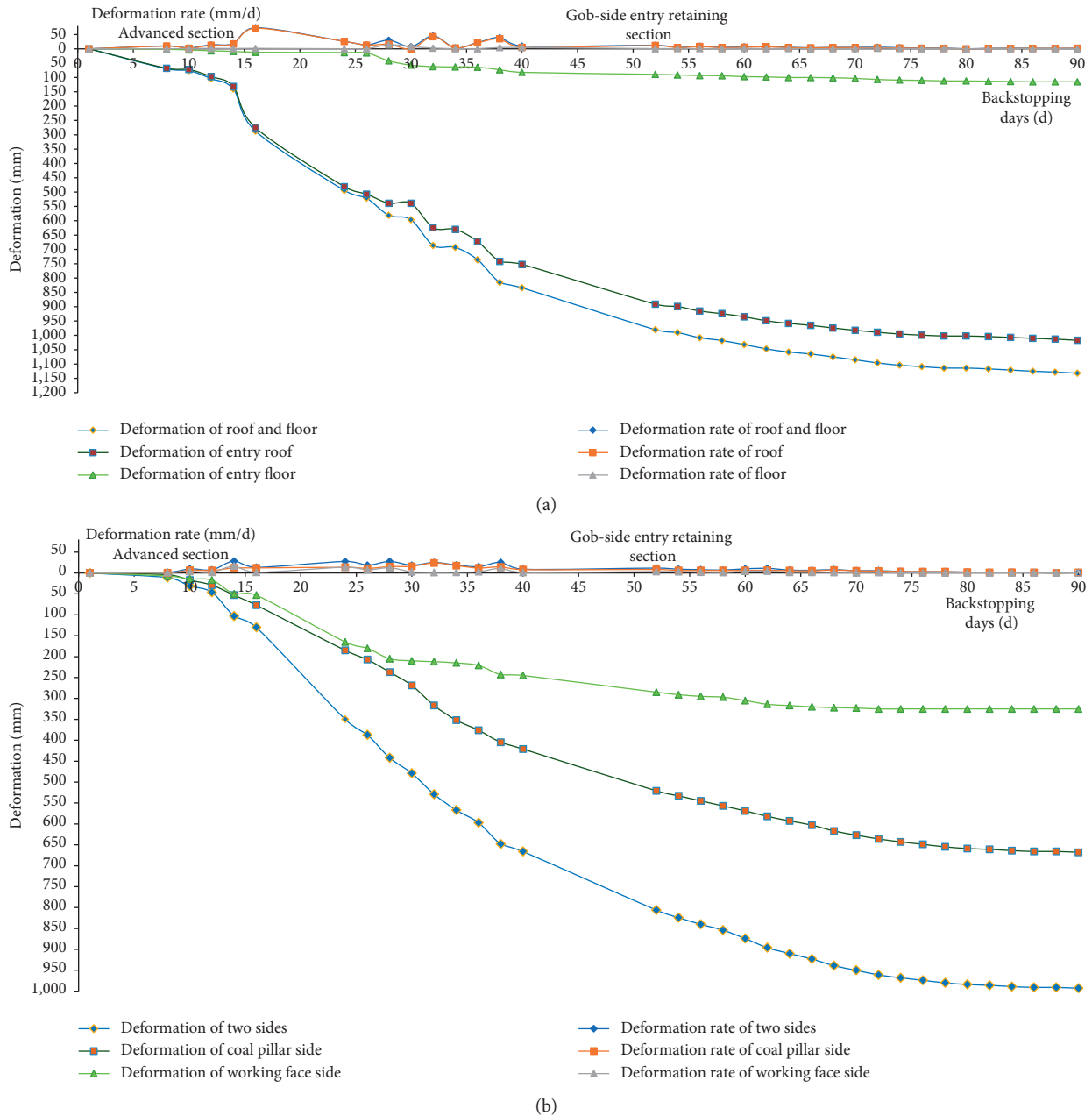
FIGURE 4: The deformation and deformation rate curve of the 2# measuring point. (a) I measuring surface. (b) II measuring surface.

30 meters after the working face. Eventually, a stable pressure was reached. After the collapse of the immediate roof, which filled the goaf, the prop pressure firstly decreased and grew stable after the main roof rotation, sinking, and contacting the gangue.

3.2.2. Filling Body Pressure Monitoring. In order to monitor the pressure change of the filling body [13–16], filling body pressure monitoring gauges were installed, respectively, at a distance of 0.3 m and 0.6 m from the edge of the filling body, as shown in Figure 6(a). The dimension of the upper load-bearing steel is $30 \times 0.25 \times 0.25$ m (thickness, length, and width, respectively). The

dimension of the lower protective steel plate was 0.25×0.3 (0.6) m, respectively. The pressure gauge observations are shown in Figure 6(b).

As shown in Figure 6, within the range of 0–18.5 m behind the working face, the pressure on the filling body due to the flexible formwork concrete near roadway increased rapidly, from 141 t at 0.3 m to 275 t at 0.6 m. Consequently, the filling body pressure gauge failed to monitor at 0.3 m due to the pipeline damage. With the range of 18.5–32.2 m behind the working face, the main roof of the stope failed, rotated, and sunk resulting in the increasing pressure of the filling body consistently. According to the pressure gauge reading, the filling body pressure at 27.6 m behind the working face increased to
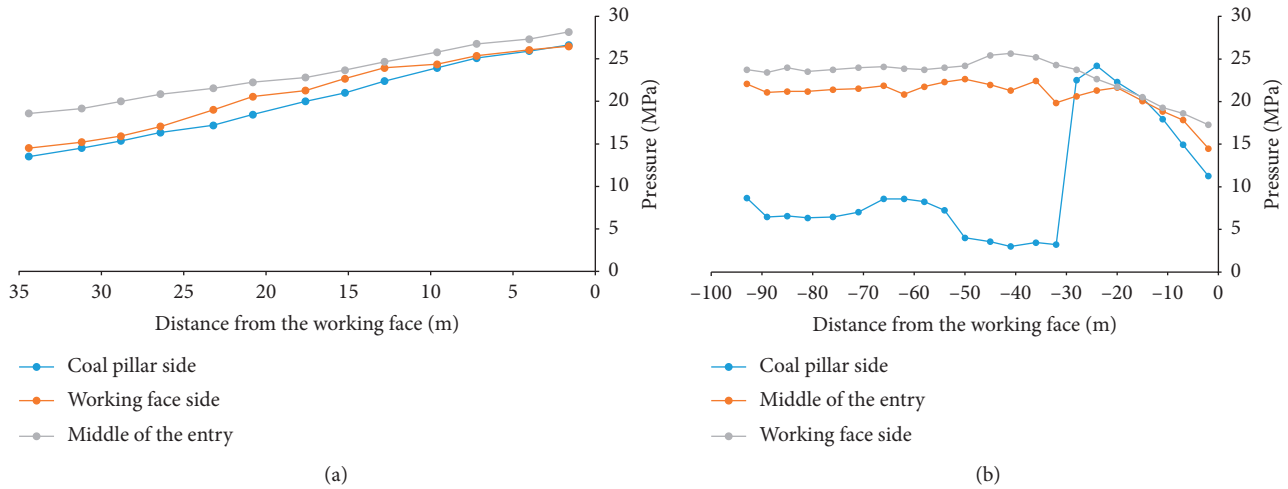
FIGURE 5: The pressure change curve of single hydraulic prop in advance support of entry. (a) Before mining. (b) After mining.
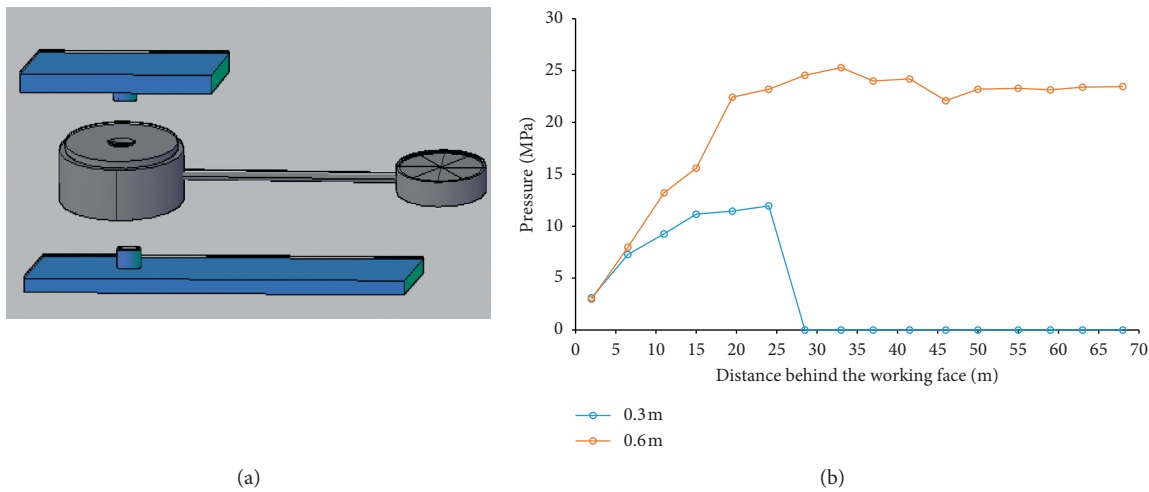
FIGURE 6: The filling body pressure monitoring. (a) The pressure gauge for the filling body. (b) The pressure gauge reading of the filling body.

308 t at 0.6 m. The pressure of the filling body fluctuated, decreased, and rose after 32.2 m behind the working face, forming a microgrowth trend. The lowest pressure was spotted at 45 m behind the working face, which may be caused by the main roof fracture. The pressure of the filling body changed little after 50 m behind the working face, indicating that the movement of roof strata tends to be stable.

4. Law of Mine Pressure of the Gob-Side Entry Retaining during the Secondary Mining Period

4.1. Reinforcement Scheme Design of the Gob-Side Entry Retaining during Secondary Mining

4.1.1. The Overall Grouting Scheme. The overall grouting scheme parameters and layout are shown in Table 5 and Figure 7, respectively.

4.1.2. Anchor Cable Reinforcement Scheme of E1316 Intake Entry. The anchor cable reinforcement scheme of E1316 intake entry is shown in Table 6 and Figure 8.

4.2. Detection and Analysis of the Surrounding Rock Stability of Entry before the Secondary Mining

4.2.1. Detection Scheme of the Surrounding Rock Structure. Based on the specific conditions of E1316 intake entry and air return entry, the borehole detector was used to detect and analyze the internal deformation and failure of the surrounding rock of entry, which provides a basis for entry evaluation and reinforcement scheme.

(1) The layout of the borehole stations: as shown in Figure 9(a), a CHK7.2 (B) type rock borehole detector developed by Xuzhou Whitton Company was adopted [17–19]. During the observation, the list of the required instruments is provided in Table 7.

TABLE 5: The details of the grouting parameters.

Related indicators	Parameters
Grouting material	Jinan reinforcement I
Grouting form	Deep and shallow hole grouting
Grouting hole layout	Three-two layout
Grouting pressure	0.7 MPa (shallow hole), 2 MPa (deep hole)
Grouting time per hole	600 s
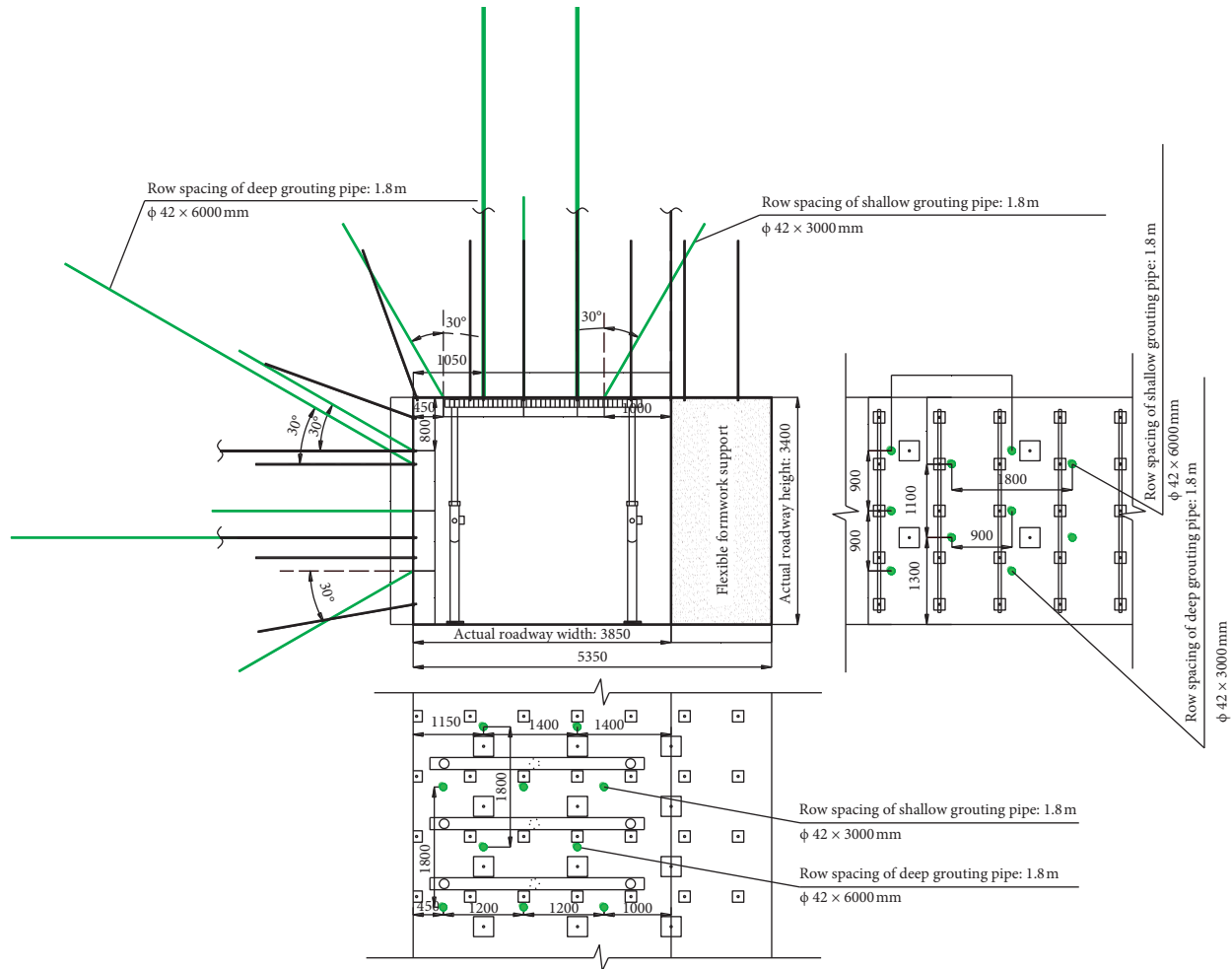
FIGURE 7: The layout of the grouting hole.

TABLE 6: The parameters of the cable reinforcement.

Name	Relevant parameters
Anchor cable specification	$\Phi 18.96 \times 5300$ mm
Pretightening force	≥ 163.3 kN
Anchorage length	1657 mm
Resin explosive roll	K2335(1), Z2360 (2)
Row and line space	Coal side: 1400 mm × 3600 mm, Roof: 1700 × 2700
Number	Coal side: 3/row, Roof: 2/row
Tray specification	300 mm × 300 mm × 16 mm
Mesh reinforcement	$\Phi 6$ steel bar, 100 mm × 100 mm mesh (repair mesh only at failure point)
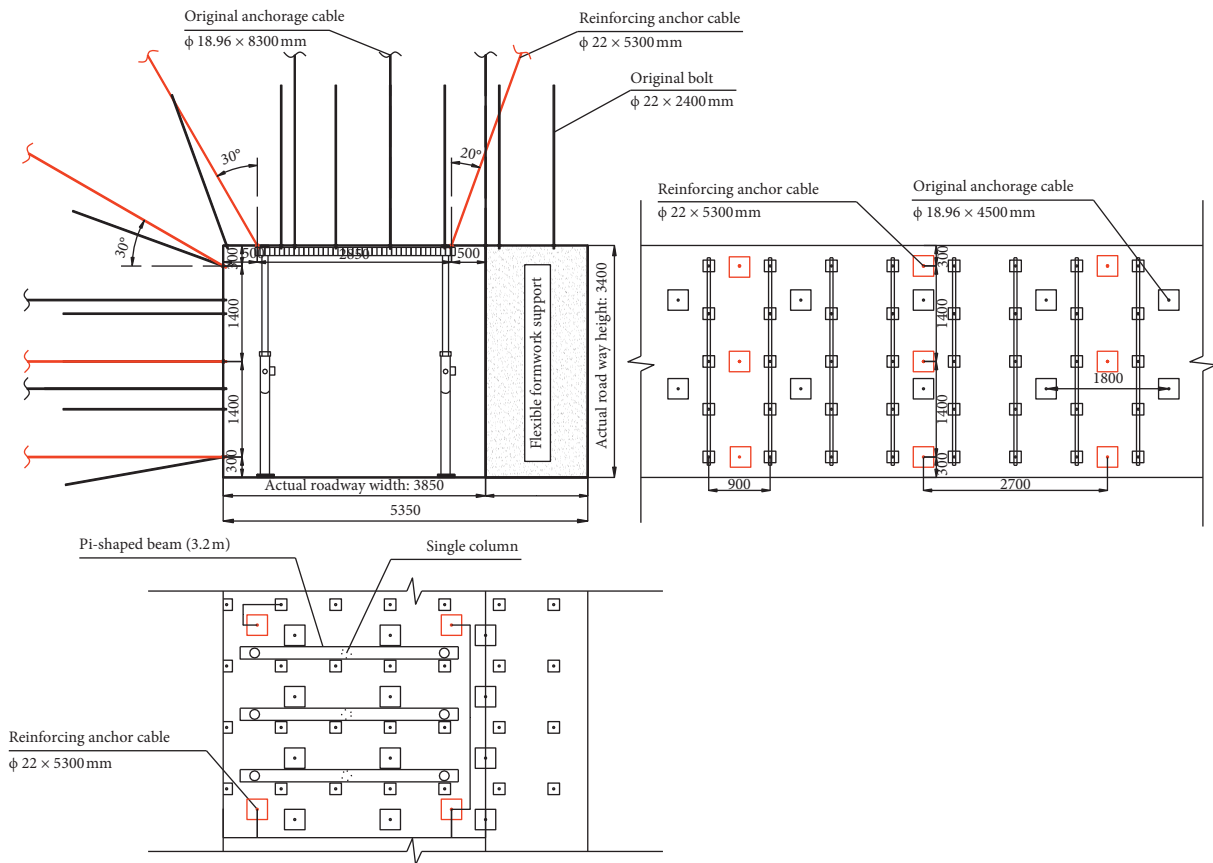
FIGURE 8: The schematic diagram of cable reinforcement of W1319 intake entry.

(a) (b) (c) (d)
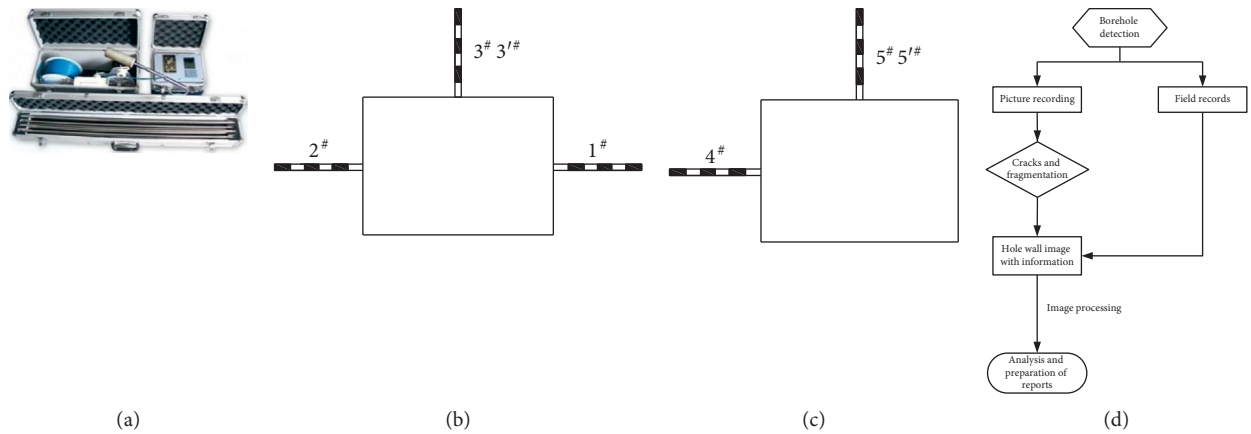
FIGURE 9: The detection scheme of the surrounding rock structure.

TABLE 7: The instrument list.

Serial number	Instrument	Quantity
1	CHK7.2 (B) type rock borehole detector	1
2	Tape measure	1

(2) The observation content: the information regarding the internal deformation and the law governing the failure of the entry surrounding rock can be collected, as well as the development of the internal cracks in the entry surrounding rock, which has been proven to be effective in evaluating the entry support and providing reference for the optimization of entry support parameters.

(3) Observation scheme: According to the specific production technical conditions of E1316 intake entry, the deformation and failure of surrounding rock were detected and analyzed by using the CHK7.2 (B) borehole detector in the early and middle working shifts on August 6, 2017. Boreholes were drilled along the roof of the entry upward and parallel to the floor along the pillar wall near E1316 intake entry, locating at 150 meters away from the cut hole. The boreholes' layout is shown in Figures 9(b) and 9(c).

A total of seven detection holes were drilled, namely, 1# (E1316 air return entry coal pillar side), 2# (E1316 air return entry solid coal side), 3# and 3'# (E1316 air return entry roof), 4# (E1316 intake entry coal pillar side), and 5# and 5'# (E1316 intake entry roof). The design parameters of each detection hole are shown in Table 8.

(4) The borehole detection and analysis: as shown in Figure 9(d), converting the borehole video into screenshot images can facilitate the analysis and processing of the borehole wall. According to the specific production technical conditions of the related roadways in E1315 and E1316 working faces of Gaohe coal mine, the borehole detection was conducted in the early and middle shifts on August 6, 2017. Through the detection and analysis of the separation and deformation of the surrounding rock, seven observation holes were drilled, and four out of seven were obtained. Some boreholes failed in the middle of the drilling, which were abandoned and excluded. Overall, a total of 22 valid video images were obtained. The law governing the internal fissures development in the surrounding rock was presented, providing the foundation for the reinforcement scheme and the selection of the supporting system.

4.2.2. Analysis of the Measurements

(1) Due to the change of stress field in tunnel excavation, the shallow deformation and destruction of coal pillar in E1316 air return entry were severe, including the failures of the boreholes. The stress concentration of solid coal pillar was high with fully developed cracks in the coal body. The overall condition was featured with fractures and cracks in the coal roof. The mudstone and the deep rock mass remained intact.

(2) The coal body of the pillar side of E1316 intake entry was mostly loose from shallow to deep with limited cracks. The coal roof was severely fractured. The separation phenomenon was observed at the joint of

coal seam with the mudstone, and the deep rock seam remained intact.

(3) The surrounding rock fragmentation of the two roadways gradually diffused from shallow to deep, and the degree of fragmentation gradually decreased from shallow to deep.

4.3. Investigation on Premining Damage of Surrounding Rock and Flexible Formwork Filling Body of E1316 Gob-Side Entry Retaining

4.3.1. Statistical Analysis of Entry Damage. In view of the situation of E1316 intake entry, the deformation and damage of coal pillar, roof, flexible formwork filling body, anchor cable, and ladder beam are counted from the cut hole of E1316 working face, as shown in Table 9.

According to the field investigation of E1316 intake entry, the main failure modes of entry include the bolt and cable failure, roof subsidence, coal pillar side moving towards the entry, severe coal body outburst at the shoulder corner of the entry, and bulging of the flexible formwork wall. The deformation mainly occurred in the roof and the coal pillar side. The estimated deformations reached about 450 mm and 300 mm, respectively. The coal body outburst at the shoulder corner can reach 550 mm. The analysis demonstrates that the deformation and destruction of the roof and the coal pillar side are severe. Meanwhile due to the high pressure, the coal pillar side and the flexible formwork wall failed. The existing supporting system faces the risk of uncontrollable entry deformations.

4.3.2. Borehole Detection and Analysis

(1) The roof of E1316 air return entry

① The distribution of the surrounding rock failure in the bolt anchorage zone presents progressive characteristics.
   The surrounding rock in the 0.1–0.8 m range of the roof anchorage zone was seriously damaged, forming obvious fractured zones. The images were selected from the detection holes and are presented in Figures 10(a) and 10(b). The surrounding rock in the anchorage zone of roof was partially broken in the range of 1.1–2.0 m, showing the plastic distribution and leading to the fracture zones with obvious development characteristics about 1 m. Image presented in Figures 10(c)–10(f) were also selected from the detection holes.

② The development of the surrounding rock outside the bolt anchorage zone (2.3–3.8 m) fissures.
   In this range, obvious cracks and fragments were found in the surrounding rock. The coal-rock boundary was 3.8 m. In other words, the top coal

TABLE 8: Design parameters of boreholes for detection.

NO	1#	2#	3#	3#	4#	5#	5'#
Diameter (mm)	33~34	33~34	33~34	33~34	33~34	33~34	33~34
Azimuth, α (°)	−90	90	—	—	90	—	—
Dip angle, β (°)	0	0	90	90	0	90	90
Length (m)	10	10	10	10	10	10	10

No, 1 # boreholes failed in the middle of drilling, which were abandoned and excluded.

TABLE 9: Questionnaire on deformation and failure of E1316 intake entry.

Mileage (m)	Description of roadway damage
15~17	Flexible formwork wall is inserted upward
23, 24, 58	The coal body at the bottom of the coal pillar side is extruded 30–50 cm, and the ladder beam is broken.
69	Fracture of the ladder beam in coal pillar side.
78	Flexible formwork wall bulge phenomenon.
82~84, 100	Fracture of the ladder beam in coal pillar side.
103~105	Metal net at the lower part of coal pillar side cracking, ladder beam fracture, and flexible formwork wall cracking.
113	The bolt of the coal pillar side failed, and the cables were laid beside it.
118	Fracture of the ladder beam near the second bolt at the bottom of coal pillar side.
132~138	Cracking of entry floor.
151~154	Two bolts in the middle of coal pillar side are pulled out by the mining stress.
163	Anchoring cable for pillar reinforcement has been removed in later period.
175~180	Extrusion and crushing at shoulder corner of the roof and coal pillar side is serious.
188	Unanchoring of the third bolt from the bottom of the coal pillar side.
190–214	Cracking of entry floor.
198~201	Four rows of ladder beams were broken in the middle and lower parts of coal pillar side.
213	The flexible formwork wall cracks in a 3-square range, the ladder beam at the bottom of the coal pillar side was broken, and the roof protruded seriously.
221	Two failure bolts in the middle of coal pillar side.
229~232	The upper and lower parts of the flexible formwork wall fall into the bag. The height is 1.2 meters, and the length is 4.5 meters.
239	The second bolt dynamometer reading at the bottom of the coal pillar wall is 24 MPa, which is abnormal; the flexible formwork wall cracks, and the middle part falls into the bag.
247~253	The damage and deformation of coal pillar side are serious, which are mainly affected by primary mining and adjacent chambers.
259~267	Roof breakage and subsidence are very serious, especially near the side of the coal pillar.
276	Unanchoring of the third and fourth bolts from the bottom of the coal pillar side.
296	Unanchoring of the third bolt from the bottom of the coal pillar side.
308	Unanchoring of the second bolt from the bottom of the coal pillar side.
311, 312	Unanchoring of the second bolt from the bottom of the coal pillar side.
320~350	The upper part of flexible formwork wall badly bulge phenomenon.
334~336	Flexible formwork wall with bulge phenomenon, bulging range is 2 meters.
352~355	Cracking of the flexible formwork wall is serious.
358	The second repaired cable at the bottom of the coal pillar side has failed.
399~406	Cracking of entry floor.
413~422	There are timbers to strengthen support in this area, and there are chambers nearby.
476~479	Over-excavation of coal pillar side is serious, and the cross section is large and irregular.
537~541	The roof is broken seriously, the displacement is large, and the flexible formwork wall has bulging problem.
581	Unanchoring of the third bolt from the bottom of the coal pillar side.
583	Unanchoring of the second bolt from the bottom of the coal pillar side.
620	The upper part of the flexible formwork wall bulges and cracks, and the third anchor bolt is removed from the bottom of the coal pillar side.
630~640	Water accumulation in entry and floor cracking.
652	The upper part of the flexible formwork wall is bulging within 2 meters.

thickness is 3.8 m. Compared with the coal seam column diagram and the situation of excavation, the top coal thickness fluctuated greatly with a thicker top. The detection results are shown in Figures 11(a)–11(d).

③ The development of the surrounding rock outside the bolt anchorage zone (3.8–10 m) is in the basic integrity state.

In this range, no obvious cracks and fractured zones were found in the surrounding rock with the good integrity.

(a)   (b)   (c)   (d)

(e)   (f)
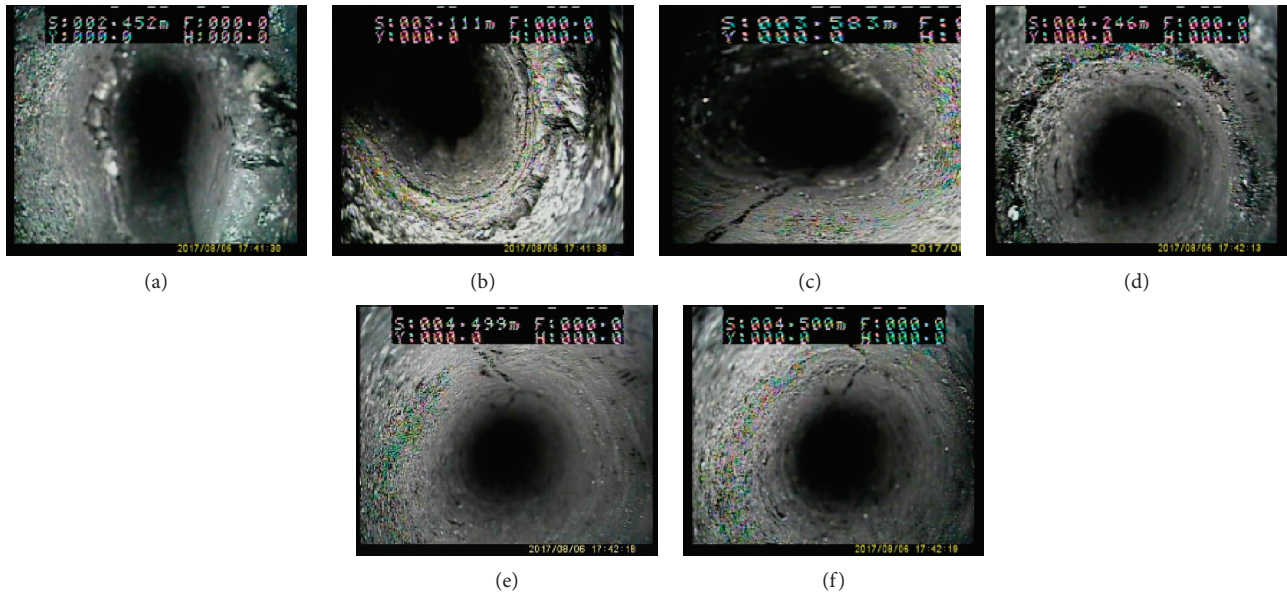
FIGURE 10: The distribution of the surrounding rock in the roof anchorage area. (a) 0.2 m. (b) 0.8 m. (c) 1.1 m. (d) 1.5 m. (e) 1.8 m. (f) 2.0 m.

(a)   (b)   (c)   (d)
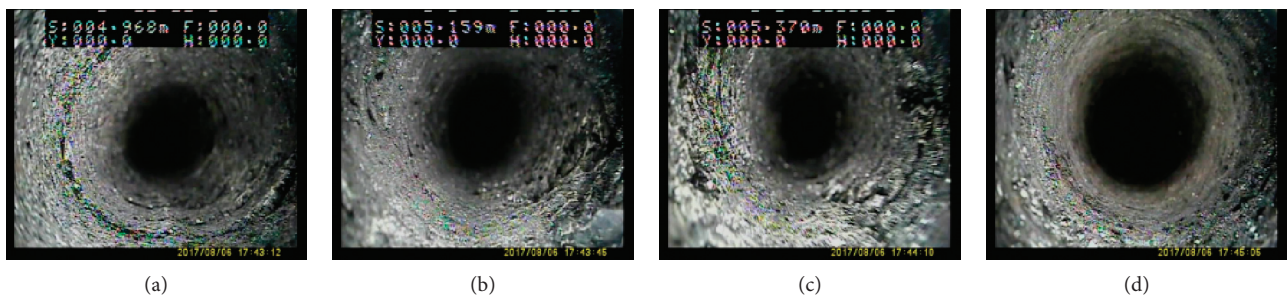
FIGURE 11: The distribution of the surrounding rock (2.5–3.8 m) outside the anchor zone. (a) 2.5 m. (b) 2.9 m. (c) 3.4 m. (d) 3.8 m.

The hole with the depth of 7.2 m was located at the junction of the direct roof and the main roof, which was relatively fragmented. A large amount of smoke and dust in the hole was within the main roof, due to the friction between the drill bit and the sandstone of the main roof. The helix characteristics were clearly observed. The detection results are shown in Figures 12(a)–12(h).

(2) The solid coal side of E1316 return entry

① Good integrity of the surrounding rock in the bolt anchorage zone.
In this range, no obvious cracks and fractured zones were found in the surrounding rock with better integrity. The preload of the bolt support was high at the initial stage. Better supporting effects were identified in the bolting range. This range of images was selected from the detection hole, and the results are shown in Figures 13(a)–13(d).

② Fracture zones found in the surrounding rock outside the bolt anchorage zone (2.3–7.8 m).
In this range, obvious crack development and fragmentation were found in the surrounding rock. The coal body was loose and fragmented, accompanied by severe granular coal caving. The detection results are shown in Figures 14(a)–14(d).

③ Good surrounding rock integrity outside the bolt anchorage zone (7.8–10 m).
In this range, no obvious cracks and fractured zones in the surrounding rock due to unmined working face were present. The overall integrity remained untouched. The coal powder accumulation in the pillar side hole was severe. This range of images was selected from the detection hole, and the results are shown in Figures 15(a)–15(d).

(3) The roof of E1316 intake entry.

① Fractured zones found in the surrounding rock of bolt anchorage zone
The integrity of the surrounding rock in 0.1–0.7 m range of the roof anchorage zone was good. The detection results are shown in Figures 16(a) and 16(b). The surrounding rock in 0.7–2.3 m range of the roof anchorage zone was partially broken, and the cracks had expanded and developed. This range of images was selected
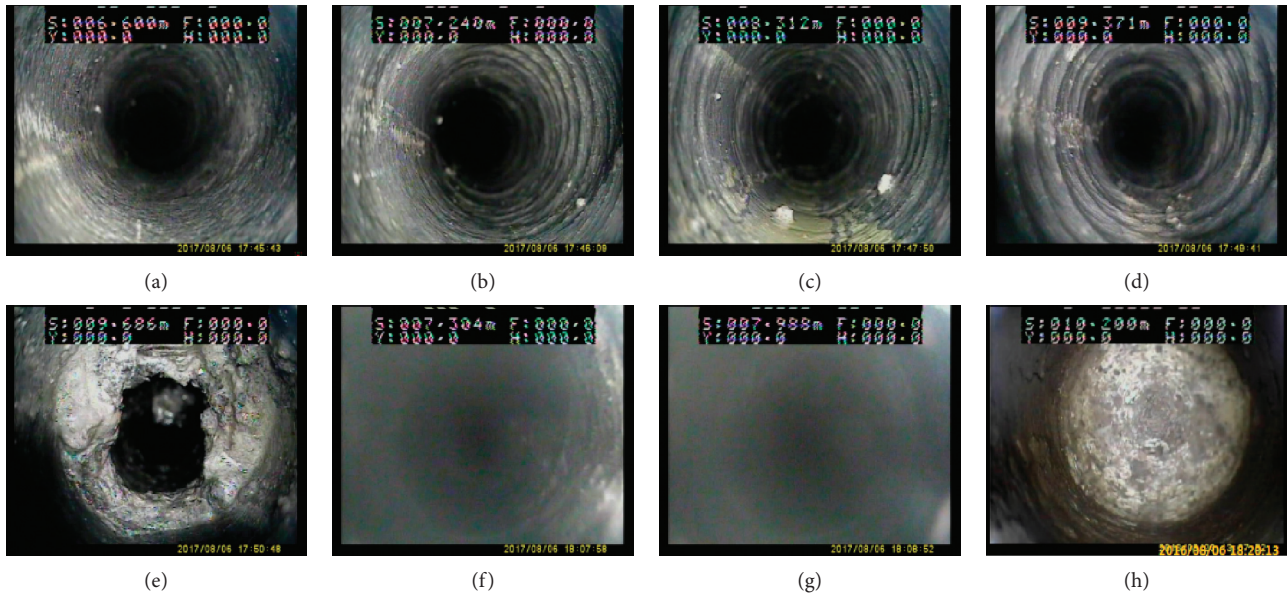
FIGURE 12: The distribution of the surrounding rock (3.8–10 m) outside the anchor zone. (a) 4.1 m. (b) 4.7 m. (c) 5.9 m. (d) 6.9 m. (e) 7.2 m. (f) 7.6 m. (g) 8.0 m. (h) 10.0 m.
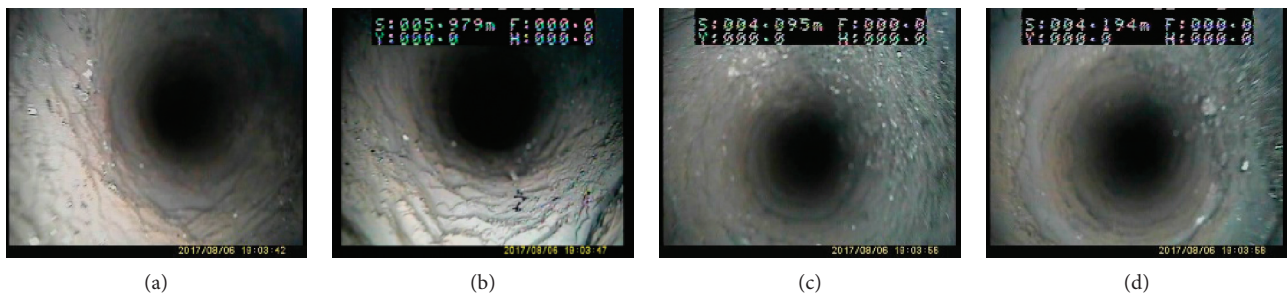
FIGURE 13: The distribution of the surrounding rock in the roof anchorage area. (a) 0.2 m. (b) 0.9 m. (c) 1.8 m. (d) 2.2 m.
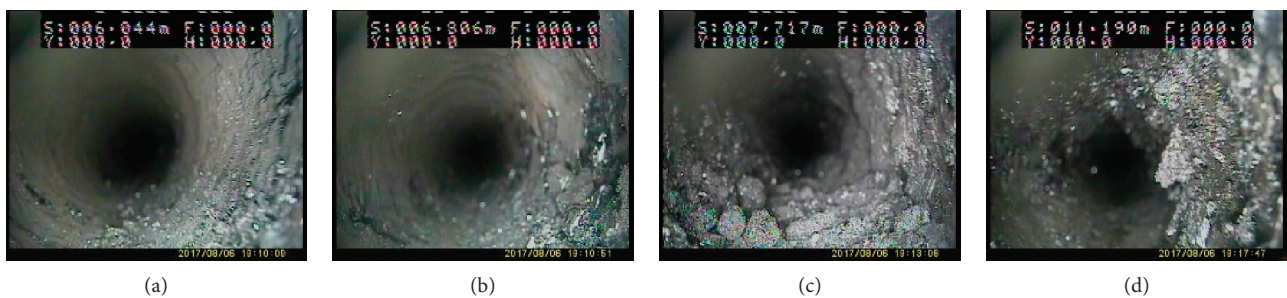
FIGURE 14: The distribution of the surrounding rock (2.3–7.8 m) outside the anchor zone. (a) 2.6 m. (b) 4.2 m. (c) 5.8 m. (d) 7.6 m.

from the detection hole, and the results are shown in Figures 16(c)–16(f).

② The development of the surrounding rock outside the bolt anchorage zone (2.3–2.8 m) fissures Fissure zones were identified in the surrounding rock. The fissures developed initially from 1.7 m in the anchorage area with a 1.1-meter penetration. Due to the softness differences between the coal body and the drill bit, the fissures can develop during drilling, and the coal-rock interface is 2.8 m. The detection results are shown in Figures 17(a)–17(d).

(a)   (b)   (c)   (d)
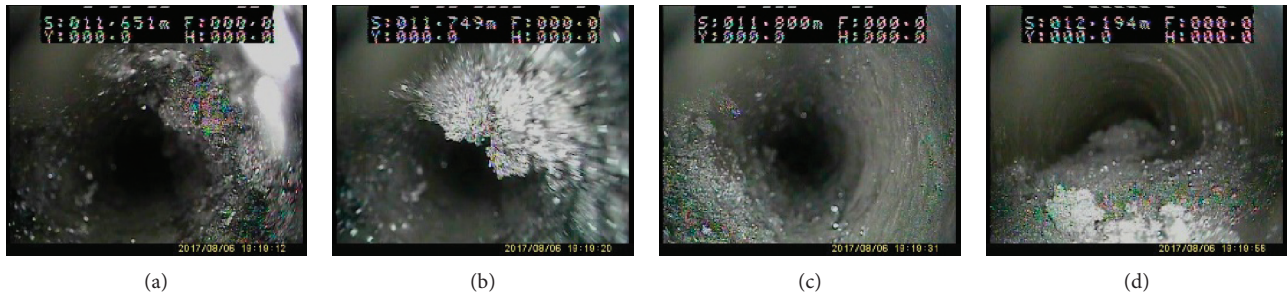
FIGURE 15: The distribution of the surrounding rock (7.8–10 m) outside the anchor zone. (a) 7.9 m. (b) 8.3 m. (c) 9.2 m. (d) 10.0 m.

(a)   (b)   (c)   (d)

(e)   (f)
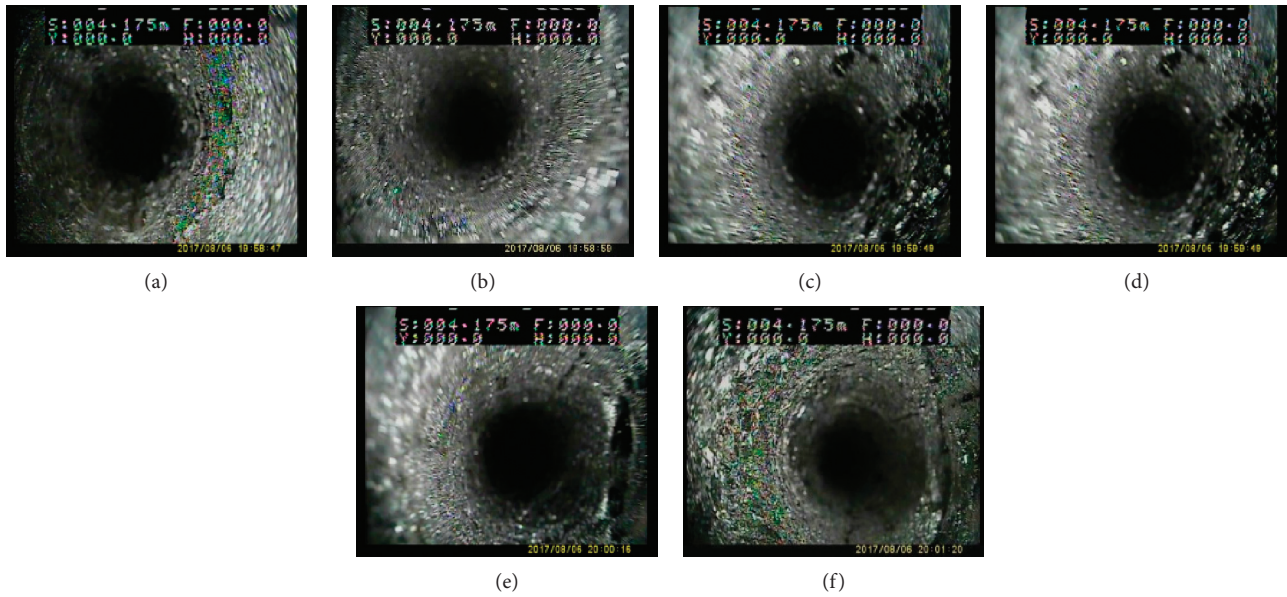
FIGURE 16: The distribution of the surrounding rock in the roof anchorage area. (a) 0.2 m. (b) 0.7 m. (c) 0.8 m. (d) 1.0 m. (e) 1.8 m. (f) 2.2 m.

(a)   (b)   (c)   (d)
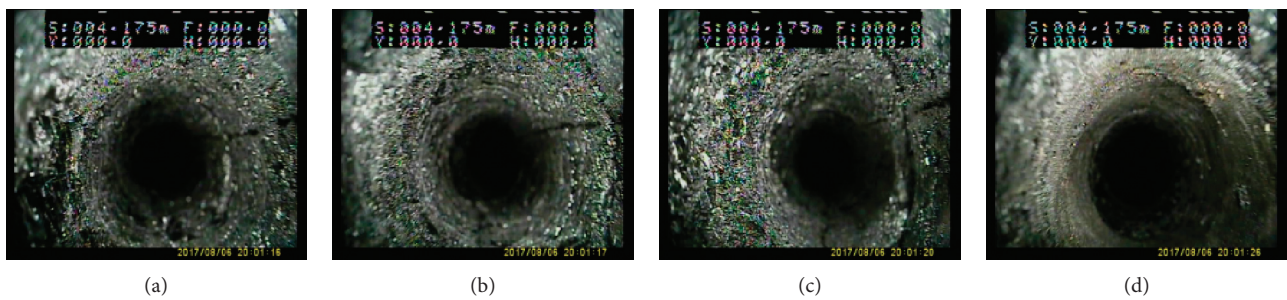
FIGURE 17: The distribution of the surrounding rock (2.3–2.8 m) outside the anchor zone. (a) 2.3 m. (b) 2.5 m. (c) 2.7 m. (d) 2.8 m.

③ The development of the surrounding rock outside the bolt anchorage zone (2.8–10 m) with basic integrity.

In this range, no obvious cracks and fractured zones were found in the surrounding rock with good integrity. The hole with a 5.7 m depth was located at the junction of the direct top and the main roof, which was relatively fragmented. The surrounding rock in the hole was intact within the main roof without any crack. The drilling process took longer. The fine sandstone of the main roof was harder, and the helix characteristics were visible. The detection results are shown in Figures 18(a)–18(h).

(4) The solid coal side of E1316 intake entry.

① Good integrity of the surrounding rock in bolt anchorage zone.
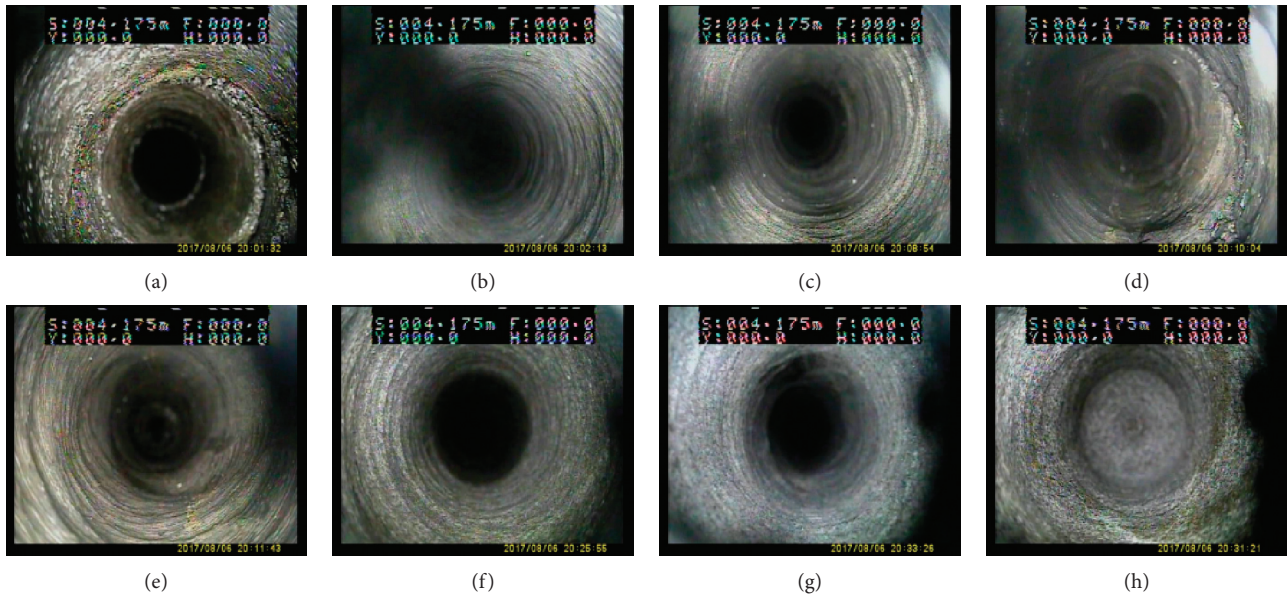
FIGURE 18: The distribution of the surrounding rock (2.8–10 m) outside the anchor zone. (a) 2.9 m. (b) 3.4 m. (c) 4.0 m. (d) 5.7 m. (e) 6.4 m. (f) 7.5 m. (g) 8.8 m. (h) 10.0 m.

In this range, no obvious cracks and fractured zones in the surrounding rock were found, but the coal body is loose and had no bearing capacity. This range of images was selected from the detection hole, and the results are shown in Figures 19(a)–19(d).

② The fracture zone in the surrounding rock outside bolt anchorage zone.

No obvious characteristics of crack development and fragmentation were found in the surrounding rock. Due to the high lateral stress caused by the mining in the upper working face, borehole fragmentation and deformation were severe with poor integrity. This range of images was selected from the detection hole, and the results are shown in Figures 20(a)–20(h).

4.4. Comprehensive Assessment on the Premining Damage of Surrounding Rock and Flexible Formwork Filling Body of E1316 Gob-Side Entry Retaining

4.4.1. Analysis of the Main Roof Structure.
Combining with the statistical analysis of entry damage and field investigation results of borehole detection in the previous section, the overburden structure of E1316 intake entry changed due to the mining of E1315 working face. During the advancing process of E1315 working face, the periodic weighting phenomena occurred in the roof. After the first weighting, the continuous advancing of the working face had made the main roof of E1315 working face prone to form "O-X" fracture structure. Due to the top coal collapse and the 2.6-meter thick immediate roof, the main roof was suffering from the fracture, rotation, and subsidence. In the mining process of E1315 working face, the flexible formwork

support was used to ensure the safety of gob-side entry retaining. Before the mining of E1316 working face, under the overall structural environment of the goaf, flexible formwork wall, and E1316 intake entry, the main roof of the section direction of E1316 intake entry can temporarily form a masonry beam structure. The fracture structure was often caused by many factors including the thickness and mechanical properties of the main roof, the immediate roof, and the coal seam, the mining depth, the stress state of the original rock, and the mining height [20–22].

According to the features of the failures of the roof of E1316 intake entry, the main roof failed at the "masonry beam" and the breaking line was above E1316 working face, suggesting that most of the weight of rock block B was above E1316 intake entry. In addition, the weight was borne by the flexible formwork wall and the coal pillar, which made the support of entry more difficult.

4.4.2. Location Analysis of the Main Roof Fracture.
The location of the fracture in the main roof of the E1316 intake entry holds an important role in the stability of the surrounding rock. Under the lateral abutment pressure of the working face, plastic zone, elastic zone, and original rock stress zone tend to appear from the edge of the coal pillar side of the entry to the depth of the coal pillar. The fracture position of the main roof was located near the junction of the elastic zone and the plastic zone in the coal body, as shown in Figure 21.

In the plastic zone, the fracture of the coal pillar was fully developed and the damage was severe. On the contrary, the damage in the elastic zone and original rock stress zone was limited. The depth of plastic zone affects the selection of support parameters. Therefore, the limit equilibrium theory was adopted to calculate the depth of the plastic zone of the
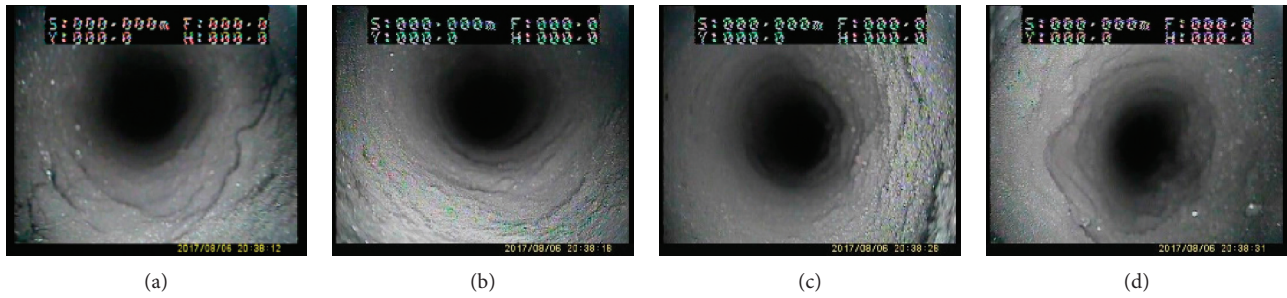
FIGURE 19: The distribution of the surrounding rock in the roof anchorage area. (a) 0.2 m. (b) 0.8 m. (c) 1.6 m. (d) 2.2 m.
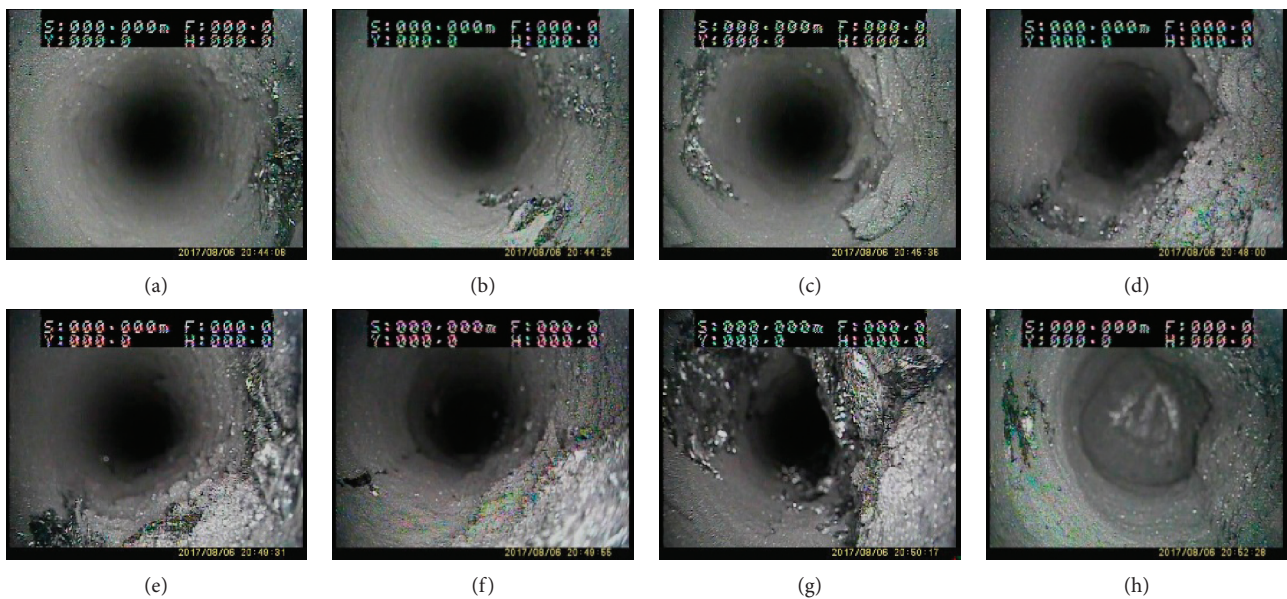
FIGURE 20: The distribution of the surrounding rock outside the anchor zone. (a) 2.6 m. (b) 3.2 m. (c) 4.8 m. (d) 5.6 m. (e) 6.6 m. (f) 7.8 m. (g) 8.9 m. (h) 10.0 m.
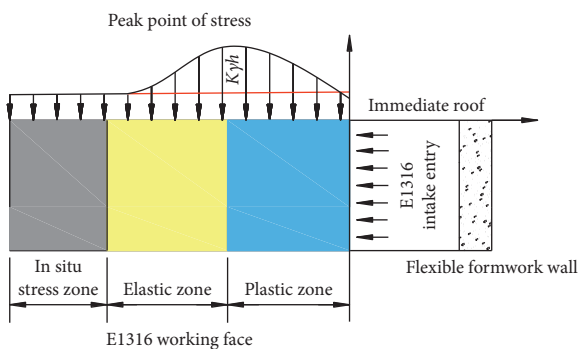
FIGURE 21: The diagrammatic sketch of stress distribution in coal pillar side.

surrounding rock for dynamic mining pressure entry such as E1316 intake entry.

According to the calculation, the limit equilibrium zone depth of E1316 intake entry was 6.14 m. In other words, the junction point of the plastic zone and elastic zone on the coal pillar side of E1316 intake entry was

6.14 m away from the coal wall. The calculation suggests that the breaking line of key block B of the main roof was above the coal pillar, which was about 6.14 m away from the coal wall.

4.4.3. Comprehensive Assessment of E1316 Gob-Side Entry Retaining. The measurement of rock mechanics properties, detection of the surrounding rock structure, and statistical study and theoretical calculation of premining failure of the surrounding rock and the flexible formwork filling body of E1316 gob-side entry retaining have suggested that the surrounding rock of E1316 intake entry had undergone great deformation and destruction. The serious damage of support structure had made the supporting system more vulnerable and fragile. In addition, due to the uneven occurrence of the layered surrounding rock, the uneven roadside support, and coal rib support, the deformation and failure of the support structure of gob-side entry retaining present nonuniform characteristics. The instability of the support structure can be jeopardized due to the significant deformation and failure occurred in the entry.

In view of the existing problems, the following solutions are proposed as follows:

(1) To solve the problem of loose bolts, the twin-nut structure is suggested. In addition, the bolt supporting density and anchoring agent should be increased to enhance the length of grip.

(2) To minimize the risk of ladder beam fracture, the ladder beam should be reinforced with the 16 mm round steel. The stress on the ladder beam should be verified. Regarding the continuous fracture area, the ladder beam can be replaced by using the steel strip for increased surface areas and strength.

(3) To minimize the risk of pallet failure, the $200 \times 200 \times 15$ mm bolt pallets and the $350 \times 350 \times 18$ mm cable pallets should be adopted. In addition, the wooden pallets and No. 12# lead wire meshes should be added to increase the surface area of pallets.

(4) To minimize the bulging and fracturing of the flexible formwork wall, a series of reinforcements and support measures for point pillars along the flexible formwork walls in the entry should be added.

(5) To minimize the floor heave of the entry, excavation measures should be taken in the floor heave.

The comprehensive analysis indicates that E1316 intake entry is subject to a high superimposed stress. Due to the low strength of the coal and rock mass, the surrounding rock cracks developed and continued to expand. With the poor bearing capacity of the entry itself, the flexible formwork wall tends to crack easily. Therefore, besides the proposed reinforcements and other preventative measures, monitoring the mine pressure constantly plays a vital role in ensuring the safety of the roadway and the E1316 working face.

5. Conclusion

(1) During the initial mining period, the roadway located at the stress increasing area was affected by mining in E1315 working face. The observation and analysis have suggested that the high pressure caused severe damage to the surrounding rock and the flexible formwork filling wall in the upper section of the entry. The roof and the flexible formwork wall experienced various levels of damage.

(2) The flexible formwork filling wall provides great strength with poor contractibility. For the severe roof subsidence at the gob-side entry retaining, the hardness of the filling wall was not compatible with the coal roof, resulting in inconsistent deformation. The deformation eventually led to the failure of the coal roof and flexible formwork filling wall, jeopardizing the entry support.

(3) The mining and roof collapse of E1315 working face lead to the formation of long cantilever beams which are not easy to collapse in the goaf on the side of the flexible formwork wall of E1316 intake entry. Most of its own weight of the cantilever beams acts on the flexible formwork filling wall, support structure, and coal pillar side, and the overall structure of the entry experienced various levels of damages.

(4) Due to the high stress, cracks developed in the top coal and the immediate roof rock layer (2.65 m above the entry), which continued to expand until the failure of the surrounding rock. Meanwhile, the coal pillar grew loose and fragmented beyond the range of 5 m. The deformation made the coal pillar become uneven and fragile, resulting in the moving out of the whole coal pillar. The deformation further jeopardized the bearing capacity of the surrounding rock. The coal pillar side experienced the most severe damage.

(5) With the reinforcements in the roof and the pillar side of the entry, the entry damage and deformation can be contained. However, more maintenance was required. Multiple long cracks and heaves were found in the immediate floor where no reinforcements were added.

The study of the coal pillarless mining technology conducted can provide both theoretical and pragmatic references to the operation of No. 3# coal in the entire Luan mining area, as well as other mining locations sharing similar conditions in Qinshui coalfield. The wide adoption of the gob-side entry retaining technology in the Luan mining area or Qinshui coalfield can bring significant economic and social benefits.

Data Availability

The data used to support the findings of this study are included within the article. And all data are obtained through experiment and test by our research team in Gaohe mine and laboratory. All the data are true and effective. The right to using data belongs to the authors before the article being published, but after it was published, the data can be referenced.

Conflicts of Interest

The authors declare no conflicts of interest.

Acknowledgments

References

[1] F.-T. Zhang, X.-Y. Wang, J.-B. Bai, G.-Y. Wang, and B.-W. Wu, "Post-peak mechanical characteristics of the high-water material for backfilling the gob-side entry retaining: from experiment to field application," *Arabian Journal of Geosciences*, vol. 13, no. 11, p. 386, 2020.

[2] G.-feng Zhang et al., "Research on the technique of no-pillar mining with gob-side entry formed by advanced roof caving in the protective seam in Baijiao coal mine," *Journal of Mining and Safety Engineering*, vol. 28, no. 4, pp. 511–516, 2011.

[3] Li Huamin, "Control design of roof rocks for gob side entry," *Chinese Journal of Rock Mechanics and Engineering*, vol. 19, no. 5, pp. 651–654, 2000.

[4] Z. Luo, Q. Hao, T. Wang, R. Li, F. Cheng, and J. Deng, "Experimental study on the deflagration characteristics of methane-ethane mixtures in a closed duct," *Fuel*, vol. 259, Article ID 116295, 2020.

[5] Z. Luo, R. Li, T. Wang et al., "Explosion pressure and flame characteristics of CO/CH4/air mixtures at elevated initial temperatures," *Fuel*, vol. 268, Article ID 117377, 2020.

[6] Z. Zhang, M. Deng, X. Wang, W. Yu, F. Zhang, and V. D. Dao, "Field and numerical investigations on the lower coal seam entry failure analysis under the remnant pillar," *Engineering Failure Analysis*, vol. 115, Article ID 104638, 2020.

[7] A. Jaiswal and B. K. Shrivastva, "Numerical simulation of coal pillar strength," *International Journal of Rock Mechanics and Mining Sciences*, vol. 46, no. 4, pp. 779–788, 2009.

[8] E. Ghasemi, M. Ataei, K. Shahriar, F. Sereshki, S. E. Jalali, and A. Ramazanzadeh, "Assessment of roof fall risk during retreat mining in room and pillar coal mines," *International Journal of Rock Mechanics and Mining Sciences*, vol. 54, pp. 80–89, 2012.

[9] M. C. He, "Control of surrounding rock structure for gob-side entry retaining by cutting roof to release pressure and its engineering application," *Journal of China University of Mining and Technology*, vol. 46, no. 5, pp. 959–969, 2017.

[10] M. C. He, "An energy-gathered roof cutting technique in no-pillar mining and its impact on stress variation in surrounding rocks," *Chinese Journal of Rock Mechanics and Engineering*, vol. 36, pp. 1314–1325, 2017.

[11] Y. Xu, J. Chen, and J. Bai, "Control of floor heaves with steel pile in gob-side entry retaining," *International Journal of Mining Science and Technology*, vol. 26, no. 3, pp. 527–534, 2016.

[12] Y.-F. Li and X.-Z. Hua, "Mechanical analysis of stability of key blocks of overlying strata for gob-side entry retaining and calculating width of roadside backfill," *Rock and Soil Mechanics*, vol. 33, no. 4, pp. 1134–1140, 2012.

[13] H. P. Kang, "In-situ stress measurements and distribution laws in Lu'an underground coal mines," *Rock and Soil Mechanics*, vol. 3, 2010.

[14] Y. Wang, Y. Gao, E. Wang, M. He, and J. Yang, "Roof deformation characteristics and preventive techniques using a novel non-pillar mining method of gob-side entry retaining by roof cutting," *Energies*, vol. 11, no. 3, p. 627, 2018.

[15] X. Zhu, "Research on the stability evaluation model of composite support pillar in backfill-strip mining," *Mathematical Problems in Engineering*, vol. 2020, no. 2, 2020.

[16] J. Zhang and Y. Li, "The stability of gob-side entry retaining in a high-gas-risk mine," *Advances in Civil Engineering*, vol. 2019, Article ID 7540749, 2019.

[17] Z. Han, C. Wang, C. Wang, X. Zou, Y. Jiao, and S. Hu, "A proposed method for determining in-situ stress from borehole breakout based on borehole stereo-pair imaging technique," *International Journal of Rock Mechanics and Mining Sciences*, vol. 127, Article ID 104215, 2020.

[18] A. M. Abudeif, M. A. Mohammed, R. E. Fat-Helbary, H. M. El-Khashab, and M. M. Masoud, "Integration of 2D geoelectrical resistivity imaging and boreholes as rapid tools for geotechnical characterization of construction sites: a case study of New Akhmim city, Sohag, Egypt," *Journal of African Earth Sciences*, vol. 163, Article ID 103734, 2020.

[19] N. T. Smith, J. Shreeve, and O. Kuras, "Multi-sensor core logging (MSCL) and X-ray computed tomography imaging of borehole core to aid 3D geological modelling of poorly exposed unconsolidated superficial sediments underlying complex industrial sites: an example from Sellafield nuclear site, UK," *Journal of Applied Geophysics*, vol. 178, Article ID 104084, 2020.

[20] G. Feng and P. Wang, "Stress environment of entry driven along gob-side through numerical simulation incorporating the angle of break," *International Journal of Mining Science and Technology*, vol. 30, no. 2, pp. 189–196, 2020.

[21] W. Huang, X. Wang, Y. Shen, F. Feng, K. Wu, and C. Li, "Application of concrete–filled steel tubular columns in gob–side entry retaining under thick and hard roof stratum: a case study," *Energy Science & Engineering*, vol. 7, no. 6, pp. 2540–2553, 2019.

[22] J. Yang, M. He, and C. Cao, "Design principles and key technologies of gob side entry retaining by roof pre-fracturing," *Tunnelling and Underground Space Technology*, vol. 90, pp. 309–318, 2019.

Research Article

Research on the First Breaking Mechanism of the Main Roof of Coal Seam with High Dip Angle

Xinyu Hu [1,2] **and Jinlong Cai** [3,4]

[1]*College of Mechanics and Civil Engineering, China University of Mining and Technology, Xuzhou, Jiangsu 221116, China*
[2]*State Key Laboratory for Geomechanics and Deep Underground Engineering, China University of Mining & Technology, Xuzhou, Jiangsu 221008, China*
[3]*School of Energy and Safety Engineering, Anhui University of Science and Technology, Huainan, Anhui 232001, China*
[4]*School of Architecture and Civil Engineering, West Anhui University, Luan, Anhui 237012, China*

Correspondence should be addressed to Jinlong Cai; 25072103@qq.com

In order to study the mechanism and characteristics of the first breaking of the roof in thick coal seams with high dip angles, a mechanical model of elastic thin plate with four clamped edges of the roof was established, and the expressions of the deflection and stress of the roof were obtained by the energy method. The influence of the change in seam dip angle on the first breaking distance of the roof was presented. Based on the stress solution, the roof breaking criterion was proposed, and the breaking distance of the roof was calculated. Combined with numerical simulation, the stress distribution characteristics of the upper and lower surfaces of the stope roof were analyzed. The results show that the first breaking distance of the roof is inversely proportional to the seam dip angle. Broken morphology of roof in high dip seam is different from the "O-X" morphology of horizontal roof. The roof breaking order of the seam with high dip angle is middle-middle upper-middle lower-upper-lower. These research results have certain theoretical guiding significance for the study of the first breaking mechanism of the main roof of highly inclined working face of coal seams.

1. Introduction

The activity of surrounding rock is closely related to mine pressure. The former is the internal source of the latter, and the latter is the external manifestation of the former. Hence, the study of roof movement in stope is the basis of mine pressure analysis [1]. As the key rock layer that affects the mine pressure, scholars at home and abroad have conducted a significant amount of in-depth research on the breaking mechanism of the main roof in near horizontal or gently inclined coal seams. Many theories of mine pressure control have been proposed, such as pressure arch hypothesis, cantilever hypothesis, masonry beam hypothesis, and moving rock beam hypothesis [2].

However, the breaking law of the inclined coal seam roof is different from that of the near horizontal coal seam. The

roof behaviors show obvious asymmetry, which cannot be described accurately by the above traditional hypotheses.

Yin et al [3] analyzed the basic laws of rock mass movement, mine pressure distribution, and ground subsidence caused by mining in large inclined working face by establishing FLAC numerical model. Based on the thin plate theory, Zhang et al. [4] analyzed the roof breaking of up-dip or down-dip mining stope. According to the theory of elastic mechanics, Wang et al. [5] established a mechanical model of the roof in the thick seam with large dip angle and analyzed its fracture characteristics. Using R–W Kane theory and Lagrange theory, Wu et al. [6–8] established the general dynamic equation of the coal seam with high dip angle and conducted in-depth research on the mechanism of the main roof fracture with high dip angle. In this paper, based on the engineering background of a mining face with high dip angle

in Luliang mining area, an elastic thin plate model with four clamped edges was established. The expressions of deflection and stress were obtained by energy method, and the influence of different inclinations on the roof deflection was analyzed. Combined with numerical calculation, the roof breaking law was analyzed and verified by on-site data.

2. General Situation of Engineering Geology

The average buried depth of working face 103 in Luliang mining area is 485 m. The main mining coal seam is No. 5 coal seam. The inclined length of working face is 185 m, the strike length is 1700 m, and the average thickness of coal seam is 4.7 m. The dip angle of coal seam is 26°–32°, with an average of 30°. The lithology of roof and floor is shown in Table 1.

2.1. Mechanical Analysis of Thin Plate Model. According to the theory of mine pressure in stope, the first fracture of main roof can be explained more reasonably by the elastic thin plate model with four edges clamped [9–11]. Generally, the working face is 150 m~200 m long, the first breaking distance of the basic roof is 20 m~50 m, and its width thickness ratio is 1/5~1/10. Hence, the main roof can be regarded as a thin plate.

2.2. Establishment of Mechanical Model. Figure 1 shows the mechanics model of the main roof before first breaking, which is an elastic thin plate with four edges clamped. For this working face, a is the advancing distance, b is the inclination length, and α is the inclination angle. For the rock in main roof, E is the elastic model, and Poisson's ratio is μ. The term h is the thickness of main roof, that is, the thickness of thin plate in elasticity. For simplification, the load $q(x)$

acting on the roof is regarded as the resultant force of the longitudinal load and the inclined load. Then, the Ritzi energy method is used for calculation [12].

2.3. Deflection and Stress Equation of Main Roof. In order to meet the asymmetrical distribution of the main roof deflection along the inclination, the following deflection functions $\omega(x, y)$ can be used:

$$w = \sum_{m=1}^{\infty} \sum_{m=1}^{\infty} c_{mn}\left(1 - \cos\frac{2\pi mx}{a}\right)\left(1 - \cos\frac{2\pi ny}{b}\right). \quad (1)$$

The boundary conditions are

$$w|_{x=0} = w|_{x=a} = w|_{y=0} = w|_{y=b} = 0,$$

$$\left.\frac{\partial w}{\partial x}\right|_{x=0} = \left.\frac{\partial w}{\partial x}\right|_{x=a} = \left.\frac{\partial w}{\partial y}\right|_{y=0} = \left.\frac{\partial w}{\partial y}\right|_{y=b} = 0. \quad (2)$$

Based on the assumption of straight line of the thin plate bending and by neglecting the middle-plane strain, its total deformation energy is obtained as follows:

$$U = \frac{\pi^2 E h^3}{6\left(1 - \mu^2\right)} \sum_{m=1}^{\infty} \sum_{n=1}^{\infty} c_{mn}^2\left(\frac{3bm^4}{a^3} + \frac{3an^4}{b^3} + \frac{2m^2n^2}{a^2b^2}\right). \quad (3)$$

The work done by the load on the plate surface is

$$W = \iint_S q\cos\alpha w\,dx\,dy + \frac{1}{2}\iint_s q\sin\alpha y\left(\frac{\partial w}{\partial y}\right)^2 dx\,dy. \quad (4)$$

The total potential energy of the plate is $\prod = U - W$. From the principle of minimum potential energy, i.e., $\partial\prod/\partial c_{mn} = 0$, each coefficient c_{mn} can be obtained. Then, the deflection expression is

$$w = \sum_{m=1}^{\infty} \sum_{n=1}^{\infty} \frac{q\cos\alpha}{\left(4\pi^2 Eh^3/12\left(1 - \mu^2\right)\right)\left(\left(3m^4/a^4\right) + \left(3n^4/b^4\right) + \left(2m^2n^2/a^3b^3\right)\right) - \left(q\sin\alpha\pi^2 n^2/b^2\right)} \left(1 - \cos\left(2\pi mx/a\right)\right)\left(1 - \cos\left(2\pi ny/b\right)\right). \quad (5)$$

Substituting equation (5) into the formula giving the relationship between the deflection and the stress of the rectangular thin plate in elastic mechanics, three stress

components of the main roof of the high dip seam are obtained as follows:

$$\sigma_x = -\frac{4\pi^2 Ezq\cos\alpha}{\left(1 - \mu^2\right)} \sum_{m=1}^{\infty} \sum_{n=1}^{\infty} \frac{\left(\left(m^2/a^2\right)\cos\left(2\pi mx/a\right)\left(1 - \cos 2\pi ny/b\right) + \mu\left(n^2/b^2\right)\cos\left(2\pi ny/b\right)\left(1 - \cos 2\pi mx/a\right)\right)}{4\pi^2 Eh^3/12\left(1 - \mu^2\right)\left(\left(3m^4/a^4\right) + \left(3n^4/b^4\right) + \left(2m^2n^2/a^3b^3\right)\right) - \left(q\sin\alpha\pi^2 n^2/b^2\right)},$$

$$\sigma_y = -\frac{4\pi^2 q\cos\alpha Ez}{\left(1 - \mu^2\right)} \sum_{m=1}^{\infty} \sum_{n=1}^{\infty} \frac{\left(\left(n^2/b^2\right)\cos\left(2\pi ny/b\right)\left(1 - \cos\left(2\pi mx/a\right)\right) + \mu\left(m^2/a^2\right)\cos\left(2\pi mx/a\right)\left(1 - \cos 2\pi ny/b\right)\right)}{\left(4\pi^2 Eh^3/12\left(1 - \mu^2\right)\right)\left(\left(3m^4/a^4\right) + \left(3n^4/b^4\right) + \left(2m^2n^2/a^3b^3\right)\right) - \left(q\sin\alpha\pi^2 n^2/b^2\right)}, \quad (6)$$

$$\tau_{xy} = -\frac{4\pi^2 q\cos\alpha Ez}{ab(1 + \mu)} \sum_{m=1}^{\infty} \sum_{n=1}^{\infty} \frac{mn\sin\left(2\pi mx/a\right)\sin\left(2\pi ny/b\right)}{\left(4\pi^2 Eh^3/12\left(1 - \mu^2\right)\right)\left(\left(3m^4/a^4\right) + \left(3n^4/b^4\right) + \left(2m^2n^2/a^3b^3\right)\right) - \left(q\sin\alpha\pi^2 n^2/b^2\right)}.$$

Roof or floor	Rock type	Thickness (m)	Lithological characteristics
Main roof	White sandstone	3.6 ~ 6.5/4.7	Light gray sandstone with medium grains, hard, with vertical fracture, undeveloped joint, compressive strength 84.8 MPa, inclination 29°
Immediate roof	Mudstone	1.0 ~ 2.1/1.5	Black mudstone with bright strip, brittle, developed joint, compressive strength 15.8 MPa, inclination 29°
Immediate floor	Mudstone	1.10 ~ 1.92/1.33	Grayish black mudstone, dense and massive, mainly composed of argillaceous components, containing a large amount of plant fossil, developed joint, compressive strength 18.5 MPa, inclination 29°
Main floor	Sandstone	2 ~ 3.1/2.5	Gray white sandstone, mainly composed of quartz, with carbon chips and carbon stripes, undeveloped joint, compressive strength 38 MPa, inclination 29°
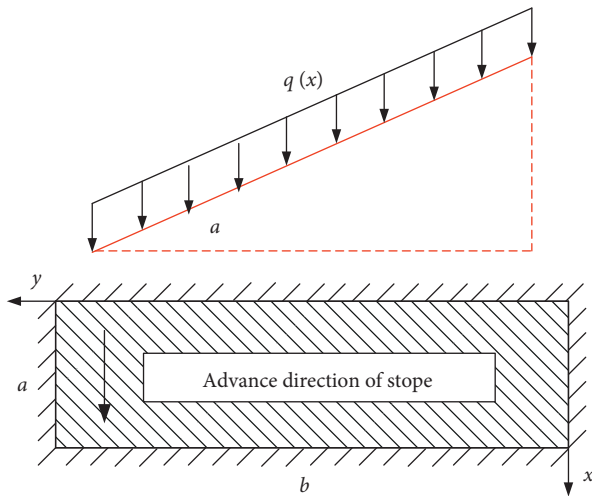
FIGURE 1: Thin plate model of main roof for mining high dip seam.

From the expressions of deflection and stress, it can be seen that the fracture shape of elastic rectangular thin plate is related to its geometric parameters.

2.4. The Criterion of Roof Breaking in High Angle Stope. The tensile strength of rock is less than its shear strength and compressive strength, and the stress release is obvious after the roof breaking. Once tensile failure has occurred at some part, other forms of failure are not considered. Therefore, the main failure mode of rectangular thin plate is tension failure.

As the inclined length of working face 103 is much longer than its other dimensions, the following criterion was set up. When the tensile stress in Y direction reaches the ultimate tensile strength, the advancing distance of working face is considered as the breaking distance of rock plate. The final solution can be approximated in the form of iteration.

3. Analysis of the First Breaking of the Main Roof in the Seam with High Dip Angle

The trial calculation of equation (5) shows that the warped surface of rock plate tends to balance gradually till $m = 20$, $n = 20$. To obtain the influence of the dip angle of seam on the first breaking distance of the main roof, and the regularity of the first breaking along the inclination of the working face, the following parameters were set in

accordance with the overlying rock parameters of working face 103. The thickness of the main roof is $h = 4.7$ m, the rock modulus of elasticity is $E = 30$ GPa, self-weight of overlying rock is 11.25 MPa, and the inclined length of working face is $b = 185$ m.

3.1. Influence of Dip Angle on the First Breaking of Main Roof. The first breaking distance of the main roof was analyzed under six inclination angles of 15°, 25°, 35°, 45°, 55° and 65°. Due to the limited space, only three cases of 25°, 35° and 45° are listed, and their warped surfaces are shown in Figures 2–4. In the figure, x, y, and z represent the inclined length of the working face, the advancing distance of the working face, and the displacement of the roof, respectively.

It can be seen from Figures 2–4 that the reverse displacement of the warped surface occurs as the working face advances, which is obviously inconsistent with the actual low-order response. Hence, it can be inferred that the roof is broken during this propulsion section. Specifically, Figure 2(a) shows that when the advancing distance of the working face is 30 m, the bending surface is normal, and the roof with an inclination of 15° is intact, while Figure 2(b) shows that when the advancing distance is 40 m, the bending surface is abnormal, and the roof is broken. This indicates that the roof is damaged at some time between 30–40 m. Figures 3 and 4 similarly illustrate the advancing distance of working face when the roofs with dip angles of 35° and 45° are broken. Through further calculation, Figure 5 shows the breaking step distance of main roof at different inclination angles of seam.

It can be seen from Figure 5 that the initial breaking distance of roof decreases with the increase in seam dip angle. More specifically, when the seam dip angle is greater than 45°, the variation of the first breaking distance is slow. When the seam dip angle is less than 45°, it becomes faster.

3.2. Variation of the Breaking Distance along the Inclination of Working Face. To analyze the change in breaking distance along the inclination of working face, the selected parameters are $\alpha = 25°$ and tensile strength of main roof rock of 10 MPa, in accordance with the specific conditions of working face 103 and the above fracture criteria. The calculation results are shown in Figure 6.

It can be seen from Figure 6 that the breaking distance on both sides of the roof is large, and the breaking distance in

(a)

(b)
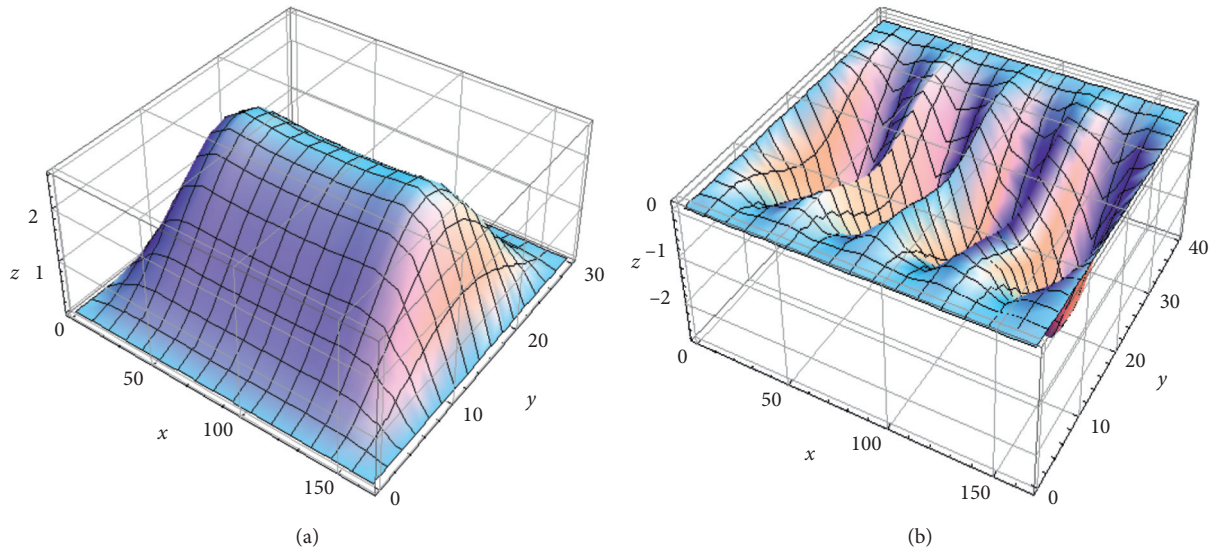
FIGURE 2: Roof deflection at an inclination angle of 25°. (a) Advancing distance of 30 m. (b) Advancing distance of 40 m.

(a)

(b)
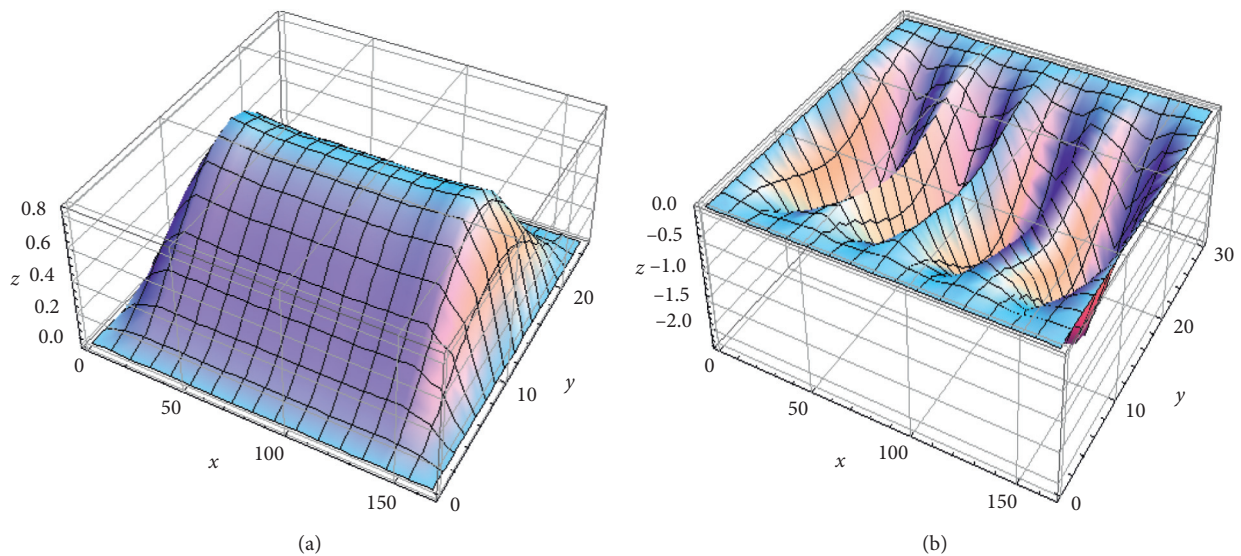
FIGURE 3: Roof deflection at an inclination angle of 35°. (a) Advancing distance of 25 m. (b) Advancing distance of 30 m.

the middle is the smallest, which forms a "V" shaped breaking surface. The maximum value of the breaking distance difference is as high as 10 m. On the whole, the first breaking distance of roof is about 30 m, which is similar to the data analyzed with warped surface.

4. Numerical Analysis of Thin Plate

4.1. Establishment of Numerical Model. To analyze the roof stress and the mechanism of roof fracture, numerical calculation was performed using a literature method [4] and the D-P strength criterion, which is closer to rock properties. It was assumed that there is main roof strata in the high dip stope, with a length of $b = 185$ m (along the inclination of working face, i.e., the y direction), a width of $a = 30$ m (the x-

direction), a thickness of $h = 4.7$ m and a dip angle of $\alpha = 30°$. Using ANSYS software, solid185 three-dimensional solid element was selected to establish the model. According to the boundary conditions before the first fracture of the main roof, its four edges can be clamped for simulation. A linear load varying along the depth is applied to the upper surface of the model, as shown in Figure 7. The angle between the load and the plate is 30°. Then, the load is divided into a component perpendicular to the plate and a component parallel to the plate.

4.2. Analysis of the First Breaking Mechanism of the Main Roof of the Steep Seam. Figures 8 and 9 show the stress distribution characteristics on the main roof surface during first breaking.

(a)

(b)
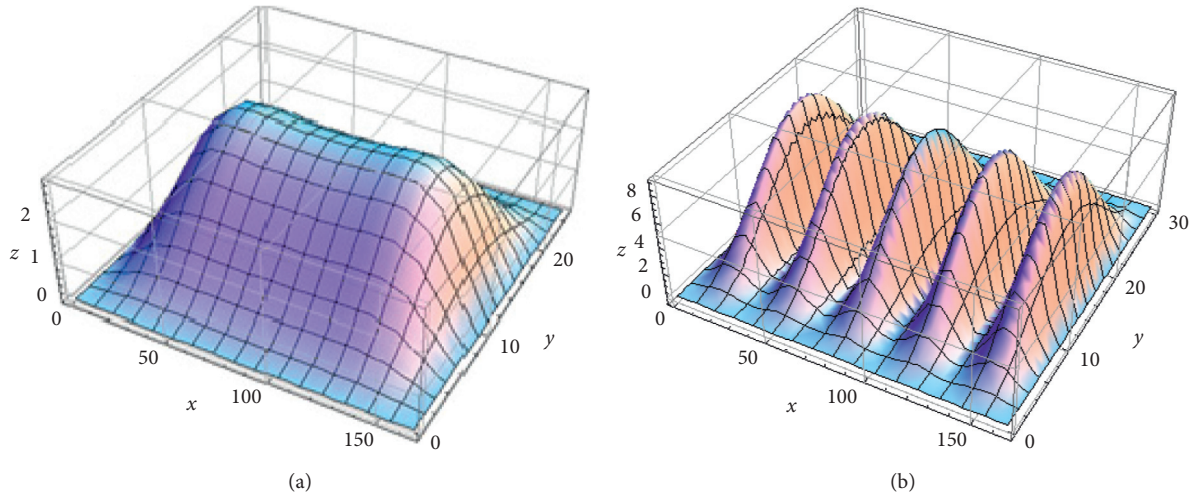
FIGURE 4: Roof deflection at an inclination angle of 45°. (a) Advancing distance of 25 m. (b) Advancing distance of 30 m.
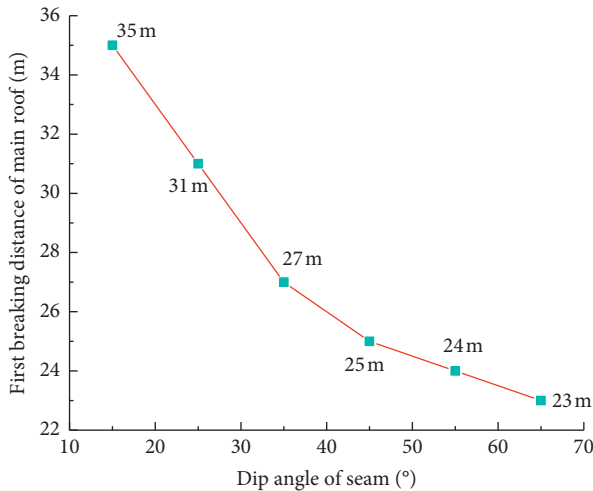
FIGURE 5: Variation of the first breaking distance of the roof with inclination angle.
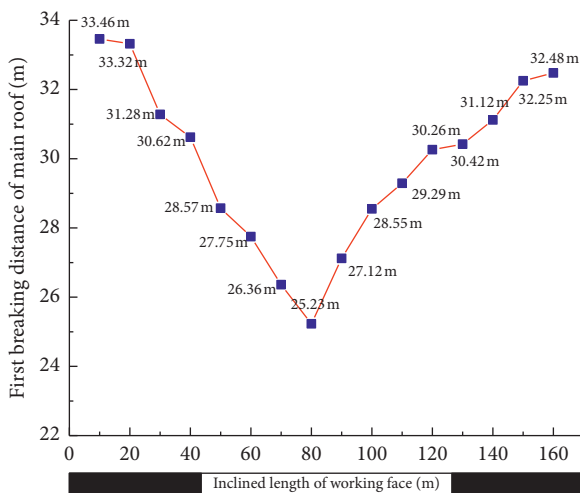
FIGURE 6: Change in the first breaking distance along the inclination of working surface.
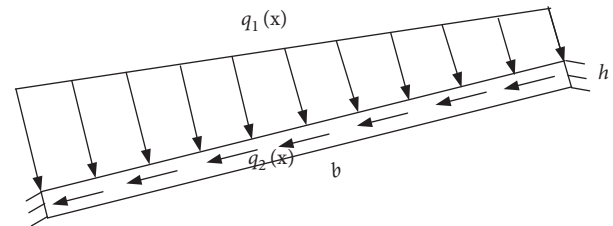
FIGURE 7: Sketch of model with applied load.

It can be seen from Figures 8 and 9 that the roof stress of the steep seam is asymmetric, which is different from that of the horizontal seam. Figure 8 shows the stress distribution in the X direction. On the upper surface, the center of the two long sides forms the maximum tensile stress area, and the center is the O-type compressive stress area. On the lower surface, the center forms the O-type tensile stress area, and the center of the two long sides is the compressive stress area.

Figure 9 shows the stress distribution in the Y direction. On the upper surface, the center of the short edge at the right end (upper part of the working face) forms the maximum tensile stress area, and the upper surface forms the "C" type tensile stress area and the triangular compressive stress area. On the lower surface, the left short edge receives the maximum compressive stress, and the lower surface forms the triangular tensile stress area. According to these distribution characteristics of the stress, it can be seen that the stress in Y direction (along the inclination of working face) causes the breaking mechanism of the roof of the steep seam to be different from that of the horizontal seam.

As a brittle material, the tensile strength of rock is far less than its compressive strength. It can be seen from the stress distribution that, on the upper surface, the central area of the two long sides (the maximum tensile stress area) will be damaged first, forming cracks that extend to both sides, and then through the central maximum tensile stress area of the short side (the upper part of the working face) on the right side to form a "U" type crack. On the lower surface, the peak

$$-0.152E + 09 \quad -0.854E + 08 \quad -0.185E + 08 \quad 0.485E + 08 \quad 0.116E + 09$$
$$\quad -0.119E + 09 \quad -0.519E + 08 \quad 0.150E + 08 \quad 0.820E + 08 \quad 0.149E + 09$$

(a)

$$-0.152E + 09 \quad -0.854E + 08 \quad -0.185E + 08 \quad 0.485E + 08 \quad 0.116E + 09$$
$$\quad -0.119E + 09 \quad -0.519E + 08 \quad 0.150E + 08 \quad 0.820E + 08 \quad 0.149E + 09$$

(b)
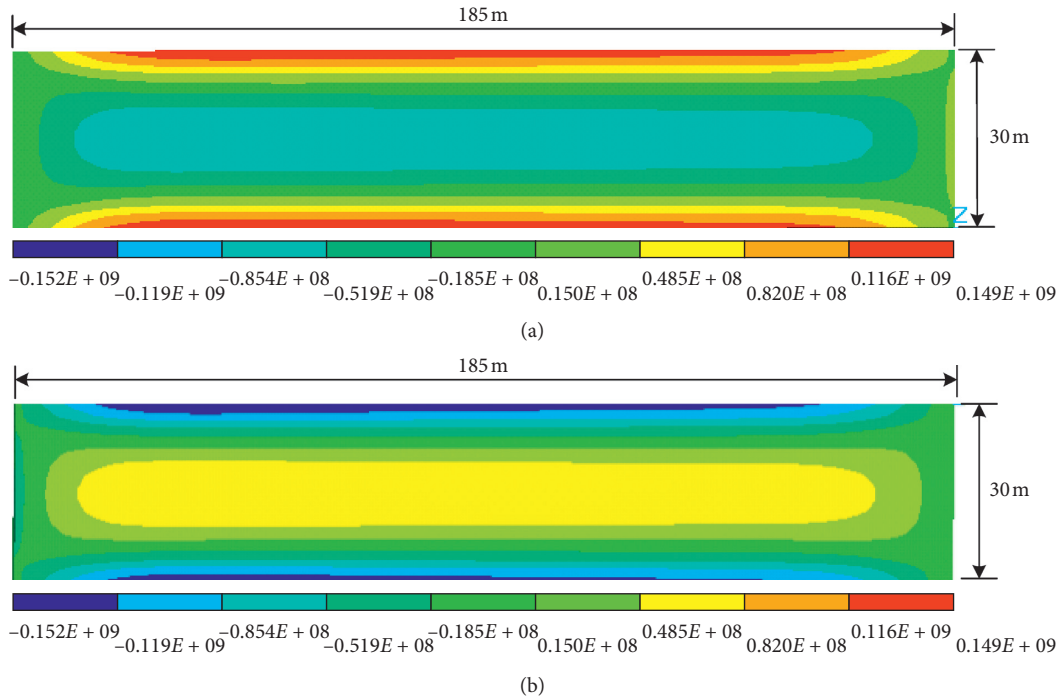
FIGURE 8: Distribution characteristics of σ_x on the main roof surface during first breaking. (a) σ_x on the upper surface. (b) σ_x on the lower surface.

$$-0.131E + 09 \quad -0.755E + 08 \quad -0.205E + 08 \quad 0.345E + 08 \quad 0.895E + 08$$
$$\quad -0.103E + 09 \quad -0.480E + 08 \quad 0.698E + 07 \quad 0.620E + 08 \quad 0.117E + 09$$

(a)

$$-0.131E + 09 \quad -0.755E + 08 \quad -0.205E + 08 \quad 0.345E + 08 \quad 0.895E + 08$$
$$\quad -0.103E + 09 \quad -0.480E + 08 \quad 0.698E + 07 \quad 0.620E + 08 \quad 0.117E + 09$$

(b)
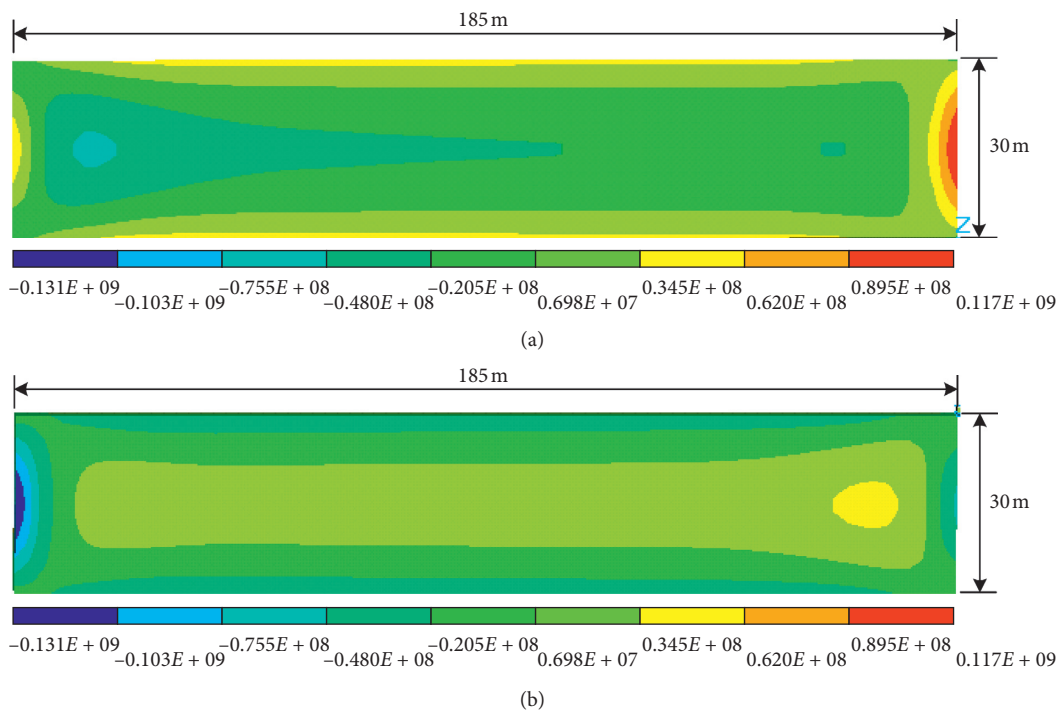
FIGURE 9: Distribution characteristics of σ_y on the main roof surface during first breaking. (a) σ_y on the upper surface. (b) σ_y on the lower surface.

tensile stress of σ_x, σ_y is obviously smaller than that of the upper surface. As the working face advances, σ_x will exceed the tensile strength, and the rock mass will be damaged to form cracks along x-direction. Moreover, influenced by σ_y,

the tensile stress concentration occurs in the area near the right side, resulting in a crack, which connects with the crack along x-direction, finally forming "Y" type crack. Therefore, unlike the "O-X" breaking of the horizontal seam roof [2],

(a)

(b)
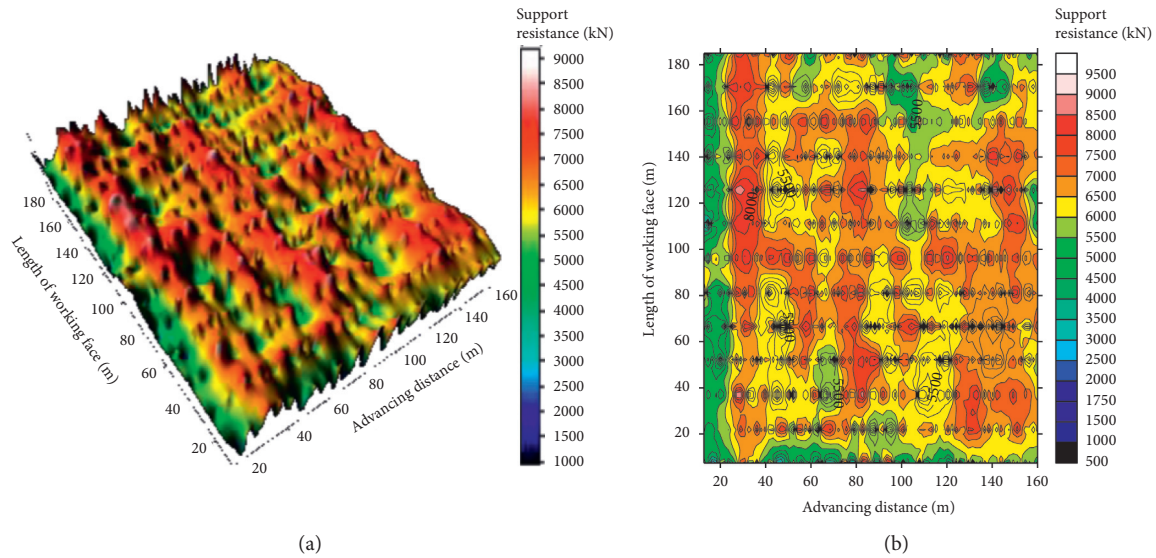
FIGURE 10: Contour map of working resistance of hydraulic support on working face. (a) Three-dimensional diagram. (b) Two-dimensional diagram.

TABLE 2: First weighting interval of the main roof of the working face.

Support location	First weighting interval (m)
Lower part	32.2
Middle lower part	30.7
Middle part	28.5
Middle upper part	31.3
Upper part	33

the high dip seam roof is characterized by a "U-Y" broken morphology. The fracture sequence of high dip seam is middle part-middle upper part-middle lower part-upper part-lower part.

5. Analysis of Project Case

With the development of science and technology, the monitoring methods of mine pressure in stope are also diversified [13–15]. In order to fully understand the roof weighting characteristics of working face 103, pressure measuring stations were arranged on the hydraulic supports of working face before backstopping (the real-time online system of support monitoring was adopted), which can also evaluate the adaptability of hydraulic support when the working face advances. The monitoring was continued until the working face was pushed to 160 m, and the maximum resistance of the hydraulic support in the monitoring data was generated into the contour map, as shown in Figure 10.

It can be seen from Figure 10 that the resistance variation of hydraulic support presents the shape of mountain fluctuation. When the advancing distance is about 30 m, the working resistance of the hydraulic supports in almost all parts of the working face reaches a large value. Combined

with other characteristics of rock pressure, it can be determined that the working face meets with first weighting of main roof at that time. The corresponding step distance is shown in Table 2.

From Table 2, the fracture step range of the main roof is 28.5 m–33 m during the first weighting, with an average of 31.1 m. Therefore, the order of the first breaking is consistent with the general trend of numerical simulation and theoretical calculation.

6. Conclusions

(1) The mechanical model of the thin plate with the general form of the first breaking of the main roof in the high dip seam was established. The expressions of deflection and stress of roof were obtained. By changing the image of deflection function, the influence of different inclinations on the first breaking of roof was analyzed, and the breaking criterion of the main roof was determined.

(2) It was found that the first breaking distance of main roof decreases with the increase in dip angle of seam.

(3) The characteristics of the first breaking of the main roof in the steep seam are different from the "O-X" breaking characteristics in the horizontal or near horizontal seam. The failure mechanism of roof is determined by its tensile stress σ_y along the inclination of working face.

(4) Based on behavior regularity of rock pressure in working face 103, the roof breaking order in space of the seam with high dip angle is middle-middle upper-middle lower-upper-lower.

Data Availability

The authors believe that the data underlying the findings of this paper are publicly available, which will help ensure that the work described in our article can potentially be replicated.

Conflicts of Interest

The authors declare that they have no conflicts of interest regarding the publication of this work.

References

[1] Z. Chen, J. Feng, C. Xiao et al., "Fracture mechanical model of key roof for fully-mechanized top-coal caving in shallow thick coal seam," *Journal of China Coal Society*, vol. 32, no. 5, pp. 449–452, 2007.

[2] M. Qian, P. Shi, and J. Xu, *Ground Pressure and Strata Control*, China University of Mining and Technology Press, Xuzhou, China, 2010.

[3] G. Yin, X. Xian, G. Dai et al., "Basic behavior of strata movement in seam with deep dip angle," *Chinese Journal of Geotechnical Engineering*, vol. 23, no. 4, pp. 450–453, 2001.

[4] Y. Zhang, J. Cheng, X. Wang et al., "Thin plate model analysis on roof break of up-dip or down-dip mining stope," *Journal of Mining and Safety Engineering*, vol. 27, no. 4, pp. 487–493, 2010.

[5] J. Wang, J. Zhang, X. Gao et al., "Fracture mode and evolution of main roof stratum above longwall fully mechanized top coal caving in steeply inclined thick coal seam (I)-initial fracture," *Journal of China Coal Society*, vol. 40, no. 6, pp. 1353–1360, 2015.

[6] Y. Wu, P. Xie, H. Wang et al., "Incline masonry structure around the coal face of steeply dipping seam mining," *Journal of China Coal Society*, vol. 35, no. 8, pp. 1252–1256, 2010.

[7] H. Wang, Y. Wu, P. Xie et al., "Practice on fully mechanized coal mining in deep inclined seam with hard roof soft coal and soft floor," *Journal of China Coal Society*, vol. 34, no. 2, pp. 287–294, 2017.

[8] Y. Wu, D. Yun, P. Xie et al., "Progress, practice and scientific issues in steeply dipping coal seams fully-mechanized mining," *Journal of China Coal Society*, vol. 45, no. 1, pp. 24–34, 2020.

[9] H. Pu, Y. Huang, and R. Chen, "Mechanical analysis for X-O type fracture morphology of stope roof," *Journal of China University of Mining & Technology*, vol. 40, no. 6, pp. 835–840, 2011.

[10] X. Wang, M. Gao, Y. Chen et al., "Analysis of fracturing characteristics of stope roof based on elastic thin plate theory," *Metal Mine*, vol. 468, no. 6, pp. 24–28, 2015.

[11] Z. Fan, D. Mao, G. Xu et al., "Analysis on the scale effect in the fully mechanized mining panel width with large mining height and dip angle," *Journal of China Coal Society*, vol. 41, no. 3, pp. 581–585, 2012.

[12] Z. Xu, *Elasticity*, Higher Education Press, Beijing, China, 4th edition, 2006.

[13] X. Meng, R. Wen, J. Liu et al., "Research on site measurement of ground behavior in fully mechanized caving mining face in high inclined seam of 1000 m deep mine," *Coal Science and Technology*, vol. 35, no. 11, pp. 14–17, 2007.

[14] K. Yang, X. Chi, and S. Liu, "Instability mechanism and control of hydraulic support in fully mechanized longwall mining with large dip," *Journal of China Coal Society*, vol. 43, no. 7, pp. 1821–1828, 2018.

[15] J. Chai, W. Du, D. Zhang et al., "Study on roof activity law in steeply inclined seams based on BOTDA sensing technology," *Chinese Journal of Rock Mechanics and Engineering*, vol. 38, no. 9, pp. 1809–1818, 2019.

Research Article

Experimental Research on Mechanical Properties of High-Temperature Sandstone with Different Cooling Methods

Minglei Zhang [1], **Runde Qiu,**[1] **Lei Yang,**[2] **and Yuting Su**[1]

[1]*Institute of Disaster Prevention, Langfang 065201, China*
[2]*Capital Construction Division, The Central Academy of Drama, Beijing 102209, China*

Correspondence should be addressed to Minglei Zhang; zml@cidp.edu.cn

Various tests including the longitudinal wave velocity tests and uniaxial compression tests have been conducted to evaluate the impact of cooling methods (including natural cooling, water cooling, and cooling by liquid carbon dioxide) on mechanical properties of sandstone under the natural status and high temperature. The acoustic emission signals were also monitored during the tests. According to the tests conducted, the sandstone sample density attenuation rate and the longitudinal wave velocity attenuation rate are higher than those of the specimen under natural status while the uniaxial compressive strength and Young's modulus are lower. Comparing with the sandstone under the natural status, the compression sections of the stress-strain curves of the high-temperature sandstone samples treated by three cooling methods are longer with lower strain peak values. The order of the acoustic emission is revealed as follows: the sample cooled by liquid carbon dioxide < the sample cooled by water < sample cooled naturally < the sample under natural status, which suggests that the rapid cooling (cooled by liquid carbon dioxide) produces the severest damage on the sample, followed by the water cooling and natural cooling methods. In addition, the relationship between the sample strength weakening coefficient and the cooling rate is defined based on the statistical data of the cooling time of the high-temperature specimen under the three cooling methods.

1. Introduction

Since the 21st century, the rapid economic development of various countries has raised higher demands to the resource, energy, and space, resulting in outstanding problems such as environmental pollution on the ground, resource shortages, and traffic congestion, which poses as a serious threat to the social health and sustainable development. Exploring the underground space and resources hidden in the depths of the earth has become the trend of future development, leading to the booming development of underground projects. Many nations have initiated various underground space construction projects [1]. Fire is one of the common disasters troubling the underground space. The high temperature and cooling effect produced during the control of fire accidents tend to modify the physical and mechanical properties of underground engineering rock mass, jeopardizing the stability and service life of underground facilities. Common fire extinguishing methods include dry powder fire extinguishing, fire extinguishing blankets, water fire extinguishing, and liquid carbon dioxide fire extinguishing, and specific fire extinguishing methods are selected in various regions based on individual fire condition, technologies available, and local economy [2]. Various fire extinguishing methods produce different cooling rates, resulting in various levels of destructive effect on the high-temperature surrounding rock. As a result, disparities are often present in the damages of the surrounding rock mass in underground facilities. Unlike the ground construction, underground facilities are usually highly concealed, resulting in more maintenance difficulties and higher expenses [3–6]. Therefore, conducting research studies to evaluate the impact of different cooling methods on the mechanical properties of underground engineering rock mass after high temperature becomes necessary.

In recent years, experts domestic and abroad have conducted a considerable number of research studies on the rock cooled after high temperature through laboratory tests and numerical simulations. Cooling methods for high-temperature rocks can be divided into the natural cooling, the water cooling, and the rapid cooling methods [7–9]. Regarding the natural cooling method, Yang et al. [10] analyzed the changes occurred to the shapes, compressive strengths, peak strains, and Young's modulus of high-temperature sandstone as well as the damage and deterioration mechanism of sandstone after the high temperature. Focusing on the tensile strength and size changes, Su et al. [11] studied the cooling impact on the red sandstone. Xu and Zhou [12] investigated the uniaxial compressive strengths of sandstone specimens under different high temperatures and obtained the temperature at the turning point of strength change trend. Zhao et al. [13] and Hou and Peng [14], respectively, studied the mechanical properties of granite and marble after high temperature, including the microscopic parameter analysis through the diffraction test and electron microscope scanning. In terms of the water cooling method, some scholars [15–18] analyzed the mechanical properties of high-temperature granite, marble, limestone, and sandstone after the water cooling, including the analysis of changes in uniaxial compressive strength, tensile strength, and Young's modulus. In terms of the rapid cooling (cooled by liquid carbon dioxide, liquid nitrogen, and calcium chloride solution), Han et al. [19], Jin et al. [20], Shen et al. [21–23], Isaka et al. [24], Hosseini [25], and Li et al. [26] studied the damage effect of granite cooled by the rapid method, including the analysis of changes in uniaxial compressive strength, tensile strength, Young's modulus, fluctuation characteristics, acoustic emission characteristics, and microscopic characteristics.

The existing research studies focus on the impact of the natural cooling and water cooling methods on the mechanic properties of sandstone. Limited studies have been conducted to evaluate the impact of rapid cooling (cooled by liquid carbon dioxide) and various cooling methods on the rock mechanical properties of the same type. During the fire accidents in the underground facilities, the surrounding rock is often heated continuously and experiences quick cooling during the fire rescue. Various extinguishing methods produce different cooling effects, resulting in different thermal shocks. The mechanical behaviors of rock change accordingly. Taking the engineering background aforementioned into consideration, the most common sandstone in the coal seam is selected as the research object. Sandstone specimens were cooled by three methods including the natural cooling, the water cooling, and the rapid cooling (cooled by liquid carbon dioxide). In addition, uniaxial compression strengths were tested with the cooling rate as the variable to explore the impact of cooling methods on mechanical properties of sandstone under high temperature.

2. Test Overview

The sandstone specimens originated from a coal mine located at Yang Quan, Shanxi province, with an average density of 2.4 g/cm^3. As shown in Figure 1, sandstones were processed into the standard cylinder specimen with a diameter of 50 mm and a height of 100 mm. Minimum three specimens were prepared for each cooling method. An electronic scale with an accuracy of 0.01 g was used to measure the quality of sandstone samples. The sizes of sandstone specimens were measured through a Vernier caliper with an accuracy of 0.02 mm. The probe frequency used for the P-wave velocity test is 50 Hz, and Vaseline is evenly applied on both ends of the sample before the test. Specimens were heat-treated in a TSX1400 muffle furnace whose setting temperature was increased at a rate of 10°C/min [12, 14, 19] until a maximum temperature of 800°C [27]. In order to ensure that the sample is heated evenly, the temperature is kept constant for 30 min each at 100°C. The sandstone was heated to 800°C and kept at constant temperature for 2 h [8, 13, 20]. The YAW-2000 test systems were adopted to evaluate the rock mechanical properties, whose loading rate was set at 0.3 mm/s. A DS5-16B acoustic emission test system was used to monitor the acoustic emissions, and the threshold of the preamplifier in the AE system is 40 dB. Specimens were divided into four groups with three in each group. Group C was selected as the reference, whose parameters were measured under the natural status. After specimens were heated to 800°C, the group N was cooled naturally and the group W was cooled to 20°C by water spraying. The group R was cooled with evenly sprayed liquid carbon dioxide from a steel cylinder controlled with a pressure relief value until the room temperature was reached. The cooling consumption time was recorded. All specimens were dried naturally indoor before tests.

3. Test Result and Analysis

3.1. Density and Longitudinal Wave Velocity. In order to quantitatively analyze the impact of three cooling methods on mechanical properties of the high-temperature sandstone, the ratio between the density reduction after and before cooling is defined as the density attenuation rate K_ρ and the ratio between the longitudinal wave velocity reduction after and before cooling is defined as the wave velocity attenuation rate K_v [18]. The detailed densities and K_ρ s corresponding to three cooling methods are provided in Table 1.

As demonstrated in Table 1, various degrees of increasement were observed in the density and K_ρ in high-temperature sandstone cooled by three different methods. During the heating process, substances with melting points below 800°C, such as cement and crystal water, were slowly melted, resulting in more cracks in the sandstone and jeopardizing the sandstone quality [13, 16]. In contrast, based on the average density reduction, the content of fusible substances contained in the sandstone is relatively low, resulting in limited density reduction.

The detailed information of longitudinal wave velocity and K_v s corresponding to three cooling methods is provided in Table 2.

As demonstrated in Table 2, various degrees of increasement were observed in the longitudinal wave
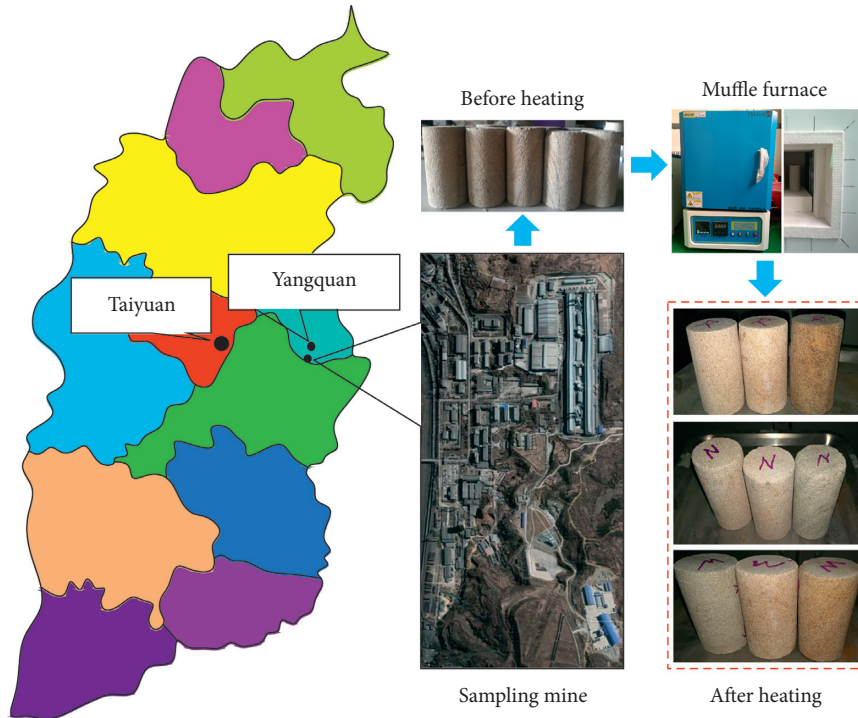
FIGURE 1: Specimen introductions.

TABLE 1: Density.

	Density before heating (g/cm³)	Average density before heating (g/cm³)	Density after heating (g/cm³)	Average density after heating (g/cm³)	K_ρ (%)
C	2.443 2.444 2.448	2.445	— — —	—	—
N	2.44 2.443 2.439	2.441	2.403 2.407 2.408	2.406	1.43
W	2.438 2.439 2.44	2.439	2.397 2.398 2.4	2.398	1.68
R	2.442 2.445 2.445	2.444	2.405 2.408 2.408	2.407	1.51

TABLE 2: Longitudinal wave velocity.

	Wave velocity before heating (km/s)	Average wave velocity before heating (km/s)	Wave velocity after heating (km/s)	Average wave velocity after heating (km/s)	K_v (%)
C	3.261 3.257 3.256	3.258	— — —	—	—
N	3.271 3.274 3.274	3.273	1.847 1.847 1.85	1.848	43.54
W	3.168 3.171 3.168	3.169	1.437 1.438 1.433	1.436	54.69
R	3.243 3.243 3.240	3.242	1.224 1.2 1.119	1.221	62.34

velocity and K_v in high-temperature sandstone cooled by three different methods. According to the wave velocity test results, comparing with the reference wave velocity obtained under the room temperature, the high-temperature sandstone specimens experienced various levels of reductions in wave velocity with increased K_v. $K_v s$ measured from the specimens cooled naturally, by water, and by liquid carbon dioxide is 43.54%, 54.69%, and 62.34%, respectively. The longitudinal wave velocity indicates the crack developing status inside sandstones, suggesting the internal damage due to different cooling methods. The heat shock produced by the natural cooling, water cooling, and rapid cooling (cooled by liquid carbon dioxide) increased accordingly, resulting in gradually decreasing destructions to the internal structure. In addition, the density attenuation rate (maximum value of 1.68%) of specimens is far lower than the wave velocity attenuation rate (maximum value of 62.34%).

3.2. Uniaxial Compressive Stress-Strain Behavior.

A series of uniaxial compression tests were conducted to the high-temperature sandstones cooled with three different methods. The stress-strain curves were developed based on the test results, as demonstrated in Figure 2.

Comparing with the sandstone under the natural status, the compression sections of the stress-strain curves of the high-temperature sandstone samples treated by three cooling methods are longer, suggesting the crack developed inside the sandstone. Groups N, W, and R demonstrated some gradually longer compression sections of the stress-strain curves, indicating more severe damages. Meanwhile, the drastic turning points occurred after the peak values suggest the characteristics of brittle material demonstrated by the high-temperature sandstone cooled differently.

3.3. Uniaxial Compressive Strength and Young's Modulus.

Figures 3(a) and 3(b) and Table 3 show the uniaxial compressive strengths and Young's modulus of high-temperature sandstone cooled differently.

The test results indicate that all cooling methods adopted have caused some reductions in the uniaxial compressive strengths and Young's modulus of sandstone. The average uniaxial compressive strength was decreased from 52.27 MPa to 42.39 MPa, by about 18.9% under the natural cooling. The average uniaxial compressive strength was decreased from 52.27 MPa to 30.80 MPa, by about 41.08% under the water cooling. The average uniaxial compressive strength was decreased from 52.27 MPa to 22.56 MPa, by about 56.84% under the rapid cooling (cooled by liquid carbon dioxide). In terms of Young's modulus, comparing with the reference group C, groups N, W, and R demonstrated a reduction of 33.88%, 48.21%, and 61.16%, respectively, which is consistent with the trend of the uniaxial compressive strength. Compared with the results of uniaxial compressive strength and Young's modulus shown in Figures 3(a) and 3(b) [19, 28, 29], the experiment demonstrated a similar trend. Based on uniaxial compressive strength and Young's modulus, various cooling methods were ranked as follows: sample cooled by liquid carbon
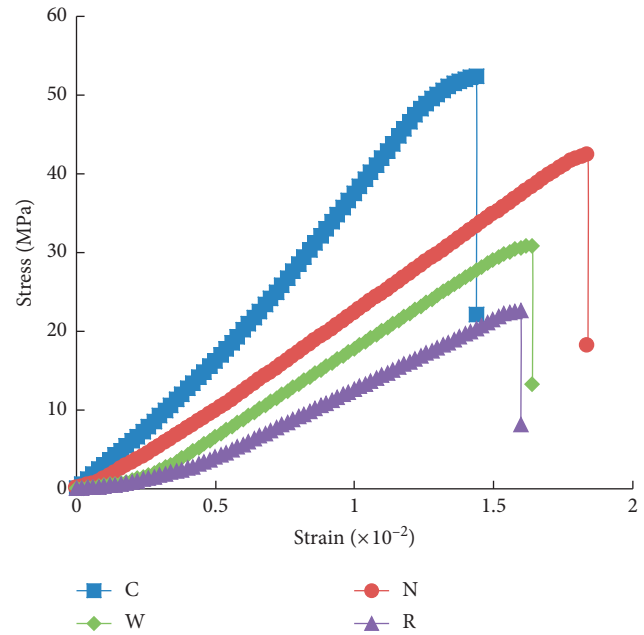
Figure 2: Stress-strain curve.

dioxide < sample cooled by water < sample cooled naturally < the sample under natural status.

Both types of tests indicate that the cooling method has a meaningful impact on the thermal shock, which is the major trigger of internal damage in sandstone. Therefore, in order to ensure the safety and service life of underground facilities, oxygen isolation or other equivalent fire extinguishing methods should be preferred during the fire rescue to minimize the internal damage to sandstone.

3.4. Acoustic Emission Characteristics.

Acoustic emission and spectrum signature can provide insightful indications of the dynamic development inside the rocks, which are widely adopted in the analysis of rock mechanical properties. Figure 4 provides the acoustic emission trends of groups C2, N1, W2, and R1 to demonstrate different levels of damages caused by three cooling methods to the high-temperature sandstone specimens.

According to Figure 4, the acoustic emission was zero or close to zero under three cooling methods. The initial cracks started to close at the stage of compression without any new damage development. As the axial stress increased, before reaching the peak, the acoustic emission increased drastically, suggesting the intensive development of cracks inside the sandstone specimens. The cracks continued to develop until rupture. Therefore, the frequency of acoustic emission can be viewed as a damage level indicator for test specimens.

Reviewing the distribution of acoustic emission under three cooling methods, the acoustic emission distributions of specimens N1, W2, and R1 are wider than specimen C2, suggesting that the progressive fracture stage of the specimen subject to high temperature and subsequent cooling is longer. Comparing four groups of specimens, the acoustic emission occurred earliest in the reference specimens,
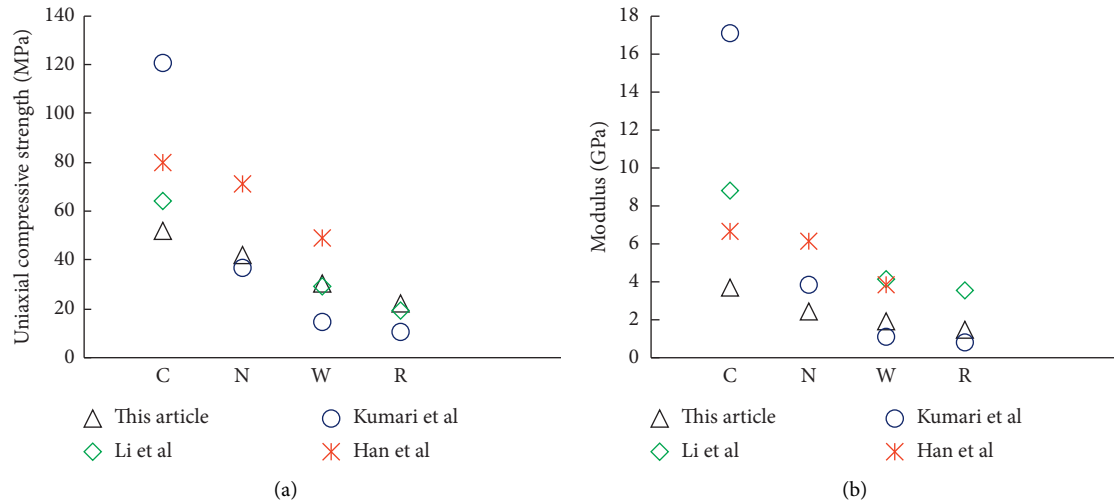
FIGURE 3: Ratio between strength and Young's modulus [19, 28, 29].

TABLE 3: Uniaxial compressive strength and Young's modulus.

	Uniaxial compressive strength (MPa)	Average (MPa)	Young's modulus (GPa)	Average (GPa)
C	53.25		3.49	
	52.3	52.27	3.65	3.63
	51.26		3.75	
N	42.3		2.56	
	42.2	42.39	2.2	2.3
	42.67		2.44	
W	31.81		1.98	
	30.94	30.8	1.96	1.88
	29.65		1.71	
R	22.58		1.27	
	21.54	22.56	1.59	1.41
	23.56		1.36	

followed by rapid-cooled specimens (cooled by liquid carbon dioxide), water-cooled specimens, and naturally cooled specimens. However, comparing with other groups of specimens (N-465s, W2-415s, and R1-405s), less time was consumed by the reference group from the initial loading to the rupture (288s), which indicates that the reference group was the last one to generate acoustic emission. After cooling, different levels of damages were produced, resulting in various numbers of cracks. The cracks not only jeopardize the strengths of specimens but also cause surface shedding, which are captured by the acoustic emission devices. The numbers of cracks due to three cooling methods impact the occurrence timings of the acoustic emissions in different groups of specimens. Early occurrences of the acoustic emission indicate more severe damage inside the sandstone. Among three cooling methods, based on the occurrence timings of the acoustic emission, the rapid cooling method (cooled by liquid carbon dioxide) produced the most severe damage, followed by the water cooling method and the natural cooling method.

In terms of morphology, the color of specimens transited from greyish white into light brownish red after the heat. The damages observed in the reference group and specimens cooled naturally were defined as the shear damage. Limited tensile cracks were observed in the specimens cooled by water and liquid carbon dioxide along with the shear damage, suggesting that more intensive thermal shocks were produced under the water cooling method and the rapid cooling method (cooled by liquid carbon dioxide) and weak planes featured with multiple orientations were formed inside.

As shown in Figure 5, the longitudinal compression tensile failure (W1 and R2) and the burst crushing failure (R3) were also observed in the specimens cooled by water and liquid carbon dioxide. Due to the influence of the internal structure and the heterogeneity of sandstone, the density and quantity of fractures produced during cooling in the high-temperature sandstone vary. Similarly, the directions of fractures are different, as well as the fracture joints. Therefore, the failure mode of the sandstone specimen with high-temperature thermal damage during the process of compression deformation is featured with significant randomness, which is not necessarily related to the cooling mode. Ruptures are more likely to occur during the uniaxial

(a)

(b)

(c)

(d)
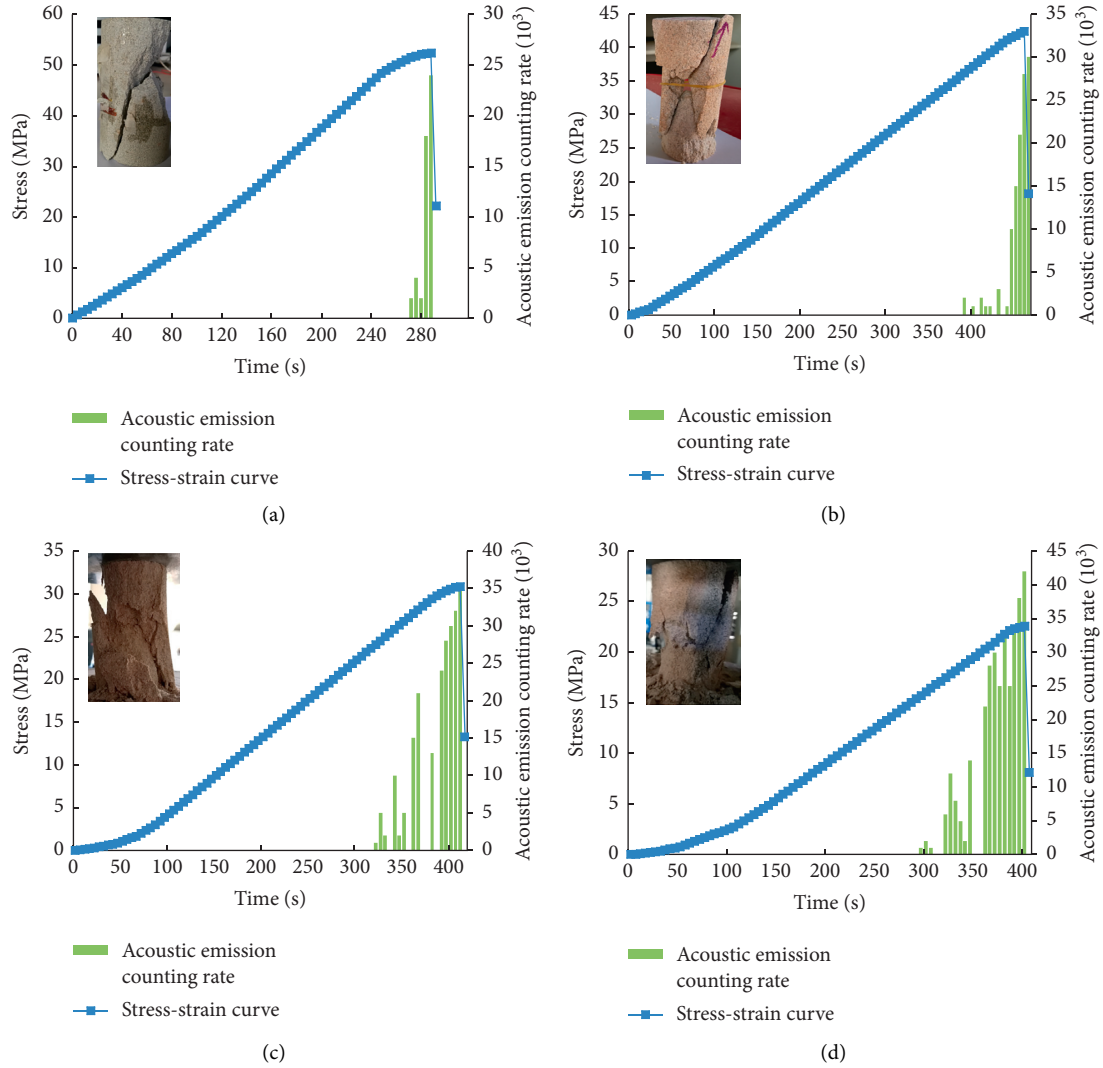
FIGURE 4: Acoustic emission response and damage. (a) C2. (b) N1. (c) W2. (d) R1.

compression tests along the weak planes, resulting in shear or tensile damage. It is not surprising that some specimens demonstrated both shear and tensile damage simultaneously. Taken together, the water cooling and rapid cooling (cooled by liquid carbon dioxide) methods tend to induce more internal cracks and tensile failures. In addition, comparing with the reference group, the thermal shocks reduced the strengths of group N, W, and R specimens due to the formation of weak planes inside.

4. The Discussion of Cooling Rate

As discussed previously, different cooling methods produce various cooling rates. Therefore, establishing the relationship between the rock parameter changes and the cooling rates is critical to evaluate the impact of various cooling methods on the high-temperature sandstone.

The changes to the density attenuation rate and the longitudinal wave velocity attenuation rate responding to various cooling rates are presented in Figure 6. The cooling rate of the heated rock is a calculated parameter obtained

by dividing the temperature decrease by the cooling time. The surface temperature of the specimen was measured by the infrared thermometer continuously until the specimen was cooled to $40°C \pm 5°C$. An infrared thermometer with an accuracy of $0.1°C$ was fixed at a specific position to test the surface temperature of a certain point of the rock specimen until the temperature of the specimen drops to $40°C \pm 5°C$ and the cooling time was recorded. If the difference between the test results within 5 minutes is less than $0.5°C$, the temperature of the test piece is considered to be stable.

The functional relationship between the density attenuation rate K_ρ and the cooling rate, the longitudinal wave velocity attenuation rate K_v and the cooling rate are developed and presented in equations (1) and (2), respectively:

$$K_\rho = -0.00008c^2 + 0.001c + 0.0139 \left(R^2 = 1 \right), \quad (1)$$

$$K_v = 0.0183c + 0.4347 \left(R^2 = 0.9827 \right), \quad (2)$$

where c refers to the cooling rate at $°C/s$.

(a)   (b)   (c)
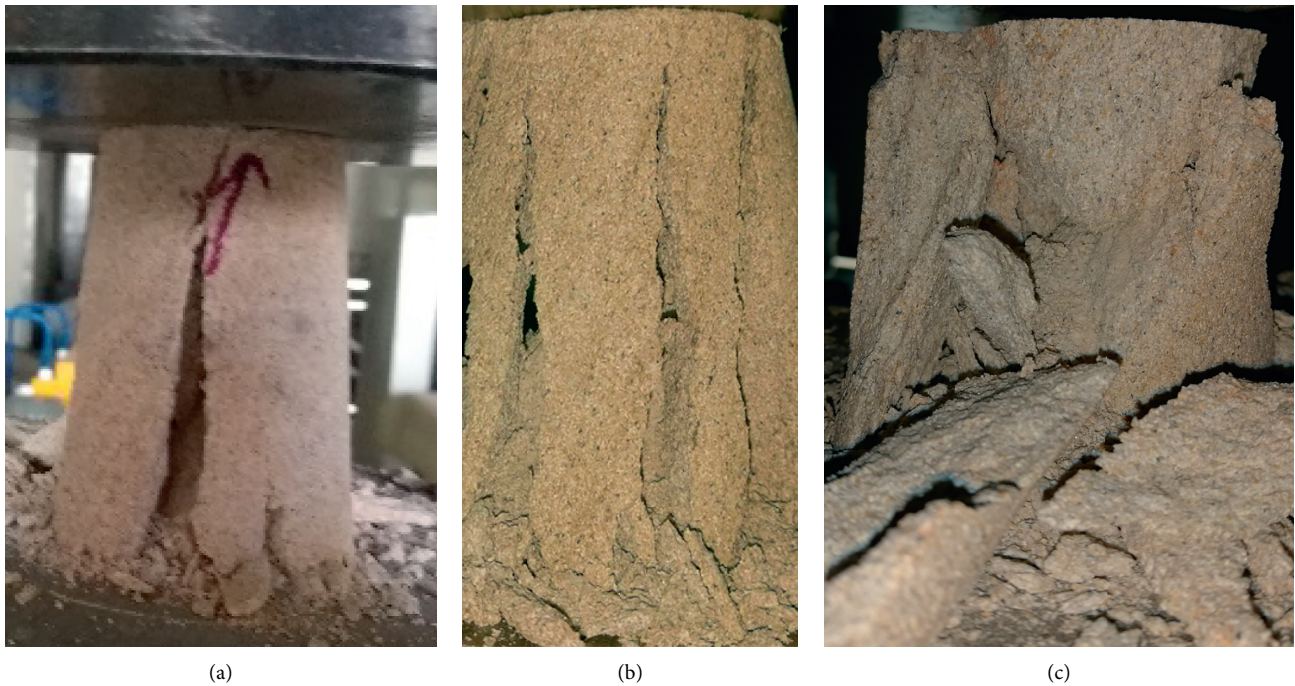
FIGURE 5: Damage form of (a) W1, (b) R2, and (c) R3.
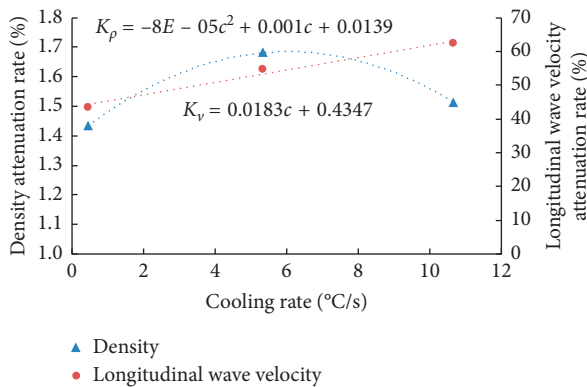
FIGURE 6: The relationship between the density attenuation rate, the longitudinal wave velocity attenuation rate, and the cooling rate.

FIGURE 7: The relationship between the strength attenuation rate, Young's modulus attenuation rate, and the cooling rate.

The functional relationship between the density attenuation rate K_ρ and the cooling rate is constructed in the form of polynomial, while the functional relationship between the longitudinal wave velocity attenuation rate K_v and the cooling rate is constructed in the form of a linear equation. Further analysis and more parameters are required to characterize the damages in rocks due to various cooling rates.

The cooling rate exerts a significant impact on the underground facility safety and service life. Under the assumption that the ratio between the strength reduction after and before cooling is defined as the strength attenuation rate K_s and Young's modulus reduction after and before cooling is defined as Young's modulus attenuation rate K_e, the strength attenuation rate and Young's modulus attenuation rate responding to various cooling rates are presented in Figure 7.

As Figure 7 demonstrates, the cooling rates increased, respectively, under the rapid cooling method (cooled by liquid carbon dioxide), the water cooling method, and the natural cooling method. A higher level of thermal shock produces more tensile stress and more severe internal damage along with more macro cracks, resulting in the decrease in the cohesion force and the lowering of internal friction angles. The compressive strength and Young's modulus deteriorate consequently. The impact of various cooling methods on the high-temperature sandstone originates from different cooling rates. Among three cooling methods, the rapid cooling method (cooled by liquid carbon dioxide) provides the highest cooling rate, resulting in the highest thermal shock and tensile stress, as well as the most

severe damage including the reduction in rock strength and Young's modulus.

The functional relationships between the strength attenuation rate K_s and the cooling rate, Young's modulus attenuation rate K_e and the cooling rate are developed and presented in equations (3) and (4), respectively:

$$K_s = 3.7001c + 18.658 (R^2 = 0.9851), \tag{3}$$

$$K_e = 2.6651c + 33.142 (R^2 = 0.9971). \tag{4}$$

Generally, the functional relationship between the density attenuation rate K_ρ and the cooling rate is constructed in the form of polynomial, which is different from the linear equations (such as the functional relationship between the longitudinal wave velocity attenuation rate K_v and the cooling rate, the functional relationship between the strength attenuation rate attenuation rate K_s and the cooling rate, and the functional relationship between Young's modulus attenuation rate K_e and the cooling rate). Although the rapid cooling method (cooled by liquid carbon dioxide) causes more serious damage to the high-temperature sandstone specimens, the specimens cooled by water suffered with more quality loss and higher density attenuation rate due to the scouring effect of water flow. Therefore, the density attenuation rate K_ρ is not suitable to characterize the damage of the high-temperature sandstone specimen caused by different cooling rates. The longitudinal wave velocity attenuation rate K_v, the strength attenuation rate attenuation rate K_s, and Young's modulus attenuation rate K_e could be used as the damage characterization index.

It is worth mentioning that this study also provides some insightful references to the rock breaking process. During the excavations of underground projects, hard rocks are often encountered. Rock blasting sometimes is used to remove the hard rocks. However, many restrictions apply to the rock blasting such as the safety concerns due to the gas explosion and smoke removal afterwards. Many experts have proposed effective alternatives to rock blasting such as the microwave technology, the ultrasound technology, and the liquid nitrogen cooling. Rock is a brittle material, indicating that the harder rock demonstrates a higher brittleness. When rocks are heated and cooled rapidly, rocks can be broken easily by taking advantage of stresses generated due to the temperature differences. The detailed application needs more research.

5. Conclusion

(1) The increase in both the density attenuation rate and the longitudinal wave velocity attenuation rate is observed in high-temperature sandstones under three cooling methods. The rapid cooling method (cooled by liquid carbon dioxide) produces the highest increasement of the density attenuation rate and the longitudinal wave velocity attenuation rate, followed by the water cooling method and the natural cooling method. The overall increasement of the density attenuation rate is relatively limited, comparing with the drastic increasement of the longitudinal wave velocity attenuation rate.

(2) Comparing with the sandstone under the natural status, the compression sections of the stress-strain curves of the high-temperature sandstone samples treated by three cooling methods are longer with lower strain peak values. The uniaxial compressive strength and Young's modulus are reduced as well. The rapid cooling method (cooled by liquid carbon dioxide) produces the highest reduction, followed by the water cooling method and the natural cooling method. Based on the acoustic emission, three cooling methods are ranked as follows: sample cooled by liquid carbon dioxide < sample cooled by water < sample cooled naturally < the sample under natural status, which suggests that the rapid cooling method (cooled by liquid carbon dioxide) produces the most severe damage to the sample, followed by the water cooling method and the natural cooling method.

(3) Only shear damage is observed in the reference group and the specimen group cooled naturally while both shear damage and tensile damage are identified in specimens cooled by water and liquid carbon dioxide.

(4) The functional relationship reflecting the synthesized strength weakening coefficient and the cooling rate provides some insightful references to the following up tests and rock blasting procedures taking advantage of stresses caused by the temperature difference in the future.

Data Availability

The data used to support the findings of this study are available from the corresponding author upon request.

Conflicts of Interest

The authors declare that there are no conflicts of interest regarding the publication of this paper.

Acknowledgments

References

[1] H. P. Xie, M. Z. Gao, J. Z. Liu et al., "Research on exploitation and volume estimation of underground space in coal mines," *Journal of China Coal Society*, vol. 43, no. 6, pp. 1487–1503, 2018, in Chinese.

[2] J. W. Wu and S. P. Chen, "Effect of heating and cooling on thermal cracking of granite under unconstrained conditions," *Chinese Journal of Underground Space and Engineering*, vol. 15, no. 1, pp. 108–115, 2019, in Chinese.

[3] C.-b. Yan, "Blasting cumulative damage effects of underground engineering rock mass based on sonic wave measurement," *Journal of Central South University of Technology*, vol. 14, no. 2, pp. 230–235, 2007.

[4] G. Hu, H. L. Fei, S. J. Bao, and Z. G. Yang, "Blasting damage accumulative effect of tunnel surrounding rock structure on HHT," *Chinese Journal of Underground Space and Engineering*, vol. 16, no. 1, pp. 249–259, 2020, in Chinese.

[5] X. Liu, P. Yan, W. B. Lu et al., "Effects of the high in-situ stress level on the acoustic detection and the damage degree evaluation of the excavation damage zone," *Advance Engineering Science*, vol. 51, no. 6, pp. 115–123, 2019, in Chinese.

[6] Z. M. Jiang, S. Z. Qin, and D. Tang, "Numerical study on accumulative damage characteristics of underground rock caverns for compressed air energy storage," *Chinese Journal of Geotechnical Engineering*, vol. 42, no. 2, pp. 230–238, 2020, in Chinese.

[7] Y. S. Luo, B. Dou, H. Tian, J. Chen, P. Xiao, and S. T. Zhang, "Comparative experimental study on physical and mechanical properties of granite after natural cooling and under real-time high temperature," *Earth Science Frontiers*, vol. 27, no. 1, pp. 178–184, 2020, in Chinese.

[8] Y. L. Zhu, J. Yu, H. D. Gao, G. Li, X. Q. Zhou, and X. Q. Zheng, "Effect of water cooling on microscopic damage and dynamic properties of high-temperature granite," *Explosion and Shock Waves*, vol. 39, no. 8, pp. 84–95, 2019, in Chinese.

[9] C. I. McDermott, A. R. L. Randriamanjatosoa, H. Tenzer, and O. Kolditz, "Simulation of heat extraction from crystalline rocks: the influence of coupled processes on differential reservoir cooling," *Geothermics*, vol. 35, no. 3, pp. 321–344, 2006.

[10] L. N. Yang, Z. Q. Jiang, W. Q. Zhang, and J. S. Geng, "Mechanical properties of sandstone after high temperature," *China Earthquake Engineering Journal*, vol. 38, no. 2, pp. 299–302, 2016, in Chinese.

[11] H. J. Su, H. W. Jing, H. H. Zhao, and Q. Yin, "Study on tensile strength and size effect of red sandstone after high temperature treatment," *Chinese Journal of Rock Mechanics and Engineering*, vol. 34, no. S1, pp. 2879–2887, 2015, in Chinese.

[12] C. B. Xu and H. S. Zhou, "Test investigation of triaxial compressive strength of coarse sandstone after high temperature," *Chinese Journal of Rock Mechanics and Engineering*, vol. 35, no. S1, pp. 2811–2818, 2016, in Chinese.

[13] Y. Y. Zhao, K. Wei, J. Q. Zhou, X. Li, and Y. F. Chen, "Laboratory study and micromechanical analysis of mechanical behaviors of three thermally damaged rocks," *Chinese Journal of Rock Mechanics and Engineering*, vol. 36, no. 1, pp. 142–151, 2017, in Chinese.

[14] D. Hou and J. Peng, "Triaxial mechanical behavior and strength model for thermally-damaged marble," *Chinese Journal of Rock Mechanics and Engineering*, vol. 38, no. S1, pp. 2603–2613, 2019, in Chinese.

[15] B. P. Xi, Y. C. Wu, Y. S. Zhao, L. Wang, B. P. Zhang, and X. M. Niu, "Experimental investigations of compressive strength and thermal damage capacity characterization of granite under different cooling modes," *Chinese Journal of Rock Mechanics and Engineering*, vol. 39, no. 2, pp. 286–300, 2020, in Chinese.

[16] Z. P. Huang, Y. Zhang, and W. D. Wu, "Analysis of mechanical and wave properties of heat-treated marble by water cooling," *Rock and Soil Mechanics*, vol. 37, no. 2, pp. 367–375, 2016, in Chinese.

[17] Z. P. Huang, Y. Zhang, Y. K. Sun, C. Y. Liu, and W. D. Wu, "Mechanical and acoustic characteristics of high temperature limestone with water cooling treatment," *Journal of Central South University (Science and Technology)*, vol. 47, no. 12, pp. 4181–4189, 2016, in Chinese.

[18] Z. W. Huang, H. T. Wen, X. G. Wu et al., "Experimental study on cracking of high temperature granite using liquid nitrogen," *Journal of China University of Petroleum*, vol. 43, no. 2, pp. 68–76, 2019, in Chinese.

[19] G. S. Han, H. W. Jing, H. J. Su, Q. Yin, J. Y. Wu, and Y. Gao, "Experimental research on mechanical behaviors of water-cooled sandstone after high temperature treatment," *Journal of China University of Mining and Technology*, vol. 49, no. 1, pp. 69–75, 2020, in Chinese.

[20] P. H. Jin, Y. Q. Hu, J. X. Shao, G. K. Zhao, X. Z. Zhu, and C. Li, "Experimental study on physical mechanical and transport properties of granite subjected to rapid cooling," *Chinese Journal of Rock Mechanics and Engineering*, vol. 37, no. 11, pp. 2556–2564, 2018, in Chinese.

[21] Y.-J. Shen, X. Hou, J.-Q. Yuan, and C.-H. Zhao, "Experimental study on temperature change and crack expansion of high temperature granite under different cooling shock treatments," *Energies*, vol. 12, no. 11, p. 2097, 2019.

[22] Y. J. Shen, X. Hou, J. Q. Yuan, S. F. Wang, and C. H. Zhao, "Thermal cracking characteristics of high-temperature granite suffering from different cooling shocks," *International Journal of Fracture*, 2020.

[23] Y. Shen, X. Hou, J. Yuan et al., "Thermal deterioration of high-temperature granite after cooling shock: multiple-identification and damage mechanism," *Bulletin of Engineering Geology and the Environment*, 2020.

[24] B. Isaka, R. Gamage, T. Rathnaweera, M. Perera, D. Chandrasekharam, and W. Kumari, "An influence of thermally-induced micro-cracking under cooling treatments: mechanical characteristics of Australian granite," *Energies*, vol. 11, no. 6, p. 1338, 2018.

[25] M. Hosseini, "Effect of temperature as well as heating and cooling cycles on rock properties," *Journal of Mining Environment*, vol. 8, no. 4, pp. 631–644, 2017.

[26] R. Li, Z. Huang, X. Wu, P. Yan, and X. Dai, "Cryogenic quenching of rock using liquid nitrogen as a coolant: investigation of surface effects," *International Journal of Heat and Mass Transfer*, vol. 119, no. 4, pp. 446–459, 2018.

[27] Z. G. Yan, Q. X. Yang, and H. H. Zhu, "Experimental study on fire in Qinling extra-long highway tunnel," *China Civil Engineering Journal*, vol. 11, pp. 96–101, 2005.

[28] Q. Li, T. Yin, X. Li, and S. Zhang, "Effects of rapid cooling treatment on heated sandstone: a comparison between water and liquid nitrogen cooling," *Bulletin of Engineering Geology and the Environment*, vol. 79, no. 1, pp. 313–327, 2020.

[29] W. G. P. Kumari, P. G. Ranjith, M. S. A. Perera, B. K. Chen, and I. M. Abdulagatov, "Temperature-dependent mechanical behaviour of Australian Strathbogie granite with different cooling treatments," *Engineering Geology*, vol. 229, pp. 31–44, 2017.

Research Article

Deformation Rules for Surrounding Rock in Directional Weakening of End Roofs of Thin Bedrocks and Ultrathick Seams

Fei Liu [ID],[1,2] **Zhanguo Ma** [ID],[1] **Yongsheng Han**,[3] **and Zhimin Huang** [ID][4]

[1]*State Key Laboratory for Geomechanics and Deep Underground Engineering, School of Mechanics and Civil Engineering, China University of Mining & Technology, Xuzhou, Jiangsu 221116, China*
[2]*School of Resources and Civil Engineering, Suzhou University, Suzhou, Anhui 234000, China*
[3]*Department of Water Resources Engineering, Shandong Water Conservancy Vocational College, Rizhao, Shandong 276826, China*
[4]*School of Materials and Physics, China University of Mining & Technology, Xuzhou, Jiangsu 221116, China*

Correspondence should be addressed to Zhanguo Ma; zhgm1044@126.com

With the deployment of China's energy strategy in the western regions, complex geological mining conditions such as thin bedrock and ultrathick seams in western China have caused a series of problems such as serious deformation of the surrounding rock at the ends of the working face and the increase in the lead abutment pressure of the roadways; the research on end roof deformation in the resource exploitation in western China has become one of the great demands of the industry. Based on the failure characteristics of rock mass, relying on the actual mining geological conditions of a coal mine in Inner Mongolia, the failure characteristics of the overlying rock strata under the influence of mining were simulated and analyzed using similar material simulation experiment, which intuitively reproduced the failure and deformation processes of the immediate roof, main roof, and key strata and revealed the mechanical mechanism of the directional weakening of the end roof. It is of great significance for the stability control of the surrounding rock at the end of the fully mechanized caving face in the thin bedrocks and ultrathick seams, reducing the abutment pressure of gate roadway and controlling the spontaneous combustion of residual coal in the goaf.

1. Introduction

The "13th Five-Year Plan" determines that China's energy production layout will continue to move westward, and the western region is still the main position of China's energy production [1]. The open roof area of the upper and lower ends of the fully mechanized caving face is large, which is located at the superposition of the strike support pressure and the inclined abutment pressure of the stope. The special geological conditions such as ultrathick seam and thin bedrock in the West further lead to a series of problems, such as serious deformation of surrounding rock at the end (as shown in Figure 1), increase of advance abutment pressure of roadway [2, 3], and low resource recovery rate [4, 5] of working face. The existing roof deformation control theory is difficult to ensure the safe and efficient production of

western mines. In order to effectively control the deformation of surrounding rock at the ends, a lot of research work has been carried out on the mechanical mechanism of deformation of end roof at home and abroad in recent years, and a large number of theoretical and technical application results have been obtained. Xiao [6] studied the structural stability of the ends of the fully mechanized caving face and believed that the supports at the ends of top-caving mining face are the difficult points for stope support and the main reason lies in the formation and stability of the arc triangle plate at the ends; Liu [7] studied the support technology at the ends of longwall fully mechanized caving face in steep thick seams; Yang and Liu [8] analyzed the caving form of the overlying strata at the ends with the method of theoretical calculation; Fang et al. [9] established the structural mechanics module of the end triangle area and analyzed the

Figure 1: Deformation diagram of surrounding rock of end roofs in test area.

mechanism of instability and failure of the arc triangle area; the scholars Sellers and Klerck [10] have found through study that the discontinuous surface generated inside the surrounding rock due to fissures and weak faces in the surrounding rock of the roadway as well as the discontinuity surface created by joint connection in the surrounding rock is one of the main reasons for the fracture spacing in the surrounding rock of the roadway. The presplitting pressure relief technology is [11] a technique to change the physical and mechanical properties of the rock mass through artificial intervention such as hydraulic fracturing or presplitting blasting, so as to weaken the structural strength of the coal rock mass and increase the fissure content, thereby achieving the purpose of permeability improvement or pressure relief. The presplitting pressure relief technology has been widely used in the prevention and control of low-permeability coal seam gas extraction, rock burst, and the control of surrounding rock in mining space [12, 13]. Dai [14] believes that presplitting blasting can eliminate the hinging effect between the fractured rocks of a hard roof, thereby promoting caving of the roof.

On-site exploration has the advantages of trustworthiness and reliability, but it features long cycle, heavy workload, high cost, and difficulty in grasping the main factors for mechanism analysis. The empirical formulas and theoretical analysis are simple and easy to operate, but there are larger calculation errors in related engineering due to the difficulty in generalization of complex mining geological conditions. A similar simulation [15–17] has the advantages of high efficiency, strong intuitiveness, good repeatability, good flexibility, and so on and can simulate the continuous dynamic deformation and failure process of the rock stratum. Therefore, in order to further investigate the deformation rules of surrounding rock in directional weakening of end roofs, in this paper, a similar material simulation experiment was used, based on the failure characteristics of rock mass and relying on the actual mining geological conditions of a coal mine in Inner Mongolia, to simulate and analyze the failure characteristics of the overlying rock strata under the influence of mining; it intuitively reproduced the failure and deformation processes of the immediate roof, main roof, and key strata and revealed the mechanical mechanism of the directional weakening of the end roof, which is of great significance for the stability control of the surrounding rock

at the end of the fully mechanized caving face in the thin bedrocks and ultrathick seams, the improvement of the mining rate of coal resources, the reduction of the abutment pressure of gate roadway, and the control of the spontaneous combustion of residual coal in the goaf.

2. Engineering Geological Conditions

The surface of the well field in Ordos Loess Plateau of the western regions is overlaid by a large area of loess and aeolian sand, and the bedrock is exposed only in larger gullies. With complex terrain and criss-cross ravines and gullies, this region has well-developed dendritic gullies. The general trend of the terrain is high in the southwest and low in the northeast at an altitude of about 1127–1346 m, with an altitude difference of 219 m. Number 6 coal seam is mainly mined in the minefield. The minable thickness of the coal seam ranges from 6.05 to 35.50 m, with an average thickness of 16.0 m, belonging to stable to relatively stable coal seams. The structure of the coal seam has a complex structure, soft in the middle, hard at the top, relatively hard at the bottom, and being with developed fissures and a lot of dirt bands. The coal seam roof is mainly semihard and has a relatively high proportion of soft rock on the floor, most of which is mudstone, claystone, and carbonaceous mudstone. Detailed lithological descriptions of the rock strata are illustrated in Figure 2.

3. Design of Similar Simulation Test

3.1. Model Bench and Related Instruments. A bench designed independently by China University of Mining and Technology was adopted to establish a similar simulation test model in which a high-speed static strain collection system was used to record the changes in the pressure cell data during the mining process, changes in rock formation displacement were observed with digital photographic measurement technology, and a hydraulic loading system was used to pressurize the overlying rock strata. PhotoInfor [18–20], a practical software system for digital photography measurement developed by China University of Mining and Technology, was used for digital image analysis. The test system is shown in Figure 3.

3.2. Similar Model Parameters. This test simulated the rock strata with a total thickness of 112.9 m from the coal seam floor-coal seam roof of the coal seam, with a coal seam thickness of 16 m. The cross section of the simulated roadway is rectangular, with a width of 5.5 m, a height of 3.7 m, and a cross-sectional area of 20.35 m^2. The model geometric similarity ratio $\alpha_l = (y_m/y_p) = (z_m/z_p) = (1/100)$, bulk density similarity coefficient [15] $\alpha_\gamma = (\gamma_{mi}/\gamma_{pi}) = 0.65$, elastic modulus similarity coefficient [15, 21] $\alpha_E = (1/154)$, and time coefficient of 1/10 were taken. Similar materials are shown in Figure 4.

3.3. Similar Material Compounding Ratio. Based on the determination of the strength of the site rock strata, combined with the principle of similar simulation test,

Thicness of strata (m)	Rock properties	Strata position
14.3	Sandy conglomerate	
5.0	Basalt	
2.6	Fine sandstone	
20.0	Medium sandstone	
8.3	Sandy mudstone	Overlying strata
6.3	Fine sandstone	
15.0	Conglomerate	
5.0	Siltstone	
1.1	Medium sandstone	
6.7	Fine sandstone	
16.0	Coal	Coal seam
10.0	Siltstone	Floor strata
2.6	Fine sandstone	
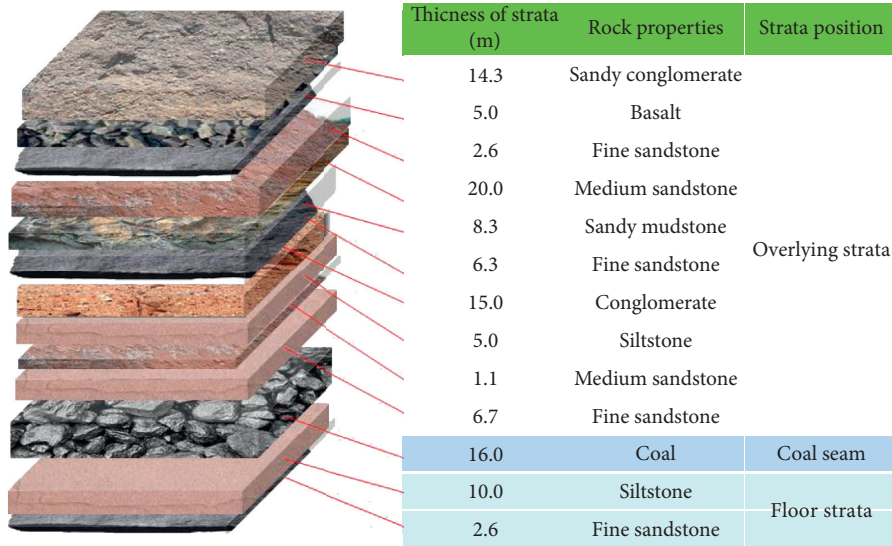
FIGURE 2: Lithological descriptions of the rock strata at number 6 coal seam.

(a)

High speed static strain acquisition system

Pressure sensor

(b)
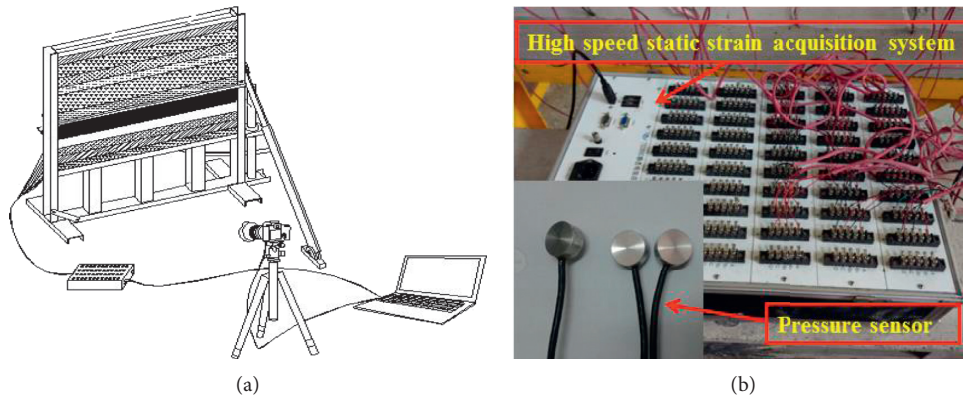
FIGURE 3: Test equipment. (a) Digital photogrammetric system and (b) rock stress collection system.

the strength of each layer in the model test was calculated. Ordinary fine-grained river sand (with a particle size of less than 3 mm) was selected as aggregate, and gypsum and calcium carbonate were used as cementing materials. For the strength of similar materials in [22–24], a test specimen with a reasonable compounding ratio was prepared for a strength verification test (as shown in Figure 5), and the parameters of each stratified material ratio in this model were finally determined as shown in Table 1.

3.4. Test Method and Arrangement of Measuring Points. This test studied the effect of changes in topping angle on pressure release from excessive pressure of coal pillars in the section between F6203 and F6024 working faces and the roadway of the F6204 working face caused by overlength suspension roof at the ends of the goaf for F6203 working face. The 30°, 45°, and 60° fissures were prefabricated in the overlying rock strata on the side of F6203 working face

from the angle of auxiliary transportation roadway on F6204. During the mining process, by caving of the overlying rock strata along the prefabricated fissures, the stress changes before and after the caving were analyzed. The pressure measuring points and displacement measuring lines were arranged as shown in Figure 6. There were three rows of pressure cells placed from bottom to top. The pressure cells in bottom row were numbered from A1 to A6 from left to right, the ones in the middle row were numbered from B1 to B6, and the ones in the top row were numbered from C1 to C6.

During the test, the model was excavated from left to right, the width of three hydraulic supports was collected, and then the top coal was drawn once for sublevel caving. Since the roof deformation is relatively large and the model stability time is relatively long during the period of drawing top coal for mining, when the drawing has a significant effect on the stress and deformation of the surrounding rock at the ends and the coal pillars in sections, stability time of 0.5 to 1.0 h is required for each measurement within the model.

(a)

(b)

(c)
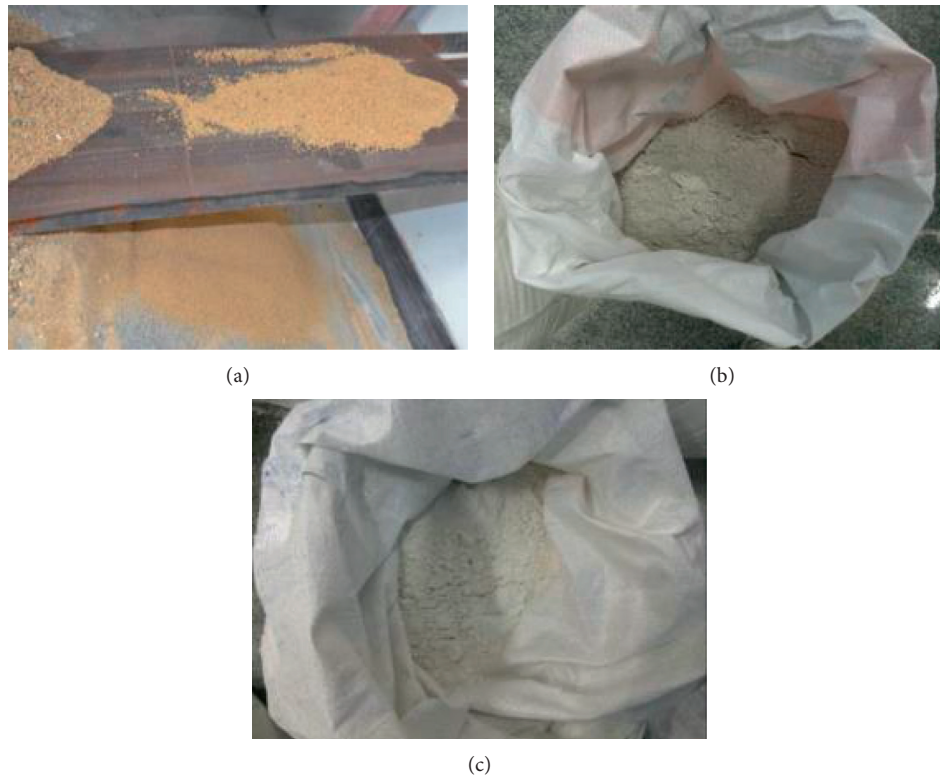
Figure 4: Similar materials. (a) River sand, (b) gypsum powder, and (c) calcium carbonate powder.

(a)

(b)

Figure 5: Strength test of similar materials [1]. (a) Sample of similar material and (b) strength test process.

4. Deformation Rules for Overlying Strata in the Fully Mechanized Sublevel Caving Face with the Thin Bedrock and Ultrathick Seam

4.1. Analysis on Limit Breaking Distance of Immediate Roof. After the coal seam is mined, the immediate roof will partially overhang. As the working face advances forward, the overhanging area continues to increase. When the suspension part of the immediate roof reaches a certain length, fracture failure will occur. The fracture forms of immediate roof are shown in Figure 7.

Figure 7 is a diagram of two fracture processes of immediate roofs. Through measurement and analysis, it can be determined that the limit fracture distance of the immediate roof is about 13 m and the fracture angle is about 63° in the test area.

4.2. Deformation Analysis of Overlying Rock Strata Structure with Caving of the Main Roof. In this test, PhotoInfor image processing software was used to track and analyze the displacement of the rock strata, and the displacement was calculated according to the pixel coordinates in the image.

TABLE 1: Ratio parameters of layered materials.

Rock layer name	Depth of stratum (m)	Model thickness (cm)	Sand (kg)	Calcium carbonate (kg)	Gypsum (kg)	Total mass (kg)
Glutenite	14.3	14.3	32.84	2.53	2.53	37.89
Basalt	5	5	11.59	1.32	0.33	13.25
Fine sandstone	2.6	2.6	5.97	0.64	0.28	6.89
Medium sandstone	20	20	44.16	4.42	4.42	52.99
Sandy mudstone	8.3	8.3	19.24	1.92	0.82	21.99
Fine sandstone	6.3	6.3	11.13	1.11	4.45	16.69
Conglomerate	15	15	35.77	3.18	0.79	39.74
Siltstone	5	5	10.60	0.79	1.85	13.25
Medium sandstone	1.1	1.1	2.55	0.11	0.26	2.91
Siltstone	6.7	6.7	15.02	1.91	0.82	17.75
Coal	16	16	37.09	2.12	3.18	42.39
Siltstone	10	10	22.42	1.22	2.85	26.50
Fine sandstone	2.6	2.6	4.59	0.69	1.61	6.89
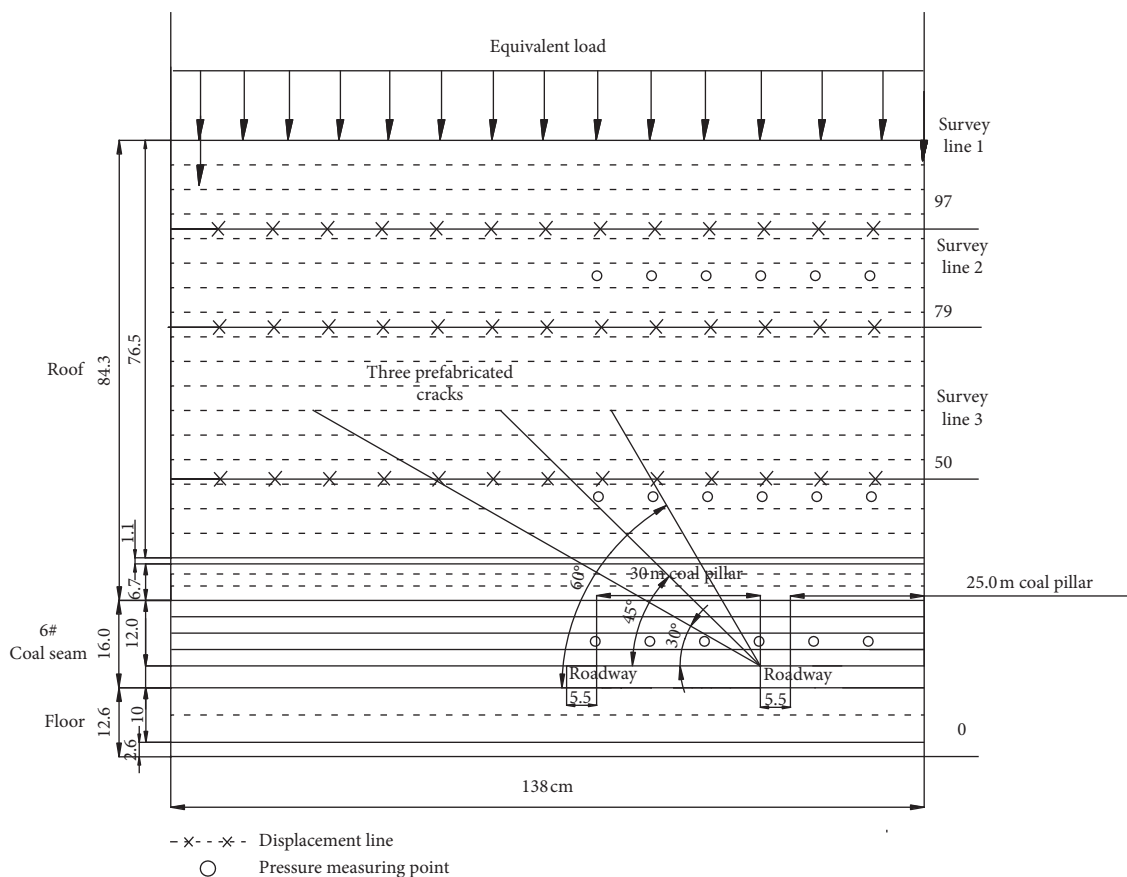
FIGURE 6: Layout of measuring points and lines of prefabricated roof fracture.

The output results were converted from pixel coordinates to actual coordinates, and the measured width of the model image of 2500 pixels was equivalent to the actual model width of 138 cm for displacement treatment. Grid partitioning is shown in Figure 8.

4.2.1. Analysis on the Test Process and Model Displacement Vector Cloud Diagram. The fracture test process diagram and model displacement vector cloud diagram for the main roof are shown in Figures 9 and 10.

As shown in Figures 9 and 10, it can be found that with the advancement of the working face, the overlying rock strata on the working face have undergone three processes of "separation-caving-compacting." The greater the cracking degree of the lower rock strata is, the smaller the cracking of the upper rock strata will be, mainly manifested by bending and subsidence. When caving of the main roof occurred for the first time, as shown in Figure 9, the displacement and deformation were mainly concentrated in the caving part. Although the displacement of the rock strata above the caving zone changed, the change was small; as excavation

(a)

(b)

(c)

(d)
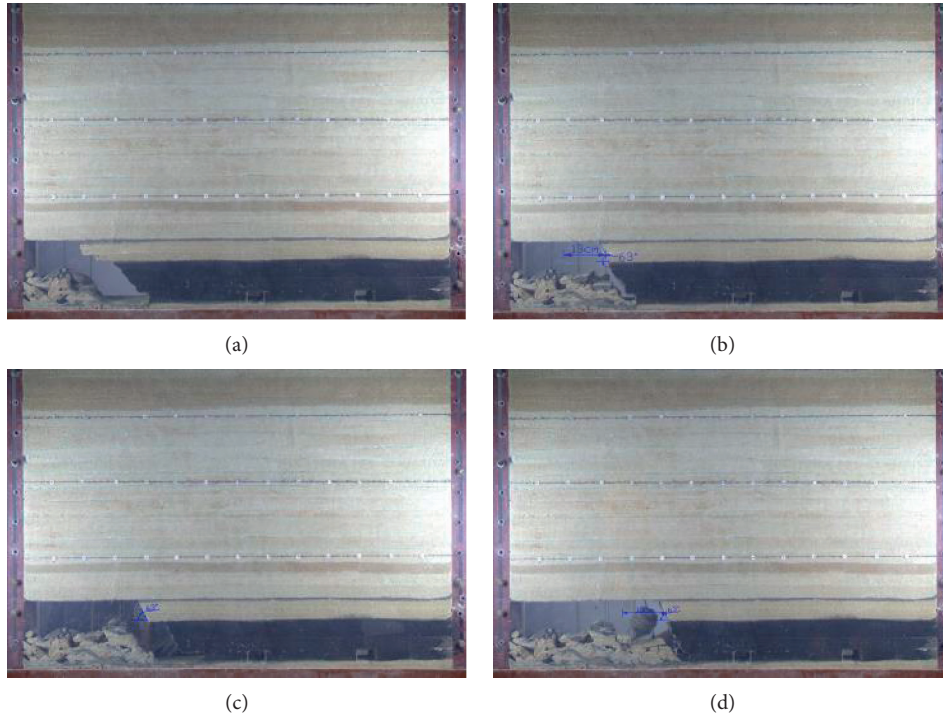
Figure 7: Breaking law of immediate roof. (a) Before the first break, (b) after the first break, (c) before the second break, and (d) after the second break.
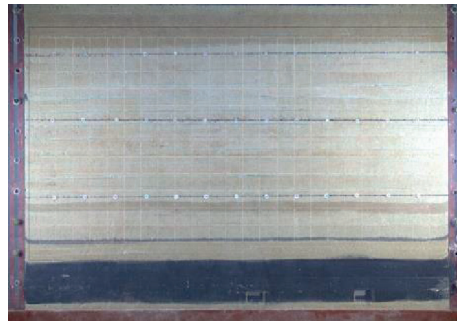
Figure 8: Grid partitioning.
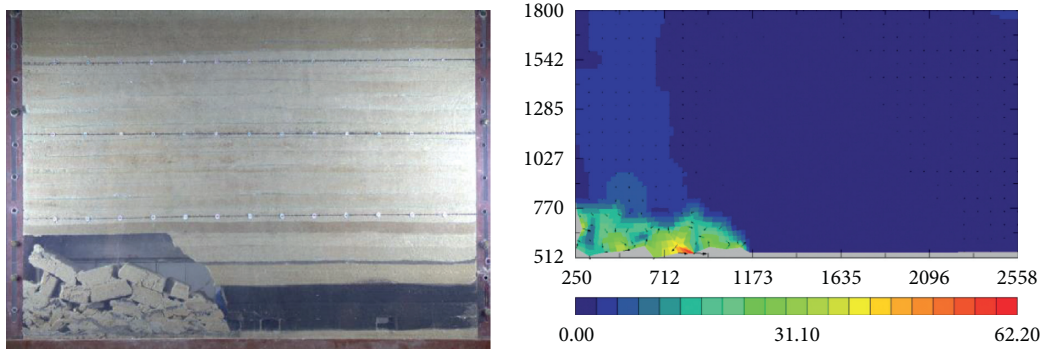
Figure 9: Model diagram and displacement vector cloud diagram of primary collapse of basic roof.
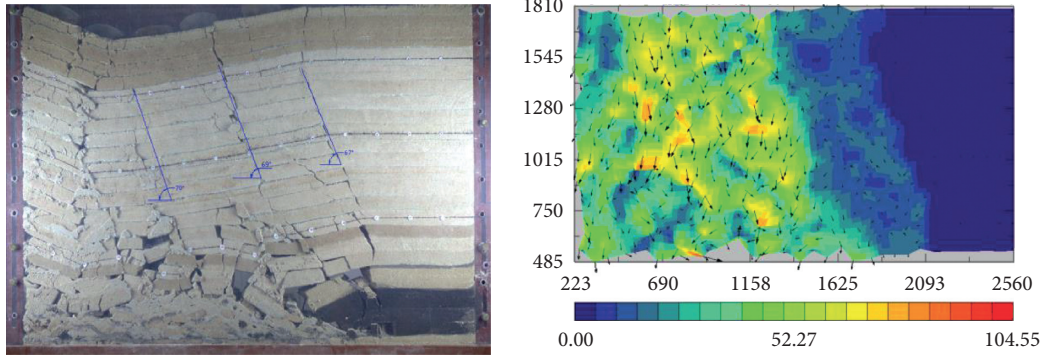
FIGURE 10: Model diagram and displacement vector cloud diagram of the third appearance of fracture zone.

continued, as shown in Figure 10, the crack zone first appeared and developed to the surface, forming obvious "three zones," namely, the caving zone, crack zone, and curved subsidence zone. Through the displacement vector flow field, with the vector direction obliquely to the lower left, it can be seen that the overlying rock strata on the working face are significantly curved and subsided, and the displacement of each rock stratum is increased compared with the initial caving; as shown in Figure 10, when the crack zone appeared for the second time, the previous crack was gradually closed, the existing goaf was compacted, and the maximum displacement became larger than when the fissure through the surface appeared for the first time; as working face advanced, as shown in Figure 10, the overlying rock strata developed through fissures for the third time. Through measurement, it was found that the angles of the three fractures in the strata were almost the same, about 69°.

4.2.2. Subsidence Curve of the Fracture Measuring Line of the Main Roof. As shown in the displacement curve in Figure 11, when caving of the main roof occurred for the first time, the three measuring lines hardly subsided, with the maximum subsidence value of 0.65 cm, and the overlying rock strata hardly had any displacement; when the crack zone first appeared, as shown in Figure 12, the "three zones" began to appear. The third measuring line subsidence was larger, with the maximum subsidence value of 13.7 cm, and the main roof of the overlying rock strata had a great displacement. When the crack zone appeared for the second time, as shown in Figure 13, the "three zones" appeared clearly. The overlying rock strata began to coordinate and subside synchronously. The first and second measuring lines had almost the same value of subsidence. The largest subsidence occurred on the third measuring line, with a maximum value of 16.1 cm, and the third measuring line showed sinusoidal bending, mainly due to the irregular caving of the lower rock strata. When the crack zone appeared for the third time, as shown in Figure 14, the three measuring lines had large subsidence, with the maximum subsidence of 16.1 cm, and the goaf at the back was gradually compacted and stabilized.
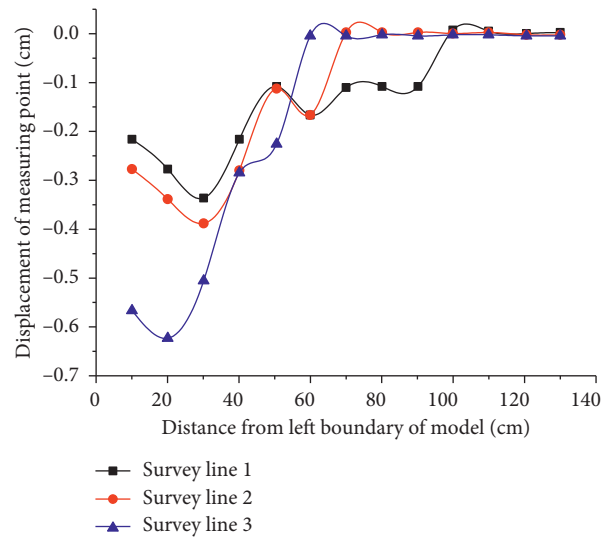
FIGURE 11: Displacement curve line of primary caving of basic roof.
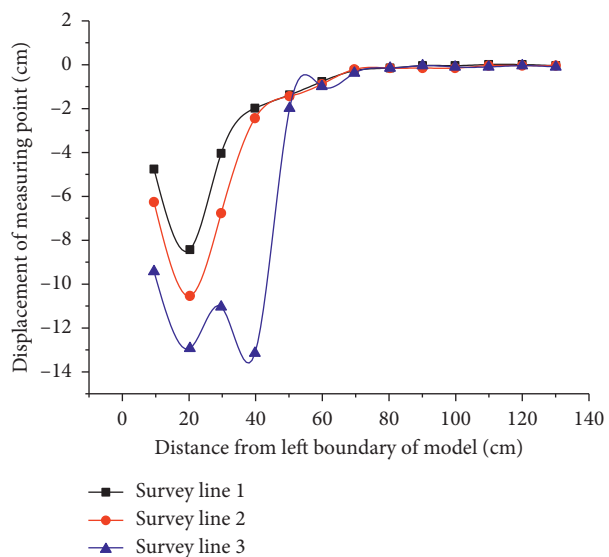
FIGURE 12: Displacement curve line of the first appearance of the fracture zone.
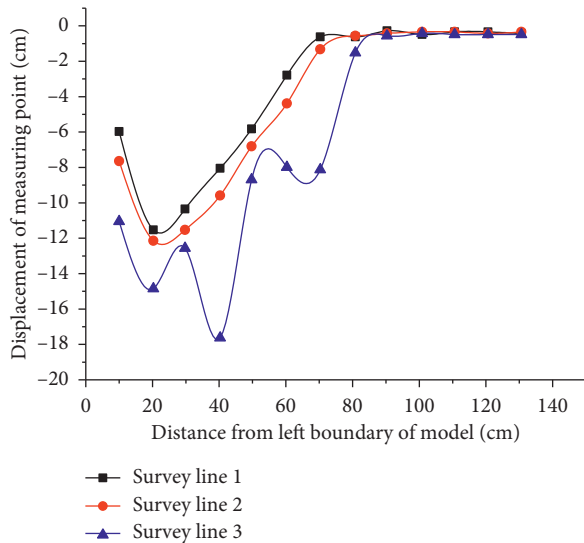
FIGURE 13: Displacement curve line of the second appearance of the fracture zone.
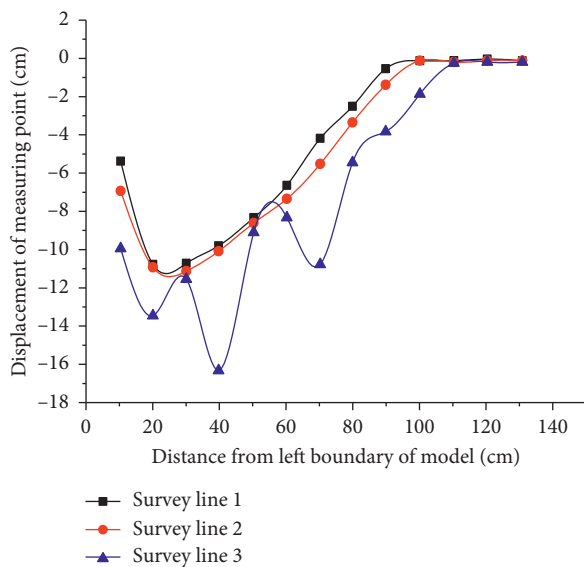
FIGURE 14: Displacement curve line of the third appearance of the fracture zone.

4.3. Key Strata Structure Analysis. According to the key strata theory, the rock strata that control the activity of some rock strata in the overlying rock strata of the stope or all rock strata to the surface are called the key strata, the former is called the inferior key strata, and the latter is called the main key strata. The deformation characteristics of the main key strata overlying the stope indicate that when the key strata subside and deform, the value of subsidence of all the overlying rock strata is synchronously coordinated; the fracture characteristics show that the fracture of key strata will cause the synchronous fracture of all overlying rock strata, leading to displacement of rock strata on a larger scale; its bearing characteristics show that the key strata take the form of "plate" (or simply "beam") as the main bearing

body of all rock strata before fracture, become the masonry beam structure after fracture, and continue to become the bearing body. By observing the entire test process, it was found that the 7.8 m–22 m rock strata above the top coal were fractured, which had a greater impact on the overlying rock strata. After fracture, it directly caused the synchronous fracture of all the overlying rock strata, which was consistent with the characteristics of the key strata, so it was initially determined as the main key strata of the mine in the test area. The specific test process is shown in Figure 15.

As shown in Figure 15(a), it was the model before the key strata fracture with no significant fissure in the middle rock strata. As excavation continued, as shown in Figure 15(b), the key strata were fractured, and the crack penetrated to the surface, causing the synchronously coordinated subsidence of upper rock strata. After fracturing, a masonry beam structure was formed to continue to support the overlying rock strata. The subsidence angle of block B is 12°, the length is 16 cm, and the length of block C is 15.5 cm.

5. Stress Analysis of Coal Pillars of the Lower Sections with Variable Angle of Topping

Affected by the F6203 working face, the auxiliary gate roadway of the F6204 working face had more significant strata pressure, the surrounding rock on the side of the coal pillar was severely fractured, and a large-scale "net bag" phenomenon occurred. It can be inferred from the analysis of the technical conditions of auxiliary transportation along the gate roadway of F6204 working face: the caving of the hard roof in the goaf on the F6203 working face will lead to the formation of a long suspension roof difficult to cave outside the goaf on the side of the auxiliary gate roadway of the F6204 working face. The rotation deformation of the suspension roof beam and the overlying pressure of overhanging rock strata will greatly increase the supporting load of the auxiliary gate roadway of the F6204 working face, thereby making the serious fracture of the top of the auxiliary gate roadway of the F6204 working face, accompanied by the sound of "coal cannon" and the large amount of displacement on both sides and at the top and bottom.

The suspension roof in the goaf of F6203 working face has a great impact on the coal pillars between F6203 and F6024 working faces and the pressure of F6204 auxiliary roadway. In the test, three fissures at 30°, 45°, and 60° were prefabricated from the angle of auxiliary gate roadway of the F6204 working face to the side of F6203 goaf. During the mining process, caving of the overlying rock strata occurred along the prefabricated fissures. The overlying strata structure after caving is shown in Figure 16.

It can be seen from Figure 16 that as the mining proceeded from left to right in the model, the overlying rock strata formed Zone A along the 30° prefabricated fissures, and the rock strata in Zone A were gradually separated for caving; the overlying rock strata formed Zone B along the 45° prefabricated fissures, and the rock strata in Zone B were gradually separated; the overlying rock strata formed Zone C along the 60° prefabricated fissures, and the rock strata in Zone C were gradually separated.

(a)

(b)

FIGURE 15: Model overview before and after key stratum breaking. (a) Before key stratum breaking and (b) after key stratum breaking.

(a)

(b)

(c)
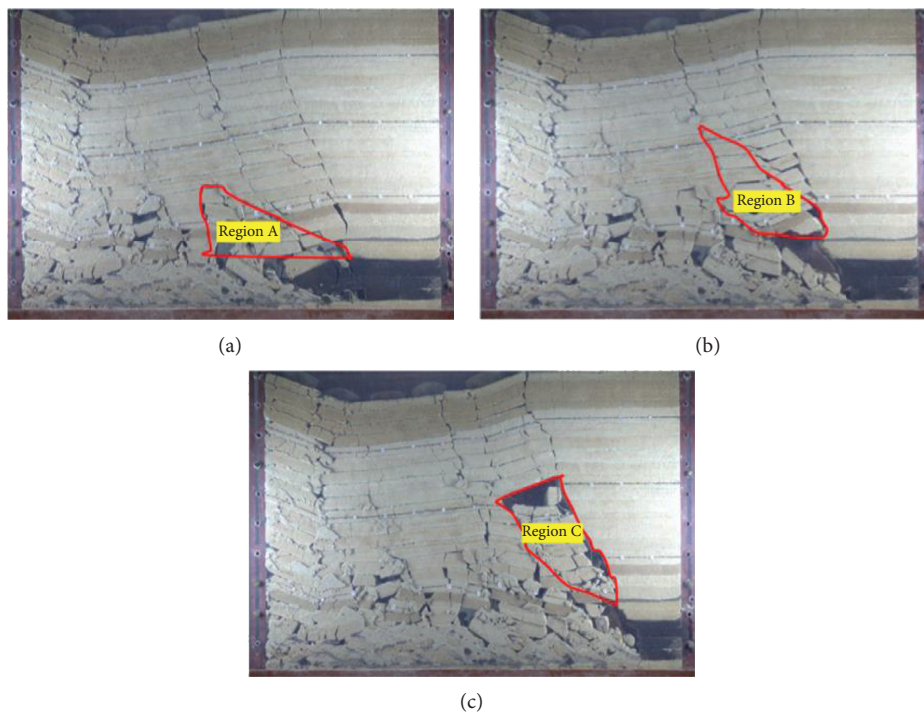
FIGURE 16: Structural form of overburden of topping fracturing. (a) Topping fracturing at 30°, (b) topping fracturing at 45°, and (c) topping fracturing at 60°.

5.1. Analysis of Stress Changes before and after Topping Fracturing at 30°. When the model was excavated to 98 cm, the rock strata in Region A were almost completely separated, and Region A tended to stabilize. The overhanging rock strata were cut along the precracked surface, filling the caving space, eliminating the suspension roof phenomenon, and reducing the load and rotation deformation force of the cantilever beam.

It can be seen from Figure 17 that after the overlying rock strata were cut along the 30° prefabricated fissure, the stresses of the A3 and A4 pressure cells decreased by 98% and 74%, respectively, and the A3 and A4 pressure cells were located at the surrounding rock in auxiliary gate roadway of the F6204 working face; the stresses of the A5 and A6 pressure cells increased by 7% and 13%, respectively. The A5

and A6 pressure cells were located in the unmined coal part on the right side of the F6204 auxiliary gate roadway. Through analysis, it can be found that the 30° prefabricated fissure cutting greatly dissipated the stress concentration degree of the surrounding rock of the auxiliary gate roadway of the F6204 working face, so that the stress concentration was transferred to the depth of the unmined coal on the right side of the auxiliary gate roadway, which greatly improved surrounding rock stress environment of F6204 auxiliary gate roadway and fundamentally optimized the structural mechanical environment in the roadway.

5.2. Analysis of Stress Changes before and after Topping Fracturing at 45°. When the model was excavated to 104.8 cm, the rock strata in Region B were almost completely
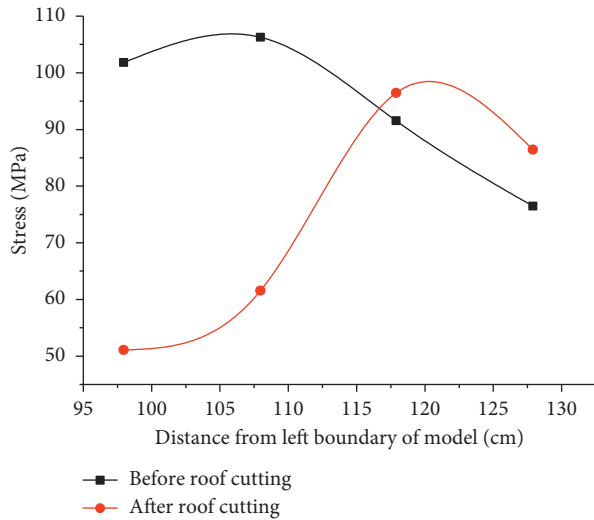
FIGURE 17: Before and after topping fracturing at 30°.
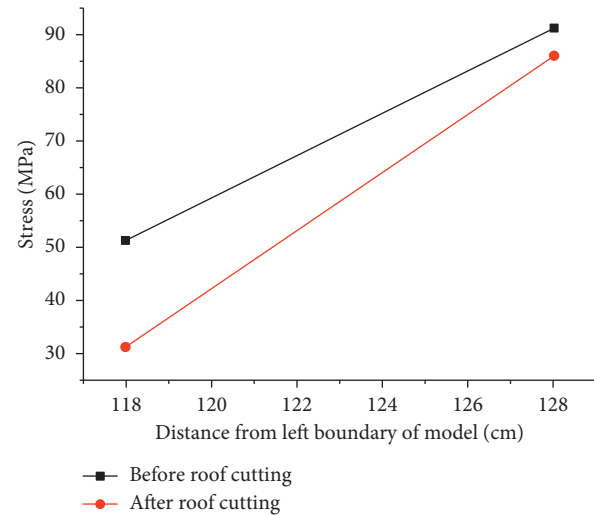
FIGURE 19: Before and after topping fracturing at 60°.
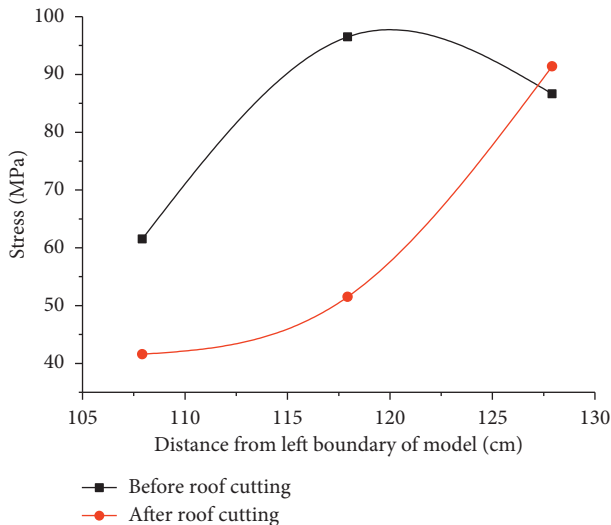
FIGURE 18: Before and after topping fracturing at 45°.

separated, and Region B tended to stabilize. The overhanging rock strata were cut along the precracked surface, filling the caving space, eliminating the suspension roof phenomenon, and reducing the load and rotation deformation force of the cantilever beam.

It can be seen from Figure 18 that after the topping of the overlying rock strata along the prefabricated fissure at 45°, the stress of the A4 pressure cell decreased by 49%, the stress of the A5 pressure cell decreased by 87%, and the stress of the A6 pressure cell increased by 6%. It can be found through analysis that the 45° prefabricated fissure topping greatly reduced the stress at the end of the auxiliary gate roadway of the F6204 working face, so that the stress is transferred to the depth of the unmined coal body.

5.3. Analysis of Stress Changes before and after Topping Fracturing at 60°. When the model was excavated to 121.8 cm, the rock strata in Region C were almost completely

separated, and Region C tended to stabilize. The overhanging rock strata were cut along the precracked surface, filling the caving space, eliminating the suspension roof phenomenon, and reducing the load and rotation deformation force of the cantilever beam.

It can be seen from Figure 19 that after the topping of the overlying rock strata along the 60° prefabricated fissure, the stress in the A5 pressure cell decreased by 63%, and the stress in the A6 pressure cell decreased by 6%. It can be found through analysis that the topping along 60° prefabricated fissure reduced the stress at the end of the auxiliary gate roadway of the F6204 working face. The degree of reduction was small, and it may be affected by the right boundary of the model.

6. Conclusion

(1) The breaking distance of the immediate roof limit was about 13 m, and the fracture angle was about 63°; upon the caving of main roof for the first time, the overlying rock strata hardly had any displacement; when the crack zone first appeared, the "three zones" began to appear, and the main roof of the overlying rock strata had great displacement; when the crack zone appeared for the second and third times, synchronously coordinated subsidence of overlying rock strata began to occur. The goaf at the back was gradually compacted and stabilized. The angles of the three cracks in the rock stratum were almost the same, about 69°.

(2) Before the key strata fractured, the "plate" structure was used as the main bearing body of all the rock strata. The key strata fractured, and the crack penetrated to the surface, causing synchronously coordinated subsidence of upper rock strata. After the fracture, the masonry beam structure formed and continued to support the overlying rock strata.

(3) The rock strata at 7.8 m–22 m above the top coal had a great impact on the overlying strata after fracturing, which directly led to the synchronous fracturing of all overlying rock strata. This is in line with the characteristics of the key strata, so it was preliminarily determined as main key strata of the mine in the test area.

(4) Compared with 45° and 60° prefabricated fissures, it can be found that the 30° prefabricated fissure topping greatly dissipated the stress concentration of the surrounding rock of the auxiliary gate roadway at the F6204 working face, so that the stress was transferred to the depth of the unmined coal on the right side of the auxiliary gate roadway, which greatly improved surrounding rock stress environment of F6204 auxiliary gate roadway and fundamentally optimized the structural mechanical environment in the roadway.

Data Availability

The data used to support the findings of this study are available from the corresponding author upon request.

Conflicts of Interest

The authors declare no conflicts of interest.

Acknowledgments

References

[1] F. Liu, Z.-G. Ma, P. Gong, and N. Cui, "Deformation mechanism of ending of surrounding rock in super-thick coal seam with thin bedrock," *Journal of Mining & Safety Engineering*, vol. 35, no. 1, pp. 94–99, 2018.

[2] Z.-Q. Yin, G.-X. Xie, Z.-X. Hu, and C.-Q. Zhu, "Investigation on fracture mechanism of coal rock on three-point bending tests under different gas pressures," *Journal of China Coal Society*, vol. 41, no. 2, pp. 424–431, 2016.

[3] Z. Q. Yin, H.-F. Ma, H. F. Ma, Z. X. Hu, and Y. Zou, "Effect of static-dynamic coupling loading on fracture toughness and failure characteristics in marble," *Journal of Engineering Science and Technology Review*, vol. 7, no. 2, pp. 169–174, 2014.

[4] Y. Xue, T. Teng, F. Dang, Z. Ma, S. Wang, and H. Xue, "Productivity analysis of fractured wells in reservoir of hydrogen and carbon based on dual-porosity medium model," *International Journal of Hydrogen Energy*, vol. 45, no. 39, pp. 20240–20249, 2020.

[5] J. Liu, X. Liang, Y. Xue, K. Yao, and Y. Fu, "Numerical evaluation on multiphase flow and heat transfer during thermal stimulation enhanced shale gas recovery," *Applied Thermal Engineering*, vol. 178, Article ID 115554, 2020.

[6] Y.-N. Xiao, "Study of end structural stability of fully mechanized caving face," *China Mining Magazine*, vol. 19, no. 2, pp. 86–103, 2010.

[7] C.-P. Liu, "Practices on face end support technology for fully mechanized top coal caving mining face in deep inclined thick seam," *Coal Science and Technology*, vol. 33, no. 10, pp. 23–25, 2005.

[8] P.-J. Yang and C.-Y. Liu, "Structure forms of basic roof and reasonable supporting parameters in ends of fully-mechanized top caving face," *Journal of Mining & Safety Engineering*, vol. 29, no. 1, pp. 26–32, 2012.

[9] X.-Q. Fang, R.-Q. Xu, and J.-J. Zhao, "Research on instability of the triangular coal alongside the goaf in a fully mechanized top-coal caving work face," *Journal of China University of Mining & Technology*, vol. 40, no. 5, pp. 678–683, 2011.

[10] E. J. Sellers and P. Klerck, "Modeling of the effect of discontinuities on the extent of the fracture zone surrounding deep tunnels," *Tunneling and Underground Space Technology*, vol. 15, no. 4, pp. 463–469, 2000.

[11] S.-C. Zhou, D. Li, F.-W. Zhang, D.-F. Shen, D.-P. Zhou, and C.-Y. Guo, "Optimization analysis of drilling layout based on blasting releasing pressure and its application," *Chinese Journal of Rock Mechanics and Engineering*, vol. 32, no. 4, pp. 807–813, 2013.

[12] C.-P. Lu, D. Li, L.-M. Dou, and X.-R. Wu, "Controlled weakening mechanism of dynamic catastrophe of coal and rock and its practice," *Journal of China University of Mining & Technology*, vol. 35, no. 3, pp. 301–305, 2006.

[13] M.-Y. Wei, E.-Y. Wang, X.-F. Liu, and C. Wang, "Numerical simulation of rockburst prevention effect by blasting pressure relief in deep coal seam," *Rock and Soil Mechanics*, vol. 32, no. 8, pp. 2539–2560, 2011.

[14] R.-G. Dai, "Preliminary analysis of the natural law of caving down the hard roof of the 15-foot coal seam at the Tu-er-ping mine and its mine pressure," *Journal of China Coal Society*, vol. 2, no. 4, pp. 40–50, 1965.

[15] P. Gong, Z.-G. Ma, R.-C. Zhang, X.-Y. Ni, F. Liu, and Z.-M. Huang, "Surrounding rock deformation mechanism and control technology for gob-side entry retaining with fully mechanized gangue backfilling mining: a case study," *Shock and Vibration*, vol. 2017, Article ID 6085941, 15 pages, 2017.

[16] Z.-G. Wang, H.-W. Zhou, and H.-P. Xie, "Experimental study of the rule of overlying strata movement and breakage in deep mining," *Journal of Experimental Mechanics*, vol. 23, no. 6, pp. 503–510, 2008.

[17] H.-W. Wang, H.-W. Zhou, and J.-P. Zuo, "Application of optical measurement method in strata movement smiulation experiment," *Journal of China Coal Society*, vol. 31, no. 3, pp. 278–281, 2006.

[18] Y.-H. Li, R.-X. Jia, and S. Yang, "Optimized method for DSCM based on progressive displacement characteristics of geotechnical materials," *Chinese Journal of Geotechnical Engineering*, vol. 37, no. 3, pp. 1490–1496, 2015.

[19] S. Yang, Y. Li, X. Tang, and J. Liu, "Experimental simulation and numerical modeling of deformation and damage evolution of pre-holed sandstones after heat treatment," *Computer Modeling in Engineering & Sciences*, vol. 122, no. 2, pp. 633–659, 2020.

[20] Y.-H. Li and H.-W. Jing, "Software development of a digital speckle correlation method and its application," *Journal of China University of Mining & Technology*, vol. 37, no. 5, pp. 635–640, 2008.

[21] D.-F. Yuan, C.-Y. Wang, and Y. Zhou, "Study on the law of the pressure of the fully mechanized mining face in deep mining," *Coal Engineering*, vol. 5, pp. 52–54, 2010.

[22] F. Luo, B.-S. Yang, and B.-B. Hao, "Mechanical properties of similar material under uniaxial compression and the strength error sources," *Journal of Mining & Safety Engineering*, vol. 30, no. 1, pp. 93–99, 2013.

[23] Y.-B. Ning, H.-M. Tang, B.-C. Zhang, P.-W. Shen, G.-C. Zhang, and D. Xia, "Research on rock similar material proportioning test based on orthogonal design and its application in base friction physical model test," *Rock and Soil Mechanics*, vol. 41, no. 6, pp. 1–11, 2020.

[24] T.-Y. Li, J.-M. Zhao, and H.-Z. Zhou, "Mixture proportioning tests of rock similar materials based on the orthogonal methods," *Journal of Water Resources and Architectural Engineering*, vol. 16, no. 4, pp. 143–147, 2018.

Research Article

Study on the Allowable Exposure Time of Temporary Goaf in the Open Stope and Backfill Mining Method with Large Structure Parameters

Xiaosheng Liu [iD],[1,2] Weijun Wang,[1] Yizhong Luo,[3] and Jin Zhan[2]

[1]*School of Resources, Environment and Safety Engineering, Hunan University of Science and Technology, Xiangtan 411201, China*
[2]*Changsha Institute of Mining Research Co., Ltd., Changsha 410012, China*
[3]*School of Resources and Safety Engineering, Central South University, Changsha 410012, China*

Correspondence should be addressed to Xiaosheng Liu; 13681996@qq.com

Based on the uniaxial rheological experiment data of iron ore rock mass and filling body in large-scale stope obtained by using the rock servo controlling creep equipment, the characteristics of the creep curve were analyzed. The creep models of iron ore and filling body which can show the attenuation creep of rock were constructed. And a nonlinear creep model was obtained. According to the rheological data of the iron ore and the filling body, the parameters of the new nonlinear creep model were identified to obtain the material parameters of the creep model. Then, the creep model parameters were fitted and reduced to calculate the reasonable exposure time of temporary goaf in the large-scale stope. The results show that the reasonable exposure time of stope is 520 ∼ 650 days, and the reasonable exposure time of filling body is 410 ∼ 520 days. The model can well describe the initial attenuation creep stage and steady creep stage in the creep curve, which proves the correctness and rationality of the model. The study provides a reference for mining design and safety production of similar mines with large-scale stope structure.

1. Introduction

In rock engineering, a large number of instability phenomena are related to the creep characteristics of rock. Rock creep is one of the important reasons for the deformation and instability of surrounding rock in rock engineering [1–3]. The rheological property of rock means that the rock presents deformation, fluidity, failure, and other properties with time under the conditions of external load and temperature, mainly presenting the properties of creep, stress relaxation, elastic aftereffect, strain rate effect, aging strength, rheological damage, and fracture [4–6]. In the past few decades, many scholars have carried out experiments on rock creep characteristics and obtained the conclusion that the rock creep continuously adjusts and recombines with time, resulting in rock stress and strain which also continuously increase and change with time [7–11].

In the process of ductile creep, the microcrack growth with time is also one of the main reasons for the failure of hard rock. In the process of brittle and ductile creep, rock samples show different time-dependent crack growth patterns in the microcosmic mechanism, leading to significant differences in macroscopic deformation behavior [12, 13]. A series of uniaxial compressive strength tests and multistage creep tests are carried out on rock specimens under different immersion conditions. The results show that the peak strength and elasticity modulus of red sandstone not only decrease with water content but also decrease with immersion time, which can be better expressed by the negative exponential function. On the basis of studying the stress-strain curve of rock, many creep models of rock have been put forward by combining with various simple creep elements, such as Maxwell model, Bingham model, Burgers model, generalized Kelvin model, and K-B model. But these models cannot describe the whole process of rock creep very

well, especially for the accelerated creep stage. Among these models, the K-B model and Burgers model are widely used and are improved to obtain good research results [13–18]. It should be pointed out that, because of the test instrument, the rock creep models under high temperature, high pressure, and anisotropy are seldom discussed, which is also the difficulty of rock creep research in the future.

In recent years, a large number of studies have been carried out on the cemented filling body strength, filling material proportion, backfill mechanical properties, and stability analysis; for example, the factors affecting the strength of tailings filling body are studied through different proportion tests [19], the damage model of tailings filling body is established through tests [20], and the mechanical properties in the roof of tailings cemented filling body are studied [21, 22]. However, there are few papers on the creep research for the cemented filling body in large-scale stope mined by the backfill mining method. Therefore, the establishing creep model of filling body to determine the reasonable exposure time of goaf is not only of theoretical value but also of great necessity to calculate and analyze the stability of filling body in engineering practice. In the whole creep process of rocks and filling body, accelerated creep is relatively difficult to simulate. The current theoretical research focuses mainly on simulating accelerated creep characteristics. In this study, through a series of uniaxial compression creep tests, an ideal nonlinear material element which can simulate accelerated creep characteristics is constructed and then combined with basic elements to simulate the whole creep process. The uniaxial creep tests are carried out on the iron ore rock and filling body under the loading conditions to study the deformation characteristics of rock and filling body under different stress states. On the basis of summarizing the damage research results of different materials, statistical damage is introduced into the composite element model, and the corresponding creep model is established. And the corresponding creep parameters are obtained by model parameter identification. Then, the creep equation is used to predict the timeliness of large-scale stope structure, and the reasonable stope exposure time is discussed from the safety.

2. Mining Conditions and Requirements of a Large Iron Mine

An iron mine in Anhui Province, China, is located about 18 km in the south of Huaihe River. The mining area is basically flat. The surface of the mining area is basically farmland and is part of the residential buildings. In order to safeguard the surface from collapse, strict protection is needed. The deposit is covered by Quaternary topsoil and strongly weathered rock stratum; its average thickness is 120 m, and the thickness of upper clay stratum is tens of meters. The integrity and stability of strongly weathered rock are poor. The occurrence of the ore body is steep, the local structural fracture zone is developed, and the rock and ore are stable. The buried depth of the main ore body is less than 150 ∼ 900 m. The ore body trend is nearly north-south and inclines to west, with a dip angle of 68° ∼ 88°. The thickness

of the ore body is 25.5 ∼ 96.5 m, the average thickness is 49.65 m, the strike length is about 2000 m, and the average geological grade is 30.69%.

The required production scale of the mine is 7.5 million t/a, the mining capacity of the stope is 2000 t/d, the ore dilution rate is less than or equal to 10%, and the ore recovery rate is more than or equal to 90%. In order to protect the earth's surface and the structures and to achieve the above technical and economic indicators, it is necessary to adopt the open-stope and backfill mining method with large structure parameter. According to research, the method is divided into three parts: drilling in sublevel, ore drawing in level, and filling in level. The space is open during mining. After mining, the ground pressure is controlled and managed by the filling body and surrounding rock. The stope is vertical to the ore body trend, with a width of 40 m, a length of about 40–80 m, and a height of 100 m. The stope is divided into a room and pillar for mining. The widths of the room and pillar both are 20 m. There is no pillar between the stope and the stope. The sublevel height is 25 m, and the whole stope is divided into 4 sublevels to drill the upward fan-shaped medium-deep holes. The mining method is shown in Figure 1.

Because the room and pillar are open during mining, the key to successfully realize the mining method is to ensure that the stope does not collapse and large-scale displacement before filling. The demonstration work is carried out through the creep principle and test.

3. Creep Experiment

There are many methods for rock creep experiment, and the most common ones are uniaxial compression experiment, triaxial compression experiment, and shear creep experiment. In order to determine the creep parameters of iron ore and filling body in the underground stope of an iron mine in a short period of time through the test, so as to study the time effect of rock stability, uniaxial compression creep experiment is chosen for the study.

3.1. Experiment Object and Uniaxial Compression Experiment. The iron ore belongs to quartz specularite. The filling body has three kinds of cement-sand ratio of 1 : 4, 1 : 6, and 1 : 8. Due to the long time of creep experiment, this study chooses the quartz specularite and the filling body with cement-sand ratio of 1 : 6 as the experiment objects.

Firstly, the conventional uniaxial compression experiment is carried out on the specimens, and the experiment results are shown in Table 1. Figure 2 shows the photos of creep experiment specimens.

3.2. Creep Experiment Instrument and Loading Mode. The strengths of the two kinds of specimens in this creep experiment are quite different. The uniaxial compressive strength of iron ore is relatively high, with an average value of 163.59 MPa, while that of the filling body is extremely low, and the average uniaxial compressive strength of the filling body with a cement-sand ratio of 1 : 6 is 3.34 MPa in 28 d. So
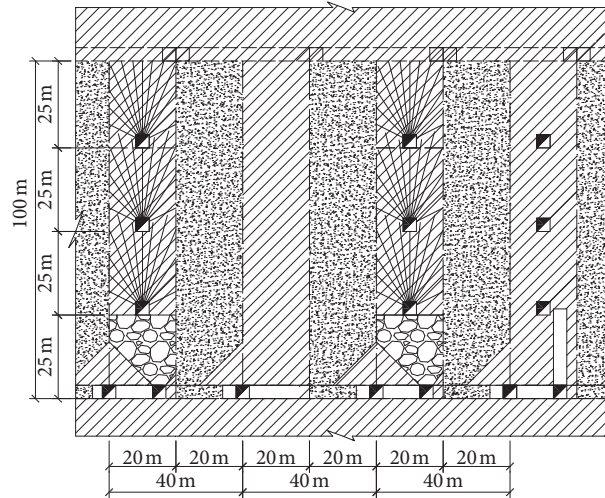
FIGURE 1: The open-stope and backfill mining method.

TABLE 1: Conventional experiment results of the specimens.

Specimens	Instantaneous uniaxial compression strength, R (MPa)	Axial ultimate strain, ε (%)	Remarks
Iron ore	163.59	0.52	Quartz specularite
Filling body	3.34	0.58	Cement-sand ratio of 1 : 6
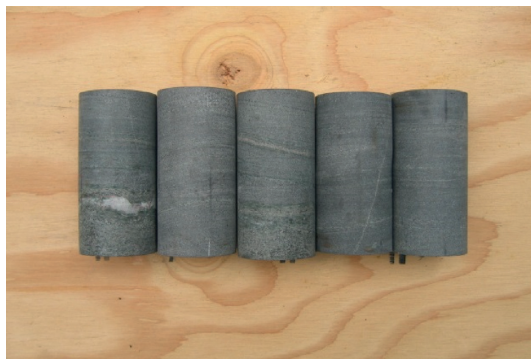
(a)	(b)

FIGURE 2: Specimens of creep experiment. (a) Iron ore specimens. (b) Filling body specimens.

it is difficult to complete the test work on the same instrument for two kinds of specimens with great strength difference. Therefore, high requirements are put forward for the experiment instrument, and it is necessary to use different tonnage testing machine for testing.

For the iron ore with high uniaxial compressive strength, an Instron 1346 servo rigid material testing machine is used for testing. For the filling samples with very low uniaxial compressive strength, the Instron 1342 servo rigid material testing machine is used for testing, with the maximum axial pressure of 250 kN and the sensor of 10 kN, and its accuracy can meet the observation value of 0.001 mm. The load control mode is adopted in the test, the test data are recorded automatically, and the test curve is drawn synchronously.

The loading mode is the constant loading mode. A group of specimens with the same rock are used to bear different constant loads. Because of the different properties of the rock specimens, the test results are discrete. However, the test results are reliable and not affected by the loading state. Therefore, the uniaxial creep experiment adopts constant load mode.

4. Creep Experiment and the Model of Ore and Rock

The uniaxial creep experiment of iron ore is carried out by using the Instron 1346 servo rigid material testing machine. Before loading, the specimens are placed indoor for 20 ∼ 30 days in the natural environment. The temperature of the experiment environment shall be controlled at 20°C ± 2°C. The constant load mode is adopted. Due to the high strength of iron ore, the loading rate is 90 kN/min, which is about
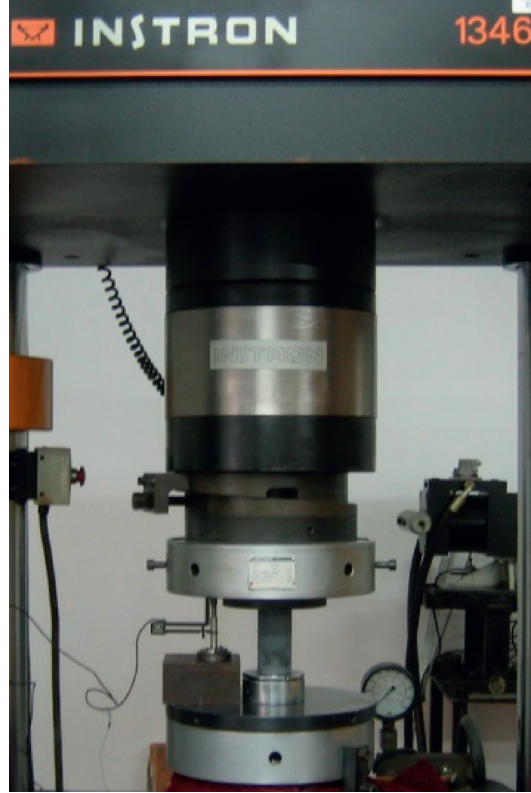
Figure 3: Creep experiment of the iron ore.

0.75 MPa/s. The axial displacement is recorded by using a displacement extensometer with a gauge distance of 5 mm. The control mode is load control. The creep experiment of iron ore is shown in Figure 3.

After loading the predetermined constant load, the strain is read immediately as the initial strain value of the load. The strain values are recorded at the intervals of 5, 10, 15, and 30 min in the first 1 h and then are recorded at intervals of half an hour.

Under the action of constant load (81.80 MPa) with a stress level of 50% R, specimen $Y2$-6 does not damage in 192 hours. Specimen $Y2$-7 also is not damaged in 192 hours under the action of constant load (98.15 MPa) with the stress level of 50% R. Under the action of constant load (114.51 MPa) of a stress level of 70% R, specimen $Y2$-8 is not damaged in 192 hours but presents a sign of possible damage. Under the action of constant load (130.87 MPa) with a stress level of 80% R, specimen $Y2$-9 gets damaged in 175 hours. The creep of each test specimen is shown in Table 2. The test curve of the relationship between axial strain and time of each test specimen is shown in Figure 4.

The iron ore belongs to hard rock, its creep is relatively small at low stress level, and its deformation tends to be stable after a short period of initial creep. But at high stress level, the creep is relatively obvious, which is also proved by this experiment. In the experiment, due to a good control on the load, the accelerated creep process is observed in two specimens besides the attenuation creep process and steady creep process.

The five element model used in rock mechanics is called the B-K model, also known as the Bingham–Vogt model,

which is composed of a Bingham body and a Kelvin (Vogt) body in series.

When $\sigma < \sigma_s$, the friction plate is a rigid body. This model has the same characteristics as the generalized Kelvin model. The constitutive equation and creep equation of the model are as follows:

$$\frac{\eta_k}{E_B + E_K}\dot{\sigma} + \sigma = \frac{E_B\eta_k}{E_B + E_K}\dot{\varepsilon} + \frac{E_B\eta_k}{E_B + E_K}\varepsilon, \tag{1}$$

$$\varepsilon = \left(\frac{1}{E_B} + \frac{1}{E_K}\right)\sigma_c - \frac{1}{E_K}\sigma_c e^{-\left(E_K/\eta_K\right)t}. \tag{2}$$

When $\sigma < \sigma_s$, the creep of the B-K model is in a stable creep. According to formula (2), when $t = 0$, only the Bingham body works, and when $t \longrightarrow \infty$, the damper cylinder does not work, which is equivalent to connecting the spring of the Bingham body and Kelvin (Vogt) body in series.

When $\sigma \geq \sigma_s$, the performance of the B-K model is similar to that of the Burgers model, but the difference is that the stress overcoming the friction resistance σ_s in the model should be removed in the B-K model. Therefore, by directly substituting $(\sigma - \sigma_s)$ for σ in the constitutive equation of the Burgers model, the constitutive equation of the B-K model is obtained as follows:

$$\ddot{\sigma} + \left(\frac{E_B}{\eta_K} + \frac{E_B}{\eta_B} + \frac{E_K}{\eta_K}\right)\dot{\sigma} + \frac{E_K E_B}{\eta_K \eta_B}(\sigma - \sigma_s) = E_B\ddot{\varepsilon} + \frac{E_K E_B}{\eta_K}\dot{\varepsilon}. \tag{3}$$

Specimens	Stress level (% R)	Creep stress (MPa)	Predetermined load (kN)	Initial strain (%)	Final strain (%)	Creep strain (%)	Creep time (h)
Y2-6	50	81.80	153.88	0.23	0.247	0.017	192
Y2-7	60	98.15	184.93	0.27	0.291	0.021	192
Y2-8	70	114.51	216.82	0.32	0.348	0.028	192
Y2-9	80	130.87	247.59	0.36	0.483	0.123	175

— Y2-6 (stress level 50% R)
— Y2-7 (stress level 60% R)
— Y2-8 (stress level 70% R)
— Y2-9 (stress level 80% R)
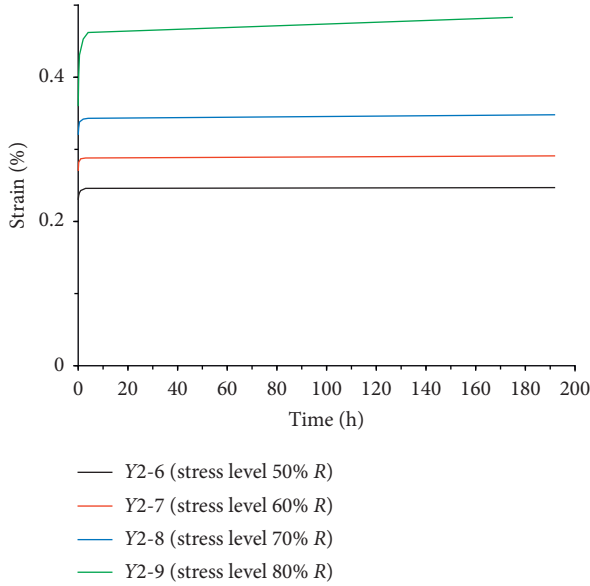
FIGURE 4: Creep curve of the iron ore specimens.

The creep and unloading equations of the B-K model can be obtained from the creep and unloading equations of the Kelvin body and Bingham body:

$$\varepsilon = \frac{\sigma_c - \sigma_s}{\eta_B} t + \frac{\sigma_c}{E_B} + \frac{\sigma_c}{E_K}\left(1 - e^{-\left(E_K/\eta_K\right)t}\right), \tag{4}$$

$$\varepsilon = \frac{t_u}{\eta_B}\left(\sigma_c - \sigma_s\right) + \frac{\sigma_c}{E}\left(1 - e^{-\left(E_K/\eta_K\right)t_u}\right)e^{-\left(E_K/\eta_K\right)\left(t_u - t\right)}. \tag{5}$$

The relaxation equation of the B-K model is too complex to be listed here. From equation (4), when $t = 0$, only the spring works, and $\varepsilon_0 = \sigma_c/E_B$. When $t \longrightarrow \infty$, $\varepsilon_\infty \longrightarrow \infty$, but the change rate tends to be constant, and the creep belongs to metastable creep. Similarly, the unloading equation of the B-K model can be obtained by the unloading equation superposition of the Maxwell body and Kelvin body. When $t \longrightarrow \infty$, $\varepsilon \longrightarrow (t_u/\eta_M)\sigma_c$, and some permanent deformation remains after unloading.

5. Creep Experiment and the Model of Filling Body

The uniaxial creep experiment of filling body is carried out by using the Instron 1342 servo rigid material testing machine. Before loading, the specimens are placed in the indoor for 20 ~ 30 days in the natural environment. The temperature of the experiment environment shall be controlled at $20°C \pm 2°C$. The constant load mode is adopted, and the loading rate is 2 kN/min, which is about 0.015 MPa/s. The axial displacement is recorded by using an LVDT displacement sensor. The control mode is load control. The creep experiment of filling body is shown in Figure 5.

After loading the predetermined constant load, the axial displacement is read immediately as the initial displacement value of the load. In the first 1 h, the axial displacement values are recorded at the intervals of 5, 10, 15, and 30 min and then are recorded every half an hour.

Under the action of constant load (1.00 MPa) with a stress level of 30% R, specimen Yc6-7 is not damaged in 200 hours. Specimen Yc6-8 also is not damaged in 200 hours under the action of constant load (1.34 MPa) with a stress level of 40% R. Under the action of constant load (1.67 MPa) with the stress level of 50% R, specimen Yc6-9 is not damaged in 200 hours but presents a sign of possible damage. Under the action of constant load (2.00 MPa) with a stress level of 60% R, specimen Yc6-10 gets damaged in 196 hours. The creep of each test specimen is shown in Table 3. The test curve of the relationship between axial strain and time of each specimen is shown in Figure 6.

The strength of filling body is low, and its creep deformation is large. When the stress level is more than 50% R, the creep is obvious, which experiences three stages: attenuation creep, steady creep, and accelerated creep. There are obvious signs before the material fracture. In the creep curve, there is an upwarping section in rapid increase of change rate.

The Burgers model can well describe the creep curve with initial creep and steady creep, and the model is simple and practical, which has been widely used. Therefore, the Burgers model is selected to describe the compression creep characteristics of the filling body.

The Burgers model is also called the M-K model, which is composed of a Maxwell body (M body) and a Kelvin body (K body) in series.

The constitutive equation and creep equation of the Burgers model are as follows:

$$\ddot{\sigma} + \left(\frac{E_B}{\eta_K} + \frac{E_B}{\eta_B} + \frac{E_K}{\eta_K}\right)\dot{\sigma} + \frac{E_K E_B}{\eta_K \eta_B}\sigma = E_B\ddot{\varepsilon} + \frac{E_K E_B}{\eta_K}\dot{\varepsilon}, \tag{6}$$

$$\varepsilon = \frac{\sigma_c}{E_B} + \frac{\sigma_c}{\eta_B}t + \frac{\sigma_c}{E_K}\left(1 - e^{-\left(E_K/E_K\right)t}\right). \tag{7}$$

According to equation (7), the creep equation of the Burgers model can be obtained by the creep equation superposition of the Maxwell body and Kelvin body. When

FIGURE 5: Creep experiment of the filling body.

TABLE 3: Uniaxial creep statistics of the filling body specimens.

Specimens	Stress level (% R)	Creep stress (MPa)	Predetermined load (kN)	Initial strain (%)	Final strain (%)	Creep strain (%)	Creep time (h)
Yc6-7	30	1.00	2.285	0.16	0.191	0.031	200
Yc6-8	40	1.34	0.071	0.21	0.252	0.042	200
Yc6-9	50	1.67	3.799	0.27	0.321	0.051	200
Yc6-10	60	2.00	4.530	0.35	0.545	0.195	196
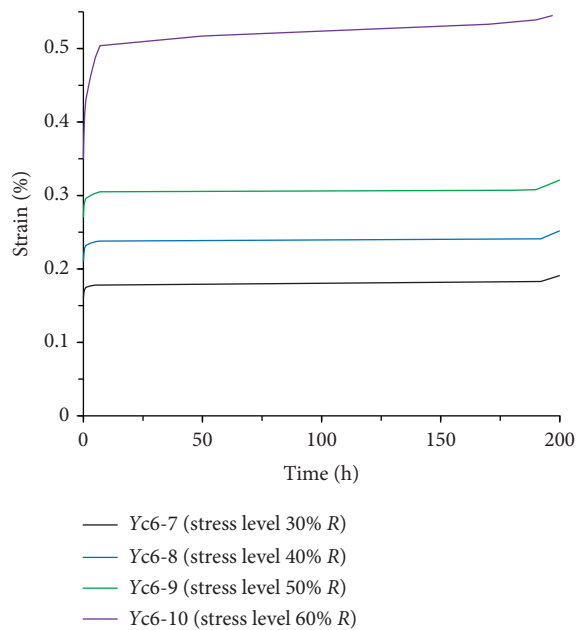
FIGURE 6: Creep curve of the filling body specimens.

$t = 0$, only the spring works, and $\varepsilon_0 = \sigma_c/E_B$. When $t \longrightarrow \infty$, ε_∞ approaches infinity, but its change rate tends to be constant and the creep belongs to metastable creep.

6. Creep Model Parameters and Exposure Time Calculation

The creep constitutive equations of iron ore and backfill in the following sections under uniaxial compression belong to a nonlinear function. In order to determine the parameters of the constitutive equations, the Marquardt method in the least squares method is used to fit the parameters of the creep model.

6.1. Fitting Value of Creep Parameters of Iron Ore. The creep constitutive model of iron ore uses the K-B model for fitting. In the K-B model, there are 5 rheological parameters need to be calculated, in which EB is the elastic modulus. When σ acts on the specimen, the elastic deformation caused by EB is completed in an instant. Therefore, when $t = 0$, the corresponding ratio of σ to ε is equal to the EB value. The initial

TABLE 4: Calculation values of creep parameters of the iron ore.

Specimens	Creep stress σ (MPa)	Σs (MPa)	E_B (GPa)	E_K (GPa)	η_K (GPa.d)	η_B (GPa.d)
Y2-6	81.80	—	35.57	23.32	1898.80	—
Y2-7	98.15	—	36.35	34.52	3839.21	—
Y2-8	114.51	—	35.78	39.74	6766.93	—
Y2-9	130.87	118.19	35.36	50.34	12765.45	6154.82

flow stress can be read directly from the creep curve. The parameters to be determined by the least squares method are EK, ηB, and ηK. The rheological parameters are related to the stress level. It is necessary to fit the creep parameters under different stress levels. During fitting the creep curves of specimens Y2-6 ~ Y2-10, the correlation coefficients are 0.92, 0.90, 0.93, 0.91, and 0.92 respectively. Table 4 shows the calculation results of creep parameters of iron ore.

6.2. Fitting Value of Creep Parameters of the Filling Body.
The creep constitutive model of filling body adopts the Burgers model for fitting. In the Burgers model, there are four rheological parameters need to be calculated, in which EB is the elastic modulus. When σ acts on the specimen, the elastic deformation caused by EB is completed in an instant. Therefore, when $t = 0$, the corresponding ratio of σ to ε is equal to the EB value. Comparing the Burgers model with the K-B model, it is found that the elastic modulus EB of the two models is exactly the same. The other three rheological parameters (EK, ηB, and ηK) are needed to be determined by the least squares method. The rheological parameters are related to the stress level. Similarly, it is necessary to fit the creep parameters of filling body under different stress levels. The correlation coefficients of the creep curves of specimens Yc6-7 ~ Yc6-11 are 0.95, 0.93, 0.93, 0.92, and 0.94, respectively. Table 5 shows the calculation results of creep parameters of the filling body.

6.3. Recommended Creep Parameters.
Because the time of indoor creep experiment is limited, the creep parameters of rock and filling body obtained by tests must have differences with the real creep parameters of rock and backfill on-site. Therefore, the fitting value of creep parameters of iron ore and filling body should be modified. The general method is to make corresponding reduction through reference to similar projects and combining with the engineering geological conditions or viscoelastic displacement inversion results.

Considering the difference between the on-site rock mass and the indoor rock specimens, referring to the research results of similar projects at home and abroad, and combined with the engineering geological conditions of the iron ore and the filling body in the mine, the fitting values of creep parameters in Tables 4 and 5 are reduced. As the joint fissures in iron ore are relatively developed, the reduction coefficient for the iron ore is selected as 0.7. For the filling body, the development degree of the joint fissures is relatively low, and the reduction coefficient is selected as 0.8. The creep parameters of on-site iron ore body and filling body after modification are shown in Tables 6 and 7, respectively.

6.4. Reasonable Exposure Time of Large-Scale Stope Structure.
On the basis of the indoor uniaxial compression creep experiment, the creep models of iron ore (quartz specularite) and filling body with a cement-sand ratio of 1:6 are established by analyzing the characteristics of the creep curve. Then, the model parameters are fitted by the least squares method, and the corresponding creep parameters are obtained. Then, the fitting value of creep parameters is modified for the engineering application. So the creep equation can be used to calculate the stability time of iron ore and filling body. This stability time is considered as reasonable exposure time.

The reasonable exposure time for the iron ore and the filling body with the cement-sand ratio of 1:6 is from the start of stope blasting to the end of roof-contacted filling. The initial setting time of the filling slurry is about 6–10 hours, and the final setting time is about 2 days. During this time, the filling body gradually develops strength and supports the roof of the stope. Because the solidification time of filling slurry is relatively short, it can be neglected in this study.

The results of the uniaxial compression creep tests are obtained as follows: the ratio of axial ultimate strain to conventional ultimate strain is 93% ~ 95% in the case of creep failure of iron ore and is 94% ~ 96% in the case of creep failure of the filling body.

The creep deformation of iron ore and filling body is related to the stress level. The finite element numerical simulation shows that the stress level of iron ore is generally lower than 100.0 MPa, namely, lower than 60% of the uniaxial compressive strength of iron ore. And the stress level of filling body is generally lower than 2.0 MPa, namely, lower than 60% of the uniaxial compressive strength of filling body.

The axial ultimate strain is 0.49 in the creep failure of iron ore, and the ratio of the axial ultimate strain to the conventional ultimate strain is about 94%. The axial ultimate strain is 0.55 in the creep failure of filling body, and the ratio of the axial ultimate strain to the conventional ultimate strain is 95%. The stress level is 50% R ~ 60% R. According to formulas (2) and (7), the stability time of iron ore and filling body is calculated, respectively.

6.4.1. Stability Time of Iron Ore.
The equation is established according to the parameters in Table 6 and the relevant initial values. When the stress level is 50% R, the equation is as follows:

$$0.49 = \left(\frac{1}{24.90} + \frac{1}{16.32}\right) \times 81.8 - \frac{81.8}{16.32} e^{-(16.32/1329.16)t}. \quad (8)$$

When the stress level is 60% R, the equation is as follows:

TABLE 5: Calculation results of creep parameters of the filling body.

Specimens	Creep stress σ (MPa)	E_B (GPa)	E_K (GPa)	η_K (GPa.d)	η_B (GPa.d)
Yc6-7	1.00	0.63	1.57	0.068	29.57
Yc6-8	1.34	0.64	3.06	0.14	56.83
Yc6-9	1.67	0.62	7.79	0.39	72.42
Yc6-10	2.00	0.57	11.23	0.60	89.50

TABLE 6: Recommended creep parameters of iron ore.

Specimens	Stress level (% R)	Σs (MPa)	E_B (GPa)	E_K (GPa)	η_K (GPa.d)	η_B (GPa.d)
Y2-6	50	—	24.90	16.32	1329.16	—
Y2-7	60	—	25.45	24.16	2687.45	—
Y2-8	70	—	25.05	27.82	4736.85	—
Y2-9	80	82.73	24.75	35.24	8935.82	4308.37

TABLE 7: Recommended creep parameters of the filling body.

Specimens	Stress level (% R)	E_B (GPa)	E_K (GPa)	η_K (GPa.d)	η_B (GPa.d)
Yc6-7	30	0.50	1.26	0.054	23.66
Yc6-8	40	0.51	2.45	0.11	45.46
Yc6-9	50	0.50	6.23	0.31	57.94
Yc6-10	60	0.46	8.98	0.48	71.60

$$0.49 = \left(\frac{1}{25.45} + \frac{1}{24.16} \right) \times 98.15 - \frac{98.15}{24.16} e^{-(24.16/2687.45)t}. \tag{9}$$

The stability time of iron ore is calculated as 658.6 days through solving equation (8) and as 527.8 days through solving equation (9). So it is suggested that the reasonable exposure time of iron ore in the stope is 520 ∼ 650 days.

The strength of quartz specularite in this mine is lower than that of magnetite in other mines. If the exposure time is determined based on the quartz specularite in the mining area, the magnetite in other mines will be more stable in the same exposure time.

6.4.2. Stability Time of the Filling Body. The equation is established according to the parameters in Table 7 and the relevant initial values. When the stress level is 50% R, the equation is as follows:

$$0.55 = \frac{1.67}{0.5} + \frac{1.67}{57.94} t + \frac{1.67}{6.23} \left(1 - e^{-(6.23/0.31)t} \right). \tag{10}$$

When the stress level is 60% R, the equation is as follows:

$$0.55 = \frac{2.00}{0.46} + \frac{2.00}{71.60} t + \frac{2.00}{8.98} \left(1 - e^{-(8.98/0.48)t} \right). \tag{11}$$

The stability time of filling body with the cement-sand ratio of 1 : 6 is calculated as 523.2 days through solving equation (10) and as 417.5 days through solving equation (11). So it is suggested that the reasonable exposure time of filling body in the stope is 410 ∼ 520 days.

There are three different cement-sand ratios for the filling slurry, including 1 : 4, 1 : 6, and 1 : 8. Among them, the filling body with the cement-sand ratio of 1 : 6 is widely used, with a reasonable strength, and its research results provide a good reference for the filling body with other two kinds of cement-sand ratio.

7. Conclusion

(1) Uniaxial compression creep tests are carried out on iron ore and filling body, respectively. The creep time of iron ore is 795 hours and that of filling body is 889 hours. The total time of two kinds of samples is 1684 hours.

(2) Through the analysis on the characteristics of creep curves, the creep models of rocks (quartz specularite) and filling body with a cement-sand ratio of 1 : 6 in the large-scale stope are established, respectively. The parameters of the models are fitted by the least squares method to obtain the corresponding creep parameters. Then, the fitting value of creep parameters is modified for the engineering application. According to the stress environment of iron ore and filling body, the creep equations are used to calculate the stability time of iron ore and filling body. The reasonable exposure time of large-scale stope is determined from the aspect of safety.

(3) The stability time of quartz specularite at the stress level of 50% R ∼ 60% R (R is the uniaxial compressive strength) is 527.8 ∼ 658.6 days, so it is

suggested that the reasonable exposure time of the large-scale stope is 520 ∼ 650 days. The stability time of the filling body with the cement-sand ratio of 1 : 6 at the stress level of 50% R ∼ 60% R is 417.5 ∼ 523.2 days, so it is suggested that the reasonable exposure time of the filling body is 410 ∼ 520 days.

Data Availability

The data used to support the findings of this study are available from the corresponding author upon request.

Conflicts of Interest

The authors declare that there are no conflicts of interest regarding the publication of this paper.

References

[1] N. Brantut, M. J. Heap, P. G. Meredith, and P. Baud, "Time-dependent cracking and brittle creep in crustal rocks: a review," *Journal of Structural Geology*, vol. 52, pp. 17–43, 2013.

[2] X. Feng, B. Chen, S. Li et al., "Studies on the evolution process of rockbursts in deep tunnels," *Journal of Rock Mechanics and Geotechnical Engineering*, vol. 4, no. 4, pp. 289–295, 2012.

[3] X.-T. Feng, S.-F. Pei, Q. Jiang, Y.-Y. Zhou, S.-J. Li, and Z.-B. Yao, "Deep fracturing of the hard rock surrounding a large underground cavern subjected to high geostress: in situ observation and mechanism analysis," *Rock Mechanics and Rock Engineering*, vol. 50, no. 8, pp. 2155–2175, 2017.

[4] A. Nicolas, J. Fortin, J. B. Regnet et al., "Brittle and semibrittle creep of tavel limestone deformed at room temperature," *Journal of Geophysical Research: Solid Earth*, vol. 122, no. 6, pp. 4436–4459, 2017.

[5] J. Renner, B. Evans, and G. Siddiqi, "Dislocation creep of calcite," *Journal of Geophysical Research: Solid Earth*, vol. 107, no. B12, pp. 6–16, 2002.

[6] N. Brantut, P. Baud, M. J. Heap, and P. G. Meredith, "Micromechanics of brittle creep in rocks," *Journal of Geophysical Research: Solid Earth*, vol. 117, no. B8, 2012.

[7] C. H. Scholz, "Mechanism of creep in brittle rock," *Journal of Geophysical Research*, vol. 73, no. 10, pp. 3295–3302, 1968.

[8] D. M. Cruden, "A theory of brittle creep in rock under uniaxial compression," *Journal of Geophysical Research*, vol. 75, no. 17, pp. 3431–3442, 1970.

[9] R. J. Martin, "Time-dependent crack growth in quartz and its application to the creep of rocks," *Journal of Geophysical Research*, vol. 77, no. 8, pp. 1406–1419, 1972.

[10] B. K. Atkinson, "Subcritical crack propagation in rocks: theory, experimental results and applications," *Journal of Structural Geology*, vol. 4, no. 1, pp. 41–56, 1982.

[11] N. L. Carter and F. D. Hansen, "Creep of rocksalt," *Tectonophysics*, vol. 92, no. 4, pp. 275–333, 1983.

[12] J. Zhao, X. T. Feng, X. Zhang, and C. Yang, "Brittle and ductile creep behavior of Jinping marble under true triaxial stress," *Engineering Geology*, vol. 258, 2019.

[13] C. Yu, S. Tang, C. A. Tang et al., "The effect of water on the creep behavior of red sandstone," *Engineering Geology*, vol. 253, pp. 64–74, 2019.

[14] N. Cristescu and U. Hunsche, *Time effects in rock mechanics*, Vol. 350, Wiley, New York, NY, USA, 1997.

[15] Ö. Aydan, T. Ito, U. Özbay et al., "ISRM suggested methods for determining the creep characteristics of rock," *Rock Mechanics and Rock Engineering*, vol. 47, no. 1, pp. 275–290, 2014.

[16] C. F. Yang and Y. J. Zeng, "Investigation on creep damage constitutive theory of salt rock," *Chinese Journal of Rock Mechanics and Engineering*, vol. 21, no. 11, pp. 1602–1604, 2002.

[17] L. S. Tsai, Y. M. Hsieh, M. C. Weng, T. H. Huang, and F. S. Jeng, "Time-dependent deformation behaviors of weak sandstones," *International Journal of Rock Mechanics and Mining Sciences*, vol. 45, no. 2, pp. 144–154, 2008.

[18] Z. Tomanovic, "Rheological model of soft rock creep based on the tests on marl," *Mechanics of Time-dependent Materials*, vol. 10, no. 2, pp. 135–154, 2006.

[19] K. Zhao, X. Yu, and S. T. Zhu, "Acoustic emission investigation of cemented paste backfill prepared with tantalum–niobium tailings," *Construction and Building Materials*, vol. 237, Article ID 117523, 2020.

[20] K. Zhao, Q. Wang, S. Gu et al., "Mining scheme optimization and stope structural mechanic characteristics for a deep and large ore body," *Journal of Minerals*, vol. 71, no. 11, pp. 4180–4190, 2019.

[21] K. Zhao, H. B. Yan, and X. Feng, "Stability analysis of pillar based on energy law," *Chinese Journal of Theoretical and Applied Mechanics*, vol. 48, no. 4, pp. 976–983, 2016.

[22] K. Zhao, Q. Wang, Y. Yan et al., "Geological structural surface evaluation model based on unascertained measure," *Geofluids*, vol. 2019, pp. 1–7, 2019.

Research Article

Investigation of Energy and Damage Evolutions in Rock Specimens with Large-Scale Inclined Prefabricated Cracks by Uniaxial Compression Test and AE Monitoring

Xiaolou Chi [iD],[1,2,3,4] **Ke Yang** [iD],[1,2,3,4,5] **and Zhen Wei** [iD][1,2,3,4]

[1]*State Key Laboratory of Mining Response and Disaster Prevention and Control in Deep Coal Mines,*
 Anhui University of Science and Technology, Huainan 232001, Anhui, China
[2]*Key Laboratory of Mining Coal Safety and Efficiently Constructed by Anhui Province and Ministry of Education,*
 Anhui University of Science and Technology, Huainan 232001, Anhui, China
[3]*National & Local Joint Engineering Research Center of Precision Coal Mining, Anhui University of Science and Technology,*
 Huainan 232001, Anhui, China
[4]*School of Energy and Safety, Anhui University of Science and Technology, Huainan 232001, Anhui, China*
[5]*Institute of Energy, Hefei Comprehensive National Science Center, Hefei 230031, Anhui, China*

Correspondence should be addressed to Xiaolou Chi; chixiaolou@163.com

To explore the energy dissipation mechanism and damage evolution characteristics of rock specimens under compressive loading, we performed the acoustic emission (AE) testing under uniaxial compression in intact rock specimens and those with large-scale prefabricated cracks. The basic mechanical properties of both types of specimens were analyzed comprehensively, and the evolution patterns of strain energy indicators (total strain, elastic, and dissipative energies) in rock specimens before the peak on the stress-strain curve were identified. We further revealed the effect of the prefabricated crack dip angle, which controlled the surplus energy conversion of the following peak deformation and failure in the rock specimens. Using the modified equation of rock specimen damage evolution characterized by the AE energy and examining the fracture surface morphology via the scanning electron microscopy (SEM), the AE distribution law for rock specimen damage was revealed. An increase in the prefabricated crack dip angle was shown to reduce the peak stress and strain of rock specimens, which experienced a transition from the tensile and splitting failure mode to shear and slip one. Cracked rock specimens exhibited strain energy accumulation at the elastic deformation stage of the stress-strain diagram and rapid energy consumption at the plastic stage. By contrast, the intact rock specimens had a smoother energy evolution pattern. As the prefabricated crack dip angle increased, the dissipated and surplus strain energies' shares increased. Moreover, the first peak of the AE energy occurred earlier, and the stress needed for its occurrence decreased as the dip angle increased. According to the damage evolution equation for rock specimens, their damage process can be subdivided into the initial damage, stable damage increase, and the accelerating damage increase stages. An increase in the prefabricated crack dip angle accelerated the damage accumulation in rock specimens. The locking effect of the sawtooth-like structures on the fracture surface was less conspicuous, and the fracture surface roughness increased. Thus, microcracks gradually developed, and rock specimens became more susceptible to sudden unstable failure.

1. Introduction

Coal mining involves roadway tunneling and stoping of working face, which usually leads to the exposure of such macroscopic geological structures as faults and joints. These structures are sources of crack initiation and propagation, in which processes jeopardize the mining production safety and require in-depth analysis. In particular, multiple studies of these phenomena have been reported in China, where coal is considered the primary source of energy in the foreseeable

future [1, 2]. Thus, Yang et al. [3, 4] studied the crack propagation and penetration mechanisms in rock specimens with prefabricated single and double cracks while Li et al. [5] characterized the mechanical properties of precracked rock specimens under uniaxial compression. Although both studies yielded essential findings on the respective governing laws, they covered mainly small-scale lengths and dip angles of prefabricated cracks in rock specimens. In contrast, in engineering practice, the scale and occurrence of macroscopic geological structures in the rock mass have a considerable impact on the degree of fragmentation and the possibility of dynamic disasters. Taking rock joints as a research object, Xue et al. [6] investigated the mechanism by which the fault scale influenced the dislocation movement of faults after activation. Yu et al. [7] analyzed two possible pathways whereby the dip angle of faults influenced the fault activation, which was found to be accompanied by energy accumulation and dissipation. The energy parameters as core indicators of dynamic disasters, including rockburst, were adopted in several studies [8–11]. Given the above, the identification of the energy evolution laws governing the damage and failure processes in rock specimens with large-scale prefabricated cracks with various dip angles is very topical.

Zhao et al. [12] experimentally studied the energy dissipation mechanism of rock specimens subjected to uniaxial compression. Zhang et al. [13] analyzed energy variation in rock specimens under the triaxial compression test conditions. Yang et al. [14] revealed the energy evolution mechanism and failure law during the loading and unloading of specimens produced by combining coal and rock mass. Wang et al. [15] reported the rock specimens' energy conversion features with nonpenetrating joints. The above studies provide a systematic analysis of the total strain, elastic, and dissipative energy components figuring in the stress-strain relationship of intact rock specimens, coal-rock mass combinations, and rock specimens with small-scale prefabricated cracks. However, the presence of macroscopic defects with increasing scales and dip angles in rock specimens increases the probability of their dynamic (impact) failure. In such cases, the surplus energy causing dynamic failure becomes a nonnegligible factor.

Besides the energy input and dissipation observed during the loading of rock specimens, their damage occurs continuously. The damage accumulation finally induces the overall failure of the rock specimen. There are many ways to define the damage variable of rock specimens [16]. Some scholars based their definitions on the elastic modulus [17] or plastic strain [18] values. However, at the compaction stage of the stress-strain relationship, the elastic modulus of a rock specimen increases. Therefore, if the damage variable is defined by the elastic modulus, a descending trend will be predicted, that is, the occurrence of "negative damage" [19]. Moreover, at the compaction stage, the strain changes rapidly, and the rock specimen damage is supposed to be small. Thus, neither the elastic modulus nor plastic strain can accurately reflect the rock specimen's damage process. Deformation and failure of the rock specimen under loading are the results of damage driven by energy. It is reasonable to

define the rock specimen's damage variable from the strain energy perspective [20]. Liu et al. [21] described the damage variable by the share of dissipative energy in the total strain energy. However, this definition was susceptible to the influence of the stiffness of the test machine and brittleness of the rock specimen. As a result, the realistic constitutive deformation could hardly be obtained. In recent years, acoustic emission (AE) testing has been increasingly applied to rock mechanics. The AE energy is highly sensitive to rock specimen damage and fracture, and this feature has been utilized to characterize the rock specimen damage [22]. However, rock specimens may retain residual strength either under uniaxial or triaxial compression. Therefore, it is necessary to refine the equation of rock specimen damage evolution characterized by the AE energy to estimate the damage evolution process under loading.

In the present study, intact rock specimens and those with large-scale prefabricated cracks were taken as the research objects. The uniaxial compression tests and AE monitoring were performed to analyze the prepeak total strain, elastic, and dissipative energy components during the stress-strain evolution. Evolutions of postpeak released energy and surplus energy under different prefabricated crack dip angles were also monitored and analyzed. The equation of rock specimen damage evolution characterized by the AE energy parameters was refined. SEM was employed to analyze the damage features of the intact and precracked rock specimens. The research findings provide theoretical guidance for disaster prevention and control of mining production safety.

2. Experimental

2.1. Rock Specimen Preparation. All rock specimens used in the experiments were collected from the fine sand strata in the roof of the 11513 working face of the Panbei Coal Mine located in Huainan city, Anhui Province of China. The large-scale rock specimens collected on-site were processed into standard cylindrical rock specimens with a diameter of 50 mm and a height of 100 mm by using laboratory rock core drill, rock cutter, and grinding machine. The unevenness at both end faces of rock specimens did not exceed 0.05 mm. A total of twelve standard rock specimens were prepared and divided into four groups. Group 1 consisted of three intact rock specimens (R_1, R_2, and R_3) while each of the remaining three groups contained three precracked rock specimens with crack dip angles of 30, 45, and 60°, respectively. The precrack dip angle was the included angle between the crack line and the end surface of the rock specimen. The precracks were made by cutting with a diamond-tipped cutter. The rock specimens in group 2 were numbered as $30°–R_1$, $30°–R_2$, and $30°–R_3$, respectively. The same intuitive numbering principle was used for specimens in groups 3 and 4. The rock specimen preparation results are depicted in Figure 1.

2.2. Experimental Setup. The experimental setup included the loading control system, AE monitoring system, digital monitoring system, and SEM monitoring system, as shown
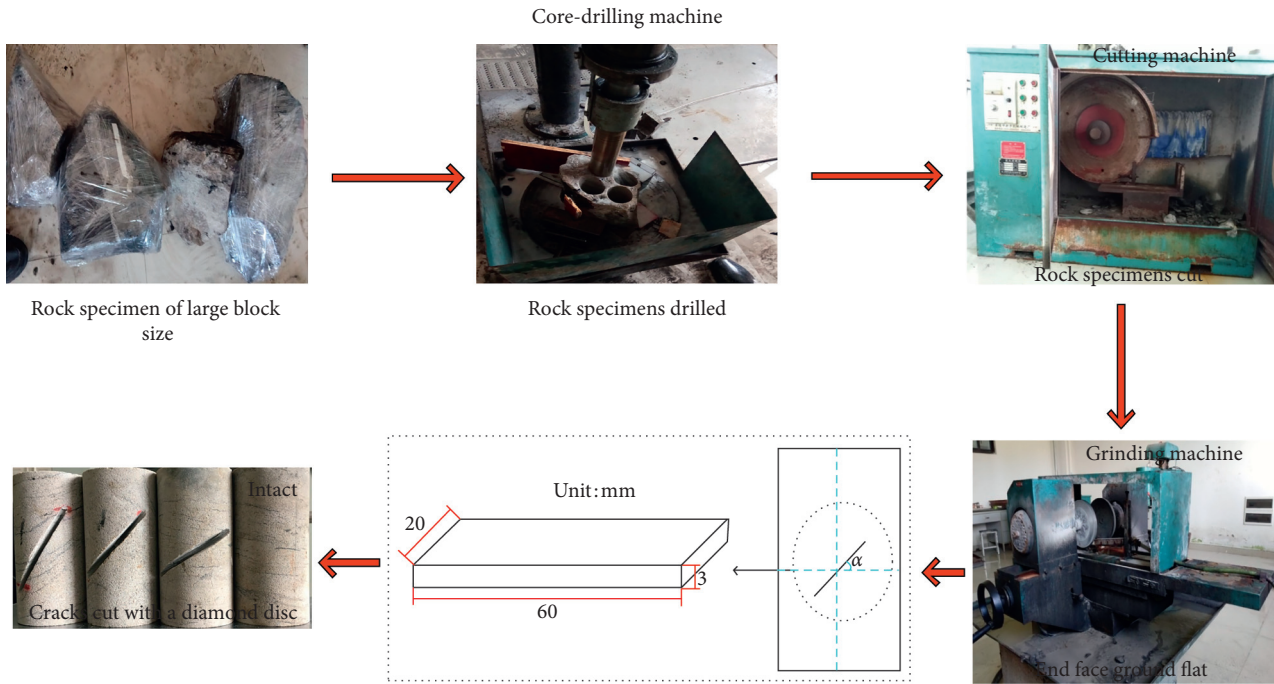
FIGURE 1: Rock specimen's processing and preparation.

in Figure 2. During the testing, the first three systems were launched simultaneously to facilitate subsequent data processing while the SEM monitoring system was used after tests to scan the macroscopic fracture surfaces in the intact and precracked rock specimens and to assess the microscopic damage features.

The loading control system used an RMT-150B multifunction automatic rigid rock material testing servo machine. This system could realize conventional uniaxial and triaxial compression test modes, along with automated data collection, processing, and display of the stress-strain curve. The load was increased at the loading rate of 0.5 kN/s until the final fracture of rock specimens.

A DS5-16B multichannel full-wave AE signal analyzer was equipped for the AE monitoring system. This system could extract such characteristic parameters as AE energy and ringdown count. Four AE transducers were installed, and the coupling agent was applied between the AE transducers and the rock specimens. Before the tests, the system calibration was performed several times to adjust its accuracy. Finally, the AE transducers' resonance frequency of 100–600 kHz, sampling rate of 3 MHz, preamplifier gain of 40 dB, and monitoring threshold value of 35 dB were preset.

A FlexSEM1000 scanning electron microscope, which could achieve a 60–300 K magnification and a 0.3–20 kV accelerating voltage, with a resolution of 4 nm, was applied in SEM examinations. A Nikon camera was provided for the digital monitoring system to capture the fracture morphology during the loading process.

2.3. Strain-Stress Relationship in Rock Specimens.

Using the RMT-150B rock testing machine, stress-strain curves of the intact and precracked rock specimens were

monitored and constructed during the loading process. For brevity sake, only four stress-strain curves of typical intact and precracked rock specimens are shown in Figure 3.

As shown in the figure, stress-strain curves of typical intact and precracked rock specimens exhibited similar variation patterns. All of them underwent the compaction stage, elastic stage, plastic stage, and residual deformation stage. As the prefabricated crack dip angle increased, the peak strength and strain of rock specimens decreased. The stress-strain curves of the intact and precracked rock specimens presented the left-shifting and compression trend. This can be attributed to the fact that the prefabricated cracks were large-scale, which affected the structural integrity of rock specimens and increased the initial damage. As the prefabricated crack dip angle increased, the axial stress component acting on the rock specimens along the dip of the prefabricated cracks increased. Under the action of the intense shear stress at the crack tip, the original cracks propagated while new ones were formed as well, thus leading to the overall failure of rock specimens. As a result, the rock specimens' peak strength and strain decreased, leading to a progressive aggravation of their brittle fracture on the macroscopic scale.

3. Mechanism of Energy Evolution in Rock Specimens

3.1. Theoretical Background.

Taking a typical intact rock specimen as an example, the assessment of prepeak and postpeak strain energies can be based on the calculation principle illustrated by Figure 4(a).
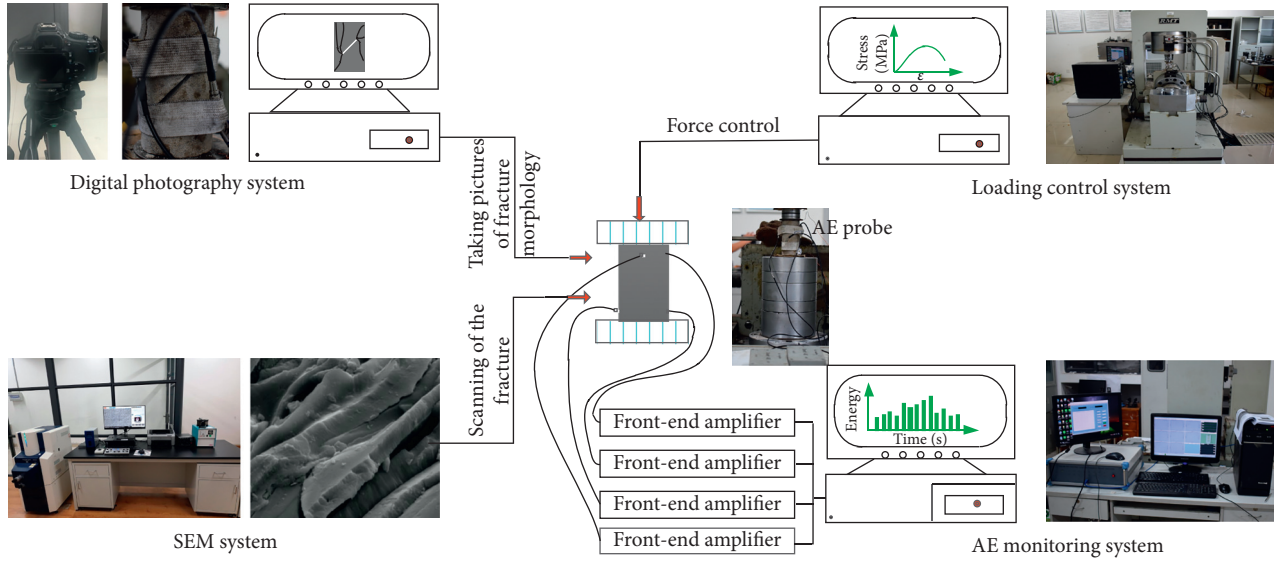
FIGURE 2: Loading and monitoring system.
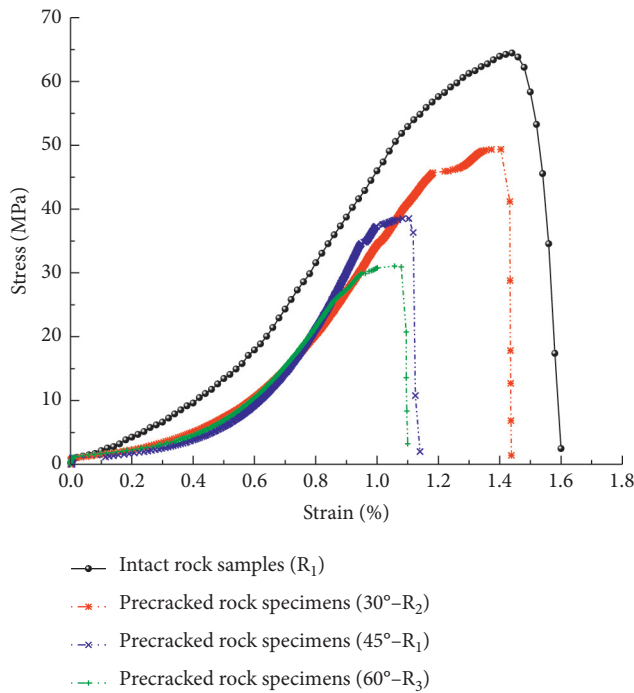
FIGURE 3: Stress-strain curves of typical intact and precracked rock specimens.

It is assumed that the energy conversion between the RMT-150B rock testing machine and rock specimens does not involve heat exchange with the environment. Then, according to the first law of thermodynamics [23],

$$U_o = U_e + U_d, \tag{1}$$

where U_o, U_e, and U_d are the prepeak total strain, elastic, and dissipative energies, respectively, of the rock specimen during the loading process, J/m³.

The averages of σ_i and σ_{i+1} corresponding to the calculus interval $d\varepsilon$ are taken. From the lower and upper bounds of calculus 0 and ε_1 [24], U_o is given by

$$U_o = \int_0^{\varepsilon_1} \frac{\sigma_i + \sigma_{i+1}}{2} \, d\varepsilon, \tag{2}$$

where σ_i is the stress at any point of the stress-strain curve, MPa, and ε_1 is the strain corresponding to the peak strain, %.

According to the curve of one loading-unloading cycle of the uniaxial compression test, the prepeak unloading path is consistent with the loading curve slope. According to Hooke's law [25, 26], U_e is given by

$$U_e = \frac{1}{2}\sigma_c\varepsilon_e \approx \frac{\sigma_i^2}{2E_0}, \tag{3}$$

where σ_c is the peak strength, MPa; ε_e is the prepeak elastic strain, %; and E_0 is the initial elastic modulus, MPa.

The prepeak total energy consists of the elastic U_e and dissipative U_d energies [24]; thus, U_d is given by

$$U_d = U_o - U_e = \int_0^{\varepsilon_1} \frac{\sigma_i + \sigma_{i+1}}{2}d\varepsilon - \frac{1}{2}\sigma_c\varepsilon_e. \tag{4}$$

The postpeak released energy U_f is the envelope area from ε_1 to ε_2 [27], and U_f is given by

$$U_f = \int_{\varepsilon_1}^{\varepsilon_2} \frac{\sigma_i + \sigma_{i+1}}{2}d\varepsilon, \tag{5}$$

where ε_2 is the peak strain, %.

Some part of the prepeak elastic energy U_e is converted into the postpeak released energy U_f, while the remaining part is converted into surplus energy U_y. The latter is derived as follows:

$$U_y = U_e - U_f = \frac{1}{2}\sigma_c\varepsilon_e - \int_{\varepsilon_1}^{\varepsilon_2} \frac{\sigma_i + \sigma_{i+1}}{2}d\varepsilon. \tag{6}$$
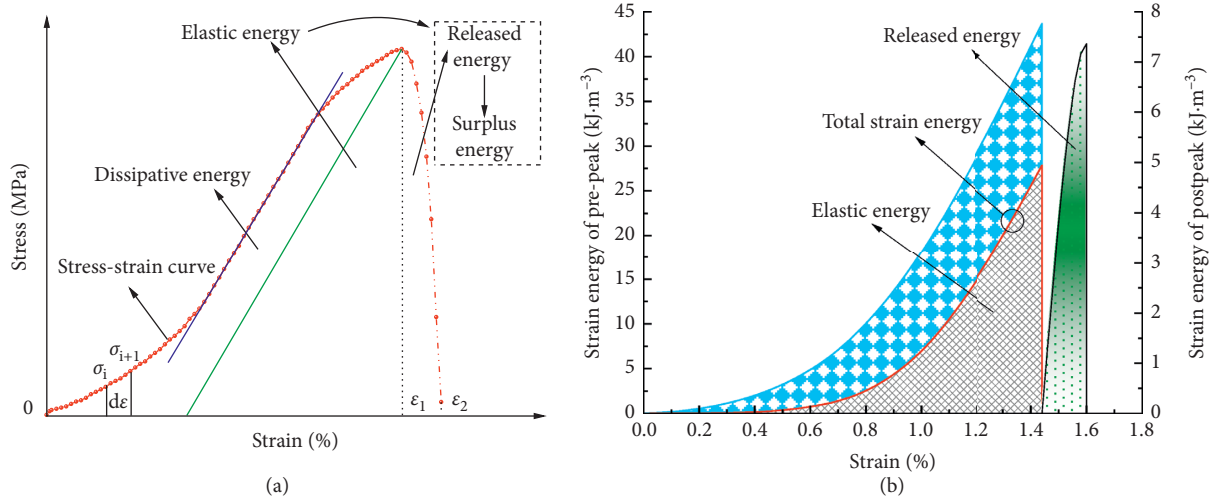
FIGURE 4: The energy conversion process of typical intact rock specimens: (a) strain energy calculation principle and (b) strain energy area.

The surplus energy can be converted into kinetic energy for rock ejection, inducing dynamic disasters. Based on the above calculation idea, the prepeak (total strain, elastic, and dissipative) energies, as well as postpeak (released and surplus) energies in typical intact rock specimens, were derived, as shown in Figure 4(b).

3.2. Energy Conversion Characteristics of the Prepeak Strain Energy.
Figure 5 depicts the relationship between the stress, prepeak strain energy, and strain in the typical intact and precracked rock specimens. It can be observed that the deformation and failure of rock specimens under loading reflect the energy evolution from the input energy from the test machine to the elastic energy accumulation in rock specimens and finally to the dissipative energy release. Energy-driven rock specimens underwent damage until macroscopic instability and failure. The total strain energy of intact and precracked rock specimens increased continuously. The elastic energy curve showed a similar trend to the stress-strain one. The dissipative energy in intact rock specimens increased gradually while that in precracked rock specimens first increased gradually and then dropped significantly, followed by a rapid rise.

At each prepeak stage of the stress-strain curve, intact and precracked rock specimens also had similar variations in the prepeak strain energy components.

(A) Compaction stage: The dissipative energy in intact and precracked rock specimens increased nonlinearly as the rock specimen deformation was aggravated. Its value was higher than the elastic energy of rock specimens because the original cracks in rock specimens developed, consuming the absorbed energy.

(B) Elastic stage: As the original cracks closed, the elastic energy of the intact and precracked rock specimens gradually increased. After the elastic energy curve intersected with the dissipative energy curve (i.e.,

their values become equal), the elastic energy of precracked rock specimens increased at an accelerating rate. In contrast, the dissipative energy curve showed an inflection point for the downward trend. In intact rock specimens, both the elastic and dissipative energies increased stably. The reason was that the prefabricated cracks changed the initially uniform bulk stress state of rock specimens. The tips of the prefabricated cracks were more likely to store elastic energy, leading to the stress concentration phenomenon. Besides, at this stage, the total strain energy increased at a constant rate, and the dissipative energy decreased.

(C) Plastic stage: When the elastic energy accumulating at the prefabricated crack tips was larger than the surface free energy needed for crack development, the original cracks propagated. In the meantime, new cracks were formed, and an inflection point for an upward trend appeared on the dissipative energy curve. As the original and new cracks continued to propagate at the prefabricated crack tips, the elastic energy stored in rock specimens was consumed, leading to a sudden dissipative energy jump.

3.3. The Precrack Dip Angle Effect on the Peak Strain Energy.
Figure 6(a) shows the relationship between the peak strain energy and precrack dip angle in typical intact and precracked rock specimens. The spheres indicate the peak values of prepeak total strain energy along the y-axis. The spheres' size indicates the peak value of the prepeak elastic energy while their color indicates the peak value of the prepeak dissipative energy. It can be seen that as the precrack dip angle increased, all peak values of strain energy decreased. The peak values of the total strain energy were 43.68, 30.07, 21.99, and 13.39 kJ·m^{-3}, respectively. Their reduction rates were 31.16, 26.87, and 39.11%, respectively. As the precrack dip angle increased, prepeak total strain energy peak values increased as well. The peak

(a)

(b)

(c)

(d)
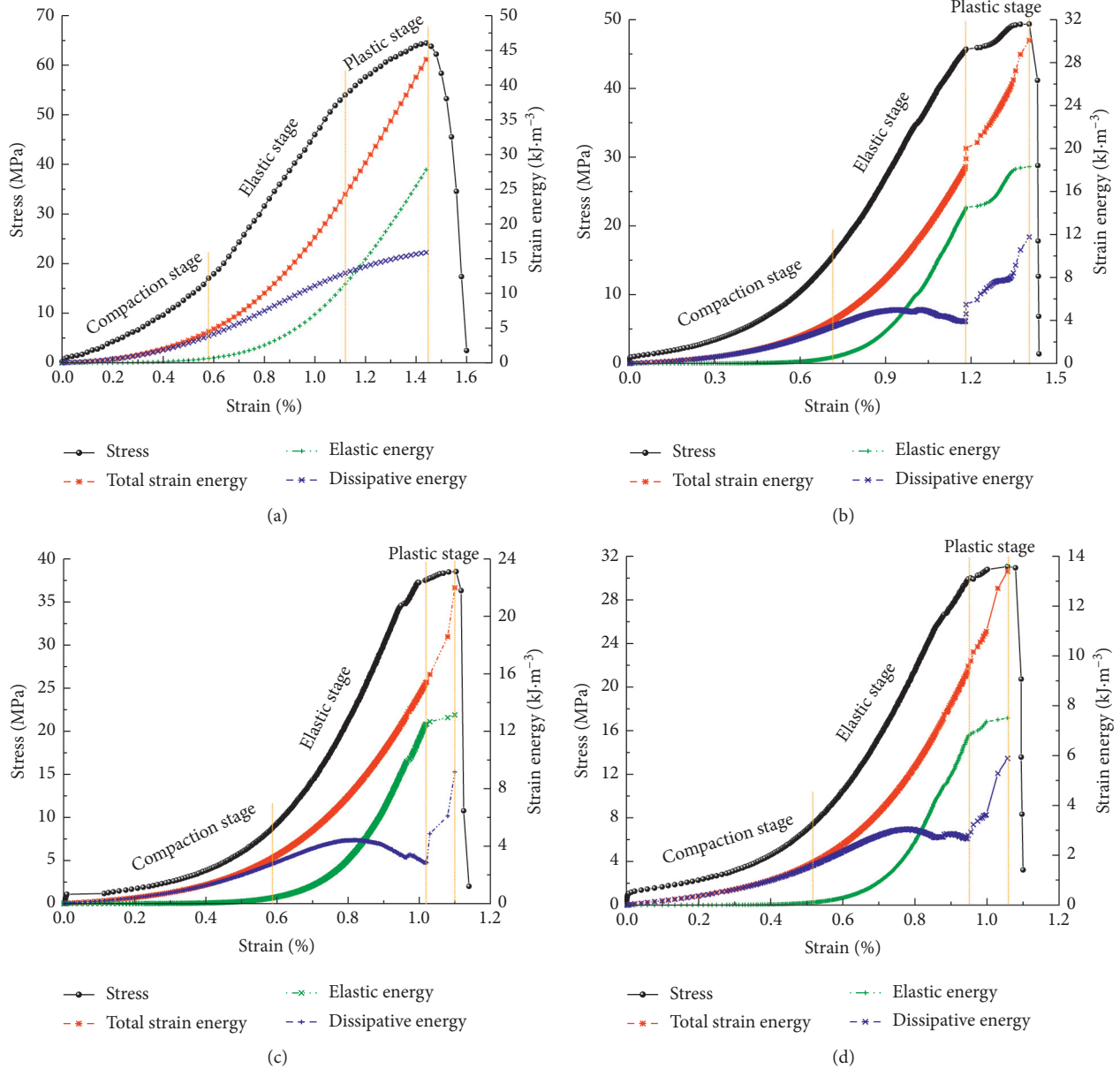
FIGURE 5: The relationships between stress, prepeak strain energy, and strain in typical intact (a) and precracked rock specimens with crack angles of 30° (b), 45° (c), and 60° (d).

values of prepeak elastic energy were 27.81, 18.31, 13.14, and 7.51 kJ·m^{-3}, respectively. The reduction rates were 34.16, 28.24, and 42.84%, respectively, being comparable to those of prepeak total strain energy's peak values. The above results indicated that the precrack dip angle had a significant impact on the rock specimens' peak strain energy. As it was already mentioned, precrack tips were more likely to store elastic energy, leading to the stress concentration phenomenon. As the precrack dip angle increased, the degree of shear stress concentration along the precrack tip increased in rock specimens under the same axial loading. Moreover, the prefabricated cracks were of a larger scale, leading to a more severe initial damage. New tips were formed and developed at the

precrack tips, which finally resulted in a decrease in the elastic energy stored in the rock specimens. Consequently, the peak total strain energy gradually dropped.

Figure 6(b) shows the relationship between the share of peak strain energy and the precrack dip angle in typical intact and precracked rock specimens. It can be seen that the peak strain energy shares before the peak in rock specimens with different precrack dip angles were 63.44, 61.02, 57.30, and 54.03%, respectively. The prepeak dissipative strain energy shares in rock specimens with different precrack dip angles were 36.54, 38.96, 42.85, and 45.97%. Thus, the peak elastic energy share before the peak significantly exceeded that of the peak dissipative energy. This strongly indicates that the total strain energy input in rock specimens before

(a)

(b)
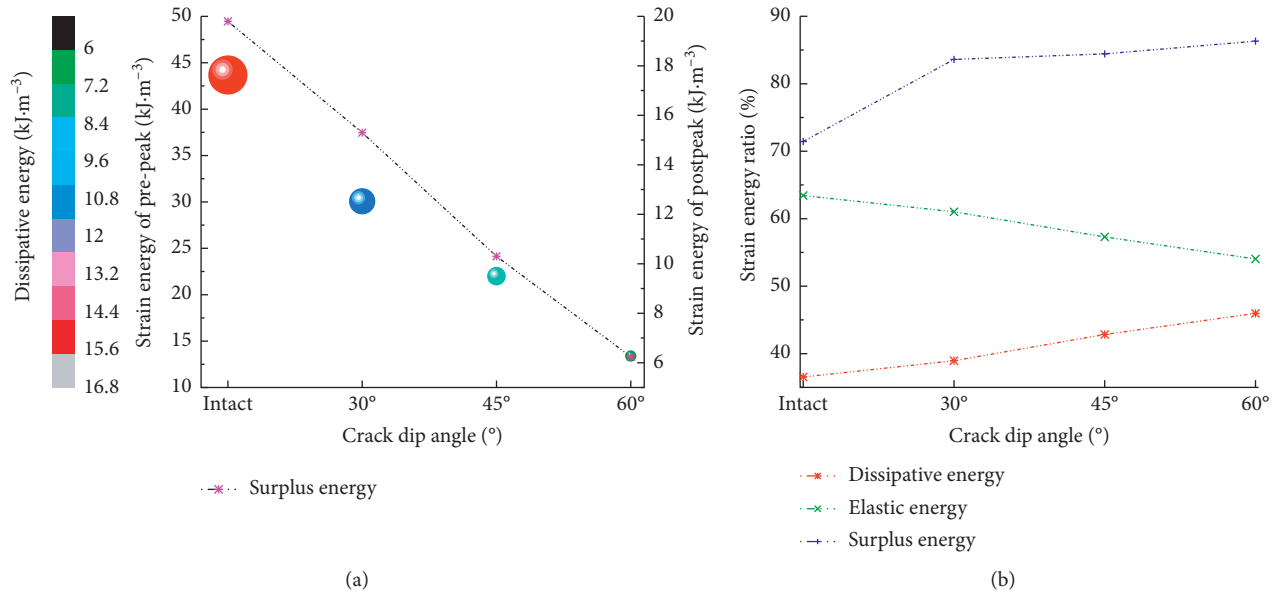
FIGURE 6: Curves depicting the relationship between the strain energy and precrack dip angle in typical intact and precracked rock specimens: (a) peak strain energy and (b) strain energy ratio (share).

the peak was mainly stored in the form of elastic energy. In contrast, only a small part of this energy was dissipated.

As the precrack dip angle increased, the peak elastic energy share before the peak decreased while that of the dissipative energy increased. This implies that, with an increase in the precrack dip angle, the damage accumulates more intensively at the precrack tips. As a result, cracks propagate more rapidly, and rock specimens become more susceptible to failure. The surplus energy is mainly spent on the ejection failure of rock specimens. As the precrack dip angle increases, the peak surplus energy drops while the peak surplus energy share is increased. This happens because the brittle failure of rock specimens is intensified, and the postpeak released energy drops at larger precrack dip angles. Consequently, the main part of the elastic energy accumulated at the precrack tips is converted into surplus energy. In other words, rock specimens acquire higher kinetic energy upon failure, which is accompanied by severe ejection of the chipped and fragmented rock specimens. Thus, the cracking sounds are emitted and recorded by the AE system.

The prepeak dissipative energy peak value shares increase at larger precrack dip angles. Therefore, rock specimens are more susceptible to failure. The peak surplus energy share increases and rock specimens are more susceptible to ejection failure. In actual roadway excavation and stoping of the coal mine working face, when large-scale and large-dip-angle defects (geological structures, such as faults and joints) are exposed, the following precautions should be taken. The fragmentation of the surrounding defective rock masses should be prevented to ensure the safe advance of the roadway and working face; energy variation near the defects should be carefully monitored; and other appropriate countermeasures should be adopted to reduce the structural impact hazards.

4. Damage Evolution Analysis of Rock Specimens

4.1. AE Energy Distribution during the Entire Process of Rock Specimen Loading. Figure 7 depicts the AE energy distribution characteristics during uniaxial loading in typical intact and precracked rock specimens. At the early loading stage, stresses generated in rock specimens are relatively small. The energy input into rock specimens is mostly consumed by the closure of the original cracks. There is little elastic energy stored in the rock specimens while shear stresses are concentrated to a lesser degree at the precrack tips. At this stage, few elastic waves are produced in rock specimens. With an increase in the load and stress in rock specimens, the energy input becomes converted into elastic stress waves. Shear stresses become more concentrated at the precrack tips. After the closure of the original cracks, new ones are formed at their tips, and more elastic waves are generated in the rock specimens. As the stress level further increases, rock specimens exhaust their ultimate ability of energy storage. The coalescence of microcracks occurs in rock specimens, and macroscopic fractures appear on the rock specimen surface, accompanied by a sudden rise in the AE energy characterized as the continuous type.

The occurrence of the first AE energy peak in intact and precracked rock specimens with dip angles of 30, 45, and 60° was revealed after 153, 101, 73, and 37 s, respectively. The corresponding axial stresses were 38.9, 25.7, 18.6, and 9.4 MPa, respectively. The first macroscopic crack (corresponding to the first peaks of AE energy and ring-down count) has appeared earlier, and the axial stress level required for the fracture was reduced with the dip angle. This result confirms the fact that the presence of prefabricated cracks significantly accelerates the failure of rock specimens.

(a)

(b)

(c)

(d)
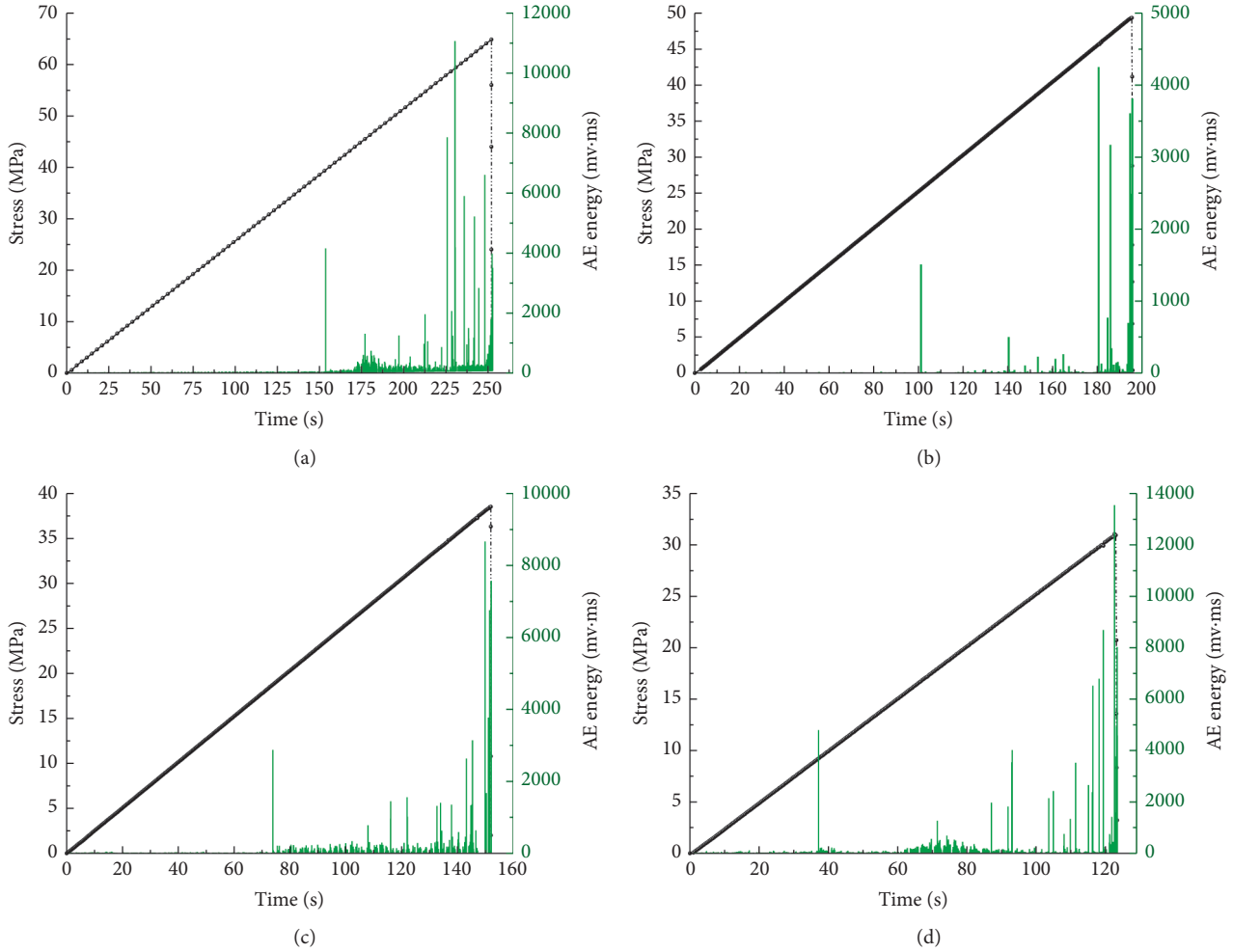
FIGURE 7: The AE energy evolution during the entire loading process of intact (a) and precracked rock specimens with a dip angle of 30° (b), 45° (c), and 60° (d).

4.2. Characterization of Rock Specimen Damage by the AE Energy Parameters.
The AE energy value is highly sensitive to the damage and fracture of rock specimens. It can intuitively reflect the initiation, propagation, and coalescence of cracks in rock specimens. Therefore, in this study, the AE energy was used as a characteristic parameter to reflect the damage evolution in intact and precracked rock specimens.

The equation of rock specimen damage evolution under uniaxial compression was elaborated based on the statistical damage theory:

$$\sigma = E(1 - D)\varepsilon_1, \tag{7}$$

where σ is the axial stress, MPa; E is the elastic modulus, MPa; and D is the damage factor, representing the ratio between the microcrack length and the size of microbodies in the rock specimen.

Assuming that the strength of microbodies in rock specimens obeys the Weibull distribution [28], the relationship between the damage factor and AE energy parameters can be expressed as follows:

$$D = \frac{N_t}{N_a}, \tag{8}$$

where N_t and N_a are the cumulative AE energy values at the loading start and complete failure instants, respectively, mv·ms.

In the triaxial compression test, rock specimens do not undergo complete failure due to the confining pressure, which contributes to their residual strength. However, in the uniaxial compression test, the rock specimens might still retain residual strength after the peak. The theoretical model depicting the relationship between the damage factor and AE parameters based on the Weibull distribution does not consider the residual strength after the failure of rock specimens under loading. Instead, it assumes that the complete failure of rock specimens occurs when $\varepsilon = \max\varepsilon$, i.e., $D = 1$, whose condition is not realistic. Therefore, the adjustment coefficient m is introduced and equation (8) is modified to the following form:

$$D = m \frac{N_t}{N_a}. \tag{9}$$

By incorporating the residual strength, m can be estimated as

$$m = \frac{\sigma_c - \sigma_p}{\sigma_c}, \tag{10}$$

where σ_p is the residual strength, MPa.

By introducing formulas (9) and (10) into (7), the equation of the rock specimen damage evolution under uniaxial compression, characterized by the AE energy, is derived as follows:

$$\sigma = E\left(1 - \frac{\sigma_c - \sigma_p}{\sigma_c} \frac{N_t}{N_a}\right)\varepsilon_1. \tag{11}$$

The normalization method was used to convert the damage variable characterized by the cumulative AE energy in typical intact and precracked rock specimens. Thus, the damage evolution process of rock specimens under uniaxial compression was obtained, as shown in Figure 8.

It can be observed that the damage evolved in both types of rock specimens follows a similar trend, which can be subdivided into three stages.

(A) The initial damage stage: At this stage, rock specimens exhibit low damage degree, and the damage variable is approximately zero. The reason is that it corresponds to the compaction stage and early elastic stage of the stress-strain curve. The energy input into rock specimens is mainly consumed by the closure of precracks. The bulk stress state of rock specimens is relatively uniform, without the formation or propagation of new cracks.

(B) The stable damage increase stage: At this stage, the rock specimen damage increases nonlinearly with a high variation rate. This happens because it corresponds to the middle and late elastic and early plastic stages of the stress-strain curve. At this time, the original cracks in rock specimens are closed. As the stress imposed by the test machine gradually increases, the original cracks further propagate after reaching the ultimate state while new cracks are formed and start to propagate.

(C) The accelerating damage increase stage. This stage, characterized by a sharp increase in rock specimen damage, is very short. The reason is that it corresponds to the middle and later plastic stage and residual deformation stage of the stress-strain curve. Microcracks in rock specimens propagate and coalesce rapidly, forming a crack network with the interpenetration of cracks. Thus, rock specimens undergo macroscopic failure.

The comparative analysis of the damage evolution processes in typical intact and precracked rock specimens revealed that an increase in the precrack dip angle reduced the initial damage stage duration. The damage accumulated
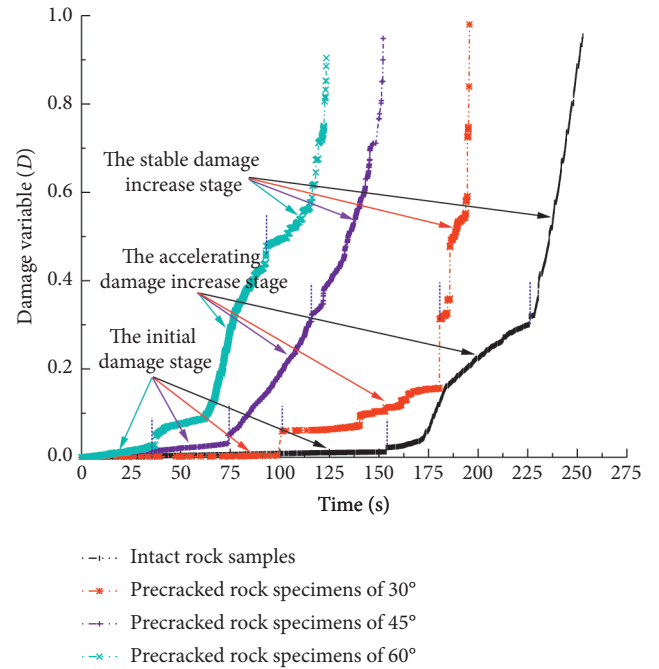
FIGURE 8: Damage evolution curves of typical intact and precracked rock specimens characterized by the AE energy.

more rapidly, promoting the evolution of rock specimens toward a "sudden instability."

4.3. Fracture Morphology of Rock Specimens.

Figure 9 presents the macrofracture morphology and SEM images of fracture surfaces of intact and precracked rock specimens. In accordance with earlier findings [29], pure tensile wing cracks were generated in the intact rock specimens and propagated to their bottom. In rock specimens with the precrack dip angle of 30°, the formation of tensile wing cracks and shear antiwing cracks being nearly normal to the precracks was observed. In the rock specimens with a precrack dip angle of 45°, tensile-shear composite wing and antiwing cracks were nearly normal to the precracks, while and tensile-shear secondary cracks were nearly parallel to them. In the rock specimens with the precrack dip angle of 60°, shear wing and shear secondary cracks were nearly parallel to the precracks formed. In all the above cases, the formed cracks propagated to reach the roof and bottom of rock specimens.

As the precrack dip angle is increased, the fracture mode of rock specimens changed from the tensile and splitting one to shear and slip fracture. There was a certain consistency in the macrofracture morphology and mutual conversion between different strain energy forms in rock specimens. Larger precrack dip angles promoted the ultimate energy storage ability exhaustion and increased the shear stress concentration at the precrack tips. Therefore, precracked rock specimens underwent fast shear and slip failure.

The morphological features of the fracture surfaces of typical intact and precracked rock specimens were instrumental in determining the damage and failure evolution
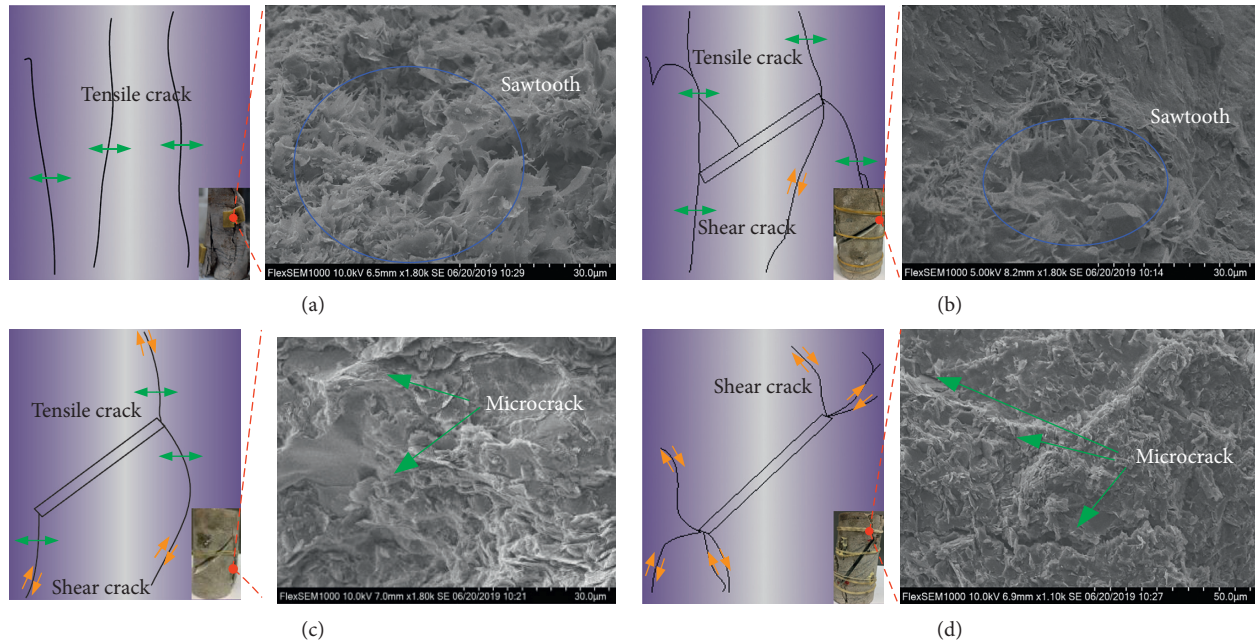
FIGURE 9: SEM images of fracture morphology and fracture surfaces of typical intact (a) and precracked rock specimens with a dip angle of 30° (b), 45° (c), and 60° (d).

patterns on the microscopic scale. The intact rock specimens had flat fracture surfaces with multiple sawtooth-like (jagged) structures. The latter structures could lock into and rub against each other, thus inhibiting the rock specimen's failure to a certain degree. As the precrack dip angle increased, sawtooth-like structures became smaller, and fracture surfaces became uneven, with developed microcracks. The above results confirm that larger precrack dip angles make specimens more susceptible to "sudden" failure, which is in concert with the damage evolution characteristics of rock specimens characterized by the AE energy.

During the uniaxial compression tests of rock specimens with small-scale prefabricated cracks [15, 30, 31], their peak strength and strain increased with the prefabricated crack dip angle. Besides, the stress-strain curve became right-shifted, in contrast to the uniaxial compression test results for rock specimens with large-scale prefabricated cracks. The prepeak energy dissipation gradually increased in rock specimens with small-scale cracks while sudden energy dissipation occurred at the plastic stage in specimens with large-scale ones. Thus, large-scale inclined prefabricated cracks severely impaired the integrity of rock specimens. In the compression tests, microcracks were more developed in the rock specimens with large-scale inclined prefabricated cracks. The fracture of rock specimens occurred in the form of collapse.

5. Conclusions

The results obtained made it possible to draw the following conclusions.

(1) Rock specimens with inclined precracks exhibited alterations in the compressive strength and deformation features, as compared to intact ones. With an increase in the precrack dip angle, their fracture mode changed from the tensile and splitting one to shear and slip fracture.

(2) In precracked rock specimens, the energy storage at an accelerating rate was observed at the elastic deformation while rapid energy dissipation occurred at the plastic stage. Both the prepeak dissipative energy and postpeak surplus energy shares in the total energy increased with the precrack dip angle. This indicates higher kinetic energy for the ejection of rocks, causing rock specimen fragmentation. Meanwhile, the kinetic energy in intact rock specimens rose more gradually.

(3) Based on the derived damage evolution equation, the rock specimens' damage process was subdivided into (i) the initial damage stage, (ii) stable damage increase stage, and (iii) the accelerating damage increase stage. As the precrack dip angle increased, the first peak of AE energy occurred earlier, and the corresponding stress level provided by the test machine was reduced. The damage in rock specimens accumulated at an accelerating rate. The sawtooth-like structures on the fracture surface were less likely to lock into each other. The fracture surface became uneven, and microcracks gradually developed. As a result, the rock specimens were more susceptible to the "sudden" failure.

Data Availability

The data used for conducting classifications are available from the corresponding author authors upon request.

Conflicts of Interest

Acknowledgments

References

[1] H. P. Xie, F. Gao, and Y. Ju, "Research and development of rock mechanics in deep ground engineering," *Chinese Journal of Rock Mechanics and Engineering*, vol. 34, no. 11, pp. 2161–2178, 2015.

[2] L. Yuan, "Scientific conception of coal mine dust control and occupational safety," *Journal of China Coal Society*, vol. 45, no. 1, pp. 1–7, 2020.

[3] S.-Q. Yang and H.-W. Jing, "Strength failure and crack coalescence behavior of brittle sandstone samples containing a single fissure under uniaxial compression," *International Journal of Fracture*, vol. 168, no. 2, pp. 227–250, 2011.

[4] S.-Q. Yang, W.-L. Tian, Y.-H. Huang, P. G. Ranjith, and Y. Ju, "An Experimental and numerical study on cracking behavior of brittle sandstone containing two non-coplanar fissures under uniaxial compression," *Rock Mechanics and Rock Engineering*, vol. 49, no. 4, pp. 1497–1515, 2016.

[5] D. Li, E. Wang, X. Kong, M. Ali, and D. Wang, "Mechanical behaviors and acoustic emission fractal characteristics of coal specimens with a pre-existing flaw of various inclinations under uniaxial compression," *International Journal of Rock Mechanics and Mining Sciences*, vol. 116, pp. 38–51, 2019.

[6] T. X. Xue, R. S. Fu, Y. W. Chen, and Z. G. Shao, "Numerical simulation of large scale fault activity and it's seismological analogy," *Progress in Geophysics*, vol. 24, no. 5, pp. 1616–1626, 2009.

[7] Q. G. Yu, H. X. Zhang, W. N. Zhang, Y. J. Zhang, and G. Y. Zhang, "Different fault activation models in mining subsidence," *Journal of China Coal Society*, vol. 44, no. 9, pp. 2777–2786, 2019.

[8] Y. L. Tan, W. J. Guo, H. Q. Xin, T. B. Zhao, and F. H. Yu, "Key technology of rock burst monitoring and control in deep coal mining," *Journal of China Coal Society*, vol. 44, no. 1, pp. 160–172, 2019.

[9] T.-b. Zhao, W.-y. Guo, Y.-l. Tan, Y.-c. Yin, L.-s. Cai, and J.-f. Pan, "Case studies of rock bursts under complicated geological conditions during multi-seam mining at a depth of 800 m," *Rock Mechanics and Rock Engineering*, vol. 51, no. 5, pp. 1539–1564, 2018.

[10] G. Cheng, L. Li, W. Zhu et al., "Microseismic investigation of mining-induced brittle fault activation in a chinese coal mine," *International Journal of Rock Mechanics and Mining Sciences*, vol. 123, Article ID 104096, 2019.

[11] O. Dorostkar and J. Carmeliet, "Potential energy as metric for understanding stick-slip dynamics in sheared granular fault gouge: a coupled CFD-DEM study," *Rock Mechanics and Rock Engineering*, vol. 51, no. 10, pp. 3281–3294, 2018.

[12] K. Zhao, X. Yu, Y. Zhou, Q. Wang, J. Wang, and J. Hao, "Energy evolution of brittle granite under different loading rates," *International Journal of Rock Mechanics and Mining Sciences*, vol. 132, Article ID 104392, 2020.

[13] Z. Zhang, M. Deng, J. Bai, X. Yu, Q. Wu, and L. Jiang, "Strain energy evolution and conversion under triaxial unloading confining pressure tests due to gob-side entry retained," *International Journal of Rock Mechanics and Mining Sciences*, vol. 126, Article ID 104184, 2020.

[14] L. Yang, F. Q. Gao, X. Q. Wang, and J. Z. Li, "Energy evolution law and failure mechanism of coal-rock combined specimen," *Journal of China Coal Society*, vol. 44, no. 12, pp. 2217–2224, 2019.

[15] G. L. Wang, L. Zhang, M. Xu, Z. Y. Liang, and B. L. Ran, "Energy damage evolution mechanism of non-across jointed rock mass under uniaxial compression," *Chinese Journal of Geotechnical Engineering*, vol. 41, no. 4, pp. 639–647, 2019.

[16] J. F. Jin, H. B. Zhong, Y. Wu, Z. Q. Guo, and X. J. Zhou, "Method selection for defining damage variable of rock subjected to static loadings and cyclic impacts," *Nonferrous Metals Science and Engineering*, vol. 4, no. 4, pp. 85–90, 2013.

[17] H. P. Xie, Y. Ju, and Y. L. Dong, "Research on plastic modulus method for classical damage mechanical definition," *Mechanical and Practice*, vol. 19, no. 2, pp. 2–6, 1997.

[18] Z. H. Guo, X. R. Liu, B. X. Liu, Z. L. Shu, and Y. Fu, "Experiment study of rock damage deformation characteristics based on plastic volumetric strain analysis," *Journal of Experimental Mechanics*, vol. 25, no. 3, pp. 223–298, 2010.

[19] Q. S. Zhang, G. S. Yang, and J. X. Ren, "New study of damage variable and constitutive equation of rock," *Chinese Journal of Rock Mechanics and Engineering*, vol. 22, no. 1, pp. 30–34, 2003.

[20] K. Zhao, H. Y. Zhao, and Q. Y. Jia, "An analysis of rock burst fracture micromorphology and study of its mechanism," *Explosion and Shock Waves*, vol. 35, no. 6, pp. 913–916, 2015.

[21] X. S. Liu, J. G. Ning, Y. L. Tan, and Q. H. Gu, "Damage constitutive model based on energy dissipation for intact rock subjected to cyclic loading," *International Journal of Rock Mechanics and Mining Sciences*, vol. 85, pp. 27–32, 2016.

[22] Z. Jia, H. Xie, R. Zhang et al., "Acoustic emission characteristics and damage evolution of coal at different depths under triaxial compression," *Rock Mechanics and Rock Engineering*, vol. 53, no. 5, pp. 2063–2076, 2020.

[23] D. Huang, R. Q. Huang, and Y. X. Zhang, "Experimental investigations on static loading rate effects on mechanical properties and energy mechanism of coarse crystal grain marble under uniaxial compression," *Chinese Journal of Rock Mechanics and Engineering*, vol. 31, no. 2, pp. 245–255, 2012.

[24] R. Solecki and R. J. Conant, *Advanced Mechanics of Materials*, Oxford University Press, London, UK, 2003.

[25] H. Xie, L. Li, R. Peng, and Y. Ju, "Energy analysis and criteria for structural failure of rocks," *Journal of Rock Mechanics and Geotechnical Engineering*, vol. 1, no. 1, pp. 11–20, 2009.

[26] R. Peng, Y. Ju, J. G. Wang, H. Xie, F. Gao, and L. Mao, "Energy dissipation and release during coal failure under conventional triaxial compression," *Rock Mechanics and Rock Engineering*, vol. 48, no. 2, pp. 509–526, 2015.

[27] G. Liu, F. K. Xiao, and T. Qin, "Rock mechanics characteristics and acoustic emission rule under small-size effect," *Chinese Journal of Rock Mechanics and Engineering*, vol. 37, no. S2, pp. 3905–3917, 2018.

[28] X. Y. Wang, H. W. Zhou, J. C. Zhong, L. Zhang, and C. S. Wang, "Study on energy evolution and permeability characteristics of damage of deep coal under triaxial cyclic loading and unloading conditions," *Chinese Journal of Rock Mechanics and Engineering*, vol. 37, no. 12, pp. 2676–2684, 2018.

[29] C. A. Tang, P. Lin, R. H. C. Wong, and K. T. Chau, "Analysis of crack coalescence in rock-like materials containing three flaws-part II: numerical approach," *International Journal of Rock Mechanics and Mining Sciences*, vol. 38, no. 7, pp. 925–939, 2001.

[30] Q. F. Guo, X. Wu, M. F. Cai, F. H. Ren, and J. L. Pan, "Crack initiation mechanism of pre-existing cracked granite," *Journal of China Coal Society*, vol. 44, no. S2, pp. 476–483, 2019.

[31] L. W. Liu, H. B. Li, X. F. Li, and R. J. Wu, "Full-field strain evolution and characteristic stress levels of rocks containing a single pre-existing flaw under uniaxial compression," *Bulletin of Engineering Geology and the Environment*, vol. 79, no. 6, pp. 3145–3161, 2020.

Research Article

Stabilization Mechanism and Safety Control Strategy of the Deep Roadway with Complex Stress

Yang Yu,[1] **Dingchao Chen** (ID),[1] **Xiangqian Zhao,**[1] **Xiangyu Wang,**[2] **Lianying Zhang,**[1] **and Siyu Zhu**[1]

¹College of Civil Engineering, Xuzhou University of Technology, Xuzhou, Jiangsu 221111, China
²School of Mines, China University of Mining & Technology, Xuzhou, Jiangsu 221116, China

Correspondence should be addressed to Dingchao Chen; 20170702129@xzit.edu.cn

With the increase of mining intensity of coal resources, some coal mines in China have gradually entered the deep mining stage. The complexity of the stress environment of the deep rock stratum leads to the difficulty of coal mining. Among them, the control of the deep roadway is one of the bottlenecks restricting the safety mining of the deep coal resources in China. By means of statistical analysis, the factors affecting the stability of the deep roadway were summed up: roadway occurrence environment, driving disturbance, and support means. The mechanical model of the deep roadway was established with the theory of elastic-plastic mechanics, the distribution characteristics of the plastic zone of the roadway were revealed, and the influence laws of lateral pressure coefficient, vertical stress, and support strength on the stability of the roadway were analyzed. Through numerical simulation, the law of stress, displacement and the plastic zone distribution evolution of the deep roadway, the mechanism of horizontal stress, and the mechanism of bolt support on the roadway were studied. On this basis, the safety control strategies to ensure the stability of the deep roadway were put forward: improving the strength of the roof and floor, especially the bearing part of the top angle and the side angle, enhancing the stability of the two sides of the roadway and controlling the floor heave, and making the surrounding rock of the deep roadway release pressure moderately, so as to make the roadway easy to be maintained under the low stress environment. These meaningful references were provided for the exploitation of deep coal resources in China.

1. Introduction

When human beings are exploring the space of the celestial body, they are expanding their exploration towards the deep of Earth at the same time, and mining engineering is the largest engineering of human beings under the deep of ground. With the enhancement of the intensity of resource exploration and development, mining is developing towards stratum under kilometers or even deeper stratum. At present, Chinese coal mining is expanding towards deeper ground in an average speed of 8–12 meters per year, and it can be predicted that deep well with kilometers shall be the main source of Chinese coal resources [1–5]. However, deep mining of coal mine presents a series of problems, such as the increase of the rock stress, the complexity of tectonic stress, intense exploiting disturbance, and the deterioration

of the stability of rock mass, which results in large deformation and serious destruction of the surrounding rock of the deep roadway, and brings in enormous threat to the safe and effective mining of deep mine. Therefore, the difficulty of controlling the surrounding rock of the deep roadway has been one of the main problems of restricting Chinese coal mining to develop to deeper part [6–10]. In allusion to deep mining and controlling the surrounding rock of the roadway, large amount of research results has been studied by scholars at home and abroad, and a certain number of research achievements have been obtained. Hou [11–13] identified the factors affecting the stability of the surrounding rock of the roadway, analyzed the influence of each influencing factor on the stability of the surrounding rock of the roadway, proposed to improve the stress state of the surrounding rock of the roadway and the mechanical

properties of the surrounding rock, rationally selected the support type of the roadway, and improved resistance and optimization of cross section of the roadway which are effective ways to control the surrounding rock of the deep roadway; Kang et al. [14–17] proposed a theory of high prestress and strong support for deep, complex, and difficult roadways in coal mines, developed a high prestress and strong support system, and successfully applied it to the 1,000 meter deep mine roadway in Xinwen mining area. For the problem that traditional rigid anchors cannot adapt to large deformation roadways, He and Guo [18, 19] have developed a constant-resistance large-deformation anchor that can provide constant working resistance and stable deformation. The anchor is suitable for soft rocks and deep roadways and can effectively control the impact of pressure engineering disasters; Bai and Hou [20–22] studied the stability of surrounding rock in deep roadways and proposed the basic methods of controlling the surrounding rock in deep roadways by increasing the strength of the surrounding rocks, transferring high stresses from the surrounding rocks, and adopting reasonable support technologies; Wang et al. [23, 24] studied the influence of support resistance on the deformation and plastic area of the surrounding rock in deep high-stress roadways and proposed that the supporting structure should meet the principle of coordinated support for large deformation of the surrounding rock. The comprehensive control technology based on "truss anchor cable" and anchor cable reinforcement is better to control the surrounding rock stability of the roadway; Li et al. [25] found that there was a regional rupture phenomenon between the fractured zone and the complete zone in the surrounding rock of the deep roadway, and it was successfully monitored by a drilling television imager in a kilometer deep well in the Huainan mining area. The research results of this phenomenon are of great significance for understanding the fracture mode and stability support of the surrounding rock in deep roadways. In response to the shortcomings of ordinary grouting in deep soft rock roadways, Liu et al. [26–29] proposed the use of a three-step grouting process to strengthen surrounding rocks, discussed the three-step grouting slurry diffusion mechanism, and carried out grouting project with the three-step grouting process; Chang and Xie [30–32] analyzed the stress evolution characteristics and deformation failure rules of the surrounding rock after the excavation of the deep rock lane, revealed the stability control mechanism of the surrounding rock in the deep well rock lane, and proposed grouting reinforcement support technology of the deep roadway with the rigid-flexible coupling of the anchor-net cable; Long [33–36] proposed the coanchoring mechanism of the surrounding rock of the deep roadway in view of the problems encountered in the control of the surrounding rock of the deep roadway and established the synergy mechanism with the structure synergy, strength synergy, stiffness synergy, anchoring timing synergy, pretension force synergy, and deformation synergy; Zuo et al. [37–40] believes that the stress gradient is an important factor that causes the surrounding rock failure of the roadway. Based on this, a theoretical model of the gradient failure of the surrounding rock failure in the deep roadway is established, and the relationship between the relative stress gradient and the average tangential stress level provided by the surrounding rock mass is determined.

However, it is still weak in aspects of the mechanism of horizontal stress, deformation and fracture feature of the roadway, and mechanism of bolt support. Thus, this paper established the mechanical model of the deep roadway through theoretical calculation and revealed the distribution characteristic of the plastic zone of the roadway on the basis of analyzing the influencing factors of stability of the surrounding rock of the deep roadway. It also researched the deformation and fracture of the deep roadway, distribution rule of stress evolution, the mechanism of horizontal stress, and the mechanism of bolt support to the deep roadway by the numerical calculation method, based on which it purposefully proposed the safety control countermeasures of the deep roadway.

2. Engineering Background

Shoushan coal mine is about 25 km from Pingdingshan City in Henan province of China, geographical coordinates: 113°21′16″ to 113°26′22″ east longitude and 33°45′45″ to 33°50′52″ north latitude. The well field is 14.5 km long from east to west and 1.1–4.6 km wide from north to south, with an area of 47 km². Shoushan coal mine is exploiting No. 15 coal seam whose average burial depth is 750 m, dip angle is 8–12°, and thickness is 3–4 m, with well-field geologic structure development and belongs to high gas extruding mine. No. 15 coal seam has the tendency of spontaneous combustion and the danger of coal dust explosion. The deformation and fracture of the roadway is serious under the combined action of high ground stress and tectonic stress, especially the deformation of floor heave and roof sink is extremely serious after excavation and mining disturbance. It forms vicious spiral of repairing after excavation in the roadway, which threats the safety production of mine seriously. The deformation and fracture situation of the roadway is shown in Figure 1.

In order to provide reliable basic parameters of rock stratum for subsequent theoretical calculation and numerical modeling, so as to reveal the deformation and stability mechanism of the deep roadway, it needs to measure physical and mechanical properties and relevant parameters by extracting No. 15 coal seam and rock samples of roof and floor. The experimental process is shown in Figure 2, and the test result is given in Table 1.

3. Influence Factors of the Stability of the Deep Roadway

The stability of the roadway under deep mining condition not only relates with the lithology and intensity of the surrounding rock but also is influenced by external stress environment. These influence factors mainly include occurrence environment, excavation disturbance, and support means.

3.1. Occurrence Environment. Ground stress is the basic parameter of the roadway stability and the design of supporting structure. The existence of tectonic stress field or

(a) (b)
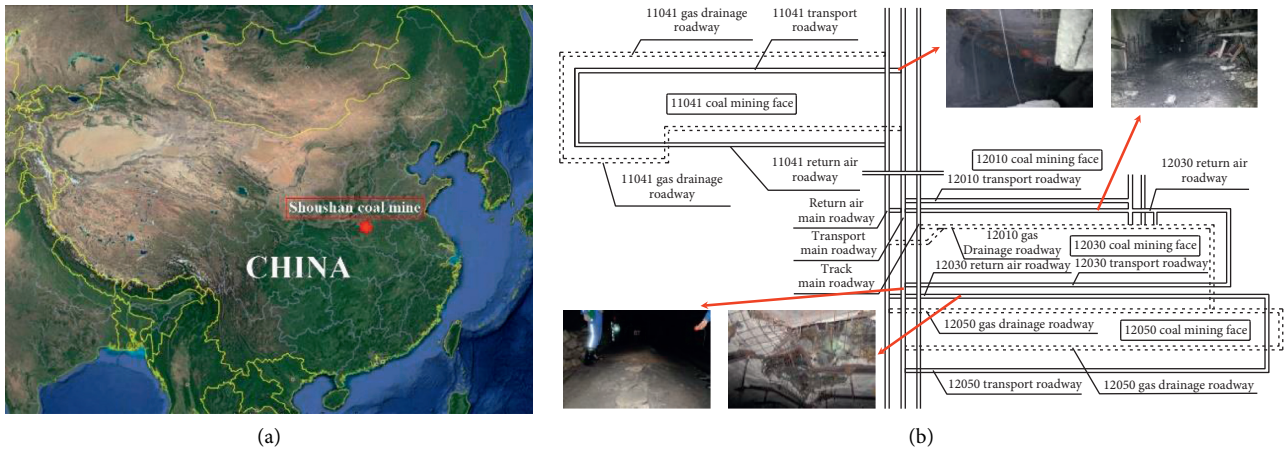
Figure 1: (a) Location of coal mine; (b) the deformation and fracture situation of the roadway.
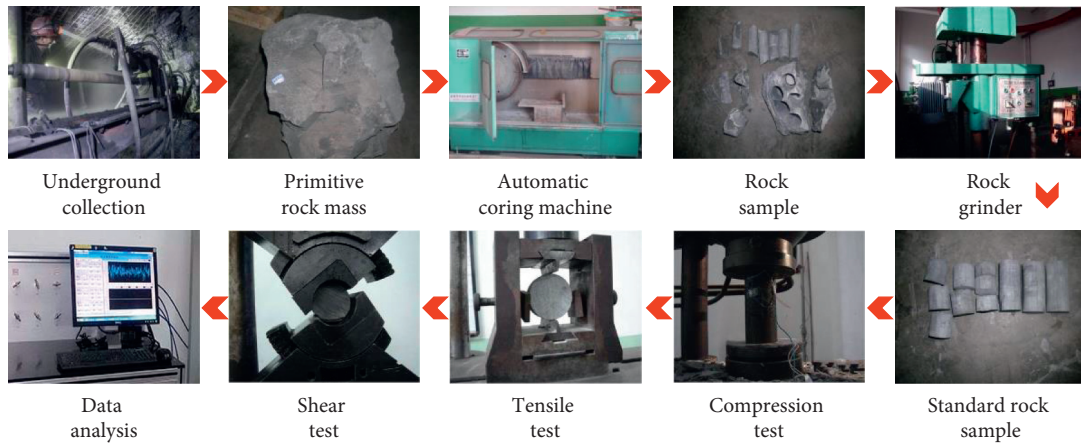
Figure 2: The experimental process.

Table 1: The physical and mechanical properties of roadway surrounding rock.

Lithology	Bulk density ($kN·m^{-3}$)	Thickness (m)	Compressive strength (MPa)	Elastic modulus (GPa)	Poisson ratio	Interfriction angle (°)	Cohesion(MPa)	Tensile strength (MPa)
Fine sandstone	27.5	32	25.7	10.0	0.20	40	6.0	6.0
Sandy mudstone	25.3	8.0	9.4	3.5	0.22	34	2.5	2.5
No. 15 coal seam	13.6	3.5	4.2	2.5	0.25	19	1.5	1.5
Mudstone	24.5	3.5	7.2	2.5	0.23	32	2.0	2.0
No. 16 coal seam	13.6	6.5	4.7	2.0	0.23	32	1.5	1.4
Fine sandstone	27.5	5.0	25.7	10.0	0.20	40	6.0	6.0
Sandy mudstone	25.3	12	9.4	4.5	0.22	34	5.0	3.2
Limestone	28.0	13	30	10.0	0.20	40	8.0	7.2

remnant tectonic stress field is ubiquitous in deep rock mass, while the superposition and accumulation of them forms high stress; the ground stress of deep rock mass possesses obvious directivity, and especially that its horizontal stress is largely influenced by geologic structure. The ground stress measured data of mine indicate that horizontal stress is larger than vertical stress, and the specific value of maximum horizontal stress and vertical stress is 0.96–2.07; under the

function of high stress, the deep rock mass converts from fragility to ductility, which shows strong rheological behavior with large deformation and obvious "time effect." In addition, high ground temperature and high water pressure also produce prominent influence on correlated characteristic of rock mass.

3.2. Excavation Disturbance. Roadway excavation changes the mechanical state of the surrounding rock, and it possesses pressure relief function to the unexcavated rock. Deviator stress and sharp release of energy caused by excavation under high ground stress condition are the basic reasons of inducing the unstability of the deep roadway, and the main forms of the surrounding rock destruction are tension crack and shear failure. Destruction is a progressive process, and the strength of the surrounding rock is weakening continuously. Under the condition without support or with small support force, the destruction of the deep roadway presents specific regional fracture phenomenon, while, under the function of strong external support, the shear slip deformation inside the surrounding rock plays a dominant role.

3.3. Support Means. Bolt support is a kind of support method widely used by coal mine. Its function mainly is reflected in the destruction period of rock, but as for rock, which has entered into yield state, small supporting resistance even can improve its residual strength remarkably and make it be capable of bearing large load. The deformation amount and speed of the roadway increases clearly after it enters deep mining. Although the deformation and fracture of rock mass is unavoidable, bolt can provide certain constraining force to prevent the rock mass from sliding. Take the advantage of horizontal stress to maintain the roof stability by installing bolt and exerting high pretightening force timely, so as to allow roof to keep in horizontal compression state and enhance the stability of the roadway.

4. Theoretical Calculation of Stabilization Mechanism of the Deep Roadway

The stability of the deep roadway in different places is different when it is under the function of high ground stress,
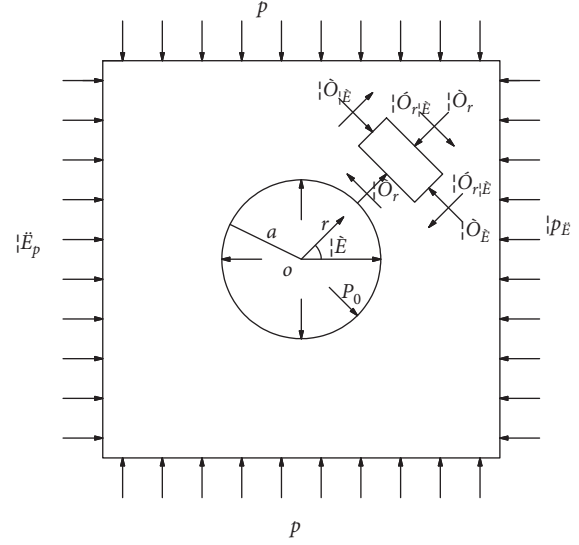
Figure 3: Mechanical model of the roadway.

and its mechanical characteristic shows that different places have different scopes of the plastic zone. Therefore, it needs to adopt the scope of the plastic zone as the evaluation index of the stability to make an analysis to the roadway stability state.

4.1. Model Establishment. The mechanical model of the roadway is shown in Figure 3. Former calculation of the plastic zone of the roadway is based on hydrostatic pressure state, while our research takes into consideration the influences of horizontal stress and supporting intensity on the roadway stability. According to the characteristics of deep stress field, it makes the following hypotheses: (1) rock mass is continuous, homogeneous, and isotropous elastic-plastic material; (2) the horizontal stress born by the roadway is λ times of vertical stress; (3) neglect the influence of dead load of the surrounding rock; and (4) the plastic zone of rock mass satisfies Mohr–Coulomb strength criterion.

4.2. Calculation of the Plastic Zone Scope. Surrounding rock stress formula of the round roadway in the elasticity zone [41]:

$$
\left.
\begin{aligned}
\sigma_r &= \frac{(1+\lambda)p}{2}\left(1-\frac{a^2}{r^2}\right)-\frac{(1+\lambda)p}{2}\left(1-\left(\frac{4a^2}{r^2}\right)+\left(\frac{3a^4}{r^4}\right)\right)\cos 2\theta+\frac{p_0 a^2}{r^2}, \\
\sigma_\theta &= \frac{(1+\lambda)p}{2}\left(1+\frac{a^2}{r^2}\right)+\frac{(1-\lambda)p}{2}\left(1+\frac{3a^4}{r^4}\right)\cos 2\theta-\left(\frac{p_0 a^2}{r^2}\right), \\
\tau_{r\theta} &= \frac{(1-\lambda)p}{2}\left(1+\left(\frac{2a^2}{r^2}\right)-\left(\frac{3a^4}{r^4}\right)\right)\sin 2\theta,
\end{aligned}
\right\}
\tag{1}
$$

where λ is the side pressure coefficient; p is the vertical stress, MPa; a is the radius of the roadway, m; r is the distance to the center of the roadway, m; P_0 is the supporting intensity, MPa; θ is the included angle with x-axis, °; σ_r is the radial direction normal stress, MPa; σ_θ is the tangential normal stress, MPa; and τr_θ is the shear stress, MPa.

One point's radial direction normal stress, tangential normal stress, and shear stress are known, and then, the principal stress of this point can be acquired by

$$\left.\begin{aligned} \sigma_1 &= \left(\frac{\sigma_r + \sigma_\theta}{2}\right) + \sqrt{\left(\frac{\sigma_r - \sigma_\theta}{2}\right)^2 + \tau_{r\theta}^2}, \\ \sigma_2 &= \frac{\sigma_r + \sigma_\theta}{2} - \sqrt{\left(\frac{\sigma_r - \sigma_\theta}{2}\right)^2 + \tau_{r\theta}^2}, \end{aligned}\right\} \quad (2)$$

where σ_1 is the maximum principal stress; and σ_2 is the minimum principal stress.

Substitute equation (1) into (2), and then, the principal stress of the surrounding rock of the round roadway in the elasticity zone can be acquired:

$$\left.\begin{aligned} \sigma_1 &= \frac{(1+\lambda)p}{2} - (\lambda - 1)\left(\frac{pa^2}{r^2}\right)\cos 2\theta + \left(\frac{p}{2}\right)\beta, \\ \sigma_2 &= \frac{(1+\lambda)p}{2} - (\lambda - 1)\left(\frac{pa^2}{r^2}\right)\cos 2\theta - \left(\frac{p}{2}\right)\beta. \end{aligned}\right\} \quad (3)$$

In the equation

$$\beta = \sqrt{\left[(1+\lambda)\left(\frac{a^2}{r^2}\right) - (\lambda - 1)\left(1 - \left(\frac{2a^2}{r^2}\right) + \left(\frac{3a^4}{r^4}\right)\right)\cos 2\theta - \left(\frac{2p_0 a^2}{pr^2}\right)\right]^2 + \left[(\lambda - 1)\left(1 + \left(\frac{2a^2}{r^2}\right) - \left(\frac{3a^4}{r^4}\right)\right)\sin 2\theta\right]^2}. \quad (4)$$

The principal stress of the point inside the plastic zone can be known by Mohr–Coulomb strength criterion:

$$\sigma_1 = \left(\frac{1 + \sin \phi}{1 - \sin \phi}\right)\sigma_2 + \left(\frac{2C \cos \phi}{1 - \sin \phi}\right), \quad (5)$$

where C is the cohesion; and φ is the internal friction angle, °.

Substituting equation (3) into (5), the scope of the plastic zone of the surrounding rock of the round roadway in deep complex stress field can be acquired:

$$\left[(1+\lambda)q - 2(\lambda - 1)\left(\frac{qa^2}{r^2}\right)\cos 2\theta\right]\sin \phi - q\beta + 2C \cos \phi = 0. \quad (6)$$

The point (r, θ) satisfying with equation (6) locates at the boundary of the elastic zone and plastic zone, and the zone inside the boundary line is the plastic zone.

4.3. Influence Factors of the Plastic Zone Scope

4.3.1. Side Pressure Coefficient λ.
Hypothesize vertical pressure $q = 15$ MPa, rock mass cohesion $c = 1.5$ MPa, internal friction angle $\varphi = 20°$, and support intensity $P_0 = 0.3$ MPa. When side pressure coefficient $\lambda = 0.5, 1, 1.5,$ and 2, the distribution range of the plastic zone can be obtained as shown in Figure 4.

It can be inferred from Figure 4 that when λ is relatively small, the plastic zone of the roadway presents symmetric distribution, and the plastic destruction scope is about 1.0 m–3.0 m; when λ increases from 0.5 to 1.5, the scope of plastic zones at two sides of the roadway is decreasing gradually from 1.24 m to 0.73 m, and the scope of roof and floor plastic zones is increasing gradually from 0.29 m to 1.34 m; when λ is greater than 1.5, the scope of the plastic

zone of the roadway increases rapidly, and the increase of humeral angle part is extremely remarkable; the scope of the plastic zone reaches to 3.47 m when $\lambda = 2$, which increases 160% than $\lambda = 1.5$, the value of λ at this time is the limit value of the roadway stability. It fully reflects the impact of horizontal stress on the stability of roof and floor of the roadway. When side pressure coefficient is greater than this value, the stability of the roadway will decreases rapidly, which coincides with a large number of field observation.

4.3.2. Vertical Pressure q.
Hypothesize side pressure coefficient $\lambda = 2$, rock mass cohesion $C = 1.5$ MPa, internal friction angle $\varphi = 20°$, and supporting intensity $P_0 = 0.3$ MPa. When vertical pressure $q = 5, 10, 15, 20$ MPa, the distribution range of the plastic zone of the roadway can be as shown in Figure 5.

It can be indicated from Figure 5 that with the increase of the burial depth of the roadway, the plastic zone is expanding constantly, and especially the diffusion from the humeral angle of the roadway towards the two sides is obvious. When vertical stress is relatively small ($q < 5$ MPa), the plastic fracture scope is less than 1.1 m, and the roadway is apt to stability at this time, but the expansion rate of the scope of the plastic zone is fast; after it enters deep part ($q > 15$ MPa), the scope of plastic fracture is more than 3.47 m, and it is difficult to keep the stability of the roadway, and the expansion rate of the plastic zone slows down.

4.3.3. Support Means.
Hypothesize side pressure coefficient $\lambda = 2$, vertical pressure $q = 15$ MPa, rock mass cohesion $C = 1.5$ MPa, and internal friction angle $\varphi = 20°$; when supporting intensity $P_0 = 0, 0.1, 0.2, 0.3, 0.4, 0.5$ MPa, the
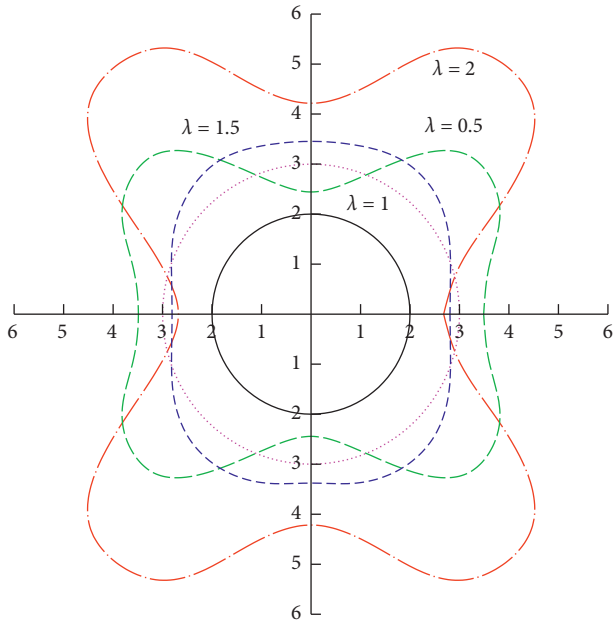
FIGURE 4: The distribution range of the plastic zone with different side pressure coefficients.
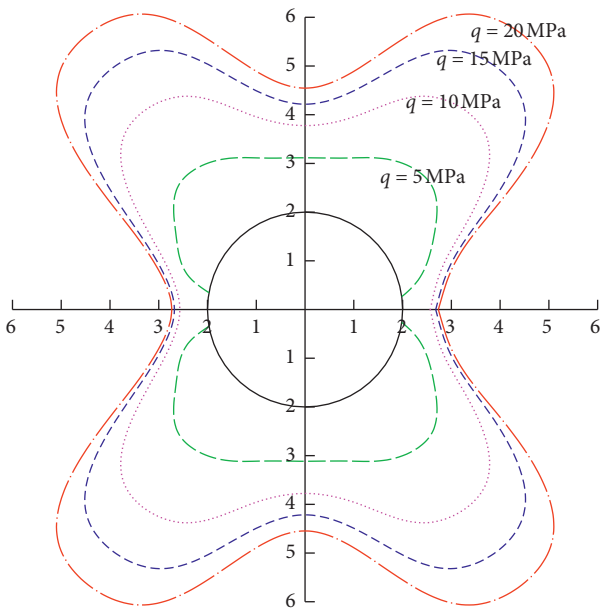
FIGURE 5: The distribution range of the plastic zone with different vertical pressure.

distribution range of the plastic zone can be as shown in Figure 6.

It can be inferred from Figure 6 that with the increase of support intensity p_0, the scope of the plastic zone L basically presents linear decrease. The linear relation is given as

$$L = 5.486 - 0.055p_0. \tag{7}$$

Although the function of bolt support to the decrease of the scope of the plastic zone is not obvious, it effectively
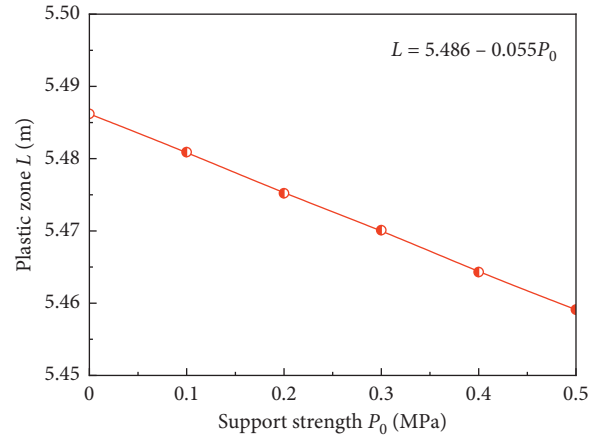
FIGURE 6: The plastic zone with different support intensity.

improves the residual strength of surrounding rock after peak [42] and restricts the further expansion of the plastic zone.

In summary, with the increase of ground stress, the stability of the roadway is becoming worse and worse; the influence of ground stress on the stability of the roadway is ununiform, that is, to say that the vertical stress mainly influences the stability of the two sides of the roadway, and the horizontal stress mainly influences the stability of roof and floor of the roadway.

5. Numerical Modeling of the Stabilization Mechanism of the Deep Roadway

5.1. Model Establishment. Taking the roadway of the 15# coal seam in Shoushan coal mine as an example, the numerical calculation model is established by making use of FLAC3D software. It makes a research on distribution and evolution rules with the stress, displacement, and the plastic zone and the influences of different intensities of horizontal stress it have on above factors. What is more, the size of the model is length × width × height = 180 m × 80 m × 83.5 m, the total number of unit is 321600, and the total number of node is 337348. The sides of this model are restricted horizontal mobility, its underside is restricted vertical shift, and its upper surface is stress boundary. Impose 15 MPa to simulate the dead weight of overlying rock mass, and the material conforms to the Mohr–Coulomb model. The numerical calculation model is shown in Figure 7. The research contents are (1) the distribution and evolution rules of stress, displacement, and the plastic zone of the roadway; (2) the influences of horizontal stress on the stability of the roadway; and (3) the function of bolt support on the deep roadway.

5.2. Distribution and Evolution Rules of Stress, Displacement, and the Plastic Zone of the Deep Roadway

5.2.1. Evolution Rule of Vertical Stress. After the excavation of the roadway, the two sides form the stress concentration zone, and the stress concentration factor increases from 1.20
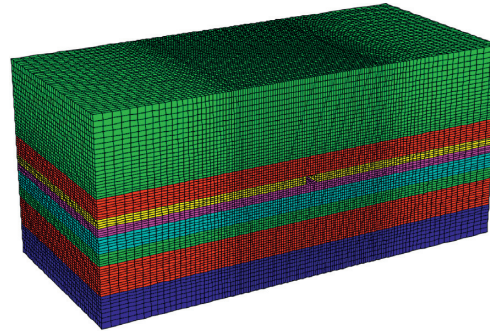
FIGURE 7: Numerical calculation model.

(a)

(b)

(c)
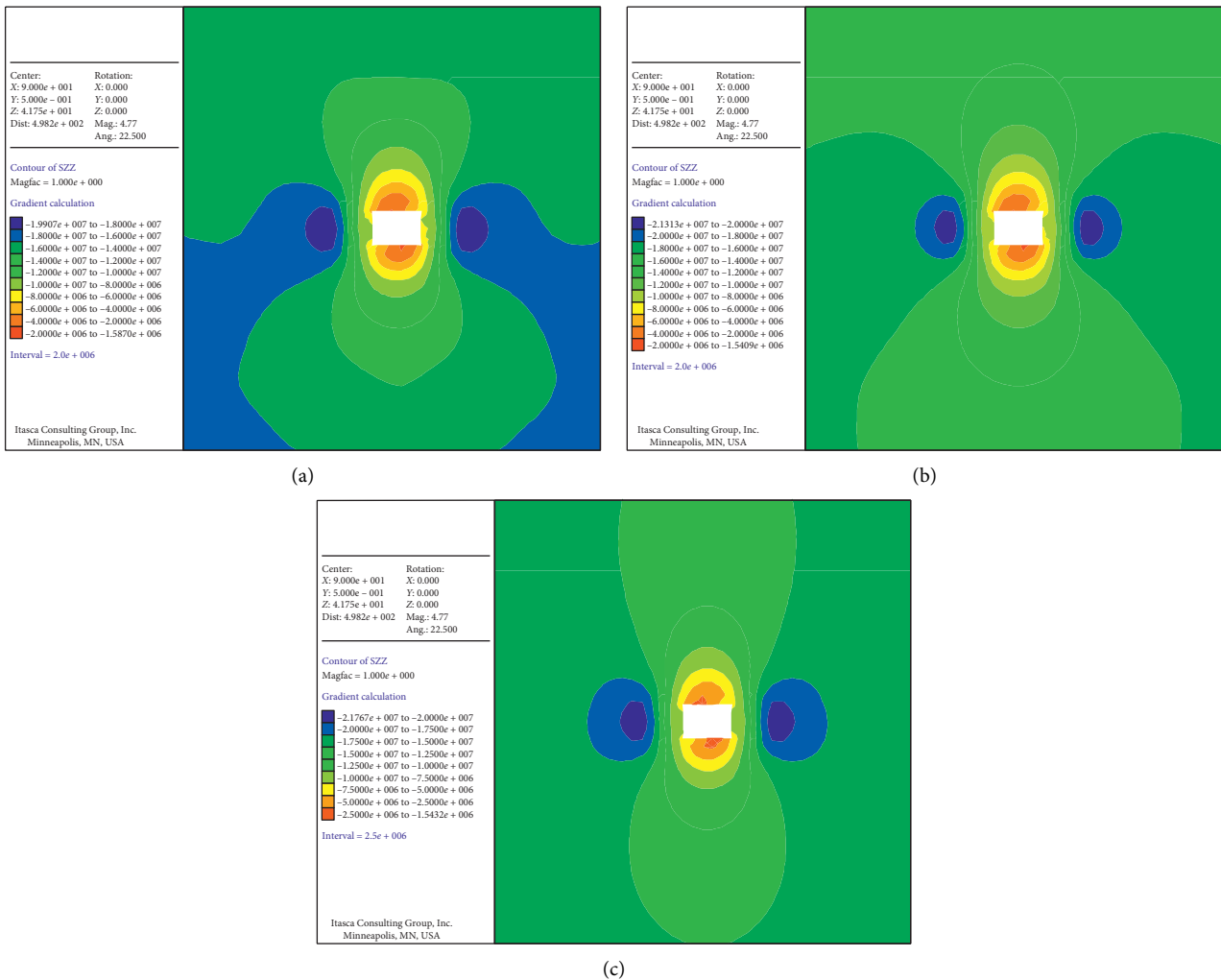
FIGURE 8: Cloud diagram of vertical stress. (a) 300 step; (b) 600 step; and (c) 2100 step.

to 1.43; the surrounding rock in certain scope of the roadway is relatively broken and forms the stress decreasing zone. After the roadway deformation tends to be stable, the stress decreasing zone presents "bowling-form" distribution at roof and floor, and the scope is relatively large. The cloud diagram of vertical stress is shown in Figure 8.

5.2.2. Distribution and Evolution Rule of Horizontal Stress.
After the excavation of the roadway, the two sides appear as large scope of the stress decreasing zone, and the floor emerges as small scope of the stress concentration zone. During the stability process of the roadway, the stress concentration zone of roof and floor is enlarging constantly, and especially in the floor of the roadway whose stress concentration zone is relatively large. Moreover, the stress distribution of the two sides is basically invariant. The cloud diagram of horizontal stress is shown in Figure 9.

5.2.3. Distribution and Evolution Rule of Shear Stress.
After the excavation of the roadway, with the increase of deviator stress $\sigma_1 - \sigma_3$, it forms the shear stress concentration zone at the four corners of the roadway. It can be known from shear stress mutual equal theory that shear stress comes in pairs, the directions of shear stress of adjacent two surfaces is opposite, and the intensity of shear stress is 6.0 MPa after the stability of the roadway. The cloud diagram of shear stress is shown in Figure 10.

5.2.4. Distribution and Evolution Rule of Displacement.
After the excavation of the roadway, the surrounding rock moves towards excavation direction. Due to that the vertical stress forms the stress concentration zone at the two sides, so the coal of the two sides bear great pressure, while the strength of coal is relatively low, so the displacement of the two sides is large. The cloud diagram of displacement is shown in Figure 11.

5.2.5. Distribution and Evolution Rule of the Plastic Zone.
After excavation of the roadway, stress concentration area appears in roof and floor. Shear failure is serious, and the two sides present small scope of tensile failure. The destruction of the roadway is mainly shear failure, and it presents small scope of the tensile-shear mixed fracture zone at the center of roof and the middle part of the two sides. The cloud diagram of the plastic zone is shown in Figure 12.

In conclusion, the two sides form the stress concentration zone under the function of vertical stress in deep stress field after the excavation of the roadway; furthermore, the roof and floor show large scope of the stress decreasing zone; under the function of horizontal stress, it appears in large scope of the horizontal stress concentration zone at the roof and floor, and the side angle appears in the shear stress concentration zone, so the roof and floor rock masses are easy to occur as shear failure. Therefore, under the function of deep high stress, the key to stabilize the deep roadway is to improve the rigidity and strength of roof and floor rock masses, and especially the important load bearing parts of vertex angle and side angle.

5.3. Horizontal Stress Action Mechanism. One of the prominent characteristics of deep ground stress is that horizontal stress is higher than vertical stress [43]. The ground stress testing results of this coal mine show that the specific value of maximum horizontal stress and vertical stress is 0.96–2.07. Therefore, the value range of side pressure coefficient selected in numerical calculation is 1-2.

5.3.1. Displacement Distribution of the Roadway

(1) The displacement of the roadway basically presents positive exponential distribution with the enlarging of distance from the roadway surface; furthermore, the horizontal displacement of the two sides keeps stable when its distance to the two sides is 4.0 m, the vertical displacement of floor keeps stable when its distance to the floor is 7.0 m, and the vertical displacement of roof keeps stable when its distance to the roof is 7.0 m.

(2) With the increase of side pressure coefficient, the surface displacement of the roadway increases constantly. The influence of horizontal stress on the stability of the roadway exists obvious boundary. In addition, when the side pressure coefficient is larger than 1.2, the roadway loses stability rapidly.

(3) The increase of horizontal stress has a great influence on the roof and floor, while it has a small influence on the two sides. The displacement distribution of the roadway is shown in Figure 13.

5.3.2. Stress Distribution of the Roadway

(1) As the distance from the roadway surface is farther, the vertical stress of the two sides first increases and then decreases; moreover, the peak stress appears at the place of 5.0 m, and the stress tends to be stable after 10 m. The horizontal stress of the two sides is increasing constantly, and there is no obvious peak value; the vertical stress of roof and floor increases constantly without obvious peak value. The horizontal stress of roof and floor first increases and then decreases, and there is a certain fluctuation in the scope of 10 m of roof and floor, and the horizontal stress gradually tends to be stable after 15 m.

(2) With the increase of side pressure coefficient, the distribution and intensity of vertical stress of two sides keep unchanged basically with small influence of horizontal stress; the vertical stress distribution of roof and floor gradually transits from "arc-shape" distribution to "ellipse shape," and the vertical stress is increasing constantly. The stress distribution of the roadway is shown in Figure 14.

5.3.3. Plastic Zone Distribution of the Roadway. With the increase of side pressure coefficient, the failure mode of the roadway keeps unchanged, which is mainly shear failure and shear-tensile failure. But, the coverage area of shear-tensile failure to the area of the roadway failure is decreasing continuously, and the scope of shear failure is increasing constantly, so horizontal stress intensifies the shear failure of the roadway. The plastic zone distribution of the roadway is shown in Figure 15.

(a)

(b)

(c)
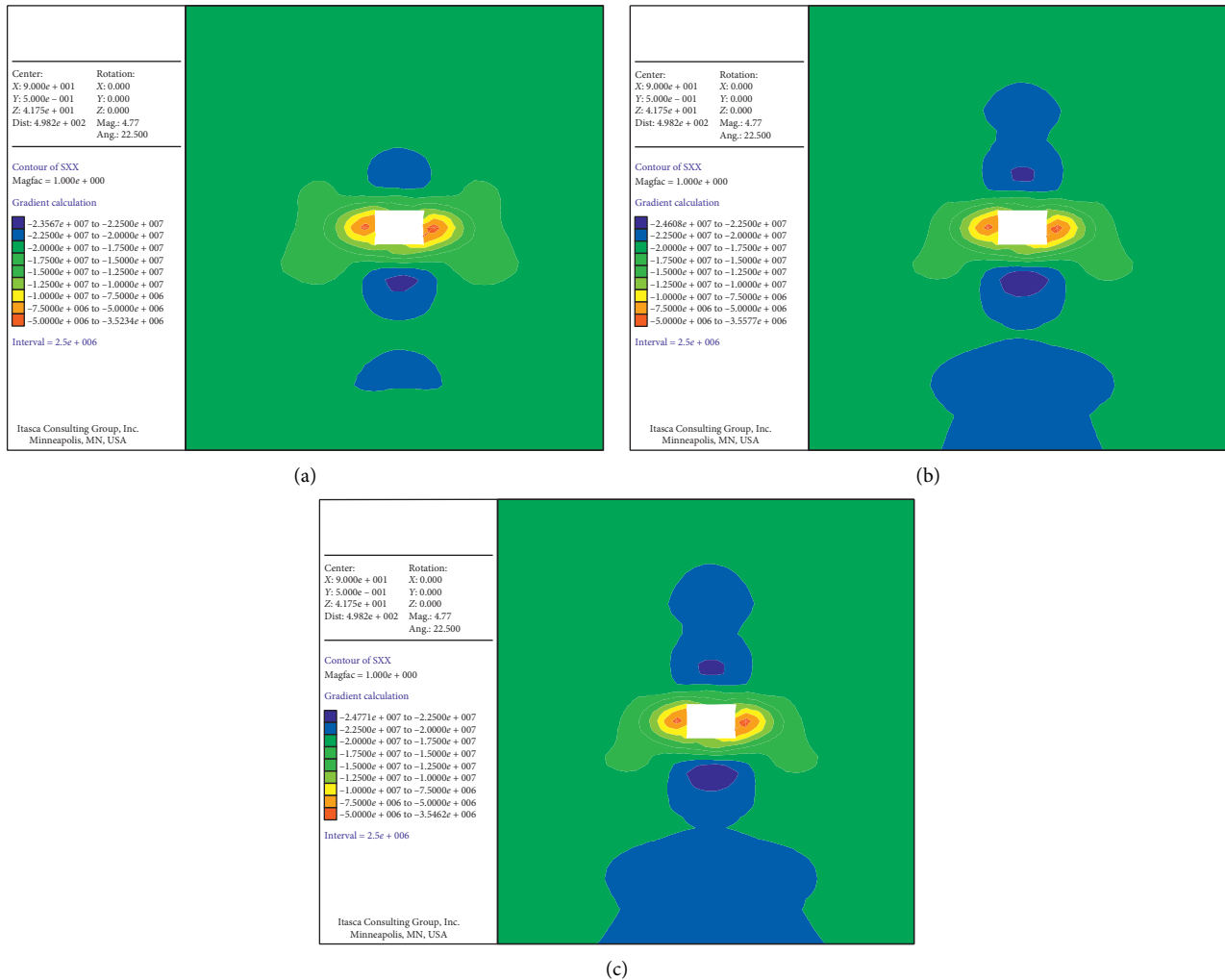
Figure 9: Cloud diagram of horizontal stress. (a) 300 step; (b) 600 step; and (c) 2100 step.

6. Bolt Support Mechanism for the Deep Roadway

As for the interaction relation between bolt and surrounding rock, scholars made large amount of research studies on the amelioration of mechanical property of rock mass after bolt strengthening, which revealed the mechanism of bolt support in different degrees. However, these achievements mainly come from shallow-buried tunnel engineering, and its research emphasis is the anchoring effect of unbroken rock and soil mass. While, under the influence of high stress and strong mining, the surrounding rock of the deep roadway especially the coal roadway occurs as large deformation and large scope of destruction; therefore, it needs to make a further study on bolt support mechanism under such condition. The bolt support structure of the roadway is shown in Figure 16. There are six bolts at roof, four bolts at each side of the two sides, row spacing is 800 mm, interspacing of anchor is 3000 mm, and row spacing of anchor is 1600 mm.

6.1. Roadway Deformation. Under the condition of with or without support, the horizontal displacement difference of the two sides is enlarging constantly when it transits from the deep of surrounding rock towards the surface of the roadway, but the maximum displacement difference is just 24 mm, and the vertical displacement of roof and floor keeps unchanged generally. Although bolt support improves the parameters of shallow surrounding rock's internal friction angle and cohesive force, the shallow surrounding rock stress of the deep roadway is still very high, and the effect of bolt support is not significant. The horizontal displacement of the two sides of the roadway is shown in Figure 17.

6.2. Roadway Stress. Compared with the condition without support, under the function of bolt support, the stress intensity and distribution rule of the roadway have no big changes. Due to that the scope of the horizontal stress decreasing zone of the two sides is large, and the stress environment is good, so the effect of bolt support of the two

(a)

(b)

(c)
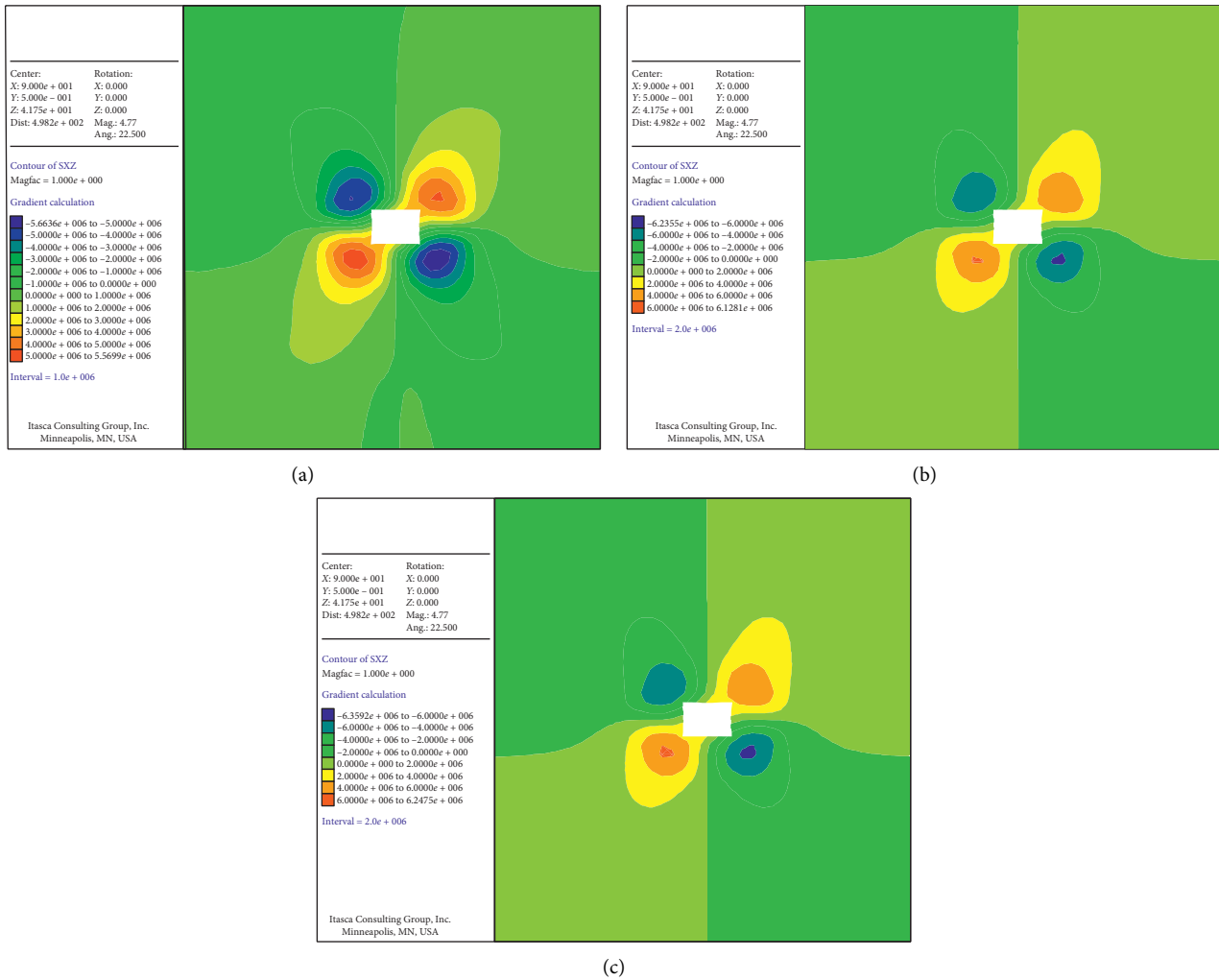
FIGURE 10: Cloud diagram of shear stress. (a) 300 step; (b) 600 step; and (c) 2100 step.

sides is more remarkable than that of roof. In addition, bolt support improves the confining pressure of the surface of the roadway, and the increase of confining pressure remarkably decreases the deformation of the roadway, on account of that the shallow surrounding rock of the roadway is mellow and broken, and it is sensitive to confining pressure. The cloud diagram of the roadway stress is shown in Figure 18.

6.3. Roadway Failure.
Compared with the condition without support, the scope of the plastic zone of the roadway decreases to some extent under the function of bolt. When there is no support, the surrounding rock in the middle part of the roadway mainly presents shear failure and tensile failure, while bolt support can effectively decrease the scope of tensile failure of the surface of the roadway, and the destruction range of roof can decrease from 3 m without support to 1 m with support, so bolt support can strengthen the stability of the roadway. The cloud diagram of the plastic zone is shown in Figure 19.

6.4. Bolt Stress.
The bolt of the roadway bears the dilatation deformation stress of the surrounding rock as it restrains the surrounding rock, so it keeps in tension state. The axial force of bolt reaches to maximum at the middle part of two sides, that of the middle part of roof takes second place, and that of vertex angle is minimum; moreover, the maximum axial force of bolt is 200 kN, and the minimum axial force of bolt is 147 kN. The maximum axial force of anchor is 304.2 kN. The bolt has entered into yield state as for bolt with BHRB335 texture and diameter of 20 mm, and the anchor also has entered into yield state as for anchor with a diameter of 15.24 mm. The force diagram of bolt and anchor is shown in Figure 20.

In conclusion, when the shallow surrounding rock stress of the roadway is relatively low, ordinary bolt support has a good effect on surrounding control, but the deformation of the roadway has not yet received an effective control on the whole, both bolt and anchor bear great tension and enter into yield state, and the supporting structure approaches destruction. Therefore, in order to

(a)

(b)

(c)
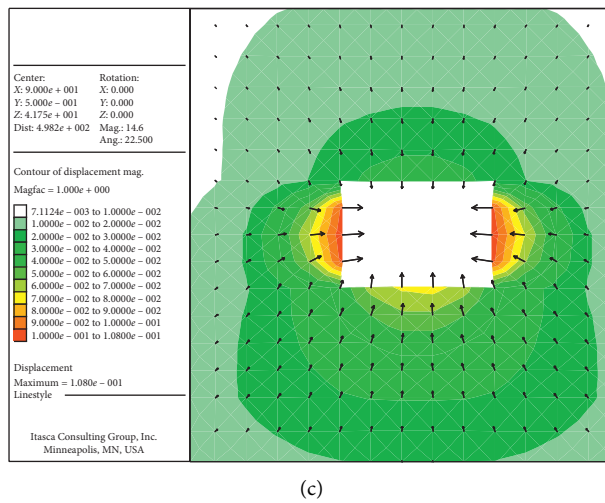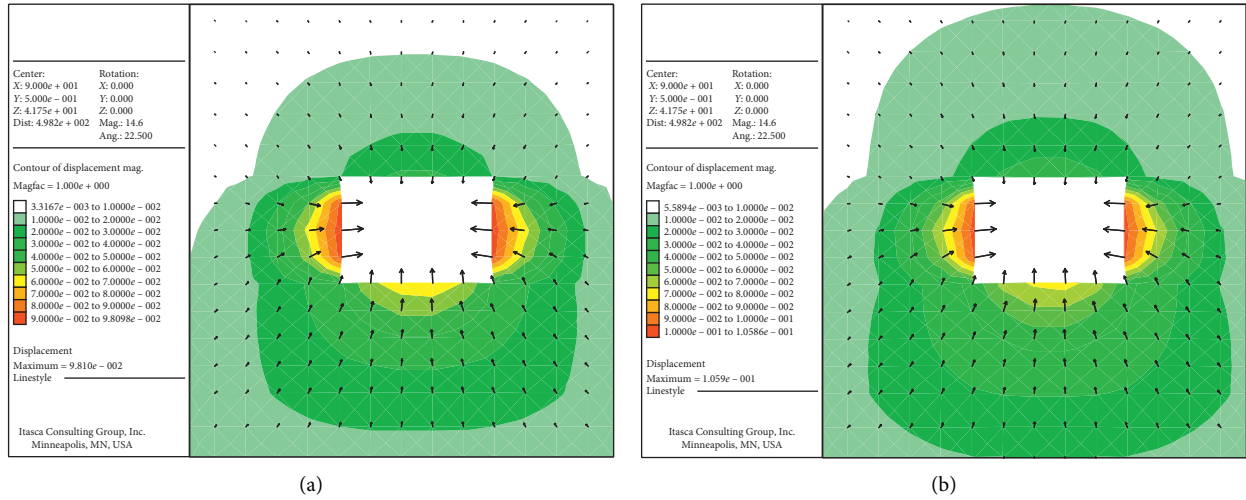
FIGURE 11: Cloud diagram of displacement. (a) 300 step; (b) 600 step; and (c) 2100 step.

(a)

(b)
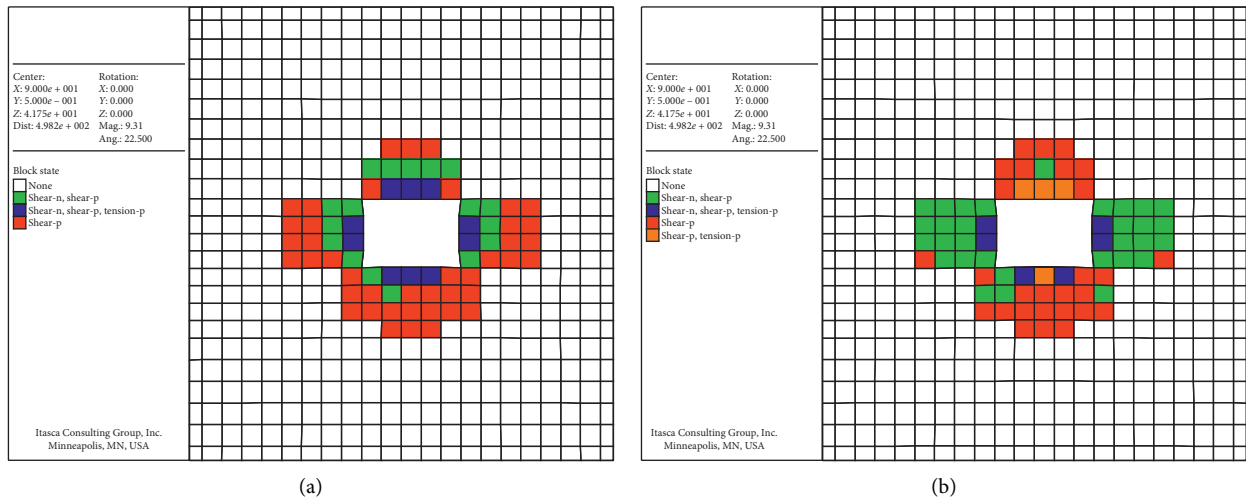
FIGURE 12: Continued.
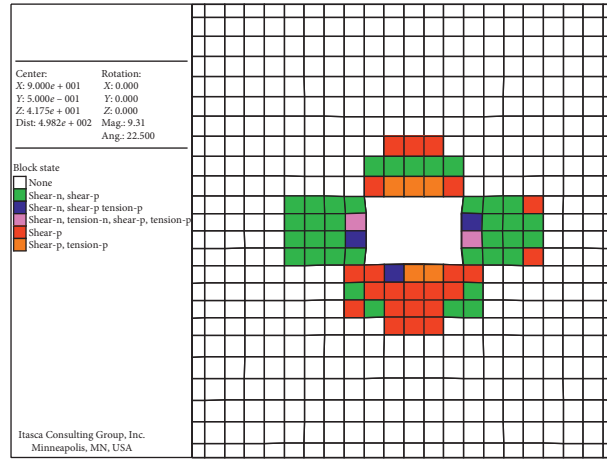
(c)

FIGURE 12: Cloud diagram of the plastic zone. (a) 300 step; (b) 600 step; and (c) 2100 step.

(a)
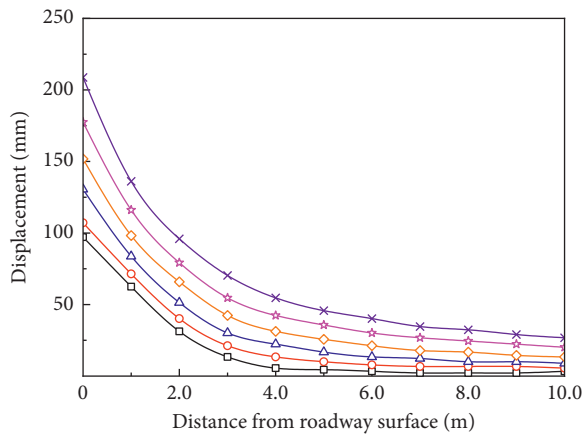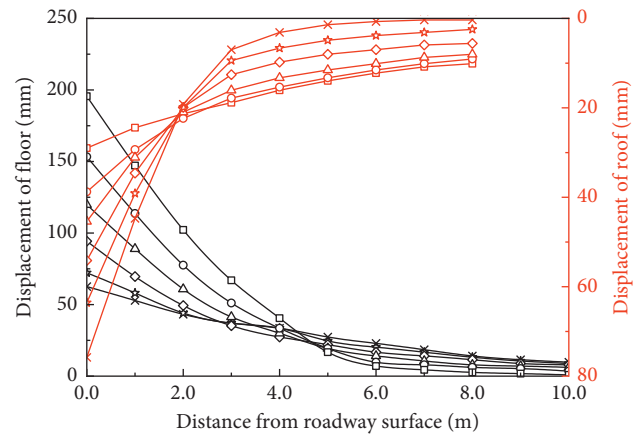
(b)

FIGURE 13: The displacement distribution of the roadway. (a) Two sides; (b) roof and floor.

(a)
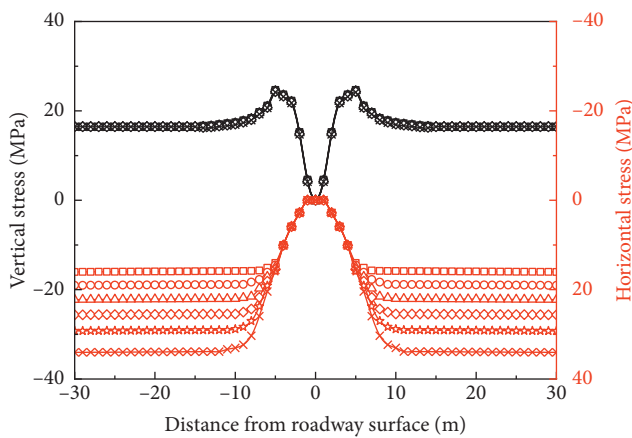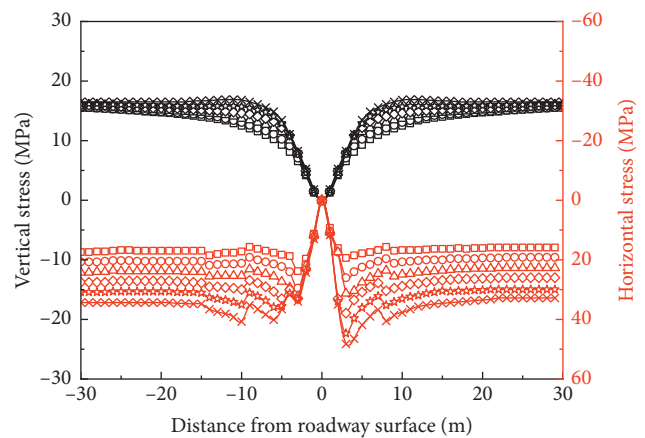
(b)

FIGURE 14: The stress distribution of the roadway. (a) Two sides; (b) roof and floor.
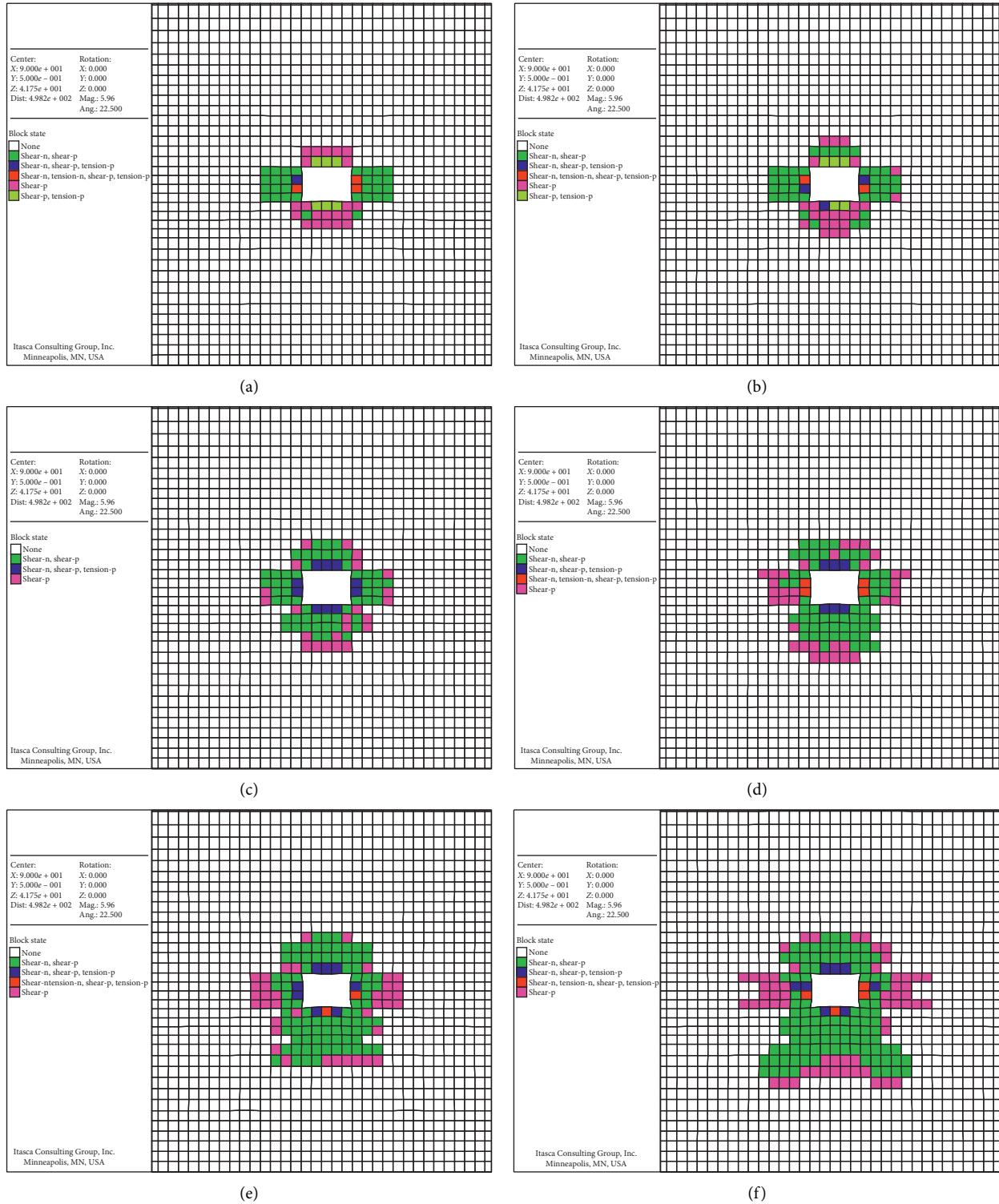
Figure 15: The plastic zone distribution of the roadway. (a) $\lambda = 1.0$; (b) $\lambda = 1.2$; (c) $\lambda = 1.4$; (d) $\lambda = 1.6$; (e) $\lambda = 1.8$; and (f) $\lambda = 2.0$.
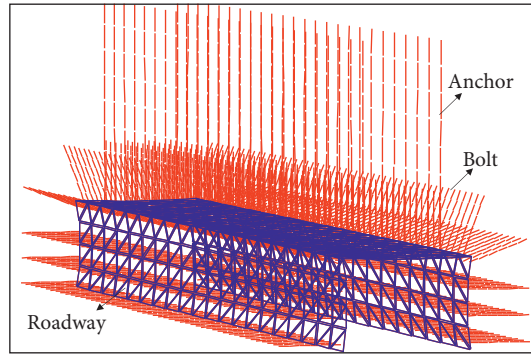
Figure 16: The bolt support structure of the roadway.
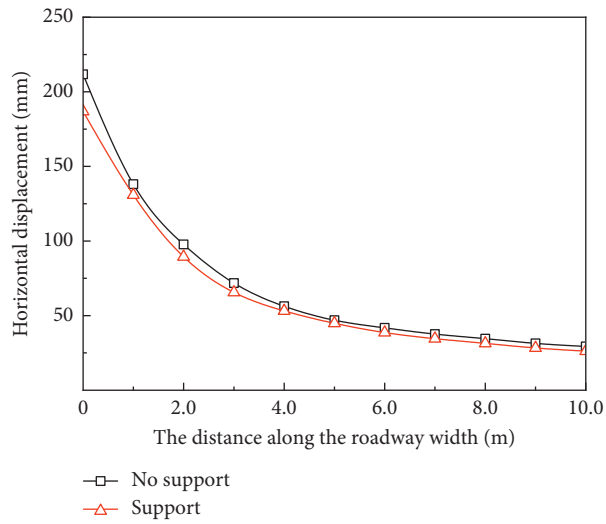
Figure 17: The horizontal displacement of the two sides of the roadway.

(a)

(b)
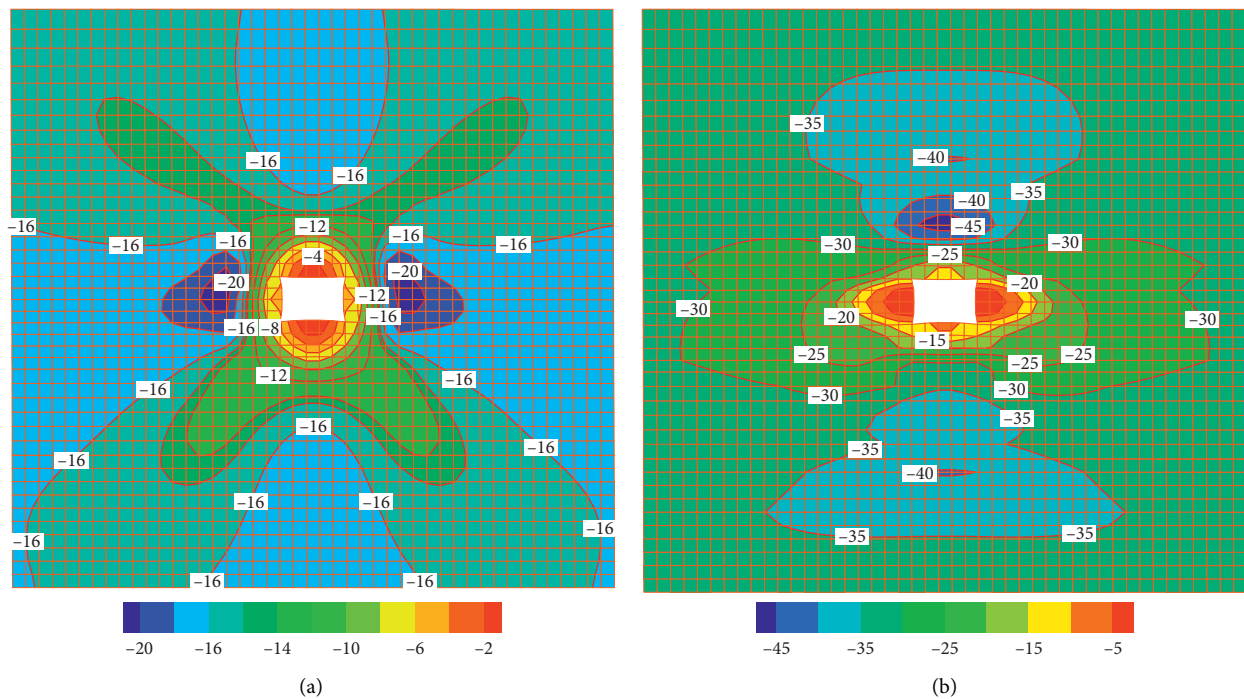
Figure 18: Continued.
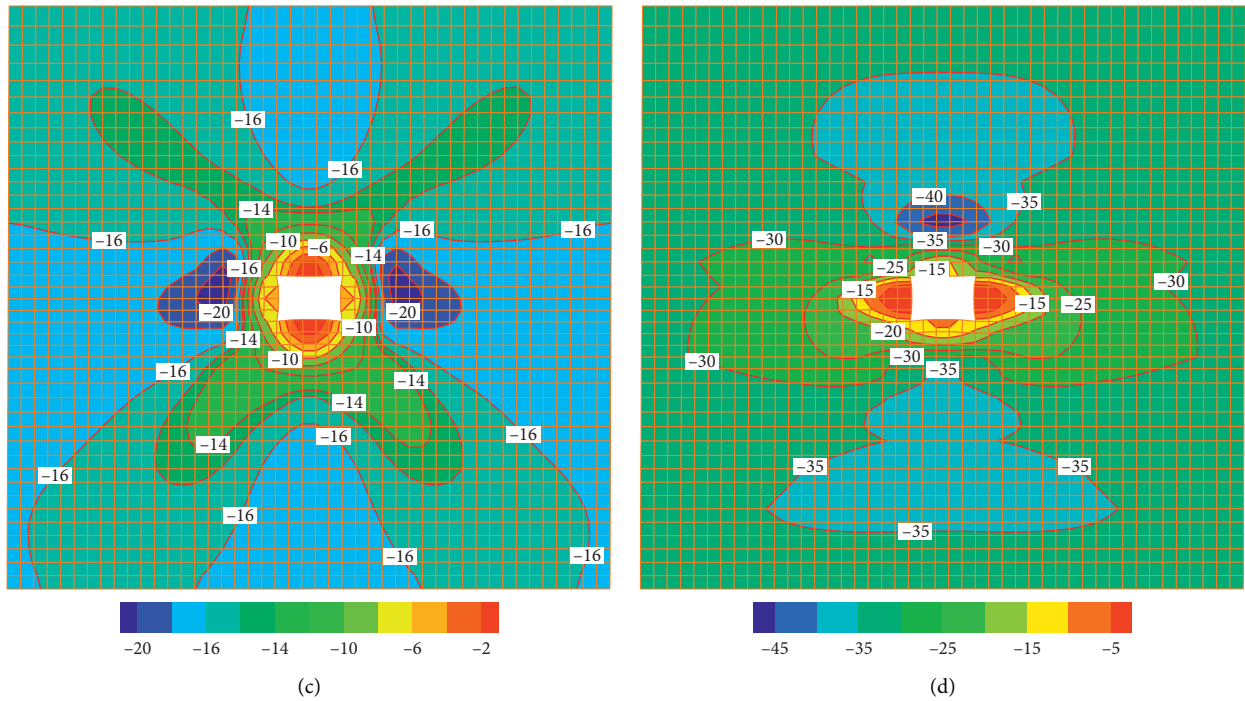
FIGURE 18: Cloud diagram of the roadway stress. (a) Vertical stress with no support; (b) horizontal stress with no support; (c) vertical stress with support; and (d) horizontal stress with support.
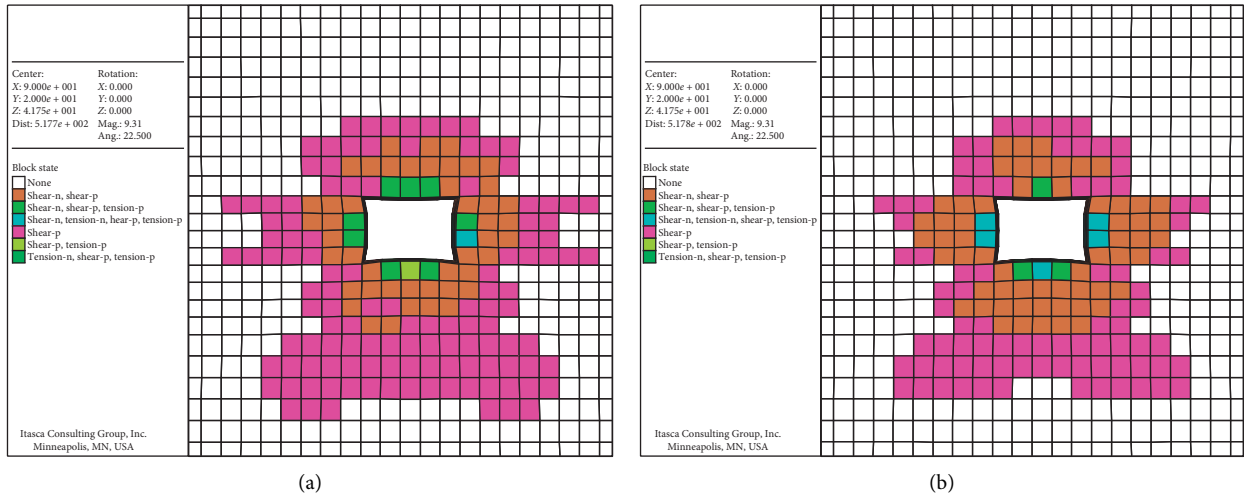
FIGURE 19: Cloud diagram of the plastic zone. (a) No support; (b) support.

ensure the stability of the deep roadway, it needs to adopt a high-strength anchor to make the surrounding rock depressurization on the basis of high support resistance, so as

to adapt to the characteristics of large and sharp deformation of the deep roadway, and make the roadway be in low stress environment, which is easy to be maintained.
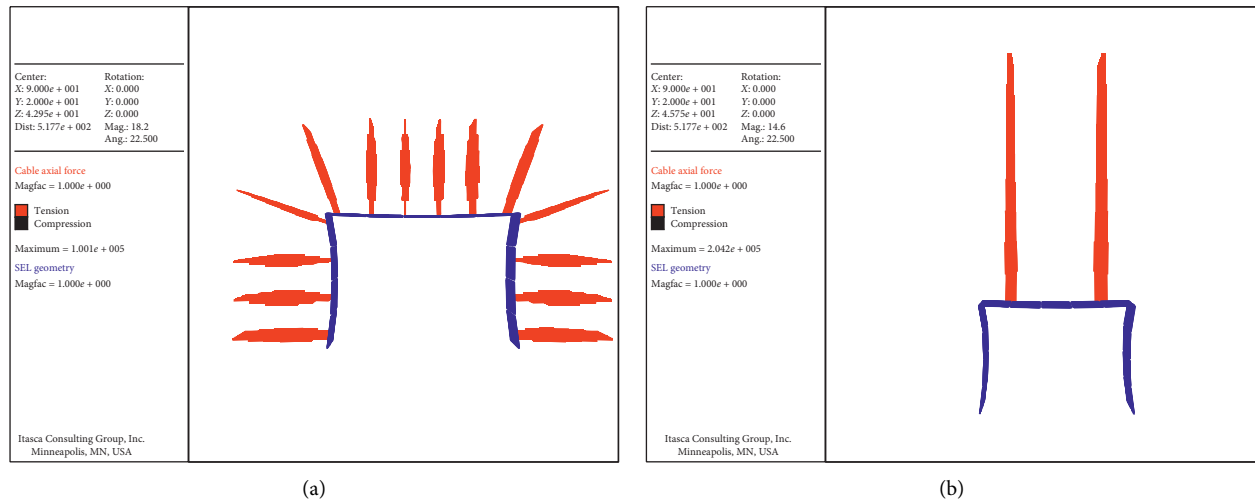
FIGURE 20: The force diagram of bolt and anchor is shown. (a) Bolt; (b) anchor.

7. Conclusion

(1) The mechanical model of the deep roadway was established, and the theoretical calculation formula of the plastic zone of the roadway is obtained. With the increase of the vertical stress, the plastic zone is expanding constantly, and especially, the diffusion from the humeral angle of the roadway towards the two sides is obvious. While, with the increase of the horizontal stress, there is the limit value of the roadway stability. The support intensity to the decrease of the scope of the plastic zone is not obvious.

(2) The distribution and evolution rule of stress, displacement, and the plastic zone of the deep roadway was obtained. The two sides form the stress concentration zone under the function of vertical stress; furthermore, the roof and floor shows large scope of the stress decreasing zone. Under the function of horizontal stress, it appears large scope of the horizontal stress concentration zone at the roof nad floor, and it appears the shear stress concentration zone at the side angle and vertex angle of the roadway, so the roof and floor rock masses are easy to occur shear failure. Therefore, the key to stabilize the deep roadway is to improve the strength of the surrounding rock, and especially the important load bearing parts of vertex angle and side angle.

(3) With the increase of horizontal stress, the surrounding rock loses stability quickly. However, when at the same place, the vertical stress of roof and floor is increasing constantly, and the vertical stress of the two sides keeps unchanged basically, while the horizontal stress of roof and floor is increasing constantly, and so as that of the two sides. The plastic zone of the roadway expands sharply, and the proportion of shear failure is bigger and bigger. Therefore, it is extremely important to enhance the stability of the two sides and control the floor heave on the basis of ensuring the stability of roof.

(4) When the shallow surrounding rock stress of the roadway is relatively low, ordinary bolt support has a good effect on surrounding control, but the deformation of the roadway has not yet received an effective control on the whole, both bolt and anchor bear great tension and enter into yield state, and the supporting structure approaches destruction. Therefore, it needs to adopt a high-strength anchor to make surrounding rock depressurization on the basis of high support resistance.

Data Availability

No data were used to support this study.

Conflicts of Interest

The authors declare that they have no conflicts of interest.

Authors' Contributions

Dingchao Chen conceived and designed the research. Xiangyu Wang performed the numerical simulation and field tests. Lianying Zhang provided theoretical guidance in the research process. Yang Yu analyzed the data and wrote the paper.

Acknowledgments

References

[1] S. C. Li, Q. Wang, H. T. Wang et al., "Model test study on surrounding rock deformation and failure mechanisms of deep roadways with thick top coal," *Tunnelling and Underground Space Technology*, vol. 47, pp. 52–63, 2015.

[2] M. Chen, S.-Q. Yang, Y.-C. Zhang, and C.-W. Zang, "Analysis of the failure mechanism and support technology for the dongtan deep coal roadway," *Geomechanics and Engineering*, vol. 11, no. 3, pp. 401–420, 2016.

[3] R.-H. Cao, P. Cao, and H. Lin, "A kind of control technology for squeezing failure in deep roadways: a case study," *Geomatics, Natural Hazards and Risk*, vol. 8, no. 2, pp. 1715–1729, 2017.

[4] X.-R. Meng, R. Peng, G.-M. Zhao, and Y.-M. Li, "Roadway engineering mechanical properties and roadway structural instability mechanisms in deep wells," *KSCE Journal of Civil Engineering*, vol. 22, no. 5, pp. 1954–1966, 2017.

[5] Q. Wang, R. Pan, B. Jiang et al., "Study on failure mechanism of roadway with soft rock in deep coal mine and confined concrete support system," *Engineering Failure Analysis*, vol. 81, pp. 155–177, 2017.

[6] G. Xue, J. Cheng, J. Guan et al., "The method for determining working resistance of advance support bracket in deep fully mechanized roadway based on flac3d," *Advances in Mechanical Engineering*, vol. 10, no. 6, 2018.

[7] J. Zhang, L. Liu, J. Cao, X. Yan, and F. Zhang, "Mechanism and application of concrete-filled steel tubular support in deep and high stress roadway," *Construction and Building Materials*, vol. 186, pp. 233–246, 2018.

[8] F. Qi and Z. Ma, "Investigation of the roof presplitting and rock mass filling approach on controlling large deformations and coal bumps in deep high-stress roadways," *Latin American Journal of Solids and Structures*, vol. 16, no. 4, 2019.

[9] Z. Xiao, J. Liu, S. Gu et al., "A control method of rock burst for dynamic roadway floor in deep mining mine," *Shock and Vibration*, vol. 2019, Article ID 7938491, 16 pages, 2019.

[10] Z. Xie, N. Zhang, X. Feng, D. Liang, Q. Wei, and M. Weng, "Investigation on the evolution and control of surrounding rock fracture under different supporting conditions in deep roadway during excavation period," *International Journal of Rock Mechanics and Mining Sciences*, vol. 123, 2019.

[11] C. J. Hou, "Effective approach for surrounding rock control in deep roadway," *Journal of China University of Mining and Technology*, vol. 46, no. 3, pp. 467–473, 2017.

[12] R. Peng, X. Meng, G. Zhao, Y. Li, and J. Zhu, "Experimental research on the structural instability mechanism and the effect of multi-echelon support of deep roadways in a kilometre-deep well," *PLoS One*, vol. 13, no. 2, Article ID e0192470, 2018.

[13] J. Zhang, L. Liu, J. Shao, and Q. Li, "Mechanical properties and application of right-hand rolling-thread steel bolt in deep and high-stress roadway," *Metals*, vol. 9, no. 3, p. 346, 2019.

[14] H. P. Kang, J. H. Wang, and J. Lin, "High pretensioned stress and intensive bolting system and its application in deep roadways," *Journal of China Coal Society*, vol. 32, no. 12, pp. 1233–1238, 2007.

[15] Z. Liu, A. Cao, G. Zhu, and C. Wang, "Numerical simulation and engineering practice for optimal parameters of deep-hole blasting in sidewalls of roadway," *Arabian Journal for Science and Engineering*, vol. 42, no. 9, pp. 3809–3818, 2017.

[16] C.-L. Dong, G.-M. Zhao, X.-Y. Lu, X.-R. Meng, Y.-M. Li, and X. Cheng, "Similar simulation device for unloading effect of deep roadway excavation and its application," *Journal of Mountain Science*, vol. 15, no. 5, pp. 1115–1128, 2018.

[17] W. Zhang, Z. He, D. Zhang, D. Qi, and W. Zhang, "Surrounding rock deformation control of asymmetrical roadway in deep three-soft coal seam: a case study," *Journal of Geophysics and Engineering*, vol. 15, no. 5, pp. 1917–1928, 2018.

[18] M. C. He and Z. B. Guo, "Mechanical property and engineering application of anchor bolt with constant resistance and large deformation," *Chinese Journal of Rock Mechanics and Engineering*, vol. 33, no. 7, pp. 1297–1308, 2014.

[19] X.-M. Sun, F. Chen, M.-C. He, W.-L. Gong, H.-C. Xu, and H. Lu, "Physical modeling of floor heave for the deep-buried roadway excavated in ten degree inclined strata using infrared thermal imaging technology," *Tunnelling and Underground Space Technology*, vol. 63, pp. 228–243, 2017.

[20] J. B. Bai and C. J. Hou, "Control principle of surrounding rocks in deep roadway and its application," *Journal of China University of Mining and Technology*, vol. 35, no. 2, pp. 145–148, 2006.

[21] S.-Q. Yang, M. Chen, H.-W. Jing, K.-F. Chen, and B. Meng, "A case study on large deformation failure mechanism of deep soft rock roadway in xin'an coal mine, China," *Engineering Geology*, vol. 217, pp. 89–101, 2017.

[22] D. Wang, Y. Jiang, X. Sun, H. Luan, and H. Zhang, "Nonlinear large deformation mechanism and stability control of deep soft rock roadway: a case study in China," *Sustainability*, vol. 11, no. 22, 2019.

[23] W. J. Wang, C. Yuan, W. J. Yu et al., "Control technology of reserved surrounding rock deformation in deep roadway under high stress," *Journal of China Coal Society*, vol. 41, no. 9, pp. 2156–2164, 2016.

[24] X. Shengrong, G. Mingming, C. Dongdong et al., "Stability influence factors analysis and construction of a deep beam anchorage structure in roadway roof," *International Journal of Mining Science and Technology*, vol. 28, no. 3, pp. 445–451, 2018.

[25] S. C. Li, H. P. Wang, Q. H. Qian et al., "In-situ monitoring research on zonal disintegration of surrounding rock mass in deep mine roadways," *Chinese Journal of Rock Mechanics and Engineering*, vol. 27, no. 8, pp. 1545–1553, 2008.

[26] Q. S. Liu, C. B. Lu, B. Liu, and X. W. Liu, "Research on the grouting diffusion mechanism and its application of grouting reinforcement in deep roadway," *Journal of Mining and Safety Engineering*, vol. 31, pp. 333–339, 2014.

[27] W. P. Huang, Q. Yuan, Y. L. Tan et al., "An innovative support technology employing a concrete-filled steel tubular structure for a 1000 m-deep roadway in a high in situ stress field," *Tunnelling and Underground Space Technology*, vol. 73, pp. 26–36, 2018.

[28] C. Wang, L. Liu, D. Elmo et al., "Improved energy balance theory applied to roadway support design in deep mining," *Journal of Geophysics and Engineering*, vol. 15, no. 4, pp. 1588–1601, 2018.

[29] Y. Yuan, W. Wang, S. Li, and Y. Zhu, "Failure mechanism for surrounding rock of deep circular roadway in coal mine based on mining-induced plastic zone," *Advances in Civil Engineering*, vol. 2018, Article ID 1835381, 14 pages, 2018.

[30] J. C. Chang and G. X. Xie, "Mechanical characteristics and stability control of rock roadway surrounding rock in deep mine," *Journal of China Coal Society*, vol. 34, no. 7, pp. 881–886, 2009.

[31] Y. Cheng, J. Bai, Y. Ma, J. Sun, Y. Liang, and F. Jiang, "Control mechanism of rock burst in the floor of roadway driven along next goaf in thick coal seam with large obliquity angle in deep well," *Shock and Vibration*, vol. 2015, Article ID 750807, 10 pages, 2015.

[32] B. Jiang, L. Wang, Y. Lu, S. Gu, and X. Sun, "Failure mechanism analysis and support design for deep composite soft rock roadway: a case study of the yangcheng coal mine in China," *Shock and Vibration*, vol. 2015, Article ID 452479, 14 pages, 2015.

[33] J. K. Long, "The mechanism of synergetic anchorage in deep roadway surrounding rock," *Journal of Mining and Safety Engineering*, vol. 33, no. 1, pp. 19–26, 2016.

[34] J. Ning, J. Wang, Y. Tan, and X. Shi, "Dissipation of impact stress waves within the artificial blasting damage zone in the surrounding rocks of deep roadway," *Shock and Vibration*, vol. 2016, Article ID 4629254, 13 pages, 2016.

[35] R. Pan, Q. Wang, B. Jiang et al., "Failure of bolt support and experimental study on the parameters of bolt-grouting for supporting the roadways in deep coal seam," *Engineering Failure Analysis*, vol. 80, pp. 218–233, 2017.

[36] H. Zhang, X. Miao, G. Zhang, Y. Wu, and Y. Chen, "Non-destructive testing and pre-warning analysis on the quality of bolt support in deep roadways of mining districts," *International Journal of Mining Science and Technology*, vol. 27, no. 6, pp. 989–998, 2017.

[37] J. P. Zuo, X. Wei, J. Wang, D. J. Liu, and F. Cui, "Investigation of failure mechanism and model for rocks in deep roadway under stress gradient effect," *Journal of China University of Mining and Technology*, vol. 47, no. 3, pp. 478–485, 2018.

[38] G. Li, F. Ma, G. Liu, H. Zhao, and J. Guo, "A strain-softening constitutive model of heterogeneous rock mass considering statistical damage and its application in numerical modeling of deep roadways," *Sustainability*, vol. 11, no. 8, 2019.

[39] Q. Li, J. Li, J. Zhang et al., "Numerical simulation analysis of new steel sets used for roadway support in coal mines," *Metals*, vol. 9, no. 5, 2019.

[40] S. Huang and S. Zheng, "Stressing state analysis of CFST arch supports in deep roadway based on NSF method," *Applied Sciences*, vol. 9, no. 20, 2019.

[41] Z. Xu, *Elasticity*, China Higher Education Press, Peking, China, 4th edition, 2006.

[42] C. Hou and P. Gou, "Mechanism study on strength enhancement for the rocks surrounding roadway supported by bolt," *Chinese Journal of Rock Mechanics and Engineering*, vol. 19, no. 3, pp. 342–345, 2000.

[43] W. Yu, B. Pan, F. Zhang, S. Yao, and F. Liu, "Deformation characteristics and determination of optimum supporting time of alteration rock mass in deep mine," *KSCE Journal of Civil Engineering*, vol. 23, no. 11, pp. 4921–4932, 2019.

Research Article

Semianalytical Solution for Large Deformation of Salt Cavern with Strain-Softening Behavior

Lina Ran ,[1] Huabin Zhang ,[2] and Qingqing Zhang [2]

[1]*PetroChina Research Institute of Petroleum Exploration & Development, 100083, China*
[2]*School of Mechanical and Engineering, Liaoning Technical University, Fuxin 123000, China*

Correspondence should be addressed to Huabin Zhang; lgd_zhb@163.com

A semianalytical solution of stress and displacement in the strain-softening and plastic flow zones of a salt cavern is presented. The solution is derived by adopting the large deformation theory, considering the nonlinear Hoek–Brown (H-B) strength criterion. The Romberg method is used to carry out numerical calculation, and then, the large deformation law of displacement is analyzed. The results are compared with those obtained by former numerical methods, and the solutions are validated. The results indicate that the displacement of the plastic zone decreases with the increase in distance away from the salt cavern. Similarly, it decreases with an increase in the geological strength index or running pressure, with the running pressure having a more significant effect on the displacement. It increases with the dilation angle, and the impact degree gradually increases. Compared with the softening parameter, h, of the plastic zone, the flow parameter, f, has little impact on the displacement. The displacement of the plastic zone obviously increased when considering the strain-softening of salt rock. When considering the shear dilation and softening behaviors of salt rock, the analytical solution obtained by employing the experiential regression Hoek–Brown (H-B) criterion, which considers many factors such as the structural characteristics of the salt formation and the rock mass quality, is safer and closer to the actual situation. This study can provide reference for many applications, including but not confined to analyzing the deformation of the surrounding rock of an underground salt cavern storage facility during construction.

1. Introduction

Salt caverns are considered the best places in the world for energy reserves [1–5]. The reason is that salt cavern storage facilities, compared to other underground storage facilities, have many advantages. For example, it has simple hydrological conditions, a wide distribution range, and a complete structure and stratum status. Moreover, the mechanical properties of rock salt, compact structure, low porosity and permeability, and damage self-recovery capability can ensure the safety of salt cavern. An underground salt cavern storage facility can be constructed using a water solution to form underground adits in deep salt formations. However, the redistribution of the stress and strain around the cavity and the damage to the mechanical properties of the surrounding rock are closely linked with the solution process. In recent years, seal failure, volume

shrinkage, excessive deformation or heavy collapse, serious ground subsidence, etc. have become among the most arduous challenges to the engineers. For example, in the Hutchison salt cavern gas storage in Kansas, USA, a ground subsidence with 90 m in diameter was observed. Internal pressure caused excessive volume shrinkage, and the Eminence salt cavern storage in Mississippi, USA, lost about 40% of its volume in 2 years [6]. Thus, analysis of the stability of underground salt cavern gas storage is very important for controlling this hazard.

In order to ensure the safety and stability of underground adits, a large number of analytical methods for the stress and deformation of the surrounding rock have been suggested for ideal underground spherical caverns in the past. For stability analysis of deep underground cavity, the Hoek–Brown (H-B) failure criterion has been found to be more suitable than the commonly used Mohr–Coulomb

(M-C) criterion. The H-B failure criterion was proposed for hard rock masses and very poor qualities of rock masses. It can reflect the inherent nonlinear damage characteristics of rock masses. Using the nonlinear H-B failure criterion, Brown et al. [7] derived a solution for the stress and displacement of the plastic zone of a tunnel. Using the nonassociated flow rules and considering three cases for the elastic strain of the plastic zone, Park and Kim [8] put forward a solution for the displacement of the plastic zone of a circular tunnel. Employing the H-B criterion, Lee and Pietruszczak [9] analyzed the stress and deformation field of circular adits with strain-softening behavior and presented a solution for the surrounding rock of a tunnel by assuming that the criterion parameters were linearly transformed with the shear strain. Introducing the nonassociated flow rules in the design of a hydropower tunnel, Rojat et al. [10] derived a closed-form solution for the surrounding rock of a tunnel using the H-B criterion. Park [11] dealt with a similarity solution for a spherical or circular adits excavated in elastic-strain-softening rock mass compatible with the M-C or H-B yield criterion. The partial differential equations from stress equilibrium, constitutive law, and consistency equations are simplified with first-order ordinary differential equations that solved via the Runge–Kutta (R-K) method. In China, Liu and Lin [12] derived the elastoplastic deformation of a tunnel by adopting the M-C criterion. Adopting the H-B strength theory and limit equilibrium equation, Yao et al. [13] and Pan et al. [14] conducted elastoplastic analyses of the surrounding rock in an idealized roadway with hydrostatic pressure. Wang et al. [15] proposed a brittle-plastic solution of a spherical cavity, and the solution is used in the strain-softening analysis. They also proposed numerical solutions and studied their application to determining stress–strain curve of strain-softening H-B rock masses. Wang et al. [16] proposed an elastic analytical solution for a spherical salt cavern with a lateral pressure coefficient (λ) and used the H-B failure criterion to derive the internal pressure limit when the plastic failure of the gas storage cavern did not appear. In order to study excavation problems for tunnels exhibiting strain-softening behavior, considering the effect of the confining stress, Wen and Yang [17] and Cai et al. [18] conducted numerical calculations by adopting the R-K method. They obtained the deformation around a tunnel and analyzed the displacement of the surrounding rock of a deep underground chamber by using the H-B criterion. Using the elastoplastic theory, Wang et al. [19], Fan et al. [20], and Hu and Zhu [21] presented analytical solutions to the expansion of spherical cavities and analyzed the effects of softening and shear dilation on the spherical expansion. Adopting the M-C criterion and nonassociated flow rule and introducing the large deformation theory, Wang and Zhu [22] obtained an elastoplastic analytical solution to the cavity expansion. Zhang et al. [23] established a multistep brittle-plastic model by simplifying the strain-softening process of the postfailure region, and they proposed analytical solutions of a spherical cavern with considering the deterioration of elastic parameters. Both M-C and H-B criteria are included in their analysis. Zhang et al. [24] analyzed the stress and deformation of the surrounding rock in a spherical salt cavern under ideal elastoplastic conditions, and they predicted the creep deformation of the surrounding rock via theoretical analysis.

The analytical elastoplastic solution for a space problem accounting for large deformation requires a complicated mathematical deduction, and, even when it is combined with a numerical method, there are a limited number of studies that can be referenced. Wang and Qian [25] proposed a finite difference method. Adopting the large deformation theory, Guan et al. [26] proposed a numerical procedure that reflects the strain-softening behavior and studied the instability problem of a plane strain axially symmetric tunnel. The above studies mainly involved two-dimensional research on circular tunnels. Jiang et al. [27] provided key information for predicting deformational performance for a tunnel undergoing large deformation problem. Zhang et al. [28] presented a large strain numerical solution of a circular tunnel for the ground reaction curve in strain-softening rock masses. In consideration of the tunnelling-induced large deformation, Mo et al. [29] analyzed the cavity contraction in M-C and H-B media.

In the previous results for salt cavern storage projects, there has been little information on the large deformation [30] properties of salt rock, and these results were obtained mainly by employing the M-C criterion. Accounting for the erosion effect of solution mining on the cavity wall, the H-B criterion, which is based on empirical regression, is especially practical with salt cavern gas storage. Hence, this paper considers the large deformation around a salt cavern by introducing the H-B criterion and taking the strain-softening property of salt rock into account. This study can have significant implications for the design and construction of a deep hollow spherical domain.

2. Mechanics Model for Spherical Salt Cavern Gas Storage

In situ investigations indicated that salt caverns have all irregular shapes; they are different from each other. Most of the salt storage caverns are pear-like in the design stage. However, in order to facilitate the theoretical analysis and derivation, we can establish a spherical symmetry model for the stability analysis of a salt cavern under hydrostatic stress (side pressure coefficient is 1). Salt cavern gas storage is here regarded as a deep hollow spherical domain subjected to internal and external pressures, the radius of the salt cavern is designated as R_0. The gas pressure (approximately homogeneous running pressure), p_i, and hydrostatic pressure, p_0, are the inner and outer boundaries of the model, respectively. Gravity and side pressure coefficient are not considered in the model. In order to meet the demands of spherical symmetry, the coordinate origin of the salt cavern mechanics model is designated in the center of the spherical adits. It agrees with the hypothesis of isotropy during the construction of a salt cavern. There exist elastic and plastic zones around the salt cavern. The far filed of the cavern ($R_2 \longrightarrow \infty$) enters into an elastic state. The stress of the elastic zone is smaller than the strength of the salt rock; as a result, the deformations can recover after unloading. At $r = R_2$, the radial stress and tangential strain are designated as σ_{R2} and ε_{R2},

respectively. The near-zone of the cavern ($R_1 \longrightarrow R_2$) enters into a strain-softening state. The rock in the strain-softening zone will undergo microcrack propagation and plastic deformation. At $r = R_1$, the radial stress and tangential strain are designated as σ_{R1} and ε_{R1}, respectively. Likewise, the near-zone of the cavern ($R_0 \longrightarrow R_1$) enters into a plastic flow state. The rock in the plastic flow zone undergoes ultimate failure. What is more, the salt rock around the cavity satisfies the continuity conditions both in the elastoplastic interface, $r = R_2$, and in the interface of the strain-softening and plastic flow zones, $r = R_1$. Figure 1 shows the elastoplastic model of the rock surrounding spherical salt cavity.

The rock salt formation where salt cavern gas storage is located has a depth arranging from 1000 to 2000 m, so surrounding rock of the salt cavern is situated in high geostress levels. In situ investigations and compression tests indicated that the large plastic deformation played an unneglectable role during the analysis of the mechanical properties of rock salt under triaxial stress. Thus, the shear dilatation and strain-softening properties of rock salt [30–33] are considered in this study, and a strain-softening mechanical model is used.

3. Strength Criterion

The generalized H-B criterion is an experiential regression strength criterion. The H-B failure criterion was proposed in 1980s originally as follows [34]:

$$\sigma_1 = \sigma_3 + \sigma_c \left(m_i \frac{\sigma_3}{\sigma_c} + 1 \right)^{1/2}, \tag{1a}$$

where σ_c is the uniaxial compressive strength of the intact rock (MPa) and m_i is a dimensionless material constant, with the value of m_i varying from 0.001 to 25.0.

To eliminate some of the deficiencies with the application of the original H-B failure criterion, a modified rock mass failure criterion has been developed and is presented by Hoek et al. [35]. Hoek et al. suggested a specific form of the strength criterion:

$$\sigma_1 = \sigma_3 + \sigma_{ci} \left(m_b \frac{\sigma_3}{\sigma_{ci}} + s \right)^a, \tag{1b}$$

where σ_{ci} is the uniaxial compressive strength of the intact rock (MPa) and m_b, s, and a are dimensionless material constants.

The H-B failure criterion was updated by discussing the use of the geological strength index (GSI) to describe the structure and condition of a wide range of types of rock masses and the selection of the disturbance factor D [36, 37]. The dimensionless material constants m_b, s, and a can be calculated by (2) [36, 37]. The parameter a varies over a range from 0.5 to 0.666, where $a = (1/2) + (1/6)(e^{-(\text{GSI}/15)} - e^{-20/3})$. Considering the difficulty to obtain theoretical solutions of nonlinear numerical problems, to simplify the calculation, the commonly used H-B strength criterion equation (1b) is used and the parameter a is given a value of 0.5 in this paper:

$$\left.\begin{aligned} m_b^{\text{peak}} &= m_i e^{\left(\left(\text{GSI}^{\text{peak}} - 100\right)/(28 - 14D)\right)} \\ s^{\text{peak}} &= e^{\left(\left(\text{GSI}^{\text{peak}} - 100\right)/(9 - 3D)\right)} \end{aligned}\right\},$$
$$\left.\begin{aligned} m_b^{\text{res}} &= m_i e^{\left(\left(\text{GSI}^{\text{res}} - 100\right)/28\right)} \\ s^{\text{res}} &= e^{\left(\left(\text{GSI}^{\text{res}} - 100\right)/9\right)} \end{aligned}\right\}, \tag{2}$$

where the superscripts "peak" and "res" represent the peak parameter and residual parameter, respectively. Hoek and Brown proposed a nonlinear relation between the major and minor principal stresses at failure, assuming independence of the intermediate principal stress [29]. In recent years, many studies on generalized three-dimensional H-B strength criterion have been carried out [38–41]. The commonly used H-B criterion is modified continuously, and the generalized three-dimensional model is the future direction in the research and application.

4. Solutions in the Elastic Zone

For the symmetry of a spherical salt cavern subjected to homogeneous internal and external pressures, the corresponding relationships between both the stresses and the strains can be written as $\sigma_1 = \sigma_2 = \sigma_\theta = \sigma_\varphi, \sigma_3 = \sigma_r$ and $\varepsilon_1 = \varepsilon_2 = \varepsilon_\theta = \varepsilon_\varphi, \varepsilon_3 = \varepsilon_r$. As a result, the salt rock around the cavern satisfies the force equilibrium equation:

$$\frac{d\sigma_r}{dr} + \frac{2}{r}\left(\sigma_r - \sigma_\theta\right) = 0. \tag{3}$$

The compressive stress is assumed to be positive, the initial in situ stress p_0 is not considered, and the stresses and strains in the elastic zone can be obtained, respectively, as follows:

$$\begin{cases} \sigma_{re} = \left(1 - \left(\dfrac{R_2}{r}\right)^3\right)p_0 + \left(\dfrac{R_2}{r}\right)^3 \sigma_{R2}, \\[4mm] \sigma_{\theta e} = \left(1 + \dfrac{1}{2}\left(\dfrac{R_2}{r}\right)^3\right)p_0 - \dfrac{1}{2}\left(\dfrac{R_2}{r}\right)^3 \sigma_{R2}, \end{cases} \tag{4}$$

$$\begin{cases} \varepsilon_{re} = \dfrac{1}{E}\left[\left(\sigma_{re} - p_0\right) - 2\mu\left(\sigma_{\theta e} - p_0\right)\right], \\[4mm] \varepsilon_{\theta e} = \dfrac{1}{E}\left[\left(\sigma_{\theta e} - p_0\right) - \mu\left(\sigma_{re} + \sigma_{\theta e} - 2p_0\right)\right]. \end{cases} \tag{5}$$

Then, the elastic strains within the elastic zone at $r = R_2$ can be written as follows:

$$\begin{cases} \varepsilon_{re} = \delta, \\[4mm] \varepsilon_{\theta e} = -\dfrac{1}{2}\delta, \end{cases} \tag{6}$$

where $\delta = (1/2G)(\sigma_{R2} - p_0)$ and $G = (E/2(1 + \mu))$.

What is more, the displacement caused by the salt cavern's construction can be derived as follows:
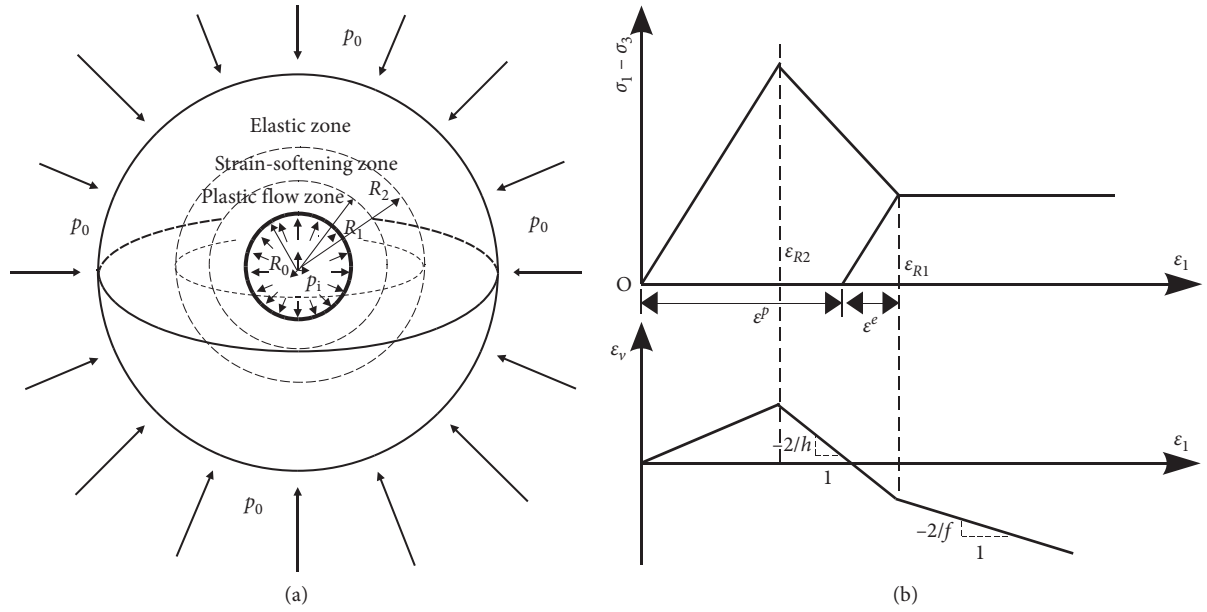
FIGURE 1: Elastoplastic model of spherical salt cavern. (a) Sketch of salt cavern deformation zones. (b) Simplified model of salt rock with strain-softening behavior.

$$u_e(r) = \frac{1}{4G}(\sigma_{R2} - p_0)\frac{R_2^3}{r^2}. \tag{7}$$

Assuming that $\sigma|_{r=R_2} = \sigma_{R2}$, σ_{R_2} represents the radial stress at $r = R_2$. The values of R_2 and σ_{R2} are not yet known. When elastic–perfectly plastic model is used, and strength parameters m and s in the H-B yield criterion are constant values, the values of R_2 and σ_{R2} can be obtained [24]. However, if strain-softening occurs in the plastic zone and if m and s in the H-B criterion change after peak strength, numerical methods have to be used to get the values of R_2 and/or σ_{R2}. Besides, the stresses and strains, on the interface between elastic zone and softening zone and on the interface between softening zone and residual zone, have to be used in the solving process; the detail determination method of the elastoplastic interface and its corresponding stress will be analyzed later. Meanwhile, the stresses and displacements at the elasto-softening interface have to be used to obtain the stresses and displacements on the softening zone and the residual zone.

5. Stress Analysis in the Plastic Zone

5.1. Stress and Radius of the Strain-Softening Zone. Within the near-zone of a salt cavern, $R_1 \leq r \leq R_2$, to build the H-B softening constitutive model, it is of critical importance to define a variable as the softening coefficient, which can reflect the linear degradation law of each softening model parameter during the strain-softening process (Figure 2). The coefficient is given as $\eta = \varepsilon_{\theta s}^p$, where $\varepsilon_{\theta s}^p$ is the tangential plastic strain in the strain-softening zone. The functional relation between $\omega(\eta)$ and η is established as follows:
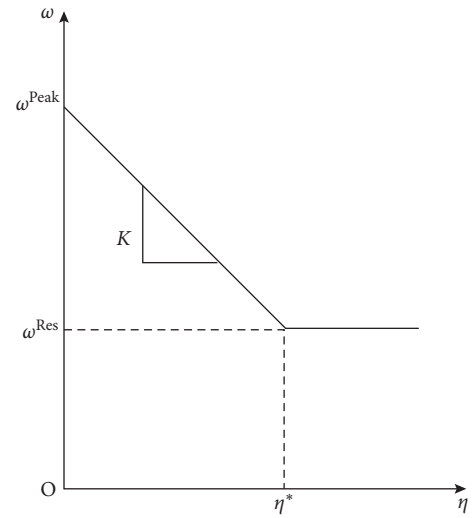
FIGURE 2: Relationships between softening coefficient and H-B parameters.

$$\omega(\eta) = \begin{cases} \dfrac{\omega^{res} - \omega^{peak}}{\eta^*}\eta + \omega^{peak}, & 0 \leq \eta < \eta^*, \\ \\ \omega^{res}, & \eta \geq \eta^*, \end{cases} \tag{8}$$

where $\omega(\eta)$ can be used to describe the H-B parameter m_b^s or s^s; ω^{peak} and ω^{res} are the corresponding peak parameter and residue parameter, respectively, and can be obtained by substituting GSI^{peak} and GSI^{res} into (2), respectively; and η^* represents the residue value of η.

According to the definition of the softening coefficient, we can obtain the following:

$$\begin{cases} K \longrightarrow \infty \,(\text{elastic} - \text{brittle} - \text{plasticity}), & \eta^* = 0, \\ K = 0 \,(\text{ideal elasto} - \text{plastic}), & \eta^* \longrightarrow \infty, \end{cases}$$
(9)

where, the parameter K is the curve slope for the strain-softening process. When $K = 0$, the elastic-brittle-plasticity model degenerated to an ideal elastoplastic model [42].

After the rock around the cavern enters the strain-softening state, $\sigma_{\theta s}(\eta)$ and $\sigma_{rs}(\eta)$ vary with the softening coefficient and conform to the H-B criterion. To determine the stress within the strain-softening zone, the classical H-B criterion can be rewritten as follows:

$$\sigma_{\theta s}(\eta) = \sigma_{rs}(\eta) + \sigma_{ci}\left[m_b^s \frac{\sigma_{rs}(\eta)}{\sigma_{ci}} + s^s \right]^{1/2}.$$
(10)

Combining (3) and (10), the radial stress can be derived as follows:

$$\frac{1}{m_b^s}\left(m_b^s \frac{\sigma_{rs}(\eta)}{\sigma_{ci}} + s^s \right)^{1/2} = \ln r + C.$$
(11)

Substituting $\sigma_{rs} = \sigma_{R2}$ into (11) at $r = R_2$, we can obtain the radial stress of the strain-softening zone as follows:

$$\sigma_{rs}(\eta) = \sigma_{R2} + 2A_1 \ln\left(\frac{r}{R_2}\right) + A_2 \ln^2\left(\frac{r}{R_2}\right),$$
(12)

where $A_1 = \sqrt{m_b^s \sigma_{ci} \sigma_{R2} + s^s \sigma_{ci}^2}$; $A_2 = m_b^s \sigma_{ci}$; m_b^s and s^s vary with the variation of softening coefficient η; and $0 \le \eta \le \eta^*$.

According to (10), the tangential stress can be determined as follows:

$$\sigma_{\theta s}(\eta) = \sigma_{rs}(\eta) + A_1 + A_2 \ln\left(\frac{r}{R_2}\right).$$
(13)

Accounting for the boundary condition at $r = R_2$, we can obtain the following:

$$3\sigma_{R2} + 2\sqrt{m_b^s \sigma_{ci} \sigma_{R2} + s^s \sigma_{ci}^2} - 3p_0 = 0,$$
(14)

where the parameters m_b^s and s^s are given the residual values.

Because (14) is a nonlinear equation, $f(\sigma_{R2}) = 0$, the iteration method can be employed to determine the value of σ_{R2} in the strain-softening zone at $r = R_2$. To determine the radius of the strain-softening zone, adding the stress–strain curve in Figure 1(b) and assuming that the elastic strain in the plastic zone abides by Hooke's law, we can express the stress in the strain-softening zone as follows:

$$\sigma_{\theta s} - \sigma_{rs} = \frac{3}{2}(p_0 - \sigma_{R2}) - \lambda\left(\varepsilon_{\theta s} - \frac{\sigma_{\theta s} - \sigma_{rs}}{E}\right),$$
(15)

where $\lambda = ((\text{GSI}^{\text{peak}} - \text{GSI}^{\text{res}})/(\varepsilon_{R1} - \varepsilon_{R2}))$.

Considering the boundary conditions at $r = R_1$ and combining (13) and (15), assuming $(R_1/R_2) = t$, we can obtain the following:

$$A_1^{R1} + A_2^{R1} \ln t - \frac{3}{2}(p_0 - \sigma_{R2}) + \lambda\left(\varepsilon_{R1} - \frac{\sigma_{\theta s} - \sigma_{rs}}{E}\right) = 0,$$
(16)

where A_1^{R1} and A_2^{R1} are obtained by m_b^s and s^s at $r = R_1$, respectively.

5.2. Stress and Radius in the Plastic Flow Zone.

Within the near-zone of a salt cavern, $R_0 \le r \le R_1$, the stress satisfies (1b) and (3). The H-B parameters m_b^r and s^r are residual values, which can be derived by combining (2) and parameter GSI$^{\text{res}}$. Combining (1b) and (3) results, we obtain the radial stress of the plastic flow zone as

$$\frac{1}{m_b^r}\left(m_b^r \frac{\sigma_{rr}}{\sigma_{ci}} + s^r \right)^{1/2} = \ln r + C.$$
(17)

Substituting $\sigma_{rr} = p_i$ into (17) at $r = R_0$ results in the radial stress:

$$\sigma_{rr} = p_i + 2B_1 \ln\left(\frac{r}{R_0}\right) + B_2 \ln^2\left(\frac{r}{R_0}\right),$$
(18)

where $B_1 = \sqrt{m_b^r \sigma_{ci} p_i + s^r \sigma_{ci}^2}$ and $B_2 = m_b^r \sigma_{ci}$.

Adding (1b), we can determine the stress of the plastic flow zone, $\sigma_{\theta r}$, as follows:

$$\sigma_{\theta r} = \sigma_{rr} + B_1 + B_2 \ln\left(\frac{r}{R_0}\right).$$
(19)

Accounting for the continuous conditions, at $r = R_1$, the stress of the plastic flow zone σ_{rr} should equal that of the strain-softening zone σ_{rs}. Combining (12) and (18), we can obtain the radial stress as

$$\sigma_{R1} = p_i + 2B_1 \ln\left(\frac{R_1}{R_0}\right) + B_2 \ln^2\left(\frac{R_1}{R_0}\right)$$
$$= \sigma_{R2} + 2A_1 \ln t + A_2 \ln^2 t.$$
(20)

Adding (20), we can determine the range of the plastic flow zone as

$$R_1 = R_0 e^{\left(\sqrt{B_1^2 + B_2 B_3} - B_1\right)/B_2},$$
(21)

where $B_3 = \sigma_{R1} - p_i$.

6. Deformation Analysis in the Plastic Zone

According to the plastic theory, the strain in the plastic zone can be divided into the elastic and plastic strains. For salt rock, the large strain theory is more suitable for the plastic strain. Generally when the degree of deformation is less than 10%, it can be expressed by engineering strain; otherwise, logarithmic strain should be used. The deformation of salt rock under triaxial stress state indicates the large deformation characteristics of salt rock under high confining pressure. Using the logarithmic strain to analyze the large deformation characteristics of salt rock is more suitable [30]. Therefore, the strain can be expressed in the logarithmic form as $\varepsilon = \int_{r_0}^r (\mathrm{d}l/l) = \ln(r/r_0)$, where r_0 and r are variables in the calculations. Then, the geometric equation can be rewritten as (22). Although the elastic strain in the plastic zone has various definitions [43], it is assumed that it conforms to Hooke's law in this study:

$$\varepsilon_r = \ln \frac{\mathrm{d}r}{\mathrm{d}r_0},$$

$$\varepsilon_\theta = \varepsilon_\varphi = \ln \frac{r}{r_0}. \tag{22}$$

6.1. Displacement Analysis in the Strain-Softening Zone.
In the zone of $R_1 \le r \le R_2$, the strains can be stated as follows:

$$\begin{cases} \varepsilon_{rs} = \varepsilon_{rs}^e + \varepsilon_{rs}^p, \\ \varepsilon_{\theta s} = \varepsilon_{\theta s}^e + \varepsilon_{\theta s}^p, \end{cases} \tag{23}$$

where the superscripts "e" and "p" denote the elastic and plastic strains of the strain-softening zone, respectively.

Employing the flow rule establishes the relationship between the components of the plastic strain. According to the nonassociated flow law, we can get the relationship between the plastic strain increments as follows:

$$\frac{\mathrm{d}\varepsilon_{rs}^p}{\mathrm{d}\varepsilon_{\theta s}^p} = -\frac{2}{h}, \tag{24}$$

where h is a function of ψ, $h = ((1 - \sin \psi)/(1 + \sin \psi))$, and ψ is the angle of dilation obtained by a triaxial compressive test.

Combining (23) and (24) results in the following:

$$h\mathrm{d}\varepsilon_{rs} + 2\mathrm{d}\varepsilon_{\theta s} = h\mathrm{d}\varepsilon_{rs}^e + 2\mathrm{d}\varepsilon_{\theta s}^e. \tag{25}$$

Based on the integration of (25) and by adding (5), we can derive the following:

$$h\varepsilon_{rs} + 2\varepsilon_{\theta s} = f_s(r), \tag{26}$$

where $f_s(r)$ can be given as $f_s(r) = (1/2G(1 + \mu))\{(h - 2\mu)\sigma_{rs} + 2(1 - \mu - h\mu)\sigma_{\theta s} - (h + 2)(1 - 2\mu)p_0\}$.

After substituting the radial stress of (12) and tangential stress of (13) into the above form for $f_s(r)$, we can obtain

$$f_s(r) = \frac{1}{2G(1 + \mu)} \left\{ C_1 + C_2 \ln\left(\frac{r}{R_2}\right) + C_3 \ln^2\left(\frac{r}{R_2}\right) \right\}, \tag{27}$$

where $C_1 = (h + 2)(1 - 2\mu)(\sigma_{R2} - p_0) + 2(1 - \mu - h\mu)A_1$, $C_2 = 2(h + 2)(1 - 2\mu)A_1 + 2(1 - \mu - h\mu)A_2$, and $C_3 = (h + 2)(1 - 2\mu)A_2$.

Combining (22) and (26) leads to the following equations:

$$h \ln \frac{\mathrm{d}r}{\mathrm{d}r_0} + 2 \ln \frac{r}{r_0} = f_s(r),$$

$$\ln\left[\left(\frac{r}{r_0}\right)^{2/h} \frac{\mathrm{d}r}{\mathrm{d}r_0}\right] = \frac{f_s(r)}{h}. \tag{28}$$

Definite integral calculation can be performed on the intervals $r_0 \in [r_0, R_2 - u_{R_2}]$ and $r \in [r, R_2]$, where u_{R_2} represents the displacement around a salt cavern in the elastic zone at $r = R_2$. Based on (7), we can obtain $u_{R_2} = (1/2)\delta R_2$.

The integration of (28) leads to the displacement for a large deformation in the strain-softening zone:

$$u_s(r) = r - r_0 = r - \left\{ \left[\left(1 - \frac{1}{2}\delta\right)R_2\right]^{(h+2)/h} - \frac{h+2}{h} \int_r^{R_2} r^{2/h} e^{-(f_s(r)/h)} \mathrm{d}r \right\}^{h/(h+2)}. \tag{29}$$

Using the method of definite integration by substitution, we can deduce (29) as follows:

$$u_s(r) = r - r_0 = r - \left\{ \left[\left(1 - \frac{1}{2}\delta\right)R_2\right]^{(h+2)/h} - \frac{h+2}{h} \int_0^1 ((R_2 - r)x + r)^{2/h}(R_2 - r)e^{-(1/2G(1+\mu))\left(\{C_1 + C_2 \ln\left(((R_2-r)x+r)/R_2\right) + C_3 \ln^2\left(((R_2-r)x+r)/R_2\right)\}/h\right)} \mathrm{d}x \right\}^{h/(h+2)}. \tag{30}$$

Furthermore, the solution of (30) can be derived based on Romberg integration. At $r = R_1$, according to (28), the tangential strain at the interface of the strain-softening zone and plastic flow zone can be given as follows:

$$\varepsilon_{R1} = \ln \frac{r}{r_0} = \ln\left\{ \left[\left(1 - \frac{1}{2}\delta\right)\frac{1}{t}\right]^{(h+2)/h} - \frac{h+2}{h}T \right\}$$

$$\Rightarrow T = \frac{h}{h+2} \left\{ \left[\left(1 - \frac{1}{2}\delta\right)\frac{1}{t}\right]^{(h+2)/h} - e^{\varepsilon_{R1}} \right\}, \tag{31}$$

where $T = \int_0^1 [((1/t) - 1)x + 1]^{2/h}((1/t) - 1)e^{(1/hE)\{C_1 + C_2 \ln((1-t)x+t) + C_3 \ln^2((1-t)x+t)\}} \mathrm{d}x$.

Combining (16) and (31), we can obtain the nonlinear differential equation for t. However, this equation has no closed-form solution. To find the values of t and ε_{R1}, the numerical iteration method is employed with the aid of MATLAB. Next, substituting $\ln t$ into (20) produces σ_{R1}. Then, substituting σ_{R1} into (21), we can obtain R_1 and R_2.

6.2. Displacement Analysis in the Plastic Flow Zone.
Likewise, in the zone of $R_0 \le r \le R_1$, the strains can be expressed as follows:

$$\begin{cases} \varepsilon_{rr} = \varepsilon_{rs}|_{r=R_1} + \varepsilon_{rr}^p, \\ \varepsilon_{\theta r} = \varepsilon_{\theta s}|_{r=R_1} + \varepsilon_{\theta r}^p. \end{cases} \tag{32}$$

Based on the nonassociated flow law, we can determine the plastic strain increments as follows:

$$\frac{d\varepsilon_{rr}^p}{d\varepsilon_{\theta r}^p} = -\frac{2}{f}, \tag{33}$$

where f is a function of ψ'; $f = ((1 - \sin \psi')/(1 + \sin \psi'))$; and ψ' can be got through a triaxial compressive test.

Combining (32) and (33), we will have the following:

$$f d\varepsilon_{rr} + 2d\varepsilon_{\theta r} = f d\varepsilon_{rr}^e + 2d\varepsilon_{\theta r}^e. \tag{34}$$

Based on the integration of (34) and by adding (5), we can derive the following:

$$f\varepsilon_{rr} + 2\varepsilon_{\theta r} = f_r(r), \tag{35}$$

where $f_r(r) = (1/2G(1 + \mu))[(\sigma_{rr} - p_0) - 2\mu(\sigma_{\theta r} - p_0)](f - h) + f_s(R_1)$.

After substituting the radial stress of (18) and tangential stress of (19) into $f_r(r)$, we can obtain

$$f_r(r) = \frac{(f - h)}{2G(1 + \mu)}\left\{ D_1 + D_2 \ln\left(\frac{r}{R_0}\right) + D_3 \ln^2\left(\frac{r}{R_0}\right) \right\} + f_s(R_1), \tag{36}$$

where $D_1 = (1 - 2\mu)(p_i - p_0) - 2\mu B_1$; $D_2 = 2(1 - 2\mu)B_1 - 2\mu B_2$; $D_3 = (1 - 2\mu)B_2$; and $f_s(R_1) = (1/2G(1 + \mu))\{C_1 + C_2 \ln(R_1/R_2) + C_3 \ln^2(R_1/R_2)\}$.

Combining (32) and (34) results in the following:

$$f \ln\frac{dr}{dr_0} + 2 \ln\frac{r}{r_0} = f_r(r),$$

$$\ln\left[\left(\frac{r}{r_0}\right)^{2/f}\frac{dr}{dr_0}\right] = \frac{f_r(r)}{f}. \tag{37}$$

Definite integral calculation can be performed on $r_0 \in [r_0, R_1 - u_{R_1}]$ and $r \in [r, R_1]$, where u_{R_1} is based on (30) and represents the displacement in the strain-softening zone at $r = R_1$. The integration of (37) leads to the displacement for a large deformation in the plastic flow zone:

$$u_r(r) = r - r_0 = r - \left\{ \left(R_1 - u_{R_1}\right)^{(f+2)/f} - \frac{f + 2}{f}\int_r^{R_1} r^{2/f} e^{-(f_r(r)/f)} dr \right\}^{f/(f+2)}. \tag{38}$$

Using the definite integration by substitution, we can deduce (38) as follows:

$$u_r(r) = r - r_0 = r - \left\{ \left(R_1 - u_{R_1}\right)^{(f+2)/f} - \frac{f + 2}{f}\int_0^1 [(R_1 - r)x + r]^{2/f}(R_1 - r)e^{\{-((f-h)/fE)[D_1 + D_2 \ln(((R_1 - r)x+r)/R_0) + D_3 \ln^2(((R_1 - r)x+r)/R_0)] - (1/f)f_s(R_1)\}} dx \right\}^{f/(f+2)}. \tag{39}$$

Then, (39) can be solved by the method of Romberg integration.

7. Discussion

When $\eta^* \longrightarrow \infty$, there is no softening behavior, and the zoned phenomenon does not remain in the plastic zone. In addition, the constitutive relationship of the salt rock is the ideal elastoplastic one. The radial stress and tangential stress in the plastic zone can be written as (40) and (41), respectively:

$$\sigma_{rp} = p_i + 2A_1 \ln\left(\frac{r}{R_0}\right) + A_2 \ln^2\left(\frac{r}{R_0}\right), \tag{40}$$

where $A_1 = \sqrt{m_b \sigma_{ci} p_i + s\sigma_{ci}^2}$, $A_2 = m_b \sigma_{ci}$, and m_b and s are stationary values obtained by substituting the parameter GSI^{peak} into (2):

$$\sigma_{\theta p} = \sigma_{rp} + A_1 + A_2 \ln\left(\frac{r}{R_0}\right). \tag{41}$$

Considering the boundary condition at $r = R_2$, we can express (14) as follows:

$$3\sigma_{R2} + 2\sqrt{m_b \sigma_{ci} \sigma_{R2} + s\sigma_{ci}^2} - 3p_0 = 0. \tag{42}$$

The radial stress at $r = R_2$, σ_{R2}, can be derived through numerical iteration. Then, plastic radius R_2 can be determined according to (40):

$$R_2 = R_0 e^{\left(\sqrt{A_1^2 + A_2 (\sigma_{R2} - p_i)} - A_1\right)/A_2}. \tag{43}$$

When calculating the displacement in the plastic zone, (26) is rewritten as follows:

$$h\varepsilon_{rp} + 2\varepsilon_{\theta p} = f_p(r), \tag{44}$$

where $f_p(r) = (1/2G(1 + \mu))\{K_1 + K_2 \ln(r/R_0) + K_3 \ln^2(r/R_0)\}$, $K_1 = (h + 2)(1 - 2\mu)(p_i - p_0) + 2(1 - \mu - h\mu)A_1$, $K_2 = 2(h + 2)(1 - 2\mu)A_1 + 2(1 - \mu - h\mu)A_2$, and $K_3 = (h + 2)(1 - 2\mu)A_2$.

Combining (22) and (44), we can obtain the following:

$$\ln\left[\left(\frac{r}{r_0}\right)^{2/h}\frac{dr}{dr_0}\right] = \frac{f_p(r)}{h}. \tag{45}$$

Moreover, definite integral calculation can be performed on $r_0 \in [r_0, R_2 - u_{R_2}]$ and $r \in [r, R_2]$, where u_{R_2} is based on (7) and represents the displacement in the elastic zone at the interface of the plastic zone and elastic zone. The integration

of (45) leads to the displacement for a large deformation in the plastic zone with an ideal elastoplastic rock mass:

$$u_p(r) = r - r_0 = r - \left\{\left(R_2 - u_{R_2}\right)^{(h+2)/h} - \frac{h+2}{h}\int_r^{R_2} e^{-f_p(r)/h}r^{2/h}dr\right\}^{h/(h+2)}. \tag{46}$$

Using the method of the definite integration by substitution, we can deduce (46) as follows:

$$u_p(r) = r - r_0 = r - \left\{\left(R_2 - u_{R_2}\right)^{(h+2)/h} - \frac{h+2}{h}\int_0^1 e^{-(1/2G(1+\mu))\left(\{K_1+K_2\ln\left(((R_2-r)x+r)/R_0\right)+K_3\ln^2\left(((R_2-r)x+r)/R_0\right)\}/h\right)}\left((R_2-r)x+r\right)^{2/h}(R_2-r)dx\right\}^{h/(h+2)}. \tag{47}$$

Furthermore, the solution of (47) can be determined based on Romberg integration.

8. Case Study

Large-scale underground salt cavern gas storage construction has been carried out in Huaian, Jiangsu, Pingdingshan, Henan, Wanzhou, Chongqing, Yunying, Hubei, etc., those storage groups will be used as oil and gas reserves. At present, there is just one underground gas storage salt cavern (Jintan gas storage) in China at running condition [44]. To show the accuracy of the proposed solutions, the results of the displacement, the radial and circumferential stresses, and the variation of (r/R_0) are compared using the dataset as shown in Table 1. Table 1 lists the salt cavity structural and rock mechanical parameters. E, μ, and ψ denote the elastic modulus, poison ratio, and dilation angle of salt rock, respectively. Table 2 lists the H-B parameters of the salt rock. After the water encroachment of salt cavity storage, the damaged quality and structure of the rock mass decrease the GSI value. Accounting for the empirical regression H-B parameter, GSI affects the displacement, with different GSI values of 60 and 70.

Primarily, through numerical iteration, σ_{R2} is calculated on the basis of (14). Furthermore, the nonlinear differential equations (48) are utilized according to (16) and (31). Then, the unknown variables t and ε_{R1} are determined with the aid of the MATLAB software. Next, σ_{R1}, R_1, and R_2 are calculated one by one. Table 3 lists the related data:

$$\begin{cases} A_1^{R1} + A_2^{R1}\ln t - \frac{3}{2}(p_0 - \sigma_{R2}) + \lambda\left(\varepsilon_{R1} - \frac{\sigma_{\theta s} - \sigma_{rs}}{E}\right) = 0, \\ \int_0^1 \theta(t)dx = \frac{h}{h+2}\left\{\left[\left(1 - \frac{1}{2}\delta\right)\frac{1}{t}\right]^{(h+2)/h} - e^{\varepsilon_{R1}}\right\}, \end{cases} \tag{48}$$

where $\theta(t) = [((1/t) - 1)x + 1]^{2/h}$ $((1/t) - 1)$ $e^{(1/hE)\{C_1+C_2\ln((1-t)x+t)+C_3\ln^2((1-t)x+t)\}}$.

First, it is particularly necessary to validate the analytical result. Therefore, the elastic-brittle-plasticity model is simplified to an ideal elastoplastic model. The solution of (47) is

derived and compared with the numerical solutions that are carried out with the use of the H-B constitutive model in FLAC3D. Figure 3 shows the principle stress and displacement of the rock masses around the cavity, respectively. It can be seen from Figure 3 that the solutions obtained with different H-B criterion parameters are in accord with the distribution law of deep spherical adits and agree with the published outcomes [24]. The variation in GSI affects the principle stress but not obviously. Without considering softening behavior, the analytical solution is closer to the numerical solution. However, when taking the softening behavior into account, the plastic zone is enlarged, and a great difference exists between the analytical and numerical results, particularly at the cavity wall. The numerical solution for the tangential stress is significantly larger than the analytical solution. It can be seen from Figure 3(b) that GSI markedly affects both the displacement at the cavity wall and the plastic radius of the surrounding rock. For example, the GSI increases by 10 and, as a result, the displacement at the cavity wall decreases from 0.72 m to 0.51 m, while the plastic radii R_1 and R_2 decrease by 6% and 12%, respectively. The influence of GSI on R_2 is more obvious. The numerical result for the displacement obtained when adopting the ideal elastoplastic model is evidently smaller than the analytical result obtained when considering the softening behavior, but it should be noted that the numerical result is fundamentally in accord with the analytical result obtained without taking the softening behavior into account. It can be seen from the results that the variation of GSI and/or the softening behavior greatly affects the results. Thus, if the effects of the two factors are not considered, the conclusions will have large deviations.

Alejano and Alonso [45] suggested a definition of dilatancy; it is a volume change caused by the shear distortion which could not recover. Hoek and Brown [46] proposed that the dilation angle of rocks may be extremely small. A dilation angle of zero shows that the volume is preserved. Three cases, $\psi = 0$, $\psi = 0.25\varphi$, and $\psi = 0.5\varphi$, are considered here. The relationships between the dilation angles and the displacements within the plastic zone of a salt cavern are illustrated in Figure 4. The figure shows that the displacement at the same point increases with the dilation angle, but

TABLE 1: Parameters.

R_0 (m)	p_0 (MPa)	p_i (MPa)	E (GPa)	μ	ψ
30	40	10	10	0.3	0, $(\varphi/4)$, $(\varphi/2)$

TABLE 2: H-B parameters of salt rock.

GSI^S	GSI^r	σ_{ci} (MPa)	m_i	D	m_b^s	s^s	m_b^r	s^r
60	34	24.4	4.1	0.2	0.84	0.0085	0.30	0.0004
70	36	24.4	4.1	0.2	1.25	0.0281	0.32	0.0005

TABLE 3: Dataset.

GSI	δ	σ_{R2}	ε_{R1}	t	σ_{R1}	R_1	R_2	A_1	A_2	B_1	B_2	B_3
60	−0.002	24.884	0.0011	0.6427	14.1971	37.5149	58.3708	$A_1(0) = 22.674$ $A_1(\eta^*) = 13.5051$	$A_2(0) = 20.496$ $A_2(\eta^*) = 7.32$	8.5696	7.32	4.1971
70	−0.0023	22.39	0.0012	0.6913	13.1540	35.4165	51.23	$A_1(0) = 27.815$ $A_1(\eta^*) = 13.950$	$A_2(0) = 30.420$ $A_2(\eta^*) = 7.808$	8.853	7.808	3.1540

(a)
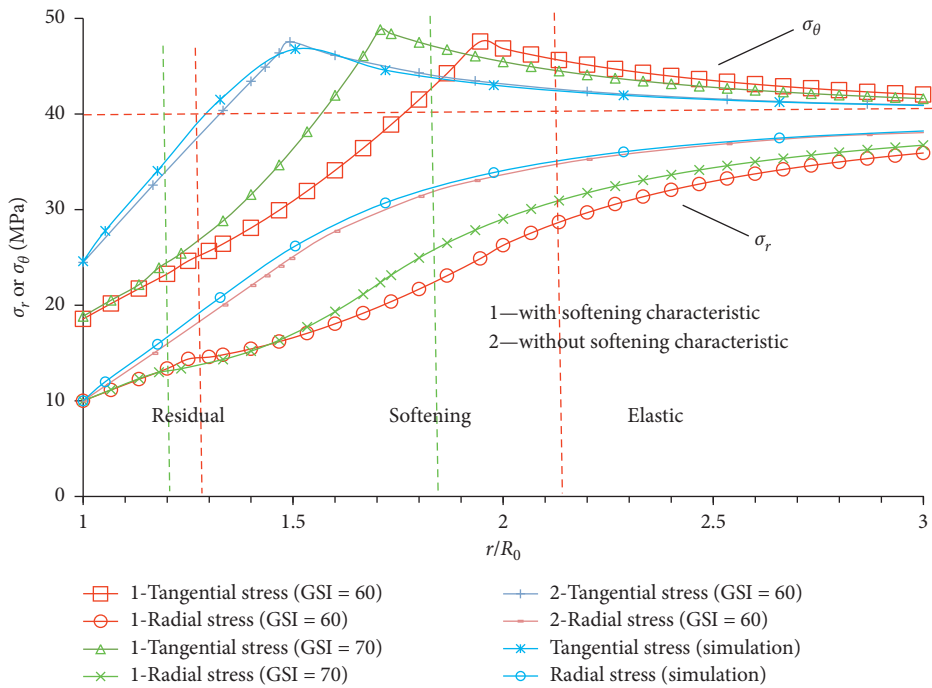
FIGURE 3: Continued.

(b)
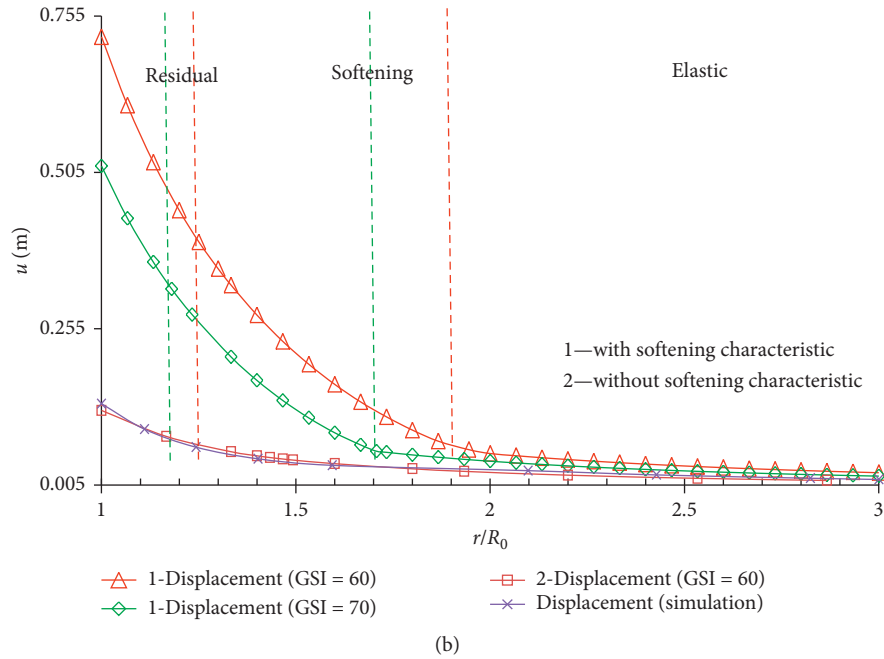
FIGURE 3: Validation of H-B solution against numerical results for spherical domain: (a) distributions of principal stresses; (b) distributions of displacements.
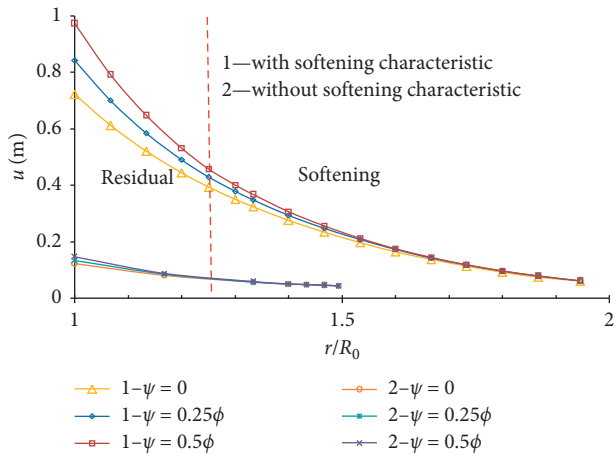
FIGURE 4: Relationships between dilation angle and displacements of salt cavern in plastic zone.

FIGURE 5: Displacements of surrounding rock in strain-softening zone.

the degree of this effect decreases with an increase in the distance away from the salt cavern. The influence of the dilation angle on the displacement at the cavity wall is the most striking. Taking the softening behavior into account, when the angle of dilation is $\psi = 0$, $\psi = 0.25\varphi$, or $\psi = 0.5\varphi$, the displacement at the cavity wall is 0.72 m, 0.84 m, or 0.97 m, respectively. Thus, the extent of the influence increases with the dilation angle. We next consider the displacements of the plastic flow zone for cases of $f = 0.7699$, $f = 0.8687$, and $f = 1$ when $h = 0.7699$ ($\psi = 0.25\varphi$) and $f \neq h$. Figure 5 illustrates that the displacement of the plastic flow zone decreases with an increase in f. In other words,

the displacement increases with dilation angle ψ', but the variations are minor. Compared to h, the effect of f on the displacement is relatively small.

Figure 6 indicates the relationships between the operating pressure and displacement at the cavity wall. As we can see from Figure 6, the displacement decreases with an increase in the operating pressure. When the operating pressure is increased six times, both the analytical results and numerical results are decreased by 80%, and the reduction rates are essentially the same. Under a pressure of 2 MPa, an analytical solution of 2.4 m is attained, but when the softening behavior is not considered, the analytical solution and numerical solution are merely 0.55 m and 0.75 m,
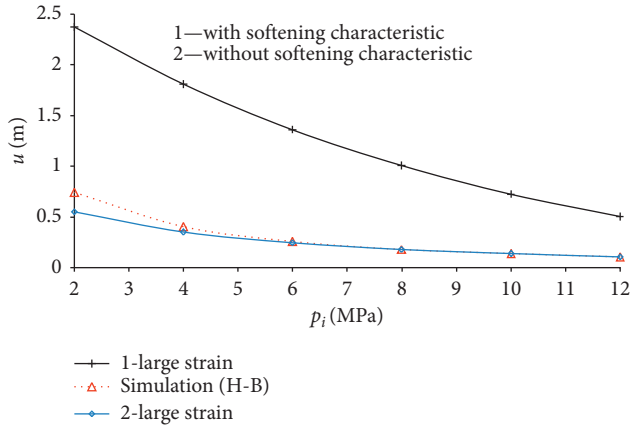
FIGURE 6: Relationships between displacement activity wall and operating pressure.

respectively. Thus, the difference is evident. The variations are caused by the fact that the numerical solution does not take the softening behavior into account, and the definition of the elastic strain within the plastic zone is different. The results demonstrate that the operating pressure has a significant effect on the displacement of the salt cavern storage at the cavity wall. In order to ensure safe operation of the reservoir, the minimum running pressure should not be too low. Thus, it is safer to design the operating pressure based on the analytical solution.

9. Conclusions

(1) Under the condition of three-dimensional model, considering the large strain characteristics of salt rock, the logarithmic strain is introduced to analyze the theoretical solution for the large deformation of the surrounding rock of salt cavity. And a semi-analytical solution is obtained via Romberg numerical method. The stress, strain, and large deformation displacement of the strain-softening and plastic flow zones of a salt cavern in H-B rock masses were obtained.

(2) The H-B parameter, GSI, was found to have a significant impact on the radius and displacement of the plastic zone. Both the plastic radius and displacement decreased with an increase in the GSI parameter, which indicated that the plastic zone and displacement decreased with an increase in the rock mass.

(3) The dilation angle also affected the distribution of the displacement in the salt cavern. The displacement was positively correlated with the angle of dilation. Compared with the impact of the strain-softening parameter, h, the flow parameter, f, had little effect on the displacement. The dilation angle and GSI affected the displacement of the salt cavern most significantly at the cavity wall.

(4) The displacement and plastic zone became obviously greater when the strain-softening behavior was

considered, especially for a poor rock mass and lower operating pressure. Therefore, the strain-softening properties cannot be ignored when designing an actual project.

Notations

R_0:	Radius of salt cavern
p_i:	Gas pressure
p_0:	Hydrostatic pressure
R_2:	Plastic radius of strain-softening zone
σ_{R2}:	Radial stress at the elastoplastic boundary
ε_{R2}:	Tangential strain at the elastoplastic boundary
R_1:	Plastic radius of plastic flow zone
σ_{R1}:	Radial stress at the interface of the strain-softening and plastic flow zones
ε_{R1}:	Tangential strain at the interface of the strain-softening and plastic flow zones
σ_c, σ_{ci}:	Uniaxial compressive strength of the intact rock
m_i, m_b, s, a:	Constants for Hoek–Brown material
GSI:	Geological strength index
D:	Disturbance factor
σ_{re}, $\sigma_{\theta e}$:	Radial stress and tangential stress of elastic zone
ε_{re}, $\varepsilon_{\theta e}$:	Radial strain and tangential strain of elastic zone
σ_{rs}, $\sigma_{\theta s}$:	Radial stress and tangential stress of strain-softening zone
ε_{rs}, $\varepsilon_{\theta s}$:	Radial strain and tangential strain of strain-softening zone
σ_{rr}, $\sigma_{\theta r}$:	Radial stress and tangential stress of plastic flow zone
ε_{rr}, $\varepsilon_{\theta r}$:	Radial strain and tangential strain of plastic flow zone
E:	Young's modulus
μ:	Poisson's ratio
G:	Shear modulus
ψ:	Dilation angle
η:	Softening coefficient
$u_e(r)$, $u_s(r)$, $u_r(r)$:	Displacement in the elastic zone, strain-softening zone, and plastic flow zone, respectively.

Data Availability

The data used to support the findings of this study are available from the corresponding author upon request.

Conflicts of Interest

The authors declare that they have no conflicts of interest regarding the publication of this paper.

Acknowledgments

References

[1] T. Wang, X. Yan, H. Yang, X. Yang, T. Jiang, and S. Zhao, "A new shape design method of salt cavern used as underground gas storage," *Applied Energy*, vol. 104, pp. 50–61, 2013.

[2] K.-H. Lux, "Design of salt caverns for the storage of natural gas, crude oil and compressed air: geomechanical aspects of construction, operation and abandonment," *Geological Society, London, Special Publications*, vol. 313, no. 1, pp. 93–128, 2009.

[3] H.-M. Kim, J. Rutqvist, D.-W. Ryu, B.-H. Choi, C. Sunwoo, and W.-K. Song, "Exploring the concept of compressed air energy storage (CAES) in lined rock caverns at shallow depth: a modeling study of air tightness and energy balance," *Applied Energy*, vol. 92, pp. 653–667, 2012.

[4] M. Raju and S. K. Khaitan, "Modeling and simulation of compressed air storage in caverns: a case study of the Huntorf plant," *Applied Energy*, vol. 89, no. 1, pp. 474–481, 2011.

[5] A. V. Novo, J. R. Bayon, D. Castro-Fresno, and J. Rodriguez-Hernandez, "Review of seasonal heat storage in large basins: watertanks and gravel–waterpits," *Applied Energy*, vol. 87, no. 2, pp. 390–397, 2010.

[6] W. Watney, "Natural gas explosions in Hutchinson, Kansas: geological factors," in *Proceedings of the 37th Annual Meeting of Geological Society of America*, Kansas City, MO, USA, 2003.

[7] E. T. Brown, J. W. Bray, B. Ladanyi, and E. Hoek, "Ground response curves for rock tunnels," *Journal of Geotechnical Engineering*, vol. 109, no. 1, pp. 15–39, 1983.

[8] K.-H. Park and Y.-J. Kim, "Analytical solution for a circular opening in an elastic-brittle-plastic rock," *International Journal of Rock Mechanics and Mining Sciences*, vol. 43, no. 4, pp. 616–622, 2006.

[9] Y.-K. Lee and S. Pietruszczak, "A new numerical procedure for elasto-plastic analysis of a circular opening excavated in a strain-softening rock mass," *Tunnelling and Underground Space Technology*, vol. 23, no. 5, pp. 588–599, 2008.

[10] F. Rojat, V. Labiouse, and P. Mestat, "Improved analytical solutions for the response of underground excavations in rock masses satisfying the generalized Hoek-Brown failure criterion," *International Journal of Rock Mechanics and Mining Sciences*, vol. 79, pp. 193–204, 2015.

[11] K. H. Park, "Similarity solution for a spherical or circular opening in elastic-strain softening rock mass," *International Journal of Rock Mechanics and Mining Sciences*, vol. 71, pp. 151–159, 2014.

[12] X. Liu and Y. Lin, "Theoretic analysis of elastoplastic deformation for the tunnel in soft rocks," *Rock and Soil Mechanics*, vol. 15, no. 2, pp. 27–36, 1994.

[13] G.-S. Yao, J.-P. Li, and S.-C. Gu, "Analytic solution to deformation of soft rock tunnel considering dilatancy and plastic softening of rock mass," *Rock and Soil Mechanics*, vol. 30, no. 2, pp. 463–467, 2009.

[14] Y. Pan, G. Zhao, and X. Meng, "Elastro-plastrc research of surrounding rock based on Hoek-Brown strength criterion," *Journal of Engineering Geology*, vol. 19, no. 5, pp. 637–641, 2011.

[15] S. Wang, S. Yin, and Z. Wu, "Strain-softening analysis of a spherical cavity," *International Journal for Numerical and Analytical Methods in Geomechanics*, vol. 36, no. 2, pp. 182–202, 2012.

[16] W. Wang, H. Xu, M. Jiang et al., "Theoretical analytical solution of stress distribution in elasticity stage of spherical cavity storage cavern in salt rock," *Chinese Journal of Rock Mechanics and Engineering*, vol. 31, no. S1, pp. 3138–3144, 2012.

[17] S. Wen and S.-Q. Yang, "Study of deformations of surrounding rock of tunnel based on Hoek-Brown criterion," *Rock and Soil Mechanics*, vol. 32, no. 1, pp. 63–69, 2011.

[18] H. Cai, H. Cheng, and C. Rong, "Analysis on rock plastic zone displacement of deep buried underground chamber based on generalized Hoek-Brown criterion," *Journal of Mining and Safety Engineering*, vol. 32, no. 5, pp. 778–785, 2015.

[19] X.-H. Wang, J.-l. Wang, and F.-Y. Liang, "Analytical solution to expansion of cawity in strain-softening materials," *Engineering Mechanics*, vol. 16, no. 5, pp. 71–76, 1999.

[20] W. Fan, M. H. Yu, L. W. Chen, and P. Sun, "Unified elastoplastic solution for surrounding rocks of openings with consideration of material dilatancy and softening," *Chinese Journal of Rock Mechanics and Engineering*, vol. 23, no. 19, pp. 3213–3220, 2004.

[21] S.-B. Hu and X.-R. Zhu, "Solution to spherical expansion of cavity in tri-linear strain-softening soil," *Bulletin of Science and Technology*, vol. 23, no. 6, pp. 848–852, 2007.

[22] P. Wang and X. Zhu, "Analysis of cavity expansion in soil with shear dilation and strain softening considering large deformation," *Journal of Zhejiang University (Engineering Science)*, vol. 38, no. 7, pp. 116–121, 2004.

[23] Q. Zhang, X.-W. Quan, L.-Y. Yu, and B.-S. Jiang, "Analytical strain-softening solutions of a spherical cavity," *Latin American Journal of Solids and Structures*, vol. 15, no. 4, pp. pp1–25, 2018.

[24] H. Zhang, Q. Zhang, and L. Wang, "Displacement solution of salt cavern with shear dilatation behavior based on Hoek-Brown strength criterion," *Advances In Civil Engineering*, vol. 2019, Article ID 6735623, 25 pages, 2019.

[25] F. Wang and D. Qian, "Difference solution for a circular tunnel excavated in strain-softening rock mass considering decayed confinement," *Tunnelling and Underground Space Technology*, vol. 82, pp. 66–81, 2018.

[26] K. Guan, W. Zhu, J. Wei, X. Liu, L. Niu, and X. Wang, "A finite strain numerical procedure for a circular tunnel in strain-softening rock mass with large deformation," *International Journal of Rock Mechanics and Mining Sciences*, vol. 112, pp. 266–280, 2018.

[27] Q. Jiang, S. Zhong, and P.-Z. Pan, "Observe the temporal evolution of deep tunnel's 3D deformation by 3D laser scanning in the Jinchuan no. 2 mine," *Tunnelling and Underground Space Technology*, vol. 97, pp. 1–17, 2020.

[28] Q. Zhang, H.-Y. Wang, Y. Jiang, M.-M. Lu, and B.-S. Jiang, "A numerical large strain solution for circular tunnels excavated in strain-softening rock masses," *Computers and Geotechnics*, vol. 114, pp. pp1–11, 2019.

[29] P.-Q. Mo, Y. Fang, and H.-S. Yu, "Benchmark solutions of large-strain cavity contraction for deep tunnel convergence in geomaterials," *Journal of Rock Mechanics and Geotechnical Engineering*, vol. 12, no. 3, pp. 596–607, 2019.

[30] J.-F. Liu, Y. Bian, and D.-W. Zheng, "Discussion on strength analysis of salt rock under triaxial compressive stress," *Rock And Soil Mechanics*, vol. 35, no. 4, pp. 919–925, 2014.

[31] S. Jia, J. Luo, and J. Yang, "An elastoplastic damage constitutive model for salt rock considering confining pressure effect," *Rock and Soil Mechanics*, vol. 36, no. 4, pp. 1549–1556, 2015.

[32] T. Meng, J. l. Xie, J. w. Ma, and Y. Yue, "Experimental study on the evolutional trend of pore structures and fractal dimension of low-rank coal rich clay subjected to a coupled

thermo-hydro-mechanical-chemical environment," *Energy*, vol. 203, Article ID 117838, 2020.

[33] T. Y. Jl, J. Ma, B. Jiao, H. Niu, L. Wen, and X. Yongbin, "Use of DC voltage fluctuation method to investigate real-time mode I and mode II subcritical crack growth behavior in gypsum rock," *Engineering Fracture Mechanics*, vol. 234, Article ID 107104, 2020.

[34] E. Yue and E. T. Brown, "Empirical strength criterion for rock masses," *Journal of the Geotechnical Engineering Division*, vol. 106, 1980.

[35] E. Hoek, D. Wood, and S. Shah, "A modified Hoek-Brown failure criterion for jointed rock masses," *International Journal of Rock Mechanics and Mining Sciences & Geomechanics*, vol. 30, no. 4, 1992.

[36] E. Hoek, C. Carranza-Torres, and B. Corkum, "Hoek-Brown failure criterion—2002 edition," in *Proceedings of the North American Rock Mechanics Society NARMS-TAC 2002*, Toronto, Canada, 2002.

[37] E. Hoek and E. T. Brown, "The Hoek-Brown failure criterion and GSI e 2018 edition," *Journal of Rock Mechanics and Geotechnical Engineering*, vol. 11, no. 3, 2019.

[38] X. Pan and J. A. Hudson, "A simplified three dimensional Hoek-Brown yield criterion," *Rock Mechanics and Power Plants*, pp. 95–103, A. A. Balkema, Rotterdam, Netherlands, 1988.

[39] N. Melkoumian, S. D. Priest, and S. P. Hunt, "Further development of the three-dimensional Hoek-Brown yield criterion," *Rock Mechanics and Rock Engineering*, vol. 42, no. 6, pp. 835–847, 2009.

[40] L. Y. Zhang and H. H. Zhu, "Three-dimensional Hoek-Brown strength criterion for rocks," *Journal of Geotechnical and Geoenvironmental Engineering*, vol. 133, no. 9, pp. 128–135, 2007.

[41] S. D. Priest, "Determination of shear strength and three-dimensional yield strength for the Hoek-Brown criterion," *Rock Mechanics and Rock Engineering*, vol. 38, no. 4, pp. 299–327, 2005.

[42] Q. Jiang, X.-T. Feng, T.-B. Xiang et al., "Observe the temporal evolution of deep tunnel's 3D deformation by 3D laser scanning in the Jinchuan no. 2 mine rockburst characteristics and numerical simulation based on a new energy index: a case study of a tunnel at 2,500 m depth," *Bulletin of Engineering Geology and the Environment*, vol. 69, pp. 381–388, 2010.

[43] C.-G. Zhang, W. Fan, and J.-H. Zhao, "New solutions of rock plastic displacement and ground response curve for a deep circular tunnel and parametric analysis," *Rock And Soil Mechanics*, vol. 37, no. 1, pp. 12–24, 2016.

[44] L. Ran, D. Zheng, T. Luo et al., "Construction & operation characteristics of salt cavern underground gas storages," *Oil & Gas Storage and Transportation*, vol. 38, no. 7, pp. 778–781, 2019.

[45] L. R. Alejano and E. Alonso, "Considerations of the dilatancy angle in rocks and rock masses," *International Journal of Rock Mechanics and Mining Sciences*, vol. 42, no. 4, pp. 481–507, 2005.

[46] E. Hoek and E. T. Brown, "Practical estimates of rock mass strength," *International Journal of Rock Mechanics and Mining Sciences*, vol. 34, no. 8, pp. 1165–1186, 1997.

Research Article

Crack Initiation Behaviors of Granite Specimens Containing Crossing-Double-Flaws with Different Lengths under Uniaxial Loading

Haiyang Pan [ID],[1,2] **Dawei Yin** [ID],[1,3] **Ning Jiang** [ID],[1] **and Zhiguo Xia** [ID][1]

[1]*State Key Laboratory of Mine Disaster Prevention and Control, Shandong University of Science and Technology, Qingdao 266590, China*
[2]*General Institute of Exploration and Research of China National Administration of Coal Geology, Beijing 10039, China*
[3]*Key Laboratory of Safety and High-Efficiency Coal Mining, Ministry of Education, Anhui University of Science and Technology, Huainan 232001, China*

Correspondence should be addressed to Dawei Yin; 949251142@qq.com

Crack initiation is an important stage in the failure process of rock masses. In this paper, crack initiation behaviors (crack initiation model, crack initiation location, crack initiation angle, and crack initiation stress) of granite specimens containing crossing-double-flaws with different lengths were investigated using PFC2^D software. Crack initiation models were all tensile wing cracks, which did not exactly initiate from the main flaw with a length of 30 mm. They can initiate from the secondary flaw with a length 20 mm at α of 30° (included angle between main flaw and horizontal direction) and β of 90° (included angle between main and secondary flaws) and from main and secondary flaws at α of 30° and β of 60°. These were mainly induced by the superposition of stress fields around the main and secondary flaws as β varied from 0° to 90°, especially the tensile force concentration zones superposition. The tensile forces concentration zone around flaw shrank towards flaw tips with the increase of flaw's inclinations measured horizontally. Under stress field superposition effects, the crack initiation stress decreased firstly and then increased with β at α of 30° and 45°. Crack initiation locations were close to flaw tips but not restricted to them. The distances between crack initiation locations and flaw tips, and the crack initiation angles depended on the flaw where first macrocracks initiated from. Microdisplacement field distributions of granite specimens to reveal the mesomechanism of crack initiation behaviors were discussed.

1. Introduction

Under different geological processes, the rock masses contain various discontinuities such as joints, fissures, cracks, and faults [1–8]. The failure process of rock masses is characterized by several distinct deformation stages, including the crack initiation, propagation, and coalescence. The crack initiation illustrates how and where new cracks start in the rock masses [9], and the corresponding crack initiation stress is the stress level marking the initiation of the microfracturing process [10]. Therefore, it is very important to investigate the crack initiation behaviors of the flawed rock masses in rock engineering.

For decades, the investigations on crack initiation behaviors have been conducted on the rock or rock-like specimens with artificial flaws by the laboratory tests and numerical simulations. Most of these studies have been performed on different materials containing single flaw [11–14], two or more parallel flaws [15–19], two or more nonparallel flaws [20–23], three flaws [24–26], and three-dimensional (3D) flaws [27–29]. Moreover, the crack initiation behaviors of rock-coal composite specimens with original coal flaw were studied by Chen et al. [30, 31] and Yin et al. [32]. In addition, to analyze the crack initiation behavior, many crack initiation criteria were proposed, which mainly include the stress-based, energy-based, and strain-

based according to the parameter evaluated around the pre-existing flaw tips [33]. Through the development and propagation of secondary shear cracks under uniaxial compression tests, the damage model based on the maximum tensile principal [34] and F-criterion [35] were proposed.

In nature, the rock mass may contain one or more sets of crossing-double-flaws [31, 36–38]. The strength and failure characteristics of rock specimens containing a set of crossing-flaws [31, 38] and two sets of crossing-flaws [36, 37] were studied, respectively. There are few studies on the crack initiation behavior of rock specimen containing crossing-flaws. In this investigation, the uniaxial compression tests on the granite specimens containing crossing-double-flaws with different lengths were simulated by Particle Flow Code (PFC). Their crack initiation behaviors were the main target of this investigation, including the crack initiation model, crack initiation location, crack initiation angle, and crack initiation stress.

2. Numerical Model and Microparameters

In the PFC software, two main bonded-particle models are provided, i.e., contact model and parallel bond model. Generally, both forces and bending moments between particles can be transmitted in the parallel bond model [31, 32], which is well selected to simulate the mechanical behaviors of the compact materials, such as rock or coal. Therefore, numerical models for granite specimens containing crossing-double-flaws of different lengths were built using the parallel bond model in this study.

2.1. Model Description.
Numerical models for granite specimens containing crossing-double-flaws of different lengths were shown in Figure 1. The model size is 70 mm × 140 mm. The uniform distribution of particles can better model the mechanical behaviors of rock. Therefore, the particle radius followed a uniform distribution ranging from 0.3 to 0.498 mm. Each intact numerical model contained 16459 particle samples. The crossing-double-flaws were created by deleting particles in the intact numerical model center. The flaw with a large length of 30 mm is described as the main flaw, and the flaw with a small length of 20 mm is the secondary flaw. The widths of main and secondary flaws are all 1 mm. The included angle between the main flaw and horizontal direction is α, which are 30° and 45°, respectively. β is taken as the included angle between main and secondary flaws, which are 0°, 30°, 45°, 60°, and 90°, respectively.

The granite specimens were loaded vertically in a constant displacement-control manner, which was performed by moving upper and lower walls. In order to ensure the granite specimens remain a quasi-static equilibrium throughout the test, upper and lower walls moved at a rate of 0.05 m/s. Loading was continuously terminated until failure occurred, which was defined as a drop of postpeak axial stress down to 80% of the peak stress.

2.2. Microparameters of Granite Specimens.
Appropriate microparameters should be selected before modeling through a calibration process. Due to the limitation of laboratory test conditions, the microparameters (Table 1) of granite specimen provided by Yin et al. [38] and Zhang et al. [39] were used to carry out the numerical tests, which were described in detail as follows. Young's modulus of the particle and parallel bond modulus are 3 GPa and 43 GPa, respectively. The ratios of normal to shear stiffness of the particle and parallel bond are all 3. The particle friction coefficient is 0.8. The parallel bond radius multiplier is 1. The tensile and shear strengths of the parallel bond are 88 MPa and 160 MPa, respectively.

Figure 2 illustrates the comparison of stress-strain curves and failure models obtained by the laboratory test and numerical simulation, respectively.

The simulated stress-strain curve and failure pattern were in excellent agreement with the laboratory test. The values of elastic modulus, peak stress, Poisson ratio, cohesive force, and internal friction angle of the numerical model were 28.4 GPa, 132.8 MPa, 0.2285, 20.87 MPa, and 43.68°, respectively. The corresponding experimental results were 28.7 GPa, 130.5 MPa, 0.2300, 15.9 MPa, and 49.86°, respectively. The elastic modulus, peak stress, and Poisson ratio of the numerical results were basically equal to the experimental results. Therefore, the macromechanical properties of the numerical model were basically coincident with the granite specimen in the laboratory test. Due to circular particles used in the numerical model, relatively large differences were found in the cohesive forces and internal friction angles obtained by the laboratory test and numerical simulation [38, 39].

2.3. Determination of Crack Initiation Behavior.
During the loading process, when the axial stress σ reaches to the crack initiation stress of granite specimen, first macrocracks initiate from the pre-existing flaw. In the parallel bond model, under σ, the parallel bond between adjacent parent particles can be broken when the stress intensity transmitted between the particles exceeds the parallel bonding strength between particles. Thus, a microcrack is generated. Each microcrack is represented as a straight line of length equal to the average value of the diameters of two parent particles. Because the individual bonds are discrete, the microcracks formed in neighbouring particles are also discrete and not connected, which are in contrast to those observed in physical tests and numerical studies based on the finite element method. To better visualize the crack initiation behavior, close enough discrete microcracks are artificially linked up to form a continuous macrocrack path. According to the previous studies, the distance of the centroids of two adjacent microcracks was defined as l, and the microcrack length was long as L. If $(l/L) \leq 1$, two microcracks would be treated to be a single continuous macrocrack and a macrocrack trace line can be then be drawn to link the centroids of two microcracks, as shown in Figure 3 [33]. A macrocrack is described to have formed when three or more microcracks are connected through this method in this study.
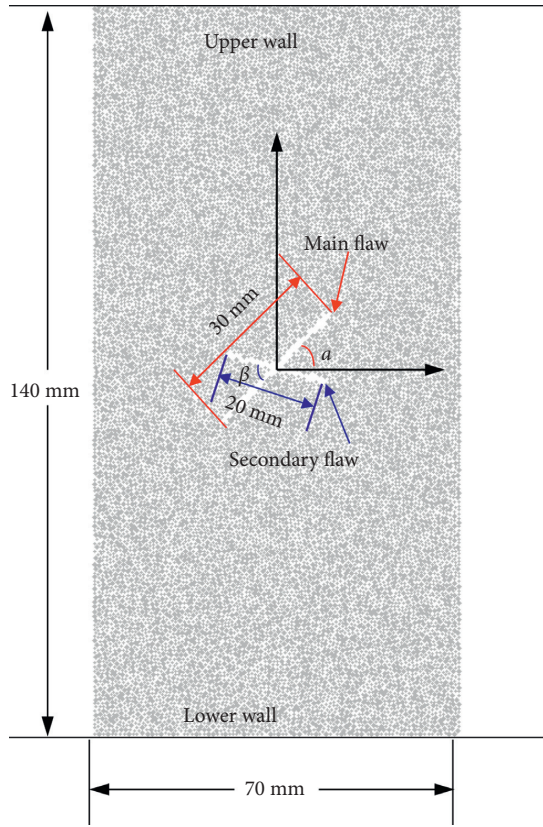
Figure 1: Numerical model for granite specimens containing crossing-double-flaws of different lengths.

Table 1: Microparameters of granite specimen [38, 39].

Microparameters	Values
Minimum particle radius (mm)	0.3
Ratio of maximum to minimum of radius	1.66
Particle density (kg/m^3)	2800
Particle friction coefficient	0.8
Young's modulus of the particle (GPa)	5
Ratio of normal to shear stiffness of the particle	3
Young's modulus of the parallel bond (GPa)	43
Ratio of normal to shear stiffness of the parallel bond	3
Tensile strength of the parallel bond	88
Shear strength of the parallel bond	160
Parallel bond radius multiplier	1

Figure 4 shows the crack initiation, propagation, and coalescence processes of the numerical model for granite specimen ($\alpha = 45°$ and $\beta = 0°$). In Figure 4, microcracks are presented in black colour. When σ reached up to 35.604 MPa (crack initiation stress), the granite specimen occurred crack initiation, and macrotensile cracks (first macrocrack) initiated from flaw tips. As σ increased further to 76.217 MPa, the secondary shear cracks initiated in the flaw areas. With the propagation and coalescence of the first and secondary cracks, the specimen failed. The peak stress of granite specimen was 86.684 MPa. The ratio of crack initiation stress to peak stress was about 0.411. The crack initiation behavior of the numerical model basically agreed with previous investigations [9–16, 33], verifying the accuracy of numerical

simulations. Numerical simulations for other granite specimens with crossing-double-flaws of different lengths were conducted to investigate their crack initiation behaviors.

3. Crack Initiation Behaviors of Granite Specimens

The crack initiation locations of first macrocracks on the flaw periphery relative to the flaw tips were d_1 and d_2, respectively, and crack initiation angles were presented as θ_1 and θ_2, respectively, as shown in Figure 5. Table 2 shows the typical first macrocracks, crack initiation stresses, crack initiation angles, and crack initiation locations of granite specimens under different simulation conditions, which were analyzed as follows.

3.1. Crack Initiation Model. First macrocracks of granite specimens under different simulation conditions were all tensile in origin, which were consistent with previous fields and experimental investigations [17, 40]. When α was 45° and β varied from 0° to 90°, first macrocracks initiated from the main flaw. When α was 30° and β was between 0° and 45°, first macrocracks originated from the main flaw. However, when α was 30° and β was 60°, first macrocracks originated from main and secondary flaws (upper tip region of main flaw and lower tip region of secondary flaw). First, macrocracks initiated from the secondary flaw at α of 30° and β of 90°. Meanwhile, these first macrocracks later propagated towards the vertical loading direction. This phenomenon was caused the superposition effects of stress fields around main and secondary flaws, which were discussed in the section of stress and displacement fields analysis.

3.2. Crack Initiation Location and Crack Initiation Angle. The initiation locations of first macrocracks were close to flaw tips but not restricted to them, which were similar to research results studied by Wong [40] through physical and numerical tests. Figure 6 gives the variations of crack initiation locations with β. The variations of crack initiation angles with β were presented in Figure 7. The d was the mean value of d_1 and d_2, and the θ was the mean value of θ_1 and θ_2.

The values of d and θ were related to the included angle of φ between the flaw (where first macrocracks initiated from) direction and horizontal direction. Generally, the crack initiation location in a single flawed specimen shifted from flaw tips towards the flaw center as φ decreased, and the crack initiation angle increased with the increase of φ [13, 14, 33]. These mean the larger φ was, the smaller d was and the greater θ was. First, macrocracks initiated from main flaw at α of 45° and β varied from 0° to 90°, and the d and θ did not obviously change with β. When α was 30° and β varied from 0° to 45°, first macrocracks initiated from the main flaw. First, macrocracks originated from main and secondary flaws at α of 30° and β of 60°, and φ was −30° along the clockwise direction. Therefore, d and θ did not also change with β varying from 0° to 60°. However, the first macrocracks originated from secondary flaw at α of 30° and β of 90°. φ was −60° along the clockwise direction. Thus, the d

(a)

(b)
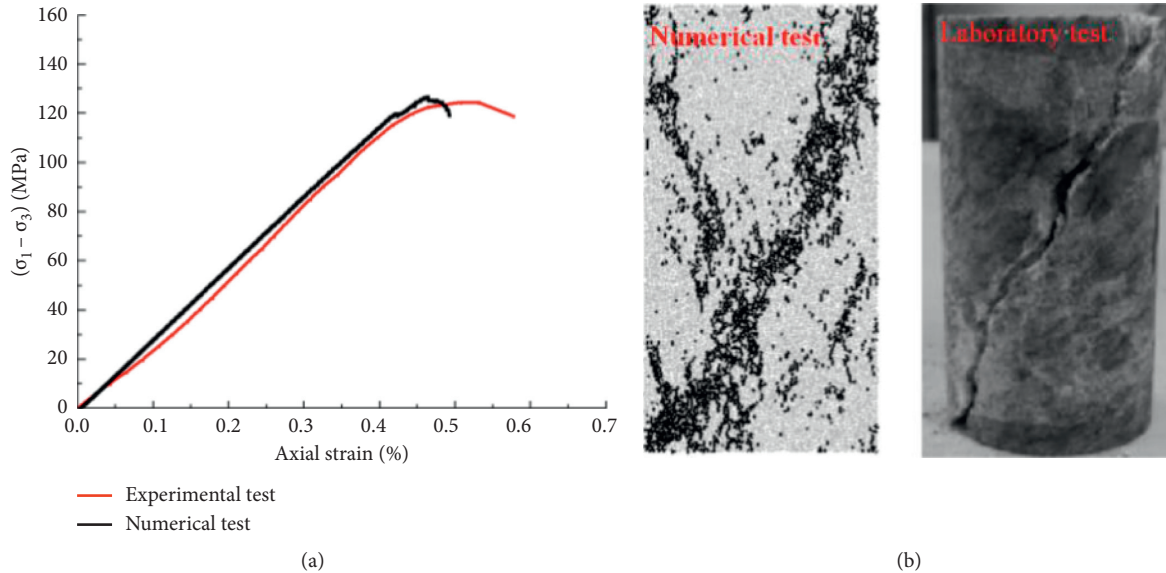
Figure 2: Comparisons of stress-strain curves and failure patterns between experimental and numerical results [38, 39]. (a) Stress-strain curve comparison. (b) Failure pattern comparison.
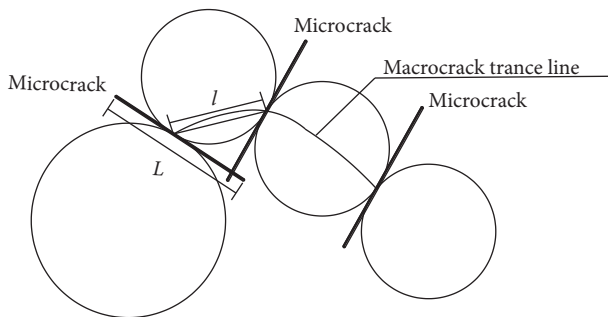
Figure 3: Constructing a macrocrack based on connecting centroids of microcracks [33].

showed a steep decrease and θ presented a steep increase α of 30° and β of 90°. In addition, the d at α of 30° was larger than that at α of 45°, and the θ at α of 30° was lower than that at α of 45° (except α of 30° and β of 90°).

3.3. Crack Initiation Stress. Crack initiation stresses of granite specimens under different simulation conditions are denoted in Figure 8. It can be obviously seen that the crack initiation stress decreased firstly and then increased gradually with an increase of β. When α was 30°, the crack initiation stress was the smallest at β of 30°. While, the crack initiation stress at β of 45° was the lowest at α of 45°. It was well known that the stress filed in the rock specimen changed due to the flaw existence. The stress concentrations were generated near the flaw. When the stress intensity factor near the flaw exceeded the fracture toughness of specimen, the flaw can fracture and first macrocracks initiated from the flaw. First, macrocracks typically initiated from the tensile stress concentration regions near the flaw. In this study, the stress filed around the secondary flaw varied with β. If the tensile force concentration regions around main and secondary flaws were overlapped, the crack initiation behavior was

strengthened and the corresponding crack initiation stress was relatively low. If the tensile force concentration region was overlapped with the compression force concentration region, the crack initiation behavior was weakened and the corresponding crack initiation stress was relatively high. And variations of crack initiation stresses with β were mainly induced by the superposition effects of stress fields around main and secondary flaws, which were analyzed as follows.

4. Stress and Displacement Field Analysis

4.1. Stress-Filed Analysis. In the parallel bond model, when the stress intensity transmitted between the particles exceeded the parallel bonding force between the particles, a microcrack was generated. In order to analyze the superposition effects of stress fields around main and secondary flaws, Table 3 gives the parallel bonding forces around the single flaw with different included angles of φ between the flaw direction and horizontal direction when first macrocracks initiated. The red segment stands for the tensile force, and the compression force is presented in the black segment. Among them, the thick blue line with an arrowhead stands for the shrink direction of tensile force concentration zone.

In Table 3, the red segments were almost around the flaw at φ of 0° except at the flaw tips. The flaw tips were only surrounded by black segments. These illustrate that the flaw perimeter was in a state of tension, and the flaw tips' areas were in a state of compression. With an increase of φ, the black segments' (compression force) regions expanded gradually from the left flaw tip towards the right flaw tip above the flaw surface and from the right tip towards the left tip beneath the flaw surface. Correspondingly, the red segments regions around the flaw perimeter gradually shrank towards the flaw tips with the increase of φ. Namely, the tensile force concentration region shrank towards flaw tips with the increase of φ. These results agreed well with that
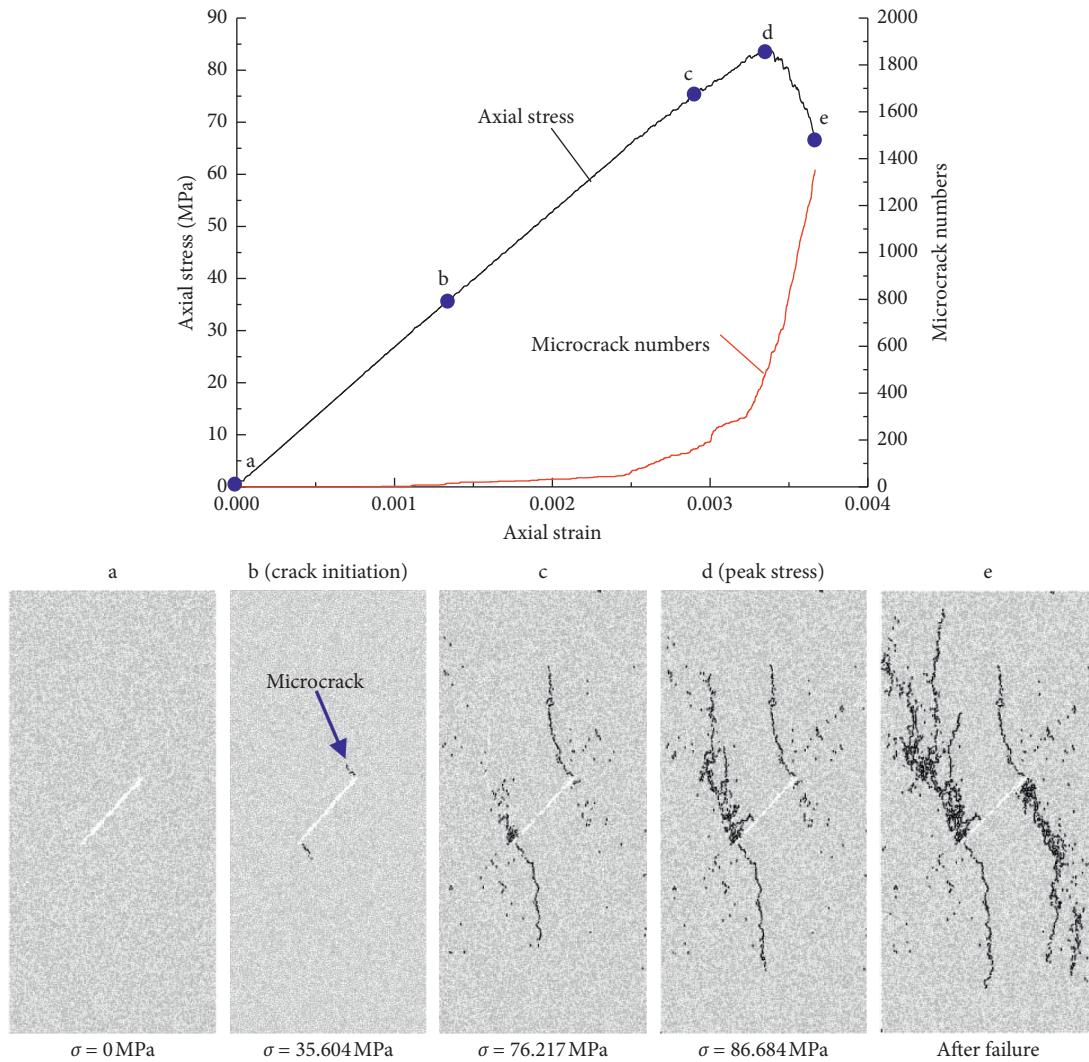
FIGURE 4: Crack initiation, propagation, and coalescence processes of the numerical model for granite specimen ($\alpha = 45°$ and $\beta = 0°$).
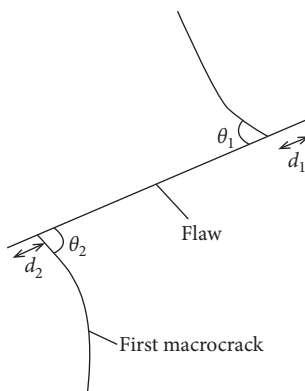
FIGURE 5: Crack initiation angles and distances between first macrocrack initiation locations and flaw tips [36].
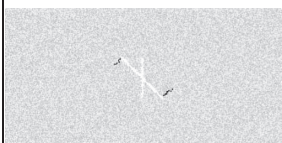
studied by Zhang and Wong [33] and Lajtai [41]. The first macrocracks typically initiated from the tensile stress concentration regions. Therefore, in this study, due to the shrink of the tensile forces' concentration region towards flaw tips,

the average distance between the crack initiation locations and flaw tips decreased with the increase of α and the average distance showed a steep decrease at α of 30° and β of 90°, as shown in Figure 6.

For the granite specimens containing crossing-double-flaws of different lengths, if the tensile force distribution regions around main and secondary flaws were superimposed, the crack initiation behavior was enhanced and first macrocracks may easily be initiated from main flaw or secondary flaw or both main and secondary flaws. The corresponding crack initiation stress was relatively large. If not, the crack initiation behavior was weakened and the corresponding crack initiation stress was relatively small. The superposition effects of stress fields around main and secondary flaws at α of 30° and 45° were analyzed as follows.

4.1.1. $\alpha = 30°$. Table 4 gives the parallel bonding forces around the crossing-double-flaws at α of 30° when first macrocracks initiate. In Table 4, the red segment stands for the tensile force and the compression force is presented in

Table 2: First macrocracks, crack initiation stresses, crack initiation angles, and crack initiation locations of granite specimens under different simulation conditions (microcracks presented in black colour).

Conditions	$\alpha = 30°$, $\beta = 0°$	$\alpha = 30°$, $\beta = 30°$	$\alpha = 30°$, $\beta = 45°$	$\alpha = 30°$, $\beta = 60°$	$\alpha = 30°$, $\beta = 90°$	$\alpha = 45°$, $\beta = 0°$	$\alpha = 45°$, $\beta = 30°$	$\alpha = 45°$, $\beta = 45°$	$\alpha = 45°$, $\beta = 60°$	$\alpha = 45°$, $\beta = 90°$
Initiation of first macrocracks										
Crack initiation stress (MPa)	30.511	30.183	30.262	32.162	33.812	35.604	34.041	33.566	33.309	36.852
θ_1, θ_2 (°)	86, 85	86, 92	86, 87	84, 85	147, 115	84, 90	89, 92	88, 94	90, 86	85, 89
d_1, d_2 (mm)	2.05, 2.45	1.96, 2.31	2.00, 2.22	1.70, 2.18	1.20, 0.71	0.45, 1.23	0.48, 1.27	0.46, 1.60	0.38, 1.55	0.42, 1.69
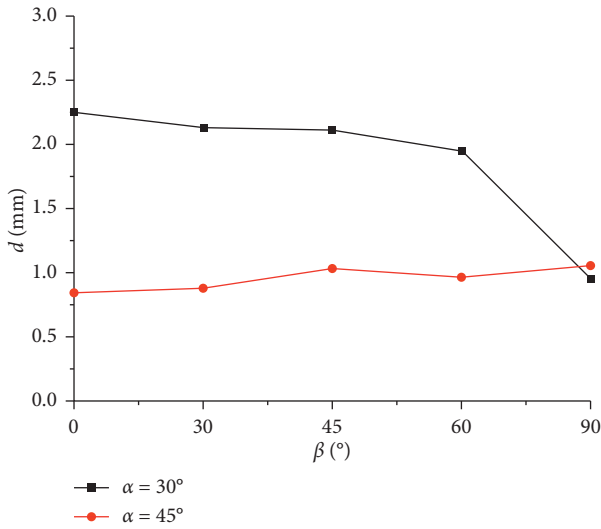
Figure 6: Variations of crack initiation locations with β.
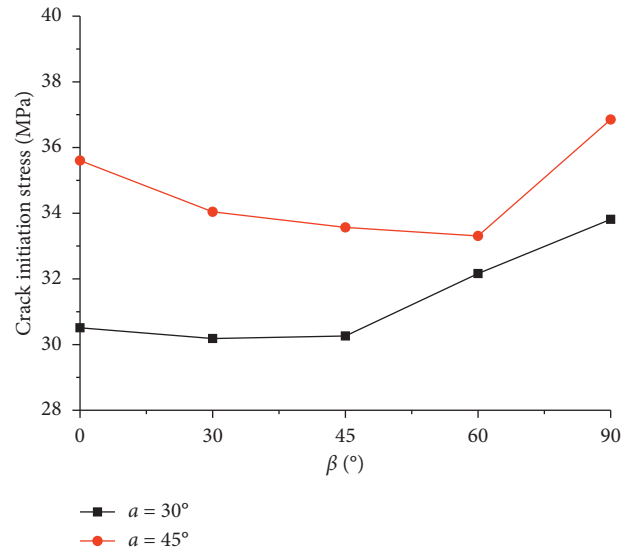
Figure 8: Variations of crack initiation stresses with β.
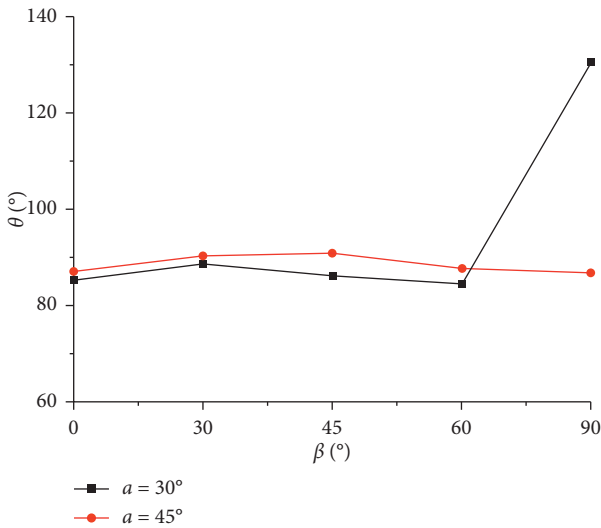
Figure 7: Variations of crack initiation angles with β.

the black segment. The thick black line with an arrowhead stands for the shrink direction of tensile force concentration zone around the main flaw. The thick red line with an arrowhead stands for the shrink direction of tensile force concentration zone around the secondary flaw. As β varied from 0° to 90°, the included angles of φ between the secondary flaw direction and horizontal direction were 30°, 0°, −15°, −30°, and −60° along the clockwise direction, respectively. When $\alpha = 30°$ and $\beta = 30°$, i.e., $\alpha = 30°$ and $\varphi = 0°$, the tensile force concentration region around the main flaw shrank towards the flaw tips, and the tensile force concentration region around the secondary flaw were almost around it except at its tips. The tensile force concentrations close to main flaw tips were enhanced by being superposed with parts of tensile forces around the secondary flaw. Also, due to the shrink of tensile force concentration region around the main flaw, the compression force concentrations

of the secondary flaw tips were weakened, which were crowded by a small number of black segment, as shown in the black boxes in Table 4. The secondary flaw tips were still under compression. Thus, the first macrocracks easily initiated from the main flaw compared that at α of 30° and β of 0°. As β varied from 30° to 90°, i.e., φ varies from −15° to −60°, the tensile force concentration zone around the secondary flaw shrank from right tip towards the left tip along the top flaw surface and from left tip towards right tip along the bottom flaw surface. That means the tensile force concentration regions around the secondary flaw moved away the main flaw tips, and the tensile force concentrations close to main flaw tips were reduced with β. Therefore, the crack initiation stress at α of 30° and β of 45° was larger than that at α of 30° and β of 30° and small than at α of 30° and β of 0°. On the one hand, the tensile force concentration zone around the secondary flaws shrank towards its tips. On the other hand, the secondary flaws tips became more and more close to the tensile force concentration zone close to main flaw tips. Therefore, the tensile force concentrations close to secondary flaw tips were enhanced with β, which were crowded by less black segments and more red segments, especially at α of 30° and β of 90°. And this may cause the first macrocrack initiate from the secondary flaw, as shown in Table 2. Thus, the corresponding crack initiation stress was relatively large due to a large value of φ and flaw length.

4.1.2. $\alpha = 45°$. Table 5 gives the parallel bonding forces around the crossing-double-flaws at α of 45° when the first macrocracks initiate. In Table 5, the red segment, thick black line with an arrowhead, and thick red line with an arrowhead are same as in Table 4. As β varied from 0° to 90°, the included angles of φ between the secondary flaw and horizontal direction were 15°, 0°, −15°, and −45° along the clockwise direction, respectively. When $\alpha = 45°$ and $\beta = 30°$, i.e., $\alpha = 45°$ and $\varphi = 0°$, the tensile force concentration zone around secondary flaw shrank from left tip towards the right

TABLE 3: Force concentrations around the single flaw with different φ when the initiation of first macrocracks.

Conditions	$\varphi = 0°$	$\varphi = 30°$	$\varphi = 45°$	$\varphi = 60°$
Stress field around single flaw				
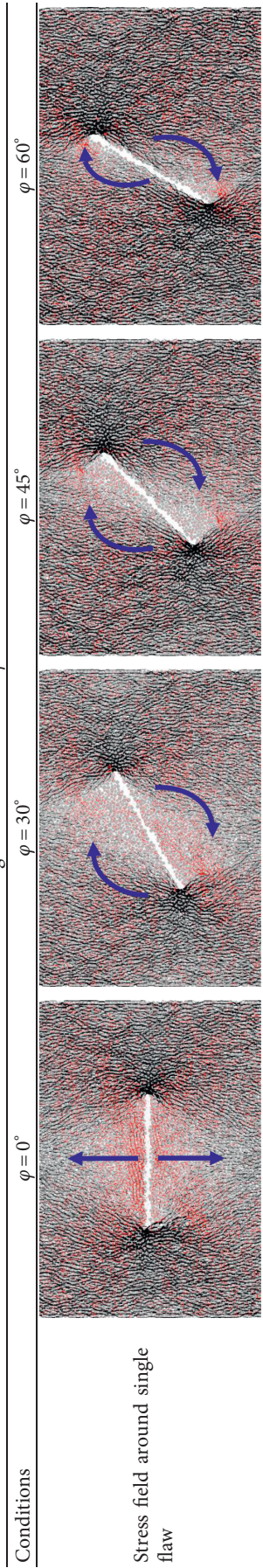
TABLE 4: Force concentrations around the crossing-double-flaws at α of 30° when the initiation of first macrocracks.

Conditions	Stress fields around crossing-double-flaws	Stress fields' rotation
$\alpha = 30°$, $\beta = 0°$		
$\alpha = 30°$, $\beta = 30°$		
$\alpha = 30°$, $\beta = 45°$		
$\alpha = 30°$, $\beta = 60°$		
$\alpha = 30°$, $\beta = 90°$		

tip along the top flaw surface, and from right tip towards left tip along the bottom flaw surface. When $\alpha = 45°$ and $\beta = 45°$, i.e., $\alpha = 45°$ and $\varphi = 0°$, the tensile force concentration region around secondary flaw were almost around the secondary flaw except at its tips. When $\alpha = 45°$ and $\beta = 60°$ or 90°, i.e., $\alpha = 45°$ and $\varphi = -15°$ or $-45°$, the tensile force concentration zone around secondary flaw shrank from right tip towards the left tip along the top flaw surface and from left tip

Table 5: Force concentrations around the crossing-double-flaws at α of 45° when the initiation of first macrocracks.

Conditions	Stress fields around crossing-double-flaws	Stress fields' rotation
$\alpha = 45°$, $\beta = 0°$		
$\alpha = 45°$, $\beta = 30°$		
$\alpha = 45°$, $\beta = 45°$		
$\alpha = 45°$, $\beta = 60°$		
$\alpha = 45°$, $\beta = 90°$		

towards right tip along the bottom flaw surface. If the shrink direction of tensile force concentration regions around the secondary flaw at α of 45° and β of 30° was taken as a reference direction, the tensile force concentration regions

around the secondary flaw expanded along the anticlockwise direction at β of 45° and shrank along the anticlockwise direction at β of 60° and 90°. These meant the tensile force concentration regions around secondary flaw

(a)

(b)

(c)

(d)

(e)
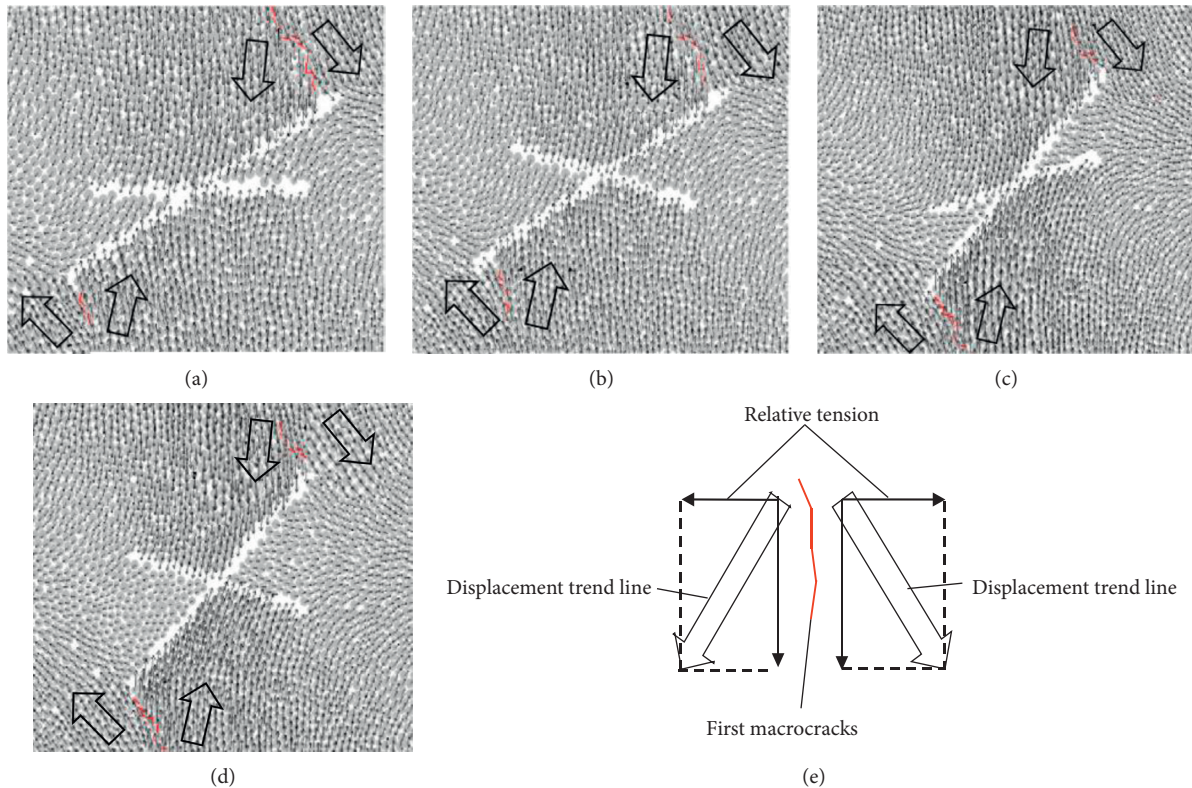
FIGURE 9: Typical microdisplacement field distributions and of displacement-filed model of granite specimens. (a) $\alpha = 30°$ and $\beta = 30°$, (b) $\alpha = 30°$ and $\beta = 45°$, (c) $\alpha = 45°$ and $\beta = 30°$, (d) $\alpha = 45°$ and $\beta = 60°$, and (e) displacement-filed model.

moved close to main flaw tips at β of 45° and moved always the main flaw tips at β of 60° and 90°. The shrink degree increased with β varying from 60° to 90°. Therefore, the tensile force concentration close to the main flaw was enhanced firstly at β of 45° and then weakened at β of 60° and 90°. The corresponding crack initiation stress decreased firstly and then increased.

4.2. Microdisplacement Field Analysis. The microdisplacement filed (MDF) distribution is helpful to reveal the micromechanism of crack initiation behavior in granite specimen containing crossing-double-flaws under uniaxial compression.

Figures 9(a)–9(d) illustrate MDF distributions of granite specimen under different simulation conditions when first macrocracks initiated. Red segments presented the microcracks. Thin black lines with arrowheads stood for displacement vectors of the particles in the numerical model. Thick black lines with arrowheads stood for the displacement trend on both sides of first macrocrack, which were not filled with a colour.

According to displacement trends of particles on both sides of first macrocracks, a type of displacement filed was obtained when the first macrocracks initiate, as shown in Figure 9(e). Firstly, the particles moved in the same direction, then they moved apart in two directions. Thus, a relative tension was formed, and microcracks were generated. Finally, a macrocrack was generated when three or

more microcracks connected in this study. The type of displacement filed was basically consistent with research results studied by Zhang and Wong [33], Huang et al. [22], and Yin et al. [38].

5. Conclusions

In this study, the uniaxial compression tests on granite specimens with crossing-double-flaws of different lengths were simulated by PFC. The crack initiation behaviors of granite specimens were studied. The following conclusions were achieved:

(1) Crack initiation models were all tensile wing cracks. First, macrocracks did not exactly initiate from the main flaw with a length of 30 mm, and they can initiate from the secondary flaw with a length of 20 mm at α of 30° and β of 90° and from the main and secondary flaws at α of 30° and β of 60°. These are mainly caused by the superposition of stress fields around the main and secondary flaws as β varies from 0° to 90°, especially the tensile force concentration zones' superposition. The tensile forces' concentration region around the flaw shrank towards flaw tips with the increase of the flaw's inclinations measured horizontally. Under superposition effects of stress fields, the crack initiation stress decreased firstly and then increased with β at α of 30° and 45°.

(2) Crack initiation locations were close to flaw tips but not restricted to them. The crack initiation angle was determined by the flaw where first macrocracks initiated from. Generally, the larger the flaw inclinations measured horizontally was, the smaller the distances between crack initiation locations and flaw tips were, and the greater the crack initiation angle was.

(3) A type of displacement filed was found when first macrocracks initiated. Firstly, the particles moved in the same direction, and then they moved apart in two directions. Thus, a relative tension was formed, and microcracks were generated. A macrocrack was generated when three or more microcracks connected in this study.

Data Availability

The data used to support the findings of this study are included within the article.

Conflicts of Interest

The authors declare that they have no conflicts of interest.

Acknowledgments

References

[1] Z. H. Zhao, W. Sun, M. Z. Zhang, X. J. Gao, and S. J. Chen, "Fracture mechanical behavior of cracked cantilever roof with large cutting height mining," *Shock and Vibration*, vol. 2020, Article ID 1641382, 10 pages, 2020.

[2] Z. Qin, H. L. Fu, and X. X. Chen, "A study on altered granite meso-damage mechanisms due to water invasion-water loss cycles," *Environmental Earth Sciences*, vol. 78, no. 14, p. 428, 2019.

[3] J. Wang, S.-C. Li, L.-P. Li, P. Lin, Z.-H. Xu, and C.-L. Gao, "Attribute recognition model for risk assessment of water inrush," *Bulletin of Engineering Geology and the Environment*, vol. 78, no. 2, pp. 1057–1071, 2019.

[4] N. Zhang, W. Liu, Y. Zhang, P. F. Shan, and X. L. Shi, "Microscopic pore structure of surrounding rock for underground strategic petroleum reserve (SPR) caverns in bedded rock salt," *Energies*, vol. 13, no. 7, p. 1565, 2020.

[5] F. Q. Ren, C. Zhu, and M. C. He, "Moment tensor analysis of acoustic emissions for cracking mechanisms during schist strain burst," *Rock Mechanics and Rock Engineering*, vol. 53, no. 1, pp. 153–170, 2020.

[6] D. K. Liu, Z. L. Gu, R. X. Liang et al., "Impacts of pore-throat system on fractal characterization of tight sandstones," *Geofluids*, vol. 2020, Article ID 4941501, 17 pages, 2020.

[7] D. Z. Ren, D. S. Zhou, D. K. Liu, F. J. Dong, S. W. Ma, and H. Huang, "Formation mechanism of the upper triassic yanchang formation tight sandstone reservoir in ordos basin—take chang 6 reservoir in jiyuan oil field as an example," *Journal of Petroleum Science and Engineering*, vol. 178, pp. 497–505, 2019.

[8] G. Feng, X. C. Wang, M. Wang, and Y. Kang, "Experimental investigation of thermal cycling effect on fracture characteristics of granite in a geothermal-energy reservoir," *Engineering Fracture Mechanics*, vol. 235, Article ID 107180, 2020.

[9] B. R. Lawn and A. G. Evans, "A model for crack initiation in elastic/plastic indentation filed," *Journal of Materials Science*, vol. 12, no. 11, pp. 2195–2199, 1997.

[10] A. Basu and D. A. Mishra, "A method for estimating crack-initiation stress of rock materials by porosity," *Journal of the Geological Society of India*, vol. 84, no. 4, pp. 397–405, 2014.

[11] B. Shen, O. Stephansson, H. H. Einstein, and B. Ghahremanl, "Coalescence of fractures under shear stresses in experiments," *Journal of Geophysical Research*, vol. 100, no. B4, pp. 5975–5990, 1995.

[12] A. Bobet, "The initiation of secondary cracks in compression," *Engineering Fracture Mechanics*, vol. 66, no. 2, pp. 187–219, 2000.

[13] L. N. Y. Wong and H. H. Einstein, "Systematic evaluation of cracking behavior in specimens containing single flaws under uniaxial compression," *International Journal of Rock Mechanics and Mining Sciences*, vol. 46, no. 2, pp. 239–249, 2009.

[14] P. Lin, R. H. C. Wong, R.-K. Wang, and W. Y. Zhou, "Crack growth mechanism failure behavior of specimen containing single flaw with different angles," *Chinese Journal of Rock Mechanics and Engineering*, vol. 24, no. 2, pp. 5652–5657, 2005.

[15] R. H. C. Wong and K. T. Chau, "Crack coalescence in a rock-like material containing two cracks," *International Journal of Rock Mechanics and Mining Sciences*, vol. 35, no. 2, pp. 147–164, 1998.

[16] R.H. Cao, P. Cao, H. Lin, C.-Z. Pu, and K. Ou, "Mechanical behavior of brittle rock-like specimens with pre-existing fissures under uniaxial loading, experimental studies and particle mechanics approach," *Rock Mechanics and Rock Engineering*, vol. 49, no. 3, pp. 763–783, 2016.

[17] X. P. Zhou, J. Bi, and Q. H. Qian, "Numerical simulation of crack growth and coalescence in rock materials containing multiple pre-existing flaws," *Rock Mechanics and Rock Engineering*, vol. 48, no. 3, pp. 1097–1114, 2015.

[18] G. M. Latha and A. Garaga, "Elasto-plastic analysis of jointed rocks using discrete continuum and equivalent continuum approaches," *International Journal of Rock Mechanics and Mining Sciences*, vol. 53, pp. 56–63, 2012.

[19] Z. H. Zhao, M. Z. Zhang, Q. Ma, and B. S. Chen, "Deviation effect of coaxiality on the rock brazilian split," *Advances in Mathematical Physics*, vol. 2020, Article ID 5782457, 8 pages, 2020.

[20] H. Lee and S. Jeon, "An experimental and numerical study of fracture coalescence in pre-cracked specimens under uniaxial compression," *International Journal of Solids and Structures*, vol. 48, no. 6, pp. 979–999, 2011.

[21] S.-Q. Yang, X.-R. Liu, and H.-W. Jing, "Experimental investigation on fracture coalescence behavior of red sandstone

containing two unparallel fissures," *International Journal of Rock Mechanics and Mining Sciences*, vol. 63, pp. 82–92, 2013.

[22] Y.-H. Huang, S.-Q. Yang, W.-L. Tian, W. Zeng, and L.-Y. Yu, "An experimental study on fracture mechanical behavior of rock-like materials containing two unparallel fissures under uniaxial compression," *Acta Mechanica Sinica*, vol. 32, no. 3, pp. 442–455, 2016.

[23] S. R. Zhang, F. Sun, C. Wang, and L. Yan, "Discrete element analysis of crack propagation in rocks under biaxial compression," *Chinese Journal of Rock Mechanics and Engineering*, vol. 32, no. 2, pp. 3083–3091, 2013.

[24] R. H. C. Wong, K. T. Chau, C. A. Tang, and P. Lin, "Analysis of crack coalescence in rock-like materials containing three flaws-part I: experimental approach," *International Journal of Rock Mechanics and Mining Sciences*, vol. 38, no. 7, pp. 909–924, 2001.

[25] C. A. Tang, P. Lin, R. H. C. Wong, and K. T. Chau, "Analysis of crack coalescence in rock-like materials containing three flaws-part II: numerical approach," *International Journal of Rock Mechanics and Mining Sciences*, vol. 38, no. 7, pp. 925–939, 2001.

[26] M. Sagong and A. Bobet, "Coalescence of multiple flaws in a rock-model material in uniaxial compression," *International Journal of Rock Mechanics and Mining Sciences*, vol. 39, no. 2, pp. 229–241, 2002.

[27] X. Z. Sun, B. Shen, and B. L. Zhang, "Experimental study on propagation behavior of three-dimensional cracks influenced by intermediate principal stress," *Geomechanics and Engineering*, vol. 14, no. 2, pp. 195–202, 2018.

[28] L. Li, R. H. C. Wong, Z. Han, L. I. Haiyun, and Y. Liu, "Experimental and theoretical analyses of three-dimensional surface crack propagation," *Chinese Journal of Rock Mechanics and Engineering*, vol. 31, no. 2, pp. 311–318, 2012.

[29] A. V. Dyskin, L. N. Germanovich, and K. B. Ustinov, "A 3-D model of wing crack growth and interaction," *Engineering Fracture Mechanics*, vol. 63, no. 1, pp. 81–110, 1999.

[30] S. J. Chen, D. W. Yin, N. Jiang, F. Wang, and Z. F. Zhao, "Mechanical properties of oil shale-coal composite samples," *International Journal of Rock Mechanics and Mining Sciences*, vol. 123, Article ID 104120, 2019.

[31] S. J. Chen, D. W. Yin, N. Jiang, F. Wang, and W. J. Guo, "Simulation study on effects of loading rate on uniaxial compression failure of composite rock-coal layer," *Geomechanics and Engineering*, vol. 17, no. 4, pp. 333–342, 2019.

[32] D. W. Yin, S. J. Chen, X. Q. Liu, and H. F. Ma, "Effect of joint angle in coal on failure mechanical behavior of rock-coal combined body," *Quarterly Journal of Engineering Geology and Hydrogeology*, vol. 51, no. 2, pp. 202–209, 2018.

[33] X.-P. Zhang and L. N. Y. Wong, "Cracking processes in rock-like material containing a single flaw under uniaxial compression: a numerical study based on parallel bonded-particle model approach," *Rock Mechanics Rock Engineering*, vol. 45, no. 5, pp. 711–737, 2011.

[34] O. Reyes and H. H. Einstein, "Failure mechanism of fractured rock-a fracture coalescence model," in *Proceedings of the Seventh International Congress on Rock Mechanics*, pp. 333–340, Aachen, Germany, 1991.

[35] B. Shen and O. Stephansson, "Modification of the G-criterion for crack propagation subjected to compression," *Engineering Fracture Mechanics*, vol. 47, no. 2, pp. 177–189, 1994.

[36] P. H. S. W. Kulatilake, B. Malama, and J. Wang, "Physical and particle flow modeling of jointed rock block behavior under uniaxial loading," *International Journal of Rock Mechanics and Mining Sciences*, vol. 38, no. 5, pp. 641–657, 2001.

[37] Y. H. Huang and S. Q. Yang, "Discrete element study on strength and failure behavior of jointed sandstone with two sets of cross-joints," *Journal of China Coal Society*, vol. 40, no. 1, pp. 76–84, 2015.

[38] D. W. Yin, S. J. Chen, X. Q. Liu, and H. F. Ma, "Simulation study on strength and failure characteristics for granite with a set of cross-joints of different lengths," *Advances in Civil Engineering*, vol. 2018, Article ID 2384579, 10 pages, 2018.

[39] X. P. Zhang, G. Wang, Y. J. Jiang, and N. Huang, "Simulation research on granite compression test based on particle discrete element model," *Rock and Soil Mechanics*, vol. 35, no. 1, pp. 99–105, 2014.

[40] L. N. Y. Wong, *Crack Coalescence in Molded Gypsum and Carrara Marble*, Massachusetts Institute of Technology, Cambridge, MA, USA, 2008.

[41] E. Z. Lajtai, "A theoretical and experimental evaluation of the Griffith theory of brittle fracture," *Tectonophysics*, vol. 11, no. 2, pp. 129–156, 1971.

Research Article

Application of Thermal Insulation Gunite Material to the High Geo-Temperature Roadway

Junhui Wang [iD],[1] **Zhijun Wan** [iD],[1] **Hongwei Zhang** [iD],[2] **Dong Wu,**[1] **Yuan Zhang,**[1] **Yi Wang,**[3] **Luchang Xiong,**[1] **and Guoli Wang**[4]

[1]*Key Laboratory of Deep Coal Resource Mining (CUMT), Ministry of Education of China, School of Mines, China University of Mining and Technology, Xuzhou 221116, Jiangsu, China*
[2]*School of Energy and Mining Engineering, China University of Mining and Technology, Beijing 100083, China*
[3]*College of Safety and Emergency Management Engineering, Taiyuan University of Technology, Taiyuan 030024, Shanxi, China*
[4]*Dananhu No. 1 Coal Mine, CHN ENERGY Investment Group Co., Ltd., Hami 839000, China*

Correspondence should be addressed to Zhijun Wan; zhjwan@cumt.edu.cn and Hongwei Zhang; hongwei@cumtb.edu.cn

Thermal insulation gunite (TIG) in roadways is an effective method for regional thermal hazard control in mines. The development of mine TIG materials is the foundation of thermal insulation technique. However, some conventional and advanced insulation materials are inapplicable to deep mines which are rather humid with high in situ stress and high geo-temperature. In this study, a kind of fly ash-inorganic mineral TIG material was developed and applied to the modelling of a high geo-temperature roadway. Moreover, the thermal insulation effect of the TIG layer was analyzed, and the temperature field characteristics of the TIG surrounding rock were discussed. Results reveal that (1) the TIG layer has a significant impact on the heat release of the wall and stability of the surrounding rock temperature field; (2) the initial temperature disturbance times, temperature disturbance ranges, and temperature drop rates differ with whether a TIG layer exists or not; (3) after the TIG roadway starts to be ventilated, the thermal flux densities tend to be consistent, which indicates the end of temperature disturbance; besides, the dimensionless temperature shares an exponential relation with the dimensionless radius; and (4) the characteristics of temperature drops vary with the radial positions of the surrounding rock. The research results provide a certain reference for thermal hazard control, temperature prediction, and ventilation network adjustment.

1. Introduction

Thermal hazards, one of the common problems in modern mines, are an inevitable geological disaster in the process of mine development to the deep [1–3]. The problem of thermal hazards appeared earlier in developed mining countries such as the United States [4], Australia [5], Poland [6], and South Africa [7]. To this day, there have been about 140 high geo-temperature mines in China [8, 9]. High geo-temperature is the main reason for the formation of thermal hazards which are inevitably brought about by deep mining [10–12]. By 2016, there have been 47 coal mines whose depths exceed 1,000 m in China [13, 14], such as the Suncun Coal Mine (1,501 m, geo-temperature 48°C), Sanhejian Coal

Mine (1,010 m, geo-temperature 46.8°C), and Zhangji Coal Mine (1,260 m, geo-temperature 51.5°C) [8], and over 150 coal mines whose depths exceed 1,000 m abroad, such as the Pniowek Coal Mine (1,000 m, geo-temperature 45°C) in Poland [6]. In addition, some coal mines which are 600–1,000 m deep have high geo-temperatures as a result of local heat accumulation, such as the Pingdingshan No. 8 Coal Mine (660 m, geo-temperature 43°C) [1]. Domestic and foreign researches on cooling of high geo-temperature mines are mainly focused on mechanical cooling technique [7, 15], including central air conditioning cooling, ice cooling, air cooling [16], electric-thermal-glycol cooling, and deep well HEMS cooling [17]. However, the high cost, large cooling capacity losses, and large energy consumption of mechanical

cooling bring considerable burden to enterprises. The thermal insulation and cooling of a roadway is to shoot the mine thermal insulation materials on the roadway surface with high surrounding rock temperature, so as to reduce heat transfer from high-temperature rock to air flow. This method, in combination with the adjustment of ventilation parameters, can achieve a good cooling effect with a relatively low cost [9]. Therefore, the research on the thermal insulation and cooling of roadways is of great significance for the control of regional thermal hazards and the efficient exploitation of resources in mines.

The development of mine thermal insulation gunite material (TIG material) is the basis for the application of thermal insulation and cooling to roadways. Mine TIG materials are required not only to feature light weight, thermal insulation, and flame retardance but also to possess high mechanical properties. These requirements make certain materials that are commonly used in construction and chemical fields unsuitable for use in mine roadways, such as form materials (EPS, XPS, phenolic foam, and polyurethane), fibrous materials (stone wool and glass wool), and advanced materials (vacuum insulation panels, gas filed panels, and aerogel) [18, 19]. Foreign scholars rarely conducted researches on TIG materials, and Chinese scholars mainly focused on inorganic mineral materials such as expanded perlite, vitrified microsphere, and vermiculite. Fly ash, a solid waste produced by the rapid oxidation of pulverized coal during thermal power generation [20], is enormously produced in China (686 million t, 2017). It features multiple holes, low density and low thermal conductivity, and is pretty economical [21, 22]. Therefore, fly ash-inorganic mineral insulation materials are advantageous in mining. The previous literature pays more attention to the development of materials and takes thermal conductivity as the evaluation standard, but the developed materials are seldom applied in the field. Li et al. [23] developed a kind of TIG material by taking vitrified microsphere, cement, sand, and aluminum powder as the raw materials. Then, through an industrial application of the material, they found that the heat release from the shotcrete roadway was reduced by 64%. By studying the composition and ratio of raw materials, Zhang [24], Yang [25], and Zhu [26] obtained thermal insulation materials with a better performance. Liu [27] and Wang [28] simulated the temperature distribution of a TIG roadway with the aid of Fluent software. Zhou [29] discussed the influence of thermophysical parameters of the TIG layer on its thermal insulation effect. It can be concluded that scholars mostly evaluated the thermal insulation effect of TIG materials in high geo-temperature roadways by means of numerical simulation. Nevertheless, since the unstable heat transfer coefficients of the roadways are difficult to determine, the simulation results differ notably from the actual situation.

Therefore, despite some previous achievements made in the development of TIG materials, there is still a lack of researches on the thermal insulation effect of mine TIG materials and the influence of TIG layers on the temperature field of surrounding rock. Physical simulation experiments provide us with solutions. Wang [30], Zhang [31], Zhu [32], and Wang [33] analyzed the temperature and humidity fields of air flow and surrounding rock with the aid of similar simulation devices, but their conclusions were all targeted at non-TIG roadways. On the basis of previous studies, the influence of the TIG layer on the geo-temperature field was investigated by using a similarity simulation device (Figure 1) in this paper. The investigation can serve to evaluate the thermal insulation effect of TIG materials. Besides, it is meaningful for the prediction of airflow and rock temperature and the adjustment and optimization of the ventilation network. Ultimately, it conduces to the control of thermal hazards in mines.

This paper is focused on the application of a kind of fly ash-inorganic mineral thermal insulation material to the high geo-temperature roadway. The specific objectives of this study are (a) to develop a kind of mine TIG material which achieves both roadway support and thermal insulation; (b) to compare and verify the thermal insulation effect of the TIG layer; and (c) to analyze the temperature field characteristics of the TIG roadway.

2. Materials and Methods

2.1. Experimental Apparatus. As displayed in Figure 2, the physical similarity simulation experimental apparatus for a high geo-temperature TIG roadway mainly consists of a surrounding rock heating system, a modelling roadway, a constant temperature and humidity ventilation system, and a data acquisition system. The apparatus has a geometric similarity constant $C_l = 20$, a time similarity constant $C_\tau = 400$, and a wind speed similarity constant $C_v = 0.05$. Detailed design of the experimental apparatus can be found in the literature [9].

The surrounding rock heating system, which contains a closed loop constituted by a rectifier, electric heating electrodes, an alloy heating net, copper plates, and other components, works by outputting low voltage and high current through the thyristor rectifier. With the aid of the alloy heating net, the system can heat the cylinder through stepless adjustment of output current in the range of 0–1000 A. The constant temperature and humidity ventilation system can provide air flow conditions in the temperature range of 5°C–45°C, the humidity range of 20%–90%, and a maximum air volume of 5000 m³/h. The modelling roadway is composed of six cylinders, each of which has a length of 1 m, an inner diameter of 0.8 m, and an outer diameter of 1 m. In the 0.1 m space between the inner wall and the outer wall, mica paper, alloy heating net, mica paper, and thermal insulation asbestos are arranged, respectively. Temperature sensors are arranged at the positions of 0.9 R, 1 R, 2 R, 3 R, and 4 R.

2.2. Materials of the Surrounding Rock and TIG Layer. Surrounding rock materials (the range of 1 R–4 R) and TIG layer materials (the range of 0.9 R–1 R) were poured or built into the cylinders, as shown in Figure 2.

The surrounding rock material was made of high-purity quartz sand and river sand as the fine aggregates and iron
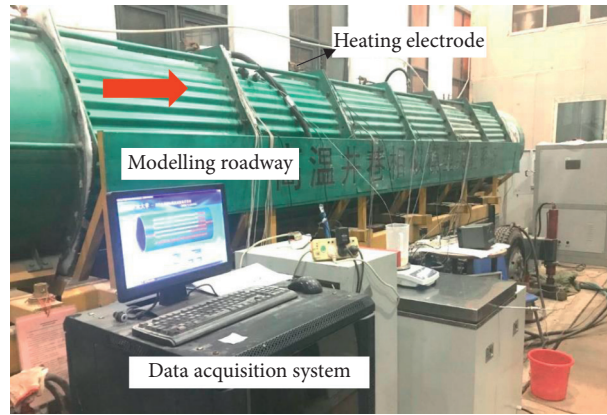
FIGURE 1: The experimental apparatus.

1	Copper sheet	6	Mica paper
2	Thermal insulation foam	7	Alloy heating net
3	Out wall of cylinder	8	Surrounding rock mass
4	Inner wall of cylinder	9	TIG layer
5	Asbestos blanket	10	Temperature sensors
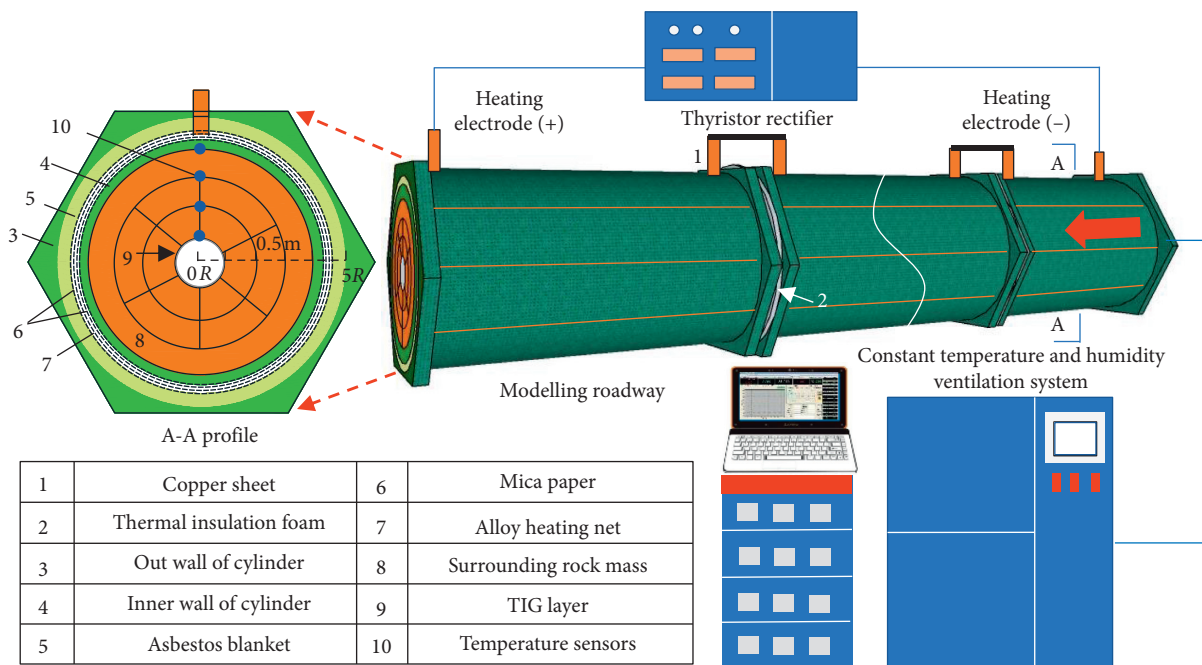
FIGURE 2: Schematic diagram of the experimental apparatus.

powder (to improve thermal conductivity) as the additive. The ratio and thermophysical properties are given in Table 1 [9, 31]. For the material, the thermal conductivity λ_2 was 1.2 W/(m·K) and the thermal diffusivity α_2 was $0.8 \times 10{-}6$ m^2/s. Three layers of surrounding rock material were arranged within the range of 1 R–4 R in the cylinders in Figure 1, of which the material within 1 R–3 R was built and cured by the mould while that within 3 R–4 R was directly poured in the cylinders.

The TIG material was composed of 425 ordinary Portland cement (28 d uniaxial compressive strength ≥ 36 MPa), river sand (particle size < 1 mm), and fly ash (particle size <0.5 mm). Besides, it was added with a certain amount of vitrified microsphere (particle size = 0.5–1 mm; thermal conductivity < 0.043 W/(m·K)) for enhancing its thermal insulation performance. The TIG layer was arranged within the range of 0.9 R–1 R in the cylinders, as in Figure 2.

2.3. Experimental Scheme

2.3.1. Development of the TIG Material. The TIG material should meet the requirements of thermal insulation, light weight, and excellent load-bearing capacity. To explore the material performance under different ratios, a three factor and three-level orthogonal experiment was designed. As listed in Table 2, the three factors are fly ash, vitrified microsphere, and river sand, and the three levels are three ratios corresponding to each raw material. Since cement can improve the mechanical properties of the material significantly, it is not researched on any more here.

The nine groups of experimental samples with varying ratios were numbered 1–9, representing level combinations A1B1C1, A1B2C2, A1B3C3, A2B1C3, A2B2C1, A2B3C2, A3B1C2, A3B2C3, and A3B3C1, respectively. In each group, three 70.7 mm × 70.7 mm × 70.7 mm cubic samples and one 400 mm × 400 mm × 30 mm plate sample were prepared.

TABLE 1: Ratio and properties of similar material for surrounding rock [9].

Cement	River sand	Quartz sand	Thermal conductive powder	Water-cement ratio	Thermophysical property	
					λ_2 (W/(m·K))	α_2 (m²/s)
1	4	0.1	0.07	0.6	1.2	$0.8 \times 10-6$

TABLE 2: Scheme of orthogonal experiment on the material ratio.

Level	Factor		
	Fly ash A (%)	Vitrified microsphere B (%)	River sand C (%)
1	40	10	60
2	50	20	80
3	60	30	100

Note. The percentages are obtained from the ratios of masses of corresponding materials to the total mass of cement and fly ash.

During sample preparation, the materials at the corresponding ratio were added with a certain amount of water and stirred evenly. Next, the evenly stirred mixture was injected into three-groove moulds, vibrated, and compacted. After 24 h, the samples were demoulded and placed in the curing room to be cured standardly (temperature $20 \pm 2°C$; humidity over 95%) for 28 d.

Three basic physical and mechanical parameters, namely, apparent density, uniaxial compressive strength (UCS), and thermal conductivity, of the nine groups of samples were measured. The apparent density was obtained by measuring the mass and volume; the compressive strength was measured by using a compression testing machine (MTS/SANS CMT5105); and the thermal conductivity was measured by the method of a plate heat flux meter (DRPL-400 thermal conductivity tester produced in Xiangtan, China).

2.3.2. Application of the TIG Material to the High Geo-Temperature Roadway. To investigate the application effect of the mine TIG material to the high geo-temperature roadway, two groups of experiments were performed with the aid of the physical similarity simulation experimental apparatus. The first group aims to investigate the temperature field of surrounding rock of a non-TIG roadway, namely, the roadway without a TIG layer (see Scheme 1 in Table 3 for the working conditions), while the second group aims to explore that of a TIG roadway, namely, the roadway with a TIG layer (see Schemes 1–4 in Table 3 for the working conditions).

2.4. Method for Data Analysis. The experimental data were subjected to dimensionless processing. After the processing, the dimensionless temperature, radius, and time expressions become $T = (t - t_f)/(t_0 - t_f)$, $R = r/r_1$, and $F_0 = \alpha_2 * r/(r1_2)$, respectively. In the expressions, T, R, and F_0 represent the dimensionless temperature, radius, and time, respectively; t_0 is the temperature of virgin rock, °C; t_f is the temperature of inlet air, °C; t is the temperature of the measuring point, °C; r is the distance from a certain point to the center of roadway,

m; r_1 is the inner radius of roadway, 0.1 m; α_2 is the thermal diffusivity of surrounding rock, m²/s; and τ is the ventilation time, s. Because the relation between dimensionless quantities is universally applicable, the experimental data need not be calculated into the real model according to the similar constant relations.

3. Results and Discussion

3.1. The Optimum Ratio of the TIG Material. Figure 3 illustrates the apparent density, thermal conductivity, and UCS data of nine groups of compounded samples. As displayed in Figure 3, the physical and mechanical properties of samples differ notably but vary in basically consistent patterns overall. For the samples, the apparent density, thermal conductivity, and UCS lie in the ranges of 1200–1630 kg/m³, 0.119–0.181 W/(m·K), and 4.8–11.7 MPa, respectively.

Table 4 gives the range analysis results of apparent density, thermal conductivity, and UCS of the nine groups of compounded samples (the data are derived from Figure 3). It can be known from Table 4 that the three factors are vitrified microsphere (B), fly ash (A), and river sand (C) in descending order of their degrees of influence on the apparent density. The optimal level combination for apparent density is A2B3C1, i.e., fly ash (50%), vitrified microsphere (30%), and river sand (60%). The three factors are vitrified microsphere (B), river sand (C), and fly ash (A) in descending order of their degrees of influence on the thermal conductivity. The optimal level combination for thermal conductivity is also A2B3C1. The three factors are river sand (C), fly ash (A), and vitrified microsphere (B) in descending order of their degrees of influence on the UCS. The optimal level combination of 28 d UCS is A1B1C2, i.e., fly ash (40%), vitrified microsphere (10%), and river sand (80%).

From the analysis of data in Figure 3 and Table 4, the apparent density, thermal conductivity, and UCS of the samples change synchronously, except some data points that vary due to experimental errors. That is, the sample with a small apparent density generally possesses a small thermal conductivity and a low UCS. The range analysis demonstrates that vitrified microsphere remarkably reduces the weight of the material and improves the thermal insulation performance, but it notably causes damage to the load-bearing capacity of the material. Hence, fly ash and cement become important factors balancing the relationship among weight reduction, thermal insulation, and load-bearing capacity.

To determine the optimal ratio of the material, the method of efficacy coefficient was adopted. It is assumed that n indexes (three indexes in this experiment, namely, apparent density, thermal conductivity, and UCS) are examined and that the efficiency coefficient of each index is di

TABLE 3: Experimental scheme.

Parameter	Scheme 1	Scheme 2	Scheme 3	Scheme 4
Virgin rock temperature t_0 (°C)	37	37	37	39
Inlet air temperature t_f (°C)	20	20	10	20
Average wind speed v (m/s)	5	7	5	5
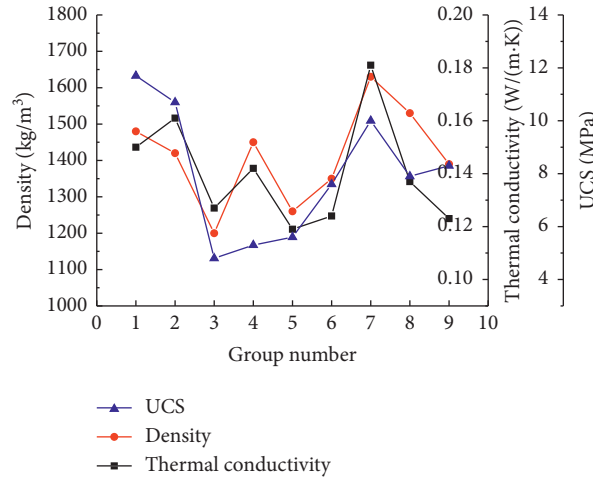
FIGURE 3: Physical and mechanical properties data of compounded samples.

TABLE 4: Range analysis results.

Parameters	Apparent density (kg/m³)			Thermal conductivity (W/(m·K))			UCS (MPa)		
	A	B	C	A	B	C	A	B	C
K_1	1367	1520	1377	0.146	0.158	0.131	9.1	9.1	8.5
K_2	1353	1403	1467	0.128	0.139	0.155	6.2	8.1	9.4
K_3	1517	1313	1393	0.147	0.125	0.135	8.7	6.9	6
Range R	164	207	90	0.019	0.033	0.024	2.9	2.2	3.4
Influence degree	B > A > C			B > C > A			C > A > B		
Optimal level	A2	B3	C1	A2	B3	C1	A1	B1	C2
Optimal combination	A2B3C1			A2B3C1			A1B1C2		

($0 \leq di \leq 1$). If the ith examined index is the optimal index, its efficiency coefficient is 1, i.e., $di = 1$. Efficiency coefficients of the other indexes are ratios of these indexes to the optimal index. Then, the total efficiency coefficient is $d = \sqrt[n]{d_1 \cdot d_2 \ldots d_n}$. The greater the total efficacy coefficient is, the better the ratio is. The results are listed in Table 5 The data are derived from Figure 3).

As can be observed from Table 5, $d = 0.86$ (fly ash 40%, vitrified microsphere 10%, river sand 60%) in Group 1 is the largest efficiency coefficient. In other words, the ratio of Group 1 is the optimal ratio. From the perspective of material properties, the thermal insulation material with this ratio can balance roadway support and thermal insulation. With a density of 1480 kg/m³, it meets the requirement for lightweight concrete 1950 kg/m³; its thermal conductivity 0.15 W/(m·K) meets the requirement for thermal insulation material 0.23 W/(m·K); and it boasts a UCS of 11.7 MPa which exceeds the strength (10 MPa) of C10 concrete.

3.2. The Heat Reduction of the TIG Layer.

The experimental data of the TIG roadway and non-TIG roadway were compared under the conditions of the virgin rock temperature $t_0 = 37$°C, inlet temperature $t_f = 20$°C, and average wind speed $v = 5$ m/s. Figures 4 and 5 exhibit the temperature distribution characteristics of radial points (1 R–4 R) in the surrounding rock and their dynamic variations with time in the two experimental cases.

When dimensionless temperature T in the surrounding rock falls to 0.99, it is considered that thermal disturbance occurs in the surrounding rock. In the non-TIG roadway, thermal disturbance occurs at 1 R and 2 R of the surrounding rock when the dimensionless time $F_0 = 0.1$; it occurs at 3 R when $F_0 = 0.2$ and at 4 R when $F_0 = 0.4$. Radial points (1 R–4 R) in the surrounding rock undergo thermal disturbance earlier for the non-TIG roadway than the TIG one.

For the non-TIG roadway wall, the initial and end dimensionless temperatures T are 0.73 ($F_0 = 0.1$) and 0.51 ($F_0 = 0.8$), respectively, while for the TIG roadway wall, the

TABLE 5: Analysis of the efficacy coefficient model.

| Group no. | Efficiency coefficient | | | Total efficiency coefficient $d = \sqrt[3]{d_1 \cdot d_2 \cdot d_3}$ |
	Apparent density (kg/m^3)	Thermal conductivity (W/(m·K))	UCS (MPa)	
1	0.81	0.79	1.00	0.86
2	0.85	0.74	0.91	0.83
3	1.00	0.94	0.41	0.73
4	0.83	0.84	0.45	0.68
5	0.95	1.00	0.48	0.77
6	0.89	0.96	0.65	0.82
7	0.74	0.66	0.85	0.75
8	0.78	0.87	0.68	0.77
9	0.86	0.97	0.71	0.84
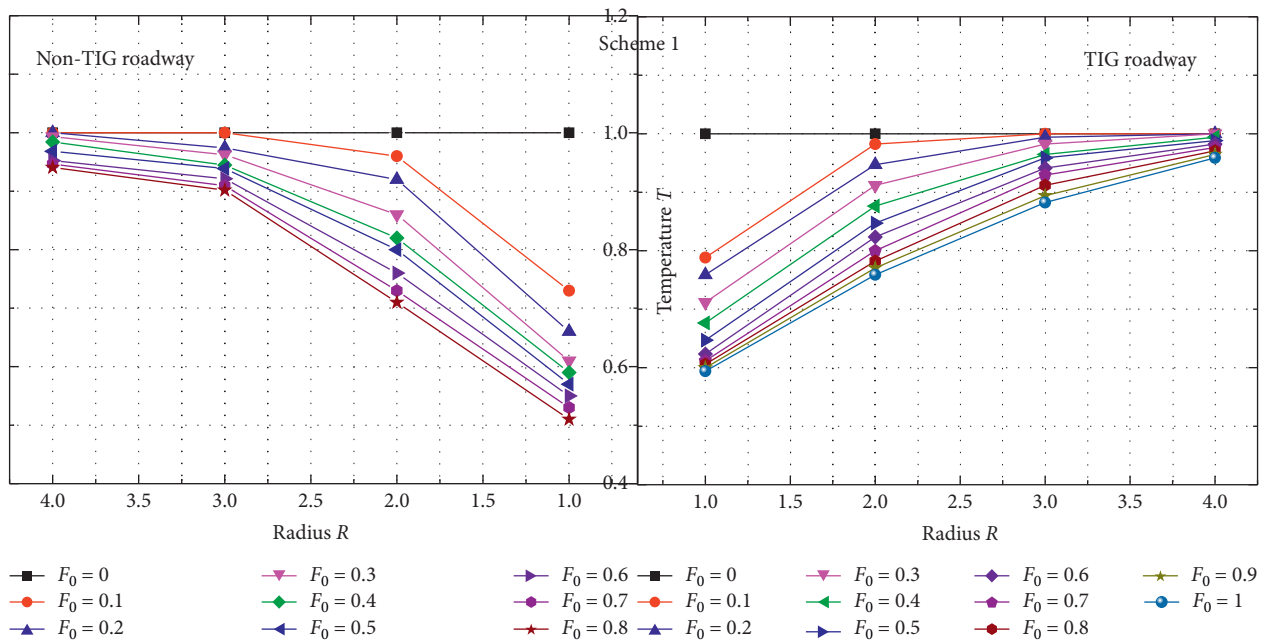
FIGURE 4: T-R curves of the TIG roadway and non-TIG roadway.
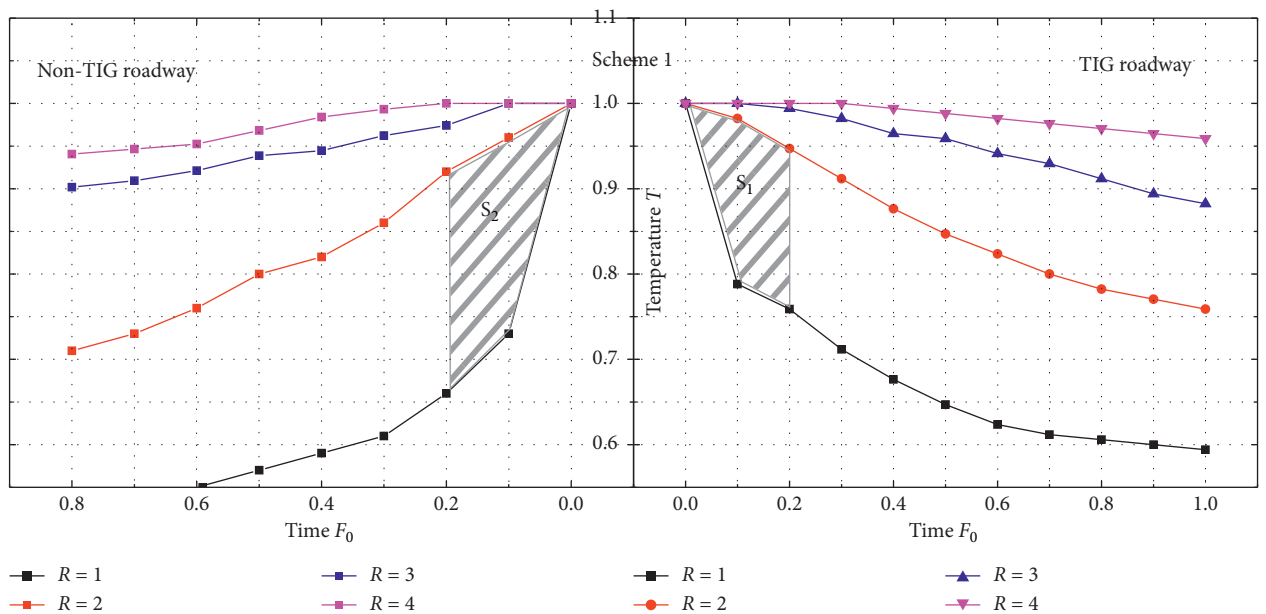
FIGURE 5: $T - F_0$ curves of the TIG roadway and non-TIG roadway.

initial and end dimensionless temperatures T are 0.79 ($F_0 = 0.1$) and 0.6 ($F_0 = 0.8$), respectively. The temperature drop range and rate of the surrounding rock (2 R–4 R) are both greater for the non-TIG roadway than for the TIG roadway. Obviously, the TIG layer prevents heat in the deep surrounding rock from dissipating to the airflow in the roadway and plays a significant role in cooling the roadway.

To interpret the thermal insulation effect of the TIG layer, it is necessary to calculate the amount of heat reduction. In engineering, the amount of heat release (or heat absorption) from surrounding rock can be calculated in accordance with the following formula:

$$Q = K_\tau UL(t_0 - t_f), \tag{1}$$

where Q is the amount of heat released from surrounding rock, W; K_τ is the coefficient of unstable heat transfer between surrounding rock and airflow, W/(m^2·K); U is the perimeter of the roadway interface, m; and L is the length of the roadway, m.

The value of the coefficient of unstable heat transfer $K_\tau = f(F_0, B_i)$ is difficult to obtain by this experimental system. The analysis indicates that it is through the roadway wall that heat dissipates from the surrounding rock in the high geo-temperature roadway to the airflow. The heat loss Q equals the integral of heat flow rate q in the unit area A to the time τ, i.e.,

$$Q = \int_0^\tau q \mathrm{d}\tau = -\int_0^\tau \lambda_2 \frac{\partial t}{\partial r} \mathrm{d}\tau. \tag{2}$$

In this experiment, the homogeneous surrounding rock material has the same thermal conductivity λ_2. The slope of curve in Figure 4 numerically equals the temperature gradient $\partial t / \partial r$ of surrounding rock (sharing a linear conversion relationship with $\partial T / \partial R$). The shadow area in Figure 5 physically means the integral term of the temperature gradient between 1 R and 2 R of surrounding rock (approximately representing the wall) over a period of time. The ratio $(S_2 - S_1)/S_2$ represents the heat reduction per unit wall in a period of time after the high geo-temperature roadway is equipped with a TIG layer. As shown in Table 6, under the experimental conditions, the heat reduction of the roadway wall is 64.2% in the initial stage of ventilation, whereas it is greatly reduced in the later stage, namely, after $F_0 > 0.3 \sim 0.4$. Thus, the TIG layer should be constructed at the early stage of ventilation.

3.3. The Temperature Field Characteristics of the TIG Roadway.

In the similarity experiment of the second group of the TIG roadway, the experimental results reveal that, after the excavation and ventilation of the TIG roadway, the temperature distributions of radial points in the surrounding rock in Schemes 1–4 develop in similar trends and so do their dynamic variations with time in Schemes 1–4, as illustrated in Figures 6–9. In Figure 6(a), Zone I is the TIG layer zone (0.9 R–1 R) and Zone II is the surrounding rock zone (1 R–4 R). Here, only the experimental data under the working conditions of Scheme 1 are analyzed.

TABLE 6: Calculation of heat reduction of the roadway wall at different periods.

F_0	S_1	S_2	Heat reduction of the roadway wall (%)
0–0.1	0.0077	0.0215	64.2
0–0.2	0.0222	0.0493	55.0
0–0.3	0.0505	0.0645	21.7
0–0.4	0.0718	0.0890	19.3
0–0.5	0.0914	0.1116	18.1
0–0.6	0.1115	0.1342	16.9
0–0.7	0.1311	0.1542	15.0
0–0.8	0.1492	0.1743	14.4

3.3.1. Relationship between Dimensionless Temperature T and Dimensionless Radius R.

As can be observed from Figure 6(a), an obvious exponential function relationship exists between T and R in the surrounding rock zone (Zone II), and the expression is $T = P_1 \exp(P_2 R) + P_3$. That is, the temperature of surrounding rock rises gradually with the increase in depth and approximates the temperature of the virgin rock. Partial fitting parameters are displayed in Table 7. The analysis shows that P_1 and P_2 are both the functions of F_0 and B_i (Biot number) under the condition of constant airflow state [31].

It can also be seen from Figure 6(a) that ① the temperature gradient between the TIG layer and the surrounding rock experiences an obvious abrupt change due to the great difference in thermal conductivity of materials; ② assuming that thermophysical properties inside the surrounding rock are constant, the thermal flux density (T/R) of the surrounding rock near the roadway wall is larger in the early stage of ventilation; the various thermal flux densities (T/R) inside the surrounding rock tend to be consistent as the ventilation time F_0 increases from 0 to 1. This indicates that the temperature field of the surrounding rock regains a balance, which marks the end of temperature disturbance.

3.3.2. Thermal Disturbance of the TIG Roadway.

From Figure 6, the temperature of the surrounding rock of the TIG roadway is slowly disturbed in the beginning, and the range of disturbance increases gradually with dimensionless time F_0.

According to the data, when $F_0 = 0.1$, the dimensionless temperatures T of 0.9 R, 1 R, and 2 R are disturbed immediately. Among them, the temperature of the TIG layer wall (0.9 R) drops to 30.6% of the initial dimensionless temperature; that of roadway wall (1R) declines to 78.8% of the initial dimensionless temperature; and that of internal surrounding rock (2 R) begins to be slightly disturbed. The dimensionless temperatures of 3 R and 4 R in the surrounding rock do not begin to be disturbed until $F_0 = 0.3$ and $F_0 = 0.5$, respectively.

3.3.3. Characteristics of Temperature Drop at Different Radial Positions of the TIG Roadway.

The temperatures at 0.9 R and 1 R on both sides of the TIG layer drop suddenly at the beginning of ventilation, but the degrees of drops differ, leading to the formation of a relatively large temperature

(a)

(b)
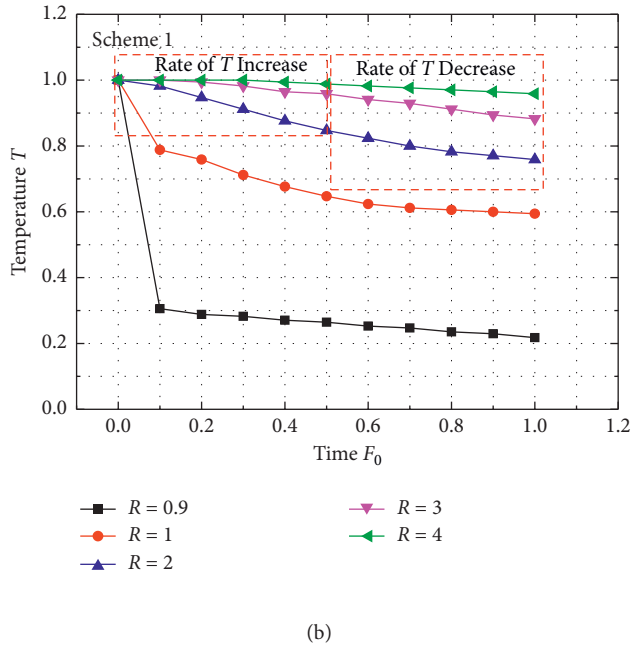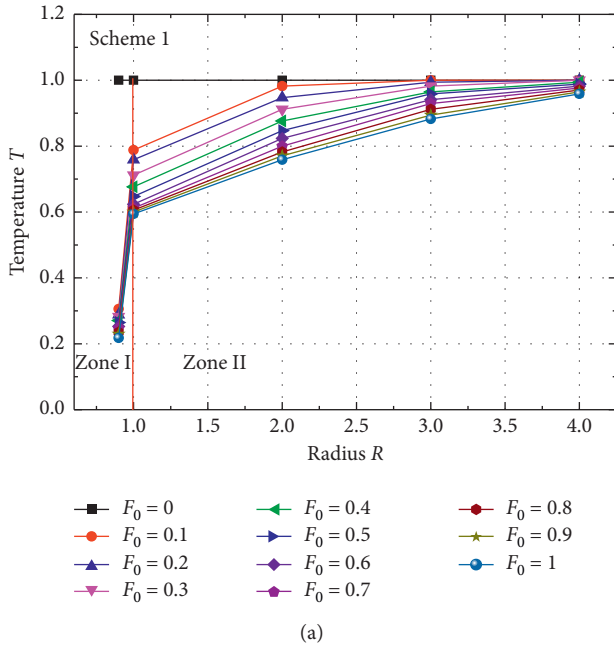
FIGURE 6: $T - R$ curve and $T - F_0$ curve under the working conditions of Scheme 1. (a) $T - R$ curve. (b) $T - F_0$ curve.

(a)

(b)
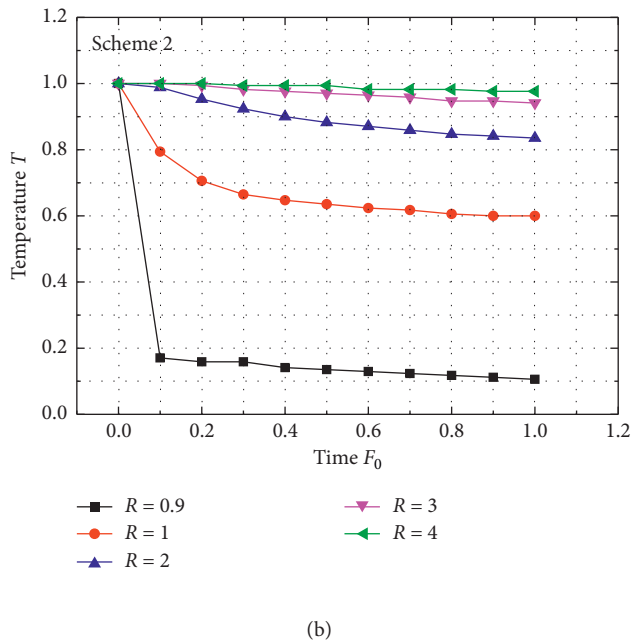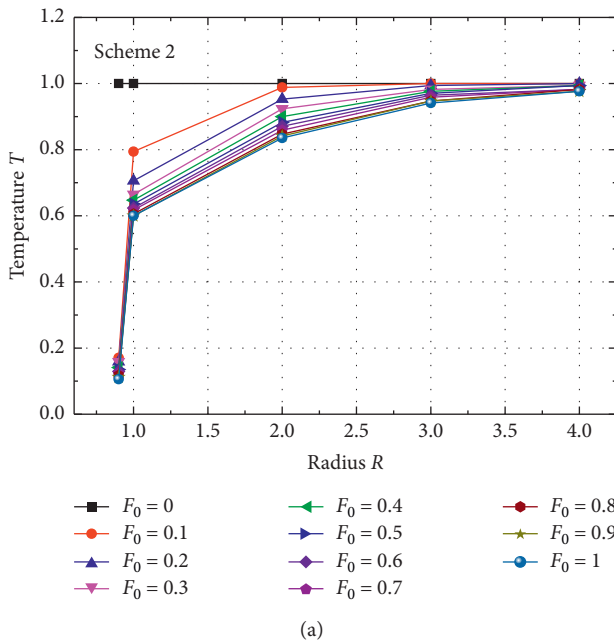
FIGURE 7: $T - R$ curve and $T - F_0$ curve under the working conditions of Scheme 2. (a) $T - R$ curve. (b) $T - F_0$ curve.

difference. The temperature outside the TIG layer (0.9 R) drops in an equal slope; the temperature inside the TIG layer (1 R) declines at a gradually reducing rate; and the temperature inside the surrounding rock (2 R) falls at an increasing rate first and at a decreasing rate later.

(1) TIG Layer Zone (Zone I). The temperature on the TIG layer wall falls sharply at the beginning of ventilation. As presented in Figure 10, after $F_0 = 0.1$, the temperature here

(0.9 R) decreases in an equal slope with the increase of F_0 under the four schemes.

(2) Surrounding Rock Zone (Zone II). According to the temperature data at 1 R and 0.9 R on both sides of the TIG layer, the temperature at 1 R drops sharply at the beginning of ventilation when $F_0 = 0.1$, but the range of drop is much smaller than that of the TIG layer wall, leading to the formation of a relatively large temperature difference on the
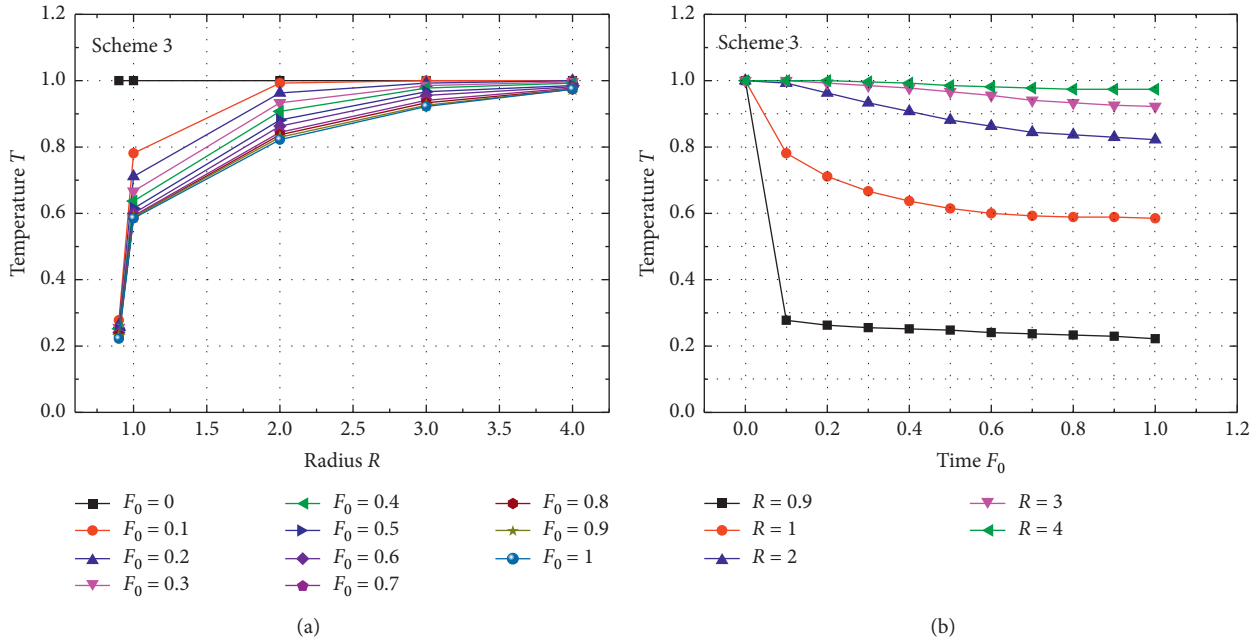
FIGURE 8: $T - R$ curve and $T - F_0$ curve under the working conditions of Scheme 3. (a) $T - R$ curve. (b) $T - F_0$ curve.
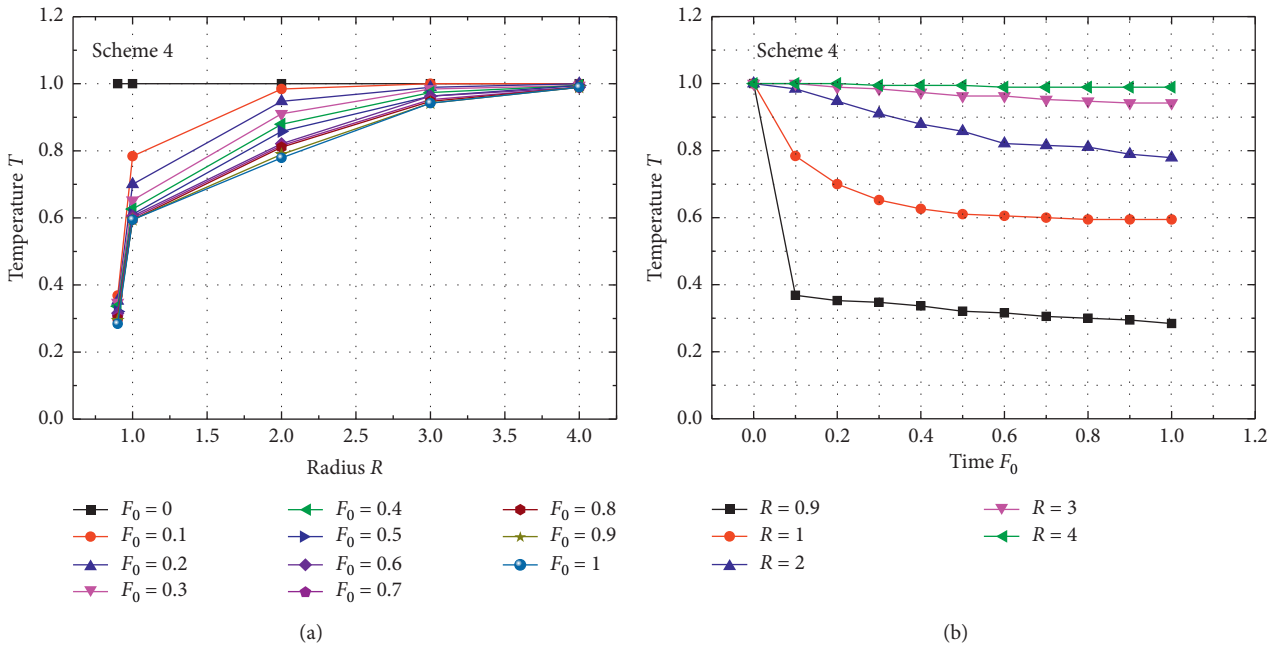
FIGURE 9: $T - R$ curve and $T - F_0$ curve under the working conditions of Scheme 4. (a) $T - R$ curve. (b) $T - F_0$ curve.

TABLE 7: Relationship between dimensionless temperature and dimensionless radius.

F_0	P_1	P_2	P_3	Correlation coefficient
0.2	−1.06	−1.47	1.01	0.99
0.4	−0.83	−0.88	1.02	0.99
0.6	−0.82	−0.67	1.04	0.99
0.8	−0.78	−0.47	1.09	0.99
1	−0.79	−0.36	1.15	0.99
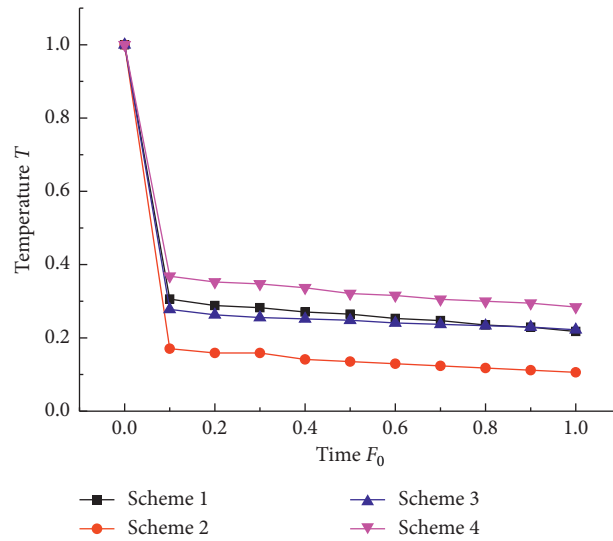
FIGURE 10: Variations of temperature T on the TIG layer wall at 0.9 R with time.
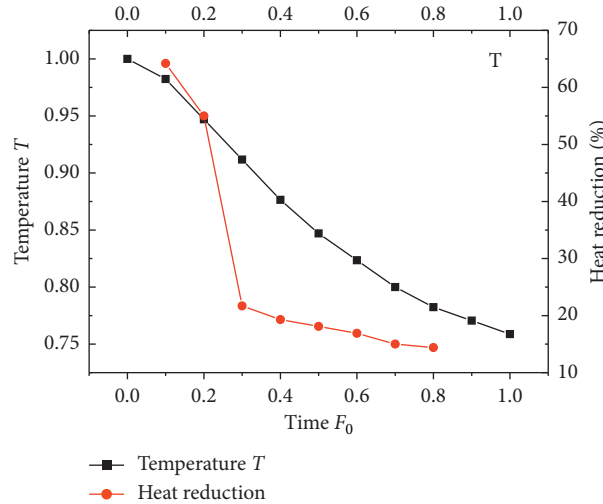
FIGURE 11: Relationship between the temperature drop at 2 R and the heat reduction of the surrounding rock under Scheme 1.

two sides. The temperature at 1 R declines at a gradually decreasing rate with the increase of F_0 and tends to level off when $F_0 = 0.8$.

The temperatures at 2 R in the surrounding rock decreases with the increase in F_0, but their temperature variation rates differ from that of the wall. The temperature drop rates keep growing before $F_0 = 0.2 \sim 0.4$, and they tend to level off after $F_0 > 0.4$, as shown in Figure 6(b). Since 3 R and 4 R are closer to the outer boundary, the above-mentioned law is not evidently exhibited at the two positions. However, it can be inferred that for the position father away from the wall, the turning point of the temperature drop rate appears later temporally. This indicates that the inside of the surrounding rock exhibits a lagging response time for the adjustment of boundary temperature disturbance, and the longer the distance is, the longer the response time is. Compared with the non-TIG roadway, the TIG roadway presents more obvious lagging response time.

By comparing Figure 6 with Figures 7–9, it is found that the variations of ventilation parameters (wind speed and wind temperature) and virgin rock temperature do not alter the variation trends of the $T − R$ curve and $T − F_0$ curve. Besides, variations of these parameters exert no significant effect on the internal temperature field of the TIG roadway in this experimental scope. As presented in Figure 10, the variations of ventilation parameters (wind speed and wind temperature) and virgin rock temperature directly affect the wall temperature, which demonstrates that the TIG layer has a significant effect on the stability of the temperature field of internal surrounding rock.

Figure 11 is a comparison between the temperature drop and the heat reduction at 2 R of the surrounding rock under Scheme 1. From Figure 11, the heat reduction of the TIG roadway is significantly lowered after $F_0 > 0.3 \sim 0.4$, which corresponds to the gentle temperature drop rates at 2 R, 3 R,

and 4 R, as in Figure 6(b). This suggests that the TIG structure should be constructed in the early stage of ventilation in order to achieve an excellent effect.

4. Conclusions

In this paper, a kind of mine TIG material that boasts light weight, thermal insulation, and large load-bearing capacity was developed by taking cement, sand, fly ash, and vitrified microsphere as raw materials and density, thermal conductivity, and UCS as evaluation indexes. Furthermore, the thermal insulation effect of the TIG layer was analyzed with the aid of a physical similarity simulation experimental apparatus independently developed by our research team. Besides, the temperature field characteristics of the surrounding rock were researched on. The following main conclusions were drawn:

(1) The thermal insulation effect of the TIG material in the high geo-temperature roadway was analyzed by means of physical similarity simulation. The temperature disturbance time, temperature drop rate, and temperature drop range of radial points in the surrounding rock of the TIG roadway and the non-TIG roadway were compared. The results show that, in the early stage of TIG layer construction, the heat reduction of the roadway wall reaches over 60%, which directly demonstrates the excellent thermal insulation performance of the TIG material. The changes in ventilation parameters (wind speed and wind temperature) and virgin rock temperature do not notably influence the internal temperature field of the surrounding rock of the TIG roadway, which suggests that the TIG layer has an important influence on the stability of the surrounding rock temperature field. This indirectly demonstrates the good thermal insulation performance of the TIG material.

(2) Characteristics of temperature field in the surrounding rock of the TIG roadway were researched on. The thermal flux density (T/R) of surrounding rock near the roadway wall is larger in the early stage of ventilation; then, the thermal flux densities tend to be consistent as the ventilation time F_0 increases from 0 to 1. This indicates that the temperature field of surrounding rock regains a balance, which marks the end of temperature disturbance. An obvious exponential function relationship exists between T and R during the entire time period.

(3) Different radial points of the surrounding rock in the TIG roadway exhibit varying characteristics of temperature drop. The temperature outside the TIG layer drops sharply as ventilation begins, and then, the temperature drop develops in an equal slope. The temperature of the inner wall of the TIG layer declines in a smaller range than that of the outer wall at the beginning of ventilation, after which the temperature drop rate decreases gradually. The temperature drop inside the surrounding rock increases

first and, then, decreases. The inside of the surrounding rock exhibits a lagging response time for the adjustment of boundary temperature disturbance; and the longer the distance is, the longer the response time is. Compared with the non-TIG roadway, the TIG roadway presents more obvious lagging response time. The stage of decreasing temperature drop rate of the surrounding rock corresponds to the stage of gentle heat reduction of the wall.

Data Availability

The data used to support the findings of this study are available from the corresponding author upon request.

Conflicts of Interest

The authors declare no conflicts of interest.

Acknowledgments

References

[1] J. Y. Wang, *Geothermology and its Application*, Science Press, Beijing, China, 2015.

[2] Z. P. Xie, "Distribution law of high temperature mine's thermal environment parameters and study of heat damage's causes," *Procedia Engineering*, vol. 43, pp. 588–593, 2012.

[3] P. Ma, "Application and research of prevention and control technique of thermal damage in deep mining of coal mine," *Value Engineering*, vol. 37, no. 3, pp. 125-126, 2018.

[4] K. Carpenter, P. Roghanchi, and C. Kocsis, "Investigating the importance of climatic monitoring and modeling in deep and hot US underground mines," in *Proceedings of 15th North American Mine Ventilation Symposium*, pp. 1–4, Virginia Tech, Virginia, 2015.

[5] B. Belle and M. Biffi, "Cooling pathways for deep Australian longwall coal mines of the future," *International Journal of Mining Science and Technology*, vol. 28, no. 6, pp. 865–875, 2018.

[6] N. Slazak, D. Obracaj, and M. Borowski, "Methods for controlling temperature hazard in Polish coal mines," *Archives of Mining Sciences*, vol. 53, no. 4, pp. 497–510, 2008.

[7] X. J. Yang, Q. Y. Han, J. W. Pang et al., "Progress of heat-hazard treatment in deep mines," *International Journal of Mining Science and Technology*, vol. 21, no. 2, pp. 295–299, 2011.

[8] Z. J. Wan, S. K. Bi, Y. Zhang et al., "Framework of the theory and technology for simultaneous extraction of coal and geothermal resources," *Journal of China Coal Society*, vol. 43, no. 8, pp. 2099–2106, 2018.

[9] Y. Zhang, *Transient Temperature Field of Surrounding Rock of the High Geothermal Roadway and its Heat Control Mechanism by Heat Insulation*, China University of Mining and Technology, Xuzhou, China, 2013.

[10] C. Kang, W. Zha, L. Zhang et al., "Control theory and technology analysis of high temperature in deep mining," *Safety in Coal Mines*, vol. 47, no. 5, pp. 89–93, 2016.

[11] M. He, X. Cao, Q. Xie et al., "Principles and technology for stepwise utilization of resources for mitigating deep mine heat hazards," *Mining Science and Technology (China)*, vol. 20, no. 1, pp. 20–27, 2010.

[12] M. G. Zhang, X. J. Zhang, and Y. Zhang, "Discussion on comprehensive control of mine heat hazard," *Advanced Materials Research*, vol. 726–731, pp. 854–858, 2013.

[13] Y. Zhang, Z.-J. Wan, B. Gu, C.-B. Zhou, and J.-Y. Cheng, "Unsteady temperature field of surrounding rock mass in high geothermal roadway during mechanical ventilation," *Journal of Central South University*, vol. 24, no. 2, pp. 374–381, 2017.

[14] H. P. Kang, G. F. Wang, P. F. Jiang et al., "Conception for strata control and intelligent mining technology in deep coal mines with depth more than 1000m," *Journal of China Coal Society*, vol. 43, no. 7, pp. 1789–1800, 2018.

[15] K. Trapani, A. Romero, and D. Millar, "Deep mine cooling, a case for Northern Ontario: Part II," *International Journal of Mining Science and Technology*, vol. 26, no. 6, pp. 1033–1042, 2016.

[16] X.-P. Feng, Z. Jia, H. Liang et al., "A full air cooling and heating system based on mine water source," *Applied Thermal Engineering*, vol. 145, pp. 610–617, 2018.

[17] M.-C. He, "Application of HEMS cooling technology in deep mine heat hazard control," *Mining Science and Technology (China)*, vol. 19, no. 3, pp. 269–275, 2009.

[18] L. Aditya, T. M. I. Mahlia, B. Rismanchi et al., "A review on insulation materials for energy conservation in buildings," *Renewable and Sustainable Energy Reviews*, vol. 73, pp. 1352–1365, 2017.

[19] S. Schiavoni, F. D'Alessandro, F. Bianchi, and F. Asdrubali, "Insulation materials for the building sector: a review and comparative analysis," *Renewable and Sustainable Energy Reviews*, vol. 62, pp. 988–1011, 2016.

[20] T. Chien Yet, R. Hamid, and M. Kasmuri, "Dynamic stress-strain behaviour of steel fiber reinforced high-performance concrete with fly ash," *Advances in Civil Engineering*, vol. 2012, 2012.

[21] Z. Zhang, Y. Zhu, H. Zhu, Y. Zhang, J. L. Provis, and H. Wang, "Effect of drying procedures on pore structure and phase evolution of alkali-activated cements," *Cement and Concrete Composites*, vol. 96, pp. 194–203, 2019.

[22] A. Noushini, K. Vessalas, G. Arabian et al., "Drying shrinkage behaviour of fibre reinforced concrete incorporating polyvinyl alcohol fibres and fly ash," *Advances in Civil Engineering*, vol. 2014, 2014.

[23] G. F. Li, *Research on Technology of Active Cooling Supporting Structure in High Temperature Road Way*, Taiyuan University of Technology, Taiyuan, China, 2010.

[24] X. L. Zhang, *The Development of Mine Thermal Insulation Material and the Expermental Study of it's Performance*, Henan Polytechnic University, Henan, China, 2012.

[25] F. Yang, *Experimental Study of High Temperature Deep Roadway New Insulation Materials*, Anhui University of Science and Technology, Anhui, China, 2016.

[26] J. Wang, C. Zhu, Q. Hou et al., "Experimental study on heat insulation of vermiculite mortar in heat harmful mine," *Safety in Coal Mines*, vol. 45, no. 9, pp. 13–15, 2014.

[27] L. Liu and J. Zhang, "Thermal insulation composite material for governance of underground thermal hazard and its application," *Journal of Shandong University of Science & Technology*, vol. 36, no. 1, pp. 46–53, 2017.

[28] F. F. Wang, D. C. Mei, and J. Y. Pang, "Research on performance of thermal insulation materials in underground high-temperature tunnels," *Coal Technology*, vol. 36, no. 2, pp. 187–189, 2017.

[29] X. H. Zhou, X. Tang, and D. P. Song, "Thermal insulation performance affected by thermal physical parameters of thermal insulation layer in active thermal insulation tunnel," *Mining Safety and Environmental Protection*, vol. 46, no. 1, pp. 18–22, 2019.

[30] Y. J. Wang, G. Q. Zhou, Y. Z. Wei et al., "Experimental research on changes in the unsteady temperature field of an airway in deep mining engineering," *Journal of China University of Mining & Technology*, vol. 40, no. 3, pp. 345–350, 2011.

[31] Y. Zhang, Z. Wan, B. Gu et al., "An experimental investigation of transient heat transfer in surrounding rock mass of high geothermal roadway," *Thermal Science*, vol. 20, no. 6, 53 pages, 2016.

[32] S. Zhu, S. Wu, J. Cheng, S. Li, and M. Li, "An underground air-route temperature prediction model for ultra-deep coal mines," *Minerals*, vol. 5, no. 3, pp. 527–545, 2015.

[33] H. Z. Wang, *Study on Characteristics of Heat and Mass Transfer in Working Face of High-Temperature Mine*, China University of Mining and Technology, Xuzhou, China, 2016.

Research Article

Transition Threshold of Granite Mechanical Characteristics at High Temperature

Hongjun Guo [iD],[1] **Ming Ji** [iD],[2] **and Dapeng Liu**[1]

[1]*Jiangsu Vocational Institute of Architectural Technology, Xuzhou 221116, China*
[2]*Key Laboratory of Deep Coal Resource Mining, Ministry of Education of China, School of Mines,
  China University of Mining & Technology, Xuzhou 221116, China*

Correspondence should be addressed to Ming Ji; jiming@cumt.edu.cn

No unified criterion exists for the transition threshold of rock mechanical characteristics. We combine rock stress-strain curves to propose an increment ratio of axial pressure based on uniaxial compression tests on granite at high temperature. The behavior of the increment ratio of strain, elastic modulus, Poisson's ratio, and energy with axial pressure is analyzed, and the following conclusions are drawn. (1) High temperatures aggravate rock deterioration, reduce failure strength, and enhance ductility characteristics. (2) Under loading, the compression-to-elasticity and elasticity-to-plasticity transition thresholds for rock occur, respectively, at 20%–35% and 75%–80% stress levels at temperatures of 25–800°C. (3) The source data for calculating rock deformation parameters or unloading points for unloading tests can be selected over the stress level range of 35%–75%.

1. Introduction

Rock mechanics tests have gathered significant attention worldwide. The tests include uniaxial and triaxial, single-stress and complex-stress paths, dry and saturated environments, freeze-thaw and high-temperature conditions, cracks and pore pressure, and natural and prefabricated samples, as well as auxiliary methods (e.g., acoustic emission, electromagnetic or infrared radiation, and computed tomography scanning) and have provided important results [1–6].

However, some qualitative conclusions are difficult to quantify from the available results as described by the following examples. (1) In the stress-strain curve, the transition zone or conversion threshold in the compaction-to-elastic and elastic-to-plastic stages is not quantified and the selection is inevitably affected by subjective factors. (2) When the stress-strain curve is used to solve for deformation parameters (elastic modulus and Poisson's ratio), the data interval selection varies from user to user and is often chosen on the premise of conforming to objective facts. (3) There is no uniform standard for selecting the unloading point in an uniaxial or triaxial unloading test. Most previous studies have chosen 80% of the peak rock strength as the unloading point (Table 1). This introduces confusion in the calculation of relevant parameters or design of complex test schemes.

In view of the abovementioned problems, Ji [19] combined conventional triaxial compression tests to explore the critical value of rock damage transitions under triaxial compression [20]. Following on this work, we further study the mechanical properties of rock after high temperature under different stress conditions.

2. Materials and Methods

The granite samples used in the tests were collected from a mine in Weifang, Shandong, China, with an average density of $2.612 \, \text{g/cm}^3$ at room temperature. The samples were processed into standard cylindrical specimens of $\Phi50 \, \text{mm} \times H100 \, \text{mm}$ (error $\pm 0.5 \, \text{mm}$) following the International Society of Rock Mechanics (ISRM) standards, as shown in Figure 1. The tests were performed using an MTS815.02 electrohydraulic servo material test system (Figure 2).

TABLE 1: Statistics of unloading level in rock unloading test.

Lithology	Unloading level (%)	Researchers
Rock masses with interlayer staggered zones	25, 40, 50, 60, 70, 80	Duan et al. [7]
Tuffaceous sandstone	65–75	Zhou et al. [8]
Granite	70–80	Duan et al. [9]
Sandstone	85–95	Liu et al. [10]
Sandstone	70, 80, 90	Liu et al. [11]
Rhyolite	80–90	Zhong et al. [12]
Rock mass inside the composite slope	80	Chang et al. [13]
Granite, red sandstone	80	Du et al. [14]
Sandstone	80	Yang et al. [15] Qin et al. [16]
Granite	80	Dai et al. [17]
Marble	80	Zhao et al. [18]

FIGURE 1: Granite specimen.

FIGURE 2: MTS815.02 testing system.

(1) The specimen was subjected to high-temperature treatment at 25, 200, 400, 600, and 800°C. To ensure uniform internal heating, the temperature was raised to the set value and held constant for 2 h and then cooled to room temperature.

(2) Axial pressure was applied using the displacement control mode at a loading rate of 0.003 mm/s until the specimen broke.

3. Results

The uniaxial compression test data of granite at high temperature are given in Table 2, and the typical data were selected to draw the stress-strain curve as shown in Figure 3.

The compression process goes through several stages including compaction, elasticity, yield, failure, and residue.

TABLE 2: Test data.

T (°C)	No.	$\varepsilon_1 \times 10^{-3}$	$\sigma_{1\,\max}$ (MPa)
25	#1	4.16	120.37
	#2	4.04	116.61
	#3	4.26	122.28
200	#1	4.83	121.77
	#2	4.72	117.77
	#3	4.88	120.21
400	#1	4.23	97.94
	#2	4.44	95.56
	#3	4.32	98.82
600	#1	5.86	54.62
	#2	5.72	53.69
	#3	5.75	58.95
800	#1	5.45	41.91
	#2	5.15	41.15
	#3	5.33	43.80
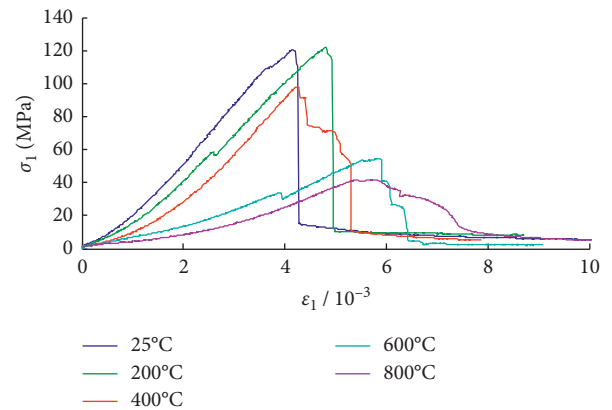
FIGURE 3: Stress-strain curves.

With increasing temperature, the strain growth rate is more prominent than the stress growth rate and ductility characteristics are observed. Rock strength is less affected when the temperature is < 200°C. Above 200°C, rock strength reduces approximately linearly. Between 400 and 600°C, the strength drop is more significant [21, 22], as shown in Figure 4.

$$\sigma_c = -0.1414T + 149.79$$
$$R^2 = 0.9624$$

Testing
Fitting
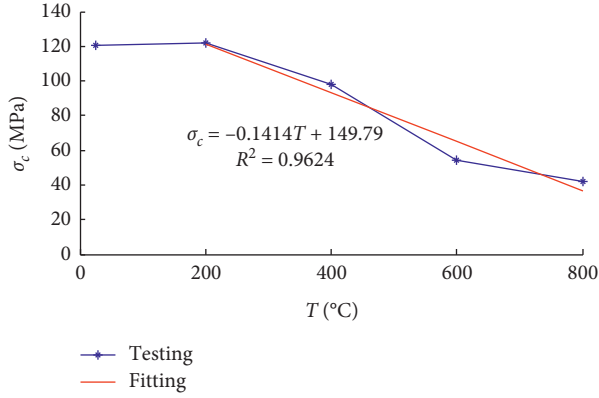
FIGURE 4: Failure strength-temperature curve.

3.1. Strain Evolution.

Under uniaxial compression, rock strain is only related to axial pressure. To study the effect of stress level, we introduce the concept of increment ratio of strain to axial pressure [19, 23–25], namely, the ratio of the increase in strain to the increase in axial pressure, which is expressed as follows:

$$\frac{\Delta\varepsilon_{1(t+1)}}{\Delta\sigma_{1(t+1)}} = \frac{\varepsilon_{1(t+1)} - \varepsilon_{1(t)}}{\sigma_{1(t+1)} - \sigma_{1(t)}}, \tag{1}$$

where $\Delta\varepsilon_{1(t+1)}$ is the increment of axial strain at $t+1$; $\varepsilon_{1(t+1)}$ and $\varepsilon_{1(t)}$ are the axial strains at $t+1$ and t; $\Delta\sigma_{1(t+1)}$ is the increment of axial pressure at $t+1$; and $\sigma_{1(t+1)}$ and $\sigma_{1(t)}$ are the axial pressures at $t+1$ and t.

The increment ratio of strain to axial pressure is a physical quantity that characterizes the rapid or slow change of strain with axial pressure. It well reflects the influence of axial pressure changes on rock deformation and damage during loading, as well as the internal structural response to the change of external macromechanical state. Larger increment ratios of strain to axial pressure are associated with higher sensitivity of rock deformation to changes of axial pressure. The relationship between the increment ratio of strain to axial pressure and stress level is obtained by combining the test data and equation (1), as shown in Figure 5.

The increment ratio of strain to axial pressure shows a peak at the approximate compression-to-elastic and elastic-to-plastic transition stages in the stress-strain curve. This indicates that the ratio can be used as an indicator for assessing a change of rock mechanical characteristics. The corresponding stress levels of axial pressure are listed in Table 3.

It should be emphasized that (1) the rock samples are heterogeneous and anisotropic, and the transition points of their mechanical characteristics should be over a small stress range; (2) some specimens also show a strong response in the increment ratio of strain to axial pressure during the compaction stage, which is related to the initial state of their internal pores and fractures.

The compaction-to-elastic transition point in the stress-strain curve changes with increasing temperature, which is

related to the internal cracks [21], whereas the elastic-to-plastic transition point remains essentially unchanged at about 80% stress level.

3.2. Deformation Parameter Evolution.

The elastic modulus and Poisson's ratio are important mechanical parameters of rock, and their changes are closely related to deformation and damage. Similarly, the increment ratio of deformation parameters to axial pressure can also be obtained:

$$\begin{cases} \dfrac{\Delta E_{t+1}}{\Delta\sigma_{1(t+1)}} = \dfrac{E_{t+1} - E_t}{\sigma_{1(t+1)} - \sigma_{1(t)}} \\[2ex] \dfrac{\Delta\mu_{t+1}}{\Delta\sigma_{1(t+1)}} = \dfrac{\mu_{t+1} - \mu_t}{\sigma_{1(t+1)} - \sigma_{1(t)}} \end{cases}, \tag{2}$$

where ΔE_{t+1} is the increment of elastic modulus at $t+1$; E_{t+1} and E_t are the elastic modulus at $t+1$ and t; $\Delta\mu_{t+1}$ is the increment of Poisson's ratio at $t+1$; and μ_{t+1} and μ_t are the Poisson ratios at $t+1$ and t.

The relationship between deformation parameters and the increment ratio to axial pressure and stress level is shown in Figures 6 and 7.

The results shown in Figures 6 and 7 are consistent with those in Figure 5, further indicating that a significant change of the increment ratio of rock parameters to axial compression can be used as an indicator of its mechanical characteristics. Table 4 lists the stress levels under different temperature conditions.

3.3. Strain Energy Evolution.

To further verify the accuracy of the results, we analyzed changes of rock strain energy. The law of energy conservation states that energy transformation occurs during rock deformation and failure. The change of thermal energy is not considered because the specimens were cooled to room temperature after heat treatment and loading was also performed at room temperature. Therefore, according to the law of thermodynamics, energy production mainly comes from the work of external forces. During uniaxial compression, the external forces on the rock specimen are only the axial pressure of the testing machine. The total energy absorbed by the rock sample is therefore the axial strain energy [18, 26], then

$$U_1 = \int_0^{\varepsilon_{1(t)}} \sigma_1 d\varepsilon_1, \tag{3}$$

where $\varepsilon_{1(t)}$ is the axial strain at any t.

According to the concept of definite integral in equation (3), we adopt the method of microelement area, which is

$$U_1 = \sum_{t=0}^{t_0} \frac{1}{2}\left(\sigma_{1(t+1)} + \sigma_{1(t)}\right)\left(\varepsilon_{1(t+1)} - \varepsilon_{1(t)}\right). \tag{4}$$

In combination with the previously described concept, the increment ratio of strain energy to axial pressure can be expressed as follows:

(a)

(b)

(c)

(d)

(e)
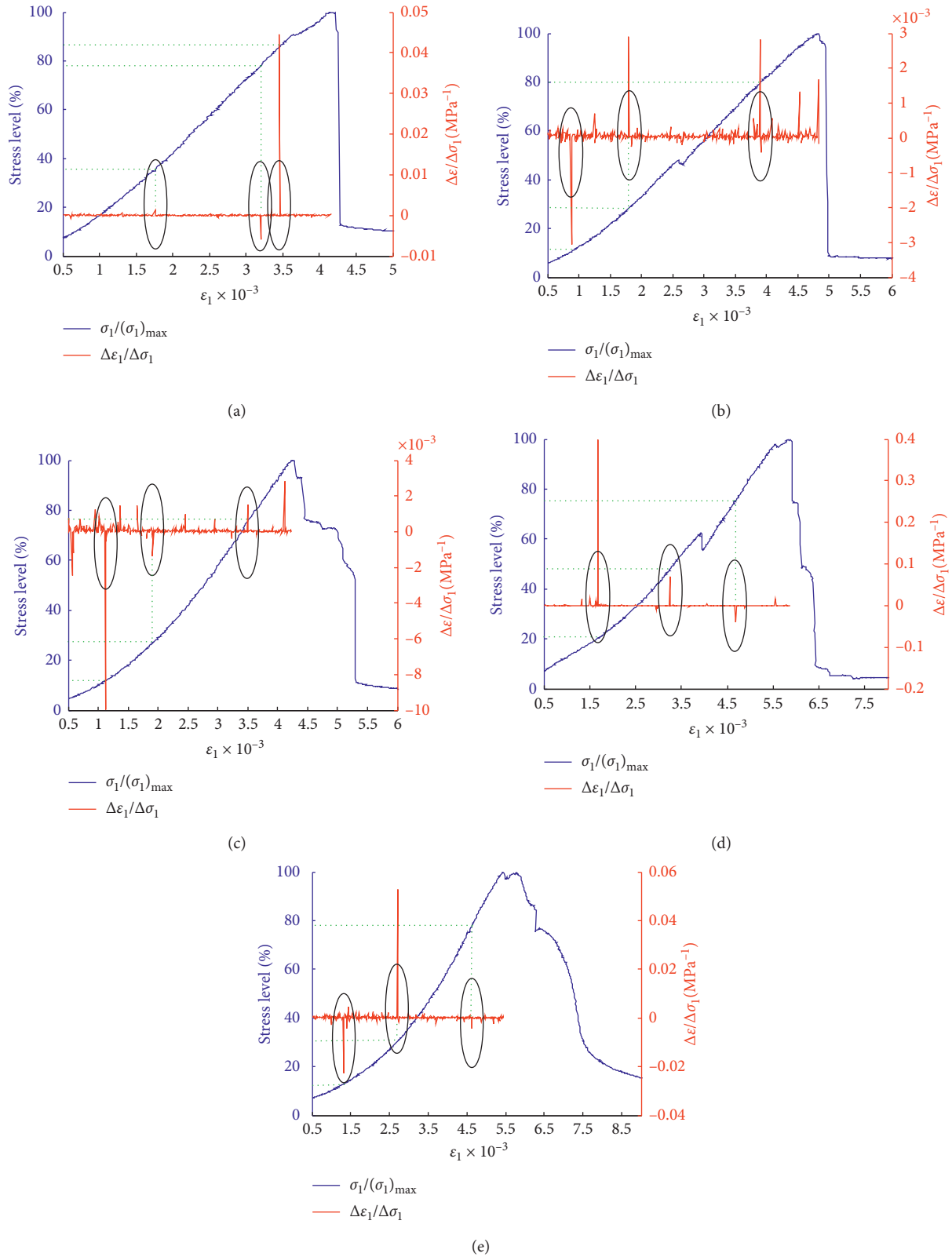
FIGURE 5: Evolution curve of the increment ratio of strain to axial pressure. (a) 25°C, (b) 200°C, (c) 400°C, (d) 600°C, and (e) 800°C.

$$\frac{\Delta U_{t+1}}{\Delta \sigma_{1(t+1)}} = \frac{U_{t+1} - U_t}{\sigma_{1(t+1)} - \sigma_{1(t)}}, \tag{5}$$

where ΔU_{t+1} is the increment of strain energy at $t + 1$, and U_{t+1} and U_t are the strain energies at $t + 1$ and t.

TABLE 3: Statistics of the incremental ratio of strain to axial pressure peak.

T (°C)	Stress level (%)	
	Compaction to elastic	Elastic to plastic
25	35.75	78.17–86.13
200	11.55–28.49	79.65
400	12.34–26.97	76.13
600	20.98	74.98
800	13.23–31.02	78.1

(a)

(b)

(c)

(d)

(e)
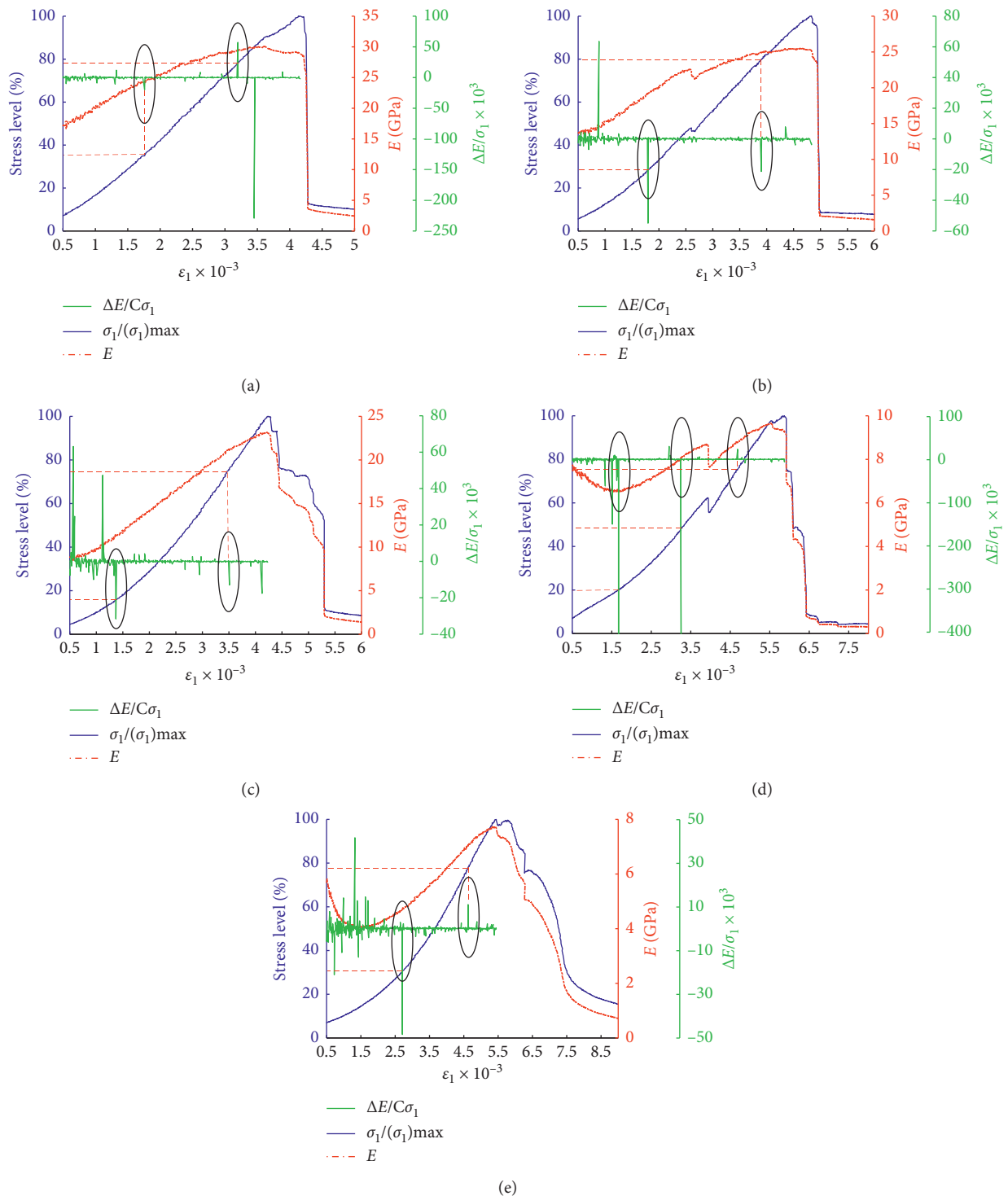
FIGURE 6: Evolution curve of the increment ratio of elastic modulus to axial pressure. (a) 25°C, (b) 200°C, (c) 400°C, (d) 600°C, and (e) 800°C.

(a)

(b)

(c)

(d)

(e)
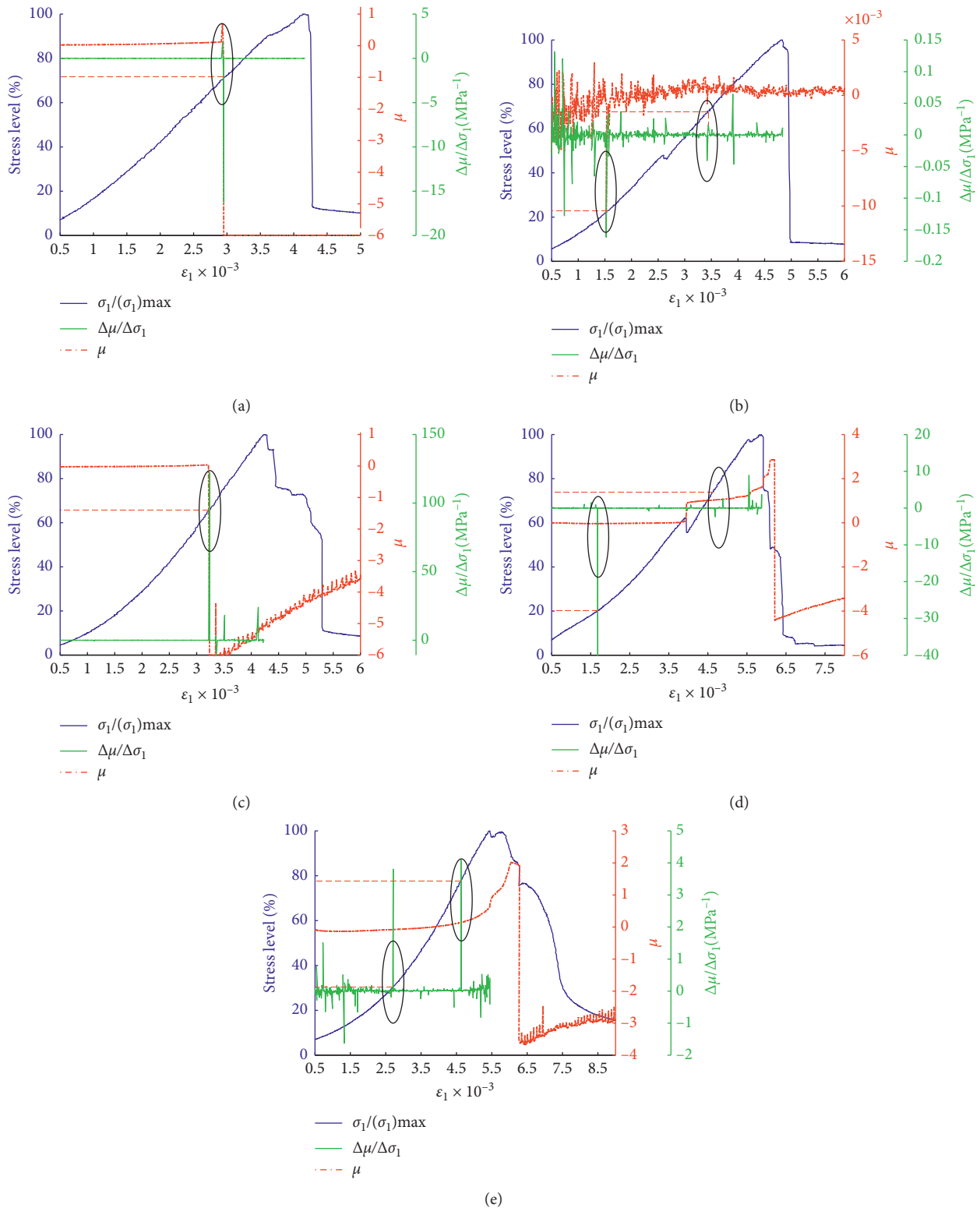
FIGURE 7: Evolution curve of the increment ratio of Poisson's ratio to axial pressure. (a) 25°C, (b) 200°C, (c) 400°C, (d) 600°C, and (e) 800°C.

Figure 8 shows the relationship between strain energy and increment ratio of strain energy to axial pressure and stress level during loading.

The threshold of rock mechanical characteristics is consistent with the conclusions obtained from strain, elastic modulus, and Poisson's ratio. The corresponding stress levels of axial pressure are listed in Table 5.

Critical points are believed to exist at the compaction-to-elasticity and elasticity-to-plasticity transitions during rock loading. A peak in the increment ratio of

TABLE 4: Statistics of the incremental ratio of deformation parameters to axial pressure peak.

T (°C)	Stress level (%)			
	(Compaction to elastic)^E	(Elastic to plastic)^E	(Compaction to elastic)$^\mu$	(Elastic to plastic)$^\mu$
25	35.75	78.17		71.68
200	28.49	79.65	23.24	67.36
400	15.96	74.4		65.83
600	19.9	75.18	20.12	74.56
800	31.02	77.86	30.31	77.86

(a)

(b)

(c)

(d)
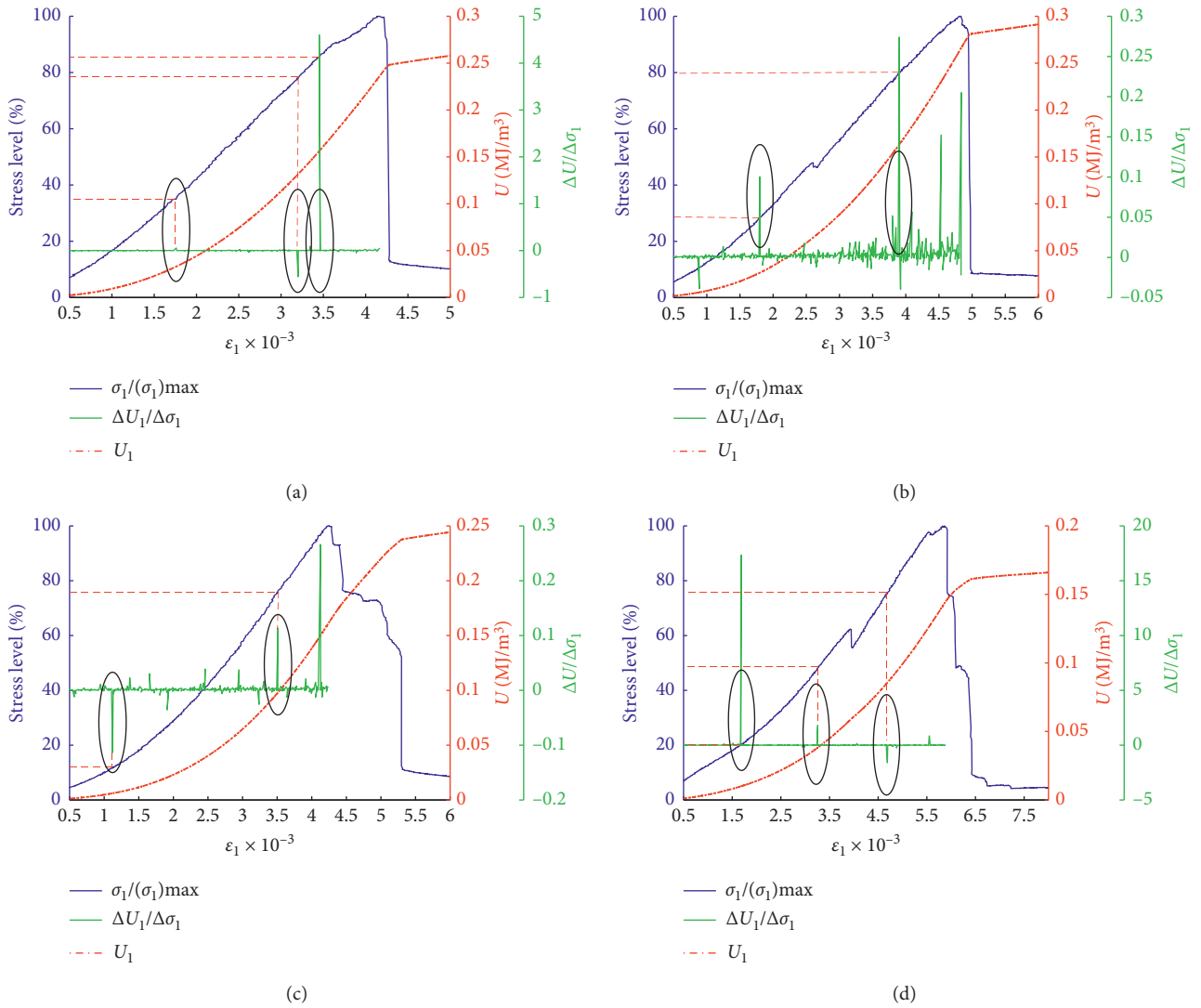
FIGURE 8: Continued.

(e)
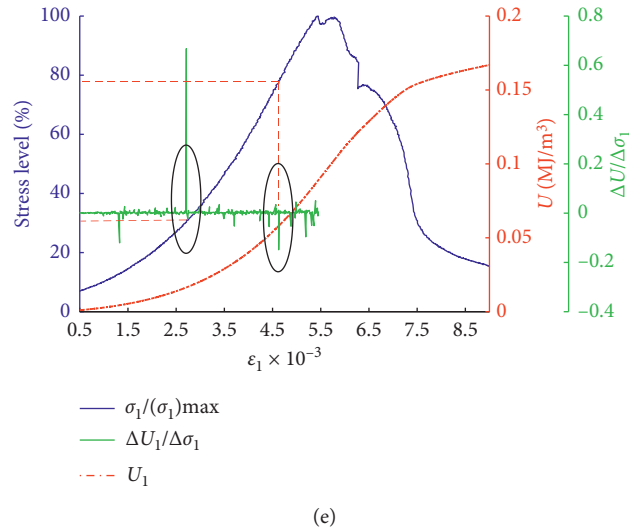
FIGURE 8: Evolution curve of the increment ratio of strain energy to axial pressure. (a) 25°C, (b) 200°C, (c) 400°C, (d) 600°C, and (e) 800°C.

TABLE 5: Statistics of the incremental ratio of strain energy to axial pressure peak.

T (°C)	Stress level (%)	
	Compaction to elastic	Compaction to elastic
25	34.97	78.49–85.85
200	28.49	80.07
400	12.34	75.56
600	20.12	75.6
800	31.02	77.86

(a)   (b)
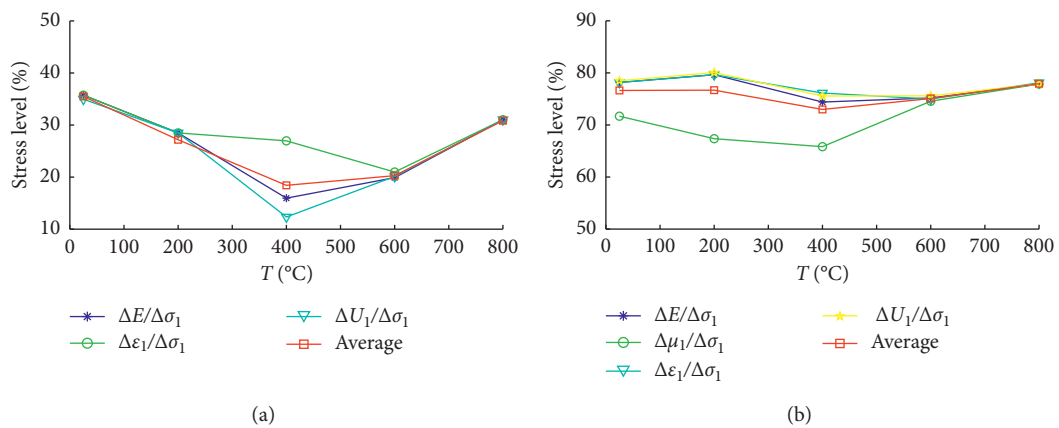
FIGURE 9: Relationship between the transition threshold of the rock mechanical characteristics and temperature. (a) Compression-to-elasticity transition. (b) Elasticity-to-plasticity transition.

different parameters to axial pressure can be used as the basis for evaluating the stress level.

4. Discussion

Figure 9 shows the loads corresponding to the critical compaction-to-elasticity and elasticity-to-plasticity transition points of granite under compression and variable temperature. The transition thresholds of rock mechanical characteristics obtained from the increment ratio of different parameters to axial pressure are in good agreement. The difference of initial rock state is enlarged to some extent at high temperature. The threshold of the compression-to-elasticity transition is therefore strongly affected by temperature. The transition threshold
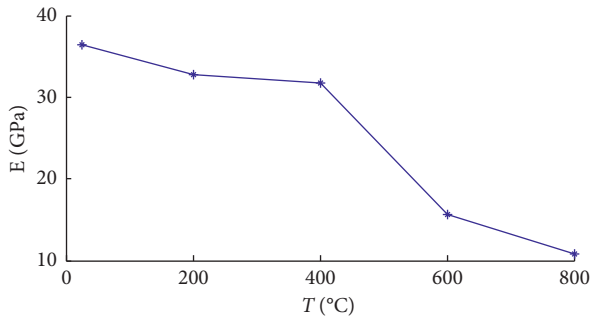
FIGURE 10: Relationship between elastic modulus and temperature.

generally occurs at the 20%–35% stress level. The rock enters the elastic stage under low-stress conditions at 400–600°C. However, the relationship between the elasticity-to-plasticity transition threshold and temperature is strong and remains at 75%–80% stress level over the full investigated temperature range (25–800°C).

Based on the above conclusions, the elastic modulus of granite under different temperatures was analyzed using data from the 40%–70% stress level range. The results are shown in Figure 10. The elastic modulus decreases irregularly with increasing temperature, which is consistent with the behavior of failure strength.

Because rock deformation in the elastic stage is reversible and does not cause substantial damage to itself, it is suggested that the unloading point be lower than the elasticity-to-plasticity transition threshold in unloading tests with complex-stress paths to avoid damage caused by higher loads later in the test.

5. Conclusions

We combine high-temperature uniaxial compression tests on granite with the concept of an increment ratio of axial pressure. The following conclusions are drawn:

(1) With increasing temperature, granite transitions from brittle to ductile failure. When the temperature exceeds 200°C, its strength decreases approximately linearly.

(2) Based on the analysis of the increment ratio of granite parameters (strain, deformation parameters, and strain energy) to axial pressure, it is considered that the transition thresholds of compaction to elasticity and elasticity to plasticity are 20%–35% and 75%–80% stress level, respectively.

(3) In general, rock deformation parameters can be calculated over the stress level range of 35%–75%. In unloading tests, we suggest that the unloading point is lower than the elasticity-to-plasticity transition threshold.

Data Availability

The data used to support the findings of the study are available from the corresponding author upon request.

Conflicts of Interest

The authors declare that there are no conflicts of interest regarding the publication of this paper.

Acknowledgments

References

[1] A. Momeni, M. Karakus, G. R. Khanlari, and M. Heidari, "Effects of cyclic loading on the mechanical properties of a granite," *International Journal of Rock Mechanics and Mining Sciences*, vol. 77, pp. 89–96, 2015.

[2] A. Singh, C. Kumar, L. G. Kannan, K. S. Rao, and R. Ayothiraman, "Estimation of creep parameters of rock salt from uniaxial compression tests," *International Journal of Rock Mechanics and Mining Sciences*, vol. 107, pp. 243–248, 2018.

[3] H. Munoz, A. Taheri, and E. K. Chanda, "Fracture energy-based brittleness index development and brittleness quantification by pre-peak strength parameters in rock uniaxial compression," *Rock Mechanics and Rock Engineering*, vol. 49, no. 12, pp. 4587–4606, 2016.

[4] H. Guo, M. Ji, Y. Zhang, and M. Zhang, "Study of mechanical property of rock under uniaxial cyclic loading and unloading," *Advances in Civil Engineering*, vol. 2018, Article ID 1670180, 6 pages, 2018.

[5] M. Ji, Y. D. Zhang, W. P. Liu, and L. Cheng, "Damane evolution law based on acoustic emission and weibull distribution of granite under uniaxial stress," *Acta Geodynamica Et Geomaterialia*, vol. 11, no. 3, pp. 269–277, 2014.

[6] M. Ji, K. Chen, and H. J. Guo, "Constitutive model of rock uniaxial damage based on rock strength Statistics," *Advances in Civil Engineering*, vol. 2018, Article ID 5047834, 8 pages, 2018.

[7] S. D. Duan, Q. Jiang, D. P. Xu, and G. F. Liu, "Experimental study of mechanical behavior of interlayer staggered zone under cyclic loading and unloading condition," *International Journal of Geomechanics*, vol. 20, no. 3, pp. 1–12, 2020.

[8] Z. Zhou, H. Zhan, J. Hu, and C. Ren, "Characteristics of unloading creep of tuffaceous sandstone in east tianshan tunnel under freeze-thaw cycles," *Advances in Materials Science and Engineering*, vol. 2019, Article ID 7547564, 16 pages, 2019.

[9] K. Duan, Y. Ji, W. Wu, and C. Y. Kwok, "Unloading-induced failure of brittle rock and implications for excavation-induced strain burst," *Tunnelling and Underground Space Technology*, vol. 84, pp. 495–506, 2019.

[10] J. Liu and J. P. Li, "Experimental Research on sandstone pre-peak unloading process under high confining pressure," *Chinese Journal of Rock Mechanics and Engineering*, vol. 30, no. 3, pp. 473–479, 2011.

[11] X. R. Liu, J. Liu, D. L. Li, J. B. Wang, Z. J. Wang, and Z. L. Zhong, "Unloading mechanical properties and constitutive model of sandstone under different pore pressures and initial unloading levels," *Journal of China Coal Society*, vol. 42, no. 10, pp. 2592–2600, 2017.

[12] Z. B. Zhong, *Experimental Study on Mechanical Properties of Microfissured Rhyolite Under Triaxial Test*, Southwest Jiaotong University, Chengdu, China, 2013.

[13] Z. Chang, Q. Cai, W. Zhou, I. M. Jiskani, and R. Wang, "Effects of the loading and unloading conditions on crack propagation in high composite slope of deep open-pit mine," *Advances in Civil Engineering*, vol. 2019, Article ID 3168481, 11 pages, 2019.

[14] K. Du, M. Tao, X.-b. Li, and J. Zhou, "Experimental study of slabbing and rockburst induced by true-triaxial unloading and local dynamic disturbance," *Rock Mechanics and Rock Engineering*, vol. 49, no. 9, pp. 3437–3453, 2016.

[15] R. Yang, D. Ma, and Y. Yang, "Experimental investigation of energy evolution in sandstone failure during triaxial unloading confining pressure tests," *Advances in Civil Engineering*, vol. 2019, Article ID 37419752, 11 pages, 2019.

[16] T. Qin, H. Sun, H. Liu et al., "Experimental study on mechanical and acoustic emission characteristics of rock samples under different stress paths," *Shock and Vibration*, vol. 2018, Article ID 4813724, 9 pages, 2018.

[17] B. Dai, G. Zhao, L. Dong, and C. Yang, "Mechanical characteristics for rocks under different paths and unloading rates under confining pressures," *Shock and Vibration*, vol. 2015, Article ID 578748, 8 pages, 2015.

[18] G.-Y. Zhao, B. Dai, L.-J. Dong, and C. Yang, "Energy conversion of rocks in process of unloading confining pressure under different unloading paths," *Transactions of Nonferrous Metals Society of China*, vol. 25, no. 5, pp. 1626–1632, 2015.

[19] M. Ji and H. Guo, "Elastic-plastic threshold and rational unloading level of rocks," *Applied Sciences*, vol. 9, no. 15, p. 3164, 2019.

[20] Q. Sun, M. Ji, L. Xue, and T. M. Su, "The influence of moisture content on the acoustic emission at threshold of rock destruction," *Acta Geodynamica et Geomaterialia*, vol. 12, no. 3, pp. 279–287, 2015.

[21] X. L. Xu, F. Gao, and Z. Z. Zhang, "Research on triaxial compression test of granite after high temperatures," *Rock and Soil Mechanics*, vol. 35, no. 11, pp. 3177–3183, 2014.

[22] X. L. Xu, F. Gao, and Z. Z. Zhang, "Influence of confining pressure on deformation and strength properties of granite after high temperatures," *Chinese Journal of Geotechnical Engineering*, vol. 36, no. 12, pp. 2246–2252, 2014.

[23] T. Li, *Siltstone's Mechanical Properties in Different Stress Paths and Research of Unloading Constitutive Model*, China University of Mining and Technology, Xuzhou, China, 2015.

[24] D.-M. Zhang, Y.-S. Yang, Y.-P. Chu, X. Zhang, and Y.-G. Xue, "Influence of loading and unloading velocity of confining pressure on strength and permeability characteristics of crystalline sandstone," *Results in Physics*, vol. 9, pp. 1363–1370, 2018.

[25] S. L. Qiu, X. T. Feng, C. Q. Zhang, H. Zhou, and F. Sun, "Experimental research on mechanical properties of deep-buried marble under different unloading rates of confining pressures," *Chinese Journal of Rock Mechanics and Engineering*, vol. 31, no. 8, pp. 1686–1698, 2012.

[26] D. Huang and Y. Li, "Conversion of strain energy in triaxial unloading tests on marble," *International Journal of Rock Mechanics and Mining Sciences*, vol. 66, pp. 160–168, 2014.

Research Article

The Research on the Effect of Humidity on the Rheological Model of Swelling Rock

Ming Ji [1] **and Yi-Dong Zhang**[2]

[1]*Key Laboratory of Deep Coal Resource Mining, Ministry of Education of China and China University of Mining & Technology, Xuzhou 221116, China*
[2]*State Key Laboratory of Coal Resources and Mine Safety, China University of Mining & Technology, Xuzhou 221116, China*

Correspondence should be addressed to Ming Ji; jiming@cumt.edu.cn

The research on the rheological mechanical behaviour of swelling rock in the condition of humidity field has a significant meaning for large rock engineering, such as deep coal mining, tunnelling, and slope engineering. Based on the Nishihara model, considering on the effect of humidity factor on swelling rock, the rheological elements are established and the effects of humidity on the damage of rock, the viscosity, and the elasticity are introduced. Moreover, the viscoelastic plasticity constitutive equations are established under the coupling of swelling rock stress and humidity. Afterward, considering the effects of humidity on the damage, elasticity, and viscosity, the creeping, unloading, and relaxation equations have been deduced. From this research, under the state of low stress ($\sigma_{3P} < \sigma_S$), the Nishihara model which considers the effect of humidity shows the properties of stable creeping. In addition, the unloading curves contain instantaneous elasticity, elastic after effect, and the viscosity flow induced by the humidity. However, under the state of high stress ($\sigma_{3P} \geq \sigma_S$), it is an unstable creeping model. The unloading curves include instantaneous elasticity, elastic after effect, and the viscosity flow induced by the stress and the humidity. This model reflects the rheological properties of swelling rock comprehensively, and it can be used for rock rheological analysis.

1. Introduction

The research on rock rheological model is an important component of the research on rock rheological mechanical theories. Moreover, it is also one of the hot and difficult topics in the field of rock mechanics. Currently, the rheological models of rock mainly have the empirical model, the component composition model, and the damage and fracture rheological model. There are plenty of studies carried out in this field in the world. For example, Xu and Xia [1] used logarithmic empirical formulas to fit creeping test results of Granite. Zhang et al. [2] performed the uniaxial compression creeping test for Gabbro rock; they mentioned the empirical formulas about the creeping law. Zhang et al. [3] used aging theory and power functions to fund nonlinear creeping equations of Mudstone. Based on traditional linear viscoelastic models, Jin and Kui-ying [4] mentioned the

nonlinear viscoelastic model. Yuan-jiang [5] used the creeping body and the fractured plastic body; these two kinds of nonlinear components found a new complex rheological model to describe soft rock. Based on the creeping test results of rock, Zhi-chun et al. [6] and Xie-xing and Chen [7] pointed out the parameters of creeping modulus and the damage equations of rock creeping which can describe damage history. Yan-yi [8] studied on the process of damage rheological fractures of jointed rock; then, he mentioned the laws of delay crack initiation and expansion and instability of rock joints under constant loading; he established the damage evolution equations of jointed rock and viscoelastic plasticity constitutive equations of damage evolution coupling. Guan et al. [9] supplied a new rheological model and applied it in mountain tunnelling. Zhang and Yang [10] suggested a nonlinear unloading rheological constitutive model based on the fractional-order

derivative. Zhao et al. [11] examined the creep properties of limestone under unloading triaxial creep test. Nedjar and Roy [12] suggested a creep mechanical model which could describe the whole creep process of granite with different temperatures. Brotons et al. [13] studied the mechanical characteristics of limestone in a 96 hour uniaxial compressive creep test and proposed a theological model and a creep function to study the creep behaviour of rock dependent on time. Cao et al. [14] defined a new nonlinear damage creep constitutive model of high-stress soft rock with improved Burgers model, Hooke model, and St. Venant model based on the nonlinear damage creep characteristics of rock and damage variable. Lu et al. [15] proposed a time-dependent model to simulate the creep aging damage, deformation, and fracture behaviour of brittle rock. Firme et al. [16] studied the elastoplastic creep characteristics of soft rock and provided an accurate explanation. Fahimifar et al. [17] modified a viscoplastic model to account for the creep deformation of rocks associated with the wide range of stress levels and implemented the model in numerical finite difference code (FLAC). Bazhin and Murashkin [18] studied the creep deformation and the stress relaxation characteristics of the material with loading and unloading condition under hydrostatic pressure and established a nonlinear rheological model.

Based on the Nishihara model in component composition model, this paper introduced the rheological components, which consider the humidity expansion effect, to establish the swelling rock viscoelastic model that considers on the humidity, the damage, and the viscosity. The research result of this paper is a useful supplement for the theory research on rock engineering.

2. Free Expansion Experiment of Rock

The rock sample which was obtained from the roof of a coal mine is mudstone, which will expand but cannot disintegrate, whose dry density is 2.74 g/cm^3.

Shaping the rock sample into a rectangle shape with length, width, and height as 5, 5, and 10 cm. The processed sample should be heated to 105°C for 24 h in the oven to remove water completely; then, the water content of rock is 0. In the experiment, length is tested by a vernier caliper whose range is 13.5 cm and precision is 0.02 mm; height is tested by an electronic balance JM10002 whose range is 1000 g and precision is 0.01 g. Taking the dry rock sample out and putting into a desiccator for cooling, then measure and record length (x), width (y), height (z), and mass (m) of the dry sample. Lay the test area of the dry sample and measure its length, width, and height with the method getting the average value by multiple measuring.

The expanding experiment was processing in the environment of 20°C. Put the sample into water and ensure it soaks completely and expands freely; then, take the sample out at an interval, dry the surface of it with absorbent paper, and measure the data: length, width, height, and mass. The standard to judge the sample whether to be water saturating is the mass of the rock increases less than 0.1 g/h one time.

Record the experimental data of every time points; the result of expansion strain and the water content is shown in Table 1:

3. The Relationship between Expansion Strain and Water Content

In [19–21], the concept of humidity stress field is shown, which held the point that humidity diffusion in the swelling rock has coupling relationship with water content, water absorption force, and volume deformation. Let the geotechnical expand freely, and it will bring a strain component as follows:

$$\varepsilon_{ij} = \alpha \delta_{ij} \Delta w. \tag{1}$$

Among the formula, α is linear expansion coefficient, δ_{ij} is a symbol of Kronecker, and Δw is a humidity changing value.

Figure 1 shows the relationship between expansion strain and volume water content and mass water content of lime mudstone in 3 directions at length, width, and height.

From Figure 1 we know that the free expansion strain has proper linear relationship with both volume water content and mass water content of the rock sample in 3 directions at length, width, and height, whose result is fit for the humidity stress field concept in [19–21]. We found the expansion coefficient of volume water content as 0.01421, 0.01603, and 0.01782 and mass water content as 0.03852, 0.04345, and 0.04831, respectively, in three directions at length, width, and height through function fitting.

The anisotropy of the experimental rock sample leads to the difference of expansion coefficient in three directions at length, width, and height, but the difference is very small from the data, so the rock sample can be approximately regarded as isotropic rock mass. So, the relationship between free expansion strain and water content of lime mudstone can be shown as follows:

$$\begin{aligned} \varepsilon &= K_m w_m, \\ \varepsilon &= K_v w_v. \end{aligned} \tag{2}$$

Among the formula, w_m and w_v, respectively, show the mass water content and volume water content and K_m and K_v show the corresponding expansion coefficients.

4. The Constitutive Model

The fundamental components of the conventional rheological model only considered the effect of the load; however, the effect of humidity factor also has obvious impact on the mechanical properties of swelling rock. Considering the effect of humidity factor and combining with the humidity stress field theory, the following hypotheses have been mentioned (Table 2).

The Nishihara model is series connected by the Hooker model, the Kelvin model, and the ideal viscoplastic model. In this paper, based on the Nishihara model, the humidity effect is introduced; then, as shown in Figure 2, the Nishihara

TABLE 1: Experiment results.

T (h)	Expansion strain (10^{-2})			Mass content	Volume content
	ε_x	ε_y	ε_z		
0	0	0	0	0	0
0.2	0.0799	0.1201	0.1406	0.031969	0.08735
0.4	0.1599	0.2002	0.2209	0.042694	0.116374
0.8	0.1998	0.2402	0.2812	0.055719	0.151665
1.2	0.2398	0.2802	0.3213	0.064906	0.176459
2	0.2798	0.3203	0.3615	0.077594	0.210701
4	0.3197	0.3603	0.4017	0.085007	0.230556
10	0.3597	0.4003	0.4419	0.091249	0.247188
24	0.3997	0.4404	0.482	0.100289	0.271352
48	0.4396	0.4804	0.5222	0.10697	0.289083
72	0.4396	0.4804	0.5423	0.111995	0.302603
96	0.4396	0.4804	0.5423	0.111995	0.302603
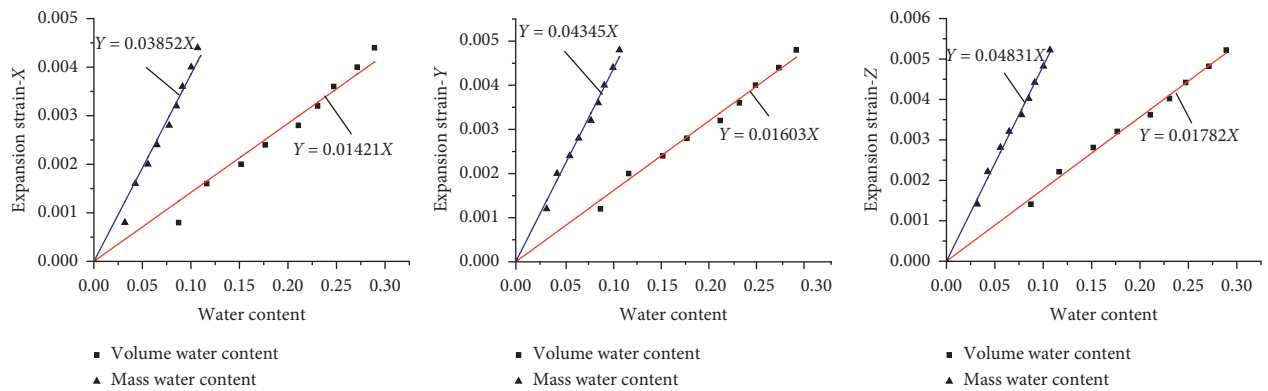
FIGURE 1: Relationship between expansion strain and water content.

TABLE 2: Rheological elements in the humidity field.

Fundamental components	Symbols	Explanation
Hooker model	σ $\xrightarrow{E, \alpha}$ σ / Δw Δw	σ Is the stress; E and a are the elasticity coefficient and the humidity expansion coefficient of Hooker model, respectively; Δw is the humidity difference of before and after two states; moreover, assume that the changes of the humidity have no effect on the Hooker law of the elastic model
Plastic model		When $\sigma < \sigma_s$, there is no strain changes; when $\sigma > \sigma_s$, the plastic model yield; σ_s is the yield limit of the material; when the stress meets the yield limit, the yield continues, no-slip in friction surface and have no relationship with the time; in the coupling of humidity and stress, the yield stress of the material is $\sigma_s(w)$ and the yield surface is $f(\sigma_s, w)$, both of them have the relationships with the humidity; moreover, assume that the yield stress is a given constant
Newton model		The stress and strain obey to sticky laws in the Newton model; there is a proportional relationship between the stress and the strain rate; the formulation is $\sigma = \eta\dot{\varepsilon}$, η is the sticky coefficient; under the coupling of the humidity and the stress, the sticky coefficient is expressed by $\eta(w)$ and it has the relationship with the humidity; moreover, assume that the sticky coefficient is a given constant
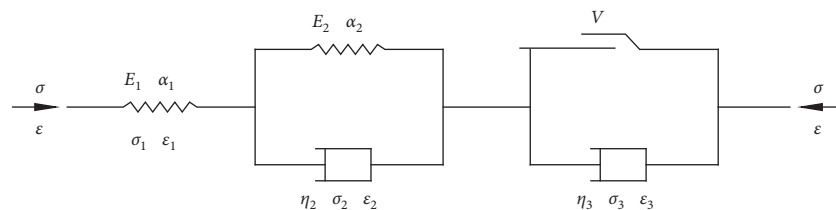
FIGURE 2: The Nishihara model under the humidity effect.

model, which considers the effect of the humidity, has been found.

Under the coupling of the humidity-stress, the stress-strain relationships in this model can be shown as follows:

$$\begin{cases} \sigma = \sigma_1 = \sigma_2 = \sigma_3, \\ \varepsilon = \varepsilon_1 + \varepsilon_2 + \varepsilon_3. \end{cases} \tag{3}$$

In these formulas, $\sigma_1 = E_1\varepsilon_1 - E_1\alpha_1\Delta w$,

$$\begin{cases} \sigma_2 = \sigma_{2E} + \sigma_{2\eta}, \\ \sigma_{2E} = E_2\varepsilon_{2E} - E_2\alpha_2\Delta w, \\ \sigma_{2\eta} = \eta_2(w)\dot{\varepsilon}_{2\eta}, \end{cases}$$

$$\begin{cases} \sigma_3 = \sigma_{3P} + \sigma_{3\eta}, \\ \sigma_{3P} = \begin{cases} 0, & \sigma_{3P} < \sigma_s, \\ \sigma_s, & \sigma_{3P} \geq \sigma_s, \end{cases} \\ \sigma_{3\eta} = \eta_3(w)\dot{\varepsilon}_{3\eta}, \end{cases} \tag{4}$$

$$\begin{cases} \varepsilon_2 = \varepsilon_{2E} = \varepsilon_{2\eta}, \\ \varepsilon_{3P} = \begin{cases} 0, & \sigma_{3P} < \sigma_s, \\ \varepsilon_3, & \sigma_{3P} \geq \sigma_s, \end{cases} \\ \varepsilon_3 = \varepsilon_{3P} = \varepsilon_{3\eta}. \end{cases}$$

In these formulas, σ is the total stress of this model; ε is the total strain of this model; Δw is the amount of the humidity changes between two states; σ_2 and ε_2 are the total stress and the total strain in the Kelvin model, respectively; σ_3 and ε_3 are the total stress and the total strain in the ideal viscoplastic model, respectively; σ_1, E_1, ε_1, and α_1 are the stress, the elastic module, the strain, and the wet expansion coefficient in the Hooker model respectively; σ_{2E}, E_2, ε_{2E}, and α_2 are the stress, the elastic module, the strain, and the wet expansion coefficient in the Kelvin model, respectively; $\sigma_{2\eta}$, $\varepsilon_{2\eta}$, and $\eta_2(w)$ are the stress of the viscous model, the strain, and the wet viscosity coefficient of the Kelvin model, respectively; $\sigma_{3\eta}$, $\varepsilon_{3\eta}$, and $\eta_3(w)$ are the stress of the viscous model, the strain, and the wet viscosity coefficient of the ideal viscoplastic model, respectively; σ_{3P}, ε_{3P}, and σ_{3S} are the stress of elastic components, the strain, and the yield limit of the ideal viscoplastic model, respectively.

Under the state of low stress $(\sigma_{3P} < \sigma_S)$, the ideal viscoplastic model has no effect and the model is the generalized Kelvin model, as shown in Figure 3.
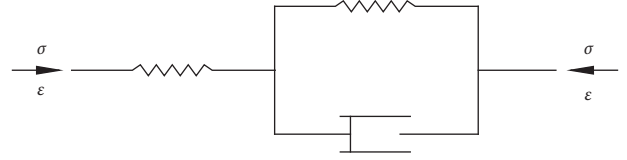
FIGURE 3: The generalized Kelvin model with the humidity effect.

In Figure 2, $\sigma_1 = \sigma_2 = \sigma$, $\varepsilon_1 + \varepsilon_2 = \varepsilon$, and $\dot{\varepsilon}_1 + \dot{\varepsilon}_2 = \dot{\varepsilon}$.

For the Hooker model, $\sigma = E_1\dot{\varepsilon}_1 - E_1\alpha_1\Delta\dot{w}$ and $\dot{\sigma} = E_1\dot{\varepsilon}_1 - E_1\alpha_1\Delta\dot{w}$.

For the Kelvin model, $\sigma = E_2\varepsilon_2 - E_2\alpha_2\Delta w + \eta_2(w)\dot{\varepsilon}_2$.

Thus, $\sigma = E_2(\varepsilon - \varepsilon_1) - E_2\alpha_2\Delta w + \eta_2(w)(\dot{\varepsilon} - \dot{\varepsilon}_1)$.

Then, the constitutive equation, which considers the effect of the humidity on the elasticity, can be deduced:

$$\frac{\eta_2(w)}{E_1}\dot{\sigma} + \left(1 + \frac{E_2}{E_1}\right)\sigma + \eta_2(w)\alpha_1\Delta\dot{w} + E_2(\alpha_1 + \alpha_2)\Delta w \\ = \eta_2(w)\dot{\varepsilon} + E_2\varepsilon. \tag{5}$$

Under high-stress state $(\sigma_{3P} \geq \sigma_S)$, as shown in Figure 1, this model has three components. Moreover, the constitutive equation can be deduced with the similar process:

$$\ddot{\sigma} + \left(\frac{E_1}{\eta_2(w)} + \frac{E_1}{\eta_3(w)} + \frac{E_2}{\eta_2(w)}\right)\dot{\sigma} + \frac{E_1 E_2}{\eta_2(w)\eta_3(w)}(\sigma - \sigma_s) \\ + E_1\alpha_1\Delta\ddot{w} + \frac{E_1 E_2(\alpha_1 + \alpha_2)}{\eta_2(w)}\Delta\dot{w} = E_1\ddot{\varepsilon} + \frac{E_1 E_2}{\eta_2(w)}\dot{\varepsilon}. \tag{6}$$

The humidity and the humidity content have dramatic effects on the creeping properties of the rock. Generally, the rock strength will decrease with the increase of the humidity; however, the rate of rock creeping will increase. According to [22], the viscosity coefficient will decrease with the increase of the humidity; moreover, it is almost a linear change. If ξ_2 and ξ_3 are presumed as the corresponding viscosity attenuation coefficient, $\eta_2'(w) = \eta_2(w) - \xi_2\Delta w$ and $\eta_3'(w) = \eta_3(w) - \xi_3\Delta w$. Then, the constitutive relationship is

$$\begin{cases} \frac{\eta_2(w) - \xi_2\Delta w}{E_1}\dot{\sigma} + \left(1 + \frac{E_2}{E_1}\right)\sigma + [\eta_2(w) - \xi_2\Delta w]\alpha_1\Delta\dot{w} + E_2(\alpha_1 + \alpha_2)\Delta w = [\eta_2(w) - \xi_2\Delta w]\dot{\varepsilon} + E_2\varepsilon, \quad \sigma_{3P} < \sigma_s, \\ \\ \ddot{\sigma} + \left(\frac{E_1}{\eta_2(w) - \xi_2\Delta w} + \frac{E_1}{\eta_3(w) - \xi_3\Delta w} + \frac{E_2}{\eta_2(w) - \xi_2\Delta w}\right)\dot{\sigma} + \frac{E_1 E_2}{[\eta_2(w) - \xi_2\Delta w][\eta_3(w) - \xi_3\Delta w]}(\sigma - \sigma_s) \\ \\ + E_1\alpha_1\Delta\ddot{w} + \frac{E_1 E_2(\alpha_1 + \alpha_2)}{\eta_2(w) - \xi_2\Delta w}\Delta\dot{w} = E_1\ddot{\varepsilon} + \frac{E_1 E_2}{\eta_2(w) - \xi_2\Delta w}\dot{\varepsilon}, \quad \sigma_{3P} \geq \sigma_s. \end{cases} \tag{7}$$

Large amounts of experiments have identified that the properties of swelling rock will be reduced after it is contacted with water; moreover, the elastic modulus will also be decreased with the increase of the humidity [23]. Thus,

introducing two damage factors (D_1 and D_2) for the Hooker element, then $E_1' = E_1(1 - D_1)$ and $E_2' = E_2(1 - D_2)$, and the constitutive equations are

$$
\begin{cases}
\dfrac{\eta_2(w) - \xi_2\Delta w}{E_1(1 - D_1)}\dot{\sigma} + \left(1 + \dfrac{E_2(1 - D_2)}{E_1(1 - D_1)}\right)\sigma + [\eta_2(w) - \xi_2\Delta w]\alpha_1\Delta\dot{w} + E_2(1 - D_2)(\alpha_1 + \alpha_2)\Delta w \\[4pt]
\qquad = [\eta_2(w) - \xi_2\Delta w]\dot{\varepsilon} + E_2(1 - D_2)\varepsilon, \hfill \sigma_{3P} < \sigma_s, \\[12pt]
\ddot{\sigma} + \left(\dfrac{E_1(1 - D_1)}{\eta_2(w) - \xi_2\Delta w} + \dfrac{E_1(1 - D_1)}{\eta_3(w) - \xi_3\Delta w} + \dfrac{E_2(1 - D_2)}{\eta_2(w) - \xi_2\Delta w}\right)\dot{\sigma} + \dfrac{E_1(1 - D_1)E_2(1 - D_2)}{[\eta_2(w) - \xi_2\Delta w][\eta_3(w) - \xi_3\Delta w]}(\sigma - \sigma_s) \\[12pt]
\qquad + E_1(1 - D_1)\alpha_1\Delta\ddot{w} + \dfrac{E_1(1 - D_1)E_2(1 - D_2)(\alpha_1 + \alpha_2)}{\eta_2(w) - \xi_2\Delta w}\Delta\dot{w} = E_1(1 - D_1)\ddot{\varepsilon} + \dfrac{E_1(1 - D_1)E_2(1 - D_2)}{\eta_2(w) - \xi_2\Delta w}\dot{\varepsilon}, \quad \sigma_{3P} \geq \sigma_s.
\end{cases}
\tag{8}
$$

4.1. Creeping Equations.

Assuming that the humidity is constant after the absorbent of the rock; then, $\Delta\dot{w} = 0$.

Under the state of low stress ($\sigma_{3P} < \sigma_S$), it has a constant value, $\dot{\sigma} = 0$. Then, the model is the generalized Kelvin model. For the Hooker model, when $\sigma = \sigma_0$, then $\varepsilon_1(t) = (\sigma_0/E_1) + \alpha_1\Delta w$. For the Kelvin model, $\sigma_0 = E_2\varepsilon_2(t) - E_2\alpha_2\Delta w + \eta_2(w)(d\varepsilon_2(t)/dt)$; then, $\varepsilon_2(t) = (\sigma_0 + E_2\alpha_2\Delta w/E_2) + Ae^{-(E_2/\eta_2(w))t}$; in this equation, A is the integration constant. When $t = 0$, $\varepsilon_2 = 0$; then, $A = -(\sigma_0 + E_2\alpha_2\Delta w/E_2)$. The creeping equation is

$$
\varepsilon(t) = \varepsilon_1(t) + \varepsilon_2(t) = \frac{\sigma_0}{E_1} + \alpha_1\Delta w + \frac{\sigma_0 + E_2\alpha_2\Delta w}{E_2}\left(1 - e^{-(E_2/\eta_2(w))t}\right).
\tag{9}
$$

When t tends to infinity, $\varepsilon(t) = (\sigma_0/E_1) + \alpha_1\Delta w + (\sigma_0/E_2) + \alpha_2\Delta w$ is the horizontal asymptote of the creeping equation and this model is under stable creeping.

Under the state of high stress ($\sigma_{3P} \geq \sigma_S$), the rock has plastic deformation. For the Hooker model, $\varepsilon_1(t) = (\sigma_0/E_1) + \alpha_1\Delta w$. For the Kelvin model, $\varepsilon_2(t) = (\sigma_0 + E_2\alpha_2\Delta w/E_2)(1 - e^{-(E_2/\eta_2(w))t})$. For the ideal viscoplastic model, $\varepsilon_3(t) = (\sigma_0 - \sigma_s/\eta_3(w))t$. The creeping equation is

$$
\varepsilon(t) = \varepsilon_1(t) + \varepsilon_2(t) + \varepsilon_3(t) = \frac{\sigma_0}{E_1} + \alpha_1\Delta w + \frac{\sigma_0 + E_2\alpha_2\Delta w}{E_2}
$$
$$
\cdot\left(1 - e^{-(E_2/\eta_2(w))t}\right) + \frac{\sigma_0 - \sigma_s}{\eta_3(w)}t.
\tag{10}
$$

This model will become larger as the time goes; the strain will be reduced gradually; this model will be under unstable creeping and the creeping will be instability finally.

The creeping equation considers the effects of humidity on elasticity and viscosity as follows:

$$
\varepsilon(t) = \begin{cases}
\dfrac{\sigma_0}{E_1} + \alpha_1\Delta w + \dfrac{\sigma_0 + E_2\alpha_2\Delta w}{E_2}\left(1 - e^{-(E_2/(\eta_2(w) - \xi_2\Delta w))t}\right), & \sigma_{3P} < \sigma_s, \\[14pt]
\dfrac{\sigma_0}{E_1} + \alpha_1\Delta w + \dfrac{\sigma_0 + E_2\alpha_2\Delta w}{E_2}\left(1 - e^{-(E_2/(\eta_2(w) - \xi_2\Delta w))t}\right) + \dfrac{\sigma_0 - \sigma_s}{\eta_3(w)}t, & \sigma_{3P} \geq \sigma_s.
\end{cases}
\tag{11}
$$

The creeping equation considers the effects of humidity on elasticity, damage, and viscosity as follows:

$$
\varepsilon(t) = \begin{cases}
\dfrac{\sigma_0}{E_1(1 - D_1)} + \alpha_1\Delta w + \dfrac{\sigma_0 + E_2(1 - D_2)\alpha_2\Delta w}{E_2(1 - D_2)}\left(1 - e^{-(E_2(1 - D_2)/(\eta_2(w) - \xi_2\Delta w))t}\right), & \sigma_{3P} < \sigma_s, \\[14pt]
\dfrac{\sigma_0}{E_1(1 - D_1)} + \alpha_1\Delta w + \dfrac{\sigma_0 + E_2(1 - D_2)\alpha_2\Delta w}{E_2(1 - D_2)}\left(1 - e^{-(E_2(1 - D_2)/(\eta_2(w) - \xi_2\Delta w))t}\right) + \dfrac{\sigma_0 - \sigma_s}{\eta_3(w) - \xi_3\Delta w}t, & \sigma_{3P} \geq \sigma_s.
\end{cases}
\tag{12}
$$

4.2. Unloading Equations. Under the state of low stress $(\sigma_{3P} < \sigma_s,)$, unloading at the time of t_1, the stress is zero. For the Hooker model, $\varepsilon_1(t) = \alpha_1 \Delta w$.

For the Kelvin model, $(d\varepsilon_2(t)/dt) + (E_2\varepsilon_2(t)/\eta_2(w)) = (E_2\alpha_2\Delta w/\eta_2(w))$; then, $\varepsilon_2(t) = \alpha_2\Delta w + Be^{-(E_2/\eta_2(w))t}$. In this equation, B is integration constant. A the time of t_1, $\varepsilon_2 = \varepsilon_{21} = (\sigma_0 + E_2\alpha_2\Delta w/E_2)(1 - e^{-(E_2/\eta_2(w))t_1})$; then, $B = (\varepsilon_{21} - \alpha_2\Delta w)e^{-(E_2/\eta_2(w))t_1}$. The unloading equation is

$$\varepsilon(t) = \varepsilon_1(t) + \varepsilon_2(t) = (\alpha_1 + \alpha_2)\Delta w + (\varepsilon_{21} - \alpha_2\Delta w) \\ e^{-(E_2/\eta_2(w))(t_1-t)}. \tag{13}$$

When t tends to infinite, $\varepsilon(t) = (\alpha_1 + \alpha_2)\Delta w$. Thus, because of the effect of humidity, the deformation of the model is not recovered to zero:

$$\varepsilon(t) = \varepsilon_1(t) + \varepsilon_2(t) + \varepsilon_3(t) = (\alpha_1 + \alpha_2)\Delta w + (\varepsilon_{21} - \alpha_2\Delta w) \\ \cdot e^{-(E_2/\eta_2(w))(t_1-t)} + \frac{\sigma_0 - \sigma_s}{\eta_3(w)}t_1. \tag{14}$$

Under the state of high stress $(\sigma_{3P} \geq \sigma_s)$, for the Hooker model, $\varepsilon_1(t) = \alpha_1\Delta w$. For the Kelvin model, $\varepsilon_2(t) = \alpha_2\Delta w + (\varepsilon_{21} - \alpha_2\Delta w)e^{-(E_2/\eta_2(w))(t_1-t)}$. For the ideal viscoplastic model, the model remains at the time of t_1 after unloading, the strain is $\varepsilon_3 = (\sigma_0 - \sigma_s/\eta_3(w))t_1$, and the deformation is the eternal plastic deformation. The unloading equation is

$$\varepsilon(t) = \varepsilon_1(t) + \varepsilon_2(t) + \varepsilon_3(t) = (\alpha_1 + \alpha_2)\Delta w \\ + (\varepsilon_{21} - \alpha_2\Delta w)e^{-(E_2/\eta_2(w))(t_1-t)} + \frac{\sigma_0 - \sigma_s}{\eta_3(w)}t_1. \tag{15}$$

When t tends to infinite, $\varepsilon(t) = (\alpha_1 + \alpha_2)\Delta w + (\sigma_0 - \sigma_s/\eta_3(w))t_1$.

Considering about the effects of the humidity on the elasticity and the viscosity, the unloading equation is as follows:

$$\varepsilon(t) = \begin{cases} (\alpha_1 + \alpha_2)\Delta w + Be^{-(E_2/(\eta_2(w) - \xi_2\Delta w))t}, & \sigma_{3P} < \sigma_s, \\ (\alpha_1 + \alpha_2)\Delta w + Be^{-(E_2/(\eta_2(w) - \xi_2\Delta w))t} + \dfrac{\sigma_0 - \sigma_s}{\eta_3(w) - \xi_3\Delta w}t_1, & \sigma_{3P} \geq \sigma_s. \end{cases} \tag{16}$$

In this equation, $B = (\varepsilon_{21} - \alpha_2\Delta w)e^{-(E_2/(\eta_2(w) - \xi_2\Delta w))t_1}$.

Considering the effects of the humidity on elasticity, damage, and viscosity, the unloading equation is as follows:

$$\varepsilon(t) = \begin{cases} (\alpha_1 + \alpha_2)\Delta w + Be^{-(E_2(1 - D_2)/(\eta_2(w) - \xi_2\Delta w))t}, & \sigma_{3P} < \sigma_s, \\ (\alpha_1 + \alpha_2)\Delta w + Be^{-(E_2(1 - D_2)/(\eta_2(w) - \xi_2\Delta w))t}\dfrac{\sigma_0 - \sigma_s}{\eta_3(w) - \xi_3\Delta w}t_1, & \sigma_{3P} \geq \sigma_s. \end{cases} \tag{17}$$

In this equation, $B = (\varepsilon_{21} - \alpha_2\Delta w)e^{-(E_2(1 - D_2)/(\eta_2(w) - \xi_2\Delta w))t1}$.

4.3. Relaxation Equations. Under the state of low stress $(\sigma_{3P} < \sigma_s,)$ and $\varepsilon = \varepsilon_0$. That is, $\dot{\varepsilon} = 0$. Then, $\dot{\sigma} + (E_1 + E_2/\eta_2(w))\sigma = (E_1/\eta_2(w))[E_2\varepsilon_0 - E_2(\alpha_1 + \alpha_2)\Delta w]$, introducing $t = 0$ and $\sigma = \sigma_0$ into it; then, $\sigma_0 = E_1\varepsilon_0$:

$$\sigma = -\frac{E_1}{E_1 + E_2}[E_1\varepsilon_0 + E_2(\alpha_1 + \alpha_2)\Delta w]e^{-(E_1 + E_2/\eta_2(w))t} \\ + \frac{E_1 E_2}{E_1 + E_2}[\varepsilon_0 - (\alpha_1 + \alpha_2)\Delta w]. \tag{18}$$

Under the state of high stress $(\sigma_{3P} \geq \sigma_s)$, for the ideal viscoplastic model, the relaxation deformation is $\varepsilon = \varepsilon_0$ $(\dot{\varepsilon} = 0)$. That is, when $t = 0$, $\sigma = \sigma_S$ and $\sigma\prime = \sigma_s$; then, the relaxation equation of the Nishihara model as follows:

$$\sigma = -\frac{E_1}{E_1 + E_2}[E_1\varepsilon_0 + E_2(\alpha_1 + \alpha_2)\Delta w]e^{-(E_1 + E_2/\eta_2(w))t} \\ + \frac{E_1 E_2}{E_1 + E_2}[\varepsilon_0 - (\alpha_1 + \alpha_2)\Delta w] + \sigma_s. \tag{19}$$

The below is the relaxation equation which considers the effects of humidity on elasticity and viscosity:
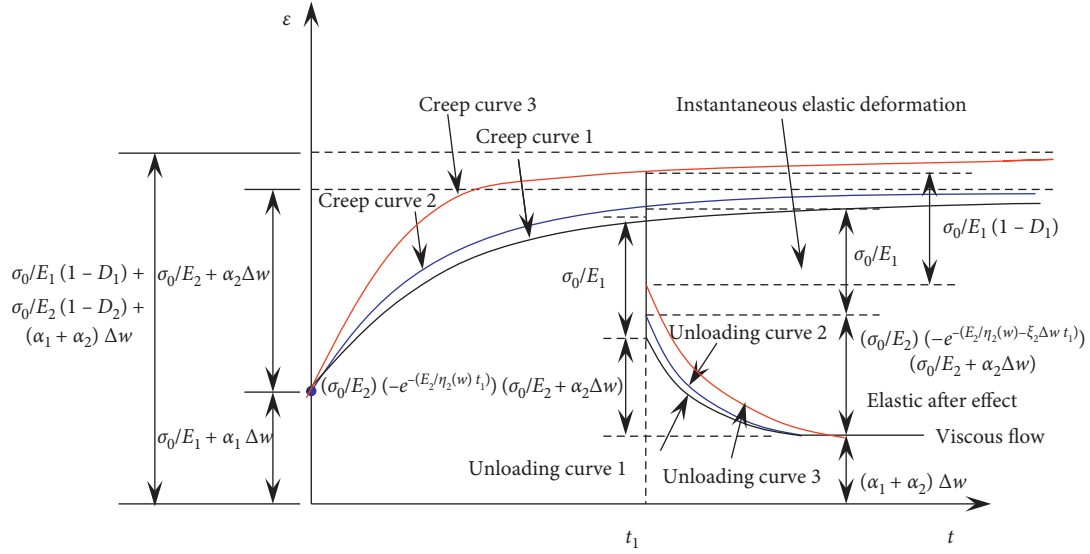
FIGURE 4: Model curves of creeping and unloading while $\sigma_{3P} < \sigma_S$.

$$\sigma = \begin{cases} \left\{ -\dfrac{E_1}{E_1 + E_2} \left[E_1 \varepsilon_0 + E_2 (\alpha_1 + \alpha_2) \Delta w \right] \right\} e^{-\left(E_1 + E_2 / (\eta_2(w) - \xi_2 \Delta w) \right)t} + \dfrac{E_1 E_2}{E_1 + E_2} \left[\varepsilon_0 - (\alpha_1 + \alpha_2) \Delta w \right], & \sigma_{3P} < \sigma_s, \\[3mm] \left\{ -\dfrac{E_1}{E_1 + E_2} \left[E_1 \varepsilon_0 + E_2 (\alpha_1 + \alpha_2) \Delta w \right] \right\} e^{-\left(E_1 + E_2 / (\eta_2(w) - \xi_2 \Delta w) \right)t} + \dfrac{E_1 E_2}{E_1 + E_2} \left[\varepsilon_0 - (\alpha_1 + \alpha_2) \Delta w \right] + \sigma_s, & \sigma_{3P} \geq \sigma_s. \end{cases} \tag{20}$$

The below is the relaxation equation which considers the effects of humidity on elasticity, damage, and viscosity.

$$\sigma = \begin{cases} \left\{ -\dfrac{E_1(1-D_1)}{E_1(1-D_1) + E_2(1-D_2)} \left[E_1(1-D_1)\varepsilon_0 + E_2(1-D_2)(\alpha_1 + \alpha_2)\Delta w \right] \right\} e^{-\left((E_1(1-D_1) + E_2(1-D_2)) / (\eta_2(w) - \xi_2 \Delta w) \right)t} \\[3mm] \quad + \dfrac{E_1(1-D_1)E_2(1-D_2)}{E_1(1-D_1) + E_2(1-D_2)} \left[\varepsilon_0 - (\alpha_1 + \alpha_2)\Delta w \right], & \sigma_{3P} < \sigma_s, \\[4mm] \left\{ -\dfrac{E_1(1-D_1)}{E_1(1-D_1) + E_2(1-D_2)} \left[E_1(1-D_1)\varepsilon_0 + E_2(1-D_2)(\alpha_1 + \alpha_2)\Delta w \right] \right\} e^{-\left((E_1(1-D_1) + E_2(1-D_2)) / (\eta_2(w) - \xi_2 \Delta w) \right)t} \\[3mm] \quad + \dfrac{E_1(1-D_1)E_2(1-D_2)}{E_1(1-D_1) + E_2(1-D_2)} \left[\varepsilon_0 - (\alpha_1 + \alpha_2)\Delta w \right] + \sigma_s, & \sigma_{3P} \geq \sigma_s. \end{cases} \tag{21}$$

Figures 4 and 5 show the creeping curves and the unloading curves of the model under two states of the stress, respectively. The creeping curve 1 and the unloading curve 1 indicate that the effect of the humidity on the elasticity is only considered on. The creeping curve 2 and the unloading curve 2 express that the effects of the humidity on the elasticity and the viscosity are considered about. The creeping curve 3 and the unloading curve 3 show that the effects of humidity on elasticity, damage, and viscosity are considered about.

According to Figures 4 and 5, under three situations, when $\sigma_{3P} < \sigma_S$, the model has a relatively fast deformation at the beginning; afterward, and it tends to stable gradually. Based on the unloading curve, the model has the instantaneous elastic deformation, elastic after effect, and the viscous flow which are caused by the humidity. At the situation of $\sigma_{3P} \geq \sigma_S$, it transfers to the unstable creeping. According to the unloading curve, it has the instantaneous elastic deformation, elastic after effect, and viscosity flow induced by both of humidity and stress. This model
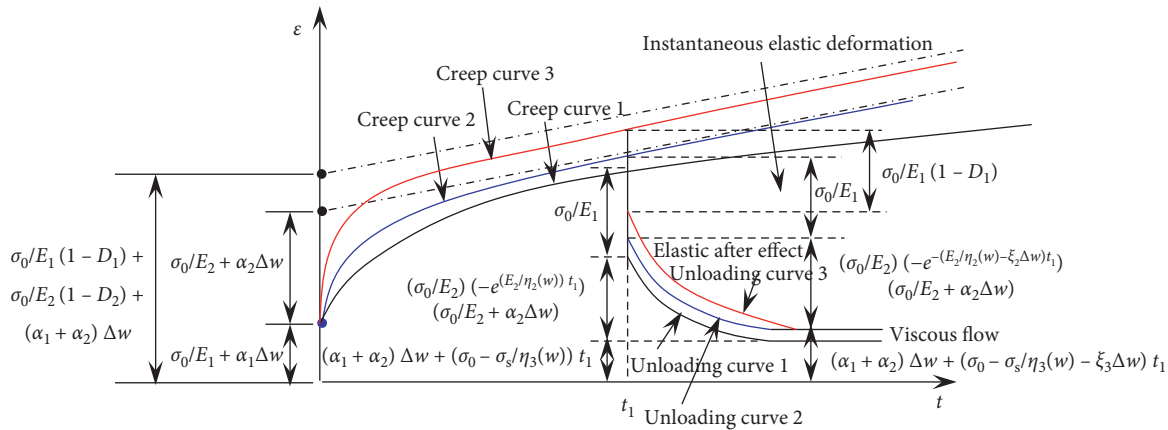
FIGURE 5: Model curves of creeping and unloading while $\sigma_{3P} \geq \sigma_S$.

indicated two creeping states of many rocks under the effect of the humidity.

From these two curves, the effects of humidity on damage, elasticity, and viscosity are introduced into this model. It can indicate the rheological properties of rock comprehensively. With the increase of humidity, viscosity, and strength of the rock will be decreased; however, the damage and the plastic will be increased. Thus, it will cause larger creeping deformation. The model in this paper can describe the rheological properties of rock which is sensitive to the change of the humidity.

5. Conclusions

(1) The expansion strain is directly proportional to the mass or volume moisture content

(2) A new Nishihara model was established by introducing the effect of humidity to improve components

(3) The constitutive equations, creeping equations, and unloading equations considering the change of damage and viscosity coefficient by the effect of humidity are deduced

(4) Under the state of low stress, the model shows stable creeping; however, when it is under high stress, the model expresses unstable creeping

(5) The elastic deformation, elastic after effect, and viscous flow are occurred in the unloading curve

Problems: the model in the paper only qualitatively shows the rheological properties of the swelling rock under the effects of humidity and humidity-relative parameters theoretically. More relative experiments and field test verification should be followed up.

Data Availability

All the data used to support the findings of the study are available from the corresponding author upon request.

Conflicts of Interest

The authors declare that there are no conflicts of interest regarding the publication of this paper.

Acknowledgments

References

[1] P. Xu and X.-L. Xia, "Testing study on creep characteristics of SAN-XIA granite," *Chinese Jounal of Geotechnical Engineering*, vol. 18, no. 4, pp. 63–67, 1996.

[2] X.-Z. Zhang, L. Wang, and D.-J. Zhang, "An experimental study on rheological characteristics of gabbro in east mountain slope of zhu-jia-bao-bao mine," *Journal of Chongqing University (Natural Science Edition)*, vol. 22, no. 5, pp. 99–103, 1999.

[3] X.-D. Zhang, Y.-J. Li, and S.-G. Zhang, "Creep theory of soft rock and its engineering application," *Chinese Journal of Rock Mechanics and Engineering*, vol. 23, no. 10, pp. 1635–1639, 2004.

[4] F.-N. Jin and P. Kui-ying, "Discussion of visco-elastic models," *Chinese Journal of Rock Mechanics and Engineering*, vol. 14, no. 4, pp. 335–361, 1995.

[5] C. Yuan-jiang, "Research on constitutive model and intelligent identification of rock rheology," Doctoral thesis, Central South University, Changsha, China, 2003.

[6] C. Zhi-chun, M. I. A. O. Xie-xing, and M. A. O. Xian-biao, "Rock creep damage evolution equation and the fatigue damage parameter determination," *Coal Science and Technology*, vol. 22, no. 8, pp. 34–36, 1994.

[7] M. Xie-xing and Z.-D. Chen, "A creep damage equation for rocks," *Acta Mechanica Solida Sinica*, vol. 16, no. 4, pp. 343–346, 1995.

[8] Y. Yan-yi, "Underlying relationship between nonlinear rheological property of fissured rocks and damage development," *Engineering Mechanics*, vol. 11, no. 2, pp. 81–90, 1994.

[9] Z. Guan, Y. Jiang, Y. Tanabashi, and H. Huang, "A new rheological model and its application in mountain tunnelling," *Tunnelling and Underground Space Technology*, vol. 23, no. 3, pp. 292–299, 2008.

[10] L. Zhang and S. Yang, "Unloading rheologi cal test and model research of hard rock under complex conditions," *Advances in Materials Science and Engineering*, vol. 2020, Article ID 3576181, 12 pages, 2020.

[11] Y. Zhao, L. Zhang, W. Wang et al., "Creep behavior of intact and cracked limestone under multi-level loading and unloading cycles," *Rock Mechanics and Rock Engineering*, vol. 50, no. 6, pp. 1409–1424, 2017.

[12] B. Nedjar and R. L. Roy, "An approach to the modeling of viscoelastic damage. Application to the long-term creep of gypsum rock materials," *International Journal for Numerical and Analytical Methods in Geomechanics*, vol. 37, no. 9, pp. 1066–1078, 2013.

[13] V. Brotóns, S. Ivorra, J. Martínez-Martínez, R. Tomás, and D. Benavente, "Estudio de la fluencia de una calcarenita: la piedra de san julián (alicante)," *Materiales de Construcción*, vol. 63, no. 312, pp. 581–595, 2013.

[14] P. Cao, Y. Wen, Y. Wang, Y. Haiping, and Y. Bingxiang, "Study on nonlinear damage creep constitutive model for high-stress soft rock," *Environmental Earth Sciences*, vol. 75, no. 10, Article ID 900, 2016.

[15] Y. Lu, D. Elsworth, and L. Wang, "A dual-scale approach to model time-dependent deformation, creep and fracturing of brittle rocks," *Computers and Geotechnics*, vol. 60, pp. 61–76, 2014.

[16] P. A. L. P. Firme, D. Roehl, and C. Romanel, "An assessment of the creep behaviour of Brazilian salt rocks using the multi-mechanism deformation model," *Acta Geotechnica*, vol. 11, no. 6, pp. 1445–1463, 2016.

[17] A. Fahimifar, M. Karami, and A. Fahimifar, "Modifications to an elasto-visco-plastic constitutive model for prediction of creep deformation of rock samples," *Soils and foundations*, vol. 55, no. 6, pp. 1364–1371, 2015.

[18] A. A. Bazhin and E. V. Murashkin, "Creep and stress relaxation in the vicinity of a micropore under the conditions of hydrostatic loading and unloading," *Doklady Physics*, vol. 57, no. 8, pp. 294–296, 2012.

[19] M. Xie-xing, "Large deformation analysis of surrounding rock of a tunnel in swelling rock mass based on the humidity stress field theory," *Journal of China University of Mining & Technology*, vol. 24, no. 1, pp. 58–63, 1995.

[20] M. Xie-xing, A.-H. Lu, and M. A. O. Xian-biao, "Numerical simulation for roadways in swelling rock under coupling function of water and ground pressure," *Journal of China University of Mining &Technology*, vol. 12, no. 2, pp. 120–125, 2002.

[21] Y Shi-lian, M. A. O. Xian-biao, and A.-H. LU, "Study of Deformation rule of swelling rock roadway under the humidity field," *Journal*, vol. 23, no. 4, pp. 402–405, 2006.

[22] F. Yan-qiu, *Expansive Rock and Engineering*, Science press, Beijing, China, 2008.

[23] X Xiao-li, "Study on the evolution of mechanical properties of granite and its micro mechanism under temperature loading," pp. 93–123, China University of Mining &Technology, Xuzhou, China, 2008, Doctoral thesis.

Research Article

Influence of Real-Time Heating on Mechanical Behaviours of Rocks

Bin Gu,[1,2] Zhijun Wan [iD],[1,2] Yuan Zhang,[2] Yangsheng Ma,[3] and Xiaodong Bernard Xu[4]

[1]*Key Laboratory of Deep Coal Resource Mining, China University of Mining & Technology, Ministry of Education of China, Xuzhou 221116, China*
[2]*School of Mines, China University of Mining & Technology, Xuzhou 221116, China*
[3]*School of Mines, Shanxi Normal University, Linfen 041000, China*
[4]*Department of Chemical Engineering, Monash University, Clayton, VIC 3800, Australia*

Correspondence should be addressed to Zhijun Wan; zhjwan@cumt.edu.cn

The rock mechanical properties under the effect of high temperature present a great significance on underground rock engineering. In this paper, the mechanical properties of sandstones, marbles, and granites under real-time heating were investigated with a servo-controlled compression apparatus. The results show that mechanical behaviours of all the three types of rocks are influenced by real-time heating to different degrees. Due to thermal cracking, the uniaxial compressive strengths decrease as the heating temperature rises from room temperature to 400°C. Above 400°C, the sandstone exhibits a significant increase in UCS because of the sintering reaction. The sintering enlarges the contact area and friction between crystal grains in the sandstone, which strengthens the bearing capacity. For marbles, the UCS continues to decrease from 400°C to 600°C due to thermal cracking. However, the carbonate in the marble begins to decompose after 600°C. The generated particles would fill the cracks in the marble and increase the strength. For granites, their UCS presents a sharp decline after 400°C because of thermal cracking. For all rock elastic modulus, they present a decreasing trend, and this indicates that the rock's ability to resist deformation gradually weakens under the effect of temperature. In general, rock mechanical behaviours under real-time heating differ from those in normal situations, and use of the parameters presented here is important for underground rock engineering related to high temperature and can improve the precision in theoretical and numerical analysis.

1. Introduction

Physical and mechanical properties of the rock have attracted significant attention in a number of research fields, such as coal mining, underground coal gasification, and geothermal resource exploitation [1–3]. In physical experimental tests, characteristics of rock matrix permeability, failure mode, and mechanical parameters present large changes after loading process [4, 5]. There is a growing demand for extensive understanding of rock behaviours under the influence of heating, especially above 200°C where material properties change dramatically [6]. Previous research on rock properties generally focused on sandstones, granites, and calcarenites. It is well known that rock

mechanical properties and the corresponding internal mechanism at high temperature are dependent on the rock type. Previous studies have shown that thermal cracking, phase transition, and decomposition all contribute to variation of rock mechanical properties [7, 8].

Sandstone is a typical sedimentary rock in the Earth crust, and some scholars have conducted a series of experiments on its physical and mechanical characteristics under different experimental conditions, such as cyclic loads [9–11] and crack angle [12]. However, with temperature changes, sandstones present a different variation than those in normal condition. Török and Hajpál [13] found that the cementing agents and minerals of sandstones undergoing thermal treatment affect the rock physicomechanical

properties. Santos et al. [14] conducted a series of tests on sandstones (including some artificial materials) under different heating regimes and reported no clear distinctions of rock mechanical properties below 200°C, while mechanical properties decrease uniformly with a temperature above 200°C. In an experimental study, Mccabe et al. [15] measured weight loss and visual surface damage to sandstones after exposure to fires and reported that the fracture structure and the soot are the primary factors that affect rock mechanical properties. The soot is hydrophobic in character, so surface permeability is reduced. The decomposition of minerals after exposure to high temperature results in an expansion of internal rock fractures, leading to weight loss and surface visual damage. Liu and Xu [16] performed a series of tests on the uniaxial compressive strength (UCS) of sandstones up to 1000°C and found that the temperature threshold for brittle-ductile deformation of sandstones is 600°C. Within this temperature range, the UCS generally decreases with increase in the temperature; UCS changes are insignificant below 800°C but increase slightly above 800°C and then decrease sharply further, as does the elastic modulus. Many similar physical tests have been conducted to measure the UCS and elastic modulus of sandstone [17–19], as summarized by Tian et al. [20]. Overall, under the effect of temperature, physicomechanical properties of sandstones differ from those in natural condition.

These factors also affect the mechanical properties of calcarenites [21–24]. Yavuz and Topal [25] conducted experiments to study the effect of drying temperature on marble physicomechanical properties and reported that higher temperature causes significant damage. Mao et al. [26] concluded that mechanical properties of limestone change pronouncedly above 600°C when samples undergo plastic deformation. The p-wave velocity of the carbonate rock has been reported to negatively correlate with temperature [27]. Carbonate rocks at 800°C have also been reported to undergo a sharp decrease in rock's UCS compared with sandstone and granite due to the composition of the carbonate [24].

However for granites, many studies concentrate on burial depths of granite and the fracture mode [28–30]. Under the effect of temperature, previous studies have shown a small decrease in UCS with temperature below 400°C, followed by a significant decrease above 400°C [31–33]. Chen et al. [34] reported a decrease in granite UCS, elastic modulus, and fracture toughness up to 800°C, above which no further changes were observed. A freeze-thaw cycling test demonstrated that granite peak strain increases with temperature, while UCS and elastic modulus decrease [35]. Kumari et al. [36] conducted a series of hydraulic fracturing experiments and reported a linear reduction of granite breakdown pressure with a temperature up to 300°C. Upon heating of granite samples, the evaporation of free water, asymmetrical thermal expansion, phase transition of quartz, and thermal cracking induced by thermal stress contribute to the propagation of cracks, all of which affect the mechanical properties of granite [6, 37–39].

The literature shows that rock mechanical properties fluctuate only slightly with temperature rising up to

approximately 400°C–600°C, above which substantial changes occur. The main factors that influence rock mechanical properties are thermal cracking and the asymmetric thermal expansion of minerals [18]. In terms of specific applications (e.g., underground coal gasification, enhanced geothermal system, and even building fire), the rock matrix is under the influence of a range of real-time temperatures. Under the real-time temperature, the rock mechanical behaviour varies significantly. The majority of previous studies are normally addressed to rock samples with heat treatment rather than under real-time temperature, and it is insufficient for conducting engineering design due to different rock categories in rock underground engineering.

In this study, we investigated igneous, sedimentary, and metamorphic rocks to better understand the different rock mechanical behaviours at high temperature and to establish a framework to compare mechanical properties of different rocks during real-time heating. The results obtained here have important implications for the prediction of rock behaviour in real high-temperature scenarios and can prevent serious damage with the help of a new technique, like 3D seismic technology [40]. We compare the rock failure mechanism of each type of rocks with a particular focus on UCS and elastic modulus.

2. Materials and Methods

2.1. Sample Collection and Specifications. Sandstone and marble samples were, respectively, collected from Jvxian, Laizhou, and Wenshang in Shandong Province, China. All samples were cut into $\phi 50 \times 100$ mm with a surface parallelism value of within 0.05 mm, in correspondence with the ISRM standard [41]. No visible flaws were observed on the sample surfaces.

2.2. Experimental Apparatus and Methods. The experimental setup included WAW-600, a furnace, and a temperature controller. As in previous studies [42], all specimens were oven-dried for 24h at 105°C to remove moisture. A temperature controller was used to heat the specimens at a rate of 2°C/min, ensuring a homogenous internal and external sample temperature, which is more representative of a natural setting. Furthermore, fast heating rates lead to larger thermal stress, which is beyond the scope of the present study.

Samples were held at the target temperature for 2 hours to allow for equilibration [43] and then compressed at a rate of 0.5 MPa/s until the sample fails. Tests were performed at room temperature (25°C), 200°C, 400°C, 600°C, and 800°C, respectively. Additional temperature points were added when appropriate to better constrain the UCS variation. At least three samples were tested at each temperature point.

3. Results

3.1. Rock Stress-Strain Characteristics. The uniaxial compression results for each rock type are shown in Figure 1. The stress-strain behaviours and failure photographs of sandstone are quite different from that of marble during the
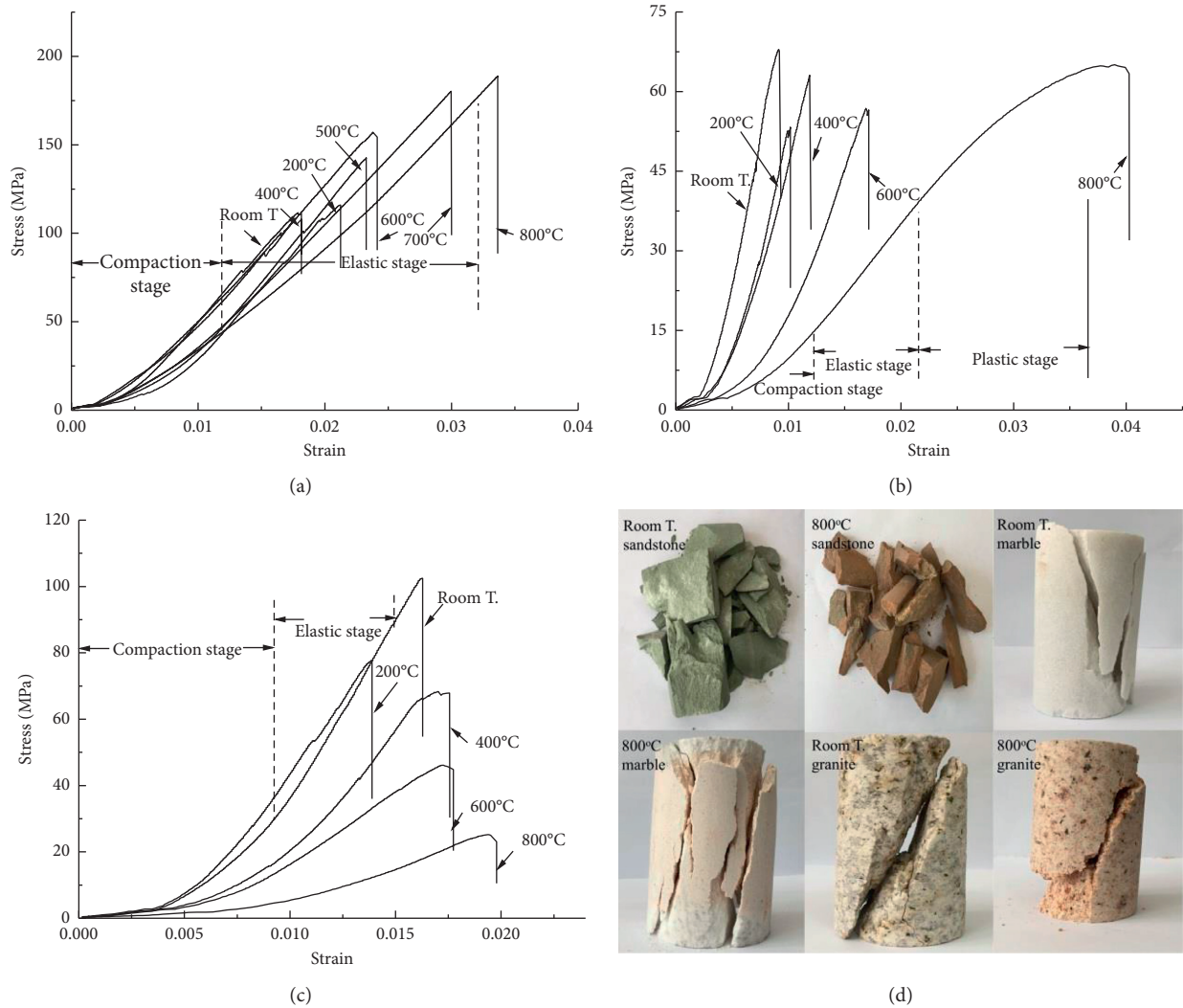
FIGURE 1: Stress-strain curve and failure photographs of rock samples as a function of temperature: (a) sandstone samples, (b) marble samples, (c) granite samples, and (d) failure photograph.

compaction and elastic stages at the same temperature (Figure 1). The stress-strain curve of marbles clearly shows a ductile stage at 800°C, as shown in Figure 1. Figure 2 shows the peak strain of rock samples at different temperatures. Before 800°C, failure pictures are similar for all temperature points.

The characteristics of peak strain variation can be summarized as follows.

The sandstone peak strain rises by 85.3% from 0.01815 at 25°C to 0.03364 at 800°C. However, no distinct plastic stage is observed after the elastic stage on the stress-strain curve (Figure 1(a)), which indicates that the failure mode of sandstone remains brittle over this temperature range.

For marbles, the peak strain increases by 325% from 0.0092 at 25°C to 0.0391at 800°C. The stress-strain curves in Figure 1(b) demonstrate the distinct failure mode transition from brittle to ductile between 600°C and 800°C.

The granite peak strain increases only by 33.36% from 0.01484 at 25°C to 0.01979 at 800°C with a continuous decrease in the peak stress. At 800°C, the compaction stage of

the stress-strain curve is extended and the elastic stage is shortened, which implies that a subsequent transition from brittle to ductile failure modes occurs at the higher temperature.

3.2. Variation Characteristics of Rock Uniaxial Compressive Strength.
The UCS is the peak stress experienced by a rock sample during the loading process. Variations in average UCS are plotted in Figure 3.

From which, the following characteristics can be summarized.

The UCS of sandstone samples below 400°C decreases gradually with the temperature from 117.16 MPa at 25°C to 108.62 MPa at 200°C and 107.3 MPa at 400°C. However, above 400°C, UCS values increase sharply, reaching 196.63 MPa at 800°C. Compared with values at room temperature, sandstone UCS changes by 34.5%, 36.4%, 45.4%, and 67.8% at 200, 400, 600, and 800°C, respectively. Therefore, the reversal point should be in the range of 400°C to 500°C.
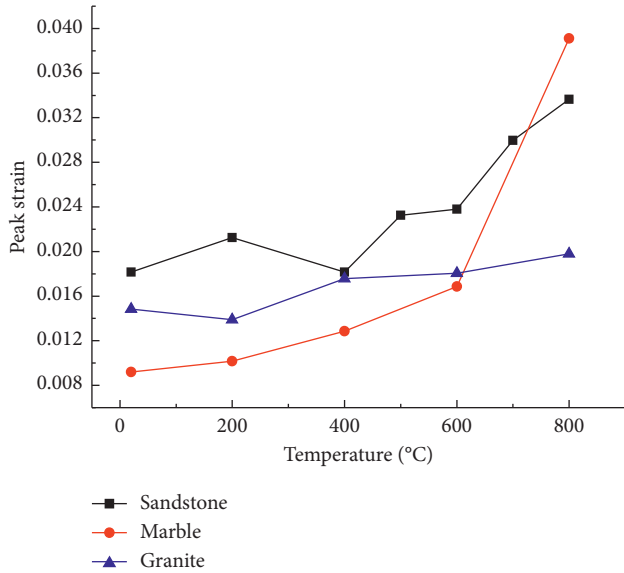
Figure 2: Peak strain for the three rock samples as a function of temperature.

The UCS of marble samples decreases linearly with temperature to a minimum of 55.84 MPa at 600°C and then increases slightly to 64.45 MPa at 800°C. Granites' UCS decreases with temperature to 32.3 MPa at 800°C, a reduction of about 70% from that at the room temperature.

In summary, the effect of temperature on UCS is strongly dependent on the rock type. Marbles' UCS values demonstrate only slight changes with an increase in the temperature, while the sandstone behaves quite differently above 400°C with a sharp increase in UCS. Below 400°C, the UCS of both types of rocks decreases slightly, demonstrating a weak temperature effect over this interval. Temperature effect above 400°C, however, is markedly different for each type of the rocks and therefore requires appropriate consideration.

3.3. Variation Characteristics of Rock Elastic Modulus.

The elastic modulus is an important rock mechanical parameter commonly used in rock engineering. The elastic modulus can be calculated as a linear fitting to the stress-strain curve. In this study, we fit curves to values from 30% to 70% of the rock UCS. Elastic modulus variations are plotted in Figure 4. In general, the elastic modulus of all samples decreases, while each type of the rock demonstrates its own specific characteristics.

The elastic modulus of sandstone samples increases from 7.97 GPa at 400°C to 8.69 GPa at 500°C, both of which are lower than the value 9.17 GPa at the ambient temperature. From Figure 1, it is observed that sandstone's UCS increases sharply at 500°C with a stronger temperature dependence than that of the peak strain, which results in the small increase in the sandstone elastic modulus. These results are also indicative of strengthening of the sandstone mechanical properties.

The elastic modulus of marbles decreases linearly from 10.03 GPa at 25°C to 2.5 GPa at 800°C. Although the marble

UCS increases between 600 and 800°C, the peak strain over the full temperature range increases by about a factor of four, and the decrease in elastic modulus is observed.

The elastic modulus of granite samples generally decreases with temperature from 10.47 GPa at room temperature to 3.32 GPa at 800°C. The elastic modulus at 400°C is higher than those values at 200°C, which we speculate to be due to mechanical property changes at this temperature that increase the data scatter.

Although the elastic modulus of both rock samples decreases with temperature, each rock type shows markedly different magnitudes. The elastic modulus of marbles decreases by several times compared with their ambient temperature, while the sandstone elastic modulus decreases by about 25%. The UCS values of marbles decrease and peak strain increases with temperature, while sandstone UCS values increase sharply above 500°C. The variations of the rock elastic modulus are influenced by the combined effect of rock strain and UCS.

4. Analysis and Discussion

Previous investigations have shown that rock mechanical properties may change at high temperature due to the evaporation of free water, microcrack propagation, mineral dehydration, decomposition, and phase changes [37, 44]. A number of tests have been conducted to evaluate the internal relationship between rock mechanical parameters and external factors.

4.1. Rock Uniaxial Compression Strength (UCS).

The temperature threshold for the α-β quartz phase change is 573°C [7], and the temperature threshold for the decomposition of calcium carbonate is about 800°C [15]. These phenomena would therefore not contribute to the increasing UCS trend observed in sandstone samples above 500°C. Furthermore, thermal cracking during heating leads to the propagation of microcracks that also diminishes rock bearing capacity.

The mineral composition of sandstone samples was measured by X-ray diffraction (XRD) (Table 1) and found to contain quartz, potassium feldspar, and TCCM (kaoline, etc., clay minerals), similar to the raw materials found in many ceramics. When temperature reached 450°C, the mineral of Fe^{2+} in sandstone experiences the following chemical reaction. In the process, the colour of sandstone changes from greyish-green into red (Figure 1(d)). Compared with the previous research work [45], the composition of sandstone is 20% mica, 30% kaolinite, 30% quartz, 15% albite, and 10% siderite, which is different with the contents of sandstone in this paper. Under real-time heating, no sintering reaction as following was found in that study, and thus sandstone UCS experienced a decreasing trend after 400°C rather than a sharp increasing trend:

$$Fe^{2+} + O_2 \xrightarrow{400-800C} Fe_2O_3 \tag{1}$$
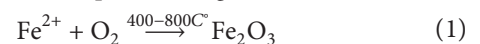
In the manufacture of certain ceramics, the percentage of potassium feldspar is usually 20% to 30%, and the temperature for the sintering reaction is 0.5 to 0.8 Tm

(a)

(b)

(c)
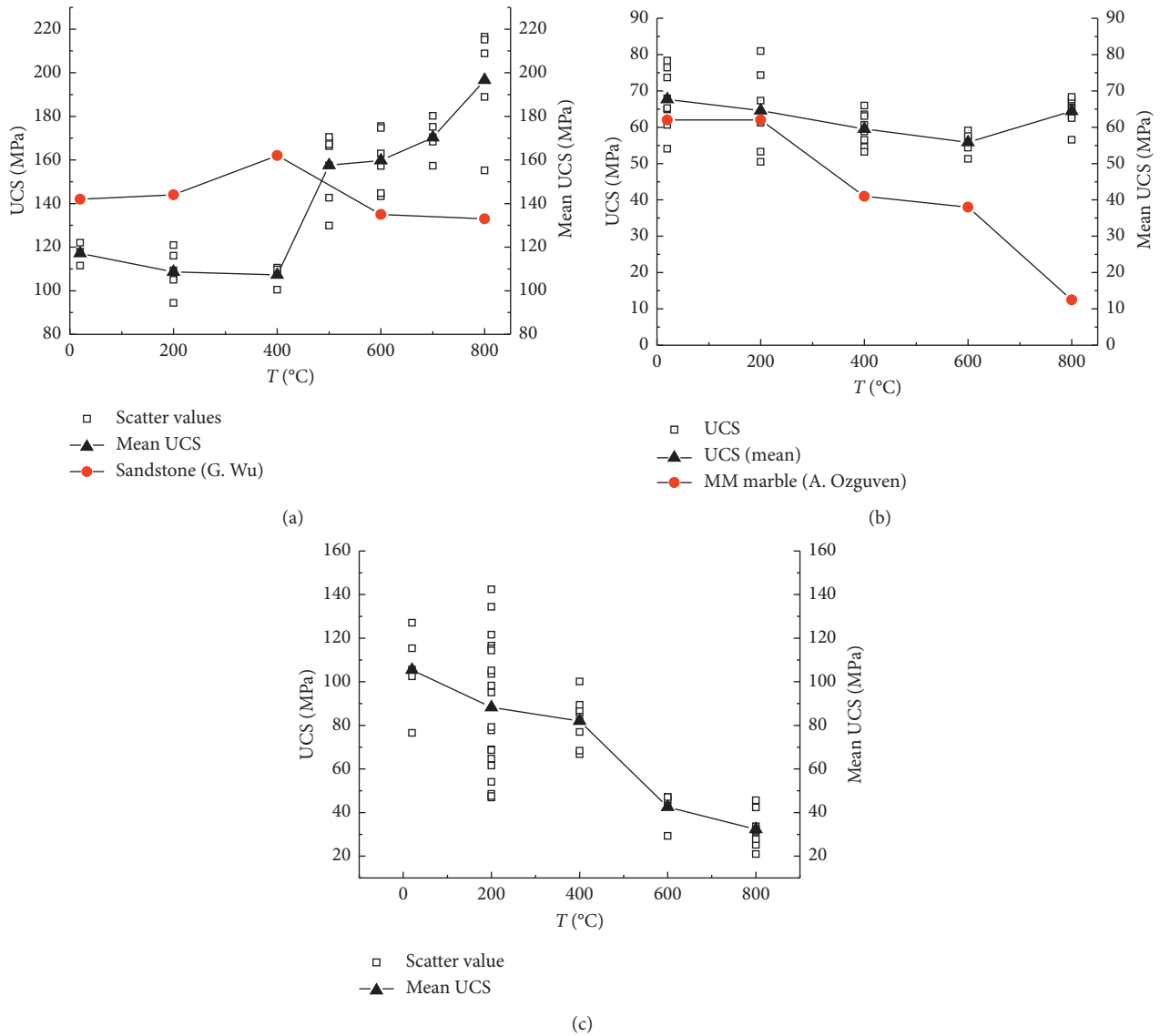
FIGURE 3: Variation of rock uniaxial compressive strength with temperature: (a) sandstone samples, (b) marble samples, and (c) granite samples.

where Tm is the melting point of the raw material. The melting point of potassium feldspar is about 1150°C, and the melting point of anorthose is between 1100 and 1150°C. When the raw material is blended with Al_2O_3 and Fe_2O_3, the melting point further decreases to about 500°C [46, 47]. The sintering reaction in sandstone can be simply described as in Figure 5.

In the initial state, the crystal grain in sandstone is in loose contact; with temperature reaching about 500°C, the generation of Fe and Al oxides gradually fills the space between crystal grains and then forms into a eutectic material under the effect of high temperature. After that, the feldspar in sandstone samples gradually softens, causing an increase in the peak strain of sandstone, and then melts into this eutectic material until forming a new close contact crystal grain (shown in Figure 5(c)). In the whole process, the contact area between mineral grains is

enlarged [48] and then leads to an increase in the sandstone UCS above 500°C.

However, for marbles and granites, the internal mechanical mechanism is similar to sandstones below 600°C and 800°C, respectively. Under the effect of real-time heating, thermal cracking induced by thermal stress and asymmetric thermal expansion prompts the propagation of microcracks and causes the decline in rock UCS. When the temperature reached 800°C, the marble UCS slightly increases compared with values obtained from the previous work, which decreases sharply at 800°C [25]. In the process, the dolomite in marble decomposes into calcium oxide and magnesium oxide at about 800°C; the marble composition is shown in Table 2. The decomposition of dolomite leads to a reduction in the size of crystal grains and increases the padding minerals between crystal grains, shown in Figure 6. In this case, the main factor for controlling marble UCS is

(a)

(b)

(c)
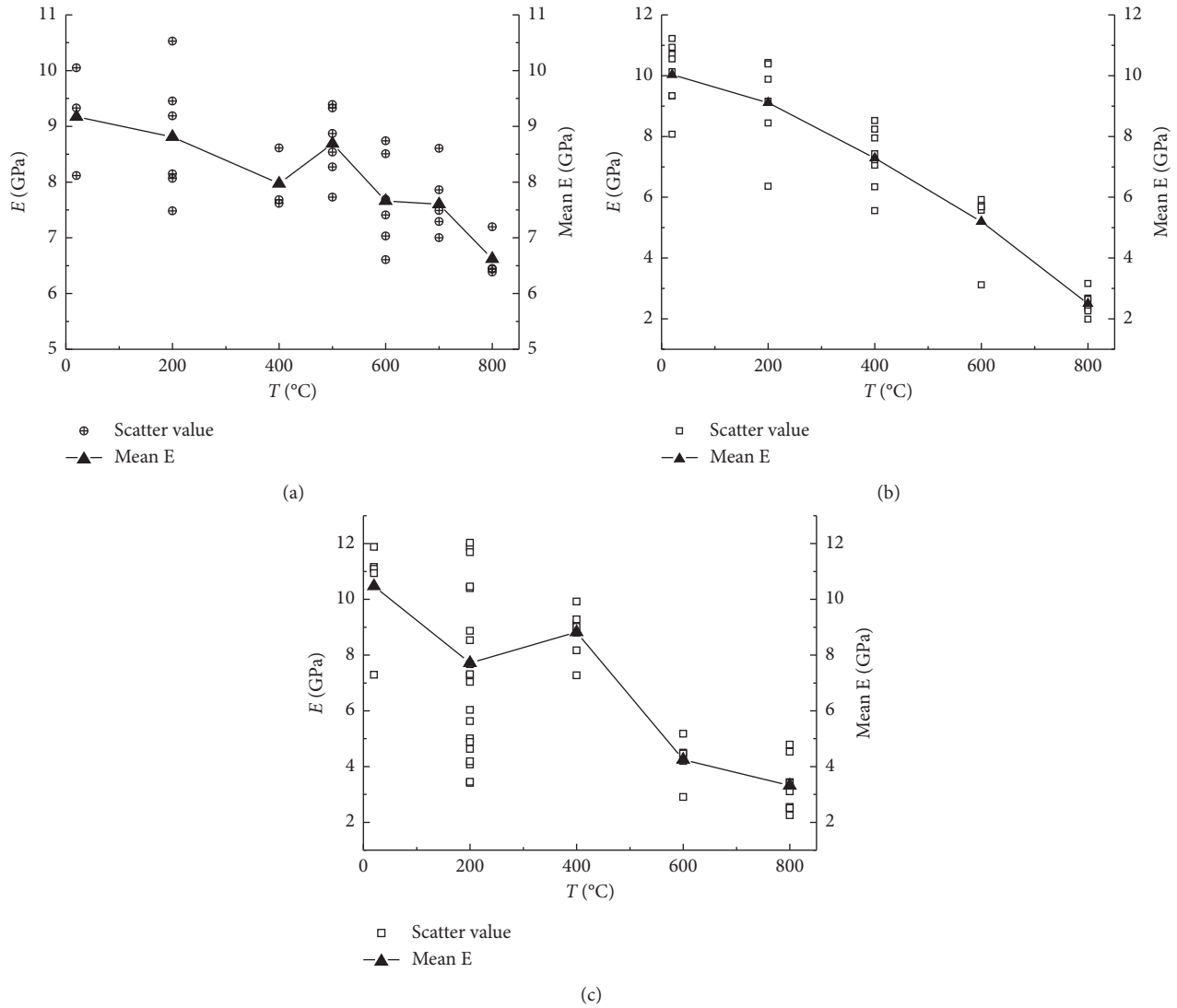
Figure 4: Change in the elastic modulus with temperature: (a) sandstone samples, (b) marble samples, and (c) granite samples.

Table 1: Mineral composition of sandstone used in this study.

Mineral	Quartz	Potassium feldspar	Anorthose	Calcite	Dolomite	TCCM
Content (%)	17.0	31.0	38.0	3.0	5.0	6.0

TCCM means clay minerals in the XRD test.

the padding mineral produced by decomposition of dolomite, filling the space between crystal grains and then enlarging the friction between crystal grains during the loading process.

4.2. Rock Elastic Modulus.

For the rock elastic modulus, they are all presenting a decreasing trend with temperature. Rock elastic modulus is a mechanical property to describe rock's ability to resist deformation. Under the real-time heating, all rock samples gradually soften which is represented by an increase in the rock peak strain. And, the failure mode of rock samples becomes from brittle failure to ductile failure.

It can be clearly seen at 800°C of marbles from its stress-strain curve. It is clear that all rock types experience a process of gradual softening under real-time heating which then diminishes the rock's ability to resist deformation.

From the above analysis, it is shown that the internal mechanism of different rock samples' mechanical properties with temperature has similarities and differences. They can be summarized as follows:

(1) Thermal cracking induced by thermal stress and asymmetric thermal expansion of crystal grains results in propagation of microcracks in all rock samples. Increase in the microcracks in rock samples

Crystal grain
Fe, Al oxide
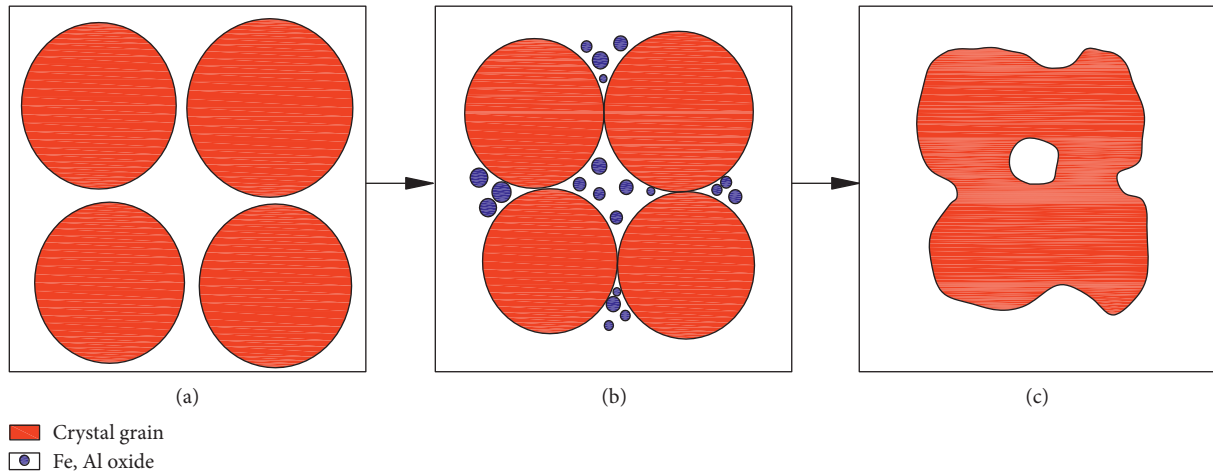
FIGURE 5: Schematic diagram of sintering reaction in sandstone: (a) initial state, (b) eutectic state, and (c) final state.

TABLE 2: Mineral composition of marble used in this study.

Mineral	Dolomite	Hornblende	White mica	Fe, Al, etc.
Content (%)	92.2	6.3	0.4	1.1

Crystal grain
Padding minerals
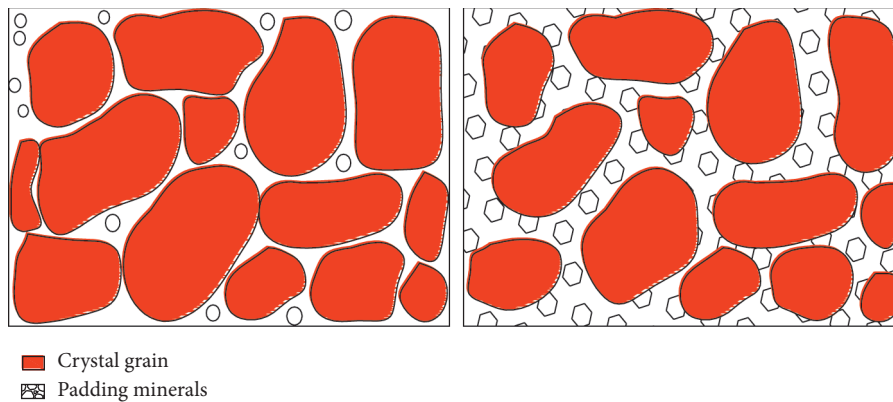
FIGURE 6: Grain model of the marble sample in this paper.

weakens the rock bearing capacity. This is the reason why sandstone, marble, and granite experience a decreasing trend in their UCS below 400°C, before 600°C, and at the whole experimental temperature range, respectively.

(2) When the rock samples consisted of quartz, potassium feldspar, anorthose, clay minerals, etc., and in a proper percentage, the sintering reaction would exist under the effect of real-time heating. In the process, the melting and recombination of crystal grain prompt enlarging of the contact area between crystal grains and then strengthening of the rock bearing capacity. Due to the lack of clay minerals in granites (shown in Table 3), no sintering reaction exists in the whole heating process, and the granite UCS continuously declines.

TABLE 3: Mineral composition of granite used in this study.

Mineral	Quartz	Potassium feldspar	Anorthose
Content (%)	33.0	23.0	44.0

(3) When the majority of the composition of rock samples is carbonate, it decomposes at about 800°C, and the generation of the related oxide filling the crystal grains would enhance the friction between crystal grains. In this case, rock bearing capacity may increase slightly compared with the last experimental temperature point.

(4) In the whole heating process, all rock crystal grains gradually soften and result in an increase in rock ductility. It can simply be demonstrated by the increase in the rock peak strain with temperature. It

shows that the temperature will weaken the rock's ability to resist deformation.

When conducting underground rock engineering, for example, underground coal gasification, it is hard to measure and monitor the deformation of the coal roof, so theoretical and numerical calculation will be adopted to calculate the relative technical parameters. In this case, some conclusions like variations of sandstone mechanical properties and its internal mechanism are helpful to evaluate the safety and economy of the underground rock engineering.

5. Conclusion

In this paper, mechanical characteristics of three types of rocks representing igneous, sedimentary, and metamorphic rocks have been investigated up to 800°C. We find that the internal mechanism of variations of mechanical properties for different rock types has similarities and differences. With the whole heating process, thermal cracking induced by thermal stress and asymmetric thermal expansion is the main controlled factor to influence the rock bearing capacity. In this case, sandstone, marble, and granite UCS experience a decreasing trend below 400°C, 600°C, and 800°C, respectively. When rock samples consisted of some particular minerals and proper percentage, like sandstone in this paper, the sintering reaction exists in these minerals under the effect of high temperature and results in enlarging the contact area between crystal grains. Then, the rock bearing capacity would be strengthened. Besides, decomposition of carbonate and generated oxide filling the space between crystal grains enlarge the friction of crystal grains, which would enhance rock bearing capacity, like marble UCS at 800°C. For the rock's ability to resist deformation, due to the effect of temperature, all three types of rocks experience a decreasing trend in the elastic modulus. The softening of the crystal grain under high temperature prompts the ductility of rock samples and then weakens the rock's ability to resist deformation.

The variation of mechanical properties of three rock types illustrates the significant importance of the real-time temperature effect. When conducting underground rock engineering involving temperature, it is necessary to consider the temperature effect on rock mechanical parameters.

Data Availability

The data used to support the findings of this study are available from the corresponding author upon request.

Conflicts of Interest

The authors declare that there are no conflicts of interest regarding the publication of this paper.

Acknowledgments

References

[1] Y. Zhao, Z. Feng, Z. Feng, D. Yang, and W. Liang, "THM (Thermo-hydro-mechanical) coupled mathematical model of fractured media and numerical simulation of a 3D enhanced geothermal system at 573 K and buried depth 6000–7000 M," *Energy*, vol. 82, pp. 193–205, 2015.

[2] Z. Yin, W. Chen, H. Hao et al., "Dynamic compressive test of gas-containing coal using a modified split hopkinson pressure bar system," *Rock Mechanics and Rock Engineering*, vol. 53, no. 2, pp. 815–829, 2020.

[3] Z.-Q. Yin, Z.-X. Hu, Z.-D. Wei et al., "Assessment of blasting-induced ground vibration in an open-pit mine under different rock properties," *Advances in Civil Engineering*, vol. 2018, Article ID 4603687, 10 pages, 2018.

[4] K. Peng, S. Shi, Q. Zou, Y. Zhang, and G. Tan, "Gas permeability characteristics and energy evolution laws of gas-bearing coal under multi-level stress paths," *Natural Resources Research*, vol. 1, pp. 1–22, 2020.

[5] G. Xie, Z. Yin, L. Wang, Z. Hu, and C. Zhu, "Effects of gas pressure on the failure characteristics of coal," *Rock Mechanics and Rock Engineering*, vol. 50, no. 7, pp. 1711–1723, 2017.

[6] Y.-L. Chen, J. Ni, W. Shao, and R. Azzam, "Experimental study on the influence of temperature on the mechanical properties of granite under uni-axial compression and fatigue loading," *International Journal of Rock Mechanics and Mining Sciences*, vol. 56, no. 15, pp. 62–66, 2012.

[7] Z.-J. Wan, Y.-S. Zhao, Y. Zhang, and C. Wang, "Research status quo and prospection of mechanical characteristics of rock under high temperature and high pressure," *Procedia Earth and Planetary Science*, vol. 1, no. 1, pp. 565–570, 2009.

[8] A. Ozguven and Y. Ozcelik, "Investigation of some property changes of natural building stones exposed to fire and high heat," *Construction and Building Materials*, vol. 38, no. 2, pp. 813–821, 2013.

[9] K. Peng, J. Zhou, Q. Zou, J. Zhang, and F. Wu, "Effects of stress lower limit during cyclic loading and unloading on deformation characteristics of sandstones," *Construction and Building Materials*, vol. 217, pp. 202–215, 2019.

[10] K. Peng, J. Zhou, Q. Zou, and F. Yan, "Deformation characteristics of sandstones during cyclic loading and unloading with varying lower limits of stress under different confining pressures," *International Journal of Fatigue*, vol. 127, pp. 82–100, 2019.

[11] K. Peng, J. Zhou, Q. Zou, and X. Song, "Effect of loading frequency on the deformation behaviours of sandstones subjected to cyclic loads and its underlying mechanism," *International Journal of Fatigue*, vol. 131, Article ID 105349, 2020.

[12] K. Peng, Y. Wang, Q. Zou, Z. Liu, and J. Mou, "Effect of crack angles on energy characteristics of sandstones under a complex stress path," *Engineering Fracture Mechanics*, vol. 218, Article ID 106577, 2019.

[13] Á. Török and M. Hajpál, "Effect of temperature changes on the mineralogy and physical proper ties of sandstones. a laboratory study," *International Journal for Restoration of Buildings & Monuments*, vol. 11, no. 4, pp. 1–8, 2005.

[14] J. P. L. D. Santos, L. G. Rosa, and P. M. Amaral, "Temperature effects on mechanical behaviour of engineered stones," *Construction & Building Materials*, vol. 25, no. 1, pp. 171–174, 2011.

[15] S. Mccabe, B. J. Smith, and P. A. Warke, "Exploitation of inherited weakness in fire-damaged building sandstone: the "fatiguing" of "shocked" stone," *Engineering Geology*, vol. 115, no. 3-4, pp. 217–225, 2010.

[16] S. Liu and J. Xu, "An experimental study on the physico-mechanical properties of two post-high-temperature rocks," *Engineering Geology*, vol. 185, no. 4, pp. 63–70, 2015.

[17] M. Li, X. Mao, L. Cao, H. Pu, R. Mao, and A. Lu, "Effects of thermal treatment on the dynamic mechanical properties of coal measures sandstone," *Rock Mechanics and Rock Engineering*, vol. 49, no. 9, pp. 3525–3539, 2016.

[18] G. Wu, Y. Wang, G. Swift, and J. Chen, "Laboratory investigation of the effects of temperature on the mechanical properties of sandstone," *Geotechnical and Geological Engineering*, vol. 31, no. 2, pp. 809–816, 2013.

[19] L. Zhang, X. Mao, and A. Lu, "Experimental study on the mechanical properties of rocks at high temperature," *Science in China Series E: Technological Sciences*, vol. 52, no. 3, pp. 641–646, 2009.

[20] H. Tian, T. Kempka, S. Yu, and M. Ziegler, "Mechanical properties of sandstones exposed to high temperature," *Rock Mechanics and Rock Engineering*, vol. 49, no. 1, pp. 321–327, 2016.

[21] B. Chakrabarti, T. Yates, and A. Lewry, "Effect of fire damage on natural stonework in buildings," *Construction & Building Materials*, vol. 10, no. 10, pp. 539–544, 1996.

[22] V. Brotóns, R. Tomás, S. Ivorra, and J. C. Alarcón, "Temperature influence on the physical and mechanical properties of a porous rock: san Julian's calcarenite," *Engineering Geology*, vol. 167, no. 4, pp. 117–127, 2013.

[23] M. Y. Koca, G. Ozden, A. B. Yavuz, C. Kincal, T. Onargan, and K. Kucuk, "Changes in the engineering properties of marble in fire-exposed columns," *International Journal of Rock Mechanics and Mining Sciences*, vol. 43, no. 4, pp. 520–530, 2006.

[24] N. Sengun, "Influence of thermal damage on the physical and mechanical properties of carbonate rocks," *Arabian Journal of Geosciences*, vol. 7, no. 12, pp. 1–9, 2014.

[25] A. B. Yavuz and T. Topal, "Effects of different drying temperatures on the physical and mechanical properties of some marbles (Muğla, Turkey) during salt crystallization tests," *Environmental Earth Sciences*, vol. 75, no. 11, pp. 1–13, 2016.

[26] X.-B. Mao, L.-Y. Zhang, T.-Z. Li, and H.-S. Liu, "Properties of failure mode and thermal damage for limestone at high temperature," *Mining Science and Technology (China)*, vol. 19, no. 3, pp. 290–294, 2009.

[27] H. Yavuz, S. Demirdag, and S. Caran, "Thermal effect on the physical properties of carbonate rocks," *International Journal of Rock Mechanics and Mining Sciences*, vol. 47, no. 1, pp. 94–103, 2010.

[28] K. Peng, Z. Liu, Q. Zou, Q. Wu, and J. Zhou, "Mechanical property of granite from different buried depths under uniaxial compression and dynamic impact: an energy-based investigation," *Powder Technology*, vol. 362, pp. 729–744, 2020.

[29] P. Kang, L. Hong, Y. Fazhi, Z. Quanle, S. Xiao, and L. Zhaopeng, "Effects of temperature on mechanical properties of granite under different fracture modes," *Engineering Fracture Mechanics*, vol. 226, Article ID 106838, 2020.

[30] P. Kang, L. Zhaopeng, Z. Quanle, Z. Zhenyu, and Z. Jiaqi, "Static and dynamic mechanical properties of granite from various burial depths," *Rock Mechanics and Rock Engineering*, vol. 52, no. 10, pp. 3545–3566, 2019.

[31] S. Liu and J. Xu, "Study on dynamic characteristics of marble under impact loading and high temperature," *International Journal of Rock Mechanics and Mining Sciences*, vol. 62, no. 5, pp. 51–58, 2013.

[32] Q. Sun, W. Zhang, L. Xue, Z. Zhang, and T. Su, "Thermal damage pattern and thresholds of granite," *Environmental Earth Sciences*, vol. 74, no. 3, pp. 2341–2349, 2015.

[33] S. Liu and J. Xu, "Mechanical properties of qinling biotite granite after high temperature treatment," *International Journal of Rock Mechanics and Mining Sciences*, vol. 71, pp. 188–193, 2014.

[34] Y.-L. Chen, S.-R. Wang, J. Ni, R. Azzam, and T. M. Fernández-Steeger, "An experimental study of the mechanical properties of granite after high temperature exposure based on mineral characteristics," *Engineering Geology*, vol. 220, pp. 234–242, 2017.

[35] Y.-L. Chen, J. Ni, L.-H. Jiang, M.-L. Liu, P. Wang, and R. Azzam, "Experimental study on mechanical properties of granite after freeze-thaw cycling," *Environmental Earth Sciences*, vol. 71, no. 8, pp. 3349–3354, 2014.

[36] W. G. P. Kumari, P. G. Ranjith, M. S. A. Perera et al., "Hydraulic fracturing under high temperature and pressure conditions with micro CT applications: geothermal energy from hot dry rocks," *Fuel*, vol. 230, pp. 138–154, 2018.

[37] E. Althaus, A. Friz-Töpfer, C. Lempp, and O. Natau, "Effects of water on strength and failure mode of coarse-grained granites at 300 C," *Rock Mechanics and Rock Engineering*, vol. 27, no. 1, pp. 1–21, 1994.

[38] R. D. Dwivedi, R. K. Goel, V. V. R. Prasad, and A. Sinha, "Thermo-mechanical properties of Indian and other granites," *International Journal of Rock Mechanics and Mining Sciences*, vol. 45, no. 3, pp. 303–315, 2008.

[39] P. Vázquez, V. Shushakova, and M. Gómez-Heras, "Influence of mineralogy on granite decay induced by temperature increase: experimental observations and stress simulation," *Engineering Geology*, vol. 189, pp. 58–67, 2015.

[40] Y. Wang, X. Shang, and K. Peng, "Relocating mining microseismic earthquakes in a 3-D velocity model using a windowed cross-correlation technique," *IEEE Access*, vol. 8, pp. 37866–37878, 2020.

[41] A. Aydin, *ISRM Suggested Method for Determination of the Schmidt Hammer Rebound Hardness: Revised Version*, Springer International Publishing, New York, NY, USA, 2008.

[42] A. W. Hatheway, "The complete ISRM suggested methods for rock characterization, testing and monitoring; 1974–2006," *Environmental & Engineering Geoscience*, vol. 15, no. 1, pp. 47-48, 2009.

[43] Y. Zhao, Z. Wan, Z. Feng, D. Yang, Y. Zhang, and F. Qu, "Triaxial compression system for rock testing under high temperature and high pressure," *International Journal of Rock Mechanics and Mining Sciences*, vol. 52, no. 6, pp. 132–138, 2012.

[44] A. Ozguven and Y. Ozcelik, "Effects of high temperature on physico-mechanical properties of Turkish natural building stones," *Engineering Geology*, vol. 183, pp. 127–136, 2014.

[45] W. U. Zhong, B. D. Qin, L. J. Chen, and Y. J. Luo, "Experimental study on mechanical character of sandstone of the upper plank of coal bed under high temperature," *Chinese Journal of Rock Mechanics & Engineering*, vol. 24, no. 11, pp. 1863–1867, 2005.

[46] W. Wang, Z. Fu, H. Wang, and R. Yuan, "Influence of hot pressing sintering temperature and time on microstructure and mechanical properties of TiB2 ceramics," *Journal of the European Ceramic Society*, vol. 22, no. 7, pp. 1045–1049, 2002.

[47] J. Martín-Márquez, J. M. Rincón, and M. Romero, "Effect of firing temperature on sintering of porcelain stoneware tiles," *Ceramics International*, vol. 34, no. 8, pp. 1867–1873, 2008.

[48] Y. Ma, C. Bao, J. Chen, S. Song, and L. Han, "Study on microstructures and mechanical properties of foam titanium carbide ceramics fabricated by reaction sintering process," *Journal of Materials Engineering & Performance*, vol. 27, no. 11, pp. 1–8, 2018.

Research Article

Analysis of Failure Characteristics and Strength Criterion of Coal-Rock Combined Body with Different Height Ratios

Tuo Wang [iD],[1] Zhanguo Ma [iD],[1,2] Peng Gong [iD],[1] Ning Li [iD],[1] and Shixing Cheng [iD][1]

[1]*State Key Laboratory for Geomechanics and Deep Underground Engineering, China University of Mining & Technology,
 Xuzhou 221116, China*
[2]*School of Mechanics and Civil Engineering, China University of Mining & Technology, Xuzhou 221116, China*

Correspondence should be addressed to Zhanguo Ma; 1044@cumt.edu.cn

In underground mining and roadway support engineering of coal mine, the coal and rock layers bear loads together; therefore, the deformation and mechanical characteristics of the coal-rock combined bodies are not the same as those of the pure coal or rock bodies. In this paper, conventional triaxial compression tests of coal-rock combined bodies with different height ratios were conducted. And the stress and deformation characteristics of coal-rock combined body were studied and the experimental results were analyzed with different strength criteria. The results show that the peak stress, elastic modulus, and strength reduction coefficient of coal-rock combined body are negatively correlated with the ratio of coal to coal-rock combination height and positively correlated with the confining pressure; the coal-rock combination shows obvious ductility under 10 MPa confining pressure. Under the conventional triaxial condition, the shear failure was the main cause of the lateral deformation of the coal body in the coal-rock combination, which was much larger than that of the rock body. The circle deformation value, volume strain value, and the deformation rate in the postpeak stage of coal-rock combination are much higher than those in the prepeak stage. Mohr–Coulomb and general Hoek–Brown strength criterion fit the experimental results well.

1. Introduction

With the continuous development and improvement of roadway support technology and theory, more and more mines choose to arrange the roadway in the coal seam to reduce the amount of rock roadway excavation. In order to maintain good roof conditions, for roadways with low coal seam strength, the roadways are generally arranged along the roof of the coal seam. Also for the mining of thin coal seams, the side of the roadway is often in the state of half coal seam and half rock. The roadway driving along the roof is shown in Figure 1(a) and the semicoal-rock roadway in Figure 1(b).

The common features of these two types of roadways are that the coal seam and roof rock of the roadway are weakly adhered. The strength of the coal body is low, and the coal seam is prone to large deformation under the action of vertical pressure. The coal seam is liable to slip and deform along the weak side of the coal-rock interface toward the roadway, causing a large series of deformation and shrinkage and then a series of deformation failure modes such as roof sinking and floor bulging [1–7].

Many experts and scholars have done tests on the mechanical properties of coal and rock masses, including conventional triaxial tests and true triaxial tests on pure coal and rock masses and experiments on rock mechanical properties under different stress paths [8–17]. However, in the underground engineering, the overburden load is carried by the coal body and the rock mass together, and the safety and stability of the roadway are determined by the roof rock and coal mass. Therefore, the deformation and failure characteristics of a single coal or rock mass cannot accurately describe the deformation and stress characteristics of such a roadway.

In recent years, some experts have studied the mechanical properties of coal-rock combined samples under different loads and obtained the precursor characteristics and acoustic emission information of failure of coal-rock

(a)   (b)
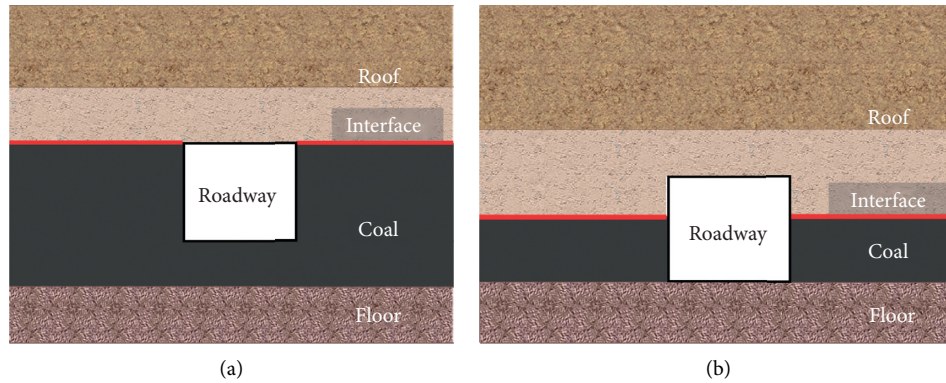
FIGURE 1: Two types of roadways. (a) Roadway driving along the roof. (b) Semicoal-rock roadway.

combined samples through experiments [18–26]. Zuo [27, 28] studied the failure behavior and strength characteristics of coal and rock masses in equal proportions, with confining pressure as a variable. Tan [29] determined the mechanical properties of coal-rock combined samples and obtained a new approach considering the influences of roof and/or floor which was proposed to evaluate the impact capability of coal seam. Huang [30] performed uniaxial compression tests on composite coal rocks under different loading rates and analyzed the effects of loading and unloading rates and paths on the mechanical properties of combined coal and rocks. Lu [31] proposed a method to reduce the impact tendency by weakening the strength of the coal-rock combined body based on the experimental results. Wang [32], in order to understand the sliding mechanism between coal and rock, studied the unstable sliding conditions of coal and rock samples, sliding types under different conditions, displacement evolution law, and AE characteristics through the sliding test between coal and rock. Li [21] used a direct shear test under constant positive load conditions to study the shear characteristics of the natural coal-rock interface and analyze the acoustic emission signals during the shear process. However, their research is based on the proportion of coal and rock, and there is a little research on the different proportion of coal height to the total height of coal-rock combined samples.

At present, many scholars have developed a variety of strength criteria based on conventional triaxial compression test data, such as Hoek [33, 34], You [35], Zuo [36], and Peng [35]. These strength criteria show good applicability and are widely used in the failure of rock structure. Based on the different thickness ratios of coal seams and roofs under different geological conditions, this paper conducted a laboratory test on the mechanical properties of coal-rock combined samples with different height ratios of coal and rock samples. The relationship between the different height ratios on the peak strength, elastic modulus, and strength reduction coefficient of coal-rock combined samples was analyzed. The strength of coal-rock combination is verified and analyzed by using the strength criterion and briefly describes the reasons for the lateral deformation of the coal-rock combination which provides a theoretical and experimental basis for understanding the characteristics of

deformation, failure, and failure of surrounding rock in roadway driving along the roof and the semicoal-rock roadway with different coal seam roof thickness ratios.

2. Experiment

2.1. Samples Preparation. The coal and rock samples of the coal-rock combined bodies were taken directly from number 3 coal seam of Zhangcun Coal Mine, Shanxi Province, China. During the transportation process, the samples are sealed with cling film to reduce water loss and reduce the degree of weathering and transport them back to the laboratory for core processing in a timely manner.

Coal and rock samples are processed to different heights, and the processing accuracy meets the requirements of the test method. After the processing was completed, the rock samples with obvious natural fissures were selected and removed, and then the RSM-SY5 (N) digital intelligent ultrasonic instrument was used to detect and select the interior of the rock. Figure 2(a) shows rock samples with good integrity and uniformity. Due to the long-term high temperature and high-pressure conditions during the formation of coal, the coal seam has a certain degree of cohesive force with the direct roof and is not a nonbonded free mode. Therefore, in the experiments, the medium-viscosity white latex was used as an adhesive to bond the coal and rock bodies and the adhesive (see Figure 2(b)). The adhesive should be coated as thin as possible and ensure uniformity (see Figure 2(c)). After the bond was completed, the coal-rock combined samples were numbered and weighed. The numbering was performed according to the following principles, such as the number RCB-1-3-1, the number "R" represents rock, "C" represents coal, "B" represents the form of bonding between coal-rock combined samples, "1-3" represents the height ratio of rock, coal is 1 : 3, and the last "1" represents sample number 1 in this group (see Figure 2(d)).

The dimensions of coal-rock combined samples were performed in accordance with the standard size of the International Rock Mechanics Society [37]. The total height of the coal and rock specimens is 100 mm and the diameter is 50 mm. Before the test, the diameter, height, and weight of the coal and the rock body were measured individually and combined. Table 1 shows the measurement results.

(a)   (b)   (c)   (d)
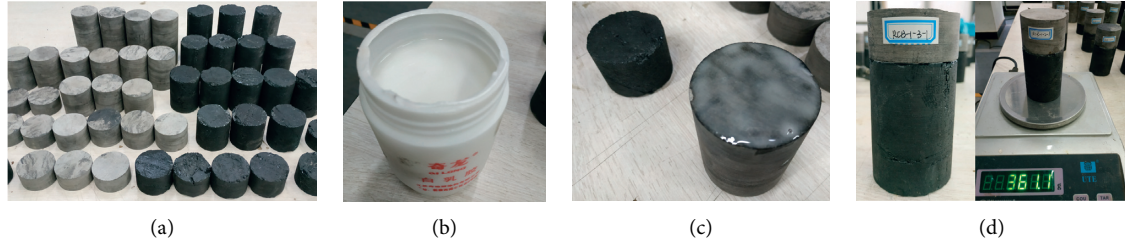
FIGURE 2: Coal and rock combined body manufacturing process. (a) Coal and rock samples. (b) White latex adhesive. (c) The adhesive applied to the interface. (d) Samples labeling and weighing.

TABLE 1: Grouping of coal-rock combined samples and their basic parameters.

Specimen number	Diameter (mm)		Height (mm)			Weight (g)		Confining pressure (MPa)	Density ρ/g·cm^{-3}
	D_r	D_c	H_r	H_c	H_t	m_r	m_c		
Rock	50.09		100.79			544.75		0	2.744
Rock	50.16		101.83			547.25		5	2.720
Rock	50.18		101.88			541.45		10	2.688
Coal		50.06		100.60			275.25	0	1.390
Coal		50.05		102.07			277.30	5	1.381
Coal		50.15		102.56			280.40	10	1.384
RCB-2-1	50.12	50.09	66.81	33.99	100.99	90.25	360.10	0	2.254
RCB-2-1	50.11	50.14	66.90	34.46	101.65	92.03	360.47	5	2.256
RCB-2-1	50.02	50.14	66.82	34.01	101.07	89.53	356.67	10	2.241
RCB-1-1	50.14	50.19	49.90	51.63	101.65	133.45	265.50	0	1.985
RCB-1-1	50.14	50.13	49.99	51.16	101.34	132.63	265.13	5	1.988
RCB-1-1	49.95	50.16	51.71	49.76	101.86	136.53	256.60	10	1.962
RCB-1-2	50.03	50.12	34.58	65.93	100.7	175.10	181.65	0	1.803
RCB-1-2	50.03	50.06	34.44	66	100.61	176.50	180.57	5	1.804
RCB-1-2	50.04	50.09	34.22	65.87	100.31	178.23	181.67	10	1.822
RCB-1-3	49.91	50.07	25.55	75.73	101.41	200.30	130.05	0	1.659
RCB-1-3	49.91	50.07	25.55	75.73	101.49	200.30	130.05	5	1.659
RCB-1-3	50.12	50.12	24.88	76.94	102.2	205.00	135.25	10	1.688

D_r and D_c represent the diameter of the rock and coal body, H_r and H_c represent the height of the rock and coal body, H_t represents the height of the coal-rock combination, m_r and m_c represent the mass of the rock and coal body, and ρ is the coal-rock combined body density. The density of coal body is between 1.378 and 1.39 g cm^{-3}, the average density is 1.383 g cm^{-3}, the density of rock body is between 2.685 and 2.736 g cm^{-3}, and the average density is 2.704 g cm^{-3}, and the average density of coal-rock combined body is between coal and rock samples.

2.2. Test Procedure.

The tests were divided into uniaxial tests and conventional triaxial tests. The samples include coal and rock samples and coal-rock combined samples. There are four groups of coal-rock combined samples with different height ratios. In the conventional triaxial test, there are six specimens in each group, and the confining pressure is 5 MPa and 10 MPa. The uniaxial tests include two specimens in each group. The experimental results excluded the data with large differences, and the remaining two groups of data were averaged. The test was completed on the MTS815.02 electrohydraulic servo rock mechanics test equipment of

China University of Mining and Technology. The equipment of MTS815.02 is shown in Figure 3.

In order to reduce the friction effect of the indenter on the end of the test piece in the conventional triaxial test, according to the research results of J. F. Labuz and Feng [38], this article used a mixture of vaseline and stearic acid to reduce the friction effect of the two ends of the sample. The test steps are as follows:

Step 1: firstly apply petroleum jelly to both ends of the samples, wrap the test piece with a thin heat shrinkable film, place the wrapped test piece on a gasket, then wrap the two layers with a heat shrinkable film, and use 20 # ethylene-propylene self-adhesive tape to wind it evenly to prevent the oil from seeping in.

Step 2: place the sample in the center of the test bench, use the force control mode, and preload 1 kN force to fix the sample.

Step 3: install the hoop extensometer and drop the triaxial cell.

Step 4: load the confining pressure to a predetermined value at a loading rate of 0.1 MPa/min.

FIGURE 3: MTS815.02 electrohydraulic servo rock mechanics test system.

Step 5: load the axial pressure and use the displacement control mode until the sample was broken. The loading rate was 0.003 mm/s.

The stress loading path of a conventional triaxial test is shown in Figure 4.

3. Experimental Results

3.1. Stress-Strain Characteristics. Pure coal and pure rock samples were subjected to uniaxial compression and conventional triaxial compression tests with confining pressures of 5 MPa and 10 MPa. The stress-strain curves of the samples are shown in Figure 5.

Under uniaxial compression, the peak stress of coal samples is 6.38 MPa, while that of rock samples is 53.32 MPa. Under 5 MPa confining pressure, the peak stress of pure coal samples is 10.03 MPa, and that of pure rock samples is 66.2 MPa. Under the confining pressure of 10 MPa, the stress peak of the pure coal samples is 17.12 MPa, and that of the pure rock samples is 90.94 MPa. The stress-strain relationship between coal and rock has a tendency to sink under uniaxial conditions, indicating that coal and rock have obvious crack compaction stages, and the pressure drops rapidly after the peak of the intensity, and the residual strength is almost zero (see Figure 5). After the confining pressure is loaded, due to the low strength of the coal bodies, there is almost no crack compaction stage, the rock strength is high, and the crack compaction stage is not obvious. The coal and rock masses have obvious postpeak softening stages and have the characteristics of ductile failure.

The stress-strain relationship of coal-rock combination under conventional triaxial compression conditions is shown in Figure 6.

The stress-strain curve of coal-rock combination under uniaxial loading condition can be divided into four parts (see Figure 6(a)):

(1) Fracture compaction stage: at this stage, the cracks in the coal-rock combined body and the gaps between the coal and rock were compressed and closed.

Because of the existence of the coal-rock interface and the natural cracks in the samples, the coal-rock combined bodies were initially loaded. The strain growth speed increases at the stage, and the stress increases at a slower rate, so the curve at this stage shows a downward trend.

(2) Elastic phase: at this stage, the internal cracks of the coal-rock combination were closed, and the stress and strain were in a linear relationship.

(3) Yielding stage: at this stage, the stress of the coal-rock combination reached the yield load, internal cracks were initiated, and cracks expanded.

(4) Uninstall phase: at this stage, the internal cracks of the coal-rock combination penetrated, and the stress suddenly dropped. The curve of the coal-rock combination after the peak unloading trend fell below 90°.

The conventional triaxial test preloaded 5 MPa and 10 MPa confining pressure on coal-rock combination. So the fracture compaction stage of the coal-rock combination is not obvious, but there are obvious elastic stage, yield stage, and postpeak softening stage. The peak stress of sample RCB-1-3 is the lowest, and the peak stress of RCB-2-1 is the highest (see Figures 6(b) and 6(d)). Increasing the pressure of surrounding rock has a significant effect on the strength of the combination, and the peak stress and the postpeak residual intensity value are significantly increased. The strength of coal-rock combined bodies with different height ratios increases, and the rate of stress drop after peaks increases accordingly. The coal-rock combined samples of different combined form are classified, and the coefficient δ value is introduced to express the percentage of coal height in the height of coal-rock assemblage, which is expressed as

$$\delta = \frac{h_{ci}}{h_M}, \tag{1}$$

where h_{ci} is the height of the coal body in the coal-rock complex and h_M is the total height of the coal-rock body.
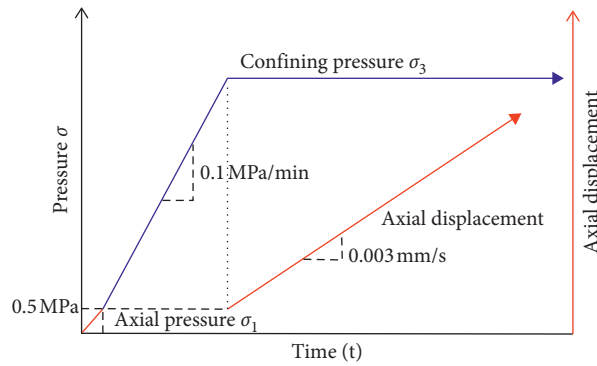
FIGURE 4: Stress loading path of the conventional triaxial test.
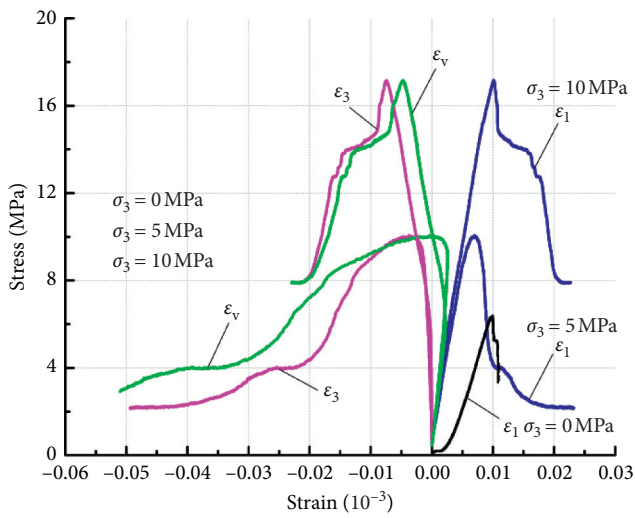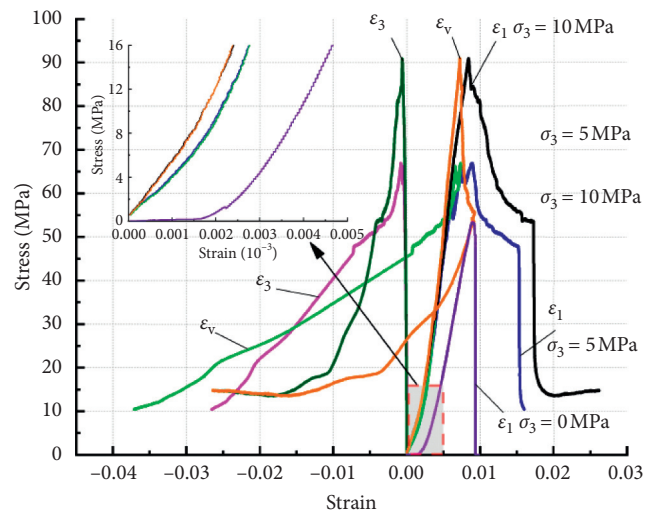
(a)

(b)

FIGURE 5: Stress-strain curves of (a) pure coal samples and (b) pure rock samples under different confining pressures.

(a)
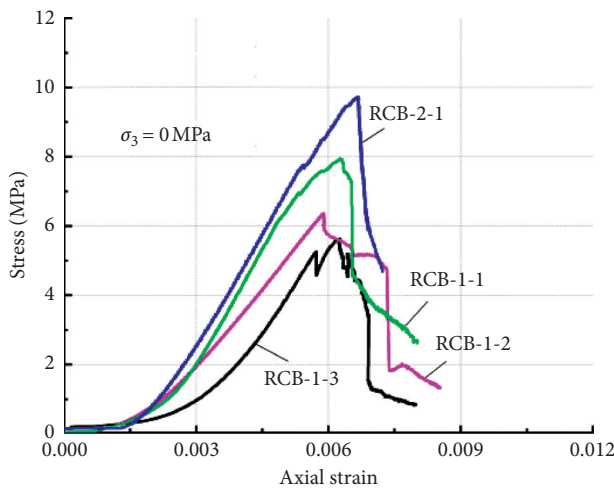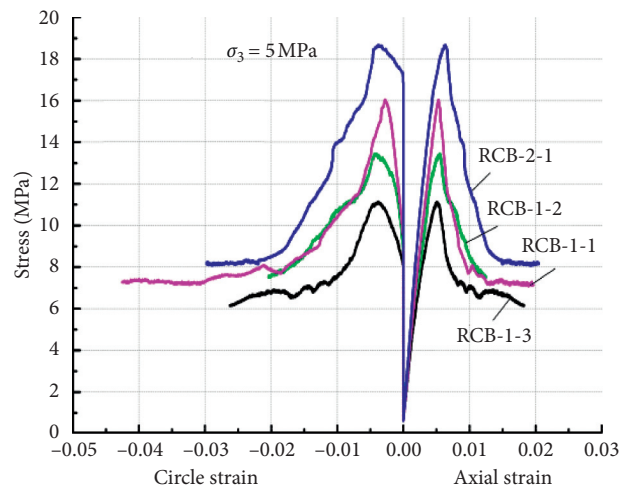
(b)

FIGURE 6: Continued.

(c)

(d)

(e)
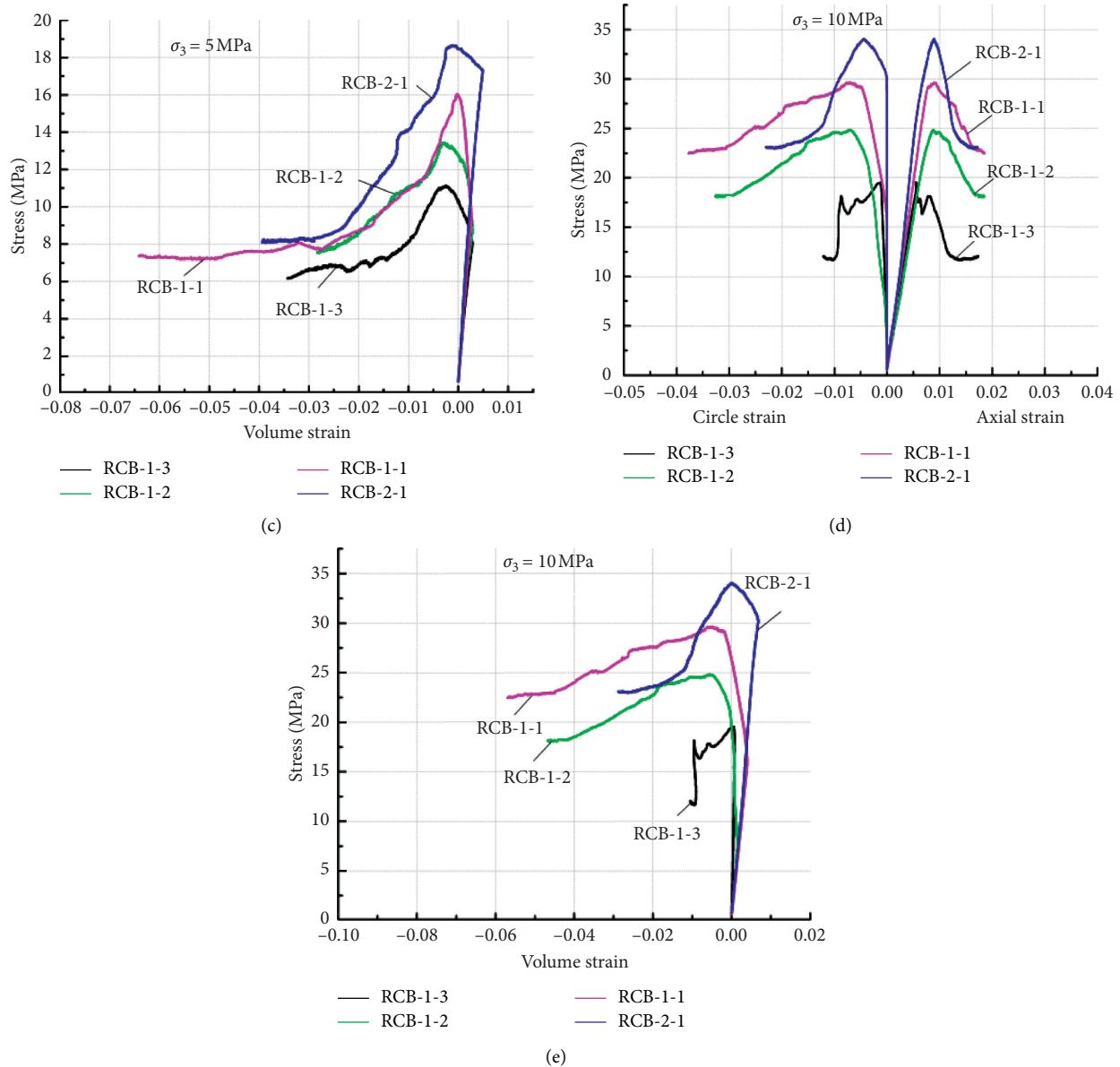
FIGURE 6: Axial stress-strain curve of coal-rock combination. (a) Axial strain of coal-rock combination under uniaxial loading. (b, c) The axial and circumferential strains and volume strains of coal-rock combined samples when the confining pressure is 5 MPa. (d, e) The axial and circumferential strains and volume strains of coal-rock combined samples when the confining pressure is 10 MPa.

The peak strength and axial strain, elastic modulus, circle strain, and volume strain of the test block are shown in Table 2. The uniaxial test only counts the axial strain.

The stress peak of coal-rock combination increases with the increase of confining pressure (see Figure 7(a)). Under the same confining pressure, the peak stress of the coal-rock combination is the greatest when $\delta = 0.33$, the strength decreases with the increase of the value of δ, and the peak stress is the smallest when $\delta = 0.75$. The peak stress of coal and rock samples and coal-rock combination increased with the increase of confining pressure. The peak stress of coal rock pure samples and coal rock combination is positively correlated with surrounding rock pressure. With the surrounding rock pressure from 0 MPa to 5 MPa, the change proportion of the pressure is basically smaller than that of

the surrounding rock pressure from 5 MPa to 10 MPa. The change ratio of rock is the smallest, which is less than 0.4. The change ratio of coal-rock combination is more than 0.7, and the maximum value is 1.1, which indicates that the surrounding rock pressure has an obvious influence on the peak strength (see Figure 7(b)).

According to the research by Yang and Liu [39, 40], it can be known that when the diameter of the rock is the same, as the height increases, the strength of the rock gradually decreases and finally tends to a fixed value. Therefore, it can be concluded that when δ decreases gradually, the strength of the coal body with smaller strength in the combination increases gradually, and the peak strength of the coal-rock combined samples increases, which proves that the experimental results are reasonable.

TABLE 2: Test results of coal and rock pure samples and coal-rock combined samples.

Samples	δ	σ_3 (MPa)	Elastic modulus (GPa)	Peak stress (MPa)	Residual strength (MPa)	Axial strain (10^{-3})	Circle strain (10^{-3})	Volume strain (10^{-3})
ROCK	0	0	6.88	53.32	0.85	9.04		
		5	7.7	66.20	6.32	8.93	−0.79	7.35
		10	9.11	90.93	14.71	8.44	−0.59	7.26
RCB-1-3	0.75	0	1.44	5.61	0.75	6.22		
		5	3.37	10.9	6.51	5.06	−3.74	−2.42
		10	3.74	18.71	12.09	7.79	−8.64	−9.49
RCB-1-2	0.67	0	1.54	6.36	1.23	5.89		
		5	3.38	12.33	7.02	5.55	−4.35	−3.15
		10	3.52	24.57	18.08	8.83	−7.14	−5.45
RCB-1-1	0.5	0	2.48	7.93	1.95	6.27		
		5	3.58	14.12	7.20	5.28	−2.67	−0.06
		10	3.89	29.51	22.7	9.05	−7.1	−5.15
RCB-2-1	0.33	0	2.19	9.72	1.21	6.68		
		5	4.48	17.92	8.13	6.32	−3.9	−1.48
		10	4.63	33.92	23.32	8.92	−6.41	−3.9
Coal	1	0	1.22	6.38	1.8	7.98		
		5	2.07	10.03	2.21	6.88	−3.33	0.22
		10	2.29	17.1	7.85	9.39	−7.58	−5.77
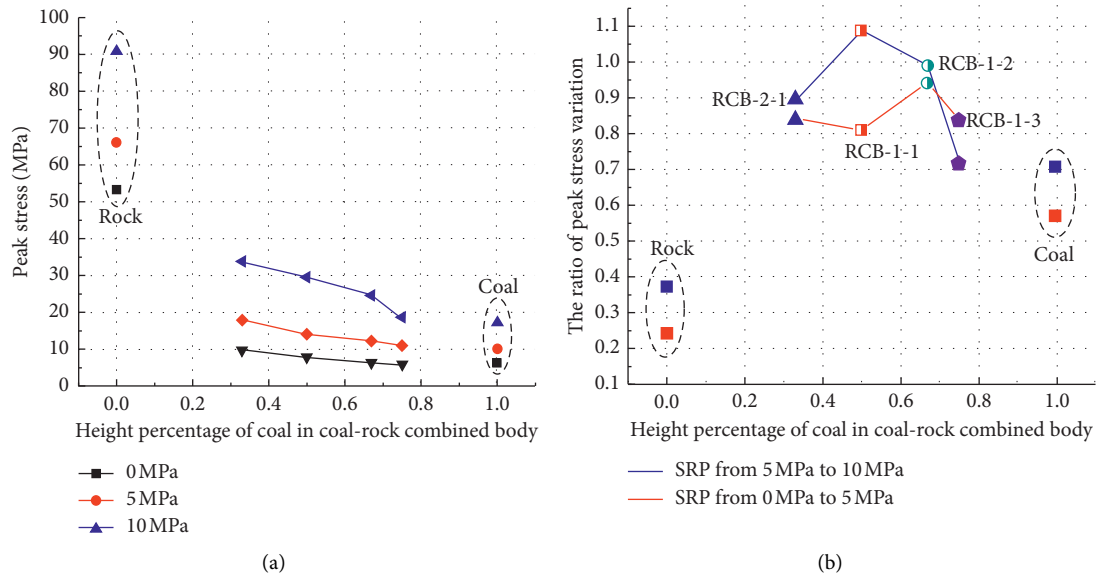
FIGURE 7: The relationship between the peak stress and its change value of coal-rock combination with δ under different confining pressures. (a) Changes in stress peaks with δ. (b) Changes in stress peaks at confining pressures from 0 MPa to 5 MPa and 5 MPa to 10 MPa.

For the coal-rock combined samples under uniaxial compression, due to the process of compaction of coal and rock interface at the initial stage, the axial strain is relatively large. Therefore, the actual axial strain of coal-rock combined samples should be the strain that removing the interface of the compressed coal-rock combination, the calculation is shown in

$$\varepsilon_1' = \varepsilon_1 - \frac{H_t - H_c - H_r}{H_t}, \qquad (2)$$

where ε_1' is the actual axial strain of the coal-rock combination, ε_1 is the axial strain obtained from the test, H_t is the height of the coal-rock combination containing the interface, H_r is the height of the rock sample, and H_c is the height of the coal sample. The measured height values have been calculated in Table 1.

The peak strain of the rock is the highest when the confining pressure is 0 MPa, and the peak strain of coal changes little under the confining pressures of 0 MPa and 5 MPa (see Figure 8). When the confining pressure reaches 10 MPa, the peak strain value increases greatly. The difference in peak strain is caused by the respective strengths of coal and rock samples. The uniaxial peak stress of the rock exceeds 50 MPa. Under the confining pressure of 10 MPa, the ductility characteristics of the rock are not obvious. On the contrary, the coal body has better ductility. When the
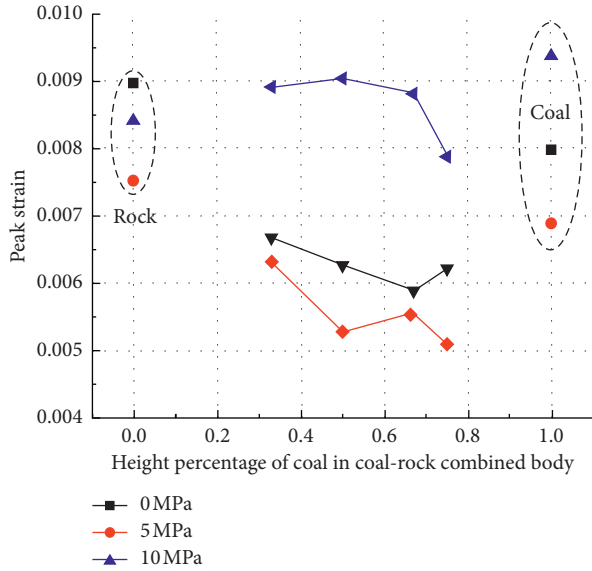
FIGURE 8: Relationship between peak strain and value of coal-rock combination under different confining pressures.

FIGURE 9: Relationship between elastic modulus and δ value of coal-rock combination under different confining pressures.

confining pressure increases from 5 MPa to 10 MPa, the peak strain increases more, indicating that the coal-rock combination shows more obvious ductility characteristics, under the confining pressure of 10 MPa.

The change of elastic modulus of coal-rock combination with δ value under different confining pressures is shown in Figure 9. The elastic modulus of the coal-rock combination increases with the increase of the confining pressure and has a positive correlation with the confining pressure. Under the same confining pressure, the elastic modulus of coal-rock combination decreases gradually with the increase of δ value. When the value of δ is greater than 0.67, the decrease in the elastic modulus slows down, the elastic modulus of coal is the smallest, and the elastic modulus of rock is the largest.

The strength reduction coefficient of the rock can characterize the brittleness of the rock. According to the calculation formula of the strength reduction coefficient proposed by Peng [41], the brittleness index of the coal-rock combination can be calculated:

$$D_s = \frac{\sigma_p - \sigma_r}{\sigma_p}, \tag{3}$$

where D_s is the strength reduction factor of the coal-rock combination and σ_p and σ_r are the stress peak and residual strength of the coal-rock combination, respectively, and their values are shown in Table 2.

The relationship between the strength reduction factor of the coal-rock combination and the percentage of coal height to the height of the coal-rock combination δ and the pressure of the surrounding rock load are calculated (see Figure 10).

When the confining pressure is 0 MPa, the D_s value of all samples is greater than 0.8, the brittleness characteristics are obvious, and the D_s value of the rock sample is 1 (see Figure 10(a)). When the confining pressure reaches 10 MPa, the D_s value of coal-rock combination and pure coal samples is less than 0.35, showing good ductility characteristics. With
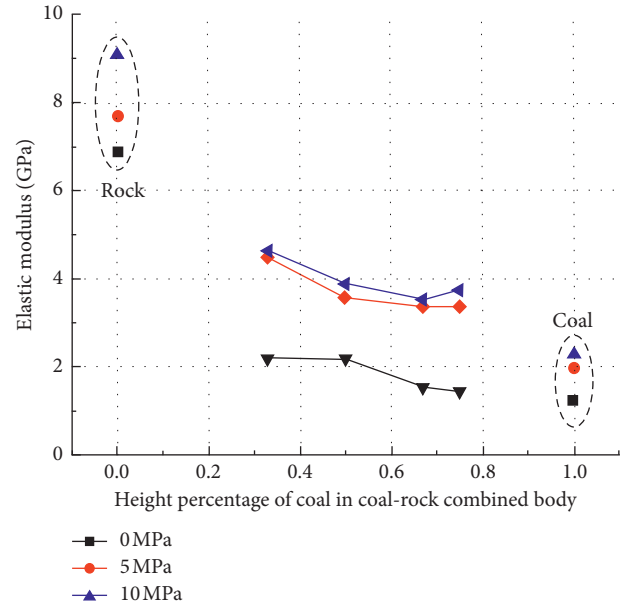
the increase of confining pressure, the D_s values of the samples decrease approximately linearly. The brittleness of pure rock samples is obvious, with D_s values being more than 0.8. The brittleness of pure coal samples and coal-rock combined samples is small under confining pressure. In the process of increasing the confining pressure, the coal-rock combined samples transform from brittleness to ductility quickly and have better ductility characteristics at low confining pressure. Under uniaxial compression, the strength reduction coefficient of coal-rock combination decreases first with the increase of δ value and then gradually flattens (see Figure 10(b)). When the confining pressure reaches 5 MPa, the overall strength reduction coefficient decreases. When the confining pressure is 10 MPa, the strength reduction coefficient shows an approximately horizontal trend. The strength reduction coefficient $D_s = 0.5$ was used to represent the boundary value between brittleness and ductility of the rock. Under the confining pressure of 10 MPa, the coal-rock combination is ductile, and under the confining pressure of 5 MPa, the ductility is only present when the value of δ is greater than 0.33.

3.2. Deformation Features.
Because the coal-rock combination and the coal and rock samples were sealed before the conventional triaxial test, the sample should be completely peeled off after the loading, especially for compressed and brittle coal-containing samples. The failure modes of coal and rock samples and coal-rock combination are shown in Figure 11.

The deformation of rock and coal samples is shown in Figures 11(a) and 11(b). During uniaxial compression, multiple macrocracks appear on the surface of the coal and rock samples, and the macrocracks are mainly vertical tension cracks with a small number of shear cracks, which

(a)

(b)
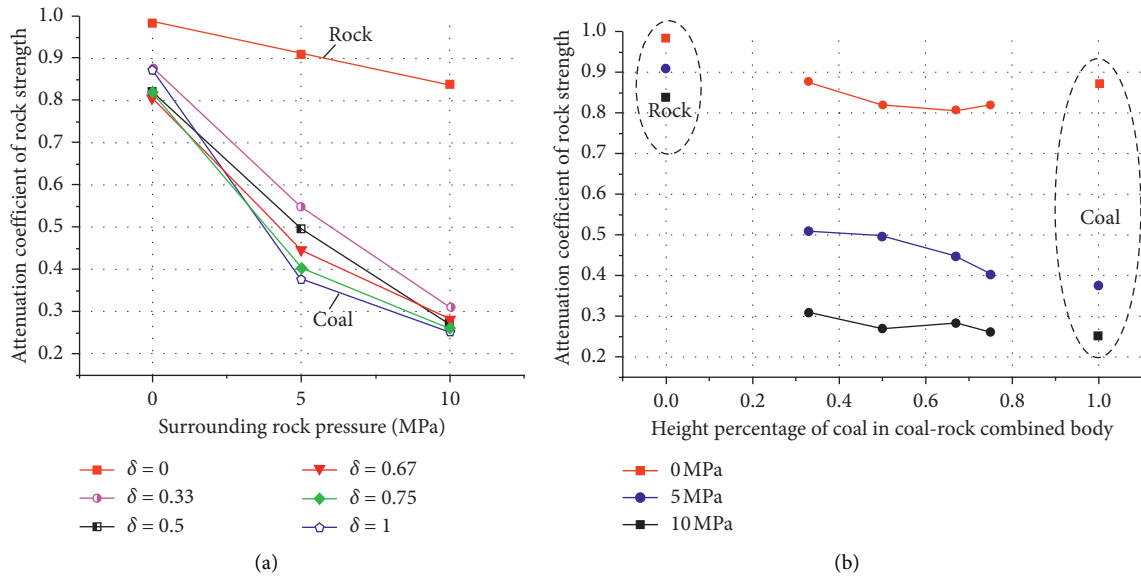
FIGURE 10: Variation trend of strength reduction coefficient of coal-rock combination. (a) Curve of strength reduction coefficient with confining pressure. (b) Curve of strength reduction coefficient with δ value.

(a)   (b)   (c)

(d)   (e)   (f)
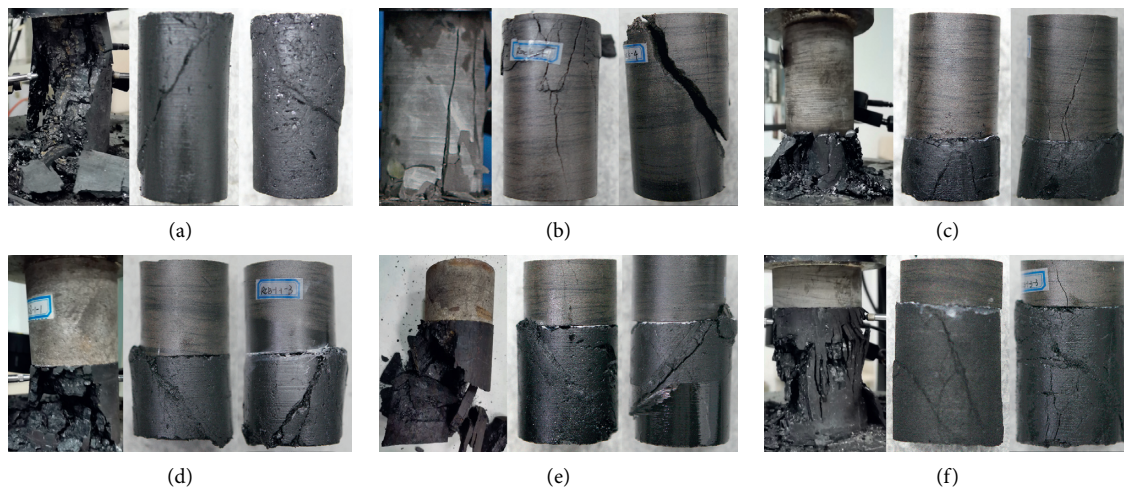
FIGURE 11: Failure patterns of coal-rock combination and the coal and rock samples under different confining pressures; from left to right, the confining pressures are 0 MPa, 5 MPa, and 10 MPa for each group of pictures. (a) Coal. (b) Rock. (c) RCB-2-1. (d) RCB-1-1. (e) RCB-1-2. (f) RCB-1-3.

indicates that the coal and rock samples are mainly tension cracks. When the confining pressure is 5 MPa, the fracture shape of the single coal is oblique shear failure. The average angle between the fracture surface and the axial direction of the sample is 34.8°. The fracture shape of the single rock is mainly oriented to tensile failure, the axial angle of the specimen is small, and the average is 12.3°. The rock failure is accompanied by multiple longitudinal cracks, which are close to the uniaxial compression failure mode. When the confining pressure is 10 MPa, the angle between the fracture surface of the coal and the axial direction becomes larger, on average 50.3°, and the breaking angle of the rock is 33.5°.

The failure mode of the RCB-2-1 tests of the coal-rock combination is shown in Figure 11(c); under uniaxial loading, the failure of the coal-rock combined samples is

mainly the longitudinal tensile fracture of the coal bodies, accompanied by multiple cracks, and the upper rock part is relatively complete. When the confining pressure is 5 MPa, the coal-rock combined samples are mainly shear failure. The average angle between the fracture surface of the fracture surface and the axial direction of the sample is 28.6°, and the rock part is intact. When the confining pressure is 10 MPa, the average angle is 30.2°.

The failure mode of the RCB-1-1 and RCB-1-2 tests of coal-rock complex is shown in Figures 11(d) and 11(e), respectively. Under uniaxial loading, the failure of the coal-rock combination is mainly the longitudinal tensile fracture of the coal body. There is a macromajor fracture surface in the middle of the coal body, the fracture angle is close to the vertical direction, and the upper rock part is relatively

complete. When the confining pressure is 5 MPa, the coal-rock combined samples are mainly shear failure. The average angle between the fracture surface of the fracture surface and the axial direction of the RCB-1-1 sample is 31.2°, while the average angle of the RCB-1-2 is 37.2° and the rock is partially intact. When the confining pressure is 10 MPa, the average angle of the RCB-1-1 sample is 39.2°, while the average angle of the RCB-1-2 is 44.6°.

The failure mode of the RCB-1-3 test for coal-rock combination is shown in Figure 11(f). Under uniaxial loading, the failure is mainly the tensile failure of the coal body and the upper rock part is relatively complete. When the confining pressure is 5 MPa, the combination is mainly the shear failure with an average angle of 34.2° and the rock part is intact. When the confining pressure is 10 MPa, the angle is 42.3° on average.

Take one group $\delta = 0.67$ as an example (see Figure 12), at the initial loading, the coal-rock combination is compressed, and the extreme point of volume compression is point C. After point C, the volume of the coal-rock combination changes from decreasing to gradually expanding, indicating that point C is the starting point of the new crack initiation in the coal-rock combination, and point B corresponding to the stress-strain curve of point C is the critical point of the elastic and plastic phases of coal-rock combination. In the elastic stage, the hoop strain of the coal-rock combination is almost zero. After reaching point A, the circle strain begins to increase at an increasing rate. The increasing starting point A corresponds to point B on the stress-strain curve, which indicates that the plastic deformation is the starting point of the increase of hoop strain. The circle deformation value, volume strain value, and deformation rate in the postpeak phase are much larger than those in the prepeak phase. At the postpeak stage, the coal body in the coal-rock combination has a shear fracture surface. The difference between the lateral deformation of the rock body and the coal body in the coal-rock combination is mainly caused by the shear expansion of the coal body. The lateral deformation of the coal body is far larger than the rock mass.

In summary, it can be considered that the confining pressure has a significant effect on the failure morphology of coal and rock samples and coal-rock combination. The greater the confining pressure, the greater the angle between the fracture surface and the axial direction and the more pronounced the shear failure. Under low confining pressure, the main failure mode is tension failure. Under normal triaxial, the circle deformation value, volume strain value, and deformation rate in the postpeak phase are much greater than in the prepeak phase; shear failure is the main reason for the large lateral deformation of coal body. δ has a significant impact on the deformation and failure of coal-rock combination. The failure of combination is mainly due to the formation of the main fracture zone in the middle of the coal body.

4. Strength Characteristics

4.1. Mohr–Coulomb Criterion.
Mohr–Coulomb strength theory has obvious physical background significance. Rock has friction and cohesion. It is a strength theory based on the
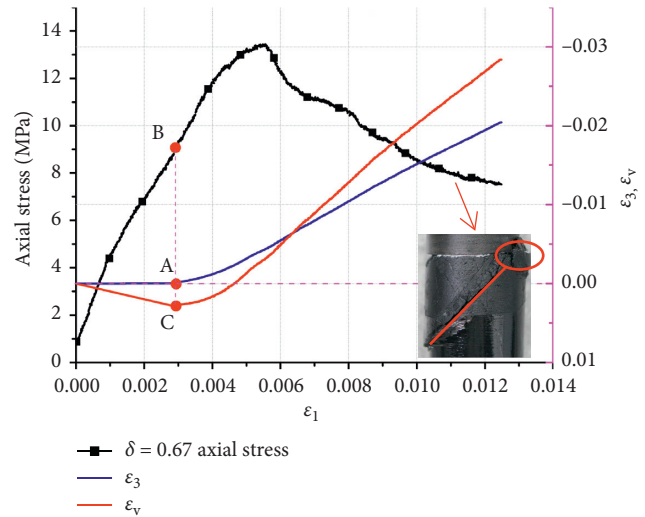
FIGURE 12: The relationship between axial strain-stress and circle and volume strain when confining pressure is 5 MPa.

summary of the results of failure tests of rock materials under normal stress. Mohr–Coulomb strength theory holds that the failure of rock is the result of the combined action of shear stress and normal stress on the material's failure surface. In the principal stress space, Coulomb criterion can be expressed as

$$\sigma_1 = Q + K\sigma_3, \tag{4}$$

where σ_1 is the primary stress of rock failure, σ_3 is the secondary stress of failure, and Q and K are parameters related to the cohesion and internal friction angle of the rock material. $K = \tan^2 \psi$, $Q = 2c \tan \psi$, ψ is the angle between the rock failure surface and the axial direction of the rock, and $\psi = 45° - \varphi/2$.

The Coulomb criterion was used to fit coal-rock combination with different height ratios. The M-C criterion fitting parameters and R^2 are shown in Table 3 and the fitting results are shown in Figure 13.

4.2. H-B Criterion.
The Hoek–Brown criterion [33] (a comprehensive consideration of the effects of multiple factors, which can better reflect the nonlinear failure characteristics of rock masses) is an empirical equation, which usually fits the test data well. The original form of the H-B criterion is expressed as

$$\sigma_1 = \sigma_3 + \sigma_c \cdot \sqrt{m \cdot \frac{\sigma_3}{\sigma_c} + 1}. \tag{5}$$

In 1992, Hoek et al. [34] improved the H-B strength criterion, called the generalized Hoek–Brown criterion. The GH-B strength criterion increases the coefficient describing the integrity of rocks, which is not only applicable to complete rock samples, but also applicable to rock samples with internal fractures. The generalized HB criterion is expressed as

TABLE 3: M-C criterion fitting parameters and R^2.

δ	Fitting curve	R^2	Cohesion	The angle of internal friction (MPa)	Theoretical value ψ	Actual value ψ
0	$\sigma_1 = 51.345 + 3.761\sigma_3$	0.968	13.24	35.4	27.3	22.9
0.75	$\sigma_1 = 5.37 + 1.277\sigma_3$	0.973	2.37	6.98	41.5	38.3
0.67	$\sigma_1 = 5.29 + 1.848\sigma_3$	0.922	1.94	17.32	36.33	40.9
0.5	$\sigma_1 = 6.38 + 2.158\sigma_3$	0.915	2.17	21.5	34.24	35.2
0.33	$\sigma_1 = 8.27 + 2.418\sigma_3$	0.917	2.65	24.5	32.74	29.4
1	$\sigma_1 = 5.81 + 1.32\sigma_3$	0.967	2.52	7.93	41.03	42.5
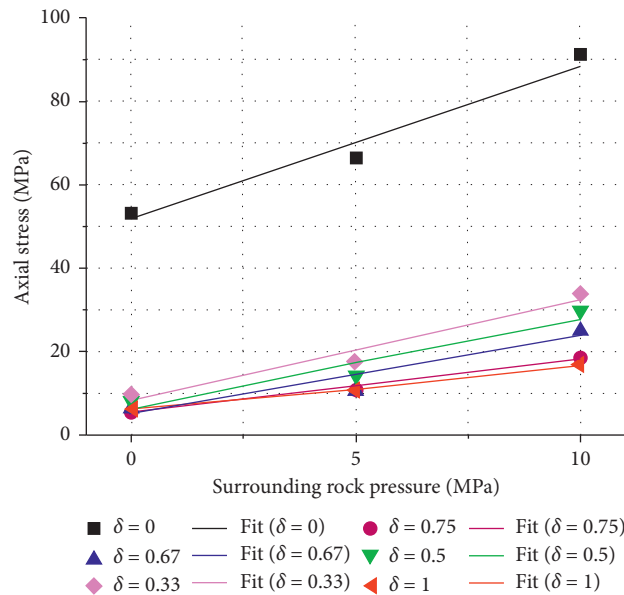
FIGURE 13: Fitting curve of Mohr–Coulomb criterion.

(a)

(b)
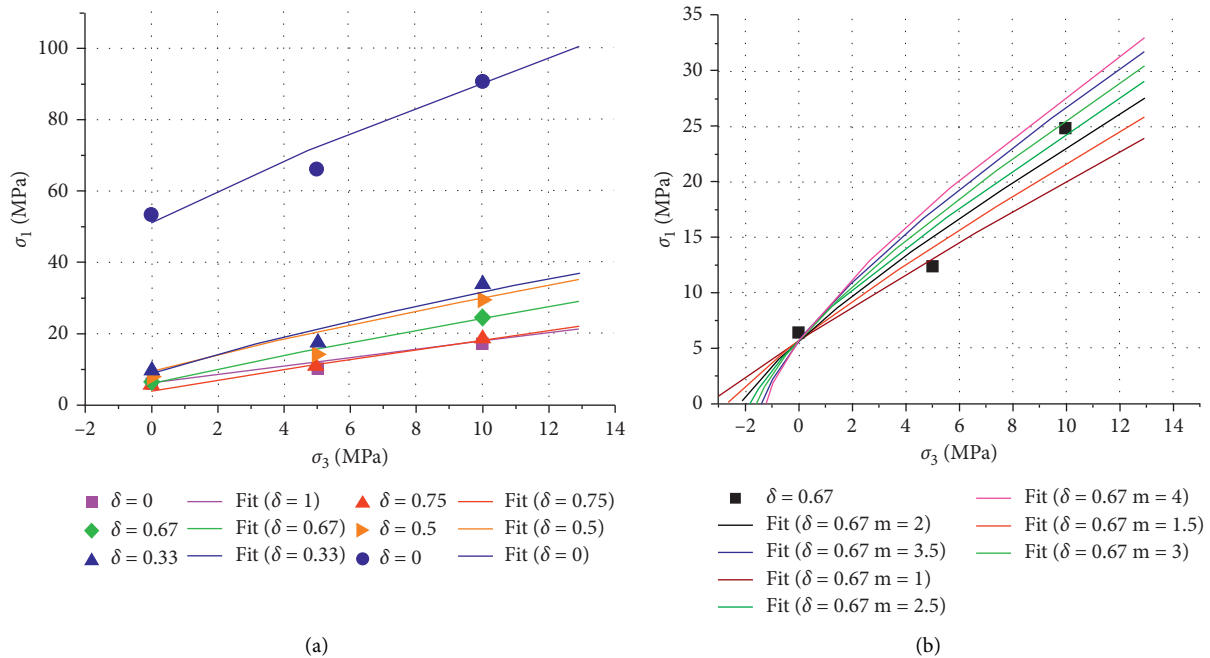
FIGURE 14: The GH-B criterion fitting curve. (a) GH-B criterion fitting curve with different a values. (b) GH-B strength criterion fitting curves with different m values, when $\delta = 0.67$.

TABLE 4: GH-B criterion fitting parameters and R^2.

δ	R^2	m	b	n
0	0.9144	7.09	0.927	0.51
0.75	0.9095	1.52	0.81	0.521
0.67	0.9803	2.465	0.82	0.525
0.5	0.912	2.741	0.833	0.524
0.33	0.924	3.674	0.88	0.541
1	0.8803	1.1	0.88	0.53

$$\sigma_1 = \sigma_3 + \sigma_c \cdot \left(m \cdot \frac{\sigma_3}{\sigma_c} + b \right)^n, \tag{6}$$

where σ_c is the uniaxial compressive strength of the rock, m and b are constants about the mechanical properties of the rock, the value of b ranges from 0 to 1, n is related to the development degree of internal cracks in the rock, the value is generally 0.5–0.65, and the value of the block with good quality is 0.5.

The test data of coal-rock combination and coal and rock samples were fitted using the GH-B criterion (see Figure 14).

The curve has a good fitting effect with experimental results (see Figure 14(a)), R^2 of the coal-rock combination reaches above 0.9, and the strength of the coal-rock combination shows an increasing trend with the increase of confining pressure. However, the increase rate gradually slows down. When $\delta = 0.5$, the strength of coal-rock combination is the largest, and the rate of strength increase is the same. The values of each parameter and R^2 are shown in Figure 14(b) and Table 4.

Among them, the m value of rock and coal is up to 7.09 and 1.1, and the m value of coal-rock combination is between them. The values of n that characterize the internal voids and fractures of the rock are between 0.5 and 0.54. Take $\delta = 0.67$ as an example, take n and b as fixed values, and change the value of m. When m is small value, the absolute value of the intersection between the curve and the abscissa is larger, and the tensile strength of the coal-rock combination is larger. When the m value is 2-3, there is a better fitting trend.

5. Summary

In this paper, the conventional triaxial tests were performed on the combination of number 3 coal seam and roof of Zhangcun Coal Mine with different height ratios and confining pressures. The peak stress, elastic modulus, and strength reduction coefficient of coal-rock assembly are negatively related to the proportion of coal height and positively related to the confining pressure.

Under uniaxial compression, the coal and rock samples and coal-rock combined samples are mainly tensile failures. The forms are mainly inclined shear failures, under conventional triaxial loading. The angle between the fracture surface and the axial direction is between 30° and 40°, the M-C criterion is used for fitting, and the calculated fracture angle is approximately equal to the actual one.

The higher the confining pressure, the larger the angle between the fracture surface and the axial direction and the more obvious the shear failure characteristics. The circumferential deformation value, volume strain value, and deformation rate in the postpeak phase are much greater than in the prepeak phase; shear failure is the main reason for the large lateral deformation of coal body.

Using different strength criteria to fit experimental data of coal and rock samples and coal-rock combination, the fitted R^2 values are all above 0.9, and the fitting effect is good.

Data Availability

The data used to support the findings of this study are included within the supplementary information files.

Conflicts of Interest

The authors declare no conflicts of interest.

Authors' Contributions

Tuo Wang and Zhanguo Ma conceived and established the experimental system; Gong Peng guided thesis writing; Shixing Cheng and Ning Li analyzed the data; Tuo Wang wrote the paper.

Acknowledgments

Supplementary Materials

The supplementary materials include the test data supporting the manuscript. (*Supplementary Materials*)

References

[1] S.-Q. Yang, M. Chen, H.-W. Jing, K.-F. Chen, and B. Meng, "A case study on large deformation failure mechanism of deep soft rock roadway in xin'An coal mine, China," *Engineering Geology*, vol. 217, pp. 89–101, 2017.

[2] Y. Lu, L. Wang, and B. Zhang, "An experimental study of a yielding support for roadways constructed in deep broken soft rock under high stress," *Mining Science & Technology*, vol. 21, pp. 89–94, 2011.

[3] B. Shen, "Coal mine roadway stability in soft rock: a case study," *Rock Mechanics and Rock Engineering*, vol. 47, no. 6, pp. 2225–2238, 2014.

[4] R. Yang, Y. Li, D. Guo, L. Yao, T. Yang, and T. Li, "Failure mechanism and control technology of water-immersed roadway in high-stress and soft rock in a deep mine," *International Journal of Mining Science and Technology*, vol. 27, no. 2, pp. 245–252, 2017.

[5] Y. Yuan, Y. Zhu, W. Wang, and W. Yu, "Failure mechanism of Mesozoic soft rock roadway in Shajihai coal mine and its

surrounding rock control," *International Journal of Mining Science and Technology*, vol. 24, no. 6, pp. 853–858, 2014.

[6] J. C. Chang and G. X. Xie, "Investigation on deformation and failure characteristics and stability control of soft rock roadway surrounding rock in deep coal mine," *Advanced Materials Research*, vol. 255-260, pp. 3711–3716, 2011.

[7] Z. Yin, Z. Hu, Z. Wei et al., "Assessment of blasting-induced ground vibration in an open-pit mine under different rock properties," *Advances in Civil Engineering*, vol. 2018, Article ID 4603687, 10 pages, 2018.

[8] Q. Liu, K. Liu, J. Zhu et al., "Study on mechanical properties of raw coal under high stress triaxial compression," *Journal of Rock Mechanics and Engineering*, vol. 33, pp. 24–34, 2014.

[9] S.-Q. Yang and Q. Sheng, "Experimental study on deformation, peak strength and crack damage behavior of hollow sandstone under conventional triaxial compression," *Engineering Geology*, vol. 213, pp. 11–24, 2016.

[10] S.-Q. Yang and Q. Sheng, "Strength and deformation behavior of red sandstone under multi-stage triaxial compression," *Canadian Geotechnical Journal*, vol. 49, no. 6, pp. 694–709, 2012.

[11] M. Mukherjee, G. D. Nguyen, A. Mir et al., "Capturing pressure- and rate-dependent behaviour of rocks using a new damage-plasticity model," *International Journal of Impact Engineering*, vol. 110, pp. 208–218, 2017.

[12] C. Lu, L. dou, X. Wu, S. Zhang, and Z. Mou, "Strength weakening of coal mine rock burst," *Journal of Engineering Science*, vol. 29, pp. 1074–1078, 2007.

[13] T. Bruning, M. Karakus, G. D. Nguyen, and D. Goodchild, "An experimental and theoretical stress-strain-damage correlation procedure for constitutive modelling of granite," *International Journal of Rock Mechanics and Mining Sciences*, vol. 116, pp. 1–12, 2019.

[14] B. Thomas, K. Murat, G. D. Nguyen, and G. David, "Experimental study on the damage evolution of brittle rock under triaxial confinement with full circumferential strain control," *Rock Mechanics & Rock Engineering*, vol. 51, pp. 3321–3341, 2018.

[15] T. Bruning, M. Karakus, G. D. Nguyen, and D. Goodchild, "An experimental and theoretical stress-strain-damage correlation procedure for constitutive modelling of granite," *International Journal of Rock Mechanics and Mining Sciences*, vol. 116, pp. 1–12, 2019.

[16] Y. Zhao, S. Gong, X. Hao, Y. Peng, and Y. Jiang, "Effects of loading rate and bedding on the dynamic fracture toughness of coal: laboratory experiments," *Engineering Fracture Mechanics*, 2017.

[17] G. Xie, Z. Yin, L. Wang, Z. Hu, and C. Zhu, "Effects of gas pressure on the failure characteristics of coal," *Rock Mechanics and Rock Engineering*, vol. 50, no. 7, pp. 1711–1723, 2017.

[18] Z. Zhou, L. Chen, X. Cai, B. Shen, J. Zhou, and K. Du, "Experimental investigation of the progressive failure of multiple pillar–roof system," *Rock Mechanics & Rock Engineering*, vol. 51, pp. 1629–1636, 2018.

[19] Q. Bai, M. Tibbo, M. H. B. Nasseri, and R. P. Young, "True triaxial experimental investigation of rock response around the mine-by tunnel under an in situ 3D stress path," *Rock Mechanics and Rock Engineering*, vol. 52, pp. 3971–3986, 2019.

[20] L. U. Qun, B. Zhang, and L. Wang, "Experimental study on strength and deformation performance of fiber recycled concrete under conventional triaxial compression," *World Earthquake Engineering*, vol. 31, pp. 243–250, 2015.

[21] D. Li, S. Zhi, X. Tao, X. Li, and P. G. Ranjith, "Energy evolution characteristics of hard rock during triaxial failure with different loading and unloading paths," *Engineering Geology*, vol. 228, 2017.

[22] D. Unteregger, B. Fuchs, and G. Hofstetter, "A damage plasticity model for different types of intact rock," *International Journal of Rock Mechanics and Mining Sciences*, vol. 80, pp. 402–411, 2015.

[23] J. Bai and W. Li, "Determination of coal–rock interface strength by laboratory direct shear tests under constant normal load," *International Journal of Rock Mechanics & Mining Sciences*, vol. 77, pp. 60–67, 2015.

[24] J. Peng, G. Rong, M. Cai, X. Wang, and C. Zhou, "An empirical failure criterion for intact rocks," *Rock Mechanics and Rock Engineering*, vol. 47, no. 2, pp. 347–356, 2014.

[25] H. Zhang, H. Li, T. Zhang, Q. Wang, and T. Guo, "Research and engineering application of high pre-stressed resistance enhancement large deformation bolt in deep soft rock roadway," *Meitan Xuebao/Journal of the China Coal Society*, vol. 44, pp. 409–418, 2019.

[26] Z. Yin, W. Chen, H. Hao et al., "Dynamic compressive test of gas-containing coal using a modified split Hopkinson pressure bar system," *Rock Mechanics and Rock Engineering*, vol. 53, pp. 815–829, 2020.

[27] J. Zuo, C. Yan, J. Zhang, J. Wang et al., "Failure behavior and strength characteristics of coal rock combination under different confining pressures," *Journal of Coal Industry*, vol. 41, pp. 2706–2713, 2016.

[28] J. Zuo, H. Xie, A. Wu et al., "Study on failure mechanism and mechanical properties of deep coal rock monomers and combinations," *Journal of Rock Mechanics and Engineering*, vol. 30, pp. 84–92, 2011.

[29] Y. L. Tan, X. S. Liu, B. Shen, J. G. Ning, and Q. H. Gu, "New approaches to testing and evaluating the impact capability of coal seam with hard roof and/or floor in coal mines," *Geomechanics and Engineering*, vol. 14, pp. 367–376, 2018.

[30] B. Huang and J. Liu, "The effect of loading rate on the behavior of samples composed of coal and rock," *International Journal of Rock Mechanics and Mining Sciences*, vol. 61, pp. 23–30, 2013.

[31] C. Lu, L. Dou, X. Wu, Z. Mou, and G. Chen, "Experimental and empirical research on frequency-spectrum evolvement rule of rockburst precursory microseismic signals of coal-rock," *Chinese Journal of Rock Mechanics & Engineering*, vol. 27, pp. 519–525, 2008.

[32] T. Wang, Y. Jiang, S. Zhan, and C. Wang, "Frictional sliding tests on combined coal-rock samples," *Journal of Rock Mechanics and Geotechnical Engineering*, vol. 6, no. 3, pp. 280–286, 2014.

[33] E. Hoek and Brown, "Empirical strength criterion for rock masses," *Geotechnical Engineering*, vol. 18, p. 23, 1981.

[34] E. Hoek, D. Wood, and S. Shah, "Modified Hoek-Brown failure criterion for jointed rock masses," *International Journal of Rock Mechanics and Mining Sciences*, vol. 30, p. A215, 1993.

[35] M. You, "True-triaxial strength criteria for rock," *International Journal of Rock Mechanics and Mining Sciences*, vol. 46, no. 1, pp. 115–127, 2009.

[36] J. Zuo, H. song, C. Yan et al., "Post peak progressive failure characteristics and nonlinear model of coal rock assemblages," *Journal of Coal Industry*, vol. 43, pp. 3265–3272, 2018.

[37] K. Franklin and S. Zhang, "Recommended method for determining rock stress by the Committee of test methods of the international society of rock mechanics," *Journal of Rock Mechanics and Engineering*, vol. 7, pp. 69–100, 1988.

[38] J. F. Labuz and J. M. Bridell, "Reducing frictional constraint in compression testing through lubrication," *International Journal of Rock Mechanics and Mining Sciences & Geomechanics Abstracts*, vol. 30, no. 4, pp. 451–455, 1993.

[39] S. Yang, C. Su, and W. Xu, "Experimental and theoretical research on size effect of rock materials," *Engineering Mechanics*, vol. 22, pp. 112–118, 2005.

[40] B. Liu and J. Zhang, "Size effect of rock compressive strength," *Journal of Rock Mechanics and Engineering*, vol. 17, pp. 611–614, 1998.

[41] J. Peng, R. Guan, M. Cai, and K. Peng, "Determining residual strength of rock based on a brittle index," *Geotechnical Mechanics*, vol. 36, pp. 403–408, 2015.

Research Article

A Damage Constitutive Model of Rock under Hydrochemical Cyclic Invasion

Lunan Sun,[1] Yu Zhang,[1] Zhe Qin [1,2] Tengfei Wang,[1] and Sheng Zhang[1]

[1]*College of Civil Engineering and Architecture, Shandong University of Science and Technology, Qingdao, China*
[2]*Shandong Key Laboratory of Civil Engineering Disaster Prevention and Mitigation,*
 Shandong University of Science and Technology, Qingdao, China

Correspondence should be addressed to Zhe Qin; chin@sdust.edu.cn

In order to analyze the stability of water-related materials, the deterioration and damage of rock strength due to circulating water intrusion in an open tailings pond were studied. Uniaxial compression tests were carried out for rocks under different hydrochemical environments and varying numbers of invasion cycles. Results show that, with increasing number of cycle times, rock peak strength and elastic modulus gradually decrease and the acidity and alkalinity of the soaking solution also degrades rock strength. The curve of the number of cycles, acidity, alkalinity, peak strength, and elastic modulus is fit numerically. Based on the principle of damage mechanics, a hydraulic-chemistry-mechanics (HCM) coupling damage variable is defined. Based on the theory of microbody strength distribution, the constitutive equation for rock damage under the coupled effect of water chemistry and cyclic water invasion is established. The results verify the validity of the established damage constitutive model.

1. Introduction

Abandoned open pits are geological bodies with increased safety risks when the original support system fails. In order to make abandoned open pits reusable and avoid wasting land resources on new tailings storage, some open pits are used as tailings ponds for nearby dressing plants [1–5]. Using an open-pit mine as a tailings pond raises two main problems. First, the waste tailings liquid contains a large amount of tailings sand and is discharged into the pit through a pipe or tanker, which causes the water level in the open pit to continuously rise. Increased groundwater flow and precipitation can also cause the water level to significantly increase. Secondly, the tailings liquid in the open pit undergoes long-term precipitation, and the tailings sand consolidates and settles. The ore pit uses the water in the pit for secondary use at various times, resulting in a decrease in water level. Therefore, after the open-pit mine is used as a tailings pond, the stability of the slope rock mass needs to be

analyzed and the influence of the rock environment and water level fluctuation on the rock strength needs to be considered. At present, many researchers have examined the strength of engineering rock masses affected by water level fluctuations, primarily including the static and dynamic rocks characteristics such as compressive strength and elastic modulus. There are numerous research results on the variation in macroscopic strength of rocks under the effect of cyclic water invasion [6–12]. The weakening of rock strength under the effect of cyclic water intrusion is the damage of the micro-meso rock structure inside. Structural control theory in engineering geology indicates that cyclic water intrusion causes the expansion of primary defects such as microcracks and micropores and also causes the development of secondary defects, eventually leading to the formation of macrocracks inside the rock mass, which affects the macrostrength of the rock. Presently, for rock mesodamage characteristics under cyclic water intrusion, scanning electron microscopy and Computed Tomography (CT) tests are

primarily used. Fractured sections of the rock are examined using advanced instruments such as nuclear magnetic resonance imagers to obtain mesostructural changes for different cyclic invasion conditions and produce a qualitative analysis of the mesodamage. Using digital image recognition technology, mesostructural information, such as fractal dimension and porosity, is extracted to quantitatively characterize the mesostructural damage [3, 13–16]. Results show that cyclic water intrusion affects the strength and structure of rocks and adversely affects the stability of the project. However, the rocks on the bank slope of the tailings reservoir are immersed in acidic or alkaline tailings for a long time. The tailings with different acidity and alkalinity will have a nonnegligible degradation effect on the macrodamage and mesodamage of the rock. For different water chemical environmental conditions, there is still a lack of necessary research on rock damage characteristics. Therefore, examining the degradation and damage characteristics of rock strength relative to water chemistry and cyclic invasion is significant, especially for wading geotechnical and coastal geotechnical engineering.

Taking the open pit as the tailings pond, the change in rock strength under the influence is examined, considering the degradation and damage to rock strength due to the coupled effect of water chemistry and cyclic invasion. Using the uniaxial compression of rocks under different hydrochemical environments, the experiment focused on analyzing the rock strength damage and established a multiparameter variation plane equation. Based on the principle of Hydraulic-Chemistry-Mechanics (HCM), coupling damage variables were defined and constructed.

2. Engineering Background

The Cangshang open pit was closed in 2005 and has remained idle. Due to the construction of an 8,000-ton ore dressing plant adjacent to the Sanshandao Gold Mine, the Cangshang open pit was converted to a tailings pond for the Sanshandao Gold Mine Concentrator in 2009. With the discharge of abandoned tailings fluids, the water level in the open-pit mine continues to rise, which severely affects the stability of the slope (Figure 1). The main sliding area is located on the north side of the slope. Obvious cracks are visible at the top of the slope, and there is significant slip on the local sliding surface as well as a substantial collapse of the adjacent house wall. The open pit water level rise and fall cycles cause irreversible deterioration to the rock strength and internal structure of the slope, especially for slopes containing weak structural planes, such alteration zones are formed during gold mineralization. The alteration zone has a certain strength, and the slope is in a relatively stable state. When the water invades, the rock strength decreases or the rock mass fails, which causes the pit slope to slip and even causes sudden slope instabilities.

The cyclic water invasion-dehydration effect weakens the rock mass strength and causes the open pit slope to slip. The YCY-3 water level automatic measuring instrument is used to monitor the surface displacement of the open pit north side and the open pit water level change (Figure 2). The water

level of the tailings dam in the figure shows an increasing trend of first falling and then rising. When the water level falls rapidly or rises rapidly, the slope structure of the bank slope is likely to be unstable, causing serious landslides, displacements, and other disasters.

3. Uniaxial Compression Test

3.1. Uniaxial Compression Test Curve. The rock samples are taken from the typical rock samples of the tailings dam slope of Sanshan Island Gold Mine. The method is to use on-the-spot sampling with the method of combining the core and the block on the slope surface. The drilled cores are encapsulated with plastic wrap in time to ensure their original moisture content. The rock sampled on-site is cut into standard rock specimens of $100 \, mm \times 50 \, mm$. Here, one cycle of water infiltration is defined as the rock being soaked in the soaking box for 24 hours and then dried in the drying box at 105°C for 24 hours. The test consists of three sets of rock samples, each group of 4 rock samples; the rock samples were subjected to 0, 5, 15, and 30 cycles of water infiltration test, and then the samples were then immersed in a solution of pH = 5, pH = 7, and pH = 9 for 24 hours. A uniaxial compression test machine is used to conduct uniaxial compression tests on rocks treated with different water chemical environments at varying cycles. The basic mechanical parameters of the rock under different conditions can be obtained based on the rock stress-strain curve (Figure 3).

According to the uniaxial compression test results, the various hydrochemical environments and cyclic states have varying degrees of influence on rock mechanical properties. The stress-strain curves show four stages, including the compaction stage, elastic stage, plastic deformation stage, and yield stage. Affected by different pH levels and cyclic water invasion, the peak strength of the rock shows a significant decrease, which is closely related to the pH and the number of cyclic water intrusions. The peak strength and elastic modulus of the rock are obtained according to the uniaxial compressive stress-strain curve. The quantitative mechanical parameters are given in Table 1:

With the increase of the number of cycles, the peak strength and elastic modulus of the rock showed an overall downward trend. The degradation rate of the rock was faster during the first 5 cycles of water intrusion, and the degradation rate after 15 cycles was relatively slow. Acid and alkali also have obvious degradation effect on rock peak strength and elastic modulus. The degradation effect of acid solution on rock is stronger than that of alkaline solution, and neutral solution has the weakest degradation effect on rock.

3.2. Degradation of Uniaxial Compressive Strength. Parameters such as rock strength weakening coefficient and elastic modulus degradation under different conditions are obtained from the uniaxial compression test results. The changes in the abovementioned mechanical parameters can be used to quantitatively characterize the degree of rock damage. Define the rock weakening coefficient and the deterioration degree of elastic modulus shown as follows:

(a)

(b)

(c)

(d)
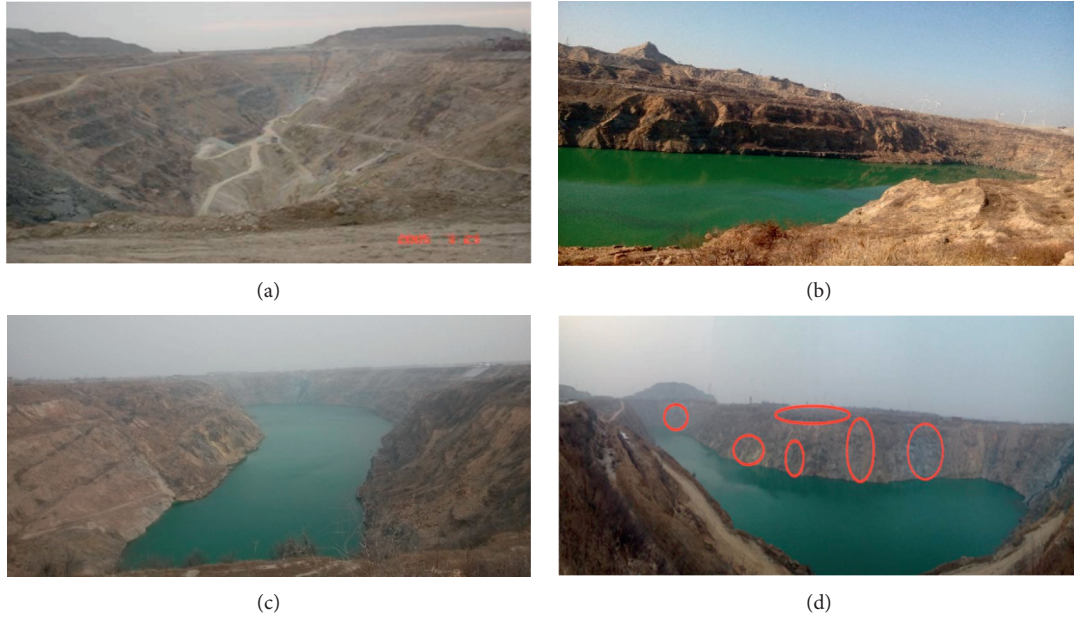
Figure 1: Cyclic invasion-dehydration process in open pit. (a) Open pit without water. (b) Water level rise. (c) Water level decline. (d) Open pit slope deformation.
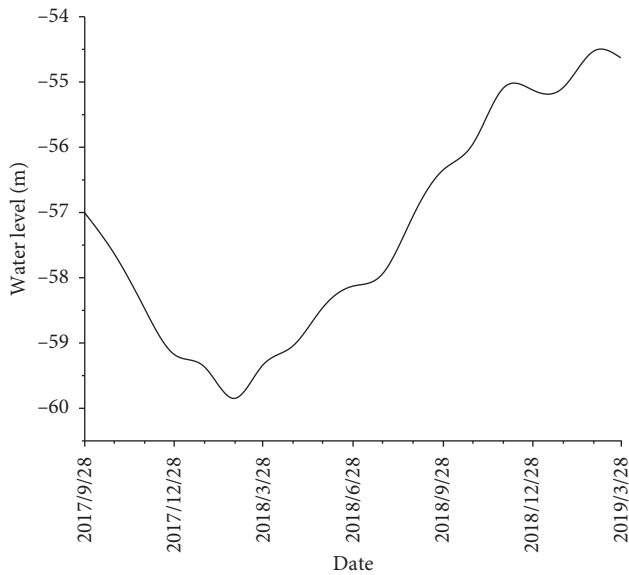
Figure 2: Water level change in the open pit.

$$\lambda = \frac{R_{t0} - R_{tn}}{R_{t0}},$$

$$D_E = \frac{E_0 - E_n}{E_0}, \tag{1}$$

where λ is the rock weakening coefficient, R_{t0} is the initial peak strength of the rock in the natural state, R_{tn} is the peak strength when the number of cycles of water intrusion is n; D_E is the degree of degradation of the elastic modulus, E_0 is the initial elastic modulus of the rock in the natural state, and E_n is the modulus of elasticity when the number of cycles of water intrusion is n.

The rock damage parameters for different hydrochemical environments and different cyclic states were obtained. The rock damage parameters under different cyclic states are shown in Table 2.

According to Table 2 and Figure 4, for the same water chemical environment, rock strength gradually decreases with increasing number of cycles. Similarly, for the same cycle number of cycles, rock strength gradually decreases under different pH levels. However, for acidic and alkaline environments, the decrease in rock strength in acidic environments is higher than in alkaline environments because the rocks are primarily carbonate rocks, and acidic ions easily breakdown carbonate, resulting in a reduction in rock strength.

By analyzing the effects of different water chemical environments and different cyclic states on the peak rock strength and elastic modulus, a mathematical fit was used to achieve a flat fit of the test results. The fitting results are shown in Figure 5 and the corresponding fitting formula is as follows.

Data were fit using the fitting toolbox in MATLAB to get the fitting formula:

$$f_1(x, y) = 11.44 - 2.03x + 12.88y + 0.03x^2 - 0.87y^2,$$

$$f_2(x, y) = -4.16 - 0.18x + 3.11y + 0.003x^2 - 0.22y^2. \tag{2}$$

4. Rock Damage Constitutive Model

Uniaxial compression tests have shown that the coupling of water chemistry and cyclic water intrusion can cause rock strength degradation, and different environmental conditions have different degrees of impact on rock strength.
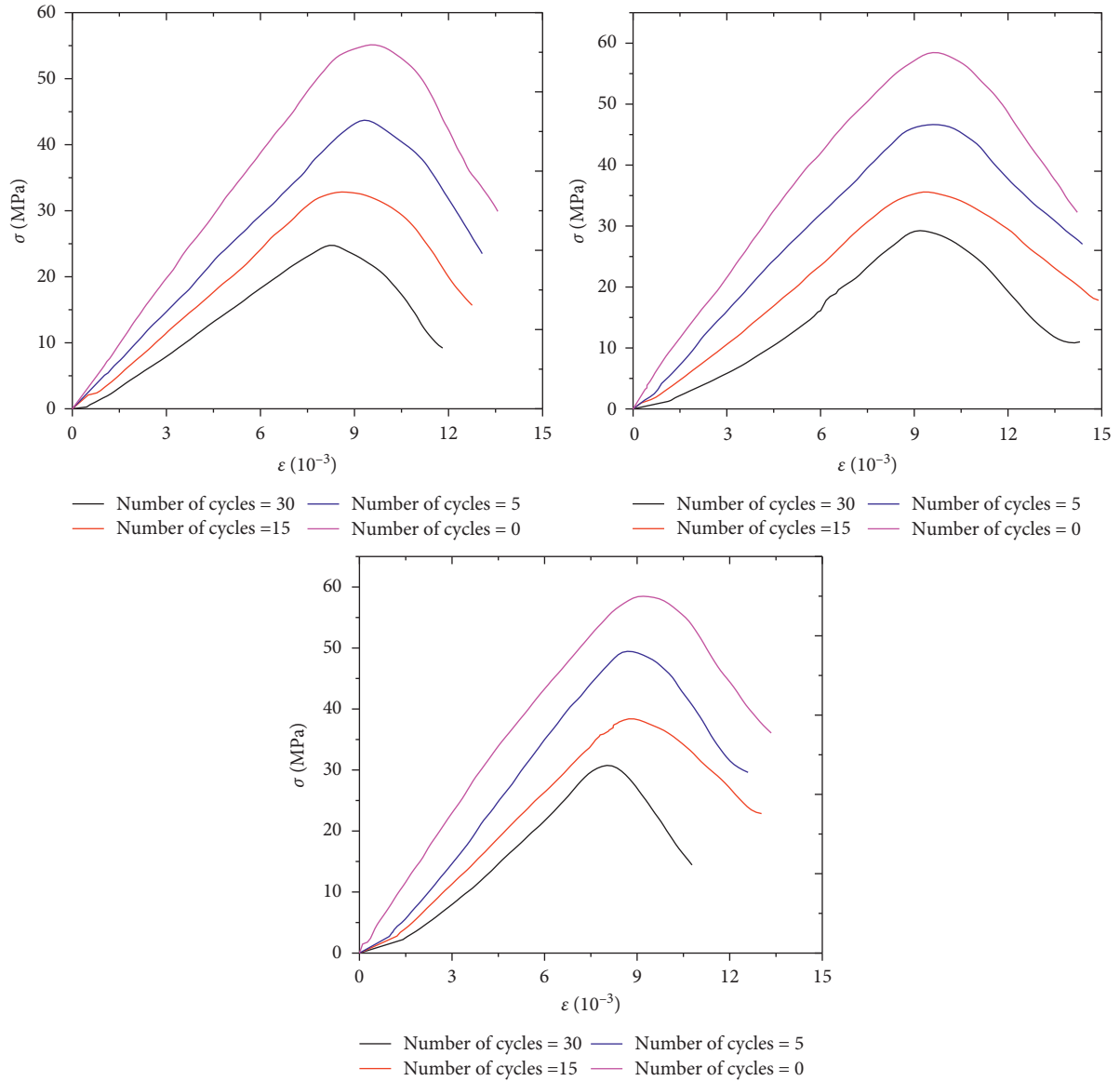
Figure 3: Stress-strain curve of rock. (a) pH = 5. (b) pH = 7. (c) pH = 9.

Table 1: Uniaxial compression test results.

n	pH = 5		pH = 7		pH = 9	
	Peak strength (MPa)	Elastic modulus (GPa)	Peak strength (MPa)	Elastic modulus (GPa)	Peak strength (MPa)	Elastic modulus (GPa)
0	55.12	6.15	58.48	6.67	58.45	6.35
5	43.70	4.82	49.45	6.35	46.65	5.22
15	32.83	4.15	38.38	4.91	35.58	4.18
30	24.75	3.29	30.75	4.46	29.24	3.04

Therefore, the coupling effect of water chemistry and cyclic water intrusion is affected by the coupling of cyclic water intrusion. Therefore, the damage variable in this paper is defined as the cyclic water invasion Hydraulic-Chemistry-Mechanics (HCM) coupling damage variable. Among them, the cyclic hydraulic (chemistry) damage variable primarily affects mechanical parameters by affecting the internal structure of the rock. According to the principle of damage mechanics, the damage variable is defined by the elastic modulus and the damage caused by mechanical loading. Since the damage is primarily due to the influence of the strength of the unit body inside the rock, the damage

TABLE 2: The rock damage parameters for different hydrochemical environments and different cyclic states.

	pH = 5		pH = 7		pH = 9	
n	Weakening coefficient (%)	Degree of elastic modulus degradation (%)	Weakening coefficient (%)	Degree of elastic modulus degradation (%)	Weakening coefficient (%)	Degree of elastic modulus degradation (%)
0	0	0	0	0	0	0
5	20.72	21.63	15.44	4.80	20.19	17.80
15	24.87	13.90	22.39	22.68	23.73	19.92
30	24.61	20.72	19.88	9.16	17.82	12.92
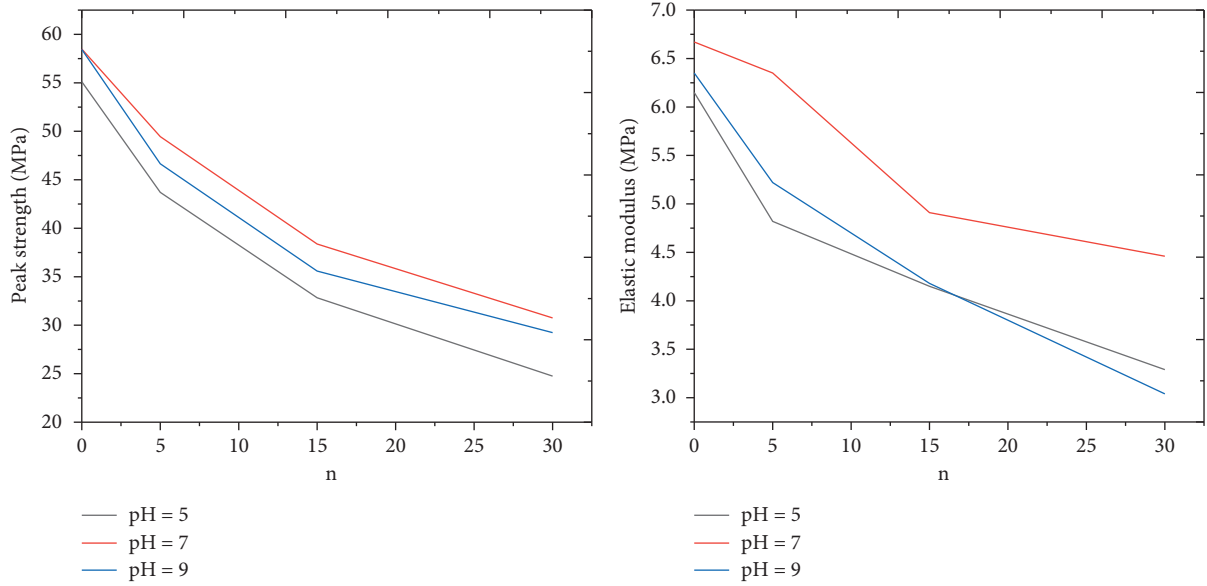
FIGURE 4: Change of mechanical parameters with the number of cycles.
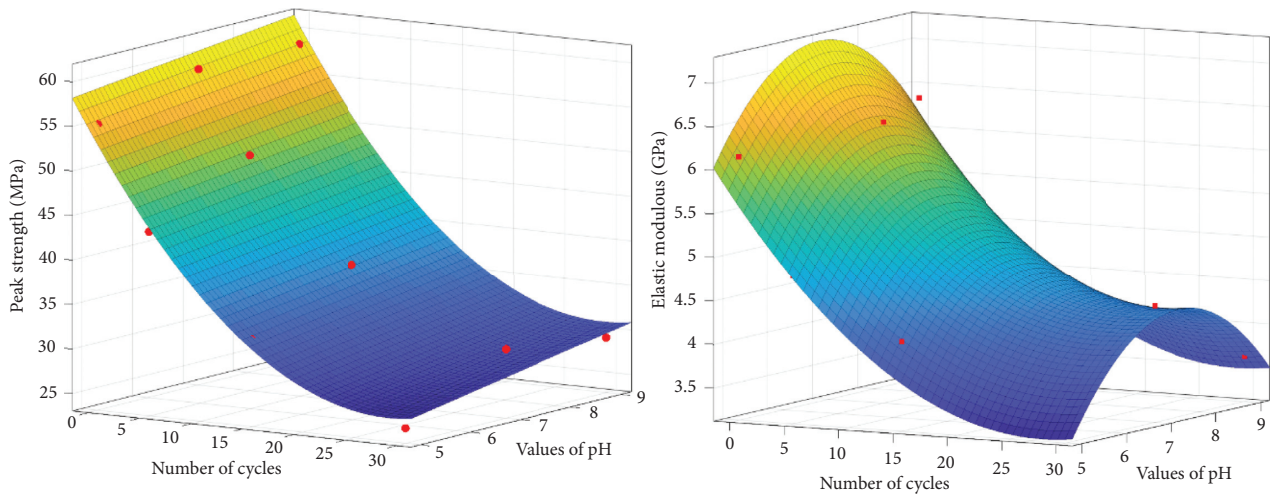
FIGURE 5: Parameter plane fitting.

variable is defined according to the change in the strength of the microbody.

(1) Hydraulic-chemistry damage variables: the hydraulic-chemistry damage variable primarily affects rock mechanical parameters by affecting the internal structure of the rock; therefore, according to the

principle of damage mechanics, the damage variable is defined by the elastic modulus:

$$D_e = \frac{E_0 - E_n}{E_0} = 1 - \frac{E_n}{E_0}, \qquad (3)$$
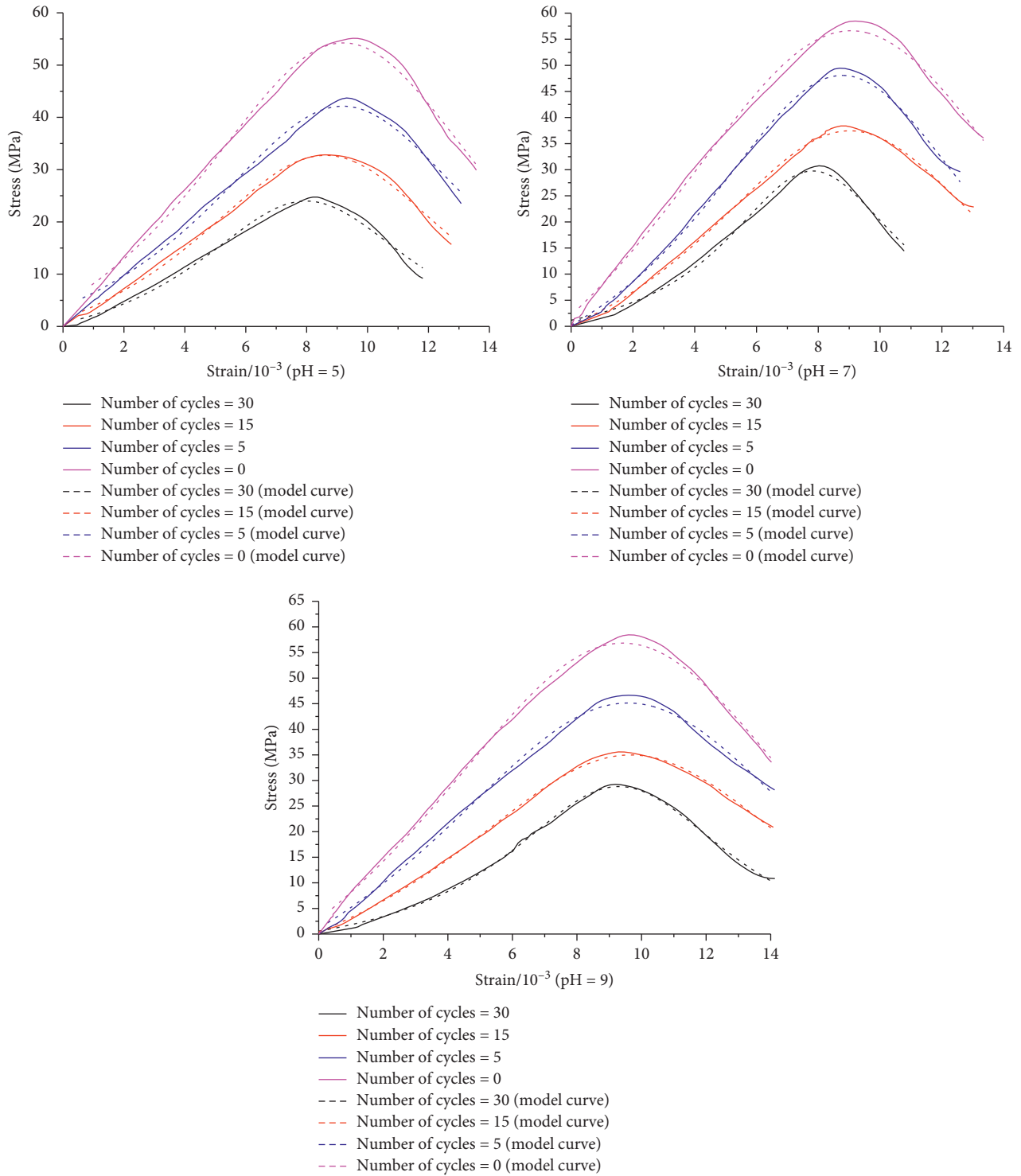
Figure 6: Comparison of test and model curves.

where D_e denotes the hydraulic-chemical damage variable; E_n is the elastic modulus at n number of cycles; and E_0 is the elastic modulus at 0 cycles.

(2) Mechanical damage variable: during the uniaxial compression test, the external load will cause random damage to the internal unit of the test rock. The strength of the unit body is mainly distributed within

a certain range, and the strength of the unit body smaller or larger than this range gradually decreases with increasing distance. Therefore, based on the knowledge of probability theory, it is assumed that the failure of the internal microunits in the rock as a whole obeys a certain probability statistical distribution, such as the Weibull distribution or Gaussian

distribution [15]. Assuming that the strength of the rock microelements obeys the Weibull distribution, the distribution probability density function is [17, 18]

$$f(x) = \frac{m}{\lambda} \left(\frac{N}{\lambda}\right)^{m-1} \exp\left[-\left(\frac{N}{\lambda}\right)^m\right], \qquad (4)$$

where m and λ are Weibull distribution parameters.

The mechanical damage variable D_m is defined as the strength failure probability of rock microelements:

$$D_m = \frac{N_b}{N} = \frac{\int_0^\varepsilon N \cdot f(x)dx}{N} = \int_0^\varepsilon f(x)dx = 1 - \exp\left(-\left(\frac{\varepsilon}{\lambda}\right)^m\right). \qquad (5)$$

Under the coupling effect of water chemistry and cyclic invasion, rocks are affected by HCM coupling of cyclic intrusion. According to formulas (3) and (5), the cyclic invasion HCM coupling damage variable is defined as follows:

$$1 - D = (1 - D_e)(1 - D_m). \qquad (6)$$

According to the above formula, the comprehensive damage variable under the HCM coupling is

$$D = 1 - \frac{E_n}{E_0} \cdot \left(\exp\left(-\left(\frac{\varepsilon}{\lambda}\right)^m\right)\right). \qquad (7)$$

Damage mechanics is a recently developed discipline for studying the failure process of materials based on continuum thermodynamics. Damage mechanics focuses on the development of defects such as micropores in rocks and is the study of the formation of macroscopic cracks in materials. The principle of damage mechanics proposes the strain equivalent principle combined with the effective stress principle, in which the basic form of the damage constitutive relationship does not change before and after the damage caused by the coupling of water chemistry and cyclic water invasion. However, the effective stress in the constitutive model will change. Therefore, based on the principle of damage mechanics, the basic form of the material's damage constitutive equation is [19–21]

$$\varepsilon = \frac{\overline{\sigma}}{E} = \frac{1}{E} \cdot \frac{\sigma}{(1 - D)}, \qquad (8)$$

where ε is the rock strain in different states, σ is the nominal stress on the rock, $\overline{\sigma}$ is the effective stress on the rock, E is the initial elastic modulus of the material, and D is the damage variable.

By combining formulas (7) and (8), a constitutive model of rock damage under the coupling of water chemistry and cyclic invasion can be deduced:

$$\sigma = E_n \cdot \left(\exp\left(-\left(\frac{\varepsilon}{\lambda}\right)^m\right)\right) \cdot \varepsilon. \qquad (9)$$

4.1. Evaluation of Rock Damage Constitutive Model. According to the uniaxial compression test results of rock under the coupling of water chemistry and cyclic invasion, the comparative analysis of the statistical damage constitutive model under the coupling of water chemistry and cyclic invasion is carried out (Figure 6).

The damage constitutive model established in the paper can effectively describe the characteristics of the test curve, and the description accuracy is greater than 90%, which illustrates the effectiveness of the established model (Figure 6). Because the damage constitutive model was built without considering the initial compaction stage, some model curves show deviations during the compaction stage of the stress-strain curve, which limits the accuracy of the constitutive model to some extent. However, the damage constitutive model considering the coupling effect of water chemistry and cyclic invasion and can describe the characteristics of rock deformation curve.

5. Conclusion

Taking an open pit as the tailings pond, the change in rock strength considering the degradation and damage caused by the coupling effect of water chemistry and cyclic invasion was analyzed using uniaxial compression tests. A constitutive model for rock damage under the coupling of water chemistry and cyclic invasion was introduced. The main research conclusions include

(1) The coupling effect of water chemistry and cyclic invasion decreases rock strength. Test results show that the peak strength and elastic modulus of the rock gradually decrease as the number of cycles increases. Specifically, the more the number of cycles is, the more obvious the damage of the peak strength and elastic modulus of the rock is. The weakening speed of the peak strength is higher than that of the elastic modulus.

(2) The acidity and alkalinity of the fluid also degrade rock strength, acidic and alkaline conditions have a significant weakening effect on the peak strength and elastic modulus of the rock, and the weakening effect of the neutral condition on the rock is slightly weaker; acidic fluids degrade rock strength more that alkaline solutions. The change curve relative to the number of cycles, pH level, peak strength, and elastic modulus of the rock was fit.

(3) Based on the principle of damage mechanics, the HCM coupling damage variable is defined. Based on the Weibull distribution theory and the strain equivalent principle, a coupling that considers water chemistry and cyclic water intrusion is constructed. The effect of the constitutive model of rock damage is verified by comparison with experimental results.

Data Availability

The processed data required to reproduce these findings cannot be shared at this time as the data also forms part of an ongoing study.

Conflicts of Interest

The authors declare that they have no conflicts of interest.

Acknowledgments

References

[1] Z. Qin, H. Fu, and X. Chen, "A study on altered granite meso-damage mechanisms due to water invasion-water loss cycles," *Environmental Earth Sciences*, vol. 78, no. 14, p. 428, 2019.

[2] Z. Qin, X. Chen, and H. Fu, "Damage features of altered rock subjected to drying-wetting cycles," *Advances in Civil Engineering*, vol. 2018, Article ID 5170832, 10 pages, 2018.

[3] X. Chen, P. He, Z. Qin et al., "Statistical damage model of altered granite under dry-wet cycles," *Symmetry*, vol. 11, no. 1, 2019.

[4] L. Li, S. Sun, J. Wang, W. Yang, S. Song, and Z. Fang, "Experimental study of the precursor information of the water inrush in shield tunnels due to the proximity of a water-filled cave," *International Journal of Rock Mechanics and Mining Sciences*, vol. 130, Article ID 104320, 2020.

[5] W. T. Li, N. Yang, and T. C. Li, "Implementation of bolt broken failure in FLAC3D and its application," *Chinese Journal of Rock Mechanics and Engineering*, vol. 35, no. 4, pp. 753–767, 2016.

[6] T. Waragai, "The effect of rock strength on weathering rates of sandstone used for Angkor temples in Cambodia," *Engineering Geology*, vol. 207, pp. 24–35, 2016.

[7] X. Liu, Z. Wang, Y. Fu et al., "Macro/microtesting and damage and degradation of sandstones under dry-wet cycles," *Advances in Materials Science and Engineering*, vol. 2016, Article ID 7013032, 16 pages, 2016.

[8] G. Wang, W. Han, Y. Jiang, H. Luan, and K. Wang, "Coupling analysis for rock mass supported with CMC or CFC rockbolts based on viscoelastic method," *Rock Mechanics and Rock Engineering*, vol. 52, no. 11, pp. 4565–4588, 2019.

[9] X.-X. Yang and W.-G. Qiao, "Numerical investigation of the shear behavior of granite materials containing discontinuous joints by utilizing the flat-joint model," *Computers and Geotechnics*, vol. 104, pp. 69–80, 2018.

[10] Q. Yao, T. Chen, M. Ju, S. Liang, Y. Liu, and X. Li, "Effects of water intrusion on mechanical properties of and crack propagation in coal," *Rock Mechanics and Rock Engineering*, vol. 49, no. 12, pp. 4699–4709, 2016.

[11] K. Bian, J. Liu, W. Zhang, X. Zheng, S. Ni, and Z. Liu, "Mechanical behavior and damage constitutive model of rock subjected to water-weakening effect and uniaxial loading," *Rock Mechanics and Rock Engineering*, vol. 52, no. 1, pp. 97–106, 2019.

[12] Z. Zhao, J. Yang, D. Zhang, and H. Peng, "Effects of wetting and cyclic wetting-drying on tensile strength of sandstone with a low clay mineral content," *Rock Mechanics and Rock Engineering*, vol. 50, no. 2, pp. 485–491, 2017.

[13] X. Chen, P. He, and Z. Qin, "Damage to the microstructure and strength of altered granite under wet-dry cycles," *Symmetry*, vol. 10, no. 12, p. 716, 2018.

[14] K. Xie, D. Jiang, Z. Sun, J. Chen, W. Zhang, and X. Jiang, "NMR, MRI and AE statistical study of damage due to a low number of wetting-drying cycles in sandstone from the three gorges reservoir area," *Rock Mechanics and Rock Engineering*, vol. 51, no. 11, pp. 3625–3634, 2018.

[15] P. Kang, L. Hong, Y. Fazhi, Z. Quanle, and L. Zhaopeng, "Effects of temperature on mechanical properties of granite under different fracture modes," *Engineering Fracture Mechanics*, vol. 226, p. 106838, 2020.

[16] T. Saksala, "Modelling of dynamic rock fracture process with a rate-dependent combined continuum damage-embedded discontinuity model incorporating microstructure," *Rock Mechanics and Rock Engineering*, vol. 49, no. 10, pp. 3947–3962, 2016.

[17] D. Kundu and R. D. Gupta, "Estimation of $rm P[Y \ll X]$for Weibull Distributions," *IEEE Transactions on Reliability*, vol. 55, no. 2, pp. 270–280, 2006.

[18] T. Wong, R. H. C. Wong, K. T. Chau et al., "Microcrack statistics, Weibull distribution and micromechanical modeling of compressive failure in rock," *Mechanics of Materials*, vol. 38, no. 7, pp. 664–681, 2006.

[19] D. Krajcinovic, "Damage mechanics," *Ceskoslovensky Casopis Pro Fyziku Sekce A*, vol. 8, no. 2-3, pp. 117–197, 1989.

[20] K. Peng, J. Zhou, Q. Zou, and F. Yan, "Deformation characteristics of sandstones during cyclic loading and unloading with varying lower limits of stress under different confining pressures," *International Journal of Fatigue*, vol. 127, pp. 82–100, 2019.

[21] K. Peng, J. Zhou, Q. Zou, and X. Song, "Effect of loading frequency on the deformation behaviours of sandstones subjected to cyclic loads and its underlying mechanism," *International Journal of Fatigue*, vol. 131, p. 105349, 2020.

Research Article

Study on the Rheological Failure Mechanism of Weakly Cemented Soft Rock Roadway during the Mining of Close-Distance Coal Seams: A Case Study

Wenkai Ru,[1] Shanchao Hu [ID],[1,2] Jianguo Ning,[1] Jun Wang,[1] Qingheng Gu,[1] Yong Guo,[1] and Jing Zuo[1]

[1]*State Key Laboratory of Mining Disaster Prevention and Control Co-Founded by Shandong Province and the Ministry of Science and Technology, Shandong University of Science and Technology, 579 Qianwangang Road, Qingdao, China*
[2]*State Key Laboratory of Coal Resources and Safe Mining, China University of Mining and Technology, No. 1 University Road, Xuzhou, China*

Correspondence should be addressed to Shanchao Hu; mining2@126.com

During the mining of the shallow-buried and close-distance multiple coal seam, the rheological failure of the surrounding weakly cemented soft rock of the roadway in the lower coal seam under the concentrated stress is very rare. However, the stress on the roof of the upper coal seam is transmitted down through the residual pillar, resulting in this situation. Taking the Gaojialiang coal mine which is located in the mining areas of western China as the research object, the failure mechanism of the roadway roof under the residual coal pillar in the shallow-buried and close-distance multiple seam is studied in combination with field monitoring and numerical simulation. Furthermore, suggestions on the roadway support under such geological conditions are proposed. The results show that the residual coal pillar in the working face of the lower coal seam gradually collapses during the mining of the shallow-buried and close-distance multiple coal seam. The concentrated stress transferred by the coal pillar increases further, which makes the roof stress of the lower coal seam roadway to increase continuously. In addition, the stress of the roadway roof also increases further due to the rotation of the broken rock above the goaf, and the peek region of stress moves to the nongoaf area. Combining the heavy concentrated stress and weakly cemented property, the shallow-buried surrounding rock shows rheological behavior and failure. Therefore, we must pay more attention on the creep failure of the roadway roof under the action of the residual coal pillar even in the shallow-buried coal seam.

1. Introduction

Shallow-buried Jurassic coalfields abound in western China widely, which boasts the abundant reserves. They are featured by rich minable coal seams and close interlayer spacing [1, 2]. When mining the close-distance coal seams, the working faces of the upper and lower coal seams are usually arranged in parallel [3]. However, due to the geological conditions such as faults and coal-free areas, staggered arrangement appears inevitably [4–6]. When the stopping roadway of the lower coal seam is arranged under the section coal pillar left by the upper coal seam, coal pillar loading can

be calculated based on the assumption that the coal pillar bears the loading of the overlying stratum [7, 8] within its influenced area according to the tributary area theory, and the concentrated stress causes the failure of the roadway [9–12].

In order to figure out the failure mechanism of the surrounding rock in the goaf, the residual coal pillar, or the solid coal, some scholars have done a lot of research on the law of mine pressure when mining the shallow-buried and close-distance coal seam by means of the field test, theoretical analysis, and numerical simulation. First of all, the physical and mechanical properties and components of the

shallow-buried weakly cemented rock have been studied. It was found that the lithology of weakly cemented rock is mainly composed of sandy mudstone and fine sandstone [13, 14]. And, mudstone contains a high proportion of clay minerals, which easily leads to disintegration and high inflation under certain stress [15]. Based on this, some scholars have used the conventional compression test [16], shear test [17], and acoustic emission test [18] and found that the failure evolution and stress distribution of the weakly cemented surrounding rock had had obvious time effects [19–21]. Furthermore, the rock crept steadily under the lighter stress [22].

Subsequently, the concentrated loading formed by the residual coal pillar in the upper coal seam will be transferred downward through the floor strata, forming a stress-concentrated area in the floor. Consequently, the concentrated stress transferring rule of the residual coal pillar should be determined [23, 24]. Using the tributary area theory, the stability analysis method of coal pillars [25] and the Wilson and Carr method [26] are developed. By establishing the stress increment model of the pressure-relief mining floor [27, 28], it can be obtained that the floor of the coal seam after pressure-relief mining can be divided into four areas in the aspects of floor rupture area (arc), stress-relaxed area (parabola), stress-concentrated area (oval), and original rock stress area. Only when the lower coal roadway is arranged in the stress-relaxed area of the coal pillar floor can the stability of the roadway be more easily guaranteed.

In the end, it is necessary to analyze the stability of the floor roadway during the mining of the close-distance coal seam. The reason is that the floor of the coal pillar is the roadway roof of the lower coal seam. Based on the elasto-plastic mechanics and fracture mechanics under unloading conditions, the dynamic distribution and evolution laws of fractures in different stress areas in the floor under the influence of mining can be achieved [29–31]. At the same time, the deformation caused by the mining of the upper coal seam to the floor is determined [32]. The failure characteristics and depth of the interval rock under different mining conditions are generally determined by theoretical analysis, field monitoring, and numerical simulation. And, numerical simulation because of its simplicity has been commonly used in longwall mining to investigate mining-induced rock mass responses [33].

It can be found that remarkable achievements have been made in the studies of strength properties of weakly cemented rock and the stress transmission of the residual coal pillar. However, due to the shallow burial of coal seams in western China, the rheological phenomenon of weakly cemented rocks under concentrated stress has not attracted people's attention. As a result, problems of rheological failure of the roadway under the long-term action of concentrated loading of coal pillars have appeared [34], which has brought safety risks during production. This paper takes the shallow-buried and close-distance coal seam in western China as the research object. In combination with the field monitoring and numerical simulation, it studies the failure mechanism of the roadway roof under the residual coal pillar in the shallow-buried and close-distance multiple seam and

provides the basis for the roadway support under similar geological conditions [35, 36].

2. Mechanical Properties of Weakly Consolidated Soft Rock

There are 6 coal layers that can be mined in the Gaojialiang coal mine in western China. Currently, 2-2 upper and 2-2 middle coal seams are mainly mined. The depth and average thickness of the 2-2 upper coal seam are 165 m and 1.71 m, respectively, while those of the 2-2 middle coal seam are 170 m and 2.73 m, respectively. The distance between the two coal seams is 6.65~11.9 m, which is counted as a close-distance coal seam. The weakly cemented rock, between the two coal seams, is composed of sandy mudstone and silt-stone. It belongs to the typical weakly consolidated soft rock strata.

For the purpose of figuring out the mechanical mechanism of deformation and failure of the surrounding rock of the roadway under the residual coal pillar and providing the basis for the design of the roadway support under similar conditions, the component analysis and the creep test of the stratum between layers of Gaojialiang are carried out.

2.1. Analysis on Components of Strata. The components and parameters of physical mechanics of the interval strata are measured, and the components of strata are shown in Table 1. The interval strata is mainly composed of sandy mudstone, and the sandy mudstone is mainly composed of kaolinite and illite. Both are common clay minerals with a low hardness. The tensile and compressive strengths of sandy mudstone are 11.5 MPa and 3.5 MPa, respectively, and its elastic modulus is 13.7 GPa. It can be seen that its strength is generally low, so the surrounding rock of the roadway belongs to the typical weakly cemented soft rock.

2.2. Creep Test on Weakly Cemented Rock. As mentioned above, some scholars have carried out rheological tests on the shallow-buried weakly cemented rock and found that it would exhibit rheological behavior under lower stress [37–39]. Therefore, the sandy mudstone obtained in the Gaojialiang mine is selected for the creep test. A core is taken to prepare a standard sample of ϕ 50 mm × 100 mm, and graded-loading creep tests are performed. The failure strength of the specimens under 1.5 MPa confining creep compression is 14.5 MPa. The time-history curve and the creep properties curve under 1.5 MPa confining pressure are shown in Figure 1.

According to the curve of creep loading and considering the axial, lateral, and volume deformation characteristics of the rock, the stress-strain isochronous curve cluster under 1.5 MPa confining pressure is drawn, as shown in Figures 2(a)–2(c). For the three-way creep isochronous curve cluster, there are two inflection points among which point A is the sign of creep deformation and B is the strongly nonlinear plasticity after deformation. The stress at point A can be regarded as the threshold value of damage generation and B as the long-term strength index σ_{∞} of the rock sample.

TABLE 1: The components of the shallow-buried strata.

Lithology	Kaolinite	Illite	Chlorite	Iraq/middle layer
Coarse sandstone	29	15	5	—
Mudstone	29	15	5	—
Fine sandstone	25.4	16.37	38.82	<10
Medium sandstone	25.4	36.93	31.12	<10
Sandy mudstone	—	55	25	—
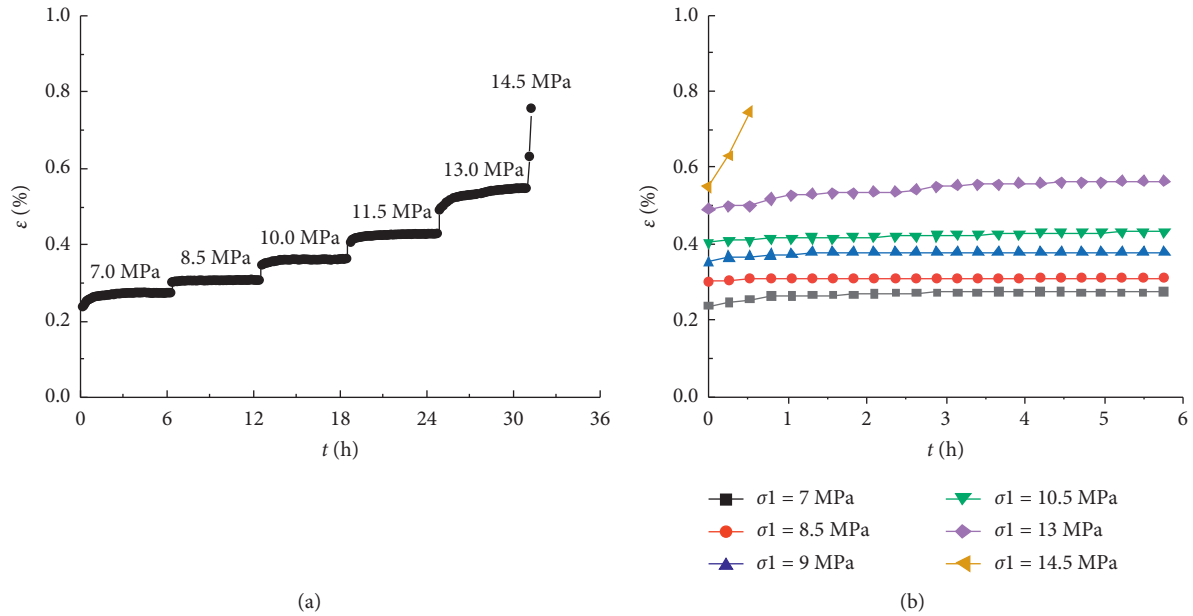
FIGURE 1: Under 1.5 MPa confining pressure, (a) time-history curve of strain and (b) creep characteristic curve.

The long-term strength of the specimen under 1.5 MPa confining pressure is 11.7 MPa. The long-term strength is slightly less than the rheological strength.

3. Geological Overview and Roadway Damage

In order to further verify the rheological failure characteristics and mechanism of weakly consolidated surrounding rock under a concentrated load, we conducted field monitoring in the Gaojialiang coal mine.

3.1. Geological Overview. At present, the 2-2 upper coal seam has been completed, while the 2-2 coal seam is being mined in the Gaojialiang coal mine. Affected by the coal-free area, most of the roadways in the 2-2 middle coal seam mined at this stage are arranged in the goaf of the 2-2 upper coal seam or the residual coal pillar. Figure 3 presents the layouts of the roadways and goafs. The 20314 auxiliary haulage roadway is located in the 2-2 middle coal seam, which is arranged in cross with multiple goafs on the overlying coal seam. And, the roadway is located under the upper coal seam goaf or the residual coal pillar. As a result, the roof of the 20314 auxiliary haulage roadway is complexly stressed. In particular, when it

is under the residual coal pillar, problems such as the sink of the roadway roof, the bulge of the floor, the rib spalling, and the break of the bolt and the anchor cable often occur.

3.2. Field Monitoring Method. In order to observe the surface and deep displacements of the surrounding rock of the roadway under the residual coal pillar in the upper coal seam, the mechanism of deformation and failure can be revealed and the basis for the surrounding rock support measures can be provided. A station is arranged in the 20314 auxiliary haulage roadway to determine the variation laws of the roadway displacement and the stress of the supporting body. Based on the intersection characteristics of the working faces of the 2-2 upper and 2-2 middle coal seams, the monitoring plan towards the lower coal seam roadway is formulated. 1# is arranged under the junction of the coal pillar and goaf, 2#, 3#, and 5# are placed under the coal pillar, and 4# is arranged under the solid coal. Two measuring points with a 5 m spacing are set in each station. Each station mainly includes the following equipment for testing: anchor (cable) dynamometer, borehole stress meter, borehole drilling TV, etc. Figure 4 depicts the arrangement of the monitoring instrument.

(a)

(b)

(c)
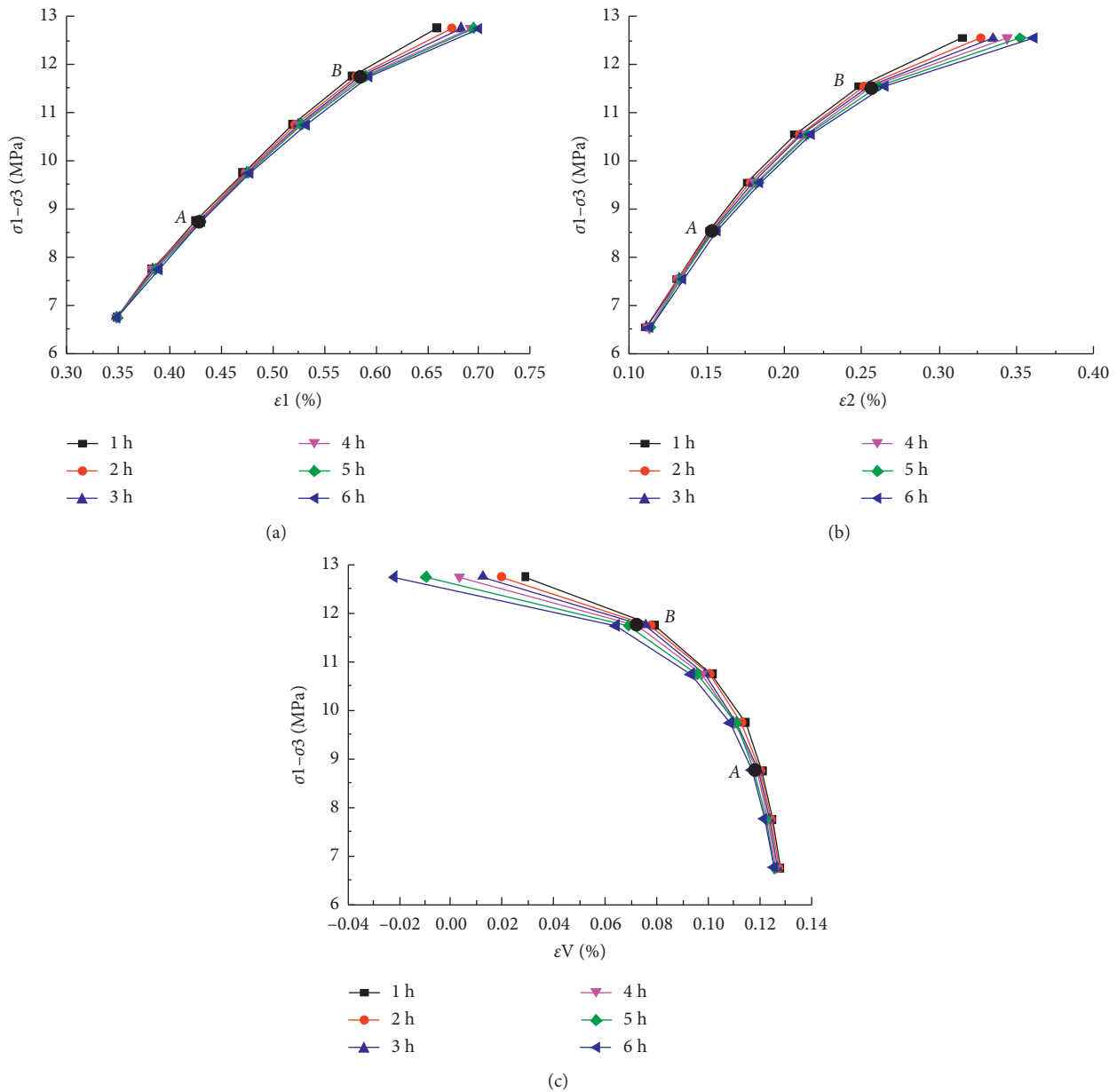
FIGURE 2: Stress-strain isochronous curve cluster: (a) axial strain; (b) lateral strain; (c) volume strain.

3.3. Deformation and Failure of Roadway

3.3.1. Macroscopic Failure of the Surrounding Rock of Roadway.

When the P20314 working face is moved to 900 m, the surrounding rock of the roadway at 44 m north of the auxiliary haulage roadway from the quadruple roadway shows deformation and failure. Problems such as the sink of the roadway roof, the bulge of the floor, and the rib spalling appear. Figure 5 reveals the deformation and failure range (54 m) of the surrounding rock. When the roadway stabilizes again, the roadway roof in the range of 6~18 m on the right side sinks in an arc way, while in the range of 18~36 m on the left side shows a step-type sinking with 0.6~0.8 m height. Due to a greater sink of the roof, some bolts (cables) are broken and dropped and some of the

single hydraulic props are crushed. Figure 6 shows the deformation and failure forms of the surrounding rock of the roadway.

3.3.2. Roadway Displacement Variation

(1) Roadway Surface Displacement. Surface displacement of the roadway includes the subsidence convergence of the roadway roof and the displacement convergence of the two sides. Surface displacements observed at 4# and 5# stations vary with time, as shown in Figures 7(a) and 7(b). It can be known that both subsidence and displacement convergences increase first and then stabilize as time goes by. In the first 12 days, the surface displacement changes barely. However, the surface displacement of the surrounding rock suddenly

Green represents gateroad in 2-2 upper coal seam   ● Measuring points

blue represents gateroad in 2-middle coal seam
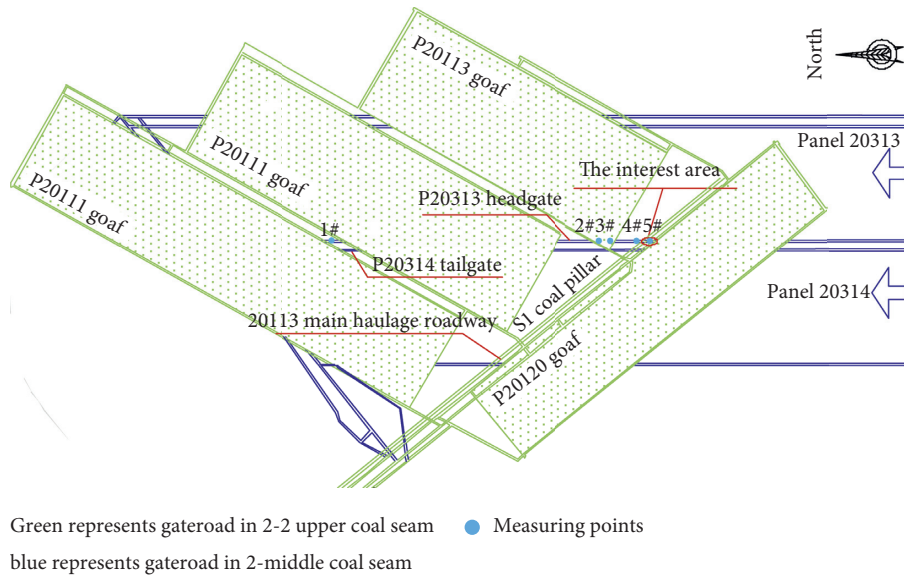
FIGURE 3: Layouts of the 2-2 upper and 2-2 middle coal seams.
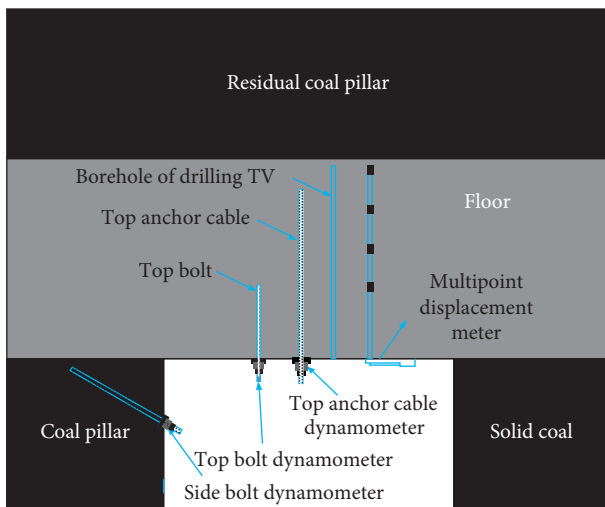
FIGURE 4: Arrangement of the monitoring instrument.

increases on the 13th day and stabilizes again after the 19th day. As the measuring points at the 5# station are located under the residual coal pillar, the surrounding rock of the roadway is seriously deformed because it suffers from a high concentrated stress. Furthermore, 5#-1 is the worst part of the station in which the maximum subsidence and displacement convergences reach 328 mm and 282 mm, respectively. By contrast, the subsidence convergence of the roof and the displacement convergence of the two sides at the 4# station change slightly, showing 27 mm and 91 mm, respectively. The reason is that the two measuring points at the 4# station are located under the solid coal, and the stress of the surrounding rock of the roadway is smaller than that of the lower part of the coal pillar.

(2) Displacement of Deep Roadway. Figures 8(a) and 8(b) show the displacement curves of the deep roadway roof at 4# and 5# stations. Similar to the variation law of the surface displacement of the roadway, the displacement of each measuring point in the deep also stabilizes first and then increases and stabilizes finally. For the shallow base point—depth measuring point with 2.5 m—two measuring points at the 4# station are located under the solid coal where point 4#-1 is far from the boundary of the solid coal and the displacement of the deep roof is 14 mm. Point 4#-2 is arranged at the boundary, which is greatly suffered from the concentrated stress than 4#-1. Consequently, the displacement of the deep roof is 16 mm. And, the two measuring points at the 5# station are arranged under the residual coal pillar, which are also greatly suffered from the concentrated stress, and the displacements are 16 mm and 13 mm, respectively. For the deep base point—depth measuring point with 4.5 m—the displacements of the deep roof of the two measuring points at the 4# station change slightly, while the displacement of the point 5#-1 is 18 mm at point 5#-2 is 12 mm.

3.3.3. Stress Variation of Roadway Support. Figures 9(a)–9(c) present the stress variations of bolts (cables) at 4# and 5# stations. As time moves, the stresses of the bolts (cables) in the roof and on the sides increase first and then stabilize. The 5#-1 measuring point is located under the residual coal pillar, with the completion of mining in the 20314 working face; the stress here is the most concentrated, and the force of the supporting body changes the most. Specifically, the forces of the anchor cable and the bolt in the roof increase by 40 kN and 32 kN, respectively, and the force of the bolt on the two sides increases by 18 kN. Correspondingly, the 4#-1 measuring point is arranged under the solid coal, which is less affected by the stopping of the P20314 working face. Therefore, the force at this point changes slightly, and forces of the anchor cable and the bolt in the roof increase by 20 kN and 12 kN, respectively. And, on the two sides, the fore of the bolt increases by 7 kN.
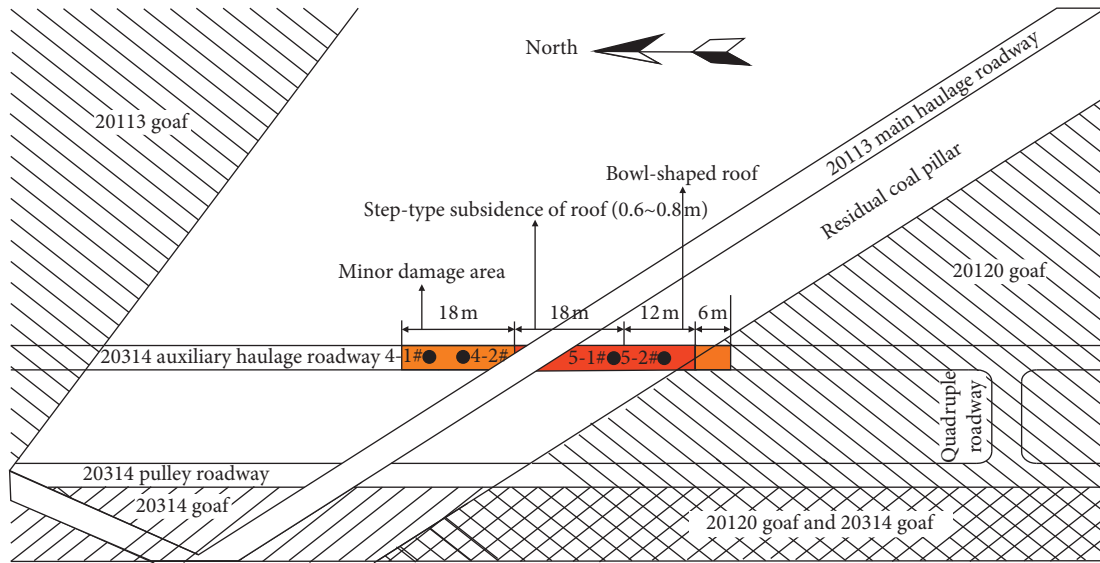
FIGURE 5: Deformation and failure range of the roadway.

(a)

(b)

(c)

(d)
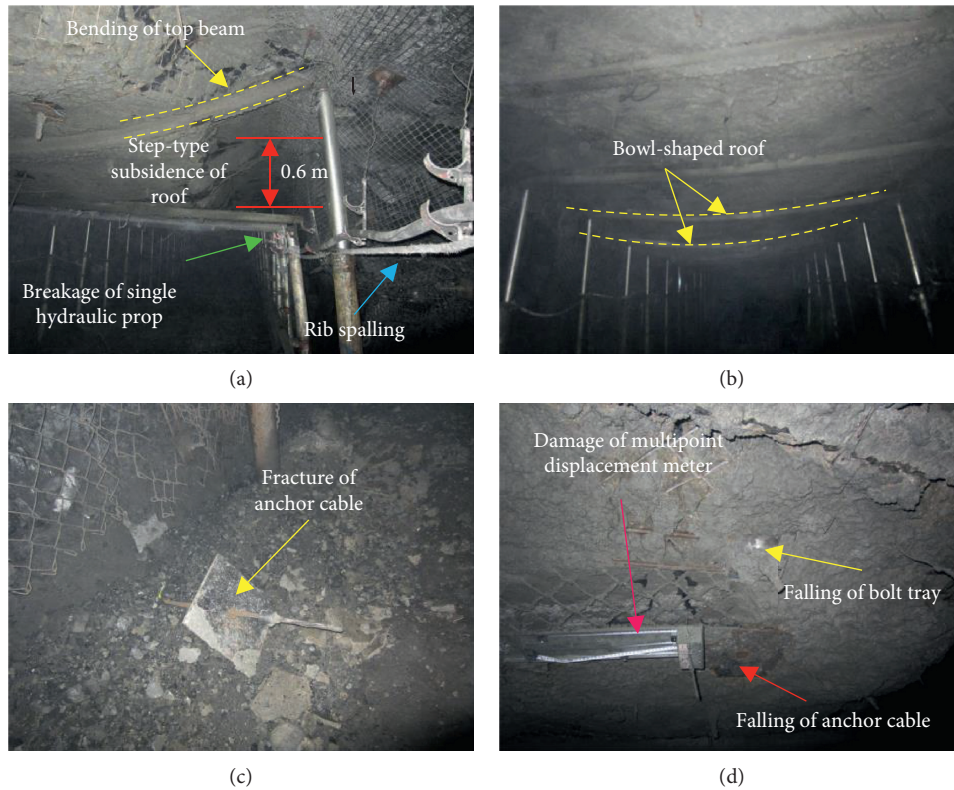
FIGURE 6: Deformation and failure forms of the surrounding rock of the roadway.

3.3.4. *Drilling TV Monitoring Results.* The monitoring results of some boreholes are shown in Figure 10. According to the peep results of the borehole, it can be obtained that there are many fracture areas within 0–2.72 m at the point 4#-2 and within 0–2.60 m at the point 5#-1. The roof rock in both these areas is seriously deformed and express rock fractures. The phenomenon of separation appears rarely. When peeping the drilling (depth) in the range of 2.72 m~3.29 m at the point 4#-2 and of 2.60 m~3.33 m at the point 5#-1, the roof rock is slightly deformed and holds overall integrity. Furthermore, when peeping the drilling (depth) over 4.7 m, the surrounding rock roof is basically intact and there is no small separation layer. It should be noted that it fails to observe the failure of the surrounding rock roof caused by
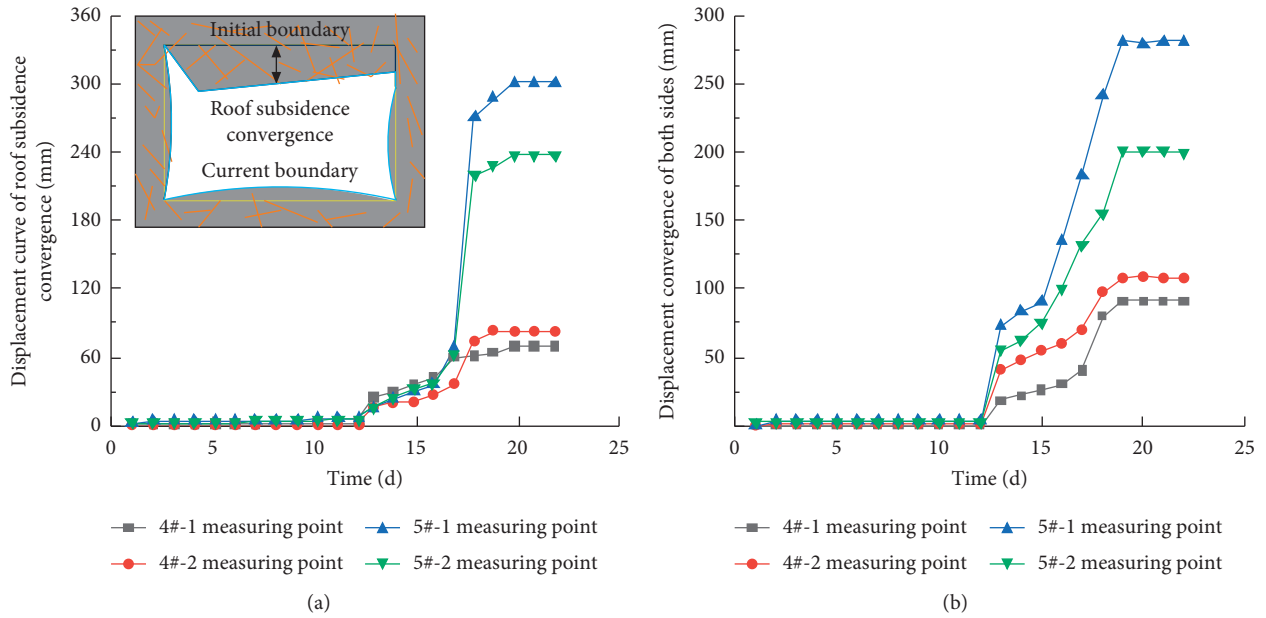
Figure 7: Displacement curve of the roadway surface: (a) displacement curve of roof subsidence convergence; (b) displacement convergence of both sides.
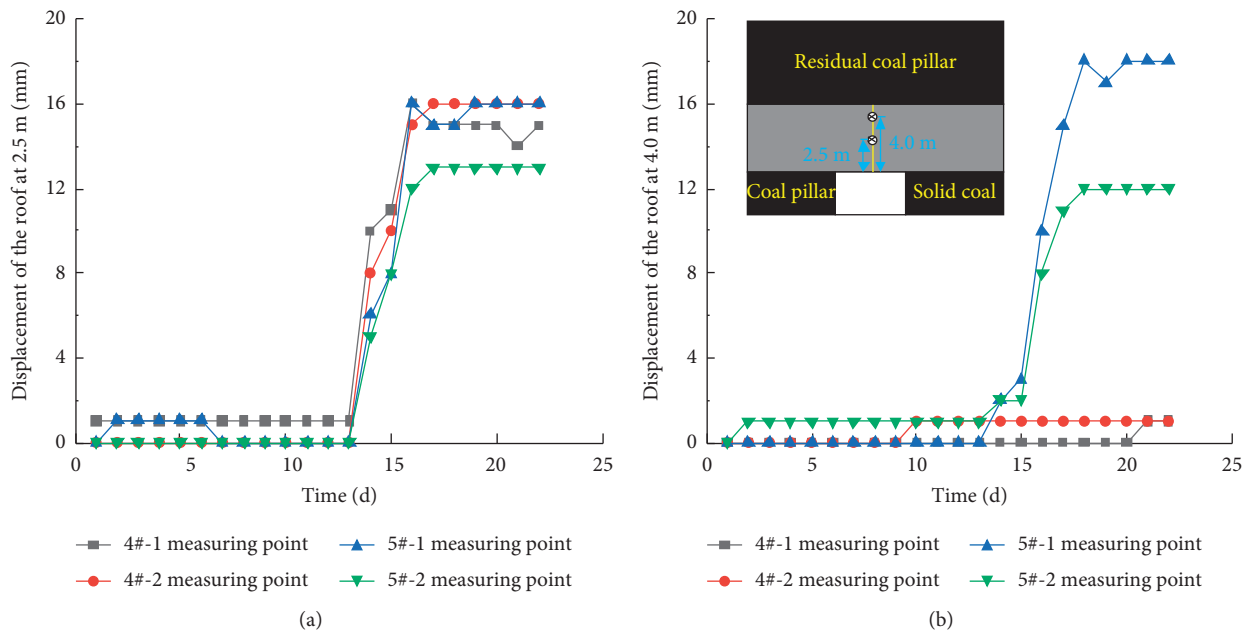
Figure 8: Displacement curve of the deep roof: (a) displacement of the roof at 2.5 m; (b) displacement of the roof at 4.0 m.

step-type subsidence at one side of the roadway because the TV drilling is arranged in the middle of the roadway in the earlier stage.

4. Numerical Simulation of Rheological Damage in Close-Distance Coal Seam Roadway

4.1. Numerical Model. In order to further study the deformation and failure law of the 2-2 middle coal seam roadway

with the stopping of working face, the numerical calculation model is established by using the ANSYS software. The model size is 400 m × 300 m × 119 m, as shown in Figure 11. Grid elements of the 20314 auxiliary haulage roadway (the main area which is observed for deformation and failure study of the surrounding rock of the roadway) are densified, and the minimum length is 0.5 m. In addition, the horizontal and vertical directions of the model are limited. A vertical load of 5.0 MPa is applied over the model to replace the unmodeled rock formation above.

(a)

(b)

(c)
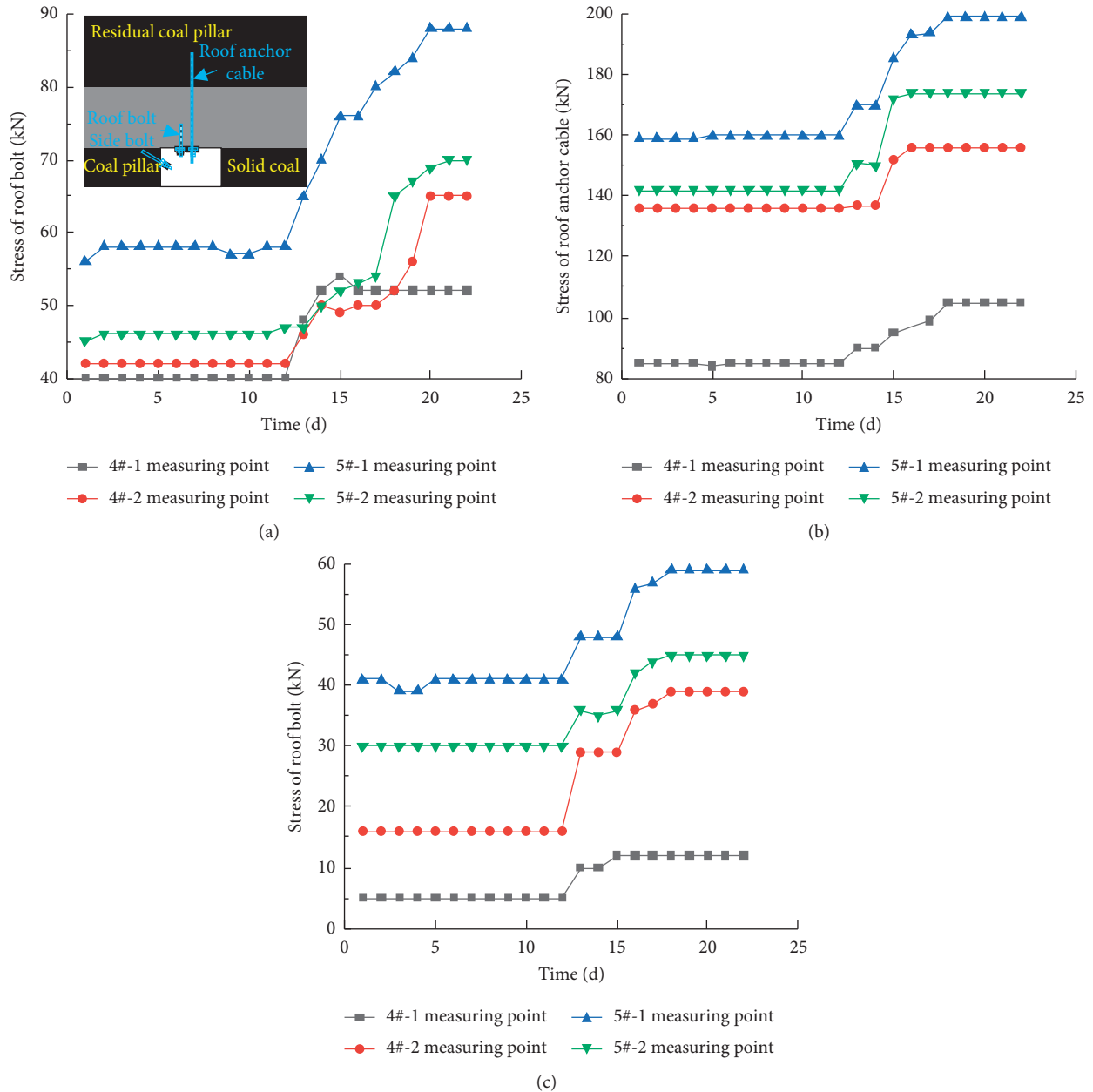
FIGURE 9: Stress curve of the anchorage body: (a) stress of the roof bolt; (b) stress of the roof anchor cable; (c) stress of the side bolt.

FLAC3D software is used in the numerical simulation, and the Mohr–Coulomb constitutive model is overall used in the calculation model. For studying the deformation and failure characteristics of the surrounding rock of the roadway in the lower coal seam under a concentrated load, the CVISC rheological constitutive model is adopted in the surrounding rock of the roadway in the active area of residual coal pillar [40]. Table 2 depicts the parameters of numerical calculation. During the numerical simulation, the roadway and the working face of the 2-2 upper coal seam are first excavated to form a goaf and a section coal pillar, and these 2-2 middle coal seams are excavated in sequence.

4.2. Numerical Simulation Results. During the mining of the 2-2 upper coal seam, a residual coal pillar with a width of 23 is formed between the 20120 goaf and the 20113 main haulage roadway. The vertical stress of the roof of the auxiliary haulage roadway under the residual coal pillar is greater than 12 MPa (Figure 12(a)). Since the 2-2 middle coal seam has not been excavated at this time, the displacement of the rock under the residual coal pillar changes slightly, ranging from 0.05 m to 0.15 m (Figure 13(a)).

As shown in Figure 12(b), during the mining of the 2-2 middle coal seam, the stresses of the residual coal pillar and the lower rock are released due to the excavation of the 20314
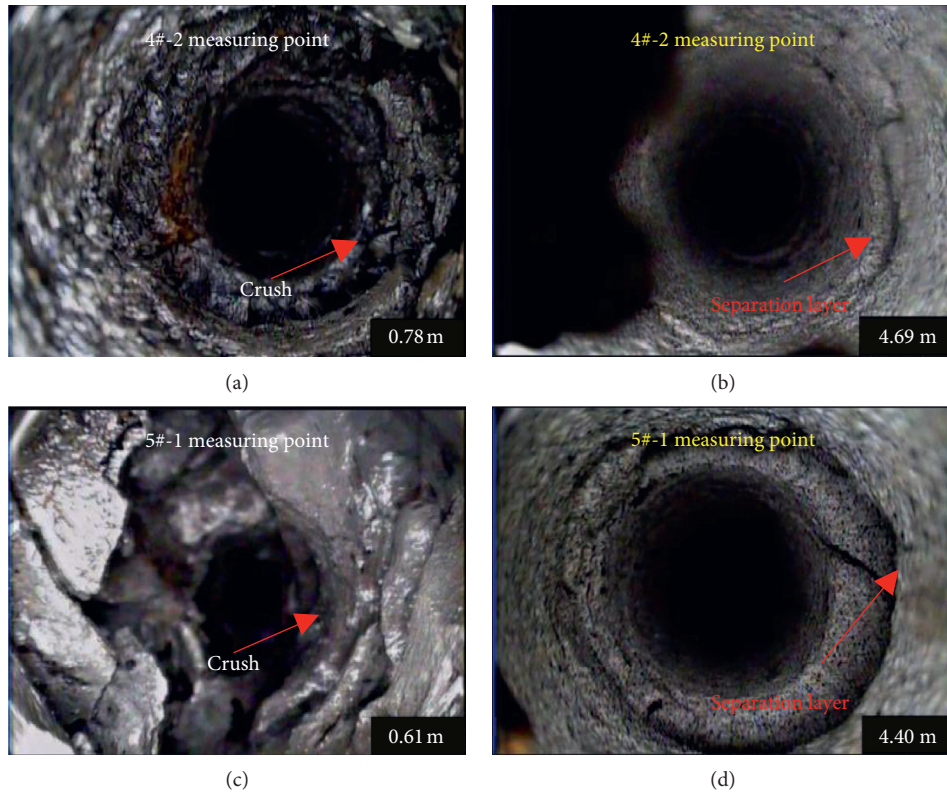
FIGURE 10: Images of different depths of borehole TV at two measuring points.
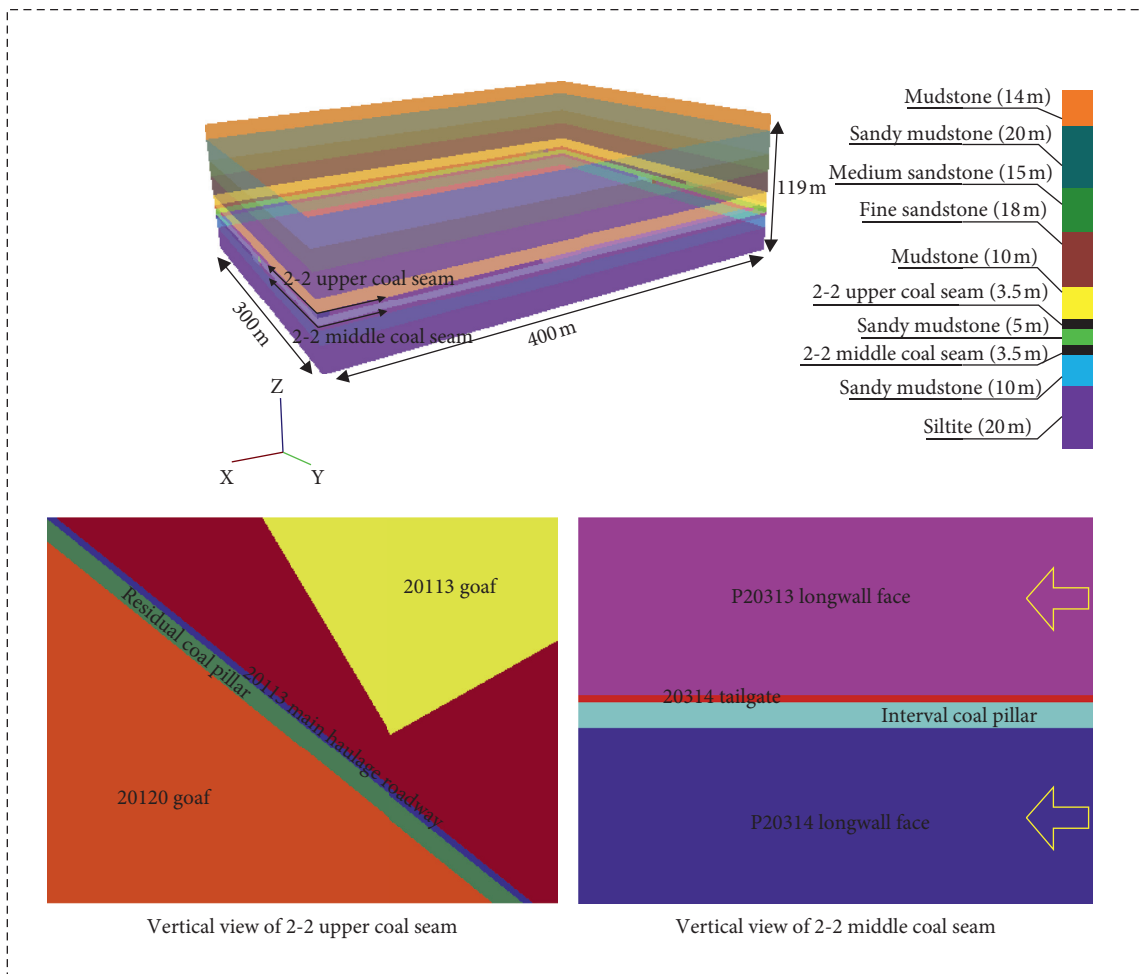
FIGURE 11: Numerical model.

TABLE 2: Mechanical properties of the coal measures that are used in the model.

Coal measures	Thickness (m)	Density (g.cm^{-3})	Young's modulus (GPa)	Shear modulus (GPa)	Tensile strength (MPa)	Cohesion (MPa)	Friction angle (°)
Mudstone	14	2.30	6.2	3.5	1.1	2.3	27
Sandy mudstone	20.8	2.52	15.4	7.3	1.2	2.2	30
Medium sandstone	15.1	2.59	16.8	8.6	1.7	5.5	29
Fine sandstone	18.2	2.49	26.8	12.1	1.2	4.5	32
Mudstone	9.8	2.3	6.2	3.5	1.1	2.3	27
2-2 上 coal	3.5	1.42	1.7	1.1	1.0	2.3 (0.8)	35 (25)
Sandy mudstone	5	2.52	15.4	7.3	1.2	2.2 (0.62)	30 (22)
2-2 中 coal	3.5	1.42	1.7	1.1	1.0	2.3 (0.8)	35 (25)
Sandy mudstone	9.5	2.52	15.4	7.3	1.2	2.2 (0.62)	30 (22)
Siltstone	17.8	2.54	17.6	8.0	1.7	5.5	32

*Numbers in parentheses are residual values.

(a)

(b)

(c)
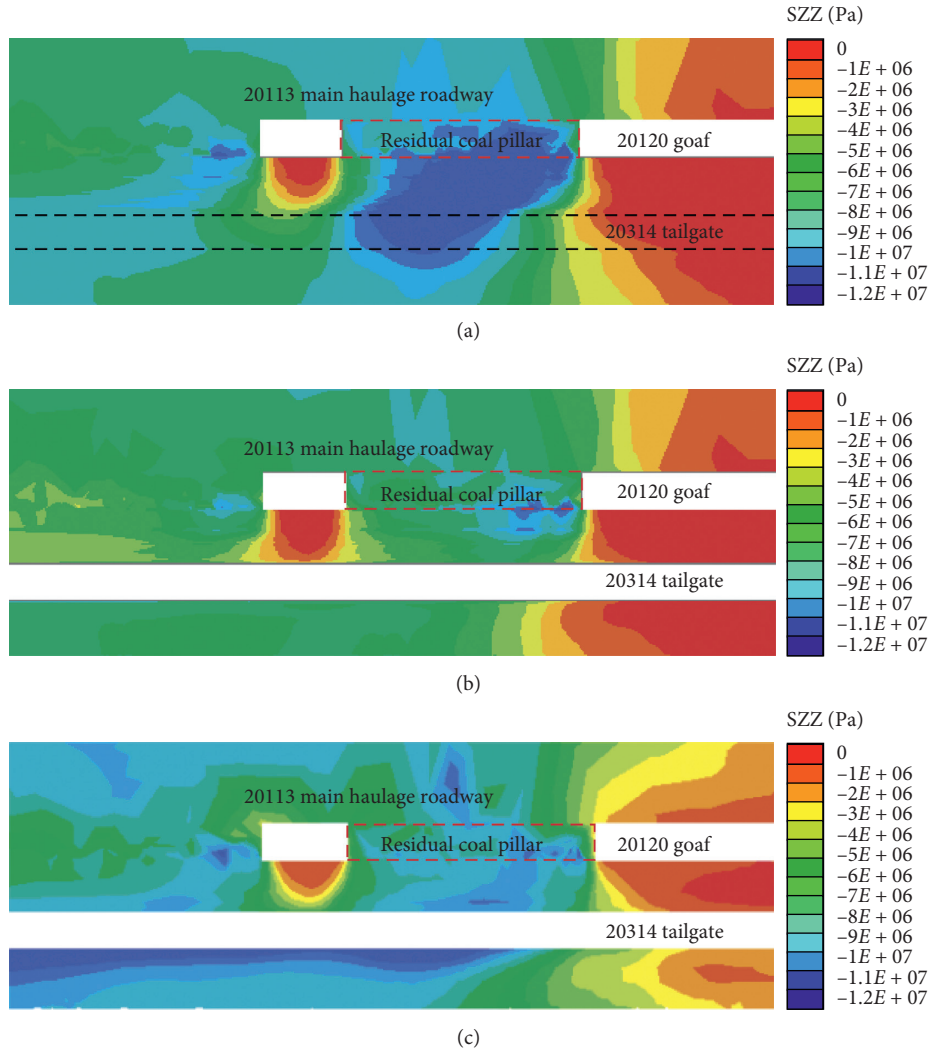
FIGURE 12: Stress variation of the 20314 auxiliary haulage roadway (parallel to the axis section of the roadway): (a) 2-2 upper coal seam excavation; (b) 20314 tailgate excavation; (c) 20314 panel excavation.
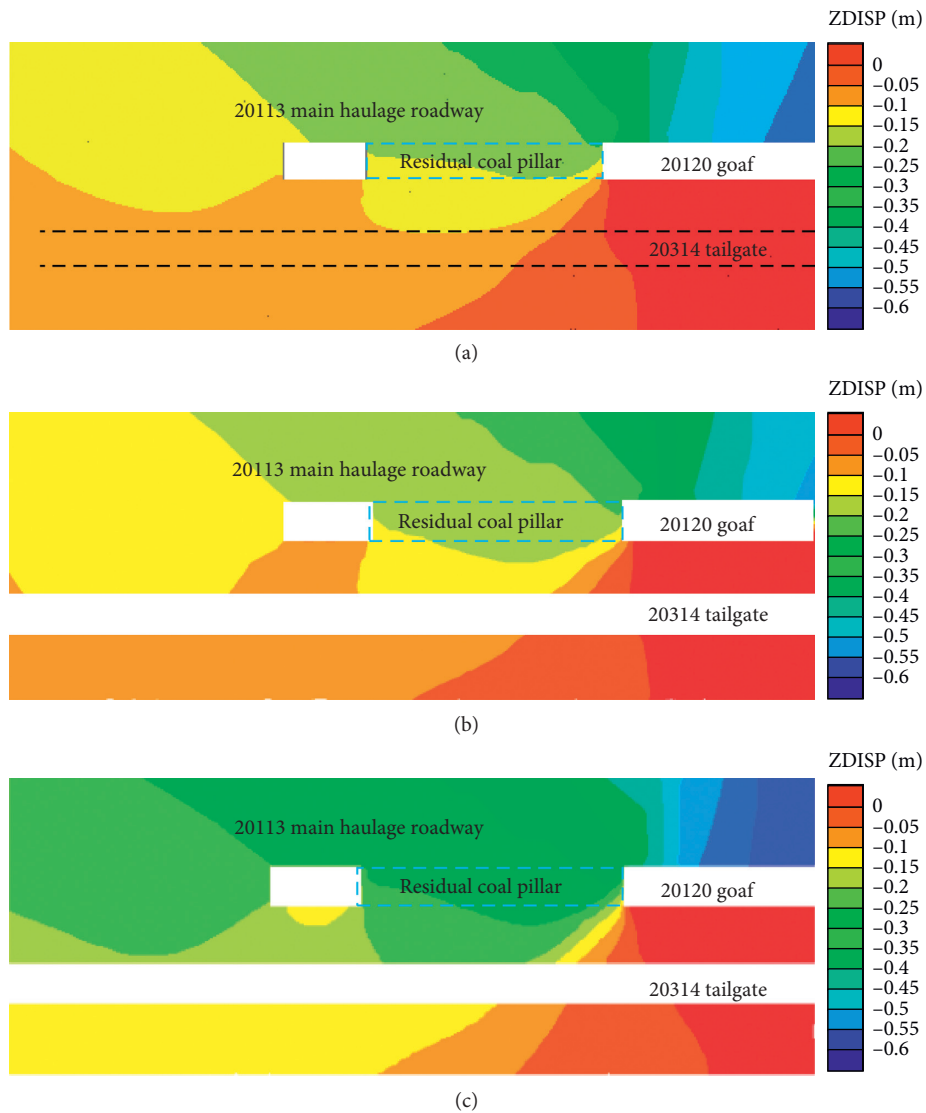
Figure 13: Displacement variation of the roof of the 20314 auxiliary haulage roadway (parallel to the axis section of the roadway): (a) 2-2 upper coal seam excavation; (b) 20314 tailgate excavation; (c) 20314 panel excavation.

auxiliary haulage roadway. Meanwhile, the vertical stress in the rock reduces significantly and is 5~9 MPa. There is no obvious displacement change of the surrounding rock of the roadway. And, the P20314 working face is further excavated. At this time, the stress concentration of the roof of the auxiliary haulage roadway appears again, and the vertical stress reaches 9~11 MPa (Figure 12(c)). Furthermore, the displacement of the roof of the 20314 auxiliary haulage roadway increases significantly (Figure 13(c)), which reaches 0.15~0.3 m.

In addition, the evolution law of the plastic area of the interval rock under the residual coal pillar during the mining of two coal seams is analyzed. It can be seen that after the excavation of the 2-2 upper coal seam, the plastic area appears in the floor (roof of the 20314 auxiliary haulage roadway) of the residual coal pillar (Figure 14(a)), but the deformation range is small. After the excavation of the 20314 auxiliary haulage roadway, the plastic area of the rock under

the residual coal pillar slightly expands (Figure 14(b)). When the P20314 working face moves to the active area of the residual coal pillar, the goafs in the 2-2 upper coal seam and the middle coal seams connect together. The broken roof develops upwards, and the increasing roof load is further transferred downward through the residual coal pillar. As a result, the plastic area of the surrounding rock of the roadway in the 2-2 middle coal seam increases sharply, and the entire thickness of the interval rock in some areas is deformed (Figure 14(c)).

Based on the above analysis, the vertical stress variation of the roof of the 20314 auxiliary haulage roadway goes through three stages. In the first stage, the remaining coal pillars are formed owing to the excavation of each roadway and working face in the 2-2 upper coal seam, which causes the vertical stress of the roadway roof to increase sharply, and the roof stress is concentrated. In the second stage, the vertical stress of the roof is partly released due to the

(a)

(b)

(c)
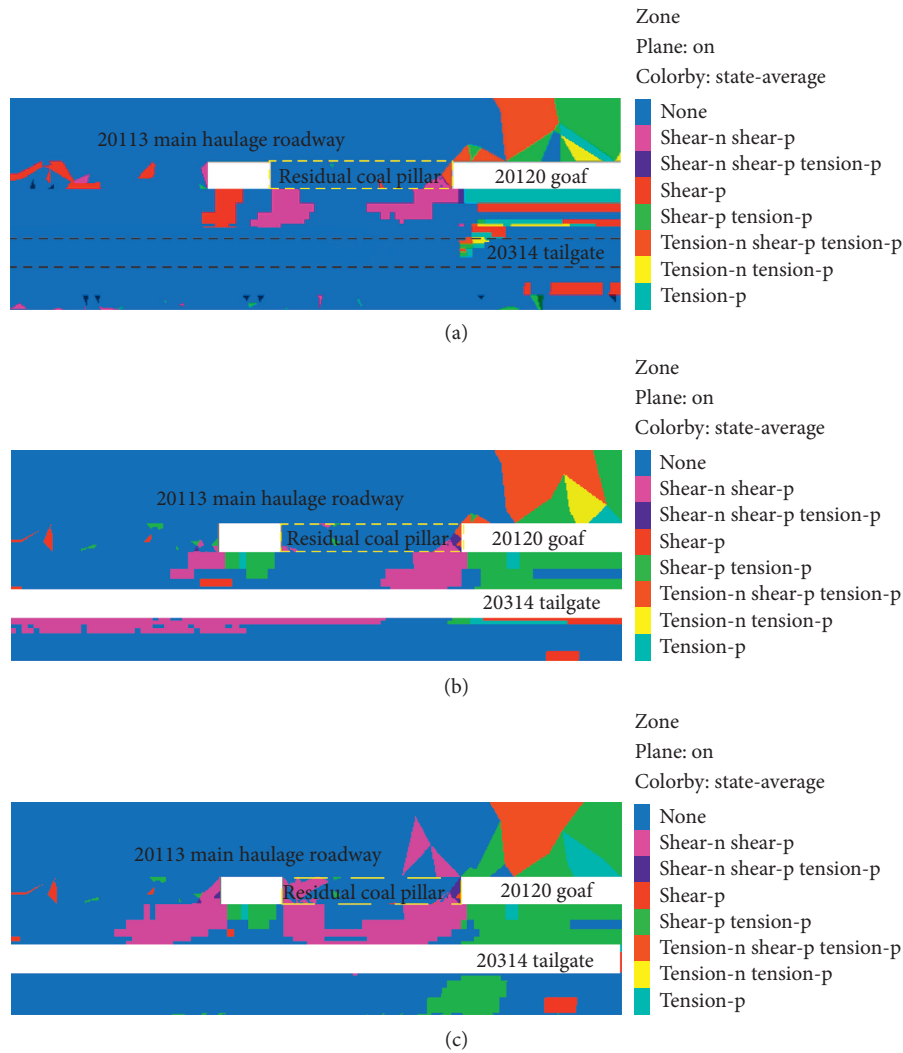
FIGURE 14: Section variation of the plastic area that is parallel to the 20314 auxiliary haulage roadway (parallel to the axis section of the roadway): (a) 2-2 upper coal seam excavation; (b) 20314 tailgate excavation; (c) 20314 panel excavation.

excavation of the 20314 auxiliary haulage roadway, and the vertical stress reduces and the roadway roof is not deformed. In the third stage, the stress concentration point of the coal pillar towards the 20113 centralized main haulage roadway is due to the stopping of the P20314 working face. At this time, the vertical stress of the roadway roof increases again, causing the deformation and failure of the roof and the surrounding rock of the roadway.

5. Analysis on Deformation and Failure Mechanism

Through the numerical simulation in Section 4, the stress on the roof of the 20314 tailgate after the excavation of the different coal face is repeated, and the evolution process of stress, displacement, and plastic zone in the process is obtained. In Section 5, the failure mechanism is analyzed based on the above evolution process. The strata above the coal seam resist caving and easily overhang for a considerable

length, and thus a roof cantilever beam can form above the goaf edge after the working face has retreated. According to the field data and theoretical analysis, it can be seen that the stress variation of the roof of the 20314 auxiliary haulage roadway undergoes the following three stages.

5.1. Stage I. As shown in Figure 15(a), due to the cantilever beam formed by the stopping of the 2012 working face in the upper coal seam, the stress of the strata under the residual coal pillar increases rapidly and the edge of the coal pillar is obviously broken. Meanwhile, area "a" is at the junction of the elastic and plastic zone, and the stress concentration is obvious. Combined with the numerical simulation results, it can be concluded that the plastic zone of the roof of the auxiliary haulage roadway is small after the completion of the 2-2 upper coal seam (Figure 16(a)), and area "a" is the stress peak area. At this time, the stress and displacement variations of the roof strata are shown in Figures 17(a) and 18(a), respectively.

(a)

(b)
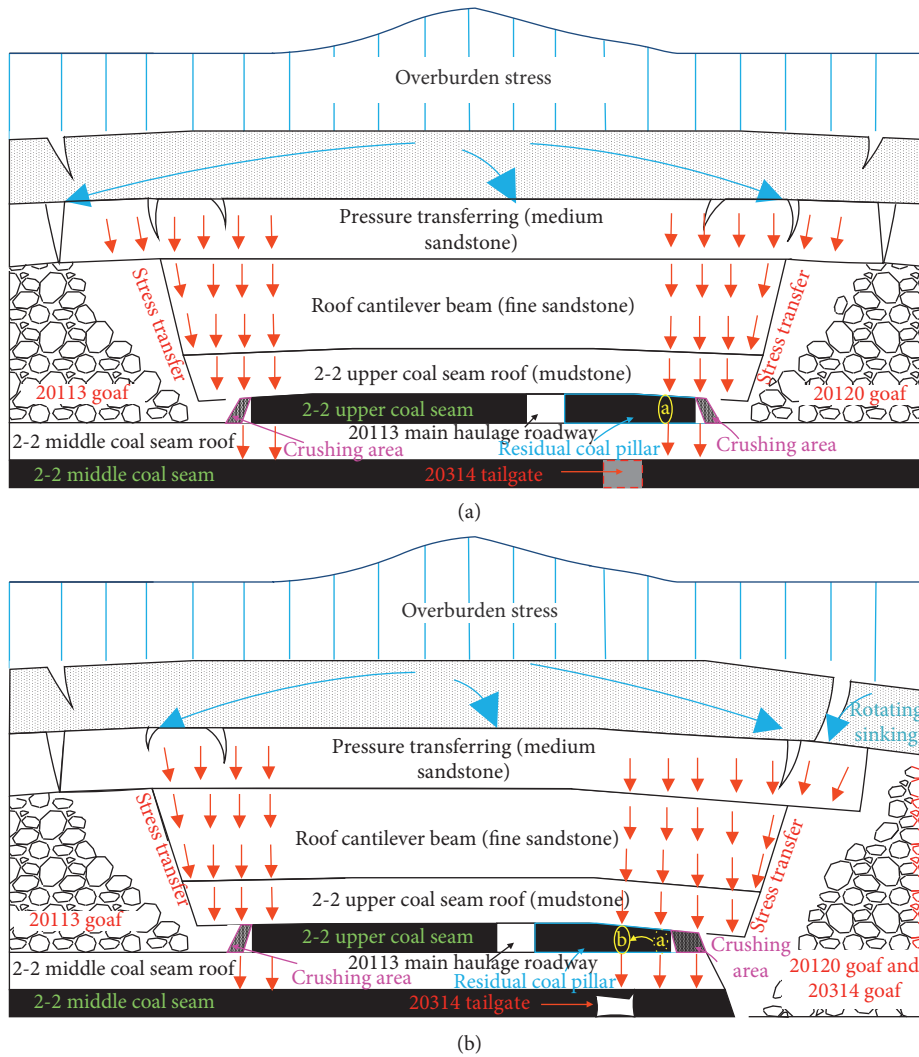
FIGURE 15: Stress changes under the coal pillar: (a) excavation of the 2-2 upper coal seam; (b) excavation of the P20314 working face.

5.2. Stage II. When mining the 2-2 middle coal seam, the roof movement of the 2-2 upper coal seam has stabilized. Since the size of the 20314 auxiliary haulage roadway is relatively small, the expansion range and displacement convergence of the plastic zone of the roadway roof are also small when excavating (Figures 16(b) and 18(b)) the auxiliary haulage roadway. The peak position of the stress is unchanged basically.

5.3. Stage III. As shown in Figure 15(b), a part of the P20314 working face is located under the 20120 goaf. With the stopping of the P20314 working face, the 20120 goaf continues to fall downward to connect with the goaf of the P20314 working face. Before the stopping of the 20120 working face, a part of the overlying strata of the roof has been broken. However, the strata of the roof is complete at this time, and the bearing capacity is large enough to carry the high stress under the residual coal pillar. With the stopping of the working face, the overlying fractured strata in the goaf develop further. The cantilever, due to the

bending and subsidence of the fractured strata, increases the pressure on the residual coal pillar. The broken and plastic areas of the goaf increase, and the stress point of the peak moves to the center of the coal pillar. Furthermore, position "b" is just above the roof of the 20314 auxiliary haulage roadway, which is consistent with the numerical simulation results of stress concentration of the roadway roof under the residual coal pillar after the stopping of the P20314 working face (Figures 16(c) and 17(c)).

Under this structure, the movement of the basic roof fault block determines the stability of the working face roadway. The fracture span a of the fracture block is related to the length b of the working face and the periodic fracture span L:

$$a = \frac{2L}{17}\left[\sqrt{\left(10\frac{L}{b}\right) + 102} - 10\frac{L}{b}\right]. \tag{1}$$

The length of the working face b is 1611.1 m, the periodic fracture span L is 12M, and a is 14.1 m. The weight directly transferred to the coal seam is [41, 42]

(a)

(b)

(c)
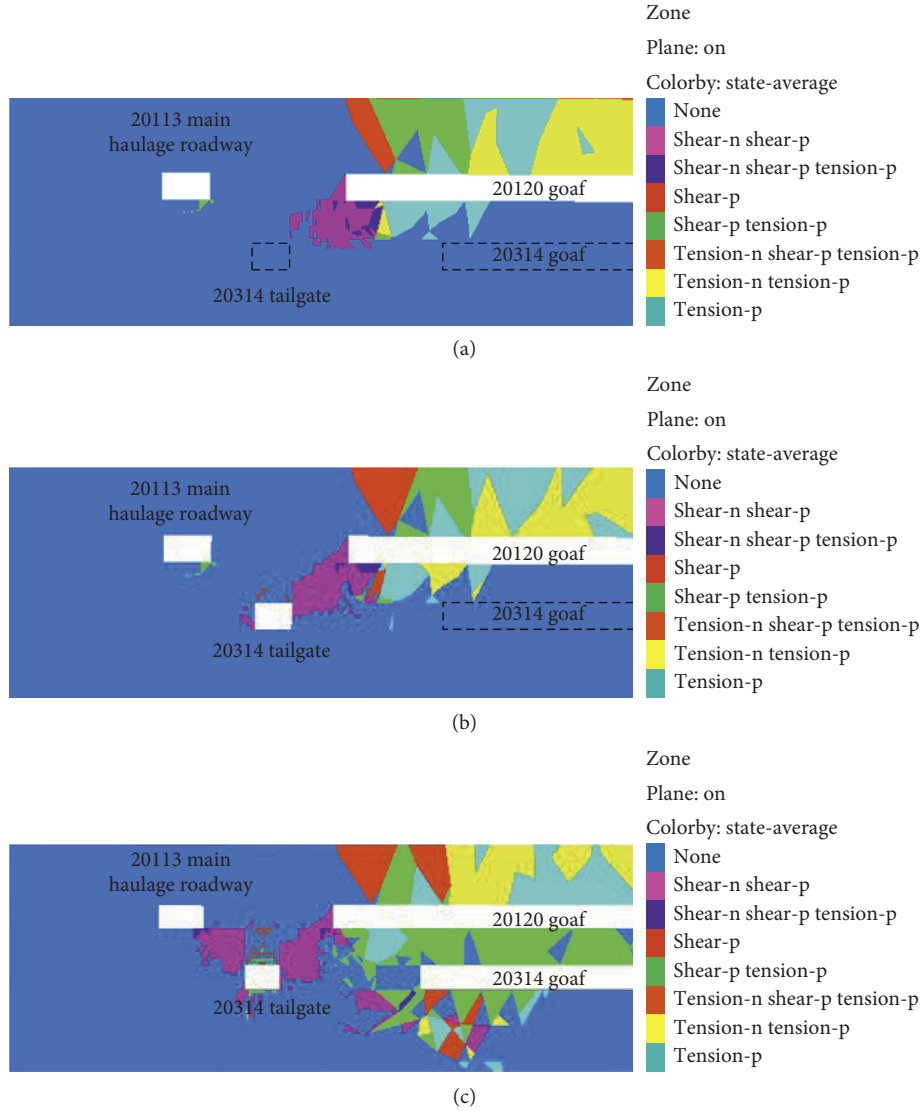
FIGURE 16: Nephogram of the plastic zone perpendicular to the section of the auxiliary haulage roadway (perpendicular to the axis section of the roadway): (a) 2-2 upper coal seam excavation; (b) 20314 tailgate excavation; (c) 20314 panel excavation.

$$Q = \frac{q}{2} = \frac{\gamma h a}{2}, \tag{2}$$

where γ is the average bulk density of the overlying strata, $25 \, kN/m^3$, h is the thickness of the rock stratum, 3 m, and Q is 528.8 kN/m. The forces transmitted to the coal seam are

$$\sigma = \begin{cases} \sigma_{max} \sin \alpha, & (0 \le x \le H), \\ 2\sigma_{max}\left(1 - \frac{x \sin \alpha}{2}\right), & (H \le x \le 2H), \\ 0, & (x \ge 2H), \end{cases} \tag{3}$$

where σ_{max} is the maximum stress $\sigma = 15.9 \, MPa$ of the fault block on the coal seam, $\sigma_{max} = Q \sin \alpha \tan \alpha / H$; H is the vertical distance from the fault block to the coal seam, 43 m; α is the stress influence angle of the block, 60°. By substituting the data, we can find that $\sigma_{max} = 18.4 \, MPa$.

When the influence angle is 60°, x is less than H, so it can be seen that $\sigma = 15.9 \, MPa$, which is larger than the long-term strength of the rock layer of 11.7 MPa, so rheological failure will occur under this condition.

Base on the field monitoring, it can be known that the deformation and failure of the surrounding rock of the roadway in the 20314 auxiliary haulage roadway occurs after a long period of time. Therefore, combined with theoretical analysis and numerical simulation results, it is obtained that the stress of the roof rock strata exceeds its bearing capacity and then causes the creep, and thus brings in the deformation and failure of the surrounding rock of the roadway. Furthermore, from the numerical simulation results of Figure 19, it can be seen that the forces on the top corners of the 20314 auxiliary haulage roadway and its goaf roof are significantly greater than that on the side of the P20313 working face. And, this complies with the step-type subsidence in the side roof of the P20314 working face goaf.
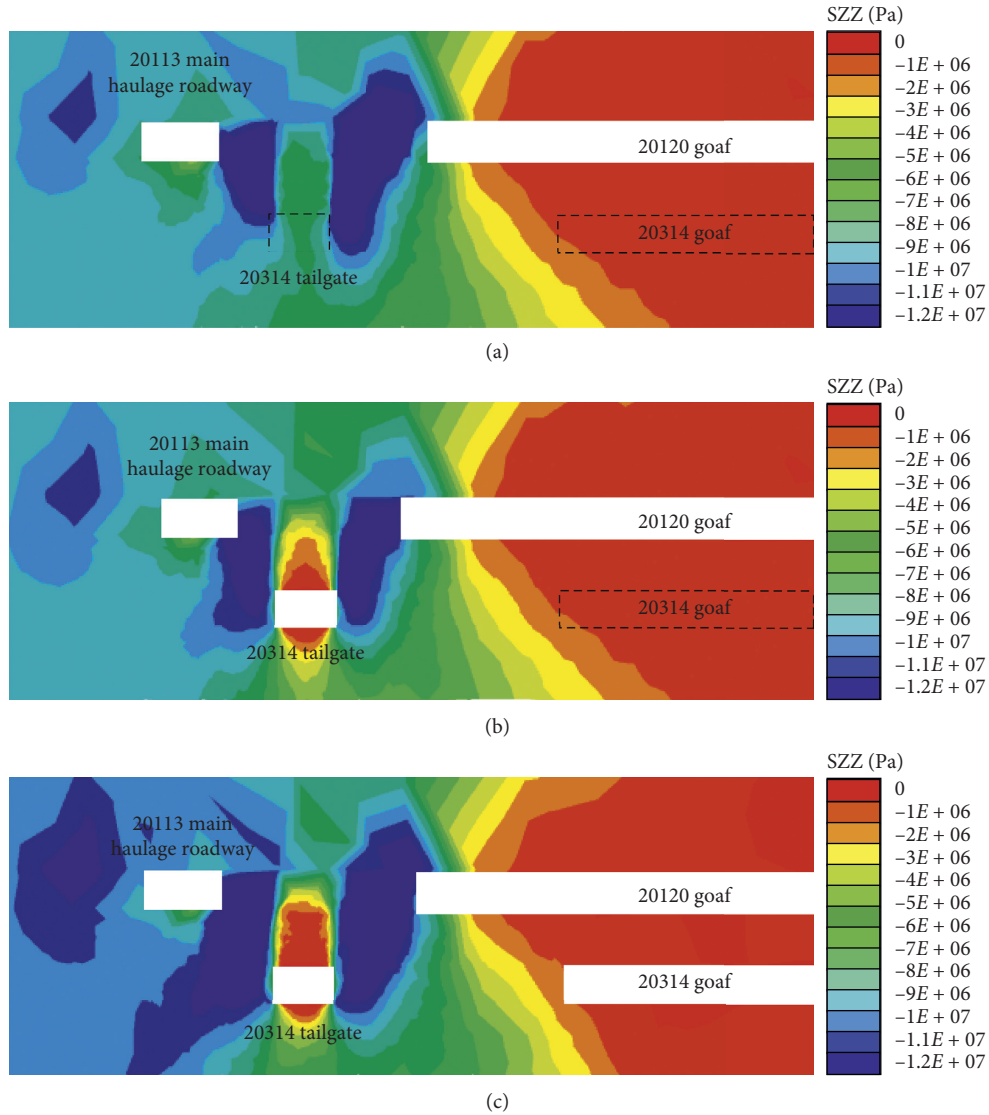
FIGURE 17: Nephogram of stress perpendicular to the section auxiliary haulage roadway (perpendicular to the axis section of the roadway): (a) 2-2 upper coal seam excavation; (b) 20314 tailgate excavation; (c) 20314 panel excavation.

Combined with the laboratory experiment results, the concentrated stress on the upper corner of the 20314 goaf of the roadway roof after the excavation of the P20314 working face is 11~12 MPa. The data are similar to the long-term strength of the roof strata, resulting in the creeping failure of the 20314 auxiliary transport roadway roof under the residual coal pillar, which caused the deformation and instability of the surrounding rock of the roadway.

6. Discussion

The roof bolt of the 20314 auxiliary haulage roadway eliminates the mutual dislocation between the rock strata of the roadway roof and makes the roof combine into a thicker roof structure of the composite rock beam. Meanwhile, due to the increase in thickness of the roof rock beam, the overall stability of the roof is improved and pressure on the roadway weakens. Besides, the span of the caving arch correspondingly reduces. Combined with relevant research studies, the mechanical model of the composite suspended rock beam is established, as shown in Figure 20. In the model, the stress acting on the structure of the roof rock beam is defined as q, the supporting stress of the roof anchor cable, the bolt, and the hydraulic prop is defined as q_1, and the constraining force at both ends are defined as R_O and R_B.

According to the mechanical equilibrium, the following conditions can be obtained:

$$\sum F_y = 0,$$
$$\sum M_o = 0. \tag{4}$$

An equation according to the force balance and moment balance can be obtained as follows:

$$R_{oy} = R_{by} = \frac{l(q - q_1)}{2}. \tag{5}$$

(a)

(b)

(c)
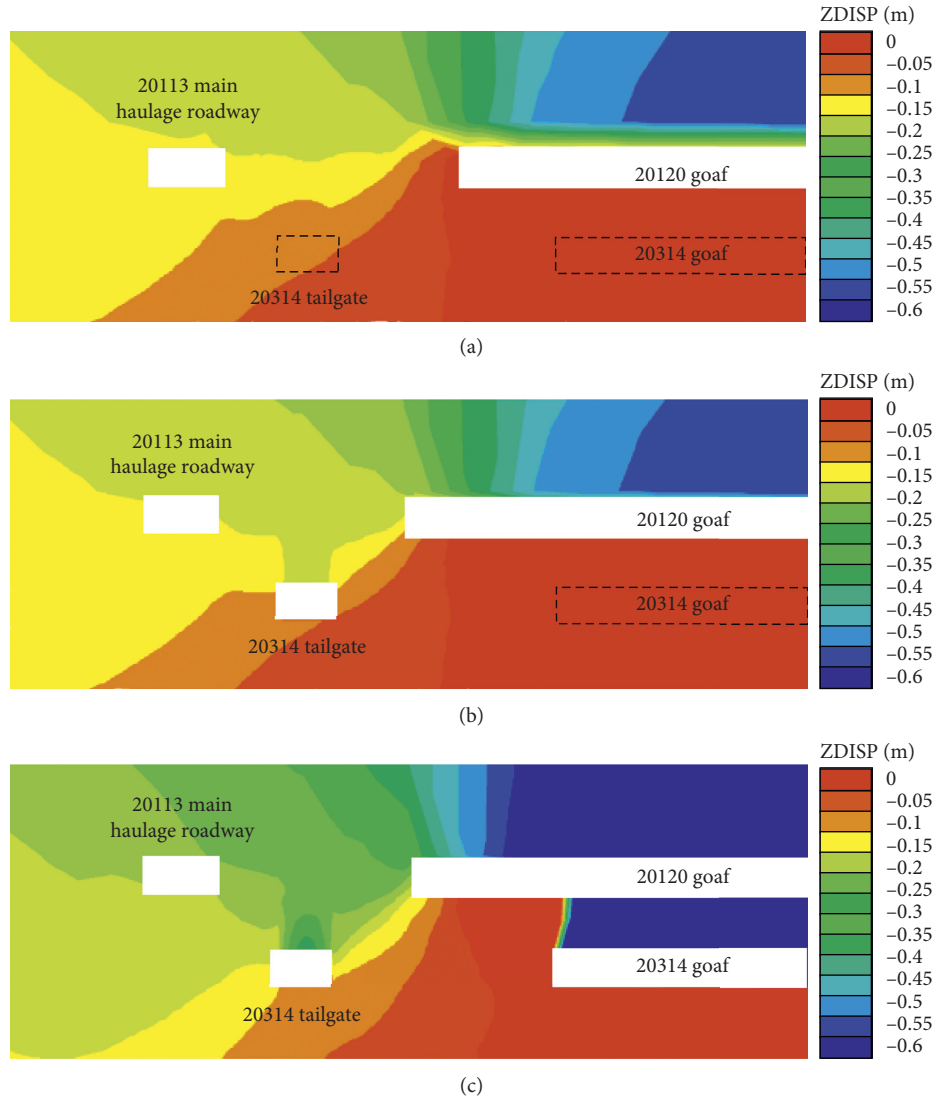
FIGURE 18: Displacement nephogram perpendicular to the auxiliary haulage roadway (perpendicular to the axis section of the roadway): (a) 2-2 upper coal seam excavation; (b) 20314 tailgate excavation; (c) 20314 panel excavation.

The bending moment on any section of the roof rock beam is

$$M(x) = \frac{1}{2}(q - q_1)x^2 - \frac{1}{2}(q - q_1)lx. \quad (6)$$

The maximum tensile stress of the roof rock beam is

$$\sigma_{\max} = \frac{M_{\max}}{W} = \frac{l^2(q - q_1)/8}{h_1^2/6} = \frac{3l^2(q - q_1)}{4h_1^2}. \quad (7)$$

The condition of no failure of the roof rock beam is

$$\sigma_{\max} \leq [\sigma], \quad (8)$$

where l (m) represents the net width of the roadway, h_1 (m) represents the thickness of the composite suspended rock beam, and the effective length of the top bolt is taken, and q (Pa) represents the force of the overburden on the rock beam structure when the pressure is applied. According to the load estimation method, it can obtained that $q = Km\gamma$ where m

(m) refers to the thicknesses sum of the interval rock (including the thickness of the upper coal seam), the immediate roof, and the main roof of the upper coal seam working face, while γ (N/m^3) represents the bulk density of overburden; K represents the dynamic load coefficient, and q_1 is the force exerted by the single hydraulic prop, bolt, and anchor cable on the roof rock beam. Furthermore, q_1 is simplified as a vertical-upward uniform load (Pa), which can be calculated as

$$q_1 = \frac{P_g}{S_b^2} + \frac{mP_s}{nlS_b} + \frac{4P_z}{(l \times 1)}, \quad (9)$$

in which P_g symbolizes the anchoring force of the bolt, P_s is the anchoring force of the cable, P_z refers to the rated working resistance of the single hydraulic props, S_b represents the spacing between the anchors, and m is the number of anchors per row. The spacing of the anchor row nS_b is an integral multiple of the row distance of the bolt in which n

(a)

(b)
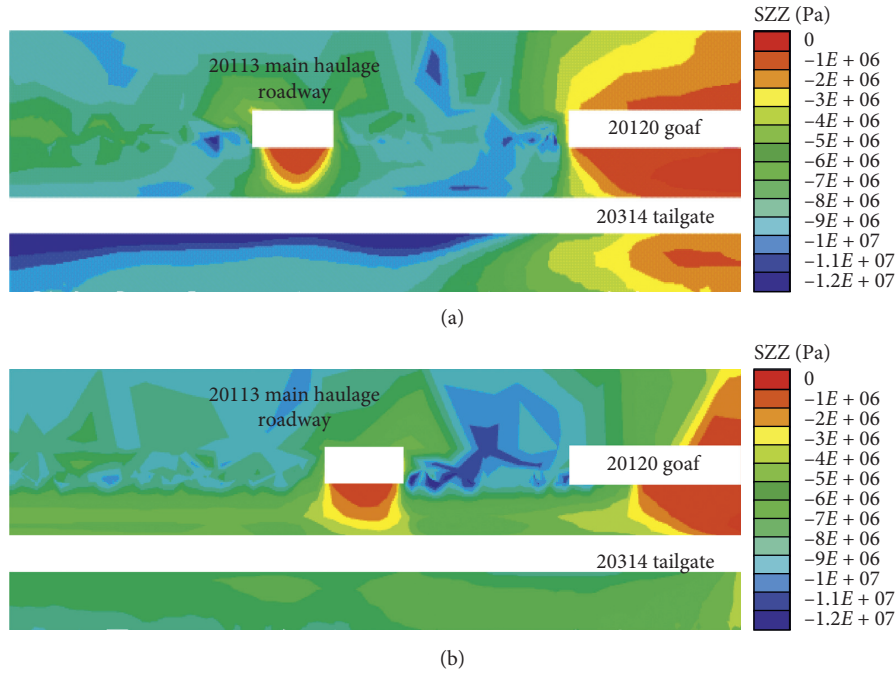
FIGURE 19: Stress on both sides of the roof of the 2031 auxiliary haulage roadway: (a) coal pillar side; (b) entity coal side.
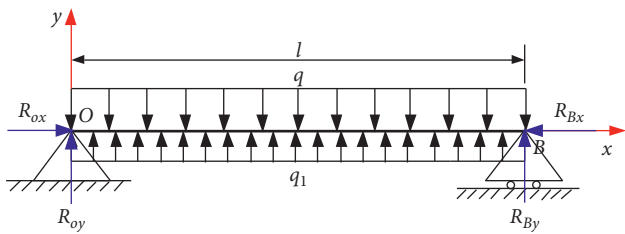
FIGURE 20: Mechanical model of the composite suspended rock beam structure.

takes a positive integer 1, 2, 3, . . ., $\sigma_{\max}$ (Pa) symbolizes the maximum tensile stress of the roof rock beam, and σ (Pa) is the tensile strength of the roof strata after anchoring.

For the auxiliary haulage roadway of the P20314 working face, the net width l is 5.2 m, the effective length h_1 of the top bolt is 2.05 m, and the spacing S_b between the anchors is 0.8 m. Figure 3 is selected for m and n. And, the maximum thickness sum (m) of the interval rock (including the upper coal seam), the immediate roof, and the main roof of the working face in the upper coal seam is 30 m. The uniform load q_1 of the anchor cable, bolt, and single hydraulic strut on the roof rock beam is 356.73 kN/m^2 (where P_g and P_s of the anchor anchoring force are 80 kN and 164 kN, respectively, and the rated working resistance of the single hydraulic prop is 250 kN).

6.1. Under Pressure of Overlying Strata Weight.
Substituting the above parameters into equation (9), it can be obtained that the maximum tensile stress on the roof rock beam is 1.9 MPa. According to relevant research studies, the tensile strength of the rock after anchoring can generally

reach from 5 MPa to 8 MPa around. It can be known that the maximum tensile stress on the roof rock beam is less than the tensile strength of the roof after anchoring. Consequently, the support system can play the role of controlling the surrounding rock when considering the overburden weight only.

6.2. Under Pressure of Stress Concentration.
With the stopping of the P20314 working face, the 20314 auxiliary haulage roadway is located under the edge of the residual coal pillar, resulting in the superimposed bearing pressure of the two working faces (working faces of 20113 and 20120 in the 2-2 upper coal seam). Therefore, coefficient 3 is taken as the stress concentration. Substituting the relevant parameters into equation (9), it can be known that the maximum tensile stress on the roof rock beam is 9.14 MPa. Based on relevant research studies, the tensile strength of the rock after anchoring can generally reach from 5 MPa to 8 MPa around. It can be seen that the maximum tensile stress on the roof rock beam is greater than the tensile strength of the roof rock after anchoring. As a result, when considering stress concentration, the supporting system cannot effectively control the surrounding rock, and auxiliary support measures such as shed supporting must be adopted.

Therefore, the roadway of the lower coal seam should be reasonably arranged to avoid the deformation and failure of its surrounding rock during the mining of multiple and close-distance coal seams [43, 44]. The reason lies in that the roadway of the lower coal seam is different in the solid coal of the upper coal seam, the residual coal pillar, and the goaf. By a perfect arrangement, it can avoid the problem that the roadway penetrates the residual coal pillar in the upper coal seam and the phenomenon of deformation and failure

caused by the excessive stress of the surrounding rock of the roadway. If the roadway arranged must penetrate the residual coal pillar in the upper coal seam due to some reasons such as coal seam occurrence and fault, some measures can be adopted according to the specific production geological conditions of the site. Under this condition, support of the high-strength and high-pretension bolt, active support of anchor cable reinforcement, passive support of the combination of the steel beam and the single hydraulic prop, and surrounding rock grouting reinforcement can be selected [41, 45–47].

7. Conclusion

In this paper, rheological failure mechanism of the weakly cemented soft rock roadway under the residual coal pillar during the mining of shallow-buried close-distance coal seams of the Gaojialiang coal mine is analyzed and studied through field monitoring, numerical simulation, and laboratory experiment. The field monitoring results show that the data of each monitoring device in the auxiliary haulage roadway start to change at the same time, and they are stable again after changing at the same time at a slower speed. Moreover, the monitoring results of the damaged areas observed by the borehole drilling TV are consistent with the displacements of the deep roofs, which prove the reliability of the monitoring data.

The results of numerical simulation suggest that the stress of the roadway roof increases first and then decreases and increases finally. Meanwhile, after the mining of the P20314 working face, the stress and displacement of the roof of the auxiliary haulage roadway under the residual coal pillar are concentrated and increased, respectively. The results comply with the variation data of the stress and displacement of field monitoring at the 5#-1 station. Besides, the side roof stress of the P20314 working face goaf is more concentrated, which is also in line with the step-type subsidence of the side roof.

The laboratory experiment shows that the roof strata belong to the weakly cemented strata, and the specimen can creep under a small pressure. On this basis, the failure mechanism of the 20314 auxiliary haulage roadway is analyzed.

(1) Coal pillar is left because of the mining of the upper coal seam. With the excavation of the upper coal seam, the stress on the roof of the 20314 auxiliary haulage roadway under the coal pillar gradually increases and is concentrated. However, the excavation of 20314 brings in the fact that the stress on the roof is partially released and reduces further. Therefore, the surrounding rock of the roadway holds its integrity.

(2) With the stopping of the P20314 working face in the lower coal seam, the goaf of the overlap part of the upper and lower coal seams is connected, and the rotation of the overlying fractured rock makes the stress of the residual coal pillar to increase. The concentrated stress is transferred to the top of the auxiliary haulage roadway roof through the residual coal pillar, and the stress concentration area is located right above the roof. But, due to the shallow burial of the coal seam, the concentrated stress is not high enough to cause the deformation of the roadway roof directly. Instead, the roof creeps with time under such a condition, and the surrounding rock of the roadway is deformed.

(3) Through analysis, it is suggested that in the design of the working system, a gateroad under an isolated residual coal pillar in the upper coal seam should be avoided when mining in close-distance seams. If it cannot be avoided, combined supports of passive plus active measures should be used to support the roadway to ensure the safety production of coal mines.

Data Availability

The data used to support the findings of this study are included within the article.

Conflicts of Interest

The authors declare that they have no conflicts of interest regarding the publication of this paper.

Acknowledgments

References

[1] Y. L. Tan, T. B. Zhao, and Y. X. Xiao, "In situ investigations of failure zone of floor strata in mining close distance coal seams," *International Journal of Rock Mechanics and Mining Sciences*, vol. 47, no. 5, pp. 865–870, 2010.

[2] J. X. Yang, C. Y. Liu, and B. Yu, "Roof structure of close distance coal strata in multi-gob condition and its effects," *Acta Geodynamica et Geomaterialia*, vol. 11, no. 4, pp. 351–359, 2014.

[3] H. Yan, M.-Y. Weng, R.-M. Feng, and W.-K. Li, "Layout and support design of a coal roadway in ultra-close multiple-seams," *Journal of Central South University*, vol. 22, no. 11, pp. 4385–4395, 2015.

[4] W.-B. Zhu, J.-L. Xu, X. Kong, D.-Y. Xuan, and W. Qin, "Study on pillar stability of wongawilli mining area in shallow close distance coal seams," *Procedia Earth and Planetary Science*, vol. 1, no. 1, pp. 235–242, 2009.

[5] Q. Bai, S. Tu, F. Wang, and C. Zhang, "Field and numerical investigations of gateroad system failure induced by hard roofs in a longwall top coal caving face," *International Journal of Coal Geology*, vol. 173, pp. 176–199, 2017.

[6] Q. Liu, W. Nie, Y. Hua, H. Peng, C. Liu, and C. Wei, "Research on tunnel ventilation systems: dust diffusion and pollution behaviour by air curtains based on CFD technology and field measurement," *Building and Environment*, vol. 147, pp. 444–460, 2019.

[7] J. Wang, J. G. Ning, L. S. Jiang, J.-Q. Jiang, and T. Bu, "Structural characteristics of strata overlying of a fully mechanized longwall face: a case study," *Journal of the Southern African Institute of Mining and Metallurgy*, vol. 118, no. 11, pp. 1195–1204, 2018.

[8] J. Wang, J. Ning, P. Qiu, S. Yang, and H. Shang, "Microseismic monitoring and its precursory parameter of hard roof collapse in longwall faces: a case study," *Geomechanics and Engineering*, vol. 17, no. 4, pp. 375–383, 2019.

[9] M. Hu, W. Zhao, Z. Lu, J. Ren, and Y. Miao, "Research on the reasonable width of the waterproof coal pillar during the mining of a shallow coal seam located close to a reservoir," *Advances in Civil Engineering*, vol. 2019, Article ID 3532784, 14 pages, 2019.

[10] H. Shang, J. Ning, S. Hu, S. Yang, and P. Qiu, "Field and numerical investigations of gateroad system failure under an irregular residual coal pillar in close-istance coal seams," *Energy Science & Engineering*, vol. 7, no. 6, pp. 2720–2740, 2019.

[11] L. Xinjie, L. Xiaomeng, and P. Weidong, "Analysis on the floor stress distribution and roadway position in the close distance coal seams," *Arabian Journal of Geosciences*, vol. 9, no. 2, p. 83, 2016.

[12] J. X. Yang, C. Y. Liu, and Y. Yang, "Study of the bearing mechanism of the coal roof and the dimension selection of the room and pillar in the shallow and close distance coal seam," *Journal of China University of Mining & Technology*, vol. 42, no. 2, pp. 161–168, 2013.

[13] Q. Gu, W. Ru, Y. Tan, J. Ning, and Q. Xu, "Mechanical analysis of weakly cemented roof of gob-side entry retaining in fully-mechanized top coal caving mining," *Geotechnical and Geological Engineering*, vol. 37, no. 4, pp. 2977–2984, 2019.

[14] X. Z. Lyu, Z. Zhao, X. Wang, and W. Wang, "Study on the permeability of weakly cemented sandstones," *Geofluids*, vol. 2019, Article ID 8310128, 14 pages, 2019.

[15] S. Zhang, G. Fan, D. Zhang, M. Chen, and C. Zhang, "Study on material properties and similar material proportion of weakly cemented water-resisting strata," *Arabian Journal of Geosciences*, vol. 12, no. 11, 2019.

[16] Q.-B. Meng, L.-J. Han, W.-G. Qiao, D.-G. Lin, and L. Yang, "Mechanism of rock deformation and failure and monitoring analysis in water-rich soft rock roadway of western China," *Journal of Coal Science and Engineering (China)*, vol. 18, no. 3, pp. 262–270, 2012, in Chinese.

[17] J. Zhu, C. Qiao, and Y. Song, "Effect of particle characteristics on shear strength of weakly cemented conglomerate in tertiary," *Journal of Harbin Institute of Technology*, vol. 5, no. 51, pp. 101–109, 2019, in Chinese.

[18] C. Y. Song, H. G. Ji, and H. Y. Jiang, "Influence of wetting-drying cycles on acoustic emission characteristics and microstruc-ture deterioration of weak cementation stratum," *Journal of China Coal Society*, vol. 43, no. 1, pp. 96–103, 2018, in Chinese.

[19] E. Maranini and M. Brignoli, "Creep behaviour of a weak rock: experimental characterization," *International Journal of Rock Mechanics and Mining Sciences*, vol. 36, no. 1, pp. 127–138, 1999.

[20] S. Liang, X. Li, Y. Mao, and C. Li, "Time-domain characteristics of overlying strata failure under condition of longwall ascending mining," *International Journal of Mining Science and Technology*, vol. 23, no. 2, pp. 207–211, 2013.

[21] S. Yin, W. Nie, Q. Liu, and Y. Hua, "Transient CFD modelling of space-time evolution of dust pollutants and air-curtain generator position during tunneling," *Journal of Cleaner Production*, vol. 239, Article ID 117924, 2019.

[22] Y. L. Li, "Experimental study of creep properties of silty mudstone under triaxial compression," *Journal of Sichuan University (Engineering Science Edition)*, vol. 44, no. 1, pp. 14–19, 2012, in Chinese.

[23] L. Kong, Y. Wang, and S. Li, "Analysis on overburden strata movement law of coal mining face under goaf of room and pillar mining face," *Coal Science & Technology*, vol. 43, no. 5, pp. 26–29, 2015, in Chinese.

[24] N.-C. Zhang, N. Zhang, J. Esterle, J.-G. Kan, Y.-M. Zhao, and F. Xue, "Optimization of gateroad layout under a remnant chain pillar in longwall undermining based on pressure bulb theory," *International Journal of Mining, Reclamation and Environment*, vol. 30, no. 2, pp. 128–144, 2016.

[25] C. Mark, F. Chase, and A. Campoli, *Analysis of Retreat Mining Pillar Stability*, West Virginia University, Morgantown, WV, USA, 1995.

[26] J. Wang, J. G. Ning, and P. Q. Qiu, "Microseismic monitoring and its precursory parameter of hard roof collapse in longwall faces: a case study," *Geomechanics and Engineering*, vol. 17, no. 4, pp. 375–383, 2019.

[27] F. H. Yu, T. B. Zhao, and Y. L. Tan, "Study on quantitative calculation method of mining roadway supporting intensity under depressurized mining," *Journal of Mining and Safety Engineering*, vol. 3, no. 33, pp. 460–466, 2016, in Chinese.

[28] R. Gao, B. Yu, and X. B. Meng, "Stress distribution and surrounding rock control of mining near to the overlying coal pillar in the working face," *International Journal of Mining Science and Technology*, vol. 29, no. 6, pp. 881–887, 2019.

[29] Z.-S. Lian, J.-R. Wang, and C.-Y. Hao, "Numerical simulation and experimental research of surrounding rock deformation of floor roadway under short-distance coal seam group combined mining," *Journal of Coal Science and Engineering (China)*, vol. 16, no. 3, pp. 230–234, 2010, in Chinese.

[30] X.-Q. Wei, H. B. Bai, H. R. Rong, Y. Jiao, and B.-Y. Zhang, "Research on mining fracture of overburden in close distance multi-seam," *Procedia Earth & Planetary Science*, vol. 2, pp. 20–27, 2011.

[31] F. He, Z. Zheng, H. Zhu, and B. Yang, "Research on failure mechanism and strengthening of broken roadway affected by upper coal pillar," *Advances in Civil Engineering*, vol. 2019, Article ID 8132817, 13 pages, 2019.

[32] J. Yang and D. Wang, "Analysis on damage characteristic of the upper coal seam mining in contiguous coal seams," *Coal Science & Technology*, vol. 7, no. 45, pp. 7–11, 2017, in Chinese.

[33] J. Zhao and G. Li, "Pressure-relief mining of the working face under the coal pillar in the close distance coal seams," *Geotechnical and Geological Engineering*, vol. 34, no. 4, pp. 1067–1077, 2016.

[34] Z. Li, H. X. Liu, Z. L. Dun, L. Ren, and J. Fang, "Grouting effect on rock fracture using shear and seepage assessment," *Construction & Building Materials*, vol. 242, 2020.

[35] T. Xiao, B. Jianbiao, X. Lei, and Z. Xuebin, "Characteristics of stress distribution in floor strata and control of roadway stability under coal pillars," *Mining Science and Technology (China)*, vol. 21, no. 2, pp. 243–247, 2011.

[36] P. Gong, T. Zhao, K. Yetilmezsoy, and K. Yi, "Mechanical modeling of roof fracture instability mechanism and its control in top-coal caving mining under thin topsoil of shallow coal seam," *Advances in Civil Engineering*, vol. 2019, Article ID 1986050, 10 pages, 2019.

[37] Y. Tan, Q. Gu, J. Ning, X. Liu, Z. Jia, and D. Huang, "Uniaxial compression behavior of cement mortar and its damage-constitutive model based on energy theory," *Materials*, vol. 12, no. 8, p. 1309, 2019.

[38] T. Li, Y. Yu, W. Cheng, Q. Xu, H. Yang, and J. Shen, "The dynamic change of pore structure for the low-rank coal with various pretreatment temperatures: a case study from southwestern ordos basin," *Geofluids*, vol. 2020, Article ID 4670812, 15 pages, 2020.

[39] W. Y. Guo, Y. Tan, F. H. Yu, and T.-B. Zhao, "Mechanical behavior of rock-coal-rock specimens with different coal thicknesses," *Geomechanics and Engineering*, vol. 15, no. 4, pp. 1017–1027, 2018.

[40] B.-Y. Jiang, S.-T. Gu, L.-G. Wang, G.-C. Zhang, and W.-S. Li, "Strainburst process of marble in tunnel-excavation-induced stress path considering intermediate principal stress," *Journal of Central South University*, vol. 26, no. 4, pp. 984–999, 2019.

[41] C. X. Wang, B. T. Shen, and J. T. Chen, "Compression characteristics of filling gangue and simulation of mining with gangue backfilling: an experimental investigation," *Geomechanics and Engineering*, vol. 20, no. 6, pp. 485–495, 2020.

[42] Z. Li, H. Zhou, D. Hu, and C. Zhang, "Yield criterion for rocklike geomaterials based on strain energy and CMP model," *International Journal of Geomechanics*, vol. 20, no. 3, 2020.

[43] M. Sun, X. Zhang, W. Zheng, and X. Zhang, "Study on causing disaster and removing danger for stress concentration of overlying residual coal pillar in ultra-close multi-seam," *Geotechnical and Geological Engineering*, vol. 37, no. 5, pp. 4009–4017, 2019.

[44] C. Xu, W. Nie, Z. Liu, H. Peng, S. Yang, and Q. Liu, "Multi-factor numerical simulation study on spray dust suppression device in coal mining process," *Energy*, vol. 182, pp. 544–558, 2019.

[45] Q. Meng, L. Han, W. Qiao, D. Lin, and J. Fan, "Support technology for mine roadways in extreme weakly cemented strata and its application," *International Journal of Mining Science and Technology*, vol. 24, no. 2, pp. 157–164, 2014.

[46] Q. Meng, L. Han, J. Sun, F. Min, W. Feng, and X. Zhao, "Experimental study on the bolt-cable combined supporting technology for the extraction roadways in weakly cemented strata," *International Journal of Mining Science and Technology*, vol. 25, no. 1, pp. 113–119, 2015.

[47] S. Hu, Y. Tan, H. Zhou et al., "Anisotropic modeling of layered rocks incorporating planes of weakness and volumetric stress," *Energy Science & Engineering*, vol. 8, no. 3, pp. 789–803, 2020.

Research Article

A Shear Strength Model for a Subsidence Backfill Body Based on Adhesion Friction Theory

Lei Liu [1,2] **Shengyou Zhang** [1,2] **Weidong Liu** [3] **Wei Sun** [1,2] **and Jinxin Li** [1]

[1]*Faculty of Land Resources Engineering, Kunming University of Science and Technology, Kunming 650093, China*
[2]*Yunnan Key Laboratory of Sino-German Blue Mining and Utilization of Special Underground Space, Kunming 650093, China*
[3]*No. 3 Mining District of Jinchuan Group Co. Ltd., Jinchang 737103, China*

Correspondence should be addressed to Wei Sun; kgblasting@qq.com

Proper determination of the shear strength of the backfill body used to fill the subsidence is the basis for subsidence restoration and the stability analysis of materials. This study developed a shear strength calculation model for the backfill body by introducing adhesive friction theory into the shear strength analysis. A direct shear test was performed in the laboratory to verify the proposed method. Test results suggested that the shear strength calculation method based on adhesive friction theory can calculate the variation in the actual contact area between grains in the tested samples undergoing shearing and estimate the peak shear strength. The actual contact area was divided into two components, namely, adhesive contact area $A_{\rm rm}$ and contact area reduction caused by shear displacement, which exhibited a maximum at $A_{\rm rmax}$. The shear strength values calculated by this method were smaller than laboratory values, and their differences increased with the rock proportion in the backfill body. The differences between the theoretical and experimental values of shear strength increased with the rock grain size. The results of theoretical calculation, combined with the results of laboratory experiments, can provide support for the proper determination of shear strength of the backfill body.

1. Introduction

Mining-induced subsidence has accounted for 50% of the total geological disasters caused by mining in China and affected an area of $314765\,\mathrm{hm}^2$. This condition has attracted widespread attention and required the effective reclamation of subsided lands [1, 2]. Traditionally, subsidence areas in mines act as disposal sites of solid wastes from the mines. In the recent years, new methods for reclaiming subsidence areas, such as filling subsidence areas with rocks blasted from surrounding mountains or with filter cakes made of tailings and converting these areas to tailing ponds, have emerged [3, 4]. These methods are effective for subsided grounds free from mining influence (which indicates that no mining activity occurs in the underlying strata), but are unsuitable for subsided grounds that are still affected by mining activities in the underlying strata [5–7]. Waste rocks and tailings in a mine in Guangxi Province are manufactured into a paste to fill the subsidence area, which is in an active state. The amount of fill required is estimated to be 5 million m^3. Considering that this area is subject to mining influence, reasonable mechanical properties of backfill body play a critical role in its successful restoration.

Existing studies have investigated the mechanical properties of fills for subsidence areas primarily through laboratory experiments and numerical simulations because subsidence areas are often dangerous. The research of Leduc and Smith on the mechanical properties of waste rock-tailing mixture discharged into a subsidence area indicated that the internal friction angle between grains in this mixture decreases with the waste rock proportion [8]. Wickland and Wilson [9] investigated the self-consolidation of tailing-waste rock mixture at different mixing ratios by using an analog device. The mixture underwent a relatively fast self-consolidation when the waste rock-to-tailing ratio was 5:1. Tian et al. [10] evaluated the powder percentage in the block filling of a subsidence area at Jinshandian Iron Ore Mine and the probability of deris flow occurrence. Results suggested

that using the cement block and waste rock mixture to fill the subsidence area can ensure safety. Tian et al. [11] found that the soil-rock mixture tends to be strong with the increase in rock content and strength, and its mechanical properties primarily depend on soil in the mixture when the rock proportion is less than 40%.

Theoretical research on the shear strength of in situ fills should be conducted because the data from laboratory experiments cannot reflect their mechanical properties. Fill materials used to fill subsidence areas are typical granular materials with a wide range of grain sizes, and their shear strength mainly depends on the friction between grains [12–14]. Adhesive friction theory is an important basis for explaining the formation mechanism of soil and rock shear strengths [15]. Horne [16] and Penman [17] provided analytic relationships between the macroscopic shear and intergranular friction strengths. Sun et al. [18] investigated the influences of waste rock content and grain size on the shear strength of a fill for subsidence areas and explained the formation of fill shear strength on the basis of adhesive friction theory. However, they failed to provide a shear strength calculation model. Tong et al. [19] developed a method for calculating the shear strength of structural planes on the basis of adhesive friction theory and proved that this method is more reliable than the strength reduction method. In the present study, a model for calculating the shear strength of fills for subsidence areas was constructed on the basis of adhesive friction theory. Then, a theoretical calculation was performed using this model, and a verification experiment was conducted. This study aimed to find a reasonable method for determining the shear strength of fills used to restore subsided lands.

A force chain network can form in granular materials, such as soil and rock, to transfer forces when they are subjected to an external load. Considering that the forces between grains within this network are significantly greater than those between grains located outside this network, the macroscopic shear strength of granular materials are determined by the friction strength between grains within the force chain network [15, 20, 21]. Studies of [15] demonstrated that the macroscopic shear strength of granular materials depends on the friction between grains. The fills used for subsidence areas are often prepared by mixing waste rock and tailings. CT scans of the mixture samples containing different waste rock proportions (Figure 1) show that the waste rock and tailing grains are randomly distributed in the samples, and the fill is a typical granular composite with a wide range of grain sizes. This condition suggests that the shear strength of the fill is determined by the friction strength between the grains in it [18, 22, 23].

2. Theory

2.1. Adhesive Friction Theory.
Adhesive friction theory states that the frictional strength of soil and rock is essentially a molecular behavior in physics, roughness is an inherent quality of all surfaces of objects regardless of their smoothness, and the contact between surfaces occurs at the microbulges scattered on them (Figure 2). In the beginning,

when two surfaces come into contact, the microbulges experience considerable stress caused by the normal forces N_S between the surfaces. After the contact stress reaches its yield strength σ_y, the microbulges experience plastic deformation. As other smaller microbulges gradually come into contact, the contact area between the surfaces continues to increase until the net forces at the contact points reach zero. At this point, firm adhesion occurs between the microbulges in contact. For an ideal elastic-plastic material, the actual total contact area between the plastically deformed microbulges on particle surfaces can be expressed as $A_r = N_S/\sigma_y$. Intergranular friction T_S is the product of A_r and frictional strength τ_{sf}, where $T_S = A_r\tau_{sf}$.

The classical theory of adhesive friction only considers the actual contact area but ignores the increase in the actual contact area caused by the relative slipping between the objects in contact. The modified theory of adhesive friction states that the normal force and friction can cause microbulges to yield and adhesive contact nodes to grow, and the actual contact area can be written as

$$A_r^2 = \left(\frac{N_s}{\sigma_y}\right)^2 + \alpha\left(\frac{T_s}{\sigma_y}\right)^2, \tag{1}$$

where α is the experimentally determined coefficient, which is larger than 1 and normally at 9. The coefficient α is usually affected by material properties, section shape, and other factors and is usually selected according to experience.

2.2. Shear Strength Theory of a Backfill Body.
Sun et al. [12, 18, 24] investigated the mechanism of shear strength of a backfill body based on the modified theory of adhesive friction. The changes in the grain size and proportion of waste rock and external pressure led to variations in the actual contact area between the grains in the backfill body, intergranular friction strength, and macroscopic shear strength of the backfill body. Therefore, the variation in the actual contact area should be first considered when constructing a shear strength model for a backfill body.

2.2.1. Variation in the Actual Contact Area of the Backfill Body Undergoing Shearing.
The actual contact area between shear planes A_r is considerably smaller than the nominal area of apparent shear plane A_0. Formula (1) suggests that A_r arises from the adhesive friction between the shear planes in the fill and varies with shear displacement. A_r is divided into adhesive contact area A_{rm} and contact area reduction caused by shear displacement, A_{rb}. A_{rm}, A_{rb}, and A_r are, respectively, given by [19]

$$A_{rm} = \sqrt{\left(\frac{N_s}{\sigma_y}\right)^2 + \alpha\left(\frac{T_s}{\sigma_y}\right)^2}, \tag{2}$$

$$A_{rb} = \frac{2\lambda A_{rm}}{\sqrt{A_0} - 2S} \cdot S, \tag{3}$$

(a) (b) (c)
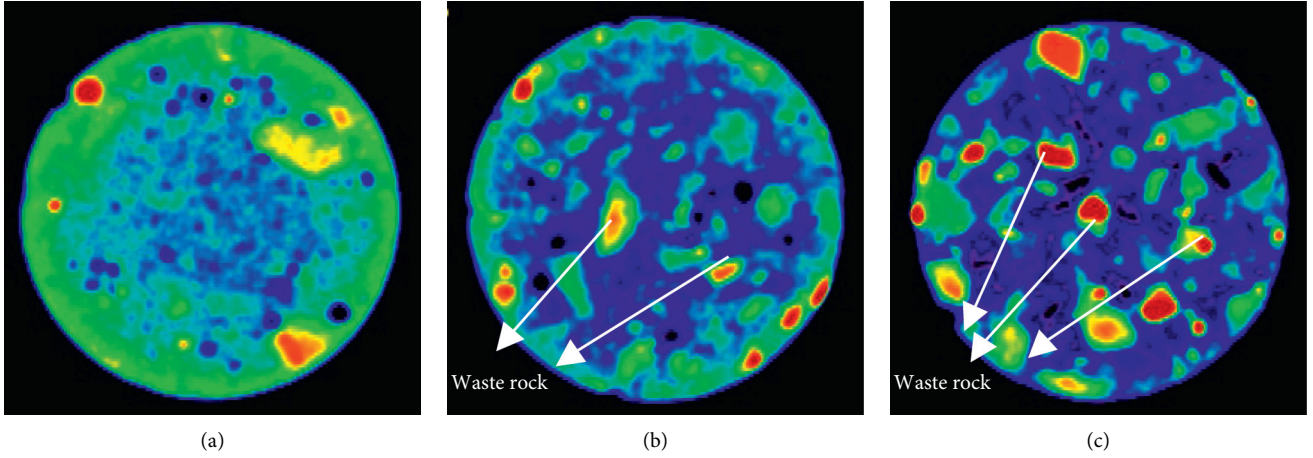
FIGURE 1: X-ray CT scan images of the backfill body with different mixture ratios [18], (a) waste rock content of 10%, (b) waste rock content of 30%, and (c) waste rock content of 50%.
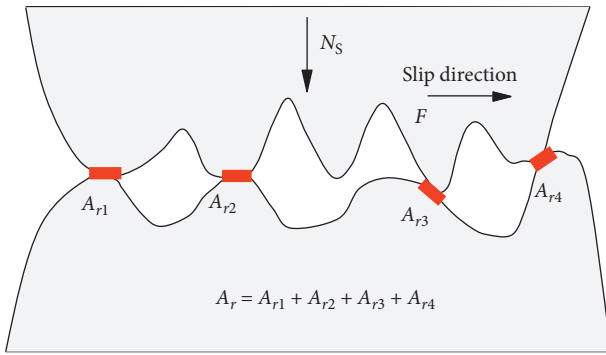
FIGURE 2: Schematic of intergranular contact [12].

$$A_r = A_{\rm rm} + A_{\rm rb} = \sqrt{\left(\frac{N_s}{\sigma_y}\right)^2 + \alpha\left(\frac{T_s}{\sigma_y}\right)^2} \cdot \left(1 - \frac{2\lambda A_{\rm rm}S}{\sqrt{A_0} - 2S}\right),$$

(4)

where S is the shear displacement, λ is the modified coefficient of adhesive friction ($\lambda = \sqrt{A_0}/S_m$, in which S_m is the shear displacement when the shear stress exceeds the shear yield strength, $S_m = 20$ mm), and α is a coefficient (normally $\alpha = 9$).

2.2.2. Determination of Shear Strength Based on Adhesive Friction Theory.

Adhesive friction theory states that the contact nodes on the shear planes are in a plastic state when the backfill body undergoes shearing. At a constant vertical stress, the friction between the shear planes is directly proportional to the actual contact area A_r. The friction between shear planes reaches its peak when A_r reaches $A_{\rm rmax}$, indicating that the shear strength at this point can be the maximum shear strength of the backfill body. Therefore, letting $A_r = A_{\rm rmax}$ at point (S_a, N_a) in the stress-strain curve $N(s)$ of the backfill body, the following relation can be obtained:

$$\frac{{\rm d}A_r}{{\rm d}s} = 0,$$

$$\frac{{\rm d}^2 A_r}{{\rm d}s^2} < 0.$$

(5)

Taking the derivative of A_r with respect to s provides

$$\frac{{\rm d}A_r}{{\rm d}s} = \frac{\alpha T}{\sqrt{N^2 + \alpha T^2}\sigma_y}\frac{{\rm d}T}{{\rm d}s}\left(1 - \frac{2\lambda s}{\sqrt{A_0} - 2s}\right) - \frac{\sqrt{N^2 + \alpha T^2}}{\sigma_y}\frac{2\lambda\sqrt{A_0}}{\left(\sqrt{A_0} - s\right)^2}.$$

(6)

Letting ${\rm d}A_r/{\rm d}s = 0$ provides

$$\frac{\alpha T}{N^2 + \alpha T^2}\frac{{\rm d}T}{{\rm d}s} = \frac{2\lambda\sqrt{A_0}}{\left(\sqrt{A_0} - s\right)\left[\sqrt{A_0} - 2(\lambda + 1)s\right]}.$$

(7)

The expression of $N(s)$ cannot be obtained because the initial value conditions of Formula (7) are unavailable. On this basis, the related measured data are used in Formula (7) to acquire point $(S_j N_j)(j = 1 \cdots$ that satisfies ${\rm d}A_r/{\rm d}s = 0$. Then, ${\rm d}^2 A_r/{\rm d}s^2 < 0$ at point $(S_j N_j)$ is evaluated to determine the point that satisfy the condition, $(S_a N_a)$. At this point, A_r reaches its maximum, the friction forces between shear planes reach their peak, and the corresponding shear strength, namely, adhesive friction strength τ_p, is obtained.

3. Experimental

3.1. Direct Shear Test.

A small modified direct shear apparatus was used to test the fill samples. The samples with 6.18 cm diameter and 5.0 cm height were obtained from tailings and waste rock in a mine. The waste rock particles have an important influence on the shear strength [25], so the waste rock was pulverized into three groups of fragments, which had grain sizes of −20, −15, and −10 mm, respectively. Considering the limited size of the shear cell, supersize waste rock was treated through equivalent substitution to ensure the continuous distribution of grain sizes.

In the experiment, mixture samples containing 10%, 20%, 30%, and 40% waste rock were prepared by mixing the

(a)

(b)

FIGURE 3: Shear test photos: (a) prepared specimens; (b) specimens destroyed.

TABLE 1: Results of the shear strength test (kPa).

Waste rock proportion (%)	Grain size (mm)	Vertical pressure (kPa)				c (kPa)	φ (°)
		100	200	300	400		
40	−20	167	245	341	444	67.3	42.8
	−15	158	220	335	408	64.3	40.8
	−10	144	236	305	399	50.7	40.6
30	−20	153	239	338	436	54.3	43.5
	−15	144	215	329	401	51	41.5
	−10	132	187	277	353	48.5	37
20	−20	144	235	308	367	77.5	36.6
	−15	142	214	276	344	77.3	33.7
	−10	139	189	265	329	68.7	32.9
10	−20	157	241	317	388	83.2	37.5
	−15	150	236	290	369	83.8	35.3
	−10	147	212	272	330	87.5	31.4

waste rock of each grain size with tailings and water, and the mass concentration ranges from 81% to 83%. The prepared paste was poured into molds with 6.2 cm diameter and 5.0 cm height. After the samples were fully air-dried at room temperature, they were released from the molds for the direct shear test. During the direct shear test, vertical stresses of 100, 200, 300, and 400 kPa were applied to each sample successively, and a lateral shear stress was rapidly applied until shear failure occurred in each sample (Figure 3).

3.2. Test Results. The direct shear test was conducted on 12 groups of samples. Table 1 shows the test results, and Figure 4 shows the shear stress-shear strain curves of some samples. The shear strength of the samples increased with the increase in vertical stress. As the proportion of waste rock increased, the shear strength initially decreased and then increased, and the minimum values were reached when the waste rock proportion was 20% or 30%. The cohesion force continuously declined, and the internal friction angle gradually increased. At the same waste rock proportion, the increase in waste rock grain size increased the shear strength, cohesion force, and internal friction angle.

Shear strength normally includes two components, namely, adhesive and frictional strengths. The calculation results indicated that the frictional strength accounted for approximately 80% of the shear strength of the backfill body and was the dominant component of shear strength. The sample containing 30% waste rock with a grain size of −20 mm displayed a frictional strength of 381.31 kPa, which was equivalent to 87.52% of its total shear strength.

4. Results and Discussion

The data from the experiment were substituted into the aforementioned formulas for calculating the contact area change and shear strength, and the theoretical and experimental values of shear strength were compared.

4.1. Actual Contact Area in the Backfill Body. The relationship of shear displacement with A_{rm}, A_{rb}, and A_r was derived by using the experimental data from the test (in which the waste rock grain size was −20 mm, the waste rock proportion was 30%, and the vertical stress was 400 kPa) and the related data in the stress-strain curve into formulas (2), (3), and (4), as shown in Figure 5.

As presented in Figure 5, adhesive contact area A_{rm} increased with the shear displacement, and the rate of increase began to decline when A_{rm} approached 0.3 cm². The contact area reduction caused by shear displacement A_{rb} increased with the shear displacement. The rate of increase
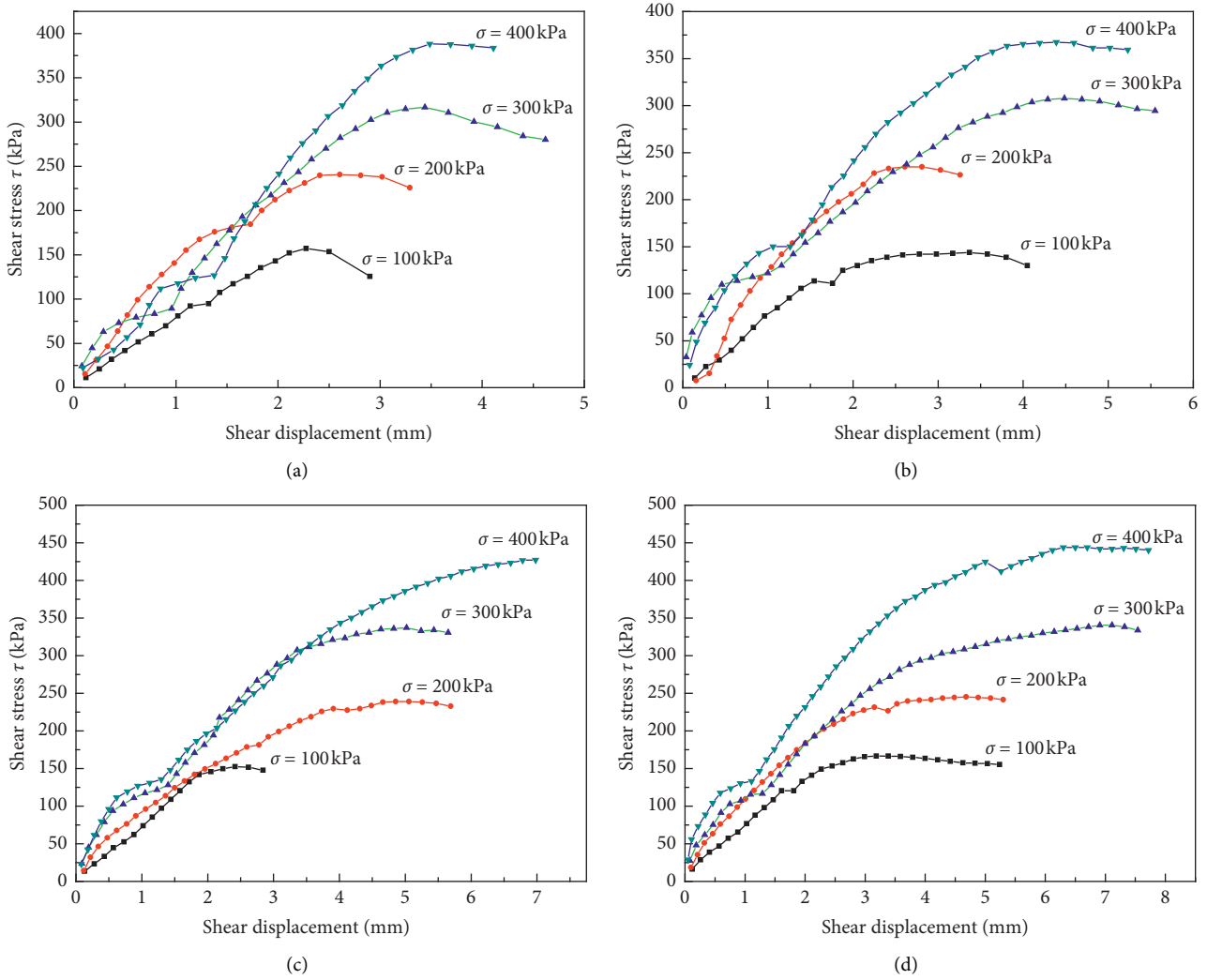
FIGURE 4: Shear stress-shear displacement curves of backfill body samples (−20 mm): (a) waste rock content of 10%, (b) waste rock content of 20%, (c) waste rock content of 30%, and (d) waste rock content of 40%.
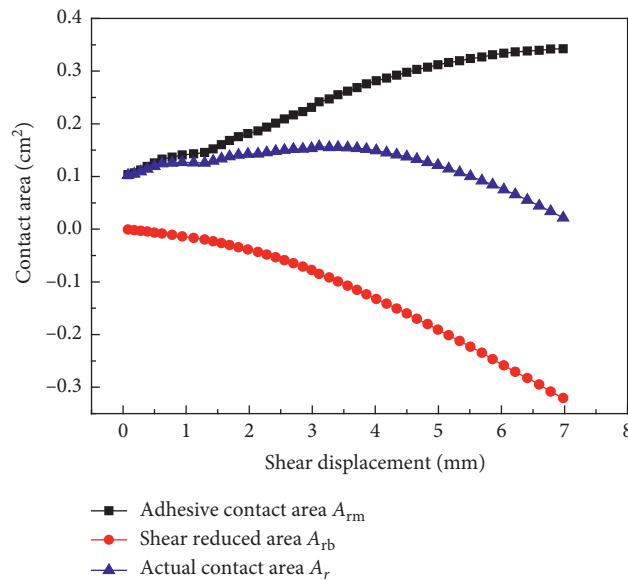
FIGURE 5: Relationship between shear displacement and the contact area.

(a)

(b)

(c)

(d)
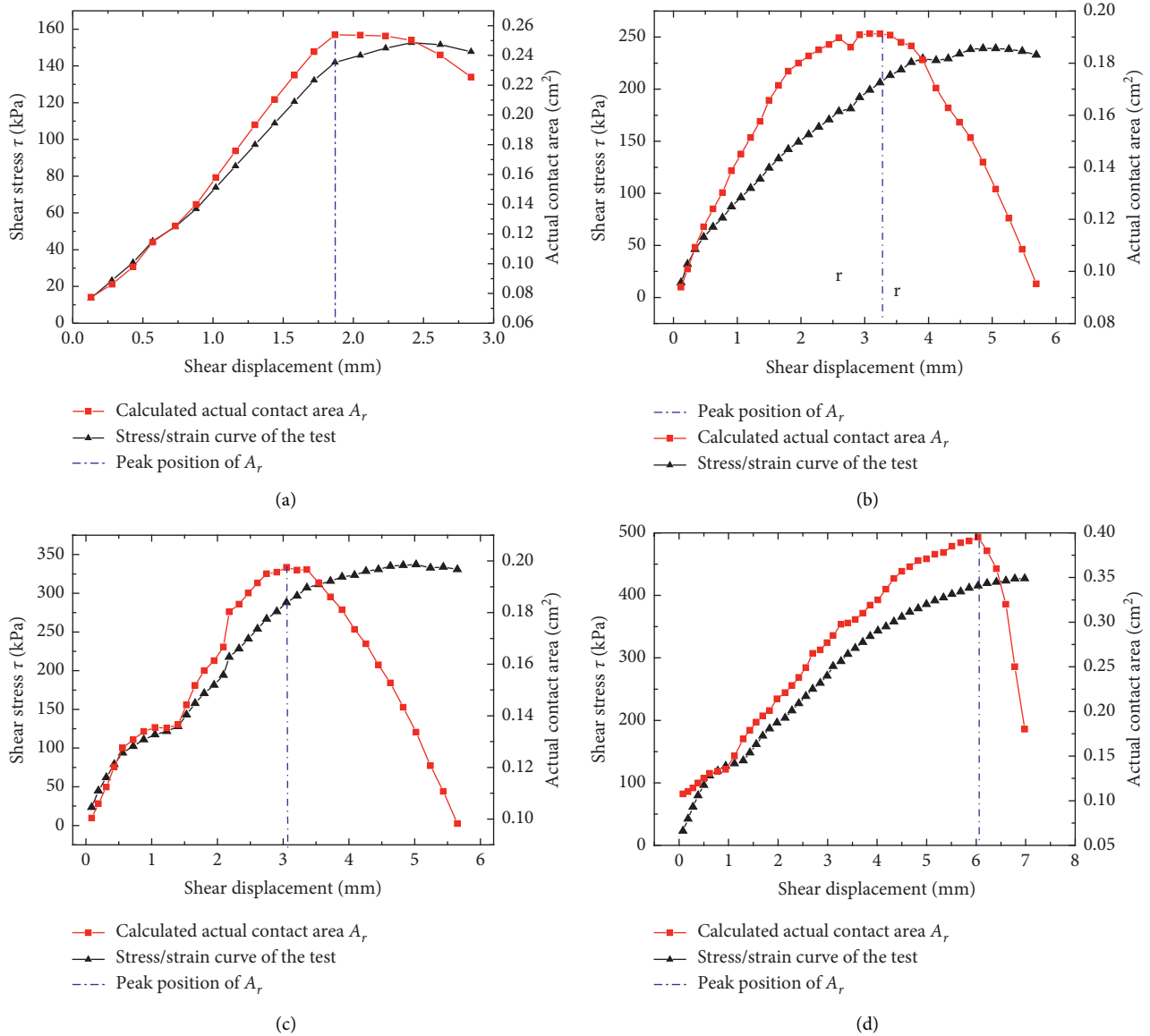
Figure 6: Relationship between shear strength and actual contact area: (a) vertical stress 100 kPa, (b) vertical stress 200 kPa, (c) vertical stress 300 kPa, and (d) vertical stress 400 kPa.

was relatively low when the shear displacement was smaller than 1.5 mm and began to grow when the shear displacement exceeded 1.5 mm. The actual contact area A_r increased and then decreased with the shear displacement and exhibited a maximum at A_{rmax}. The shear strength reached its peak at A_{rmax}, and the corresponding shear strength obtained through calculation was considered the maximum shear strength of the backfill body.

4.2. Shear Strength Calculation. After A_{rmax} was determined, the strength of adhesive friction τ_p was calculated using Formula (7). Then, the relationship between shear strength and the actual contact area was obtained using the experimental data from the tests (in which the waste rock grain size was −20 mm, the waste rock proportion was 30%, and

the vertical stresses were 100, 200, 300, and 400 kPa) into the formula, as shown in Figure 6.

As presented in Figure 6, the samples demonstrated theoretical adhesive friction strengths of 141.9, 218.7, 288.1, and 415.6 kPa, which were 92.7%, 91.5%, 85.23%, and 95.3% of the experimental values of maximum shear strength, respectively, when the waste rock grain size was −20 mm, waste rock proportion was 30%, and vertical stresses were 100, 200, 300, and 400 kPa. Therefore, the calculated values of adhesive friction strength were smaller than the corresponding experimental values of shear strength.

4.3. Factors Influencing the Theoretical Adhesive Friction Strength. Fills used to restore subsided lands are a typical type of granular composites made from waste rock and
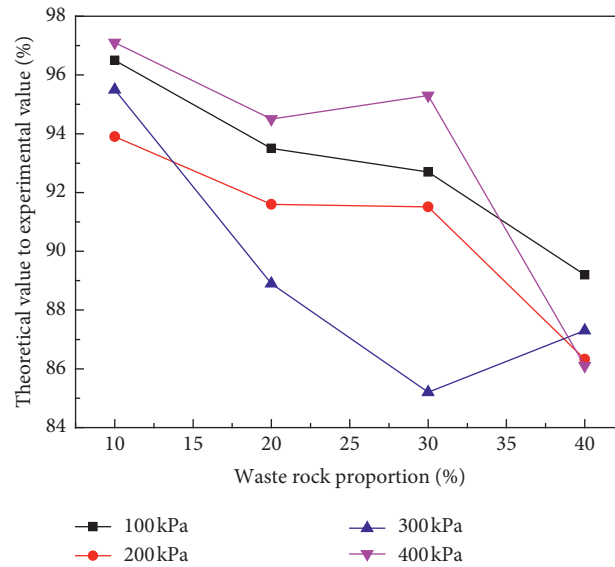
FIGURE 7: Relationship between the waste rock proportion and the ratio of the theoretical value to experimental value of shear strength.
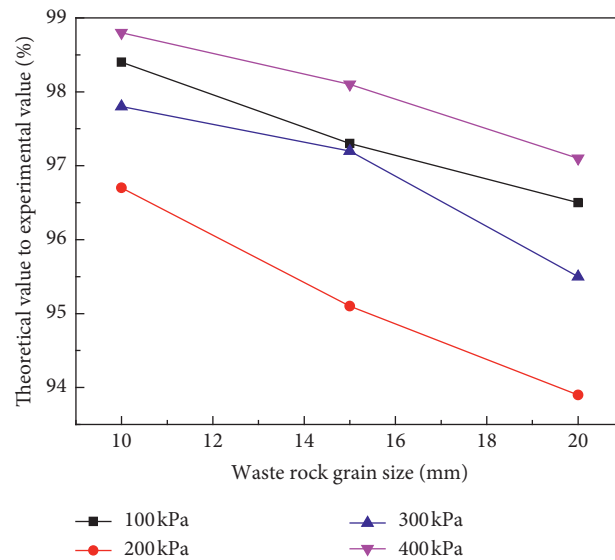
FIGURE 8: Relationship between waste rock grain size and the ratio of the theoretical value to experimental value of shear strength.

tailings. The variation pattern of the difference between the theoretical and experimental values of adhesive friction strength varied between samples with different mixing ratios. As shown in Figure 7, the theoretical values of shear strength were close to the experimental values when the waste rock proportion was low, and their differences increased with the increase in waste rock proportion. The relationship between vertical stress and theoretical shear strength did not exhibit an evident pattern. As the waste rock grain size increased, the difference between the theoretical and experimental results

exhibited a continued increase, and its relationship with vertical stress did not exhibit a pattern, as shown in Figure 8.

The results suggest that the proposed shear strength calculation method based on adhesive friction theory is applicable to homogeneous granular materials, and the values calculated using the method are close to the experimental results. Considering that the theoretical values of shear strength were smaller than the experimental values, they can be used in practical applications to ensure the stability of in situ fills for subsidence areas.

5. Conclusions

In this study, a shear strength calculation method for the backfill body used to fill subsidence areas was developed on the basis of adhesive friction theory, and a verification experiment was conducted in the laboratory. The theoretical calculation results were compared with experimental results. This study presents the following conclusions:

(1) Actual contact area A_r is divided into two components, namely, adhesive contact area A_{rm} and contact area reduction caused by shear displacement, A_{rb}. Actual contact area A_r exhibited a maximum at A_{rmax}, and the shear strength reached its peak at this point. Then, the corresponding shear strength obtained through calculation was considered the maximum shear strength of the backfill body.

(2) The values of shear strength calculated based on adhesive friction theory were smaller than those obtained from the laboratory experiment. The theoretical values of shear strength were close to the experimental values when the waste rock proportion was low, and their differences increased with the increase in waste rock proportion. The increase in waste rock grain size increased the differences between the theoretical and experimental results.

(3) The shear strength calculation model based on adhesive friction theory applies to homogeneous mixtures. This model can be used to estimate the maximum shear strength of in situ fills and in related computational analyses.

This study presents a preliminary discussion of the theoretical method for calculating the shear strength of fills used to restore subsided grounds. Although further corrections and improvement are necessary, this research can provide a new insight into the theoretical shear strength of materials with a wide range of grain sizes, such as the waste rock-tailing mixture. The results of theoretical calculation, combined with the results of laboratory experiments, can provide support for the proper determination of the shear strength of fills used to restore subsided lands.

There are still some deficiencies in this study, which need to be improved in the future. Firstly, a lot of experiments are carried out to improve the theoretical model; secondly, field in situ experiments are carried out to make up for the shortcomings of small-scale tests; finally, the effects of parameters such as the amount of waste rock added, the size of waste rock particles, and the shear rate on the shear strength are studied.

Data Availability

The data used to support the findings of this study are included within the article.

Conflicts of Interest

The authors declare that they have no conflicts of interest regarding the publication of this paper.

Authors' Contributions

Lei Liu and Wei Sun designed experiments; Wei Sun and Shengyou Zhang carried out the experiments; Jinxin Li analyzed the experimental results; Weidong Liu analyzed the data and developed analysis tools; and Wei Sun and Lei Liu wrote the manuscript.

Acknowledgments

References

[1] F. He, Y. N. Xu, and G. Qiao, "Distribution characteristics of mine geological hazards in China," *Geological Bulletin of China*, vol. 31, pp. 476–485, 2012.

[2] S. Cao, G. Xue, and E. Yilmaz, "Flexural behavior of fiber reinforced cemented tailings backfill under three-point bending," *IEEE Access*, vol. 7, pp. 139317–139328, 2019.

[3] H. Chen, Z. M. Sun, and G. H. Yao, "Feasibility study on the program of eliminating potential accident at veinlet belt orebody of Tongkeng mine," *China Mineralogical Magazine*, vol. 17, pp. 100–106, 2008.

[4] H. Lu, C. Qi, Q. Chen, D. Gan, Z. Xue, and Y. Hu, "A new procedure for recycling waste tailings as cemented paste backfill to underground stopes and open pits," *Journal of Cleaner Production*, vol. 188, pp. 601–612, 2018.

[5] Y. B. Hou, J. Tang, and S. X. Wei, "Research on tailings cementation and discharging technology," *Metal Mine*, vol. 6, pp. 59–62, 2011.

[6] Z. Yin, W. Chen, H. Hao et al., "Dynamic compressive test of gas-containing coal using a modified split hopkinson pressure bar system," *Rock Mechanics and Rock Engineering*, vol. 53, no. 2, pp. 815–829, 2020.

[7] W. Sun, H. Wang, and K. Hou, "Control of waste rock-tailings paste backfill for active mining subsidence areas," *Journal of Cleaner Production*, vol. 171, pp. 567–579, 2018.

[8] M. Leduc and M. E. Smith, "Tailings co disposal-innovation for cost saving and liability reduction," *Latin America Mining Record*, vol. 16, pp. 1–15, 2003.

[9] B. E. Wickland and G. W. Wilson, "Self-weight consolidation of mixtures of mine waste rock and tailings," *Canadian Geotechnical Journal*, vol. 42, no. 2, pp. 327–339, 2005.

[10] Y. H. Tian, X. C. Li, and N. Wei, "Experimental study of characteristics of compression and pulverization for cemented tailings blocks," *Rock and Soil Mechanics*, vol. 32, pp. 3597–3603, 2011.

[11] H. N. Tian, Y. Y. Jiao, and H. Wang, "Research on biaxial test of mechanical characteristics on soil-rock aggregate (SRA) based on particle flow code simulation," *Chinese Journal of Rock Mechanics and Engineering*, vol. 34, pp. 3564–3573, 2013.

[12] W. Sun, A. X. Wu, and H. J. Wang, "Experimental research on shear behavior of subsidence backfill body mixed by unclassified tailings and waste rocks," *Chinese Journal of Rock Mechanics and Engineering*, vol. 32, pp. 917–925, 2013.

[13] Z. Q. Yin, Z. X. Hu, Z. D. Wei et al., "Assessment of blasting-induced ground vibration in an open-pit mine under different rock properties," *Advances in Civil Engineering*, vol. 2018, Article ID 4603687, 10 pages, 2018.

[14] S. Cao and W. Song, "Effect of filling interval time on the mechanical strength and ultrasonic properties of cemented coarse tailing backfill," *International Journal of Mineral Processing*, vol. 166, pp. 62–68, 2017.

[15] C. Thornton and L. Zhang, "On the evolution of stress and microstructure during general 3D deviatoric straining of granular media," *Géotechnique*, vol. 60, no. 5, pp. 333–341, 2010.

[16] M. R. Horne, "The behaviour of an assembly of rotund, rigid, cohesionless particles. III," *Proceedings of the Royal Society of London. A. Mathematical and Physical Sciences*, vol. 310, no. 1500, pp. 21–34, 1969.

[17] A. D. M. Penman, "Shear characteristics of a saturated silt, measured in triaxial compression," *Géotechnique*, vol. 3, no. 8, pp. 312–328, 1953.

[18] W. Sun, A. Wu, K. Hou, Y. Yang, L. Liu, and Y. Wen, "Real-time observation of meso-fracture process in backfill body during mine subsidence using X-ray CT under uniaxial compressive conditions," *Construction and Building Materials*, vol. 113, pp. 153–162, 2016.

[19] Z. Y. Tong, C. X. Chen, and J. Xu, "Selection of shear strength of structural plane based on adhesion friction theory," *Chinese Journal of Geotechnical Engineering*, vol. 30, pp. 1367–1371, 2008.

[20] X. Z. Li, C. Z. Qi, Z. S. Shao, and C. Xia, "Effects of crack inclination on shear failure of brittle geomaterials under compression," *Arabian Journal of Geosciences*, vol. 10, no. 23, pp. 529–541, 2017.

[21] C.-P. Lu, Y. Liu, T.-B. Zhao, and H.-Y. Wang, "Experimental research on shear-slip characteristics of simulated fault with zigzag-type gouge," *Tribology International*, vol. 99, pp. 187–197, 2016.

[22] M. Wang, L. Liu, X.-Y. Zhang, L. Chen, S.-Q. Wang, and Y.-H. Jia, "Experimental and numerical investigations of heat transfer and phase change characteristics of cemented paste backfill with PCM," *Applied Thermal Engineering*, vol. 150, pp. 121–131, 2019.

[23] L. Liu, C. Zhu, C. Qi, B. Zhang, and K.-I. Song, "A microstructural hydration model for cemented paste backfill considering internal sulfate attacks," *Construction and Building Materials*, vol. 211, pp. 99–108, 2019.

[24] W. Sun, K. Hou, and Z. Y. Yang, "X-ray CT three-dimensional reconstruction and discrete element analysis of the cement paste backfill pore structure under uniaxial compression," *Construction and Building Materials*, vol. 138, pp. 69–78, 2017.

[25] C. S. Wen, V. Marzulli, F. Cafaro, K. Senetakis, and T. Pöschel, "Micromechanical behavior of DNA-1A lunar regolith simulant in comparison to ottawa sand," *Journal of Geophysical Research: Solid Earth*, vol. 124, no. 8, pp. 8077–8100, 2019.

Research Article

A Study of the Differences in the Gas Diffusion and Migration Characteristics of Soft and Hard Coal in High Gas Coal Seams

Anying Yuan (ID)

State Key Laboratory of Mining Response and Disaster Prevention and Control in Deep Coal Mines,
Anhui University of Science and Technology, Huainan City, Anhui Province 232001, China

Correspondence should be addressed to Anying Yuan; ayyuan@aust.edu.cn

At the present time, it is of major significance to examine the differences in the gas diffusion and migration characteristics of soft and hard coal in order to prevent and control safety hazards in high gas coal seams. In this study, the differences in the gas diffusion and migration characteristics between soft coal and hard coal were examined in detail using macrostructural, mesostructural, and microstructural research methods. The root causes of the differences in the gas diffusion and migration between soft coal and hard coal were revealed in the obtained research results. The study shows that, in terms of the macrostructures, the soft coal particle grains were flakey and with shapes resembling fingernails. Meanwhile, the hard coal particle grains were observed to be in the shapes of complete blocks. In addition, in terms of the mesostructures of the different coal types, it was found that the proportion of granular coal below the particle size limit of 6 mm in the soft coal was much higher than that of the hard coal. Also, from the aspect of the characteristics of the microstructures, the pores and fissures on the soft coal surfaces were observed to be better developed, and the BJH specific surface areas of the soft coal were more than twice those of the hard coal. That is to say, the gas diffusion and migration conditions of the soft coal were better than those of the hard coal. At the same time, the increments of the specific surface areas and volumes of the pores of soft coal were above 100 nm, which provided channels for gas diffusion and migration at rates of more than twice those of the hard coal. Therefore, the soft coal was more conducive to gas emissions. This study conducted gas desorption experiments on both soft and hard coal samples and found that the initial gas desorption speed of the soft coal was significantly higher than that of the hard coal. Since the instantaneous gas emissions of the soft coal were significantly higher than those of the hard coal, it was considered to be more likely that gas outbursts and transfinite accidents could potentially occur in the soft coal layers of a project site. This study's results provided a foundation and basis for effective gas control measures in coal seams composed of soft coal layers, which will be of major significance to the safety of coal mining activities in the future.

1. Introduction

Gas emissions are a type of disastrous gas hazard which may potentially impact the safe production processes of coal mines [1]. Coal seams that contain high content levels of gas are known to be easily affected by gas outburst accidents resulting in casualties and property losses [2–4]. However, within the same coal seam, different types of coal bodies may display significant differences in gas emission amounts, which pose greater challenges for the prevention and control of gas emissions in mine working faces [5–7].

It was determined that several of the examined examples of coal and gas outbursts indicated that outburst accidents with prediction and effect inspection indexes not exceeding the standard limits had occurred in the soft layers of the coal seam, and the gas desorption laws of the soft and hard coal bodies were quite different [8–10]. It was observed that using the desorption laws of hard coal to test the gas content levels in soft coal seams, along with the gas desorption indexes of drill cuttings, would potentially lead to large errors in the test results.

Previously, many experts and scholars in the field have conducted in-depth research regarding the characteristics of

gas diffusion and migration in coal seams [11–13]. Some researchers believe that the majority of coal and gas outburst accidents occur on the roadways of driving faces and at both ends of working faces. This is due to the fact that the aforementioned areas tend to be disturbed by mining activities, and a general phenomenon of stress concentration is present, which plays a leading role in gas outburst events [14–17]. Second, some researchers have theorized that coal deposits, as the main carrier of coal and gas outbursts, are the objects of the gas outbursts, and the mechanical characteristics, pore structure characteristics, and other factors of the coal bodies themselves play important roles in the gas emission processes [18–22].

Therefore, in view of the gas emission laws of coal bodies, experts in the field have adopted many research methods, including gas adsorption and desorption experiments, microscanning, micropore structure analyses, and mercury injection experiments [23–25]. However, the majority of the research studies generally utilize one or two of the aforementioned methods to examine the gas desorption laws of coal bodies. As a result, different research findings have been presented. In particular, there have been relatively few studies conducted regarding the phenomena observed in soft and hard coal bodies within the same coal seam.

In the present research, from the aspects of the macrostructures, mesostructures, and microstructures of soft coal and hard coal, gas desorption experiments were conducted in order to comprehensively analyze the root causes of the differences in the characteristics of gas diffusion and migration in soft coal and hard coal. The results of the experimental processes revealed the mechanism of the differences in the gas emissions of soft coal and hard coal, which provided a foundation and basis for the prevention and control of coal seam gas disasters under similar conditions, which was considered to be of major significance to future coal mining projects.

2. Differences in the Characteristics of the Macrostructures and Mesostructures of Soft Coal and Hard Coal

In order to examine the differences in the gas diffusion processes between the soft coal and hard coal in high gas coal seams, the characteristics of macrostructures and mesostructures of soft and hard coal samples were first analyzed. In this study, soft coal and hard coal samples obtained from the No. 6 and No. 11 high gas coal seams of the Xieqiao Coal Mine in China's Huainan mining area were selected. The No. 6 coal seam and No. 11 coal seam both contained soft layers (hereinafter referred to as the soft coal), and the physical and mechanical properties of soft layers and normal coal bodies (hereinafter referred to as the hard coal) were obviously different.

Figure 1 shows the macro characteristics of the soft coal and hard coal in each coal seam. It can be seen in the figure that the soft coal in each coal seam generally contained no large blocks, and the coal particles were generally uniform in size, displaying approximately nail-shaped flakey particles. Meanwhile, the hard coal was mainly in the form of blocks.

An artificial crushing method was adopted in this study to simulate the crushing processes, which occur during the mining of a working face. A standard sieve was used to screen the soft coal and hard coal samples in order to obtain the fine particle size distribution law of the soft coal and hard coal, as shown in Figure 2. The results indicated that there was a particle size limit during the process in which the particle sizes influenced the desorption and diffusion of the coal particle gas. The limit of the particle size was considered to be the inherent particle size of the coal, which was related to the degree of damage and metamorphism of the coal, with a maximum size of no more than 6 mm. It was observed that, in the ranges less than the particle size limit, the gas desorption strength and attenuation coefficient decreased with the increases in the coal particle sizes. However, when the coal particle sizes were larger than the particle size limit (6 mm), the decreasing trends of the gas desorption strength and attenuation coefficient with the increases in the coal particle sizes were not obvious. Therefore, this study selected a 6 mm particle size as the boundary for the purpose of analyzing the particle size distributions in the raw coal.

The results of this study's comparative analysis showed that the proportions of coal particles below 6 mm in the soft coal of the No. 6 and No. 11 coal seams were 54.63% and 68.54%, respectively. The proportions of the coal particles below 6 mm in the hard coal of the No. 6 and No. 11 coal seams were determined to be 17.72% and 21.45%, respectively. Therefore, the proportions of coal particles below 6 mm in soft coal were more than 3 times those of the hard coal. In other words, the proportions of coal particles below 6 mm in the soft coal of each examined coal seam were far higher than those of the hard coal.

3. Differences in the Micropore Structures of the Soft Coal and Hard Coal

In order to further explore the underlying mechanism of the differences in the gas diffusion and migration between the soft coal and hard coal, this study examined the micropore structures of each type of coal. A Micrometrics ASAP 2460 multistation specific surface and porosity analyzer was used for the determination of the micropore structural parameters, as shown in Figure 3.

3.1. Comparative Analysis of the Specific Surface Areas of the Soft Coal and Hard Coal. Figure 4 shows this study's comparative analysis diagram of the BET specific surface areas and BJH specific surface areas of the soft coal and hard coal in the different coal seams. Table 1 shows this study's pore structural parameters of the soft coal and hard coal in the different coal seams. It can be seen in Figure 4 and Table 1 that the BET specific surface areas of the soft coal and hard coal in the No. 6 coal seam were 3.5421 m^2/g and 1.8008 m^2/g, respectively. That is to say, the BET specific surface area of soft coal in the No. 6 coal seam was
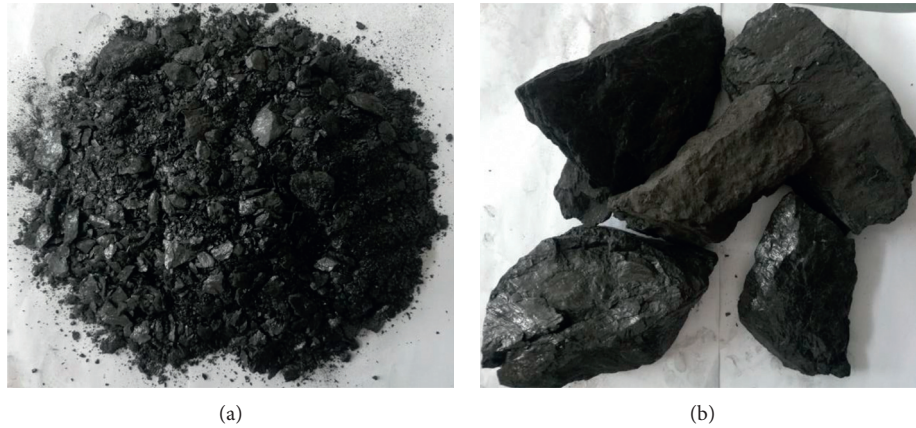
FIGURE 1: Macroscopic characteristics of soft coal and hard coal. (a) Soft coal. (b) Hard coal.
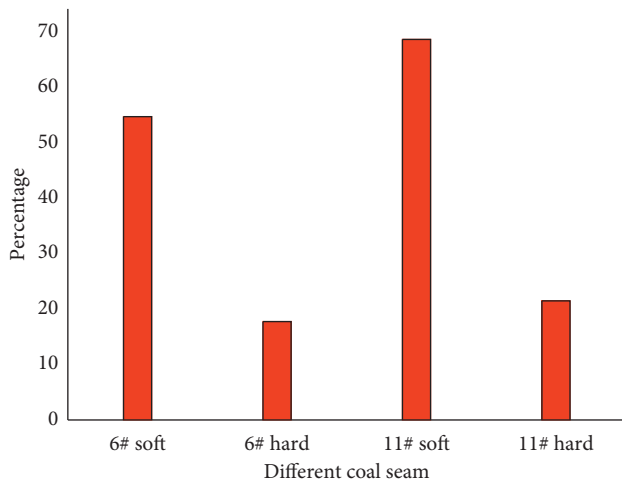
FIGURE 2: Percentages of soft coal and hard coal with particle sizes less than 6 mm in each coal seam.

FIGURE 3: ASAP 2460 multistation specific surface and porosity analyzer.
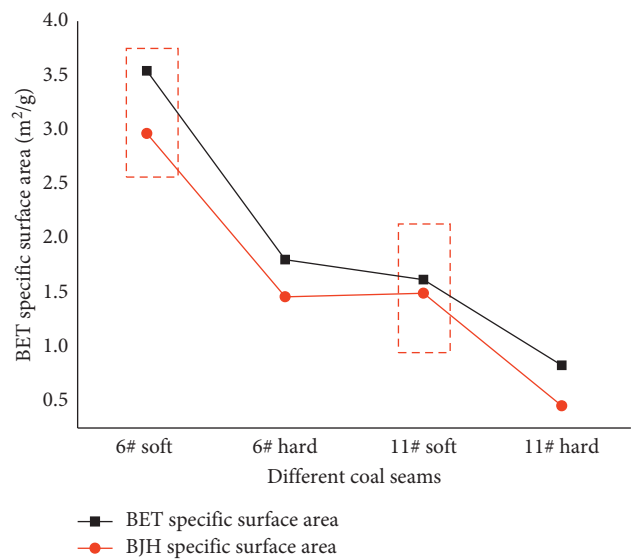
FIGURE 4: Specific surface areas of the coal bodies in the different coal seams.

approximately twice that of the hard coal, which indicated that the gas adsorption conditions of the soft coal in the No. 6 coal seam were superior to those of the hard coal. In addition, it was determined that the BET specific surface areas of the soft coal and hard coal in the No. 11 coal seam were $1.6179 \, m^2/g$ and $0.8278 \, m^2/g$, respectively. Therefore, the BET specific surface area of the soft coal in the No. 11 coal

seam was confirmed to be approximately twice that of the hard coal, indicating that the gas adsorption conditions of the soft coal in the No. 11 coal seam were also better than those of the hard coal. As detailed in Figure 3, the BJH specific surface areas of the soft coal and hard coal in the No. 6 coal seam were $2.9642 \, m^2/g$ and $1.4593 \, m^2/g$, respectively. Therefore, the BJH specific surface areas of the soft coal were more than twice those of the hard coal, which indicated that the gas diffusion and migration conditions of the soft coal in the No. 6 coal seam were superior. The BJH specific surface areas of the soft coal and hard coal of the No. 11 coal were $1.4921 \, m^2/g$ and $0.453 \, m^2/g$, respectively. Therefore, it was determined that the BJH specific surface areas of the soft coal were more than three times those of the hard coal, which indicated that the gas diffusion and migration conditions of the soft coal in the No. 11 coal seam were better than those of the hard coal within the same coal seam.

In conclusion, the BET specific surface areas and BJH specific surface areas of soft coal were found to be

significantly larger than those of the hard coal. As a result, it was concluded that the conditions for gas adsorption and diffusion migration of the soft coal were stronger than those of the hard coal.

3.2. Relationships between the Pore Sizes, Specific Surface Areas, and Pore Volumes.

Figures 5 and 6 show the relationships between the increments of the pore sizes and specific surface areas, as well as the relationships between the increments of pore sizes and pore volumes, of the soft coal and hard coal in the No. 6 coal seam, respectively. It can be seen in the aforementioned figures that the increments of the specific surface areas and pore volumes corresponding to the soft coal pore sizes above 100 nm were significantly larger than those of the hard coal. The maximum increment of the pore volumes corresponding to the pore sizes greater than 100 nm in the soft coal was 9×10^{-5} cm^3/g. In addition, the maximum increment of the pore volume corresponding to the pore sizes above 100 nm in the hard coal was 3.5×10^{-5} cm^3/g. Therefore, the increment of the soft coal was approximately 2.6 times that of the hard coal, as shown in the blue-dashed boxes in Figures 5(b) and 6(b).

Figures 7 and 8 show the relationships between the increments of the pore sizes and specific surface areas and the relationships between the increments of the pore sizes and pore volumes of the soft and hard coal in the No. 11 coal seam, respectively. It can be seen in the figure that the increments of the specific surface areas and pore volumes corresponding to the pore sizes greater than 100 nm in the soft coal were significantly larger than those of the hard coal, wherein the maximum increment of pore volume corresponding to the pore sizes greater than 100 nm in the soft coal was 12.5×10^{-5} cm^3/g. The maximum increment of the pore volume corresponding to the pore sizes greater than 100 nm in the hard coal was determined to be 6.2×10^{-5} cm^3/g. Therefore, the increment of the soft coal was approximately 2 times that of the hard coal, as indicated in the blue-dashed boxes in Figures 7(b) and 8(b).

Based on the above analysis of the increments of the pore diameter and specific surface areas and the increments of the pore volumes of the soft coal and hard coal in the two examined coal seams, it was concluded that the pore specific surface area increments and the pore volume increments of the soft coal with apertures larger than 100 nm were more than twice those of the hard coal. These findings indicated that the soft coal provided better conditions for gas diffusion and migration. In other words, the soft coal was determined to be more conducive to gas desorption and diffusion.

3.3. Comparative Analysis Results of the Microscanning of the Soft Coal and Hard Coal.

In the present study, a FlexSEM 1000 scanning electron microscope was used to conduct microscopic scanning of the soft coal and hard coal, respectively. The results are shown in Figure 9. It can be seen in the figure that the soft coal surfaces of the two coal seams were very rough and uneven, and the gas pores were relatively developed (as shown in Figures 9(a) and 9(c)). The pore edges were mainly zig-zagged in appearance, with significant differences observed in the pore sizes. In addition, pores ranging from several microns to dozens of microns were developed. The most direct impact of these relatively developed pores in the high gas coal seam was the corresponding increases in the gas adsorption capacity. There were many crush marks and stepped fracture scale structures were also observed. These structures had greatly increased the surface areas of the coal bodies, which had contacts outside the coal seams. At the same time, the crush marks formed under the action of the structural compressive stress had led to the obvious development of microcracks, as well as good connectivity between the pores. This had resulted in the formations of dominant channels for gas flow. In contrast, the surfaces of the hard coal were found to be more complete, with the characteristics of thin-layer shear fractures, thin sections, and crumpled deformations. In addition, local roughness and unevenness, scattered minerals, and coal chips on the surfaces were observed, with few pores in local areas and no obvious cracks. Therefore, based on the above analysis results, it was concluded that the development of pores and fractures in the soft coal had provided "good" conditions for gas adsorption and desorption, respectively. Therefore, more attention should be paid to the gas emissions of soft coal during coal mining processes.

3.4. Differences in the Gas Desorption and Diffusion Laws of the Soft Coal and Hard Coal.

Figure 10 shows the gas desorption speeds of the soft coal and hard coal and the change laws of the gas desorption amounts with time. It can be seen in Figure 10(a) that the gas desorption speeds of the soft coal and hard coal continuously decreased with the increases of time. During the initial stage of the desorption, the gas desorption speeds had decreased violently. Then, with the increases in duration, the gas desorption speeds slowly decreased. It can be seen from the curve in the red-dotted line box of Figure 10(a) and the data in Table 2 that the initial gas desorption speed of the soft coal was significantly higher than that of the hard coal. Due to the fact that the initial gas desorption speed represents the initial instantaneous gas emission in a coal body, the instantaneous gas emission of the soft coal was found to be significantly higher than that of the hard coal. Therefore, it was considered to be more likely to cause gas outbursts and transfinite accidents in the project site. It was ascertained from the data shown in Figure 10(b) and Table 2 that the gas desorption capacities of the soft coal and hard coal in each coal seam had gradually increased with time. However, the increasing trend had gradually slowed down. It was observed that the gas desorption capacity of the soft coal was also significantly higher than that of the hard coal, and the gas desorption speed and gas desorption capacity of the No. 6 coal seam were higher than those of the No. 11 coal seam.

TABLE 1: Pore structural parameters of the soft coal and hard coal in the different coal seams.

Pore structural parameters (m²/g)	Soft coal and hard coal bodies of the different coal seams			
	No. 6 soft	No. 6 hard	No. 11 soft	No. 11 hard
BET specific surface areas	3.5421	1.8008	1.6179	0.8278
BJH specific surface areas	2.9642	1.4593	1.4921	0.453

(a)

(b)
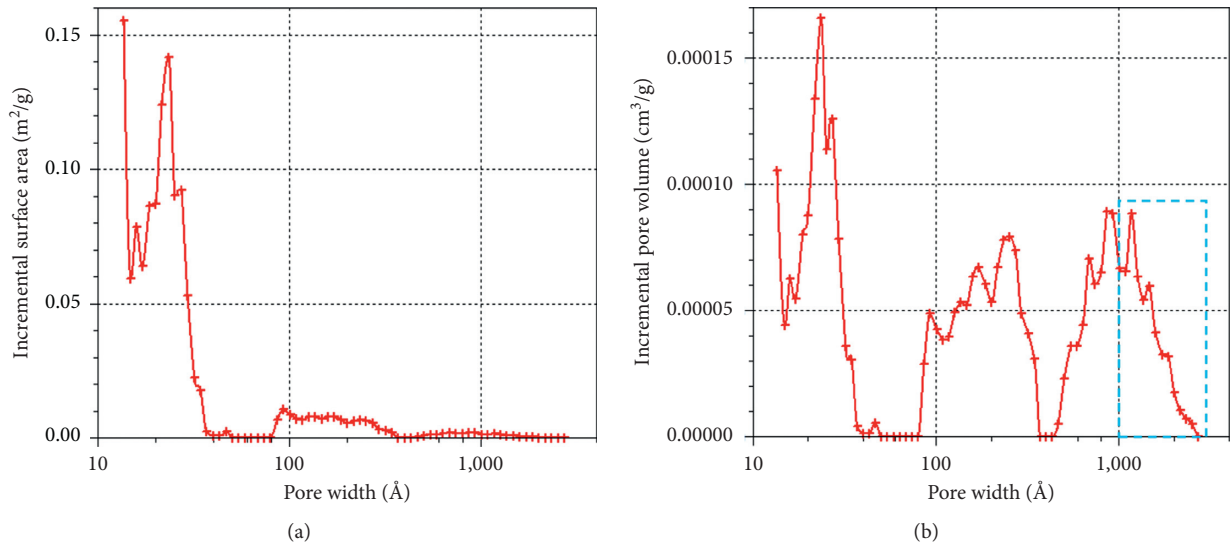
FIGURE 5: Diagram of the relationships between the increments of the pore sizes and the specific surface areas and the increments of the pore volumes of the soft coal of the No. 6 coal seam. (a) Relationships between the increments of the pore sizes and the specific surface areas. (b) Relationship between the increments of the pore sizes and the pore volumes; A is 10^{-1} nm.

(a)

(b)
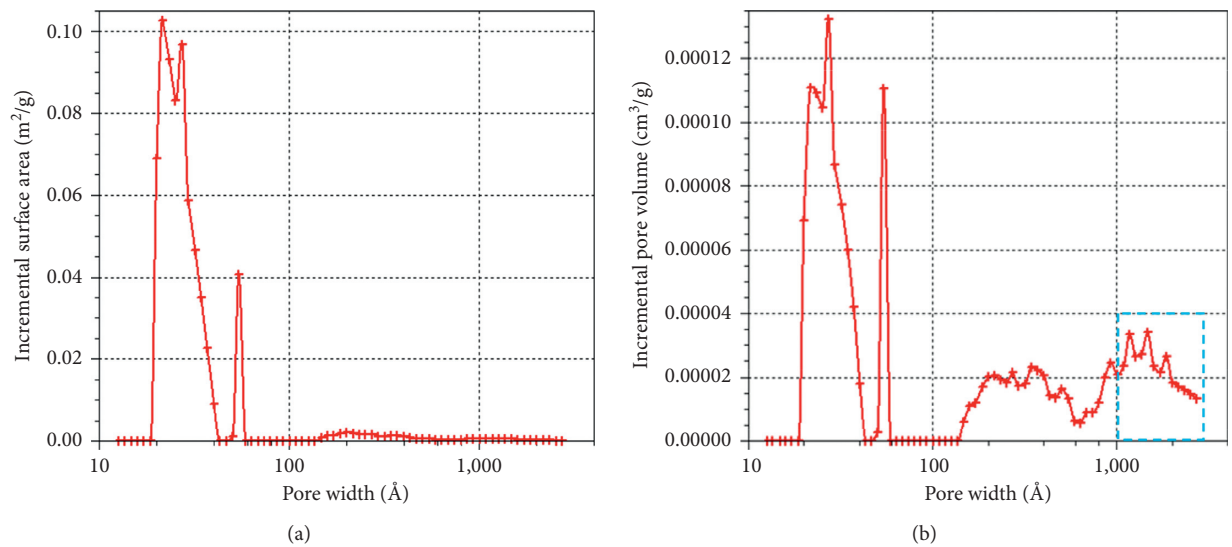
FIGURE 6: Diagram of the relationships between the increments of the pore sizes and the specific surface areas and the increments of the pore volumes of the hard coal in the No. 6 coal seam. (a) Relationships between the increments of the pore sizes and the specific surface areas. (b) Relationships between the increments of the pore sizes and the pore volumes; A is 10^{-1} nm.

(a)

(b)
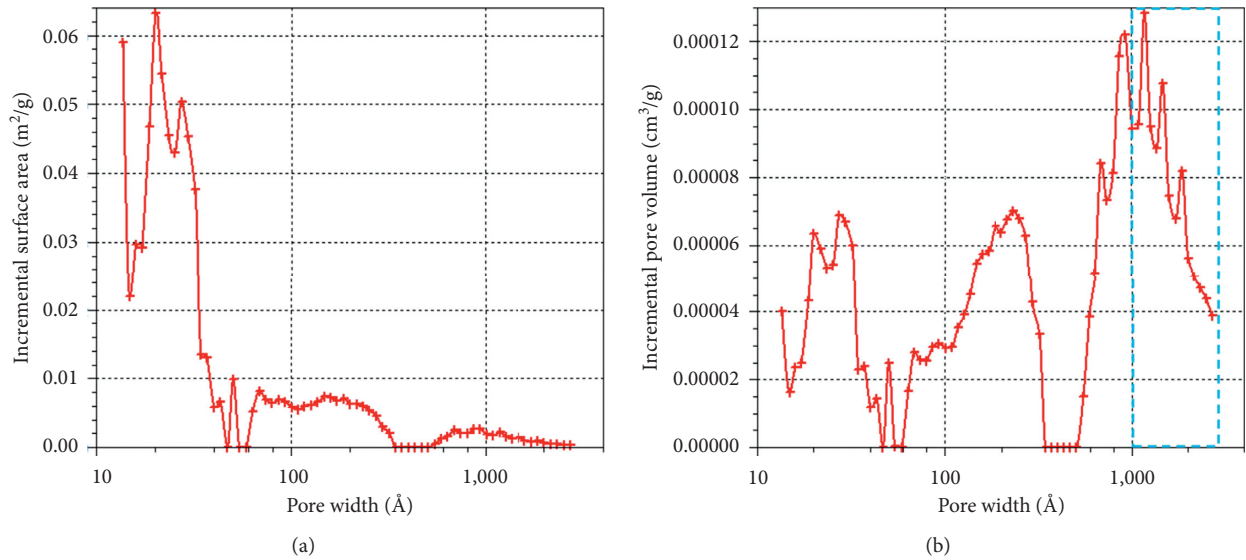
FIGURE 7: Diagram of the relationships between the increments of the pore sizes and the specific surface areas and the increments of pore volumes of the hard coal of the No. 11 coal seam. (a) Relationships between the increments of the pore sizes and the specific surface areas. (b) Relationships between the increments of the pore sizes and the pore volumes; (A) is 10^{-1} nm.

(a)

(b)
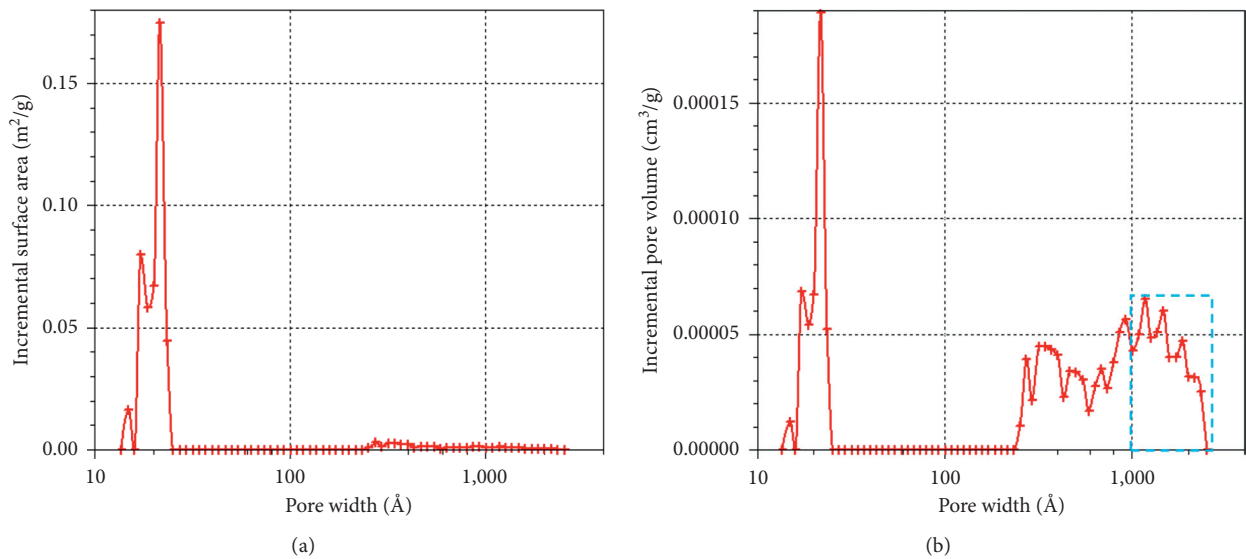
FIGURE 8: Diagram of the relationships between the increments of the pore sizes and the specific surface areas and the increments of the pore volumes of the hard coal of the No. 11 coal seam. (a) Relationships between the increments of the pore sizes and the specific surface areas. (b) Relationships between the increments of the pore sizes and the pore volumes; (A) is 10^{-1} nm.

4. Differential Mechanism Analysis of the Gas Diffusion and Migration Processes in the Soft Coal and Hard Coal

In accordance with the pore classification method, micropores and pores provide the majority of the specific surface areas in pore structures and are the main sites for gas adsorption and storage. The BET specific surface areas of the soft coal and hard coal were found to be quite different, which indicated that the gas adsorption capacities of the soft coal and hard coal were also different. The increments of the specific surface areas and pore

volumes of the mesopores and large pores of the soft coal were found to be much larger than those of the hard coal. In addition, since the mesopores and large pores were the main paths and channels for gas desorption in the micropores and small pores, the increases of the specific surface areas and pore volumes of the mesopores and large pores provided more spacious and advantageous channels for gas diffusion in the micropores and small pores. That is to say, the smaller the damage degree of the coal dust was (e.g., the greater the firmness coefficient), the longer the paths of the gas diffusion in the micropores and small pores would be and in turn the greater the
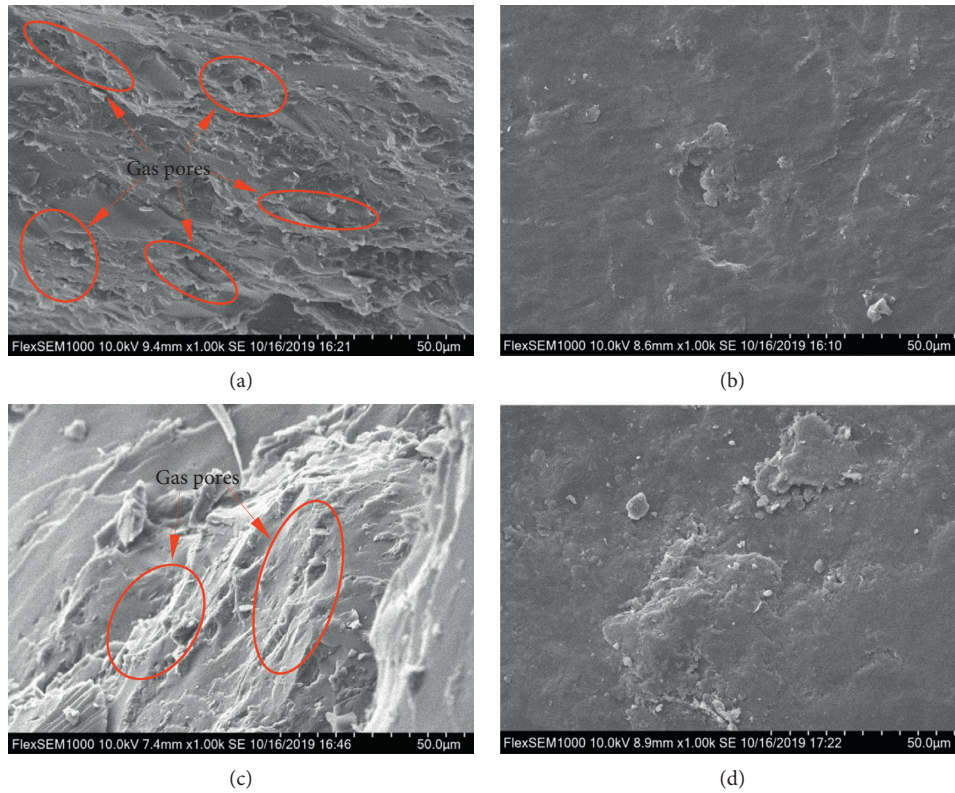
FIGURE 9: Microscanning results of the soft coal and hard coal. (a) No. 6 soft coal. (b) No. 6 hard coal. (c) No. 11 soft coal. (d) No. 11 hard coal.
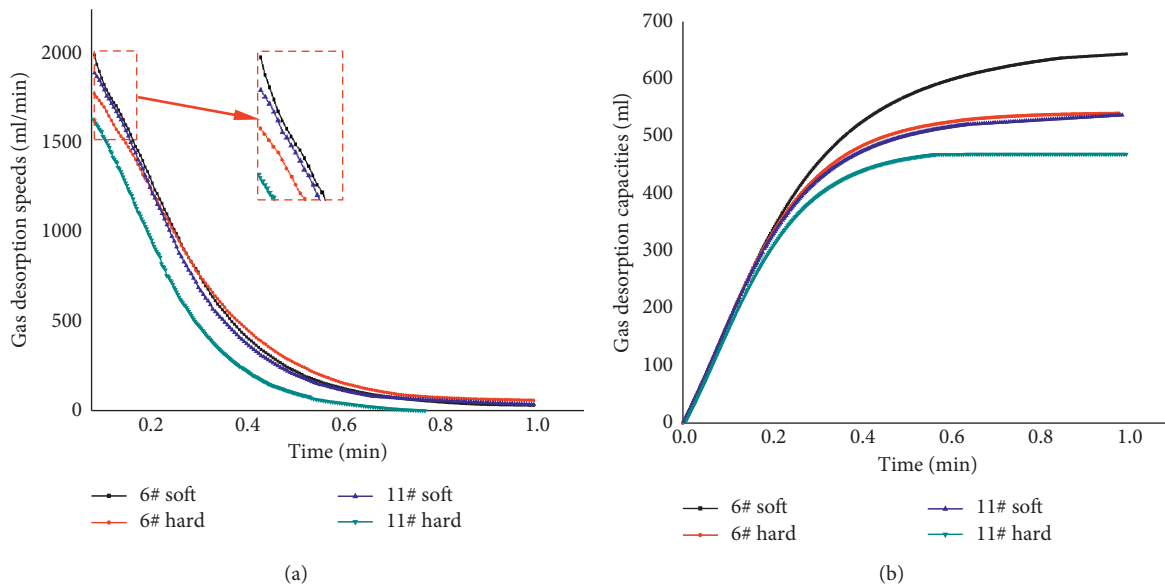
FIGURE 10: Gas desorption laws of the soft coal and hard coal. (a) Gas desorption speeds of the soft coal and hard coal. (b) Gas desorption capacities of the soft coal and hard coal.

resistance would be. Therefore, the increases in the damage degrees were equivalent to widening the channels for gas desorption in the micropores and small pores, which subsequently shortened the paths of gas diffusion and reduced the resistance of gas diffusion. This resulted

in increases in the initial velocity of the gas released in the micropores and small pores. The mesopores of the soft coal were observed to be much larger than those of the hard coal. It was found that when the gas stored in the mesopores was desorbed, it did not need to directly

TABLE 2: Gas desorption parameters of the soft coal and hard coal in the different coal seams.

Gas desorption parameters	Soft coal and hard coal bodies of the different coal seams			
	No. 6 soft	No. 6 hard	No. 11 soft	No. 11 hard
Initial speed of the gas desorption (ml/min)	1993.26	1775.02	1924.53	1695.36
Gas desorption (ml)	643.45	539.74	630.98	532.02
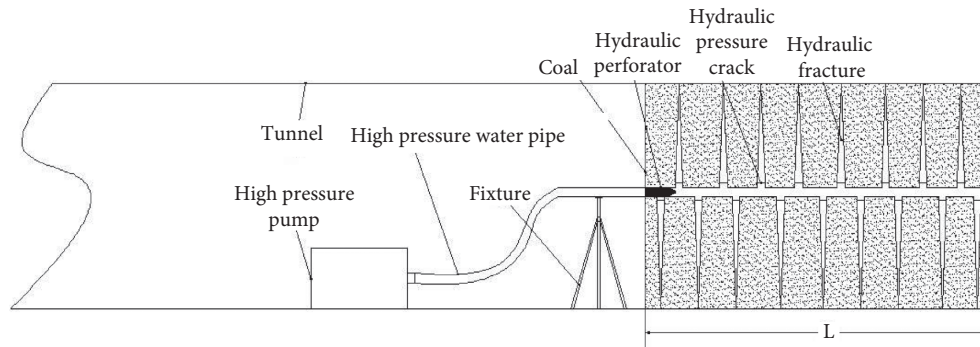
FIGURE 11: Schematic diagram of hydraulic perforation-hydraulic fracturing-gas drainage.
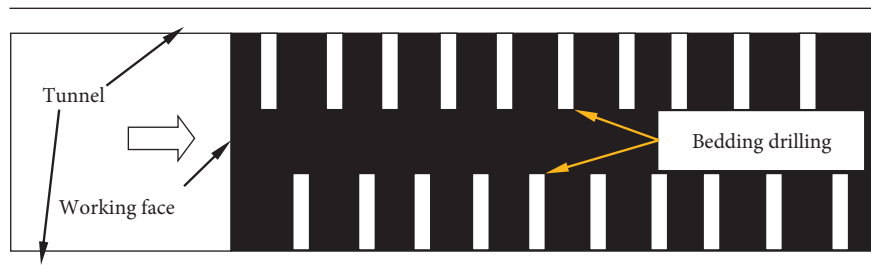
FIGURE 12: Gas drainage diagram of coal seam in working face.
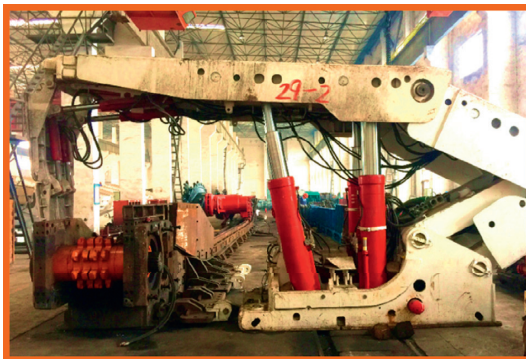
FIGURE 13: "Rigid support + flexible metal mesh" new rigid flexible composite active support system.

diffuse to the large pores or coal surfaces through the micropores or small pores. This had resulted in the initial velocity of the mesopore gas diffusion of the soft coal to be much faster than that of the hard coal. It was concluded in this study that this was the basic reason why the gas diffusion coefficient of the soft coal was larger than that of the hard coal. Therefore, the differences in the gas diffusion paths stored in different pores and locations could be considered as the reason why the gas diffusion coefficient of the coal particles had changed with time.

5. Engineering Case

According to the above research results, the combined mode of hydraulic perforation-hydraulic fracturing-gas drainage was adopted in the tunneling process of Xieqiao coal mine to preextract the gas in the coal body during the tunneling process, as shown in Figure 11. Before mining the coal seam in the working face, the bottom plate was used to dig the gas predrainage roadway to extract part of the gas in the coal seam. Before mining in the working face, the gas in the coal seam was extracted by drilling along the seam, as shown in Figure 12.

Due to the fact that the soft coal body has the problems of soft crushing and being easy to slice, we designed and adopted a new type of rigid flexible composite active support system of "rigid support + flexible metal net," which solved the problem of easy slicing of soft coal body in the coal seam and effectively prevented the sudden gas emission caused by the slice of coal wall, as shown in Figure 13. The effect is very good.

6. Conclusions

In the current research study, the differences in the characteristics of gas diffusion between soft coal and hard coal were examined from macroaspects, mesoaspects, and microaspects. The basic mechanism of the gas diffusion differences between the soft coal and hard coal was revealed and verified by the

results of this study's gas desorption experiments. Through the above analysis and research results for soft coal and hard coal, there are important guiding significance and promotion value for gas regional control in the field construction process of working face. The following conclusions were obtained:

(1) In view of the special situation of gas emission in coal mines, this paper makes an in-depth study on the nature of abnormal gas emission law of soft coal and hard coal from macroaspects, mesoaspects, and microaspects. The mechanism of gas emission difference between soft coal and hard coal is revealed, which provides basis for the prevention and control of coal seam gas disaster under similar conditions, and has important significance.

(2) In the macroaspects and mesostructures of the soft coal, the particles were observed to be flakey with fingernail-like shapes, and there were generally no complete blocks. However, the hard coal was mainly composed of complete block structures. In addition, the proportion of coal particles sized below the particle size limit (6 mm) of the soft coal was much higher than that of the hard coal.

(3) The pores and fissures of the soft coal were found to be more developed than those of the hard coal. The BET and BJH specific surface areas of the soft coal were found to be more than twice those of the hard coal. Furthermore, the pore specific surface area increments and pore volume increments of the soft coal particles greater than 100 nm were found to be more than twice those of the hard coal. Therefore, the gas adsorption and diffusion migration conditions of the soft coal were superior to those of the hard coal.

(4) The experimental results of the soft coal and hard coal gas desorption showed that the gas desorption speeds, gas desorption capacities, initial gas desorption speeds, and other parameters were significantly higher for the soft coal than for the hard coal. Therefore, it was concluded that the soft coal was more likely to cause gas outbursts and transfinite accidents in a project site.

(5) A combined method of hydraulic perforation-hydraulic fracturing-gas extraction was put forward to extract the gas in the process of roadway excavation. The gas in the working face is extracted by drilling along the layer. According to the problems of soft coal, such as being soft and broken and being easy to slice, we designed a new type of rigid flexible composite active support system of "rigid support + flexible metal net," which solved the problem easy slicing of soft coal in the coal seam and effectively prevented the coal wall slice from causing the gas to gush out suddenly. The effect is very good.

Data Availability

The data used to support the findings of this study are included within the article.

Conflicts of Interest

The author declares that there are no conflicts of interest regarding the publication of this paper.

Acknowledgments

References

[1] Q. Xu and K. Xu, "Mine safety assessment using gray relational analysis and bow tie model," *Plos One*, vol. 13, no. 3, Article ID e0193576, 2018.

[2] Y. Yuan, Z. Chen, X. Zhang, and Z. Wang, "Intermediate coal pillar instability and permeability evolution in extremely thin protective seam by auger mining," *Arabian Journal of Geosciences*, vol. 12, no. 10, 2019.

[3] Q. Sun, J. Zhang, Q. Zhang, W. Yin, and D. Germain, "A protective seam with nearly whole rock mining technology for controlling coal and gas outburst hazards: a case study," *Natural Hazards*, vol. 84, 2016.

[4] W. Zhao, Y. Cheng, P. Guo, K. Jin, and H. Wang, "An analysis of the gas-solid plug flow formation: new insights into the coal failure process during coal and gas outbursts," *Powder Technology*, vol. 305, pp. 39–47, 2016.

[5] A. T. Zhou, K. Wang, T. A. Kiryaeva, and V. N. Oparin, "Regularities of two-phase gas flow under coal and gas outbursts in mines," *Journal of Mining Science*, vol. 53, no. 3, pp. 533–543, 2017.

[6] L. Cheng, "A sequential approach for integrated coal and gas mining of closely-spaced outburst coal seams: results from a case study including mine safety improvements and greenhouse gas reductions," *Energies*, vol. 11, p. 11, 2018.

[7] A. Zhou and W. Kai, "A new gas extraction technique for high-gas multi-seam mining: a case study in Yangquan Coalfield, China," *Environmental Earth Sciences*, vol. 77, p. 150, 2018.

[8] G. Lu, C. Wei, J. Wang, J. Zhang, and L. Soh Tamehe, "The variation of surface free energy in the process of methane adsorption in the nanopores of tectonically deformed coals: a case study of middle-rank tectonically deformed coals in the huaibei coalfield," *Energy & Fuels*, vol. 77, 2019.

[9] X. Zhang, P. G. Ranjith, and M. S. A. Perera, "Gas transportation and enhanced coalbed methane recovery processes in deep coal seams: a review," *Energy & Fuels*, vol. 30, p. 11, 2016.

[10] H. Zhang, Y. Cheng, L. Yuan, L. Wang, and Z. Pan, "Hydraulic flushing in soft coal sublayer: gas extraction enhancement mechanism and field application," *Energy Science and Engineering*, vol. 7, no. 1, 2019.

[11] M. Ya and L. Zhiping, "Experimental comparisons of gas adsorption, sorption induced strain, diffusivity and permeability for low and high rank coals," *Fuel*, vol. 234, pp. 914–923, 2018.

[12] Q. Tu, Y. Cheng, P. Guo, J. Jiang, L. Wang, and R. Zhang, "Experimental study of coal and gas outbursts related to gas-enriched areas," *Rock Mechanics & Rock Engineering*, vol. 49, no. 9, pp. 3769–3781, 2018.

[13] K. Jin, Y. Cheng, T. Ren, W. Zhao, Q. Tu, and J. Dong, "Experimental investigation on the formation and transport mechanism of outburst coal-gas flow: implications for the role of gas desorption in the development stage of outburst," *International Journal of Coal Geology*, vol. 194, pp. 45–58, 2018.

[14] Q. Liu, E. Wang, X. Kong, Q. Li, S. Hu, and D. Li, "Numerical simulation on the coupling law of stress and gas pressure in the uncovering tectonic coal by cross-cut," *International Journal of Rock Mechanics and Mining Sciences*, vol. 103, pp. 33–42, 2018.

[15] B. Lin, Q. Zou, Y. Liang, J. Xie, and H. Yang, "Response characteristics of coal subjected to coupling static and waterjet impact loads," *International Journal of Rock Mechanics and Mining Sciences*, vol. 103, pp. 155–167, 2018.

[16] Z. Wang, J. Pan, Q. Hou, B. Yu, M. Li, and Q. Niu, "Anisotropic characteristics of low-rank coal fractures in the Fukang mining area, China," *Fuel*, vol. 211, pp. 182–193, 2018.

[17] P. Guo, Y. Cheng, K. Jin, W. Li, Q. Tu, and H. Liu, "Impact of effective stress and matrix deformation on the coal fracture permeability," *Transport in Porous Media*, vol. 103, no. 1, pp. 99–115, 2017.

[18] L. Zhang, Z. Ye, J. Tang, and D. Hao, "Comparative experiment study on nitrogen injection and free desorption of methane-rich bituminous coal under triaxial loading," *Archives of Mining Sciences*, vol. 62, no. 4, pp. 911–928, 2017.

[19] Q. Zhang, Y. Cheng, Q. Liu et al., "Investigation of the formation mechanism of coal spallation through the cross-coupling relations of multiple physical processes," *International Journal of Rock Mechanics and Mining Sciences*, vol. 105, pp. 133–144, 2018.

[20] M.-Y. Jiang, Y.-P. Cheng, J.-C. Wang, H.-R. Li, and N. Wang, "Experimental investigation on the mechanical characteristics of gas-bearing coal considering the impact of moisture," *Arabian Journal of Geosciences*, vol. 12, no. 18, 2019.

[21] G. Haijun, Y. Liang, C. Yuanping et al., "Effect of moisture on the desorption and unsteady-state diffusion properties of gas in low-rank coal," *Journal of Natural Gas Science and Engineering*, vol. 57, pp. 45–51, 2018.

[22] B. Hu, Y. Cheng, Z. Wang, X. He, and L. Wang, "Effect of pulverization on the microporous and ultramicroporous structures of coal using low-pressure CO_2 adsorption," *Energy & Fuels*, vol. 2019, 2019.

[23] W. Szott, A. Gołąbek, K. Sowiżdżał, and P. Łętkowski, "Numerical studies of improved methane drainage technologies by stimulating coal seams in multi-seam mining layouts," *International Journal of Rock Mechanics and Mining Sciences*, vol. 108, pp. 157–168, 2018.

[24] G. Słota-Valim, Z. Yin, L. Wang, Z. Hu, and C. Zhu, "Effects of gas pressure on the failure characteristics of coal," *Rock Mechanics and Rock Engineering*, vol. 50, no. 7, pp. 1711–1723, 2017.

[25] Z. Yin, W. Chen, H. Hao et al., "Dynamic compressive test of gas-containing coal using a modified split Hopkinson pressure bar system," *Rock Mechanics and Rock Engineering*, vol. 53, no. 2, pp. 815–829, 2020.

Research Article

Analysis of the Damage Characteristics and Energy Dissipation of Rocks with a Vertical Hole under Cyclic Impact Loads

Bing Dai [1,2,3] Xinyao Luo,[1] Li Chen,[2] Yakun Tian [1] Zhijun Zhang [1,3] Ying Chen [1,3] and Qiwei Shan[1]

[1]*School of Resources Environment and Safety Engineering, University of South China, Hengyang, China*
[2]*Deep Mining Laboratory of Gold Group Co., Ltd, Laizhou, China*
[3]*Hunan Province Engineering Technology, Research Center for Disaster Prediction and Control on Mining Geotechnical Engineering, 421001 Hengyang, China*

Correspondence should be addressed to Yakun Tian; 1090596259@qq.com and Ying Chen; csu_chenying@csu.edu.cn

This study systematically investigates the failure patterns, energy dissipation, and fracture behavior of rock specimens containing a vertical hole under impact loads. First, an improved damage calculation equation suitable for the analysis of rock specimens with a vertical hole is obtained based on the one-dimensional stress wave theory and the interface continuity condition. After that, the Hopkinson pressure bar (SHPB) device was used to conduct cyclic impact tests with different impact pressures and impact modes (impact pressures with equal amplitude and unequal amplitude). The experimental results suggest that, under the equal-amplitude high pressure and unequal-amplitude pressure, the degree of damage of the rock significantly increased, the bearing capacity greatly reduced, and the rock gradually transitions from having good ductility to experiencing brittle failure. The cumulative specific energy absorption value gradually increases with the increase in the cyclic impact. Compared to that of the equal impact condition, the degree of damage to the rock is more severe for the case of equal-amplitude high pressure and unequal impact, and the failure mode undergoes a transformation from transverse tensile failure to transverse tensile failure-axial splitting failure combination and axial splitting failure. Through the analysis of rock energy changes and rock failure patterns during cyclic impact, it will be helpful to predict and control the fracture caused by local stress concentration during excavation, thus can reduce the cost of support and reinforcement in excavation and improve the stability of surrounding rocks.

1. Introduction

Unexpected swift increases in urbanization throughout the world have brought the demand for more land and faster transportation between cities or intercity. In order to keep pace with the demand, more and more underground engineering, highways, and railways are under construction [1–3]. In these constructions, it is unavoidable to encounter the excavation work. Blast and mechanical excavations are the usual way to accomplish this process. As the main medium in various underground projects, rock is inevitably subjected to dynamic loads, such as mechanical drilling and blasting, during the construction of a tunnel or city underground engineering, which causes the internal structure

and energy of the surrounding rocks to change, and long-term accumulation will cause hidden safety risks.

Therefore, many scholars have performed substantial research on the dynamic mechanical properties, damage, and energy dissipation of rocks under dynamic loads [4–6]. Zhu et al. [7] used a large-diameter SHPB device to conduct cyclic impact tests, analyzed the mechanical characteristics and energy absorption trends of granite, and obtained a damage model based on the Weibull distribution. Gong et al. [8] used a modified triaxial SHPB system to analyze the relationship between high strain rate, low yield pressure, and the dynamic mechanical properties of sandstone. Shu et al. [9] heat treated granite under a cyclic impact load test and obtained the relationship between the rock energy and

failure patterns with the temperature. Peng et al. [10, 11] revealed the effects of confining pressure on physical quantities, such as the stress-strain and damage factor, by using different confining pressures for tests on sandstone and gained the relationship among the strain rate, energy, and damage degree. Tao et al. [12] studied the dynamic failure process of granodiorite rock including an elliptical hole, and the results indicated that the elliptical hole in rock may lead to obvious stress concentration and energy accumulation which can cause considerable decreases in the strength parameters.

In the practical underground engineering, undisturbed rock mass encompasses various defects such as fissures, joints, weak surfaces, pores, and cavities [13]. The instability and failure of a rock mass usually begins with initial defects, such as holes and fissures. At present, there are few reports on studies of rock with defects under dynamic loading. Zhou [14, 15] analyzed the crack propagation and failure process of prefabricated cracks and holes in layered sandstone and marble, respectively, by using a high-speed camera and described the effects of the crack inclination, hole shape, and size on the dynamic compressive strength. Li et al. [16] carried out experiments on prismatic marble specimens containing a single flaw using a modified SPHB and revealed that the geometry of the flaws may have a slight effect on the failure modes of flawed rock under impact loading. Tao et al. [17] prefabricated round holes in granite and observed the failure process of the specimen under different combinations of static and dynamic stress with a high-speed camera. Based on the true triaxial static load and vertical dynamic load, Liu et al. [18] carried out rock burst tests on the sandstone samples with holes in the center and compared and analyzed the characteristics of fragments and energy dissipation after failure obtained by the two loading methods. Wu et al. [19] analyzed the fracture morphology on the axial surface by using the SHPB device, and the results showed that the energy absorption rate and energy consumption density decrease firstly and then increase.

In the cumulative process of damage under cyclic dynamic loads, the mechanical properties of the rock become gradually degraded, the ability to withstand external dynamic load becomes lower, and the integrity becomes worse. In addition, the original rock stress further aggravates the damage of the rock, resulting in the reduction of the bearing capacity and stability of the rock mass. Therefore, rock damage under dynamic loading and its evolution law are the important research topics in rock dynamics. The methods for defining rock mass damage variables include elastic modulus method, ultrasonic wave velocity method, density and gravity method, energy method, strain method [20], CT method, and acoustic emission cumulative number method [21]. In addition, many scholars have derived constitutive models which were suitable for defining the rock mass damage through research. Zhu et al. [22] proposed a linear damage model for rock mass based on cyclic loading times and fatigue life, but its accuracy was far from the actual situation. Based on the deformation characteristics of rocks under cyclic loading, Zheng et al. [23] established a fatigue damage model related to failure factors under triaxial cyclic

loading, which could be applied to engineering practice. Meng et al. [24] established a dynamic statistical damage constitutive model under Weibull distribution, which was suitable for dynamic load conditions, and its calculation curve was in good agreement with the test curve. Wu et al. [25] proposed a quantitative method of rock impact fatigue performance for the engineering application under repeated blasting. Chen et al. [26] selected different damage variables from different perspectives with respect to the random distribution of microscopic unit strength of rocks and established two damage constitutive models subject to lognormal distribution, which were effectively proved by triaxial compression test data.

With respect to the rock with various defects, research on prefabricated cavity rocks in the energy and damage fields is also very important. Zhou et al. [27] tested the marble specimens with single or two rectangular holes in different layouts under uniaxial compression and revealed the relationship between absorption energy per unit volume and the degree of crushing of the specimens. Based on the theory of particle discrete element, Scholtès and Donzé [28] carried out numerical simulation of compression failure process of tuffaceous sandstone with holes under the conditions of uniaxial, biaxial, and triaxial, and the results showed that the strain energy and dissipation could reflect the rock destruction process and degree of the sliding and friction of the mesoscopic particles. Liu et al. [18] conducted true triaxial static load and vertical dynamic load rockburst tests on sandstone samples with central hole, analyzed the relationship between the number of debris particles and energy dissipation, and concluded that the energy dissipation of the rockburst test was greater than that of the uniaxial compression test. In terms of damage research, Matvienko et al. [29] used electronic speckle interferometry (ESPI) to measure the deformation response of local materials caused by hole defects under low-period fatigue load and proposed and verified a new method for quantitative determination of damage accumulation in the stress concentration area.

As shown in Figure 1, in previous research on the dynamic characteristics of rock with holes, transverse holes were prefabricated in the vertical direction of the dynamic load. Few scholars have studied the damage accumulation and energy dissipation of vertical hole rocks distributed in the direction of the dynamic load. In the study of rock failure mechanism in underground excavation engineering, rocks are usually divided into two types. The first type regards the hole as the excavation cavern, such as tunnel [30] and chamber [31]. The second type regards the hole as the initial defect inside the rocks [17, 18]. If the hole is regarded as a cavern, the transverse hole and the vertical hole can be regarded as the propagation of stress wave on the hole plane and the propagation on the vertical hole plane. If the hole is regarded as the initial defect, the difference between them is the distribution in the rocks relative to the stress wave propagation direction. The disturbance of two-way excavation in tunnel engineering usually acts in the direction of the hole. When the two-way excavation of the tunnel is close to penetration, the drilling and blasting of the tunnel on one side greatly affects the stability of the surrounding rock of the
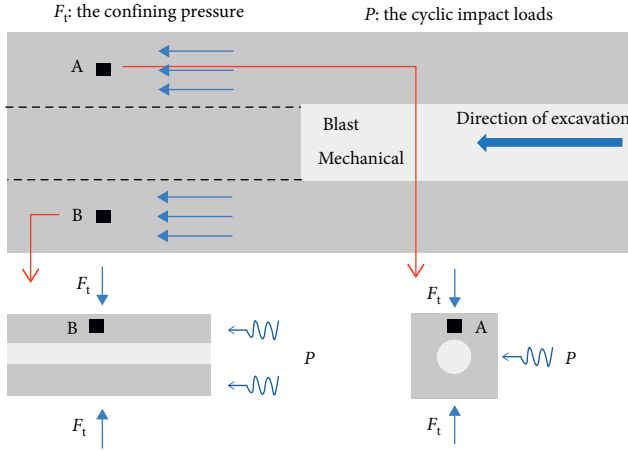
FIGURE 1: Sketch of rock mass subjected to cyclic dynamic loads in excavation.

tunnel on the other side. The impact load generated by actual drilling and blasting often varies [32]. Therefore, this article will use a SHPB device to carry out cyclic impact tests of equal and unequal pressures on granite with vertical holes, compare and analyze the cumulative damage and energy dissipation characteristics of rock samples, and explore the response characteristics of rocks under different pressure impacts. A theoretical reference will also be provided for correctly understanding the granite failure mechanism and the engineering confining pressure stability under actual conditions.

2. Methodology: Establishment of the Damage Model

Jiefang et al. [33] deduced the expression for wave impedance from incident waves, reflected waves, and transmitted waves based on one-dimensional stress wave theory. The results show that the damage variables defined based on the wave impedance exist in the rock fatigue mechanical properties from the initial stage to the low-speed stage and the acceleration stage, which have the same trend as the damage variables defined by the P-wave velocity. Therefore, the wave impedance of the specimen is used to define the change in the damage to the rock in this cyclic impact test. The degree of damage D to the specimen can be expressed as

$$D = 1 - \left(\frac{\overline{\rho C}}{\rho C}\right)^{1.6}, \tag{1}$$

where $\overline{\rho C}$ is the wave impedance in a certain damage state of the rock and ρC is the wave impedance in the initial state of the rock. The vertical hole is prefabricated in the center of the cylindrical rock sample in this test, so the cross-sectional areas of the elastic rod and the test specimen are not equal. The equation for calculating the wave impedance derived by Jin cannot be directly applied to this experiment. It is assumed that the contact surface between the rock and the elastic rod is a two-elastic half-space contact surface

with displacement discontinuity. At this time, the propagation of the stress wave at the contact surface can be transformed to solve the boundary value problem of the wave equation.

As shown in Figure 2, when the stress wave enters the specimen from the rod part, the wave resistance changes from m_t to m_s at the interface according to the one-dimensional stress wave theory [34]. The continuous condition on I-II has the following equations:

$$P_R = \lambda P_I, \tag{2}$$

$$P'_T = (1 - \lambda)P_I, \tag{3}$$

$$m_t = \rho_t C_t A_t, \tag{4}$$

$$m_s = \rho_s C_s A_s, \tag{5}$$

$$\lambda = \frac{m_t - m_s}{m_t + m_s}, \tag{6}$$

where P_I, P_R, and P'_T are the incident wave, reflected wave, and transmitted wave in the specimen, respectively; A_t, A_s, ρ_t, ρ_s, C_t, and C_s are the cross-sectional area, density, and P-wave velocity of the elastic rod and the specimen, respectively; and λ is the reflectance of the one-dimensional longitudinal wave when it enters the specimen from the incident rod.

In actual experiments, since the reflected wave and the incident wave are measured by the same strain gauge, the incident wave may still be present when the reflected wave is present, and then the starting point of the reflected wave will be greatly affected by the incident wave. At this time, the corresponding time is difficult to be determined, which can cause data errors, but the starting point of the transmitted wave will not be disturbed by the incident wave, so equation (3) can be used to derive the damage model. Then, the incident wave and the transmitted wave are functions of time, and equation (3) is transformed into a continuous condition on interface III-IV to obtain the following equation:

$$\sigma_T(t_i) = \left(1 - \lambda^2\right)\sigma_I(t_i). \tag{7}$$

Knowing the wave impedance of the elastic rod and the rock specimen, the time relationship between the wave impedance and the wave can be obtained by combining equations (6) and (7):

$$f(t_i) = \frac{\sigma_T(t_i)}{\sigma_I(t_i)} = \frac{4m_t m_s}{(m_t + m_s)^2}, \tag{8}$$

where $\sigma_I t_i$ and $\sigma_T t_i$ are the incident wave and transmission wave of the i-th impact wave, respectively, and $f(t_i)$ is the ratio of the i-th shock transmitted wave to the incident wave. By bringing equations (4) and (5) into equation (8) and solving the root of the quadratic equation by the inverse function transformation and global substitution, the effective expression of the wave impedance of the rock specimen at the i-th impact at a certain moment can be obtained:
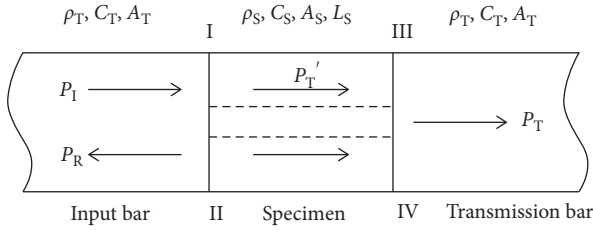
FIGURE 2: Transmission and reflection of the one-dimensional longitudinal wave in the specimen.

$$\rho_i C_i = \zeta \frac{2 - f(t_i) - 2\sqrt{1 - f(t_i)}}{f(t_i)} \rho_t C_t, \qquad (9)$$

$$\zeta = \frac{A_s}{A_t}. \qquad (10)$$

The following expression of rock damage can be obtained by substituting equation (9) into equation (1):

$$D = 1 - \left(\zeta \frac{2 - f(t_i) - 2\sqrt{1 - f(t_i)}}{f(t_i)} \frac{\rho_t C_t}{\rho C} \right)^{1.6}, \qquad (11)$$

where $\rho_i C_i$ is the wave impedance value of the i-th impact rock specimen and ζ is the cross-section proportionality coefficient between the specimen and the elastic rod. In this test, the average diameter of the granite section is $\overline{D} = 4.85$ cm, and the average diameter of the pores is $\overline{d} = 1.10$ cm. The result is $\overline{\zeta} = 0.8925$. Since one impact of the specimen is the result of incident and multiple reflections, the wave impedance value of the rock specimen is always changing throughout the process. Li [33, 35] pointed out that when $t \leq (2L_s/C_s)$, the measured reflected and transmitted waves will not be affected by secondary and more reflections and transmissions, and the wave impedance change trend is relatively gentle during this period. Figure 3 shows the relationship between the wave impedance and time when D-0.6-1 is impacted. It can be seen from the figure that there is a relatively stable area of wave impedance after point A, and it has a similar slope of change. After point B, a downward trend begins. At this time, the fissures inside the rock initiate and further expand. Therefore, a point on AB in the $(0, 2L_s/C_s)$ time section is selected as the fixed time point for the calculation of the wave impedance.

3. Experimental Design

3.1. Sample Preparation.

The rock sample is granite with good integrity and homogeneity, with a density of 2790 kg/m³, a P-wave velocity of 5345 m/s, and an elastic modulus of approximately 40.7 GPa. Figure 4 shows a prefabricated granite specimen with vertical holes. The test specimen is made into a cylindrical rock sample with a growth diameter ratio of 2 : 1, a size of ϕ50 mm × 100 mm, and a vertical hole in the center of the circular cross section with a diameter of 10 mm. Before testing, the two ends and sides of the specimen are carefully polished to ensure that their
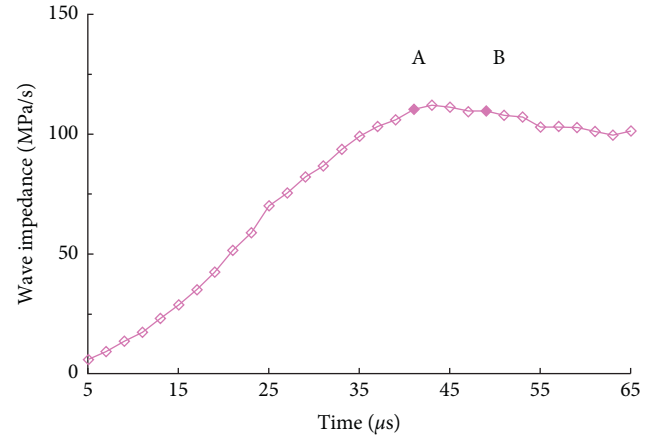
FIGURE 3: The trend of the wave impedance of the specimen over time.

nonparallelism and nonverticality are less than 0.02 mm. High-pressure water cutting technology is used to precast vertical holes in the center of the circular cross section of the specimen with a water jet cutting machine to avoid mechanical damage to the rock sample body caused by the process of smoothing the hole surface.

3.2. Experimental Equipment.

The test equipment is a 50 mm diameter Hopkinson pressure bar (SHPB) device from Central South University. The punch, incident rod, transmission rod, and absorption rod of the device are made of 40Cr alloy steel. The longitudinal wave velocity is 5400 m/s, the density is 7810 kg/m³, the elastic modulus is 240 GPa, and the wave impedance is 4.2×10^7 MPa/s. Two sets of strain gauges are attached to the incident rod and the transmission rod, and the deformation of the rod is collected and displayed with the help of a CS-1D superdynamic strain gauge and a DL-750 oscilloscope. In the launch cavity, PC vibration is eliminated to achieve half-sine wave loading, thereby achieving a constant strain rate loading. Figure 5 shows a schematic diagram of the SHPB test system and testing equipment.

3.3. Experimental Plan

3.3.1. The Method.

To study the law and to compare the strain damage and energy dissipation of granite under cyclic impact with equal amplitude and cyclic impact with unequal amplitude, the impact air pressure was set to 0.6 MPa, 0.7 MPa, and 0.8 MPa for cyclic impact. The cyclic effects of varying loads on the rock mass during blasting were simulated using impact pressures of 0.6–0.7 MPa and 0.7–0.8 MPa with different amplitudes. The number of specimens with equal and unequal impacts is represented as D-0.6-1 and B-0.6-1, respectively, where D and B represent the equal and unequal amplitudes, respectively, and 0.6 represents the equal and unequal impact pressures. The initial impact air pressure, 1, is the test group number. There are a total of 5 test groups, and each group is cyclically impacted until failure. The details of the test protocol are shown in Table 1.
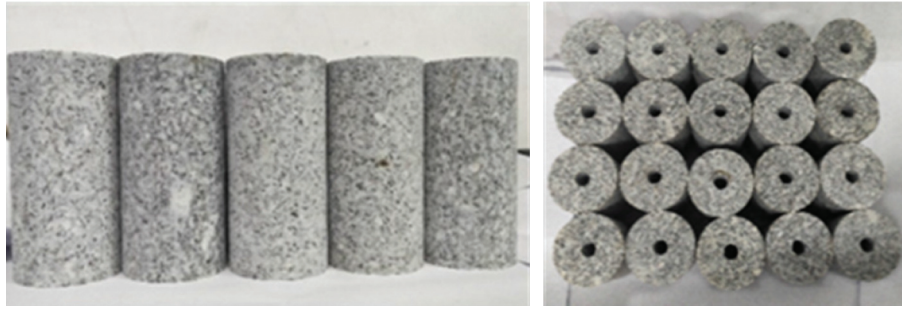
FIGURE 4: Granite specimen with a vertical hole.
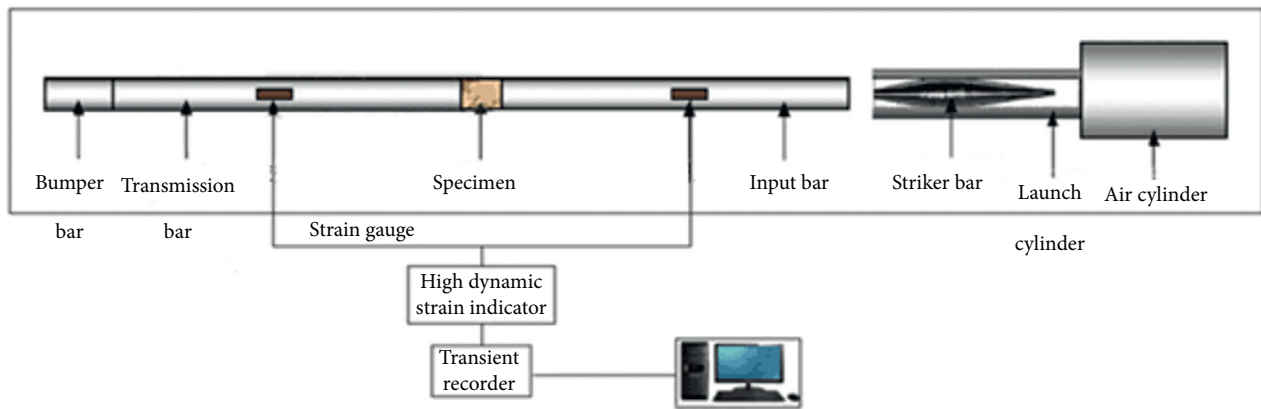
FIGURE 5: Schematic diagram of the SHPB test system and testing equipment [36].

TABLE 1: Scheme of the impact experiment.

Experimental group	Aspect ratio	Impact air pressure (MPa)
	2.0	0.6
Constant-amplitude pressure shock load	2.0	0.7
	2.0	0.8
Uneven-amplitude air pressure shock load	2.0	0.6–0.7
	2.0	0.7–0.8

3.3.2. The Procedure

(i) Before the start of the test, the incident rod and the transmission rod are closely pressed for a test punch, and the trend of the incident wave and the transmitted wave on the oscilloscope is observed to ensure that the two rods are properly connected so that the specimen can achieve stress balance during the test

(ii) During the test, butter is evenly applied to both ends of the specimen to ensure that the two ends are in good contact with the incident rod and the transmission rod since butter can reduce the impact of the friction between the rock and the rod interface during the test

(iii) The position of the punch in the transmitting cavity is adjusted, and it is confirmed that the position is fixed each time to equalize the incident stress wave on the incident rod

(iv) The cylinder air pressure is changed to the planned set value, and the strain gauge and oscilloscope are turned on for data recording

4. Results and Analysis

4.1. Experimental Results. According to the one-dimensional stress wave theory and the law of the conservation of energy, the incident energy $\sigma_I(t)$, reflected wave $\sigma_R(t)$, and transmitted wave $\sigma_R(t)$ recorded on the DL-750 oscilloscope are used to calculate the incident energy during cyclic impact, reflection energy, transmission energy, average strain rate, and absorbed energy per unit volume, and then the degree of damage after each impact is obtained from equation (11). Due to space limitations, Table 2 only lists the results of some test specimens. Table 2 shows that with the increase in the number of cyclic impacts, the absorbed energy per unit volume and the average strain rate of the specimen gradually increase and the wave impedance gradually decreases. The dynamic peak

TABLE 2: Experimental results for some granite specimens under cyclical impact loads.

Specimen number	Impact air pressure (MPa)	Number of impacts	Wave impedance (MPa/s)	Incident energy (J)	Absorption energy per unit volume (J/cm³)	Average strain rate (s⁻¹)	Dynamic peak stress (MPa)
D-0.6-2	0.6	1	127.83	78.83	0.123	24.82	113.89
		2	108.55	80.05	0.152	30.86	85.39
		3	103.68	81.86	0.156	31.14	83.09
		4	99.36	81.88	0.156	30.23	88.63
		5	93.57	75.76	0.165	32.41	82.68
		6	72.72	77.87	0.206	38.02	59.37
D-0.7-3	0.7	1	125.04	123.47	0.186	30.84	131.63
		2	111.38	126.64	0.194	31.73	129.46
		3	95.88	123.04	0.263	39.37	95.58
		4	63.03	126.11	0.291	42.09	76.46
D-0.8-3	0.8	1	117.34	163.35	0.255	36.76	150.38
		2	88.36	162.27	0.311	41.75	137.02
		3	41.09	157.22	0.415	51.67	98.94
B-0.6-1	0.6–0.7	1	123.41	83.23	0.165	27.15	74.90
		2	34.77	127.49	0.276	35.51	118.77
B-0.7-3	0.7–0.8	1	118.23	113.31	0.157	28.61	101.65
		2	26.87	152.21	0.330	39.83	129.68

stress decreases gradually during equal-amplitude impact generally, but it increases during uneven-amplitude impact.

4.2. Damage Evolution Characteristic Curve. Figure 6 shows the relationship between the degree of damage and the number of impacts during cyclic loading. From the analysis of the graph, it can be seen that the damage accumulation of rock specimens with vertical holes increases as the number of impacts increases, and basically, as the impact load increases, the cumulative damage growth rate of its cyclic impact also increases. The number of impacts gradually decreases. Due to the existence of hole defects, a large number of cracks are generated near the hole wall during the impact process, and the rock itself contains initial cracks. The analysis shows that each group of specimens has a larger damage value after the first impact. The range of this value is 0.2~0.3. Subsequent shocks are affected by the magnitude and change in the pressure of the shock, and the change law of the damage is also different.

The damage accumulation of the granite specimen D-0.6-2 slowly increased during the second to fourth impacts. At this stage, the curve change trend was relatively gentle, and the dynamic peak stress and the average strain rate were basically unchanged. After the impact, initial microcracks and pore compaction appeared inside the rock, while the crack initiation and propagation process around the hole continued, reflecting the overall situation that the deformation characteristics were relatively stable, and the rock samples had good ductility characteristics. The degree of damage to the test specimen continued to increase. At this stage, cracks occurred in various directions in the rock and around the hole. Cracks with an inclination greater than the internal friction angle began to rapidly expand and penetrate due to the insufficient bearing capacity of the specimen. The yield area of the cross section of the rock continued to increase until the specimen was damaged. The damage
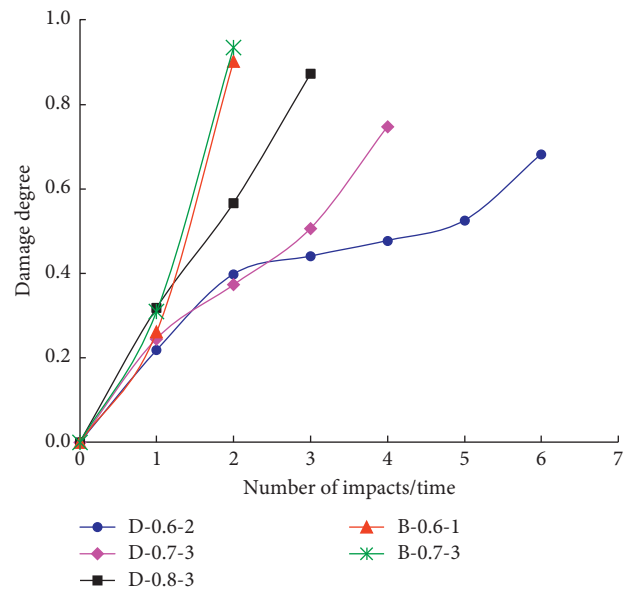
FIGURE 6: Relationship between the damage degree and number of impacts.

evolution curve for the entire process includes the process from the initial stage to the low-speed stage and the acceleration stage, which can better characterize the fatigue mechanical properties of rocks under cyclic impact. Comparing specimen D-0.6-2 and specimen D-0.7-3, due to the increase in the impact gas pressure, the damage accumulation rate in the whole process is accelerated, the number of impacts is reduced, the low-speed stage of the rock damage evolution disappears, and the dynamic peak stress gradually decreases with the number of impacts. When the dynamic load is further increased to an impact pressure of 0.8 MPa, the damage accumulation rate of specimen D-0.8-3 is much greater than that of the previous two groups, the degree of

damage increases approximately linearly, the number of impacts decreases, and the rock brittleness increases. The damage during the initial and final failure stages is also larger than that of the previous two groups. It can be considered that this result occurs because the specimen exhibited more cracks in the first impact stage, and the final impact specimen had a higher degree of fragmentation.

Both specimens B-0.6-1 and B-0.7-3, under different amplitude impacts, were destroyed after two impacts. The phenomenon occurred because the damage was small under the first impact, and the second incident was caused by the increase in the air pressure. The stress wave amplitude and strain rate increase accordingly, the impact damage accumulation sharply increases, and the relationship between the degree of damage and the number of impacts exponentially increases. Compared with that of specimen D-0.6-2 and specimen D-0.7-3, the degree of damage to the rock at this time exhibits a more dramatic, sudden increase, and the final degree of damage is also more severe. Compared with those following the equal-amplitude impact, the mechanical properties of the specimens with unequal-amplitude impact deteriorate faster, and the rock exhibits significant brittle failure characteristics. The reasons for this phenomenon will be discussed in conjunction with the energy dissipation.

Except for specimen D-0.6-2, with an impact pressure of 0.6 MPa, the peak stress value of the rock significantly decreases with an increase in the number of impacts. The crack growth rate of the vertical hole granite is greater than the strength capacity of the rock structure required after compaction. At this time, the magnitude of the impact load exceeds the critical value of the dynamic load that disappears at the low-speed stage. During the multiple impacts of the specimen, the internal cracks continue to sprout, expand, and penetrate, resulting in increased specimen damage and reduced load carrying capacity.

4.3. Analysis of the Average Strain Rate and Damage Characteristics.

The damage model deduced from the continuous condition of the interface shows that the degree of damage D is a function of the ratio of the transmitted wave $\sigma_T(t)$ to the incident wave $\sigma_I(t)$, which represents the gradual weakening of the cohesion in the rock and the degree of volume unit failure. Assuming that the rock stress is uniform and without attenuation, the strain rate $\dot{\varepsilon}$ is a function of the reflected wave $\sigma_R(t)$ in the two-wave method, which represents the rate of change of the rock strain. Therefore, there is a certain degree of damage D and strain rate $\dot{\varepsilon}$ during impact contact. Figure 7 shows the change in the degree of damage with the average strain rate under different impact air pressures of the same amplitude impact. The analysis shows that when the impact gas pressure is constant, the damage to the specimen increases with the increase in the average strain rate, which indicates that as the strain rate increases, the degree of structural deterioration caused by crack initiation and propagation in the rock is more serious. Increasing the impact air pressure causes the specimen damage accumulation curve as a whole to shift to the right, and the size of the damage under a high strain rate increases, which shows that the increase in rock damage under high pressure impact is
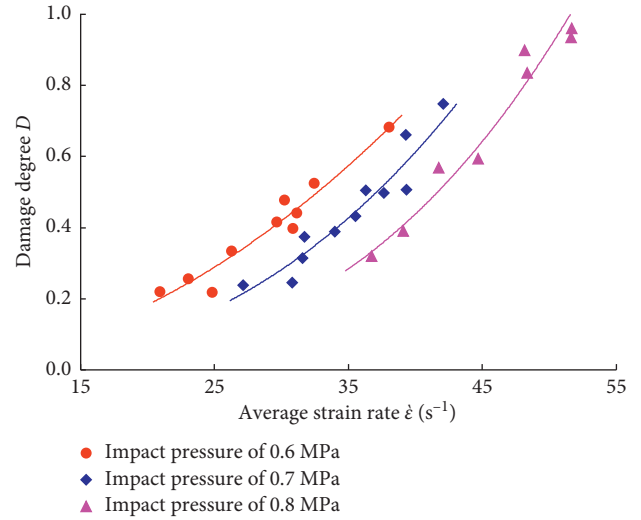
FIGURE 7: Relationship between the degree of damage and the average strain rate under different pressures of equal amplitude.

greater as the average strain rate increases. Therefore, it can be considered that the increase in the impact pressure weakens the impact strength of granite and accelerates the damage evolution rate of the internal structure under impact loading, and the larger the impact pressure within a certain range is, the faster the damage evolution rate of the specimen is.

To investigate the relationship between the rock damage and the average strain rate under more impact pressures, the power function $D = \alpha\dot{\varepsilon}^{\beta}$ was used to fit the data in Figure 6 to obtain the relationship between the degree of damage and the average strain rate at different impact pressures:

$$P_n = 0.6\,\text{MPa}, \quad D = 4.01 \times 10^{-4}\dot{\varepsilon}^{2.0439}, \quad R^2 = 0.913,$$
$$P_n = 0.7\,\text{MPa}, \quad D = 2.92 \times 10^{-5}\dot{\varepsilon}^{2.6972}, \quad R^2 = 0.910,$$
$$P_n = 0.8\,\text{MPa}, \quad D = 2.73 \times 10^{-6}\dot{\varepsilon}^{3.2490}, \quad R^2 = 0.965.$$
$$(12)$$

The impact pressure is fitted to the parameters α and β to obtain the following equation:

$$\begin{cases} \alpha = 1.22 \times 10^3 \cdot e^{-24.9467P_n}, & R^2 = 0.998, \\ \beta = 6.03P_n - 1.5544, & R^2 = 0.997. \end{cases} \quad (13)$$

By substituting equation (13) into the power function $D = \alpha\dot{\varepsilon}^{\beta}$, we can obtain the expression for the relationship between the degree of damage to the rock and the impact pressure and the average strain rate:

$$D = \left(1.22 \times 10^3 \cdot e^{-24.9467P_n}\right)\dot{\varepsilon}^{6.03-1.5544}. \quad (14)$$

Figure 8 shows the comparison between the test result fitting and the equation theoretical curve at $P_n = 0.7$ MPa. It can be seen from the figure that the fitted curve and the experimental curve are almost coincident, there are only slight differences in the high-strain section, and the overall trend of the numerical changes is the same. The average strain rate-degree of damage curve calculated by the theoretical equation is very similar to the experimental fit curve. Using equation (14), the relationship between the degree of
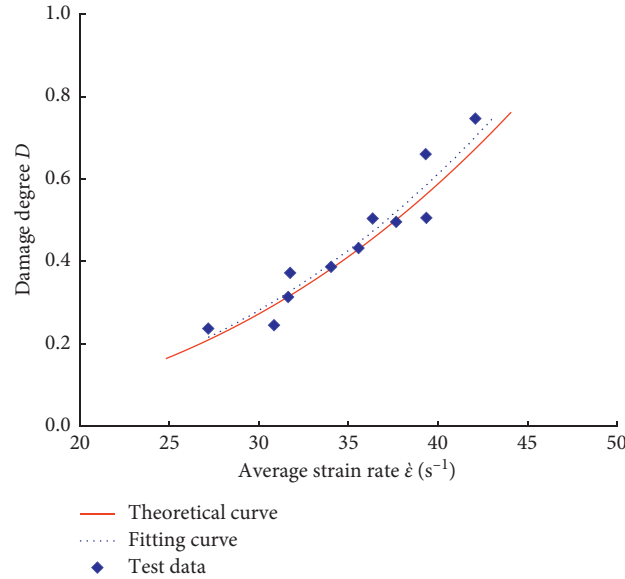
FIGURE 8: Relationship between the average strain rate and the degree of damage for $P_n = 0.7$ MPa.

damage and the average strain rate under other pressure shocks can be calculated, and the relationship between the development rate of internal defects and the degree of structural damage when the load is applied on the granite with different impacts can be obtained. Because the experimental data of the unequal-amplitude experimental group are small and the relationship between the strain rate and damage evolution under alternating impact pressure is relatively complicated, the theoretical equation for such cases is not discussed.

4.4. Relationship between the Absorbed Energy per Unit Volume and Strain Rate. Figure 9 shows the relationship between the absorbed energy per unit volume and the average strain rate during the cyclic impact of the specimen under constant and unequal pressure. It can be seen from the figure that under the action of equal- and unequal-amplitude air pressure shocks, the absorption energy per unit volume of the rock increases linearly with the increase in the average strain rate.

Figure 9(a) shows the fitting of the relationship between the absorbed energy per unit volume and the average strain rate under different air pressures of equal-amplitude impact. As the increase in the impact air pressure leads to an increase in the punch speed, the average strain rate generated by the specimen also increases overall. The slope of the linear fitting is greater under high pressure, and the absorption energy per unit volume increases rapidly with the strain rate. On the other hand, the slope of the linear fitting under low pressure is smaller, and the absorption energy per unit volume increases slowly with the strain rate. By examining the impact of different impact modes on the law of rock damage, as shown in Figures 9(b) and 9(c), when the average strain rate is small, the energy values are not very different, and under a high average strain rate, the energy absorption efficiency of the specimen under the impact of unequal amplitude is stronger than that under equal amplitude, which indicates

that the energy absorption efficiency of the specimen is improved under the impact of high air pressure.

The analysis shows that under the action of a large impact load, the development rate of internal defects in the rock will gradually increase. At this time, the looser the specimen is, the smaller the wave impedance value is and the higher the degree of damage is. If the same average strain rate occurs, a specimen impacted by a high pressure must absorb more energy to do work on more crack slip surfaces, so the slope of the absorbed energy per unit volume and the average strain rate during cyclic impact will increase with the increase in the impact pressure.

4.5. Relationship between the Number of Impacts and Specific Energy Absorption. To explore the relationship between the number of impacts of rock and the damage under cyclic impact loading, the cumulative specific energy absorption value ϑ is defined as the accumulated energy absorbed per unit volume of the specimen during cyclic impact:

$$\vartheta = \sum_{i=0}^{n} E_{V(i)}, \tag{15}$$

where ϑ is the cumulative specific energy absorption value, $E_{V(i)}$ is the absorbed energy per unit volume generated by the i-th impact of the specimen, and n is the number of impacts of the cyclic load. The relationship between the cumulative specific energy absorption value of the rock and the number of impact loads can be obtained from the test results and equation (15). Figure 10 shows the relationship between the cumulative specific energy absorption of rock and the number of impacts under different impact pressures and impact modes.

With constant amplitude impact, as the pressure of the impact gas increases, the rate of increase of the specific energy of the specimen increases and the number of impacts decreases accordingly. The last impact incident energy is mainly used for specimen failure [37], resulting in a

(a)

(b)

(c)
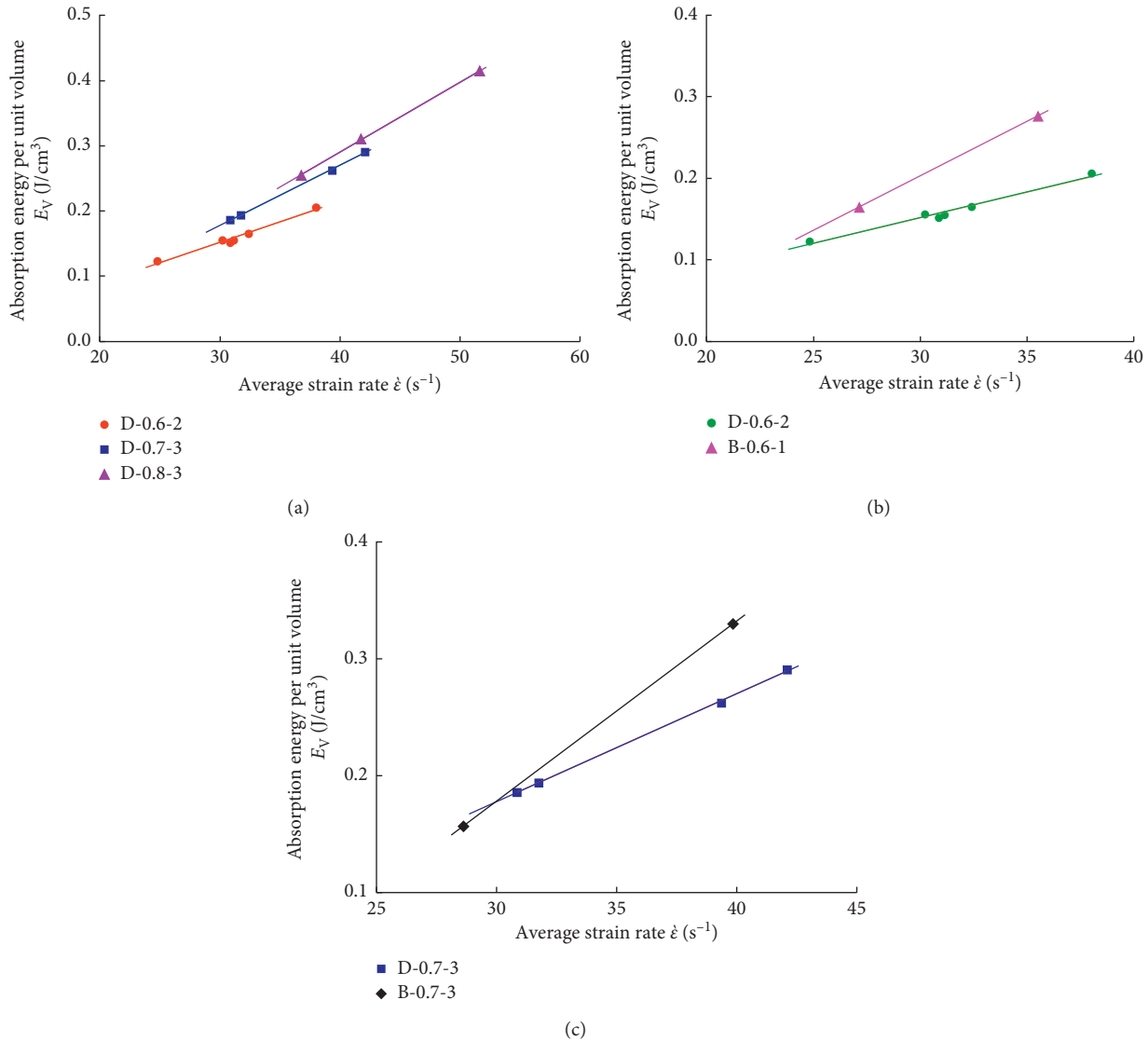
FIGURE 9: Variation laws of the absorbed energy per unit volume with the strain rate. (a) Pressure shocks of 0.6 MPa, 0.7 MPa, and 0.8 MPa. (b) Pressure shocks of 0.6 MPa and 0.6 MPa-0.7 MPa. (c) Pressure shocks of 0.7 MPa and 0.7 MPa-0.8 MPa.

relatively large absorbed energy of the specimen. This test showed a significant increase in the last absorption energy under high pressure impact. Specimen D-0.8-3 showed an increase by 50.39% and 29.89% in the last unit volume compared to that of specimens D-0.6-2 and D-0.7-3, respectively. Figure 10 shows the failure mode of a granite specimen with holes under constant amplitude impact. At an impact pressure of 0.6 MPa, specimen D-0.6-2 undergoes lateral tensile failure near the middle, with some spalling at the edges; at 0.7 MPa, the failure degree of specimen D-0.7-3 is incomplete. The secondary rock block undergoes lateral stretching and axial splitting along the diameter section of the hole, and the surface of the main rock block undergoes longitudinal tensile cracking that extends to the edge of the hole with a circular cross section; under the impact of 0.8 MPa, specimen D-0.8-3 breaks into three main blocks, there is a lateral stretching zone and an axial splitting zone,

and the flaking and fragmentation of the rock edge is more severe.

For the case of unequal-amplitude impact, the number of impacts of the rock is significantly reduced compared to the number of equal-amplitude impacts, and the accumulated specific energy at the time of the final failure is also greatly reduced. Compared with specimen D-0.6-2 and specimen D-0.7-3, specimen B-0.6-1 and specimen B-0.7-3 both produced a greater accumulated specific energy due to the subsequent increase in the impact gas pressure. The growth rate increased by 25.45% and 11.85%, respectively. The failure morphology of the rock specimen under unequal-amplitude impact is shown in Figure 11. The failure mode of specimen B-0.6-1 under pressures of 0.6-0.7 MPa is a combination of lateral stretching and axial splitting failure, and under a pressure of 0.8 MPa, specimen B-0.7-3 exhibits a complete axial splitting failure
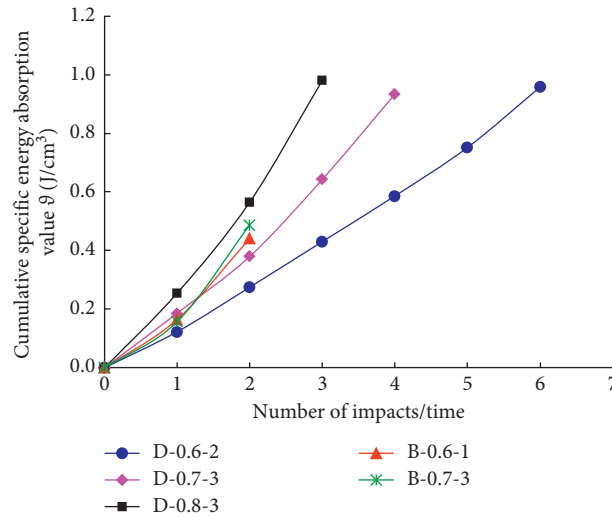
FIGURE 10: Relationship between the value of the cumulative specific energy and time of the impact loads.

FIGURE 11: Fracture failure morphology of granite specimens with a vertical hole under different impact pressures of equal-amplitude impact.

mode, and rock blocks spall and break at both ends of the specimen.

5. Discussion

With the increase in the impact pressure and the change in the impact mode, the failure mode of the rock undergoes a transformation from lateral tensile failure to lateral tensile-axial splitting combination and axial splitting failure and is affected by the size effect of granite. The degree of the final fracture of the specimen is not serious. The explosion stress wave reflection tensile theory assumes that rock failure is caused by the stress wave in the rock, forming a reflected tensile wave after the free surface is reflected, and the tensile stress in the rock is greater than its tensile strength. When the stress wave is transmitted from the incident rod to the specimen, a short elastic deformation displacement difference occurs in the interface area due to the difference in the elastic modulus. During the entire impact process, there are multiple transreflective stress waves. Each time the stress wave is transmitted to the interface between the specimen and the rod, a relative displacement will be produced. With the increase in the number of times, the stress wave propagates in the specimen, the microcracks will propagate

and penetrate in succession, resulting in the enhanced deformation capacity of the rock, and the relative displacement generated each time will gradually increase. In addition, due to the lack of axial compression constraints, the transmission rod will undergo a certain displacement after being subjected to several transmission stress waves. At a certain reflection and reflection stage, a side of the specimen will form a hollow surface with the elastic rod and generate reflected tensile waves [38]. The existence of holes intensifies the crack propagation rate in each reflective process and reduces the net cross-sectional area of the active surface, which results in the lateral tensile failure of the rock. Increased impact air pressure leads to the initiation of the concentrated tensile stress generated near the hole wall, causing the split-through surface to develop in the axial direction. Under the high pressure of unequal-amplitude impact, the stress concentration around the hole is further intensified. Before the formation of hysteresis, the test specimen will split and break because the tensile stress around the hole exceeds its tensile strength. The excessive local compressive stress causes a certain crushing.

According to the theoretical analysis, during microcrack initiation and propagation, slippage will inevitably occur. As the cyclic impact progresses, the penetration crack surface

FIGURE 12: Fracture failure morphology of the granite specimen with a vertical hole under different impact pressures with unequal-amplitude impact.

will continue to increase. At this time, the work required to overcome the friction of the section slip will incrementally increase. The absorbed energy per unit volume of the rock will also increase, causing the cumulative specific energy absorption value to gradually increase, while the damage accumulation of the rock will increase one after another. In this experiment, with the increase in the equal-pressure impact gas pressure, the degree of fracture and the area of fracture of the specimen increase correspondingly and the impact strength also weakens successively. Under unequal-amplitude impact, the specimen exhibits a more severe degree of fragmentation at a lower cumulative specific energy absorption value. Compared with that of equal-amplitude impact, the impact resistance of the specimen under unequal-amplitude impact is greatly reduced and the damage evolution is more severe. The high-pressure shock aggravates the propagation rate of the microdefects inside the test specimen after the low-pressure shock, and the stress concentration around the hole initiates more cracks. When most of the cracks have not yet initiated and propagated, the test specimen A section has been loaded with a low capacity, and a large crack density expands, penetrates, and breaks. According to Figures 11 and 12, the through surface usually forms along the section where the diameter of the hole is located. Therefore, in engineering practice, when the rock is subjected to large dynamic loads and varying dynamic loads, construction personnel should pay attention to locations with defects and take corresponding measures to support and strengthen the surrounding rocks [39–41].

6. Conclusions

This paper proposed a damage constitutive model defined by wave impedance, which can quantify the damage degree of the granite with a hole paralleled with the load direction, and provided a new method for predicting the damage process of confining pressure in engineering practice. Through the constitutive model, it can be found that the degree of damage and the change rate of cumulative specific energy absorption value of the specimens accelerated, and the impact strength significantly decreases as the number of impacts increases. During the experiment, the specimens with holes showed

significant brittle failure characteristics, and the failure mode underwent the transformation of transverse tensile failure to transverse tension-axial splitting combination and axial splitting failure. Through the analysis of rock energy changes and rock failure patterns during cyclic impact, it will be helpful to predict and control the fracture caused by local stress concentration during excavation, thus can reduce the cost of support and reinforcement in excavation and improve the stability of the surrounding rocks.

Data Availability

The data used to support the findings of this study are available from the corresponding author upon request.

Conflicts of Interest

The authors declare that they have no known conflicts of interest that could influence the work reported in this paper.

Authors' Contributions

Bing Dai was responsible for methodology; Li Chen conceptualized the study; Yakun Tian was involved in investigation and data curation; Xinyao Luo wrote the original draft; Ying Chen was responsible for resources and writing (reviewing and editing); Zhijun Zhang supervised the study; Qiwei Shan was involved in validation and visualization.

Acknowledgments

References

[1] P.-X. Li, X.-T. Feng, G.-L. Feng, Y.-X. Xiao, and B.-R. Chen, "Rockburst and microseismic characteristics around lithological interfaces under different excavation directions in deep tunnels," *Engineering Geology*, vol. 260, Article ID 105209, 2019.

[2] X. Xu, M. He, C. Zhu, Y. Lin, and C. Cao, "A new calculation model of blasting dam-age degree-based on fractal and tie rod damage theory," *Engineering Fracture Mechanics*, vol. 220, 2019.

[3] X. B. Li, T. S. Lok, and J. Zhao, "Dynamic characteristics of granite subjected to intermediate loading rate," *Rock Mechanics and Rock Engineering*, vol. 38, no. 1, pp. 21–39, 2005.

[4] X. Luo, N. Jiang, M. Wang, and Y. Xu, "Response of leptynite subjected to repeated impact loading," *Rock Mechanics and Rock Engineering*, vol. 49, no. 10, pp. 4137–4141, 2016.

[5] J. Fan, J. Chen, D. Jiang, S. Ren, and J. Wu, "Fatigue properties of rock salt subjected to interval cyclic pressure," *International Journal of Fatigue*, vol. 90, pp. 109–115, 2016.

[6] S. H. Li, W. C. Zhu, L. L. Niu, M. Yu, and C. F. Chen, "Dynamic characteristics of green sandstone subjected to repetitive impact loading: phenomena and mechanisms," *Rock Mechanics and Rock Engineering*, vol. 51, no. 6, pp. 1921–1936, 2018.

[7] J. J. Zhu, X. B. Li, F. Q. Gong, and S. M. Wang, "Dynamic characteristics and damage model for rock under uniaxial cyclic impact compressive loads," *Chinese Journal of Geotechnical Engineering*, vol. 35, no. 3, pp. 531–539, 2013.

[8] F.-Q. Gong, X.-F. Si, X.-B. Li, and S.-Y. Wang, "Dynamic triaxial compression tests on sandstone at high strain rates and low confining pressures with split Hopkinson pressure bar," *International Journal of Rock Mechanics and Mining Sciences*, vol. 113, pp. 211–219, 2019.

[9] R.-H. Shu, T.-B. Yin, X.-B. Li, Z.-Q. Yin, and L.-Z. Tang, "Effect of thermal treatment on energy dissipation of granite under cyclic impact loading," *Transactions of Nonferrous Metals Society of China*, vol. 29, no. 2, pp. 385–396, 2019.

[10] K. Peng, J. Zhou, Q. Zou, and F. Yan, "Deformation characteristics of sandstones during cyclic loading and unloading with varying lower limits of stress under different confining pressures," *International Journal of Fatigue*, vol. 127, pp. 82–100, 2019.

[11] K. Peng, J. Zhou, Q. Zou, and X. Song, "Effect of loading frequency on the deformation behaviours of sandstones subjected to cyclic loads and its underlying mechanism," *International Journal of Fatigue*, vol. 131, Article ID 105349, 2020.

[12] M. Tao, H. Zhao, A. Momeni, Y. Wang, and W. Cao, "Fracture failure analysis of elliptical hole bored granodiorite rocks under impact loads," *Theoretical and Applied Fracture Mechanics*, vol. 107, Article ID 102516, 2020.

[13] B. Dai and Y. Chen, "A novel approach for predicting the height of the water-flow fracture zone in undersea safety mining," *Remote Sensing*, vol. 12, no. 3, p. 358, 2020.

[14] Z.-l. Zhou, Y. Zhao, Y.-h. Jiang, Y. Zou, X. Cai, and D.-y. Li, "Dynamic behavior of rock during its post failure stage in shpb tests," *Transactions of Nonferrous Metals Society of China*, vol. 27, no. 1, pp. 184–196, 2017.

[15] X. Li, Z. Zhou, T.-S. Lok, L. Hong, and T. Yin, "Innovative testing technique of rock subjected to coupled static and dynamic loads," *International Journal of Rock Mechanics and Mining Sciences*, vol. 45, no. 5, pp. 739–748, 2008.

[16] X. Li, T. Zhou, and D. Li, "Dynamic strength and fracturing behavior of single-flawed prismatic marble specimens under impact loading with a split-hopkinson pressure bar," *Rock Mechanics and Rock Engineering*, vol. 50, no. 1, pp. 29–44, 2017.

[17] M. Tao, M. Ao, W. Cao, X. Li, and F. Gong, "Dynamic response of pre-stressed rock with a circular cavity subject to transient loading," *International Journal of Rock Mechanics and Mining Sciences*, vol. 99, pp. 1–8, 2017.

[18] D. Liu, D. Li, F. Zhao, and C. Wang, "Fragmentation characteristics analysis of sandstone fragments based on impact rockburst test," *Journal of Rock Mechanics and Geotechnical Engineering*, vol. 6, no. 3, pp. 251–256, 2014.

[19] H. Wu, G. Zhao, W. Liang, and E. Wang, "Dynamic mechanical characteristics and failure modes of sandstone with artificial surface cracks," *Journal of Central South University (Science and Technology)*, vol. 50, no. 02, pp. 106–115, 2019.

[20] D. Han, K. Li, and J. Meng, "Evolution of nonlinear elasticity and crack damage of rock joint under cyclic tension," *International Journal of Rock Mechanics and Mining Sciences*, vol. 128, Article ID 104286, 2020.

[21] Q. Meng, M. Zhang, L. Han, H. Pu, and Y. Chen, "Acoustic emission characteristics of red sandstone specimens under uniaxial cyclic loading and unloading compression," *Rock Mechanics and Rock Engineering*, vol. 51, no. 4, pp. 969–988, 2018.

[22] D. Zhu, Y. Wu, Z. Liu, X. Dong, and J. Yu, "Failure mechanism and safety control strategy for laminated roof of wide-span roadway," *Engineering Failure Analysis*, vol. 111, Article ID 104489, 2020.

[23] Q. Zheng, E. Liu, P. Sun, M. Liu, and D. Yu, "Dynamic and damage properties of artificial jointed rock samples subjected to cyclic triaxial loading at various frequencies," *International Journal of Rock Mechanics and Mining Sciences*, vol. 128, Article ID 104243, 2020.

[24] Q. Meng, M. Zhang, L. Han, H. Pu, and T. Nie, "Effects of acoustic emission and energy evolution of rock specimens under the uniaxial cyclic loading and unloading compression," *Rock Mechanics and Rock Engineering*, vol. 49, no. 10, pp. 3873–3886, 2016.

[25] H. Wu, G. Zhao, and W. Liang, "Mechanical properties and fracture characteristics of pre-holed rocks subjected to uniaxial loading: a comparative analysis of five hole shapes," *Theoretical and Applied Fracture Mechanics*, vol. 105, Article ID 102433, 2020.

[26] K. Chen, M. Tang, and Z. Guo, "Comparative study on three-dimensional conventional and modified statistical damage constitutive models," *Multiscale and Multidisciplinary Modeling, Experiments and Design*, vol. 2, no. 4, pp. 259–267, 2019.

[27] Z. Zhou, L. Tan, W. Cao, Z. Zhou, and X. Cai, "Fracture evolution and failure behaviour of marble specimens containing rectangular cavities under uniaxial loading," *Engineering Fracture Mechanics*, vol. 184, pp. 183–201, 2017.

[28] L. Scholtès and F.-V. Donzé, "Modelling progressive failure in fractured rock masses using a 3d discrete element method," *International Journal of Rock Mechanics and Mining Sciences*, vol. 52, pp. 18–30, 2012.

[29] Y. Matvienko, V. Pisarev, and S. Eleonsky, "The effect of low-cycle fatigue parameters on damage accumulation near a hole," *Engineering Failure Analysis*, vol. 106, Article ID 104175, 2019.

[30] D. Li, Q. Zhu, and X. Li, "Research on the effect of cavity shapes for the progressive failure and mechanical behavior of marb," *Journal of Underground Space and Engineering*, vol. 14, no. 1, pp. 58–66, 2008.

[31] C. Zhang, J. Tang, J. Teng, and C. Li, "Experimental study of influences of pore number and pore size on mechanical properties of marble," *Rock and Soil Mechanics*, vol. 38, no. S2, pp. 41–50, 2017.

[32] J. Qiu, L. Luo, X. Li, D. Li, Y. Chen, and Y. Luo, "Numerical investigation on the tensile fracturing behavior of rock-shotcrete interface based on discrete element method," *International Journal of Mining Science and Technology*, 2020.

[33] J. Jiefang, L. Xibing, Y. Zhiqiang, and Z. Yang, "A method for defining rock damage variable by wave impedance under

cyclic impact loadings," *Rock and Soil Mechanics*, vol. 32, no. 5, pp. 1385–1393, 2011.

[34] D. Ai, Y. Zhao, Q. Wang, and C. Li, "Crack propagation and dynamic properties of coal under SHPB impact loading: experimental investigation and numerical simulation," *Theoretical and Applied Fracture Mechanics*, vol. 105, Article ID 102393, 2020.

[35] J. G. Cai and J. Zhao, "Effects of multiple parallel fractures on apparent attenuation of stress waves in rock masses," *International Journal of Rock Mechanics and Mining Sciences*, vol. 37, no. 4, pp. 661–682, 2000.

[36] F.-Q. Gong and G.-F. Zhao, "Dynamic indirect tensile strength of sandstone under different loading rates," *Rock Mechanics and Rock Engineering*, vol. 47, no. 6, pp. 2271–2278, 2014.

[37] L. Xibing, G. Fengqiang, Z. Jian, G. Ke, and Y. Tubing, "Test study of impact failure of rock subjected to one-dimensional coupled static and dynamic loads," *Chinese Journal of Rock Mechanics and Engineering*, vol. 29, no. 02, pp. 251–260, 2010.

[38] W. Dang, H. Konietzky, T. Frühwirt, and M. Herbst, "Cyclic frictional responses of planar joints under cyclic normal load conditions: laboratory tests and numerical simulations," *Rock Mechanics and Rock Engineering*, vol. 53, no. 1, pp. 337–364, 2020.

[39] W. Dang, H. W. Wu, and J. Qian, "Effect of shear-induced aperture evolution on fluid flow in rock fractures," *Computers and Geotechnics*, vol. 114, Article ID 103152, 2019.

[40] W. Dang, L. H. Konietzky, and T. Frühwirt, "Velocity-frequency-amplitude-dependent frictional resistance of planar joints under dynamic normal load (DNL) conditions," *Tunnelling and Underground Space Technology*, vol. 79, no. 9, pp. 27–34, 2018.

[41] Y. Luo, F. Q. Gong, X. B. Li, and S. Y. Wang, "Experimental simulation investigation of influence of depth on spalling characteristics in circular hard rock tunnel," *Journal of Central South University*, vol. 27, no. 3, pp. 891–910, 2020.

Research Article

Experimental Study of the Rock Mechanism under Coupled High Temperatures and Dynamic Loads

Huaming An [ID],[1] Tongshuai Zeng,[1] Zhihua Zhang,[2] and Lei Liu [ID][2]

[1]*Faculty of Public Security and Emergency Management, Kunming University of Science and Technology,
Kunming 650093, China*
[2]*Faculty of Land Resources Engineering, Kunming University of Science and Technology, Kunming 650093, China*

Correspondence should be addressed to Lei Liu; explosive.lab@outlook.com

With the development of modern society, geomaterials are widely used for infrastructure. These materials often experience dynamic loading and high temperature, which significantly influences the mechanical behaviour of the materials. This research focuses on the effects of the loading rate and high temperature on rock mass in terms of rock mechanism. A state-of-the-art review of rock mechanism under coupled dynamic loads and high temperatures is conducted first. The rock mechanism under static and dynamic loads is introduced. The marble is taken as the rock material for the test, while the split-Hopkinson pressure bar system is used to take the dynamic tests. In addition, the principles of the split-Hopkinson pressure bar are introduced to obtain the dynamic parameters. The fracture patterns of the uniaxial compressive strength test and the Brazilian tensile strength test are obtained and compared with those well documented in the literature. Some curves for the relationships among the loading rate, strain, temperature, compressive or tensile strengths are explained. It is conduced that with the increase of the loading rate, the rock strength increases, while with the increase of the temperature, the rock strength decreases.

1. Introduction

It is well known that the rock materials are widely used in many geostructures, such as foundations, tunnels, dam, and slops. However, the physical and chemical properties of the rock materials will be changed if they experience a high-temperature environment. This change will eventually affect the rock behaviours. In addition, rock mass in a deep tunnel or deep mine might be disturbed by explosion, earthquake, and sudden and natural disasters [1]. In this condition, the rock mass is experiencing an impact, i.e., dynamic loading. Although the dynamic behaviour of the rock mass has been intensively studied, the knowledge on the mechanism of the rock mass under dynamic loads is still limited us to a better understating of the dynamic behaviour of rock mass. Moreover, for rock mass under the coupled condition of high temperature and dynamic loading, the mechanism of rock failure will be more complicated. Thus, it is necessary to study the rock behaviour under coupled high temperatures and

dynamic loading. To better understand the background of the study on the dynamic behavior of rock after heat treatment, a literature review is conducted in the following section. The main experimental equipment, i.e., split-Hopkinson pressure bar, is introduced [2, 3]. Then, static and dynamic tests for the rock after heat treatment are reviewed.

2. State-of-the-Art Review of Rock Mechanism under Dynamic Loads and High Temperatures

This section mainly reviews the rock fracture studies under high temperatures and dynamic loads. As the split-Hopkinson pressure bar (SHPB) is the most widely used technique to carry out the rock fracture mechanism under dynamic loads, the development of the technique is reviewed first. Then, many dynamic tests, such as the uniaxial compression test and Brazilian tensile strength test using SHPB, are reviewed. Among them, the influence of the loading rate

on the rock strength is intensively studied. After that, the rock mechanism under temperatures is reviewed. The review focuses on the physical properties of rock after high-temperature treatment and the static and the dynamic rock mechanism of rock under high temperature. Since the numerical studies of the dynamic rock fracture and fragmentation have been intensively studied and reviewed by the authors and more details can be found in the literature [4–14], the numerical studies of rock mechanism under high temperature are not reviewed herein.

2.1. Experimental Study of Rock Mechanism under Dynamic Loads

2.1.1. Development of the Split-Hopkinson Pressure Bar. As for the rock under dynamic loading, sources of dynamic loads could be explosion, impact, and seismic events [2, 3]. For research on the dynamic mechanism of rock, the split-Hopkinson pressure bar might be the most widely used technique [15–19]. Thus, the development of the split-Hopkinson pressure bar is introduced first. Kolsky used a pressure bar to test the pulse waveform, and it was the first time to measure the mechanical properties of rock under dynamic loads [20]. Kolsky improved the Hopkinson bar system, which is mainly divided into striker, incident bar, and transmission bar. As the system is comprised of several separated components, the system was called split-Hopkinson bar system [21]. Then, the system is used to study the rock mechanism at the strain rates within $10^1 \sim 10^4 S^{-1}$. Some of the brittle materials, such as rock, are heterogeneous and contain defects such as crack texture. Therefore, large enough materials are needed to reduce the impact of material's heterogeneity. As the size of the specimen increased, a larger diameter pressure bar was needed, so the large-diameter Hopkinson bar developed rapidly since the 1970s. The adoption of the large-diameter Hopkinson bar challenges the traditional theoretical assumptions of Hopkinson bar, i.e., one-dimensional stress wave hypothesis and uniform hypothesis. In addition, wave dispersion, stress unevenness, and cross section friction are the main problems needed to be solved for the large-diameter Hopkinson bar. The dispersion problem is caused by the ignorance of the inertia motion of particles in the Hopkinson bar with a large diameter [22]. For section friction, butter is generally applied to both ends of the specimen to reduce friction [22]. Moreover, since constant strain rate loading is very important for studying the constitutive relations under dynamic loads of rocks, many scholars have studied the realization of constant strain rate loading by the SHPB. For the first time, Samanta added a pad at the front end of the incident bar to realize constant strain rate loading [23]. The pad is made of the same material and size as the sample. Frew et al. pasted a copper sheet on the front end of impact bars to realize constant strain rate loading [24].

2.1.2. Rock Mechanism under Dynamic Loads. Most rock experiments techniques for carrying out the rock dynamic tests are developed from those techniques for static tests. At present, the standard dynamic experiment methods recommended by the international society of rock mechanics are uniaxial compression test, the Brazilian disk test, and semidisc with the prefabricated crack test. Tedesco et al. applied the Hopkinson pressure bar to conduct an impact test on cement and studied the influence of loading rate on cement strength [25]. Galvez et al. conducted impact tests on ceramic materials with the application of the Hopkinson pressure bar, and the study showed that the loading rates influence the tensile strength of the materials significantly [26]. Sukontasukkul et al. have studied the effect of loading rate on the damage of concrete using SHPB [27]. They concluded that the specimens subjected to impact loading were found to suffer higher damage than those subjected to static loading. Uniaxial and triaxial compressive strength tests have been conducted by Zhao, and the results showed that compressive strength will increase due to the increased loading rate [28]. Zhang et al. studied the influences of the loading rate on the rock fracture process and concluded that the number of cracks increases with the increasing loading rate [29]. Many researchers indicate the same conclusion that the loading rate significantly influences the behaviour of the brittle materials [27–34]. Wang et al. studied the fracture process of rock under high pressure by the Hopkinson pressure bar, and the study showed that the tensile strength and elastic modulus of rock under high strain rate were several times higher than those under static condition [35]. Dai et al. proposed a method for measuring dynamic mode-I rock fracture parameters using a cracked chevron notched semicircular bend (CCNSCB) specimen loaded by a split-Hopkinson pressure bar (SHPB) apparatus [31]. Zhou et al. studied the mechanical behaviour of rock under both dynamic and static loads from the theoretical and experimental perspectives [36]. The theoretical and experimental results show that when the stress wave front propagation is relatively slow, the disk can reach a stress equilibrium and the disk is split by the loading diameter [36]. When the force wave front is relatively fast, the Brazilian disk is not suitable for calculating the tensile strength of rock due to the uneven distribution of stress [36]. Mahanta et al. studied the effects of strain rate on fracture toughness and energy release rate of gas shales [33]. Peng used the split-Hopkinson pressure bar to conduct the Brazilian disc test and concluded that the time required to achieve a uniform stress state in specimen for the half-sine incident pulse is noticeably shorter than that for the perfectly rectangular incident pulse [37].

2.2. Experimental Study of Rock Mechanism under High Temperatures

2.2.1. Static Rock Mechanism under High Temperatures. In deep geotechnical engineering, such as deep mining, deep burial treatment of radioactive nuclear waste, coal gasification and exploitation, and utilization of geothermal resources, the physical and mechanical properties of rock are all affected by the high-temperature environment. Due to complex physical and chemical changes in the high-temperature environment, the physical and mechanical

behaviours of rock are different from those of normal temperature. Thus, the influence of temperature on rock mechanical properties has been widely studied worldwide. The influence of temperature on rock is mainly manifested in the following two aspects. On the one hand, the temperature field has an influence on the physical behaviour of rock. On the other hand, the change of thermodynamic parameters related to rock deformation affects the temperature field. On the contrary, the change of temperature field affects the mechanical properties of rock. Generally, when the temperature increases, the mechanical properties of the rock become weak, and the stiffness, compressive strength, tensile strength, elastic modulus, and other parameters of the rock will be reduced. At the same time, the increase of the temperature will also change the mineral composition of the rock, resulting in the increasing of the microfractures and joint fractures. Then, the study for physical property and the static rock mechanism under high temperature is reviewed as follows.

Van der Molen summarized the mechanical properties of rocks in high-temperature environments and analysed the changes of granite while it experiences high temperature under high confining pressure [38]. It is concluded that the porosity between the particles in the granite decreases when the temperature reaches 200°C, and the porosity between granite particles expands when the temperature is between 200°C and 840°C. Heard measured the thermal expansion coefficient and permeability of quartz, and the studies have shown that temperature has a significant effect on the thermal expansion coefficient of rocks. The higher the temperature, the higher the thermal expansion coefficient [39]. Yan studied the effects of high temperature on density, P-wave velocity, uniaxial compressive strength, and elastic modulus for granite, tuff, and breccia [40]. Fengchen studied the change law of the physical properties of sandstone with temperature and found that the bulk density of sandstone decreased with increasing temperature, and the porosity and permeability gradually increased with increasing temperature [41]. Zhao and Chen et al. studied the thermal expansion behaviour of limestone [42, 43]. It was found that the thermal expansion behaviour of limestone has a nonlinear relationship with temperature, and the porosity increases with temperature.

2.2.2. Dynamic Rock Mechanism under High Temperatures.
During mining for deep resources, excavation for the deep tunnel by blasts, and gas explosion in mine coal, the underground rock mass is in the extreme environment of impact load and high temperature. Thus, it is essential to study the rock mechanism under dynamic loading and high temperature. Li used an experimental system with the function of coupling dynamic loads and high temperatures to carry out the rock behaviour test for siltstone and concluded that dynamic peak strength of siltstone increases with the increase of temperature in the range of 20°C–100°C and decreases with the increase of temperature when it exceeds

100°C [44]. Yin carried out uniaxial dynamic compression experiments on sandstone cooled under the action of high temperature from room temperature to 800°C by using SHPB and analysed the change rule of rock density, longitudinal wave, and strength with temperature [45]. In addition, they also analysed the dynamic fracture characteristics of sandstone after high temperature from the failure form of sample and fragments. The results show that with the increase of temperature, the mechanical parameters such as density, P-wave velocity, and peak strength of the sample decrease gradually. Yin studied the dynamic mechanical properties of granite under the condition of temperature compression coupling. The results showed that the dynamic strength of granite decreased with the increase of temperature, while the peak strain increased with the increase of temperature [46]. Xu and Liu carried out impact compression experiments of marble at different temperatures and loading rates [47]. The results show that the peak strength and peak strain of marble increase with the increase of loading rate at different temperatures. When the temperature rises to 800°C, the peak strength of marble becomes less obvious with the change of loading rate The modulus decreases with the increase of temperature. When the temperature rises to 1000°C, the modulus of elasticity shows a basically constant trend with the increase of loading rate. Liu analysed the dynamic splitting tensile test of marble after high-temperature treatment and found that the tensile strength of marble after high-temperature treatment is significantly higher than that under static condition. Under the same impact pressure, the tensile strength of marble increases first and then decreases with the increase of temperature [48].

3. Materials and Methods

3.1. Preparation for the Rock Specimen.
In this research, the marble from Gejiu Kafang tin mine in Yunnan Province of China is used to study the rock behaviour under the high temperatures and dynamic loads. The strata in the mining area are mainly divided into Triassic (t2 g) hydrochloride rock strata. The fold structure in the sampling area is mainly anticline, and the fault structure in the mining area is mainly east-west fault. The rock material is taken from the depth of 700 m in the mine. According to the geometry suggested by ISRM, the samples are made into cylinders with 50 mm in the diameter and 100 mm in length for the uniaxial compressive strength test under static loading. The sample with 40 mm in the diameter and 40 mm in length are made for the Brazilian tensile strength test under static loading and compressive strength test under dynamic loading.

3.2. Principles for the Rock Tests under Static Loads.
Figure 1 depicts the geometrical model for the uniaxial compressive strength (UCS) test and the Brazilian tensile strength (BTS) test under static loads. For the UCS test as illustrated in Figure 1(a), it includes two loading plates under
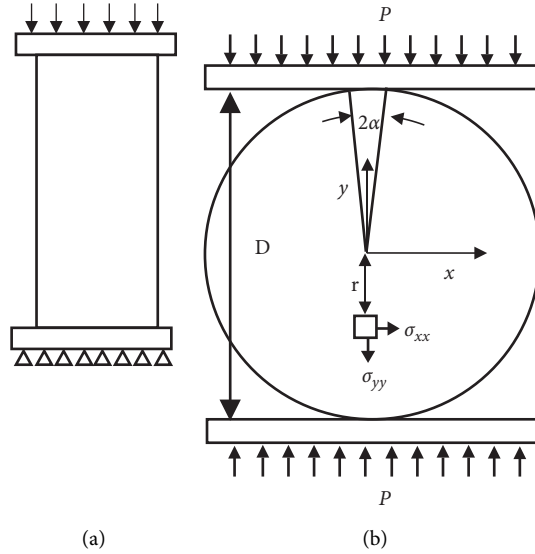
FIGURE 1: Geometrical model for UCS and BTS test. (a) Geometrical model for UCS test. (b) Geometrical model of BTS test.

the top and bottom of the rock specimen, while the sample is placed between the two loading plates. During testing, the two loading plates will move at a constant speed, as the loading plates contact the rock sample, the compressive stresses are produced immediately and propagate along the length of the specimen. After the stress increases and reaches the strength of the rock, fractures are produced. The compressive strength can be calculated according to

$$\sigma_c = \frac{P}{A}, \tag{1}$$

where P is the force on the top and bottom of the sample and A is the cross-sectional area of the top and bottom of the sample.

For the tensile strength test under static loading, the BTS test is used to obtain the tensile strength of the rock as illustrated in Figure 1(b). Since Akazawa and Carneiro [49, 50] developed the Brazilian disc test independently at almost the same time, the Brazilian disc test has gained its popularity for calculating the tensile strength and toughness. It is also widely used to study rock fracture initiation and propagation. Hondors [51] gave a complete stress solution for disc under diametral compression valid for both plane stress and plane strain conditions. This stress solution is then widely used to verify the numerical results of Brazilian disc test [52, 53].

Figure 1(b) shows the geometrical model of the BTS test. As shown in Figure 1(b), two plates are placed between the specimens. The two plates will move toward each other. The loads from the plates could be assumed to be radially applied over a short strip of the circumference with a radius of 2α, as shown in Figure 1(b). A complete stress solution along the loading diameter is given by Hondros as follows:

$$\sigma_{xx} = \frac{P}{\pi R t \alpha} \left\{ \frac{\left[1 - (r/R)^2\right] \mathrm{Sin}\, 2\alpha}{1 - 2(r/R)^2 \mathrm{Cos}\, 2\alpha + (r/R)^4} \right.$$
$$\left. - \tan^{-1}\left[\frac{1 + (r/R)^2}{1 - (r/R)^2} \tan(\alpha)\right] \right\}, \tag{2}$$

$$\sigma_{yy} = -\frac{P}{\pi R t \alpha} \left\{ \frac{\left[1 - (r/R)^2\right] \mathrm{Sin}\, 2\alpha}{1 - 2(r/R)^2 \mathrm{Cos}\, 2\alpha + (r/R)^4} \right.$$
$$\left. + \tan^{-1}\left[\frac{1 + (r/R)^2}{1 - (r/R)^2} \tan \alpha\right] \right\}, \tag{3}$$

where P is the applied load, R is the disc radius, r is the distance from the centre of the disc, t is the disc thickness, 2α is the angular distance of load arc, and σ_{xx} and σ_{yy} are the stresses along with the horizontal and vertical directions, respectively.

Thus, taking into account the specimen thickness t, the tensile strength can be calculated by (3) [54]:

$$\sigma_t = \frac{2P}{\pi D t}, \tag{4}$$

where σ_t is the tensile strength, P is the applied load, and R is the diameter.

3.3. Principles of Split-Hopkinson Pressure Bar (SHPB).
Figure 2 shows the conventional split-Hopkinson pressure bar (SHPB), which comprises a striker bar, an incident bar, and a transmission bar. The sample is placed between the incident and transmission bars during the dynamic experimental process. In the SHPB dynamic experiments, a gas
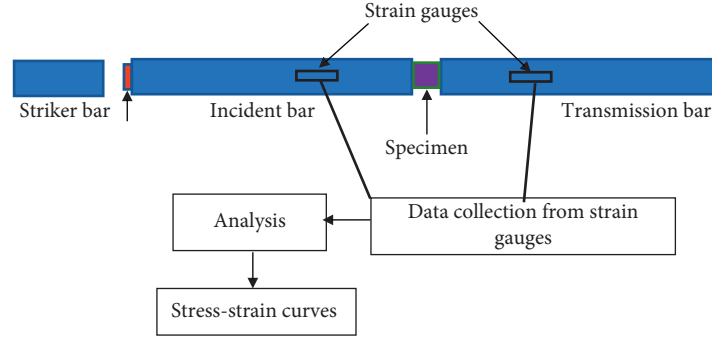
FIGURE 2: Schematic of conventional split-Hopkinson pressure bar (SHPB).

gun is used to launch the striker bar at the incident bar. Meanwhile, the elastic compression wave is produced to travel in the incident bar towards the sample. During the interaction between the striker bar and the sample, an elastic compression wave transmits into the transmission bar while an elastic tensile wave is reflected in the incident bar. It can be seen from Figure 2 that there are two strain gauges on the incident bar and the transmission bar. The incident strain pulse ε_i and reflected ε_r are measured by strain gauges on the incident bar, while the transmitted ε_t strain pulse is measured from the strain gauge on the transmitted bar.

Figure 3 shows the schematic diagram of the Hopkinson pressure bar during the dynamic test, and this diagram is used to explain the principle of the test. When the striker bar hits the incident bar, a compressive stress pulse wave of approximately one-dimensional propagation is generated in the incident bar. When the stress propagates to the interface where the incident bar and the transition bar are in contact (the 1-1 interface in Figure 3), a part of the compressive stress pulse wave continues to propagate into the sample, and the other part is reflected into the incident bar since the material of the sample is different from the incident bar in terms of wave impedance.

When the compressive stress pulse wave propagating into the rock sample reaches the contact surface of the sample and the transmission bar (the 2-2 interface in Figure 3), reflection and transmission are generated. A portion of the compressive stress pulse wave is reflected back into the sample at interface 2-2, while the other portion is transmitted into the transmission bar. When the compressive stress pulse wave is reflected back and forth for 3 to 6 times through the interfaces 1-1 and 2-2 in the rock sample, the stress equilibration is established in the rock sample.

In Figure 3, the cross-sectional area of the incident bar and the transmission bar is A_0. The cross-sectional area and length of the specimen are A and L. The stress at the interface of 1-1 is $\sigma_1(t)$, while the stress at the interface of 2-2 is $\sigma_2(t)$, and the stress of the specimen is $\sigma(t)$. The wave velocity and the elastic modulus of the incident bar and the transmission bar are C_0 and E_o, respectively, and the strain of the incident wave in the incident bar is ε_i and the reflected wave strain is ε_r. The transmission wave in the transmission rod is ε_t. The mass velocity at the interface of specimen 1-1 is u_1, and the particle velocity at the interface of specimen 2-2 is u_2. If the average strain in the specimen is ε, the strain rate is $\dot{\varepsilon}$. Based on the continuity condition of displacement and the one-dimensional stress hypothesis of stress wave, the following equations can be achieved.

Velocity on the interface1-1 is

$$u_1(t) = C_0[\varepsilon_i(t) - \varepsilon_r(t)]. \tag{5}$$

Velocity on the interface 2-2 is

$$u_2(t) = C_0\varepsilon_t(t), \tag{6}$$

Strain rate in the rock sample is

$$\dot{\varepsilon}(t) = \frac{u_1(t) - u_2(t)}{L} = \frac{C_0}{L}[\varepsilon_i(t) - \varepsilon_r(t) - \varepsilon_t(t)]. \tag{7}$$

Strain during time t is

$$D = f(\varepsilon, \dot{\varepsilon}). \tag{8}$$

Stress on 1-1 interface is

$$A\sigma_1(t) = A_0E_0[\varepsilon_i(t) + \varepsilon_r(t)]. \tag{9}$$

Stress on 2-2 interface is

$$A\sigma_2(t) = A_0E_0\varepsilon_t. \tag{10}$$

Average stress in specimen is

$$\sigma(t) = \frac{[\sigma_1(t) + \sigma_2(t)]}{2} = \frac{A_0E_0}{2A}[\varepsilon_i(t) + \varepsilon_r(t) + \varepsilon_t(t)]. \tag{11}$$

When the stress pulse wave propagates several times to and fro in the specimen, the stress equilibrium state is established. In this case, the three strains are equal as shown in equation (8):

$$\varepsilon_i + \varepsilon_r = \varepsilon_t. \tag{12}$$

Thus, by submitting (8) to (1)~(7), the following equations can be achieved:

$$\dot{\varepsilon}(t) = -\frac{2C_0}{L}\varepsilon_r(t), \tag{13}$$

$$\varepsilon(t) = -\frac{2C_0}{L}\int_0^t \varepsilon_r(t)dt, \tag{14}$$
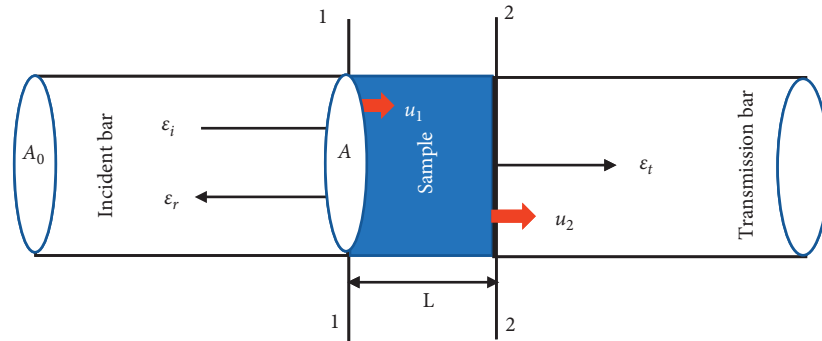
FIGURE 3: Schematic diagram of the rock sample under impact by SHPB.

$$\sigma(t) = \frac{A_0 E_0}{A}\varepsilon_t(t). \qquad (15)$$

Equations (12)~(15) can be used to calculate stress, strain, and strain rate in the research.

4. Rock Behaviours under Static Loading with Various High Temperatures

In this research, a chamber-type electric resistance furnace (Figure 4) is employed to heat the rock sample to a specific temperature for testing the rock behaviour experiencing various high temperatures and under different loading rates. The temperatures are set as indoor temperature (25°C), 100°C, 200°C, 400°C, 600°C, and 800°C, respectively. Figure 5 illustrates the cooled and dried rock samples after experiencing the above high temperatures. As illustrated in Figure 5(a), the colour of the marble sample lightened to a certain extent after cooling at a temperature of 100°C~400°C, but the volume and surface flatness did not change significantly. After experiencing the high temperature of 600°C, the colour of the rock gradually turns gray and white, and the surface flatness changes slightly. At 800°C (Figure 5(b)), the colour changes significantly, i.e., the marble turns white. Moreover, the volume of the specimen expands and obvious cracks appear. In addition, the surface of the specimen becomes very rough. This indicates that the specimen is damaged under the action of temperature and the internal structure of the rock has undergone obvious deterioration.

4.1. Uniaxial Compressive Strength (UCS) Test. As illustrated in Figure 6, YAW-2000 computer-controlled automatic pressure testing machine is used to carry out the UCS test and BTS test under static loads. In order to mitigate the end effects due to the frictions initiating from the two loading contacts, i.e., contacts of the sample ends and the loading plates, some lubricating oil is placed on the loading contacts. At the beginning of the testing, the loading plate is moving at a speed of 0.002 mm · s^{-1}. After the loading plate contacts the specimen, the loading plate is then applying the load of 1 kN · S^{-1} to the specimen until the specimen fails.

The averages of the rock parameters obtained from the test are recorded in Table 1, while Figure 7 shows the rock fracture patterns of the UCS test for those specimens under

FIGURE 4: XH7L chamber-type electric resistance furnace.

different temperatures. From the indoor temperature to 600°C, the rock fracture patterns are not significantly changed as the temperature increases. The rock mainly fractures along an inclined line or the vertical line which demonstrated typical characteristics of brittle materials under compression. According to the numerical study of the rock fracture process in the UCS test by a hybrid finite-discrete element method, the fractures are a mix of mode I-II damage (Figure 7(h)), i.e., mixed pure mode I fracture (Figure 7(g)) and pure mode II fracture.

Table 1 lists the obtained average compressive strength, strain on the vertical direction, and the Young modulus. The three parameters are significantly influenced by the increase of the temperature. With the increase of the temperature, those three parameters decrease significantly.

Figure 8 illustrates the stress-strain curves for those rock samples under various temperatures, while in general, as illustrated in Figure 8, the shape of the stress-strain curve is roughly the same, and each curve has experienced four stages: compaction stage, elastic stage, plastic deformation

(a)

(b)
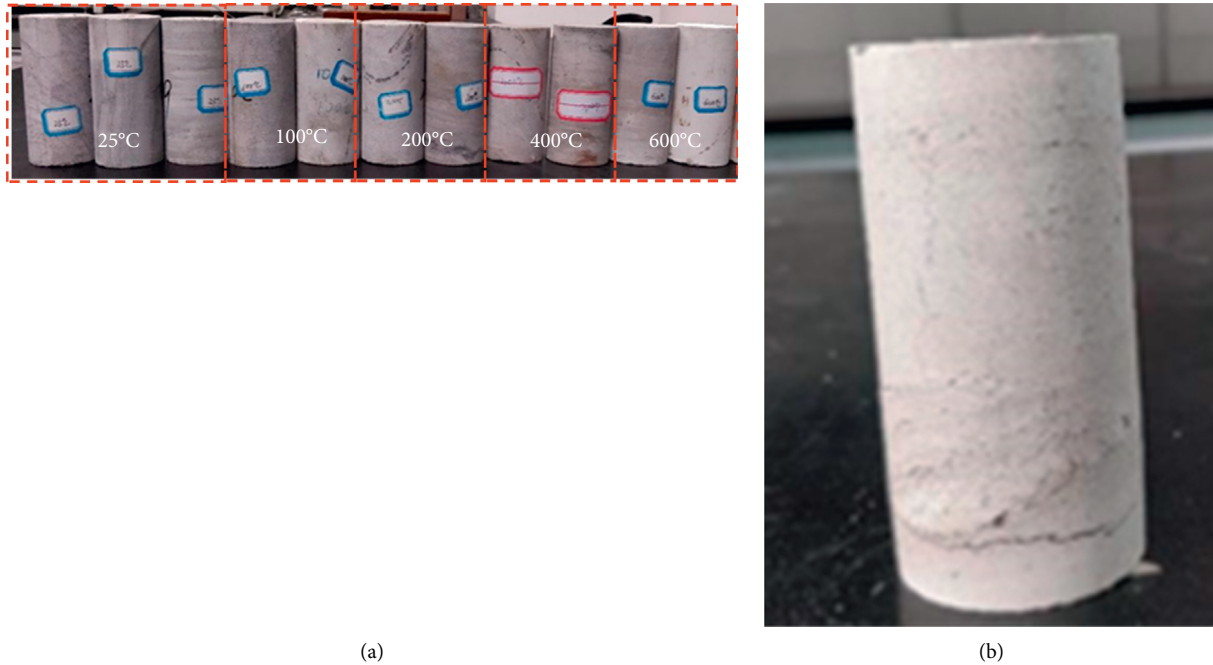
FIGURE 5: Rock sample for uniaxial compressive strength test after undergoing various temperatures. (a) Rock sample after experiencing the temperature from 25°C to 600°C. (b) Rock sample after undergoing 800°C.

FIGURE 6: YAW-2000 computer-controlled automatic pressure testing machine.

TABLE 1: Rock parameters obtained from the uniaxial compressive test under various temperatures.

Temperature (°C)	Compressive strength σ (MPa)	Strain ε (10^{-3})	Young's modulus E (GPa)
25	80.6	2.12	34.7
100	74.5	2.15	31.8
200	65.4	4.03	29.6
400	48.3	5.92	22.93
600	49.6	11.2	19.34
800	34.2	14.64	4.6

stage, and failure stage. In other words, the overall change trend for each curve is the same. When the marble temperature increases gradually, the slope of the compaction stage, i.e., the straight line of each curve, decreases, which indicates that the elastic modulus decreases with the increase of the temperature. This trend is confirmed by the elastic modulus in Table 1. For the specimen under the high temperature beyond 400°C, the peak stress of the rock decreases obviously, and the time to reach the peak stress increases, which indicates that the temperature has a great influence on the strength of the rock. As the temperature of the specimen increases gradually, the axial strain tends to increase, which is mainly due to the weakening and ductility of the material brittleness. By comparing the stress-strain whole-process curves in the above temperature ranges, it can be seen that with the increase of temperature, the brittleness, ductility, and peak strength of the rocks decrease. The curves still show the characteristics of brittle material failure process.

Figure 9 shows the relationship between the uniaxial compressive strength and the temperature. The temperatures have a significant impact on the strength of the rock. As can be seen from Figure 9, the strength of the rock decreased significantly from approximately 78 MPa to 20 MPa with the increase of the temperature from the indoor temperature to 800°C.

4.2. Brazilian Tensile Strength Test. Figure 10 illustrates the fracture patterns for the BTS test under different temperatures. The specimens mainly fracture along the loading diameter, and the main fractures separate the specimen into two halves. The fracture pattern is not significantly influenced by temperature.

Table 2 gives the tensile strength of the rock under different temperatures, while Figure 11 illustrates the corresponding curve.

(a)　　　　　　　　(b)　　　　　　　　(c)　　　　　　　　(d)　　　　　　　　(e)

Mode II damage

Mixed-mode I-II damage

(f)　　　　　　　　　　　　(g)　　　　　　　　　　　　(h)
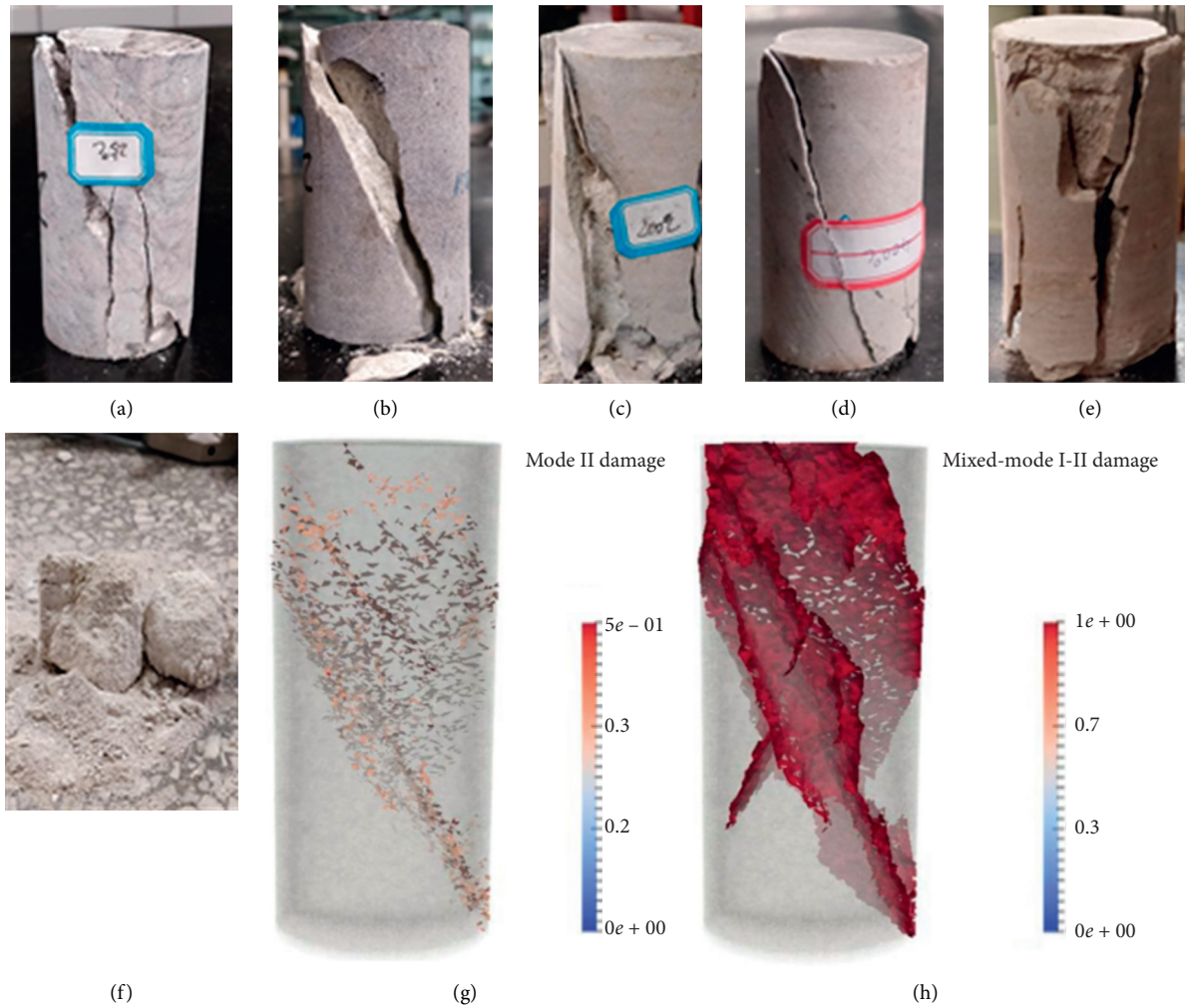
FIGURE 7: Fracture patterns for the UCS test under different temperatures: (a–f) experimental results; (g) mode II damage [55]; and (h) mixed-mode I-II damage [55]. (a) 25°C. (b) 100°C. (c) 200°C. (d) 400°C. (e) 600°C. (f) 800°C.
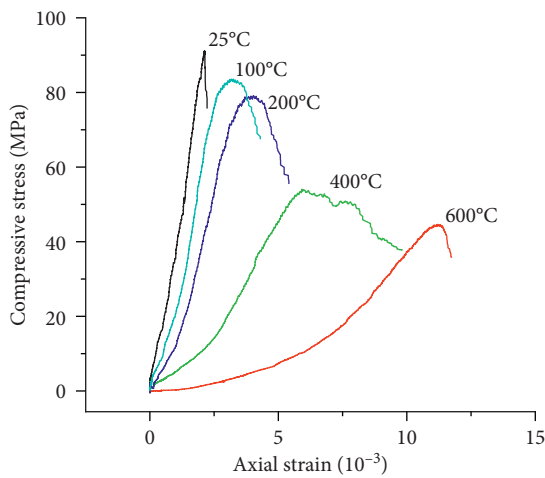
FIGURE 8: Stress-strain curve for uniaxial compressive strength test.

$$\sigma = 76.86843 - 0.04623\,T$$
$$-2.49 * 10^{-5} T^2$$
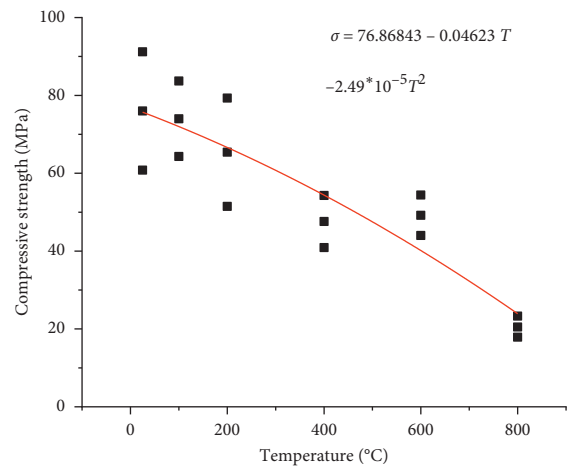
FIGURE 9: The strength-temperature curve for uniaxial compressive strength test.

As shown in Figure 11, the average results of static splitting tensile strength experiments show that the splitting tensile strength of marble at each temperature has a large

dispersion. In general, the splitting tensile strength of marble is 6.98 MPa at room temperature. After that, the tensile strength kept floating around 6.5 MPa until it reached about
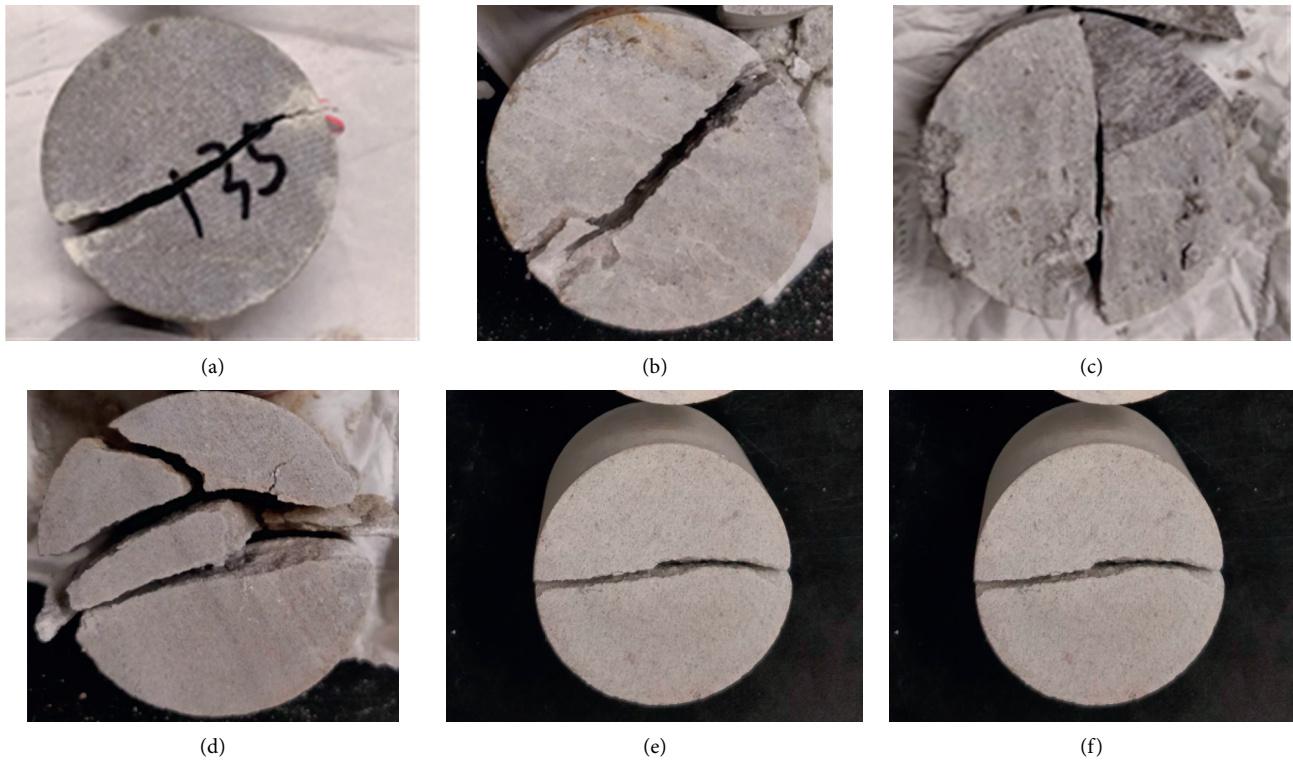
FIGURE 10: Rock fracture patterns for BTS test under various temperatures. (a) 25°C. (b) 100°C. (c) 200°C. (d) 400°C. (e) 600°C. (f) 800°C.

TABLE 2: Tensile strengths of the rock under different temperatures.

Temperature (°C)	25	100	200	400	600	800
Tensile strength σ (MPa)	6.82	6.64	6.44	6.8	6.48	3.4
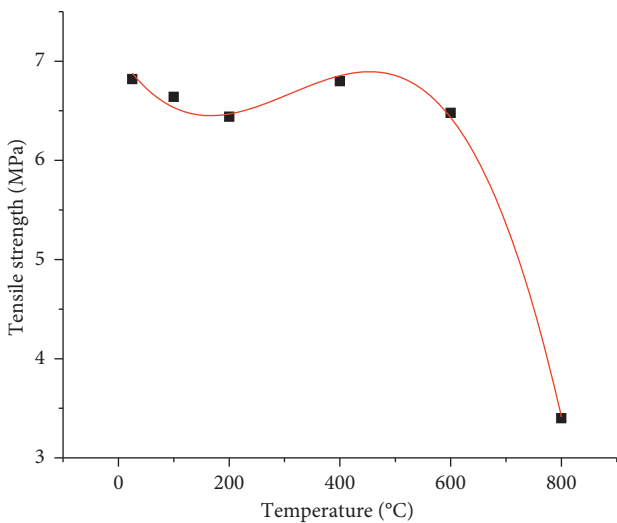
FIGURE 11: Tensile strength of the marble under different temperatures.

600°C. For the temperature of 800°C, the tensile strength of marble is only 3.40 MPa, about 43% decrease compared that at room temperature.

5. Rock Behaviours under Dynamic Loading and Different Temperatures

Figure 12 illustrates the HSPB system used for dynamic rock behaviour tests. The main components are gas gun, striker, incident bar, transmission bar, and dynamic strain meter system. Firstly, the striker is accelerated by gas gun to impact one end of the incident bar. Then, a dynamic compressive strain wave is induced in the incident bar and propagates toward the other end of the incident bar. Some portion of the compressive strain wave will be reflected at the interface between the incident bar and the specimen, and the reflected wave will turn into a tensile wave. The remaining portion will propagate into the specimen still as compressive strain wave. As the transmitted compressive strain wave reaches the interface of the specimen and the transmission bar, the disk is subjected to dynamic loading.

The rock material for the dynamic compression strength is the same as that used for the static test in the last section. The diameter of the cylinder is 50 mm, while the length is 40 mm. The temperature gradient of this experiment is divided into six degrees, i.e., 25°C, 100°C, 200°C, 40°C, 600°C, and 800°C. The heating rate of the resistance furnace is set as 10°C/min. When the temperature reaches the prescribed temperature, it is then heated at a constant temperature for another three hours to obtain marble samples under uniform high temperature. Then SHPB experiment under high temperature is carried out. In the experiment, impact speed is set as 10 m/s, 12.5 m/s, and 14.5 m/s, respectively.
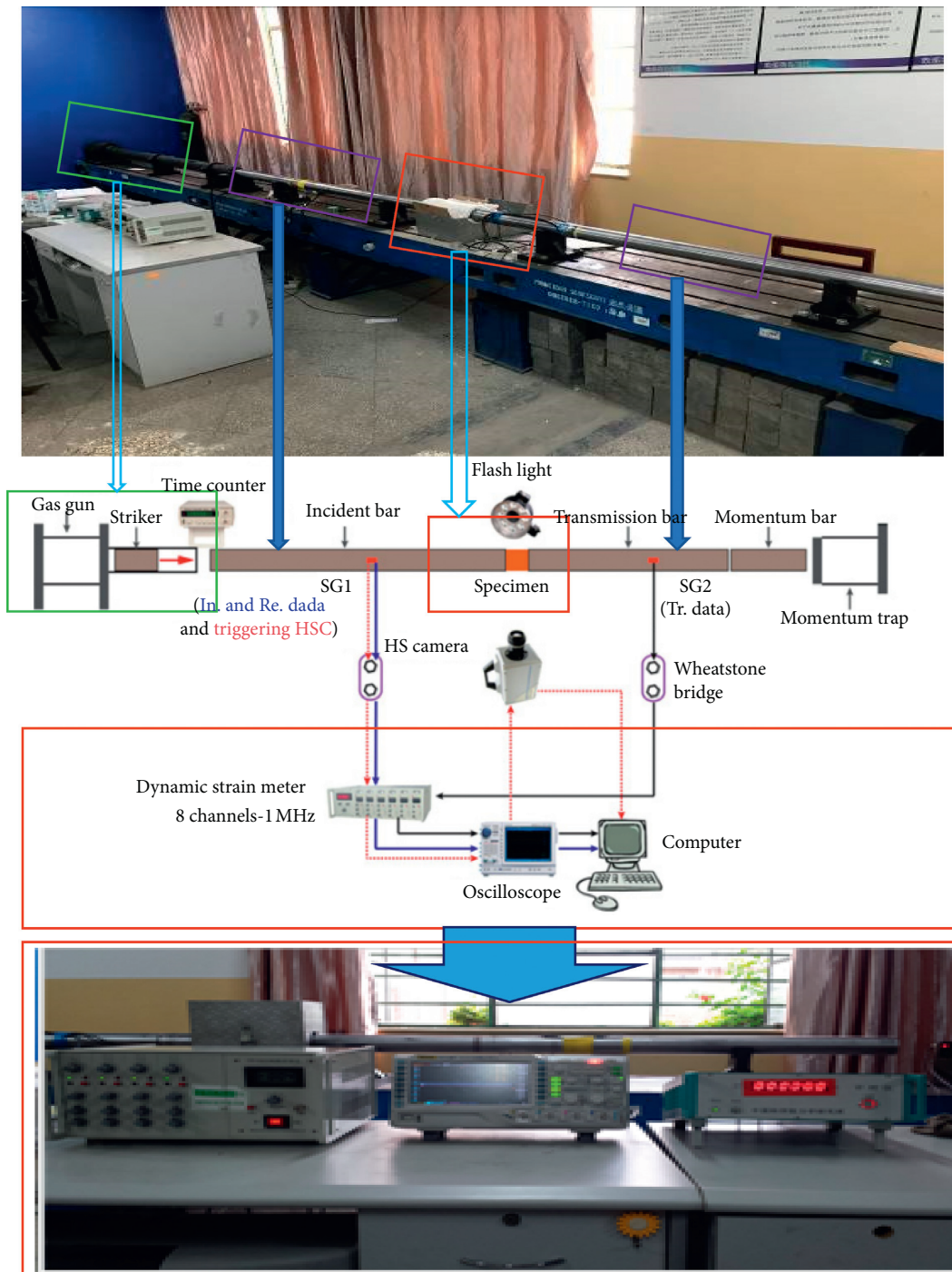
FIGURE 12: SHPB system (the schematic of the SHPB is adopted from Zhang and Zhao (2013) [56]).

5.1. Dynamic Uniaxial Compressive Strength (UCS) Test for Rock Specimens under Various Temperatures. Figure 13 illustrates the fragments produced by the dynamic UCS test. The strain rate significantly influences the test results in terms of the fragment size and size distribution. The larger the strain rate is, the finer the fragments produced for the specimen under the same temperature are. In addition, with the temperature increases, the size of the fragments decreases under the same loading rate.

Table 3 shows the influences of the impact strain rate, peak stress, peak strain, and Young's modulus by the impact speed and the temperature. In general, for a specific temperature, with the increase of the impact speed, the strain rate, peak stress, peak strain, and Young's modulus also increase. On the contrary, for a specific impact speed, with the increase of the impact speed, the strain rate increases, while the peak stress, peak strain, and Young's modulus decreases. More details for the relationship among those parameters are analysed from Figures 14–18.

(a)

(b)

(c)
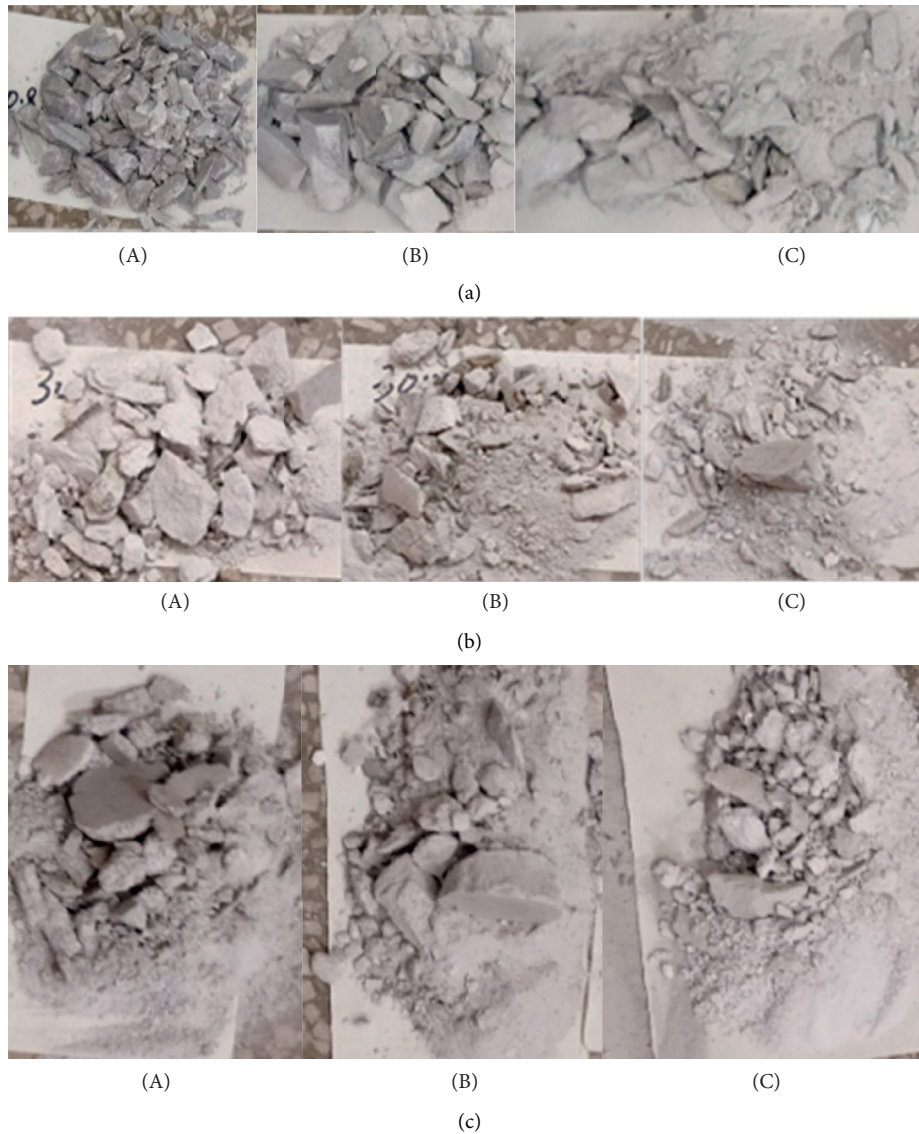
FIGURE 13: Rock fragments produced by the UCS test under coupled temperatures and strain rates. (a) I 25°C: (A) 84.7 s^{-1}, (B) 87.1 s^{-1}, and (C) 127.8 s^{-1}. (b) II 400°C: (A) 104.7 s^{-1}, (B) 07.1 s^{-1}, and (C) 137.8 s^{-1}. (c) III 600°C: (A) 200.7 s^{-1}, (B) 217.1 s^{-1}, and (C) 57.8 s^{-1}.

Figure 14 illustrates the stress-strain curves for the rock under different impact speed and temperatures. All the curves show a typical brittle rock failure process. Take the curves under the temperature of 25°C as an example (Figure 14(a)). The curves could be divided into four stages:

(i) OA: as the strain increases, the existing micro-fractures are closed. The duration of this stage is very short.

(ii) AB: the stage of AB is considered as linear elastic and deformation is fully recoverable.

(iii) BD: the stage of BD is the nonlinear elastic stage. During this stage, the fracture propagates stably. If the load is removed, the fracture propagation will be stopped.

(iv) DF: DF is the unstable fracture propagation stage. D is the yielding point, and beyond this point, the

permanent deformation develops and it is not recoverable even if the load is removed.

Compared with those figures (Figures 14(a)–14(f)), all the curves demonstrate the same trend although under various loading rates and high temperature. For an individual figure in Figure 14, it is indicated that with the increase of the loading rate, the rock strength increases. Compared with curves in different figures, it is indicated that with the increase of the temperature, the rock strength decreases.

Since the peak stress, peak strain, and Young's modulus of the brittle materials are significantly influenced by the strain rates and the temperature, relationships among them are discussed according to Figures 15–17. As illustrated in Figures 15 and 16, with the increase of temperature, the peak stresses of the rock specimens under three different impact speeds decrease dramatically (Figure 15), while with the

TABLE 3: Parameters obtained during the dynamic compressive strength tests.

Temperature T (°C)	Impact speed V (m/s)	Strain rate $*\varepsilon$ (s^{-1})	Peak stress σ_d (MPa)	Peak strain ε_d (10^{-3})	Young's modulus E_c (GPa)
25	10.0	96.09	199.73	3.56	25.39
	12.5	108.44	224.68	4.15	33.10
	14.5	117.90	246.70	11.25	36.00
100	10.0	100.12	191.14	1.77	33.21
	12.5	108.08	196.26	6.87	30.02
	14.5	118.08	205.76	8.99	31.96
200	10.0	118.70	152.99	3.05	34.56
	12.5	122.44	168.14	8.1	30.73
	14.5	135.93	240.71	12.91	28.68
400	10.0	122.63	146.69	6.02	29.86
	12.5	139.37	161.15	8.48	15.44
	14.5	161.25.	213.27	11.38	23.12
600	10.0	135.29	85.16	6.42	5.48
	12.5	160.19	104.29	9.96	12.26
	14.5	174.05	151.90	13.7	13.50
800	10.0	206.78	33.00	8.14	1.92
	12.5	215.47	35.91	18.03	2.63
	14.5	222.66	59.44	18.87	3.48

increase of the strain rate, the peak stresses increase fast (Figure 16). The relationship between dynamic peak stress and temperature change of marble specimens at different impact velocities can be fitted as shown in the following equations:

$$10.0 \, \text{m/s} \; \sigma = -0.28\left(\frac{T}{100}\right)^3 + 2.5\left(\frac{T}{100}\right)^2 - 23.4\left(\frac{T}{100}\right)$$
$$+ 205.72 \quad R^2 = 0.978,$$

$$12.5 \, \text{m/s} \; \sigma = -0.73\left(\frac{T}{100}\right)^3 + 7.77\left(\frac{T}{100}\right)^2 - 40\left(\frac{T}{100}\right)$$
$$+ 230.85 \quad R^2 = 0.986,$$

$$14.5 \, \text{m/s} \; \sigma = -0.24\left(\frac{T}{100}\right)^3 + 0.85\left(\frac{T}{100}\right)^2 - 0.06\left(\frac{T}{100}\right)$$
$$+ 240.20 \quad R^2 = 0.989.$$

(16)

Figure 17 illustrates the peak strain-temperature curves of rock under different impact loads. In general, with the increase of the temperatures, the peak strains increase. For the impact velocity of 10 m/s, the peak strain increases almost linearly. For the impact velocities of 12.5 m/s and 14.5 m/s, the peak strains increase fast when the temperature is beyond 400°C.

The relationship between the dynamic peak strain of marble specimen under different impact velocities and the change of temperature can be fitted as follows:

$$10.0 \, \text{m} \cdot \text{s}^{-1} \; \sigma = -8.76\left(\frac{T}{1000}\right)^3 + 10.4\left(\frac{T}{1000}\right)^2 + 4\left(\frac{T}{1000}\right)$$
$$+ 2.64 \quad R^2 = 0.959,$$

$$12.5 \, \text{m} \cdot \text{s}^{-1} \; \sigma = 119.56\left(\frac{T}{1000}\right)^3 - 130.45\left(\frac{T}{1000}\right)^2$$
$$- 46.43\left(\frac{T}{1000}\right) + 3.18 \quad R^2 = 0.999,$$

$$14.5 \, \text{m} \cdot \text{s}^{-1} \; \sigma = 42.54\left(\frac{T}{100}\right)^3 - 34.13\left(\frac{T}{1000}\right)^2$$
$$- 10.91\left(\frac{T}{1000}\right) + 10.19 \quad R^2 = 0.871.$$

(17)

Figure 18 illustrates the relationship between Young's modulus and the temperature under three different impact velocities. Before 200°C, with the increase of the temperature, Young's modulus is not influenced. However, after 200°C, Young's modulus decreases dramatically.

The relationship between the dynamic modulus of elasticity of marble specimens with different impact velocities and the change of temperature can be fitted as follows:

$$10.0 \, \text{m} \cdot \text{s}^{-1} \sigma = 0.41\left(\frac{T}{100}\right)^3 - 5.89\left(\frac{T}{100}\right)^2 + 18.49\left(\frac{T}{100}\right)$$
$$+ 20.34 \quad R^2 = 0.975,$$

(18)
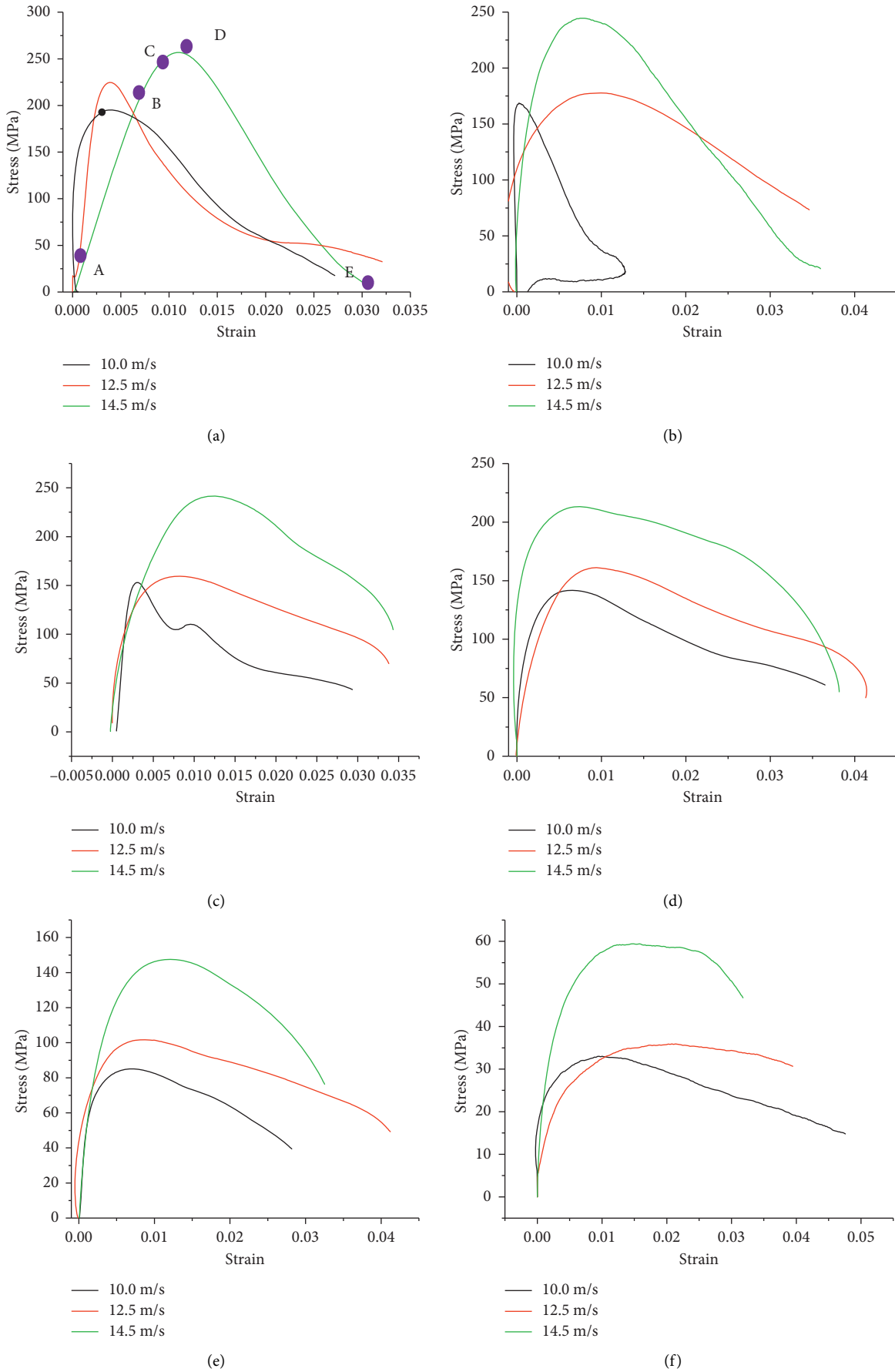
FIGURE 14: Stress-strain curves of rock under different impact speeds and different temperatures. (a) 25°C. (b) 100°C. (c) 200°C. (d) 400°C. (e) 600°C. (f) 800°C.
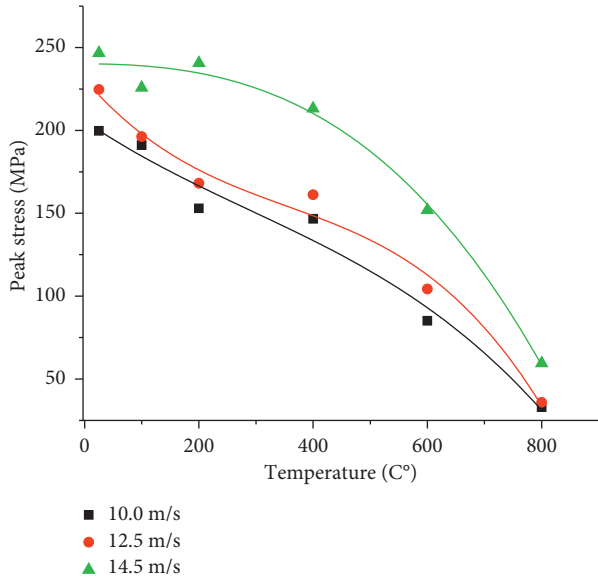
FIGURE 15: Peak stress-temperature curves of rock under different impact speeds and different temperatures.
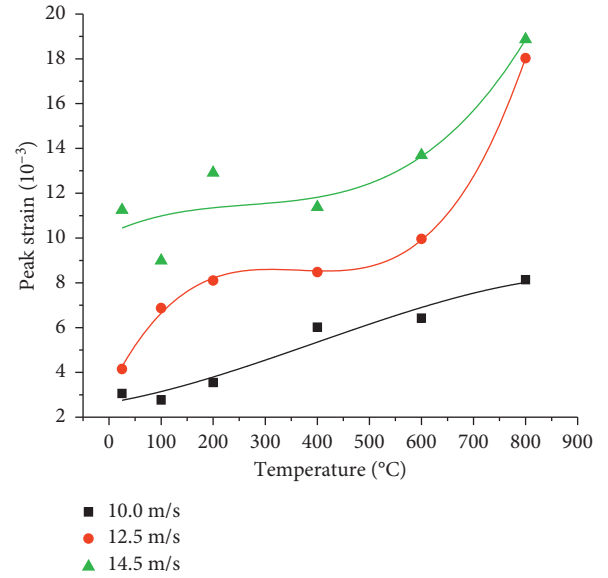
FIGURE 17: Peak strain-temperature curves of rock under different impact speeds and different temperatures.
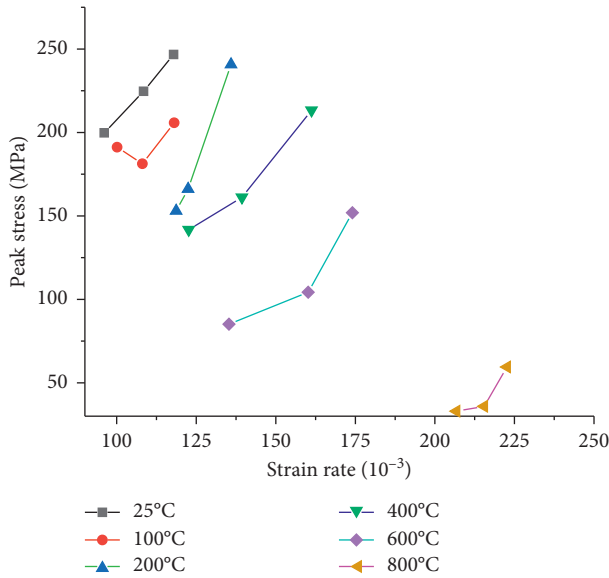
FIGURE 16: Peak stress-strain rate curves of rock under different impact speeds and different temperatures.
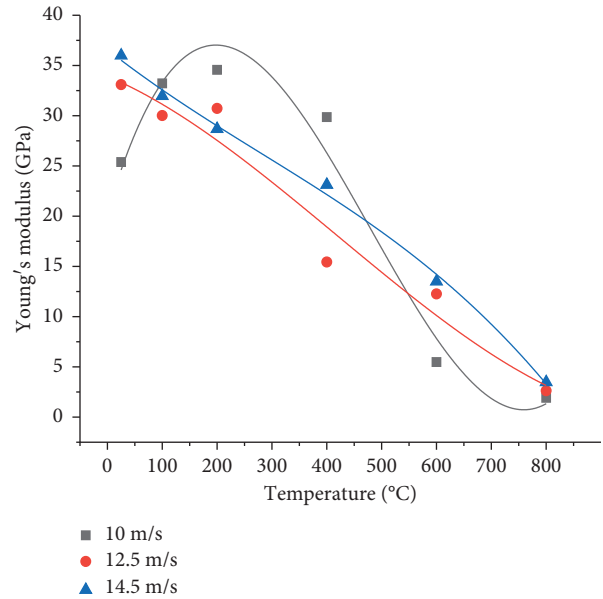
FIGURE 18: Young's modulus-temperature curves of rock under different impact speeds and different temperatures.

5.2. Dynamic Tensile Strength Test for Rock Specimens under Various Temperatures.

For the dynamic tensile strength test, the impact velocities for bullet are 5 m/s, 7 m/s, and 9 m/s, respectively. The temperatures for rock specimens are still set as 25°C, 100°C, 200°C, 40°C, 600°C, and 800°C. The specimen cylinder for the dynamic BTS test is prepared with a diameter of 50 mm and a height of 40 mm. The signals obtained by SHPB during the dynamic test can be processed by (12)–(14).

Figure 19 illustrates the rock fracture process during the dynamic BTS test. As can be seen from Figure 19 under

$$
12.5 \, \text{m} \cdot \text{s}^{-1} \, \sigma = 0.043 \left(\frac{T}{100}\right)^3 - 53.50 \left(\frac{T}{100}\right)^2 \\
- 2.29 \left(\frac{T}{100}\right) + 33.92 \quad R^2 = 0.963, \tag{19}
$$

$$
14.5 \, \text{m} \cdot \text{s}^{-1} \, \sigma = -0.039 \left(\frac{T}{100}\right)^3 + 0.33 \left(\frac{T}{100}\right)^2 - 4.29 \left(\frac{T}{100}\right) \\
+ 36.58 \quad R^2 = 0.997. \tag{20}
$$

(a)

(b)

(c)

(d)
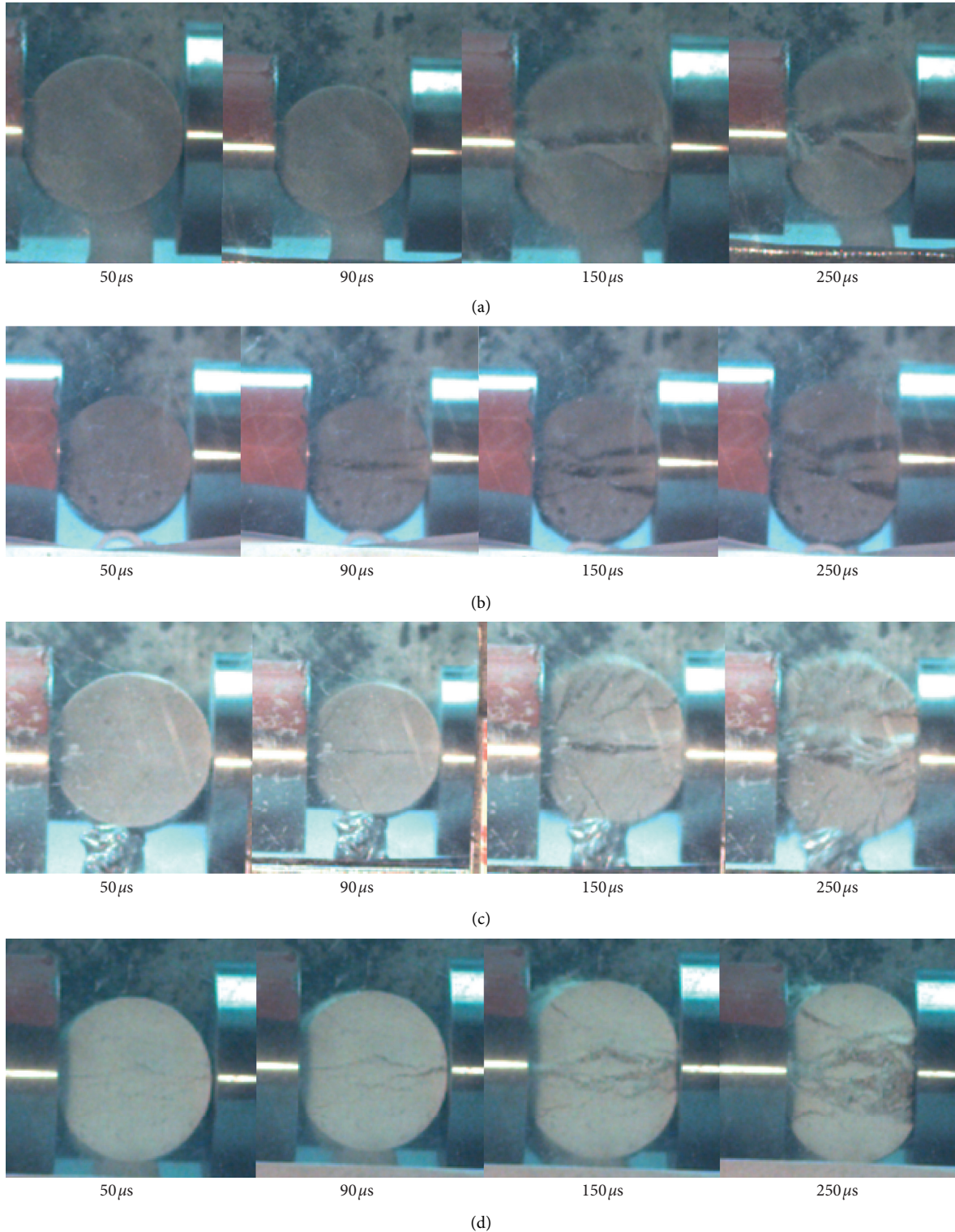
FIGURE 19: Failure process of marble under temperature from 200°C to 800°C obtained by a high-speed camera. (a) 200°C. (b) 400°C. (c) 600°C. (d) 800°C.

various temperatures, in the process of marble failure under different temperature conditions under high strain rate, the marble specimen first breaks into two parts along the radial (impact loading) direction, accompanied by a small amount of debris. In addition, some secondary cracks are produced at the loading end, forming a nearly triangular fragmented block. With the increase in temperature, the area of triangular breakage increases gradually. With the increase of the temperature, the fragments produced by the impact loading increase.

(a)

(b)

(c)

(d)

(e)

(f)
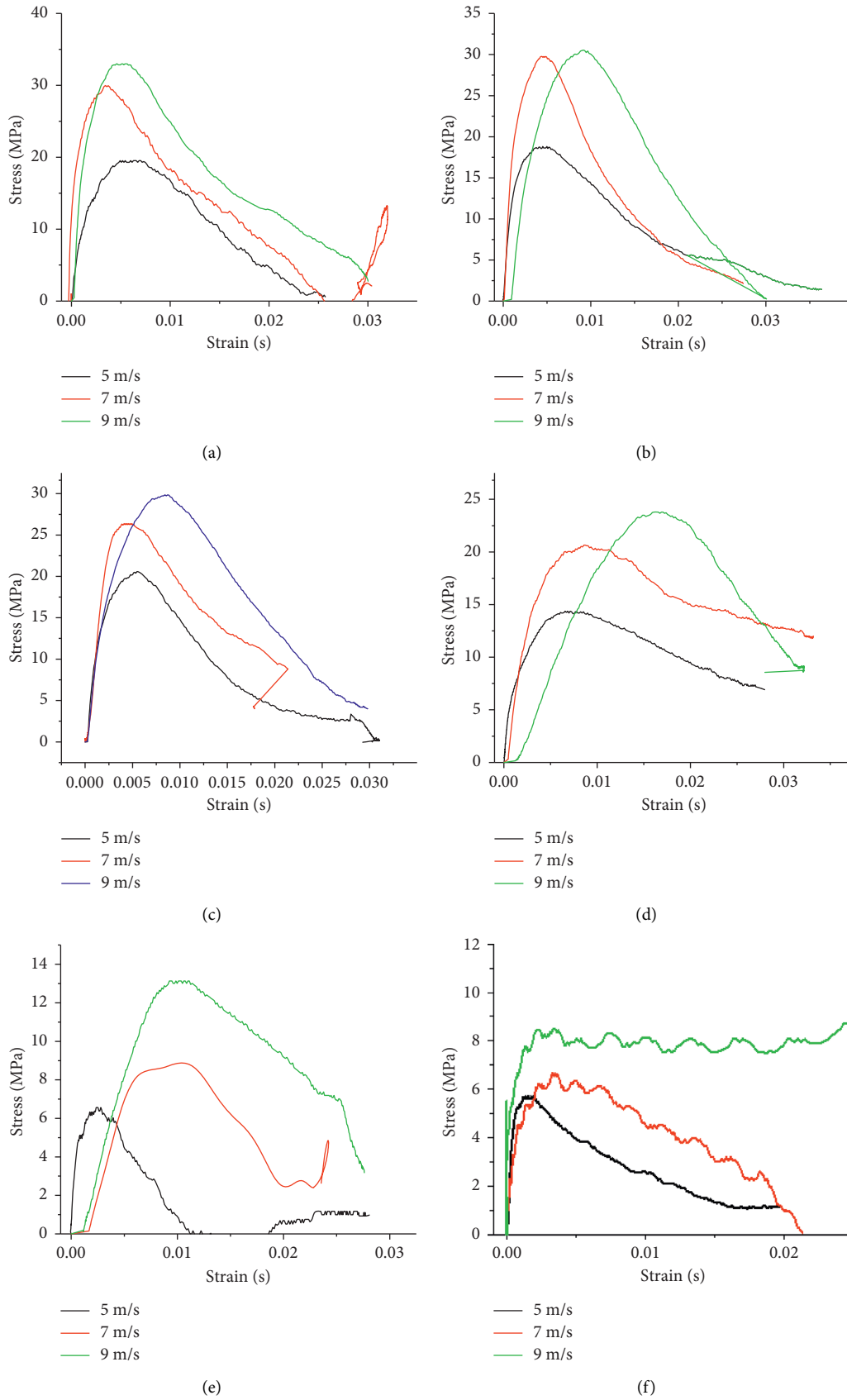
FIGURE 20: Stress-strain curves for the rock under different dynamic loads and temperature during dynamic BTS tests. (a) 25°C. (b) 100°C. (c) 200°C. (d) 400°C. (e) 600°C. (f) 800°C.

The stress-strain curves for the specimens under different loading rates and various temperatures are illustrated in Figure 20. For all the curves, they indicate that the impact speed of the bullet significantly influences the tensile strength of the rock. However, with the increase of the temperature, the tensile strength (peak stress) decreases. As can be seen in Figure 20(a), the peak strength is about 20 MPa at the impact speed of 5 m/s and room temperature, while it is only about 5.8 MPa (Figure 20(f)) at the same impact speed but under the temperature of 800°C. Thus, the temperature has an obvious influence on the tensile strength of the specimen. In addition, under the same temperature, for all the curves, the peak stress of the curve with a higher impact speed is much larger than that with a lower impact speed. Thus, the loading rate severely influences the tensile strength of the rock specimen.

6. Conclusions

This research has studied rock behaviour under the coupled dynamic loads and high temperatures. The SHPB system is used to carry out the test under different temperatures. The influences of the loading rate and the temperature are analysed. It is concluded that

(i) Under static loading, with the increase of temperature, the compressive strength of rock decreases. Before 400°C, the strength is not significantly influenced by the temperature, while after 400°C, the temperature plays a critical role in the rock strength under static loading.

(ii) Under the same impact velocity, the peak strength of marble decreases with the increase of temperature. However, with the increase of temperature, the peak strain of marble under high temperature increases. The dynamic elastic modulus of marble decreases with the increase of temperature, while the dynamic peak strength of marble decreases with the increase of temperature.

(iii) For the BTS test, the tensile strength increases with the increase of the loading rate. However, the tensile strength decreases with the increase of the temperature.

(iv) The failure modes of the dynamic BTS test are similar to those under static loading. The specimen is split into two halves along the loading diameter. Many fragments are produced at the top and bottom loading areas. With the increase of the loading rate, more fragments at the loading area are produced.

Data Availability

The data used to support the findings of this study are included within the article.

Conflicts of Interest

The authors declare that there are no conflicts of interest regarding the publication of this paper.

Acknowledgments

References

[1] Z. Yin, W. Chen, H. Hao et al., "Dynamic compressive test of gas-containing coal using a modified split Hopkinson pressure bar system," *Rock Mechanics and Rock Engineering*, vol. 53, no. 2, pp. 815–829, 2020.

[2] J. Zhao, Y. X. Zhou, A. M. Hefny et al., "Rock dynamics research related to cavern development for ammunition storage," *Tunnelling and Underground Space Technology*, vol. 14, no. 4, pp. 513–526, 1999.

[3] Z.-Q. Yin, "Assessment of blasting-induced ground vibration in an open-pit mine under different rock properties," *Advances in Civil Engineering*, vol. 2018, Article ID 4603687, 10 pages, 2018.

[4] H. An, S. Hou, and L. Liu, "Experimental and numerical study of the concrete stress and fracture propagation processes by blast," *Engineering Letters*, vol. 27, no. 4, pp. 669–675, 2019.

[5] H. An and H. Liu, "Hybrid finite-discrete element modelling of dynamic fracture of rock and resultant fragment arching by rock blast," in *Proceedings of the ISRM International Symposium-8th Asian Rock Mechanics Symposium*, International Society for Rock Mechanics, Sapporo, Japan, October 2014.

[6] H. M. An, H. Y. Liu, H. Han, X. Zheng, and X. G. Wang, "Hybrid finite-discrete element modelling of dynamic fracture and resultant fragment casting and muck-piling by rock blast," *Computers and Geotechnics*, vol. 81, pp. 322–345, 2017.

[7] H. An, H. Liu, X. Wang, J. Shi, and H. Han, "Hybrid finite-discrete element modelling of blast-induced excavation damaged zone in the top-heading of deep tunnels," *Stavební Obzor—Civil Engineering Journal*, vol. 26, no. 1, pp. 22–33, 2017.

[8] H. An, "Hybrid continuum-discontinuum modelling of rock fracutre process in brazilian tensile strength test," *Civil Engineering Journal-Stavebni Obzor*, vol. 26, no. 3, pp. 237–249, 2017.

[9] H. M. An and L. Liu, "Numerical study of dynamic behaviors of concrete under various strain rates," *Archives of Civil Engineering*, vol. 65, no. 4, pp. 21–36, 2019.

[10] H. An, "Hybrid finite-discrete element method modelling of Brazilian disc tests," in *Proceedings of the International Conference on Civil, Transportation and Environment (ICCTE 2016)*, pp. 371–377, Guangzhou, China, January 2016.

[11] H. An, "Hybrid finite-discrete element method modeling of rock failure processes in Brazilian disc tests," *Electronic Journal of Geotechnical Engineering*, vol. 21, 2016.

[12] S. Jianjun and A. Huaming, "Simulation research on collapse vibration caused by demolition blasting," in *Proceedings of the 2013 Fourth International Conference on Digital*

Manufacturing and Automation (ICDMA), IEEE, Qingdao, China, June 2013.

[13] H. Liu and H. An, "Hybrid finite-discrete modelling of dynamic fracture of rock under impact loads and resultant fragment grinding," in *International Conference on Geomechanics, Geo-Energy and Geo-Resources (IC3G 2016),* Melbourne, Australia, September 2016.

[14] H. Y. Liu, H. Han, H. M. An, and J. J. Shi, "Hybrid finite-discrete element modelling of asperity degradation and gouge grinding during direct shearing of rough rock joints," *International Journal of Coal Science & Technology,* vol. 3, no. 3, pp. 295–310, 2016.

[15] A. Kumar, "The effect of stress rate and temperature on the strength of basalt and granite," *Geophysics,* vol. 33, no. 3, pp. 501–510, 1968.

[16] Z. P. Bazant, S.-p. Bai, and R. Gettu, "Fracture of rock: effect of loading rate," *Engineering Fracture Mechanics,* vol. 45, no. 3, pp. 393–398, 1993.

[17] T. Blanton, "Effect of strain rates from 10-2 to 10 sec-1 in triaxial compression tests on three rocks," *International Journal of Rock Mechanics and Mining Sciences & Geomechanics Abstracts,* vol. 81, no. 1, pp. 47–62, 1981.

[18] G. Johnson, *Numerical Algorithms in a Lagrangian Hydrocode,* DTIC Document, Fort Belvoir, VA, USA, 1997.

[19] X. B. Li, T. S. Lok, and J. Zhao, "Dynamic characteristics of granite subjected to intermediate loading rate," *Rock Mechanics and Rock Engineering,* vol. 38, no. 1, pp. 21–39, 2005.

[20] H. Kolsky, "Stress waves in solids," Courier Corporation, Chelmsford, MA, USA, 1963.

[21] H. Kolsky, "An investigation of the mechanical properties of materials at very high rates of loading," *Proceedings of the Physical Society. Section B,* vol. 62, no. 11, pp. 676–700, 1949.

[22] H. Zhang, *Experimental research on Dispersion Behavior of BIg diameter SHPB,* Kunming Univeristy of Sceince and Technology (Sceicne Version), Kunming, China, 2010.

[23] S. K. Samanta, "Dynamic deformation of aluminium and copper at elevated temperatures," *Journal of the Mechanics and Physics of Solids,* vol. 19, no. 3, pp. 117–135, 1971.

[24] D. J. Frew, M. J. Forrestal, and W. Chen, "Pulse shaping techniques for testing brittle materials with a split Hopkinson pressure bar," *Experimental Mechanics,* vol. 42, no. 1, pp. 93–106, 2002.

[25] J. W. Tedesco, M. L. Hughes, and C. A. Ross, "Numerical simulation of high strain rate concrete compression tests," *Computers & Structures,* vol. 51, no. 1, pp. 65–77, 1994.

[26] F. Gálvez, J. Rodríguez, and V. Sánchez, "Tensile strength measurements of ceramic materials at high rates of strain," *Le Journal de Physique IV,* vol. 7, no. C3, pp. C3-151–C3-156, 1997.

[27] P. Sukontasukkul, P. Nimityongskul, and S. Mindess, "Effect of loading rate on damage of concrete," *Cement and Concrete Research,* vol. 34, no. 11, pp. 2127–2134, 2004.

[28] J. Zhao, "Applicability of Mohr-Coulomb and Hoek-Brown strength criteria to the dynamic strength of brittle rock," *International Journal of Rock Mechanics and Mining Sciences,* vol. 37, no. 7, pp. 1115–1121, 2000.

[29] Z. X. Zhang, S. Q. Kou, L. G. Jiang, and P.-A. Lindqvist, "Effects of loading rate on rock fracture: fracture characteristics and energy partitioning," *International Journal of Rock Mechanics and Mining Sciences,* vol. 37, no. 5, pp. 745–762, 2000.

[30] F. Dai, S. Huang, K. Xia, and Z. Tan, "Some fundamental issues in dynamic compression and tension tests of rocks using split Hopkinson pressure bar," *Rock Mechanics and Rock Engineering,* vol. 43, no. 6, pp. 657–666, 2010.

[31] F. Dai, K. Xia, H. Zheng, and Y. X. Wang, "Determination of dynamic rock mode-I fracture parameters using cracked chevron notched semi-circular bend specimen," *Engineering Fracture Mechanics,* vol. 78, no. 15, pp. 2633–2644, 2011.

[32] E. Eissa and A. Kazi, "Relation between static and dynamic Young's moduli of rocks," *International Journal of Rock Mechanics and Mining Sciences & Geomechanics Abstracts,* vol. 25, no. 6, pp. 479–482, 1988.

[33] B. Mahanta, A. Tripathy, V. Vishal, T. N. Singh, and P. G. Ranjith, "Effects of strain rate on fracture toughness and energy release rate of gas shales," *Engineering Geology,* vol. 218, pp. 39–49, 2017.

[34] Z. Zhang, *Laboratory Studies of Dynamic Rock Fracture and In-Situ Measurements of Cutter Forces for a Boring Machine,* CRC Press, Boca Raton, FL, USA, 2001.

[35] Q. Wang, W. Li, and X. Song, "A method for testing dynamic tensile strength and elastic modulus of rock materials using SHPB," *Pure and Applied Geophysics,* vol. 163, no. 5-6, pp. 1091–1100, 2006.

[36] Z. Zhou, X. Li, Y. Zou, Y. Jiang, and G. Li, "Dynamic Brazilian tests of granite under coupled static and dynamic loads," *Rock Mechanics and Rock Engineering,* vol. 47, no. 2, pp. 495–505, 2014.

[37] K. Peng, "Experimental and numerical evaluation of rock dynamic test with split-Hopkinson pressure bar," *Advances in Materials Science and Engineering,* vol. 2017, Article ID 2048591, 12 pages, 2017.

[38] I. Van der Molen, "The shift of the α-β transition temperature of quartz associated with the thermal expansion of granite at high pressure," *Tectonophysics,* vol. 73, no. 4, pp. 323–342, 1981.

[39] S. O. Heard, "Lipopolysaccharide-induced myocardial depression is not mediated by thromboxane a2," *Critical Care Medicine,* vol. 18, no. 4, p. S258, 1990.

[40] Z.-G. Yan, "Experimental study on longitudinal wave characteristics of tuff, granite and breccia after high temperature," *Yantu Gongcheng Xuebao (Chinese Journal of Geotechnical Engineering),* vol. 28, no. 11, pp. 2010–2014, 2006.

[41] T. Fengchen, "Repair of below pairt nasal defec by auricular compound tissue flap," *Chinese Journal of Reparative and Reconstructive Surgery,* vol. 4, p. 4, 1990.

[42] H. Zhao and L. Chen, "Experimental study of thermal expansion property of limestone," *Rock and Soil Mechanics,* vol. 32, no. 6, pp. 1725–1730, 2011.

[43] L. Chen, "Experimental research on heat swelling power of sandstone and limestone," *Journal of China University of Mining & Technology,* vol. 37, no. 5, pp. 670–674, 2008.

[44] X. Li, "Study of dynamic properties of siltstone under coupling effects of temperature and pressure," *Chinese Journal of Rock Mechanics and Engineering,* vol. 29, no. 12, pp. 2377–2384, 2010.

[45] T. Yin, *Study on Dynamic Behavior of Rocks Considering Thermal Effect,* Central South University, Changsha, China, 2012.

[46] T.-b. Yin, "Energy dissipation of rock fracture under thermomechanical coupling and dynamic disturbances," *Chinese Journal of Rock Mechanics and Engineering,* vol. 32, no. 6, pp. 1197–1202, 2013.

[47] J. Xu and S. Liu, "Effect of impact velocity on dynamic mechanical behaviors of marble after high temperatures," *Chinese Journal of Geotechnical Engineering,* vol. 35, no. 5, pp. 879–883, 2013.

[48] S. Liu, "Experimental research on mechanical behaviors of marble after high temperatures subjected to impact loading," *Chinese Journal of Rock Mechanics and Engineering*, vol. 32, no. 2, pp. 273–280, 2013.

[49] T. Akazawa, "New test method for evaluating internal stress due to compression of concrete (the splitting tension test) (part 1)," *Journal of Japan Society of Civil Engineers*, vol. 29, pp. 777–787, 1943.

[50] F. Carneiro, "A new method to determine the tensile strength of concrete," in *Proceedings of the 5th Meeting of the Brazilian Association for Technical Rules*, Springer, Berlin, Germany, 1943.

[51] G. Hondros, "The evaluation of Poisson's ratio and the modulus of materials of a low tensile resistance by the Brazilian (indirect tensile) test with particular reference to concrete," *Australian Journal of Applied Science*, vol. 10, no. 3, pp. 243–268, 1959.

[52] W. C. Zhu and C. A. Tang, "Numerical simulation of Brazilian disk rock failure under static and dynamic loading," *International Journal of Rock Mechanics and Mining Sciences*, vol. 43, no. 2, pp. 236–252, 2006.

[53] D. Li and L. N. Y. Wong, "The Brazilian disc test for rock mechanics applications: review and new insights," *Rock Mechanics and Rock Engineering*, vol. 46, no. 2, pp. 269–287, 2013.

[54] S. Timoshenko and J. Goodier, *Theory of Elasticity*, McGraw-Hill, New York, NY, USA, 1970.

[55] D. Fukuda, "Development of a 3D hybrid finite-discrete element simulator based on GPGPU-parallelized computation for modelling rock fracturing under quasi-static and dynamic loading conditions," *Rock Mechanics and Rock Engineering*, vol. 53, no. 3, pp. 1072–1112, 2020.

[56] Q. B. Zhang and J. Zhao, "Determination of mechanical properties and full-field strain measurements of rock material under dynamic loads," *International Journal of Rock Mechanics and Mining Sciences*, vol. 60, pp. 423–439, 2013.

Research Article

Interval Nonprobabilistic Reliability Analysis for Ancient Landslide considering Strain-Softening Behavior: A Case Study

Zilong Zhou, Chenglong Lin, Xin Cai [ID], and Riyan Lan

School of Resources and Safety Engineering, Central South University, Changsha 410083, China

Correspondence should be addressed to Xin Cai; xincai@csu.edu.cn

Uncertainties in geotechnical parameters significantly affect the stability evaluation of an ancient landslide, especially when considering the strain-softening behavior. Due to the great difficulty in obtaining the probability density distribution of geo-parameters, an interval nonprobability reliability analysis framework combined with numerical strain-softening constitutive relations was established in this paper. Interval variables were defined as the uncertain parameters in the strain-softening model. The interval nonprobabilistic reliability was defined as the minimum distance from the origin point to the failure surface in the standard normal space, which is the key index for describing the ability of a system to tolerate the variation of uncertain parameters. The proposed method was used to evaluate the reliability of Baishi ancient landslide. The parameter sensitivity analysis was also conducted. Through the proposed method, it is considered that Baishi ancient landslide is safe and stable, and the strain threshold k_r is the dominant parameter. The results calculated by the proposed method agree well with the actual situation. This indicates the proposed method is more applicable than the traditional probability method when the data are scare.

1. Introduction

Considerable uncertainties exist in landslide engineering [1–5]. Traditional deterministic analysis cannot account for the uncertainty explicitly in most cases [6, 7]. Overestimation or conservative estimation of stability is very common [8]. Therefore, the reliability analysis considering the effect of uncertainties should be proposed for exactly evaluating the landslide stability.

The reliability method has been developed for different fields since 1930s [9]. The reliability of engineering structure is defined as the ability to perform the predetermined function in the specified time under the specified conditions. In landslide engineering, the basic steps of reliability analysis are as follows [9, 10]: (1) determining the input variables; (2) determining the performance function of the limiting state; (3) calculating the reliability index. Great achievements have been made on landslide reliability calculation. The uncertainties in geomaterial properties and subsurface stratigraphic and other aspects of landslide engineering were well considered [11–13]. However, the strain-softening behavior,

as a common characteristic in geomaterial deformation, was usually neglected [14, 15]. It is necessary to consider the strain-softening behavior to evaluate the slope stability accurately [16–19].

Limited studies can be found to analyze the landslide reliability considering the strain-softening behavior. Terzaghi and Peck [20] firstly took notice of the strain-softening behavior of soil. Bishop [21] proposed the concept of progressive failure of slopes. Skempton [22] defined the average residual factor R over a slip surface as the proportion of slip surface length over which the shear strength has reduced to a residual value. In a long time, residual factor R has been the most commonly used parameter to describe the strain-softening behavior in reliability analysis. Grivas and Chowdhury [23] firstly developed the probabilistic reliability analysis for strain-softening slopes. Stability factor F_s was obtained by the limit equilibrium method with residual factor R, and a simple probabilistic reliability analysis was conducted under "$\varphi = 0$" assumption (ignoring the internal friction angle). Chowdhury et al. [24] considered the correlations between shear parameters. In recent years, Metya

et al. [25] conducted a probabilistic reliability analysis based on the first-order reliability method; the performance function ($F_s - 1$) based on the Bishop simplified method was adapted to take strain-softening into account in terms of residual factor R. Bhattacharya et al. [26] regraded residual factor R as a random variable, and the influence of R was comprehensively analyzed and compared under different probability density distributions. These probabilistic reliability analyses can well describe the uncertainties in the strain-softening slope. However, these methods require the probability density distribution of uncertain parameters, which significantly affects the results of reliability evaluations. Usually, it is hard to obtain the adequate data describing the strain-softening behavior of landslide. The independent normal or log-normal distribution assumption can also cause some errors in the strain-softening relation. For examples, strength parameters may be negative based on normal distribution assumption. There are always some possibilities that the residual strength even exceeds the peak strength due to the long-tail curve in the independent normal or log-normal distribution assumption ($c_r > c_p$, $\varphi_r > \varphi_p$, in which c_r and c_p are the peak and residual cohesion, respectively, and φ_r and φ_p are the peak and residual frictional angle respectively). In addition, the randomness of some uncertain parameters needs further discussion. Fortunately, the interval theory may provide a new strategy. This new idea was usually used in structure engineering [27–29]. Reliability was used to describe the ability of a system to tolerate the variation of uncertain parameters instead of failure probability. Interval values can better describe the uncertainties in stain-softening relations when the data are scare. The bounds of the interval value can also guarantee the correct relations between peak and residual strength ($c_p > c_r$, $\varphi_p > \varphi_r$). Therefore, interval nonprobability reliability method has great application prospect in landslide engineering [30–32].

In this paper, an interval nonprobabilistic reliability analysis framework combined with numerical strain-softening constitutive relations was established. The proposed method requires only the boundary values instead of specific probability density distribution functions of uncertain parameters describing the strain-softening behavior, greatly decreasing the demanding for data. Nonprobabilistic reliability index η instead of a deterministic safety factor F_s or traditional probability of failure was used to describe the stability. The method was used to verify the stability of Baishi ancient landslide. Results of the proposed method were compared with the results of the traditional probabilistic method and the in situ investigation to prove the applicability. The sensitivity analysis was also discussed to make a reference for similar engineering.

2. Methodology

2.1. Interval Variables in Strain-Softening Model.
To consider the uncertainties as well as the strain-softening behavior, numerical strain-softening constitutive model is commonly used [33]. In the simplified constitutive model, the strain-softening behavior is characterized by five parameters: peak

cohesion c_p, peak friction angle φ_p, residual cohesion c_r, residual friction angle φ_r, and the threshold parameter when strength reduces from peak to residual k_r.

The uncertainty of different parameters needs to be confirmed. As shown in Figure 1, k_r was a parameter describing the malleability of strain-softening materials [33]. When k_r increases from 0 to ∞, materials change from brittleness to malleability, and the strength of geomaterials changes from residual to peak state. Considering the noticeable malleability effect in soil deformation, k_r is considered as a variable in this paper. k_r is also greatly associated with the residual factor R [22]; they are the cause and effect in negative correlation. Peak and residual shear strength (c_p, φ_p, c_r, and φ_r) are the common parameters with great uncertainties describing the inherent quality of geomaterials [15, 26]. Therefore, all these parameters in numerical strain-softening constitutive model (c_p, φ_p, c_r, φ_r, and k_r) are confirmed as interval variables to consider the uncertainties. It is noted that interval variables are assumed mutually independent.

2.2. Determination of Safety Factor F_s.
The response interval of F_s controlled by interval variables is obtained based on the numerical model in FLAC 3D. Each response of F_s against each group of interval variables is calculated by the shear strength reduction (SSR) method, which is commonly used in landslide engineering [34, 35]. The SSR method can truly represent stress-strain relations in the progressive failure process [33], thus very suitable for landslide with strain-softening behavior. In this method, the safety factor is defined as the ratio of the actual shear strength to the reduced shear strength at failure (equations. (1) and (2)). Zhang et al. [36] extended this method to solve F_s of a homogeneous slope with a strain-softening behavior:

$$c'_f = \frac{c'}{Fs}, \tag{1}$$

$$\varphi'_f = \arctan\left(\tan \frac{\varphi'}{F_s}\right), \tag{2}$$

where Fs is the safety factor; c'_f and φ'_f are the real strength parameters at failure; and c' and φ' are the original strength parameters.

Interval variables c_p, φ_p, c_r, φ_r, and k_r are the input parameters. Specially, the strength reduction process is only conducted in the slip zones [37]. The accumulations and the bedrock layer remain unchanged with the Mohr–coulomb model. In other words, slip zones are considered as the overriding potential slip surface. The reason is that failures usually occur in local weaker materials firstly in the ancient landslide.

2.3. Performance Function M.
Performance function M presenting the limit state of system is established based on F_s as

$$M = F_s - 1 = g\left(c_p, \varphi_p, c_r, \varphi_r, k_r\right). \tag{3}$$
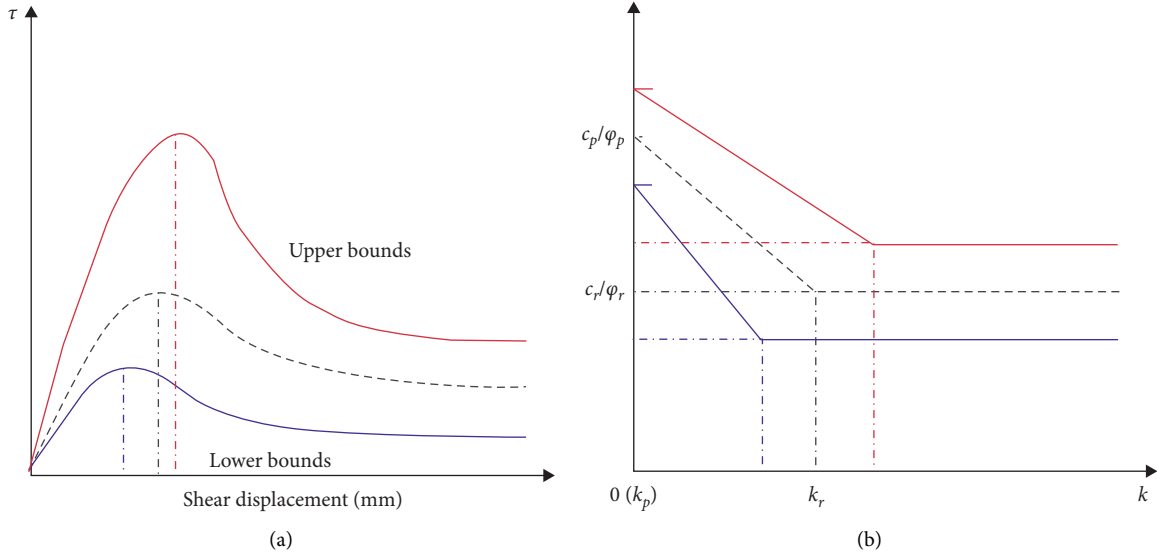
FIGURE 1: (a) Shear stress-displacement curves under a certain vertical stress. (b) Numerical strain-softening constitutive model (Conte et al.) [33].

However, numerical method cannot give an explicit relationship between M and interval variables. In this paper, the explicit expression of M was obtained by response surface fitting [38] via a series of deterministic tests. Usually, the explicit expression needs to be assumed in advance [10, 39, 40]. Some preliminary treatment is made to optimize the performance function in this paper. According to the expression obtained by the limit equilibrium method [26], F_s can be written as

$$F_s = R\left(\frac{c_r + \gamma z * \cos^2 i * \tan \varphi_r}{\gamma z * \sin i * \cos i}\right)$$
$$+ (1 - R)\left(\frac{c_p + \gamma z * \cos^2 i * \tan \varphi_p}{\gamma z * \sin i * \cos i}\right). \tag{4}$$

For simplification, F_s could be rewritten as

$$F_s = w_1 F_p + w_2 F_r, \tag{5}$$

where R is the residual factor, $w_1 = 1 - R, w_2 = R, F_r = (c_r + \gamma z * \cos^2 i * \tan \varphi_r)/(\gamma z * \sin i * \cos i)$ is the residual safety factor, and $F_p = (c_p + \gamma z * \cos^2 i * \tan \varphi_p)/ (\gamma z * \sin i * \cos i)$ is the peak safety factor.

In equation (5), each subitem (w_1, F_p, w_2, F_r) was assumed as a linear or quadratic polynomial for convenience. As introduced in Section 2.1, when $k_r = 0$, materials are brittle, strength of whole slip surface are in residual state, and then $w_1 = 0, w_2 = 1$. Therefore, the assumed expressions of each subitems are written as

$$F_p = a_1 + a_2 c_p + a_3 \varphi_p + a_4 \varphi_p^2, \tag{6}$$

$$F_r = b_1 + b_2 c_r + b_3 \varphi_r + b_4 \varphi_r^2, \tag{7}$$

$$w_1 = c_1 k_r + c_2 k_r^2, \tag{8}$$

$$w_2 = 1 - \left(c_1 k_r + c_2 k_r^2\right), \tag{9}$$

where $a_1, a_2, a_3, a_4, b_1, b_2, b_3, b_4, c_1, c_2$ are the undetermined coefficients.

Substituting equations (6)–(9) into equation (3), the performance function can be expressed as

$$M = \left(c_1 k_r + c_2 k_r^2\right)\left(a_1 + a_2 c_p + a_3 \varphi_p + a_4 \varphi_p^2\right)$$
$$+ \left(1 - c_1 k_r - c_2 k_r^2\right)\left(b_1 + b_2 c_r + b_3 \varphi_r + b_4 \varphi_r^2\right) - 1. \tag{10}$$

After fitting a series of deterministic results $((c_p, \varphi_p, c_r, \varphi_r, k_r), M)$, the explicit expression of M in equation (10) can be obtained.

2.4. Reliability Analysis Based on Interval Theory.
Interval nonprobability reliability index η, representing the ability of a system to tolerate the variation of uncertain parameters, is defined as the minimum distance between original point and failure surface in the standard normal space [27–29] (as shown in Figure 2).

For $\forall M = g(x_1, x_2, \ldots, x_n)$, where M is the performance function, $(x_1, x_2, \ldots, x_n)$ are the controlling interval variables, there are $\forall x_i \in [x_i^{\min}, x_i^{\max}]$ $(i = 1, 2, \ldots, n)$, where $x_i^{\min}$ and $x_i^{\max}$ are the lower and upper bounds of x_i respectively. Then, the performance function M is also an interval $M = [M^{\min}, M^{\max}]$ to response, where $M^{\min}$ and $M^{\max}$ are the lower and upper bounds of M, respectively. M^c and M^r are defined as the mean and radius of M, respectively (equations (11) and (12)). Then, the interval nonprobability reliability index η is defined as in equation (13):

FIGURE 2: Schematic diagram of interval nonprobability reliability.

$$M^c = \frac{1}{2}\left(M^{\min} + M^{\max}\right), \tag{11}$$

$$M^r = \frac{1}{2}\left(M^{\max} - M^{\min}\right), \tag{12}$$

$$\eta = \frac{M^c}{M^r}, \tag{13}$$

where $M = g(x_1, x_2, \ldots, x_n) = 0$ is the failure plane, and this hypersurface divides the space into the failure domain and the security domain. When $M = g(x_1, x_2, \ldots, x_n) < 0$, the system is in failure state and the opposite it is in safe state. According to equations (11)–(13), if $\eta > 1$, then $\forall x_i \in [x_i^{\min}, x_i^{\max}]$ $(i = 1, 2, \ldots, n)$, $M = g(x_1, x_2, \ldots, x_n) > 0$, and the system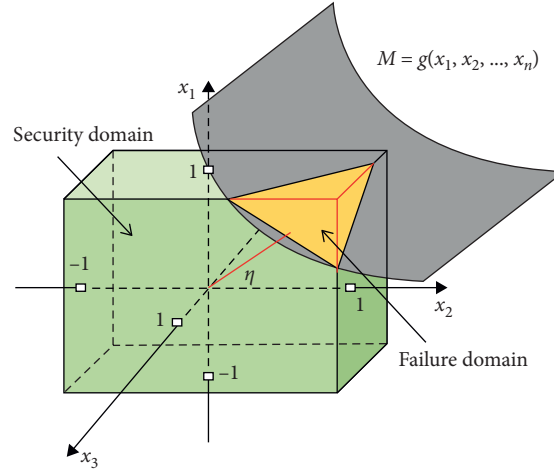 is safe and reliable. If $\eta < 1$, then $\forall x_i \in [x_i^{\min}, x_i^{\max}]$ $(i = 1, 2, \ldots, n)$, $M = g(x_1, x_2, \ldots, x_n) < 0$ and the system fails. If $-1 \leq \eta \leq 1$, then $\forall x_i \in [x_i^{\min}, x_i^{\max}]$ $(i = 1, 2, \ldots, n)$, $M = g(x_1, x_2, \ldots, x_n) < 0$ or $M = g(x_1, x_2, \ldots, x_n) > 0$ or $M = g(x_1, x_2, \ldots, x_n) = 0$ are all possible. As a result, the system could be safe or in failure. And, the larger the value of η, the safer the system [32].

3. Case Study: Baishi Ancient Landslide

3.1. Geological Background. To verify the applicability of our reliability analysis method, we took a strain-softening landslide, i.e., Baishi ancient landslide, as an example. Baishi ancient landslide is located at the south mountains area in Guangxi province, China (Figure 3(a)). Geographic, geomorphic, elevation, and other information is shown in Figure 3(b). Geologically, Baishi landslide is an accumulated ancient landslide with obvious ancient slip bands. The geomaterial distribution could be described as three uneven layers: (1) argillaceous sandstone bedrock downmost, (2) slip bands with strain-softening behavior in-between, and (3) soil-gravel accumulations uppermost.

3.2. Parameter Collection. Some critical parameters used for simulation were collected from geological surveys or engineering experience as listed in Table 1.

3.3. Interval Variables and Numerical Model in Case Study. According to in situ data and engineering experience [15, 33, 41], interval variables of Baishi ancient landslide are set in Table 2. Correlation relation of parameters ($c_p > c_r$; $\varphi_p > \varphi_r$) in strain-softening constitutive is well presented.

The numerical model in FLAC 3D of Baishi ancient landslide is established on the real geological information. According to some preliminary computation and in situ surveys, profile A-A′ in Area I is chosen as the main research object (shown in Figure 4). In this model, the ancient slip zones are abstracted as a 2 m thick band. The mesh of slip zones is almost all quadrangles of $1\,m \times 1\,m$, and the grid division is enough for computation.

4. Results and Discussion

4.1. Stability Analysis. Table 3 presents some results of deterministic analysis of Baishi ancient landslide. Three examples are conducted. In example 1, safety factor F_s is calculated in peak strength when the peak strength parameters (c_p, φ_p) are set as the maximum, mean, and minimum values, respectively. In example 2, safety factor F_s is calculated in residual strength when the residual strength parameters (c_r, φ_r) are set as the maximum, mean, and minimum values, respectively. In example 3, safety factor F_s is calculated considering the strain-softening behavior when k_r is set as the maximum, mean, and minimum values, respectively. In these three examples, all the parameters are set as mean values except for the assigned parameters. In examples 1 and 2, results are also calculated by the Spencer method to make a comparison with that by the SSR method.

Results in examples 1 and 2 indicate that, when F_s is calculated only in peak or residual strength, uncertainties of shear strength parameters (c_p, φ_p; c_r, φ_r) can cause great differences. The values of c_p, φ_p and c_r, φ_r should be thus considered as variables. Results calculated by SSR and Spencer methods are in good agreement, which indicates that the numerical model and method in this paper are valid. Results in example 3 indicate that when F_s is calculated considering the strain-softening behavior, the results are significantly influenced by the value of k_r. Also, k_r is set as a variable. Moreover, calculation results of F_s are 1.695, 1.095, and 1.414, respectively,

(a)

→ North direction − − − Boundary
--→ Sliding direction − − − Planned road

(b)
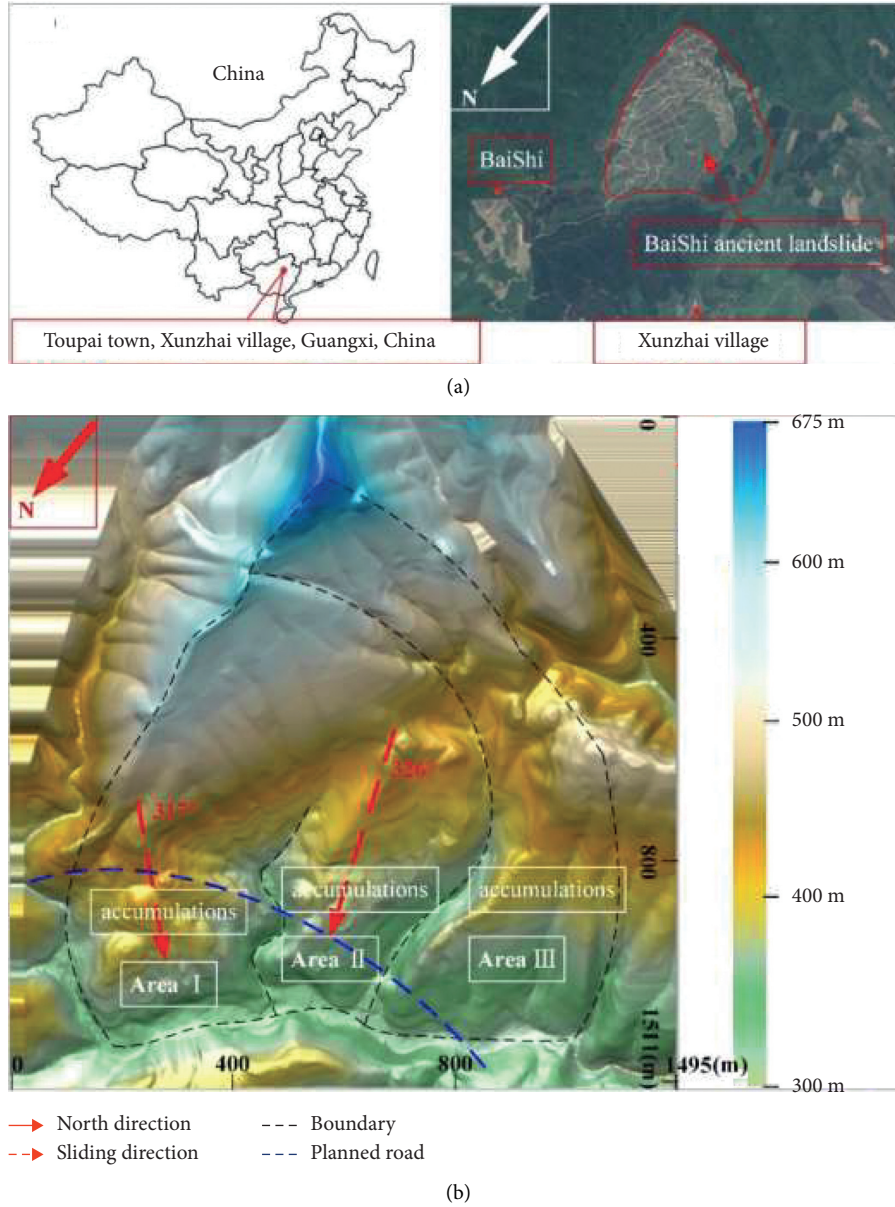
FIGURE 3: (a) Location and (b) digital elevation model of Baishi ancient landslide.

TABLE 1: Physical and mechanical parameters of Baishi ancient landslide.

Item	Accumulations	Bedrock	Slip bands
Constitutive relation	Mohr–Coulomb	Mohr–Coulomb	Strain-softening
E (GPa)	1	10	0.1
ν	0.3	0.3	0.3
ρ (kg·m^3)	1960	2130	2450
c (kPa)	26	130	—
φ (°)	29	42	—
c_p (kPa)	—	—	12.5~16.8
φ_p (°)	—	—	17.9~24.7
c_r (kPa)	—	—	3.1~12.5
φ_r (°)	—	—	10.6~17.9

Note: only the shear strength parameters of slip bands were collected in detail.

TABLE 2: Interval variables in the case study.

Interval variables	Units	Range
c_p	kPa	[12.5, 16.8]
φ_p	°	[17.9, 24.7]
c_r	kPa	[3.1, 12.5]
φ_r	°	[10.6, 17.9]
k_r	—	[0, 0.1]

Note: only the parameters of slip zones are considered with the strain-softening behavior and abstracted as interval variables.

when parameters (c_p, φ_p; c_r, φ_r) are set as the mean value of peak strength and residual strength and in the case of considering the strain-softening behavior. Result indicates that the strain-softening behavior should be considered in the stability evaluation of Baishi ancient landslide.
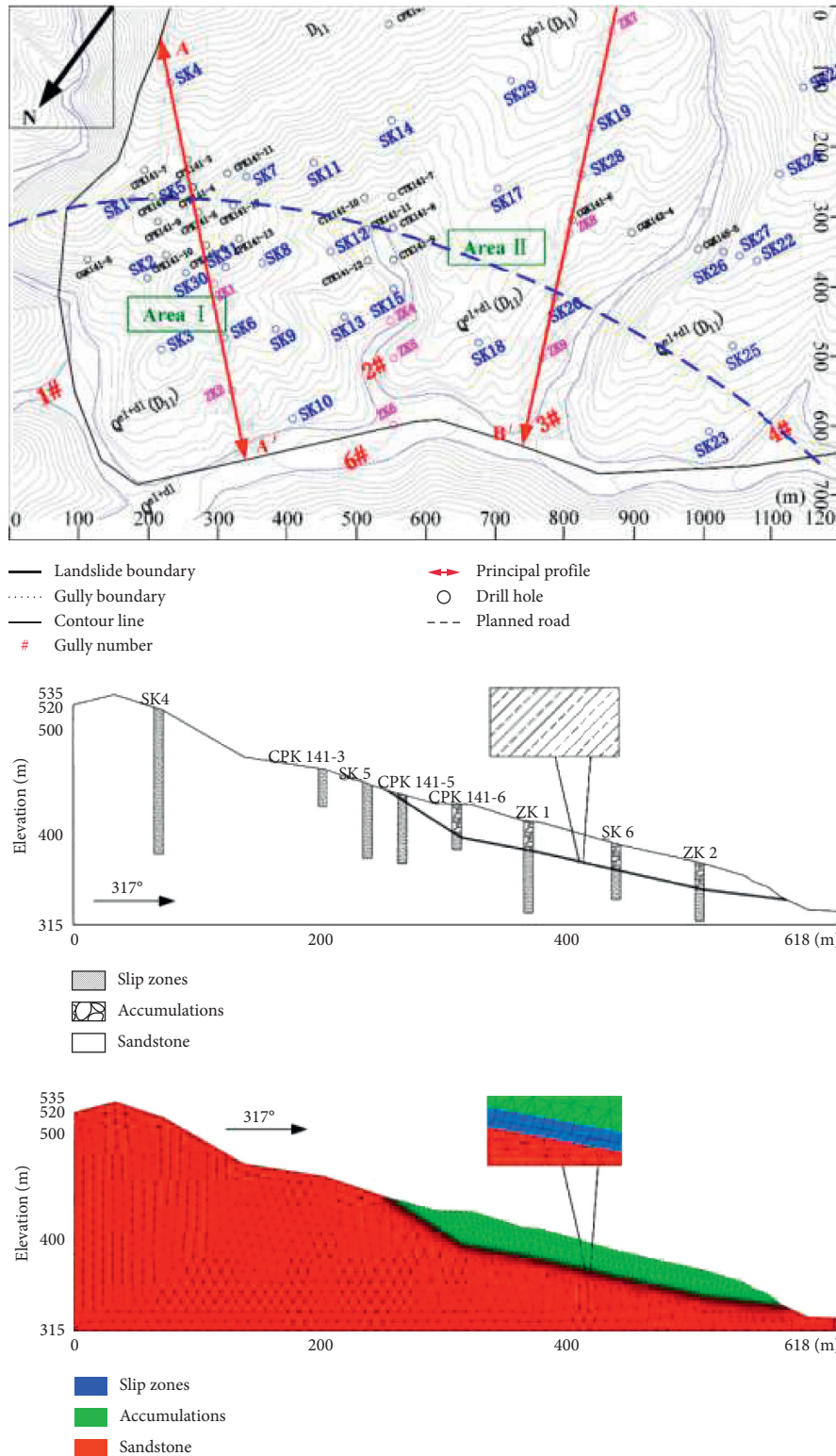
FIGURE 4: Geological information and numerical model of the case study.

4.2. Performance Function Analysis

4.2.1. Results of Performance Function.
Table 4 presents some results of deterministic tests for fitting the performance function. The central composite design was used to conduct the deterministic stability computation. As shown in Table 3, numbers 1–32 are the 2^5 groups of two-level design of five variables (c_p, φ_p, c_r, φ_r, and k_r); numbers 33–37 are 5 groups of extension tests for nonlinear influence checkout; numbers 38–42 are 5 groups of random tests on the limited interval.

TABLE 3: Comparison of F_s considering three different strength states.

Item	Variable		F_s (SSR)	F_s (spencer)	Relative errors (%)
Example 1	c_p, φ_p	Max.	1.997	1.997	0.000
		Mean	1.695	1.698	0.177
		Min.	1.402	1.406	0.284
Example 2	c_r, φ_r	Max.	1.402	1.406	0.284
		Mean	1.095	1.092	0.274
		Min.	0.793	0.794	0.126
Example 3	k_r	Max.	1.535	—	—
		Mean	1.414	—	—
		Min.	1.097	—	—

TABLE 4: Results of central composite design in FLAC 3D.

Number	c_p (kPa)	φ_p (°)	c_r (kPa)	φ_r (°)	k_r	F_s-FLAC 3D
1	16.80	24.70	12.50	17.90	0.00	1.408
2	12.50	24.70	12.50	17.90	0.00	1.405
3	16.80	17.90	12.50	17.90	0.00	1.408
4	12.50	17.90	12.50	17.90	0.00	1.405
5	16.80	24.70	3.10	17.90	0.00	1.364
6	12.50	24.70	3.10	17.90	0.00	1.364
7	16.80	17.90	3.10	17.90	0.00	1.364
8	12.50	17.90	3.10	17.90	0.00	1.359
9	16.80	24.70	12.50	10.60	0.00	0.852
10	12.50	24.70	12.50	10.60	0.00	0.852
11	16.80	17.90	12.50	10.60	0.00	0.852
12	12.50	17.90	12.50	10.60	0.00	0.853
13	16.80	24.70	3.10	10.60	0.00	0.793
14	12.50	24.70	3.10	10.60	0.00	0.793
15	16.80	17.90	3.10	10.60	0.00	0.793
16	12.50	17.90	3.10	10.60	0.00	0.796
17	16.80	24.70	12.50	17.90	0.10	1.834
18	12.50	24.70	12.50	17.90	0.10	1.817
19	16.80	17.90	12.50	17.90	0.10	1.421
20	12.50	17.90	12.50	17.90	0.10	1.402
21	16.80	24.70	3.10	17.90	0.10	1.821
22	12.50	24.70	3.10	17.90	0.10	1.804
23	16.80	17.90	3.10	17.90	0.10	1.406
24	12.50	17.90	3.10	17.90	0.10	1.392
25	16.80	24.70	12.50	10.60	0.10	1.714
26	12.50	24.70	12.50	10.60	0.10	1.697
27	16.80	17.90	12.50	10.60	0.10	1.278
28	12.50	17.90	12.50	10.60	0.10	1.260
29	16.80	24.70	3.10	10.60	0.10	1.701
30	12.50	24.70	3.10	10.60	0.10	1.681
31	16.80	17.90	3.10	10.60	0.10	1.267
32	12.50	17.90	3.10	10.60	0.10	1.249
33	14.65	21.30	7.80	14.25	0.00	1.097
34	14.65	21.30	7.80	14.25	0.04	1.364
35	14.65	21.30	7.80	14.25	0.05	1.414
36	14.65	21.30	7.80	14.25	0.06	1.454
37	14.65	21.30	7.80	14.25	0.10	1.535
38	12.64	18.22	3.91	11.39	0.01	0.928
39	13.66	19.90	6.19	12.91	0.04	1.261
40	15.14	21.96	9.26	15.14	0.07	1.561
41	16.13	23.63	10.36	16.61	0.09	1.731
42	16.33	24.23	11.47	17.59	0.10	1.798

The nonlinear-fitting function is used to solve the undetermined coefficients by least squares regression. Results of undetermined coefficients are listed in Table 5. The comparisons of F_s in FLAC 3D obtained by the response function are shown in Figure 5. F_s obtained from the response surface and that from FLAC 3D agree well. This means that the fitting of the performance function is valid.

Substituting the results of Table 5 into equations (3) and (6)–(9), we obtain the explicit expression of performance function as

$$M = \left(14.46171k_r - 67.9998k_r^2\right)\left(0.350237 + 0.005312c_p + 0.035093\varphi_p + 0.001088\varphi_p^2\right) + \left(1 - 14.46171k_r + 67.9998k_r^2\right)\left(0.065479 + 0.005458c_r + 0.061833\varphi_r + 0.00053\varphi_r^2\right) - 1,$$

(14)

$$F_p = 0.350237 + 0.005312c_p + 0.035093\varphi_p + 0.001088\varphi_p^2,$$

(15)

$$F_r = 0.065479 + 0.005458c_r + 0.061833\varphi_r + 0.00053\varphi_r^2,$$

(16)

$$w_1 = 14.46171k_r - 67.9998k_r^2,$$

(17)

$$w_2 = 1 - 14.46171k_r + 67.9998k_r^2.$$

(18)

4.2.2. Sensitivity of Safety Factor to Variables. The response result of F_p induced by c_p and φ_p, response result of F_r induced by c_r and φ_r, and response result of w_1 and w_2 induced by k_r are shown in Figures 6(a)–6(c), respectively. These results indicate that φ_p has a greater influence on the peak safety factor F_p than c_p; φ_r has a greater influence on the residual safety factor F_r than c_r. The nonlinear influence of shear strength parameters $(c_p, \varphi_p; c_r, \varphi_r)$ is not obvious on respective intervals. However, k_r greatly affects the weight function w_1 and w_2, and the nonlinear influence is obvious even on the small interval $k_r = [0, 0.1]$.

Sensitivity of safety factor F_s to variables is shown in Figure 7. Each interval variable is analyzed with the others fixed at the mean value. Results indicate that all the interval variables have some influence to safety factor F_s; however, the influence of c_p and c_r is not so obvious. The sensitivity to interval variables can be ranked as $k_r > \varphi_p > \varphi_r > c_r > c_p$.

Under the assumptions in Section 2.3, w_1 and w_2 are equal to the weight functions to control the contributions of F_p and F_r to F_s. That is to say, k_r is equal to a weight coefficient to control the contributions of $(c_p, \varphi_p; c_r, \varphi_r)$ to F_s. Therefore, the interval response of F_s induced by each interval variables under different k_r is shown in Figure 8 k_r values are set to 0.00, 0.02, 0.04, 0.06, 0.08, and 0.10, respectively. When an interval variable is analyzed, others are

TABLE 5: Results of undetermined coefficients by regression.

Coefficient	Value
a_1	0.350237
a_2	0.005312
a_3	0.035093
a_4	0.001088
b_1	0.065479
b_2	0.005458
b_3	0.061833
b_4	0.00053
c_1	14.46171
c_2	−67.99980
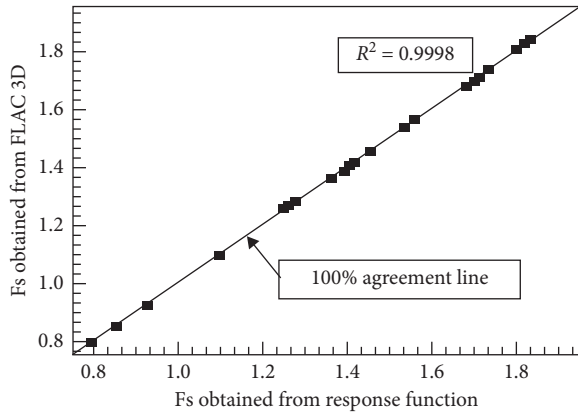
FIGURE 5: Results of F_s comparison between the response surface and FLAC 3D.

fixed at the mean value. Results indicate that, with k_r increasing, the interval response of F_s induced by c_r and c_p changes slightly. In detail, the value of F_s induced by c_r decreases, induced by φ_p increases. However, with k_r increasing, the interval response of F_s induced by φ_r decreases and that induced by φ_p increases. The average level of interval response of F_s increases with the growth of k_r. Therefore, it is considered that all the interval variables are of great significance to safety factor F_s, where k_r is the most outstanding one.

4.3. Reliability Analysis

4.3.1. Results of Reliability. According to the result in equation (14), the monotony of performance function M can be obtained. For $\forall k_r \in [0, 0.1]$, $w_1 \in [0, 0.7662]$ and $w_2 \in [0.2338, 1]$. For $\forall (c_p, \varphi_p, c_r, \varphi_r)$ on their interval, $F_p \in [1.3934, 1.9701]$ and $F_r \in [0.7974, 1.4103]$. For each single interval variable, function M is continuous monotonic. However, k_r is at least more than 0.04 in Baishi ancient landslide according to the literature [41]. In fact, the strength of whole slip surface is in residual state when $k_r \longrightarrow 0$, which is unreal for an ancient landslide with prolonged dormancy. Therefore, in Baishi ancient landslide, we adopt $k_r \in [0.04, 0.1]$, and the interval nonprobability reliability is solved as

$$M^{\min} = 0.0773,$$

$$M^{\max} = 0.8392,$$

$$\eta = \frac{M^c}{M^r} = \frac{1/2 \left(M^{\min} + M^{\max} \right)}{1/2 \left(M^{\max} - M^{\min} \right)} \quad (19)$$

$$= \frac{0.5 \times (0.0773 + 0.8392)}{0.5 \times (0.8392 - 0, 0773)} = 1.2029.$$

Result of η indicates that Baishi ancient landslide is reliable and safe ($\eta > 1$) under the natural condition, agreeing well with the actual situation. In fact, the planned highway began the construction several months ago, and this landslide was also safe during the disturbance of construction.

The reliability analysis is also conducted by the traditional probabilistic method to make a comparison. According to the literature [26], c_p, φ_p, c_r, φ_r, and k_r are considered as random variables. c_p, φ_p, c_r, and φ_r are assumed as log-normal distribution, but k_r is assumed as beta distribution. Mean values are fixed as the same as the mean of intervals in this paper, and coefficients of variation are chosen from the literature [26]. The probability reliability index is also defined as the minimum distance from the origin point to the failure surface in the standard normal space. Some results are listed in Table 6.

Results in Table 6 indicate that the reliability is greatly influenced by the probability density distribution. The probability reliability index η can be little to 0.8364 with nearly 10% probability of failure. It can be also large to 2.1075 but with nearly 35% probability of failure. These results cannot be used in landslide engineering. However, bounds of interval variables can well solve this problem. The robustness of interval nonprobability reliability makes it more suitable to evaluate a landslide with the strain-softening behavior when the probability density is unknown.

4.3.2. Sensitivity of Interval Nonprobability Reliability Index on Variables. For each interval variable, $x_i = x_i^c + \delta_i x_i^r$, where x_i^c is the center value, x_i^r is the radius of interval and $\delta_i = [-1, 1]$. x_i^c and x_i^r are the controlling indexes of an interval.

The influence of interval radius to interval nonprobability reliability index η is shown in Figure 9. Fix the center value x_i^c of an interval variable at original value; change the radius x_i^r from 0 to original maximum radius, presented by axis from 0 to 1 (Figure 9), while other interval variables are set as usual. Results indicate that when the interval radius of k_r and φ_r decreases, η significantly improves; the fall of the radius of c_p and c_r contributes little to the improvement of η; the drop in radius of φ_p even makes η decrease. Therefore, the influence of variable radius is ranked as follows: $k_r > \varphi_r > c_r > c_p > \varphi_p$. It is worth noting that decreasing variable radius of φ_p declines η as well. The reason is that, when the radius of φ_p decreases to 0, φ_p eventually converges to a mean value. It indicates that the center value x_i^c of interval variable is also of great importance.

(a)

(b)

(c)
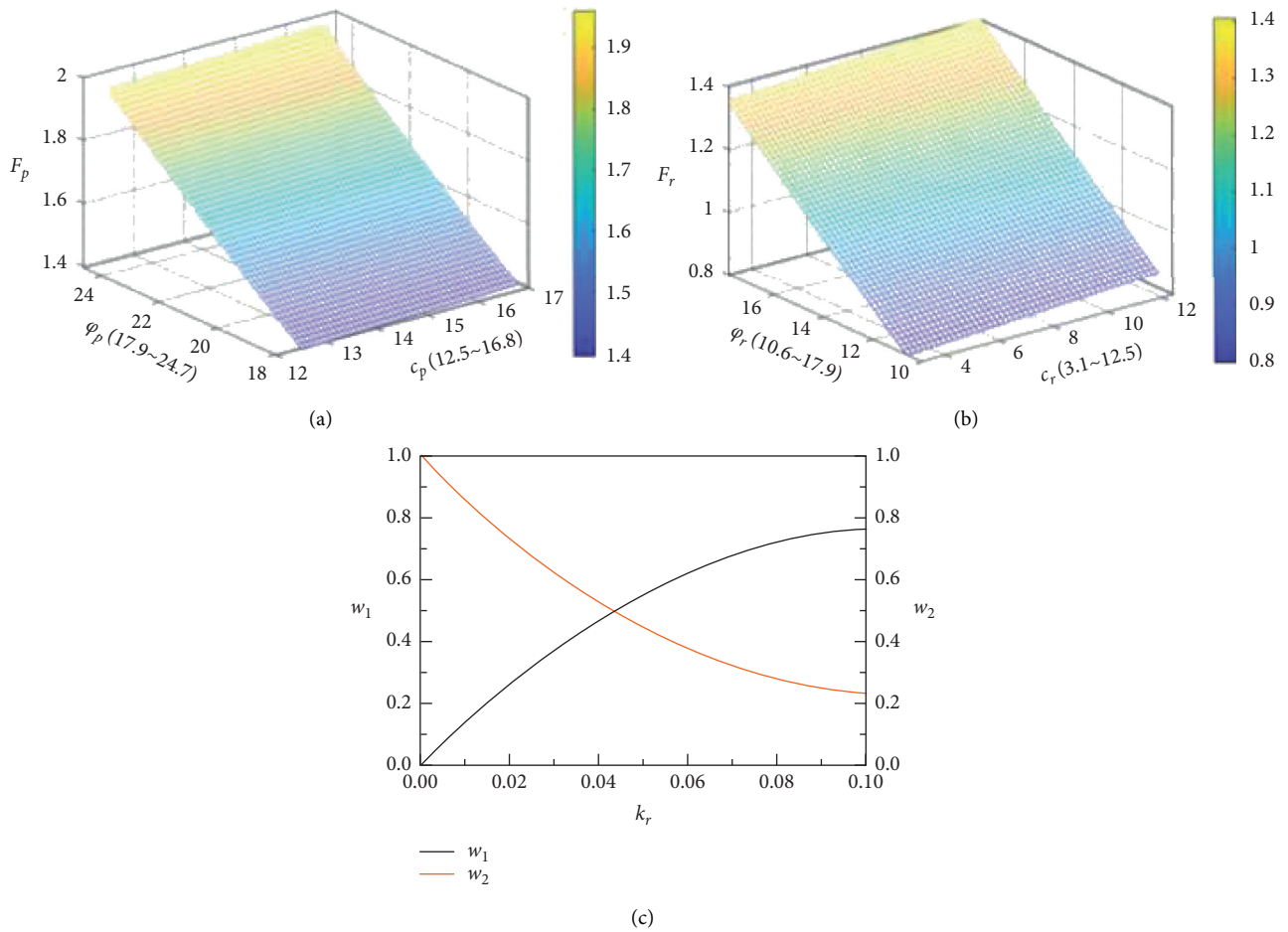
FIGURE 6: (a) Response result of F_p induced by c_p and φ_p. (b) Response result of F_r induced by c_r and φ_r. (c) Response results of w_1 and w_2 induced by k_r.
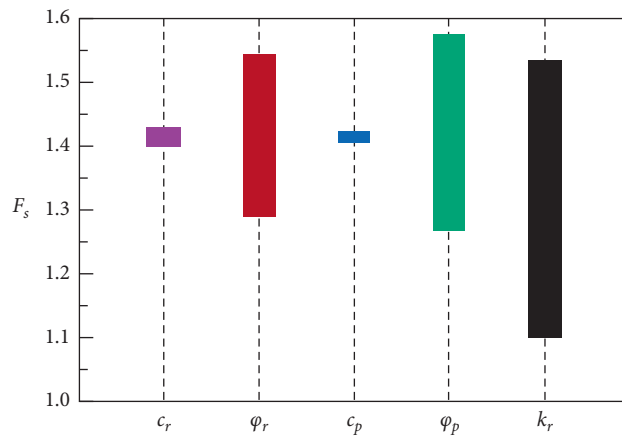
FIGURE 7: Interval response of F_s induced by each interval variables.

The influence of interval center value to η is shown in Figure 10. The radius x_i^r of an interval variable is fixed at 0; the interval center value changes from minimum to maximum on the interval, presented by axis from −1 to 1 (Figure 10), while other interval variables are set as usual. Results indicate that when the center value of interval variables k_r and φ_r increases, η significantly increases. And,

the line of φ_r grows faster. When the center value of interval variables c_r, c_p, φ_p increases, the growth of η is not so obvious.

The interval response of η induced by interval variables $(c_p, \varphi_p, c_r, \varphi_r)$ under different k_r is shown in Figure 11. Set k_r to 0.00, 0.02, 0.04, 0.06, 0.08, and 0.10, respectively. The radius x_i^r of an interval variable is fixed at 0; the interval
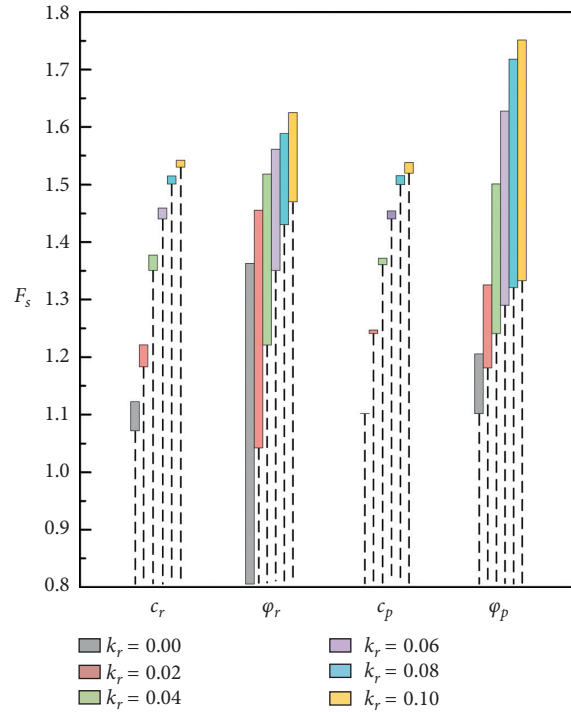
Figure 8: Interval response of F_s induced by the interval variables ($c_p, \varphi_p; c_r, \varphi_r$) under different k_r values.

Table 6: Results in probabilistic reliability calculations under different variable distributions.

COV of log-normal variables				Beta distribution parameters		p_f (%)	PRI-η	INPRI-η
c_p	c_r	φ_p	φ_r	q	r			
0.2	0.2	5	5	1	6	10.85	0.9443	
0.5	0.5	10	10	1	6	34.76	0.8364	
0.2	0.2	5	5	6	6	10.71	1.4016	
0.5	0.5	10	10	6	6	34.91	1.3567	1.2029
0.2	0.2	5	5	6	2	11.36	2.1075	
0.5	0.5	10	10	6	2	35.75	1.7697	

Note: COV: coefficient of variation, q and r are the parameters describing the probability density distribution, p_f is the probability of failure, PRI-η is the probability reliability index, and INPRI-η is interval nonprobability of failure. More details are shown in the literature [26].

Figure 9: Results of reliability index η influenced by the interval radius of five variables.

FIGURE 10: Results of reliability index η influenced by the interval center of five variables.
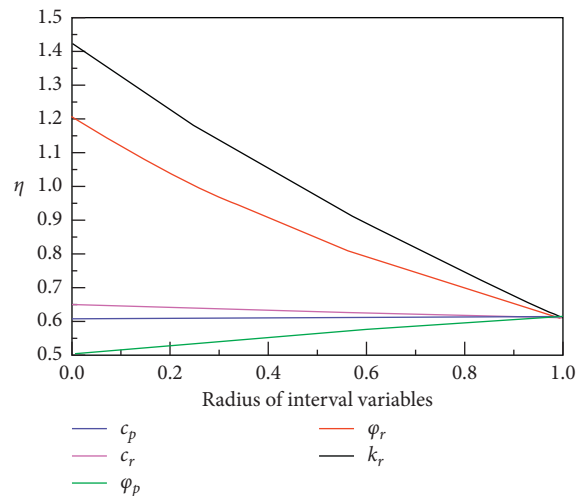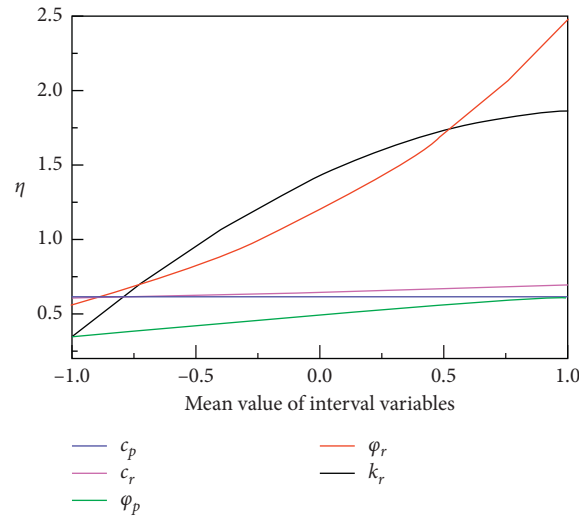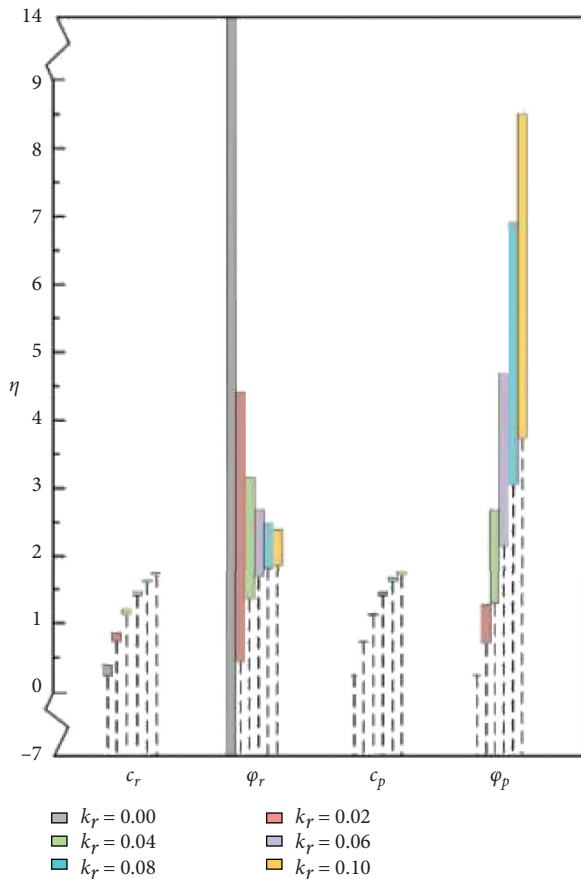

FIGURE 11: Interval response of reliability index η induced by interval variables ($c_p, \varphi_p, c_r, \varphi_r$) under different k_r values.

decreases and that induced by φ_p increases. However, with k_r increasing, the interval response of η induced by φ_r quickly decreases and that induced by φ_p quickly increases. In summary, both the center value and range of all interval variables are important to η. The k_r is the most significant factor which should be preferentially determined.

5. Conclusions

In the present study, an interval nonprobability reliability analysis framework combined with numerical strain-softening constitutive relations was established to evaluate the reliability of Baishi ancient landslide. The main conclusions can be drawn as follows:

(1) The uncertainties of geomaterial properties significantly affect the stability evaluation of the ancient landslide. To correctly and effectively consider these uncertainties when data are scarce, an interval nonprobability reliability analysis framework combined with numerical strain-softening constitutive relations is established.

(2) The proposed reliability analysis method is verified by Baishi ancient landslide as a case study. Uncertain parameters (c_p, φ_p, c_r, φ_r, and k_r) in the strain-softening numerical constitutive relation are set as interval variables. The interval nonprobability reliability index η is defined as the minimum distance from the origin point to the failure surface in the standard normal space. This index is used to describe the ability of a system to tolerate the variation of uncertain parameters.

(3) The interval nonprobability reliability index η of Baishi is 1.2029 (>1), indicating that Baishi ancient landslide is safe under the nature condition. The results calculated by the proposed method agree with the reality. However, the reliability index η in the probability method ranges greatly; Baishi ancient landslide holds a

center value is changed from the minimum value to the maximum on the interval, while other interval variables are set as usual. Results in Figure 11 indicate that, with k_r increasing, the interval response of η induced by c_r and c_p changes slightly. In detail, the value of η induced by c_r

35% probability of failure. Therefore, the interval nonprobability method is more suitable.

(4) The sensitivity analysis indicates that k_r is the most significant variable controlling both safety factor F_s and interval nonprobability reliability index η. In addition, k_r is equivalent to a weight coefficient that can affect the influence of (c_r, φ_r) and (c_p, φ_p). When k_r increases, the influence of (c_r, φ_r) decreases but that of (c_p, φ_p) increases.

(5) Interval nonprobability reliability method combined with numerical strain-softening constitutive relation can accurately present the relation of parameters between peak and residual strength with a few data and obtain robust results. It provides a great complement for traditional probabilistic methods.

Data Availability

The data used to support the findings of this study are included within the article.

Conflicts of Interest

The authors declare that there are no conflicts of interest regarding the publication of this paper.

Acknowledgments

References

[1] Z. Zhou, X. Cai, X. Li, W. Cao, and X. Du, "Dynamic response and energy evolution of sandstone under coupled static-dynamic compression: insights from experimental study into deep rock engineering applications," *Rock Mechanics and Rock Engineering*, vol. 53, no. 3, pp. 1305–1331, 2020.

[2] X. Cai, Z. L. Zhou, L. H. Tan, H. Z. Zang, and Z. Y. Song, "Fracture behavior and damage mechanisms of sandstone subjected to wetting-drying cycles," *Engineering Fracture Mechanics*, vol. 234, Article ID 107109, 2020.

[3] X. Cai, Z. L. Zhou, and X. M. Du, "Water-induced variations in dynamic behavior and failure characteristics of sandstone subjected to simulated geo-stress," *Rock Mechanics and Rock Engineering*, vol. 130, Article ID 104339, 2020.

[4] Z. Zhou, H. Wang, X. Cai, L. Chen, Y. E, and R. Cheng, "Damage evolution and failure behavior of post-mainshock damaged rocks under aftershock effects," *Energies*, vol. 12, no. 23, p. 4429, 2019.

[5] D. Ma, H. Duan, X. Li, Z. Li, Z. Zhou, and T. Li, "Effects of seepage-induced erosion on nonlinear hydraulic properties of broken red sandstones," *Tunnelling and Underground Space Technology*, vol. 91, Article ID 102993, 2019.

[6] T. Bong and Y. Son, "Probabilistic analysis of weathered soil slope in South Korea," *Advances in Civil Engineering*, vol. 2018, Article ID 2120854, 12 pages, 2018.

[7] Y. Li, H. Zhang, X. Liu, G. Liu, D. Hu, and X. Meng, "Time-varying compressive strength model of aeolian sand concrete considering the harmful pore ratio variation and heterogeneous nucleation effect," *Advances in Civil Engineering*, vol. 2019, Article ID 8267601, 15 pages, 2019.

[8] E. Conte, A. Donato, L. Pugliese, and A. Troncone, "Analysis of the maierato landslide (Calabria, southern Italy)," *Landslides*, vol. 15, no. 10, pp. 1935–1950, 2018.

[9] Q.-j. Pan, X.-r. Qu, and X. Wang, "Probabilistic seismic stability of three-dimensional slopes by pseudo-dynamic approach," *Journal of Central South University*, vol. 26, no. 7, pp. 1687–1695, 2019.

[10] E. Shamekhi and D. D. Tannant, "Probabilistic assessment of rock slope stability using response surfaces determined from finite element models of geometric realizations," *Computers and Geotechnics*, vol. 69, pp. 70–81, 2015.

[11] D. V. Griffiths, J. Huang, and G. A. Fenton, "Probabilistic infinite slope analysis," *Computers and Geotechnics*, vol. 38, no. 4, pp. 577–584, 2011.

[12] X. Wang, H. Wang, and R. Y. Liang, "A method for slope stability analysis considering subsurface stratigraphic uncertainty," *Landslides*, vol. 15, no. 5, pp. 925–936, 2018.

[13] Z.-P. Deng, D.-Q. Li, X.-H. Qi, Z.-J. Cao, and K.-K. Phoon, "Reliability evaluation of slope considering geological uncertainty and inherent variability of soil parameters," *Computers and Geotechnics*, vol. 92, pp. 121–131, 2017.

[14] K. Terzaghi, R. B. Peck, and G. Mesri, *"Soil Mechanics in Engineering Practice"*, John Wiley & Sons, Hoboken, NJ, USA, 3rd edition, 1996.

[15] S.-l. Zhang, Z.-h. Zhu, S.-c. Qi, Y.-x. Hu, Q. Du, and J.-w. Zhou, "Deformation process and mechanism analyses for a planar sliding in the Mayanpo massive bedding rock slope at the Xiangjiaba hydropower station," *Landslides*, vol. 15, no. 10, pp. 2061–2073, 2018.

[16] Y. Zhao, X.-p. Zhou, and Q.-h. Qian, "Progressive failure processes of reinforced slopes based on general particle dynamic method," *Journal of Central South University*, vol. 22, no. 10, pp. 4049–4055, 2015.

[17] G. Zhang and L. Wang, "Stability analysis of strain-softening slope reinforced with stabilizing piles," *Journal of Geotechnical and Geoenvironmental Engineering*, vol. 136, no. 11, pp. 1578–1582, 2010.

[18] X.-r. Wang, Q.-g. Rong, S.-l. Sun, and H. Wang, "Stability analysis of slope in strain-softening soils using local arc-length solution scheme," *Journal of Mountain Science*, vol. 14, no. 1, pp. 175–187, 2017.

[19] L. Zhao, S. Zuo, D. Deng, Z. Han, and B. Zhao, "Development mechanism for the landslide at Xinlu village, Chongqing, China," *Landslides*, vol. 15, no. 10, pp. 2075–2081, 2018.

[20] K. Terzaghi and R. B. Peck, *"Soil Mechanics in Engineering Practice"*, Wiley, New York, NY, USA, 1948.

[21] A. W. Bishop, "The influence of progressive failure on the choice of the method of stability analysis," *Géotechnique*, vol. 21, no. 2, pp. 168–172, 1971.

[22] A. W. Skempton, "Long-term stability of clay slopes," *Géotechnique*, vol. 14, no. 2, pp. 77–102, 1964.

[23] D. A. Grivas and R. N. Chowdhury, "Probabilistic $\varphi = 0$ stability analysis in strain-softening soil," *Structural Safety*, vol. 1, no. 3, pp. 199–210, 1982.

[24] R. N. Chowdhury, W. H. Tang, and I. Sidi, "Reliability model of progressive slope failure," *Géotechnique*, vol. 37, no. 4, pp. 467–481, 1987.

[25] S. Metya, G. Bhattacharya, and R. Chowdhury, "Reliability analysis of slopes in strain-softening soils considering critical

slip surfaces," *Innovative Infrastructure Solutions*, vol. 1, no. 1, pp. 1–7, 2016.

[26] G. Bhattacharya, R. Chowdhury, and S. Metya, "Residual factor as a variable in slope reliability analysis," *Bulletin of Engineering Geology and the Environment*, vol. 78, no. 1, pp. 147–166, 2019.

[27] K. Karuna and C. S. Manohar, "Inverse problems in structural safety analysis with combined probabilistic and non-probabilistic uncertainty models," *Engineering Structures*, vol. 150, pp. 166–175, 2017.

[28] Y. Wang, P. Zhang, and G. Qin, "Non-probabilistic time-dependent reliability analysis for suspended pipeline with corrosion defects based on interval model," *Process Safety and Environmental Protection*, vol. 124, pp. 290–298, 2019.

[29] X.-X. Liu and I. Elishakoff, "A combined importance sampling and active learning Kriging reliability method for small failure probability with random and correlated interval variables," *Structural Safety*, vol. 82, Article ID 101875, 2020.

[30] L. Dong, D. Sun, X. Li, and Z. Zhou, "Interval non-probabilistic reliability of a surrounding jointed rockmass in underground engineering: a case study," *IEEE Access*, vol. 5, pp. 18804–18817, 2017.

[31] L. Dong, D. Sun, and X. Li, "Theoretical and case studies of interval nonprobabilistic reliability for tailing dam stability," *Geofluids*, vol. 2017, Article ID 8745894, 11 pages, 2017.

[32] H. Su, J. Li, Z. Guo, and Z. Wen, "Nonprobabilistic reliability evaluation for in-service gravity dam undergoing structural reinforcement," *IEEE Transactions on Reliability*, vol. 67, no. 3, pp. 970–986, 2018.

[33] E. Conte, F. Silvestri, and A. Troncone, "Stability analysis of slopes in soils with strain-softening behaviour," *Computers and Geotechnics*, vol. 37, no. 5, pp. 710–722, 2010.

[34] Z. Nie, Z. Zhang, and H. Zheng, "Slope stability analysis using convergent strength reduction method," *Engineering Analysis with Boundary Elements*, vol. 108, pp. 402–410, 2019.

[35] Y. Chen and H. Lin, "Consistency analysis of Hoek-Brown and equivalent Mohr-coulomb parameters in calculating slope safety factor," *Bulletin of Engineering Geology and the Environment*, vol. 78, no. 6, pp. 4349–4361, 2019.

[36] K. Zhang, P. Cao, and R. Bao, "Progressive failure analysis of slope with strain-softening behaviour based on strength reduction method," *Journal of Zhejiang University-Science A (Applied Physics & Engineering)*, vol. 14, no. 2, pp. 26–34, 2013.

[37] G.-H. Yang, Z.-H. Zhong, X.-D. Fu, Y.-C. Zhang, Y. Wen, and M.-F. Zhang, "Slope analysis based on local strength reduction method and variable-modulus elasto-plastic model," *Journal of Central South University*, vol. 21, no. 5, pp. 2041–2050, 2014.

[38] X.-P. Zhou and X.-C. Huang, "Reliability analysis of slopes using UD-based response surface methods combined with LASSO," *Engineering Geology*, vol. 233, pp. 111–123, 2018.

[39] D.-Q. Li, D. Zheng, Z.-J. Cao, X.-S. Tang, and K.-K. Phoon, "Response surface methods for slope reliability analysis: review and comparison," *Engineering Geology*, vol. 203, pp. 3–14, 2016.

[40] H. Basahel and H. Mitri, "Probabilistic assessment of rock slopes stability using the response surface approach—a case study," *International Journal of Mining Science and Technology*, vol. 29, no. 3, pp. 357–370, 2019.

[41] D. R. Bhat, R. Yatabe, and N. P. Bhandary, "Study of pre-existing shear surfaces of reactivated landslides from a strength recovery perspective," *Journal of Asian Earth Sciences*, vol. 77, pp. 243–253, 2013.

Research Article

Research on Surface Failure Law of Working Faces in Large Mining Height and Shallow Buried Coal Seam

Zhenhua Li,[1] Yingkun Pang,[1] Yongsheng Bao [ID],[2] and Zhanyuan Ma[2]

[1]*School of Energy Science and Engineering, Henan Polytechnic University, Jiaozuo 454000, Henan, China*
[2]*Datong Coal Mine Group Co. Ltd., Datong 037003, Shanxi, China*

Correspondence should be addressed to Yongsheng Bao; yongshengbao@126.com

In the process of high-intensity and large-space mining in Shendong mining area, various surface cracks are generated on the surface, resulting in serious damage to the surface buildings and the local ecological environment. To study the influence of overlying rock movement on surface failure of near-field single key strata of near-shallow buried and large mining height working face, the relationship between overburden movement, strata pressure appearance, and surface failure at working face 52307 in Daliuta mining area was analyzed by field measurement and numerical simulation. The results show the following: (1) there is only one thick and hard key stratum in the overburden of large mining height and near-shallow buried working face. Under the condition of presplitting roof blasting, the first weighting step is still as high as 95 m, and the periodic breaking step of roof is 20–30 m. During the weighting, the working resistance of support is still close to the rated resistance. (2) The single key stratum plays an obvious role in controlling overburden movement. After the first weighting of the working face, a stepped subsidence crack appears on the surface within a short time, and the crack lags behind the working face for about 5 m. (3) During each periodic weighting process, the breaking and subsidence of key blocks are accompanied by surface cracks.

1. Introduction

In the coal mining of working faces, the surface usually has a certain response. For example, surface soil strata can be seriously deformed, and mining cracks appear on the surface [1, 2]. This kind of destruction is quite remarkable and poses a great threat to surface buildings, roads, and railways [3, 4]. Therefore, it is necessary to analyze and study the mechanism of surface cracks.

Many scholars have studied the development mechanism of mining-induced surface fracture. In 1981, Singh et al. [5] concluded that surface subsidence is caused by overburden fault movement. This is the beginning of a deep study on the surface and spatial-temporal evolution of overburden strata. Ghose [6], Greco [7], and Homoud [8] used fracture mechanics and plastic mechanics theory to study the mechanical mechanism of mining landslide. Luo [9] applied computer simulation technology to investigate the dynamic deformation calculation model of mining slope.

The basic laws of surface cracks have also been studied. Herrera et al. [10] and Camec and Delacourt [11] monitored land subsidence through D-InSAR and detected tensile deformation area. Hahn et al. [12] used the equipment to investigate and classify surface cracks.

With the westward movement of China's coal mining, large-space and high-intensity mining of shallow and thin bedrock coal seam has caused irreversible impact on the surface and local ecology under the special geological conditions in Northwest China [13, 14]. A lot of research on the mechanism and development of mining-induced cracks in western mining area has been performed [15, 16]. Liu et al. [17] analyzed the mechanism and the dynamic development law of surface cracks and surface subsidence. This study provides technical references for the placement of surface cracks. The movement of overlying strata in shallow seam mining is characterized by the full cutoff of roof strata and the large bedrock fracture angle; and the fracture directly develops to the surface, forming significant subsidence

cracks [18]. In addition, under the condition of high-intensity mining, the surface cracks have secondary development characteristics, and there are two development cycles and corresponding two peaks [19, 20]. At the same time, the development mechanism of surface cracks under the condition of wide and fast advance working face was analyzed in detail [21, 22]. Hu et al. [23, 24] focused on in-depth study of surface subsidence and surface cracks in aeolian sand area and proposed suggestions on the restoration of ecological environment after the destruction of aeolian sand mining. This study provides a basis for ecological restoration at that time. Sun et al. [25] put forward a "quasi-hyperbolic" settlement model on the basis of key strata theory and basic mechanics. This study provides a new theoretical basis for the study of surface subsidence and damage. Ju and Xu. [26] studied the spatial and temporal effects of different failure structures in different locations of key strata on surface damage by changing the location of key strata through similar simulation methods. Yan et al. [27], Yang et al. [28], and Zhou et al. [29] performed a lot of research on the occurrence and disaster causing of surface cracks in shallow coal seam mining and provided favorable measures for the restoration of surface ecological environment and land reclamation. Other studies on the mechanism and development characteristics of surface cracks in shallow seam mining in Western China were conducted [30–32], contributing to local ecological protection and safe mining.

However, the above studies are focused on the shallow seam mining [33, 34]. There are few studies on the mechanism and development of surface cracks in the near-shallow seam mining (coal seam depth > 150 m) [35]. Based on the geological environment of working face 52307 with shallow burial and high mining height in the Daliuta mining area, the spatial-temporal relationship between surface damage and breakage of key strata is explored in this study. In this paper, the generation and development of surface cracks under the condition of near-shallow burial is explained. This study provides a theoretical basis for the research on mining-induced cracks.

2. Overview of Working Face

2.1. Geological Conditions of Mining Working Face.
Daliuta Coal Mine is located in Wulanmulun Town, Shenmu County, Yulin City, Shaanxi Province. With the border to Ordos city of Inner Mongolia autonomous region, this mine belongs to Shendong Coal Group. With the subordinate of Daliuta Well and Huojitu, this mine is a supersize, high-yield, and high-efficiency mine in China, with an annual output of more than 20 million tons. Figure 1 shows the geographic location of the Daliuta Coal Mine.

Working face 52307 is a fully mechanized mining face with large mining height in the Daliuta mine, the ground elevation is +1120.2–1217.1, and the coal seam floor elevation is +987.7–1025.5. Most of the surface overburden strata are Quaternary loose sediments, which is 32 m in working face 52307, and the thickness of overlying bedrock is 158 m. The strike length of the working face is 4462.6 m and the inclination length is 301 m. The roadway layout of
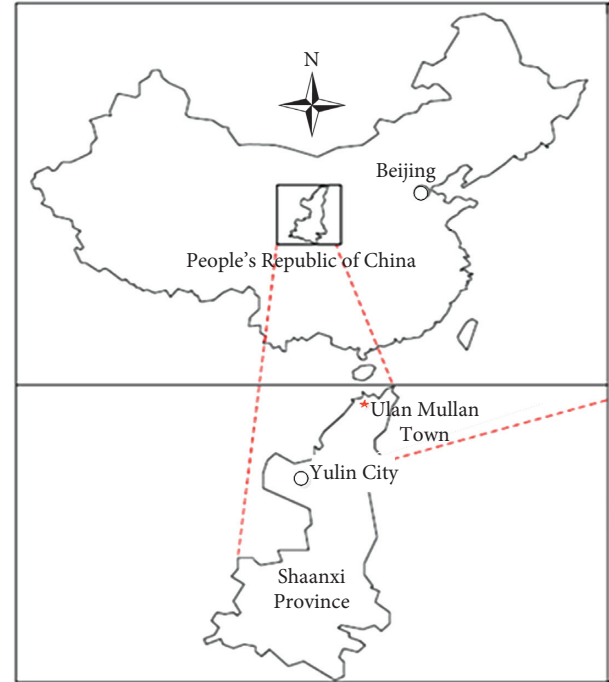

FIGURE 1: Geographical location of Daliuta Coal Mine.

the working face is shown in Figure 2(a). Coal 5–2 is the main working face with an average coal thickness of 7.2 m, an average coal seam depth of 190 m, and there is a stratum of giant fine-grained sandstone with a thickness of nearly 31 m at 4 m above the coal seam, as shown in Figure 2(b).

In the advance process of working face, various types of surface cracks appear, as shown in Figure 3. Surface cracks in Figure 3 are placed in other coal mine nearby the Daliuta mining area. Since the geological and mining conditions in coal mining area nearby the Daliuta mine are similar, the characteristics and mechanism of surface cracks caused by underground mining are the same.

2.2. Discrimination for Key Strata Location.
The location of key strata is judged by two criteria of critical strata [36], namely, stiffness criterion and strength criterion. The criterion of stiffness is

$$q_{n+1} < q_n, \tag{1}$$

where q_{n+1} and q_n are the loads on the key strata of the first strata when calculated to $n + 1$ strata and n strata, respectively.

To judge whether $n + 1$ strata can be the key strata, the strength criterion should be satisfied, namely, the breakage distance of the lower strata should be less than that of the upper strata, shown as follows:

$$l_{n+1} > l_n, \quad n = 1, 2, \ldots, k, \tag{2}$$

where l_n is the breakage distance of the n-th strata and k is the determined number of hard rock strata in equation (1).

Based on the results of stiffness and strength discrimination of key strata and field settlement measurement of

(a)

(b)
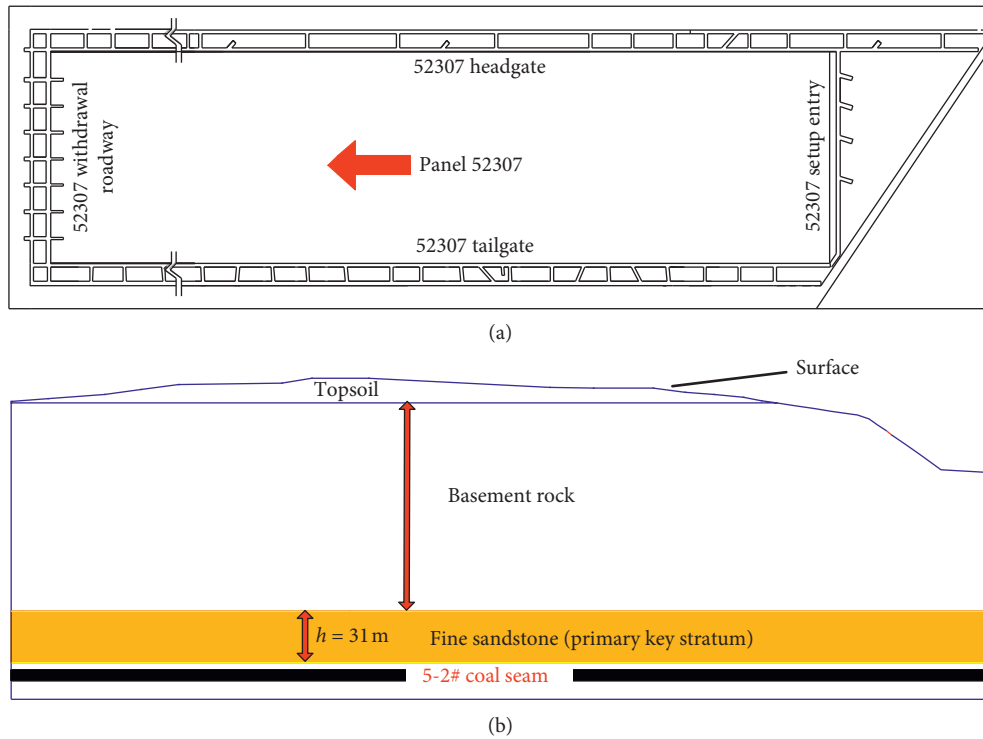
FIGURE 2: Roadway layout and overburden occurrence of working face 52307. (a) Roadway layout of working face 52307. (b) Overburden occurrence of the working face.

(a)

(b)
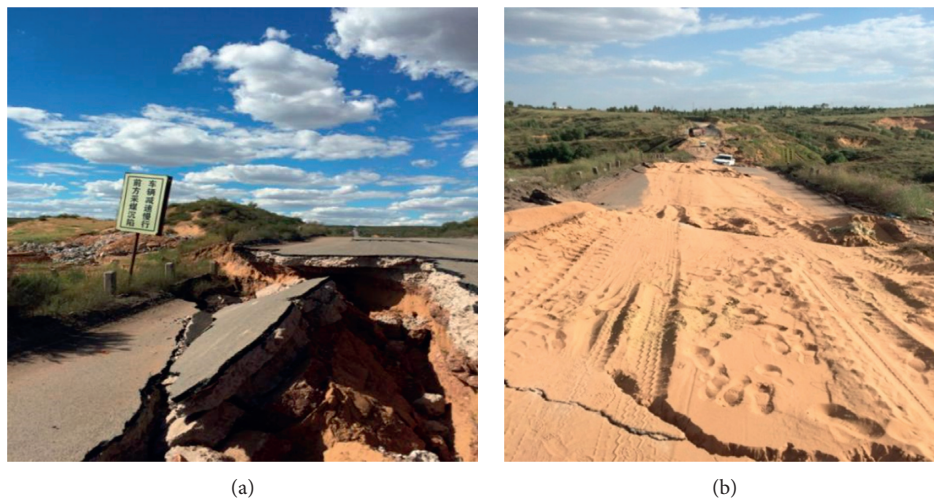
FIGURE 3: Surface cracks caused by underground mining. (a) 50 meters away from the open-off cut; (b) 120 meters away from the open-off cut.

overburden, fine-grained sandstone with a thickness of about 31 m in working face 52307 is determined as the main key strata in overburden strata of working face. Table 1 shows parameters of the roof and floor strata of working face.

3. Analysis of Weighting Law of Working Face

The mining pressure data of working face 52307 were collected by the monitored research group in the initial mining stage. Six Uloka pressure gauges are arranged at the head of the working face machine, which are located at 39#, 40#, 42#, 43#, and 44# brackets, respectively. Eight Uloka pressure gauges are arranged at the middle of the working face, which are located at 70#, 71#, 72# (the center of the working face), 73#, 74#, 75#, and 76# brackets, respectively. Five Uloka pressure gauges are arranged at the tail of the working face machine, located at 114#, 115#, 116#, 117#, and 118# brackets. Uloka data are collected once every 1 s. Figure 4 shows the layout of extension.

TABLE 1: Partial table of strata parameters.

Horizon	Lithology	Thickness (m)	Depth (m)
Roof	Fine sandstone	31	175.62
	Siltstone	0.6	176.22
	Medium sandstone	0.7	176.92
	Siltstone	2.41	179.33
Coal	Coal seam 5–2#	7.69	187.02
Floor	Siltstone	3.58	190.60
	Sandy mudstone	2.82	193.42
	Siltstone	4.4	197.82

FIGURE 4: Diagram of pressure gauge distribution.

In this paper, the bracket in the middle of the working face is selected to analyze the pressure data of the bracket. Figure 5 shows the working resistance of the bracket.
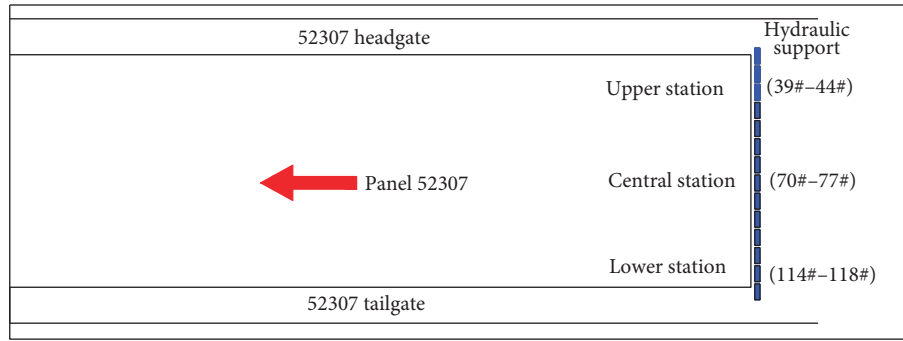
The formula of weighting criterion is

$$P_t^p = \overline{p}_t + \sigma_{pi}, \tag{3}$$

where $\overline{p}_t$ is the mean end-cycle resistance and σ_{pi} is the mean square deviation.

As shown in Figure 5, when the working face advances to 955 m, the support resistance increases rapidly, and the first weighting of the working face occurs, namely, the first weighting of the working face (when the cantilever of the main roof reaches its limit, the fracture of the main roof forms a three-hinged arch-like balance, while the broken rock blocks rotate unstably, resulting in a sharp drop of the working full roof. The load on the bracket is generally increased, and this phenomenon is called the initial weighting of the main roof). The weighting step is about 95 m. When the working face advances to 120 m, the second weighting occurs, namely, the first periodic weighting of the working face (the roof weighting phenomenon caused by periodic instability of rock strata in fracture zone is called periodic weighting of the working face roof), and the weighting step is 25 m. When the working face advances to 140 m, the second periodic weighting occurs, and the weighting step is 20 m; within the 204 m range of the working face advance, there are six types of obvious periodic weighting. The largest weighting step exceeds 30 m, averaging about 20 m. Under the special overburden condition of single thick and hard main key strata in the near field, presplitting blasting is carried out at the cutting end of the working face, but the distance between the initial mining weighting step and throwing step can reach 95 m, and the interval between periodic weighting step is also in the range of 20 m–30 m.

Through detailed analysis of data, it is concluded that the average end-cycle resistance of the bracket is 17111.04 kN during weighting and 10451.08 kN during nonweighting.

4. Relationship between Generation of Surface Cracks and Weighting of Working Face

In the initial mining stage of working face 52307 in the Daliuta Mining Area, there is a stratum of fine sandstone about 31 m thick above the working face. Then this stratum is determined as the main key strata of the working face by the discriminant condition. The first weighting of the basic roof fracture occurs when the working face advances to 95 m. The step subsidence of 50 cm is generated near the direction of 70 m, and the subsidence of the surface measuring point is 746.7 mm. The relationship between underground periodic pressure and surface fracture is obtained, as shown in Table 2.

The negative value in the table represents the distance between the ground fracture lagging behind the underground pressure point, while the positive value represents the distance between the ground fracture ahead of the underground pressure point. According to Table 2, when the pressure of the underground working face is applied, cracks will occur above the surface; if pressure is not applied on the working face, there are no cracks. It indicates that cracks can be generated in the working surface 52307 during nonweighting period. It further shows that the influence of overburden movement on surface deformation is intense.
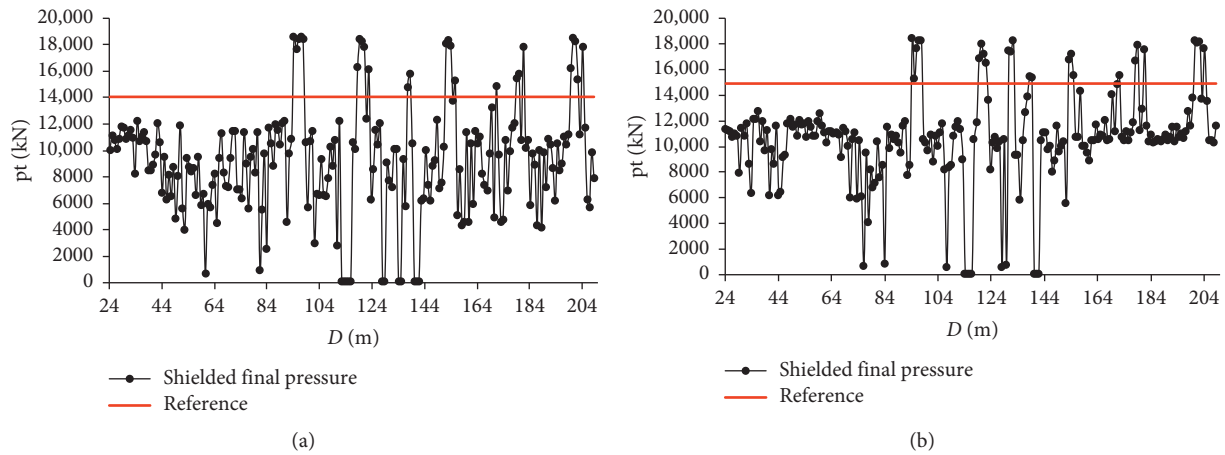
FIGURE 5: Resistance curve of the on-site monitoring bracket. (a) 71# bracket and (b) 72# bracket.

TABLE 2: Statistical table of periodic pressure and surface cracks.

Date	Advance distance (m)	Pressure point (m)	Pressure value (kN)	Fracture range (m)	Weighting distance (m)
3.11	112.3	109.1	15837.3	(−23.5 to −4.9) 18.6	22.6
3.14	129.7	128.1	16838.3	(−17.7~1.3) 19	19
3.18	152.3	142	17856.3	(−11.8 to −5.1) 6.3	13.9
3.21	172.1	161	15517.9	(−14.3~6.2) 20.5	19
3.23	188.8	—	—	16	—
3.24	195.5	190.4	17663.1	(−18.2 to −7) 11.2	29.6

The upper and lower wells with surface cracks are plotted, according to the periodic weighting length at the three upper and lower positions of the working face.

Three different locations in the working face are selected to arrange the hydraulic support of the Euloka station to ensure the accuracy of data collection.

The setup entry is the starting place of 52307 working face, as shown in Figure 6, during the initial weighting process of the working face, the "fixed supported beam" structure of the key bearing strata breaks in the middle, and the overburden subsides and forms a tensile force toward the middle. The overburden breaks and subsides on both sides of the corresponding surface and forms a tensile action to form the surface crack. The surface crack is shaped like a funnel in the "C" shape and the "C" direction (as shown in black box). In the latter weighting process, the periodic weighting step of the support in the middle of the working face is obviously smaller than that of the support at both ends, which results in unequal weighting step. The overburden rock in the middle of the working face has been broken, but the overburden rock at both ends has not been broken [37]. Besides, there is a "dislocation." The first fracture and subsidence of the middle roof overburden directly form a tensile force on the upper surface loess strata of this part, so that the surface cracks appear in the "C" shape during the period of periodic weighting.

In the face of the periodic weighting, when the key stratum of the middle support of the working face is broken, typical cracks on the surface are compared. According to the field observation, the surface is often accompanied by various kinds of cracks during each weighting, as shown in Figure 7.

5. Relationship between Fracture Development and Surface Subsidence

5.1. Fracture Genesis Analysis. With the advance of the working face, uneven settlement will occur on the surface. The horizontal displacement and subsidence of the surface soil in adjacent positions are different, which will inevitably lead to the deformation of the surface overburden soil. Because of small tensile and poor shear capacity of the Quaternary loose strata [38], surface cracks occur when the tensile deformation reaches the maximum tensile deformation energy of the surface soil.

To fully study the actual deformation of the surface, an observatory is set up on the surface above the open-off cut. The horizontal section of the observatory is shown in Figure 8.

The actual length of the observation station is 626 m, the distance between the observation points is 20 m, and the number of working observation points is 23 m. By observing the surface movement and deformation of the working face and the calculation of observation data, the surface movement curve is obtained. The subsidence curve of the survey line in each observation period is shown in Figure 9.

The average depth of working face 52307 is 190 m, and the length of working face is 301 m; the mobile basin with stable mining will be fully exploited. During the last observation, the working face 52307 is advanced to 637.4 m, the
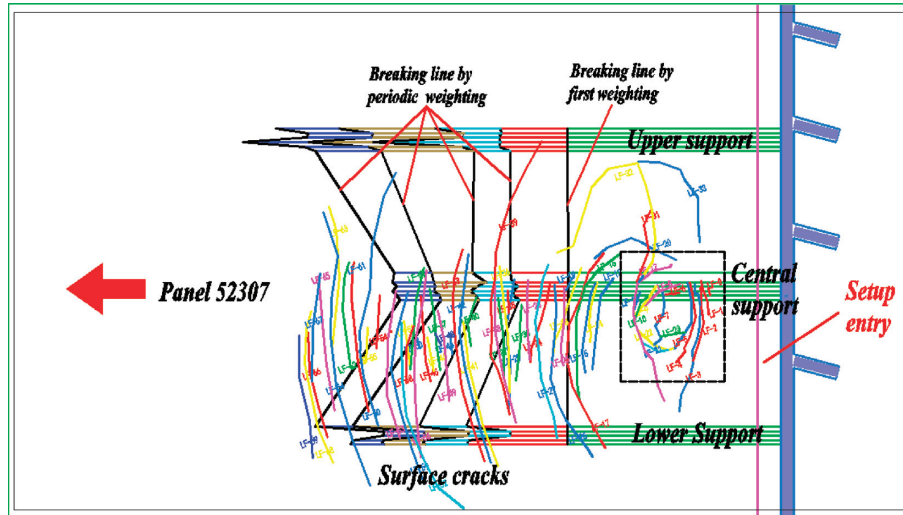
FIGURE 6: Spatial-temporal relationship between weighted breakage distance and surface cracks.
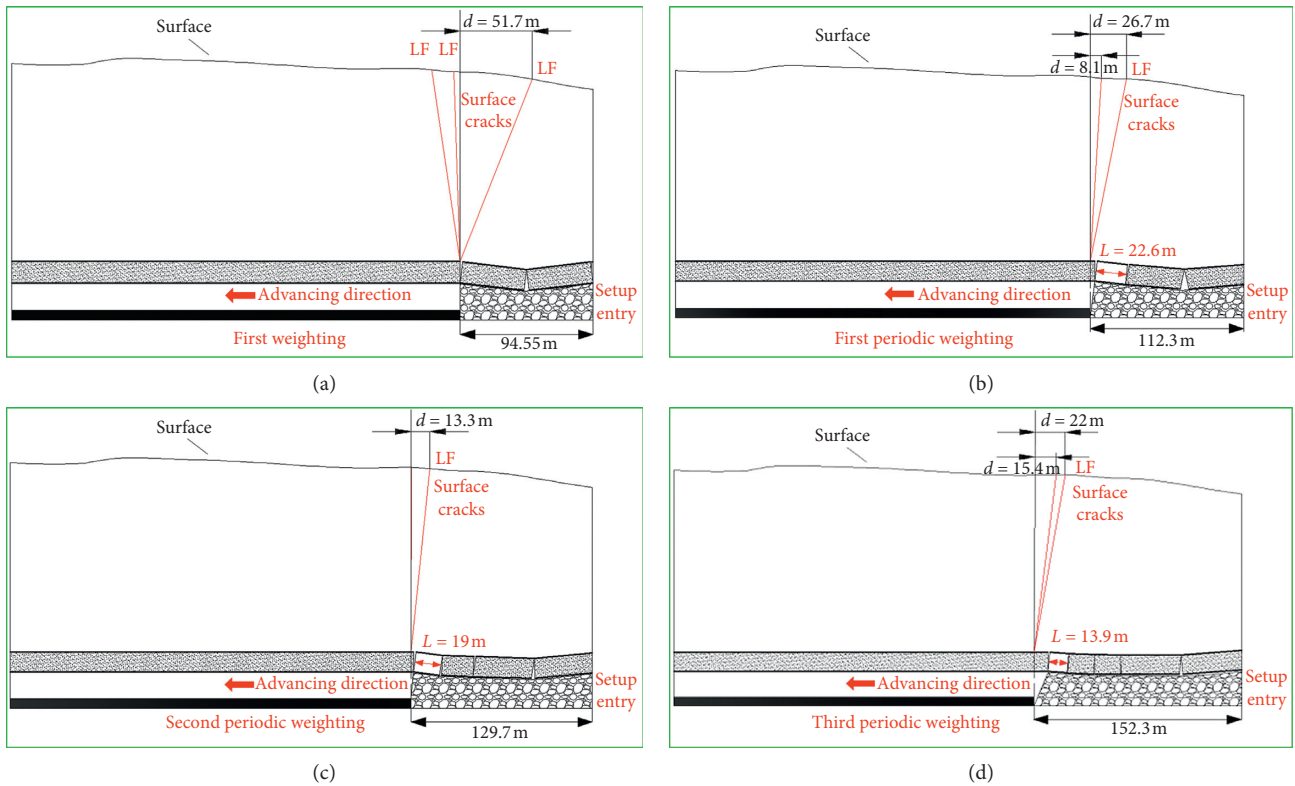
FIGURE 7: Contrast of broken blocks in key strata with surface-fractured wells. (a) The first weighting stage of working face, (b) the first periodic weighting stage, (c) the second periodic weighting stage, and (d) the third periodic weighting stage.

working face has reached full mining, the maximum subsidence point A22 is not changed, and the maximum value is 3560 mm.

According to the definition of horizontal deformation, the horizontal deformation of each measurement point on the advance line can be calculated by the moving value of each measurement point in different time periods on the advance line of the working face. Then a horizontal deformation curve can be drawn, as shown in Figure 10.

From the horizontal deformation curve in the advance direction of the working face, with the mining of the working face, the horizontal deformation value of surface water increases gradually, the maximum value of tensile deformation is 46.1 mm/m, and the maximum value of compressive deformation is −32.4 mm/m.
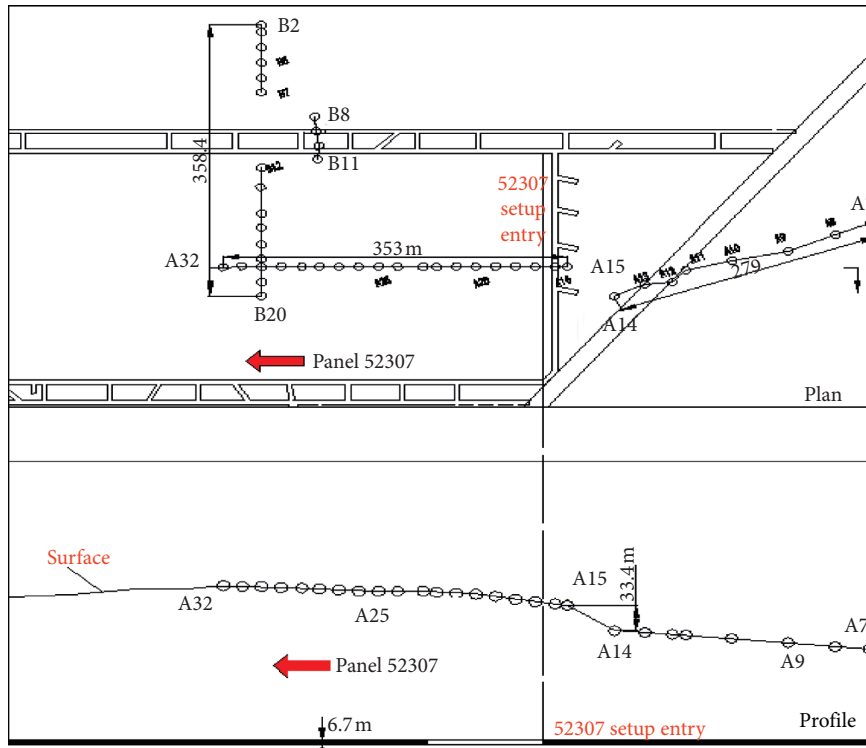
FIGURE 8: Horizontal section diagram of the observation station.
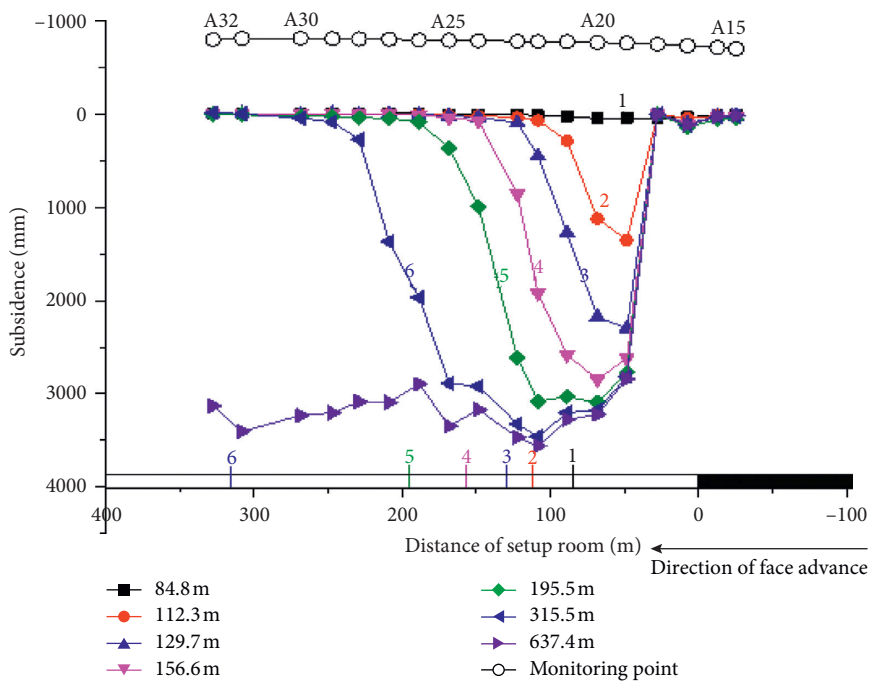
FIGURE 9: Subsidence curves.

According to Figures 9 and 10, in the advance of the working face, the surface subsides under the influence of mining, and the horizontal deformation of the surface soil changes with fluctuations. Near the measurement point A23, the maximum of surface deformation is accompanied by the maximum horizontal deformation. It indicates that the surface movement is intense, different forms of surface cracks will be formed in this area, and even multiple cracks will appear. In the actual observation, with the advance of working face, the speed of surface subsidence in the working face is fast, and the intense surface horizontal movement can be observed. The movement of the overburden subsidence
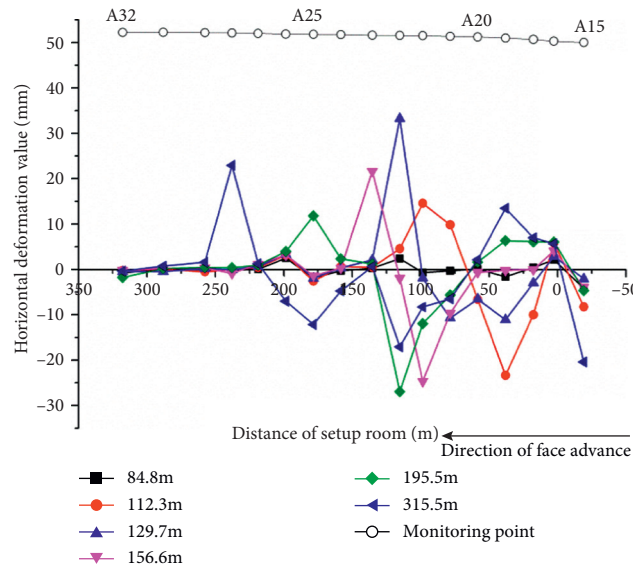
FIGURE 10: Horizontal deformation curves.

results in a sharp subsidence of the topsoil strata. However, there exists the uneven subsidence because the subsidence speed between adjacent soils is not uniform in time. At this moment, the soil bears great tensile stress. When the tensile force is greater than the limit bearing force of the soil, dislocation is caused between the adjacent soils in the vertical direction, and surface cracks are generated.

5.2. Field Measurement of Surface Crack Morphology. Surface cracks in the stations are recorded, and the characteristics of ground deformation and cracks are studied. The crack situation is shown in Figure 11. With the advance of the working face, surface cracks are generated.

The distribution of cracks in the middle of the surface is basically parallel to the working face, some of which bend towards the goaf, and the overall shape of the cracks presents a "C" shape. At the beginning of mining in the working face, the surface dynamic cracks are mainly distributed in the middle of the working face. When the working face advances to about 450 m, fewer permanent cracks are found above the open-off cut, along the grooves on both sides of the working face and the adjacent areas. Meanwhile, surface subsidence is serious in the process of on-site investigation and mining, and there will be different forms of surface cracks in the field, as shown in Figure 12. Surface cracks caused by underground mining can be classified as tensile cracks, hysteretic extrusion crack, and stepped cracks. Tensile cracks are caused by tensile stress, hysteretic extrusion cracks are caused by compressive stress, and stepped cracks are caused by shearing stress in Quaternary loose sediments.

Through the analysis of the surface tensile cracks and the advance of the underground working face, it is known that the position of the cracks always lags behind the mining position of the working face for a certain distance. Stepped cracks are formed by mining-induced overburden breakage and surface subsidence, generally lagging behind the

working face. Their mechanism can be divided into basic roof breaking principle based on thin plate theory and key strata theory. Based on the analysis of stepped cracks in working face 52307 of Daliuta, it is considered that the occurrence of stepped cracks is closely related to the lag distance of cracks, subsidence value, and horizontal deformation value of surface points of cracks. These cracks are located in the tensile deformation area, rather than the extrusion area, and their deformation value and subsidence value are relatively large.

Traditionally, it is generally believed that dynamic cracks open first and then close gradually with the advance of the working face. The width of cracks generally presents a single peak period and increases from small to large and finally tends to close. Based on the statistics of all cracks in working face 52307, the development time of tensile, extrusion, and stepped cracks are analyzed, respectively. Tensile crack, which is located behind the working face in Daliuta, generally undergoes the process of "opening-large-closing." It has a small deformation value and short duration (averaging 4.8 days). The maximum distance pushed by the working face is 40 m, the minimum is 17.4 m, and the average is 24.8 m. In the advance process of the working face, some cracks do not close after opening but only undergo the process of "opening-large-unchanged." These cracks are generally located near the open-off cut of the working face, with an average duration of 7.6 days. The maximum distance pushed by the working face is 48.9 m, the minimum is 33.3 m, and the average is 41.5 m. Stepped cracks are destructive cracks. They have small change range and rarely change after the generation, undergoing the process of "opening-unchanged." These cracks generally lie behind the working face and last for an average of 5.2 days. The maximum distance pushed by the working face is 27.8 m, the minimum is 19.7 m, and the average is 24.3 m. The extrusion crack is the same as the stepped
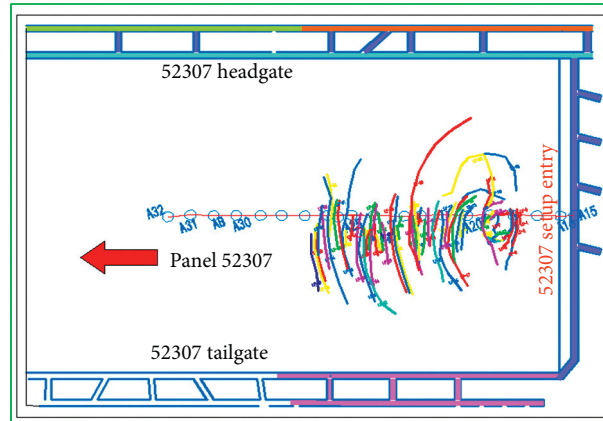
FIGURE 11: Contrast map for surface cracks in working face 52307 and observation station.
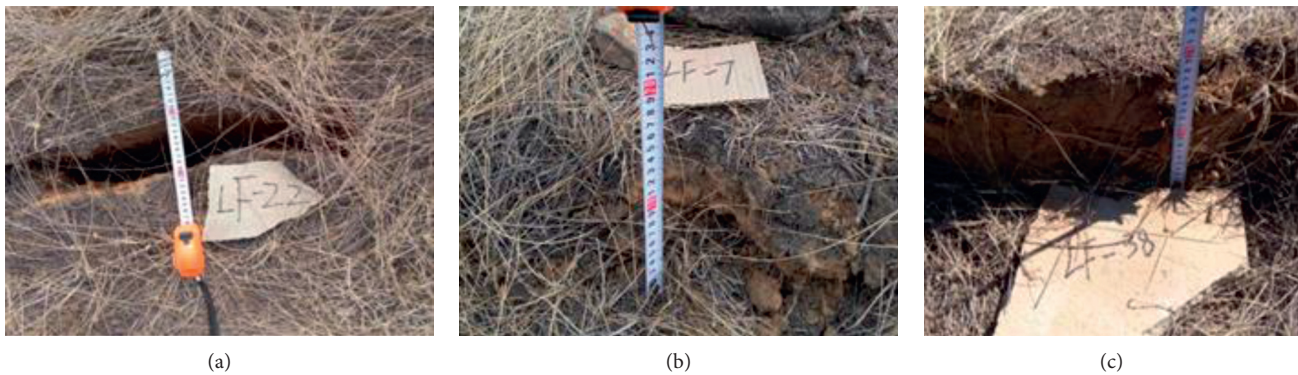

| (a) | (b) | (c) |

FIGURE 12: Classification of surface cracks in the working face. (a) Tensile cracks, (b) hysteretic extrusion crack, and (c) stepped cracks.

crack, but the damage degree of extrusion crack is far less than the stepped crack. They have small change range and rarely change after the generation, undergoing the process of "opening-unchanged." These cracks generally lie behind the working face and last for an average of 5.3 days. The maximum distance pushed by the working face is 33.3 m, the minimum is 21.8 m, and the average is 29.5 m.

6. Verification and Analysis of Numerical Simulation of Working Face

6.1. Model Design. CDEM software is the abbreviation for Continuum-Based Discrete Element Method, which is the coupling of continuous medium algorithm (such as finite element) and discontinuous medium algorithm (such as discrete element), developed by Institute of Mechanics, Chinese Academy of Sciences. By controlling the block (finite element calculation in the block, discrete element calculation in the boundary), to simulate the deformation and movement characteristics of materials in discontinuous and continuous states, the failure process of materials can be realized. The numerical model of the hydraulic support is embedded in the simulation. According to the data of drilling strata in the initial mining stage of the working face, the model has 45 strata and the strike length is 600 m; Table 3 shows rock mechanics parameters in numerical simulation. In numerical simulation, the upper boundary is free face, and the bottom boundary is the vertical displacement restriction; the right and left boundary are both the horizontal displacement restriction. The constitutive model of hydraulic support adopts the numerical constitutive model which characterizes the relationship between the support shrinkage and the working resistance of the support. According to the calculation principle and characteristics of the software, to eliminate the influence of boundary effect, 100 m boundary pillars are left on both sides, the actual mining length is 400 m, and the simulated working face advances 400 m along the open-off cut. The establishment of surface morphology is based on the field data such as the contrast map, the layout map of surface survey lines, as shown in Figure 13. There are 9065 block units in the model. According to the different lithology and thickness of each stratum, the block size of each stratum is different, and the characteristics of overburden breakage in situ can be restored to the greatest extent. And the plane numerical model is suitable for reflecting the relationship between underground mining and surface cracks.

TABLE 3: Rock mechanics parameters in numerical simulation.

No.	Lithology	Thickness (m)	Tensile strength (GPa/MPa)	Modulus of elasticity (MPa/GPa)	Density (kg·m^{-3})
45	Loess strata	11	—	—	1643
44	Sandy mudstone	5	1.59	1.34	2280
43	Siltstone	2	2.97	2.16	2312
42	Sandy mudstone	3	3.09	2.63	2287
41	Siltstone	1	2.86	1.92	2309
40	Sandy mudstone	2	2.41	4.19	2325
39	Mudstone	4	2.52	4.2	2323
38	Siltstone	2	2.56	4.51	2282
37	Sandy mudstone	6	2.58	4.83	2345
36	Coarse-grained sandstone	14	1.08	2.08	1997
35	Medium-grained sandstone	4	1.65	2.95	2111
34	Sandy mudstone	3	3.95	7.72	2318
33	Coarse-grained sandstone	2	4.68	5.68	2372
32	Sandy mudstone	5	5.37	7.72	2352
31	Fine-grained sandstone	2	2.75	35	2593
30	Siltstone	8	3.73	6.92	2367
29	Sandy mudstone	3	4.4	5.53	2405
28	Sandy mudstone	2	5.66	6.15	2363
27	Siltstone	3	3.73	6.92	2367
26	Sandy mudstone	3	6.54	12.4	2606
25	Fine-grained sandstone	3	5.35	10	2343
24	Sandy mudstone	3	6.54	12.4	2606
23	Siltstone	2	3.73	6.92	2367
22	Argillaceous sandstone	7	5.75	7.5	2366
21	Fine-grained sandstone	2	3.56	4.19	2263
20	Mudstone	4	5.2	8.21	2374
19	Fine-grained sandstone	4	5.71	16.3	2295
18	Fine-grained sandstone	3	6.01	15.6	2406
17	Sandy mudstone	2	6.79	6.8	2425
16	Siltstone	2	6.27	11.7	2403
15	Sandy mudstone	4	5.47	6.08	2446
14	Siltstone	6	8.08	15.7	2494
13	Medium-grained sandstone	5	5.62	9.78	2256
12	Siltstone	1	7.21	9.3	2387
11	Sandy mudstone	4	5.6	7.7	2482
10	Fine-grained sandstone	31	4.93	14.1	2360
9	Siltstone	4	9.26	14	2430
8	Coal 5–2	7	1.08	2.08	1290
7	Siltstone	4	7.84	12.9	2512
6	Sandy mudstone	3	8.58	11	2482
5	Siltstone	4	7.22	18.5	2546

Groups 1, 2, 3, and 4 are the groups of scaffolds in the simulation.

6.2. Simulation Process and Result Analysis

6.2.1. Simulation Process.
The working face starts from the open-off cut and excavates 5 m each time. Then the advance of 5 m in the working face is simulated. As a result, the mining of working face can be stimulated in a rapid a process.

Because the main key stratum belongs to the near-field key strata, according to the theoretical formula, the stratified breakage supplementary caving zone is generated at the thickness of 16 m, and the remaining 15 m is the basic top of the key strata, that is, the key bearing strata of the whole overburden. When the working face advances 95 m, the "fixed beam" on the basic top of the key strata breaks the first weighting of the working face, and then surface cracks occur, as shown in Figure 14.

Due to the existence of tensile force, there are two obvious surface cracks on both sides above the open-off cut, the support and the coal wall, respectively. The cracks above the open-off cut are permanent cracks, which will not close with the advance of working face; the width of the cracks above the working face and the coal wall is between 0.5 m and 1 m. The penetration depth of the crack is about 5 m, and the crack hysteresis working face is 10 m.

The first periodic weighting occurs when the working face advances to 115 m. The tensile cracks formed in the upper stage are closed due to the extrusion force behind them, while the breaking and subsidence of the key bearing blocks lead to the generation of new surface cracks.

According to Figure 15(a), two surface cracks are formed in this stage, both of which are hysteretic surface cracks. The first crack lags the working face within the
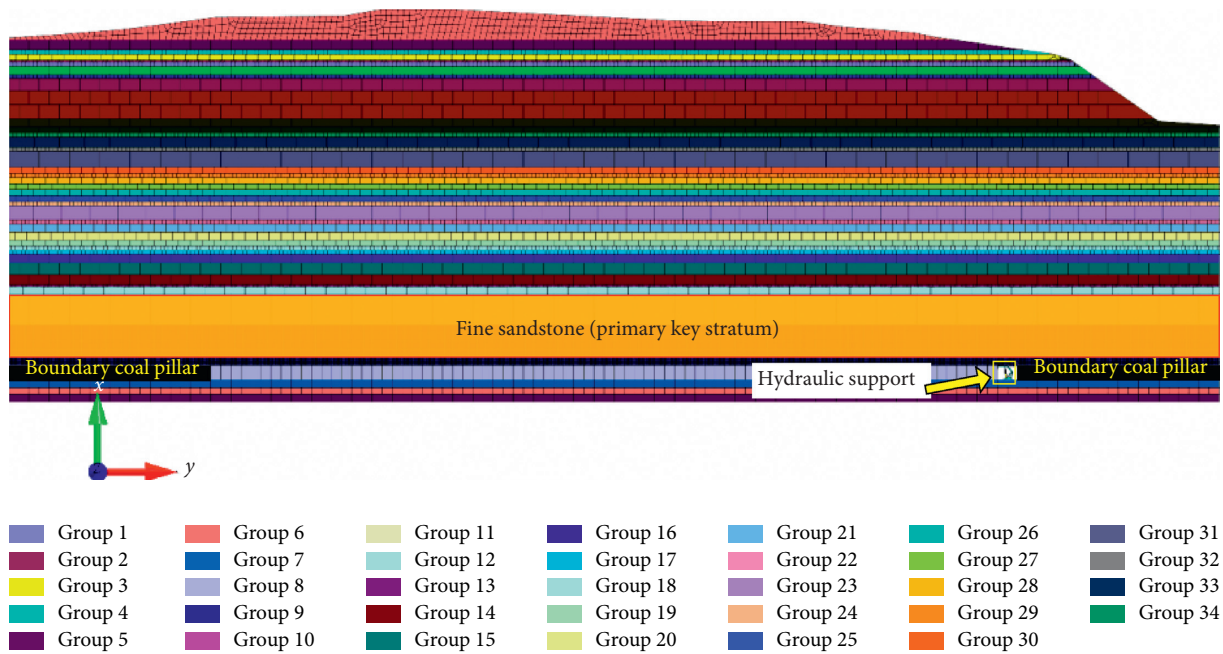
Fine sandstone (primary key stratum)

Boundary coal pillar

Hydraulic support   Boundary coal pillar

Group 1	Group 6	Group 11	Group 16	Group 21	Group 26	Group 31
Group 2	Group 7	Group 12	Group 17	Group 22	Group 27	Group 32
Group 3	Group 8	Group 13	Group 18	Group 23	Group 28	Group 33
Group 4	Group 9	Group 14	Group 19	Group 24	Group 29	Group 34
Group 5	Group 10	Group 15	Group 20	Group 25	Group 30	

FIGURE 13: Numerical simulation.

Surface cracks

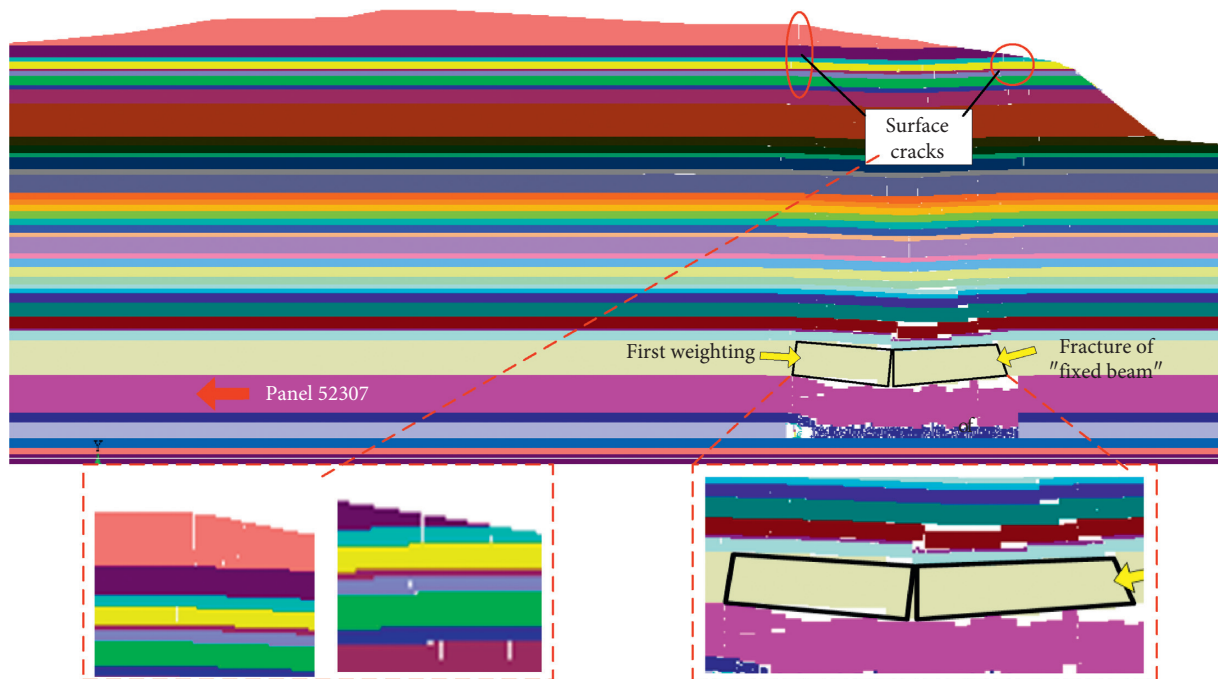First weighting   Fracture of "fixed beam"

Panel 52307

FIGURE 14: Initial weighting of working face.

range of 6–9 m, the second surface crack lags the working face is about 25 m. Due to the different distance from the side of goaf, the farther the distance, the greater the tension effect. Thus, the penetration depth of the first crack is greater than that of the second one. There is little difference in the lag distance of cracks at this stage in the simulation and in the field. The second periodic weighting occurs when the working face advances 130 m, as shown in Figure 15(b).

The key blocks of the key bearing strata break down and subside, and the surface cracks are very obvious. The crack lags behind the working face between 12 m and 15 m, and the width of the crack opening is about 1 m, which is larger than that of the first periodic weighting and deeper penetration into the bedrock.

Because there is only one key strata structure in the working face, and it belongs to the near-field key strata,
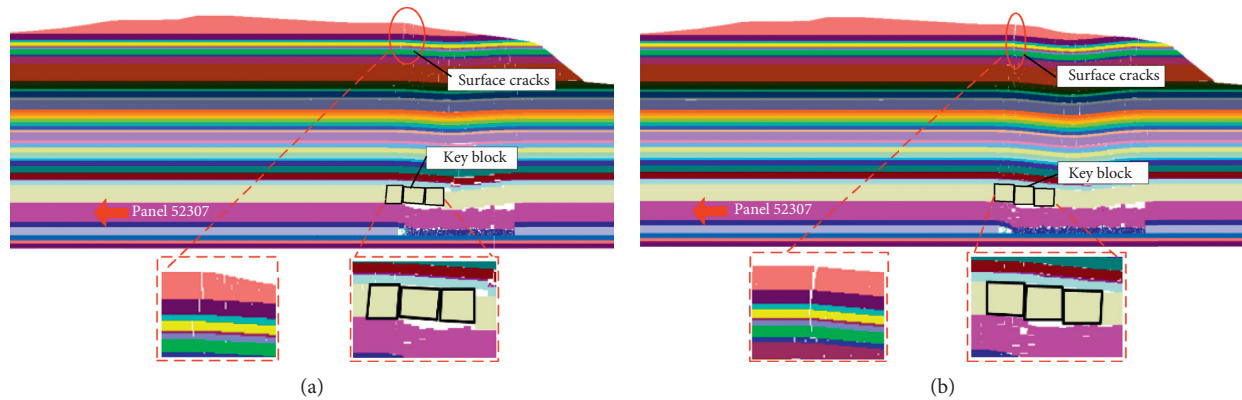
FIGURE 15: Periodic weighting of working face. (a) First periodic weighting. (b) Second periodic weighting.
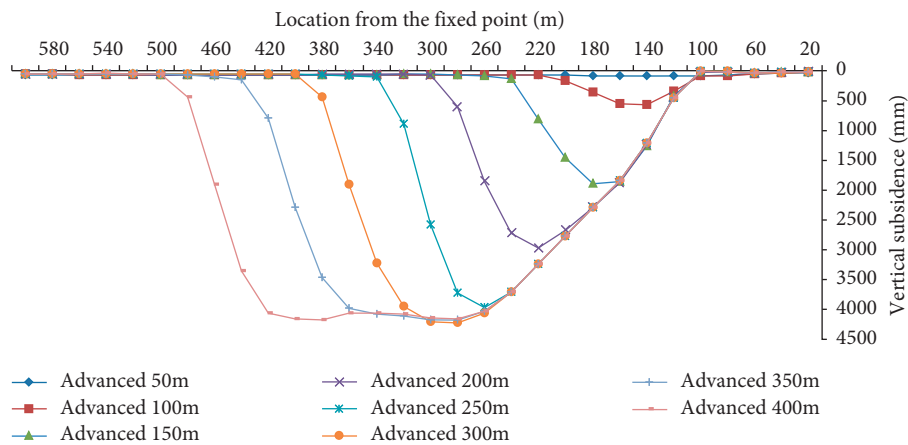

FIGURE 16: Surface subsidence curve.

when the key block of the key bearing strata breaks and has the subsidence displacement, the overburden bedrock will show the breakage and the subsidence displacement simultaneously. As a result, the surface also shows subsidence displacement, and the working face the first weighting. Within the initial weighting range of the working face, the key strata basic top break first subsides displacement, the overlying strata above follow, and the surface also has a certain subsidence at this time.

In the numerical simulation, the measured points are arranged along the surface of the model, and the surface subsidence at each step of excavation is monitored in real time. Figure 16 shows the surface subsidence curve.

As shown in Figure 16, when the initial weighting range of the working face is pushed to 100 m, the surface has already subsided. When the working face advances to 100, the maximum subsidence of surface survey points is 571 mm. When the working face advances 400 m, that is, when the excavation of the model is completed, the final subsidence of the surface survey line is 4,175 mm, and the surface subsidence value is 3,560 mm in the field measurement. Although there are some errors in the field measurement, the errors are unavoidable due to the difference between the numerical simulation and the rock strata change in the field.

7. Conclusions

(1) By distinguishing the overburden lithology and key strata of working face 52307 with shallow burial and high mining height in the Daliuta mining area, it is concluded that fine-grained sandstone with a thickness of 31 m or so above the coal seam is the main key strata of the overburden of the working face. According to the analysis of support pressure data of working face, after a roof prefracturing project, the first weighting step of working face still reaches about 95 m, and the periodic weighting step is in the range of 30 m–20 m, which indicates that the weighting step of working face is larger.

(2) Through the analysis of statistical results of the observation stations on the surface above the working face, after fully mining, the surface survey lines are observed; the maximum subsidence of the surface is 3560 mm from the last observation, because the key strata can control the whole overburden movement from the key strata to the surface. At the same time, the horizontal deformation curve also shows that the surface deformation is serious along with the advance of the working face. According to the statistics of the cracks, with the

breaking movement of the overburden, various types of surface cracks appear on the surface, mainly tensile ground cracks, which lag behind the working face.

(3) Through the validation of numerical simulation, with the advance of the working face, the key bearing strata breaks and subsides, and the overburden bedrock moves as a whole, resulting in obvious lagging surface cracks.

Data Availability

The data used to support the findings of this study are included within the article.

Conflicts of Interest

The authors declare that they have no conflicts of interest.

Acknowledgments

References

[1] E. H. Bai, W. B. Guo, Y. Tan, and D. M. Yang, "Special features and mechanism of the surface response to the high-intensity mining in the thick seam mining activities," *Journal of Safety and Environment*, vol. 18, no. 2, pp. 503–508, 2018.

[2] J. R. Kang, "Analysis of the effect of fissures caused by underground mining on ground movement and deformation," *Chinese Journal of Rock Mechanics and Engineering*, vol. 27, no. 1, pp. 59–64, 2008.

[3] D. Ma, J. Wang, X. Cai et al., "Effects of height/diameter ratio on failure and damage properties of granite under coupled bending and splitting deformation," *Engineering Fracture Mechanics*, vol. 220, p. 106640, 2019.

[4] Q. F. Hu, X. M. Cui, D. B. Yuan, and X. B. Deng, "Formation mechanism of surface cracks caused by thick seam mining and hazard analysis," *Journal of Mining and Safety Engineering*, vol. 29, no. 6, pp. 864–869, 2012.

[5] M. Singh and M. F. Dunn, "Investigation of problems and benefits of underground multiple seam coal mining," Final Technical Report, US Department of Energy, Washington, DC, USA, 1981.

[6] A. K. Ghose, "Green mining-unifying concept for mining industry," *Journal of Mines, Metals & Fuels*, vol. 52, no. 12, pp. 393–395, 2004.

[7] V. R. Greco, "Efficient Monte Carlo technique for locating critical slip surface," *Journal of Geotechnical Engineering*, vol. 122, no. 7, pp. 517–525, 1996.

[8] A. I. Homoud, *Studying Theory of Displacement and Deformation in the Mountain Areas under the Influence of Underground Exploitation*, AGH University of Science and Technology, Kraków, Poland, 1999.

[9] Y. Luo and S. S. Peng, "Integrated approach for predicting mining subsidence in hilly terrain," *Mining Engineering*, vol. 51, no. 6, pp. 100–104, 1999.

[10] G. Herrera, M. I. Álvarez Fernández, R. Tomás et al., "Forensic analysis of buildings affected by mining subsidence based on Differential Interferometry (Part III)," *Engineering Failure Analysis*, vol. 24, pp. 67–76, 2012.

[11] C. Tomás and C. Delacourt, "Three years of mining subsidence monitored by SAR interferometry, near Gardanne, France," *Journal of Applied Geophysics*, vol. 43, no. 1, pp. 43–54, 2000.

[12] C. J. Hahn, S. W. Kim, and H. S. Jung, "Satellite observation of coal mining subsidence by persistent scatter analysis," *Engineering Geology*, vol. 92, pp. 1–13, 2007.

[13] D. Ma, H. Duan, W. Liu, X. Ma, and M. Tao, "Water-sediment two-phase flow inrush hazard in rock fractures of overburden strata during coal mining," *Mine Water and the Environment*, vol. 39, no. 2, pp. 308–319, 2020.

[14] Y. Xue, T. Teng, F. Dang, Z. Ma, S. Wang, and H. Xue, "Productivity analysis of fractured wells in reservoir of hydrogen and carbon based on dual-porosity medium model," *International Journal of Hydrogen Energy*, pp. 1–10, 2019.

[15] W.-l. Shen, J.-b. Bai, W.-f. Li, and X.-y. Wang, "Prediction of relative displacement for entry roof with weak plane under the effect of mining abutment stress," *Tunnelling and Underground Space Technology*, vol. 71, pp. 309–317, 2018.

[16] Z. Z. Cao, P. Xu, Z. H. Li, M. X. Zhang, Y. Zhao, and W. L. Shen, "Joint bearing mechanism of coal pillar and backfilling body in roadway backfilling mining technology," *CMC-computers Materials & Continua*, vol. 54, no. 2, pp. 137–159, 2018.

[17] H. Liu, C. G. He, K. Z. Deng, S. G. Lei, and A. B. Zhang, "Analysis of forming mechanism of collapsing ground fissure caused by mining," *Journal of Mining and Safety Engineering*, vol. 30, no. 3, pp. 380–384, 2013.

[18] Q. X. Huang, "Roof structure theory and support resistance determination of longwall face in shallow seam," *International Journal of Coal Science & Technology*, no. 2, pp. 21–24, 2003.

[19] D. W. Zhou, K. Wu, Z. H. Bai et al., "Formation and development mechanism of ground crack caused by coal mining: effects of overlying key strata," *Bulletin of Engineering Geology and the Environment*, vol. 78, no. 2, pp. 1025–1044, 2017.

[20] L. Li, K. Wu, Z. Q. Hu, Y. K. Xu, and D. W. Zhou, "Analysis of developmental features and causes of the ground cracks induced by oversized working face mining in an aeolian sand area," *Environmental Earth Sciences*, vol. 76, no. 3, p. 135, 2017.

[21] Y. Xu, K. Wu, L. Li, D. Zhou, and Z. Hu, "Ground cracks development and characteristics of strata movement under fast excavation: a case study at Bulianta coal mine, China," *Bulletin of Engineering Geology and the Environment*, vol. 78, no. 1, pp. 325–340, 2019.

[22] Y. Xue, P. G. Ranjith, F. Dang et al., "Analysis of deformation, permeability and energy evolution characteristics of coal mass around borehole after excavation," *Natural Resources Research*, pp. 1–19, 2020.

[23] Z. Hu, C. Chen, W. Xiao, X. Wang, and M. Gao, "Surface movement and deformation characteristics due to high-intensive coal mining in the windy and sandy region," *International Journal of Coal Science & Technology*, vol. 3, no. 3, pp. 339–348, 2016.

[24] Z. Hu and C. Cao, "Impact of underground coal mining on land ecology and its restoration in windy and sandy region," *Journal of Mining Science and Technology*, vol. 1, no. 2, pp. 120–130, 2016.

[25] Y. Sun, J. Zuo, M. Karakus, and J. Wang, "Investigation of movement and damage of integral overburden during shallow coal seam mining," *International Journal of Rock Mechanics and Mining Sciences*, vol. 117, pp. 63–75, 2019.

[26] J. Ju and J. Xu, "Surface stepped subsidence related to top-coal caving longwall mining of extremely thick coal seam under shallow cover," *International Journal of Rock Mechanics and Mining Sciences*, vol. 78, pp. 27–35, 2015.

[27] W. Yan, H. Dai, and J. Chen, "Surface crack and sand inrush disaster induced by high-strength mining: example from the Shendong coal field, China," *Geosciences Journal*, vol. 22, no. 2, pp. 347–357, 2018.

[28] X. L. Yang, G. C. Wen, L. C. Dai, H. T. Sun, and X. L. Li, "Ground subsidence and surface cracks evolution from shallow-buried close-distance multi-seam mining: a case study in Bulianta coal mine," *Rock Mechanics and Rock Engineering*, vol. 58, no. 2, pp. 2835–3852, 2019.

[29] H. Zhuo, B. T. Qin, Q. L. Shi, and L. Li, "Development law of air leakage fractures in shallow coal seams: a case study in the Shendong coalfield of China," *Environmental Earth Sciences*, vol. 77, no. 23, pp. 1–11, 2018.

[30] H. Liu, K. Deng, S. Lei, and Z. Bian, "Mechanism of formation of sliding ground fissure in loess hilly areas caused by underground mining," *International Journal of Mining Science and Technology*, vol. 25, no. 4, pp. 553–558, 2015.

[31] D. Ma, H. Duan, X. Li, Z. Li, Z. Zhou, and T. Li, "Effects of seepage-induced erosion on nonlinear hydraulic properties of broken red sandstones," *Tunnelling and Underground Space Technology*, vol. 91, p. 102993, 2019.

[32] S. S. Peng, "Topical areas of research needs in ground control - a state of the art review on coal mine ground control," *International Journal of Mining Science and Technology*, vol. 25, no. 1, pp. 1–6, 2015.

[33] X. Y. Yu, P. Wang, and X. L. Li, "Analysis on characteristics of surface subsidence with Han Jia Wan coal mine," *Advanced Materials Research*, vol. 524-527, pp. 520–524, 2012.

[34] F. Wang, C. Zhang, X. Zhang, and Q. Song, "Overlying strata movement rules and safety mining technology for the shallow depth seam proximity beneath a room mining goaf," *International Journal of Mining Science and Technology*, vol. 25, no. 1, pp. 139–143, 2015.

[35] Q. H. Huang, "Ground pressure behavior and definition of shallow seam," *Chinese Rock Mechanics and Journal*, vol. 21, no. 8, pp. 1174–1177, 2002.

[36] M. G. Qian, S. P. Wu, and J. L. Xu, *Mine Pressure and Strata Control*, pp. 66–90, China University of Mining and Technology Press, Xuzhou, China, 2010.

[37] D. Ma, J. Wang, and Z. Li, "Effect of particle erosion on mining-induced water inrush hazard of karst collapse pillar," *Environmental Science and Pollution Research*, vol. 26, no. 19, pp. 19719–19728, 2019.

[38] X. Y. Yu, W. B. Guo, B. C. Zhao, and F. L. Wang, "Study on mining subsidence law of coal seam with thick overlying loEss stratum," *Coal Science and Technology*, vol. 43, no. 7, pp. 6–10, 2015.

Research Article

Energy Evolution and AE Failure Precursory Characteristics of Rocks with Different Rockburst Proneness

Feng Pei [1,2] **Hongguang Ji** [1,2] **Jiwei Zhao,**[1,2] **and Jingming Geng**[1,2]

[1]*School of Civil and Resource Engineering, University of Science and Technology Beijing, Beijing 100083, China*
[2]*Beijing Key Laboratory of Urban Underground Space Engineering, University of Science and Technology Beijing, Beijing 100083, China*

Correspondence should be addressed to Hongguang Ji; 1078938768@qq.com

Mastering the precursory information of rock failure is the basis of scientifically predicting rockburst, and AE technology is an effective means to solve this problem. The conventional uniaxial loading and cyclic loading/unloading tests of metagabbro and granite were carried out with GAW-2000 uniaxial electrohydraulic rigid testing machine to evaluate rockburst proneness. The energy evolution and AE characteristics of rocks with different rockburst proneness during loading are revealed. The results show that the rockburst proneness of granite is obviously stronger than that of metagabbro based on the comprehensive evaluation method of multiple rockburst proneness index. The reasons for different rockburst proneness are analyzed from the perspective of mineral composition and microstructure. Rockburst proneness is positively correlated with energy storage capacity. The elastic energy ratio of granite is obviously larger than that of metagabbro before peak stress. The intensity of AE signals generated in the failure process of strong rockburst rock (granite) is significantly higher than that of moderate rockburst rock (metagabbro). However, the peak frequency bands and amplitude all increase obviously before failure. The *b*-value and memory characteristics of rock with different rockburst proneness have obvious similar change rules.

1. Introduction

With the depletion of shallow resources, a great number of countries have gradually entered the deep mining stage. Rockburst disaster occurred frequently, which posed a great threat to the safety of equipment, life, and property. Rock is a heterogeneous material due to its petrographic, mineralogical, and internal microstructure features that affect the engineering properties of this rock. Rock stores elastic energy in the form of elastic strain, while it consumes energy in the form of crack propagation and damage. When the rock is loaded to its ultimate bearing capacity, aggregated strain energy in rock mass is released rapidly, thereby causing massive attack. In the meantime, a large number of AE signals are released in the form of elastic waves. AE signals contain a lot of information about crack propagation and coalescence. It could infer internal structure alteration and failure mechanism under different stress levels, and then the rockburst could be effectively predicted based on AE signals.

Considerable research on rock energy evolution has been undertaken, and scholars have achieved many important research results. Xie et al. [1, 2], for example, reveal the essential characteristics of rock instability and failure from the energy point of view, which lays a foundation for energy evolution analysis of rock mechanics. Nonlinear characteristics and energy distribution proportion of red sandstone were investigated by Zhang and Gao [3, 4] through uniaxial and triaxial cyclic loading/unloading testing. The relationship between energy conversion and rock fragmentation was clarified [5]. Li et al. [2] carried out uniaxial loading/unloading tests of rocks at different loading speeds and obtained the variation of releasable strain energy and dissipation energy. In addition, a large number of scholars have studied the relationship between rock damage and energy evolution [6–8]. However, little attention has been paid to

study the differences in the energy evolution of rocks with different rockburst proneness.

The deformation and failure of rocks have been investigated by analyzing AE signals, and studies have shown that information from the AE signals can be used to monitor the development of internal cracks in rocks and serve as an early warning for the instability and failure of rocks. Scholars have done a lot of research studies on AE signals from characteristic parameters and spectrum characteristics. On the one hand, AE signals are used to study the evolution process of rock fracture development by characteristic parameters such as ring counting rate, event rate, and energy rate. On the other hand, the combination of characteristic parameters such as RA (rising time/amplitude) [9, 10] and AF (counting/duration) is used to study the variation of parameters in the loading process. In the research of spectrum characteristics, Ji [11, 12] pointed out that the sudden increase of high-frequency and high-amplitude AE signals indicates that granite will be destabilized with the increase of stress level. The main frequency distribution band of AE signals in the process of rockburst is revealed [13–16].

Rockburst proneness is the inherent property of rock. The research of rockburst proneness is the basis of predicting and preventing rockburst and has important guiding significance for dynamic disasters. Engineering practice shows that rock is commonly loaded cyclically during construction. However, there are few comparison studies on energy evolution and AE characteristics of rocks with different rockburst proneness during cyclic loading/unloading. In this study, uniaxial cyclic loading/unloading testing is conducted on rocks with different rockburst proneness, and energy evolution and AE characteristics of rocks with different rockburst proneness are obtained. Felicity ratio was used to characterize the damage memory characteristics of two kinds of rocks during loading/unloading. At the same time, the development law of AE b-value is revealed, which provides a theoretical basis for the prediction of rock failure. The relationship between damage evolution, energy accumulation and release, and AE precursor information before the failure of rocks with different rockburst proneness is clarified.

2. Comprehensive Evaluation of Rockburst Proneness Based on Multiple Criteria

Rockburst must have two necessary conditions [17]: (1) rock has the ability to store high strain energy, which releases enormous energy in the failure process, and (2) excavation disturbance brings about local energy concentration, which provides energy for rockburst. In this work, a large number of laboratory experiments have been carried out for the first necessary condition. In view of the limitation of a single index to evaluate rockburst proneness, the rockburst proneness is evaluated by brittleness coefficient B, maximum elastic energy density Es, and rockburst tendency index Wet.

2.1. Brittleness Coefficient B.
The strength brittleness coefficient could be defined as the ratio of uniaxial compressive strength (σ_c) to uniaxial tensile strength (σ_t):

$$B = \frac{\sigma_c}{\sigma_t}, \tag{1}$$

where σ_c is the uniaxial compressive strength and σ_t is the tensile strength. The average tensile strength of granite and metagabbro is 7.82–9.14 MPa and 6.75–8.64 MPa, respectively.

2.2. Maximum Elastic Energy Density Es.
The maximum elastic strain energy density before the peak strength indicates the energy storage capacity of rock, which provides sufficient energy support for the dynamic impact of rock after failure. Several typical uniaxial compression curves and failure patterns are shown in Figure 1:

$$Es = \frac{R_c^2}{2E}, \tag{2}$$

where σ_c is the uniaxial compressive strength (UCS), MPa; E is Young's modulus, MPa.

2.3. Rockburst Proneness Index Wet.
The rockburst proneness index is a quantitative parameter, which corresponds to the ratio between the storage energy and the consumption energy in the loading stage, i.e., the loading measures 80–90% of the peak strength and the unloading measures 5% of the peak stress. The rockburst proneness index is the ratio between the elastic strain energy recovered during the unloading process and the dissipation energy in the loading process. The larger the rockburst proneness index is, the more likely an impact occurs in case of failure. Typical loading and unloading curves and failure patterns are shown in Figure 2.

Based on the comprehensive evaluation result in Table 1, it could be concluded that although there are small differences in rockburst proneness discriminant results between the different criteria, metagabbro shows a weak or moderate rockburst proneness, while granite shows a strong rockburst proneness. The impact intensity of granite is obviously stronger than that of metagabbro.

3. Microstructure Characteristics

Many research studies have clarified that the mechanical behavior of rock and energy storage capability are essentially determined by mineral composition, micromorphology, and combination mode [18–25]. The mineral composition and micromorphology characteristics of two kinds of rocks are obtained by combining powder X-ray diffraction (XRD) and binocular transmission polarization microscopy. The results are shown in Figures 3 and 4.

The metagabbro is grey-green, with scaly-columnar and fibrous metamorphic textures and banded and massive structures. It is mainly composed of amphibole (30%), feldspar (45%), quartz (15%), biotite (5%), kaolin (3%), and chlorite (2%). The composition is not uniform, which mainly shows the difference of altered mineral content caused by different alteration intensity. The minerals have the characteristics of directional arrangement under the microscope.
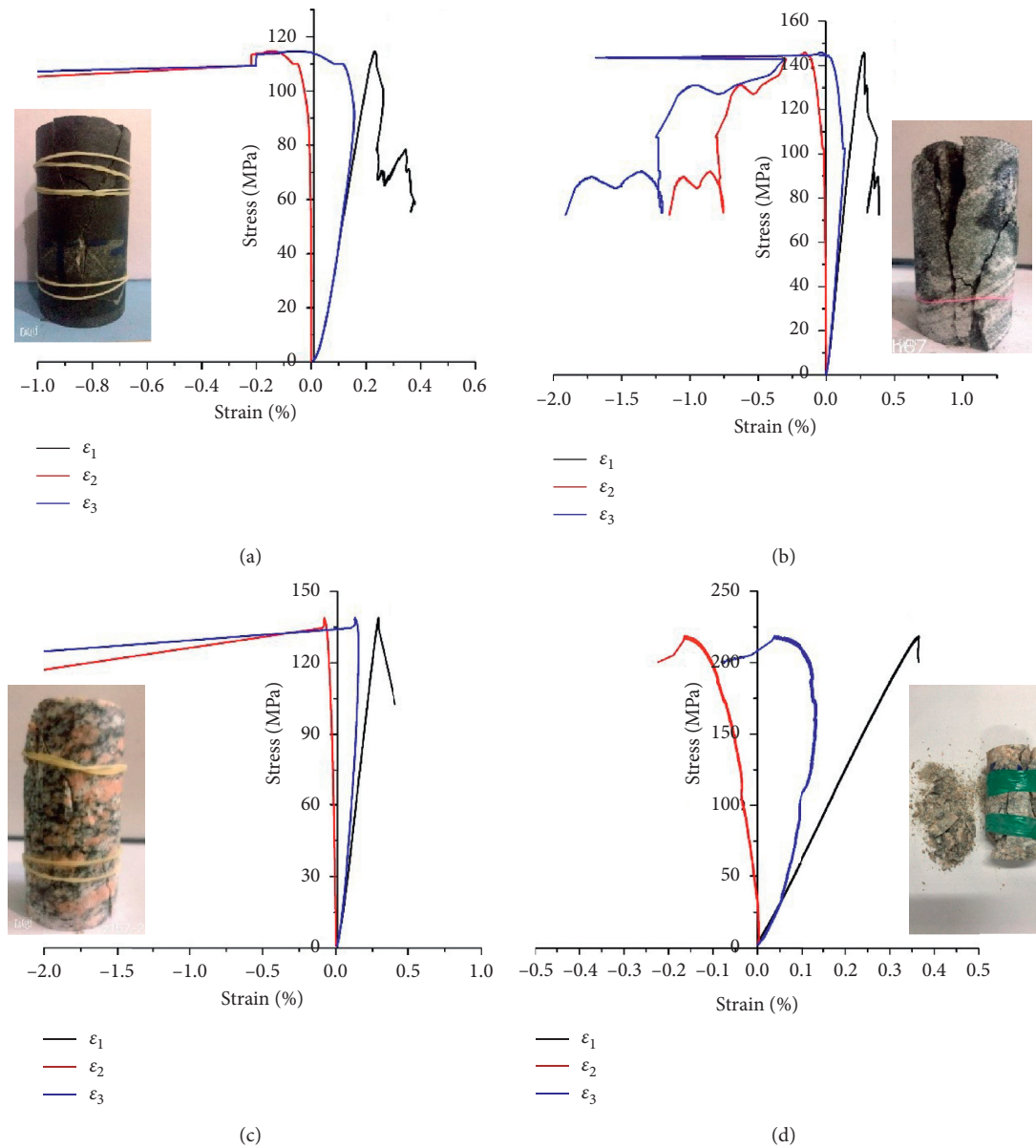
(a)

(b)

(c)

(d)

Figure 1: (a) Metagabbro-1, (b) metagabbro-2, (c) granite-1, and (d) granite-2.

The particle size distribution is shown in Figure 3(d), and the equivalent radius is mainly distributed in the range of 0.04–0.2 mm.

Comprehensive analysis shows that the granite has a porphyry-like structure with obvious schistosomiasis. The porphyry is feldspar (60%) with a grain size of about 0.5 mm. The matrix is mainly quartz (30%). The dark minerals are mainly biotite (5%) with directional arrangement. Other minerals include chlorite (about 3%) and pyrite (about 2%). The equivalent radius is mainly distributed in the range of 0.2–0.75 mm.

Quartz has compact structure, high stiffness, good mechanical properties, and small dispersion. The texture of feldspar is relatively soft than that of quartz, and its mechanical properties are relatively discrete. Mica is a soft material with obvious pore structure and great dispersion of mechanical properties. Quartz and feldspar with stable

mechanical properties in granite are obviously higher than that in metagabbro, which is the key element affecting rock impact proneness. Meanwhile, the crystallization degree is also the key factor affecting rockburst proneness.

4. Energy Evolution Characteristics

4.1. Specimen Preparation. Samples used in the experiments are granite and metagabbro, which were collected from the main shaft geological exploration hole of Shanling gold mine in Laizhou, Shandong Province. According to the method recommended by ISRM, samples were cylindrical cores drilled with diameters of 50 mm and lengths of 100 mm. To reduce the dispersion of experimental results caused by the natural differences in rock specimens, specimens with fewer cracks and no obvious defects were selected for experiments.
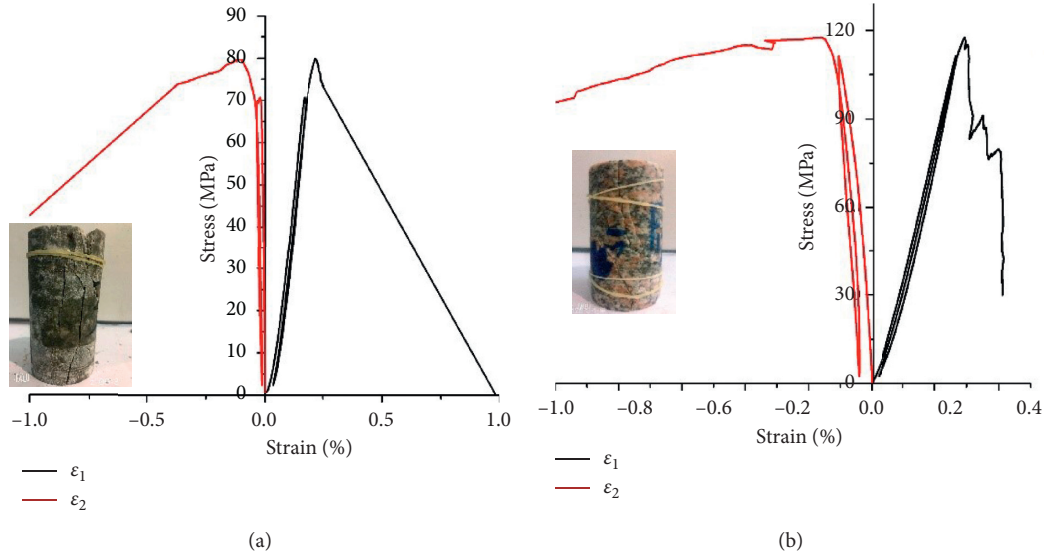
(a)

(b)

Figure 2: The loading and unloading curves of (a) metagabbro and (b) granite.

Table 1: Rockburst prediction results based on multiple criteria.

Lithology	Depth (m)	Maximum elastic strain energy density		Brittleness index		Rockburst proneness index	
		Es	Level	B	Level	Wet	Level
Metagabbro	761	172.9	III	14.9	III	3.76	III
Metagabbro	965	145.5	III	14.7	III	3.47	II
Metagabbro	1090	146.8	III	13.4	III	3.82	III
Granite	1415	247.0	IV	16.77	III	7.98	IV
Granite	1524	321.0	IV	19.5	IV	6.32	IV
Granite	1526	410.59	IV	21	IV	5.16	IV

II: weak rockburst proneness; III: moderate rockburst proneness; IV: strong rockburst proneness.

4.2. Test Procedures. The testing schemes were as follows: granite and metagabbro specimens were loaded/unloaded at a rate of 0.01 mm/min in steps of 30 kN. In order to prevent the specimen from sliding off the compression head, the loading was only unloaded to 2 kN in each cyclic step. The loading/unloading cycles were repeated until the specimen failed. AE signals were recorded with a processing system using a gain of 40 dB and a trigger amplitude threshold of 40 dB. AE monitoring systems and the loading system were turned on simultaneously to acquire the AE data and the mechanical parameters.

4.3. Energy Evolution. The relationship between energy density and strain in uniaxial cyclic loading/unloading is depicted in Figure 5.

It can be seen that energy density has an obvious nonlinear relationship with strain and the energy evolution of rock with different rockburst proneness demonstrates obvious similarity characteristics.

The input energy density and elastic strain energy density almost coincide, and storing elastic strain energy is dominated in the elastic deformation stage. Due to internal crack initiation and propagation with stress level

enhancement, input energy density deviates from elastic strain energy gradually. Small-scale crack propagation is dominated, and dissipation energy density increases slowly. Small-scale cracks are generating continuously and large-scale cracks are starting to develop, more energy was consuming when entering the unsteady crack propagation stage, and the closer to the peak strength is, the greater the increase of dissipated energy density is until destroyed. The storage elastic energy density of granite and metagabbro at the peak strength is 0.248 MJ·m^{-3} and 0.152 MJ·m^{-3}, respectively. The stronger the impact proneness is, the larger the energy storage capacity is.

In order to characterize the relationship between energy distribution ratios in the loading process, the energy storage ratio is defined as the ratio of elastic strain energy density to input energy density, and the ratio of dissipated energy density to input energy density is energy dissipation ratio. Energy storage ratio and energy dissipation ratio are calculated in Figure 6. As shown from Figure 6 that the dissipation ratio could be divided into four stages: decreasing, stabilization, slow increase, and sharp increase. In Figure 6, the dissipation ratio of metagabbro in the compaction stage is 0.267;however the dissipation ratio of granite in the compaction stage is 0.133. The dissipation ratio of

(a)

1-Quartz
2-Feldspar
3-Hornblende
4-Kaolin
5-Biotite
6-Chlorite

(b)

- Hornblende
- Feldspar
- Quartz
- Biotite
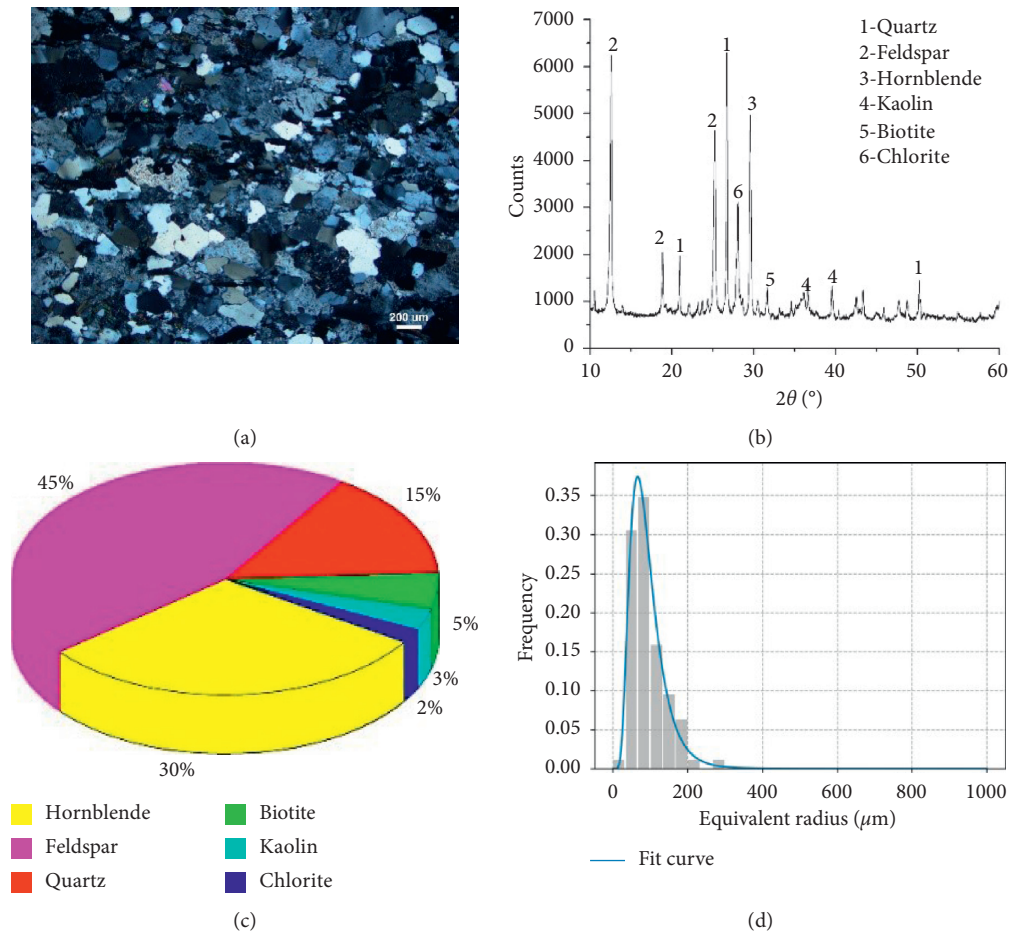- Kaolin
- Chlorite

(c)

—— Fit curve

(d)

FIGURE 3: Mineral composition and microstructure of metagabbro. (a) Observation under a polarizing microscope. (b) XRD diffraction pattern. (c) Mineral composition. (d) Equivalent radius distribution curve of particles.

metagabbro is obviously higher than that of granite at low-stress level.

There are many defects and fractures in the metagabbro, and the compaction stage is more obvious, so the input energy is used to improve the stiffness of the rock. The dissipation energy ration of metagabbro and granite is stable in 0.06–0.1 and 0.05–0.09 during the elastic deformation stage. Distribution ratio is approximately the same, and the ratio of elastic energy density to dissipation energy density is about 9 : 1 in the linear development stage. The dissipation energy ratio increases with the stress level increase, and the closer to the peak strength is, the larger the increasing extent is. The dissipation energy ratio at the peak strength of metagabbro and granite is 0.15 and 0.13, respectively. The extension of the elastic stage and reduction of the plastic stage lead to obvious improvement of rock energy storage capacity, and rock energy is released quickly at the moment of failure, which then causes strong impact failure.

5. AE Characteristics

5.1. AE Parameter Characteristics at Different Stress Levels. Given that AE signals are very sensitive to the initiation and growth of cracks in materials and structures, it has been widely used to evaluate damage mechanisms of rock. AE

transducers were attached to the specimen to record AE data and to avoid background noise, and the trigger threshold was set to 40 dB, where the peak definition time (PDT), hit definition time (HDT), and hit locking time (HLT) were set to 50, 100, and 500 μs, respectively, for the test. A layer of ultrasonic gel and tape were applied to provide better contact between the transducer and surface sample. The relationship among AE count, cumulative counts, AE energy, and load with time is depicted in Figure 7.

Compared with conventional uniaxial loading, rock under cyclic loading/unloading also undergoes compaction, linear development, stable crack propagation, unstable crack propagation, and rapid decline after peak. On the whole, the AE signals showed a slow increase in the elastic stage, a significant increase in unstable crack propagation, and a sharp increase in the failure stage.

Under the first cycle, the specimens are mainly in the compaction stage. There are fewer AE events as a result of crack closure and compaction. The cumulative counting curve shows the first rising step, but AE signals of the metagabbro in the compaction stage are obviously stronger than those of the granite, and even high-energy AE signals appear locally. The occurrence of local high-energy signals may be related to the rapid adjustment of the internal structure of metagabbro. At relatively low
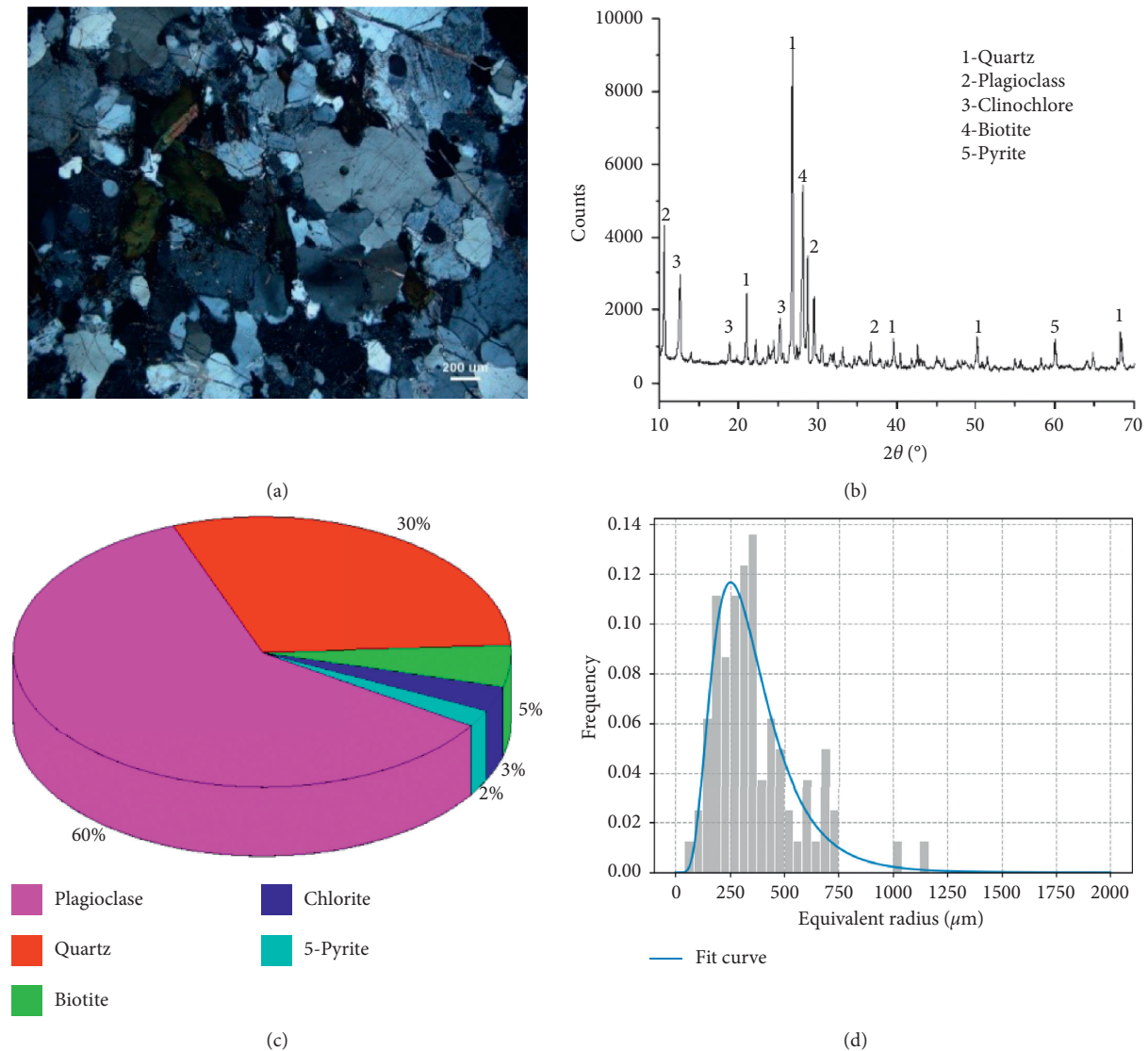
(a)

(b)

(c)

(d)

FIGURE 4: Mineral composition and microstructure of granite. (a) Observation under a polarizing microscope. (b) XRD diffraction pattern. (c) Mineral composition. (d) Equivalent radius distribution curve of particles.

stress, the stress did not play a primary role in the extension of microcrack intensity; microcrack propagation was related to the initial microcrack size, position, and direction.

Afterwards, the rock samples enter the elastic deformation stage corresponding to 47.4% and 65.7% stress levels, respectively. Elastic deformation is predominant and almost no new cracks occur. Although the cumulative ringing count curve of granite increases like a step, the gradient is small, and the cumulative ringing curve of metagabbro is nearly horizontal. During 47.4%–63.2% and 65.7%–76.4% stress level corresponding to granite and metagabbro, respectively, AE signals are gradually active, but the energy release is still at a lower level. As shown in Figure 7(a), the AE signals are almost symmetrically distributed at the maximum stress of this cycle, indicating that crack propagation stops immediately after unloading to last peak stress, and the rock sample is still in a weak damage state.

During 63.2% and 76.4% stress level to peak strength, the AE ringing count and energy release increase suddenly, and the cumulative ringing count increases abruptly. Obviously, the quiet phase of AE signals in the prepeak phase was not observed. Even at a lower stress level, the AE signals are still active in the unloading stage. In the unloading process, because of the elastic recovery of the element in the elastic state, there must be a friction effect between the elastic-plastic parts (elements or particles). This friction should also be one of the physical mechanisms of AE during unloading.

New cracks and original cracks will continue to grow in rock under low stress level. When rock sample reaches its peak stress, a large amount of elastic energy stored in the rock sample will suddenly release along the direction most vulnerable to damage and then produce high-energy AE signals.

Before the failure of samples, the AE ringing count rate of granite is obviously higher than that of metagabbro. The AE energy released at the peak strength of granite is
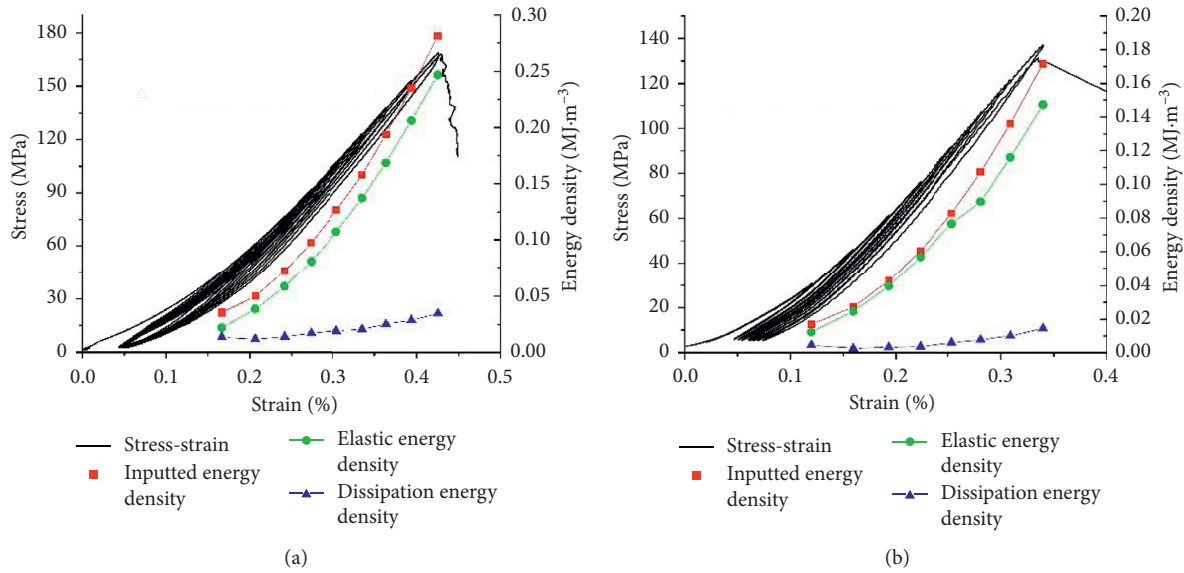
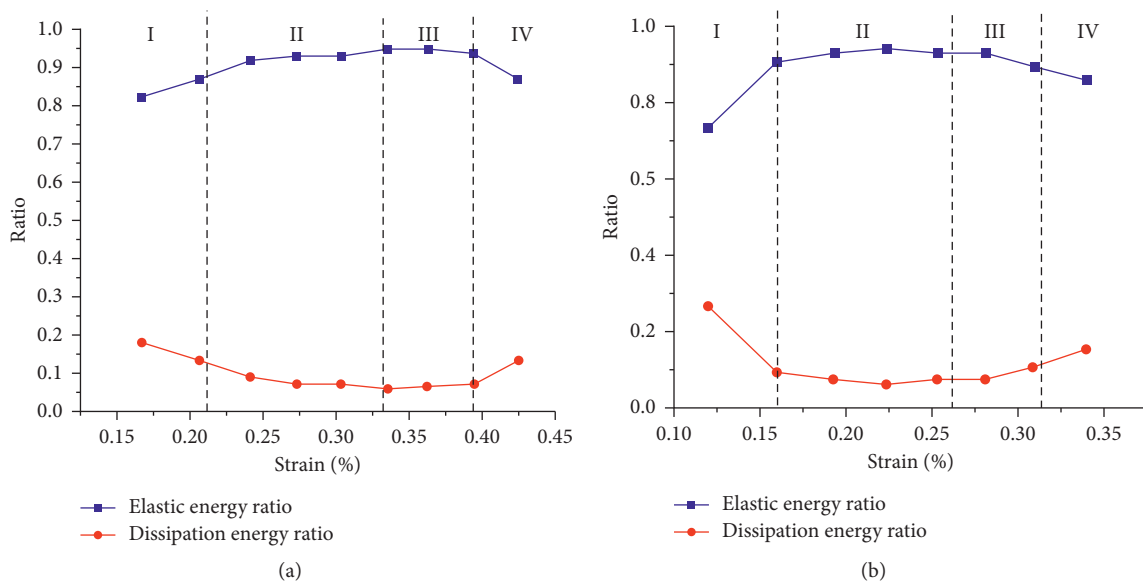Figure 5: Energy evolution of (a) granite and (b) metagabbro.

Figure 6: Energy distribution ratio of (a) granite and (b) metagabbro.

2×10^6 aJ, and that energy released by metagabbro is about 6.5×10^4 aJ. The maximum release energy at the peak strength of granite is 30.77 times that of metagabbro, which indicates the severity of rock destruction. Therefore, it can be concluded that the rockburst proneness of rock is positively related to the AE energy released during failure.

5.2. AE Spectrum Characteristics.

AE amplitude is a direct characterization parameter of crack propagation strength. The AE spectrum characteristics are determined by different crack growth modes. Therefore, amplitude and spectrum characteristics are of great significance to analyze the mechanism of rock crack, and AE spectrum characteristics under cyclic loading and unloading are depicted in Figure 8.

AE amplitudes of granite and metagabbro generated by cracks closure are concentrated in 40–60 dB and 40–45 dB, respectively. AE amplitudes are generally less than 50 dB in the elastic development stage. High-amplitude AE signals appear at each peak stress of loading/unloading and the AE amplitudes increase gradually with the stress level increase. However, at the same stress level, the AE amplitude of granite is generally higher than that of metagabbro. The amplitude of granite at the crack propagation stage changes with time in the form of arch bridge, which results in the absence of 40 dB–45 dB AE signals. When loading stress exceeds a certain stress level, the crack propagation is dominant in samples, and some crack initiation signals are concealed. But metagabbro did not occur above phenomena, and this is related to internal structure adjustment. The
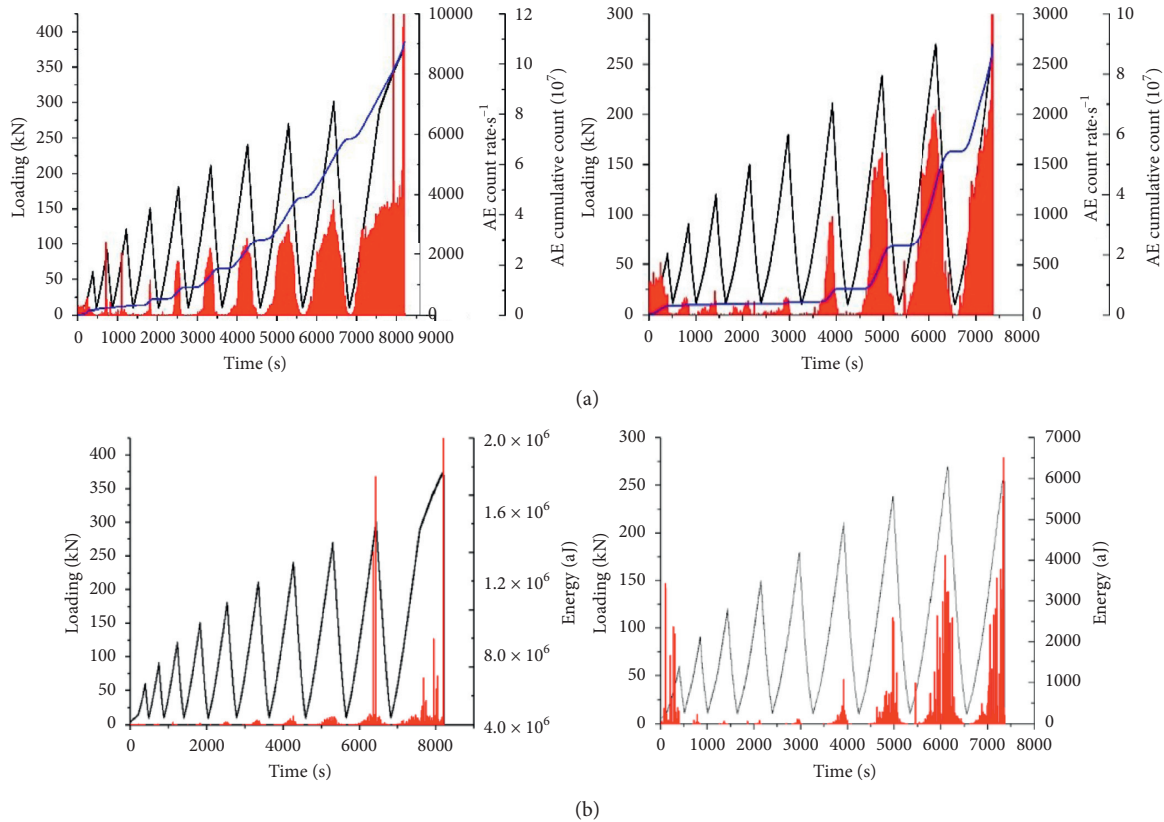
FIGURE 7: (a) AE count rate and cumulative count; (b) AE energy (left: granites; right: metagabbro).

maximum amplitude of granite and metagabbro at peak strength is 91 dB and 72 dB, which also shows the intensity of released energy when samples are destroyed.

Throughout the whole cyclic loading/unloading process, the peak frequency of granite is mainly concentrated in the 20 kHz and 50 kHz bands. The frequency bands near 50 kHz are dominant due to crack closure, and local high-frequency signals of 155–165 kHz appear. New cracks are constantly generated in rock, and large-scale crack propagation occurs locally in the stable and unstable crack propagation stage, and the frequency range is 60–80 kHz. Therefore, it can be inferred that the large-scale crack propagation is concentrated in the frequency range of 60–80 kHz. AE signals of 155 kHz high-frequency band appear near the peak strength of granite, and the high-frequency AE signals appear earlier than the peak strength. Therefore, the sudden increase of high-frequency signals indicates that macrofracture surface will occur in rock and it is about to enter the instability stage. The signal characteristics in the frequency band of metagabbro are similar to granite. In the unsteady crack propagation stage, 60–80 kHz frequency band also appears, and the AE signals in 155 kHz high-frequency band also appear at the peak strength. During 80–100% stress level, the internal cracks expand fully and the AE signals increase obviously in the low-frequency range.

5.3. AE Felicity Ratio. The discovery of Kaiser effect was first made in metals by Dr Joseph Kaiser and reported in his doctoral thesis. Then it was extended to rock materials, and a

lot of research studies on rock memory effect were carried out. Kaiser effect refers to the ability of rock to remember the maximum loading history. It is affected by loading history, loading mode, time effect, rock structure, and rock composition. Among these factors, loading history has the most significant effect on the AE characteristics of rock.

Kaiser effect is not obvious with the stress level increase, and rock memory deteriorates with the damage increase, and this phenomenon is called Felicity effect. The accuracy of Kaiser effect can be measured by the Felicity ratio, which is inversely proportional to the internal damage:

$$R_F(i) = \frac{\sigma_{AE}}{\sigma_{(i-1)}}, \tag{3}$$

where $R_F(i)$ is the Felicity ratio in i-th cycle. σ_{AE} is the stress level when the effective AE is restored during i-th loading process; $\sigma_{(i-1)}$ is the maximum stress level reached by $(i$-1)th loading. In view of the ambiguity of the definition of "significant increase" of AE signals, in this paper, the stress threshold for σ_{AE} is set at AE counts greater than 100 for the granite and metagabbro specimens.

The variation in AE Felicity ratio of rocks with different rockburst proneness was basically consistent with cycle numbers (Figure 9). The R_F of granite and metagabbro can be divided into three phases, Phases I, II, and III. In Phase I, R_F is greater than one under low stress level (corresponding to below 58.3% and 77.8% stress levels, respectively), indicating that rocks have an obvious memory as a result of less damage. Rock samples are repeatedly compacted under
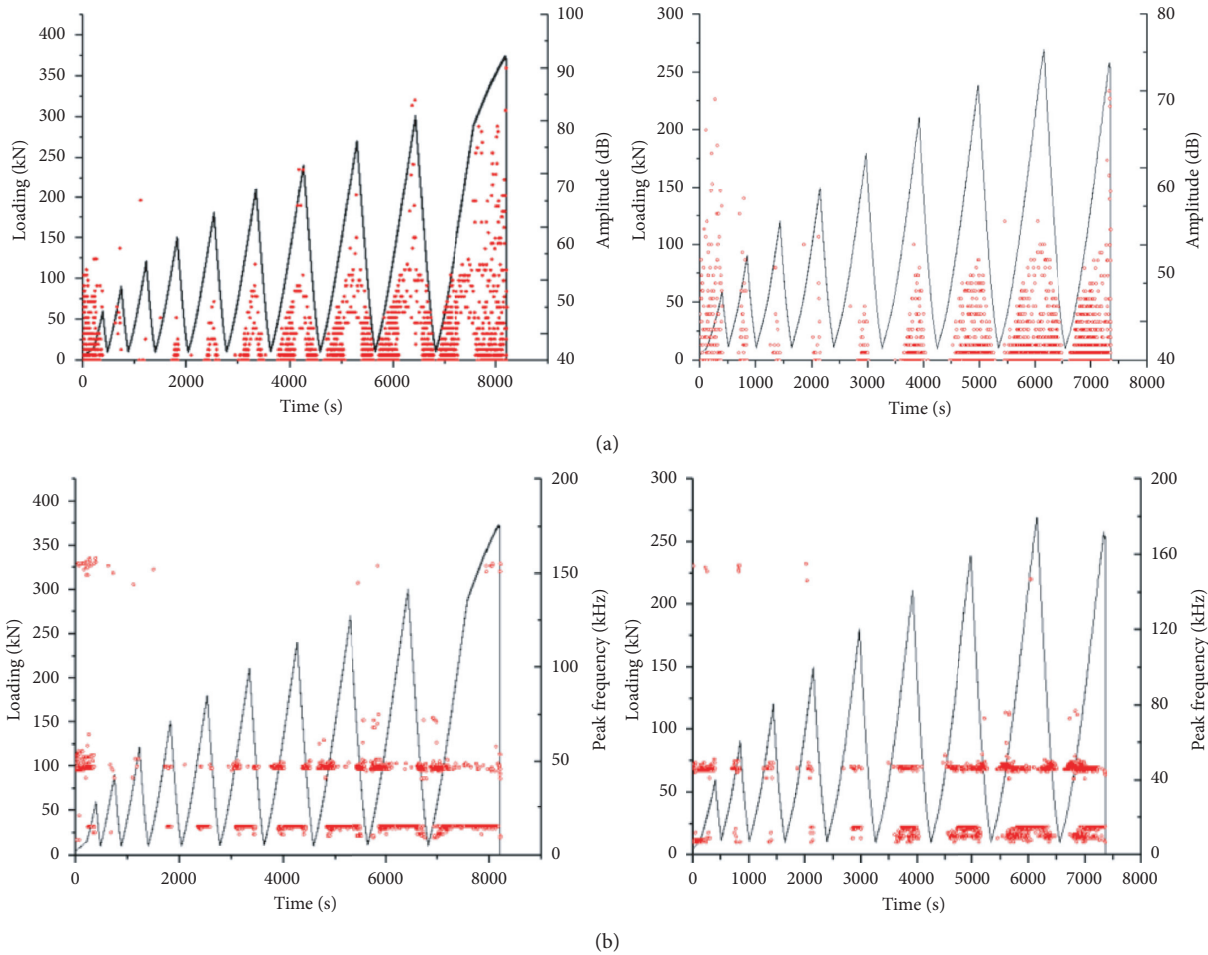
FIGURE 8: (a) AE amplitude and (b) AE peak frequency (left: granites; right: metagabbro).
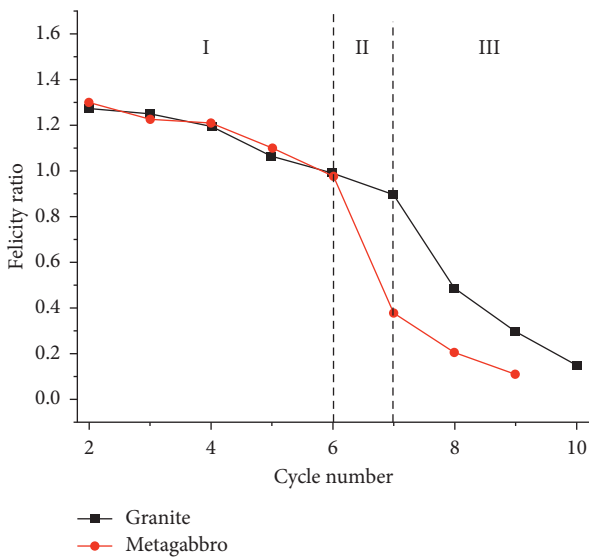

FIGURE 9: The relationship between Felicity ratio and cycle number.

loading, only the load exceeds previous maximum stress, and the significant AE signals will be generated. According to the energy distribution theory, the input energy is mainly stored in the form of elastic energy, while the dissipated energy by internal crack propagation is less.

In Phase II, $0.4 < R_F < 1$, the R_F gradually declines as a result of increased damage. With the further increase of stress level, the cracks parallel to the loading direction expanded. R_F of metagabbro decreased by 0.6 from 0.98 to 0.38, while R_F of granite decreased by 0.41 from 0.9 to 0.49. The decline extent of R_F can be used to indicate the damage degree. The maximum drop of metagabbro is significantly greater than that of granite, stating clearly that the damage degree of metagabbro with the same stress increase is greater than that of granite. The internal damage of rock samples is mainly caused by the initiation and expansion of internal cracks, and the dissipation energy of rock samples increases gradually.

In Phase III, the R_F of granite and metagabbro decreased linearly after the eighth and seventh cycles, respectively, and the internal cracks were further extended due to the action of high-stress level. Owing to accumulated damage in rock samples, the cracks could expand continuously even at low-stress level and produce violent AE signals.

Overall, the changes in R_F for granite are generally the same as the changes in metagabbro. However, in the loading and unloading processes, the AE signals of granite
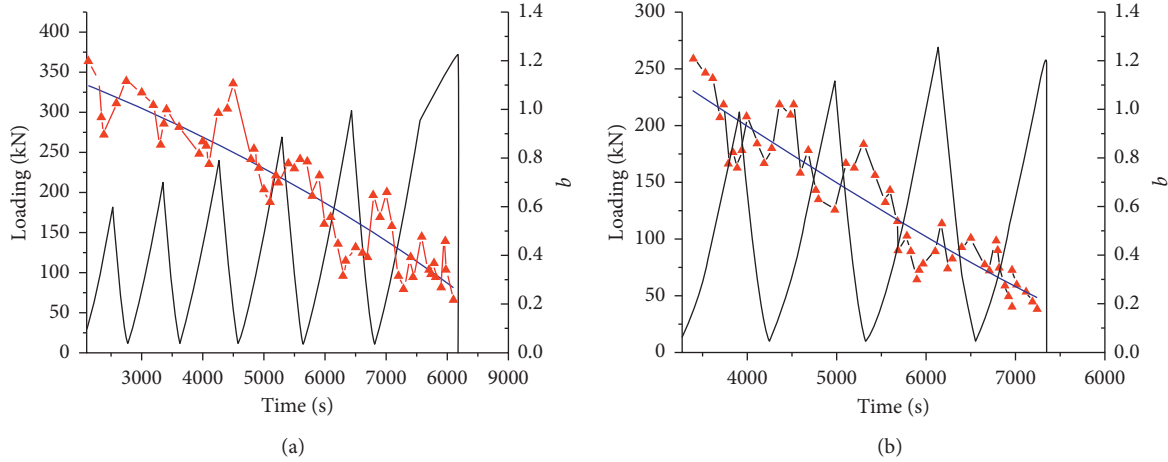
Figure 10: b-value variation with time of (a) granite and (b) metagabbro.

with strong storage energy capacity are stronger than those of metagabbro. Due to the release of elastic energy, the stress level of rapid R_F decline of granite is lower than that of metagabbro. However, the definition of R_F indicates that its value can only be used to determine the damage degree of rocks in the previous cycle, while this cycle damage can only be reflected in the next cycle, with a certain hysteresis.

5.4. AE b-Value.

In consideration of the hysteresis of using Felicity ratio to characterize damage, this section studies the evolution of AE b-value during loading to discuss on the precursory information of rock failure.

In the field of earthquake seismology, it is well known that small-magnitude earthquakes frequently occur, whereas large-magnitude earthquakes occur rarely. Gutenberg and Richter [26] conducted a statistical analysis of a large number of seismic activities and obtained the following relationship between earthquake magnitude and frequency [27–30]:

$$\lg N = a - bM, \tag{4}$$

where M is the magnitude, N is the earthquake frequency within ΔM range, a and b are constants, and b-value is an important parameter to evaluate the seismic activity level in a certain region. Since there is no concept of magnitude in AE, the magnitude M is usually replaced by the monitored AE amplitude during the experiment:

$$M_L = \frac{m}{20}. \tag{5}$$

M_L represents the magnitude in the testing process, b-value was calculated by using the least square method, and the amplitude interval was equal to 0.5. In order to avoid the experimental error caused by too few AE events at a certain stress level, this paper took 1000 acoustic emission events as a set of data and 100 acoustic emission events as sliding for calculation and obtained the variation law of b-value at different stress levels.

b-value is the crack growth scale, reflecting the propagation and damage of cracks during loading. The decrease of b-value means that the proportion of major events in rock mass increases, so the large-scale microcracks increase. The changing trend of AE b-value is the result of the game of crack scale development.

The b-value variation of granite and metagabbro during loading/unloading is investigated and shown in Figure 10, and the overall evolutionary law is similar. There is a clear downward trend with loading stress level increase, but the b-values of granite and metagabbro show their own characteristics at the same loading stress level. The AE b-values of granite and metagabbro are calculated from the 5th and 6th cycles, respectively. The AE signals produced at the lower stress level in the early stage are less, in order to ensure the calculation accuracy, and the AE b-values are not calculated at the lower stress level. AE b-values under medium stress level are relatively large, which concentrates in the range of 0.8–1.2 and 0.62–1.12, respectively. In the elastic development stage, the crack growth level and scale are limited mainly with low energy release rate. Under stable and unstable crack growth stage, high-stress level promotes some particles reaching its maximum bearing capacity, and the local stress is highly concentrated, leading to cracks growing and expanding. Therefore, AE signals with high amplitude and high energy are generated, and the AE b-values decrease continuously. The b-values of granite and metagabbro decrease rapidly after ninth cycles and eighth cycles, while b-values fluctuate but remain at a low level. The nearer the peak stress is, the lower the b-value is.

In conclusion, the trend of b-value decrease with loading level increase also indicates that crack growth in different scales is a gradual development process from small scale to large scale. The damage degree of granite after peak stress is more severe than that of metagabbro, which is mainly due to less damage in front of the peak and rapid release of energy at the peak strength.

For each cycle, the b-value change tendency shows V-shape, and the V-shape is obvious under the condition of medium stress level, but V-shape gradually disappears with

the increase of stress level. AE b-value is a function of crack growth, and crack propagation and coalescence lead to a decline of b-value. However, crack grown stops immediately with stress drop under low-stress level, and almost no large-scale cracks occur, so the b-value rises subsequently. However, with the cycle number increase, the cumulative damage will also generate obvious AE signals even at low-stress level. Large-scale cracks will be generated continuously through the internal cracks interaction, and AE b-value will continue to decline. Accumulative internal damage results in new and existing crack expansion even at unloading stage, so the AE b-value does not increase significantly, adversely continuing to decline. Under the last loading cycle, both granite and metagabbro show a rapid decrease of b-value. At this time, the internal cracks develop rapidly, macrofracture surface is produced, and dissipation energy increases sharply. However, the b-value of granite at the peak strength is obviously higher than that of metagabbro. The elastic stage of strong impact proneness granite takes up a relatively long proportion. Rock failure often concentrates in an instant. The overall loss of rock strength tends to be concentrated in a relatively short period of time. The large size crack monitored by AE signals before peak stress is smaller, so the b-value is larger. The lower the impact proneness is, the more fully the prepeak crack expands and the lower the sudden release of energy at the peak strength is. Although stress-induced changes in the b-value intuitively indicate the state of damage, one difficulty related to the use of the b-value to predict failure is that detectable changes in the b-value are generally the result of large changes in stress.

6. Discussion

With the stress increase, the crack size and numbers enlarge and then AE b-value decreases obviously, showing fluctuating decline characteristics. However, with the further increase of stress level, the local stress concentration is easy to occur at the edge of large-scale cracks, and then microcracks are further developed at the edge of large-scale cracks. The number of microcracks is obviously larger than that of small-scale cracks, and then the low-amplitude and low-energy AE signals are released. At this time, the AE b-value increases slightly, which is the main reason for the fluctuating decline under higher stress level.

Under a higher stress level, the internal damage of rock sample accumulates, and the obvious AE phenomenon occurs during the unloading stage. This indicates that even at unloading stage, rock damage continues to increase and damage caused by unloading cannot be neglected. According to the definition of Felicity ratio, the Felicity ratio is the memory of the cumulative damage of rock mass, which cannot reasonably reflect the damage to rock mass caused by the last loading to the maximum point, and its value should be higher than the calculated value. The calculation definition of Felicity ratio illustrates that its value can only be used to determine the damage degree in the previous cycle, while the damage in this cycle needs to be reflected in the next cycle, which has a hysteretic effect.

The single b-value or Felicity ratio cannot accurately predict rock failure, so it is of great significance to improve the accuracy of rock failure prediction by considering the change rule of both before peak strength.

7. Conclusion

(1) Based on the comprehensive evaluation method of multiple rockburst proneness index, granite is mainly prone to strong rockburst and metagabbro is mainly prone to moderate rockburst. There is no obvious plastic deformation stage before the peak stress of two kinds of rocks, and the stress drops instantaneously after the peak strength.

(2) Rockburst proneness is positively correlated with mineral components with stable mechanical properties. Quartz and feldspar with stable mechanical properties in granite are obviously higher than that in metagabbro, which is the key element affecting rock impact tendency.

(3) Rocks with different rockburst proneness have similar energy evolution characteristics. The energy storage and dissipation capacity of rock are the direct reasons for rock impact in failure. The stronger the rockburst proneness is, the more the elastic strain energy is stored before the rock peak, and the less the dissipation energy is.

(4) The AE ring counts and energy of rocks with strong rockburst proneness and moderate rockburst proneness have similar evolution law. In quantity, rocks with strong rockburst proneness are obviously more than those with moderate rockburst proneness. In the aspect of AE spectrum, the peak frequency distribution of rocks with strong rockburst tendency is wider than that of rocks with moderate rockburst tendency.

(5) The peak frequency distribution of AE signals before the critical main fracture of rock shows the phenomenon of frequency band increase. Before the critical main fracture of rock with stronger rockburst proneness, the frequency distribution is more dispersed and the number of frequency bands is more.

(6) The single b-value and Felicity ratio can characterize the rock fracture process but both cannot accurately predict rock failure. Combining the change rule of both before peak strength is an effective way to improve the criterion of discrimination.

Data Availability

The data used to support the findings of this study are available from the corresponding author upon request.

Conflicts of Interest

The authors declare that there are no conflicts of interest regarding the publication of this paper.

References

[1] H. P. Xie, Y. Ju, L. Y. Li, and R. D. Peng, "Energy mechanism of deformation and failure of rock masses," *Chinese Journal of Rock Mechanics and Engineering*, vol. 27, no. 9, pp. 1729–1740, 2008.

[2] L. Y. Li, H. P. Xie, Y. P. Ju, X. Ma, and L. Wang, "Experimental investigations of releasable energy and dissipative energy within rock," *Engineering Mechanics*, vol. 28, no. 3, pp. 35–40, 2011.

[3] Z. Z. Zhang and F. Gao, "Research on nonlinear characteristics of rock energy evolution under uniaxial compression," *Chinese Journal of Rock Mechanics and Engineering*, vol. 31, no. 6, pp. 1198–1207, 2012.

[4] Z. Z. Zhang and F. Gao, "Confining pressure effect on rock energy," *Chinese Journal of Rock Mechanics and Engineering*, vol. 34, no. 1, pp. 1–11, 2015.

[5] Y. Y. Li, S. C. Zhang, Z. J. Wen et al., "Energy conversion and fragment distribution characteristics of coal sample under uniaxial cyclic loading," *Journal of China Coal Society*, vol. 44, no. 5, pp. 1411–1420, 2019.

[6] F. N. Jin, M. R. Jiang, and X. L. Gao, "Defining damage variable based on energy dissipation," *Chinese Journal of Rock Mechanics and Engineering*, vol. 23, no. 12, pp. 1976–1980, 2004.

[7] X. B. Yang, H. M. Cheng, J. Q. Lv et al., "Energy consumption ratio evolution law of sandstones under triaxial cyclic loading," *Rock and Soil Mechanics*, vol. 40, no. 10, pp. 1–8, 2019.

[8] H. P. Xie, R. D. Peng, Y. Ju, and H. Zhou, "On energy analysis of rock failure," *Chinese Journal of Rock Mechanics and Engineering*, vol. 24, no. 15, pp. 2063–2068, 2000.

[9] A. Farhidzadeh, A. C. Mpalaskas, T. E. Matikas, H. Farhidzadeh, and D. G. Aggelis, "Fracture mode identification in cementitious materials using supervised pattern recognition of acoustic emission features," *Construction and Building Materials*, vol. 67, no. 2, pp. 129–138, 2014.

[10] A. Behnia, H. K. Chai, and T. Shiotani, "Advanced structural health monitoring of concrete structures with the aid of acoustic emission," *Construction and Building Materials*, vol. 65, pp. 282–302, 2014.

[11] H. G. Ji, H. W. Wang, S. Z. Cao, Z. Hou, and Y. Jin, "Experimental research on frequency characteristics of acoustic emission signals under uniaxial compression of granite," *Chinese Journal of Rock Mechanics and Engineering*, vol. 31, no. 1, pp. 2900–2905, 2012.

[12] P. Zeng, Y.-J. Liu, H.-G. Ji, and C.-J. Li, "Coupling criteria and precursor identification characteristics of multi-band acoustic emission of gritstone fracture under uniaxial compression," *Chinese Journal of Geotechnical Engineering*, vol. 39, no. 3, pp. 509–517, 2017.

[13] M. C. He, F. Zhao, S. Du, and M.-J. Zheng, "Rockburst characteristics based on experimental tests under different unloading rates," *Rock and Soil Mechanics*, vol. 35, no. 10, pp. 2737–2747, 2014.

[14] M. C. He, F. Zhao, Y. Zhang, and S. Du, "Feature evolution of dominant frequency components in acoustic emissions of instantaneous strain-type granitic rockburst simulation tests," *Rock and Soil Mechanics*, vol. 36, no. 1, pp. 1–8, 2015.

[15] Y. B. Zhang, P. Liang, B. Z. Tian, X. Yao, L. Sun, and X. Liu, "Multi parameter coupling analysis of acoustic emission signals of granite disaster and the precursor characteristics of the main rupture," *Chinese Journal of Rock Mechanics and Engineering*, vol. 35, no. 11, pp. 2248–2258, 2016.

[16] Y.-B. Zhang, G.-Y. Yu, B.-Z. Tian, X.-X. Liu, P. Liang, and Y.-D. Wang, "Experimental study of acoustic emission signal dominant-frequency characteristics of rockburst in a granite tunnel," *Rock and Soil Mechanics*, vol. 38, no. 5, pp. 1258–1266, 2017.

[17] M. F. Cai, D. Ji, and Q. F. Guo, "Study of rockburst prediction based on in-situ stress measurement and theory of energy accumulation caused by mining disturbance," *Chinese Journal of Rock Mechanics and Engineering*, vol. 32, no. 10, pp. 1973–1980, 2013.

[18] S. J. Wang, "Geological nature of rock and its deduction for rock mechanics," *Chinese Journal of Rock Mechanics and Engineering*, vol. 28, no. 3, pp. 433–450, 2009.

[19] E. Johansson, *Technological Properties of Rock Aggregates*, Lule University of Technology, Luleå, Sweden, 2011.

[20] X. E. Li and S. H. Cai, "The microscopic analysis of the mechanical properties of granite in dam foundation of the Three Gorges Project," *Journal of Chinese Electron Microscopy Society*, vol. 14, no. 5, pp. 379–384, 1995.

[21] A. Tugrul and I. H. Zarif, "Correlation of mineralogical and textural characteristics with engineering properties of selected granitic rocks from turkey," *Engineering Geology*, vol. 51, no. 4, pp. 303–317, 1999.

[22] R. Prikryl, "Some microstructural aspects of strength variation in rocks," *International Journal of Rock Mechanics & Mining Sciences*, vol. 38, no. 5, pp. 671–682, 2001.

[23] T. Keikha and H. Keykha, "Between mineralogical characteristics and engineering properties of granitic rocks," *The Electronic Journal of Geotechnical Engineering*, vol. 18, pp. 4055–4065, 2013.

[24] X. Wang, W. Yuan, Y. T. Yan, and X. Zhang, "Scale effect of mechanical properties of jointed rock mass: a numerical study based on particle flow code," *Geomechanics and Engineering*, vol. 21, no. 3, pp. 259–268, 2020.

[25] G. Zhang, P. G. Ranjith, D. Li, A. Wanniarachchi, and B. Zhang, "In-situ synchrotron X-ray microtomography observations of fracture network evolution of coal due to waterflooding," *Geophysical Research Letters*, vol. 47, no. 10, Article ID e2020GL087375, 2020.

[26] B. Gutenberg and C. F. Richter, "Earthquake magnitude, intensity, energy, and acceleration," *Bulletin of the Seismological Society of America*, vol. 32, no. 3, pp. 163–191, 1942.

[27] S. J. D. Cox and P. G. Meridith, "Micro cracking formation and material softening in rock measured by monitoring acoustic emissions," *International Journal of Rock Mechanics and Mining Sciences*, vol. 30, no. 1, pp. 11–24, 1983.

[28] D. L. Turcotte, W. L. Newman, and R. Shcherbakov, "Micro and macroscopic models of rock fracture," *Geophysical Journal International*, vol. 152, no. 3, pp. 712–728, 2003.

[29] C. G. Hatton, I. G. Main, and P. G. Meredith, "A comparison of seismic and structural measurements of scaling exponents during tensile sub-critical crack growth," *Journal of Structural Geology*, vol. 15, no. 12, pp. 1485–1495, 1993.

[30] M. V. M. S. Rao and K. J. P. Lakshmi, "Analysis of b-value and improved b-value of acoustic emissions accompanying rock fracture," *Current Science*, vol. 89, no. 9, pp. 1577–1582, 2005.

Research Article

Experimental Study on Dynamic Mechanical Properties and Energy Evolution Characteristics of Limestone Specimens Subjected to High Temperature

Qi Ping [1,2,3] **Chuanliang Zhang,** [1,2,3] **Haipeng Su,** [1,2,3] **and Hao Zhang** [1,2,3]

[1]*State Key Laboratory of Mining Response and Disaster Prevention and Control in Deep Coal Mine,*
 Anhui University of Science and Technology, Huainan, Anhui 232001, China
[2]*Research Center of Mine Underground Engineering, Ministry of Education, Anhui University of Science and Technology,*
 Huainan, Anhui 232001, China
[3]*School of Civil Engineering and Architecture, Anhui University of Science and Technology, Huainan, Anhui 232001, China*

Correspondence should be addressed to Qi Ping; ahpingqi@163.com

To study the effect of high temperature on the dynamic mechanical properties and energy evolution characteristic of limestone specimens, the basic physical parameters of limestone specimens that cool naturally after experiencing high temperatures of room temperature (25°C), 200°C, 400°C, and 600°C were tested. In addition, compression tests with 6 impact loading conditions were conducted using SHPB device. The changes of basic physical properties of limestone before and after temperature were analyzed, and the relationship among dynamic characteristic parameters, energy evolution characteristics, and temperature was discussed. Test results indicated that, with the increase of temperature, the surface color of specimen changed from gray-black to gray-white, and its volume increased, while the mass, density, and P-wave velocity of specimen decreased. The dynamic compressive stress-strain curve of limestone specimens after different high-temperature effects could be divided into three stages: elasticity stage, yield stage, and failure stage. Failure mode of specimen was in the form of spalling axial splitting, and the degree of fragmentation increased with the increase of the temperature and incident energy. With the increase of the temperature, the reflection energy, the absorption energy, the dynamic compressive strength, and dynamic elastic modulus of rock decreased, while its transmission energy, the dynamic peak strain, and strain rate increased. The dynamic compressive strength, dynamic elastic modulus, dynamic strain, and strain rate of limestone specimens all increased with the increase of incident energy, showing a quadratic function relationship.

1. Introduction

Rock engineering safety problem induced by high temperature had become an important topic in rock mechanics research [1–3]. High-temperature rock mechanical behavior was different from normal temperature, and its physical and mechanical properties were closely related to the temperature; hence, studying the mechanical behavior of rock after high temperature had important theoretical and engineering significance [4–6].

Based on the response of rock to strain rate, the strength and deformation characteristics of rock after high

temperature could be divided into static and dynamic aspects. Under static loads, Xi et al. [7] investigate the thermal damage characteristic of granite after different high-temperature effects, and the shear failure strength criterion of granite under thermomechanical coupling was established; in addition, test results indicated that temperature had significant effect on the failure characteristic of granite specimen. Su et al. [8] conducted the static compressive tests on fine-grained sandstone after high temperature, and the effects of temperature on static compressive strength and structure characteristics of sandstone were also investigated using X-ray diffraction and scanning electron microscope

technique; the test found that 600°C could be used as a threshold temperature of strength conversion of fine-grained sandstone samples. Considering the stress state of rock in engineering, Xu et al. [9] carried out the triaxial compressive tests on granite and studied the strength and deformation properties of granite under different confining pressures and high-temperature effects. Under dynamic loads, scholars conducted dynamic impact tests with the help of split Hopkinson pressure bar (SHPB) device to investigate the strength and deformation characteristic of rock at high strain rate. Yin et al. [10] investigate the dynamic mode I fracture toughness of granite with different temperatures and strain rates under coupling static and dynamic loads. The mechanical behavior and failure mode of biotite granite under combined action of cycle loading and high temperature (20°C, 200°C, 400°C, and 600°C) were studied using a modified SHPB device [11]; test results revealed that a threshold temperature for biotite granite may have existed between 400°C and 600°C. Wong et al. [12] found that the peak stress and fragment size of marble sample after heating were inversely related to the heating temperature, and most of energy was dissipated through plastic deformation. Liu and Xu [13] conducted dynamic impact tests on marble with various high temperatures and air pressures, and the relationship between dynamic stress-strain curve characteristic and failure mode was studied.

Limestone was one of the most widely distributed mineral resources in the Earth's crust, which was the main raw material for burning lime and cement; moreover, it was also the requisite flux for steelmaking and ironmaking [14–16]. Hence, it was valuable to study the physical and mechanical properties of limestone after high temperature. Rock material was composed of mineral particles of various chemical compositions and different crystallinities, and energy was an internal factor for the destruction of rock, which was accompanied by the entire deformation and destruction process [17–19]. Additionally, energy dissipation was the driving force for the destruction of material, and rock deformation and failure could be regarded as the result of mutual conversion between different forms of energy, which produced irreversible energy dissipation [20–27]. Yin et al. [28] investigated the damage degree and energy dissipation characteristic of rock after high-temperature treatment, and results showed that, with the increase of high temperature, the reflected energy increased, while both transmitted energy and absorbed energy decreased.

From the above investigation, it could be concluded that the research results of high-temperature limestone mainly focus on the static loads, and the dynamic mechanical properties and energy dissipation of limestone were limited. In this research, the basic physical parameters, such as color, volume, mass, density, and longitudinal wave velocity of the specimen after experiencing high temperatures of room temperature (25°C), 200°C, 400°C, and 600°C, were compared. Moreover, the dynamic compressive tests on sandstone after high-temperature effects were carried out with 6 impact pressures (0.4 MPa, 0.5 MPa, 0.6 MPa, 0.7 MPa, 0.8 MPa, and 0.9 MPa), and the dynamic stress-strain curves and failure modes of sandstone specimen with various test

conditions were studied. Finally, the relationships among dynamic compressive strength, dynamic elastic modulus, dynamic strain, and strain rate, as well as the failure mode of sandstone specimen and temperature, were analyzed from the energy perspective.

2. Basic Physical Properties before and after High Temperature

2.1. Processing and High-Temperature Heating of Limestone Specimens. Rock specimens were collected from Shungeng mountain in Anhui province, China. To enhance the contrast of the test results, test specimens used were taken from the same rock block with good compactness and homogeneity [29]. According to the recommendations of the international institute of rock mechanics [30] and the China rock mechanics and engineering society's "Technical specification for testing method of rock dynamic properties" [31], the size of the limestone specimen was determined to be 50 mm × 25 mm. Rock sample processing equipment such as ZS-100 drilling sampler, DJ-1 rock cutting machine, and SHM-200 double-end grinder was used to core, cut, and grind and polish to control the unevenness of the two ends of rock specimen less than ±0.05 mm, and the error of the end surface perpendicular to the axis of the test piece was less than ±0.25°, ensuring that the machining accuracy meets the test requirements.

A box-type resistance furnace equipped with an automatic temperature control system was used to heat the limestone specimen at high temperature, as shown in Figure 1. The size of the working room was 300 mm × 200 mm × 120 mm, and the designed maximum heating temperature was 1200°C. First, place limestone specimens evenly in the furnace with a certain distance between two specimens. Subsequently, the heating was performed slowly at a heating rate of 10°C/min until reaching the set temperature. The temperature set values were 200°C, 400°C, and 600°C, respectively, in addition, a set of room temperature (25°C) was added for comparison. In order to ensure that rock specimens were uniformly heated, temperature would keep constant temperature for 4 h after heating to the set temperature. Finally, the heated limestone specimens were cooled to normal temperature in the furnace by natural cooling.

2.2. Apparent Morphological Characteristics of Specimens after High Temperature. In this test, the apparent morphology of limestone specimens subjected to room temperature (25°C), 200°C, 400°C, and 600°C is shown in Figure 2. It could be noticed that the color of the limestone specimen at room temperature was gray-black; moreover, the surface color of the specimen changed significantly and become gray-white after the high temperature. When the temperature increased to 600°C, a small amount of powder particles appeared on the surface of rock specimen, which illustrated that high temperature action showed damage effect on the structure of limestone and caused degradation of mechanical properties.
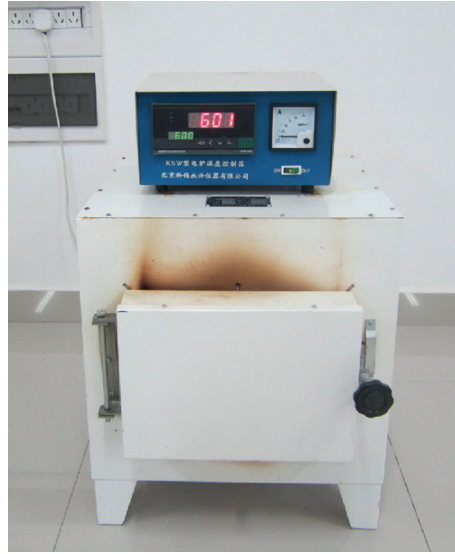
FIGURE 1: Box-type resistance furnace heated at high temperature.

(a) (b) (c) (d)

FIGURE 2: Apparent morphology of limestone specimens after high temperature. (a) 25°C. (b) 200°C. (c) 400°C. (d) 600°C.

2.3. Changes in Volume, Mass, Density, and Longitudinal Wave Velocity. According to the "Standard for test method of engineering rock mass" [32], the diameter, height, and quality of the limestone specimen after different temperature effects were measured and calculated, and the C61 type nonmetal ultrasonic detector was used to obtain its longitudinal wave velocity. The volume, mass, density, and longitudinal wave velocity of limestone specimen before and after the high temperature are shown in Figure 3.

It can be seen from Figure 3(a) that the limestone specimens showed volume expansion after different high-temperature effects, and the increase rate of volume increased with the increase of temperature. After 200°C, 400°C, and 600°C, the volume increased by 0.40%, 1.03%, and 2.81%, respectively, compared with that after room temperature. This phenomenon was caused by the volume expansion of the mineral particles composed of limestone due to high temperature, and the original micropores and microcracks inside the specimen began to germinate new cracks, which caused the expansion of specimen volume. After different high-temperature effects, the limestone specimens lost mass, and the mass reduction rate increased slightly with the increase of action temperature. After 200°C and 400°C, the mass reduction rate of specimen was only 0.02% and 0.04%, respectively. When the action temperature increased to 600°C, the mass loss rate of rock specimen increased slightly, and the mass reduction rate was 0.97%.

Figure 3(b) indicates that density of rock specimen decreased with increasing temperature after high temperature. The density of limestone specimens at room high temperature was 2.711–2.721 g/cm^3, while after 200°C, 400°C, and 600°C, the average density was 2.711 g/cm^3, 2.692 g/cm^3, and 2.604 g/cm^3, which was 0.37%, 1.05%, and 3.94% less compared with that after room temperature. Figure 3(c) shows that the longitudinal wave velocity of the limestone specimen without high-temperature effect ranged from 3975 m/s to 4117 m/s. With the increase of temperature, the longitudinal wave velocity of the limestone specimen showed a downward trend. After 200°C, the longitudinal wave velocity of the specimen was 3793 m/s, which was 7.87% less compared with that after room temperature. When the temperature increased to 400°C and 600°C, the velocity of the longitudinal wave was reduced by 32.69% and 51.98%, respectively. The main reasons could be concluded in two aspects: On one hand, due to the effect of high temperature, the constituent minerals inside the limestone specimen were expanded and new cracks were caused by different expansion coefficients. When the action temperature increased, the rock structure degradation degree increased, and powder particles appeared on the surface of the specimen. On the other hand, the pore volume caused by the evaporation of various types of water in the test piece increased. The increase of pores and the deterioration of
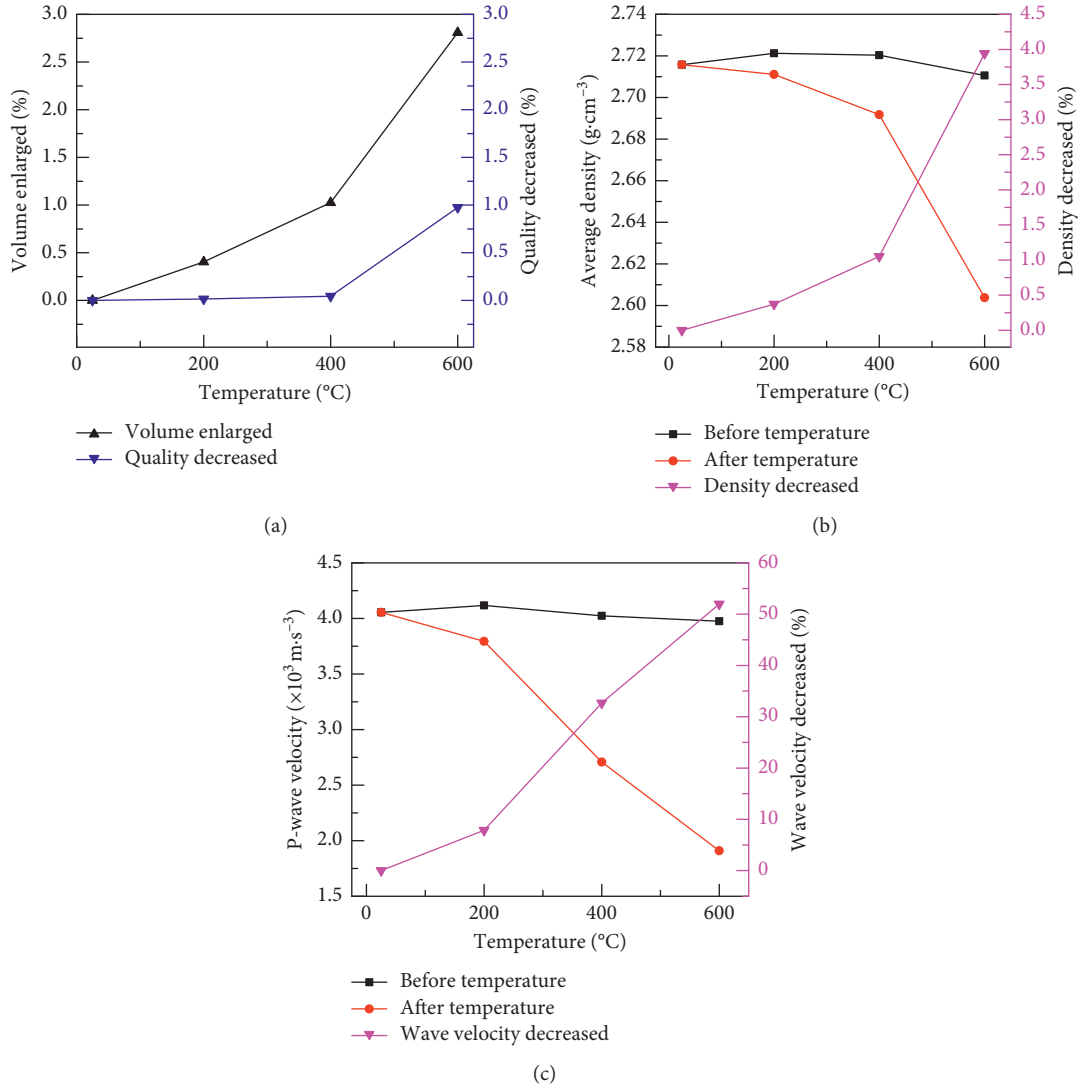
(a)

(b)

(c)

FIGURE 3: Relationship between basic physical parameters of limestone and temperature. (a) Volume and mass. (b) Density. (c) Longitudinal wave velocity.

internal structure caused by new cracks had a blocking effect on the propagation of stress waves, which caused the attenuation of stress wave propagation energy in the specimen and the decrease of wave velocity.

3. The Basic Principle and Test Result of SHPB Test

3.1. SHPB Test Device and Its Basic Principle. SHPB test device in the state key laboratory of mining response and disaster prevention and control in deep coal mine (as shown in Figure 4) was used to perform impact tests on limestone specimen with various temperature effects.

During SHPB test, the same impact velocity and loading waveform could be obtained using the same impact air pressure. When the incident stress pulse reached the interface between the incident bar and rock specimen, transmission and reflection occurred due to the different wave impedances. The stress pulse signal propagating in the

pressure bar could be obtained from the strain gauges mounted on the incident and transmitted bar, respectively, as shown in Figure 5.

SHPB experimental principle was based on the assumption of one-dimensional stress wave and stress uniformity [33]. The three-wave method was used to obtain dynamic mechanical parameters such as stress $\sigma(t)$, strain $\varepsilon(t)$, and strain rate $\dot{\varepsilon}(t)$ of the specimen:

$$
\left.
\begin{aligned}
\sigma(t) &= \frac{AE}{2A_s}\left[\varepsilon_I(t) + \varepsilon_R(t) + \varepsilon_T(t)\right], \\
\varepsilon(t) &= \frac{C}{L_s}\int_0^\tau\left[\varepsilon_I(t) - \varepsilon_R(t) - \varepsilon_T(t)\right]\mathrm{d}t, \\
\dot{\varepsilon}(t) &= \frac{C}{L_s}\left[\varepsilon_I(t) - \varepsilon_R(t) - \varepsilon_T(t)\right],
\end{aligned}
\right\} \tag{1}
$$

where A, E, C were the cross-sectional area, elastic modulus, and elastic longitudinal wave velocity of the compression
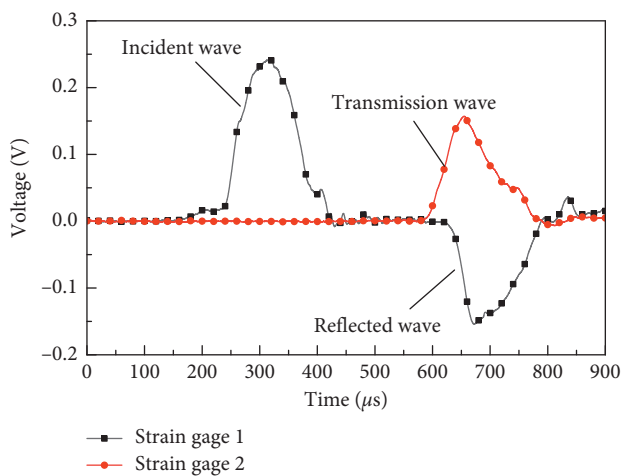
FIGURE 4: SHPB test device.

FIGURE 5: Measured strain signal in SHPB test of limestone specimen.

bar, respectively; A_S and L_S were the specimen cross-sectional area and specimen length, respectively; $\varepsilon_I(t)$, $\varepsilon_R(t)$, and $\varepsilon_T(t)$ were the incident, reflected, and transmitted wave strain signals, respectively; τ was the duration of stress loading.

3.2. Dynamic Compressive Stress-Strain Curves of Rock Specimen. SHPB test device was used to carry out impact compression test with 6 kinds of impact gas pressures on the limestone specimen under room temperature (25°C), 200°C, 400°C, and 600°C. The dynamic compressive stress-strain curves of limestone specimen after different temperature effects were obtained and are shown in Figure 6.

Figure 6 reveals that the dynamic compressive stress-strain curves of limestone specimens after room and high temperature could be divided into three stages: elasticity stage, yield stage, and failure stage. In elastic stage, the relationship between stress and strain was proportional, and its slope increased with the increase of impact pressure; moreover, the ratio of elastic stage gradually decreased with the increase of temperature. In yield stage, the curve slope gradually decreased, and the slope of the curve was 0 when it reached the peak value; in addition, the decline rate of curve

slope slowed down with the increase of temperature, and the ratio of yield stage gradually increased with the increase of temperature, which was due to the continuous evolution and development of fissures inside rock. Final, the internal cracks of the rock penetrated to form macrofailure and the slope of the curve was negative. The curves of limestone specimens showed upward trend with the increase of the impact pressure, and under the same loading conditions, the curve showed downward trend with the increase of the temperature.

3.3. Dynamic Failure Mode of Rock Specimen. The dynamic failure modes of rock specimens with various temperature effects are shown in Figure 7. It could be noticed that, for limestone specimens, after experiencing different high temperatures, the fragment failures were mainly sheet-shaped and axial splitting failure shape. Under the same action temperature, with the increase of impact air pressure, the incident energy generated increased, and the fracture surface of the specimen and degree of fragmentation gradually increased, while the size of the fragment decreased. Under the same impact pressure, the incident energy generated was basically the same, and the crushing degree of the specimen increased with the increase of temperature. The damage degree of limestone after 600°C high temperature was higher than the same loading condition at room temperature. When the impact gas pressure was relatively low, the limestone specimen could not be completely destroyed, and the number of fragments and specimen size was small. As the impact air pressure increased, the incident energy increased, and the fragmentation degree increased, the damage fragments were significantly increased, and the size of the fragments becomes significantly smaller. Under small impact air pressure, the incident energy acting on the specimen was relatively small. The random microcracks randomly distributed in the direction were developing in an orderly direction, and the number of broken blocks was small. With the incident energy acting on the test piece being increased, the cracks in the test piece were fully developed, resulting in a decreased size of fragments.
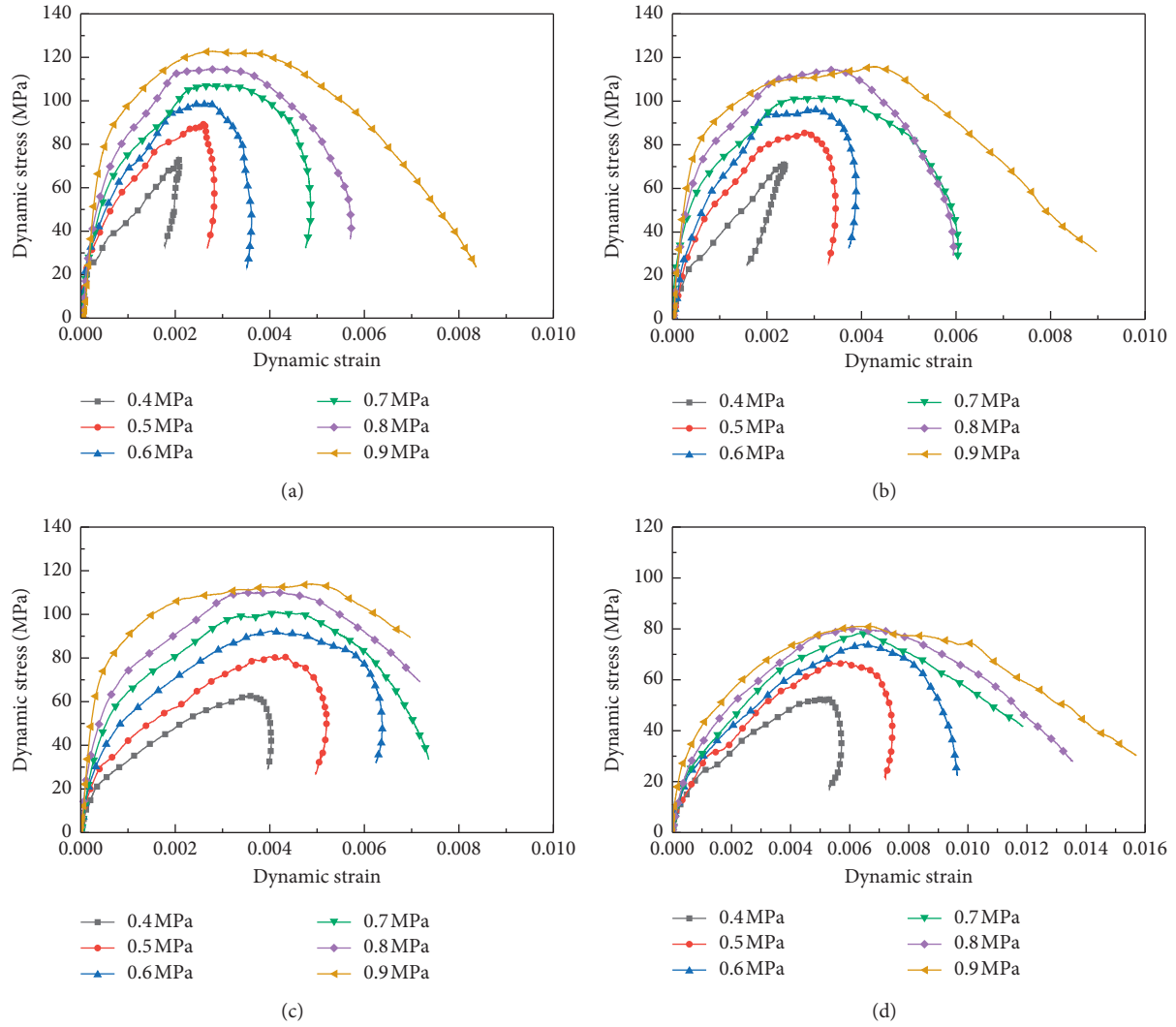
FIGURE 6: Dynamic compressive stress-strain curves of limestone specimen after different temperature effects. (a) 25°C. (b) 200°C. (c) 400°C. (d) 600°C.

4. Dynamic Characteristic Parameters and Energy Evolution of SHPB Test

4.1. Energy Composition in SHPB Test. In SHPB compressive tests, from the beginning of loading to the unloading process, the energy carried by the incident wave $\varepsilon_I(t)$, the reflected wave $\varepsilon_R(t)$, and the transmitted wave $\varepsilon_T(t)$ could be obtained by equation (2) [34, 35]:

$$\left.\begin{aligned} E_I(t) &= E_0 C_0 A_0 \int_0^\tau \varepsilon_I^2(t) dt, \\ E_R(t) &= E_0 C_0 A_0 \int_0^\tau \varepsilon_R^2(t) dt, \\ E_T(t) &= E_0 C_0 A_0 \int_0^\tau \varepsilon_T^2(t) dt, \end{aligned}\right\} \tag{2}$$

where $\varepsilon_I(t)$, $\varepsilon_R(t)$ and $\varepsilon_T(t)$ were the incident energy, reflected energy, and transmitted energy, respectively.

In SHPB test, since the lubricant was applied on the contact surface between the rock specimen and the pressure

rod, the energy consumed by the friction between the contact interfaces and between the specimen and the pressure rod could be ignored. Hence, according to the principle of energy conservation, the absorbed energy of limestone specimen could be obtained:

$$E_A(t) = E_I(t) - [E_R(t) + E_T(t)]. \tag{3}$$

The absorbed energy by the rock specimen was mainly dissipated in the following three aspects:

$$E_A(t) = E_{FD}(t) + E_K(t) + E_O(t), \tag{4}$$

where $E_{FD}(t)$ was energy consumption, mainly used for the propagation of original cracks inside the test piece and the generation of new fracture surfaces; $E_K(t)$ was ejection kinetic energy, mainly referring to the energy carried by the flying pieces of rock specimen. $E_O(t)$ was another energy consumption, such as acoustic energy, thermal energy, radiant energy, and other forms of dissipated energy.
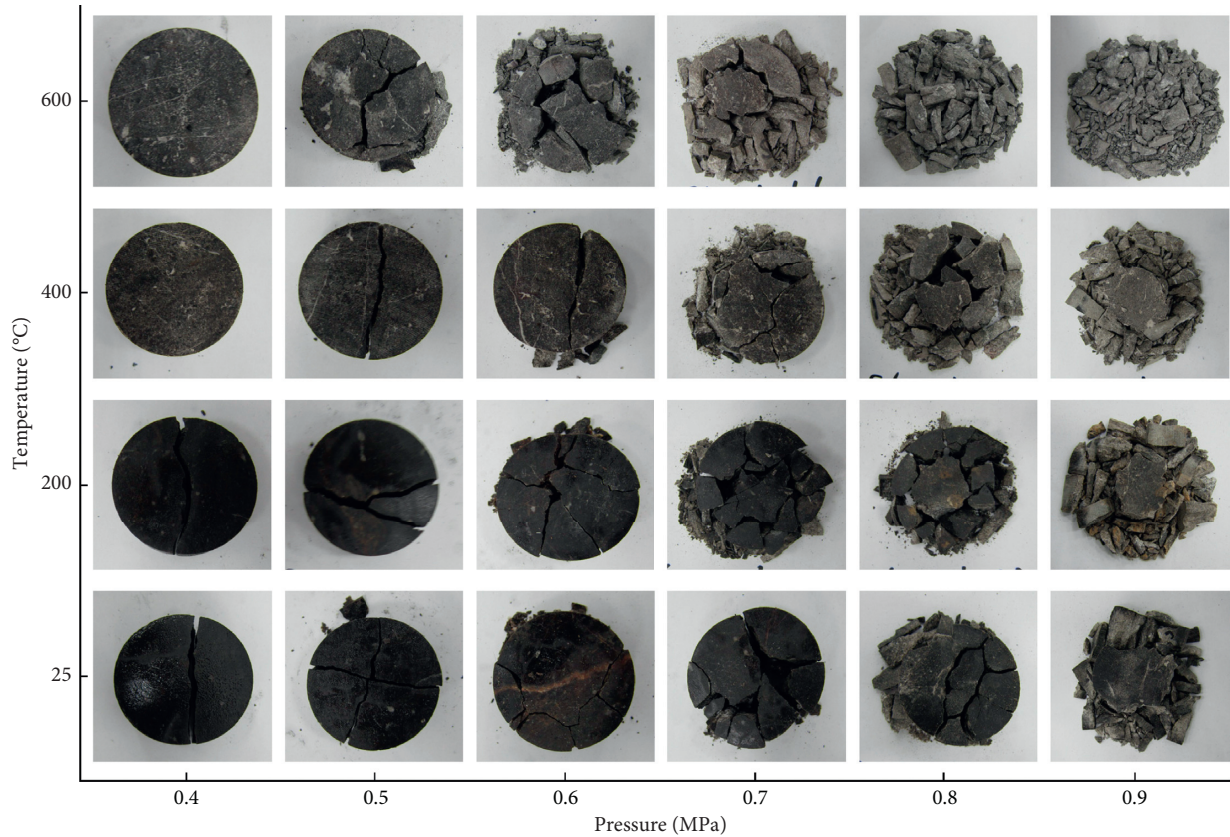
FIGURE 7: The failure modes of limestone specimen with various high temperatures under different impact air pressures.

Previous investigation showed that the ratio of $E_O(t)$ was relatively small and could be ignored [36]; hence

$$E_A(t) = E_{FD}(t) + E_K(t). \tag{5}$$

Zhang et al. and Hong [37, 38] found that $E_{FD}(t)$ was about 95% of $E_S(t)$; hence, the rock absorption energy $E_A(t)$ was used to replace rock energy consumption $E_{FD}(t)$.

4.2. Relationship between Energies in the SHPB Test.
According to the obtained wave singles and calculation method, the incident energy, reflected energy, and transmitted energy of limestone specimen during the SHPB test could be calculated and are shown in Figure 8.

Figure 8 shows that incident energy, reflected energy, transmitted energy, and specimen absorbed energy all increased with the duration of loading, and the energy remains basically constant after reaching a certain value. The total incident wave loading time was about $207\,\mu s$. Figure 8(a) indicates that, at low impact air pressure (0.4 MPa), the transmission energy accounted for the largest proportion, about 71% of the incident energy, while the proportion of reflected energy was the smallest, only 4% of the incident energy. Moreover, the absorbed energy of the rock specimen was slightly higher than the reflected energy, accounting for about 24% of incident energy, and reached peak value at $133.2\,\mu s$. Figure 8(b) illustrates that, at high-impact air pressure (0.9 MPa), transmitted energy and reflected energy account for

approximately 24% and 39% of the incident energy, respectively, and the absorption energy of specimen was about 37% of the incident energy, which reached peak value at $199.7\,\mu s$. For rock at room temperature (25°C), under the low impact pressure, the degree of damage is small, and the energy absorbed by the specimen is relatively small. Most of the incident energy was transmitted to the transmitted bar through limestone specimen, and only a small part of them reflected to the incident bar. The rock specimen was damaged, caused by high temperature. After 600°C, under the effect of higher-impact pressure, the destruction degree of the specimen was severe, and the energy absorbed by the specimen increased. Most of the incident energy reflected to the incident bar. Most of the energy absorbed by limestone specimen was dissipated in the damage evolution process of the microcrack; hence, the original disordered crack in the test piece gradually developed in an orderly direction, and finally a macroscopic main crack was formed, which led to the structure failure of test specimen.

When the SHPB test was carried out using 6 kinds of impact air pressures of 0.4 MPa, 0.5 MPa, 0.6 MPa, 0.7 MPa, 0.8 MPa, and 0.9 MPa, the similar incident energy could be obtained under the same loading conditions, and the incident energy increased with the increase of impact air pressure, showing positive correlation, as shown in Figure 9.

Figure 10 shows the relationship among reflected energy, transmitted energy, and absorbed energy of limestone with incident energy. The reflected energy, transmitted energy,
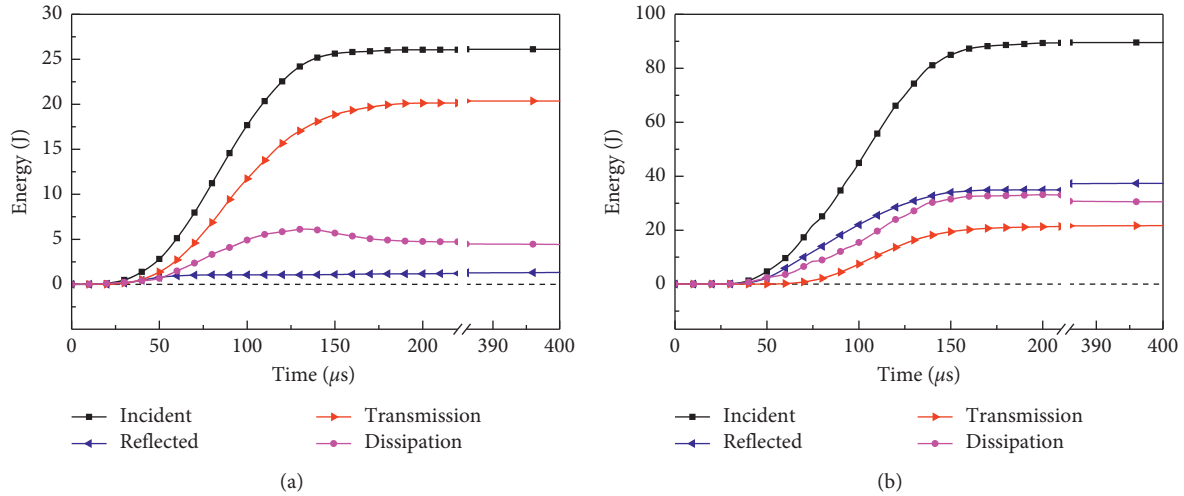
FIGURE 8: Time-history curve of energy change in SHPB compression test of limestone (a) $T = 25°C$, $p = 0.4$ MPa. (b) $T = 600°C$, $p = 0.9$ MPa.
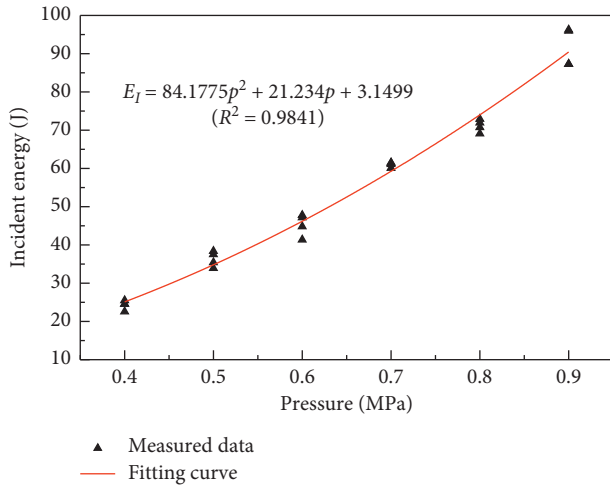

FIGURE 9: Relationship between incident energy and impact air pressure.

and absorbed energy all increased with the increase of incident energy, showing quadratic function relationship, and the fitted minimum correlation coefficients were 0.9772, 0.9273, and 0.9607, respectively.

Figure 10(a) revealed that, with the increase of temperature, the fitting curve of reflected energy and incident energy showed an upward trend, and the increase magnitude of reflected energy gradually increased with the increase of acting temperature. For example, the reflected energy of specimen at room temperature increased from 1.09 J to 7.25 J, while the reflection energy of the specimen after the 600°C increased from 4.88 J to 34.95 J. Figure 10(b) indicated that, with the increase of temperature, the fitted curve of transmission energy and incident energy showed a downward trend, and the increase magnitude of reflected energy gradually decreased with the increase of temperature. After 600°C, the transmission energy increased from 10.41 J to 23.77 J when the incident energy increased from 24.55 J to 95.95 J. Figure 10(c) illustrates that, with the increase of

incident energy, the increase gradient of absorbed energy of rock specimen after high temperature was basically the same.

4.3. Relationship between Dynamic Compressive Strength and Incident Energy.

In this test, the dynamic compressive strength of limestone was defined as the peak dynamic stress in stress-strain curve. The dynamic compressive strength of limestone with various temperature effects is shown in Figure 11.

It could be observed from Figure 11 that the dynamic compressive strength of limestone specimens increased with increasing incident energy after different high-temperature effects, showing quadratic function relationship, as shown in

$$\sigma_T = aE_I^2 + bE_I + c, \tag{6}$$

where σ_T was the dynamic compressive strength of limestone after high temperature, MPa; a, b and c were the fitting parameters, and their calculation values are shown in Table 1.

Figure 11 also indicates that the σ_T–E_I fitting curve showed a downward trend with the increase of temperature, and the dynamic compression strength of the specimen decreased. The dynamic compressive strength decreased by 3.5% and 7.9% when the action temperature increased to 200°C and 400°C, respectively. After 600°C, the dynamic compressive strength was obviously reduced, with a 28.3% decrease amplitude. This was caused by the thermal stress expanding the microcracks inside the specimen and initiating new cracks, causing the deterioration of the internal structure of the rock specimen.

4.4. Relationship between Dynamic Elasticity Modulus and Incident Energy.

The dynamic elasticity modulus of limestone with various temperature effects is shown in Figure 12.

Figure 12 shows that the dynamic elasticity modulus of limestone specimens increased with increasing incident
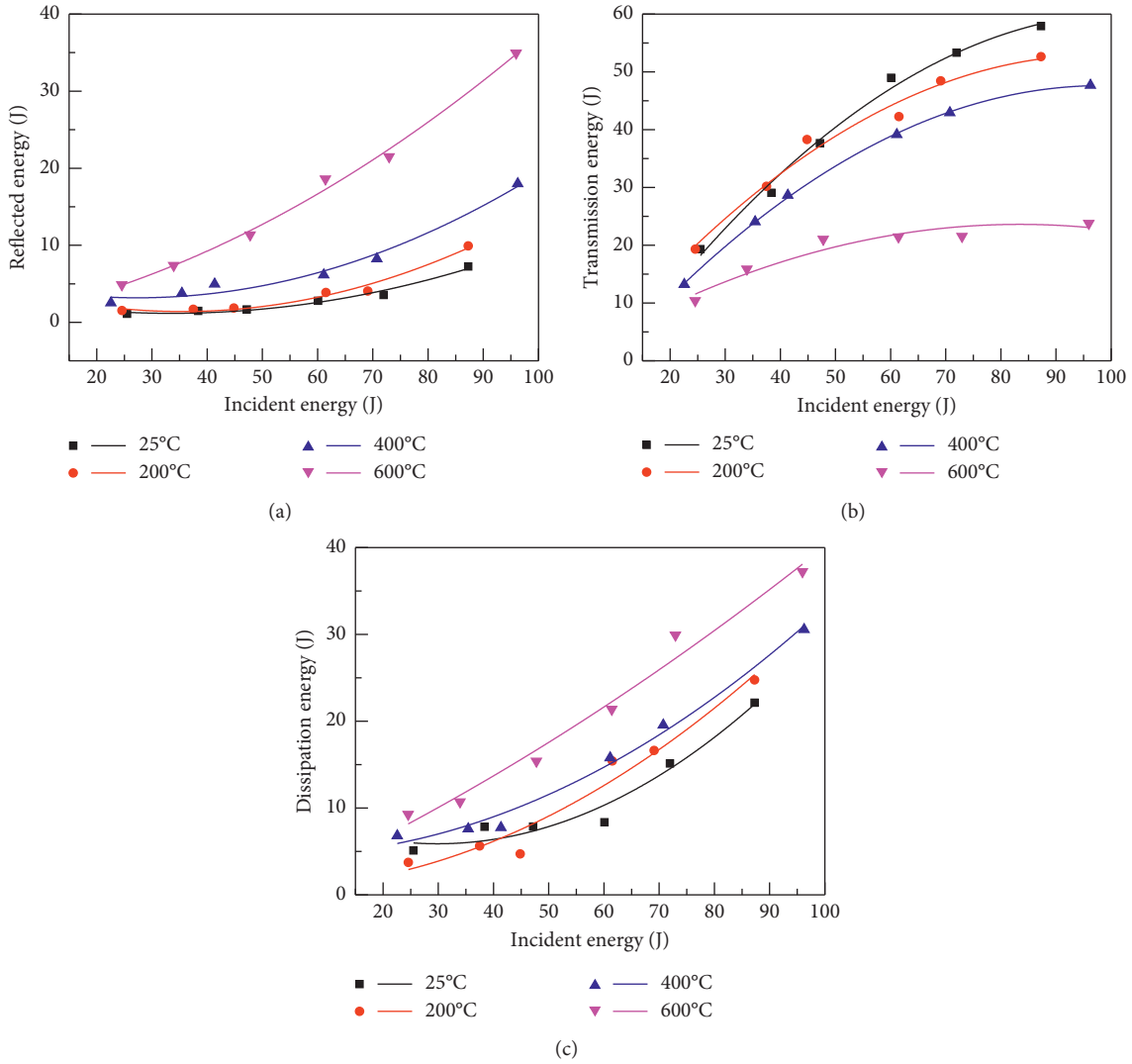
(a)

(b)

(c)

Figure 10: Relationship among reflected energy, transmitted energy, and absorbed energy of limestone with incident energy. (a) Reflected energy. (b) Transmission energy. (c) Dissipation energy (absorbed energy).
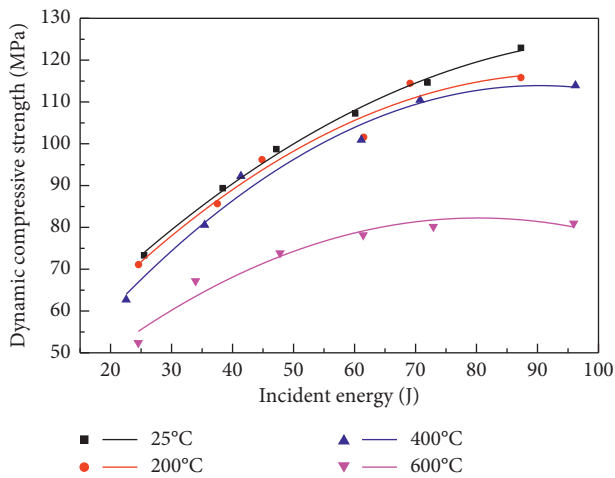

Figure 11: Relationship between dynamic compressive strength and incident energy.

Table 1: Parameter values of dynamic compressive strength and incident energy.

T (°C)	a	b	c	Correlation coefficient R^2
25	−0.0075	1.6243	37.4229	0.9972
200	−0.0092	1.7498	33.7856	0.9688
400	−0.0109	1.9628	25.2459	0.9809
600	−0.0087	1.4030	25.9517	0.9565

energy after different high-temperature effects, showing a quadratic function relationship, as shown in

$$Y_T = dE_I^2 + eE_I + f, \qquad (7)$$

where Y_T was the dynamic elasticity modulus of limestone after high temperature, GPa; d, e and f were the fitting parameters, and their calculation values are shown in Table 2.
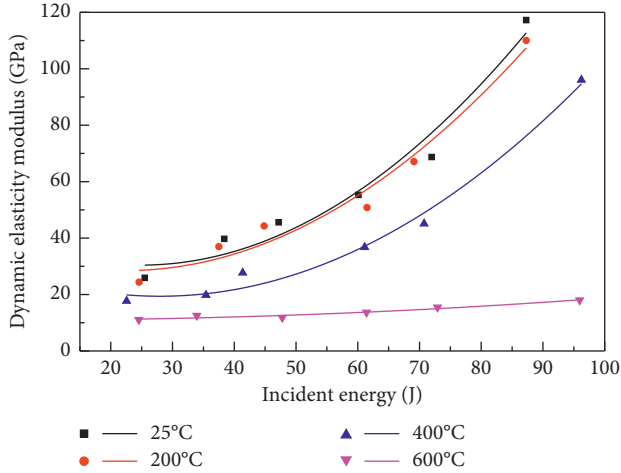
FIGURE 12: Relationship between dynamic elasticity modulus and incident energy.
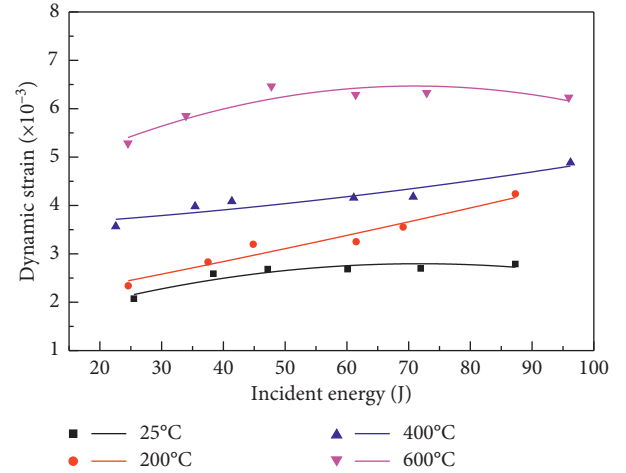

FIGURE 13: Relationship between dynamic peak strain and incident energy.

TABLE 2: Parameter values of dynamic elasticity modulus and incident energy.

T (°C)	d	e	f	Correlation coefficient R^2
25	0.0211	−1.0492	43.4581	0.9675
200	0.0186	−0.8274	37.6388	0.9719
400	0.0161	−0.9026	32.0116	0.9879
600	0.0008	−0.0048	10.9194	0.9524

TABLE 3: Parameter values of dynamic peak strain and incident energy.

T (°C)	i	j	k	Correlation coefficient R^2
25	−2.98E−4	0.0428	1.2616	0.8629
200	3.44E−5	0.0236	1.8426	0.9480
400	6.78E−5	0.0069	3.5238	0.8906
600	−4.93E−4	0.0700	3.9821	0.8658

Figure 12 reveals that the Y_T–E_I fitting curve showed a downward trend with the increase of temperature. The dynamic elasticity modulus decreased by 5.4% and 34.5% when the action temperature increased to 200°C and 400°C, respectively. The dynamic elasticity modulus decreased, 72.9%, after 600°C. With the increase of the incident energy, dynamic elastic modulus of the limestone specimen increased rapidly at 25°C, 200°C, and 400°C. When the action temperature increased to 600°C, the fitting curve approximates horizontal line, and the dynamic antielastic modulus was 11.03 GPa–17.99 GPa, which was obviously reduced compared with that after room temperature. After high-temperature effect, the microcracks in the limestone specimen gradually expand, which reduced the ability of the specimen to resist deformation. In addition, when the action temperature exceeded a certain value, the internal mineral composition of the rock changed due to high temperature, which also weakened resist deformation ability of rock specimen.

4.5. Relationship between Dynamic Peak Strain and Incident Energy. The dynamic peak strain was the strain corresponding to peak stress; the dynamic peak strain of limestone with various temperature effects is shown in Figure 13. After the same temperature gradient, the dynamic peak strain of the specimen was not significantly affected by the incident energy, and the strain scopes were 2.07–2.79×10^{-3}, 2.34–4.24×10^{-3}, 3.57–4.89×10^{-3}, and 5.29–6.46×10^{-3} after 25°C, 200°C, 400°C, and 600°C, respectively. However, dynamic peak strain increased with increasing temperature,

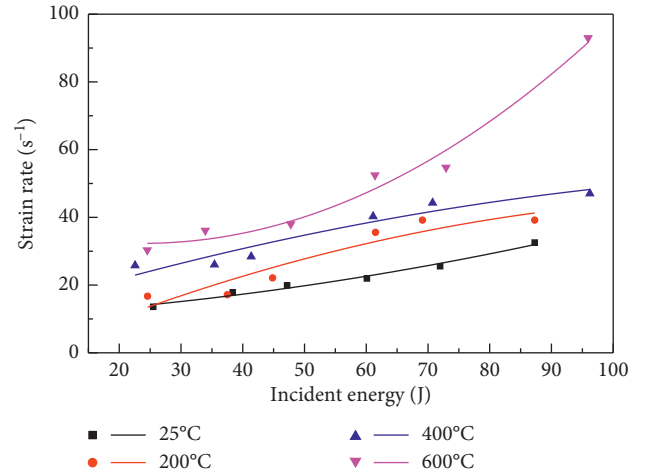

FIGURE 14: Relationship between strain rate and incident energy.

and the strain of limestone specimens after 200°C, 400°C, and 600°C was 1.2 times, 1.6 times, and 2.4 times compared with that after room temperature.

After different temperatures, the dynamic strain of the limestone specimen increased with the increase of the incident energy, showing a quadratic function relationship:

$$\varepsilon_T = iE_I^2 + jE_I + k, \tag{8}$$

where ε_T was the dynamic peak strain of limestone after high temperature, GPa; i, j and k were the fitting parameters, and their calculation values are shown in Table 3.

TABLE 4: Parameter values of strain rate and incident energy.

T (°C)	i	j	k	Correlation coefficient R^2
25	0.0016	0.1018	10.6275	0.9835
200	−0.0032	0.7980	−4.2451	0.8976
400	−0.0019	0.5652	11.1425	0.9258
600	0.0114	−0.5429	38.7897	0.9785

4.6. Relationship between Energy Dissipation and Strain Rate. The relationship between strain rate and incident energy is shown in Figure 14.

The strain rate of limestone specimen increased with the increase of incident energy after different high temperatures, which showed a quadratic function relationship, as shown in

$$\dot{\varepsilon}_T = lE_I^2 + mE_I + n, \tag{9}$$

where $\dot{\varepsilon}_T$ was the strain rate of limestone after high temperature, s^{-1}; l, m and n were the fitting parameters, and their calculation values are shown in Table 4.

5. Conclusions

The SHPB test device was used to perform compression tests on limestone after 25°C, 200°C, 400°C, and 600°C with 6 impact air pressures. The effects of high temperature on the basic physical properties, dynamic characteristic parameters, and energy of limestone specimens were analyzed.

(1) The color of limestone specimen at room temperature was gray-black, and the specimens become gray-white after high temperature. When the action temperature increased to 600°C, powder particles appeared on the surface of rock specimen, which showed that the high temperature effect damages the limestone structure. With the increase of temperature, the volume of the limestone specimen increased, while the mass, density, and longitudinal wave velocity decreased.

(2) The dynamic compressive stress-strain curve of limestone specimens after different high-temperature effects could be divided into elasticity stage, yield stage, and failure stage. Under the same temperature gradient, the curve showed upward trend with the increase of impact air pressure, while the curve shows a downward trend with the increase of the temperature

(3) The limestone specimen failure with exfoliated axial splitting, and the crushing degree of specimen increased with the increase of temperature. The reflected energy, transmitted energy, and absorbed energy increased with the increase of incident energy, showing a quadratic function relationship. The dynamic compressive strength, dynamic elastic modulus, dynamic peak strain, and strain rate of limestone specimens all increased with the increase of incident energy, showing a quadratic function relationship.

Data Availability

The datasets generated and analyzed during the current study are available from the corresponding author upon reasonable request.

Conflicts of Interest

The authors declare that there are no conflicts of interest regarding the publication of this paper.

References

[1] S. Liu and J. Xu, "Investigation of impact compressive mechanical properties of sandstone after as well as under high temperature," *High Temperature Materials and Processes*, vol. 33, no. 6, pp. 585–591, 2014.

[2] W. Yao, Y. Xu, W. Wang, and P. Kanopolous, "Dependence of dynamic tensile strength of longyou sandstone on heat-treatment temperature and loading rate," *Rock Mechanics and Rock Engineering*, vol. 49, no. 10, pp. 3899–3915, 2016.

[3] Z. L. Wang and G. Y. Shi, "Effect of heat treatment on dynamic tensile strength and damage behavior of medium-fine-grained huashan granite," *Experimental Techniques*, vol. 41, no. 4, pp. 365–375, 2017.

[4] L. L. Cao, H. Pu, P. T. Qiu, and L. Zhang, "Analyzing creeping properties of mudstone at high temperature based on variable-order fractional calculus," *Journal of Mining & Safety Engineering*, vol. 34, no. 1, pp. 148–154, 2017.

[5] R. Lei, Y. Wang, L. Zhang et al., "The evolution of sandstone microstructure and mechanical properties with thermal damage," *Energy Science & Engineering*, vol. 7, no. 6, pp. 3058–3075, 2019.

[6] S. Liu and J. Xu, "Effect of strain rate on the dynamic compressive mechanical behaviors of rock material subjected to high temperatures," *Mechanics of Materials*, vol. 82, pp. 28–38, 2015.

[7] B. P. Xi, Y. C. Wu, S. Wang, G. Xiong, and Y. s. ZHAO, "Experimental study on mechanical properties of granite taken from Gonghe basin, Qinghai province after high temperature thermal damage," *Chinese Journal of Rock Mechanics and Engineering*, vol. 39, no. 1, pp. 69–83, 2020.

[8] C. D. Su, S. J. Wei, B. D. Qin, and Y. Yu-shun, "Experimental study of influence mechanism of high temperature on mechanical properties of fine-grained sandstone," *Rock and Soil Mechanics*, vol. 38, no. 3, pp. 623–630, 2017.

[9] X. L. Xu, F. Gao, and Z. Z. Zhang, "Influence of confining pressure on deformation and strength properties of granite after high temperatures," *Chinese Journal of Geotechnical Engineering*, vol. 36, no. 12, pp. 2246–2252, 2014.

[10] T. Yin, L. Bai, X. Li, X. Li, and S. Zhang, "Effect of thermal treatment on the mode I fracture toughness of granite under dynamic and static coupling load," *Engineering Fracture Mechanics*, vol. 199, pp. 143–158, 2018.

[11] Z. L. Wang, H. Shi, and J. G. Wang, "Mechanical behavior and damage constitutive model of granite under coupling of

temperature and dynamic loading," *Rock Mechanics and Rock Engineering*, vol. 51, no. 10, pp. 3045–3059, 2018.

[12] L. N. Y. Wong, Z. Li, H. M. Kang, and C. I. Teh, "Dynamic loading of carrara marble in a heated state," *Rock Mechanics and Rock Engineering*, vol. 50, no. 6, pp. 1487–1505, 2017.

[13] S. Liu and J. Xu, "Study on dynamic characteristics of marble under impact loading and high temperature," *International Journal of Rock Mechanics and Mining Sciences*, vol. 62, pp. 51–58, 2013.

[14] Q. Ping, Z. H. Fang, D. D. Ma, and H. Zhang, "Coupled static-dynamic tensile mechanical properties and energy dissipation characteristic of limestone specimen in SHPB tests," *Advances in Civil Engineering*, vol. 2020, Article ID 7172928, 11 pages, 2020.

[15] G. Wu, N. G. Teng, and Y. Wang, "Physical and mechanical characteristics of limestone after high temperature," *Chinese Journal of Geotechnical Engineering*, vol. 33, no. 2, pp. 259–264, 2011.

[16] Q.-b. Meng, W. Qian, J.-f. Liu, M.-w. Zhang, M.-m. Lu, and Y. Wu, "Analysis of triaxial compression deformation and strength characteristics of limestone after high temperature," *Arabian Journal of Geosciences*, vol. 13, no. 4, 2020.

[17] Q. Ping, M. J. Wu, P. Yuan et al., "Experimental study on dynamic mechanical properties of sandstone under coupled actual high temperature and impact loads," *Chinese Journal of Rock Mechanics and Engineering*, vol. 38, no. 4, pp. 782–792, 2019.

[18] Q. Ping, M. J. Wu, H. Zhang et al., "Experimental study on dynamic mechanical characteristics of sandstone under actual high temperature conditions," *Chinese Journal of Underground Space and Engineering*, vol. 15, no. 3, pp. 691–698, 2019.

[19] Q. Sun, C. Lü, L. Cao, W. Li, J. Geng, and W. Zhang, "Thermal properties of sandstone after treatment at high temperature," *International Journal of Rock Mechanics and Mining Sciences*, vol. 85, pp. 60–66, 2016.

[20] T. B. Yin, X. B. Li, W. Z. Cao et al., "Effects of thermal treatment on tensile strength of laurentian granite using Brazilian test," *Rock Mechanics and Rock Engineering*, vol. 48, no. 6, pp. 2212–2223, 2015.

[21] P. Wang, J. Xu, X. Fang, and P. Wang, "Energy dissipation and damage evolution analyses for the dynamic compression failure process of red-sandstone after freeze-thaw cycles," *Engineering Geology*, vol. 221, pp. 104–113, 2017.

[22] L. F. Fan, Z. L. Wu, Z. Wang, Z. J. Wu, Z. Wan, and J. W. Gao, "Experimental investigation of thermal effects on dynamic behavior of granite," *Applied Thermal Engineering*, vol. 125, pp. 94–103, 2017.

[23] S. Liu and J. Xu, "An experimental study on the physico-mechanical properties of two post-high-temperature rocks," *Engineering Geology*, vol. 185, pp. 63–70, 2015.

[24] S. Liu and J. Xu, "Mechanical properties of Qinling biotite granite after high temperature treatment," *International Journal of Rock Mechanics and Mining Sciences*, vol. 71, pp. 188–193, 2014.

[25] Z. Yin, W. Chen, H. Hao et al., "Dynamic compressive test of gas-containing coal using a modified split Hopkinson pressure bar system," *Rock Mechanics and Rock Engineering*, vol. 53, no. 2, pp. 815–829, 2020.

[26] Z. Q. Yin, Z. Hu, Z. D. Wei et al., "Assessment of blasting-induced ground vibration in an open-pit mine under different rock properties," *Advances in Civil Engineering*, vol. 2018, Article ID 4603687, 10 pages, 2018.

[27] K. Peng, J. Zhou, Q. Zou, and F. Yan, "Deformation characteristics of sandstones during cyclic loading and unloading with varying lower limits of stress under different confining pressures," *International Journal of Fatigue*, vol. 127, pp. 82–100, 2019.

[28] T. Yin, X. Li, K. Xia, and S. Huang, "Effect of thermal treatment on the dynamic fracture toughness of laurentian granite," *Rock Mechanics and Rock Engineering*, vol. 45, no. 6, pp. 1087–1094, 2012.

[29] The National Standards Compilation Group of the People's Republic of China, "Code for investigation of geotechnical engineering," China Architecture and Building Press, Beijing, China, GB50021–2019, 2019.

[30] R. Ulusay, *The ISRM Suggested Methods for Rock Characterization, Testing and Monitoring; 2007–2014*, pp. 51–68, Springer International Publishing, Cham, Switzerland, 2015.

[31] Chinese Society for Rock Mechanics & Engineering, "Technical specification for testing method of rock dynamic properties[EB/OL]," T/CSRME 001–2019, 2019, http://www.ttbz.org.cn/Home/Show/10253.

[32] The National Standards Compilation Group of the People's Republic of China, "Standard for test method of engineering rock mass," GB/T50266–2013, China Planning Publishing House, Beijing, China, 2013.

[33] L. L. Wang, *Foundation of Stress waves*, pp. 39–64, National Defense Industry Press, Beijing, Chian, 2nd edition, 2010.

[34] R. R. Zhang, L. W. Jing, and Q. Y. Ma, "Experimental study on thermal damage and energy evolution of sandstone after high temperature treatment," *Shock and Vibration*, vol. 2018, Article ID 3845353, 9 pages, 2018.

[35] R. R. Zhang and P. Yuan, "Effect of hydrothermal coupling on physical and dynamic mechanical properties of sandstone," *Advances in Civil Engineering*, vol. 2019, Article ID 7318768, 14 pages, 2019.

[36] S. Liu, J. Y. Xu, J. Z. Liu et al., "Analysis on energy of sericite-quartz schist and sandstone in the dy-namic fracture process," *Chinese Journal of Under-ground Space and Engineering*, vol. 7, no. 6, pp. 1181–1185, 2011.

[37] Z. X. Zhang, S. Q. Kou, L. G. Jiang, L. G. Jiang, and P.-A. Lindqvist, "Effects of loading rate on rock fracture: fracture characteristics and energy partitioning," *International Journal of Rock Mechanics and Mining Sciences*, vol. 37, no. 5, pp. 745–762, 2000.

[38] L. Hong, "Size effect on strength and energy dissipation in fracture of rock under impact loads," Ph. D. thesis, Central South University, Changsha, China, 2008.

Research Article

Seepage Property of Crushed Mudstone Rock in Collapse Column

Bo-Yang Zhang and Zhi-Bin Lin [ID]

School of Civil Engineering, Henan Polytechnic University, Jiaozuo 454000, China

Correspondence should be addressed to Zhi-Bin Lin; linzhibin@hpu.edu.cn

The karst collapse column composed of crushed rocks and fine argillaceous or clay particles is easy to form the fissure channels between the coal seam working face and the confined limestone aquifer under mining and causes water inrush disasters with the loss of underground water resource, economic losses, and casualties. It is of great necessity to understand the seepage properties of crushed rock in karst collapse column for the prevention of water inrush and the protection of underground water resource. A self-developed seepage test system is used in this paper to conduct laboratory experiments on seepage properties of crushed mudstone specimens. The effects of the particle size distribution, the porosity (specimen height), and the hydraulic pressure on the water flow velocity and the permeability of crushed specimen are analyzed. The results indicate that the permeability of specimen increases with the particle size, porosity, and hydraulic pressure. It can be known from the comparative experiments of progressive hydraulic pressure on one specimen and variable hydraulic pressure on different specimens with constant particle size and porosity that more fine particles leak out from the specimen with repeated application of hydraulic pressure on one specimen. Therefore, the permeability of one specimen is bigger than that of different specimens under the condition of same hydraulic pressure.

1. Introduction

The karst collapse column is a special geological structure widely distributed in North China, which is composed of fillings such as crushed rocks and fine argillaceous or clay particles. In the process of coal mining in these areas, it is easy to form the fissure channels between the coal seam working face and the confined limestone aquifer (Figure 1), thereby causing water inrush disasters which results in the loss of underground water resource, economic losses, and casualties [1–3]. Therefore, it is of great significance to study the seepage property of this special geological material [4–6].

At present, there are few experiments on this special geological material. The collapse column is easy to disintegrate under disturbance, which causes the difficulty to drill an intact sample. Meanwhile, the sampling of collapse column may result in the water inrush disasters on site. Hence, most experimental researches were carried out on the crushed rocks and fine clay particles to describe the seepage property of collapse column [7]. Liu et al. [8] obtained the

relation between the axial stress and the permeability of broken rock through the steady-state seepage experiment. In fact, the external axial stress affected the seepage behavior of broken rock by changing its structure such as fissure channels. In addition to the effect of external stress, the role of hydraulic pressure on the structure was also worthy of attention. So Miao et al. constructed the nonlinear dynamic flow theory for describing the non-Darcy flow within broken rock [9, 10]. Based on this theory, the effects of porosity and particle size on the non-Darcy flow parameters of crushed rock were investigated [11, 12]. In addition, Ma et al. considered that the lithology of rock was an important factor to affect the non-Darcy flow property of crushed rock [13]; then the seepage properties of crushed mudstone, limestone, and sandstone under different porosities and particles sizes were studied [14]. The above studies focused on the nonlinear seepage behavior of crushed rocks; the erosion inside the structure was not taking full account. During the mining process, on the one hand, the fracture network of the rock mass is fully developed under the action of disturbance. On
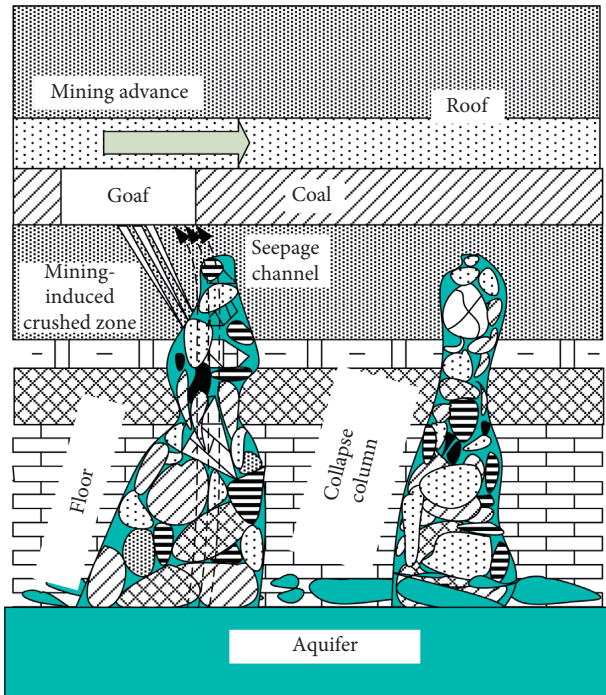
Figure 1: Seepage channel of collapse column under mining.

the other hand, the fine particles absorb water and swell to deteriorate the fracture structure of the rock mass. Under the effect of underground confined water, these fine particles are easily dissolved with water, and the two-phase fluid composed of fine particles and water migrates and is lost in the fracture network of collapse column to further expand its channels. When the small particles with cohesive effect are lost to a certain extent, the framework structure of the collapse column is failed to cause the water inrush disaster with sharp increase of seepage velocity. Garner and Fannin [15] considered that the material susceptibility, hydraulic load, and stress condition were the key factors of this erosion. Marot et al. [16] indicated that the erosion of clay and sand causes the failure of the structure under high gradients. Ke and Takahashi [17] proved that the fine particles in structure gradually migrate through the voids among the coarse particles, which results in the porous framework with low strength. Obviously, the erosion inside the structure should also be related to time; even under low hydraulic pressure, the long-term effect of erosion can also cause the seepage mutation [18]. It can be seen that the research about the seepage behavior of collapse column should consider both its nonlinearity and erosion.

A large amount of coal is distributed in North China [19–21]. Most of the collapse columns in the areas with high risk of water inrush are in the consolidation state. The fine argillaceous or clay particles are an important factor influencing the seepage characteristics of collapse column [22–24]. However, the seepage properties of crushed mudstone were rarely carried out in the above study. In addition, previous study of collapse column focused on the particle size mixture, and no study on fine particles of the single range has been reported to fill this study gap. The

seepage behavior of the collapse column is unclear. Therefore, the crushed mudstone with different single particle size ranges was sampled to obtain fine particles material in this paper. The seepage test was carried out to understand its seepage behavior. The laws of flow velocity that varied with particle size range, specimen height (porosity), hydraulic pressure, and time were analyzed during the seepage. The relation between the permeability and porosity was obtained.

2. Experimental Method

2.1. Experimental Material and System. The experimental material is crushed mudstone (Figure 2).

The experimental system for testing the seepage property of crushed rock was designed as shown in Figure 3, which was comprised of four parts: (A) hydraulic pressure system, (B) axial displacement system, (C) permeability system, and (D) data acquisition and analysis system.

(A) Hydraulic pressure system was used to provide hydraulic pressure for the specimens. This system was composed of oil pump, water pump, dual-acting hydraulic cylinder, connection pipeline, and globe valve.

(B) Axial displacement system can load and control axial displacement and provide axial pressure for the specimens to control the porosity of the specimens.

(C) Permeability system was used to test the seepage property of crushed rock. It was composed of a permeameter, a pallet, and an overflow tube.

(D) Data acquisition and analysis system was used to obtain the seepage and mechanical parameters including hydraulic pressure, oil pressure, flow rate, axial stress, and axial displacement, and it was composed of a pressure sensor, a mass flowmeter, a data acquisition system, and a computer.

2.2. Experimental Procedures. The experimental procedures are as follows:

(1) Crushed mudstone specimen with fixed particle size range (Table 1) and piston (Figure 3) were placed into the permeameter successively, and then the percolation cylinder was put into the base (substructure).

(2) The permeability system was placed on the material testing system (MTS) 816 experimental table, and the piston was lowered by MTS 816 to compress the specimen to a fixed height for controlling the porosity of the specimen (Table 1).

(3) We added water into the dual-acting hydraulic cylinder by the water pump (Figure 3), closed the globe valve between dual-acting hydraulic cylinder and water pump, and opened the globe valve between dual-acting hydraulic cylinder and the permeameter. The constant hydraulic pressure (Table 1) in the dual-acting hydraulic cylinder was injected
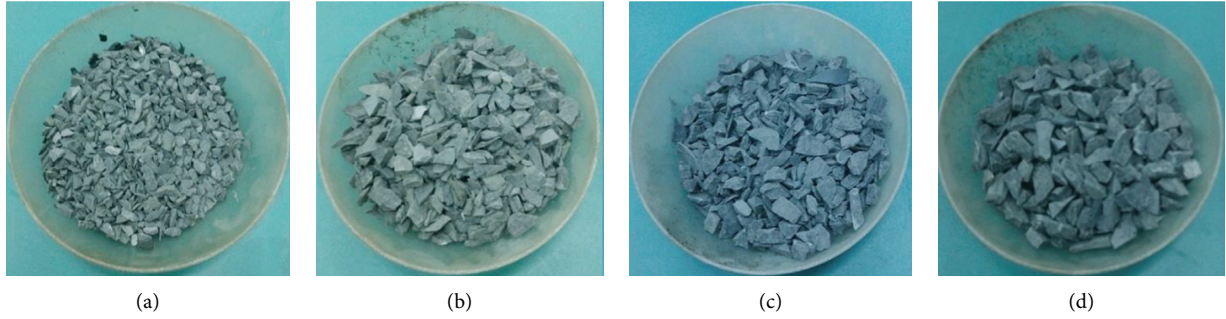
Figure 2: Experimental materials. (a) 5.0 mm ~ 7.5 mm. (b) 7.5 mm ~ 10.0 mm. (c) 10.0 mm ~ 12.5 mm. (d) 12.5 mm ~ 15.0 mm.
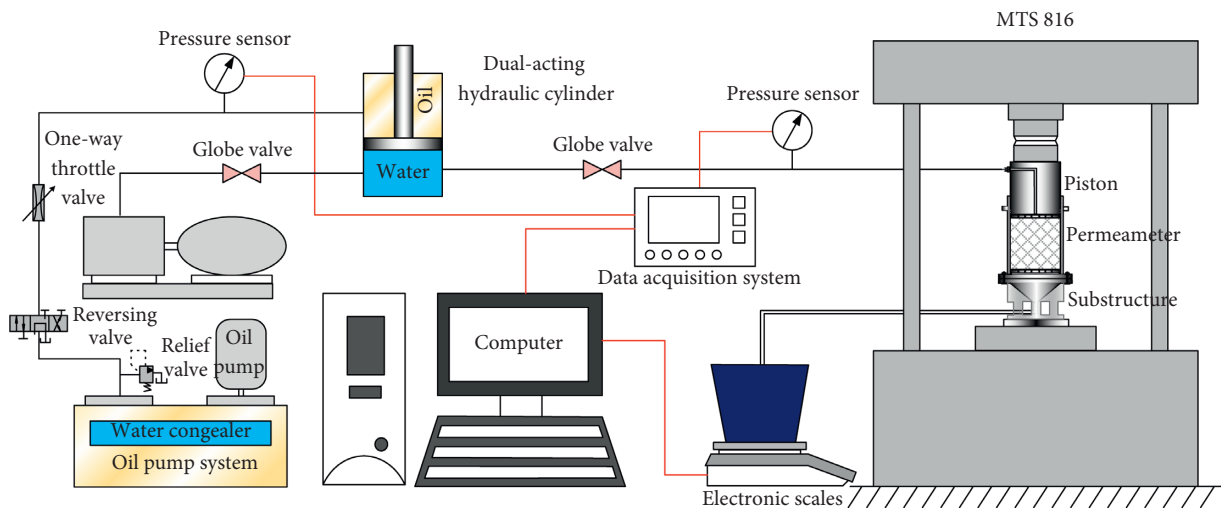

Figure 3: Experimental system [25].

Table 1: Experimental program.

Specimen group	Specimen no.	Particle size (mm)	Porosity	Hydraulic pressure (MPa)
	1a	5.0~7.5	0.19	0.7
	1b	7.5~10.0	0.19	0.7
1	1c	10.0~12.5	0.19	0.7
	1d	12.5~15.0	0.19	0.7
	2a	10.0~12.5	0.15	0.7
	2b	10.0~12.5	0.19	0.7
2	2c	10.0~12.5	0.23	0.7
	2d	10.0~12.5	0.27	0.7
	3a	7.5~10.0	0.19	0.3
	3b	7.5~10.0	0.19	0.7
3	3c	7.5~10.0	0.19	1.1
	3d	7.5~10.0	0.19	1.5

into the permeameter by means of the oil pump. The test began.

(4) The seepage and mechanical parameters including hydraulic pressure, oil pressure, flow rate, axial stress, and axial displacement were recorded by the data acquisition system (Figure 3).

2.3. Calculation Theory

2.3.1. The Calculation Method of Velocity. The velocity is calculated as follows:

$$v_{j,t=i} = \frac{M_{j,t=i} - M_{j,t=i-1}}{\rho A_s},$$

(1)

where $v_{k,t=i}$ is the velocity of specimen no. j in Table 1, m/s, M_k is the water loss mass of specimen no. j, kg, ρ is the density of water, which is assumed to be 1,000 kg/m³ as the experiments are carried out at room temperature, and A_s is cross-section area of permeameter, which is 7.85×10^{-3} m².

2.3.2. The Calculation Method of Permeability. The permeability is calculated by Darcy equation as follows:

$$\frac{\Delta p_j}{\Delta h_j} = -\frac{\mu}{k_j} v_j, \tag{2}$$

where Δp_j is the hydraulic pressure difference between the two ends of the specimen no. j, MPa, Δh_j is the height of specimen no. j, k_j is the permeability of specimen no. j, m², and μ is the dynamic viscosity of water, which is assumed to be 1.01×10^{-3} Pa·s.

2.3.3. The Calculation Method of Porosity. The porosity is calculated as follows:

$$\varphi_j = \frac{A_S \Delta h_j - V_b}{A_S \Delta h_j}, \tag{3}$$

where φ_j is the porosity of specimen no. k and V_b is the volume of crushed rock, which is 9.03×10^{-4} m³.

3. Experimental Results and Discussion

3.1. Particle Size. Specimen no. 1a was taken as an example to illustrate the calculation process of flow velocity. We measured the variation curve of water mass with time in the experiment as shown in Figure 4 and calculated the variation curve of water flow velocity with time (Figure 4) by (1). The permeability of the specimen was calculated by (2). The curves of hydraulic pressure and permeability of the first group (Table 1) over time are shown in Figure 5. Figures 5(c) and 5(d) are taken as examples to illustrate the seepage experimental process. We recorded the hydraulic pressure and water mass while opening the oil pump. In the first stage, the hydraulic pressure gradually increased after the experiment initiation. The water flowed rapidly into the seepage cylinder, forming a water hammer effect to impact on the specimen, and the water mass flowing out from outlet increased rapidly. The water leaking out from the outlet appeared black at the beginning of the experiment, gradually turned gray, and finally turned clear. With the weakening of water hammer, the flow rate and hydraulic pressure tended to be stable (i.e., stable seepage stage). However, seepage mutation often occurs in the overall experimental process. In Figure 5(d), we can find that when the experiment started at 180 ~ 190 s, the flow rate rapidly increased and the hydraulic pressure slightly decreased, with a small amount of fine particles flowing out from the outlet. At this time, the water leaking out from the outlet appeared black. Before the seepage mutation occurred, the water pipe connected to the inlet twitched slightly. When the experiment was carried out to about 500 s, a rapid increase of the flow rate and a rapid decrease of the hydraulic pressure occurred, accompanied by
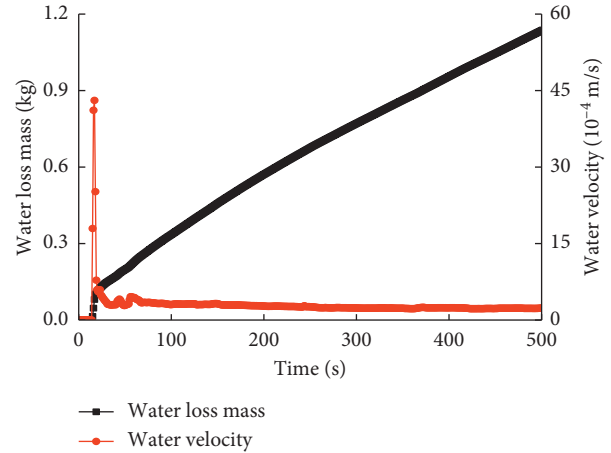

Figure 4: Water loss mass and velocity of specimen no. 1a variation curves with time.

a large number of fine particles leaking from outlet, resulting in a significant seepage mutation. In order to ensure the safety of the experimenter, the test is usually terminated quickly when the seepage mutation occurs.

For this experiment, the average permeability in the stable seepage stage without seepage mutation stage was taken as the permeability of the specimen. The variation curve of permeability with particle size range number (1 for particle size range 5.0 ~ 7.5 mm, 2 for particle size range 7.5 ~ 10.0 mm, 3 for particle size range 10.0 ~ 12.5 mm, and 4 for particle size range 12.5 ~ 15.0 mm) is shown in Figure 6. The permeability of the crushed mudstone was on the magnitude of 10^{-14} m² ~ 10^{-13} m². The permeability of particle size range numbers 1, 2, 3, and 4 was 2.19×10^{-14} m², 4.74×10^{-14} m², 19.55×10^{-14} m², and 42.17×10^{-14} m², respectively. Under the condition of constant porosity (0.19) and hydraulic pressure (0.7 MPa), the permeability of the specimen increased with particle size range number. It may be due to two reasons: first, as the volume and porosity of crushed specimen were the same, there were less pore and bigger pore diameters in the specimen with big particle size range number, which resulted in more effective seepage channels in this specimen. So the specimen with big particle size range number demonstrated higher permeability. Second, the specimen with small particle size range number was composed of more fine particles, which expanded with water and blocked the seepage channels of crushed rock specimen. Therefore, the specimen with small particle size range number showed lower permeability.

3.2. Porosity. Figure 7 is hydraulic pressure and permeability (calculated by (2)) variation curves of second group specimens (Table 1) with time. As can be seen from Figure 7(d), when the water was injected into permeameter about 340 s, the flow rate and hydraulic pressure decreased rapidly. This is because of the closing of the experimental instrument. The maximum range of the electronic balance used in the experiment was 5.2 kg. Considering the mass of the water container, the experiment will be stopped when the mass of
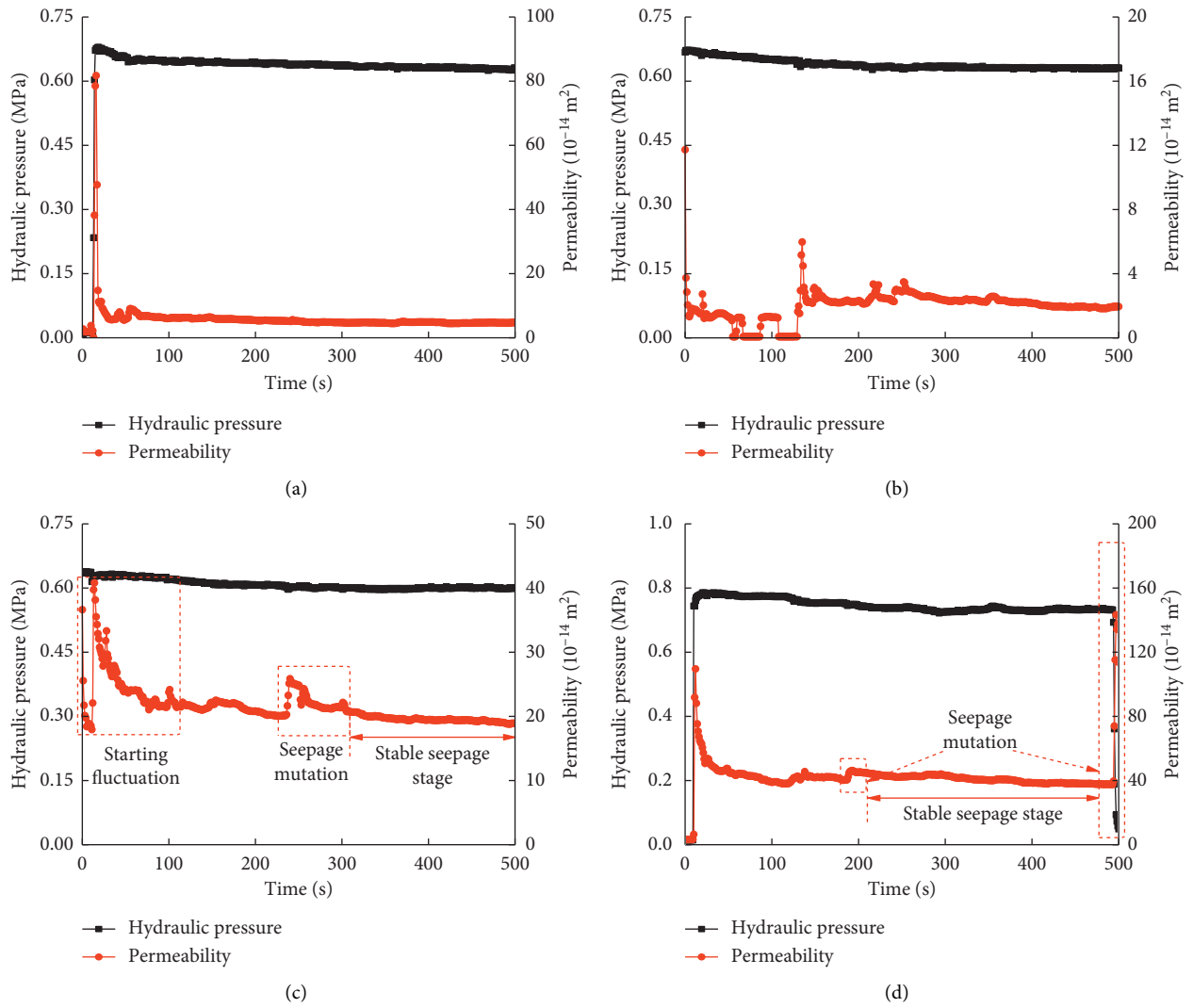
Figure 5: Hydraulic pressure and permeability variation curves of first group specimens with time. (a) 5.0–7.5 mm. (b) 7.5–10.0 mm. (c) 10.0–12.5 mm. (d) 12.5–15.0 mm.
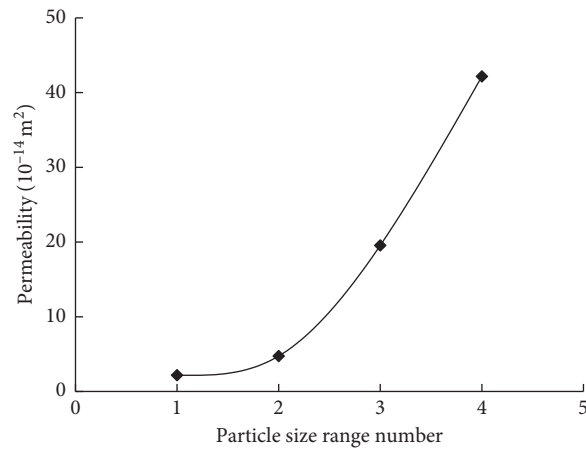

Figure 6: Permeability variation curve with particle size range number.
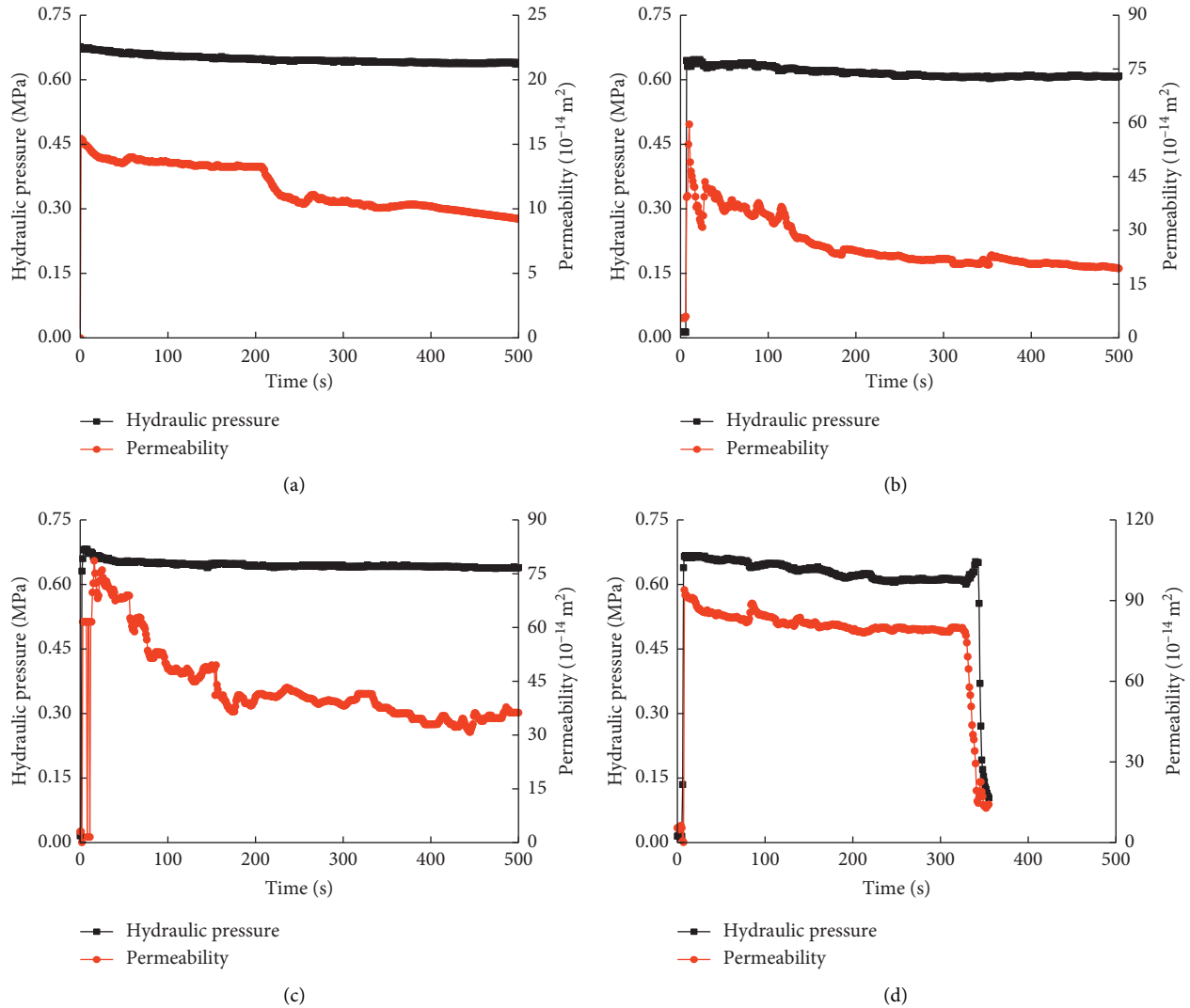
(a)

(b)

(c)

(d)

Figure 7: Hydraulic pressure and permeability variation curves of second group specimens with time. (a) 0.15. (b) 0.19. (c) 0.23. (d) 0.27.

the water flowing from outlet (in Figure 3) reached about 4.5 kg. In contrast, the permeability of specimen no. 2d (Table 1) is higher and the flow rate is faster in Figure 7(d), and the experiment only lasted for 340 s. However, the experiment of other specimens can usually last more than 500 s.

The porosities of the specimens were calculated by (3). Figure 8 is permeability variation curve with porosity (the permeability was obtained from the average value of the stable stage in Figure 7). The porosities of specimens 2a, 2b, 2c, and 2d (Table 1) were 0.15, 0.19, 0.23, and 0.27, respectively. The corresponding permeability of specimens was $9.97 \times 10^{-14}\,\mathrm{m}^2$, $19.92 \times 10^{-14}\,\mathrm{m}^2$, $39.31 \times 10^{-14}\,\mathrm{m}^2$, and $79.89 \times 10^{-14}\,\mathrm{m}^2$, respectively. Under the condition of constant hydraulic pressure (0.7 MPa) and particle size (10.0 ~ 12.5 mm), permeability increased with the increase of porosity. A number of models have been developed for finding out the relationship of permeability and porosity [26–29]. The proportional coefficient of permeability k_k/k_0 was defined as ratio of permeability and minimum permeability in the following three models:

$$\frac{k_j}{k_0} = \left(\frac{1 - \varphi_0}{1 - \varphi_j}\right)^2 \left(\frac{\varphi_j}{\varphi_0}\right)^3, \tag{4}$$

$$\frac{k_j}{k_0} = \left[\frac{(1 - \varphi_0)(1.275 - 1.5\varphi_j)}{(1 - \varphi_j)(1.275 - 1.5\varphi_0)}\right]^2 \left(\frac{\varphi_j}{\varphi_0}\right)^3, \tag{5}$$

$$\frac{k_j}{k_0} = \left(\frac{\varphi_j}{\varphi_0}\right)\left(\frac{1 - \varphi_0}{1 - \varphi_j}\right)^2, \tag{6}$$

where k_0 is the minimum permeability of second specimen group (which is $9.97 \times 10^{-14}\,\mathrm{m}^2$) and φ_0 is the minimum porosity of second specimen group (which is 0.15).

The three models of (4)–(6) were fitted for indicating the relationship of permeability and porosity (Figure 9). The fitting correlation index R^2 [29] of (4)–(6) was 0.997, 0.919, and 0.579, respectively. Therefore, it can be seen that the experimental materials of crushed mudstone adopted (4) in this paper.
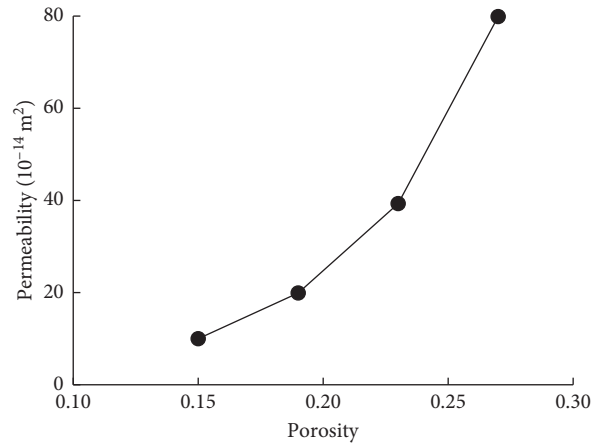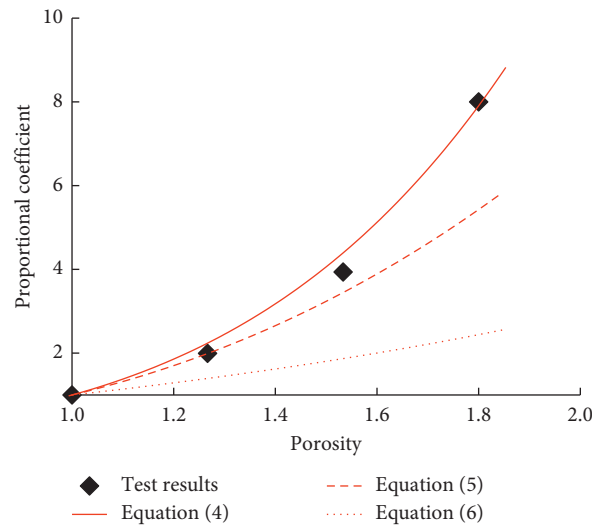
FIGURE 8: Permeability variation curve with porosity.

FIGURE 9: Proportional coefficient variation curve with porosity.

3.3. Hydraulic Pressure. Figure 10 is hydraulic pressure and permeability (calculated by (2)) variation curves of third group specimens (Table 1) with time. The particle size of the third group was $7.5 \sim 10.0$ mm and the porosity was 0.19. The initial hydraulic pressure was set to 0.3 MPa, 0.7 MPa, 1.1 MPa, and 1.5 MPa, respectively. During the experiment, the head of the oil pump was kept unchanged, but the hydraulic pressure decayed gradually. The hydraulic pressure of specimens Nos. 3a, 3b, 3c, and 3d in the experiment decayed 9.6%, 8.6%, 5.8%, and 4.3%, respectively.

Figure 11 is permeability (calculated according to the average value of the stable seepage stage) and velocity (calculated by (1)) variation curves with hydraulic pressure. As can be seen from Figure 11, the velocity changed approximately linearly with the hydraulic pressure. It can be known from (2) that the hydraulic pressure and permeability of the specimen will remain the uniform growth proportion, as the specimen was under the condition of constant particle size range, porosity, dynamic viscosity, and specimen height. However, the hydraulic pressure in the experiment increased from about 0.3 MPa to about 1.5 MPa by a factor of 5.0, and

the velocity in the experiment increased from 0.72×10^{-4} m/s to 9.12×10^{-4} m/s, increasing by a factor of about 12.8. Therefore, the permeability increased with hydraulic pressure in Figure 11. The reason may be that the water with different hydraulic pressure was repeatedly injected into the same specimen (i.e., this is only one specimen in the third specimen group). The fine particles were migrated to the bottom of the specimen and then leaked from the specimen into the outlet with water in each hydraulic pressure level. It resulted in the increase of the porosity in the specimen, and the permeability obviously increased. In order to find out the actual pressure-permeability law, further experiments were carried out with the specimen changed in every hydraulic pressure level. Figure 12 is permeability and velocity of different specimens with same particle size variation curves with hydraulic pressure. It can be seen from Figure 12 that permeability and velocity of variable specimen also increased with hydraulic pressure, which indicated that fine particles will be migrated and leak out from the specimen in each seepage experiments, and more fine particles will leak out resulting in bigger porosity with high hydraulic pressure.
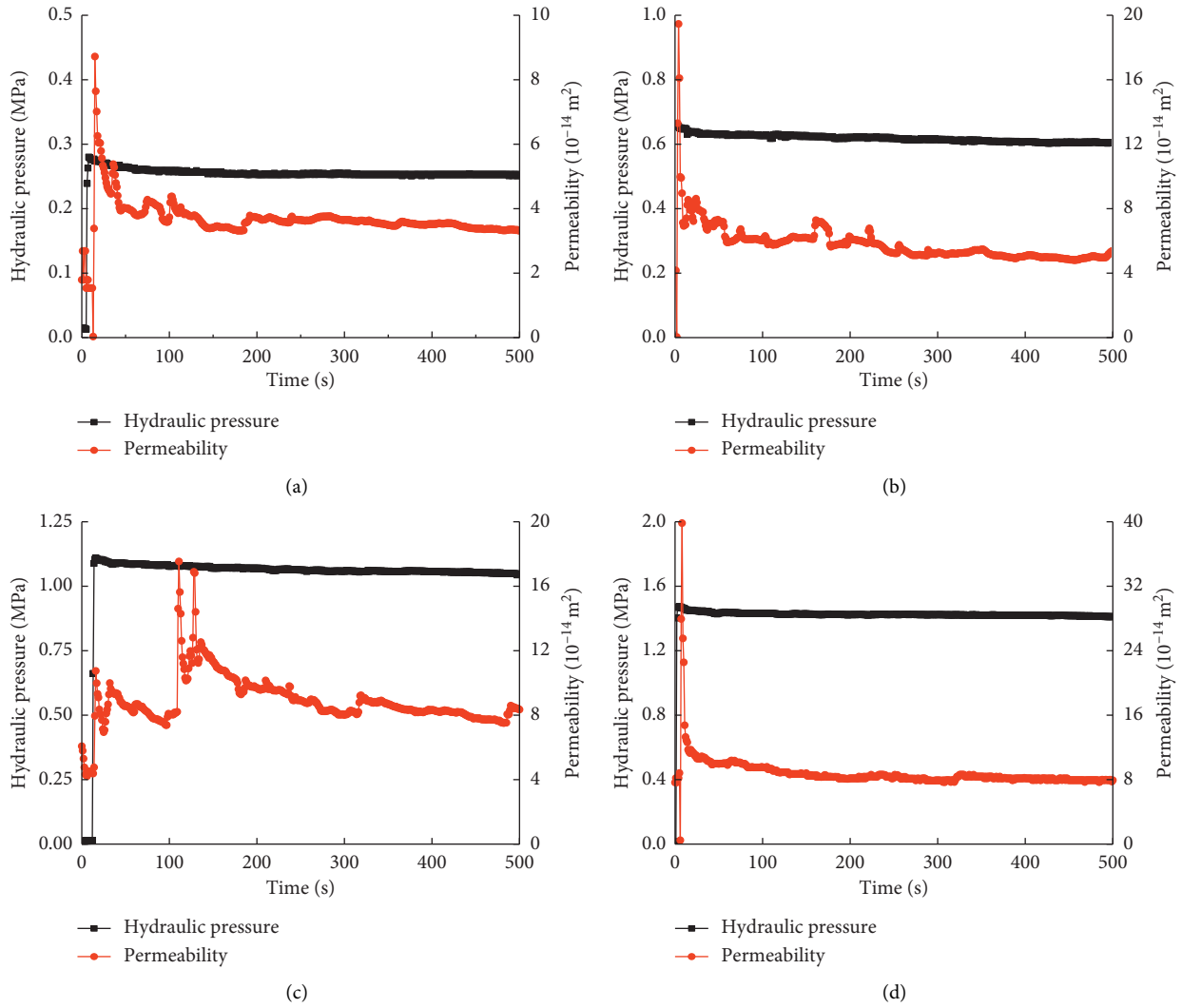
(a)

(b)

(c)

(d)

Figure 10: Hydraulic pressure and permeability variation curves of third group specimens with time. (a) 0.3 MPa. (b) 0.7 MPa. (c) 1.1 MPa. (d) 1.5 MPa.
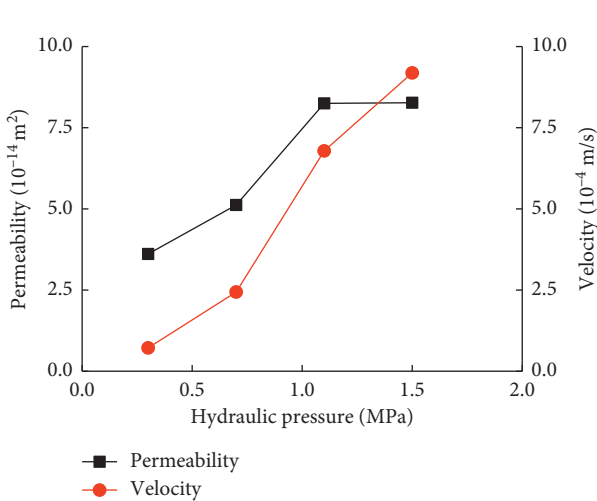

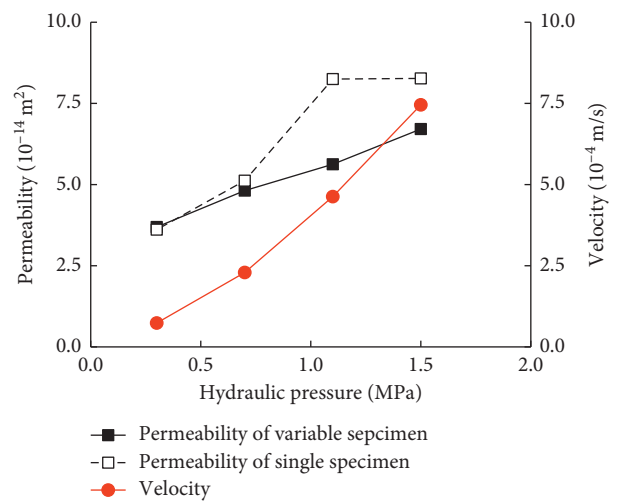Figure 11: Permeability and velocity variation curves with hydraulic pressure.

Figure 12: Permeability and velocity different specimens with same particle size variation curves with hydraulic pressure.

However, the permeability increase amplitude of variable specimen was less than that of single specimen. It indicated that the porosity of specimen will further increase with application of repeated hydraulic pressure.

4. Conclusion

A self-developed seepage test system is used to study the seepage property of crushed mudstone specimens in this paper. The following conclusions can be drawn from the experimental results:

(1) In the initial stage of seepage experiments of crushed rock mass, water hammer effect exists, and hydraulic pressure increases rapidly. After that, the seepage tends to be stable, and the hydraulic pressure and flow rate remain basically unchanged. In some stages of individual experiments, seepage mutation phenomena such as rapid decrease of hydraulic pressure and increase of flow rate will occur.

(2) The permeability of crushed mudstone is on the order of $10^{-14}\,\mathrm{m}^2 \sim 10^{-13}\,\mathrm{m}^2$. Under the condition of constant porosity and hydraulic pressure, fine particles expanding with water and less effective seepage pore in the small particle size range number result in the permeability of the specimen increasing with particle size range number.

(3) Under the condition of constant particle size and hydraulic pressure, permeability increases with porosity. In order to find out the criterion of permeability and porosity, the experimental results are fitted to three models developed by predecessors, and the fitting results show (4) is applicable to the experimental results in this paper.

(4) Permeability increases with hydraulic pressure whether one crushed mudstone specimen with progressive hydraulic pressure or different specimens with variable hydraulic pressure. More fine particles leak out from the specimen with repeated application of hydraulic pressure on one specimen, so the permeability of one specimen is bigger than that of different specimens under the condition of same hydraulic pressure.

Symbols

A_s: Cross-section area of permeameter, m^2
h: The height of the crushed rock specimen, m
i: The time series, 1
j: The crushed rock specimen number, 1
k: The permeability of crushed rock, m^2
k_0: The minimum permeability of second specimen group, m^2
M: The gushed water mass, kg
p: The hydraulic pressure, MPa
t: Time, s
V_b: Crushed rock volume, m^3
v: The flow velocity of the water, m/s
ρ: Water density, $\mathrm{kg/m}^3$

μ: The dynamic viscosity of water, Pa·s
φ: The porosity of crushed rock, 1
φ_0: The minimum porosity of second specimen group, 1.

Data Availability

The raw/processed data required to reproduce these findings cannot be shared at this time as the data also form part of an ongoing study.

Conflicts of Interest

The authors declare that they have no conflicts of interest to this work.

Acknowledgments

References

[1] T. H. Yang, P. Jia, W. H. Shi, P. T. Wang, H. L. Liu, and Q. L. Yu, "Seepage-stress coupled analysis on anisotropic characteristics of the fractured rock mass around roadway," *Tunnelling and Underground Space Technology*, vol. 43, no. 7, pp. 11–19, 2014.

[2] Z. Q. Yue and Q. Xu, "Fundamental drawbacks and disastrous consequences of current geotechnical safety design theories for slopes," *Chinese Journal of Geotechnical Engineering*, vol. 36, no. 9, pp. 1601–1606, 2014, in Chinese.

[3] D. Boldini and A. Graziani, "Remarks on axisymmetric modelling of deep tunnels in argillaceous formations II: fissured argillites," *Tunnelling and Underground Space Technology*, vol. 28, no. 3, pp. 80–89, 2012.

[4] N. Koronakis, P. Kontothanassis, N. Kazilis, and N. Gikas, "Stabilization measures for shallow tunnels with ongoing translational movements due to slope instability," *Tunnelling and Underground Space Technology*, vol. 19, no. 4-5, p. 495, 2004.

[5] M. G. Sweetenham, R. M. Maxwell, and P. M. Santi, "Assessing the timing and magnitude of precipitation-induced seepage into tunnels bored through fractured rock," *Tunnelling and Underground Space Technology*, vol. 65, pp. 62–75, 2017.

[6] L. C. Li, T. H. Yang, Z. Z. Liang, W. C. Zhu, and C. A. Tang, "Numerical investigation of groundwater outbursts near faults in underground coal mines," *International Journal of Coal Geology*, vol. 85, no. 3-4, pp. 276–288, 2011.

[7] T. H. Yang, J. Liu, W. C. Zhu, D. Elsworth, L. G. Tham, and C. A. Tang, "A coupled flow-stress-damage model for groundwater outbursts from an underlying aquifer into mining excavations," *International Journal of Rock Mechanics and Mining Sciences*, vol. 44, no. 1, pp. 87–97, 2007.

[8] W. Liu, X. Fei, and J. Fang, "Rules for confidence intervals of permeability coefficients for water flow in over-broken rock

mass," *International Journal of Mining Science and Technology*, vol. 22, no. 1, pp. 29–33, 2012.

[9] X. X. Miao, S. C. Li, and X. W. Huang, "Experimental study of seepage properties of non-darcy flow in granular gangues," *Journal of University of Mining and Technology*, vol. 16, no. 2, pp. 105–109, 2006, in Chinese.

[10] X.-x. Miao, S.-c. Li, and Z.-q. Chen, "Bifurcation and catastrophe of seepage flow system in broken rock," *Mining Science and Technology (China)*, vol. 19, no. 1, pp. 1–7, 2009, in Chinese.

[11] X. Miao, S. Li, Z. Chen, and W. Liu, "Experimental study of seepage properties of broken sandstone under different porosities," *Transport in Porous Media*, vol. 86, no. 3, pp. 805–814, 2011.

[12] H. Kong, Z. Chen, L. Wang, and H. Shen, "Experimental study on permeability of crushed gangues during compaction," *International Journal of Mineral Processing*, vol. 124, pp. 95–101, 2013.

[13] D. Ma, H. Y. Duan, J. F. Liu, X. B. Li, and Z. L. Zhou, "The role of gangue on the mitigation of mining-induced hazards and environmental pollution: an experimental investigation," *Science of The Total Environment*, vol. 664, pp. 636–448, 2019.

[14] D. Ma, X. X. Miao, G. H. Jiang, H. B. Bai, and Z. Q. Chen, "An experimental investigation of permeability measurement of water flow in crushed rocks," *Transport in Porous Media*, vol. 105, no. 3, pp. 571–595, 2014.

[15] S. J. Garner and R. J. Fannin, "Understanding internal erosion: a decade of research following a sinkhole event," *International Journal on Hydropower and Dams*, vol. 17, no. 3, pp. 93–98, 2010.

[16] D. Marot, F. Bendahmane, F. Rosquoet, and A. Alexis, "Internal flow effects on isotropic confined sand-clay mixtures," *Soil and Sediment Contamination: An International Journal*, vol. 18, no. 3, pp. 294–306, 2009.

[17] L. Ke and A. Takahashi, "Strength reduction of cohesionless soil due to internal erosion induced by one-dimensional upward seepage flow," *Soils and Foundations*, vol. 52, no. 4, pp. 698–711, 2012.

[18] R. Moffat, R. J. Fannin, and S. J. Garner, "Spatial and temporal progression of internal erosion in cohesionless soil," *Canadian Geotechnical Journal*, vol. 48, no. 3, pp. 399–412, 2011.

[19] G. Xie, Z. Yin, L. Wang, Z. Hu, and C. Zhu, "Effects of gas pressure on the failure characteristics of coal," *Rock Mechanics and Rock Engineering*, vol. 50, no. 7, pp. 1711–1723, 2017.

[20] Z. Q. Yin, Z. X. Hu, Z. D. Wei et al., "Assessment of blasting-induced ground vibration in an open-pit mine under different rock properties," *Advances in Civil Engineering*, vol. 2018, Article ID 4603687, 10 pages, 2018.

[21] Z. Yin, W. Chen, H. Hao et al., "Dynamic compressive test of gas-containing coal using a modified split hopkinson pressure bar system," *Rock Mechanics and Rock Engineering*, vol. 53, no. 2, pp. 1–15, 2019.

[22] A. Aydin, R. I. Borja, and P. Eichhubl, "Geological and mathematical framework for failure modes in granular rock," *Journal of Structural Geology*, vol. 28, no. 1, pp. 83–98, 2006.

[23] L. Z. Wang, Z. Q. Chen, and H. L. Kong, "Influences on penetration laws of broken mudstone with mass loss from talbol power exponents," *Electronic Journal of Geotechnical Engineering*, vol. 19, pp. 3681–3692, 2014.

[24] D. Ma, X. X. Miao, H. B. Bai et al., "Impact of particle transfer on flow properties of crushed mudstones," *Environmental Earth Sciences*, vol. 75, no. 7, p. 593, 2016.

[25] J. Wu, G. Han, M. Feng et al., "Mass-loss effects on the flow behavior in broken argillaceous red sandstone with different particle-size distributions," *Comptes Rendus Mécanique*, vol. 347, no. 6, pp. 504–523, 2019.

[26] S. N. Rogak and R. C. Flagan, "Stokes drag on self-similar clusters of spheres," *Journal of Colloid and Interface Science*, vol. 134, no. 1, pp. 206–218, 1990.

[27] S. Veerapaneni and M. R. Wiesner, "Hydrodynamics of fractal aggregates with radially varying permeability," *Journal of Colloid and Interface Science*, vol. 177, no. 1, pp. 45–57, 1996.

[28] D. J. Lee, G. W. Chen, Y. C. Liao, and C. C. Hsieh, "On the free-settling test for estimating activated sludge floc density," *Water Research*, vol. 30, no. 3, pp. 541–550, 1996.

[29] D. Ma, M. Rezania, H.-S. Yu, and H.-B. Bai, "Variations of hydraulic properties of granular sandstones during water inrush: effect of small particle migration," *Engineering Geology*, vol. 217, pp. 61–70, 2017.